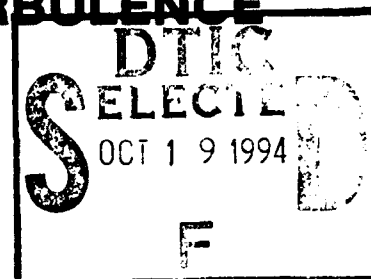


PREPRINTS FOR THE

THIRTEENTH SYMPOSIUM ON TURBULENCE

September 21-23, 1992



DEPARTMENT OF CHEMICAL ENGINEERING
CONTINUING EDUCATION
UNIVERSITY OF MISSOURI-ROLLA

Directed by

X B Reed, Jr.
University of Missouri-Rolla

Honorary Co-Chairmen

Gary K. Patterson
University of Missouri-Rolla

Jacques L. Zakin
The Ohio State University

This document has been approved
for public release and sale; its
distribution is unlimited.

5718
94-32577



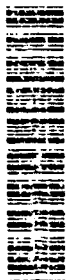
UMR

MISSOURI'S TECHNICAL UNIVERSITY

THE UNIVERSITY OF MISSOURI-ROLLA

DTIC QUALITY INSPECTED 8

AD-A285 661



REPORT DOCUMENTATION PAGE

1a. REPORT SECURITY CLASSIFICATION Unclassified			1b. RESTRICTIVE MARKINGS None	
SECURITY CLASSIFICATION AUTHORITY Contract was not classified- NoDD254			3. DISTRIBUTION/AVAILABILITY OF REPORT None	
2b. DECLASSIFICATION/DOWNGRADING SCHEDULE Not applicable as above				
4. PERFORMING ORGANIZATION REPORT NUMBER(S) None			5. MONITORING ORGANIZATION REPORT NUMBER(S) None	
6a. NAME OF PERFORMING ORGANIZATION The Curators of the University of Missouri-Rolla		6b. OFFICE SYMBOL (If applicable) 4B849	7a. NAME OF MONITORING ORGANIZATION Office of the Naval Research	
6c. ADDRESS (City, State, and ZIP Code) G-2 Parker Hall Rolla, MO 65401			7b. ADDRESS (City, State, and ZIP Code) Chicago Regional Office Federal Building, Room 208 536 S. Clark St. Chicago, IL 60605-1588	
8a. NAME OF FUNDING/SPONSORING ORGANIZATION Department of the Navy		8b. OFFICE SYMBOL (If applicable) AGO Code:N62880	9. PROCUREMENT INSTRUMENT IDENTIFICATION NUMBER N00014-92-J-1770	
8c. ADDRESS (City, State, and ZIP Code) Office of the Chief of Naval Research 800 North Quincy Street, Code 1513:GBP Arlington, Virginia 22217-5000			10. SOURCE OF FUNDING NUMBERS	
			PROGRAM ELEMENT NO. N/A	PROJECT NO. R&T 4322807-04
			TASK NO. S.O. Code:1132F	WORK UNIT ACCESSION NO. N00179
11. TITLE (Include Security Classification) Thirteenth Symposium on Turbulence				
12. PERSONAL AUTHOR(S) Proceedings were edited by Dr. X.B. Reed, Jr. and Co-editors Dr. Gary Patterson and Dr. J.L. Zakin				
13a. TYPE OF REPORT Summary		13b. TIME COVERED FROM 92/05/01 TO 93/04/30		14. DATE OF REPORT (Year, Month, Day) 92/09/21-23
15. PAGE COUNT 175±				
16. SUPPLEMENTARY NOTATION Report of Proceedings for the Thirteenth Symposium on Turbulence				
17. COSATI CODES			18. SUBJECT TERMS (Continue on reverse if necessary and identify by block number)	
FIELD	GROUP	SUB-GROUP	Turbulence, fine scale, large scale, coherent structure	
			statistics, closures, dispersed phase, Lagrangian, Eulerian,	
NOT AVAILABLE			vortex dynamics, helicity, dissipation rate, intermittancy,	
19. ABSTRACT (Continue on reverse if necessary and identify by block number)				
<p>Fundamentals of turbulence, both experimental and theoretical; turbulent instrumentation and future experimental techniques; full field measurements, multipoint and multitime image velocity and concentration measurements; scalar mixing, including turbulent chemical reactions; experimental techniques in and fluid physics of high speed compressible or reacting flows undergoing significant changes of indices of refraction.</p> <p>Possible Topics</p> <p>Coherent structures and their relation to smaller scales in turbulent shear flows; implications of chaos for turbulence and transition, chaotic behavior in experimental fluid mechanics; homogeneous turbulence, including closures and statistical properties; turbulence in compressible fluids; fine scale structure at high turbulence Reynolds numbers; direct numerical simulation, subgrid scale, and other turbulent transport,</p>				
20. DISTRIBUTION/AVAILABILITY OF ABSTRACT <input type="checkbox"/> UNCLASSIFIED/UNLIMITED <input type="checkbox"/> SAME AS RPT. <input checked="" type="checkbox"/> OTIC USERS			21. ABSTRACT SECURITY CLASSIFICATION Unclassified	
22a. NAME OF RESPONSIBLE INDIVIDUAL David Wyner, ONR Resident Representative			22b. TELEPHONE (Include Area Code) (312) 353-6065	22c. OFFICE SYMBOL ONR-chi/1432

18. Subject Terms Continued:

energy spectrum, isotropy, anisotropy, homogeneous, chemical reactions, drag reduction, flow modification, riblets, compliant, simulation, stochastic estimation, laser Doppler and hot wire anemometry, autocorrelation, particle image velocimetry, electrochemical probes, multiprobes.

19. Abstract continued:

including its effect on chemical reactions and its interactions with combustion; high-speed wall boundary and free shear layers; Lagrangian turbulence; turbulent flows containing particles, bubbles, and drops, turbulence in non-Newtonian liquids; buoyancy effects in turbulent flows; laser-Doppler, hot wire, and hot film anemometry; novel measurement techniques; flow visualization, holography, image analysis; boundary layer modification and control; interactions of turbulence with wave structures; wind-generated waves and other oceanographic applications; atmospheric boundary layers and turbulence; implications of turbulence in the environment (including pollution, estuarial and tidal channel flows, plumes, cloud physics); industrial, aeronautical, and astronautical applications.

Accession For	
NTIS CRA&I	<input checked="" type="checkbox"/>
DTIC TAB	<input type="checkbox"/>
Unannounced	<input type="checkbox"/>
Justification	
By	
Distribution /	
Availability Codes	
Dist	Avail and/or Special
A-1	

Preprint Volume of the
Thirteenth Symposium on Turbulence

September 21-23, 1992

Editor: X B Reed, Jr.

Co-editor: G. K. Patterson
J. L. Zakin

Assistant Editors and Steering Committee:

Dr. R. J. Adrian
Professor of Theoretical and
Applied Mechanics
University of Illinois

Dr. R. S. Brodkey
Professor of Chemical Engineering
Ohio State University

Dr. J. R. Herring
National Center for Atmospheric
Research
Boulder, CO

Dr. J. C. Hill
Professor of Chemical Engineering
Iowa State University

Dr. Fazle Hussain
Professor of Mechanical Engineering
University of Houston

Dr. G. B. Jones
Professor and Chairman of Nuclear
Engineering
University of Illinois

Dr. O. P. Manley
Department of Energy
Germantown, MD

Dr. J. McMichael
Air Force Office of Scientific
Research
Washington, D.C.

Dr. R. B. Miles
Professor of Mechanical and
Aerospace Engineering
Princeton University

Dr. G. K. Patterson, Honorary
Co-Chairman
Associate Dean of Engineering
University of Missouri-Rolla

Dr. L. P. Purtell
Office of Naval Research
Arlington, VA

Dr. X B Reed, Jr.
Professor of Chemical Engineering
University of Missouri-Rolla

Dr. M. M. Reischman
Associate Dean of Engineering
Pennsylvania State University

Dr. A. J. Smits
Professor of Mechanical and
Aerospace Engineering
Princeton University

Dr. C. G. Speziale
ICASE
NASA Langley Research Center

Dr. D. E. Stock
Professor of Mechanical Engineering
Washington State University

Dr. W. G. Tiederman
Professor of Mechanical Engineering
Purdue University

Dr. J. M. Wallace
Professor of Mechanical Engineering
University of Maryland

Dr. J. L. Zakin, Honorary
Co-Chairman
Professor and Chairman of Chemical
Engineering
Ohio State University

Chemical Engineering Department

Continuing Education
University of Missouri-Rolla

This work is supported by Department of Navy Grant N00014-92-J-1770 issued by the Office of Naval Research. The United States Government has a royalty-free license throughout the world in all copyrightable material contained herein.

Thirteenth Symposium on Turbulence

September 21-23, 1992
Rolla, Missouri USA

Table of Contents

Paper No.

Invited Lectures

"Statistics of the Small Scales", Robert H. Kraichnan, Santa Fe, NM	IL1
"Experimental Studies of the Fine Scale Structure of Mixing in Turbulent Flows", Werner J.A. Dahm, University of Michigan	IL2
"Investigation of Closure Models for Turbulent Reacting Flows Using Direct Numerical Simulations", James J. Riley, University of Washington . .	IL3
"Particle Transport in Turbulent Dispersed Flows", Thomas J. Hanratty, University of Illinois	IL4
"Coherent Structure in Turbulent Jets", Reda Mankbadi, NASA-Lewis Research Center	IL5
"New Approaches to Vortex Dynamics: Core Dynamics, Helicity, Helical Waves, and Interaction With Fine Scale Turbulence", Fazole Hussain, University of Houston	IL6

Fine Scale Structure of Turbulence

Chairmen: J.R. Herring, L.P. Purtell, O.P. Manley, and F. Hussain

"Evidence of Local-Axisymmetry in the Small Scales of a Turbulent Planar Jet", Hussein J. Hussein, Vanderbilt University	A1
"Response of Fine-Scale Turbulence to External Pressure Fields", Hussein J. Hussein and Michael A. MacMillan, Vanderbilt University	A2
"Measured and Modelled Component (ϵ_{11}) of the Dissipation Rate Tensor", D. Aronsson and L. Löfdahl, Chalmers University of Technology	A3
"An Empirical Evaluation of Universal Multi-fractal Indices and Order of Divergence of Moments for Atmospheric Wind Turbulence", François Schmitt and Pans Schertzer, Université de Paris	A4
"Multi-fractal Aspects of the Intermittency Corrections to the Spectrum of Temperature Fluctuations in Isotropic Turbulence", Bhimsen Shivamoggi, University of Central Florida	A5
"The Renormalization Group Theory of Turbulence and Waves on the β -Plane", B. Galperin, University of South Florida; S. Sukoriansky, Ben Gurion University of the Negev; and I. Staroselsky, Princeton University	A6

Passive Additive Turbulent Fields

Chairmen: J.C. Hill, J.R. Herring, and I B Reed, Jr.

"Isotropy and Anisotropy in Turbulent Scalar Transport", Robert Sanderson and J.C. Hill, Iowa State University	A7
---	----

- "Differential Diffusion of Passive Scalars in Stationary Isotropic Turbulence", P.K. Yeung, Georgia Institute of Technology; and S.B. Pope, Cornell University A8
- "Linear Eddy Simulations of Mixing in a Homogeneous Turbulent Flow", Todd C. Gansauge and Patrick A. McMurtry, University of Utah; Alan R. Kerstein, Sandia National Laboratories A9
- "Diffusive Mixing in Turbulent Jets as Revealed by a pH Indicator", A.F. Corriveau and W.D. Baines, University of Toronto A10
- "A Novel Finite Element Approach to CFD", William D. Webster and K.J. Berry, GMI Engineering and Management Institute A11

Turbulent Chemical Reactions

Chairmen: R.S. Brodkey, J.C. Hill, and G.K. Patterson

- "Simulations of Chemical Selectivity in Turbulent Flows", Mitali Chakrabarti and J.C. Hill, Iowa State University A12
- "Study of Reacting Flows in Stationary Isotropic Turbulence Using One-Point PDF and Two-Point Correlation Functions", Kuochen Tsai and Edward E. O'Brien, State University of New York at Stony Brook A13
- "A Linear Eddy Subgrid Model of Turbulent Combustion" Patrick A. McMurtry, University of Utah; Alan Kerstein, Sandia National Laboratories; and Suresh Menon, Georgia Institute of Technology A14
- "The Effect of Chemical Reactions on Turbulent Diffusivities", H.L. Toor, Carnegie-Mellon University A15
- "Chemically Reacting Turbulent Mixing Layers Without Heat Release", Robert A. Gore, Michigan Technological University and Francis H. Harlow, Los Alamos National Laboratory A16
- "O'Brien's Statistical Independence Hypothesis", W. Zheng and X B Reed, Jr., University of Missouri-Rolla A17

Drag Reduction and Flow Modification

Chairman: J.L. Zakin, W.G. Tiederman, and M.M. Reischman

- "Turbulence and Polymer Solution Structure in Viscoelastic Turbulent Flow", B. Gampert and A. Rensch, Universität Essen A18
- "Turbulence Measurements in a Drag Reducting Surfactant System", Zdanka Chara, Jiri Myska, and Jacques Zakin, Ohio State University A19
- "Heterogeneous Flow Drag Reduction in a Turbulent Boundary Layer", J.J. Manzano-Ruiz, Universidad Simon Bolivar A20
- "Investigation of the Interaction of a Compliant Surface with a Turbulent Boundary Layer", W.H. Schwarz and T. Lee Johns Hopkins University A21
- "Modelling the Time Dependent Flow Over V - and U - Shaped Riblets", S. Tullis and A. Pollard, Queen's University at Kingston A22
- "An Experimental Study of the Flows Associated with Circular Cavities", E. Savory and N. Toy, University of Surrey A23

Modelling, Direct Numerical, and Large Eddy Simulation

Chairmen: C.G. Speziale, G.K. Patterson, and J.C. Hill

- "Towards a Direct Numerical Simulation Procedure for Inhomogeneous Turbulence in High-Speed Flows", **Foluso Ladeinde**, SUNY at Stony Brook A24
- "A Preliminary Study of Two-Dimensional Turbulent Channel Flow Utilizing Parallel Computation", **M.S. Pervaiz**, **P.R. Smith**, and **G.A. Reynolds**, New Mexico State University A25
- "Questions to Modellers of Turbulent Flows", **D.P. vd Merwe**, Rand Afrikaans University A26
- "Prediction of Turbulent Flow Through Curved Tubes of Large Radius of Curvature", **S. Jayanti** and **G.P. Hewitt**, Imperial College of London; **N.S. Wilkes**, AEA Technology A27
- "An Improved $k-\epsilon$ Model for Prediction of Adverse Pressure Gradient Turbulent Flows", **G. Chukkapalli** and **Ö.F. Turan**, McMaster University A28
- "Two Variations of the $k-\epsilon$ Model and Their Application to Wall-Bounded Flows", **H.A. Becker**, **E.W. Grandmaison**, **H. Ozem**, **A. Pollard**, **A. Sobiesiak**, and **C.P. Thurgood**, Queen's University of Kingston A29
- "Necessity of Curvature Corrections to Reynolds Stress Model in Computation of Turbulent Recirculating Flows", **Myung Kyoong Chung**, Korea Advanced Institute of Science and Technology; and **Sang Keun Dong**, Korea Institute of Energy Research A30
- "Accuracy of Low Order Turbulence Models in Predicting Elliptical Flows", **A. Aroussi**, Nottingham University A31
- "Implications of Lagrangian Transport Analysis for Large Eddy Simulations", **Amy L. Rovelstad**, Naval Research Laboratory; **Peter S. Bernard**, University of Maryland; **Robert A. Handler**, Naval Research Laboratory A32
- "Large Eddy Simulation of Flow in a Square Duct", **E. Balaras** and **C. Benocci**, von Karman Institute for Fluid Dynamics A33
- "Stochastic Estimation of Near Wall Closure for Large Eddy Simulation", **Ted G. Bagwell** and **Ronald J. Adrian**, University of Illinois at Urbana-Champaign; **Robert D. Moser** and **John Kim**, NASA Ames Research Center A34

Coherent Structures

Chairmen: **Fazle Hussain**, **R.S. Brodkey**, **James McMichael**, and **L.P. Purtell**

- "Certain Pattern of Information Transmission Effects in Turbulent Pipe Flow", **Włodzimierz Kozłowski**, Institute of Nuclear Chemistry and Technology, Warsaw A35
- "Correlation Between Reattachment Length Downstream a Backstep and Structure of the Incident Flow", **A. Aroussi** and **A. Senior**, Nottingham University A36
- "The Formation of Coherent Turbulent Vortex Rings in Periodic Flow", **H. Büchner**, **Chr. Hirsch**, and **W. Leuckel**, University of Karlsruhe A37
- "Quasi-Two-Dimensional Turbulence and Stochastic Traveling Waves in Stratosphere and Laboratory", **H. Branover**, **A. Bershadskii**, **A. Eidelman**, and **M. Nagorny**, Ben Gurion University of the Negev A38

"Vorticity and Mixing Dynamics in Axially Perturbed Coflowing Jets",
C. Cuerno and A. Viedma, Universidad Politécnica de Madrid A39

"Longitudinal Vortices Imbedded in the Turbulent Channel Flow", Susanne Lau and
Venkatesa I. Vasanta Ram, Ruhr-Universität Bochum A40

"Measurements of Turbulent Length Scales Using LDV", R.D. Gould and L.H.
Benedict, North Carolina State University; A.S. Nejad and S.A. Ahmed, Wright
Laboratory A41

Compressible Flows, Shock/Turbulence Interactions

Chairmen: A.J. Smits, R.B. Miles, and J.L. Zakin

"Prediction of the Turbulent Compressible Flow Through Labyrinth Seals
for High Speed Turbomachinery", Hassan A. El-Gamal, Alexandria
University B1

"The Formation of Streamwise Vortices around the Circumference of
Underexpanded Supersonic Axisymmetric Jets", S.A. Arnette, M. Samimy,
and G.S. Elliott, Ohio State University B2

"Measurements of Mean and Fluctuating Heat Transfer in a Shock Wave
Turbulent Boundary Layer Interaction", T. Evans and A.J. Smits, Princeton
University B3

"Preliminary Results from a Tangentially Injected Shock Wave/Turbulent
Boundary Layer", J.F. Donovan, McDonnell Douglas Research Laboratories B4

"Large-Scale Structures Dynamics in the Simulation of Supersonic Mixing
Layer", Choong-Kun Oh and Eric Loth, University of Illinois at
Urbana-Champaign; Rainald Löhner, George Washington University B5

"Closure Approximations for the Reynolds Stress Transport Equation for
Variable-Density Turbulence", Lance R. Collins, Pennsylvania State
University B6

Complex Turbulent Flows

Chairmen: L.P. Purtell, J. McMichael, M.M. Reischman, and J.L. Zakin

"Turbulent Flow of an Annulus With Inner Rotating Cylinder and a Dead
End Wall", Parviz Merati and Joseph C. Parker, Western Michigan
University; William V. Adams, Durametallic Corporation B7

"Effects of Inlet Configuration and Boundary Layer Control on Flow
Through an Offset Duct", J.A. Mathis and Tong Wu, Wichita State
University B8

"Turbulence in a Two-Dimensional Wall-Jet: Experiments and Modeling",
H. Abrahamsson, B. Johansson, and L. Löfdahl, Chalmers University of
Technology; H.I. Andersson, The Norwegian Institute of Technology B9

"The Development of the Interface Region Between Twin Circular Jets
and a Normal Crossflow", N. Toy, E. Savory, and S. McCusker, University
of Surrey; P.J. Disimile, University of Cincinnati B10

"Mixing Between a Sharp-Edged Rectangular Jet and a Transverse Cross
Flow", A.J. Humber, E.W. Grandmaison, and A. Pollard, Queen's
University at Kingston B11

"LDA Measurements of the Turbulent Flow in Gas Cyclones", T.L. Lien
and H.E.A. van den Akker, Delft University of Technology B12

"Two-component Velocity Measurements in Top Submerged Gas Injection Systems", D.D. Atapattu and N.B. Gray, The University of Melbourne; Y.S. Moris, Swinburne University of Technology B13

"Hot-wire Measurements of Turbulent Heat Fluxes Between Bank Tubes", Y.S. Moris and W. Yang, Swinburne Institute of Technology B14

"Turbulent Energy Dissipation in Flow Through Porous Media", Charles D. Morris, University of Missouri-Rolla B15

"Wind Induced Water Penetration of Buildings", A. Aroussi and A. Senior, Nottingham University B16

"Flow Regimes in Aluminum Reduction Cells", E.E. Khalil and M.F. El-Demerdash, Cairo University B17

Turbulence in Two-phase Flows

Chairmen: O.P. Manley, D.E. Stock, G.B. Jones, I B Reed, Jr., and R.J. Adrian

"Concentration Structure of Granular Shear Flows", Michael M. Cui and Ronald J. Adrian, University of Illinois at Urbana-Champaign B18

"Experiments on Bubble/Eddy Interactions", Michael Cebzynski and Eric Loth, University of Illinois at Urbana-Champaign B19

"Visualization of Turbulence Modulation Due to Large Particles", Frans Davis and Eric Loth, University of Illinois at Urbana-Champaign B20

"Numerical Study of Interaction Between Turbulence Modulation and Bubble Dispersion", Mohammad Taeibi-Rahni and Eric Loth, University of Illinois at Urbana-Champaign; Gretar Tryggvason, University of Michigan . . . B21

"A Spectral Model for the Autocorrelation of Density Fluctuations in a Turbulent Particle-Fluid System", Shivshankar Sundaram and Lance R. Collins, Pennsylvania State University B22

"An Analysis of Lift Forces on Aerosols in a Wall-Bounded Turbulent Shear Flow", John B. McLaughlin, Clarkson University B23

"Vector Eigenfunction Expansions in the Solution of the Linearized Navier-Stokes Equation in Spherical Geometries", I B Reed, Jr., University of Missouri-Rolla B24

"Methods to Solve Forced Convection Interphase Mass Transfer Problems for Droplets in General Stokes Flows", L. Kleinman and I B Reed, Jr., University of Missouri-Rolla B25

Experimental Methods

Chairmen: W.G. Tiederman, R.J. Adrian, A.J. Smits, and R.B. Miles

"Evaluation of Ejection Detection Schemes in Turbulent Wall Flows", Renard G. Tubergen and William G. Tiederman, Purdue University B26

"Algorithms for Fully Automatic Three-Dimensional Particle Image Velocimetry", Nizar Trigui, Yann Guezennec, and Robert Brodkey, Ohio State University; Chris Kent, Ford Motor Company B27

"Full Field Velocity Measurements of a Radiant Heat Flux Driven Thermocapillary Flow", Mark P. Wernet and A. Pline, NASA-Lewis Research Center B28

"Spatial Resolution of Wall-Transfer Probes", B. Py, Institut Universitaire de Technologie B29

"How to Estimate Zero Wavenumber Turbulence Energy", R.E. Kronauer, Harvard University; P.G. Hollis and K.J. Bullock, University of Queensland; J.C.S. Lai, Australian Defence Force Academy B30

"Relation Between Spectra of Hot Wire Anemometer Signals and Velocity Components in Highly Turbulent Flows", S. Ramamoorthy, P.K. Rajan, and S. Munukutla, Tennessee Technology University B31

"Acoustic Velocity Profiler for Measurements in Turbulent Flow", U. Lemmin and T. Rolland, Ecole Polytechnique Fédérale de Lausanne; R. Lhermitte, University of Miami B32

"Liquid Backmixing in Bubble Columns via Computer Automated Particle Tracking (CARPT)", Y.B. Yang, N. Devanathan, and M.P. Duduković, Washington University B33

"The Influence of Instantaneous Velocity Gradients on Turbulence Properties Measured with Multi-Sensor Hot-Wire Probes", Seong Ryong Park and James M. Wallace, University of Maryland B34

Wall, Channel, and Duct Flows

Chairmen: R.J. Adrian, J.M. Wallace, and A.J. Smits

"Turbulence Characteristics of Two-Dimensional, Incompressible Entry Flow", Jack W. Backus and Merle C. Potter, Michigan State University; Bashar S. AbdulNour, University of Wyoming B35

"Two Half-Power Regions in Turbulent Decreasing Adverse Pressure Gradient Flows", G.A. Kopp and Ö.F. Turan, McMaster University B36

"Vortical Motion Contributions to Stress Transport in Turbulent Boundary Layers", J.C. Klewicki and J.A. Murray, University of Utah; R.E. Falco, Michigan State University B37

"The Zero-Pressure Gradient Turbulent Boundary Layer Revisited", William K. George, Pierre Knecht, and Daniel R. Bower, State University of New York at Buffalo B38

"Coherent Structures in Smooth and Rough Wall Turbulent Boundary Layer Flows", Atul Kohli and David G. Bogard, University of Texas at Austin B39

"The Development of Intermittency in Turbulent Channel Flow with Decreasing Reynolds Number", Kile S. Watson and Kenneth S. Ball, University of Texas at Austin, Robert A. Handler, Naval Research Laboratory B40

"Turbulence-driven Secondary Flow in a Duct of Square Cross-Section", G. McGrath, D.G. Petty, and R. Cheesewright, Queen Mary and Westfield College B41

STATISTICS OF THE SMALL SCALES

Robert H. Kraichnan

369 Montezuma 108
Santa Fe, New Mexico 87501-2626, U. S. A.

Abstract

Some salient empirical features of the small-scale structure of isotropic incompressible turbulence at various Reynolds numbers are reviewed. Attention is focussed on the energy spectrum and the probability distributions of velocity and space derivatives of velocity. A progress report is given for a current effort to approximate small-scale statistics from the Navier-Stokes (NS) equation by the systematic use of dynamic stochastic models in physical space.

The small scales of near-isotropic turbulence present a variety of intriguing features at modest as well as large values of Taylor microscale Reynolds number \mathcal{R}_λ . For the entire range $\mathcal{R}_\lambda \geq 15$, the wavenumber spectrum of kinetic energy $E(k)$ falls off exponentially with k for k larger than values where most of the dissipation occurs. For this range of \mathcal{R}_λ , the probability distribution function (pdf) of a vorticity component ω_1 deviates markedly from Gaussian. In particular, the flatness factor $\langle \omega_1^4 \rangle / \langle \omega_1^2 \rangle^2$ exceeds the Gaussian value 3 and the pdf has wide skirts at large $|\omega_1|$. These deviations from Gaussian form increase with \mathcal{R}_λ . It is unclear from existing data whether the deviations saturate or increase without limit as $\mathcal{R}_\lambda \rightarrow \infty$. Other statistics, including the pdf of pressure fluctuations, also deviate markedly from values for a Gaussian velocity field.

Kolmogorov's 1941 theory of the small scales (K41), together with modifications suggested by Kolmogorov and others starting in 1962, has provided the language and mind-set that underly most efforts to classify and understand empirical data and to construct models of the small scales. Surprisingly, it is difficult, even fifty years later, to say how correct are his ideas. The most celebrated prediction of K41 is the $E(k) \propto k^{-5/3}$ inertial-range spectrum. This spectrum, or something close to it, seems definitely to be supported by a large body of experimental and simulation data. But the cascade ideas behind the spectrum are less clearly supported. In particular, the existence of well-defined ropelike structures with large ratio of length to diameter and sheetlike structures with large ratio of extent to thickness implies statistical dependence that extends over a considerable

range of scales. If these ratios increase without limit as $\mathcal{R}_\lambda \rightarrow \infty$, that would be inconsistent with the concept of information-destroying cascade that underlies both K41 and the later corrections to K41.

The dissipation of turbulent kinetic energy by viscosity is notably intermittent at modest as well as large \mathcal{R}_λ . But there is a difference in character as well as magnitude of the intermittency at low versus high \mathcal{R}_λ . At large \mathcal{R}_λ there are strong hot spots that dominate the higher moments of the dissipation fluctuation while occupying only a small fraction of the flow volume. However the volume averaged dissipation seems, even at large \mathcal{R}_λ , to be supported mostly by the regions between the hot spots where the velocity field is not too far from Gaussian. At low \mathcal{R}_λ , the intensity of dissipation varies gently on energy-range spacial scales. The exponential shape of the spectrum at large k , together with this gentle variation, results in strong spacial intermittency of the velocity field if the latter is passed through a high-pass filter in k space. This is demonstrated by recent simulation.

A large number of models of the small scales have been offered in the past few decades that involve eddy-mitosis scenarios and fractal or multifractal statistics. These models become ever more elaborate, but typically have little or no contact with the NS equation. Their relation to empirical data is hard to weigh because the models typically offer only inertial-range scaling. It is difficult to quantify the dissipation-range corrections and other corrections that must be applied to finite- \mathcal{R}_λ data in order to make meaningful comparisons.

Most attempts to obtain turbulence statistics by actual analysis of the NS equation have been based on renormalized perturbative schemes of one kind or another. A fundamental difficulty here is that the radius of convergence in \mathcal{R}_λ probably is zero so that the resummations and truncations that characterize perturbation-theoretic approximations are completely uncontrolled. Model dynamical systems are a valuable device in this situation. Here the statistics of a tractable dynamical system are followed exactly, and this assures certain basic consistency properties. Inspection of the model system can give a feel for what NS physics is retained in the model and what is lost or distorted.

A central role is played by the direct-interaction approximation (DIA). This approximation is, at the same time, a truncation of renormalized perturbation theory and the exact representation of a model system. For homogeneous turbulence, the latter can be obtained by putting stochastic phase factors in all the interaction coefficients of triads of wave-vector modes. Thereby the model keeps the correct strength of each triad interaction and the detailed energy conservation, but it totally scrambles the relative phases of distinct interactions. The spacial structures characteristic of the small scales of turbulence clearly do not survive in this model. Surprisingly, the model nevertheless does a good job (without adjustable parameters) of reproducing the spectrum of isotropic turbulence at all wavenumbers up through those that carry most of the dissipation, and at \mathcal{R}_λ values up to 200. It also predicts an exponential fall of $E(k)$ in the far dissipation range, in accord with data.

At large enough \mathcal{R}_λ , the DIA is invalidated because it does not portray correctly the sweeping of small scales through space by the energy-range excitation. A modification, based on Lagrangian statistical functions, cures this problem and gives good absolute agreement (again using no adjustable constants) with the inertial- and

dissipation-range spectrum at $Re_\lambda = 3000$. Like the original DIA, this approximation cannot portray the spacial structures that characterize the small scales of real turbulence.

The implications of the success of low-order closure approximations like DIA and its Lagrangian counterpart in predicting the energy spectrum are not fully clear. One strong possibility is that the structures so important in shaping the higher statistics of the small scales are, in effect, just ornaments to the basic energy transfer process. There is evidence that the latter involves principally regions of the flow whose statistics are not far from Gaussian. In any event, approximations of the DIA type totally fail to predict intermittency of NS turbulence.

In the past several years, an attempt has been made to construct model dynamics in physical space in order to capture the highly non-Gaussian character of the pdf's of vorticity and other velocity derivatives. A brief progress report is given in this talk. The basic device is to approximate actual turbulent fields by nonlinear transformations, or mappings, of fields (called *reference fields*) with known statistics. The latter have been Gaussian fields in the work to date. The mapping transformations that have been used are locally-determined changes of field amplitude and distortions of the space in which the Gaussian reference field lives. If the mapping functions are known at a given time, the rate of change of one-point pdf's can be found exactly from the Gaussian statistics of the reference field. The mapping functions can then be changed self-consistently with time in order that the model fields have statistics that reproduce the evolution of chosen one-point pdf's under the dynamical equations. The method is wholly non-perturbative. This mapping approach has been spectacularly successful, both qualitatively and quantitatively, in predicting the highly non-Gaussian statistics of evolving Burgers turbulence. Applications to NS dynamics are currently under development. The mapping representation of the pressure term in the NS equation is of crucial interest.

An excellent reference for the current state of knowledge of the statistics of small scales and the progress of active research trends is the Kolmogorov anniversary number of the Proceedings of the Royal Society [Proc. Roy. Soc. London A **434**, 1-240 (1991)].

EXPERIMENTAL STUDIES OF THE FINE SCALE STRUCTURE OF MIXING IN TURBULENT FLOWS

WERNER J.A. DAHM

Gas Dynamics Laboratories
Department of Aerospace Engineering
The University of Michigan
Ann Arbor, MI 48109-2140 USA

Abstract

Results are presented from two experimental techniques allowing direct laboratory measurement of the four-dimensional spatio-temporal structure and dynamics of the dissipative scales in turbulent flows, via gigabyte-sized data spaces containing a level of resolution and detail comparable to direct numerical simulations. The first of these deals with fully-resolved measurements of the structure and topology of the scalar energy dissipation rate field associated with large Schmidt number mixing in turbulent flows. The second allows the fine structure and dynamics of the underlying velocity gradient field to be extracted from such measurements, allowing direct experimental studies of the vector vorticity and tensor strain rate fields on the inner scales of turbulent flows.

1. Introduction

The study of turbulent flows has, over the past decade, undergone such a dramatic change as to fairly qualify this as a revolution. In this newest phase of turbulence research, highly detailed four-dimensional spatio-temporal information about the structure and dynamics of turbulent flows, of a type that would previously have been inconceivable, has become almost routinely available. The earliest source of this type of information, and still by far the best known, is direct numerical simulation (DNS) of the full Navier-Stokes equations. Generally less well known are more recent advances in experimental techniques for whole field measurements in turbulent flows, which are beginning to allow direct experimental studies of the structure and dynamics of velocity and scalar fields in turbulence at a level of resolution and detail entirely comparable to DNS and at parameter values inaccessible to such numerical simulations. These techniques are beginning to demonstrate a potential that would have been unthinkable as recently as five years ago. They are proving to be the next stage in this revolutionary progress in providing the researcher detailed access to turbulence structure and dynamics, permitting studies of real flows in nonperiodic domains, at conditions beyond the reach of DNS.

Reviews of some relevant techniques are given by Adrian (1986, 1991), Merzkirch (1987), and Lauterborn & Vogel (1984). This paper gives an overview of two other techniques, aimed at studies of the dissipative scales of turbulence. The first, in §2 and Ref. 5, pertains to studies of mixing in turbulent flows, allowing fully-resolved, four-dimensional, spatio-temporal measurements of the scalar energy dissipation rate field $(ReSc)^{-1} \nabla \zeta \cdot \nabla \zeta(\mathbf{x}, t)$ of a dynamically passive, conserved scalar quantity $\zeta(\mathbf{x}, t)$ in the flow. The second, described in §3 and Ref. 11, is derived from the scalar field measurements and allows extraction of the underlying vector velocity field $\mathbf{u}(\mathbf{x}, t)$, along with the vector vorticity and tensor strain rate fields, at the dissipative scales of turbulent flows.

2. Four-Dimensional Scalar Field Measurements

Studies of the fine scale structure and dynamics associated with the molecular mixing of conserved scalar quantities in turbulent flows are a major branch of turbulence research. In the mixing of such a conserved quantity ζ , the scalar field $\zeta(\mathbf{x}, t)$ satisfies the advection-diffusion equation

$$\left[\frac{\partial}{\partial t} + \mathbf{u} \cdot \nabla - \frac{1}{ReSc} \nabla^2 \right] \zeta(\mathbf{x}, t) = 0. \quad (1)$$

where the Schmidt number $Sc \equiv (\nu/D)$ characterizes the ratio of the vorticity and scalar diffusivities. From (1),

the scalar energy per unit mass $\frac{1}{2}\zeta^2(\mathbf{x},t)$, defined analogous to the kinetic energy per unit mass $\frac{1}{2}u^2(\mathbf{x},t)$, follows an exact transport equation in which $(ReSc)^{-1}\nabla\zeta\cdot\nabla\zeta(\mathbf{x},t)$ gives the rate of scalar energy dissipation per unit mass, namely the local instantaneous rate at which non-uniformities in the scalar energy field are being reduced by molecular mixing in the flow. Here we describe a laser imaging diagnostic specifically designed for very highly resolved, four-dimensional, spatio-temporal measurements of the conserved scalar field $\zeta(\mathbf{x},t)$ and the associated scalar energy dissipation rate field $\nabla\zeta\cdot\nabla\zeta(\mathbf{x},t)$ in turbulent flows. Measurements with this technique have been obtained in the self-similar far field of axisymmetric turbulent jets at outer-scale Reynolds numbers $Re_\delta \equiv (u\delta/\nu)$ as high as 6000, and with resolution finer than the local strain-limited molecular diffusion scale λ_D in the underlying scalar gradient field. Since the imaged volume in the flow is quite small in comparison with the local outer flow scale δ , and comparable to the inner scale λ_v of the turbulence, the resulting measured turbulent scalar field fine structure is essentially independent of the Reynolds number and the flow. Features of the fine structure in the scalar energy dissipation rate fields captured within these four-dimensional data spaces should thus, to a large degree, be generic to large Schmidt number mixing in all high Reynolds number turbulent flows. Additional details of the technique and results are given in Ref. 5.

2.1 Experimental technique

Briefly, the technique involves measurement of the aqueous concentration of a dynamically passive laser fluorescent dye carried by one of the fluids. The dye mixture fraction is a conserved scalar with $Sc \approx 2075$. This is measured in time throughout a small three-dimensional volume in a turbulent flow by imaging the laser induced fluorescence from a collimated laser beam onto a high-speed planar photosensitive array. A pair of very low inertia, galvanometric mirror scanners are used to synchronously sweep the beam in a raster scan fashion through the desired volume in the flow field. The resulting laser induced fluorescence intensity is measured with a 256×256 imaging array, having center-to-center pixel spacings of $40\mu\text{m}$. The array is synchronized to the same clock that drives the scanners, and can be driven at variable pixel rates up to 11 MHz, allowing measurement of successive data planes at a continuous rate in excess of 140 planes per second. The fluorescence data from the array is serially acquired through a programmable digital port interface, digitized to 8-bits, and then routed into a 16 MB buffer from which it can be continuously written in real time to a 3.1 GB high-speed parallel transfer disk rank. The overall sustained data throughput rate to the disks, accounting for all line and frame overhead cycles, is up to 9.3 MB/sec. The 3.1 GB disk capacity can accommodate more than 50,000 of these 256^2 spatial data planes, yielding a four-dimensional spatio-temporal data space structured as shown in Fig. 1. The spatial separation between adjacent points within each data plane, and between adjacent data planes within each data volume, is smaller than the local strain-limited molecular diffusion lengthscale λ_D of the scalar field. Similarly, the temporal separation between adjacent data planes within each data volume and, depending on the number of spatial planes, between the same data plane in successive data volumes, is shorter than the local molecular diffusion scale advection time λ_T/μ . This resolution, together with the high signal quality attained, allows accurate differentiation of the measured conserved scalar data in all three space dimensions and in time to determine the components of the local instantaneous scalar gradient vector field $\nabla\zeta(\mathbf{x},t)$ at every point in the four-dimensional data space.

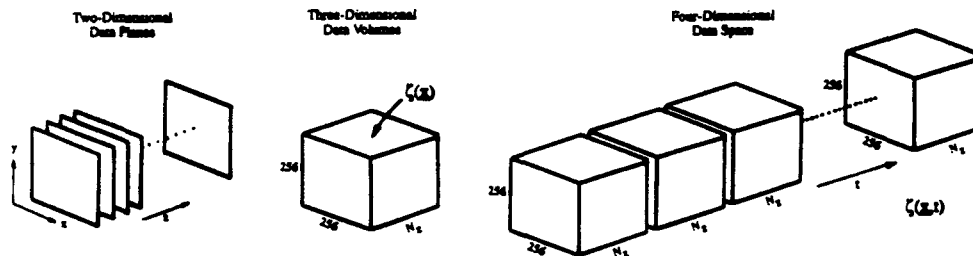


Figure 1. Structure of the experimentally measured, four-dimensional, spatio-temporal conserved scalar data space $\zeta(\mathbf{x},t)$ as a temporal progression of three-dimensional spatial data volumes, each consisting of a sequence of two-dimensional spatial data planes, each composed of a 256×256 array of data points. The data space typically consists of more than 3 billion individual point measurements. The spatial and temporal resolution achieved is sufficient to allow direct differentiation of the conserved scalar data in all three space dimensions and in time, allowing the evolution of the true molecular mixing rate field $\nabla\zeta\cdot\nabla\zeta(\mathbf{x},t)$ to be directly determined.

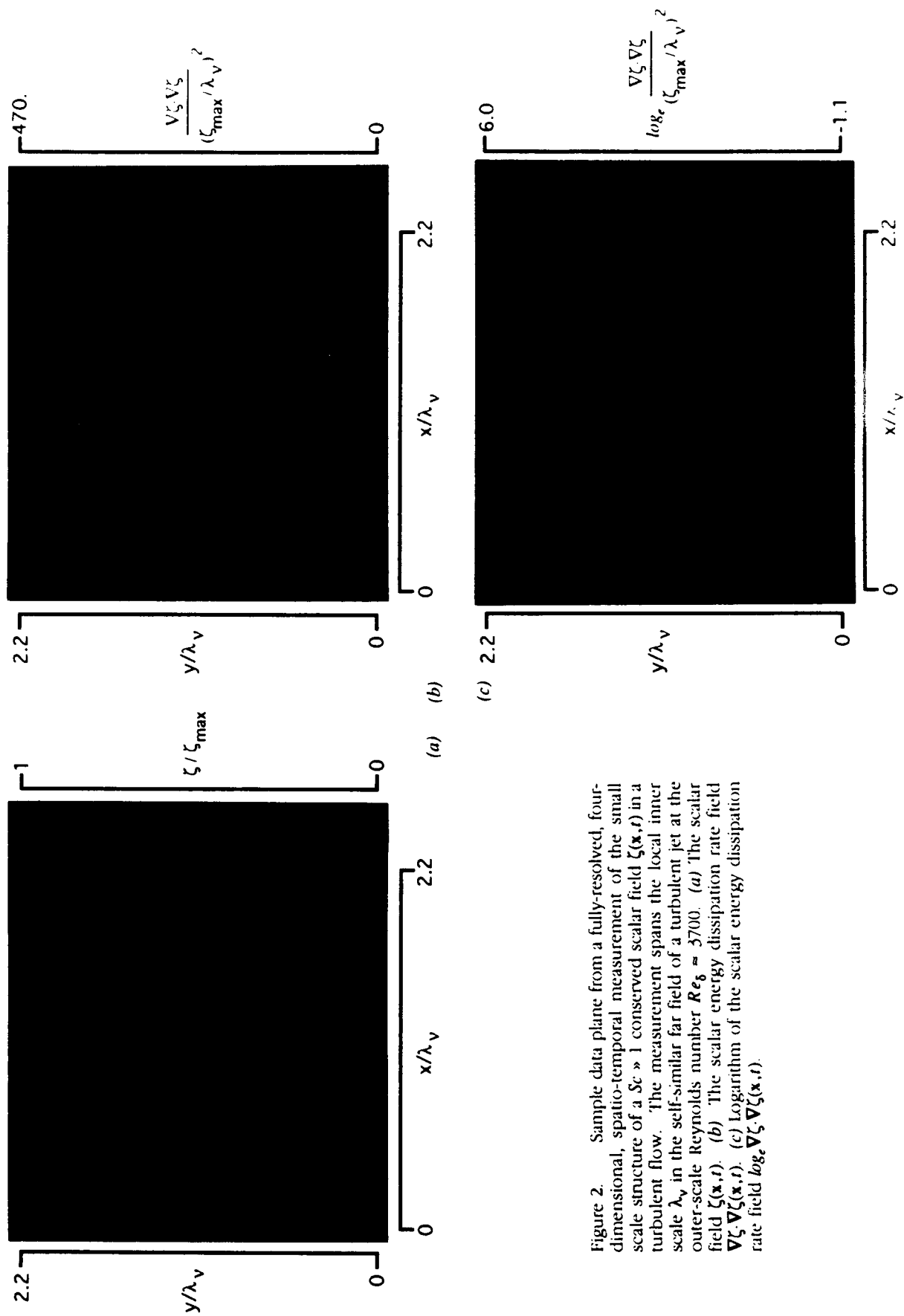


Figure 2. Sample data plane from a fully-resolved, four-dimensional, spatio-temporal measurement of the small scale structure of a $Sc \gg 1$ conserved scalar field $\zeta(\mathbf{x}, t)$ in a turbulent flow. The measurement spans the local inner scale λ_v in the self-similar far field of a turbulent jet at the outer-scale Reynolds number $Re_\delta \approx 3700$. (a) The scalar field $\zeta(\mathbf{x}, t)$. (b) The scalar energy dissipation rate field $\nabla \zeta \cdot \nabla \zeta(\mathbf{x}, t)$. (c) Logarithm of the scalar energy dissipation rate field $\log_e \nabla \zeta \cdot \nabla \zeta(\mathbf{x}, t)$.

2.2 Spatial and Temporal Resolution

The inner scales in obtaining the scalar gradient field from the measured conserved scalar field via direct differentiation of the data are the spatial and temporal resolution and the signal quality achieved by the measurements. First, in the measured laser beam diameter, together with the pixel size and the image ratio, the volume $(\Delta x \Delta y \Delta z)$ imaged onto each pixel can be determined. Similarly, the pixel clock rate and array size set the time between acquisition of successive data planes within each spatial data volume, and between the same data plane in successive data volumes. To assess the resulting relative resolution, these must be compared with the finest local spatial and temporal scales on which gradients in the conserved scalar field can be locally sustained in the flow. In both the vorticity and scalar fields, the effect of the local time-varying strain rate ϵ is to establish a competition between strain and molecular diffusion, leading to an equilibrium strain-limited diffusion layer thickness $\lambda \sim (D/\epsilon)^{1/2}$. With the peak strain rates locally in the flow scaling as $\epsilon \sim (v/\delta) \cdot Re_\delta^{1/2}$, the strain-limited scalar diffusion scale is $(\lambda_P \delta) \sim Sc^{-1/2} \cdot Re_\delta^{3/4}$, with $\lambda_v = \lambda_D \cdot Sc^{1/2}$. Recent measurements give this proportionality constant as approximately 11.2. Note that the scales λ_v and λ_D are respectively proportional to the classical Kolmogorov and Batchelor scales, but are about an order of magnitude larger.

The results presented here are from measurements in the self-similar far field of an axisymmetric turbulent jet, located 235 jet momentum diameters (1.15 m) downstream of the jet source and 13 cm off the jet centerline. To estimate the resulting resolution, note that $\delta(x) = 0.44 \cdot x$ and $u(x) = 7.2 (J/\rho)^{1/2} \cdot x^{-1}$, where J is the jet source momentum flux and ρ is the ambient fluid density. At an outer scale Reynolds number of 3700 and with $Sc = 2075$, the local strain-limited molecular diffusion lengthscale estimate is $\lambda_D = 262 \mu\text{m}$ and the local convection timescale estimate is $(\lambda_P/u) = 105 \text{ msec}$. With the measurements having an image ratio of 2.7, the in-plane spatial resolution was $\Delta x = \Delta y = 108 \mu\text{m}$, with the inter-plane resolution $\Delta z = 120 \mu\text{m}$, indicating that the scalar field measurements are essentially fully-resolved.

2.3 Sample results

Figure 2 shows the conserved scalar dissipation rate data in a typical 256×256 spatial data plane. All quantities are normalized by the inner scale reference values λ_v and (v/λ_v) of the underlying turbulent flow. The $\nabla \zeta \cdot \nabla \zeta(x, t)$ field was obtained by direct differentiation of the data in the three adjacent scalar planes centered on that in Fig. 2a. Linear central differences were used to evaluate the three components of the scalar gradient vector field $\nabla \zeta(x, t)$, with no explicit smoothing or filtering of the results. Owing to the wide range of dissipation rates, the logarithmic compression $\log_e \nabla \zeta \cdot \nabla \zeta(x, t)$ in Fig. 2c allows the structure at low dissipation rates to be examined. Fine structure maps such as these show that essentially all of the molecular mixing occurs in thin sheet-like layers. Numerical analysis of the detailed internal structure of the molecular mixing within these layers has confirmed that strain-limited solutions of the Burgers (1948, 1950) and Townsend (1951) form give a remarkably accurate description of the scalar energy dissipation profiles within these layers.

Our present interests are principally in the topology which the scalar dissipation layers assume as a result of their repeated stretching and folding by the turbulent strain rate and vorticity fields. The aim is to obtain measurements of the scalings which this topology satisfies, and relate these to the dynamics of the "turbulent cascade" represented by this stretching and folding process. We are motivated by recent successes in comparatively simple two-dimensional chaotic flows (Otuno 1992; Muzzio, Meneveau, Swanson & Otuno 1992), where a periodic stretching and folding of the scalar layers leads to scalings for the distribution of dissipation layer separations that can be reconciled with simple physical arguments. From the three-dimensional spatial character of the turbulent dissipation rate field in any given data volume (see Fig. 2c), we construct the surface of local layer-normal dissipation maxima. We can then compute the distribution of dissipation layer separations $\lambda \cdot \lambda_v$, as shown in Fig. 3. The roughly lognormal form appears consistent with the scalings obtained in the simple periodic flows (Refs. 9, 10), but for large layer separations we find the power law form shown in Fig. 4. The λ^{-3} scaling obtained is consistent with simple volume-preserving constraints and suggests a multiplicative process consistent with a self-similar repeated stretching and folding of the layers.

3. Four-Dimensional Velocity Field Measurements

This section describes a technique for measurement of the fully-resolved, four-dimensional, vector velocity field $u(x, t)$ on the inner scales of turbulent flows. It is based on the technique described above for obtaining fully-resolved, four-dimensional measurements of the fine scale structure of the $Sc \gg 1$ conserved scalar field $\zeta(x, t)$. The method involves inverting the exact conserved scalar transport equation throughout the

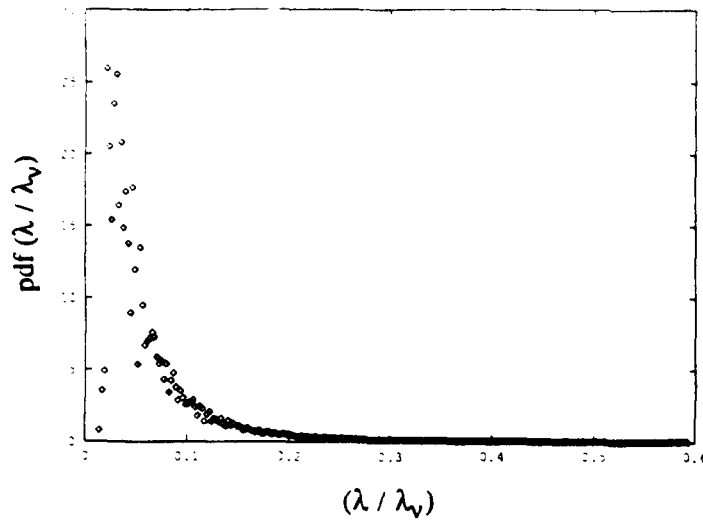


Figure 3. Measured distribution of the scalar dissipation layer separation distances λ/λ_v , obtained from the particular three-dimensional data volume containing the data plane shown in Figure 2. Note the quasi-lognormal form obtained for small layer separation values. See also Fig. 4.

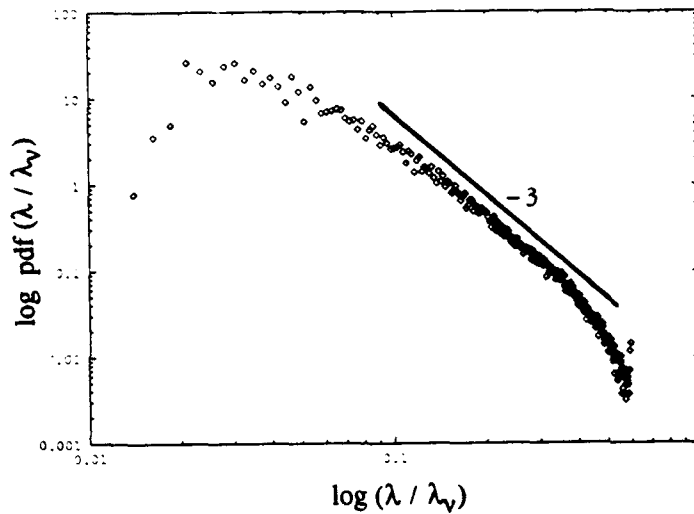


Figure 4. Log-log form of the measured distribution of scalar dissipation layer separation distances λ/λ_v in Fig. 3. Notice in particular the -3 power law form obtained for large layer separation values, and the cutoff value for small separations. The -3 slope is consistent with simple volume preserving arguments for a multiplicative process underlying the repeated stretching and folding of scalar dissipation layers by the turbulent flow field.

dense, four-dimensional, spatio-temporal data space to directly yield the velocity component field $u_{||}(\mathbf{x}, t)$ along the local scalar gradient vector $\nabla\zeta(\mathbf{x}, t)$. An examination of the corresponding gradient field $\nabla u_{||}(\mathbf{x}, t)$ then allows the extraction of the full vector velocity field $\mathbf{u}(\mathbf{x}, t)$. A detailed discussion is given in Ref. 11.

3.1 Extraction of $\mathbf{u}(\mathbf{x}, t)$ from $\zeta(\mathbf{x}, t)$

Since the conserved scalar field $\zeta(\mathbf{x}, t)$ follows the advective-diffusive transport equation given in Eq. (1), the influence of $\mathbf{u}(\mathbf{x}, t)$ on the scalar field is strictly through the $\mathbf{u} \cdot \nabla\zeta$ term. This can be written as $u_{||}|\nabla\zeta|$, where $u_{||}$ is the component of the local velocity vector along the local scalar gradient vector direction, namely

$$u_{||}(\mathbf{x}, t) = \mathbf{u}(\mathbf{x}, t) \cdot \hat{e}_{\nabla\zeta}(\mathbf{x}, t) \quad (2a)$$

with

$$\hat{e}_{\nabla\zeta}(\mathbf{x}, t) \equiv \nabla\zeta(\mathbf{x}, t) / |\nabla\zeta(\mathbf{x}, t)| \quad (2b)$$

Four-dimensional measurements of the scalar field $\zeta(\mathbf{x}, t)$, with resolution and signal quality sufficient to allow accurate direct differentiation in both space and time, allow extraction of this velocity component throughout the spatio-temporal data space as

$$u_{||}(\mathbf{x}, t) = \left[\frac{1}{ReSc} \nabla^2 \zeta(\mathbf{x}, t) - \frac{\partial \zeta(\mathbf{x}, t)}{\partial t} \right] / |\nabla\zeta(\mathbf{x}, t)| \quad (3)$$

Measurements of $u_{||}(\mathbf{x}, t)$ using Eq. (3) for the relatively simple flow field represented by an axisymmetric laminar vortex ring have been reported in Ref. 12. These show that remarkably clean first- and second-derivative fields are indeed obtainable from measured four-dimensional conserved scalar field data, allowing

accurate differentiation of the scalar field in all three space dimensions and in time to determine the components of the instantaneous time derivative field $(\partial/\partial t)\zeta(\mathbf{x}, t)$, the scalar gradient vector field $\nabla\zeta(\mathbf{x}, t)$, and the Laplacian field $\nabla^2\zeta(\mathbf{x}, t)$ involved in Eq. (3).

The value of $u_i(\mathbf{x}, t)$ differs between any two points \mathbf{x} and $\mathbf{x}+d\mathbf{x}$ due to (i) the change in the gradient vector direction, which is known, and (ii) the change in $\mathbf{u}(\mathbf{x}, t)$. This can be expressed formally as

$$\nabla u_i = \mathbf{u} \cdot \nabla \hat{e}_{\nabla\zeta}^T + \nabla \mathbf{u}^T \cdot \hat{e}_{\nabla\zeta} \quad (4)$$

In Eq. (4) the $u_i(\mathbf{x}, t)$ field and the scalar gradient vector orientation field $\hat{e}_{\nabla\zeta}(\mathbf{x}, t)$ are known from the measured scalar field data. The unknowns are the three components of the velocity field $\mathbf{u}(\mathbf{x}, t)$ and the nine components of its gradient field $\nabla \mathbf{u}(\mathbf{x}, t)$. However, the nine components of $\nabla \mathbf{u}(\mathbf{x}, t)$ result directly from relations among adjacent values of $\mathbf{u}(\mathbf{x}, t)$, and thus the availability of such adjacency information from the three-dimensional spatial character of the scalar field measurements motivates an iterative procedure to find the velocity field $\mathbf{u}(\mathbf{x}, t)$ in Eq. (4).

For large Sc scalar mixing in turbulent flows, we can expect that the scalar gradient field $\nabla\zeta(\mathbf{x}, t)$ will contain considerably more fine structure than the velocity gradient field $\nabla \mathbf{u}(\mathbf{x}, t)$. The velocity gradient field $\nabla \mathbf{u}(\mathbf{x}, t)$ will be linear over lengthscales of the order of λ_v , while $\nabla\zeta(\mathbf{x}, t)$ is linear over $\lambda_D = \lambda_v \cdot Sc^{-1/2}$. For $Sc = 2075$ this ratio of scales is about 45, so the underlying velocity field which we are aiming to extract from the scalar field measurements is considerably smoother than the scalar data itself. We can therefore expect $\hat{e}_{\nabla\zeta}$ in Eq. (4) to vary with $d\mathbf{x}$ more rapidly than will \mathbf{u} . This allows a starting solution for the velocity field by assuming that for small $d\mathbf{x}$, $\delta \mathbf{u} \cdot \hat{e}_{\nabla\zeta}$ in Eq. (4) is small in comparison with $\mathbf{u} \cdot \delta \hat{e}_{\nabla\zeta}$. The u_i 's found at three different points in a small neighborhood around any point \mathbf{x} are then essentially the projections of a single local velocity vector \mathbf{u} onto the three different unit vectors $\hat{e}_{\nabla\zeta}$. If the points are selected so that the three $\hat{e}_{\nabla\zeta}$'s are sufficiently non-colinear, then the local velocity vector $\mathbf{u} = (u, v, w)$ can be obtained from the measured $u_i(\mathbf{x}, t)$ via the inverse of this local projection matrix. Of course, in any such small neighborhood, there are in principle many combinations of points from which estimates for the local velocity vector \mathbf{u} can be obtained. This high level of redundancy leads to a strong probability of finding at least one set of points for which the projection matrix is sufficiently nonsingular to allow its accurate inversion. Moreover, this redundancy affords considerable opportunities for incorporating explicit noise reduction, if needed, in this zeroth estimate of $\mathbf{u}(\mathbf{x}, t)$.

This starting solution can be improved by writing Eq. (4) as a sequence of successive approximations as

$$\nabla u_i = \mathbf{u}^k \cdot \nabla \hat{e}_{\nabla\zeta}^T + (\nabla \mathbf{u}^{k-1})^T \cdot \hat{e}_{\nabla\zeta} \quad (5)$$

The iterative procedure begins for $k = 1$ with the result of the zeroth iteration, $\mathbf{u}^0(\mathbf{x}, t)$, from which we find $\nabla \mathbf{u}^0(\mathbf{x}, t)$. Equation (5) then involves only the three unknown velocity components \mathbf{u}^k , which we can obtain from the three components of this equation based on the measured $u_i(\mathbf{x}, t)$ and $\hat{e}_{\nabla\zeta}(\mathbf{x}, t)$ fields. Successive iterations based on Eq. (5) can then be made until the velocity field \mathbf{u}^k converges to a self-consistent result. While various constrained iteration schemes that explicitly require $\nabla \cdot \mathbf{u} = 0$, or that even enforce the vorticity transport equation explicitly, are possible if needed to accelerate convergence to the velocity field $\mathbf{u}(\mathbf{x}, t)$, our results show that stable, relatively rapid, and accurate convergence is achieved without the need to resort to any such measures.

To validate this scalar imaging velocimetry technique and assess its potential accuracy, we have applied it to a number of test cases in which synthetically generated scalar fields as well as actual measured turbulent flow scalar fields (see Fig. 5) are numerically advected in time under various imposed velocity fields. An example is shown in Fig. 6, where the imposed velocity field consists of two vortical structures. The velocity field obtained after four iterations leads to the vorticity and strain rate tensor components compared in Fig. 6 with the exact flow field. Note that all the major structural features of the vorticity and strain rate component fields are accurately extracted, and that continuity is remarkably well satisfied by the resulting velocity field.

3.2 Sample turbulent flow measurement

To demonstrate the application of this scalar imaging velocimetry technique, Figs. 7a-c show the full vector velocity field $\mathbf{u}(\mathbf{x}, t)$ in the scalar field data plane from Fig. 5, obtained from the third iteration in Eq. (5) with nothing imposed. The resulting u - and v -component fields are at least qualitatively consistent with the fluid motion apparent in the x - y plane from the time evolution of the measured scalar field data. The velocity projections, which are common in whole field velocimetry techniques, are shown in Fig. 7d, though it is apparent that the individual color-coded velocity component planes give a far better indication of the resulting structure in the measured vector velocity field.

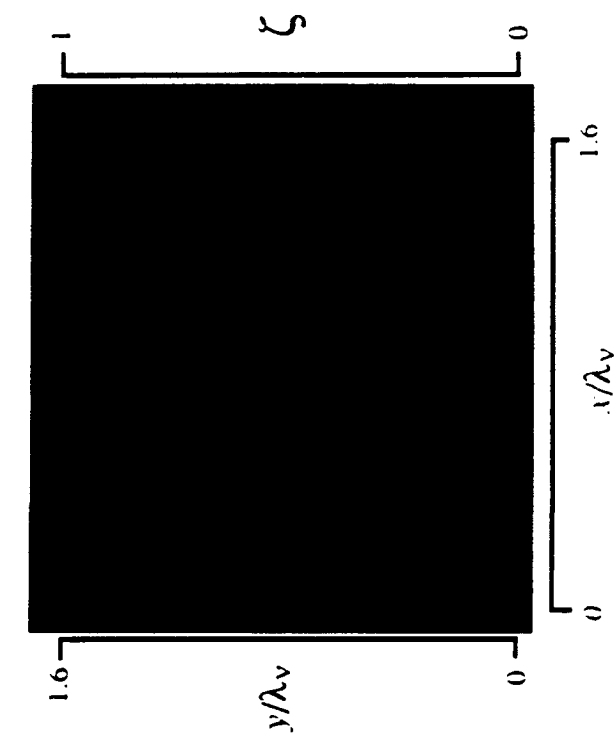


Figure 5 A single data plane from a measured four dimensional turbulent flow scalar field data space $\zeta(\mathbf{x}, t)$, used for the test case in Fig. 6. The underlying vector velocity field $\mathbf{u}(\mathbf{x}, t)$, extracted from this scalar field, is shown in Fig. 7. Various turbulence fields associated with this velocity field are shown in Fig. 8. The scalar field data were measured in the self-similar far field of an axisymmetric turbulent jet at $Re_\delta = 6,000$. The area shown spans approximately 1.6 times the local inner turbulent flow scale λ_v on either side (based on the earlier value of 25 for the proportionality constant), corresponding to about 1.17 of the local outer scale δ .

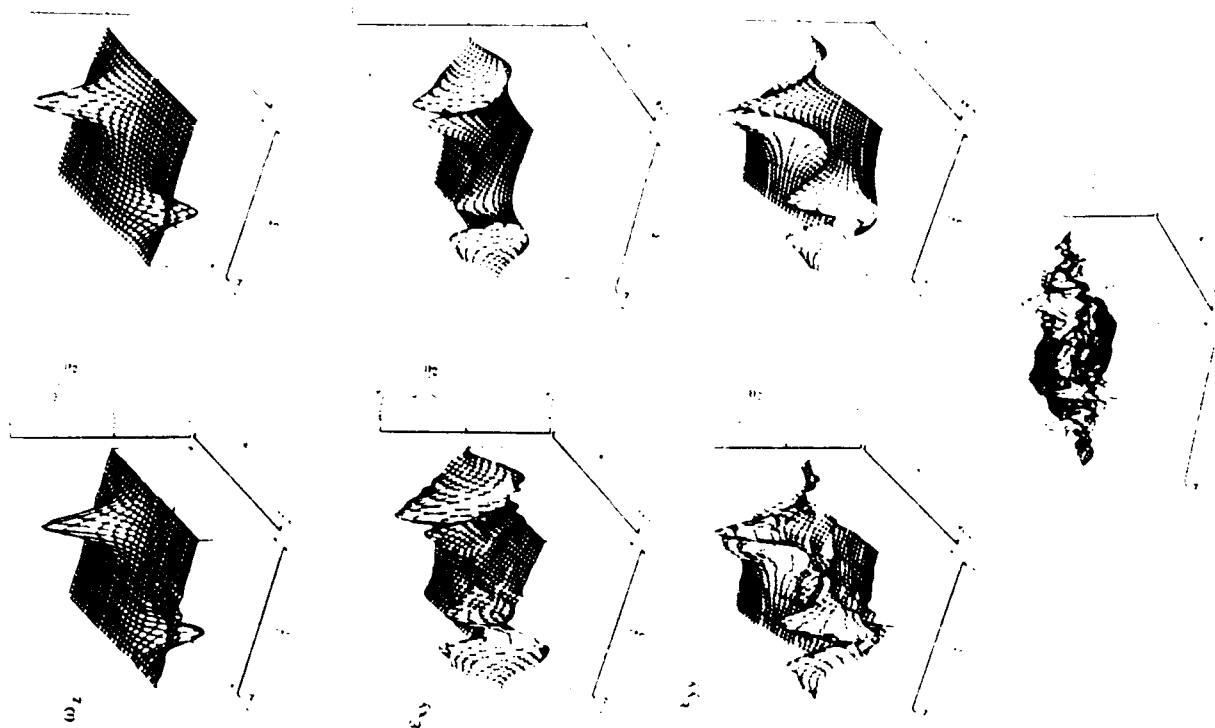


Figure 6 Vorticity and strain rate tensor component fields obtained from a test of the scalar imaging velocimetry technique, in which the measured turbulent scalar field in Fig. 5 was numerically advected with an imposed velocity field. Results obtained for these fields are shown on the left. The exact results are shown for comparison on the right. The resulting divergence $\nabla \cdot \mathbf{u}(\mathbf{x}, t)$ is shown at the bottom.

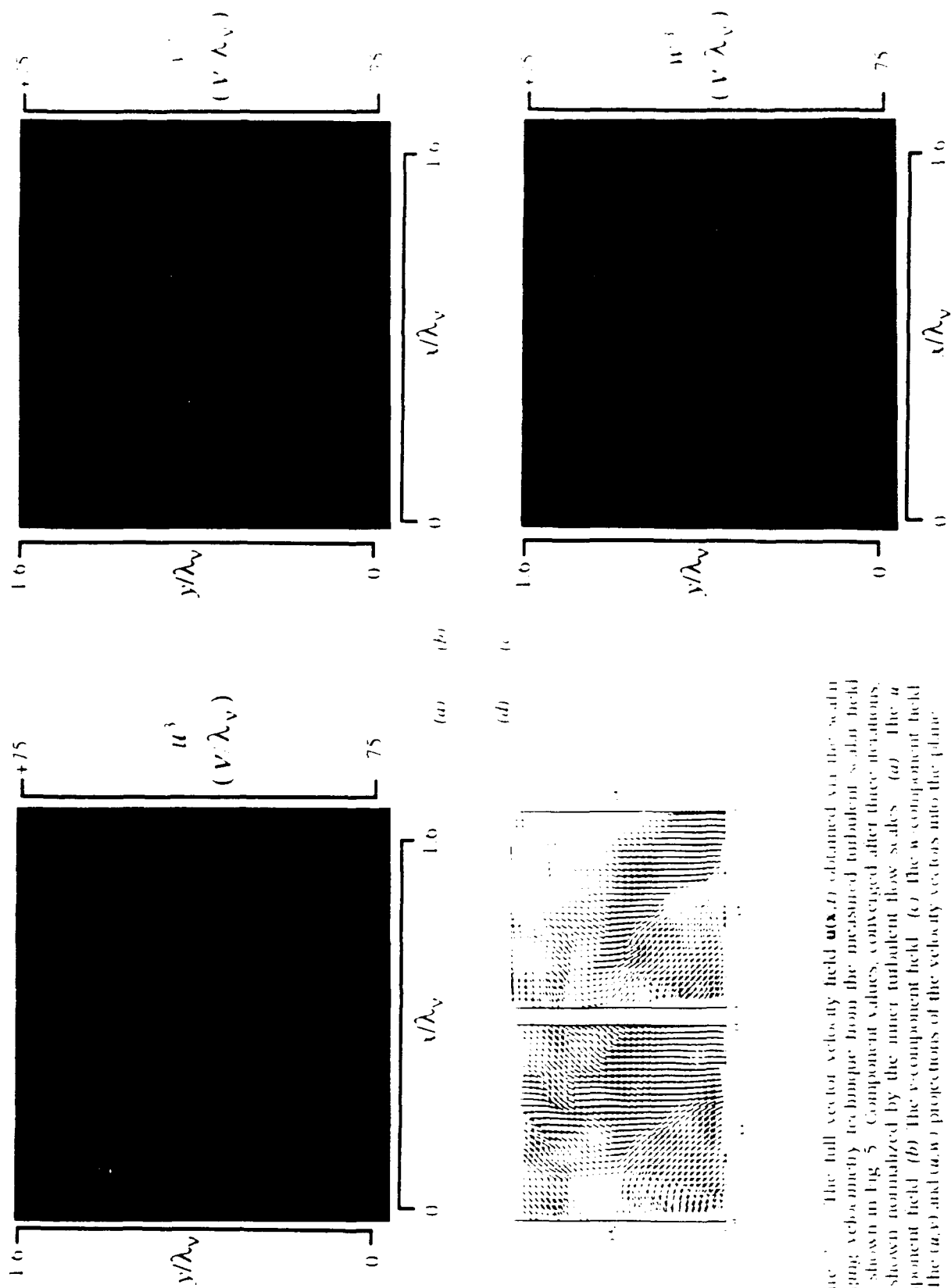


Figure 7. The full vector velocity field $\mathbf{u}(\mathbf{x}, t)$ obtained via the scalar imaging velocimetry technique from the measured turbulent scalar field data shown in Fig. 5. Component values, converged after three iterations, are shown normalized by the inner turbulent flow scales. (a) The u component field. (b) The v component field. (c) The w component field. (d) The (u, v) and (u, w) projections of the velocity vectors into the plane.

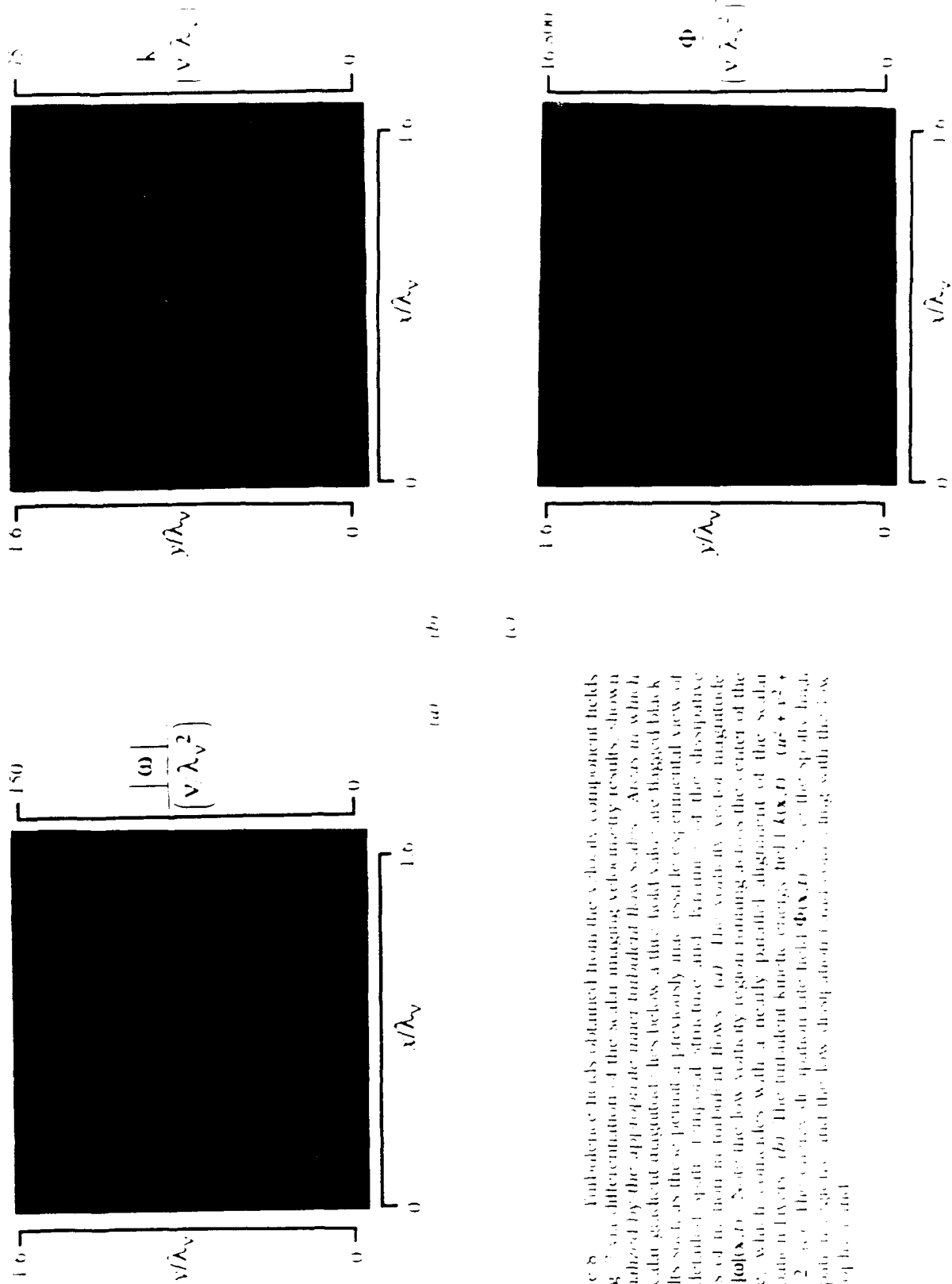


Figure 8: Turbulence fields obtained from the velocity component fields in Fig. 7 via differentiation of the scalar imaging velocimetry results, shown normalized by the appropriate inner turbulent flow scales. Areas in which the scalar gradient magnitude lies below a three-fold value are flagged black. Results such as these permit a previously inaccessible experimental view of the detailed spatial temporal structure and dynamics of the dissipative scales of motion in turbulent flows. (a) The velocity vector magnitude field $|u|(\mathbf{x}, t)$. Note the low velocity region running across the center of the plane, which coincides with a nearly parallel alignment of the scalar dissipative layers. (b) The turbulent kinetic energy field $k(\mathbf{x}, t) = (u^2 + v^2 + w^2)/2$. (c) The energy dissipation rate field $\Phi(\mathbf{x}, t) = \nu \nabla^2 k$. (d) The energy dissipation rate field $\Phi(\mathbf{x}, t)$ and contour plot with the low energy region highlighted.

A wealth of other information is available from the structure and dynamics of the more dynamically insensitive vorticity gradient field and vorticity associated turbulent energy field. Figure 5 shows examples of some of the detailed information which these results provide direct access to. Shown are the instantaneous vorticity magnitude field, the turbulent kinetic energy field, and the energy dissipation rate field. A wealth of other experimental information, such as the temporal dynamics of the alignment between the vorticity and scalar gradient vectors and the strain rate tensor eigenvectors, as well as critical point characterizations of the structure of the flow at the dissipative scales, can be derived from four-dimensional spatio-temporal laboratory data such as these.

4. Conclusions

Results from this fully-resolved, four-dimensional, spatio-temporal, scalar field imaging technique, as well as the scalar imaging velocimetry technique derived from it, provide a new means for experimentally investigating the precise fine structure and dynamics of real turbulent flows at a level of detail previously conceivable only from large-scale DNS computations. These methods, together with other whole field velocimetry techniques based on particle imaging methods and with advances in visualization techniques for large four-dimensional data spaces, are contributing to the next phase of a revolution that is rapidly providing remarkable new access into the nature of turbulence.

Acknowledgements

The results presented have been obtained with Mr. Kenneth B. Southerland and Mr. Lester K. Su of the Aerospace Engineering Department at Michigan. Discussions with D.R. Dowling of the MEAM Department at Michigan, and with J.M. Ottino, are also gratefully acknowledged. The work is supported by the Air Force Office of Scientific Research (AFOSR) under Grant No. 89-0541 and Grant No. 91-2953.

References

1. Adrian, R.J. (1991) Particle-imaging techniques for experimental fluid mechanics. Ann. Rev. Fluid Mech. **23**, 261-304.
2. Adrian, R.J. (1986) Multi-point optical measurements of simultaneous vectors in unsteady flow - a review. Int. J. Heat & Fluid Flow **7**, 127-145.
3. Merzkirch, W. (1987) Flow Visualization. Academic Press, New York.
4. Lauterborn, W. & Vogel, A. (1984) Modern optical techniques in fluid mechanics. Ann. Rev. Fluid Mech. **12**, 223-249.
5. Dahm, W.J.A., Southerland, K.B. and Buen, K.A. (1991) Direct, high resolution, four-dimensional measurements of the fine scale structure of scalar molecular mixing in turbulent flows. Phys. Fluids A **3**, 1115-1127.
6. Burgers, J.M. (1948) A mathematical model illustrating the theory of turbulence. Adv. Appl. Mech. **1**, 171-199.
7. Burgers, J.M. (1950) The formation of vortex sheets in a simplified type of turbulent motion. Proc. Acad. Sci. Amst. **53**, 122.
8. Townsend, A.A. (1951) On the fine-scale structure of turbulence. Proc. Roy. Soc. Lond. A **208**, 53-542.
9. Ottino, J.M. (1992) Mixing distributions produced by multiplicative stretching in chaotic flows. Int'l. J. Bifurcations and Chaos **2**, 37-50.
10. Muzzio, J.E., Meneveau, C., Swanson, P.D. and Ottino, J.M. (1992) Scaling and multifractal properties of mixing in chaotic flows. Phys. Fluids A **4**, 1439-1458.
11. Dahm, W.J.A., Su, L.K. and Southerland, K.B. (1992) A scalar imaging velocimetry technique for fully-resolved four-dimensional vector velocity field measurements in turbulent flow. To appear in Phys. Fluids A.
12. Southerland, K.B., Porter, J.R., Dahm, W.J.A. and Buen, K.A. (1991) An experimental study of the molecular mixing process in an axisymmetric laminar vortex ring. Phys. Fluids A **3**, 1385-1392.

PARTICLE TRANSPORT IN TURBULENT DISPERSE FLOWS

T. J. Hanratty
University of Illinois
Urbana, IL 61801

Abstract

Considerable progress has been made in understanding the dynamics of particles in a homogeneous isotropic turbulence and in understanding the additional forces on particles that arise in non-homogeneous flow fields. This work is reviewed and its use in describing gas-liquid annular flow, sediment transport and aerosol deposition is explored.

1. Introduction

Particles in a turbulent field assume a turbulent motion because of their response to fluid velocity fluctuations. An understanding of this phenomenon is central to solving many problems in multiphase flow. This paper concentrates on the behavior of dilute suspensions for which particle-particle interaction is unimportant and for which the influence of the particles on fluid turbulence can be ignored.

The particles do not follow the fluid exactly because of inertia effects and because the gravitational field can cause a drift relative to the fluid. Considerable progress has been made in understanding the dynamics of particles that originate from a point source in a homogeneous field. Nonhomogeneities in the flow field, that can dramatically change this behavior have also been quantified. However, no generally accepted solution for dispersion from a point source in a non-homogeneous field is available.

The principal focus of this paper is the utilization of these advances to analyze multiphase systems. Particular attention is given to describing the distribution of particles and the deposition on a wall.

Droplet behavior in vertical gas-liquid annular flow is described by considering the wall layer to be a series of differential sources of drops. In this system the inertia of the drops is large enough that they move through the viscous wall region in free-flight. As a consequence, a first order approximation can be obtained by assuming a homogeneous flow field. This approximation is also reasonable for horizontal gas-liquid annular flows and sediment transport. However, the influence of the gravitational field must be taken into account.

Aerosol particles have much smaller inertia than droplets or sediment particles. They impact on a wall by a free-flight which originates within the viscous wall region, where large spatial variations of the turbulence properties of the fluid are found. As a consequence, an understanding of the effect of non-homogeneities in the flow field are of first order importance. Here, the principal problem is understanding the details of the free-flight. Computer

experiments offer the opportunity of obtaining much needed information on this phenomenon.

2. Dispersion of fluid particles from a point source in a homogeneous flow

A starting point for understanding particle transport is Taylor's (1921) description of diffusion from a point source. The spread of particles may be characterized by the mean-square of the x-component of a large number of particles from the place where they originated, $\overline{X^2}$. For molecular diffusion, Einstein derived the relation

$$\frac{1}{2} \frac{d\overline{X^2}}{dt} = D \quad (1)$$

where D is the molecular diffusion coefficient.

Taylor assumed a homogeneous, isotropic field and showed that

$$\frac{1}{2} \frac{d\overline{X^2}}{dt} = \overline{u^2} \int_0^t R_F^L(s) ds \quad (2)$$

Here $\overline{u^2}$ is the mean-square of the x-component of the velocity fluctuations and R_F^L is the Lagrangian correlation defined as

$$R_F^L(s) = \frac{\overline{u(s)u(0)}}{\overline{u^2}} \quad (3)$$

The numerator is the average of the product of the velocity of a particle at times zero and s . For small s , $\overline{u(0)u(s)} \cong \overline{u^2}$ and $R_F^L(s) \rightarrow 1$. For large times, $u(s)$ is not related to $u(0)$ so that $u(0)u(s)$ can be plus as often as it is minus. Consequently $\overline{u(0)u(s)} \rightarrow 0$ for $s \rightarrow \infty$. The integral in (2) for $s \rightarrow \infty$ is a constant, defined as the Lagrangian time scale of the fluid,

A Lagrangian turbulent diffusion coefficient, $\epsilon_F(t)$, can be defined by (1). For $t \rightarrow 0$, $\epsilon_F = \overline{u^2}t$ and for $t \rightarrow$

$$\tau_{LF} = \int_0^\infty R_F^L(s) ds \quad (4)$$

∞ , $\epsilon_F = \overline{u^2}\tau_{LF}$. Consequently the turbulent diffusion coefficient is time-dependent. It varies linearly with time for small time and is a constant for large time.

An alternate method to describe diffusion from a point source is to use random flight models. These give the path of the particle over a number of discrete time intervals, Δt , as

$$\frac{dx_i}{dt} = u_i \quad (5)$$

where u_i , the x-component of the velocity of the particle at the beginning of time interval, Δt_i , is allowed to vary randomly with time. An example of this approach is the Langevin equation (van Dop et al, 1985),

$$du_i = -\frac{u_i}{\tau_{LF}} dt + \left(2 \frac{\overline{u^2}}{\tau_{LF}}\right)^{1/2} d\omega_i, \quad (6)$$

where $d\omega_i$ is a random acceleration which is uncorrelated from time step to time step. Equations (5) and (6) are solved for the initial condition that u_i is a random variable specified by a Gaussian distribution with variance $\overline{u^2}$.

This solution gives a model of one of the possible paths for a fluid particle originating from the origin at time zero. An average over a large number of paths gives

$$\overline{X^2} = 2 \overline{u^2} \tau_{LF}^2 \left(\frac{t}{\tau_{LF}} - 1 + e^{-\frac{t}{\tau_{LF}}} \right) \quad (7)$$

This is a solution of (2) if $R_F^L = \exp(-t/\tau_{LF})$.

3. Dispersion of heavy particles from a point source in a homogeneous isotropic field

Turbulence properties of particles can be defined analogous to those for the fluid: $\overline{v^2}$, τ_{LP} , and ε_P . The goal of a theory for heavy particle dispersion is to predict the turbulence properties of the particles from given turbulence properties of the fluid. The approach that is taken is to solve the equation of motion of a particle in a randomly varying fluid field and to take an average over a large number of possible particle paths.

The simplest form of this equation and the one used in this paper is

$$V_P \left(\rho_P + \frac{\rho_F}{2} \right) \frac{d\vec{v}}{dt} = \vec{g} V_P (\rho_P - \rho_F) + f_D \frac{1}{2} \rho_F (\vec{u} - \vec{v}) [\vec{u} - \vec{v}] \quad (8)$$

Here V_P is the volume of the particle, the $\rho_F/2$ term on the left side is the added mass, the first term on the right is the force of gravity and the second term on the right is the fluid drag. The drag coefficient, f_D , is obtained from a steady flow correlation.

From (8) an inertial time constant can be defined as

$$\tau_P^{-1} = \beta = \frac{3f_D \rho_F [\vec{u} - \vec{v}]}{2 d_P (2\rho_P + \rho_F)} \quad (9)$$

For a Stokesian resistance

$$\beta_S = \frac{36 \mu_F}{(2\rho_P + \rho_F) d_P^2} \quad (10)$$

and (8) is linear in \vec{v} . When time is large enough the average acceleration of the particles is zero, and the average

of (8) gives a drift (or free-fall) velocity, designated by V_T , for the particles due to the gravitational field.

More complete forms of the equation of motion have been considered. In particular, the works of Tchen (1947), Corrsin & Lumley (1956), and Maxey & Riley (1983) should be mentioned. Complications arise because of the treatment of the added mass effect, fluid pressure variations, non-linear drag and the effect of unsteadiness on drag. A detailed assessment of these problems has recently been given by Mei (1990).

The solution of (8) for Stokesian drag gives the following average results (Friedlander, 1957):

$$\overline{v^2} = \overline{u^2} \beta_s \int_0^\infty t^{-\beta} s^\beta R(s) ds \quad (11)$$

$$\overline{X_p^2} = 2 \overline{u^2} \int_0^t (t-s) R(s) ds \quad (12)$$

$$\varepsilon_p (t \rightarrow \infty) = \overline{u^2} \int_0^\infty R(s) ds \quad (13)$$

The turbulence properties of the particles are, thus, defined in terms of the fluid turbulence properties, $\overline{u^2}$ and $R(s)$. The coefficient, $R(s)$, correlates fluid velocity fluctuations seen by the particle as it moves through the field. It is not equal to the Eulerian or to the Lagrangian correlation coefficient; it cannot be measured, directly, in laboratory.

As pointed out by Lumley (1957), this presents a fundamental non-linearity. Equation (12) gives the mean-squared position of the particle, but in order to specify $R(s)$ the position needs to be known.

A major breakthrough is the approximate resolution of this problem made by Reeks (1977), Pismen & Nir (1978) and Nir & Pismen (1979). They applied Corrsin's (1959) independence approximation by assuming that the Lagrangian correlation $R_L(s)$ at time s equals a spatial average of the Eulerian space-time correlation at time s :

$$R_{ij}(s) = \frac{1}{3} \iiint R_{ij}^E(\vec{x}, s) p(\vec{x}, s) d\vec{x} \quad (14)$$

Here $p(\vec{x}, s)$ is the probability that a particle has a displacement \vec{x} after time s . It is assumed to be Gaussian with variance $\overline{X_p^2}$.

An iterative procedure is used to solve (12) and (14). A function for $R(s)$ is assumed and $\overline{X_p^2}(s)$ is calculated from (12). A first approximation of $p(\vec{x}, s)$ is obtained and a second approximation of $R(s)$ is obtained from (14).

Reeks, Pismen & Nir explored an Eulerian space-time correlation of the form

$$R_{ij}^E(x, s) = R_{ij}^E(\vec{x}) R^E(s) \quad (15)$$

The Eulerian spatial correlation is calculated from isotropic relations using

$$f(r) = \exp \left(- \frac{\pi r^2}{4L_E^2} \right) \quad (16)$$

and the Eulerian time correlation is specified as

$$R^E(s) = \exp \left(- \frac{\pi s^2}{4\tau_E^2} \right) \quad (17)$$

Here L_E and τ_E are the Eulerian length of time scales. The ratio $(\overline{u^2})^{1/2} \tau_E / L_E$ was fixed.

Reeks, Pismen and Nir found for correlation function (15-17) that $\overline{v^2} < \overline{u^2}$ and that the long-time turbulent diffusivity of the particles is larger than the long time turbulent diffusivity of the fluid, if the time constant of the particle is large and if V_T is negligible. For a very small particle time constant the particle diffusivity is the same as the fluid and $\overline{u^2} = \overline{v^2}$. Increasing values of V_T were found to cause a decrease in the long time turbulent diffusivity of the particle, in agreement with the crossing of trajectories concept of Yudine (1959). In the limit of very large V_T asymptotic relations were derived by Csanady (1963):

$$R(\theta) = R^E(x - V_T t, y=0, z=0) \quad (18)$$

$$\epsilon_x = \sqrt{2\pi} / \frac{V_T}{(\overline{u^2})^{1/2}} \quad (19)$$

$$\epsilon = \frac{1}{2} \epsilon_{xx} \quad (20)$$

Mei (1990) has extended the work of Reeks, Pismen and Nir to include the effects of non-linear drag. This work, as well as a study by Lumley (1978), shows that $\beta_x \neq \beta_y = \beta_z$, where x is the direction of particle settling, in contrast to a linear drag for which these three reciprocal time constants would be equal.

Another approach toward understanding particle turbulence in a homogeneous field is the description of individual particle paths by the use of random flight models. However, the adaptation of methods developed to describe Lagrangian statistics for the fluid is not clearcut. So, the results of different investigators are not in agreement. One of the first papers in this area was by Hutchinson, Hewitt & Dukler (1971). Other works along this line are by Shuen et al (1983), Kallio & Reeks (1988), Burnage & Moon (1990), Ormancey & Martinon (1984), Berlemont et al (1990).

4. Experiments

Laboratory studies of particle turbulence have been performed by Snyder & Lumley (1971) and Wells & Stock

(1983) in grid generated turbulence. Studies in pipe flow were carried out by Calabrese & Middleman (1979), Lee, Adrian & Hanratty (1991).

The latter two studies are of particular importance to this paper. These showed that, within experimental error, the long-time turbulent diffusivities of the particle and the fluid are approximately equal. The ratio of the particle and fluid turbulence were found to be given by

$$\frac{\overline{v_r^2}}{\overline{u_r^2}} = \frac{\beta \tau_{LF}}{0.7 + \beta \tau_{LF}} \quad (21)$$

For $V_T / u^* > 1$ the long time diffusivity of the particles becomes smaller than the long time diffusivity of the fluid.

An experimental approach that has been most fruitful is to carry out computer studies of particle turbulence. This can involve the use of a direct numerical simulation (McLaughlin, 1989; Brooke et al, 1992; Squires & Eaton, 1991) or various versions Kraichnan's (1970) kinematic representation of isotropic Gaussian turbulence with Fourier series (Maxey, 1987; Mei, 1990).

5. Effects of flow non-homogeneities

A consideration of particle dispersion in non-homogeneous flow fields introduces a number of phenomena not seen in homogeneous turbulence. Gradients of the turbulence cause particles to have a time average drift away from maxima in the energy. The drift velocity for this turbophoresis phenomenon (Reeks, 1983; Caporaloni, 1975) has been given as

$$V_{Di} = - \frac{1}{\beta_s} \frac{\partial (\overline{v_i v_j})}{\partial x_j} \quad (22)$$

for a Stokesian particle.

For a fully-developed particle field in a cylindrical polar coordinate system the drift velocity defined by Reeks would be given as

$$\beta_s \nabla_{Dr} = \frac{\partial \overline{v_r^2}}{\partial r} + \frac{\overline{v_r^2}}{r} - \frac{\overline{v_\theta^2}}{r} \quad (23)$$

However in considering the effect of non-homogeneities one must also take into account their influence on the time-averaged pressure gradient in the fluid (as discussed by Young & Hanratty, 1991a).

$$- \frac{\partial \overline{p}}{\partial r} = \rho_F \left[\frac{\partial \overline{u_r^2}}{\partial r} - \frac{\overline{u_\theta^2}}{r} + \frac{\overline{u_r^2}}{r} \right] \quad (24)$$

This exerts an average force on the particles so that from (23) and (24) the average drift velocity due to turbulence non-homogeneities is given as

$$\beta \nabla_{Dr} = \left(\frac{\partial \vec{v}_r^2}{\partial r} + \frac{\vec{v}_r^2}{r} - \frac{\vec{v}_\theta^2}{r} \right) - \alpha \left(\frac{\partial \vec{u}_r^2}{\partial r} + \frac{\vec{u}_r^2}{r} - \frac{\vec{u}_\theta^2}{r} \right) \quad (25)$$

where $\alpha = 3\rho_F / (2\rho_P + \rho_F)$. For $\rho_P = \rho_F$ it is noted that $\nabla_{Dr} = 0$.

A simple interpretation (Young & Hanratty, 1991a) of these results can be obtained if one considers that the right side of (23) is a time-averaged acceleration, either of a fluid particle or of a solid particle. If it is a fluid particle the acceleration is associated with a time-average pressure gradient in the fluid. If it is a solid particle, the acceleration is not balanced by pressure gradients in the fluid. At approximately equilibrium conditions the acceleration equals a drag force on the particle, given by $\beta \nabla_{Dr}$ for a Stokesian particle, where ∇_{Dr} is the radial component of the slip velocity.

Lift forces transverse to the direction of particle slip the (x-axis) can be caused by particle rotation (Rubinow & Keller, 1961) or by a mean velocity gradient in the fluid (Saffman, 1965, 1968). The particular results obtained by Saffman for Stokesian particles are restricted to values of $(dU_x / dy) d_p^2 / \nu$ which are small, but still much larger than the particle Reynolds number, $d_p |\vec{U} - \vec{V}| / \nu$. McLaughlin (1991) has extended the analysis of Saffman for Stokesian particles so that a small value of $d_p (dU_x / dy) / |\vec{U} - \vec{V}|$ need not be assumed. The interesting finding is that the lift starts to decrease significantly for values of this ratio of the order of unity and that it is negligible for large slip velocities. The lack of an appreciation of this effect has led to errors in a number of analyses that have appeared in the literature. Lift forces associated with velocity gradients appear to exist, also, for large particle Reynolds numbers, but clearcut theoretical guidance is not available.

When particles approach a wall a number of important effects can occur. The fluid drag in directions perpendicular and parallel to the wall increase (Brenner, 1961; Goldman et al, 1967; Cox & Brenner, 1967; Young & Hanratty, 1991b). Furthermore, when particles approach a wall very closely there is a lift force away from the wall that results from an inhibition of fluid displacement. This was discovered by Cox & Hsu (1977) and by Vasseur & Cox (1977) in their analysis of particles sedimenting in a stationary fluid. These results have been confirmed experimentally by Cherukat & McLaughlin (1990).

A number of experiments have been performed which clearly show the effects of a non-homogeneous flow field on particle distribution. In their study of the motion of 100 micron copper and glass spheres in downwardly flowing turbulent water, Young & Hanratty (1991b) found that the particles can be trapped in necklace formations that move parallel to the wall slowly at a distance of less than one particle diameter from the wall. Measurements of concentration profiles of the particles show a maximum in the center of the pipe and gradients toward the wall, indicating that particles are transported toward the wall by turbulent diffusion. The trapping phenomenon is interpreted as occurring when the Saffman lift force toward the wall overcomes the ability of fluid turbulence to mix the particles. The location of trapped particles is dictated by a balance between the Saffman lift force and the wall-

induced force associated with the displacement of fluid as a particle moves parallel to the wall.

Sun & Lin (1986), in their studies of aerosol particles, reported on an accumulation of particles close to the wall, so that a maximum in the concentration is close to the wall and there is a gradient of particle concentration away from the wall. Computer experiments by Kallio & Reeks (1989) and by McLaughlin (1989) have shown the same behavior. This can be explained by a drift toward the wall by turbophoresis, which is counterbalanced by turbulent diffusion away from the wall (Brooke et al, 1992).

6. Scaling

From the arguments presented in the previous sections three dimensionless groups emerge as being particularly important in understanding the behavior of dilute dispersed systems.

One of these is the ratio of the Lagrangian time scale to the inertial time scale of the particle, $\beta\tau_{LP}$. As $\beta\tau_{LP}$ decreases the ability of particles to follow the turbulence decreases. This is exhibited in (21) where it is seen that $(\overline{v^2})^{1/2} / (\overline{u^2})^{1/2}$ decreases with decreasing $\beta\tau_{LP}$. At $\beta\tau_{LP} = 1$, the ratio of particle and fluid root-mean-square velocity fluctuations equals 0.77.

The quantity $\tau_p = (1/\beta)$ multiplied by a velocity gives the stopping distance of a particle with that velocity in a stationary fluid. The thickness of the viscous wall region where the flow is highly non-homogeneous is given as $30\nu/u^*$, where the friction velocity, u^* , is of the order of the turbulent velocity fluctuations outside the viscous wall region. The dimensionless group $\tau_p^+ = u^* \tau_p / \left(\frac{\nu}{u^*} \right)$ is a measure of the ratio of the stopping distance of the

particle to the thickness of the viscous wall region. Thus, a correlation of particle deposition data presented by McCoy & Hanratty (1975) shows for $\tau_p^+ < 20$ that the dimensionless deposition constant, k_D/u^* varies with τ_p^{+2} or with particle diameter to the fourth power. This reflects the very large effect of turbulence non-homogeneities on deposition since particles with $\tau_p^+ < 20$ have stopping distances less than the thickness of the viscous wall region. For $\tau_p^+ > 20$ the data indicate k_D/u^* is only weakly dependent on τ_p^+ . This arises because particles with $\tau_p^+ > 20$ have stopping distances greater than the thickness of the viscous wall region; their deposition rate is not sensitive to the details of the non-homogeneities close to the wall.

The ratio of the particle terminal velocity to the friction velocity, V_T/u^* , is a measure of the influence of the crossing of trajectories on the long time turbulent diffusivity, so that for $(V_T/u^*) > 1$ the particle diffusivity will be less than the fluid diffusivity. For $V_T/u^* \leq 1$ the two diffusivities are roughly equal.

7. Formulation of a diffusion model

For cases in which $\tau_p^+ > 20$ it is of interest to explore the applicability of a diffusion model to describe particle distribution and particle deposition. A fully-developed turbulent flow is considered. When an Eulerian framework is used the concentration field for a horizontal flow is defined by the equation

$$\nabla_x \frac{\partial C}{\partial x} + \nabla_y \frac{\partial C}{\partial y} = \frac{\partial}{\partial y} \left(E_p \frac{\partial C}{\partial y} \right) \quad (26)$$

where E_p is the Eulerian diffusion coefficient and diffusion in the flow direction has been neglected. Velocity component ∇_y is a constant equal to the negative of the free-fall velocity, V_T . Values of ∇_y less than V_T are sometimes used to account for hindered settling. However, little recognition has been given to the possibility that the particles might not have been in the field long enough to reach their free-fall velocity. For a vertical flow $\nabla_y = 0$.

The specification of boundary conditions presents difficulties. Unlike the case of molecular transport, the transport of particles from and to the boundary is not described by a gradient model, whereby the flux equals $-E_p (\partial C / \partial y)$, and the concentration is not zero at a completely absorbing boundary. As a consequence, boundary conditions are usually specified empirically.

In an Eulerian framework the influence of the time-dependency of turbulent diffusion cannot be taken into account directly; it is usually absorbed in the specification of the spatial variation of E_p (Hanratty, 1956, 1958; Hanratty & Flint, 1958; Eckelman & Hanratty, 1972). However, in some circumstances the time-dependency cannot be overlooked. Vertical annular flow is an example.

Because the spatial scale characterizing turbulent diffusion can become quite large the paths of droplets entrained in the gas phase in an annular flow can sometimes be characterized by unidirectional flights from one wall to the other, and not by the usual zig-zag motion of diffusional processes (Andreussi & Azzopardi, 1983). Under these circumstances dispersion is governed by the small time asymptote of (2), whereby the turbulent diffusivity varies linearly with the time the particles have been in the field,

$$E_p = \bar{v}^2 t \quad (27)$$

For the reasons cited above the physics emerges in a more natural way if a Lagrangian formulation is used. The concentration field is pictured as resulting from a distribution of point sources. The critical physical problem is to describe the behavior of one of these sources.

One approach would be to use the random flight analysis outlined in section 2. However, different viewpoints exist on how to use random flight methods to describe particle dispersion in a homogeneous field; their application to a non-homogeneous field must be regarded as speculative. In addition, a large number of random flights must be calculated to get a proper statistical average. This could make it cumbersome to study an extensive parameter space.

As a consequence, it seems reasonable to explore, initially, a homogeneous turbulence that uses Taylor's theory to describe a wall source. This is justified for $\tau_p^+ > 20$ since particles start their free-flight to the wall beyond the viscous wall region.

8. Gas-liquid annular flow and sediment transport

(a) Outline of a homogeneous model for a wall source

The behavior of a differential source that entered a homogeneous, isotropic field at time t' and at \vec{x}' field is conveniently calculated as a solution of the following equation (Batchelor, 1949; Hanratty, 1956; Binder & Hanratty, 1992):

$$\frac{\partial C}{\partial t} = \frac{1}{2} \frac{d\bar{v}^2}{dt} \nabla^2 C - \nabla_y (t - t') \frac{\partial C}{\partial y} + S \delta(y(0)) \delta(t/t') \quad (28)$$

where ∇^2 is defined by (2), S is the source strength at \vec{x}', t' , having the units of mass per unit area, and the δ 's are delta functions having the units of reciprocal length and reciprocal time. The first term on the right side represents the spread due to turbulent motion. The second term represents the y-component of the average deterministic velocity of the particles associated with the gravitational field. The mean flow is in the x-direction so that ∇_y is zero for a vertical system. A plug flow is assumed so that

$$dt = dx / \nabla_x \quad (29)$$

and the mean particle velocities, ∇_x , ∇_y are functions only of (t, t') .

Velocity ∇_y is defined by

$$m_p \frac{d\nabla_y}{dt} = -\frac{1}{2} \rho f_D A_p |\vec{V} - \vec{U}| (\nabla_y - U_y) - g m_p \left(1 - \frac{\rho_F}{\rho_P}\right) \quad (30)$$

Here $|\vec{V} - \vec{U}|$ is the mean relative velocity between the solid and the fluid; $U_y = 0$ since there is no net fluid motion in the y-direction; A_p is the projected area of the particle; m_p is the particle mass; f_D is the particle drag-coefficient. In the context of (28) and (30) the x-component of the velocity enters the problem in the calculation of $|\vec{V} - \vec{U}|$ and in relating the time coordinate to the space coordinate in (29). Velocity ∇_x is defined by the equation

$$m_p \frac{d\nabla_x}{dt} = -\frac{1}{2} \rho f_D |\vec{V} - \vec{U}| (\nabla_x - U_x) \quad (31)$$

Particles can enter the field from a wall source with a range of sizes and velocities. Equations (28-31), in general, would have to be solved for each member of this population. In order to simplify the problem the calculations in this paper assume the particles could be represented by a single size and a single velocity. Thus, at t' , $\nabla_x = \nabla_{x0}$ and $\nabla_y = \nabla_{y0}$. For a source on the bottom wall of a horizontal system the average velocity ∇_y will be less than ∇_{y0} for $t > t'$. For t much large than t' there will be an average drift toward the wall given by $\nabla_y = -\nabla_T$.

The boundary conditions to be used in solving (28) require special consideration. For annular flow, the wall is considered to be a perfect absorber. For a process involving only molecular diffusion the assumption of perfect absorption implies a zero concentration at the boundary. However, this is not the case for droplet deposition, for which the length scale of droplet motion can be large compared to the scale characterizing the droplet concentration. This can be seen by using a radiation boundary condition

$$-\epsilon_p \frac{\partial C}{\partial y} \Big|_w = VC(w) \quad (32)$$

where V is the velocity with which drops move to the boundary. If ϵ_p is represented by the product of V and a characteristic length L then (32) can be rewritten as

$$-VL \frac{\partial C}{\partial y} \Big|_w \equiv VC(w) \quad (33)$$

If L is small (as in the case for molecular diffusion) and $(\partial C/\partial y)_w$ is finite, then $C(w) = 0$. However, if L is of the order of the length scale characterizing $\partial C/\partial y$, then $C(w)$ needs to be a finite number.

Lee et al (1989b) give the following formulation for the boundary condition:

$$\frac{\partial C}{\partial y} \Big|_w (t-t') = \sqrt{\frac{2}{\pi}} \left(\frac{v^2}{v^2} \right)^{1/2} C f \quad (34)$$

The function f is the fraction of the particles moving toward the wall.

The Lagrangian correlation is taken to be

$$R_p^L = \exp \left[- (t - t') / \tau_{LP} \right] \quad (35)$$

Following arguments of Binder & Hanratty (1991), $f(t)$ may be approximated as

$$f(t) = \frac{1}{2} \left[1 - \exp \left(-t - t' / \tau_{LP} \right) \right] \quad (36)$$

Initially all of the particles from a wall source are moving away from the wall so $f(0) = 0$. The function $f(t)$ approaches 1/2 asymptotically at large times with the same time dependence as the diffusivity.

(b) Analysis of vertical annular flow

Binder & Hanratty (1991) used the approach outlined in the previous section to analyze vertical gas-liquid annular flow in a pipe under conditions that the concentration field is fully-developed. Here, the droplet field is pictured to result from a series of differential ring sources along the wall whose behavior are described as a solution to (28) with $\nabla_y = 0$, subject to boundary condition (34).

For vertical gas-liquid annular flows $\beta \tau_{LF}$ is typically in the range of 0.01 to 0.2, $\tau_p^+ > 20$ and $V_T / u^* < 1$. This means that the droplets are not following the turbulence

$\left(\frac{v^2}{v^2} \neq \frac{u^2}{u^2} \right)$, but that $\varepsilon_p = \varepsilon_F$. From (21), $\left(\frac{v^2}{v^2} \right)^{1/2} / \left(\frac{u^2}{u^2} \right)^{1/2} = 0.1$ to 0.5 and $\tau_{LP} / \tau_{LF} = 0.014$ to 0.28 for gas-liquid

annular flow. Characteristic Lagrangian lengths scale can be defined as $L^P = \left(\frac{v^2}{v^2} \right)^{1/2} \tau_{LP}$ and as $L_F = \left(\frac{u^2}{u^2} \right)^{1/2} \tau_{LF}$

so that $L_P / L_F = 10$ to 2.

Figure 1 shows typical calculation for a single ring source by Binder & Hanratty (1991). Values of $\tau_{LF} u^* / 2a = 0.046$ and $\frac{u^2}{u^2} \approx 0.9a$, given by Vames & Hanratty (1988), were used. Because of a lack of information about the details of how the droplets enter the field it was assumed that they were initially fully entrained in the flow field; that is, $\nabla_{x0} = U_x$ and the turbulence characteristics of the particles entering the field are given by (21).

The ordinate in figure 1 is $C_D u^* / R_A$, where R_A is the rate of atomization of the liquid wall layer per unit area. The abscissa is the dimensionless radial distance, r/a . The parameter for the different curves is the dimensionless time. The calculations are for quite sluggish drops, $\beta \tau_{LF} = 0.01$. At small times $f \approx 0$, so that there is no droplet deposition on the wall. A maximum occurs at the wall because there is a diffusion of drops away from the wall. As

f takes on values different from zero, deposition occurs and there is diffusion both to the wall and away from the wall. As a consequence, the maximum in the concentration profile occurs away from the wall. As time increases the concentration profile becomes more diffuse. At long enough times the maximum is at the pipe center and diffusion occurs only toward the wall. Eventually, all the drops redeposit and the concentration is zero over the whole pipe cross section.

The rate of deposition on the wall is given by

$$R_D = \sqrt{\frac{2}{\pi}} \left(\overline{v^2} \right)^{1/2} f(t-t') C_w(t-t') \quad (37)$$

For large enough times this can be looked upon as the sum of diffusion and free-flight resistances. Diffusion governs the concentration at the wall and free-flight is the final mechanism for deposition. According to (21), $(\overline{v^2})^{1/2}$ decreases with decreasing $\beta\tau_{LF}$. It is expected that the free-flight mechanism controls for $\beta\tau_{LF} \rightarrow 0$ and that the concentration gradients at the wall become very small. Thus, calculations for $\beta\tau_{LF} = 1.0$, shown in figure 2, give larger spatial variations of the droplet concentration for larger times than shown in figure 1 for $\beta\tau_{LF} = 0.01$.

Fully developed concentration profiles for large t can be calculated by summing the contributions from sources at different t' :

$$C = \int_0^t C_{SS}(t-t') dt' \quad (38)$$

Figure 3 shows results for values of $\beta\tau_{LF}$ calculated from the drops size measurements of Azzopardi (1985) and the friction velocity measurements of Asali et al (1985) to correspond to experiments of Gill et al (1965). The calculations and the measured profiles are seen to agree reasonably well.

A deposition constant can be defined for these fully developed concentration profiles as

$$k_D = R_D / C_B \quad (39)$$

where C_B is the bulk-averaged concentration. The calculations show that k_D / u^* varies with $\beta\tau_{LF}$. For large $\beta\tau_{LF}$ (or small particles) k_D / u^* approaches a constant value. As $\beta\tau_{LF}$ decreases (the particles increase in size) k_D / u^* decreases because $\overline{v^2} / u^{*2}$ decreases. With decreasing $\beta\tau_{LF}$ the relative role of free-flight becomes more important and, at small enough $\beta\tau_{LF}$, free-flight is completely controlling. Good agreement was obtained between the calculated values of k_D / u^* and laboratory measurements (Binder & Hanratty, 1991).

(c) Analysis of horizontal annular flow

Binder & Hanratty (1992) analyzed gas-liquid annular flow in a horizontal rectangular channel, using the methods outlined in the previous two sections. The range of $\beta\tau_{LF}$, τ_p and V_T / u^* characterizing the droplet behavior in this flow is the same as for vertical gas-liquid annular flow. The values of V_T / u^* , usually encountered, are small enough that the long-time turbulent diffusivities of the particles are approximately equal to the long-time turbulent

diffusivities of the fluid. However, it is large enough that the droplets are asymmetrically distributed and that the liquid layer on the top wall is thinner than the liquid layer on the bottom wall.

The analysis of this flow requires the introduction of another dimensionless group, a Froude number defined as $Fr = u^2 / gH$, where H is the channel height. For Stokesian particles,

$$Fr\beta\tau_{LF} = 0.046 u^*/V_T \quad (40)$$

Therefore, the reciprocal of $Fr\beta\tau_{LF}$ may be looked upon as a measure of the ratio of settling velocity to the magnitude of the velocity fluctuations of the fluid.

The walls are represented by a series of infinitesimal line sources. The strength of the sources on the bottom wall are greater than on the top wall because the wall layer is thicker. The behavior of these sources is obtained by solving (28), (29) and (30). Binder & Hanratty used $\nabla_{y0} = \sqrt{2/\pi} (\overline{v^2})^{1/2}$ where $\overline{v^2}$ is given by (21). A reasonable assumption for the initial x-component of the velocity is $\nabla_{x0} = S_0 \overline{U}_x$, where \overline{U}_x is the bulk average fluid velocity in the x-direction and S_0 is the initial slip ratio. Because of a lack of information about how the drops enter the flow, S_0 was taken as unity.

Deposition at the boundaries occurs by the parallel mechanism of turbulence and gravitational settling where R_{DT} is given by (37). The contribution due to settling is

$$R_D = R_{DT} + R_{DS} \quad (41)$$

$$R_{DS} = -C(o, t-t') \nabla_y (t-t') \quad (42)$$

at the bottom wall and

$$R_{DS} = C(H, t-t') \nabla_y (t-t') \quad (43)$$

at the top wall.

From a consideration of the behavior of these line sources the fraction of the drops originating from the bottom wall ($y = o$) that deposit on the top, F_{OH} , and on the bottom wall, F_{OO} , can be calculated. Similarly F_{HO} and F_{HH} can be calculated for sources on the top wall. From conservation of mass the ratio of the rates of deposition on the top, R_{DH} , and on the bottom, R_{DO} , walls can be calculated for a fully developed droplet field

$$\frac{R_{DH}}{R_{DO}} = \frac{F_{OH}}{F_{HO}} \quad (44)$$

Figure 4 gives the results of a calculation of R_{DH} / R_{DO} versus $Fr\beta\tau_{LF}$, which varies inversely with V_T / u^* . It is noted that results for different $\beta\tau_{LF}$ collapse, approximately, on a single curve. This plot may be interpreted as flow regime map. For $Fr\beta\tau_{LF} < 0.5-0.7$ deposition of droplets on the top wall is extremely small. This would seem to correspond to the stratified-annular flow defined by Williams (1990). For $0.5 - 0.7 < Fr\beta\tau_{LF} < 7.9$ an asymmetric annular flow exists for which the liquid is unequally distributed on the walls and the droplets in the gas phase are stratified. For $Fr\beta\tau_{LF} > 7.9$ gravitational settling is relatively unimportant and the liquid in the gas phase is distributed symmetrically.

Concentration profiles downstream of a wall source, similar to those shown in figures 1 and 2 can be calculated

for droplets that enter the field at time t' from infinitesimal line sources on the top and bottom walls. Fully-developed profiles can then be calculated by summing the contributions from a large number sources with (38). Example calculations for $\beta\tau_{LF} = 0.01$ and 1.0 are shown in figure 5. These correspond to values of $0.1 < Fr\beta\tau_{LF} < 1000$, or $0.00092 < V_T / u^* < 0.40$. The curves for $Fr\beta\tau_{LF} = 0.1$ and 0.5 represent a stratified-annular flow; the curves for $Fr\beta\tau_{LF} = 1.0$ and 5.0 , an asymmetric annular flow; the curves for $Fr\beta\tau_{LF} = 10.0$ and 100 , a symmetric annular flow. The parameter R_{AH} / R_{AO} is the ratio of the rates of atomization from the top and bottom walls. Because the flow is fully developed $(R_{AH} / R_{AO}) = (R_{DH} / R_{DO})$.

(d) Analysis of sediment transport

The distribution of droplets in gas-liquid annular flow has strong similarities to sediment transport. Here a solid-liquid mixture flows through a horizontal enclosed space of height H . Because of gravitational effects, the particles distribute asymmetrically in the liquid and settle out on the bottom of the channel. If the liquid velocity is large enough, the rate at which settled particles are removed from the wall is such that complete suspension occurs. However, at low liquid velocities the rate of removal is smaller and a bed forms on the bottom wall.

Binder (1991) used the Lagrangian analysis outlined in part a of this section to calculate concentration profiles of suspended sediment and the load carried by the fluid. The concentration is considered small enough that the fluid turbulence is not affected by the presence of the particles and that particle-particle interactions are not important. The bottom of the channel is supplying particles to the system at a rate per unit area defined as R_A and particles are depositing at a rate per unit area of R_D . The approach taken by Binder was to consider the concentration field as resulting from a distribution of sources along the sediment bed, which have a strength proportional to R_A . A fully developed condition was considered for which $R_A = R_D$.

Sediment transport differs from horizontal annular flow in that the particles do not lose their identity when they reach the top boundary, as do liquid drops. One approach is to assume a perfectly reflecting boundary at the top. This would be treated in the manner outlined by Hanratty (1956). The boundary at $y = H$ would be ignored but a fictitious source would be located at $y = 2H$ at $t = t'$ of the same strength as the one at $y = 0$. This fictitious source would be analyzed with (28) except that $\nabla_y (t-t')$ would be calculated by using a negative gravitational constant.

Binder used a different assumption. He viewed the particles that strike the wall to fall out of an eddy so that the turbulence characteristics of particles coming off the wall are uncorrelated with the turbulence characteristics of particles approaching the wall. Following this viewpoint, Binder argued that the particles reaching the top boundary form new sources.

Another difference from gas-liquid annular flow is that the range of parameters characterizing the dynamics of the particles is different. For sediment transport $1 < \beta\tau_{LF} < 100$, $V_T / u^* \leq 1$ and $\tau_p^+ > 20$. For these conditions the turbulence characteristics of the particles are approximately the same as the turbulence characteristics of the fluid. However, τ_p^+ is large enough that particles move in free-flight through the viscous wall region. The calculations presented by Binder used the simplifying assumption that $\nabla_{y0} = \sqrt{2\pi} (\overline{v^2})^{1/2}$ and that $\nabla_{x0} = U_x$.

The rate of deposition to the bottom wall may be considered as the sum of contributions due to turbulence and gravitational settling as described by (37), (41) and (42). Figure 6 a plot of the ratio of the contributions due to turbulence and settling, R_{DT} / R_{DS} . These results are not strongly affected by changes in $\beta\tau_{LF}$. Furthermore the

particle Reynolds number, d_p^+ , is only important when the particles are non-Stokesian. As with gas-liquid annular flow the parameter $Fr\beta\tau_{LF}$ is a good means of characterizing the flow pattern.

For $Fr\beta\tau_{LF} > 2$ the deposition by turbulence is ten times greater than the deposition by settling. For $Fr\beta\tau_{LF} > 0.03$ the deposition by settling is ten times greater than that by turbulence. For $0.03 < Fr\beta\tau_{LF} < 2$ both turbulence and settling are important.

Fully developed concentration profiles are presented in figure 7 for $Fr = 0.01$ and $d_p^+ = 10$. In the ordinate the concentration is made dimensionless with the bulk concentration. In the abscissa the distance from the lower boundary is made dimensionless with the height of the channel. The profiles in figure 7 are characteristic of the regime where both turbulence and settling are important contributors to deposition. It is noted that the profile becomes increasingly stratified as R_{DT} / R_{DS} changes from 6 to 0.2. A depth, δ , of the suspended particles can be calculated if δ / H is defined as the location where $C / C_{wall} = 0.01$. In this way, values of $\delta / H = 0.22$ and $\delta / H = 0.40$ are calculated for $Fr\beta\tau_{LF} = 0.05, 0.1$. Using this criterion the suspended solids fill the entire channel for $Fr\beta\tau_{LF} = 0.5, 1.0$. This would suggest that there is a fuzzy liquid slurry interface for small $Fr\beta\tau_{LF}$ and that this interface ceases to exist at a value of $Fr\beta\tau_{LF}$ between 0.1 and 0.5.

9. Aerosol deposition

Aerosol deposition, unlike the situations treated in the previous section, is characterized by $\tau_p^+ \leq 10$. The classical theory by Friedlander and Johnstone (1957) (for particles large enough that Brownian motion is not important) is that particles are transported by turbulent diffusion to a location in the viscous wall region from which they move in free-flight to the wall. The rate of deposition is very sensitive to changes in the free-flight location because the turbulent diffusivity and the turbulent velocity fluctuations vary dramatically with distance from the wall.

A number of modifications of the original implementation of this idea have been proposed but no physically sound explanation of measurements of the rate of deposition has evolved. McLaughlin (1989) and Brooks et al (1992) have shown how computer experiments can be used to obtain the type information about free-flight that is needed to make theoretical progress with the problem. The experiments are carried out in a direct numerical simulation of turbulent flow in a channel. The flow is seeded with aerosol particles and the paths of these particles are followed by solving the equation of motion of the particles. Results from these studies are quite different from classical ideas.

Figure 8 shows a calculated concentration profile for particles with $\tau_p^+ = 5$. In this experiment the particles originated in the $y^+ = 40$ plane at time zero. The only force considered was Stokesian drag. The lift force, the Magnus force and wall effects were ignored. At times of the order of $t^+ = 300$ an approximately stationary state is observed in the region displayed in figure 8.

The picture that emerges from these experiments is different from that given by Friedlander & Johnstone. It is noted that there is an accumulation of particles close to wall. Particles are brought to the wall by the turbophoretic phenomenon described in section 5. This is actually opposed by turbulent diffusion. The particles start a unidirectional flight to wall from different distances, rather than from a fixed distance. The average velocity of particles on this free-flight is much larger than the local $\overline{v^2}$ or the local $\overline{u^2}$.

The solid curve in figure 8 is the result of an analysis carried out by Brooke et al (1992), based on the physical picture outlined above. This calculation required information on the variation of $\overline{v^2}$ with y , the variation of the

turbulent diffusion coefficient with y and a distribution function characterizing the distance from the wall at which free-flight began. Consequently, it is by no means a complete theory.

Acknowledgement

This work is supported by the Transport Phenomena Program of the National Science Foundation and by the Basic Engineering Sciences Program of the United States Department of Energy.

REFERENCES

- Andreussi, P. & B. J. Azzopardi 1983 Droplet deposition and interchange in annular flow. *Int. J. Multiphase Flow*, **9**, 691-696.
- Asali, J. C., Hanratty, T. J. & P. Andreussi 1985 Interfacial drag and film height for vertical annular flow. *A.I.Ch.E. J.*, **31**, 895-902.
- Azzopardi, B. J. 1985 Drop sizes in annular two-phase flow. *Expts. Fluids*, **3**, 53-59.
- Batchelor, G. K. 1949 Diffusion in a field of homogeneous turbulence. *Australian J. Sci. Res.*, **2**, 437.
- Berlemont, A., Desjonqueres, P. & G. Gousebet 1990 Particle Lagrangian simulation in turbulent flows. *Int. J. Multiphase Flow*, **16**, 19-34.
- Binder, J. L. 1991 Use of Lagrangian methods to describe particle deposition and distribution in dispersed flow. Ph.D. thesis, Univ. of Illinois, Urbana.
- Binder, J. L. & T. J. Hanratty 1991 A diffusion model for droplet deposition in gas/liquid annular flow. *Int. J. Multiphase Flow*, **17**, 1-11.
- Binder, J. L. & T. J. Hanratty 1992 Use of Lagrangian methods to describe drop deposition and distribution in horizontal gas-liquid annular flows. To be published *Int. J. Multiphase Flow*.
- Brenner, H. 1961 Slow motion of a sphere through viscous fluid toward a plane surface. *Chem. Eng. Sci.*, **16**, 242.
- Brooke, J. W., Hanratty, T. J. & J. B. McLaughlin 1992 The influence of turbophoresis on aerosol deposition, in publication.
- Brooke, J. W., Kontomaris, K., Hanratty, T. J. & J. B. McLaughlin 1992 Turbulent deposition and trapping of aerosols at a wall. *Phys. Fluids A*, **4**, 825-834.
- Burnage, H. & S. Moon (1990) Predetermination de la dispersion de particules matérielles dan un écoulement turbulent. *C.R. Acad. Sci. Paris*, **310**, Serie II, 1595-1600.
- Calabrese, R. V. & S. Middleman 1979 The dispersion of discrete particles in a turbulent fluid field. *A.I.Ch.E. J.*, **25**, 1025-1035.
- Caporaloni, M., Tamprieri, F., Trombetti, F. & O. Vittori 1975 Transfer of particles in nonisotropic air turbulence. *J. Atmos. Sci.*, **32**, 565-568.
- Cherukat, P. & J. B. McLaughlin 1990 Wall-induced lift on a sphere. *Int. J. Multiphase Flow*, **16**, 899.
- Corrsin, S. 1959 Progress report on some turbulent diffusion research. *Adv. in Geophys.*, **6**, 116-184.
- Corrsin, S., & J. Lumley 1956 On the equation of motion for a particle in a turbulent fluid. *Appl. Sci. Res.*, **A6**, 114-116.
- Cox, R. G., & H. B. Brenner 1967 The slow motion of a sphere through a viscous fluid towards a plane surface: II. small gap widths, including inertial effects. *Chem. Eng. Sci.*, **22**, 173.
- Cox, R. G., & S. K. Hsu 1977 The lateral migration of solid particles in a laminar flow near a plane. *Int. J. Multiphase Flow*, **3**, 201.
- Csanady G. T. 1963 Turbulent diffusion of heavy particles in the atmosphere. *J. Atmos. Sci.*, **20**, 201-208.
- Eckelman, L. D. & T. J. Hanratty 1972 Interpretation of measured variations of the eddy conductivity. *Int. J. Heat Mass Transfer*, **15**, 2231.
- Friedlander, S. K. 1957 Behavior of suspended particles in a turbulent fluid. *A.I.Ch.E. J.*, **3**, 381.
- Friedlander, S. K. & H. F. Johnstone 1957 Deposition of suspended particles from the turbulent gas streams. *Ind. Engng. Chem.*, **49**, 1151-1156.
- Gill, L. E., Hewitt, G. F. & P.M.C. Lacey 1965 Sampling probe studies of the gas core in annular two phase flow: part 2. Studies of the effect of two-phase rates on phase and velocity distribution. *Chem. Eng. Sci.*, **19**, 665-682.
- Goldman, A. J., Cox, R. G. & H. B. Brenner 1967 Slow viscous motion of a sphere parallel to a plane wall: couette flow. *Chem. Eng. Sci.*, **22**, 653.
- Hanratty, T. J. 1956 Heat transfer through a homogeneous isotropic turbulent field. *A.I.Ch.E. J.*, **4**, 132-136.
- Hanratty, T. J. 1958 Note on the analogy between momentum transfer and heat or mass transfer for a homogeneous isotropic turbulent field. *A.I.Ch.E. J.*, **4**, 495-496.

- Hanratty, T. J. & D. L. Flint 1958 Velocity profile for fully-developed turbulent pipe flow, *A.I.Ch.E. J.*, **4**, 132-136.
- Hutchinson, P., Hewitt, G. F. & A. E. Dukler 1971 Deposition of liquid or solid dispersions from turbulent gas streams: A stochastic model. *Chem. Eng. Sci.*, **26**, 419.
- Kallio, G. A. & M. W. Reeks 1989 A numerical simulation of particle deposition in turbulent boundary layers. *Int. J. Multiphase Flow*, **15**, 433-446.
- Kraichnan, R. H. 1970 Diffusion by a random velocity field. *Phys. Fluids*, **13**, 22-31.
- Lee, M. M., Hanratty, T. J. & R. J. Adrian 1989a An axial viewing photographic technique to study turbulence characteristics of particles. *Int. J. Multiphase Flow*, **15**, 787-802.
- Lee, M. M., Hanratty, T. J. & R. J. Adrian 1989b The interpretation of droplet dispersion measurements with a diffusion model. *Int. J. Multiphase Flow*, **15**, 459-469.
- Lumley, J. L. 1957 Some problems connected with the motion of small particles in turbulent fluids, Ph.D. thesis, The Johns Hopkins University, Baltimore, MD.
- Lumley, J. L. 1978 Two-phase and non-Newtonian flows, Chapter 7 from *Turbulence* Bradshaw (ed.), Springer Verlag, Berlin.
- Maxey, M. R. & J. J. Riley 1983 Equation of motion for a small rigid sphere in a nonuniform flow. *Phys. Fluids*, **26**, 863-889.
- Maxey, M. R. 1987 The gravitational settling of aerosol particles in homogeneous turbulence and random flow fields. *J. Fluid Mech.*, **174**, 441-465.
- McCoy, D. D. & T. J. Hanratty 1975 Rate of deposition of droplets in annular dispersed flow. *Int. J. Multiphase Flow*, **3**, 319-331.
- McLaughlin, J. B. 1989 Aerosol particle deposition in numerically simulated channel flow. *Phys. Fluids A*, **1**, 1211.
- McLaughlin, J. B. 1991 Inertial migration of a small sphere in linear shear flows. *J. Fluid Mech.*, **224**, 261-274.
- Mei, R. 1990 Particle-dispersion in isotropic-turbulence and unsteady particle dynamics at finite Reynolds number. Ph.D. thesis, Univ. of Illinois, Urbana.
- Nir, A. & L. M. Pismen 1979 The effect of steady drift in the dispersion of a particle in turbulent fluid. *Fluid Mech.*, **94**, 369-381.
- Ormaney, A. & A. Martinon 1984 Prediction of particle dispersion in particle flows. *Physico-Chem. Hydrodynamics*, **5**, 229-240.
- Pismen, L. M. & A. Nir 1978 On the motion of suspended particles in a stationary homogeneous turbulence. *J. Fluid Mech.*, **84**, 193-206.
- Reeks, M. W. 1977 On the dispersion of small particles suspended in an isotropic turbulent field. *J. Fluid Mech.*, **83**, 529-546.
- Reeks, M. W. 1983 The transport of discrete particles in inhomogeneous turbulence. *J. Fluid Mech.*, **83**, 529.
- Rubinow, S. I. & J. B. Keller 1961 The transverse force on a spinning sphere moving a viscous fluid. *J. Fluid Mech.*, **11**, 447-459.
- Saffman, P. G. 1965 The lift on a small sphere in a slow shear flow. *J. Fluid Mech.*, **22**, 385.
- Saffman, P. G. 1968 Corrigendum to the lift on a small particle in a slow shear flow. *J. Fluid Mech.*, **31**, 624.
- Shuen, J. S., Chen, L. D. & G. M. Faeth 1983 Evaluation of a stochastic model of particle dispersion in a turbulent round jet. *A.I.Ch.E. J.*, **29**, 167-170.
- Snyder, W. H. & J. L. Lumley 1971 Some measurements of particle velocity autocorrelation functions in a turbulent flow. *J. Fluid Mech.*, **48**, 41-71.
- Squires, K. D. & J. K. Eaton 1990 The interaction of particles with homogeneous turbulence. Rept. MD-55, Thermal Division, Stanford Univ., Stanford, CA.
- Sun, Y. F. & S. P. Lin 1986 Aerosol concentration in a turbulent flow. *J. Colloid. Interface Sci.*, **113**, 315.
- Taylor, G. I. 1921 Diffusion by continuous movements. *Proc. Lond. Math. Soc.*, **151**, 196.
- Tchen, C. M. 1947 Mean value and correlation problems connected with the motion of small particles suspended in a turbulent fluid. Ph.D. thesis, Delft University, The Netherlands.
- Vames, J. S. & T. J. Hanratty 1988 Turbulent dispersion of droplets for air flow in a pipe. *Expts. Fluids*, **6**, 94-104.
- van Dop, H., Nieuwstadt, F.T.M. & J.C.R. Hunt 1985 Random walk models for particle displacements in inhomogeneous unsteady turbulent flows. *Phys. Fluids*, **28**, 1639-1651.
- Vasseur, P. and R. G. Cox 1977 On the motion of a small spheroidal particle in a viscous liquid. *Int. J. Multiphase Flow*, **3**, 201.
- Wells, M. R. & D. E. Stock 1983 The effects of crossing trajectories on the dispersion of particles in a turbulent flow. *J. Fluid Mech.*, **136**, 31-62.
- Williams, L. R. 1990 Effects of pipe diameter on horizontal annular flow, Ph.D. thesis, Univ. of Illinois, Urbana.
- Young, J. B. & T. J. Hanratty 1991a Optical studies of the turbulent motion of solid particles in a pipe flow. *Fluid Mech.*, **231**, 665-688.
- Young, J. B. & T. J. Hanratty 1991b Trapping of solid particles at a wall in a turbulent flow. *A.I.Ch.E. J.*, **37**, 1529-1536.

Yudine, M. I. 1959 Physical considerations on heavy particle diffusion. *Atmospheric Diffusion and Air Pollution Adv. Geophys.*, 6, 185.

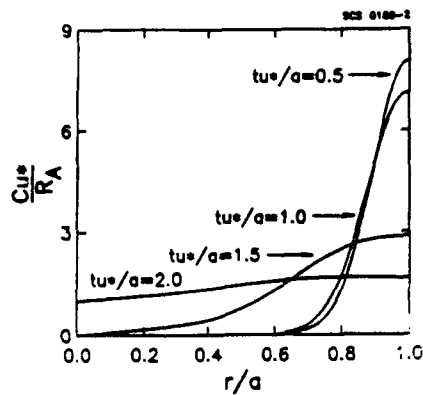


Figure 1. Concentration profiles at various times after turning on one instantaneous ring source ($\beta\tau_{LF} = 0.010$).

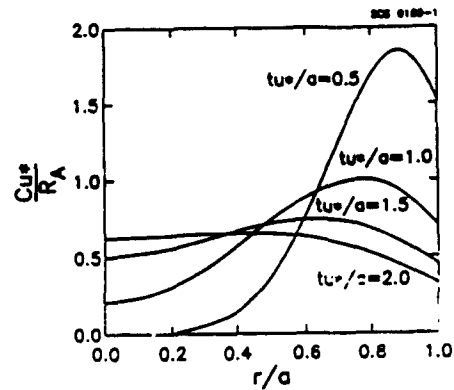


Figure 2. Calculated concentration fields for a ring source in vertical annular flow; $\beta\tau_{LF} = 1.0$.

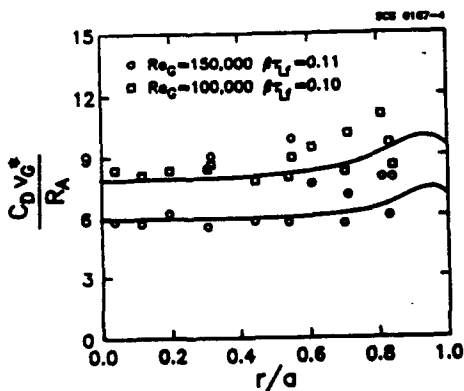


Figure 3. Comparison of measurements by Gill et al (1965) of gas-liquid annular flow with calculations.

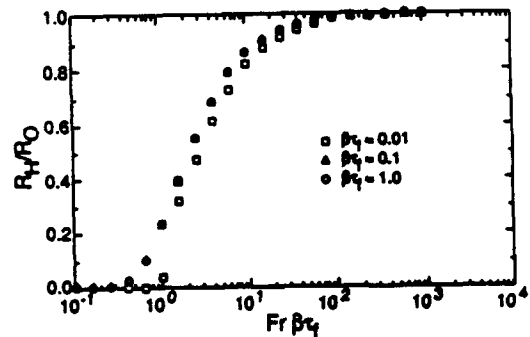


Figure 4. Relative rates of deposition to the top wall (R_H) and to the bottom wall (R_B) as a function of $Fr\beta\tau_{LF}$.

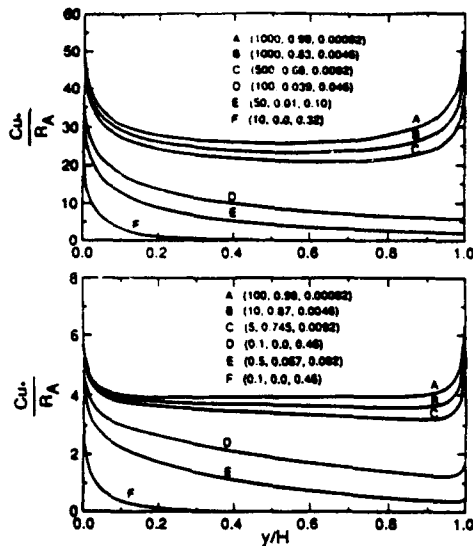


Figure 5. Fully developed concentration profiles in horizontal annular flow. The numbers in parentheses represent $(Fr, R_{AH}/R_{AO}, V_T/u^*)$; (a) $Fr\beta\tau_{LF} = 0.01$, (b) $Fr\beta\tau_{LF} = 1.0$.

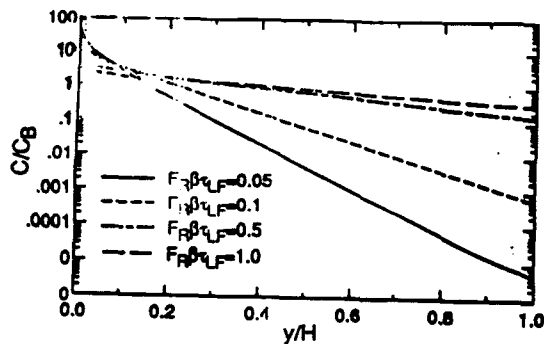


Figure 7. Calculated fully developed concentration profiles obtained by summing the contributions from multiple sources.

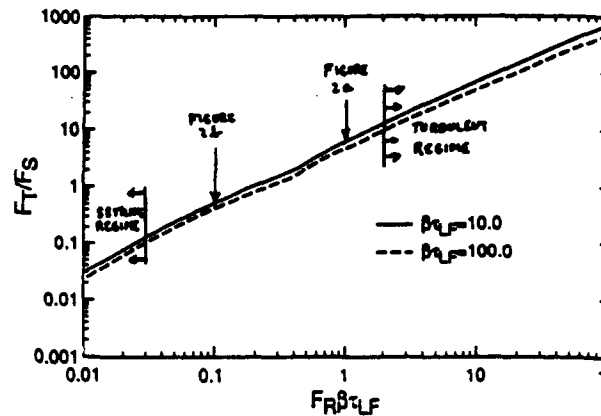


Figure 6. Ratios of the contributions of turbulence and of settling to particle deposition in slurry transport.

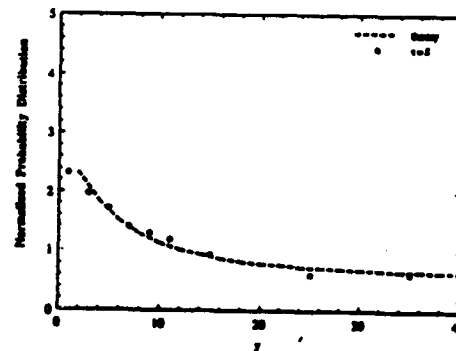


Figure 8. Concentration profile of aerosols for $\tau^+ = 5$. The open points are the computer simulation.

DYNAMICS OF COHERENT STRUCTURES IN TURBULENT JETS

Reda R. Mankbadi
National Aeronautics and Space Administration
Lewis Research Center
Cleveland, Ohio 44135

1. INTRODUCTION

The existence of large-scale coherent structures in shear flows has now been confirmed by an overwhelming number of experimental observations. The earlier work of Browand & Weidman (1976), Brown & Roshko (1974), Crow & Champagne (1971), and Winant & Browand (1974) demonstrated that the developing flow in both axisymmetric jets and two-dimensional shear layers is dominated by large-scale, wavelike coherent structures. Subsequently, coherent structures have been observed in other configurations, such as wakes (e.g., Miksad et al. 1982 and Wygnanski, Champagne & Marasli 1986), the initial region of planar jets (Antonia et al. 1986; Gutmark & Wygnanski 1976; Thomas & Chu 1989; Thomas & Goldschmidt 1986; and Wygnanski & Weisbrot 1987), elliptic jets (Gutmark & Ho 1983a; Husain & Hussain 1983; Tso & Hussain 1989; and Tso, Kovaszny & Hussain 1981), and the self-similar region of jets (e.g., Hussain 1986 and Thomas & Brehob 1986). These observations indicate that the structure starts as an instability wave on the shear layer, the amplitude of which reaches a maximum and then decays gradually downstream. The structures can merge with their neighbors as the shear layer develops downstream. The importance of coherent structures has warranted several reviews from different perspectives (e.g., Browand 1980; Cantwell 1981; Ho & Huerre 1984; Hussain 1983, 1986; Liu 1988, 1989; Lumley 1981; Roshko 1976, and Wygnanski & Petersen 1987).

Numerical simulations have succeeded in revealing some features of coherent structures (e.g., Acton 1976; Claus 1986; Corcos & Lin 1984; Corcos & Sherman 1984; Gatski & Liu 1980; Knight 1979; Mansour & Barr 1987; Patnaik, Sherman & Corcos 1976; Riley & Metcalfe 1980; and Scott 1987). Although as pointed out by Ho & Huerre (1984) the extraction of detailed information regarding the intrinsic scales of motion is more involved in the numerical simulation case, the numerical simulation has been quite helpful in clarifying several features. For instance, the dependence of the coalescence of two vortices on the initial phase difference was first obtained through numerical simulations. The numerical results can be compared with flow visualization and seem to yield a realistic modeling of the rollup of the shear layer and vortex pairing in the two-dimensional case.

The subject of coherent structures is a salient example in which the initial research objective was only to understand the basic physics involved, but soon after, this understanding provided the technological basis for using coherent structure ideas in flow control. Controlling the mixing of two fluids can be quite helpful in several technical applications, such as combustion, chemical processes, diffusion flames, and ejectors. Several experimental observations indicate that coherent structures and vortex interaction play a key role in shear layer growth. Winant & Browand (1974) demonstrated that successive merging of the vortices is responsible for most of the entrainment in the mixing layers. Browand & Weidman (1976) found that the vortex-pairing process promotes the transverse momentum and hence the mixing rate. Ho & Huang (1982) also showed that if a mixing layer is perturbed at very low forcing levels

near a subharmonic of the most amplified frequency, the spreading rate of the mixing layer is greatly manipulated. In addition, the experimental observations of Ahuja et al. (1982), Favre-Marinet & Binder (1979), Zaman & Hussain (1980), and others show that the growth of coherent structure increases the intensity of the fine-grained background turbulence, which is of technological importance. Such coherent structure investigations have also helped in understanding some aspects of the laminar-turbulent transition (Reshotko 1985, 1986) and in putting some of the coherent structure observations into practical applications. For a review on the use of coherent structure ideas in technologically important situations, the reader is referred to Hussain & Husain (1987) and Rice & Zaman (1987).

The objective of this review is to examine our current understanding of some of the coherent structure features as explained by the nonlinear stability theory. Emphasis is placed on turbulent jets for their obvious technological importance. The hope is that this understanding will enhance our ability to exercise further control over turbulent flows.

2. SYMBOLS

A	amplitude
a_{ij}, c	constants
a_0	speed of sound
C_r	total velocity component in observer's direction
cc	complex conjugate
D	differentiated with respect to r
d	nozzle diameter
dis	turbulence dissipation
$E(x)$	integrated kinetic energy in a slice of the jet
f	frequency, Hz
$G(\theta)$	normalization function
g	variable
I	integral that is a function of θ , ω , and N
I_{MA}	mean-flow advection integral
I_{MT}	mean-flow production integral of random turbulence
I_{MW}	mean-flow production integral of wave component
I_{TA}	turbulence advection integral
I_{WA}	wave advection integral
	imaginary
M_c	convection Mach number
MT	mean-flow production of turbulence
MW	mean-flow production of wave components
N	azimuthal wavenumber
P	pressure
Q	kinetic energy of wave
q	kinetic energy of turbulence
R	nozzle radius
R_{oc}	distance between observation point and jet exit
Re	Reynolds number
	real part
r	radial coordinate

$\bar{\tau}_{ij,mn}$	wave-induced stresses
S	Strouhal number
T	time scale for return to isotropy
T_{ij}	Lighthill's stress tensor
t	time
t_r	retarded time
U_e	exit mean velocity
U_i	mean velocity
u'_i	background, fine-scale random turbulence
\bar{u}_i	periodic component
V	mean-flow radial velocity
v	radial velocity
WT	energy transfer between waves and turbulence
WW	interaction between one wave and other existing waves
w	azimuthal velocity (angular velocity)
x	axial distance
y	transversal coordinate
α	complex wavenumber corresponding to frequency ω
β	phase angle of streamwise oscillatory velocity component
β_{12}	initial phase difference between waves of Strouhal numbers S_1 and S_2
β_{23}	initial phase difference between waves of Strouhal numbers S_2 and S_3
Δ	azimuthal angle at jet centerline
δ	displacement thickness
δ_{ij}	Kroneker's delta
δ_0	initial boundary-layer thickness
γ	angle between wave-induced stresses and strains
ϵ	dissipation
ζ	emission angle
θ	momentum thickness
ρ	fluid density
λ_0	initial wavelength
σ	argument of I
τ	period
ϕ	azimuthal angle
ψ	phase angle
ω	frequency, rad/sec
Subscripts:	
A	advection
$crit$	critical
e	jet exit
eff	effective

ex	excited
f	fundamental
i	initial
i,j,k,l,m,n	indices: 1,2,3
M	mean flow
oc	exit, centerline
p	peak
r	radial direction
s	subharmonic
T	turbulence
t	turbulence
ux	unexcited
W	wave
x	axial coordinate
θ	based on momentum thickness
ϕ	azimuthal angle
0	initial conditions

Superscripts:

—	time average of flow quantity
~	wavelike
*	complex conjugate
·	eigenfunction
'	differentiated with respect to r
ψ	phase

3. HYDRODYNAMIC STABILITY THEORY AND COHERENT STRUCTURES

Coherent structures in mixing layers can be viewed as a composition of interacting instability waves that propagate and amplify in the downstream direction. The observations of Bechert (1988), Binder & Favre-Marinet (1973), Crow & Champagne (1971), Dimotakis, Miake-Lye & Papantoniou (1983), Drubka, Reisenthal & Nagib (1989), and Moore (1977), among others, lend strong support to the traveling-wave representation of the large-scale structure. For example, Crow & Champagne (1971) showed that linear stability theory can predict some of the observed features of the preferred mode of an axisymmetric jet. Also, Crighton & Gaster (1976) took the divergence of the jet into consideration and calculated the preferred mode of the velocity profile two diameters downstream of the nozzle. The suitability of the spatial formulation, over the temporal one, in describing the initial growth stage of the shear layer instability was established by several experiments, such as those of Browand (1966), Cohen & Wygnanski (1987a,b), Gutmark & Ho (1983b), Ho & Huang (1982), Mattingly & Chang (1974), and Thomas & Chu (1989), as well as by analytical studies, such as those of Huerre & Monkewitz (1985) and Monkewitz & Huerre (1982). As pointed out by Liu (1988), if one extends the physical ideas from nonlinear hydrodynamic stability and transition in laminar flows (e.g., Stuart 1963, 1965), it is not entirely surprising that such instabilities and transitional structures should also occur in the geometrically similar turbulent shear flows.

The fluid motion can therefore be split into three kinds of motion: a time-averaged motion $\bar{U}_i(\underline{x})$; a periodic, organized, large-scale wavelike structure $\tilde{u}_i(\underline{x},t)$; and a background, fine-scale random turbulence $u_i'(\underline{x},t)$. Thus,

$$u_i(\underline{x}, t) = \overline{u_i(\underline{x})} + \tilde{u}_i(\underline{x}, t) + u_i'(\underline{x}, t) \quad (1)$$

and the pressure P is similarly split. The usual time average of a given quantity q is denoted by an overbar and is defined as

$$\overline{q(\underline{x})} = T^{-1} \int_0^T q(\underline{x}, t) dt, \quad (2)$$

where T is at least greater than the period τ of the large-scale structure. The conditional average, which is here the phase average, is denoted by $\langle \rangle$ and is defined as

$$\langle q(\underline{x}, t) \rangle = \lim_{N \rightarrow \infty} N^{-1} \sum_{n=0}^N (q(\underline{x}, t + n\tau)). \quad (3)$$

The process of using averaging to separate the governing equations has been discussed in detail by Hussain & Reynolds (1970).

By using ideas from the nonlinear stability theory (Ko, Kubota & Lees 1970; Liu 1971; and Stuart 1960, 1967, 1971), the coherent structure component can be written as a superposition of several interacting Fourier components, which, in polar coordinates, takes the form

$$\tilde{u}_i = \sum_{m,n} |A_{mn}(\underline{x})| \tilde{u}_{i,mn}(r, \theta) \exp[i\psi_{mn}(\underline{x}) - i\omega_m t + iN\phi] + cc \quad (4)$$

The assumption here is that the Fourier coefficient can be separated into an amplitude that is a function of the downstream coordinate x and a transversal shape function of the transversal coordinate (r or y) at a given location along the jet. The amplitude A is to be determined from nonlinear analysis; the transversal profile $\tilde{u}_{i,mn}(r, \theta)$ is taken as the eigenfunction given by the locally parallel linear stability theory (e.g., Michalke 1971). The phase angle ψ can be assumed to be given by the linear theory, as was done in numerous investigations, or to be governed by its own nonlinear evolution equation as was done in Lee (1988), Lee & Liu (1989), and Mankbadi (1986, 1991). Here N is the azimuthal number and cc denotes the complex conjugate.

The assumption that the profiles of the coherent components are given by the locally parallel linear theory follows from the fact that the governing momentum equation of the coherent components reduces to the Orr-Sommerfeld equation upon linearization. The comparisons in Mankbadi & Liu (1981) between the theoretically calculated transversal profiles based on the locally parallel linear stability theory and the measurements of Favre-Marinet & Binder (1979) confirm this assumption. This issue has also been addressed in greater detail by Strange & Crighton (1981); by comparing the linear theory with their measurements, they concluded that although the amplification rate of coherent components is not well predicted by the linear theory, the transverse distribution of the coherent quantities is well predicted by the linear theory. The same conclusion has now been confirmed by other experimenters, such as Cohen & Wygnanski (1987a,b), Gaster, Kitt & Wygnanski (1985), Thomas & Chu (1989), Weisbrodt (1984), Wygnanski & Petersen (1987), and Zhang, Ho & Monkewitz (1985).

In the triple decomposition the time-averaged momentum equation is replaced by a phase-averaged one. The classical time-averaged Reynolds stresses are also replaced by phase-averaged ones $\langle u_i' u_j' \rangle$. These phase-averaged stresses can then be split into the time-averaged component and oscillatory modulated component:

$$\langle u_i' u_j' \rangle = \overline{u_i' u_j'} + \tilde{\tau}_{ij} \quad (5)$$

The closure problem now is not only for the classical time-averaged Reynolds stresses but also for the wave-induced stresses \bar{r}_{ij} . The latter are defined as the difference between the conditional and the time average of the instantaneous fine-grained turbulent stresses. These modulated stresses play an essential role in the energy exchange between the large-scale structure and the fine-grained turbulence. By time averaging the product of these stresses with the appropriate wave rates of strain, one can explain the local kinetic energy transfer mechanism.

4. DYNAMICS OF ENERGY TRANSFERS AMONG DIFFERENT SCALES OF MOTION

4.1. GOVERNING INTEGRAL EQUATIONS

To understand the energy transfer mechanisms, we consider here the kinetic-energy equations of the different scales of motion in a turbulent axisymmetric jet. The integral kinetic energy equation of the mean flow can be obtained by applying boundary-layer approximations to the mean quantities, that is, $\partial(\bar{\cdot})/\partial x \ll \partial(\bar{\cdot})/\partial r$, $\nabla \ll U$. These approximations are applied to the averaged equations of motion, viscous terms are neglected, and the equations are integrated over r and ϕ . The resulting mean-flow energy equation is given by

$$\frac{1}{2} \frac{d}{dx} \int_0^\infty \bar{U}^3 r dr = - \int_0^\infty -\bar{u}\bar{v} \frac{\partial \bar{U}}{\partial r} r dr - \int_0^\infty -\overline{u'v'} \frac{\partial \bar{U}}{\partial r} r dr, \quad (6a)$$

which can be written symbolically as

$$\frac{d\theta}{dx} \frac{1}{2} \frac{d}{d\theta} \int_0^\infty \bar{U}^3 r dr = -MW - MT \quad (6b)$$

where θ is the momentum thickness and MW and MT are the first and second integrals, respectively, on the right side of equation (6a). Equation (6) states that the growth of the momentum thickness (the drain of the mean-flow energy) is governed by the mean-flow production of the wave components MW and by the mean-flow production of the turbulence MT .

The integral energy equation for the random turbulence is obtained by applying boundary-layer approximations to the mean quantities and by handling the viscous dissipation terms in the usual manner. After integrating over r and ϕ , the turbulence kinetic energy equation reduces to

$$\frac{d}{dx} \int_0^\infty \bar{q} \bar{U} r dr = \int_0^\infty -\overline{u'v'} \frac{\partial \bar{U}}{\partial r} r dr + \int_0^\infty \left[\bar{r}_{ij} \frac{\partial \bar{u}_i}{\partial x_j} - \frac{\bar{v}}{r} \bar{r}_{\phi\phi} + \frac{\bar{w}}{r} \bar{r}_{r\phi} \right] r dr - \frac{1}{Re} \int_0^\infty \frac{\partial u'_i}{\partial x'_k} \frac{\partial u'_j}{\partial x'_k} r dr \quad (7a)$$

which can be written as

$$\frac{d}{dx} \int_0^\infty \bar{q} \bar{U} r dr = MT + WT - (dis). \quad (7b)$$

Equation (7) states that the development of the turbulence energy is governed by its production by the mean flow MT , by the energy transfer from the wave to turbulence WT , and by the turbulence dissipation (dis) .

The integral energy equation for the mn-wave component is obtained from the full energy equation in the same manner:

$$\begin{aligned} \frac{d}{dx} \int_0^\infty U Q_{mn} r dr = \int_0^\infty -\bar{u}_{mn} \bar{v}_{mn} \frac{\partial U}{\partial r} r dr - \int_0^\infty -\Phi_{mn} r dr \\ + \int_0^\infty \left[\langle \bar{u}_i \bar{u}_j \rangle_{mn} \frac{\partial \bar{u}_{i,mn}}{\partial x_j} + \frac{\bar{v}_{mn}}{r} \langle \bar{w}^2 \rangle_{mn} - \frac{\bar{w}_{mn}}{r} \langle \bar{w} \bar{v} \rangle_{mn} \right] r dr, \end{aligned} \quad (8a)$$

where

$$-\phi = \bar{r}_{ij,nn} \frac{\partial \bar{u}_{i,mn}}{\partial x_j} + \frac{1}{r} \overline{\bar{v}_{mn} \bar{r}_{\phi\phi,mn}} - \frac{\bar{w}_{mn}}{r} \bar{r}_{r\phi,mn}$$

This system of equations can be written in the form

$$\frac{d}{dx} \int_0^\infty U \bar{Q}_{mn} r dr = MW_{mn} - WT_{mn} + WW_{mn} \quad (8b)$$

Equation (8) states that the development of the wave energy is governed by the mean-flow production of this particular wave MW_{mn} , by the energy transfer between this wave and the turbulence WT_{mn} , and by the interactions between this wave and other existing waves WW_{mn} .

4.2. MODE DECOMPOSITION AND INTERACTIONS

In the mean-flow energy equation (6) the production of all waves is given by

$$MW = - \int_0^\infty - \bar{u}\bar{v} \frac{\partial U}{\partial r} r dr \quad (9)$$

With the use of equation (4) the waves' Reynolds stress $\bar{u}\bar{v}$ can, in general, be written as

$$\bar{u}\bar{v} = \sum_{m,n} \left(u_{mn} v_{mn}^* + cc \right) + \sum_{\substack{m,k,\ell \\ l \neq \ell}} \left\{ u_{mk} v_{m\ell}^* \exp[i(N_k - N_\ell)\phi] + cc \right\} \quad (10)$$

The first summation is over the product uv^* of the same wave. These terms are axisymmetric irrespective of their azimuthal number. The second summation over the product uv^* is produced by waves of the same frequency but different azimuthal numbers. These terms are not axisymmetric and therefore destroy the symmetry of the mean flow. Note that these terms vanish unless there is more than one azimuthal component of the same frequency. Thus, this is consistent with Cohen & Wygnanski's (1987a,b) conclusion that single-mode excitation cannot destroy the axisymmetry of the mean flow. The azimuthally dependent terms in equation (10) vanish when integrated over ϕ . Therefore they redistribute the mean-flow energy in the azimuthal direction but do not contribute to the total energy integrated over ϕ . Because the mean-flow energy in equation (6) is integrated over ϕ , these nonaxisymmetric terms vanish and the mean-flow production of the wave can be written as

$$MW = \sum_{m,n} MW_{mn} \quad (11)$$

with

$$MW_{mn} = \int_0^\infty u_{mn} v_{mn}^* \frac{\partial U}{\partial r} r dr + cc \quad (12)$$

Therefore the mean-flow productions of the waves are given by the linear superposition of the individual mean-flow production of each wave.

In the turbulence energy equation (7) the energy transfer between the waves and the turbulence WT is given by

$$WT = \int_0^\infty \left(\bar{r}_{ij} \frac{\partial \bar{u}_i}{\partial x_{ij}} - \frac{\bar{v}}{r} \bar{r}_{\phi\phi} + \frac{\bar{w}}{r} \bar{r}_{r\phi} \right) r dr \quad (13)$$

where the wave-induced stresses are $\bar{r}_{ij} = \langle u_i' u_j' \rangle - u_i' u_j'$. Now let us decompose \bar{r}_{ij} as we did for \bar{u} , that is,

$$\bar{r}(x,r,\phi,t) = \sum_{m,n} \bar{r}_{mn}(x,r) \exp(-i\omega_m t + iN_n \phi) + cc \quad (14)$$

Thus $\overline{\tilde{u}\tilde{u}}$ is generally given by

$$\overline{\tilde{u}\tilde{u}} = \sum_{m,n} \left(r_{mn} u_{mn}^* + cc \right) + \sum_{\substack{m,k,\ell,n \\ l \neq \ell}} \left\{ r_{n\ell} u_{mk}^* \exp[i(N_k - N_\ell)\phi] + cc \right\} \quad (15)$$

The first summation is over the product produced by the same wave. The second summation is over the product produced by two waves of the same frequency and different azimuthal numbers. This second summation vanishes upon integration over ϕ . Thus with the energy defined as integrated over ϕ we can write

$$WT = \sum_{m,n} WT_{mn}$$

with

$$WT_{mn} = \int_0^\infty \left(\overline{\tilde{r}_{ij,mn}} \frac{\partial \tilde{u}_{i,mn}}{\partial x_j} - \frac{\tilde{v}_{mn}}{r} \overline{\tilde{r}_{\phi,mn}} + \frac{\tilde{w}_{mn}}{r} \overline{\tilde{r}_{r,mn}} \right) r \, dr \quad (16)$$

Therefore the turbulence energy exchange with the waves is given by the linear superposition of the energy exchanges between the turbulence and each individual wave.

Next we consider the wave-wave interactions appearing in equation (8a): namely,

$$WW_{mn} = \int_0^\infty \left(\overline{\langle \tilde{u}_i \tilde{u}_j \rangle_{mn}} \frac{\partial \tilde{u}_{mn}}{\partial x_j} + \frac{\tilde{v}_{mn}}{r} \overline{\langle \tilde{w}^2 \rangle_{mn}} - \frac{\tilde{w}_{mn}}{r} \overline{\langle \tilde{w} \tilde{v} \rangle_{mn}} \right) r \, dr \quad (17)$$

Because of the time averaging and the azimuthal integration these terms are generally zero unless ω and N simultaneously satisfy one of the following sets of conditions:

$$\begin{aligned} \omega_m &= \omega_k + \omega_\ell & \text{and} & & N_n &= N_k + N_\ell \\ \text{or} & & & & & \\ \omega_m &= \omega_k - \omega_\ell & \text{and} & & N_n &= N_k - N_\ell \end{aligned} \quad (18)$$

These are the same relations given by Cohen & Wygnanski (1987a,b). Equation (18) is not quite a restrictive condition because if one starts with only two frequency components, they can amplify other frequency components that satisfy the conditions of equation (18). If the process is repeated, an enormous number of frequency components can be amplified. This analysis is applicable to an unlimited number of components. Mankbadi (1991) considered the interactions among only six wave components: three axisymmetric frequency components and three first-helical frequency components. The frequencies of the helical components matched those of the axisymmetric components. In principle, these initial wave components can interact with each other to generate an enormous number of other frequency and azimuthal components. However, only the interactions among these initial components were considered. Thus other frequency and azimuthal components that could be nonlinearly generated were forced to be identically zero. The frequencies were chosen to satisfy the harmonic relations: that is, with $m = 1, 2, 3$. Thus each two consecutive frequencies are related to each other by subharmonic-fundamental relations

$$\omega_m = (2)^{m-1} \omega \quad (19)$$

The lower frequency denotes that of the subharmonic, and the higher denotes that of the fundamental under these conditions.

The wave-wave interactions can be classified into three groups: (1) interactions among the axisymmetric waves, which can be manipulated to be in the form of subharmonic-induced stresses multiplied by fundamental-induced strains, (2) interactions among the helical waves, which produce nonaxisymmetric terms that vanish upon integrating over ϕ (thus with the energy defined as that integrated over ϕ the integrated interactions among the helical modes

are identically zero; this is an interesting result because it indicates that, unlike the axisymmetric modes, two first-helical frequency components cannot generate other frequency components), and (3) mixed interactions between the axisymmetric and the helical waves. The interactions between the first-helical and the axisymmetric components are formed by two subharmonic frequency components of different azimuthal numbers interacting with the first-helical fundamental component. The general form of the wave-wave interactions is given by

$$\begin{aligned}
 w_{ij,k\ell,mn} = & \int_0^{\pi} \left[\tilde{u}_{ij} \tilde{u}_{k\ell} \frac{\partial \tilde{u}_{mn}}{\partial x} + \tilde{v}_{ij} \tilde{u}_{k\ell} \frac{\partial \tilde{v}_{mn}}{\partial x} + \tilde{w}_{ij} \tilde{u}_{k\ell} \frac{\partial \tilde{w}_{mn}}{\partial x} \right. \\
 & + \tilde{u}_{ij} \tilde{v}_{k\ell} \frac{\partial \tilde{u}_{mn}}{\partial r} + \tilde{v}_{ij} \tilde{v}_{k\ell} \frac{\partial \tilde{v}_{mn}}{\partial r} + \tilde{w}_{ij} \tilde{v}_{k\ell} \frac{\partial \tilde{w}_{mn}}{\partial r} \\
 & + \frac{1}{r} \left(\tilde{u}_{ij} \tilde{w}_{k\ell} \frac{\partial \tilde{u}_{mn}}{\partial \phi} + \tilde{v}_{ij} \tilde{w}_{k\ell} \frac{\partial \tilde{v}_{mn}}{\partial \phi} + \tilde{w}_{ij} \tilde{w}_{k\ell} \frac{\partial \tilde{w}_{mn}}{\partial \phi} \right) \\
 & \left. + \frac{1}{r} \left(\tilde{w}_{ij} \tilde{v}_{k\ell} \tilde{v}_{mn} - \tilde{v}_{ij} \tilde{w}_{k\ell} \tilde{w}_{mn} \right) r \, dr \right]
 \end{aligned} \tag{20}$$

5. NONLINEAR DEVELOPMENT OF AMPLITUDE

5.1. PERTURBATION METHODS

Rational perturbation or expansion procedures have been applied to determine the nonlinear development of amplitude. This approach is dependent on weak nonlinearities or on a near-equilibrium situation in which the amplification rate is small (Stuart 1960). Monkewitz (1988) considered the weakly nonlinear interaction between the fundamental and subharmonic modes in an inviscid, parallel mixing layer. He has shown that a critical fundamental amplitude has to be reached before the subharmonic becomes phase locked with the fundamental and exhibits a modified growth rate. Cohen & Wygnanski (1987a,b) obtained a series solution in terms of a small parameter representing the amplitude of the wave and were able to obtain improvement in the saturation of the wave when their results were compared with the experimental results of Gaster, Kit & Wygnanski (1985).

Asymptotic analysis of critical-layer nonlinearity has also been used to explain some of the coherent structure observations. The critical layer is laterally located where the mean-flow velocity equals the phase speed. In this approach it is demonstrated that once the instability wave amplitude becomes sufficiently large, nonlinear effects become important in the critical layer but the flow outside the critical layer remains governed by the linear mechanisms. Goldstein & Hultgren (1988) demonstrated that the critical-layer nonlinearity causes the fundamental instability to undergo saturation upstream of the linear neutral stability point. Also, Goldstein & Leib (1988) and Hultgren & Goldstein (1990) have used the critical layer to investigate the rollup of the instability wave. Recently Hultgren (1991) studied the nonlinear spatial equilibration of an externally excited instability wave in a free shear layer. The flow in the critical layer is governed by a nonlinear vorticity equation that includes a spatial-evolution term. Expansions for the various streamwise regions of the flow were recombined into a single formula accounting for both shear-layer spreading and nonlinear effects. Good agreement with Thomas & Chu's (1989) experimental results was obtained.

5.2. INTEGRAL-ENERGY METHOD

The integral-energy method for determining the nonlinear development of coherent structures has been quite successful in describing many of their observed features. Therefore particular emphasis is placed here on this method and how it can interpret most features of the observed coherent structures. In this method, the integral-energy

equations (eqs. (6) to (8)), coupled with radial shape assumptions, are used to derive the nonlinear ordinary differential equations that describe the energy exchanges between the different scales of motion.

Because of the shape assumptions involved and the finite number of coherent modes considered, the integral-energy method is only an approximate one. However, it allows the study of the strong nonlinear interactions, whereas weakly nonlinear theories are necessarily restricted to small amplitudes. Applications of this method to different flow situations have been reviewed by Liu (1988, 1989). This method is illustrated here by considering the coherent structure and its interactions in a turbulent round jet.

The integral-energy equations (eqs. (6) to (8)) are a set of ordinary differential equations representing the energy exchanges among the different scales of motion. But shape assumptions for the mean flow, the waves, and the turbulence are required in order to perform the radial integration in the energy equations. As discussed in section 3 the shape of the local profile of each coherent component is taken as the eigenfunction obtained from the locally parallel linear stability solution at the corresponding parameters. The mean flow can be described by the two-stage hyperbolic tangent profile in terms of (r, θ) that was proposed by Michalke (1971) and used by several researchers to describe the mean flow in the initial region of the jet. The mean flow is thus characterized by the momentum thickness θ rather than by the axial distance. Therefore functional dependence on x in the integrals involved in the energy equations is replaced by functional dependence on θ .

As for the random turbulence several experimental observations (e.g., Bradshaw, Ferriss & Johnson 1964 and Davies, Fisher & Barratt 1963) have suggested that the radial distribution of the turbulent stresses can be represented by a Gaussian distribution in the form

$$\overline{u_i' u_j'} = a_{ij} E(x) G(\theta) \exp(-\eta^2) \quad (21)$$

$$\eta^2 = \frac{(r - 1)^2}{\theta^2 c}$$

where

Both a_{ij} and c are constants given in Mankbadi (1985a). The normalization function $G(\theta)$ is introduced such that $E_t(x)$ is the fine-grained turbulence energy over a section of the jet.

Such a turbulence model is based on a quasi-steady assumption (i.e., that the characteristics of the turbulence, in terms of radial profile and ratio of stresses, are not affected by the unsteadiness), although the intensity of turbulence is affected by unsteadiness. Some arguments are given in Mankbadi (1991) to justify this quasi-steady assumption, which has not yet been fully addressed experimentally for free shear flows. The use of rapid-distortion theory to account for such unsteady effects on the characteristics of turbulence seems to be promising (Mankbadi & Liu 1991).

An eddy viscosity model for the wave-induced stresses is inappropriate because it cannot predict the reversal of energy transfer from the mean flow to the coherent structure and from the coherent structure to the turbulence (this issue is discussed further in section 8). Instead, Mankbadi & Liu (1981) obtained a dynamic equation for the wave-induced stresses by considering the unaveraged equation for $u_i' u_j'$ and subtracting the time-averaged one from the phase-averaged one. The resulting equations for \tilde{r}_{ij} are linearized, producing a set of simultaneous linear equations for determining the radial distribution of \tilde{r}_{ij} across the jet. From the linearized form it can be shown that \tilde{r}_{ij} takes the form

$$\tilde{r}_{ij, mn} = |A_{mn}(x)| E_t(x) \tilde{r}_{ij, mn} \exp \left[i \left(\psi_{mn}(x) - \omega_m t + i N_n \phi \right) \right] + cc, \quad (22)$$

where $\tilde{r}_{ij, mn}$ are obtained from the resulting algebraic equations (Mankbadi & Liu 1981).

With these shape assumptions the energy equations (eqs. (6) to (8)) can be integrated across the jet to yield the following system of simultaneous ordinary differential equations: The mean-flow momentum thickness $\theta(x)$ is given by

$$\frac{1}{2} \frac{dI_{MA}}{d\theta} \frac{d\theta}{dx} = I_{MT}E_t - \sum_{m,n} I_{MW,mn}E_{mn}. \quad (23)$$

The turbulence kinetic energy $E_t(x)$ is given by

$$\frac{d}{dx} (I_{TA}E_t) = I_{MT}E_t + \sum_{m,n} I_{WT,mn}E_{mn}E_t - I_\epsilon E_t^{3/2}. \quad (24)$$

The energy of the mn wave $E_{mn}(x)$ is given by

$$\frac{d}{dx} (I_{WA,mn}E_{mn}) = I_{WM}E_{mn} - I_{WT,mn}E_{mn}E_t + WW_{mn}. \quad (25)$$

The phase angle $\psi_{mn}(x)$ is given by

$$E_{mn}I_{WA} \frac{d\psi_{mn}}{dx} = \pi S_{mn}E_{mn} + WW_{mn}, \quad (26)$$

Here $E_{mn} = |A_{mn}|^2$, S is the Strouhal number defined as $S = \omega d / 2\pi U_0$, and d is the nozzle diameter. In this system of equations I represents an integral that is, in general, a function of the momentum thickness θ , the Strouhal number S , and the azimuthal number N . These integrals are given in Mankbadi & Liu (1981) and Mankbadi (1985a). The left side of equation (23) is the mean-flow advection. The first term on the right side of equation (23) is the mean-flow production of the turbulence, and the second term is the production of each individual wave. In the turbulence energy equation (eq. (24)), I_{TA} is the integral of the turbulence advection by the mean flow. The first term on the right side of equation (24) is the turbulence produced by the mean flow, the second term is the turbulence energy exchanged with the waves, and the last term is the viscous dissipation. The first term on the right side of equation (25) is the wave production by the mean flow, the second term is the interaction with the turbulence, and the last term is the interaction of the mn wave with other waves. The phase-development equation (eq. (26)) is obtained in a manner similar to that used by Mankbadi (1986).

This system of equations (eqs. (23) to (26)) is subject to the initial conditions at $x = 0$, $\theta(0) = \theta_i$, $E_t(0) = E_{ti}$, and $E_{mn}(0) = E_{mni}$ and to the initial phase angle $\psi_{mn}(0) = \beta_{mn}$ with respect to a given reference.

6. DEVELOPMENT OF SINGLE-FREQUENCY COHERENT MODE

The development of a single-frequency instability wave in free shear flows has been investigated by an overwhelming number of researchers. One of the early experiments, in which the excitation level was considerably large, is that of Binder & Favre-Marinet (1973). In this experiment well-controlled unsteady forcing of a round jet was imposed by means of a rotating butterfly valve upstream of the nozzle exit. The phase-averaging technique, with the frequency of forcing as a reference, was used to reduce the large-scale structure from the total fluctuations. The physical picture derived from the experiment is that the large-scale structure first grows, because of extraction of energy from the mean flow, and subsequently decays downstream, because of the energy transfer to the fine-grained turbulence and the possible transfer of some of its energy back to the mean flow. The fine-grained turbulence is enhanced because it obtains energy from the mean flow and through the large-scale structure. Although the amplitude of the coherent structure in Binder & Favre-Marinet's (1973) experiment reached considerable levels (40 percent of the mean flow), the integral energy technique predicted results in close agreement with experiment (Mankbadi & Liu 1981).

6.1. STROUHAL NUMBER EFFECTS

The development of a single-frequency component in a turbulent round jet for various Strouhal numbers (Mankbadi & Liu 1981) is shown in figure 1. The figure shows that the streamwise lifespan of the wave is inversely proportional to the Strouhal number. Because the wavelength $2\pi/\alpha_r$ is the primary dimension that describes the wave geometry, it seems that the wave "recognizes" physical dimensions relative to its wavelength. For instance, for all Strouhal numbers considered, the wave decays to an amplitude of 0.1 A after an axial distance of about four times its wavelength. That is, for any Strouhal number, the wave makes four cycles along the jet before it disappears. Figure 3 also shows that the location of the peak moves closer to the nozzle exit with increasing Strouhal number. Thus high-frequency components dominate upstream and low-frequency ones dominate farther downstream, as one might expect (Alper & Liu 1978; Liu 1974; and Merkin & Liu 1975).

The "peak" or "most amplified" Strouhal number at a given axial location decreases with distance, as illustrated in figure 2. The peak Strouhal number is inversely proportional to x , which is consistent with Chan's (1974) experimental observations that the amplitudes of the pressure oscillations along the jet for different Strouhal numbers become similar if plotted against S_p .

The maximum attainable amplification as a function of Strouhal number is shown in figure 3 for a low excitation level of $10^{-6.5}$. At such a low excitation level the peak Strouhal number is about 0.7, but the results in Mankbadi & Liu (1981) show that the peak Strouhal number decreases to about 0.35 when the excitation level is increased to 10^{-3} .

6.2. SATURATION WITH INCREASING EXCITATION LEVEL

For low levels of excitation the maximum attainable peak of the coherent component is linearly proportional to its initial level. However, at higher excitation levels a saturation mechanism comes into effect (Mankbadi & Liu 1981). The production of the coherent component by the mean flow is proportional to the energy of the coherent component and inversely proportional to the local momentum thickness. Therefore higher initial levels of the coherent component cause excessive energy drain from the mean flow. This energy drain leads to rapid growth of the momentum thickness, and hence less energy is available for the subsequent development of the coherent component. Thus the coherent structure "chokes" from its own energy, further increase of the excitation level causes saturation, and the coherent component can no longer amplify.

This saturation mechanism has been observed experimentally by Fiedler & Mensing (1985) and Oster & Wygnanski (1982) in a turbulent mixing layer and by Raman, Rice & Mankbadi (1988) in a round jet. The ratio of the momentum thickness of the excited to the unexcited case at $x/d = 9$ is shown in figure 4 versus the excitation velocity. Both the theory of Mankbadi & Liu (1981) and experiment of Raman et al. (1988) point to the saturation trend in enhancing the momentum thickness via excitation. However, the theory underestimates the saturation value of the momentum thickness because the theory in this case ignores the appearance of the subharmonic, which becomes important downstream as discussed later.

This saturation effect points to the limitation of using single-frequency plane wave excitation to enhance jet mixing. Therefore using devices that provide higher levels of single-frequency excitation may not yield better jet mixing. More effective methods of flow control, such as simultaneous excitation of the fundamental and subharmonic waves, should be considered in order to obtain greater jet mixing enhancement.

6.3. TURBULENCE EFFECTS ON JET EXCITABILITY

The growth of the fundamental is due to the imbalance between its mean-flow production and its energy drain to turbulence (see eq. (24)). Increasing the initial turbulence energy reduces the growth of the instability components in two ways: directly, because increasing the turbulence level increases the energy drain from the stability component to the turbulence; and indirectly, because higher initial levels of the turbulence cause higher rates of energy transfer from the mean flow to the turbulence and consequently less mean-flow energy becomes available for amplifying the wave

component. The two mechanisms combined cause the initial turbulence to suppress the growth of instability components. The large-scale structure could thus be reduced, or possibly eliminated, by increasing the initial level of random turbulence as observed experimentally by Chandrsuda, Mehta, Weir & Bradshaw (1978).

6.4. EFFECT OF INITIAL MEAN-FLOW VELOCITY PROFILE

Crighton & Gaster (1976), Husain & Hussain (1979), Hussain & Zedan (1978a,b), and Oster, Wygnanski, Dziomba & Fiedler (1978) emphasized the importance of the initial mean-flow velocity profile for the stability of the developing shear layer. The role of initial mean-flow velocity profile can be investigated by using the integral approach and varying the initial momentum thickness θ_i . If $\theta_i = 0^\circ$, the mean-flow velocity profile resembles a tophat, and as θ increases, the initial profile becomes smoother. Because the tendency toward instability decreases with increasing θ (lower $(dU/dy)_{\max}$), the amplification of the coherent structure was found to decrease with increasing θ . Therefore the development of the coherent structure can be suppressed by designing the nozzle for a smoother mean-flow velocity profile, as was done in the experiment of Chan & Templin (1974).

7. FUNDAMENTAL-SUBHARMONIC INTERACTION AND VORTEX PAIRING

The early observations of Browand & Weidman (1976) and Winant & Browand (1974) indicate that the coherent structure develops into vortices that can pair downstream. Winant & Browand (1974) injected a filament of dye into the flow. The dye rolled into lumps that proceeded to pair with their neighbors, generating a larger and more sparsely distributed structure. The later experiments of Browand & Laufer (1975), Hussain & Clark (1981), Laufer & Zhang (1983), and Petersen (1978), among others, also confirm that the interactions between the vortices in an axisymmetric shear layer dominate the near-field flow dynamics.

The importance of the subharmonic in vortex pairing is indicated by the analytical and computational results of Patnaik, Sherman & Corcos (1976), Kelly (1967), and Riley & Metcalfe (1980), among others. In the experiment of Kibens (1980) a circular jet was excited with an azimuthally coherent perturbation at the most-amplified instability. The perturbation organized the large-scale structures in the shear layer into a sequence of successive vortex-pairing stages at fixed streamwise locations. After each pairing the peak frequency of the spectrum was found to be halved, indicating the amplification of the subharmonic. The connection between the subharmonic and vortex pairing was underscored by Ho & Huang (1982), who showed that for a mixing layer pairing of vortices is the product of the subharmonic instability. They found pairing to occur at the downstream location where the subharmonic saturates. Hence Ho & Huang (1982) viewed the subharmonic as a catalyst for vortex pairing. These experimental investigations suggest that vortex pairing can be viewed as the interaction between a fundamental instability wave and its subharmonic.

Considering a laminar shear layer, Liu & Nikitopoulos (1982), Nikitopoulos (1982), and Nikitopoulos & Liu (1984, 1987) split the total disturbance into fundamental and subharmonic components and used the integral energy technique to follow the development of each component. Their results (shown here as fig. 5) indicate good agreement with the experiments of Ho & Huang (1982) until the fine-grained turbulence becomes sufficiently important. The existence of multisubharmonics in a two-dimensional shear layer was also considered by Nikitopoulos & Liu (1989). The extension of the laminar shear layer case to the turbulence case was considered by Kaptanoglu (1984) and Liu & Kaptanoglu (1984, 1987).

Vortex pairing in a turbulent round jet was studied by Mankbadi (1985a), who used the integral-energy method. The total disturbance was split into coherent and random components. The coherent component was then considered to be composed of a fundamental one and successive harmonics or subharmonics. Vortex pairing was viewed as occurring when the subharmonic interacts with the fundamental and exceeds the level of the fundamental to become the dominant instability component (see fig. 6). Excitation at low-to-moderate Strouhal numbers was found to result in amplifying only the first subharmonic, which was found to be most pronounced if the excitation Strouhal number is

in the range 0.6 to 1.0. The results are in close agreement with the experimental data of Hussain & Zaman (1980) and Zaman & Hussain (1980). Excitation at higher Strouhal numbers results in the amplification of several subharmonics, which is in accordance with observations of Drubka (1981), Ho & Huang (1982), Hussain & Hussain (1983), Laufer & Zhang (1983), and Zaman & Hussain (1980). Increasing the Strouhal number moves the location of the first pairing closer to the nozzle exit, as also observed by Ho & Huang (1982) for the plane shear-layer case. The location of the subharmonic's peak was found to coincide with the rapid decay of the fundamental.

Zaman & Hussain (1980) adopted the view that for a circular jet rolled-up vortex rings undergo pairing under two distinctive conditions of excitation: the "shear-layer mode," and the "jet-column mode." The shear-layer mode is similar to the plane mixing-layer mode and is observed for the circular jet when the excitation Strouhal number based on the momentum thickness is about 0.012 and the exit boundary layer is laminar. It involves pairing of the near-exit thin vortex rings. Zaman & Hussain defined the jet-column mode as involving pairing of the thick vortex rings farther downstream. They are observed for both laminar and turbulent exit boundary layers when the excitation Strouhal number based on diameter is about 0.85. They concluded that the jet-column mode of pairing can form independently of the shear-layer mode, or from evolution of the shear-layer mode, or when the jet is excited directly in the jet-column mode. The predicted growth of the first subharmonic at the excitation Strouhal number range $S = 0.6$ to 1.0 in Mankbadi (1985a) did not account for the presence of the shear-layer mode and is therefore consistent with Zaman & Hussain's (1980) conclusion that the jet-column mode can occur independently of the shear-layer mode. But on the other hand the calculated development of the fundamental and its subharmonic in Mankbadi (1985a) indicates that there is a continuous response as the excitation Strouhal number increases. The especially pronounced amplification of the subharmonic when the jet is excited with a fundamental at $S = 0.8$ (fig. 6(b)) is attributed to the growth of the subharmonic being governed by both its interaction with the mean flow and the fundamental. It is well known that the most-preferred frequency associated with the mean-flow velocity profile of a jet corresponds to $S = 0.4$ (e.g., Gutmark & Ho 1983b; Hussain & Zaman 1981). When the jet is excited at a fundamental Strouhal number of 0.8, the corresponding subharmonic is at 0.4, which is the "preferred" Strouhal number of the jet, causing the subharmonic amplification to be particularly strong. Thus the specially strong pairing at a fundamental Strouhal number of 0.8, corresponding to the jet-column mode, is attributed to the characteristics of the mean-flow instability in addition to the fundamental-subharmonic interaction.

7.1. EFFECT OF EXCITATION LEVEL

The results in Mankbadi (1985a) indicate that the strength of the fundamental-subharmonic interaction increases nonlinearly with increasing initial level of the fundamental (fig. 7). The peak of either the fundamental or the subharmonic moves upstream as the initial level of the fundamental increases, as indicated by Laufer & Yen's (1983) measurements. However, beyond a certain level any further increase in the initial level of the fundamental reduces or suppresses the growth of the subharmonic. Large forcing levels can thus result in suppressing the vortex-pairing process as observed experimentally by Reynolds & Bouchard (1981). This saturation is caused by the excessive drain of the mean-flow energy by the fundamental, which reduces the available mean-flow energy for the subsequent growth of either the fundamental or the subharmonic. Thus there is an optimum excitation level that will produce maximum subharmonic amplification, as also concluded by Monkewitz (1982) for the two-dimensional shear-layer case.

7.2. ENERGY TRANSFERS

The study of the energy transfers between the different flow components along the jet indicates that the significance of each mechanism involved depends on the Strouhal number and on the streamwise location (Mankbadi 1985a). At moderate Strouhal numbers the fundamental's production by the mean flow is the dominant mechanism close to the exit (fig. 8). Subsequently the fundamental decays through three equally significant mechanisms: turbulence damping, generation of its subharmonic, and "negative production," in which energy is transferred from the

coherent component back to the mean flow. The fundamental amplifies the subharmonic through direct and indirect mechanisms. In the direct mechanism it transfers some of its energy to the subharmonic. In the indirect mechanism the enhanced level of the subharmonic results in increasing its direct production by the mean flow. The subharmonic decays mainly through turbulence dissipation. At higher Strouhal numbers the subharmonic can amplify a second or even higher subharmonic, which constitutes an additional decay mechanism for the first subharmonic.

8. REVERSAL OF REYNOLDS STRESSES

8.1. NEGATIVE MEAN-FLOW PRODUCTION OF COHERENT STRUCTURE

The stability wave grows by absorbing energy from the mean flow, but as the flow diverges in the downstream direction, the linear theory predicts a damped solution. This results in a negative mean-flow production of the coherent stability component (fig. 8), which signals the decay of the coherent component by returning some of its energy back to the mean flow. Because the mean-flow gradient does not change sign, this negative production results from reversal of the sign of the time-averaged coherent Reynolds stresses.

The reversal in the Reynolds stresses is not restricted to the streamwise location where the coherent component is decaying. Figure 9 (from Mankbadi 1985b) shows that at the streamwise location where the waves are growing the transverse distribution of the time-averaged coherent stresses shows transversal regions of negative stresses. This indicates that even if the net radially integrated energy transfer is from the mean flow to the coherent components, it can locally reverse direction.

Browand (1980) was the first to comment on the significance of negative production and its relation to the pairing process. It was also observed by Fielder, Dziomba, Mensing & Roegen (1981), Weisbrot & Wygnanski (1988), and Zaman & Hussain (1980) for a plane shear layer. Hussain & Zaman's (1980) measured contours of the phase-averaged coherent stresses are shown here as figure 10; the alternate regions of positive and negative values are quite apparent in the figure. This change in sign represents a reversal in the direction of energy transfer between the mean flow and the coherent structure.

Browand & Ho (1983) interpreted the negative Reynolds stresses as resulting from the tilt of the vorticity distribution. If the tilt is upstream on the low-speed side, the resulting momentum flux is away from the mixing layer, resulting in negative Reynolds stresses. As far as the stability theory is concerned, this negative production results from the phase alignment of the coherent velocity components as given by the eigenfunctions of the locally parallel linear stability solution. This phase alignment becomes negative particularly when the solution becomes damped; an explanation that is not in contradiction with the favorable or unfavorable tilt advocated by others. The success of the integral energy nonlinear stability theory in predicting such reversals in the energy transfer should be underscored because this "negative production" is quite significant in interpreting several observations but cannot be predicted by eddy viscosity models.

8.2. REVERSAL OF ENERGY TRANSFER BETWEEN LARGE-SCALE STRUCTURE AND TURBULENCE

The energy transfer between the coherent structure and the fine-grained turbulence is governed by the wave-induced stresses. The relative phase between \bar{v}_{ij} and the rates of strain determines the direction of this transfer. The total energy transfer between the large-scale structure and the fine-grained turbulence is the sum of the local transfers integrated across the jet. Typical transverse distribution of this energy is shown in figure 11 (from Mankbadi & Liu 1981). Because most of the local energy transfer is positive, the direction of the net total energy transfer is from the large-scale structure to the fine-grained turbulence, as expected. However, it is also clear from the figure that the local energy transfer can be in either direction and that it is not restricted from the large-scale structure to the fine-grained turbulence.

In earlier work eddy viscosity was used to model these wave-induced stresses (Liu 1971, 1974; Merkin & Liu 1975; and Morris 1974). However, such an eddy viscosity model implies one-way energy transfers from the mean flow

to the large-scale structure and from the large-scale structure to the fine-grained turbulence. Although this assumption may be generally true, the local energy exchange can, in fact, go either way, as shown in figure 11, from the large to the small or vice versa. This indicates the intrinsic weakness of the eddy viscosity model. Thus an eddy viscosity model ignores the detailed physical picture of the energy transfer mechanism although it has been useful in assessing the overall process. Favre-Marinet & Binder (1979) also concluded from his experiment that an eddy viscosity model for the wave-induced stresses is incorrect locally. Therefore the interaction between the large-scale structure and the fine-grained turbulence must be based on the detailed physical mechanisms of the wave-induced stresses.

9. EFFECT OF INITIAL PHASE-DIFFERENCE ANGLE BETWEEN FUNDAMENTAL AND SUBHARMONIC

Direct numerical simulations of vortex-pairing interactions in two-dimensional mixing (e.g., Patnaik, Sherman & Corcos 1976 and Riley & Metcalfe 1980) show that the pairing process is dependent on the phase difference between the fundamental and subharmonic instability waves. Monkewitz (1982) extended Kelly's (1967) temporal instability analysis of a spatial periodic mixing layer to include an arbitrary phase difference between the fundamental and the subharmonic. He concluded that an arbitrary initial phase difference leads to transients with two angles where the subharmonic growth rate is initially increased or decreased depending on the initial phase difference. Although Kelly and Monkewitz did not consider the influence of the subharmonic on the fundamental, Nikitopoulos (1982) and Nikitopoulos & Liu (1987) used the integral-energy method to study the fundamental-subharmonic interaction in a laminar shear layer, allowing the subharmonic to react nonlinearly on the fundamental. The fundamental-subharmonic interaction in a turbulent round jet (Mankbadi 1985a) was found to be dependent on an effective phase-difference angle $\psi_{\text{eff}} = \psi_f - 2\psi_s$, where ψ_f and ψ_s are the phase angles of the fundamental and subharmonic, respectively. Using weakly nonlinear stability theory, Monkewitz (1988) considered the spatial evolution of a fundamental mode and its subharmonic on an inviscid parallel mixing layer. His results show that a critical fundamental amplitude α_{crit} has to be reached before the subharmonic becomes phase locked with the fundamental and exhibits a modified growth rate. Monkewitz's results for the effect of the initial phase difference on the growth of the subharmonic are shown herein as figure 12. His analytical results, as well as those of Mankbadi (1985a, 1986), Nikitopoulos (1982), and Nikitopoulos & Liu (1987), show that the initial phase difference has a weak damping effect on the growth of the fundamental but a strong influence on the subharmonic. Depending on the initial phase difference, the fundamental-subharmonic interaction can either amplify or suppress the growth of the subharmonic as compared with its growth resulting from the mean-flow instability alone.

This dependence on the initial phase-difference angle has been confirmed in Zhang, Ho & Monkewitz's (1985) experiment in which a shear layer was subjected to a bimodal excitation. Their results show that significantly different vortex-merging patterns can occur as a result of changing the initial phase difference between the fundamental and the subharmonic. The experiments of Arbey & Ffowcs-Williams (1984), Ng & Bradley (1988), and Raman & Rice (1989) for a round jet also indicate that the subharmonic can be amplified or suppressed depending on the initial phase difference with respect to the fundamental.

The experimentally observed "jitter" in the location of pairing (e.g., Brown & Roshko 1974; Browand & Weidman 1976; Hussain 1986; Oster et al. 1978; Oster & Wygnanski 1982; and Zaman & Hussain 1980) can be explained by dependence on the initial phase-difference angle. If the subharmonic at the jet exit is at the proper phase-difference angle, it will be amplified, resulting in vortex pairing. If it is not at the proper phase-difference angle, the pairing process will be altered or possibly eliminated. The net outcome is the random variation in the location of pairing.

The jet instability thus acts as an amplifier not only with respect to selective frequencies, but also with respect to selective phase differences between the fundamental and the subharmonic (Mankbadi 1985a, 1986). In natural, uncontrolled conditions the phase of the initial components at the fundamental and subharmonic frequencies would vary randomly, resulting in a random initial phase difference between the two. The mean flow acts as the first

amplifier to amplify the stability component according to its frequency. The fundamental instability wave associated with the mean-flow profile will then act as a second amplifier that will amplify or dampen the subharmonic according to its relative phase difference. For a given frequency the most amplified subharmonic is thus the one with the proper phase difference.

9.1. EFFECT ON SPREADING RATE

Because vortex pairing is an important mechanism in the growth of a shear layer, the initial phase angle can, in turn, control the development of the shear layer. Figure 13 (from Mankbadi 1986) shows that the growth of a laminar, axisymmetric shear layer is governed by the initial phase and that it is maximum when the subharmonic is subjected to maximum amplification. In fact, choosing the initial phase difference to be the one predicted theoretically as the optimum results in the corresponding predicted growth of the shear layer being in good agreement with the corresponding experimental observations of Laufer & Zhang (1983). The stepwise development of the momentum thickness shown in figure 13 was also obtained by Nikitopoulos (1982) and Nikitopoulos & Liu (1987, 1989) for the two-dimensional mixing-layer case. Their results agree favorably with the corresponding experimental data of Ho & Huang (1982). The momentum thickness first increases as the fundamental grows by draining energy from the mean flow. The fundamental subsequently decays by returning some of its energy back to the mean flow, tending to increase the mean-flow energy and reduce the momentum thickness. But this is balanced by the growth of the subharmonic, which amplifies partially by draining energy from the mean flow. The net outcome is a balance between the two mechanisms, resulting in the no-growth stage shown in the figure. Once the fundamental is fully decayed, the growth of the subharmonic by draining energy from the mean flow takes over, resulting in the subsequent growth of the momentum thickness, as shown in the figure.

9.2. SPATIAL DEVELOPMENT OF PHASE

The phase angle ψ is not fixed at its initial value but varies along the jet. In Mankbadi (1985a,b,c), Nikitopoulos (1982), and Nikitopoulos & Liu (1987) the phase was assumed to vary in the streamwise direction according to the linear theory. It seems irrational to assume that the phase behaves linearly while the amplitudes behave nonlinearly. Therefore Mankbadi (1986) used the integral approach to formulate the nonlinear development of the phase-difference angle. Figure 14 (from Mankbadi et al. 1989) shows the development of the phase-difference angle obtained according to the nonlinear analysis of Mankbadi (1986) in comparison with the corresponding experimental results. The agreement seems to be acceptable.

The nonlinear behavior of the phase-difference angle is also apparent in the experimental data of Thomas (1990) for an angled shear layer. The experimental results in Mankbadi et al. (1989) for the development of the phase-difference angle at various initial conditions (shown here as fig. 15) also clearly indicate that the development of the phase-difference angle is a nonlinear process, particularly farther downstream, where the amplitudes reach considerable levels. The nonlinear development of the phase-difference angle described in Mankbadi (1986) is therefore more appropriate than the linear assumption previously adopted.

10. CONDITIONS FOR RESONANCE INTERACTION

Cohen & Wygnanski (1987a,b) examined the conditions for resonance interactions between two instability waves for a nondivergent mean flow. The two interacting waves were assumed to be small with respect to the mean flow, and the wave resulting from the interaction of the two waves to be much smaller than either of the two interacting waves. By examining the second-order terms in the momentum equation of the disturbances, they have shown that the particular solution becomes secular when it satisfies one of the following conditions:

$$\omega_m = \omega_l + \omega_k, \quad n_m = n_l + n_k, \quad \text{and} \quad \alpha_m = \alpha_l = \alpha_k \quad (27a)$$

or

$$\omega_m = \omega_k - \omega_\ell \quad n_m = n_k - n_\ell \quad \text{and} \quad \alpha_m = \alpha_k - \alpha_\ell \quad (27b)$$

where ω is the frequency, n is the azimuthal wavenumber, and α is the complex streamwise wavenumber. Subscripts k and ℓ denote the interacting waves, and m denotes the resulting wave. Combining the conditions on streamwise wavenumber and frequency results in the equality of phase velocity as a condition for the fundamental-subharmonic resonance interaction. The shortcoming of this result is that it cannot explain the dependence of the subharmonic resonance on the initial phase difference, which, even if the phase velocities are equal, can lead either to amplification or suppression of the subharmonic. Also, some experimental results (e.g., Corke 1990) indicate that resonance can occur, even if the phase velocities are not equal.

On the basis of the energy transfers a nonlinear analysis of the condition of resonance interaction in a diverging jet is given in Mankbadi et al. (1989). The conditions on the frequency and azimuthal wavenumbers remain the same as in equation (27). But the condition on the wavenumbers is replaced by the condition that the fundamental-induced strain must align with the subharmonic-induced stresses, which can be written as

$$\psi_m = \psi_k - \psi_\ell - \sigma \quad (28a)$$

$$\psi_m = \psi_k + \psi_\ell - \sigma \quad (28b)$$

where σ is the argument of the fundamental-subharmonic interaction integral WW and ψ is the phase angle in equation (4).

To understand the physical significance of this condition, we write the wave-wave interaction WW symbolically as

$$WW = \int_0^\infty \bar{u}_i \bar{u}_{j,k} \frac{\partial \bar{u}_{i,m}}{\partial x_j} r \, dr \approx \bar{\mathbf{R}} \cdot \bar{\mathbf{S}} = |\bar{\mathbf{R}}| |\bar{\mathbf{S}}| \cos \gamma \quad (29)$$

where $\gamma = \psi_m - \psi_k \pm \psi_\ell + \sigma$ and $\bar{\mathbf{R}}$ and $\bar{\mathbf{S}}$ are vectors representing the radially averaged wave-induced stresses and strains, respectively. Resonance interaction occurs when the stresses and strains are in phase. That is, if $\gamma = 0$, we obtain maximum positive energy transfer to the output wave, resulting in the resonance condition. But, if $\gamma = 180^\circ$, we obtain the highest energy drain from the output wave, resulting in its suppression and the experimentally observed vortex shredding.

The situation is analogous to the mean flow-turbulence interaction. There the turbulence growth is governed by the scalar product of the mean-flow strains and the turbulence-induced Reynolds stresses. The energy transfers between the fundamental and the subharmonic are analogous to those between the mean flow and the turbulence, but the wave-induced stresses and strains are now vectorial quantities. The energy transfer is no longer a scalar product but a vectorial dot product governed by the phase-difference angle between the two vectors representing the stress and the strain.

The experimental data in figure 16(a) (from Raman & Rice 1989) show that the subharmonic is either amplified or suppressed depending on the initial phase-difference angle. The effect is pronounced immediately after the flow leaves the nozzle. The phase velocity based on the linear stability theory (shown in fig. 16(b)) is independent of the initial phase difference, and the results of the linear stability theory indicate that the phase velocities of the fundamental and the subharmonic become close to each other only for $x/d > 3$ although the difference in the subharmonic amplification is quite pronounced much before that. Therefore the equality of phase velocities cannot explain the observed differences in the amplification rate of the subharmonic when the initial phase difference is changed.

The resonance amplification or suppression of the subharmonic is determined in the initial region of the jet. The wave-wave interaction mechanism is efficient only at low momentum thicknesses close to the jet exit (Mankbadi 1985a). Thus only the initial behavior of $\cos \gamma$ matters (say, for $x/d < 0.2$). Later values of $\cos \gamma$ are insignificant because the wave-wave interaction mechanism becomes less efficient as the jet spreads and the subsequent growth of the waves is dominated by its interaction with the mean flow and the turbulence. The angle γ between the wave-induced stresses and strains in the initial region of the jet is shown in figure 16(c). The figure shows that if the initial phase-difference angle is such that $\cos \gamma$ is initially positive, the energy transfers from the fundamental to the subharmonic, resulting in strong amplification of the subharmonic. On the other hand, if the initial phase-difference angle is such that $\cos \gamma$ is initially negative, energy drains from the subharmonic, causing suppression of the subharmonic's growth in accordance with observations.

The condition of equation (28) replaces the previously reported condition that the two waves must have the same phase velocity in order for the subharmonic resonance to occur. The initial phase-difference angle between the two imposed waves controls the stress-strain angle and determines whether the fundamental-subharmonic interaction suppresses or amplifies the growth of the subharmonic. It is shown in Mankbadi et al. (1989) that this condition reduces to that of equation (27) under the following simplifications: (1) the linear stability theory provides a valid approximation to the phase angles of the waves, (2) the initial phase-difference angle between the two interacting waves is ignored, and (3) the argument of the wave-wave interaction integral σ is set to zero. However, the experimental results in Mankbadi et al. (1989) indicate (1) that phase-difference angle development is a nonlinear process that cannot be adequately described by the linear theory, (2) that the effect of initial phase-difference angle on the resonance interaction is now supported by several experimental observations (Arbey & Ffowcs-Williams 1984, Ng & Bradley 1988, Raman & Rice 1989, and Zhang et al. 1985) and cannot be ignored, and (3) that the variation of the argument σ is considerable along the jet (Mankbadi 1985a) and cannot be neglected. Therefore it appears that the alignment of the wave-induced stresses and strains, as a condition for resonance, reduces to the equality of the phase velocities, only under crude approximations. The main conclusions are that the equality of phase velocities for resonance interaction is only an approximate condition that need not be precisely satisfied in order for resonance to occur and that the alignment of the wave-induced stresses and strains is a better description of the resonance condition.

11. MULTIFREQUENCY EXCITED JETS

In a natural situation the coherent structure is not restricted to discrete single- or two-frequency components but occurs in a broad band of frequencies. Furthermore when in a laboratory experiment a jet is excited by a single- or two-frequency component, other frequency components amplify as well. A study of the interactions among several coherent components is therefore necessary to understand such excitation experiments, the natural coherent structure, and the later stages of the transition process. In Mankbadi (1991) the interactions among several frequency components were considered by using the integral-energy method. The situation becomes quite complicated, as demonstrated in figure 17, even if the interactions of only three components are considered. The figure shows the streamwise energy peak of each wave normalized by its initial value as a function of the initial phase-difference angles. With three frequency components there are two initial phase-difference angles, β_{12} and β_{23} . The nonlinear interactions depend on the initial energy level, which is taken to be the same for the three waves and is varied in the figure from 10^{-6} to 10^{-3} . At low levels nonlinear interaction is negligible, and each wave behaves as if the others were not present. With increasing initial energy level, nonlinearity becomes quite evident and the interactions become dependent on the two phase-difference angles. In the natural situation there is no such control over these angles. Therefore the observed amplification of the waves is irregular, which perhaps explains the irregularity in the flow

structure. One can even go further and consider this irregularity caused by random initial phase-difference angles to be the first key, as far as the nonlinear instability theory is concerned to the chaotic nature of turbulence.

At much higher initial levels a saturation condition is reached in which the waves can no longer amplify each other and the dependence on the initial phase-difference angle diminishes (fig. 17). This saturation is caused by the excessive energy drain from the mean flow, which makes the individual wave-wave interaction negligible with respect to the interaction of each wave with the mean flow.

12. MODULATION OF SPREADING RATE BY CONTROLLING COHERENT STRUCTURE

Exciting a jet by a wavelike coherent component can either enhance or reduce the mixing rate, depending on the forcing Strouhal number (see fig. 18, from Mankbadi 1985c).

12.1. ENHANCEMENT OF MIXING AND SPREADING

12.1.1. Low Strouhal numbers. - At Strouhal numbers less than 0.5, the momentum thickness increases monotonically with the forcing level, and the effect is pronounced for forcing levels higher than 0.5% of the jet exit velocity. This increase in the spreading rate with forcing was experimentally observed by Gutmark & Ho (1983b), Ho & Huang (1982), and Reynolds & Bouchard (1981), to mention only a few. At such low Strouhal numbers the pairing activities are insignificant (Mankbadi 1985c and Reynolds & Bouchard 1981). The forced fundamental component enhances the mixing rate directly by absorbing energy from the mean flow and indirectly by enhancing the random turbulence, which in turn absorbs energy from the mean flow.

12.1.2. Intermediate Strouhal numbers. - If the forcing Strouhal number is in the range 0.6 to 1.0, which corresponds to about twice the "preferred mode of the jet," the increase in the mixing rate is pronounced even at forcing levels as low as 0.01% of the jet exit velocity. The first subharmonic of the fundamental is amplified, indicating the formation of a single vortex pairing. The enhancement of the momentum thickness in this range of Strouhal numbers is due to the growth of the fundamental and also due to the enhancement of the turbulence, as in the low-Strouhal-number case. But now the vortex-pairing process forms an additional mechanism that enhances the mixing further. This is in accordance with the early observations of Browand & Weidman (1976) and Winant & Browand (1974), among others, which indicate that vortex pairing is responsible for most of the entrainment in mixing layers. This additional mechanism for mixing enhancement is due to the generated subharmonic, which absorbs additional energy from the mean flow and pumps some of this energy to the turbulence, resulting in further increases in the mean-flow energy drain by the production of turbulence. Thus, because of the subharmonic amplification, forcing at this Strouhal number range is quite effective in enhancing the mixing rate.

12.1.3. Mixing enhancement by bimodal excitation. - Because the vortex pairing is an important mechanism, one might expect that direct bimodal forcing at both the fundamental and subharmonic frequencies would be quite effective in intensifying the vortex pairing process, leading to further increase in the growth rate. The results in Mankbadi (1985b) demonstrate that simultaneous forcing at Strouhal numbers of 0.4 and 0.8 results in considerable enhancement of the mixing rate relative to single-frequency excitation.

The use of two-frequency forcing to extend the range over which the flow can be controlled has now been explored experimentally in several investigations, such as those of Ng & Bradley (1988), Raman & Rice (1989), Thomas (1990), and Weisbrot & Wignanski (1988). The experimental results of Weisbrot & Wignanski (1988) are shown here as figure 19, which demonstrates that combined forcing at two frequencies makes the shear layer grow faster than forcing at either frequency alone at the same forcing level.

12.1.4. Highly turbulent jets. - Although the growth and pairing of coherent structures are important direct mechanisms in laminar or weakly turbulent jets (typical of laboratory experiments), the situation is different for highly turbulent jets (typical of technological applications). Examining the energy transfers in highly turbulent jets (Mankbadi 1991) reveals that the enhancement in the momentum thickness is dominated by the mean-flow turbulence

production, rather than by the fundamental-subharmonic interaction or growth. But, although the coherent components do not appear to be directly responsible for the enhanced mixing in turbulence, they still play a major indirect role. The coherent components are responsible for enhancing the turbulence by pumping energy from the mean flow to the turbulence, which in turn increases the mixing rate by increasing the direct mean-flow production of the turbulence. Thus, although the role of instability waves and their interaction is directly responsible for the mixing rate of laminar or weakly turbulent jets, their role in highly turbulent jets becomes mainly an indirect one through enhancing the turbulence.

12.2. REDUCTION OF MIXING RATE

If the Strouhal number is large enough that the Strouhal number based on the momentum thickness is close to that of the "shear-layer mode," the forcing can result in reducing the spreading rate (fig. 18). This is explained in Mankbadi (1985c) as follows: Forcing at this Strouhal number range results in amplifying several subharmonics. The forced fundamental grows by absorbing energy from the mean flow, but it rapidly decays by dissipating some of its energy back to the mean flow in the form of "negative production." It also decays by transferring some of its energy to the next subharmonic, but its energy transfer to the turbulence is negligible. The subsequent subharmonic behaves similarly. The growth of the fundamental and its first subharmonic thus results in initially increasing the momentum thickness very close to the jet exit ($x/d < 0.5$). But because for such Strouhal numbers these waves are not effective in enhancing the turbulence, and because the momentum thickness is initially enhanced, leaving less mean-flow energy for turbulence production, the turbulence is initially suppressed. The subsequent spreading of the jet in this case is dominated by the mean-flow turbulence production. Because this production is proportional to the turbulence intensity, which is suppressed in the initial region, the mean-flow energy drain to the turbulence and the spreading are therefore reduced.

Although the effect of excitation in enhancing the mixing rate is well documented by several experiments, only rare experimental data are available on mixing suppression. Suppression has been observed in Husain's (1982) experiment, which is shown here as figure 20 along with the corresponding theoretical predictions of Mankbadi (1985c). The figure shows that forcing can result in either enhancement or suppression, depending on the Strouhal number. The theory indicates an increase in the momentum thickness when excited at $S = 0.8$, and the experiment indicates a similar increase at $S = 0.92$. But at higher Strouhal numbers the situation is different. For $S_\theta = 0.01244$ the theory indicates a slight increase in the momentum thickness very close to the jet exit ($x/\theta_i < 260$) but an apparent reduction in the momentum thickness for the rest of the jet. The same features are qualitatively apparent in the data. At $S_\theta = 0.0134$ the data show a slight increase in the measured momentum thickness very close to the exit ($x/\theta_i < 200$) but a pronounced reduction in the momentum thickness for the rest of the jet.

13. TURBULENCE ENHANCEMENT OR SUPPRESSION DUE TO EXCITATION

13.1. ENHANCEMENT

At low-to-intermediate Strouhal numbers Favre-Marinet & Binder (1979), Fiedler & Mensing (1985), Husain & Hussain (1979), Hussain & Thompson (1980), and Thomas & Goldschmidt (1986), among others, observed that increasing the level of coherent structure through excitation results in enhancing the random turbulence. Browand & Weidman (1976) found that the pairing process is responsible for the production of Reynolds stresses and can therefore increase the turbulence intensity. The mechanisms by which vortex pairing can enhance turbulence are classified in Mankbadi (1985a) as follows: (1) the fundamental absorbs energy from the mean flow and pumps it to the turbulence as it decays, (2) the nonlinear growth of the fundamental amplifies the subharmonic, which in turn pumps energy from the mean flow to the turbulence, and (3) these two mechanisms amplify the turbulence energy and the turbulent Reynolds stress, increasing the direct production of the turbulence by the mean flow. This latter mechanism was also

suggested by Ho & Huang (1982), who speculated that the large strain rates resulting from the coalescence of the coherent structures are responsible for the generation of small-scale eddies.

The question of what is the optimum excitation Strouhal number was addressed in Mankbadi (1990a), which considered a jet excited at a dominant Strouhal number but allowed the forced component to interact with the naturally present coherent components at other Strouhal numbers. The study reveals that the high-frequency waves are effective in pumping energy from the mean flow to the turbulence only close to the jet exit. But on the other hand, low-frequency waves have a longer streamwise lifespan and therefore are more effective than high-frequency waves in pumping energy from the mean flow to the turbulence in a wider streamwise domain (fig. 21).

13.2. SUPPRESSION

At higher Strouhal numbers based on diameter the experimental observations of Vlasov & Ginevsky (1974) and Zaman & Hussain (1981) for a circular jet indicated that turbulence is suppressed under excitation. Zaman & Hussain (1981) show that suppression occurs for the Strouhal number range 1.2 to 2.4, and their results are presented here as figure 22. The figure illustrates the ratio of the longitudinal peak fluctuation intensity under excitation u_{ex} to the unexcited value u_{ux} . Suppression is optimum at a Strouhal number $S_g = 0.017$. This suppression is explained in Mankbadi (1985a) as follows: At high Strouhal numbers the streamwise lifespan of a coherent component is short and therefore the component pumps almost no energy to the turbulence. But, because it drains energy from the mean flow, less mean-flow energy is available for the subsequent production of turbulence. Consequently the turbulence is suppressed when the jet is excited at such high Strouhal numbers.

14. THREE-DIMENSIONAL EFFECTS

Numerous experiments have pointed to the three dimensionality of the coherent structure in the form of spanwise periodicity in the plane shear-layer case or in the form of spiral modes in axisymmetric jets (e.g., Alvarez & Martinez-Val 1984; Bernal & Roshko 1986; Browand & Troutt 1980, 1985; Huang 1985; Jimenez, Cogollos & Bernal 1985; Lasheras, Cho & Maxworthy 1986; Miksad 1972; Thomas & Brehob 1986; and Thomas & Prakash 1991). We first consider here the development of a single three-dimensional (spiral) mode; then we consider the interaction among various azimuthal modes.

4.1. DEVELOPMENT OF FIRST HELICAL MODE IN TURBULENT JET

Linear stability analyses (Mattingly & Chang 1974; Michalke 1971; and Plaschko 1979) indicate that the initial region of the jet is equally unstable to both the axisymmetric and first helical ($n = 1$) modes and that higher azimuthal modes are less unstable. Cohen & Wygnanski (1987a,b), Drubka (1981), Drubka et al. (1989), Rice, Raman & Reshotko (1990), and Strange & Crighton (1981) document experimentally the existence of these two modes in the initial region of the jet. Corke, Shakib & Nagib's (1991) and Strange & Crighton's (1981) experimental results confirm that the axisymmetric and first-order helical modes have comparable growth rates in the initial region of the jet. However, Corke et al.'s short-time spectral estimates show that these two modes do not exist at the same time or space. The apparent nondeterministic switching observed between these two modes is attributed to the jet's response to stochastic input of axisymmetric or nonaxisymmetric disturbances.

Although the linear stability theory predicts almost the same growth rate for both the axisymmetric and first helical modes, their nonlinear developments in a turbulent jet may be different, as the study of Mankbadi & Liu (1981) reveals. The nonlinear growth of both modes is shown in figure 23. At low Strouhal numbers the mean-flow production of the $n = 1$ mode is higher than that of the $n = 0$ axisymmetric mode, and therefore the initial nonlinear growth of the $n = 1$ mode is higher than that of the $n = 0$ mode as long as the Strouhal number is low. However, for all Strouhal numbers considered, the $n = 1$ mode decays much faster than the $n = 0$ mode. This is attributed to the azimuthal actions of the $n = 1$ mode that produce azimuthal stresses not present in the

axisymmetric case. This additional stress causes the energy transfer mechanism between the large-scale structure and the fine-grained turbulence to be more efficient for the $n = 1$ mode. The decay of the waves through dissipation of their energy to the turbulence is therefore stronger for $n = 1$. This causes the helical modes to be restricted to a smaller region next to the jet exit than when $n = 0$ at the same Strouhal number. Thus for the subsequent region of the potential core the observations would most likely show the $n = 0$ mode to be the dominant one, as observed by Michalke & Fuchs (1975).

The effectiveness of an instability wave in pumping energy to the turbulence is governed by its efficiency, its maximum attainable amplitude, and its streamwise lifespan. The helical modes are quite efficient in pumping energy to the turbulence, but their streamwise lifespan is short because of their rapid decay. The net outcome is that the helical modes are still slightly more effective in enhancing the turbulence and the growth rates than the corresponding axisymmetric component (Mankbadi & Liu 1981). This trend was confirmed in the experiment of Strange (1981), where the turbulence was observed to increase noticeably when the jet was excited with helical modes. This suggests that if somehow the azimuthal mode could be sustained for a longer distance along the jet, such as by combined bimodal forcing, it could be quite a powerful tool in jet control.

14.2. THREE-DIMENSIONAL MODE-MODE INTERACTION

Cohen & Wygnanski (1987a,b) experimentally studied the azimuthal interactions in a circular jet. Their results show that the interactions can produce steady azimuthal variation of the mean flow. These results showed that the mean-flow profile remains axisymmetric if it is forced with either the axisymmetric mode or the first helical mode alone. This was also confirmed theoretically by Cohen & Wygnanski (1987a,b) and Mankbadi (1991). But when the modes are excited simultaneously at the same frequency, there are substantial deviations from axial symmetry, as the figure illustrates.

Corke & Kusek (1991) experimentally considered the mode-mode interaction in a round jet. They forced first helical modes of $n = \pm 1$ along with an axisymmetric mode at the harmonic frequency. Their results indicate that the axisymmetric mode develops according to linear theory throughout the initial region of the jet. The initial growth of the forced helical mode was according to linear theory. But this initial growth was followed by a sharp change indicating an enhanced secondary growth of this mode (shown here as fig. 24). Their results also indicate that the downstream development of the momentum thickness is characterized by strong azimuthal distribution. The total, azimuthally summed, momentum thickness was three times more than the natural jet (shown here as fig. 25).

Corke & Kusek (1991) also studied the interactions resulting from seeding a pair of first helical modes ($n = \pm 1$) at a Strouhal number close to the natural helical mode, but more importantly where it could couple with the natural jet-column mode instability. This occurs through a difference interaction between the forced mode and the natural axisymmetric mode. The results of this lead to a highly organized jet, with numerous discrete modes that are all derivable from the interactions with the jet-column mode. They also found the near-subharmonic modes to show a secondary enhanced growth that is comparable to that of the previous exact subharmonic resonance case.

Raman (1991) and Raman, Rice & Reshotko (1990) have considered the interaction between the axisymmetric and helical modes in a round jet with emphasis on the Strouhal number range relevant to the jet-column mode. They examined the effect of combined forcing of the axisymmetric and first helical modes on the spreading rate by measuring the jet velocity at various cross sections. The results indicate that combined forcing results in considerable enhancement of the mixing rate (see fig. 26) and also in severe distortion in the jet cross section.

On the theoretical side some aspects of the three-dimensional mode interactions were studied by Corcos & Lin (1984), Pierrehumbert & Widnall (1982), and Metcalf et al. (1987). The first analysis of three-dimensional interactions in the initial region of a round jet was given by Lee (1988) and Lee & Liu (1985, 1987, 1989). They considered the nonlinear interactions among five modes: three at the fundamental frequency ($n = 0, 1, 2$) and two at the subharmonic

frequency ($n = 0,1$). Their results, shown here as figure 27, indicate that the axisymmetric and helical modes grow almost identically in the initial region until the energy densities of the fundamental modes reach peak values. When the initial energy densities of the fundamental and subharmonic modes are equal, the initial growth of the shear-layer momentum thickness and the fundamental energy densities is mainly governed by the energy transfer from the mean flow to the fundamental modes. The subharmonic energy reaches peak values at earlier or later streamwise positions than in the linear case, depending on the energy transfer between the fundamental and the subharmonic, which is controlled by the initial phase-difference angle. The results of Lee & Liu (1989) confirm the experimental observations of Bernal (1981), Huang (1985), and Jimenez (1983) that in the two-dimensional mixing layer the number of three-dimensional spanwise-periodic coherent structures lessens with the downstream distance; that is, the spanwise wavenumber decreases with x . Their results also show that the axisymmetric mode persists longer in the streamwise direction than does the first helical mode.

REFERENCES

- Acton, E., 1976, "The Modelling of Large Eddies in a Two-Dimensional Shear Layer," J. Fluid Mech., vol. 76, pp. 561-592.
- Ahuja, K.K., Lepicovsky, J., Tam, C.K.W., Morris, P.L.J., and Burrin, R.H., 1982, "Tone-Excited Jet: Theory and Experiments," NASA CR-3538.
- Alper, A. and Liu, J.T.C., 1978, "On the Interactions Between Large-Scale Structure and Fine-Grained Turbulence in a Free Shear Flow, Part II, The Development of Spatial Interactions in the Mean," Proc. Roy. Soc. London A, vol. 359, pp. 497-523.
- Alvarez, C. and Martinez-Val, R., 1984, "Visual Measurement of Streamwise Vorticity in the Mixing Layer," Phys. Fluids, vol. 27, pp. 2367-2368.
- Antonia, R.A., Chambers, A.J., Britz, D., and Browne, L.W.B., 1986, "Organized Structures in the Turbulent Plane Jet: Topology and Contribution to Momentum and Heat Transport," J. Fluid Mech., vol. 172, pp. 211-229.
- Arbey, H. and Ffowcs-Williams, J.E., 1984, "Active Cancellation of Pure Tones in an Excited Jet," J. Fluid Mech., vol. 149, pp. 445-454.
- Bechert, D.W., 1988, "Excitation of Instability Waves in Free Shear Layers, Part 1, Theory," J. Fluid Mech., vol. 186, pp. 47-62.
- Bernal, L.P., 1981, "The Coherent Structure of Turbulent Mixing Layers," Ph.D. Thesis, California Institute of Technology, Pasadena.
- Bernal, L.P. and Roshko, A., 1986, "Streamwise Vortex Structure in Plane Mixing Layers," J. Fluid Mech., vol. 170, pp. 499-525.
- Binder, G. and Favre-Marinet, M., 1973, "Mixing Improvement in Pulsating Turbulent Jets," in Fluid Mechanics of Mixing, Uram, E.M. and Goldschmidt, V.W., eds., ASME, New York, pp. 167-172.
- Bishop, K.A., Ffowcs-Williams, J.E., and Smith, W., 1971, "On the Noise Sources of Unsuppressed High Speed Jet," J. Fluid Mech., vol. 50, pp. 21-31.
- Bradshaw, P., Ferriss, D.H., and Johnson, R.F., 1964, "Turbulence in the Noise-Producing Region of a Circular Jet," J. Fluid Mech., vol. 19, pp. 591-624.
- Browand, F.K., 1966, "An Experimental Investigation of the Instability of an Incompressible, Separated Shear Layer," J. Fluid Mech., vol. 26, pp. 281-307.
- Browand, F.K., 1980, "A Physical Description of the Turbulent Mixing Layer," Bull. Am. Phys. Soc., vol. 25, p. 1102.
- Browand, F.K. and Ho, C.M., 1983, "The Mixing Layer: An Example of Quasi-Two-Dimensional Turbulence," J. Mec., pp. 99-120.

- Browand, F.K. and Laufer, J., 1975, "The Role of Large-Scale Structures in the Initial Development of Circular Jets," in Turbulence in Liquids, Zakin, J.L. and Patterson, G.K., eds., Science Press, pp. 333-345.
- Browand, F.K. and Troutt, T.R., 1980, "A Note on Spanwise Structure in the Two-Dimensional Mixing Layer," J. Fluid Mech., vol. 97, pp. 771-781.
- Browand, F.K. and Troutt, T.R., 1985, "The Turbulent Mixing Layer: Geometry of Large Vortices," J. Fluid Mech., vol. 158, pp. 489-509.
- Browand, F.K. and Weidman, P.D., 1976, "Large Scales in the Developing Mixing Layer," J. Fluid Mech., vol. 76, pp. 127-144.
- Brown, G.L. and Roshko, A., 1974, "On Density Effects and Large Structure in Turbulent Mixing Layers," J. Fluid Mech., vol. 64, pp. 775-816.
- Cantwell, B.J., 1981, "Organised Motion in Turbulent Flow," Ann. Rev. Fluid Mech., vol. 13, pp. 457-515.
- Chan, Y.Y., 1974, "Spatial Waves in Turbulent Jets," Phys. Fluids, vol. 17, pp. 46-53.
- Chan, Y.Y. and Templin, J.T.T., 1974, "Suppression of Spatial Waves by Distortion of the Jet Velocity Profile," Phys. Fluids, vol. 17, pp. 2124-2125.
- Chandrsuda, C., Mehta, R.D., Weir, A.D., and Bradshaw, P., 1978, "Effect of Freestream Turbulence on Large Structures in Turbulent Mixing Layers," J. Fluid Mech., vol. 85, pp. 693-704.
- Claus, R.W., 1986, "Direct Numerical Simulations of a Temporally Evolving Mixing Layer Subject to Forcing," NASA TM-88896.
- Cohen, J. and Wygnanski, I., 1987a, "The Evolution of Instabilities in the Axisymmetric Jet, Part 1, The Linear Growth of Disturbances Near the Nozzle," J. Fluid Mech., vol. 176, pp. 191-219.
- Cohen, J. and Wygnanski, I., 1987b, "The Evolution of Instabilities in the Axisymmetric Jet, Part 2, The Flow Resulting From the Interaction Between Two Waves," J. Fluid Mech., vol. 176, pp. 221-235.
- Cohen, J., 1985, "Instabilities and Resonance in Turbulent Free Shear Flows," Ph.D. Thesis, Univ. Arizona, Tuscon.
- Cohen, J. and Wygnanski, I., 1987b, "The Evolution of Instabilities in the Axisymmetric Jet, Part 2, The Flow Resulting from the Interaction Between Two Waves," J. Fluid Mech., vol. 176, pp. 221-235.
- Corcos, G.M. and Lin, S.J., 1984, "The Mixing Layer: Deterministic Models of a Turbulent Flow, Part 2, The Origin of the Three-Dimensional Motion," J. Fluid Mech., vol. 139, pp. 67-96.
- Corcos, G.M. and Sherman, F.S., 1984, "The Mixing Layer: Deterministic Models of a Turbulent Flow, Part 1, Introduction and the Two-Dimensional Flow," J. Fluid Mech., vol. 139, pp. 29-65.
- Corke, T.C., 1990, "Effect of Controlled Resonant Interactions and Mode Detuning on Turbulent Transition in Boundary Layers," in Laminar-Turbulent Transitions, Arnal, D. and Michel, R., eds., Springer-Verlag, Berlin-Heidelberg.
- Corke, T.C. and Kusek, S.M., 1991, "Resonance in Axisymmetric Jets With Controlled Helical Mode Input," AIAA Paper 91-0319.
- Corke, T.C., Shakib, F., and Nagib, H.M., 1991, "Mode Selection and Resonant Locking in Unstable Axisymmetrical Jets," J. Fluid Mech., vol. 223, pp. 253-311.
- Crighton, D.G., 1975, "Basic Principles of Aerodynamic Noise Generation," Prog. Aerospace Sci., vol. 16, pp. 31-96.
- Crighton, D.G., 1981, "Acoustics as a Branch of Fluid Mechanics," J. Fluid Mech., vol. 106, pp. 261-298.
- Crighton, D.G. and Gaster, M., 1976, "Stability of Slowly Diverging Jet Flow," J. Fluid Mech., vol. 77, pp. 397-413.
- Crow, S.C., 1972, "Acoustic Gain of a Turbulent Jet," Bull. Am. Phys. Soc., Paper IE.6.
- Crow, S.C. and Champagne, F.H., 1971, "Orderly Structure in Jet Turbulence," J. Fluid Mech., vol. 48, pp. 547-591.
- Davies, P.O.A.L., Fisher, M.J., and Barratt, M.J., 1963, "The Characteristics of the Turbulence in the Mixing Region of a Round Jet," J. Fluid Mech., vol. 15, pp. 337-367.

- Dimotakis, P.E., Miake-Lye, R.C., and Papantoniou D.A., 1983, "Structure and Dynamics of Round Turbulent Jets," Phys. Fluids, vol. 26, pp. 3185-3192.
- Drubka, R.E., 1981, "Instabilities in the Near Field of Turbulent Jets and Their Dependence on Initial Conditions and Reynolds Number," Ph.D. Thesis, Illinois Institute of Technology, Chicago.
- Drubka, R.E., Reisenthal, P., and Nagib, H.M., 1989, "The Dynamics of Low Initial Disturbance Turbulent Jets," Phys. Fluids A, vol. 1, pp. 1723-1735.
- Favre-Marinet, M. and Binder, G., 1979, "Structure des Jets Pulsants," J. Mec., vol. 18, pp. 357-394.
- Ffowcs-Williams, J.E. and Kempton, A.J., 1978, "The Noise from the Large-Scale Structure of a Jet," J. Fluid Mech., vol. 84, pp. 673-694.
- Fiedler, H.E., Dziomba, B., Mensing, P., and Roegen, T., 1981, "Initiation, Evolution and Global Consequences of Coherent Structures in Turbulent Shear Flows," in The Role of Coherent Structures in Modelling Turbulence and Mixing, Jimenez, J., ed., Lecture Notes Phys., vol. 136, Springer-Verlag, pp. 219-251.
- Fiedler, H.E. and Mensing, P., 1985, "The Plane Turbulent Shear Layer With Periodic Excitation," J. Fluid Mech., vol. 150, pp. 281-309.
- Gaster, M., Kit, E., and Wygnanski, I., 1985, "Large-Scale Structures in a Forced Turbulent Mixing Layer," J. Fluid Mech., vol. 150, pp. 23-39.
- Gatski, T.B. and Liu, J.T.C., 1980, "On the Interactions Between Large-Scale Coherent Structure and Fine-Grained Turbulence in a Free Shear Flow, Part III, A Numerical Solution," Philos. Trans. Roy. Soc. London Ser A, vol. 293, pp. 473-509.
- Goldstein, M.E. and Hultgren, L.S., 1988, "Nonlinear Spatial Evolution of an Externally Excited Instability Wave in a Free Shear Layer," J. Fluid Mech., vol. 197, pp. 295-330.
- Goldstein, M.E. and Leib, L.S., 1988, "Nonlinear Roll-Up of Externally Excited Free Shear Layers," J. Fluid Mech., vol. 191, pp. 481-515.
- Goldstein, M.E. and Leib, L.S., 1989, "Nonlinear Evolution of Oblique Waves on Compressible Shear Layers," J. Fluid Mech., vol. 207, pp. 73-96.
- Gutmark, E. and Ho, C.M., 1983a, "Near Field Pressure Fluctuations of an Elliptic Jet," AIAA Paper 83-0663.
- Gutmark, E. and Ho, C.M., 1983b, "Preferred Modes and the Spreading Rates of Jets," Phys. Fluids, vol. 26, pp. 2932-2938.
- Gutmark, E. and Wygnanski, I., 1976, "The Planar Turbulent Jet," J. Fluid Mech., vol. 73, pp. 465-495.
- Ho, C.M. and Huang, L.S., 1982, "Subharmonics and Vortex Merging in Mixing Layers," J. Fluid Mech., vol. 119, pp. 443-473.
- Ho, C.M. and Huerre, P., 1984, "Perturbed Free Shear Layers," Ann. Rev. Fluid Mech., vol. 16, pp. 365-424.
- Huang, L.S., 1985, "Small-Scale Transition in a Two-Dimensional Mixing Layer," PhD Thesis, Univ. Southern California, Los Angeles.
- Huerre, P. and Monkewitz, P.A., 1985, "Absolute and Convective Instabilities in Free Shear Layers," J. Fluid Mech., vol. 159, pp. 151-168.
- Hultgren, L.S., 1991, "Nonlinear Spatial Equilibration of an Externally Excited Instability Wave in a Free Shear Layer," J. Fluid Mech. (submitted for consideration).
- Hultgren, L.S. and Goldstein, M.E., 1990, "Nonlinear Spatial Evolution of Externally Excited Instability Waves in Free Shear Layers," in International Symposium on Unsteady Fluid Dynamics, Miller, J.A. and Telionis, D.P., eds., ASME, New York, pp. 417-426. (Also, J. Fluid Mech., vol. 197, pp. 295-330).
- Husain, Z.D., 1982, "An Experimental Study of Effects of Initial and Boundary Conditions on Near and Far Fields of Jet Flows," Ph.D. Dissertation, Univ. Houston, Houston, Texas.

- Hussain, Z.D. and Hussain, A.K.M.F., 1979, "Axisymmetric Mixing Layer: Influence of the Initial and Boundary Conditions," AIAA J., vol. 17, pp. 48-55.
- Hussain, H.S. and Hussain, A.K.M.F., 1983, "Controlled Excitation of Elliptic Jets," Phys. Fluids, vol. 26, pp. 2763-2766.
- Hussain, A.K.M.F., 1983, "Coherent Structures - Reality and Myth," Phys. Fluids, vol. 26, pp. 2816-2850.
- Hussain, A.K.M.F., 1986, "Coherent Structures and Turbulence," J. Fluid Mech., vol. 173, pp. 303-356.
- Hussain, A.K.M.F. and Clark, A.R., 1981, "On the Coherent Structure of the Axisymmetric Mixing Layer: A Flow Visualization Study," J. Fluid Mech., vol. 104, pp. 263-294.
- Hussain, A.K.M.F. and Hussain, H.S., 1987, "Passive and Active Control of Jet Turbulence," in Turbulence Management and Relaminarization, Leipman, H.W. and Narasimha, R., eds., Springer-Verlag, New York, 1988, pp. 445-458.
- Hussain, A.K.M.F. and Reynolds, W.C., 1970, "The Mechanics of an Organized Wave in Turbulent Shear Flow," J. Fluid Mech., vol. 41, pp. 241-258.
- Hussain, A.K.M.F. and Thompson, C.A., 1980, "Controlled Symmetric Perturbation of the Plane Jet - An Experimental Study in the Initial Region," J. Fluid Mech., vol. 100, pp. 397-431.
- Hussain, A.K.M.F. and Zaman, K.B.M.Q., 1980, "Vortex Pairing in a Circular Jet Under Controlled Excitation, Part 2, Coherent Structures Dynamics," J. Fluid Mech., vol. 101, pp. 493-544.
- Hussain, A.K.M.F. and Zaman, K.B.M.Q., 1981, "The Preferred Mode of the Axisymmetric Jet," J. Fluid Mech., vol. 110, pp. 39-71.
- Hussain, A.K.M.F. and Zedan, M.F., 1978a, "Effects of the Initial Condition on the Axisymmetric Free Shear Layer: Effects of the Initial Fluctuation Level," Phys. Fluids, vol. 21, pp. 1475-1481.
- Hussain, A.K.M.F. and Zedan, M.F., 1978b, "Effects of the Initial Condition on the Axisymmetric Free Shear Layer: Effects of the Initial Momentum Thickness," Phys. Fluids, vol. 21, pp. 1100-1112.
- Jimenez, J., 1983, "A Spanwise Structure in the Plane Shear Layer," J. Fluid Mech., vol. 132, pp. 319-336.
- Jimenez, J., Cogollos, M., and Bernal, L.P., 1985, "A Perspective View of the Plane Mixing Layer," J. Fluid Mech., vol. 152, pp. 125-143.
- Kaptanoglu, H.T., 1984, "Coherent Mode Interactions in a Turbulent Shear Layer," Sc.M. Thesis, Brown Univ.
- Kelly, R.E., 1967, "On the Stability of an Inviscid Shear Layer Which is Periodic in Space and Time," J. Fluid Mech., vol. 27, pp. 657-689.
- Kibens, V., 1980, "Discrete Noise Spectrum Generated by an Acoustically Excited Jet," AIAA J., vol. 18, pp. 434-441.
- Kibens, V., 1981, "The Limits of Initial Shear-Layer Influence on Jet Development," AIAA Paper 81-1960.
- Knight, D.D., 1979, "Numerical Investigation of Large-Scale Structures in the Turbulent Mixing Layer," in Sixth Biennial Symposium on Turbulence, Univ. Missouri-Rolla, pp. 24-1 to 24-9.
- Ko, D.R.S., Kubota, T., and Lees, L., 1970, "Finite Disturbance Effect on the Stability of a Laminar Incompressible Wake Behind a Flat Plate," J. Fluid Mech., vol. 40, pp. 315-341.
- Lasheras, J.C., Cho, J.S., and Maxworthy, T., 1986, "On the Origin and Evolution of Streamwise Vortical Structures in a Plane Free Shear Layer," J. Fluid Mech., vol. 172, pp. 231-258.
- Laufer, J. and Yen, T.C., 1983, "Noise Generation by a Low Mach Number Jet," J. Fluid Mech., vol. 134, pp. 1-31.
- Laufer, J. and Zhang, J.P., 1983, "Unsteady Aspects of a Low Mach Number Jet," Phys. Fluids, vol. 26, pp. 1740-1750.
- Lee, S.S., 1988, "Multiple Coherent Mode Interaction in a Developing Round Jet," Ph.D. Thesis, Brown Univ., Providence, RI.
- Lee, S.S. and Liu, J.T.C., 1985, "Multiple Mode Interactions in a Round Jet," Bull. Am. Phys. Soc., vol. 30, p. 1715.

- Lee, S.S. and Liu, J.T.C., 1987, "Helical and Axisymmetric Mode Interactions in a Round Jet," Bull. Am. Phys. Soc., vol. 32, p. 2044.
- Lee, S.S. and Liu, J.T.C., 1989, "Multiple Coherent Mode Interaction in a Developing Round Jet," AIAA Paper 89-0967.
- Lighthill, M.J., 1952, "On Sound Generated Aerodynamically, Part I, General Theory," Proc. Roy. Soc. London A, vol. 211, pp. 564-587.
- Liu, J.T.C., 1971, "Nonlinear Development of an Instability Wave in a Turbulent Wake," Phys. Fluids, vol. 14, pp. 2251-2257.
- Liu, J.T.C., 1974, "Developing Large-Scale Wavelike Eddies and the Near Jet Noise Field," J. Fluid Mech., vol. 62, pp. 437-464.
- Liu, J.T.C., 1986, "Large-Scale Coherent Structures in Free Shear Flows and Their Aerodynamic Sound," in Recent Advances in Aerodynamics, Krothapalli, A. and Smith, C.A., eds., Springer-Verlag, Berlin, pp. 297-334.
- Liu, J.T.C., 1988, "Contributions to the Understanding of Large-Scale Coherent Structures in Developing Free Turbulent Shear Flows," Adv. Appl. Mech., vol. 26, pp. 183-309.
- Liu, J.T.C., 1989, "Coherent Structures in Transitional and Turbulent Free Shear Flows," Ann. Rev. Fluid Mech., vol. 21, pp. 285-315.
- Liu, J.T.C. and Kaptanoglu, H.T., 1984, "Multiple-Mode Interactions in a Turbulent Mixing Layer," Bull. Am. Phys. Soc., vol. 29, p. 155.
- Liu, J.T.C. and Kaptanoglu, H.T., 1987, "Control of Free Shear Layers," AIAA Paper 87-2689.
- Liu, J.T.C. and Nikitopoulos, D., 1982, "Mode Interactions in Developing Shear Flows," Bull. Am. Phys. Soc., vol. 27, p. 1192.
- Lumley, J.L., 1981, "Coherent Structures in Turbulence," in Transition and Turbulence, Meyer, R.E., ed., Academic Press, New York, pp. 215-242.
- Lush, P.A., 1971, "Measurements of Subsonic Jet Noise and Comparison With Theory," J. Fluid Mech., vol. 46, pp. 477-500.
- Mankbadi, R.R., 1985a, "On the Interaction Between Fundamental and Subharmonic Instability Waves in a Turbulent Round Jet," J. Fluid Mech., vol. 160, pp. 385-419.
- Mankbadi, R.R., 1985b, "The Effect of Bi-Modal Excitation on the Spreading Rate of a Circular Jet," AIAA Paper 85-0572.
- Mankbadi, R.R., 1985c, "The Mechanism of Mixing Enhancement and Suppression in a Circular Jet Under Excitation Conditions," Phys. Fluids, vol. 28, pp. 2062-2074.
- Mankbadi, R.R., 1986, "The Effect of Phase Difference on the Spreading Rate of a Jet," AIAA J., vol. 24, pp. 1941-1948.
- Mankbadi, R.R., 1990a, "Turbulence Enhancement in Free Shear Flows Under Multifrequency Excitation," in Forum on Turbulent Flows - 1990, Bower, W.M., Morris, M.J., and Samimy, M., eds., ASME, pp. 105-113.
- Mankbadi, R.R., 1990b, "The Self Noise From Ordered Structures in a Low Mach Number Jet," J. Appl. Mech., vol. 57, pp. 241-246.
- Mankbadi, R.R., 1991, "Multifrequency Excited Jets," Phys. Fluids A, vol. 3, pp. 595-605.
- Mankbadi, R.R. and Liu, J.T.C., 1981, "A Study of the Interactions Between Large-Scale Coherent Structures and Fine-Grained Turbulence in a Round Jet," Philos. Trans. Roy. Soc. London A, vol. 298, pp. 541-602.
- Mankbadi, R.R. and Liu, J.T.C., 1984, "Sound Generated Aerodynamically Revisited: Large-Scale Structures in a Turbulent Jet as a Source of Sound," Philos. Trans. Roy. Soc. London A, vol. 311, pp. 183-217.

- Mankbadi, R.R. and Liu J.T.C., 1991, "Near-Wall Response in Turbulent Shear Flows Subjected to Imposed Unsteadiness," J. Fluid Mech. (to appear).
- Mankbadi, R.R., Raman, G., and Rice, E.J., 1989, "Phase Development and its Role on Subharmonic Controls," NASA TM-101477, AIAA Paper 90-0503.
- Mansour, N.N. and Barr, P.K., 1987, "Simulation of Turbulent Mixing Layers," in Proceedings Fifth Symposium on Turbulent Shear Flows, Durst, F., ed., Springer-Verlag, New York, pp. 3.33 to 3.38.
- Mattingly, G.E. and Chang, C.C., 1974, "Unstable Waves on an Axisymmetric Jet Column," J. Fluid Mech., vol. 65, pp. 541-560.
- Merkine, L.O. and Liu, J.T.C., 1975, "On the Development of Noise Producing Large-Scale Wavelike Eddies in a Plane Turbulent Jet," J. Fluid Mech., vol. 70, pp. 353-368.
- Metcalfe, R.W., Orszag, S.A., Brackett, M.E., Menon, S. & Riley, J.J., 1987, "Secondary Instability of a Temporary Growing Mixing Layer," J. Fluid Mech., vol. 184, pp. 207-243.
- Michalke, A., 1971, "Instability of a Compressible Circular Free Jet With Consideration of the Influence of the Jet Boundary Layer Thickness (Instabilität eines Kompressiblen runden Freistrahls unter Berücksichtigung des Einflusses der Stralgrenschichtdicke), Z Flugwiss., vol. 19, pp. 319-328. (Translation, NASA TM-75190.)
- Michalke, A. and Fuchs, H.V., 1975, "On Turbulence and Noise of an Axisymmetric Shear Flow," J. Fluid Mech., vol. 70, pp. 179-205.
- Miksad, R.W., 1972 "Experiments on the Nonlinear Stages of Free Shear Layer Transition," J. Fluid Mech., vol. 56, pp. 695-719.
- Miksad, R.W., Jones, F.L., Powers, E.J., Kim, Y.C., and Khadra, L., 1982, "Experiments on the Role of Amplitude and Phase Modulations During Transition to Turbulence," J. Fluid Mech., vol. 123, pp. 1-29.
- Mollo-Christensen, E., 1967, "Jet Noise and Shear Flow Instability Seen From an Experimenter's Viewpoint," J. Appl. Mech., vol. 89, pp. 1-7.
- Monkewitz, P.A., 1982, "On the Effect of Phase Difference Between Fundamental and Subharmonic Instability in a Mixing Layer," UCLA Internal Report.
- Monkewitz, P.A., 1988, "Subharmonic Resonance, Pairing, and Shredding in the Mixing Layer," J. Fluid Mech., vol. 188, pp. 223-252.
- Monkewitz, P.A. and Huerre, P., 1982, "Influence of the Velocity Ratio on the Spatial Instability of Mixing Layers," Phys. Fluids, vol. 25, pp. 1137-1143.
- Moore, C.J., 1977, "The Role of Shear-Layer Instability Waves in Jet Exhaust Noise," J. Fluid Mech., vol. 80, pp. 321-367.
- Morris, P.J., 1974, "A Model for the Structure of Jet Turbulence as a Source of Noise," AIAA Paper 74-1.
- Nikitopoulos, D.E., 1982, "Nonlinear Interaction Between Two Instability Waves in a Developing Shear Layer," Sc.M Thesis, Brown Univ., Providence, RI.
- Nikitopoulos, D.E. and Liu, J.T.C., 1984, "Triple-Mode Interactions in a Developing Shear Layer," Bull. Am. Phys. Soc., vol. 29, p. 1548.
- Nikitopoulos, D.E. and Liu, J.T.C., 1987, "Nonlinear Binary-Mode Interactions in a Developing Mixing Layer," J. Fluid Mech., vol. 179, pp. 345-370.
- Nikitopoulos, D.E. and Liu, J.T.C., 1989, "Nonlinear Coherent Mode Interactions and the Control of Shear Layers," in Structure of Turbulence and Drag Reduction, Gyr, A., ed., Springer-Verlag, New York.
- Ng, T.T. and Bradley, T.A., 1988, "Effect of Multifrequency Forcing on the Near-Field Development of a Jet." AIAA J., vol. 26, pp. 1201-1207.

- Oster, D. and Wygnanski, I., 1982, "The Forced Mixing Layer Between Parallel Streams," J. Fluid Mech., vol. 123, pp. 91-130.
- Oster, D., Wygnanski, I., Dziomba, B., and Fiedler, H., 1978, "On the Effect of Initial Conditions on the Two-Dimensional Turbulent Mixing Layer," in Structure and Mechanisms of Turbulence I, Fiedler, H., ed., Springer-Verlag, vol. 75, pp. 48-65.
- Panda, J., 1990, "Experiments on the Instabilities of Swirling and Non-Swirling Jets," Ph.D. Thesis, Pennsylvania State Univ.
- Panda, J. and McLaughlin, D.K., 1991, "Experiments on the Instabilities of Swirling and Non-Swirling Jets," J. Fluid Mech. (submitted).
- Patnaik, P.C. Sherman, F.S., and Corcos, G.M., 1976, "A Numerical Simulation of Kelvin-Helmholtz Waves of Finite Amplitude," J. Fluid Mech., vol. 73, pp. 215-240.
- Petersen, R.A., 1978, "Influence of Wave Dispersion on Vortex Pairing in a Jet," J. Fluid Mech., vol. 89, pp. 469-495.
- Pierrehumbert, R.T. and Widnall, S.E., 1982, "The Two- and Three-Dimensional Instabilities of a Spatially Periodic Shear Layer," J. Fluid Mech., vol. 114, pp. 59-82.
- Plaschko, P., 1979, "Helical Instabilities of Slowly Divergent Jets," J. Fluid Mech., vol. 92, pp. 209-215.
- Raman, G., 1991, "An Experimental Study of Natural and Forced Modes in an Axisymmetric Jet," Ph.D. Thesis, Case Western Reserve Univ.
- Raman, G. and Rice, E.J., 1989, "Subharmonic and Fundamental High-Amplitude Excitation of an Axisymmetric Jet," AIAA Paper 89-0993. (Also NASA TM-101946.)
- Raman, G., Rice, E.J., and Mankbadi, R.R., 1988, "Saturation and the Limit of Jet Mixing Enhancement by Single Frequency Plane Wave Excitation: Experiment and Theory," NASA TM-100882, AIAA Paper 88-3613.
- Raman, G., Rice, E.J., and Reshotko, E., 1990, "Forced Axisymmetric and Helical Modes in a Round Jet," Bull. Am. Phys., vol. 35, p. 232.
- Reshotko, E., 1985, "Control of Boundary Layer Transition," AIAA Paper 85-0562.
- Reshotko, E., 1986, "Stability and Transition, How Much Do We Know?," 10th U.S. National Congress of Applied Mechanics, Lamb, J.P., ed. ASME, New York, pp. 421-434.
- Reynolds, W.C. and Bouchard, E.E., 1981, "The Effect of Forcing on the Mixing Layer Region of a Round Jet," in Unsteady Turbulent Shear Flows, Michel, R., Cousteix, J., and Houdeville, R., eds., Springer-Verlag, New York, pp. 401-411.
- Rice, E., Raman, E., and Reshotko, E., 1990, "Measurement of Naturally Occurring Modes in a Round Jet," Bull. Am. Phys., vol. 35, p. 2322.
- Rice, E.J. and Zaman, K.B.M.Q., 1987, "Control of Shear Flows by Artificial Excitation," NASA TM-100201 and AIAA Paper 87-2722.
- Riley, J.J. and Metcalfe, R.W., 1980, "Direct Numerical Simulation of a Perturbed, Turbulent Mixing Layer," AIAA Paper 80-0274.
- Roshko, A., 1976, "Structure of Turbulent Shear Flows: A New Look," AIAA J., vol. 14, pp. 1349-1357.
- Scott, J.N., 1987, "Numerical Simulation of Self-Sustained and Forced Oscillations in Jet Shear Layers," in Forum on Unsteady Flow Separation, Ghia, K.N., ed., ASME, New York, pp. 123-130.
- Strange, P.J.R., 1981, "Spinning Modes in Orderly Jet Structure," Ph.D. Thesis, Univ. of Leeds, England.
- Strange, P.J.R. and Crighton, D.G., 1981, "Spinning Modes on Axisymmetric Jets," J. Fluid Mech., vol. 134, pp. 231-245.
- Stuart, J.T., 1960, "On the Nonlinear Mechanics of Wave Disturbances in Stable and Unstable Parallel Flows, Part I, The Basic Behaviour in Plane Poiseuille Flow," J. Fluid Mech., vol. 9, pp. 353-370.

- Stuart, J.T., 1963, "Hydrodynamic Stability," in Laminar Boundary Layers, Rosenhead, L., ed. Clarendon Press, Oxford, pp. 492-579.
- Stuart, J.T., 1965, "Hydrodynamic Stability," Appl. Mech. Rev., vol. 18, pp. 523-531.
- Stuart, J.T., 1967, "On Finite Amplitude Oscillations in Laminar Mixing Layers," J. Fluid Mech., vol. 29, pp. 417-440.
- Stuart, J.T., 1971, "Nonlinear Stability Theory," Ann. Rev. Fluid Mech., vol. 3, pp. 347-370.
- Taghavi, R., Rice, E.J., and Farokhi, S., 1988, "Controlled Excitation of a Cold Turbulent Swirling Free Jet," J. Vibr. Acoust. Stress Rel. Des., vol. 110, pp. 234-237.
- Taghavi, R., Rice, E.J., and Farokhi, S., 1989, "Large Amplitude Acoustic Excitation of Swirling Turbulent Jets," NASA TM-101950 and AIAA Paper 89-0970.
- Thomas, F.O., 1990, "An Experimental Investigation into the Role of Simultaneous Amplitude and Phase Modulation in the Transition of a Planar Jet," Phys. Fluids A, vol. 2, pp. 553-574.
- Thomas, F.O., 1991, "Structure of Mixing Layers and Jets," Appl. Mech. Rev., vol. 44, pp. 119-153.
- Thomas, F.O. and Brehob, E.G., 1986, "An Investigation of Large-Scale Structure in the Similarity Region of a Two-Dimensional Turbulent Jet," Phys. Fluids, vol. 29, pp. 1788-1795.
- Thomas, F.O. and Chu, H.C., 1989, "An Experimental Investigation of the Transition of a Planar Jet: Subharmonic Suppression and Upstream Feedback," Phys. Fluids A, vol. 1, pp. 1566-1587.
- Thomas, F.O. and Goldschmidt, V.W., 1986, "Structural Characteristics of a Developing Turbulent Planar Jet," J. Fluid Mech., vol. 163, pp. 227-256.
- Thomas, F.O. and Prakash, K.M.K., 1991, "An Experimental Investigation of the Natural Transition of an Untuned Planar Jet," Phys. Fluids A, vol. 3, pp. 90-105.
- Tso, J. and Hussain, F., 1989, "Organized Motions in a Fully Developed Turbulent Axisymmetric Jet," J. Fluid Mech., vol. 203, pp. 425-448.
- Tso, J., Kovasznyai, L.S.G., and Hussain, A.K.M.F., 1981, "Search for Large-Scale Coherent Structures in the Nearly Self-Preserving Region of a Turbulent Axisymmetric Jet," J. Fluids Eng., vol. 103, pp. 503-508.
- Vlasov, Y.V. and Ginevsky, A.S., 1974, "Generation and Suppression of Turbulence in an Axisymmetric Turbulent Jet in the Presence of an Acoustic Influence," NASA TT-F-15721.
- Weisbrot, I., 1984, "A Highly Excited Turbulent Mixing Layer," M.S. Thesis, Tel-Aviv Univ.
- Weisbrot, I. and Wygnanski, I., 1988, "On Coherent Structures in a Highly Excited Mixing Layer," J. Fluid Mech., vol. 195, pp. 137-159.
- Winant, C.D. and Browand, F.K., 1974, "Vortex Pairing, the Mechanism of Mixing Layer Growth at Moderate Reynolds Number," J. Fluid Mech., vol. 63, pp. 237-255.
- Wygnanski, I., Champagne, F., and Marasli, B., 1986, "On the Large-Scale Structures in Two-Dimensional Small-Deficit, Turbulent Wakes," J. Fluid Mech., vol. 168, pp. 31-71.
- Wygnanski, I. and Petersen, R.A., 1987, "Coherent Motion in Excited Free Shear Flows," AIAA J., vol. 25, pp. 201-213.
- Wygnanski, I. and Weisbrot, I., 1987, "On the Pairing Process in an Excited Plane Turbulent Mixing Layer," in Turbulence Management and Relaminarization, Narasimha, R., ed., Springer-Verlag, New York, pp. 409-422.
- Zaman, K.B.M.Q., 1985, "Far-Field Noise of a Subsonic Jet Under Controlled Excitation," J. Fluid Mech., vol. 152, pp. 83-112.
- Zaman, K.B.M.Q., 1986, "Flow Field and Near and Far Sound Field of a Subsonic Jet," J. Sound Vibr., vol. 106, pp. 1-16.

- Zaman, K.B.M.Q. and Hussain, A.K.M.F., 1980, "Vortex Pairing in a Circular Jet Under Controlled Excitation, Part I, General Jet Response," *J. Fluid Mech.*, vol. 101, pp. 449-491.
- Zaman, K.B.M.Q. and Hussain, A.K.M.F., 1981, "Turbulence Suppression in Free Shear Flows by Controlled Excitation," *J. Fluid Mech.*, vol. 103, pp. 133-160.
- Zaman, K.B.M.Q. and Hussain, A.K.M.F., 1984, "Natural Large-Scale Structures in the Axisymmetric Mixing Layer," *J. Fluid Mech.*, vol. 138, pp. 325-351.
- Zhang, Y.Q., Ho, C.M., and Monkewitz, P., 1983, "The Mixing Layer Forced by Fundamental and Subharmonic," in *Laminar-Turbulent Transition*, IUTAM Symposium Novosibirsk, USSR, Kozlov, V.V., ed., Springer-Verlag, New York, pp. 385-395.

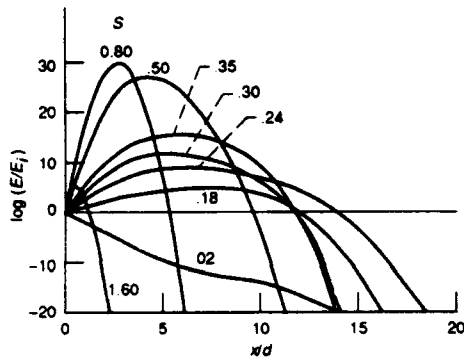


Figure 1 —Large-scale-structure kinetic energy ratio along a round jet for several Strouhal numbers. (From Mankbadi & Liu 1981.)

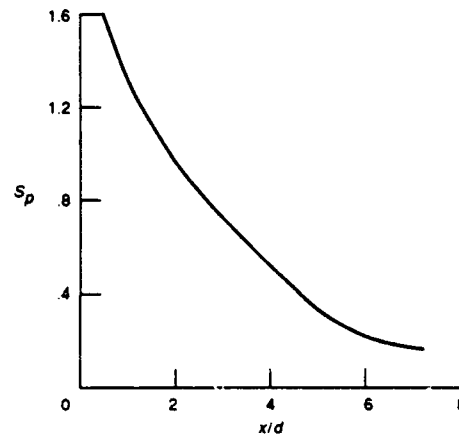


Figure 2.—Peak Strouhal number along a circular jet.

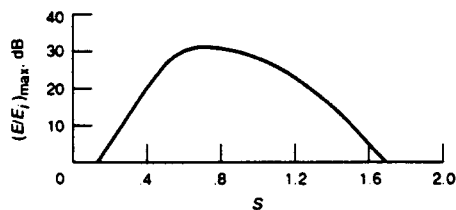


Figure 3 —Maximum amplification in coherent-structure kinetic energy E as a function of Strouhal number.

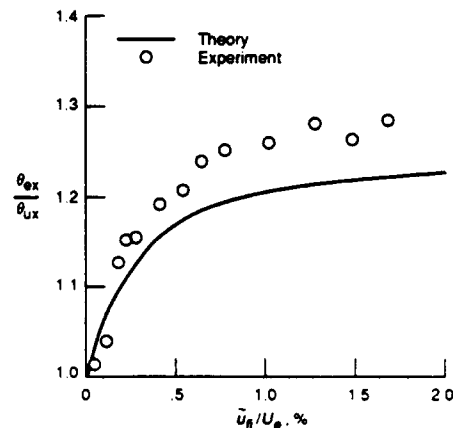
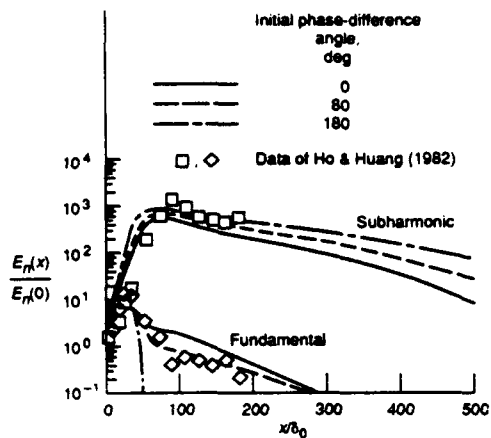
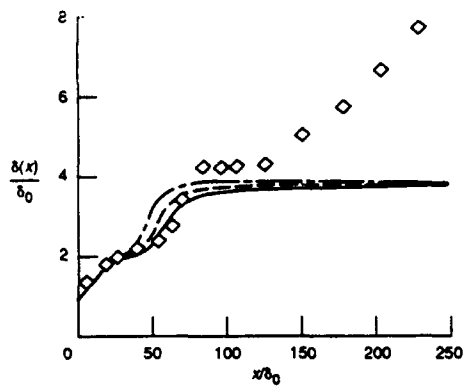


Figure 4 —Measurements of momentum thickness at $x/d = 9$ against excitation level compared with predictions of integral method. (From Raman et al 1988)



(a) Development of modal energy content.



(b) Mean-flow growth.

Figure 5.—Theoretical prediction of Nikitopoulos & Liu (1987) compared with Ho & Huang (1982) experiment.
($E_{10} = 0.16 \times 10^{-4}$, $E_{20} = 0.48 \times 10^{-3}$, $\beta_1 = 0.26$, $Re_1 = 81$).
(From Nikitopoulos & Liu 1987.)

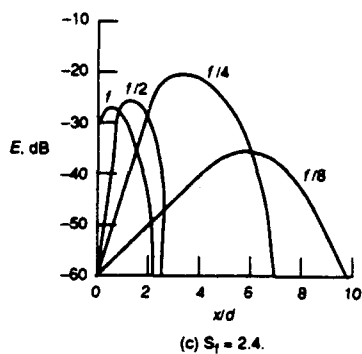
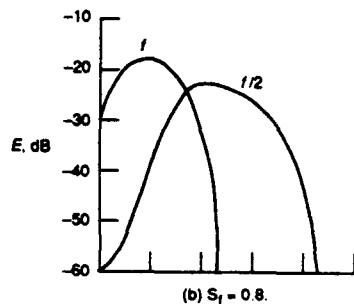
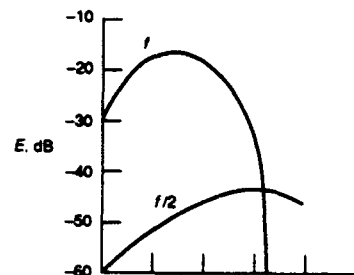


Figure 6.—Fundamental and subharmonic energies along jet at three fundamental Strouhal numbers.

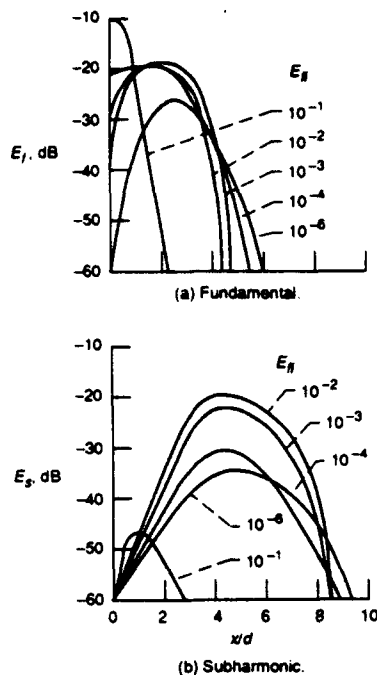


Figure 7—Effect of initial excitation level E_R on the development of $S = 0.8$. $E_{R1} = 10^{-6}$.

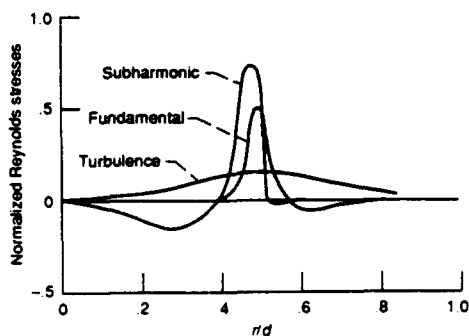


Figure 9—Coherent and random Reynolds shear stresses at $x/d = 1.5$ normalized by peak total Reynolds shear stress.

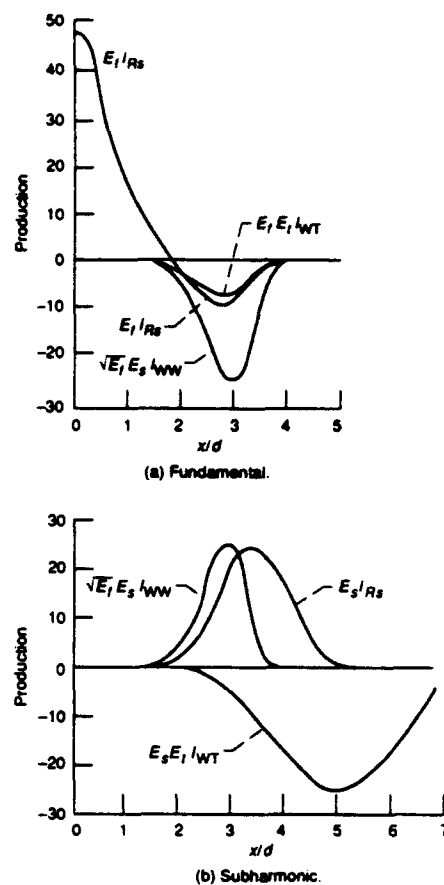


Figure 8—Energy transfer terms of $S = 0.8$ and initial excitation level $\bar{U}_R = 3\% U_0$.

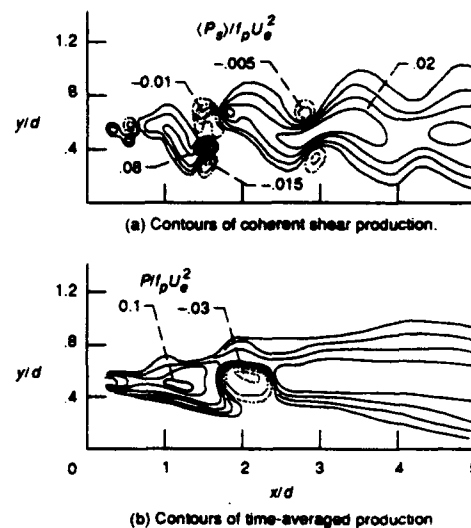


Figure 10—Coherent structures in near field of axisymmetric jet at instant of pairing in jet-column mode at $x/d = 1.75$, where U_0 is jet exit velocity. (From Hussain & Zaman 1980)

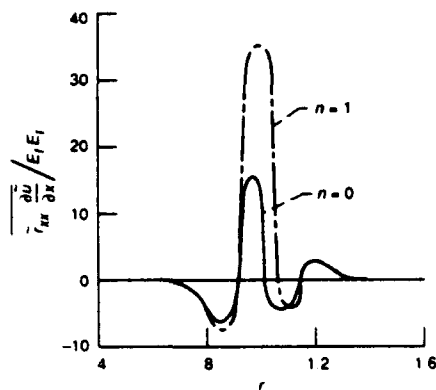
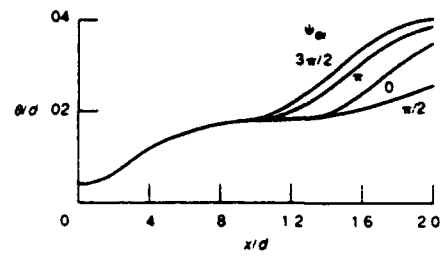
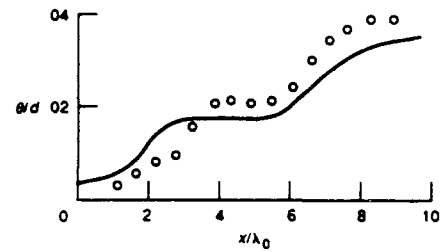


Figure 11 —xx-contribution to energy transfer from large-scale structure to turbulence in axisymmetric ($n = 0$) and helical ($n = 1$) modes. $S = 0.5$, $\theta/R = 0.08$. Note the local reverse in the direction of energy transfer (From Mankbadi & Liu 1981.)

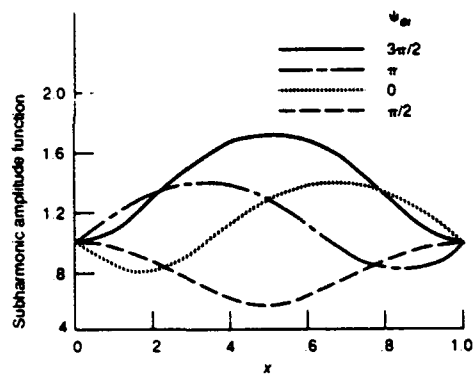


(a) Effect of initial phase difference at $S = 2.4$

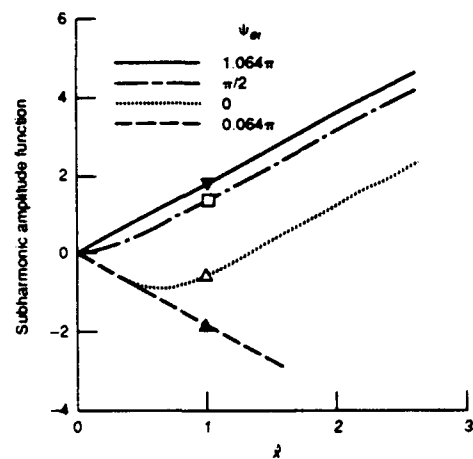


(b) Comparison with Laufer & Zhang's (1983) experiment.

Figure 13 —Development of momentum thickness

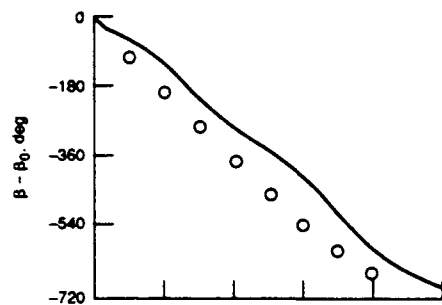


(a) Below critical amplitude

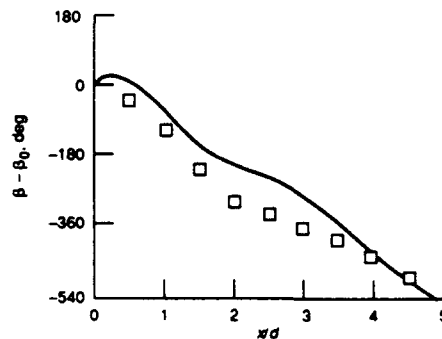


(b) Above critical amplitude

Figure 12 —Streamwise variation of subharmonic amplitude function at different initial phase-difference angles for fundamental α_{crit} (From Monkewitz 1988.)



(a) $\beta_1 = 90^\circ$



(b) $\beta_1 = 270^\circ$

Figure 14 —Predicted and measured development of phase-difference angle for two initial difference angles (From Mankbadi et al 1989.)

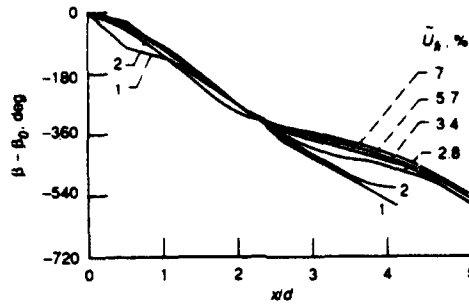


Figure 15.—Nonlinear development of phase-difference angle under various initial levels of fundamental. (From Mankbadi et al. 1969.)

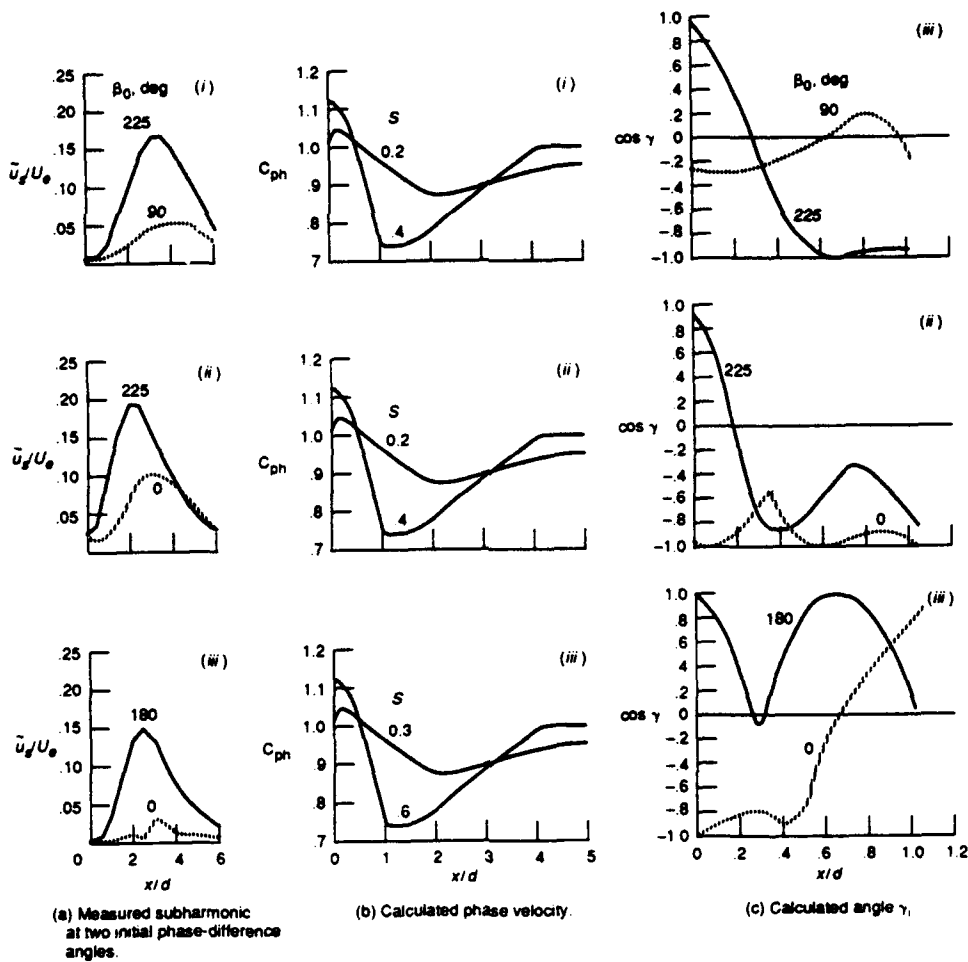


Figure 16.—Dependence of subharmonic amplification on angle γ_1 between wave-induced stresses and strains. Where in each part (i) $S = 0.2$ and 0.4 ; $u_n = u_e = 7\%$ and 0.5% . (ii) $S = 0.2$ and 0.4 ; $u_n = u_e = 3\%$. (iii) $S = 0.3$ and 0.6 ; $u_n = 3\%$, $u_e = 0.2\%$

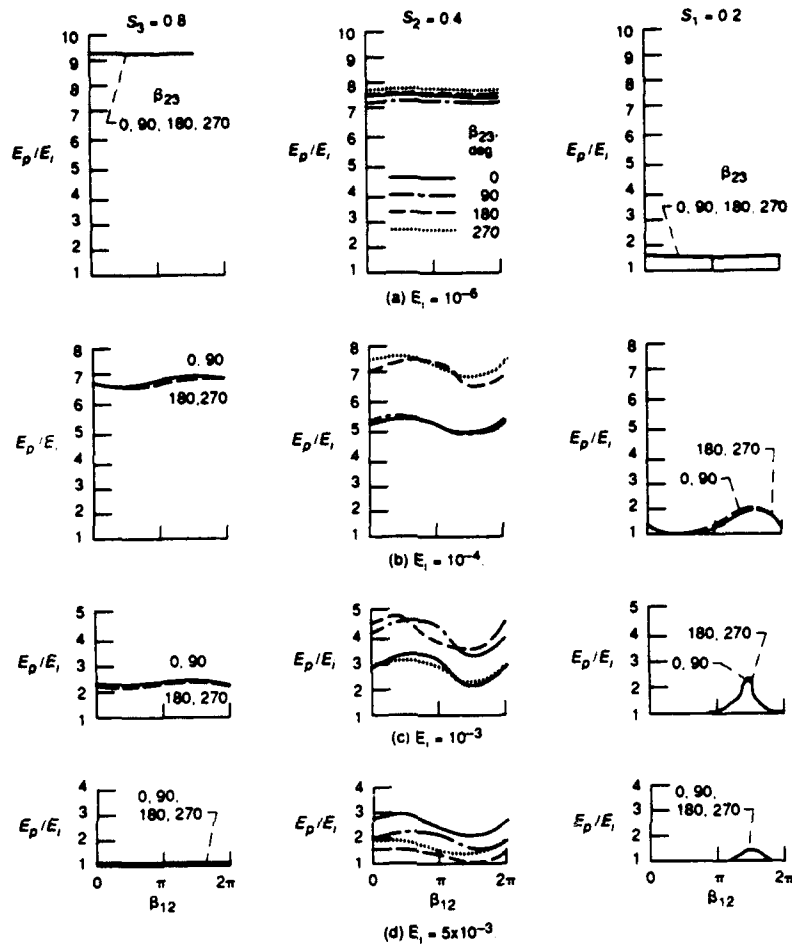


Figure 17 —Effect of phase-difference angles β_{12} and β_{23} on peak of each frequency component (three Strouhal numbers) for equal initial energy levels E_i .

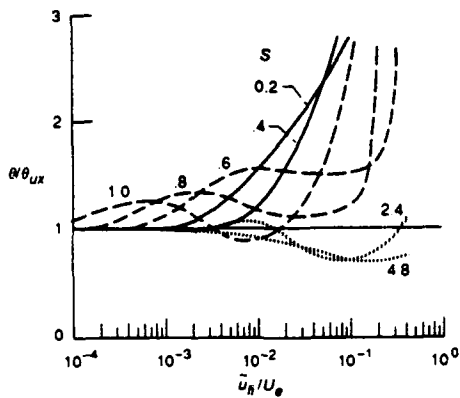


Figure 18 —Effect of forcing level at several Strouhal numbers on momentum thickness at $x/d = 3$

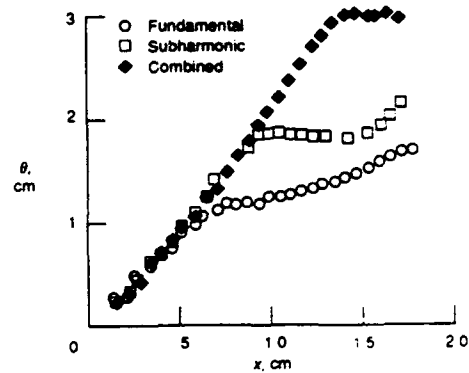


Figure 19 —Lateral growth of mixing layer excited by fundamental alone, - by subharmonic alone, or by both (From Weisbrodt & Wygnanski 1988)

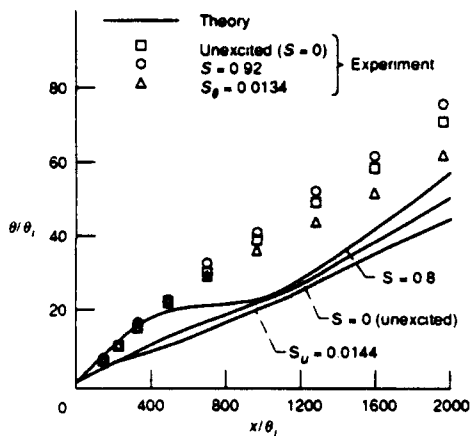


Figure 20 — Calculated momentum thickness (Mankbadi 1985c) under several forcing Strouhal numbers in comparison with Hussain's (1982) measurements. Exit conditions: $u'/U_\infty = 0.3\%$, forcing level, 1%, unexcited level of coherent components, 0.1%.

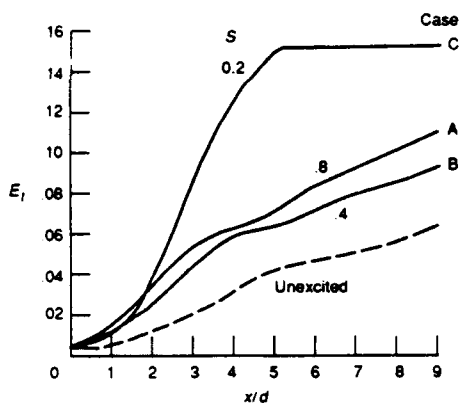
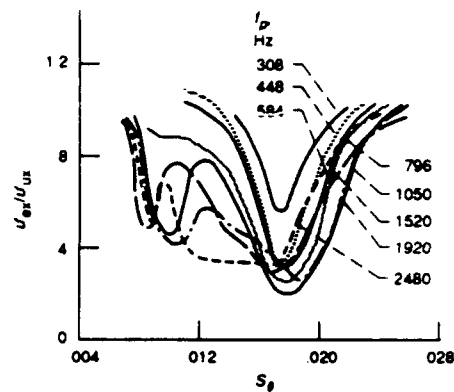
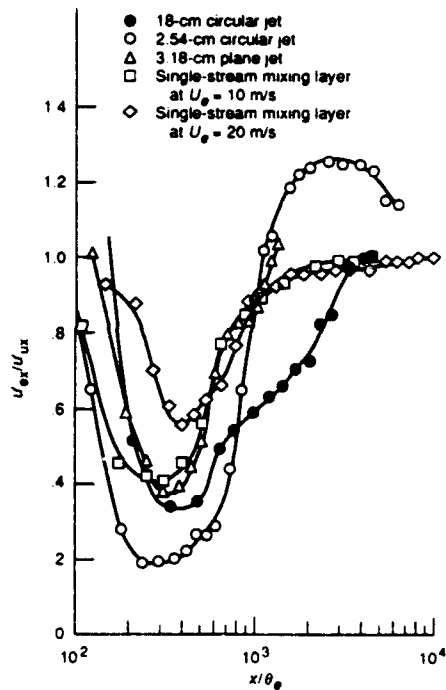


Figure 21 — Turbulence enhancement under various ratios of initial energy levels. Case A: initial phase differences $\beta_{12} = 270^\circ$, $\beta_{23} = 90^\circ$; initial energy levels, $E_{11} = 0.0005$, $E_{21} = 0.0005$, $E_{31} = 0.005$. Case B: $\beta_{12} = 270^\circ$, $\beta_{23} = 270^\circ$, $E_{11} = 0.0005$, $E_{21} = 0.005$, $E_{31} = 0.0005$. Case C: $\beta_{12} = 270^\circ$, $\beta_{23} = 180^\circ$, $E_{11} = 0.005$, $E_{21} = 0.0005$, $E_{31} = 0.0005$.



(a) Dependence of u'_{ex}/u'_{ux} on S_θ measured on the centerline of 2.54-cm jet at $x/d = 4$ for different peak frequencies.



(b) Downstream variation of u'_{ex}/u'_{ux} for $S_\theta = 0.017$, measured along a constant y line near the lip.

Figure 22 — Turbulence suppression in shear flows. (From Zaman & Hussain 1981, and Hussain 1986.)

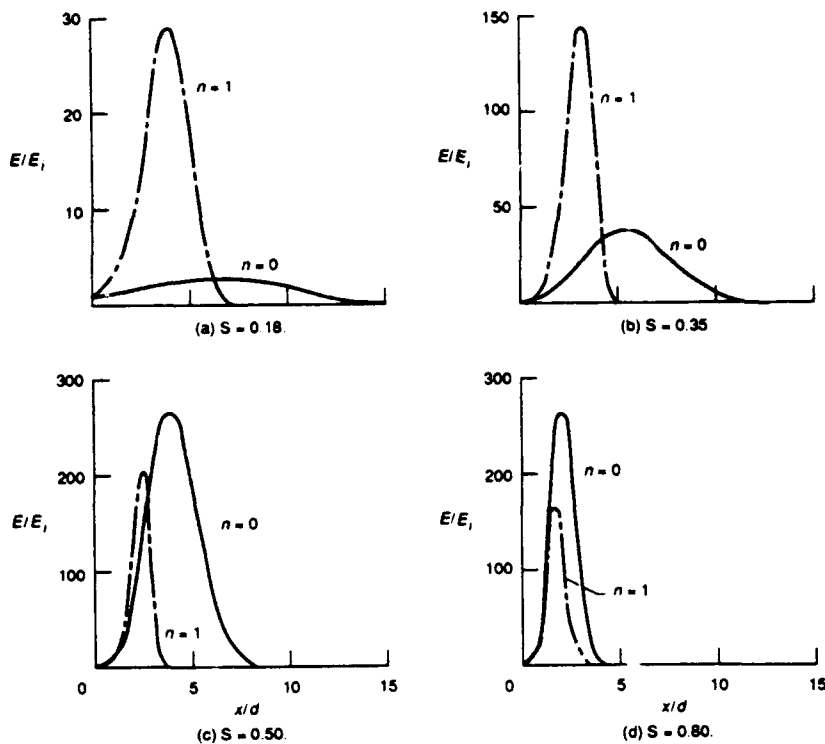


Figure 23—Large-scale structure kinetic energy ratio along jet: comparison between the $n = 0$ and $n = 1$ modes.

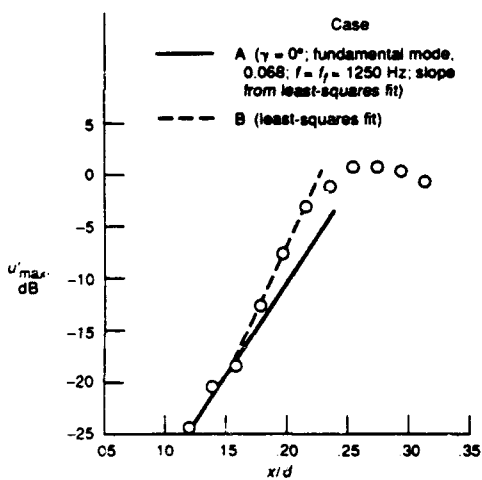


Figure 24—Comparison of streamwise growth of maximum fluctuations in seeded helical modes for two cases. Case A: plane wave at fundamental frequency $f_1 = 2500$ Hz plus pair of azimuthal waves ($n = \pm 1$) at subharmonic frequency $f_3 = 1250$ Hz. Case B: a pair of azimuthal waves ($n = \pm 1$) at frequency $f_3 = 1250$ Hz. (From Corke & Kusek 1991)

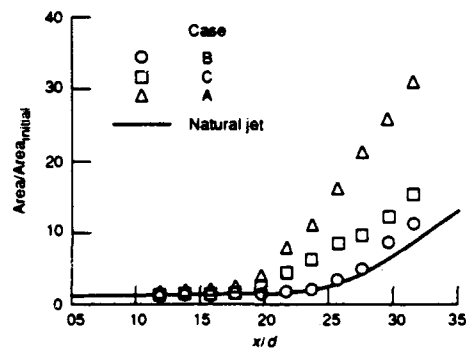


Figure 25—Streamwise development of azimuthally summed momentum thickness for three cases and natural jet. Case A: plane wave at fundamental frequency $f_1 = 2500$ Hz plus pair of azimuthal waves ($n = \pm 1$) at subharmonic frequency $f_3 = 1250$ Hz. Case B: a pair of azimuthal waves ($n = \pm 1$) at frequency $f_3 = 1250$ Hz. Case C: a pair of azimuthal waves ($n = \pm 1$) at frequency $f_1 = 2500$ Hz. (From Corke & Kusek 1991)

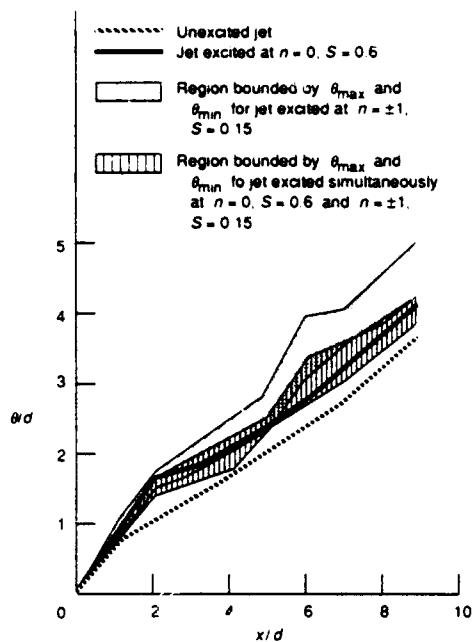
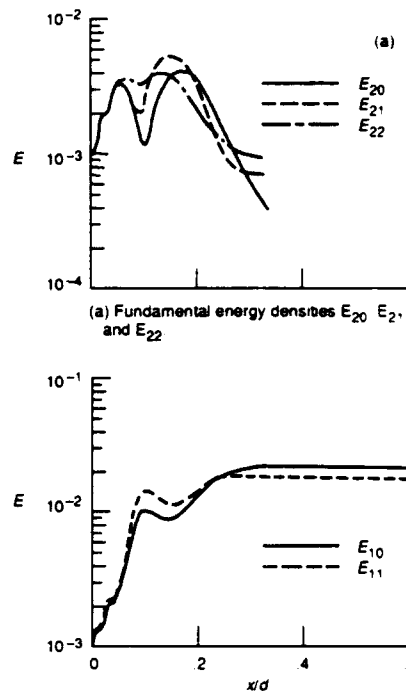


Figure 26 — Multimodal excitation (forcing levels: $\bar{u}_y/U_0 = 0.06$, $S = 0.6$, $n = 0$; $\bar{u}_y/U_0 = 0.02$, $S = 0.15$, $n = \pm 1$). (From Raman 1991)



(a) Fundamental energy densities E_{20} , E_{21} , and E_{22}

(b) Subharmonic energy densities E_{10} and E_{11} . $E_{10i} = E_{20i} = E_{21i} = E_{22i} = 10^{-3}$ and $\psi_{0i} = -\pi$.

Figure 27 — Development of energy densities for five wave modes. (From Lee & Liu 1989)

Understanding turbulence via vortex dynamics: some new perspectives

FAZLE HUSSAIN

*Department of Mechanical Engineering
University of Houston, Houston
TX 77204-4792, U.S.A.*

Abstract: This lecture will review some new aspects of vortex dynamics, which are elucidated by direct numerical simulation of the Navier-Stokes equations. Recognizing from our study of the reconnection mechanism that vortex lines associated with coherent structures are frequently helical, we study first the evolution of a laminar vortex column with nonuniform core and then its evolution in the presence of fine-scale homogeneous turbulence. We show that core dynamics, although ignored so far, consists of travelling vorticity wavepackets and can be very significant in vortex dynamics and vortex interactions, and can be better explained by *complex helical wave decomposition*, a new mathematical tool, than in terms of swirl and meridional flow. Our results reveal a new mechanism for direct coupling between coherent structures and fine-scale turbulence and hence for the failure of the hypothesis of local isotropy.

1. Core Dynamics

Here we build on our long-standing proposal that coherent structures in fluid turbulence should be characterized by coherent vorticity, the underlying instantaneously space-correlated vorticity, and that vortex dynamics is a tractable avenue for understanding evolutionary dynamics of coherent structures, their role in turbulent transport phenomena, and their interaction with fine-scale turbulence.

Investigation of vortex lines in the bridges during reconnection of two antiparallel vortex tubes (Melander & Hussain, 1988, referenced as MH) revealed that these lines are helical, hence inducing flow along the vortex axes; as a result of this, there is an inviscid 'vorticity smoothing mechanism' that causes enstrophy production opposite to that which would otherwise be expected and counters vorticity augmentation caused by vortex stretching in the same cross section. In order to focus on the axial flow in the bridges, we have idealized this problem to that of an axisymmetric vortex with a

sinusoidal variation of core size. This way we eliminate the complications of curvature and the flow induced by the threads (MH). Because of the axial variation of the core diameter, there is also an axial variation of swirl and hence twisting of vortex lines soon after $t = 0$. Figure 1 shows a schematic of the vortex at a time $t > 0$ with vortex lines lying on the shaded surface denoting an axisymmetric vortex surface (not a vorticity level surface, but $rv = \text{constant}$); a 90° cutaway is introduced to enhance comprehension of meridional streamlines, and swirl and axial velocity profiles. The vortex evolves as a result of the interaction between meridional flow and swirl. The velocities u, v , and w in the (r, θ, z) coordinates are governed by the following equations:

$$D_t \zeta = \text{viscous term}; \quad \zeta = rv; \quad (1.1)$$

$$D_t \eta = r^{-4} \partial \zeta^2 / \partial z + \text{viscous term}; \quad \eta = \omega_\theta / r \quad (1.2)$$

where $D_t = \partial_t + u \partial_r + w \partial_z$ denotes the material derivative in the meridional flow, whose streamfunction ψ is related to u, w and ω_θ as follows:

$$u = \psi_z / r, \quad w = -\psi_r / z \quad \text{and} \quad r \omega_\theta = \psi_{rr} - \psi_r / r + \psi_{zz}.$$

The axial variation of the swirl, ζ , produces coiling of vortex lines and hence axial pumping of fluid in a direction that will tend to smooth out core size variation which is opposite to the axial variation of $|\omega|$ (i.e., w is opposite to the vorticity flux). Swirl is large where core size is small and *vice versa*. Also, the twisting is stronger near the axis than at the outer edges. Note that both swirl and meridional flow would have undergone uneventful decay were it not for the coupling term $r^{-4} \partial \zeta^2 / \partial z$ between the two fields. Azimuthal vorticity, ω_θ , initially zero, is thus immediately created by axial expansion and contraction of the vortex tube via the coupling term. This is the basic mechanism for motion of waves along the vortex axis. Maximum twisting of the vortex lines occurs at the inflection points of $\zeta^2(z)$. The creation of ω_θ is necessary to induce the meridional flow. Since the meridional flow first forms counter circulating cells (we call them primary cells), the vorticity peak (at the smallest initial core) bifurcates into two parts which travel in opposite directions. We may also think of this phenomenon as a wavepacket which bounces back and forth while undergoing viscous decay. The first rebound induces a meridional flow reversal within each primary cell, thereby generating a secondary cell, which soon dominates by pushing out the primary cell. The wavepacket behavior of the vorticity is associated with enstrophy production P_ω , which can be related to ψ for

inviscid flows as:

$$P_\omega = - \frac{4\omega_z^2}{r^2} \frac{\partial \psi}{\partial z} \quad (1.3)$$

Thus, P_ω can be inferred at any time from the meridional flow streamline pattern.

It is important to focus on the generation of meridional flow, hence $\eta = \omega_\theta / r$. We find that for inviscid flow,

$$D_t \eta = (\text{axial vorticity}) \times (\text{differential rotation}),$$

the rotation being along an axisymmetric vortex surface; thus, the instantaneous value of η does not affect instantaneous material generation of η , i.e. $D_t \eta$. Because of axial transport of vorticity as wavepackets, η and $D_t \eta$ also oscillate in time, η leading $D_t \eta$ by a phase shift of about 90° ; this phase shift controls η -transport. The two η -transport mechanisms (convection of η by meridional flow and η -generation by differential rotation along the axis) are in opposite directions (hence slower η -transport) in the primary cell, but in the same direction (hence faster η -transport) in the secondary cell.

By investigating this flow for increasingly higher Re we have found that the core size variations do not decay in the high Re -limit. Moreover, we find that the wavemotion is more rapid at higher Re , albeit the wavespeed remains finite as $Re \rightarrow \infty$. This result has significant implications for computational vortex filament models (e.g. Moore & Saffman, 1972) where it is assumed that core variations are smoothed out by the above wavemotion. This assumption becomes dubious in the light of our findings.

2. Helicity and Helical Wave Decomposition

The helical nature of flow has become the focus of considerable interest in recent years (Moffatt 1969). Of the three quantities: helicity density $h = \mathbf{u} \cdot \boldsymbol{\omega}$, relative helicity $h_r = h / (|\mathbf{u}| |\boldsymbol{\omega}|)$, and helicity integral $H = \int \mathbf{u} \cdot \boldsymbol{\omega} dV$, only the last is Galilean invariant and is a conserved quantity for inviscid flow. From $|\boldsymbol{\omega} \wedge \mathbf{u}|^2 = u^2 \omega^2 / (1 - h_r^2)$ and the Navier-Stokes equations:

$$\mathbf{u}_t + \boldsymbol{\omega} \wedge \mathbf{u} = -\nabla(P/\rho + u^2/2) + \nu \Delta \mathbf{u}, \quad (2.1)$$

it is common to claim that cascade is small if $h_r \equiv \pm 1$. But such thinking is fraught with many pitfalls. First, although $h_r \equiv \pm 1$ does imply small $|\boldsymbol{\omega} \wedge \mathbf{u}|$, it

does not imply small $\nabla \wedge \omega \wedge u$ as high frequency oscillations of $\omega \wedge u$ are possible. In some frames, $\omega \wedge u$ can be large but purely potential so that vorticity obeys the purely diffusion equation and hence there is no cascade. A rectilinear vortex provides a glaring example. Thus, for cascade suppression, Beltramization (i.e., $h_r = 1$) is sufficient, but not necessary. An example of cascade suppression for which $\nabla \wedge \omega \wedge u = 0$ is not satisfied is a laminar vortex ring which travels at a constant speed.

Thus, while H is a topological property, h and h_r are of questionable use. But recognizing that local helical structure in a flow contains some essential physics, we propose that complex helical wave decomposition (Moses 1971; Lesieur 1990) is the relevant tool for understanding vortex dynamics and interactions. This decomposition in essence expands the field variables (e.g., u, ω) in terms of the eigenfunctions of the curl operator, which has only real eigenvalues in a periodic box or in infinite space. Moreover, the eigenfunctions can be chosen to form a complete set of orthonormal basis functions. In Fourier space, for each wavevector k there are two eigenmodes corresponding to the positive and negative eigenvalues k and $-k$. All functions which are linear combinations of eigenfunctions of positive eigenvalues can be called *right-handed* as trajectories or vector lines locally form right-handed helices. Similarly, we call linear combinations of eigenfunctions corresponding to negative eigenvalues *left-handed*. Thus for an incompressible velocity field, $u = u_R + u_L + \nabla \phi$. Since $\nabla \phi$ is the projection of u onto the eigenspace corresponding to the eigenvalue $k = 0$ of the curl operator, and since $\nabla \cdot u = 0$, we have $\Delta \phi = 0$. If the potential part of the flow is constant at infinity, or for a periodic box, $\nabla \phi$ is a constant. Thus u_R and u_L are unique, and both translationally and rotationally invariant. Similarly, $\omega = \omega_R + \omega_L$ (assuming no rotation at infinity).

The decomposition of a flow field into polarized (i.e. right- and left-handed) components is rooted in the intrinsic physical nature of the Navier-Stokes equations: the eigenmodes of the curl operator are exact solutions of the Euler equation and constitute a special class of solutions called Beltrami flows with constant abnormality (i.e. $\omega = \text{constant } u$). Because of orthogonality of the eigenfunctions of the curl operator, helicity takes the simple form

$$H = H_R + H_L \quad (2.2)$$

where

$$H_R = \int u_R \cdot \omega_R dV \geq 0; \quad H_L = \int u_L \cdot \omega_L dV \leq 0. \quad (2.3)$$

The decomposition also provides a clearer insight into the flow physics:

cascade is inhibited wherever $(\omega_R + \omega_L) \wedge (u_R + u_L)$ and its first spatial derivative are small. One can also easily show that cascade from interactions of modes is small when the modes are of the same parity (*i.e.* same handedness) but large when they are of opposite parity. One can thus infer that polarized vortices are persistent, hence "coherent," features of the flow.

We apply the decomposition to obtain some understanding of our axisymmetric vortex in the physical space. Remember that vector lines of $\omega_R(\omega_L)$ are right-handed (left-handed) helices. In general the physical space distributions of ω_R and ω_L overlap. The ω_R and ω_L distributions of our vortex are shown as functions of time in Figure 2 (note identical distributions of $|\omega_R|$ and $|\omega_L|$ at $t = 0$ in Figure 2a). This evolution is much more revealing than the evolution of the h_r field (not shown). The polarized components move in opposite directions. Aside from the nonlinear interaction between ω_R and ω_L there is an obvious resemblance to d'Alembert formula for the 1-D wave equation!

Note that $|\omega_R|$ is antisymmetric to $|\omega_L|$ in z with respect to $z = l$ at all times, coinciding in frame (a). The helical decomposition thus gives unique separation of ω into ω_R and ω_L components, a feature we think is essential for deeper understanding of coherent structures in turbulent flows. Note that the $|\omega_R|$ peak moves to the left instead of to the right as one would expect; this is a consequence of nonlinear interaction (discussed below). In fact, in the case of an isolated vortex with only right-handed polarization, the $|\omega_R|$ peak does indeed move to the right. In Figure 2 we see that as they move, the wavepackets deform: they broaden by diffusion, but also elongate and form a bubble by nonlinear effects. The nonlinearity is also responsible for the breakup of the initial front-back symmetry, *i.e.* steepening at the front with a tail at the back.

To understand the nonlinear interactions between polarized components, we extract each component by the projection operators (P^+ , P^-). Here we discuss only $|\omega_R|$ (by symmetry, the ω_L equation is obvious):

$$\begin{aligned} \frac{\partial \omega_R}{\partial t} = & \underbrace{-(\nabla \wedge (\omega_R \wedge u_R))}_{\text{I}} + \underbrace{\{P^+[\nabla \wedge (\omega_R \wedge u_R)]\}}_{\text{II}} - \underbrace{\{P^+[u_L \cdot \nabla \omega_R]\}}_{\text{III}} \\ & + \underbrace{\{P^+[\omega_R \cdot \nabla u_L]\}}_{\text{IV}} - \underbrace{P^+[\nabla \wedge (\omega_L \wedge u)]}_{\text{V}} + \underbrace{\left\{\frac{1}{\text{Re}} \Delta \omega_R\right\}}_{\text{VI}} \end{aligned} \quad (2.4)$$

Term I is the inviscid self-evolution; term II is the generation of ω_L by

evolution of ω_R ; term III is the contribution to ω_R by its advection by u_L ; term IV is stretching of ω_R by u_L ; term V is the ω_R generation by ω_L , consisting of self-interaction of ω_L and the right-handed part of stretching and advection of ω_L by u_R ; and term VI is the viscous diffusion term. Terms II-V represent coupling between the left- and right-handed components. We have evaluated these terms for the vortex and find that in general their dominance in decreasing order are as follows: III, I, V, IV, VI, and II.

The evolution of ω_R can be largely understood in terms of two effects: self-evolution and advection by the u_L field. The self-evolution (term I) attempts to move the ω_R -packet to the right by adding vorticity at the front and deleting it at the back. But because u_L moves the ω_R -packet to the left, the leftward motion dominates, although it is slower than u_L . Also, because the velocity field has the largest axial component on the axis, it pushes the front of the packet backward at a faster rate near the axis (Figure 2g), hence causing the formation of a low enstrophy bubble (Figure 2i). The enhanced elongation is a combined effect of terms III and V.

The above gives a glimpse of how helical wave decomposition provides a new tool for analysis of core dynamics in terms of tractable interaction of polarized velocity and vorticity wave packets (see Melander & Hussain 1991a for details). Such physical insight into the core dynamics is impossible via the usual tools of vortex dynamics such as Biot-Savart law and local induction approximation. We hope many other important vortex phenomena (one discussed briefly below) can be understood better by this approach. Vortex breakdown is another obvious candidate (subject of a separate study by us).

3. Interaction with Fine-scale Turbulence

In an attempt to understand the coupling between large-scale coherent structures and fine-scale turbulence, we have repeated the simulation reported earlier with the axisymmetric sinusoidal coherent vortex (called CV) immersed in a background of isotropic fine-scale incoherent turbulence. Care was taken to assure that the initial rms level was sufficiently high for the fine-scale turbulence to survive long enough to dynamically interact with CV. The fine-scale size was chosen to be the smallest permitted by the resolution, but still with a spectral gap between it and that of CV. We find that the scales in the background incoherent vorticity grow progressively, so that at the end of the simulation the largest incoherent scales are comparable to CV. The spectral gap is gradually filled not by diffusive mechanisms, but by interaction between incoherent turbulence and CV. While the size of the incoherent turbulence remains uniform in space, the strength is higher at the boundary of CV, where it is wrapped around CV and energized by stretching. This is not dissimilar from the growth of axisymmetric vortices on an

impulsively rotated rod except that in our case the curved vortices around CV are intrinsically asymmetric, induced by the shear in the boundary of CV.

The spiral structures formed from organization of the incoherent turbulence are indeed quite different from the spiral sheet-like structures proposed by Lundgren (1982). The structures we find are rod-like spiral patterns wrapped around CV with senses aligned or opposed to the swirl of CV (Figure 3). The helical wave decomposition is also helpful in understanding the coupling between CV and incoherent turbulence. The spiral structures are found to have a tendency to be highly polarized: they are either predominantly right-handed or predominantly left-handed. We indeed find a strong correspondence between peaks of incoherent turbulence in the boundary of CV and high values of the degree of polarization. The incoherent turbulence spirals undergo growth through merger by the (truly inviscid) pairing mechanism and not by fusion through viscous decay and diffusion. In order for the spiral vortices to pair, their transport (axial to CV) is essential. There are two distinct mechanisms for such transport: i) transport of nearby opposite-signed vortices as dipoles, and ii) self-induced transport due to curvature of the azimuthally aligned vortices (not present in the 2D case). Because of the shear of CV, the small-scale vortex spiral undergoes differential stretching, which provides the spiral an intrinsic tendency to become polarized.

In virtually all turbulence theory, local isotropy, which also forms the cornerstone of Kolmogorov's hypothesis, is universally assumed and implies decoupling of large and fine scales. By extrapolating our results (Figure 3), we conjecture, for the case of very high Re , a hierarchy of structures of successively smaller scales, i.e. a fractal cascade. This supports our long-held doubt regarding the validity of the concept of local isotropy. Of course, local isotropy does not require individual fine scales to be isotropic, but merely suggests the lack of any statistical preference for the fine-scale structure's orientation. We think that the fine scales retain some preferred orientation with respect to the coherent structures.

The CV-in-turbulence naturally decays, and these unforced flows will eventually laminarize, in a time scale depending on both Re and the initial rms turbulence level. If the level is too low, CV recovers axisymmetry; if it is too high, CV is completely disrupted. For intermediate values interactions discussed above occur. In this case, however, there is the interesting possibility of excitation of bending waves on CV. Without bending waves, the spiral structures tend to be axisymmetric as they wrap around CV, thus diminishing their stretching by CV. When bending waves are excited, CV ceases to be axisymmetric and is then in a position to continue the stretching of the spiral incoherent turbulence. This is an example of feedback (or backscatter) from the smaller scales to CV. Thus, we have a mechanism of coherent structure/fine-scale interaction: the former organizes the latter by

vortex stretching and the latter, if Re is high enough, induces bending waves in the former to generate the mechanism of its own survival.

Thus, for very high Reynolds numbers we propose a fractal scenario of vorticity cascade from the largest scale CV to the smallest scales. Since the smallest scales are closely coupled with the CV, which will have preferred orientations in any turbulent shear flow, this study provides a direct challenge to the hypothesis of local isotropy, as well as provides a mechanism for small-scale anisotropy.

This lecture is based on joint research collaboration with Professor M. V. Melander of the Southern Methodist University in Dallas, Texas. This is a progress report of our continuing research activities on vortex dynamics and their connection to coherent structures in shear flow turbulence. This research is funded by the Office of Naval Research and the Air Force Office of Scientific Research.

References

- KIDA, S., TAKAOKA, M. & HUSSAIN, F., 1989 Reconnection of the two vortex rings. *Phys. Fluid A* 1, 630-632.
- LESIEUR, M., 1990 Turbulence in Fluids (Kluwer Acad. Publ.).
- LUNDGREN, T. S., 1982 Strained spiral vortex model for turbulent fine structure. *Phys. Fluids*. 25, 2193 .
- MELANDER, M. V. & HUSSAIN, F., 1988 Cut-and-connect of two antiparallel vortex tubes CTR Report S88, Stanford U., 254-286.
- MELANDER M. V. & HUSSAIN, F., 1990 Topological Aspects of Vortex Reconnection. In *Topological Fluid Mechanics*. eds. H.K. Moffatt & A. Tsinober, 485-499 (Cambridge U. Press).
- ANDER, M. V. & HUSSAIN, F., 1991a Vortex core dynamics, helical waves and organization of fine-scale turbulence (submitted).
- MELANDER, M. V. & HUSSAIN, F., 1991b Viscous generation of helicity, and non-trivial topology of vortex lines in coherent structures (submitted).
- MOFFATT, H. K., 1969 The degree of knottedness of tangled vortex lines. *J. Fluid Mech.* 35, 117.
- MORE, D. W. & SAFFMAN, P. G., 1972 The motion of a vortex filament with axial flow. *Phil. Trans. Roy. Soc. A* 272, 403-429.
- MOSES, H. E., 1971 Eigenfunction of the curl operator, rotationally invariant Helmholtz theorem and application to electromagnetic theory and fluid mechanics. *SIAM J. Appl. Math.* 21, 114-144.

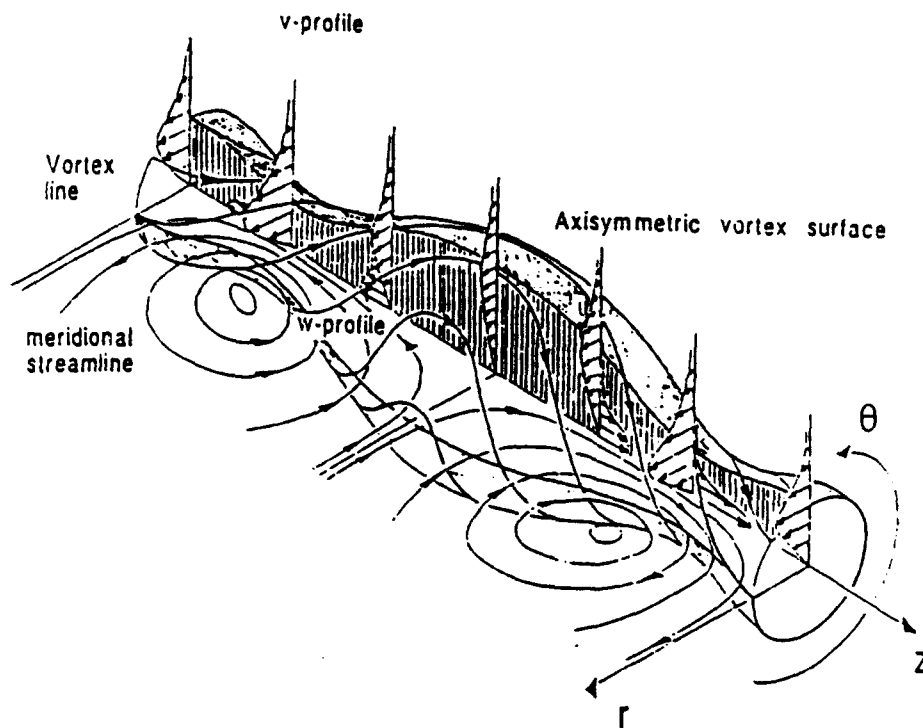


Fig. 1. Axisymmetric vortex surface with a 90° cutaway on which vortex lines lie. Also shown are streamlines in a meridional plane, and $v(r)$ and $w(r)$ profiles.

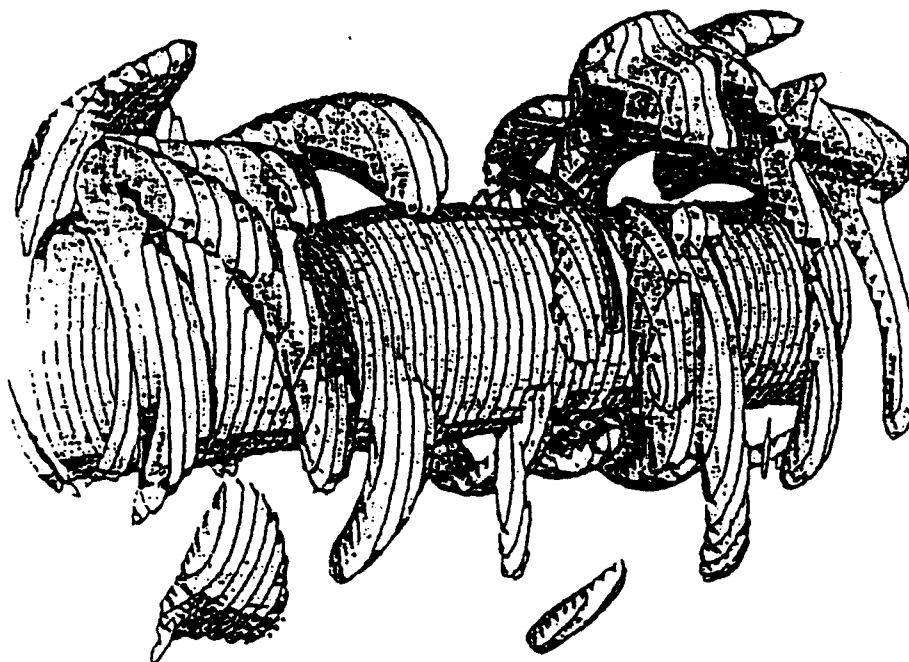


Fig. 3 . $|\omega|$ surface at 10% of the peak value.

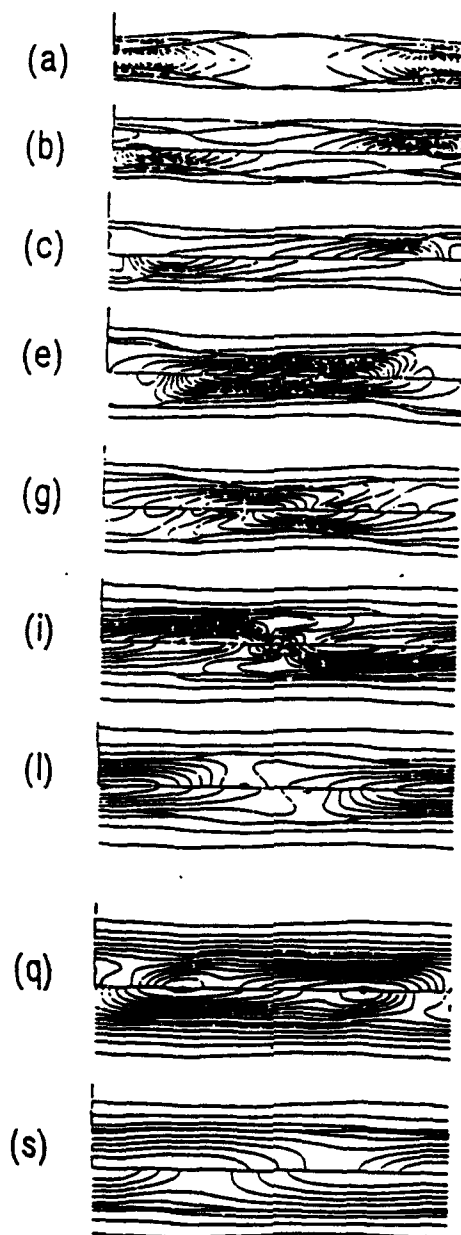


Fig. 2 Evolution of $|\omega_R|$ (above) and $|\omega_L|$ (below) the axis, with the $N_k = 1$ contour overlaid.

Evidence of Local-Axisymmetry in the Small Scales of a Turbulent Planar Jet

Hussein J. Hussein
Department of Mechanical Engineering
Vanderbilt University
Nashville, TN 37235

Abstract

The small scale characteristics of turbulent flow resulting from a jet exhausting into a quiescent environment is investigated. The Reynolds number based on exit conditions is approximately 20,000. Second order derivative moments are obtained using a flying hot-wire anemometry.

The measured derivative moments are used to evaluate both deviations from the requirements of local-isotropy and the conditions for turbulence which is locally invariant about a preferred direction. Results of the rate of dissipation of kinetic energy are presented.

1 Introduction

The present work consists of an investigation of the small scales in a planar turbulent jet using flying hot-wire anemometry. The overall objective is to provide a basis for evaluating turbulence closure hypotheses from measurements of the moments of the velocity and the rate of dissipation of turbulence energy. The secondary objectives are: evaluation of deviations from local isotropy and a direct measurement of the dissipation.

The high turbulence intensity in a jet gives rise to cross-flow and rectification errors on hot-wires (Tutu and Chevray 1975). These errors as well as the effect of the fluctuating convection velocity on the measured derivatives can be reduced by superimposing a velocity on the hot-wire, thereby reducing the effective turbulence intensity. This was accomplished by using hot-wires mounted on a flying wire system which reduced the effective turbulence intensity from 28% to 13% at the centerline of the jet and to a maximum of 30% at the outer edge.

Measurements of the dissipation rate of energy have in the past relied on the assumption of local isotropy. The concept of local isotropy is of prime importance to the theory of turbulent flows since it implies the universality of the small scale structures and the loss of all directional preferences at the dissipative scales. Although this leads to considerable simplifications in determining the turbulent dissipation rate, its validity is limited to flows with sufficiently large Reynolds numbers. Recent measurements of the fine scale structures in laboratory turbulent jets show deviations from the conditions of local isotropy, Antonia et al (1987), George and Hussein (1991) and Praskovsky, et al (1990). Extensions of the theory of local isotropy and introduction of the concept of local-axisymmetry which accounts for the directional preferences due to the finite

Reynolds number of these laboratory flows have recently been developed, George and Hussein (1991). These experimental results show that the velocity derivative correlations in a large number of flows are not well described by the conditions of local-isotropy.

The objective of this work is to provide experimental evidence of deviations from local isotropy in a planar turbulent jet. Earlier experiments on planar jets by Antonia et al (1986) give credence to deviations of the small scales from the requirements of local isotropy. The present investigation addresses these and other questions on the nature of local-isotropy at laboratory range Reynolds numbers. Since one of the primary consequences of local isotropy is on the determination of the dissipation rates of turbulence, the best test for local isotropy is one in which different sets of the measured velocity derivative correlations are compared relative to each other. In the present investigation, this was accomplished using flying hot wire anemometry to obtain measurements of the streamwise and cross-flow derivatives of the velocity. These investigations of the dissipative scales of turbulence reveal dependence of the small scale structures on the large-scale anisotropic turbulent motion. This is exhibited in the deviations of the small scales from the requirements of local-isotropy. It is well known that this effect becomes more negligible as the Reynolds number tends to infinity. The importance of this large-scale and small-scale interaction is exhibited in all moderate Reynolds number flows. Since a large portion of fluid systems in laboratory flows are in this Reynolds number region, the reported research is of importance to understanding of the nature of the energy transfer in shear flows.

2 Small Scale Turbulence

2.1 Local Isotropy

One of the cornerstones of turbulence theory over the past fifty years has been the hypothesis of local isotropy. Introduced by Kolmogorov in 1941, local isotropy assumes that the small scale turbulence satisfies the relationships for isotropic turbulence, regardless of the anisotropy of the large scale energy-containing motions. The principal applications of local-isotropy have been the determination of the rate of dissipation of turbulence kinetic energy. In general, determination of the dissipation requires the measurement of twelve different derivative moments. (To-date, this has never been accomplished). The assumption of local isotropy reduces this requirement to the measurement of only a single derivative moment -- usually $\langle \partial u_i / \partial x_i \rangle^2$, the streamwise gradient of the streamwise velocity. Modellers of the kinetic energy and Reynolds stress equations also depend on local isotropy to reduce the component dissipations to a single isotropic dissipation.

There has been an increasing body of literature over the past 10 years documenting experimental results taken in a variety of flows which do not satisfy the isotropic derivative relations. For example, Browne et al. (1987) measured nine of the twelve derivative moments necessary to determine the dissipation in a plane wake, and showed clearly that local isotropy was not an appropriate description of at least that flow. Their best estimate of the actual dissipation differed by about a factor of two from the isotropic value. Similar results were obtained recently by Hussein and George (1989) in a round jet at much higher turbulence Reynolds number. Deviations from the requirements of local isotropy can be quantified by comparing the magnitudes of various mean square derivatives across the jet.

2.2 Locally-axisymmetric homogeneous turbulence

For a Newtonian fluid with a kinematic viscosity, ν , the rate of dissipation of turbulence kinetic energy per unit volume, ϵ , is given by

$$\begin{aligned} \epsilon = 2\nu \left\{ \left[\left\langle \frac{\partial u_1}{\partial x_1} \right\rangle^2 + \left\langle \frac{\partial u_2}{\partial x_2} \right\rangle^2 + \left\langle \frac{\partial u_1}{\partial x_3} \right\rangle^2 \right] \right. \\ \left. + \frac{1}{2} \left[\left\langle \frac{\partial u_1}{\partial x_2} \right\rangle^2 + \left\langle \frac{\partial u_1}{\partial x_3} \right\rangle^2 + \left\langle \frac{\partial u_2}{\partial x_1} \right\rangle^2 \right. \right. \\ \left. \left. + \left\langle \frac{\partial u_2}{\partial x_3} \right\rangle^2 + \left\langle \frac{\partial u_3}{\partial x_1} \right\rangle^2 + \left\langle \frac{\partial u_3}{\partial x_2} \right\rangle^2 \right] + \left[\left\langle \frac{\partial u_2}{\partial x_1} \right\rangle \left\langle \frac{\partial u_1}{\partial x_2} \right\rangle \right. \right. \\ \left. \left. + \left\langle \frac{\partial u_3}{\partial x_1} \right\rangle \left\langle \frac{\partial u_1}{\partial x_3} \right\rangle + \left\langle \frac{\partial u_3}{\partial x_2} \right\rangle \left\langle \frac{\partial u_2}{\partial x_3} \right\rangle \right] \right\} \end{aligned} \quad (1)$$

The direct measurement of the average dissipation and mean square vorticity clearly requires measurements of various components of the spatial derivatives. Because of the near impossibility of this in practice, investigators have usually relied on the assumption of local isotropy and Taylor's frozen field hypothesis in determining the dissipation.

For isotropic turbulence (Hinze 1975):

$$2 \left\langle \frac{\partial u_1}{\partial x_1} \right\rangle^2 = \left\langle \frac{\partial u_1}{\partial x_2} \right\rangle^2 = \left\langle \frac{\partial u_1}{\partial x_3} \right\rangle^2 = \left\langle \frac{\partial u_2}{\partial x_1} \right\rangle^2 = \left\langle \frac{\partial u_2}{\partial x_3} \right\rangle^2 = \left\langle \frac{\partial u_3}{\partial x_1} \right\rangle^2 = \left\langle \frac{\partial u_3}{\partial x_2} \right\rangle^2 \quad (2)$$

$$\left\langle \frac{\partial u_1}{\partial x_1} \right\rangle^2 = \left\langle \frac{\partial u_2}{\partial x_2} \right\rangle^2 = \left\langle \frac{\partial u_3}{\partial x_3} \right\rangle^2 \quad (3)$$

$$\left\langle \frac{\partial u_1}{\partial x_2} \right\rangle \left\langle \frac{\partial u_2}{\partial x_1} \right\rangle = \left\langle \frac{\partial u_1}{\partial x_3} \right\rangle \left\langle \frac{\partial u_3}{\partial x_1} \right\rangle = \left\langle \frac{\partial u_2}{\partial x_3} \right\rangle \left\langle \frac{\partial u_3}{\partial x_2} \right\rangle = -\frac{1}{2} \left\langle \frac{\partial u_1}{\partial x_1} \right\rangle^2 \quad (4)$$

Thus only measurement of $\langle \partial u_1 / \partial x_1 \rangle^2$ is necessary. This has been usually accomplished by measuring only the temporal derivative of the longitudinal components of the velocity and using Taylor's frozen field hypothesis.

The assumption of local isotropy simplified the experiments significantly but the accuracy of the results were impaired by the fact that shear flows such as the jet did not usually satisfy the relations for local isotropy. For the jet, this anisotropy of the small scales becomes more pronounced the further one gets from the centerline.

From the measurement of seven of the terms in equation (2) it was clear from the data that these derivative measurements did not satisfy the conditions for local isotropy. However, they were found to satisfy the conditions for axisymmetric homogeneous turbulence (Batchelor 1946, Chandrasekhar 1950) to within the experimental error. Thus it is appropriate to use the concept of locally axisymmetric turbulence introduced by George and Hussein (1991) for which

$$\left\langle \frac{\partial u_1}{\partial x_2} \right\rangle^2 = \left\langle \frac{\partial u_1}{\partial x_3} \right\rangle^2 \quad (5)$$

$$\left\langle \frac{\partial u_2}{\partial x_1} \right\rangle^2 = \left\langle \frac{\partial u_3}{\partial x_1} \right\rangle^2 \quad (6)$$

$$\left\langle \frac{\partial u_2}{\partial x_2} \right\rangle^2 = \left\langle \frac{\partial u_3}{\partial x_3} \right\rangle^2 \quad (7)$$

$$\left\langle \frac{\partial u_2}{\partial x_3} \right\rangle^2 = \left\langle \frac{\partial u_3}{\partial x_2} \right\rangle^2 \quad (8)$$

$$\left\langle \frac{\partial u_2}{\partial x_2} \right\rangle^2 = \frac{1}{3} \left\langle \frac{\partial u_1}{\partial x_1} \right\rangle^2 + \frac{1}{3} \left\langle \frac{\partial u_2}{\partial x_3} \right\rangle^2 \quad (9)$$

$$\left\langle \frac{\partial u_1}{\partial x_2} \right\rangle \left\langle \frac{\partial u_2}{\partial x_1} \right\rangle = \left\langle \frac{\partial u_1}{\partial x_3} \right\rangle \left\langle \frac{\partial u_3}{\partial x_1} \right\rangle = -\frac{1}{2} \left\langle \frac{\partial u_1}{\partial x_1} \right\rangle^2 \quad (10)$$

$$\left\langle \frac{\partial u_2}{\partial x_3} \right\rangle \left\langle \frac{\partial u_3}{\partial x_2} \right\rangle = \frac{1}{6} \left\langle \frac{\partial u_1}{\partial x_1} \right\rangle^2 - \frac{1}{3} \left\langle \frac{\partial u_2}{\partial x_3} \right\rangle^2 \quad (11)$$

From equation (3) it follows immediately that

$$\epsilon = \nu \left[\frac{5}{3} \left\langle \frac{\partial u_1}{\partial x_1} \right\rangle^2 + 2 \left\langle \frac{\partial u_1}{\partial x_2} \right\rangle^2 + 2 \left\langle \frac{\partial u_2}{\partial x_1} \right\rangle^2 + \frac{8}{3} \left\langle \frac{\partial u_2}{\partial x_3} \right\rangle^2 \right] \quad (12)$$

For isotropic turbulence equation (1) reduces to the familiar result,

$$\epsilon = 15\nu \left\langle \frac{\partial u_1}{\partial x_1} \right\rangle^2 \quad (13)$$

3 Experimental facility and techniques

3.1 The jet facility

The experimental program was carried out in the far field of a planar turbulent jet issuing into a quiescent environment. Driving the air jet was a 3-hp paddle blower. Swirl, spatial inhomogeneities in the mean flow and turbulence intensities were removed using wire screens and plastic straws. A smooth fifth order polynomial contraction ensures a top hat velocity profile at the exit. The experiments were performed in a large 4mx4mx10m room. The results presented in this report were carried out at X/d of 100 and 120 for experiments with exit Reynolds number for the experiments was 20000.

3.2 Data acquisition and sampling considerations

The hot-wire signals were digitized using a 15 bit, 16 channel A/D converter with a throughput rate of 150 kHz. The anti-aliasing filters used were Bessel Low-Pass Filters (manufactured by Frequency Devices, Model 848 P8195) and were tunable over a frequency range of 200 Hz to 51.2 kHz. Measurements of all of the components of the velocity and a number of the velocity derivatives were made. Care was taken to ensure that record lengths were long enough to ensure that statistical convergence was achieved.

3.3 Description of hot-wire probes

An array of standard cross-wire probes were used for the experiments. All the wires used on the probes were Wollaston (Pt-10%Rh) with 2.5 micron diameter. Compared to the Kolmogorov scales in this flow which are about 0.16mm at the centerline of the jet, the wires were sufficiently short so that the variances of the measured derivatives were not affected by length effects ($l_w \ll \eta$ where η is the Kolmogorov microscale, Wyngaard 1968). The small diameter of the wires was chosen since smaller diameter wires have higher resistance and hence better signal to noise ratio.

The anemometers used were Dantec 56C17 constant temperature anemometers operated with 0.6 overheat ratio. To avoid aliasing of the signals, signal conditioners were used to low pass the signals. The highest frequency in the flow (corresponding to the Kolmogorov microscale) was 12 kHz, so the low pass setting for the filters was at 15 KHz. This cutoff frequency was calculated using the sum of jet velocity and the superimposed velocity (flying wire speed) as the convection velocity.

The cross wire array made up of two standard cross-wire probes was selected to measure all the terms in the dissipation equation assuming locally axisymmetric homogeneous turbulence (George and Hussein 1991). The criteria used in design of this probe were that it have the least amount of probe interference, and acceptable spatial resolution for the derivative measurements. The spacing between the two cross wire probes was approximately 0.4 mm which is close enough in regards to the Kolmogorov microscale to avoid spatially filtering the derivative signal. This probe was used in two different experiments. In the first, the probe was aligned with the jet in such a way that the terms $\langle \partial u_1 / \partial x_1 \rangle^2$, $\langle \partial u_2 / \partial x_1 \rangle^2$, $\langle \partial u_2 / \partial x_3 \rangle^2$, $\langle \partial u_1 / \partial x_3 \rangle^2$, were measured. In the second, the probe was rotated 90 degrees to obtain $\langle \partial u_1 / \partial x_1 \rangle^2$, $\langle \partial u_3 / \partial x_1 \rangle^2$, $\langle \partial u_3 / \partial x_2 \rangle^2$, $\langle \partial u_1 / \partial x_2 \rangle^2$.

The hot-wires were calibrated in a low turbulence intensity calibration tunnel. The error in predicting the measured velocity from measured voltages was typically less than 0.1% over the entire range. Once the calibration coefficients were found, they were used for the determination of instantaneous velocity from the instantaneous voltages sampled by the A/D. The calibration data was verified at

the end of each experiment to insure that the calibration did not shift during the course of the experiment. The angle calibration for the cross-wires was done using a modified cosine law with a velocity-dependent k-factor (Beuther et al. 1987).

3.4 Differentiation

The streamwise gradients of the velocity components were computed from Taylor's hypothesis using

$$\frac{\partial}{\partial x} = \frac{1}{U_c} \frac{\partial}{\partial t} \quad (14)$$

where U_c is the convection velocity usually taken as the local mean velocity.

The differentiation of the electronic signal was accomplished by utilizing the high-pass filter characteristics of the Dantec 55N26 signal conditioning unit. It is well-known that the differentiation corresponds to +6dB/octave frequency response function which is also the low asymptote of a single-pole high pass filter. To ensure that deviations from this asymptote near the breakpoint were negligible, the high pass cutoff frequency was chosen about five times higher than the highest frequency of interest in the signal, that corresponds to a high frequency cutoff of 50 KHZ for these experiments. The time derivatives were computed from the output using the following relation which can be readily derived from linear system theory:

$$\frac{de_i}{dt} = 2\pi f_{HP} e_o \quad (15)$$

where e_i is the voltage of the signal to be differentiated, e_o is the voltage of the differentiated signal and f_{HP} is the setting of the high pass filter. Because of the severe attenuation at the lowest frequencies by the high-pass filter, the amplifier gain was set at 100 to provide additional amplification.

The measurements of the spatial derivatives were done by measuring the velocity components at two points that are in close proximity to each other, and taking the difference to approximate the velocity gradient. The noises in the difference signal are due to either quantization and electronic noise or to uncertainty in the calibration of the two wires. The voltage to velocity transformation is accurate to within 1% and the quantization error is of order of 0.6 mv, and rms electronic noise is of the order of 3mv. For this work the spacing between the wires is given by $\Delta = 2\eta$. The velocity from each wire and the corresponding spatial difference was computed from sampled voltages.

3.5 Rationale for flying probe

The numerous problems associated with the use of standard hot-wire anemometry in high turbulence intensity flows are well known. The errors due to cross-flow and the effect of the fluctuating convection velocity on the measured derivative both scale with the turbulence intensity, $\langle u^2/U^2 \rangle$. These hot-wire errors can be avoided by reducing the effective turbulence intensity. This is accomplished in this work

by moving hot-wires through the flow so that the effective mean velocity seen by the probe is that of the flow plus that of the wire, thereby reducing the effective turbulence intensity.

Flying hot wires in turbulent flows were used in the past by various investigators. Uberoi (1965) used a flying wire in his study of entrainment in shear flows. Cantwell and Coles (1983), Watmuff et al (1983), Panchapakesan and Lumley (1987) are other investigators that applied the moving wire techniques in a wind-tunnel, wake and heated jet respectively. There are various reasons why the moving wires were used. In this work the object is two-fold: to decrease the errors due to cross-flow and rectification, and to enable a correct implementation of Taylor's frozen field hypothesis, Lumley (1965) and George et al (1989).

3.6 Description of the flying wire system

Depending on the method by which probes are moved relative to the flow, flying hot-wire methods require special considerations that are not important for conventional hot-wire anemometry. The first is the possible wake and obstruction effects from the probe support mechanism. The second is the possible need for slip rings or optical methods for the transmission of velocity signal from the probes to the data acquisition equipment. The third is the need for an accurate determination of the position and velocity of the probe relative to the flow.

Figure 1 shows the flying wire system that was used for the experiments reported here. The design of this apparatus ensures that a constant traverse velocity is obtained and that the probe vibrations have scales which are smaller than the Kolmogorov microscales. A rake of multiple hot-wire probes is mounted on a streamlined cantilever beam. The beam which is mounted on a computer controlled track, extends from a traversing platform to a position that enables the probes to be in the measurement location of interest. The probes are traversed parallel to the axis of the jet.

In the flying hot-wire system, a rake of hot-wire probes are mounted on a cantilevered airfoil which attached is to a one-dimensional track. This mechanism enables the superposition of a steady uniform velocity on the hot-wire probes. A computer controlled optical encoder that enables the support mechanism to be traversed at constant velocities. During an experimental run, the mechanism is traversed towards the jet in a trajectory that is parallel to the jet axis. This enables the superposition of a uniform velocity on the hot-wire probes. This was accomplished by using an encoder pulse that triggered the A/D converter to collect the data. The short charging time of the sample and hold of the A/D (nanoseconds) insured that the measurement was effectively taken at a point. The data was sampled along the track at specified locations along the track and 4800 samples were taken for a number of selected locations across the jet.

The effect of the wing on the flow was carefully studied. The wing had a low coefficient of drag C_d of 0.003 and a Reynolds number of 1500 at 1 m/s. The large scale characteristics of the flow around the wing were observed with smoke wires. There are minimal amounts of flow disturbances on the jet as the wing is traversed through it.

Measurements of the velocity field were obtained at $X/d = 100$ and 120. The problems associated with the support mechanism being continuously in the path of the flow is overcome by waiting for the flow to readjust after each traverse. The probe speed was selected so that the velocity derivative information can be resolved. The location and velocity of the beam were obtained from an optical encoder along the track. The signal is transmitted through a set of cables embedded inside the beam and which are connected directly to the A/D converter, enabling the measurements to be carried out without the use of slip-rings.

4 Experimental Results

The mean axial velocity normalized by the centerline velocity, U/U_c , is plotted versus the non-dimensional radial coordinate, y/b_0 , in Figure 2. The virtual origin of the jet is 5.2 and the jet spread constant is 0.093. The jet spread result obtained by Goldschmidt (1983) is 0.095 which means that the previous results indicate a jet spread which is wider than that of the present investigation. Even though the results are close, it is important to note that the difference can be explained by the fact that the earlier stationary wire measurements are expected to read higher velocity readings due to cross-flow errors. This is consistent with the expectation that the stationary wires measure wider jet growth than the moving wire results, Hussein and George (1989).

The streamwise derivatives of the three velocity components were calculated from their corresponding measured temporal derivatives of $\langle \partial u_1 / \partial t \rangle$, $\langle \partial u_2 / \partial t \rangle$, $\langle \partial u_3 / \partial t \rangle$. The issue of the applicability of Taylor's hypothesis was addressed by utilizing the flying wire mechanism. The effect of the fluctuating convection velocity is most prominent in the breakdown of Taylor's frozen field hypothesis (Lumley 1965). The contribution of the terms depending on the fluctuating velocity are less than 4% for the flying wire results, and they therefore are close to the actual values of $\langle \partial u_i / \partial x_j \rangle^2$.

Figure 3 shows the profiles of the velocity derivatives in the streamwise direction. These derivatives satisfy the isotropic relations near the centerline, but progressively deviate from them as the radius increases. On this figure, $\langle \partial u_1 / \partial x_1 \rangle^2$, $\langle \partial u_2 / \partial x_1 \rangle^2$ and $\langle \partial u_3 / \partial x_1 \rangle^2$ measured with the cross-wire probes are plotted as a function of transverse positions across the jet.

The velocity derivatives in the azimuthal direction, $\langle \partial u_1 / \partial x_3 \rangle^2$ and $\langle \partial u_2 / \partial x_3 \rangle^2$ measured with two cross probes in close proximity to each other shown on Figure 4. The other experiment which was performed by rotating the probes by 90° to measure the velocity derivatives in the transverse direction. The results from this experiment, $\langle \partial u_1 / \partial x_2 \rangle^2$ and $\langle \partial u_3 / \partial x_2 \rangle^2$ are also shown on Figure 4. Local-Axisymmetry requires that the terms $\langle \partial u_3 / \partial x_2 \rangle^2$ be equal to $\langle \partial u_2 / \partial x_3 \rangle^2$ and that $\langle \partial u_2 / \partial x_1 \rangle^2$ be equal to $\langle \partial u_3 / \partial x_1 \rangle^2$. These terms are shown on Figures 2 and 3, and the results shown to within the accuracy of the measurements that the flow appears to be truly axisymmetric in the small scales.

The full implications of this local axisymmetry is presented in George and Hussein (1991). The most significant consequence for the present experiment is that the entire set of derivative correlations can be represented in terms of four invariants which in turn, depend only on measurable quantities. Thus the determination of the dissipation and mean square fluctuating vorticity is limited only by the measurement accuracy of the four independent derivatives.

Figure 5 shows the comparison between ϵ_{axs} obtained with the assumption of local axisymmetry and ϵ_{iso} calculated from $\langle \partial u_1 / \partial x_1 \rangle^2$ and assuming local isotropy. For the jet, the isotropic results differ from the dissipation by about 25% at the centerline and by about 40% near the point of maximum mean shear ($y/y_{1/2} = 0.9$).

5. Summary and Conclusions

The statistical correlations of a number of the mean square velocity derivatives in the dissipation tensor are presented for the planar turbulent jet. Three of the mean square derivatives were computed from their corresponding measured temporal derivatives. The use of the flying wire probe which reduces the effective turbulence intensity provides the only way to measure these terms

accurately in this flow, since Taylor's frozen field hypothesis does not accurately apply to the stationary wire results. Having obtained a set of data with and without moving the wire, an assessment of the breakdown of this hypothesis was done. The issue of cross-flow and rectification errors was addressed with pertinence to the use of hot wires in flows with turbulence intensities that is higher than 30%. Comparisons between the results of the moving wire and stationary wire enabled the evaluation of these errors.

This work also provides a considerable amount of data on the dissipative scales of turbulence for the isothermal axisymmetric jet. It was proven that the jet is not locally isotropic but rather locally axisymmetric in the small scale. The direct measurement of the dissipation is presented for this type of flow.

ACKNOWLEDGEMENTS

This work was carried out at the Fluid Mechanics Laboratory at Vanderbilt University. The author wishes to acknowledge the assistance of David DeLapp in constructing the experimental setup.

This research was supported by the ASME Engineering Foundation under Grant Number RI-A-89-9.

References

- [1] Antonia, R.A., F. Anselmet and A.J. Chambers. (1986) Assessment of local isotropy using measurements in turbulent plane jet. J. Fluid Mech., 163, 365-391.
- [2] Batchelor, G.K. (1946) The theory of axisymmetric turbulence. Proc. R. Soc. Lond. A, 186, 480-502.
- [3] Beuther, P.D., A. Shabbir and W.K. George (1987) X-Wire response in turbulent flows with high intensity turbulence and low mean velocity, ASME Proc. Symp. on thermal anemometry, Cincinnati, OH.
- [4] Brown, L.W.B., Antonia, R.A. and Shah, D.A. (1987) Turbulent energy dissipation in a wake. J. Fluid Mech., 179, 307-326.
- [5] Cantwell B., and D. Coles (1983) An experimental study entrainment and transport in the turbulent near wake of the circular cylinder. J. of Fluid Mech., 136, 321-374.
- [6] Chandrasekhar S. (1950) The theory of axisymmetric turbulence. Proc. R. Soc. Lond. A, 242, 557-577.
- [7] Hussein, H.J. and George, W.K. (1989) Measurements of small scale turbulence in an axisymmetric jet using moving hot wires. Proc. 7th Sym. on turbulent shear flows, Stanford Univ. August 14-18 (Reynolds et al. eds).
- [8] George, W.K., and H.J. Hussein. (1991) Locally Axisymmetric Turbulence. J. Fluid Mech., 233, 1-23.

- [9] George, W.K., H.J. Hussein and S. Woodward, (1989) An evaluation of the effect of fluctuating convection velocity on the validity of Taylor's hypothesis, proceedings of the 10th Australasian Fluid Mechanics Conference , Melbourne, Australia.
- [10] Goldshmidt V.W., M.D. Moallemi and J.W. Oler, (1983) Structure and flow reversal in a turbulent plane jet. Physics of Fluids, 26,1983.
- [11] Hinze J.O. (1975) Turbulence, McGraw-Hill, NY.
- [12] Lumley (1965), Interpretation of time spectra measured in high-intensity shear flows. Physics of Fluids , 8, 1056-1062.
- [13] Panchapakesan, N.R. and J.L. Lumley (1987), Shuttle Mounted X-Wire Measurements in a Round Jet, Bull. of American physical society, division of fluid mechanics meeting, Eugene, OR.
- [14] Praskovsky, Kuznetso V.Y. and Karyakin M.Y. (1990) Anisotropy of turbulent fine scale structures. 3rd European Turb. Conf, July 3-6 .
Tutu and Chevray (1975), Cross-wire Anemometry in High Intensity Turbulence. J. of Fluid Mech. , 71, 786-800
- [15] Uberoi, M.S. (1975) Presentation at APS/DFD 36th Annual Meeting, College Park, MD 20.
- [16] Watmuff, M.D. J.H, A.E. Perry and M.S. Chang (1983), A Flying Hot-Wire System. Experiments in Fluids, 1, 63-71
- [17] Wyngaard, J.C. (1968) Measurement of small scale turbulence structure with hot-wires. J. Sci. Instrum. 1., 1105-1108.

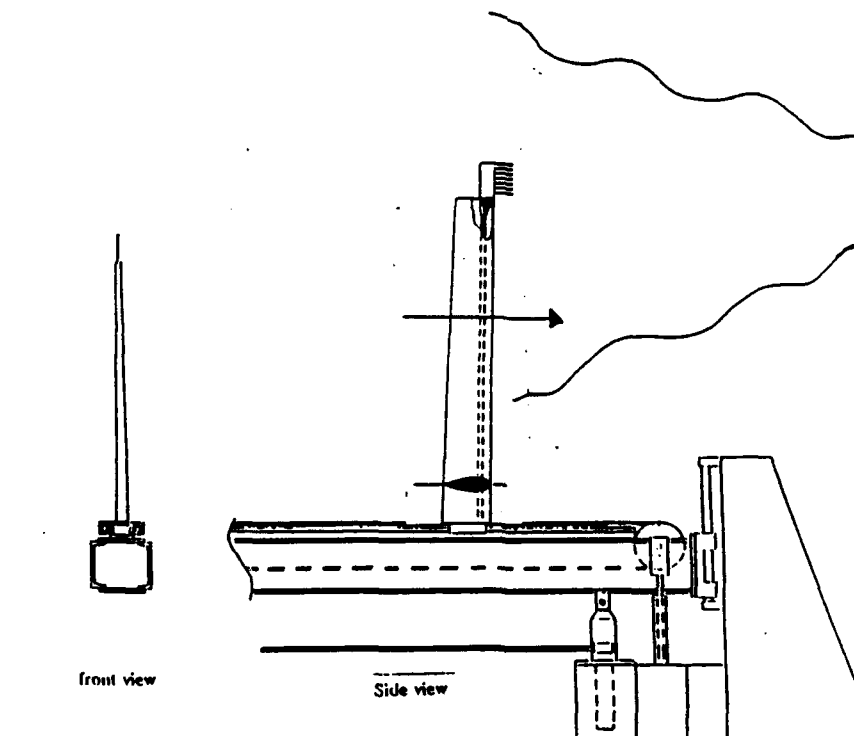


Figure 1. Jet Facility with a sketch of moving wire apparatus

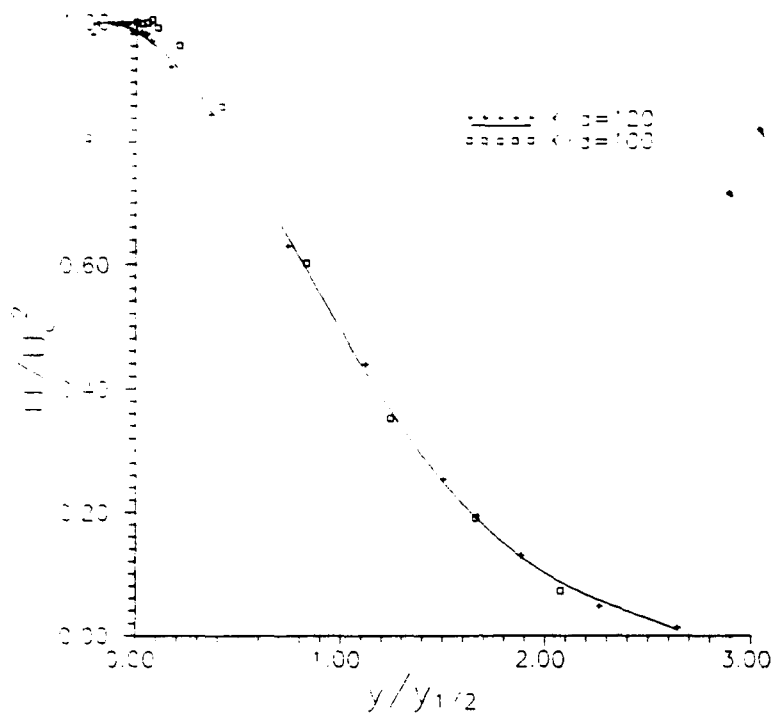


Figure 2. Mean velocity profile

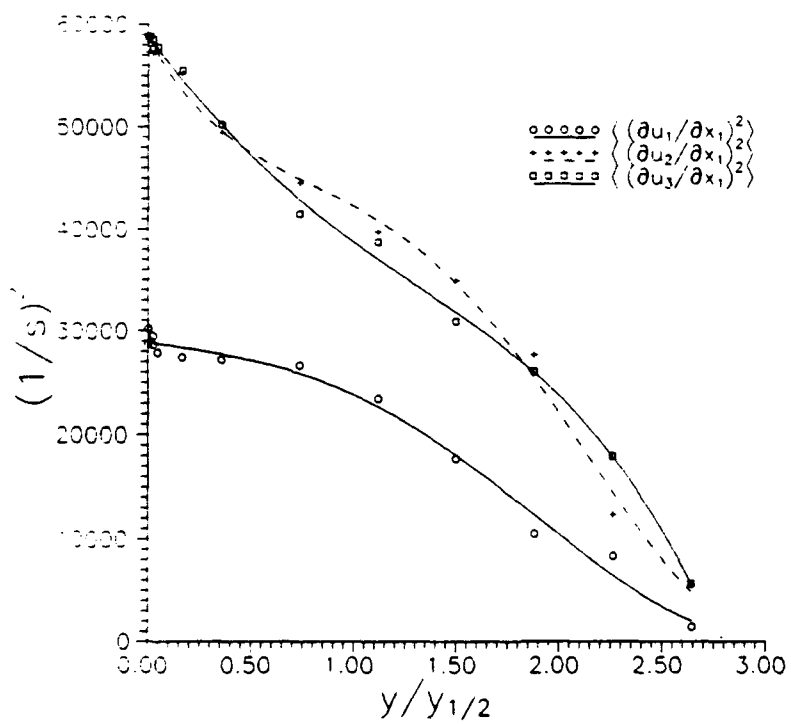


Figure 3. Velocity derivatives in streamwise direction

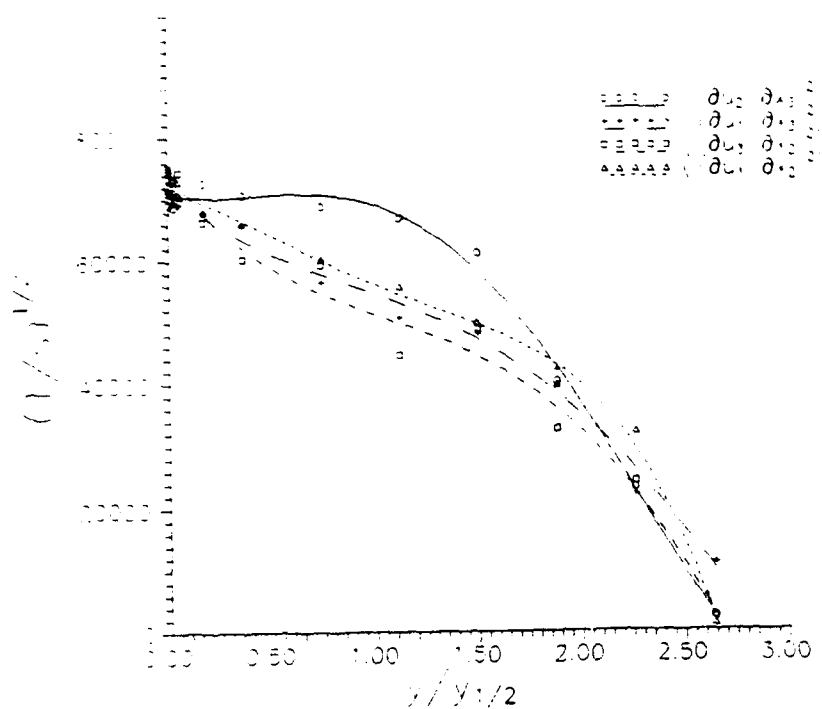


Figure 4. Velocity derivatives in cross-stream directions

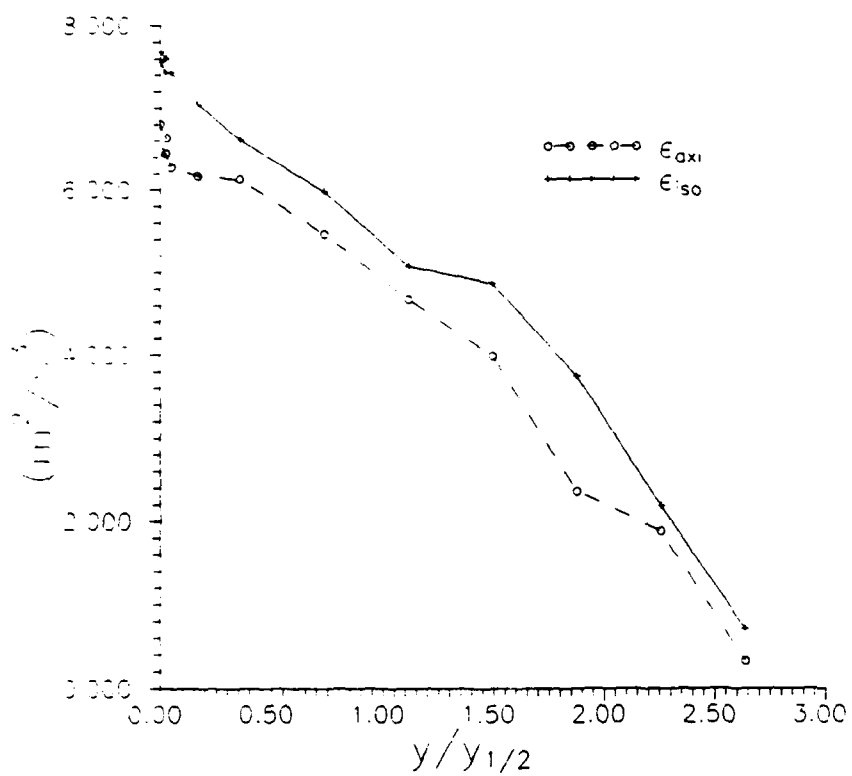


Figure 5. Dissipation profile

RESPONSE OF FINE-SCALE TURBULENCE TO EXTERNAL PRESSURE FIELDS

Hussein J. Hussein and Michael A. MacMillan
Department of Mechanical Engineering
Vanderbilt University
Nashville TN 37235

Abstract

Grid generated turbulent flow has been subjected to a local disturbance in the form of a pressure force on the mean. This is accomplished by a standing acoustic wave in the cross-flow direction. This radiation pressure disturbance appears as a single spike in the energy spectrum and corresponds to external forcing at the selected frequency. With this kind of external forcing, the amplitude and the frequency of the excitation can be varied independently. Response of the flow to the excitations are presented by reporting the evolution of the energy rate and estimates of the dissipation.

1. Introduction

The practical relevance of local-isotropy in turbulent flows is of prime importance in both the measurement of the dissipation rate as well the premise that the smallest scale motions do not receive energy directly from the mean flow. Traditional methods of studying these phenomena have relied on experiments on the dissipation and vorticity field of turbulent flows. Of interest are both the description of both the statistical nature of the fine scales as well as the response of turbulent flow to superimposed disturbances. More recently numerical simulations on distant triadic interactions by Yeung and Brasseur (1991) have indicated the persistence of anisotropy even at large Reynolds numbers. Attempts to corroborate these results have relied on the developments of techniques that utilize disturbances that are local in nature. In this attempt, one would prefer known disturbances that can be assumed to be ideal spherical shells in wavenumber space. In the case of anisotropic flow, these superimposed disturbances on the fluid velocity produce an external distortion that would persist to the small scales. The nature of the transfer of the energy mechanisms are key to understanding inter-scale coupling as well as deviations from local-isotropy.

The existence of universal similarity of the small scales of turbulent flow fields is observed for flows with sufficiently high turbulent Reynolds numbers. Recent measurements of the fine scale characteristics of laboratory turbulent jets by Antonia et al (1986) and George and Hussein (1991), show considerable deviations from the requirements of local isotropy. Measurements by Praskovsky et al, (1990) in elliptic jets at turbulence Reynolds numbers of about 2000 also corroborate these results. Since Kolmogorov's universal similarity hypothesis is based on dimensional arguments for the infinite Reynolds number limit, these deviations are

expected for moderate Reynolds number flows. Questions have been raised on the validity of the hypothesis even at large Reynolds numbers. The physical implications of these results are that the small-large scale couplings not only exist at low Reynolds numbers but also persist even at relatively large Reynolds numbers. This leads to the possibility of influencing the structure of the fine scales by superimposing external excitations on the large scale motion. Of particular interest are experiments in which the characteristics of the small scales are influenced by external forces at the small wavenumbers. These simulations which are carried out at low Reynolds numbers have no experimental verifications. The present work involves an experimental program in which the flow is loaded at specific low frequencies with standing acoustic waves. The experiments are performed in grid turbulent flow in a low turbulent intensity wind tunnel.

2. Description of Experiment

2.1 The wind tunnel facility

The experiments reported here were carried out in the wind tunnel illustrated in Figure 1. The facility which is the same used by Han (1988) for studying the effect of contraction in grid generated turbulence consists of five main units: blower, flow conditioning unit, grid and test section, contraction and a traversing section. The turbulence generator was a biplane grid constructed of circular steel rods with 40 percent solidity. The test section followed the grid and consisted of a 4 ft circular section with a diameter of 19.25 in. The operating point for the system was selected so that the tunnel velocity was 2.4 m/s. The velocity corresponding to the grid Reynolds number of 4000 and at $X/M=25$ (where the forcing is applied as described below) and the turbulent Reynolds number $Re_\lambda=27$.

2.2 Forcing technique

In this paper, we present a technique using a sound field as an external force in grid generated turbulence. Earlier investigators have avoided using acoustic excitations primarily because of the associated inherent compressibility effects and the corresponding complexities in the balance of the governing equations. Selecting acoustic waves (rather than screen of low solidity as others have used), Itsweire and Van Atta (1984) has advantage of avoiding wake effects. It also enables the possibility of adjusting the amplitude and frequency of the disturbance independently. The results from the earlier measurements do not lend themselves to a comparison with the theory specifically because of the complicated wake interactions.

Two kinds of terms exist in the force on a flow which is from a sound field: The first is from a radiation pressure, the second is the effect of the compressibility of the flow. In the present application the former dominates, since the flow has a very low turbulent Mach number. The forcing was superimposed at 25M downstream from the grid.

3. Results

The measurements were taken along the centerline of the tunnel with a free-stream velocity setting of 2.4 m/s. These measurements were aimed at identifying the effect of the external disturbance on the characteristics of the flow. Results of the streamwise component of the Reynolds Stress, the mean-square velocity derivative in the axial direction and one component of the spectral tensor are presented for a number of X/M locations. Evolution of the energy, and an estimate of the dissipation rate are inferred from these measurements for both the forced

and unforced cases. Figure 2 shows the evolution of the streamwise component of the Reynolds stress u^2 , for both the forced and unforced cases. As shown on the Figure, the external power input compensates on the viscous dissipation. Figure 3 shows an estimate of the dissipation rate assuming local isotropy, $\epsilon = 15(\partial u / \partial x)^2$. As shown on the Figure, close to the position at which the disturbance is superimposed ($X/M=25$), the dissipation is less than that of the incoming turbulence. This is due to the increased energy cascade from the inertial range to the viscous range.

The spectral results are presented on Figures 4 and 5. Figure 4 shows the streamwise velocity spectrum normalized by the Kolmogorov length and velocity scales at several X/M locations for the unforced case. As shown on the Figure even though the tunnel characteristics do not provide for a large inertial subrange, the turbulent Reynolds number is considerably larger than those attained with direct numerical simulations. Figure 5 shows the spectrum for the forced case under the same flow conditions. As shown on the figure, the disturbance is in the energy containing scales and show as a single spike in wavenumber space. In the high wavenumber region there is a larger magnitude of loss of energy in the longitudinal power spectrum. This is consistent with the results obtained in numerical simulations.

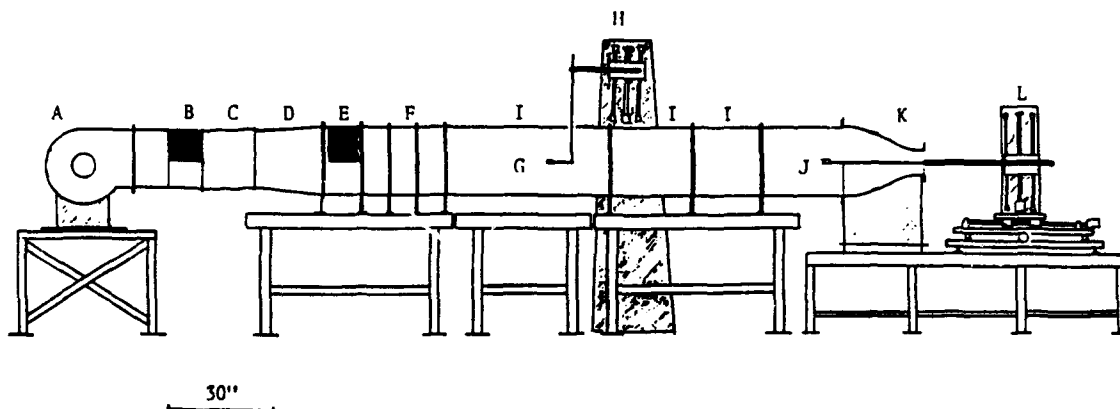
In summary, the experimental data gives considerable confidence in the local nature of the disturbance. We have presented a forcing technique that is capable of forcing the flow in such a manner that the assumption of a local disturbance at a single wavenumber holds. The question of the nature of equi-partition of energy and the issue of balancing the energy equations can be achieved with a set of measurements that include both the streamwise and the cross-flow components of the velocity field.

Acknowledgements

The ideas expressed here developed over discussions with Professor J. Brasseur

References

- [1] Antonia, R.A, F. Anselmet and A.J. Chambers. (1986) Assessment of local isotropy using measurements in turbulent plane jet J. Fluid Mech., 163, 365-391.
- [2] George, W.K., and H.J. Hussein. (1991) Locally Axisymmetric Turbulence. J. Fluid Mech., 233, 1-23.
- [3] Han Y.O. (1988) The effect of a contraction on grid generated turbulence, Ph.D. Dissertation, Univ. at Buffalo, SUNY.
- [4] Itsweire E.C., and C.W. Van Atta (1984) An experimental study of the response of nearly isotropic turbulence to a spectrally local disturbance. J. Fluid Mech., 145, 423-445.
- [5] Praskovsky, Kuznetso V.Y. and Karyakin M.Y. (1990) Anisotropy of turbulent fine scale structures. 3rd European Turb. Conf, July 3-6 .
- [6] Yeung P.K. and J.G. Brasseur (1991) The Response of Isotropic Turbulence to Isotropic and Anisotropic Forcing at the Large Scales Physics of Fluids A, 3, 884-896.



A: Blower B & E: Honeycombs C: Rubber Bellows D: Diffuser
 F: Flow Stabilizing Unit with Three Screens G: X-Wire H: Vertical Traversing System
 I: Interchangeable Test Sections; 48M, 24M and 20M lengths. (Grid locates between two of these)
 J: X-wire K: Contraction L: 3-Dimensional Traversing System

FIG. 1 Sketch of Experimental Facility

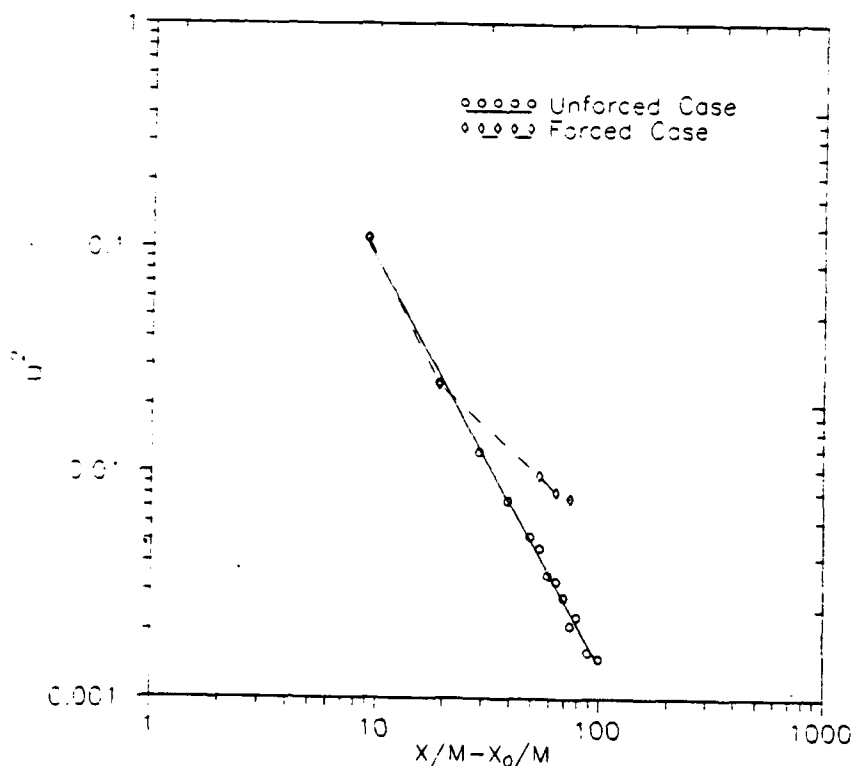


Figure 2. Development of the streamwise component of the Reynolds stress

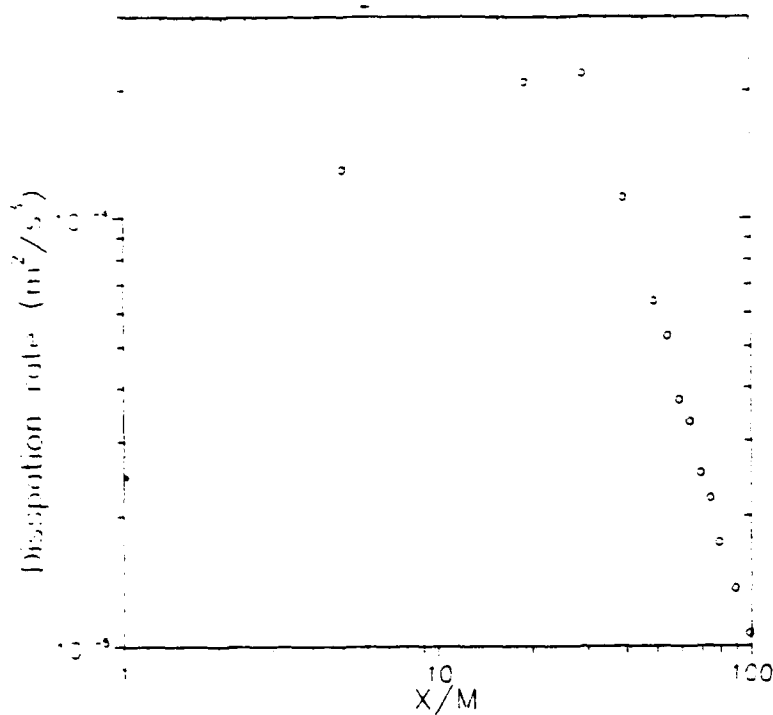


Figure 3 Dissipation rate

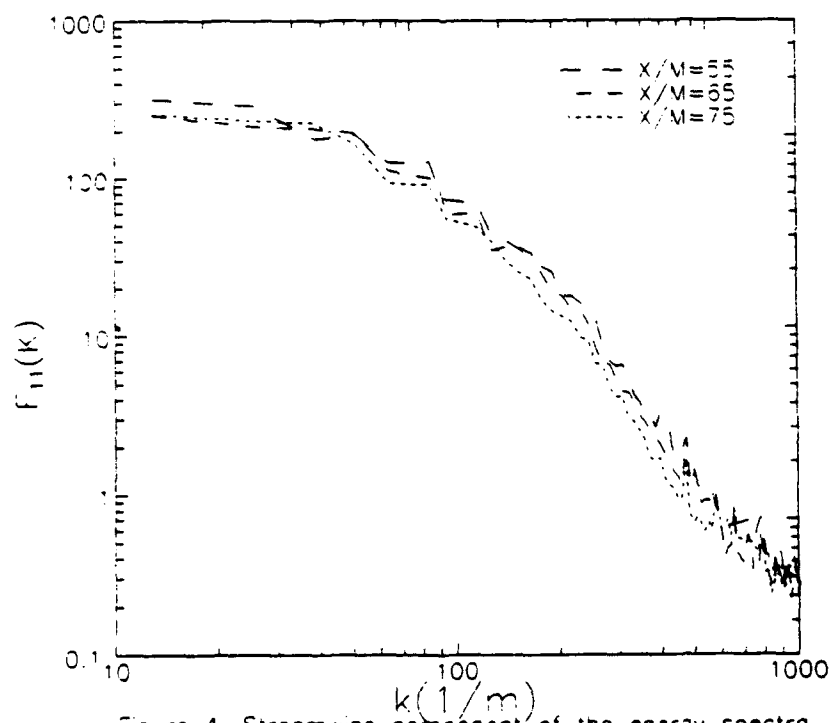


Figure 4. Streamwise component of the energy spectra, unforced case

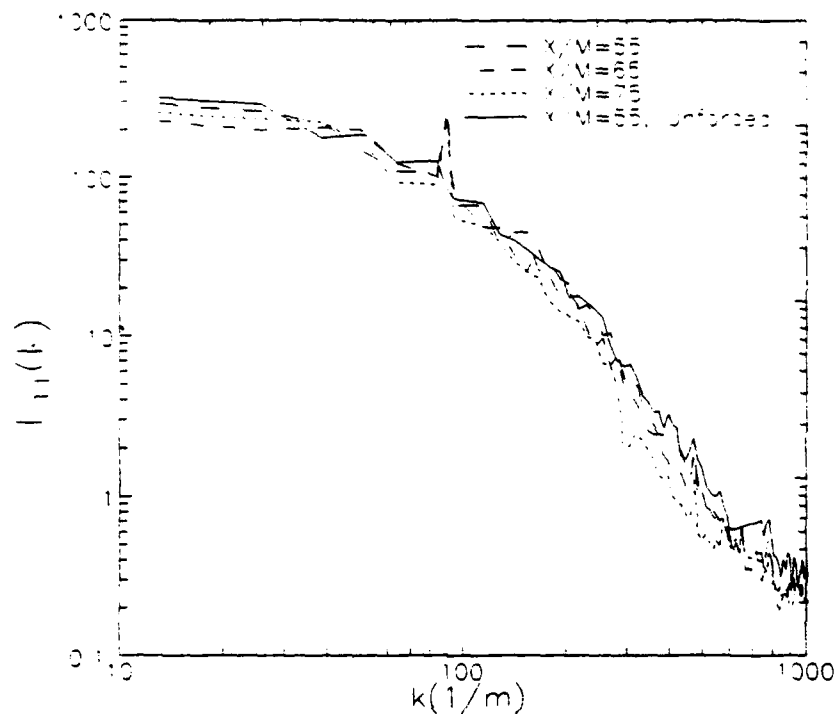


Figure 5. Streamwise component of the energy spectra, forced case

**MEASURED AND MODELLED
COMPONENT (ϵ_{11}) OF THE
DISSIPATION RATE TENSOR.**

D. Aronson and L. Löfdahl
Thermo- and Fluid Dynamics
Chalmers University of Technology
412 96 Göteborg
Sweden

Abstract

The anisotropy of the dissipation rate tensor has been studied in the self-preserving region of a cylinder wake. Hot-wire techniques have been employed to measure the derivative moments in the streamwise, lateral and normal direction. From these measurements the streamwise component of the dissipation rate tensor was determined and compared to an anisotropic dissipation model component. It was found that the dissipation rate anisotropy could essentially be accounted for by the employed model. In this flow field triple velocity correlations were also measured and a comparison with the corresponding modelled profiles has been made.

1. Introduction.

Much of the research in the area of turbulence modelling is today directed towards an improved generality of the closure models for the Reynolds stress transport equations. An important part of this work is the experimental determination of the dissipation rate tensor and the triple velocity correlations. The anisotropy of the dissipation rate tensor and its coupling to the anisotropy of the Reynolds stress tensor has been shown to be quite useful in the modelling, see Browne et al. (1987), Hussein and George (1989), and Hallböck et al. (1989). For a more complete discussion of the closure problem and today's turbulence modelling see e.g. George & Taulbee (1990) and in Groth (1991).

A key element in obtaining the components of the dissipation rate tensor is the measurement of the velocity gradients. Due to limitations in current experimental techniques a determination of all components in the dissipation rate tensor is impossible. However, if the flow is symmetric in some coordinates, like the axisymmetric case of Hallböck et al. (1989), the number of components is reduced. In order to assess the applicability of the results obtained in the aforementioned fundamental investigations, the present experiment was carried out in a more complex flow, the self-preserving region of a cylinder wake. Measurements are presented of the dissipation rate and triple velocity correlations, and comparisons are made to theoretical models.

2. Experimental Arrangements.

All measurements were performed in a low-speed closed circuit wind-tunnel, with a test section of 3.0 m x 1.8 m x 1.2 m. The self-preserving wake was generated by a circular cylinder, of a diameter of 4.0 mm, which was mounted in the midplane of the test section. In the measurements a free stream velocity of 7.0 m/s was used, giving a Reynolds number, based on the cylinder diameter, of 1840. All measurements of velocity derivatives were made in the self-preserving part of the wake at $x_1/(2\theta) = 440$.

For the determination of the free stream velocity a micro manometer and a Prandtl tube was used. For turbulence measurements were carried out using a standard DANTEC constant-temperature hot-wire anemometer and standard DANTEC hot-wires (55P01 and 55P61). The output voltages of the anemometers were filtered and amplified, the low-pass filter setting was 3.0 kHz. (This value was appropriate since the Kolmogorov frequency was approximately 2300 Hz). The signals from the micro manometer, the anemometer and the signal conditioner were subsequently sampled using a twelve bit A/D converter with a sample and hold unit.

A hot-wire method based on single- as well as cross-wires was developed to enable these measurements. For the cross-wire measurements this method uses a look-up table, Lueptow, Breuer & Haritonidis (1988), in the calibration routines for the improvement of the angular sensitivity and the elimination of correction factors due to the probe geometry. A more comprehensive description of the hot-wire method can be found in Aronson (1991). In order to obtain a satisfactory spatial resolution in the determination of the velocity derivatives, George & Hussein (1991) and Johansson (1992) stressed that the spatial extension of the employed sensor must be of the order of the Kolmogorov microscale. The experimental conditions used here gives the advantage of the relatively large size of the Kolmogorov microscale, ranging from 0.47 mm at the centre line to about 0.8 mm near the edge of the wake, needed to obtain a satisfactory spatial resolution.

In the transport equation for the average turbulent kinetic energy the dissipation rate is given by (e.g. Hinze (1975))

$$\epsilon = \nu \left(\frac{\partial u_i}{\partial x_j} + \frac{\partial u_j}{\partial x_i} \right) \frac{\partial u_i}{\partial x_i} \quad (1)$$

The streamwise components e.g. $(\partial u_1/\partial x_1)^2$ may be rewritten, using Taylors hypothesis,

$$\overline{\left(\frac{\partial u_1}{\partial x_1} \right)^2} = \frac{1}{U_1^2} \overline{\left(\frac{\partial u_1}{\partial t} \right)^2} = \frac{2 \overline{u_1^2}}{U_1^2 \lambda_1^2} \quad ; \quad \lambda_1^2 = 2 \overline{u_1^2} / \overline{\left(\frac{\partial u_1}{\partial t} \right)^2} ,$$

where λ_1 is defined as the Taylor microscale. Since a transformation from a spatial to a temporal derivative is necessary the validity of Taylors hypothesis was established according to the criteria of Lin (1953), and for all parts of the self-preserving wake it was found that the employment of the hypothesis was justified.

In order to correctly compute this microscale it is important to choose an appropriate sampling frequency or time between samples (Δt) when measuring. If Δt is too short effects of electrical noise and insufficient resolution in the AD-converter will give a too low value of the microscale, on the other hand if Δt is too long the fine scales will not be resolved yielding a too large value.

$$\left(\frac{\lambda_{tm}}{\lambda_t}\right)^2 = 1 + \beta \left(\frac{\Delta t}{\lambda_t}\right)^2 \quad \text{where} \quad \lambda_{tm}^2 = 2 \overline{u_1^2} / \left(\overline{\left(\frac{u_1(t + \Delta t) - u_1(t)}{\Delta t} \right)^2} \right) \quad (2)$$

As shown in figure 1 the measured time scale, λ_{tm} , in the intermediate region ($0.1 < \Delta t / \lambda_t < 0.4$) closely adheres to relation (2). This makes it possible to accurately obtain the wanted microscale, λ_t , from extrapolation of measurements. These results are in close agreement with the results of Hallbäck et al. (1989).

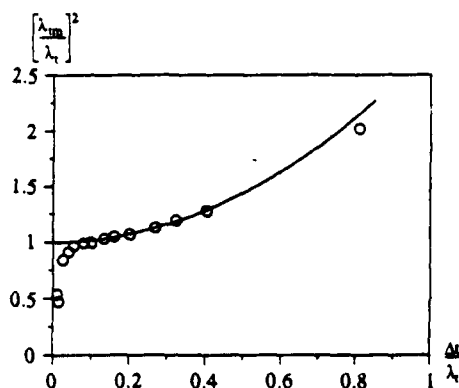


Figure 1. The measured microscale λ_{tm} normalized by λ_t as a function of $\Delta t/\lambda_t$.

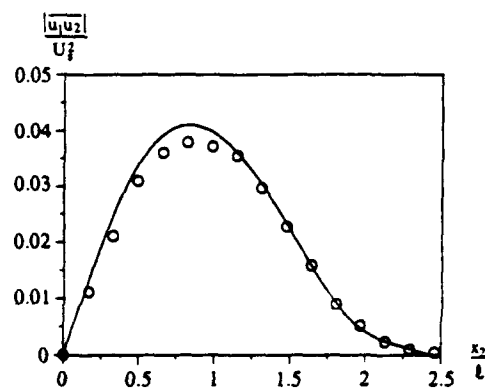


Figure 2. The normalized distribution of Reynolds shear stress.

To obtain $\overline{(\partial u_1 / \partial x_2)^2}$ and $\overline{(\partial u_1 / \partial x_3)^2}$ a similar technique was used, Δt is then replaced by the spatial separation Δx_2 and Δx_3 resp. According to Wyngaard (1969) the present probe geometries would give an 90% response, or better, during the gradient measurements.

3. Results and discussions.

3.1 The self-preservation of the cylinder wake.

In the plane two-dimensional wake behind a cylinder, sufficiently far downstream, the transverse distributions of mean-velocity and Reynolds stresses are assumed to be self-preserving. That is, these distributions assume functional forms which are independent of x_1 when normalized by the characteristic velocity and length scales.

These conditions can be expressed in the form;

$$U_1 = U_\infty - g_1(x_2/l), \quad \overline{u_1^2} = U_\infty^2 g_2(x_2/l) \quad \text{and} \quad \overline{u_1 u_2} = U_\infty^2 g_3(x_2/l), \quad (3, 4, 5)$$

where the characteristic velocity, U_s , is defined as the maximum value of the mean-velocity defect at that position, and the characteristic length, ℓ , is defined as the distance from the centerline to the position where the mean-velocity defect is $0.5 U_s$, following Tennekes & Lumley (1972). In the self-preserving region U_s and ℓ , the normalized velocity and length scales should vary as

$$\frac{U_s}{U_\infty} = A \left(\frac{x_1 - x_0}{2\theta} \right)^{-1/2} \quad \text{and} \quad \frac{\ell}{\theta} = B \left(\frac{x_1 - x_0}{2\theta} \right)^{1/2}, \quad (6, 7)$$

where A and B are universal constants, θ is the momentum thickness (here $\theta = 1.90$ mm) and x_0 is the virtual origin. Measurements were made at distances ranging from 210 to 880 momentum thicknesses downstream of the cylinder. The data obtained indicated that some 400 momentum thicknesses downstream the velocity scale U_s was proportional to $(x_1 - x_0)^{-1/2}$, and the width of the wake ℓ was proportional to $(x_1 - x_0)^{1/2}$. In this region the coefficients A and B take the values 1.25 and 0.41 respectively and $x_0/(2\theta) = -112$. These values of the coefficients are in good agreement with the corresponding values reported by Wygnanski, Champagne & Marsali (1986) who found $A=1.24$ and $B=0.41$.

To assess the quality of the turbulence data we checked if the directly measured Reynolds shear stress agreed with the value calculated from the mean momentum equation. For a two-dimensional, small-deficit wake the mean momentum equation can be approximated to

$$U_\infty \frac{\partial U_1}{\partial x_1} + \frac{\partial \overline{u_1 u_2}}{\partial x_2} = 0. \quad (8)$$

Here the Reynolds number is assumed to be sufficiently large for viscous and diffusive terms to be neglected, and the streamwise gradients of the normal stress have also been neglected by using the boundary layer approximation. The Reynolds shear stress $\overline{u_1 u_2}$ can be calculated using eq. (3), eq. (5) and integrating eq. (8) across the wake. This yields the normalized distribution of $\overline{u_1 u_2}$.

$$g_3 = a \int_0^{\bar{x}} g_1 d\bar{x} - b \bar{x} g_1, \quad (9)$$

where

$$a = \frac{U_\infty}{U_s^2} \frac{dU_s}{dx_1} \ell + \frac{U_\infty}{U_s} \frac{d\ell}{dx_1}, \quad b = \frac{U_\infty}{U_s} \frac{d\ell}{dx_1} \quad \text{and} \quad \bar{x} = x_2/\ell.$$

The use of eq. (6) and (7) indicates that a of eq. (9) should be zero so that eq. (9) can be simplified to

$$\frac{\overline{u_1 u_2}}{U_s^2} = - \frac{B}{4A} \frac{x_2}{\ell} \frac{U_\infty - U_1}{U_s}. \quad (10)$$

In figure 2 the measured Reynolds shear stress is compared to the calculated value from eq.(10). At the position of maximum shear stress the largest difference between the experimental and the calculated values is about 6%. Based on a number of measurements, we estimate the error in U_s to be $\pm 5.5\%$ and the uncertainty in $\overline{u_1 u_2}$ to be

$\pm 5\%$. Using the propagation of errors approach, the resulting uncertainty in the measured $\overline{u_1 u_2} / U_s^2$ is estimated to $\pm 9\%$. At $x_2 / \ell = 1$, near the position of maximum shear stress, $U_\infty - U_1$ is exactly $U_s / 2$, yielding that the only uncertainty in the calculated shear stress is the uncertainty in B/A , which is estimated to be approximately 2%, so the agreement between the momentum balance and the direct measurements of the shear stress is satisfying.

3.2 Average turbulent kinetic energy budget and the anisotropy factors.

An approximation to the transport equation for the average turbulent kinetic energy ($k = 1/2 \overline{u_i u_i}$) is given by (Townsend (1949))

$$U_\infty \frac{\partial k}{\partial x_1} + \overline{u_1 u_2} \frac{\partial U_1}{\partial x_2} + \frac{\partial}{\partial x_2} [\overline{u_2 (k + p/\rho)}] + \epsilon = 0 \quad (11)$$

Estimates were made for all the terms in eq.(11) except for the pressure diffusion term which was determined by difference. The gradient $\partial k / \partial x_1$ was inferred from the streamwise variations of U_s and ℓ , and the lateral derivatives of U_1 and $\overline{u_2 k}$ were obtained by fitting a curve to the data and then performing a differentiation. Since one component of $\overline{ku_2}$, $\overline{u_3^2 u_2}$, was not measured, we inferred our distribution for $\overline{u_3^2 u_2}$ from our $\overline{u_1^2 u_2}$ data via the relation

$$(\overline{u_3^2 u_2})_{\text{present}} = (\overline{u_1^2 u_2})_{\text{present}} \left(\frac{\overline{u_3^2 u_2}}{\overline{u_1^2 u_2}} \right)_{\text{Browne}} ; \quad (\text{Browne et al. (1987)})$$

In general, the magnitude of $\overline{u_3^2 u_2}$ is sufficiently smaller than $\overline{u_1^2 u_2}$ or $\overline{u_2^3}$ to suggest that the determination of $\overline{u_3^2 u_2}$ is not critical in the context of obtaining $\overline{ku_2}$. The various terms in eq.(11), normalized by multiplying with ℓ / U_s^3 , are plotted in figure 3. Assuming symmetry with respect to $x_2 / \ell = 0$ the diffusion terms should satisfy the following two integral constraints

$$\int_{-\infty}^{\infty} \frac{\partial}{\partial x_2} (\overline{ku_2}) dx_2 = 0, \quad \int_{-\infty}^{\infty} \frac{\partial}{\partial x_2} (\overline{p/\rho u_2}) dx_2 = 0.$$

The diffusion of k satisfies the integral constraint by about 3%. However the pressure diffusion term, obtained by difference, is small compared to the diffusion of k , and does not satisfy the integral constraint. This demonstrates that in this case the pressure diffusion is inaccurate due to the assumption of an isotropic dissipation rate and is an indication of the need for a better estimate of the dissipation rate.

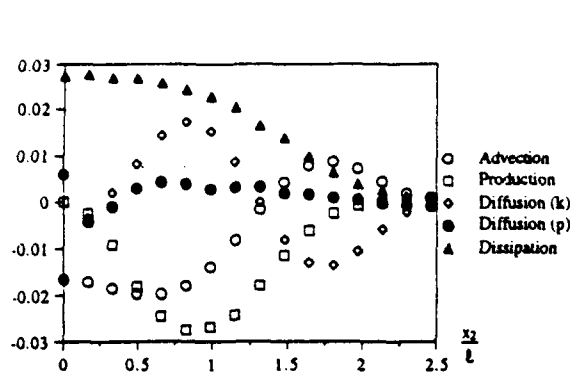


Figure 3. Budget of average turbulent kinetic energy

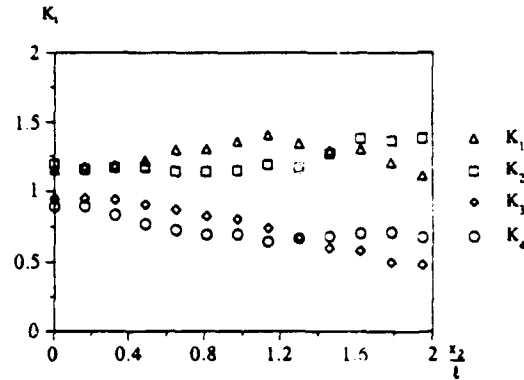


Figure 4. The distribution of the ratios K_1 through K_4 .

If the assumption of isotropy in the self-preserving region of a cylinder wake would be correct, the ratios K_1 through K_4 should be 1.0. Here K_1 through K_4 are defined as:

$$K_1 = 2 \frac{(\partial u_1 / \partial x_1)^2}{(\partial u_2 / \partial x_1)^2} \quad K_2 = 2 \frac{(\partial u_1 / \partial x_1)^2}{(\partial u_3 / \partial x_1)^2}$$

$$K_3 = 2 \frac{(\partial u_1 / \partial x_1)^2}{(\partial u_1 / \partial x_2)^2} \quad K_4 = 2 \frac{(\partial u_1 / \partial x_1)^2}{(\partial u_1 / \partial x_3)^2}$$

In Figure 4 the distributions of the ratios K_1 through K_4 of the present flow case are shown. As is evident in this Figure these ratios are never equal to unity, indicating that the condition of isotropy is not fulfilled, and further emphasizes the need for a better estimate of the dissipation rate. It may, however, be noted that $K_1 = K_2 > 1$ and $K_3 = K_4 < 1$, an observation in full agreement with what has been suggested by George and Hussein (1991) as a case of local axisymmetric turbulence.

3.3 Dissipation Model.

To investigate the assumed relation between the anisotropy of the dissipation rate tensor and the stress tensor the streamwise component (ϵ_{11}) of the dissipation rate tensor was measured as well as computed using a dissipation model based on the anisotropies of the Reynolds stress tensor. In the measurements, terms in ϵ_{11} requiring the use of more than one cross-wire have been estimated using the assumption of isotropy, thus yielding

$$\epsilon_{11} = 2\nu \left[\left(\frac{\partial u_1}{\partial x_1} \right)^2 + \left(\frac{\partial u_1}{\partial x_2} \right)^2 + \left(\frac{\partial u_1}{\partial x_3} \right)^2 \right] \quad (13)$$

The here employed dissipation model was suggested by Hallbäck, Groth and Johansson (1990), and is basically an extension of a model originally suggested by Rotta (1951) and later developed by Hanjalic and Launder (1976). This dissipation model satisfies both the weak and the strong realizability conditions, due to Pope (1985).

$$\epsilon_{ij} = \epsilon \left(e_{ij} + \frac{2}{3} \delta_{ij} \right) \quad (14)$$

where

$$e_{ij} = a_{ij} + \alpha \left\{ \left(\frac{1}{2} \Pi_a - \frac{2}{3} \right) a_{ij} - \left(a_{ik} a_{kj} - \frac{1}{3} \Pi_a \delta_{ij} \right) \right\} ,$$

$$a_{ij} = \frac{\overline{u_i u_j}}{k} - \frac{2}{3} \delta_{ij} \quad \text{and} \quad \Pi_a = a_{ik} a_{ki} .$$

The value of α in this comparison was chosen to be 0.75. In figure 5 a comparison between the experimental and modelled distributions of the streamwise component (ϵ_{11}) of the dissipation rate tensor is shown. (the various terms in eq.(13) and eq.(14) are normalized by multiplying with U/U_s^3 .) It is seen that the isotropic estimate of ϵ_{11} is smaller than the measured value across the whole wake, at the centerline of the wake the difference is about 5%, at $x_2/\ell = 1$ about 15%, and near the edge of the wake the isotropic estimate of ϵ_{11} is 25% smaller than the measured value. It is seen that the modelled distribution of ϵ_{11} agrees well with the measured distribution of ϵ_{11} . However, eq.(13) does overpredict the dissipation rate at the centerline of the wake by about 3%. This result shows that the model used, which describes the anisotropies of the dissipation rate tensor in terms of the anisotropies of the Reynolds stress tensor, to some extent can predict the anisotropies of the small scales in this case. Here it should be pointed out that the Reynolds number of this investigation is relatively low, a fact that can be in favour of the model.

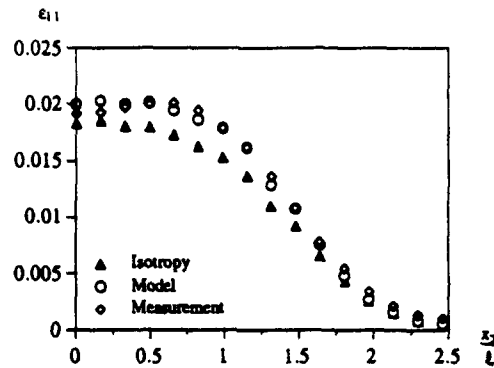


Figure 5. The distribution of ϵ_{11} .

3.4 Triple velocity correlations.

In the beginning of the seventies Hanjalic and Launder (1972) suggested a model for the triple velocity correlations. Looking at high Reynolds number flow and referring to measurements in a plane axisymmetric channel they neglected the viscosity and pressure dependent parts, and suggested the following model.

$$-\overline{u_i u_j u_k} = c_s \frac{k}{\epsilon} \left[\overline{u_i u_m} \frac{\partial \overline{u_j u_k}}{\partial x_m} + \overline{u_j u_m} \frac{\partial \overline{u_i u_k}}{\partial x_m} + \overline{u_k u_m} \frac{\partial \overline{u_i u_j}}{\partial x_m} \right] . \quad (15)$$

The model parameter c_s was set to 0.11, due to Launder, Reece & Rodi (1975). The from eq. (15) calculated triple velocity correlations were compared to the present measured profiles of the triple velocity correlations. Shown in Figures 6 and 7 are the comparison for the total streamwise and the total lateral transport correlations. (The different correlations have been normalized by dividing with U_1^3 .) In general the shape of the predicted profiles similar to those measured, however, it can be seen that the model underpredicts the experimental profile for the streamwise transport. For the lateral transport eq.(15) predicts the measured profile better, but the predicted values are consistently lower than the measured values.

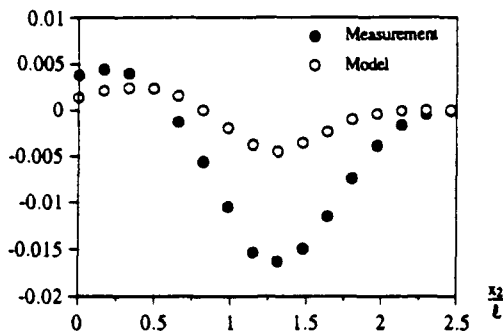


Figure 6. Streamwise transport $1/2 \overline{U_1 U_1 U_1}$.

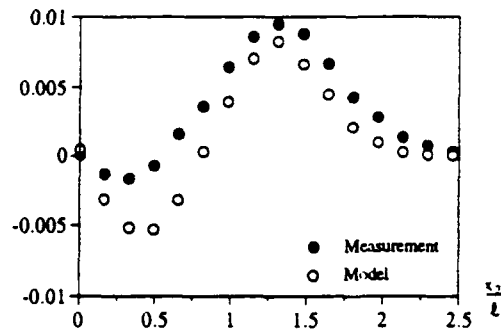


Figure 7. Lateral transport $1/2 \overline{U_2 U_1 U_1}$.

4. Conclusions.

An investigation has been carried out in which the derivative moments have been measured, employing hot-wire methods. The streamwise component ϵ_{11} of the dissipation rate tensor was determined and compared to the corresponding quantity computed with an algebraic dissipation model. From these comparisons the following conclusions can be made.

- * The present experimental arrangement fulfils the requirement of a two dimensional, self-preserving cylinder wake flow. For the studied Reynolds number, 1840, the dissipation rate terms have been shown to have a non-isotropic structure.
- * The measured profile of the streamwise component of the dissipation rate tensor agrees well with the profile predicted by the dissipation rate model of Hallbäck et al. (1989). As compared to corresponding quantities obtained under the assumption of isotropy, large deviations can be noted.
- * The profiles for the third moments predicted by the model of Hanjalic and Launder (1972) show similar shaped profiles with those measured, but they are different in magnitude.

Support from the Swedish Board for Industrial and Technical Development (NUTEK) is gratefully acknowledged. The authors are grateful to Professor Håkan Gustavsson for valuable comments on the manuscript.

5. References.

- Browne, L.W.B., Antonia, R.A. and Shah, D.A. 1987 Turbulent Energy Dissipation in a Wake, *J. Fluid Mech.*, Vol. 179, pp 307.
- George, W.K. and Hussein, H.J. 1991 Local Axisymmetric turbulence, *J. Fluid Mech.*, Vol. 233, pp 1.
- Hallback, M., Groth, J. and Johansson, A.V. 1990 An algebraic model for nonisotropic turbulent dissipation rate in Reynolds stress closures, *Phys. Fluids A*, Vol. 2, pp 1859.
- Hallback, M., Groth, J. and Johansson, A.V. A Reynolds stress closure for the dissipation in anisotropic turbulent flows, in *Proceedings of the Seventh Symposium on Turbulent Shear Flows*, Stanford, August 1989.
- Hanjalic, K. and Launder, B.E. 1972 A Reynolds stress model of turbulence and its application to thin shear flows, *J. Fluid. Mech.*, vol. 52, pp 609.
- Hanjalic, K. and Launder, B.E. 1976 Contribution towards a Reynolds stress closure for low-Reynolds number turbulence, *J. Fluid. Mech.*, vol. 74, pp 593.
- Hinze, J.O. 1975 *Turbulence*, McGraw-Hill Book Company.
- Hussein, H.J. and George, W.K. Influence of wire spacing on derivative measurement with parallel hot-wire probes, in *Proceedings of the Seventh Symposium on Turbulent Shear Flows*, Stanford, August 1989.
- Johansson, A.V. 1992 Private communications.
- Lin, C.C. 1953 On Taylor's Hypothesis and the Acceleration Term in the Navier-Stokes Equations, *Quarterly of Applied Mathematics*, Vol. 10, pp 295.
- Lueptow, R.M., Breuer, K.S. and Haritonidis, J.H. 1988 Computer-aided calibration of X-probes using a look-up table, *Experiments in Fluids*, no. 6, pp. 115.
- Rotta, J.C. 1951 Statistische Theorie nichthomogener Turbulenz ", *Z. Phys.* vol. 131, pp. 51.
- Tennekes, H. and Lumley, J.L. 1987 *A First Course in Turbulence*, The MIT Press.
- Wynanski, I., Champagne, F. and Marsali, B. 1986 On the large-scale structures in two dimensional, small-deficit, turbulent wakes, *J. Fluid Mech.*, vol. 168, pp 31.
- Wyngaard, J.C. 1969 Spatial Resolution of the Vorticity Meter and other Hot-wire Arrays, *J. Sci. Instr.*, Vol. 2, pp. 983.

RENORMALIZATION GROUP THEORY OF TURBULENCE AND WAVES ON THE β -PLANE

Boris Galperin
Department of Marine Science,
University of South Florida,
St. Petersburg, FL 33701

Semion Sukoriansky
Department of Mechanical Engineering,
Ben Gurion University of the Negev,
Beer Sheva 84105, Israel

Ilya Staroselsky
Applied and Computational Mathematics,
Princeton University, Princeton, NJ 08544

Abstract

The two-dimensional, forced, barotropic vorticity equation on the β -plane is studied using the Renormalization Group (RNG) technique. It is shown that the β -term does not renormalize in the process of infra-red ($k \rightarrow 0$) renormalization. As $k \rightarrow 0$, the RNG viscosity develops significant anisotropy, due to the β -effect. The RNG viscosities were used for calculations of energy transfer, energy spectra and two-parametric viscosity in the energy sub-range. It was found that, as $k \rightarrow 0$, the energy spectrum becomes substantially anisotropic, with energy concentrated in a zonal flow and zonally propagating Rossby waves. Such a spectrum is consistent with the spectral energy transfer that has local negative maxima at $\phi = 0, \pi$ and $\phi = \pm\pi/2$. These results have important implications for geophysical fluid dynamics.

1. Introduction

The two-dimensional (2-D) barotropic vorticity equation has long been recognized as one of the simplest models relevant to geophysical flows. It describes non-vortex-stretching large-scale horizontal motions and, when forced, its non-linearity supports well-observed energy and enstrophy spectra, inverse energy and direct enstrophy cascades. Numerical simulations with this equation reveal generation and evolution of coherent structures which may be isolated or multiple vortices [1-3]. Such structures can be reproduced in the laboratory settings [4,5]. In the geophysical context of differentially rotating flows, this equation is supplemented by the β -term that reflects the variation of the planetary vorticity. Then, the vorticity equation on the β -plane supports large-scale Rossby waves and describes the interaction between these waves and two-dimensional turbulence. The β -effect tends to destroy the coherent structures characteristic of purely 2-D turbulence thus improving the applicability of statistical theories to β -plane turbulence [6].

Without dissipation, this equation constitutes preservation of potential vorticity on both f - and β -planes, the evolution of which is believed to be the dominant factor determining large-scale, wind-driven oceanic circulation [7]. This equation can also be generalized to include effects of stratification, bottom topography, friction and three-dimensionality [8-10]. Extensive reviews of different properties of the barotropic vorticity equation can be found in [8, 11-13].

Pioneering studies of turbulence and waves on the β -plane were conducted by Rhines [14] who found that at large k the flow is relatively unaffected by the differential rotation and behaves largely like two-dimensional turbulence. With decreasing k , inverse energy cascade halts and flow evolves towards the regime of linear Rossby waves. The transitional wave number introduced by Rhines [14] is related to β and velocity scale U as $k_\beta = (\beta/2U)^{1/2}$. Holloway and Hendershott [15] corroborated Rhines's results using the Test Field Model (TFM) by Kraichnan [16]; they defined k_β based upon the rms vorticity, to assure the Galilean invariance. Later, Rhines's suggestion on the inhibition of the inverse energy cascade by the β -effect was given an important implementation in the theory of geophysical predictability where k_β was identified with the maximum scales which can be attained by the initially small-scale errors [17].

Despite the great effort invested in studies of barotropic vorticity equation, its basic non-linear features are still poorly understood. Furthermore, enstrophy dissipation is often neglected or, when included in numerical models, is parameterized by ad-hoc eddy- and/or hyper-viscosities. There exist only a few analytical studies of the flow anisotropization due to differential rotation (see, for instance, [15]); this phenomenon has usually been demonstrated via numerical experimentation [14, 18].

This paper is aimed to advance our understanding of the analytical properties of the fully non-linear and dissipative barotropic vorticity equation on the β -plane. For this purpose, the RNG formalism, recently developed for purely two-dimensional turbulence [20], will be extended to account for the β -effect. Unlike the standard quasi-geostrophic approximation, in our approach not only weak non-linearity is not assumed *a priori* but, on the contrary, strong non-linear interactions are responsible for renormalization and rescaling of all flow parameters in the process of small scales elimination.

2. Mathematical Formulation

The basic equation of the present study, the barotropic vorticity equation on the β -plane, is:

$$\frac{\partial \zeta}{\partial t} + J(\psi, \zeta) + \beta \frac{\partial \psi}{\partial x} = \nu_0 \nabla^2 \zeta, \quad (1)$$

where ψ is the stream function, $\zeta = \nabla^2 \psi$ is the relative vorticity, β describes the differential rotation (implying that the Coriolis parameter, f , is given by $f = f_0 + \beta y$, y is directed northward and β is a constant), ν_0 is the molecular viscosity and $J(\psi, \zeta)$ is the Jacobian. This equation can be re-written in the self-contained form:

$$\frac{\partial \zeta}{\partial t} + \epsilon_{ab} \left(\frac{\partial}{\partial x_a} \nabla^{-2} \zeta \right) \frac{\partial \zeta}{\partial x_b} + \beta \frac{\partial}{\partial x} (\nabla^{-2} \zeta) = \nu_o \nabla^2 \zeta, \quad (2)$$

where ϵ_{ab} is the unit antisymmetric tensor and ∇^{-2} is the inverse Laplacian which renders the problem non-local. Following [20], Eq. (2) can be Fourier-transformed resulting in

$$\zeta(\hat{k}) = G^o(\hat{k}) \epsilon_{ab} k_a \int q_b \frac{\zeta(\hat{q}) \zeta(\hat{k} - \hat{q})}{q^2} \frac{d\hat{q}}{(2\pi)^{d+1}} + G^o(\hat{k}) \xi. \quad (3)$$

Here, $\hat{k} \equiv (\mathbf{k}, \Omega)$, $G^o(\hat{k}) = (i\Omega + i\beta k_x k^{-2} + \nu_o k^2)^{-1}$ is the bare propagator that includes the β -effect, and $d = 2$ is the dimension of space. The random, zero-mean, white Gaussian stirring force ξ in the rhs of Eq. (3) accounts for the steady energy input localized in the vicinity of a wave number k_o . This term maintains a fully developed nondecaying turbulence for the unbounded homogeneous system under consideration and is equivalent to the stirring force introduced by Yakhot and Orszag [19]. As was shown in [20], the effect of the localized random stirring on the 2-D flow field in the RNG formalism is equivalent to introducing, in the renormalized equation, of the spatially- and temporarily-distributed forcing with the correlator

$$\langle \xi(\mathbf{k}, \Omega) \xi(\mathbf{k}', \Omega') \rangle = 2D_o k^{-y+2} (2\pi)^{d+1} \delta(\mathbf{k} + \mathbf{k}') \delta(\Omega + \Omega'), \quad (4)$$

where y and D_o are different for $k \ll k_o$ and $k \gg k_o$. The region $k \ll k_o$ corresponds to the inverse energy cascade for which $y = 2$ and $D_o \propto \bar{\epsilon}$, $\bar{\epsilon}$ being the constant energy injection rate; the region $k \gg k_o$ corresponds to the direct enstrophy cascade with the constant rate $\bar{\eta}$; in that region $D_o \propto \bar{\eta}$ and $y = 4$.

Similarly to the case of purely two-dimensional turbulence [20], Fourier-coefficients of the relative vorticity can be separated into "small scale" and "large scale" modes, $\zeta^>(k)$ and $\zeta^<(k)$, where $0 < k < \Lambda_o$, Λ_o being the vorticity analog of the Kolmogorov length scale, i.e., the scale of the viscous dissipation of enstrophy. Then, the modes from the interval $\Lambda_o - \delta\Lambda_o < k < \Lambda_o$ are eliminated; the remaining modes $\zeta^<(k)$ are defined over a reduced domain $0 < k < \Lambda_o - \delta\Lambda_o$. Equation (2), written for $\zeta^<(k)$, now contains a new (subgrid) term accounting for the unresolved scales; its Fourier-transform represents correction to the Green function defined by Eq. (3) and is the same as given in [20]:

$$\delta G(\hat{k})^{-1} = \int^> \frac{k^2 q^2 - (\mathbf{k} \cdot \mathbf{q})^2}{k^4} \left(\frac{1}{q^2} - \frac{1}{|\mathbf{q} - \mathbf{k}|^2} \right) G(\hat{k} - \hat{q}) |G(\hat{q})|^2 D_o q^{-y+2} \frac{d\hat{q}}{(2\pi)^{d+1}}, \quad (5)$$

where $\int^>$ denotes an integration over the band of wave numbers being removed. Frequency integration is straightforward; in the limit $\Omega \rightarrow 0$ the subgrid-scale correction to the Green function becomes

$$\delta G(\mathbf{k})^{-1} = k^{-2} \int^> \left(\frac{1}{q^2} - \frac{1}{|\mathbf{q} - \mathbf{k}|^2} \right) \frac{D(q) [k^2 q^2 - (\mathbf{k} \cdot \mathbf{q})^2]}{2\mu(q) [\mu(q) + \mu(\mathbf{k} - \mathbf{q})]} \frac{d^d q}{(2\pi)^d}, \quad (6)$$

where $\mu(q) = \nu q^2 + i\beta q_x q^{-2}$. Considering the limit $k \rightarrow 0$ and retaining only the terms up to $O(k^2)$, one calculates corrections to β and ν given by $O(k^{-1})$ and $O(k^2)$ terms, respectively. It can be easily seen that in the process of infra-red renormalization Eq. (6) produces only $O(k^n)$, $n > 0$ terms, which essentially means that the β -term does not renormalize. Although this result has been implied in all large-scale geophysical

modeling, it is non-trivial and its mathematical justification has not been widely discussed. Still, the β -term renormalization is possible if an ultra-violet ($k \rightarrow \infty$) renormalization is considered.

3. Renormalized Viscosity and Energy Spectra

The $O(k^2)$ terms generate an integro-differential equation for RNG viscosity $\nu(k)$. This equation can be re-casted in terms of the non-dimensional parameter $M = \nu k^3/\beta$:

$$\frac{dM(x, \phi)}{dx} = \frac{3}{9-\epsilon} \cdot \frac{M}{x} + \frac{1}{2} \cdot \frac{1}{9-\epsilon} \cdot \frac{1}{2\pi} \int_0^{2\pi} \frac{d\theta}{2\pi} \frac{F(M, \theta, \phi)}{M^2}, \quad (7)$$

where $\epsilon = 4 + y - d$, $x \equiv D_0 k^{9-\epsilon}/\beta^3$ and

$$F(M, \theta, \phi) = \frac{(1 - \cos^2 \theta) \{M^2(1 - 6 \cos^2 \theta) + \cos(\theta + \phi) \cos \theta [\cos \phi - 2 \cos(\theta + \phi) \cos \theta]\}}{M^2 + \cos^2(\theta + \phi)}. \quad (8)$$

The renormalized viscosity $\nu(k)$ given by Eq. (7) is depicted in Fig. 1 in cylindrical surface coordinates.

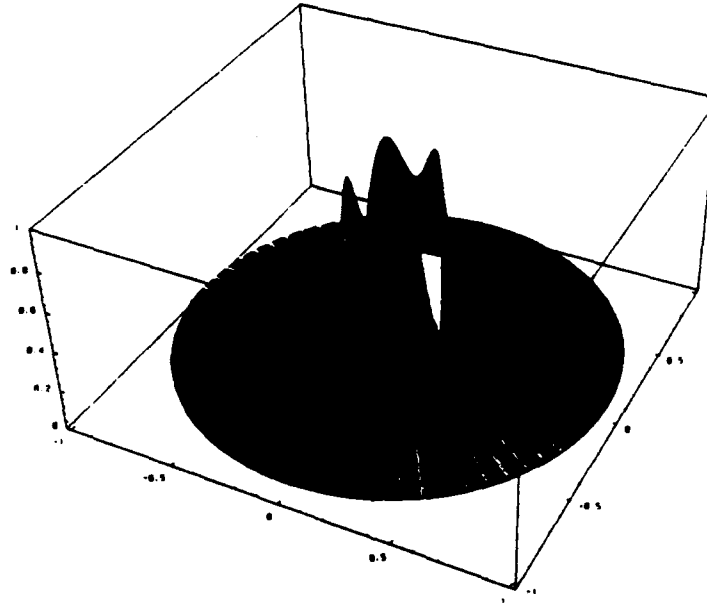


Figure 1. Renormalized viscosity $\nu(k)$.

One can see that for relatively large wave vectors, $x \gg 1$, $\nu(k)$ is isotropic and is growing monotonically as $k^{-\epsilon/3}$ with decreasing k , consistently with the results for purely 2-D turbulence [20]. The anisotropy induced by the β -effect develops as $k \rightarrow 0$; while $\nu(k)$ grows sharply for $\phi \in [\pi/4, 3\pi/4]$ and $\phi \in [5\pi/4, 7\pi/4]$, it abruptly decreases to zero along $\phi = 0, \pi$. Such a behavior of $\nu(k)$ causes singularity in Eq. (7) at $x \approx 0.04$ thus making its numerical solution impossible at smaller wave numbers.

The relative importance of processes associated with turbulence and Rossby waves can be measured by the ratio of the respective time scales, the turnover time, $\tau_{ts} = (\nu k^2)^{-1}$, and the Rossby wave period, $\tau_R = (\beta \cos \phi/k)^{-1}$:

$$\frac{\tau_{ts}}{\tau_R} = \frac{\beta \cos \phi}{\nu k^3} = \frac{\cos \phi}{M(k, \phi)}. \quad (9)$$

For $\tau_{tu}/\tau_R < 1$, turbulence dominates, while in the range $\tau_{tu}/\tau_R > 1$, Rossby waves prevail. Figure 2a shows the behavior of $\tau_{tu}/\tau_R = \cos \phi / M(k, \phi)$. One can see that at large k , this ratio is smaller than 1 and the flow is turbulence-dominated. At $x < 1$, the ratio becomes substantially anisotropic: it remains much smaller than 1 for the directions close to $\phi = \pm\pi/2$ but rapidly increases in the vicinity of $\phi = 0$ and π . Figure 2b shows only the region where $\tau_{tu}/\tau_R \geq 1$, which is dominated by Rossby waves. One can see that this region excludes the vicinities of $\phi = \pm\pi/2$ where Rossby waves cannot propagate; the effect of Rossby waves dramatically increases as $k \rightarrow 0$, particularly along $\phi = 0, \pi$.

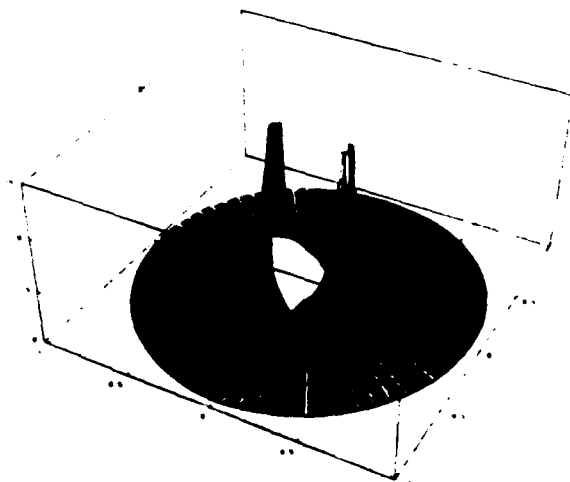


Figure 2a. Turbulence to Rossby waves time scales ratio, $\cos \phi / M(k, \phi)$.

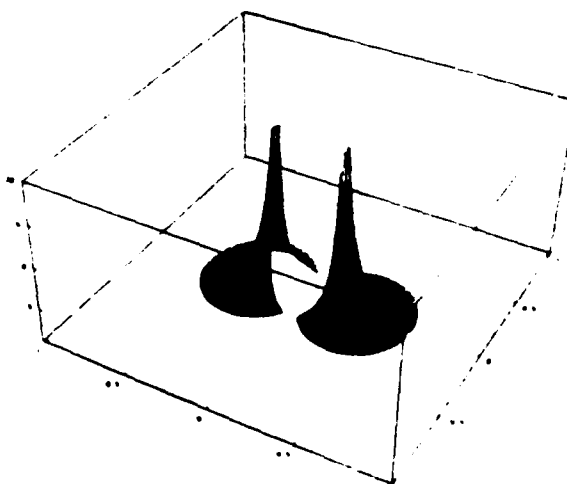


Figure 2b. Region of Rossby waves domination, $\cos \phi / M(k, \phi) > 1$.

These results indicate that as $k \rightarrow 0$, the β -term significantly affects the nature of the flow field making it anisotropic and either turbulence- or waves-dominated. One would expect that the energy spectrum would also become ϕ -dependent and thus an anisotropic spectrum $E(k, \phi)$ must be considered.

The energy spectrum, $E(k, \phi)$, can be related to the vorticity correlator $U(k, \phi)$ which in turn can be expressed in terms of the stirring force correlator:

$$E(k, \phi) = \pi \frac{U(k, \phi)}{k}, \quad (10)$$

$$U(k, \phi) = U(k) = \langle \zeta(k) \zeta(-k) \rangle = \frac{\langle \xi(k) \xi(-k) \rangle}{\nu(k) k^2}. \quad (11)$$

Figures 3a,b show compensated energy spectra $E(k, \phi) k^{5/3}$ and $E(k, \phi) k^{7/2}$, respectively. One can see that for large k , $E(k, \phi)$ is isotropic and proportional to $k^{-5/3}$, which is characteristic of the energy subrange of purely 2-D turbulence. As $k \rightarrow 0$, the spectral anisotropy develops: Fig. 3b indicates that $E(k, \phi) \propto k^{-7/2}$ is a good approximation for $\phi = 0, \pi$. One could speculate that this spectrum is generated by strongly interacting non-linear Rossby waves. One should note, however, that the $k^{-7/2}$ spectrum is rather qualitative since it occupies a very small range of k and therefore should be taken cautiously.

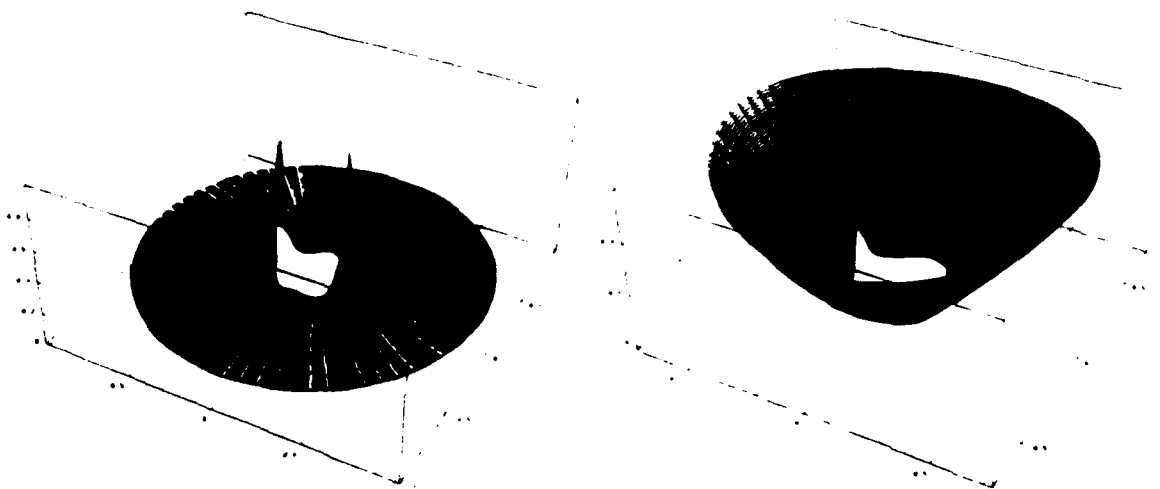


Figure 3a. Compensated energy spectrum, $E(k)k^{5/3}$. Figure 3b. Compensated energy spectrum, $E(k)k^{7/2}$.

4. Two-Parametric Viscosity and Spectral Energy Transfer

The RNG viscosity given by Eq. (7) characterizes the flow field in the limit $k \rightarrow 0$; it allows to calculate spectra of energy and enstrophy but does not directly relate to their transfer. To gain a deeper insight into energy and enstrophy transfer processes, a two-parametric viscosity, $\nu(k|k_c)$, should be introduced following Kraichnan [21]. This quantity is a measure of enstrophy and energy transfer from all subgrid wave numbers outside of the circle limited by the cut-off wave number k_c to the given wave number k , $k < k_c$. The two-parametric viscosity correctly accounts for the direct enstrophy and inverse energy cascades, it implies energy and enstrophy conservation and it was shown in [21] to be a powerful tool for description of isotropic 2-D turbulence.

The RNG-based, 3-D, spectral energy transfer derivation was given in [22]. Similar procedure can be performed for the vorticity equation describing 2-D turbulence [20]; it is based on a fixed point solution for the resolved scales, $\zeta^<(k) = G_r \xi$, G_r being the renormalized Green function, and leads to the enstrophy equation in the second order of ϵ -expansion:

$$\left(\frac{\partial}{\partial t} + 2\nu(k, t)k^2 \right) U(k, t) = T(k, t), \quad (12)$$

where

$$T(k, t) = \iint_D T(k, p, q, t) dp dq, \quad (13)$$

and

$$T(k, p, q) = \Theta_{-k, p, q}(p^2 - q^2) \sin \alpha \left[\frac{p^2 - q^2}{p^2 q^2} U(p)U(q) - \frac{k^2 - q^2}{k^2 q^2} U(q)U(k) + \frac{k^2 - p^2}{k^2 p^2} U(p)U(k) \right] + \text{similar terms}. \quad (14)$$

Here, α is an angle between the vectors \mathbf{p} and \mathbf{q} ; $\mathbf{k}, \mathbf{p}, \mathbf{q}$ form a triangle, $\mathbf{k} + \mathbf{p} + \mathbf{q} = 0$, and the integration domain, D , is defined by $|\mathbf{k} - \mathbf{p}| < q < \mathbf{k} + \mathbf{q}$. Note that Eq. (12) depends not only on k , but also on its direction, in anticipation of the anisotropy introduced by the β -term. Not shown in (14) are the terms that correspond to the mirror image of the triangle with respect to \mathbf{k} .

In the limit $t \rightarrow \infty$, an anisotropic two-parametric viscosity, $\nu(\mathbf{k}|k_c)$, is defined by

$$\nu(\mathbf{k}|k_c) = \frac{T(\mathbf{k}|k_c)}{2k^2 U(\mathbf{k})}, \quad (15)$$

where

$$T(\mathbf{k}|k_c) = \iint_{\Delta} T(\mathbf{k}, \mathbf{p}, \mathbf{q}) d\mathbf{p} d\mathbf{q}, \quad (16)$$

and where Δ denotes integration over all such triangles that p and/or q are greater than k_c . For the β -plane turbulence, the triad relaxation time, $\Theta_{-\mathbf{k}, \mathbf{p}, \mathbf{q}}$, in (14) is given by

$$\Theta_{-\mathbf{k}, \mathbf{p}, \mathbf{q}} = \frac{\nu_{\mathbf{k}} + \nu_{\mathbf{p}} + \nu_{\mathbf{q}}}{(\nu_{\mathbf{k}} + \nu_{\mathbf{p}} + \nu_{\mathbf{q}})^2 + (\omega_{-\mathbf{k}} + \omega_{\mathbf{p}} + \omega_{\mathbf{q}})^2}, \quad (17)$$

where

$$\nu_{\mathbf{k}} \equiv \nu(\mathbf{k})k^2 \quad \text{and} \quad \omega_{\mathbf{k}} \equiv \frac{\beta k_x}{k^2}. \quad (18)$$

Expressions similar to (12-14, 17, 18) were derived in [15] based on a Test Field Model.

It is useful to mention that if $M(k)k/k_x + M(p)p/p_x + M(q)q/q_x \rightarrow 0$, then

$$\Theta_{-\mathbf{k}, \mathbf{p}, \mathbf{q}} \rightarrow \pi \delta(\omega_{-\mathbf{k}} + \omega_{\mathbf{p}} + \omega_{\mathbf{q}}),$$

which corresponds to the results obtained from weak turbulence theory [12, 23, 24]; expression (13) is then converted into Boltzmann integral of the kinetic theory.

Figure 4 presents $\nu(k|k_c)$ for isotropic 2-D turbulence ($\beta = 0$) calculated using the RNG viscosity (here, the angular integration has been performed). Similarly to [21], $\nu(k|k_c)$ in this case has a sharp positive cusp near k_c and becomes negative as $k \rightarrow 0$. Numerical values of the RNG-based $\nu(k|k_c)$ are close to those derived in [21].

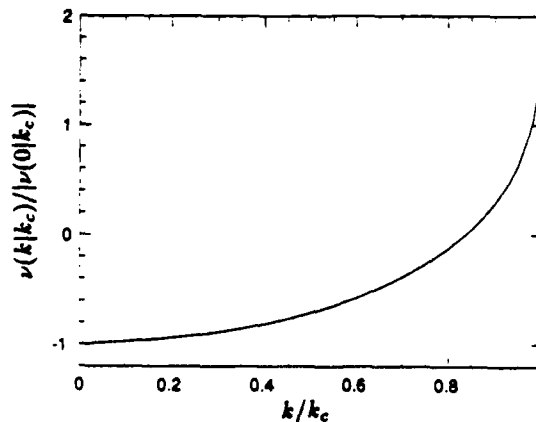


Figure 4. Two-parametric viscosity for isotropic ($\beta = 0$) 2-D turbulence, $\nu(k|k_c)$.

Figure 5a shows an angle-dependent, RNG-based $\nu(k|k_c)$ for isotropic 2-D turbulence ($\beta = 0$). Obviously, it is the body of revolution formed by the curve shown in Fig. 4. The isotropy of Fig. 5a is broken in Fig. 5b, where $\nu(k|k_c)$ is shown for $x_c \equiv D_0 k_c^{9-\epsilon}/\beta^3 = 10^3$. For approximately $0.5 < k/k_c < 1$, the β -effect is weak and $\nu(k|k_c)$ behaves quite similarly to the purely 2-D turbulence; there is a sharp positive cusp and then $\nu(k|k_c)$ becomes negative. As $k \rightarrow 0$, the effect of the β -term becomes stronger; $\nu(k|k_c)$ remains negative in the vicinity of $\phi = \pm\pi/2$ but increases in other directions. The negativeness of $\nu(k|k_c)$ along $\phi = \pm\pi/2$ is indicative of the strong inverse energy transfer to these directions which, in physical space, corresponds to a zonal flow $u = u(y)$. This is an important result demonstrating that zonal flows, typical of the Earth's and planetary circulations [25, 26] can be generated and maintained by the quasi-2-D turbulence on the β -plane, forced at relatively small scales.

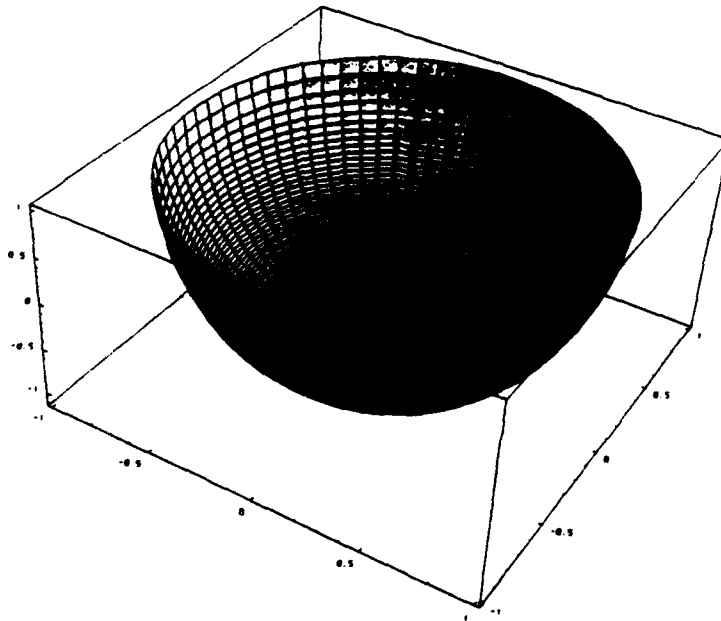


Figure 5a. Two-parametric viscosity for isotropic ($\beta = 0$) 2-D turbulence, $\nu(k|k_c)$.

To single out the mechanism causing $\nu(k|k_c)$ to remain negative along $\phi = \pm\pi/2$ for small k , which is the mechanism of zonalization in the physical space, $\nu(k|k_c)$ was calculated with the RNG-based vorticity correlator (11) for isotropic turbulence, such that the β -term was retained only in the relaxation time, $\Theta_{-k,p,q}$. Figure 5c shows that $\nu(k|k_c)$ in this case has the same general features as the two-parametric viscosity calculated with the full model, Fig. 5b. Particularly, strong negative values along $\phi = \pm\pi/2$ are also present in Fig. 5c. This result indicates that the zonalization is rather the result of the β -effect on $\Theta_{-k,p,q}$ than on the correlator $U(k)$.

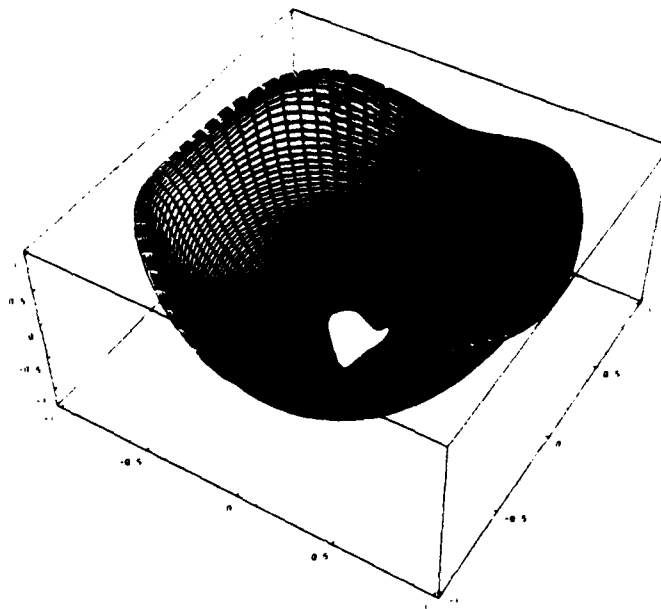


Figure 5b. Two-parametric viscosity $\nu(k|k_c)$; $x_c = 10^3$.

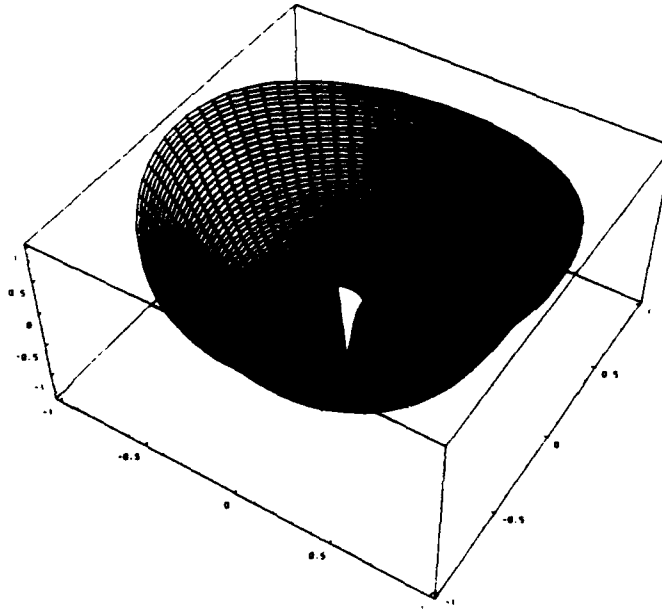


Figure 5c. Two-parametric viscosity $\nu(k|k_c)$ with isotropic $U(k)$, $x_c=8.0$.

Finally, let us consider the spectral energy transfer, $\mathcal{T}_e(k|k_c) = 2k^2\nu(k|k_c)E(k)$. By definition, this function accounts for the total energy transfer, which may be due to turbulence or non-linear waves. Figure 6 shows $\mathcal{T}_e(k|k_c)$ calculated for $x_c = 10^3$. For relatively large k , the spectral transfer function behaves similarly to $\nu(k|k_c)$, Fig. 5b. However, as $k \rightarrow 0$, $\mathcal{T}_e(k|k_c)$ develops two negative dips, along $\phi = \pm\pi/2$ and, much stronger, along $\phi = 0, \pi$. The former has been identified earlier with the flow zonalization. The

interpretation of the latter is more subtle. As was shown on Fig. 2b, the region in the vicinity of the clips along $z = 0, \tau$ is strongly dominated by Rossby waves. Thus, $T_e(k|k_c)$ is consistent with this result showing that along with the energy flux into a zonal flow there is also a significant energy flux into zonally propagating Rossby waves. The arising structure of the large-scale flow consisting of zonal jets and zonally propagating Rossby waves is consistent with results of numerical simulations [14, 18].

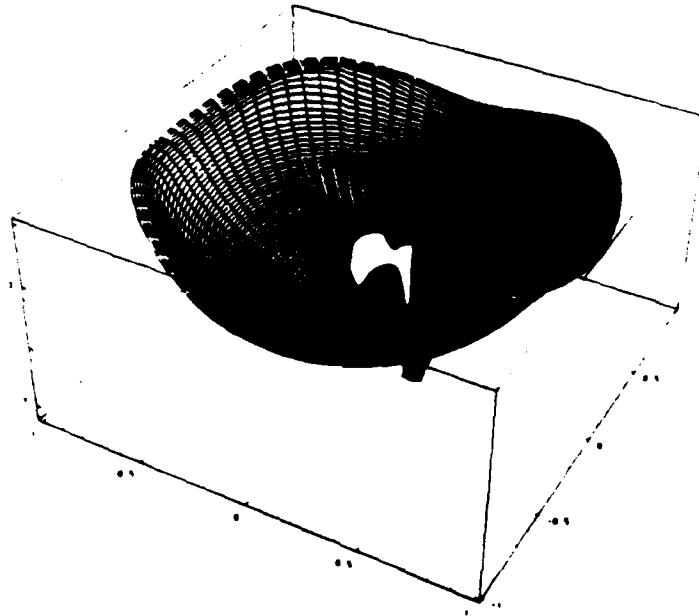


Figure 6. Spectral energy transfer, $T_e(k|k_c)$, $z_c = 10^3$.

5. Conclusions and Discussion

Renormalization Group theory of turbulence was applied to barotropic vorticity equation on the β -plane. In this framework, the complex interaction between 2-D turbulence and Rossby waves was studied from first principles. It was shown that at relatively small scales, the β -effect is weak and the flow structure resembles that of purely 2-D turbulence. At large scales, the β -effect dominates and results in anisotropization of the renormalized viscosity and energy spectrum. Consideration of the spectral energy transfer reveals that as $k \rightarrow 0$, the energy is preferably transmitted to zonal flows and zonally propagating Rossby waves. This study provides the first analytical evidence that zonal flows can be sustained by 2-D turbulence on the β -plane.

Two problems of the method should be mentioned. First, the forcing introduced in (2) is assumed isotropic. It is not clear *a priori* if it indeed is isotropic at large scales where β -effect is significant. Second, it was shown that the β -term does not renormalize in infra-red renormalization. It is possible that the situation will change in the process of ultra-violet renormalization. Then, the renormalized β will characterize the Rossby frequency shift. Such a shift was discussed in [12, 23, 27] but whether or not it indeed exists is not clear at the present time. Both problems are difficult and require further investigation.

Acknowledgments

This research has been partially supported by ONR Grant N00014-92-J-1363 and NSF Grant OCE 9010851.

REFERENCES

- [1] J. C. McWilliams, *J. Fluid Mech.* **146**, 21 (1984).
- [2] V. D. Larichev and J. C. McWilliams, *Phys. Fluids* **A3**, 938 (1991).
- [3] M. Briscolini and P. Santangelo, *IBM J. Res. Devel.* **35**, 119 (1991).
- [4] R. C. Kloosterziel and G. J. F. van Heijst, *J. Fluid Mech.* **223**, 1 (1991).
- [5] P. Tabeling, S. Burkhart, O. Cardoso and H. Willaime, *Phys. Rev. Lett.* **67**, 3772 (1991).
- [6] M. E. Maltrud and G. K. Vallis, *J. Fluid Mech.* **228**, 321 (1991).
- [7] H. D. I. Abarbanel and W. R. Young, eds. *General Circulation of the Ocean*. Springer-Verlag (1987).
- [8] P. B. Rhines, *Ann. Rev. Fluid Mech.* **11**, 401 (1979).
- [9] G. Holloway, *J. Fluid Mech.* **184**, 463 (1987).
- [10] J. C. McWilliams, *J. Fluid Mech.* **198**, 199 (1989).
- [11] R. Kraichnan and D. Montgomery, *Rep. Prog. Phys.* **43**, 547 (1980).
- [12] G. Holloway, *Ann. Rev. Fluid Mech.* **18**, 91 (1986).
- [13] A. Mirabel and A. S. Monin, *Adv. Mech. Poland* **2**, 47 (1979).
- [14] P. B. Rhines, *J. Fluid Mech.* **69**, 417 (1975).
- [15] G. Holloway and M. C. Hendershott, *J. Fluid Mech.* **82**, 747 (1977).
- [16] R. H. Kraichnan, *J. Fluid Mech.* **47**, 513 (1971).
- [17] C. Basdevant, B. Legras, R. Sadourny and B. Béland, *J. Atmos. Sci.* **38**, 2305 (1981).
- [18] G. P. Williams, *J. Atmos. Sci.* **35**, 1399 (1978).
- [19] V. Yakhot and S. A. Orszag, *J. Sci. Comput.* **1**, 3 (1986).
- [20] S. Sukoriansky and I. Staroselsky, 43rd Annual Meeting of APS, Div. Fluid Dynamics (1990).
I. Staroselsky and S. Sukoriansky, Renormalization Group Approach to Two-Dimensional Turbulence.
In: *Advance in Turbulence Research*, Progress Series of the AIAA, in press.
- [21] R. H. Kraichnan, *J. Atmos. Sci.* **33**, 1521 (1976).
- [22] W. P. Dannevik, V. Yakhot, and S. A. Orszag, *Phys. Fluids*, **30**, 2021, 1987.
- [23] G. K. Carnevale and P. C. Martin, *Geophys. Astrophys. Fluid Dyn.*, **20**, 131 (1982).
- [24] R. Salmon, Geostrophic Turbulence. In: *Topics in Ocean Physics, Proc. Int. Sch. Phys. Enrico Fermi, Varenna, Italy*, 30 (1982).
- [25] J. Pedlosky, *Geophysical Fluid Dynamics*, Second Edition. Springer-Verlag (1987).
- [26] A. P. Ingersoll, *Science*, **248**, 308 (1990).
- [27] B. Legras, *Geophys. Astrophys. Fluid Dyn.*, **15**, 253 (1980).

DIFFERENTIAL DIFFUSION OF PASSIVE SCALARS IN STATIONARY ISOTROPIC TURBULENCE

P.K. Yeung † and S.B. Pope ‡

† School of Aerospace Engineering
Georgia Institute of Technology
Atlanta, GA 30332, U.S.A.

‡ Sibley School of Mechanical and Aerospace Engineering
Cornell University
Ithaca, NY 14853, U.S.A.

ABSTRACT

The differential diffusion of passive scalars of different diffusivities is studied by direct numerical simulations of statistically stationary isotropic turbulence at low Reynolds number. The statistical correlation between different scalars is closely linked to that between the gradients of different scalars. At small times the scalars de-correlate fairly rapidly, at a rate proportional to the square of the diffusivity difference. At large times the variance of each scalar decays exponentially in time at a slightly different rate, and the correlation coefficients continue to decrease, but only slowly. The question of whether the scalars ultimately become completely de-correlated (and remain so) requires further investigation.

INTRODUCTION

If two passive scalars of different molecular diffusivities are introduced into a turbulent flow and made identical-valued at some initial time instant, differing rates of diffusion cause them to subsequently become displaced and statistically de-correlated from each other. This phenomenon of differential diffusion has important effects on the structure of turbulent flames in which multiple diffusing species, including heat, of different diffusivities are almost always involved.

Most theoretical models of turbulent diffusion flames effectively ignore differential diffusion by assuming (a) the molecular diffusivities of all species, and of heat, to be equal, and (b) the effects of molecular diffusion to be negligible compared to turbulent diffusion. Assumption (a) is equivalent to taking the Lewis numbers of all species to be unity. These assumptions lead to great simplifications. However, Bilger and Dibble¹ pointed out that they are questionable at the low and moderate Reynolds numbers often encountered in turbulent flames. More recently, based on results reported by Chen *et al.*², Pope³ noted that methods based on the equal-diffusivities assumption could not match experimental data.

As a basic fluid mechanics problem, the mixing of *multiple* scalars is not well understood, perhaps considerably less so than the mixing of a *single* scalar. For instance, there is little definite knowledge of the time scale on which two initially identical scalars de-correlate, and of whether the correlation coefficient between the two scalars attains a non-zero asymptotic value at large times. These are questions we address

in the present work

We consider the differential diffusion between three passive scalars (taken in pairs) in numerically simulated isotropic turbulence. To provide a simplified setting in which to study the scalars, the hydrodynamic field is kept statistically stationary in time using the forcing scheme of Eswaran and Pope ⁴. Direct numerical simulations are carried out using the pseudo-spectral algorithm of Rogallo ⁵ on a 64^3 grid. The time-averaged Taylor scale Reynolds number is 38, corresponding to one of the (hydrodynamic) simulations of Yeung and Pope ⁶. Three initially Gaussian-distributed passive scalars ϕ_1 , ϕ_2 and ϕ_3 , at Schmidt numbers (Sc) 0.25, 0.5 and 1.0 respectively are introduced into the flow and allowed to evolve. High wavenumber spectra of the scalars are well resolved at these Schmidt numbers. After a transient period the decay of scalar variances becomes approximately exponential in time, consistent with the results of Eswaran and Pope ⁷. Subsequently ϕ_1 and ϕ_2 are made identical to ϕ_3 (the scalar with unity Schmidt number). Differential diffusion effects become important in the ensuing evolution.

Our results show that the correlation coefficient decays rapidly at early times, but more slowly at later times. The small-time behavior is compared to an approximate analysis of the pure diffusion equation (with velocity field removed). The difference in diffusivities, rather than the ratios between them, is an important parameter. At large times the ensemble-averaged correlation coefficients appear to change slowly with no clear indication of approaching asymptotic values.

In the following sections, we give the basic equations governing differential diffusion, and an overview of the numerical simulations. Results are then presented for discussion. The path of further investigations is addressed.

BASIC EQUATIONS

Consider a set of σ passive scalars $\phi_1, \phi_2, \dots, \phi_\sigma$ evolving in a field of homogeneous isotropic turbulence. In the absence of mean scalar gradients, the mean value of each scalar may be taken to be zero without loss of generality. Then the fluctuation of each scalar ϕ_α ($\alpha = 1, \dots, \sigma$, with no sum over Greek indices) evolves by the equation

$$\frac{\partial \phi_\alpha}{\partial t} + u_i \frac{\partial \phi_\alpha}{\partial x_i} = D_\alpha \frac{\partial^2 \phi_\alpha}{\partial x_i \partial x_i}, \quad (1)$$

where $u_i = u_i(\underline{x})$ is the fluctuating velocity field, and D_α is the diffusivity of the scalar ϕ_α . The diffusivity is constant but (in general) different for each scalar. As mixing proceeds, the scalar variance $\langle \phi_\alpha^2 \rangle$ decays according to

$$\frac{\partial \langle \phi_\alpha^2 \rangle}{\partial t} = -2D_\alpha \left\langle \left(\frac{\partial \phi_\alpha}{\partial x_i} \right)^2 \right\rangle \equiv -\chi_\alpha, \quad (2)$$

where χ_α is the dissipation rate of the scalar ϕ_α .

In studies of differential diffusion the covariance of two scalars, $\langle \phi_\alpha \phi_\beta \rangle$, is important. It evolves by

$$\frac{\partial \langle \phi_\alpha \phi_\beta \rangle}{\partial t} = -(D_\alpha + D_\beta) \left\langle \frac{\partial \phi_\alpha}{\partial x_i} \frac{\partial \phi_\beta}{\partial x_i} \right\rangle \equiv -\chi_{\alpha\beta}, \quad (3)$$

where $\chi_{\alpha\beta}$ denotes the "joint" dissipation. (Unlike χ_α , when $\alpha \neq \beta$, $\chi_{\alpha\beta}$ is not necessarily positive.) From Eqs. 2 and 3 it may be shown that the cross-correlation coefficient between the scalars ϕ_α and ϕ_β , i.e.,

$$\rho_{\alpha\beta} \equiv \frac{\phi_\alpha \phi_\beta}{(\phi_\alpha^2 \phi_\beta^2)^{1/2}}$$

evolves by

$$\frac{\partial \rho_{\alpha\beta}}{\partial t} = [(\phi_\alpha^2 \phi_\beta^2)^{-3/2}] - (\phi_\alpha^2 \phi_\beta^2 \chi_{\alpha\beta} - \frac{1}{2} (\phi_\alpha \phi_\beta / ((\phi_\alpha^2 \chi_\beta + \phi_\beta^2 \chi_\alpha)))]. \quad (4)$$

Equation 4 may be viewed as a "budget" equation for the two-scalar cross-correlation coefficient. This equation directly confirms two qualitative expectations. First, consider that the two scalars be made identical valued at some initial instant t_0 . Since the scalar fluctuations are differentiable in time, a simple Taylor expansion shows that the correlation coefficient must depart from unity quadratically in time. Consistent with this fact, Eq. 4 indicates that $\partial \rho_{\alpha\beta} / \partial t = 0$ at $t = t_0$. The second expectation is that if the variances of both scalars as well as the their covariance decay exponentially with time at the same rate, then their cross-correlation coefficient does not change. In this case $\langle \phi_\alpha^2 \rangle$, $\langle \phi_\beta^2 \rangle$ and $\langle \phi_\alpha \phi_\beta \rangle$ are all proportional to $\exp(-ct)$, where c is some positive constant. Substituting the corresponding forms for the dissipations (via Eqs. 2 and 3) in Eq. 4 again leads to a vanishing time derivative for the two-scalar correlation coefficient.

Clearly, the correlation between the *gradients* of two scalars, through the joint dissipation, plays an important role. In the results section, we study the dynamics of the correlation between pairs of scalars and between their gradients with reference to the equations presented above.

OVERVIEW OF SIMULATIONS

The exact Navier-Stokes equations are solved together with the scalar transport equation (1) numerically to obtain velocity and scalar fluctuations. This is accomplished by carrying out direct numerical simulations (DNS) of homogeneous isotropic turbulence using the Fourier pseudo-spectral algorithm of Rogallo⁵ in the form implemented by Yeung and Pope⁶. The solution domain is a 64^3 uniform grid with periodic boundary conditions imposed in three dimensions. The hydrodynamic field is made statistically stationary in time using the forcing scheme of Eswaran and Pope⁴. The time-averaged Taylor-scale Reynolds number is 38, with all hydrodynamic statistics corresponding closely to those of the first-listed simulation in Yeung and Pope⁶. (In effect, numerical parameters are chosen to obtain different realizations of statistically the same flow.)

The scalars are introduced first using Gaussian distributed random numbers in conjunction with a specified wavenumber spectrum. This Gaussian state is unphysical because it implies Gaussian distributed scalar gradients as well. However, when the scalar is allowed to evolve, after a transient period it attains a self-similar state, independent of the details of the initial spectrum. Self-similarity of the scalar is characterized by approximate exponential decay of variance with time, a Gaussian probability density function (p.d.f.) for the scalar but not for the gradients, and a collapse of the high-wavenumber scalar spectrum under Kolmogorov scaling. The case of $Sc = 1$ is taken as reference, and after it has remained self-similar for a few eddy-turnover times, two other scalars at $Sc = 0.25$ and $Sc = 0.5$ are introduced and made identical-valued to the $Sc = 1$ scalar. We choose Schmidt number values not exceeding unity so that, like the hydrodynamic field, the scalar fields remain well-resolved at the small scales. The drawback is that for small Schmidt numbers (say 0.25)

the scalar spectrum quickly becomes dominated by the large scales. This contributes to statistical variability since relatively few samples of the large-scale modes exist in the solution domain.

Unlike the forced hydrodynamic field, the scalar fields are not statistically stationary and thus time averages are not taken. Consequently, each run represents only one realization, and considerable differences between realizations can be expected. Indeed, the numerical results presented in this paper exhibit significant statistical variability, especially at long diffusion times. This necessitates performing ensemble averaging over multiple independent realizations that are statistically identical but different in detail. Different realizations are created by introducing randomness via the initial conditions, and via the forcing scheme which is based on a stochastic process. Since each simulation covered as long as 16 eddy-turnover times, the velocity and scalar fields at the beginning and end may be considered statistically independent. Thus, the final conditions for each run are conveniently taken to be the initial conditions for the next run, with each run then representing a different realization. We have obtained and processed 11 realizations in this manner. For the forcing scheme, since only a small number of large scale modes are forced, insufficient sampling of the forced modes leads to large temporal fluctuations in volume-averaged flow statistics, as previously discussed by Yeung and Pope ⁶.

Differential diffusion occurs when the three scalars of different diffusivities are subsequently allowed to evolve together. Results are presented in the next few sections. For convenience, time is measured from the instant at which the scalars are made identical, and the scalar variances at this time (called *initial time* hereafter in this article) are normalized to unity.

RESULTS AND DISCUSSION

In this section, we describe and discuss the temporal evolution of scalar variances, covariances and cross-correlation coefficients. The behavior at small and large times are separately discussed further. In view of the statistical variability at (especially) large diffusion times, ensemble averaging is performed over multiple realizations created in the manner described in the previous section.

Figure 1 shows the evolution of scalar variances and covariances, which are equal at the initial time at which the scalar fluctuations are made identical valued. The dissipation of scalar fluctuations by mixing occurs faster for more strongly diffusing scalars with lower Schmidt numbers. A transient period necessarily occurs during which the scalars adjust to the different rates of mixing. At large times the data suggest exponential decay of the variances in time, represented by approximately straight lines of constant slopes on the linear-log plot. Exponential decay at large times was also observed in forced stationary turbulence by Eswaran and Pope ⁷ who used very different initial conditions for the scalars.

True exponential decay of the variance implies a constant decay time scale, defined as the ratio of variance to dissipation. Eswaran and Pope ⁷ used only one Schmidt number of 0.7. To compare the decay time scales of different scalars of different Schmidt numbers among themselves and to that of the velocity field, we show in Fig. 2 the evolution of the mechanical-to-scalar time scale ratios

$$\tau_a = (q^2/\epsilon) (\chi_a / \langle \phi_a^2 \rangle) .$$

(Here $q^2/2$ and ϵ are the mean turbulence kinetic energy and dissipation rate respectively.) Except during

an initial transient period, the time scale ratio τ_a oscillates around a value slightly greater than 5, which is qualitatively consistent with the results of Eswaran and Pope ⁷ (in which the definition of scalar dissipation was half of that used in this paper). However, a slight but systematic dependence of the decay time scale on Schmidt number can be discerned. Lower Schmidt number is seen to be associated with a larger mechanical-to-scalar time scale ratio, and hence a smaller decay time scale and larger decay rate for the scalar variance.

The transient period observed in Fig. 2 appears to be less than one eddy-turnover time. Concurrently, the spectra of the two initially-perturbed scalars ($Sc = 0.25$ and 0.5) are found to adjust rapidly to a statistically steady shape under Kolmogorov scaling. Figure 3 shows the scaled steady-state spectra for all three scalars, using the same scaling as Kerr ⁹. The spectra are well resolved, with small or no turn-up at the high wavenumber end. The spectral collapse at later times is consistent with self-similar decay of each scalar. The p.d.f. of each scalar remains near-Gaussian throughout the simulations. We also observe that, as expected, the spectra of scalars of lower Schmidt numbers have more low wavenumber content.

Figure 4 shows the correlation coefficient between the $Sc = 0.25$ and $Sc = 1$ scalars for 11 different realizations, up to 16 eddy-turnover times. This pair of scalars has the largest diffusivity difference among the three scalars used. The sample mean and standard deviation are also indicated. It may be seen that at early times (less than one eddy-turnover time) the correlation coefficient decreases fairly rapidly with little statistical uncertainty. In contrast, the different realizations differ widely at later times. The possibility of asymptotic values at large times is explored further at the end of this section.

The correlation coefficients of all three pairs of scalars are compared in Fig. 5. Besides the sample means, 90% confidence intervals for the ensemble averages are also indicated. (That is, at each given time the ensemble-averaged correlation coefficient falls inside the marked intervals with 90% probability.) Differential diffusion between the $Sc = 0.25$ and $Sc = 1$ scalars is clearly much more pronounced than for the other two pairs. The pairs $Sc = 0.25, 0.5$ and $Sc = 0.5, 1.0$ share the same diffusivity ratio. However, the correlation coefficient is consistently lower for the *former*—i.e., the pair with higher diffusivities and larger diffusivity differences.

According to Eq. 3, the rate of de-correlation of scalar fluctuations is tied to the de-correlation of the gradients of different scalars. Figure 6 shows the evolution of the scalar-gradient correlation coefficients $g_{\alpha\beta}$ (defined similarly to $\rho_{\alpha\beta}$) averaged over different realizations and (in view of isotropy) over different coordinate components. Clearly, the scalar gradients are persistently more strongly de-correlated than the scalars themselves. Statistical variability, as measured by the size of the confidence intervals, is substantially less than that for the scalars. Since the gradients are more closely related to the small scales, this comparison is consistent with the expectation that the statistical uncertainty arises mainly at the large scales. At large times the correlation coefficient between the scalar gradients appears to approach a quasi-steady value, or at least changes very slowly.

Small-time behavior

At sufficiently small times it is natural to expect differential diffusion to be largely determined by the small scales (which have the shortest time scales) at which molecular effects are most important. Thus

an approximate analysis can be made based on the pure diffusion equation, (Eq. 1 with the advective term removed)

$$\frac{\partial \phi_a}{\partial t} = D_a \nabla^2 \phi_a \quad (5)$$

Let $\dot{\phi}_a(\underline{k}, t)$ be the Fourier transform of the scalar field $\phi_a(\underline{x}, t)$, where \underline{k} is the wave-vector with magnitude k . The Fourier-space equivalent of Eq. 5 is

$$\frac{\partial \dot{\phi}_a}{\partial t} = -D_a k^2 \dot{\phi}_a \quad (6)$$

which upon integration gives

$$\dot{\phi}_a(\underline{k}, t) = \dot{\phi}_0(\underline{k}) \exp(-D_a k^2 t) \quad (7)$$

where the subscript '0' denotes initial conditions which are identical for all scalars. The scalar spectrum is given by

$$E_{aa}(\underline{k}, t) = \langle \dot{\phi}_a \dot{\phi}_a^* \rangle = E_0(\underline{k}) \exp(-2D_a k^2 t) \quad (8)$$

and so the variance can be expressed as

$$\langle \phi_a^2 \rangle = \int E_0(\underline{k}) \exp(-2D_a k^2 t) d\underline{k} \quad (9)$$

where the integral is taken over all Fourier modes. Similarly, the covariance is given by

$$\langle \phi_a \phi_b \rangle = \int E_0(\underline{k}) \exp[-(D_a + D_b) k^2 t] d\underline{k} \quad (10)$$

The correlation coefficient is hence

$$\rho_{ab} = \frac{\int E_0(\underline{k}) e^{-(D_a + D_b) k^2 t} d\underline{k}}{\left\{ \int E_0(\underline{k}) e^{-2D_a k^2 t} d\underline{k} \int E_0(\underline{k}) e^{-2D_b k^2 t} d\underline{k} \right\}^{1/2}} \quad (11)$$

By expanding the exponentials, $\langle \phi_a \phi_b \rangle$ can be written in terms of even moments of the initial scalar spectrum:

$$I_p = \int E_0(\underline{k}) k^p d\underline{k} \quad (12)$$

where $p = 0, 2, 4, \dots$, and I_0 is just the initial variance.

Consider now times so small that Eq. 11 can be expanded as a binomial series, with higher order terms neglected. After straightforward algebra, the final result is:

$$\rho_{ab}(t) = 1 - \frac{1}{2} (D_a - D_b)^2 [I_4/I_0 - (I_2/I_0)^2] t^2 + O(t^4) \quad (13)$$

The factor $I_4/I_0 - (I_2/I_0)^2$ depends on the shape of the initial scalar spectrum. In general, $I_4/I_0 > (I_2/I_0)^2$, so that $\rho_{ab}(t)$ initially decreases quadratically with time. This analysis also shows that, at least initially, the rate of de-correlation is proportional to the square of the diffusivity difference. The result (13) is compared to numerical data in Fig. 7. To accentuate the quadratic behavior, we have plotted $1 - \rho_{ab}(t)$ versus time on log-log-scales. Since the early time evolution is a small scale process, time is normalized by the Kolmogorov time scale (which is $0.136 T_E$ in this flow). The agreement is evidently close at sufficiently small diffusion times. Also, the range of validity of (13) is longer for lower Schmidt numbers at which the diffusive effects are stronger compared to the convective effects.

There is natural interest in whether the scalar and scalar-gradient correlation coefficients approach zero, representing complete de-correlation, or other asymptotic value at long enough diffusion times. Figures 5 and 6 indicate that asymptotic values, if they do occur, are not yet reached after 16 eddy-turnover times. Within the limits of statistical uncertainty, the correlation coefficients show a continuing but slow trend of approximately linear decrease with time. If the ensemble-averaged joint-scalar correlation coefficients are extrapolated linearly in time, they would reach zero at nearly 45 eddy-turnover times for the $Sc = 0.25$ and 1.0 pair, and as long as 160 eddy-turnover times for the $Sc = 0.5$ and 1.0 pair.

The question of long-time asymptotic behavior can be addressed further using Eq. 4. The rate of change of the joint-scalar correlation coefficient is determined by two competing effects. A positive joint-scalar correlation coefficient tends to reinforce itself, while a positive correlation of the scalar gradients tends to de-correlate the scalars. The relative magnitudes of these effects are compared in Fig. 8, where they are seen to nearly balance. The overall rate of change is indeed small—on average, for the $Sc = 0.25$ and 1.0 scalars, it takes some 5 eddy-turnover times for the correlation coefficient to decrease by 0.1. (For comparison, according to Fig. 1, in the same time interval the scalar variances decay by a factor of of order at least 10^3 .)

We earlier remarked that if the scalar variances and covariances all decay at the same rate, the correlation coefficients would become constant. However, the decay time scales are seen in Fig. 2 to be different for each scalar. Considering also the trends observed in Fig. 5 and 6, it seems more likely that, on average, the correlation coefficients would continue to decrease. Nevertheless, this statement needs to be tested by further numerical simulations over extended periods of time. We may note that if the scalars and their gradients become perfectly uncorrelated at some time, then Eq. 4 indicates that the correlation coefficients would pass through another inflection point at which the first-order time derivative $\partial \rho_{\alpha\beta}/\partial t$ vanishes. Additional interesting deductions may be drawn from Eq. 4, but will be reported elsewhere.

CONCLUSIONS AND FURTHER WORK

We have studied the differential diffusion of passive scalars with different diffusivities, a problem especially important in turbulent combustion, in the case of statistically stationary isotropic turbulence. The dimensionless parameters are a Taylor-scale Reynolds number of 38, and Schmidt numbers of 0.25, 0.5 and 1.0.

It is shown that each scalar attains a self-similar state and decays exponentially in time with a slightly different decay time scale. The scalars are initially identical but subsequently de-correlate due to differential diffusion. At small diffusion times the joint-scalar correlation coefficient departs from unity quadratically in time, proportionally to the square of the diffusivity difference, and to a parameter describing the shape of the scalar spectrum.

At large diffusion times the data show considerable statistical variability among different realizations. The ensemble-averaged correlation coefficients between different scalars and between the gradients of different scalars appear to decrease slowly up to 16 eddy-turnover times and beyond. A definitive answer to the question

of long-time asymptotic behavior awaits further investigations.

This work will be extended in several directions. The numerical simulations will be extended to cover longer diffusion times. Whereas this paper is largely based on statistical analysis in physical space, useful insights may also be gained using Fourier-space descriptions and three-dimensional visualization. The effects of Reynolds number, and of different types of initial conditions are also to be studied.

REFERENCES

- ¹ R.W. Bilger and R.W. Dibble, "Differential molecular diffusion effects in turbulent mixing," Comb. Sci. & Tech. **28**,161 (1982).
- ² J-Y. Chen, R.W. Bilger and R.W. Dibble, "PDF modeling of turbulent nonpremixed $CO/H_2/N_2$ jet flames with reduced mechanisms," Twenty-Third Symposium (International) on Combustion, The Combustion Institute, 775 (1990).
- ³ S.B. Pope, "Computations of turbulent combustion: progress and challenges," Twenty-Third Symposium (International) on Combustion, The Combustion Institute, 591 (1990).
- ⁴ V. Eswaran and S.B. Pope, "An examination of forcing in direct numerical simulations of turbulence," Comput. & Fluids **16**, 257 (1988).
- ⁵ R.S. Rogallo, "Numerical experiments in homogeneous turbulence," NASA TM 81315 (1981).
- ⁶ P.K. Yeung and S.B. Pope, "Lagrangian statistics from direct numerical simulations of isotropic turbulence," J. Fluid Mech. **207**, 531 (1989).
- ⁷ V. Eswaran and S.B. Pope, "Direct numerical simulations of the turbulent mixing of a passive scalar," Phys. Fluids **31**, 506 (1988).
- ⁸ P.K. Yeung and S.B. Pope, "An Algorithm for tracking fluid particles in numerical simulations of homogeneous turbulence," J. Comput. Phys. **79**, 373 (1988).
- ⁹ R.M. Kerr, "Higher-order derivative correlations and the alignment of small-scale structures in isotropic numerical turbulence," J. Fluid Mech. **153**, 31 (1985).

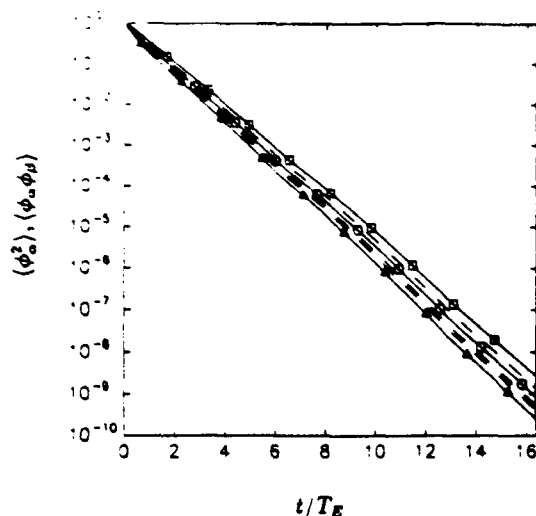


Fig. 1. The decay of variances and covariances with time normalized by the eddy-turnover time (T_E , the ratio of longitudinal integral length scale to the root-mean-square velocity). Schmidt numbers for variances are: 0.25 (ϕ_1 , Δ), 0.5 (ϕ_2 , \circ) and 1.0 (ϕ_3 , \square). Covariances are shown as dashed lines, with $\langle \phi_2 \phi_3 \rangle > \langle \phi_1 \phi_3 \rangle > \langle \phi_1 \phi_2 \rangle$ at all times.

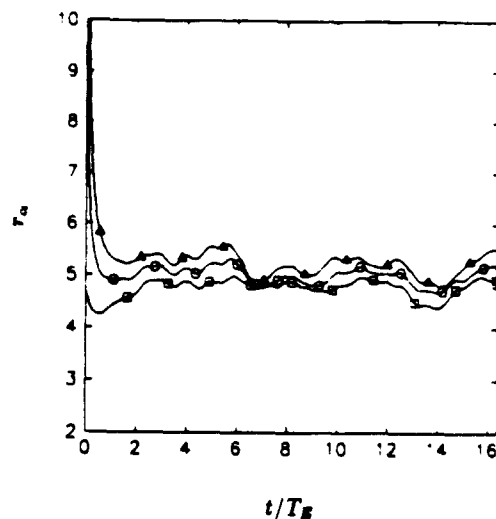


Fig. 2. Evolution of the mechanical-to-scalar time scale ratio r_m for the three scalars, shown in normalized time. Schmidt numbers are: 0.25 (Δ), 0.5 (\circ) and 1.0 (\square).

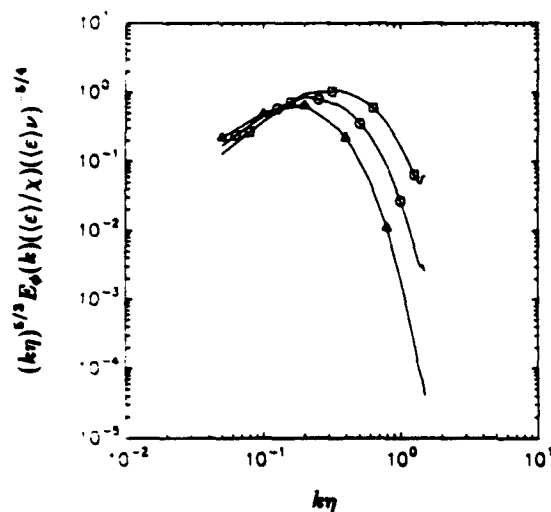


Fig. 3. Three-dimensional scalar spectra ($E_\phi(k)$) in the self-similar period of decay, shown in Kolmogorov scaling (ν is the kinematic viscosity, and η is the Kolmogorov length scale). Schmidt numbers are: 0.25 (Δ), 0.5 (\circ) and 1.0 (\square).

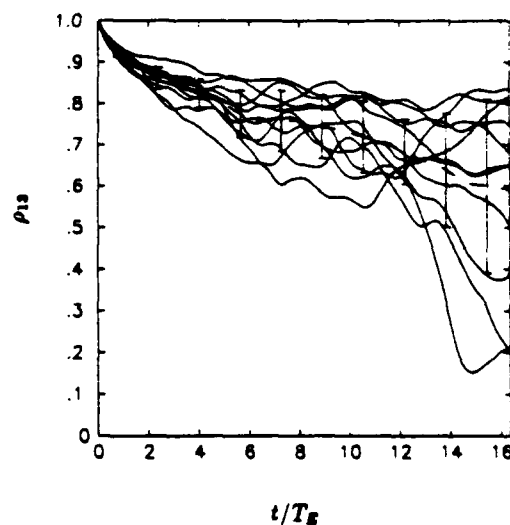


Fig. 4. Evolution of the correlation coefficients between the $Sc = 0.25$ (ϕ_1) and $Sc = 1$ (ϕ_3) scalars shown in normalized time. Each solid line represents a different realization. The dashed line represents the average over all (11) realizations, and the vertical bars indicate one standard deviation above and below the mean.

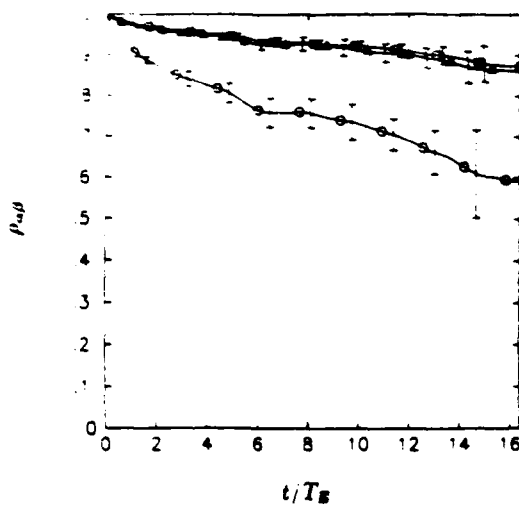


Fig. 5. Evolution of the correlation coefficients between different scalars taken in pairs: $Sc = (0.25, 0.5)$ (Δ), $Sc = (0.25, 1.0)$ (\circ), and $Sc = (0.5, 1.0)$ (\square), shown in normalized time. The lines shown are averages over multiple realizations. Vertical bars denote bounds of 90% confidence intervals (calculated using Student's t distribution because sample size is small) for the respective ensemble averages.

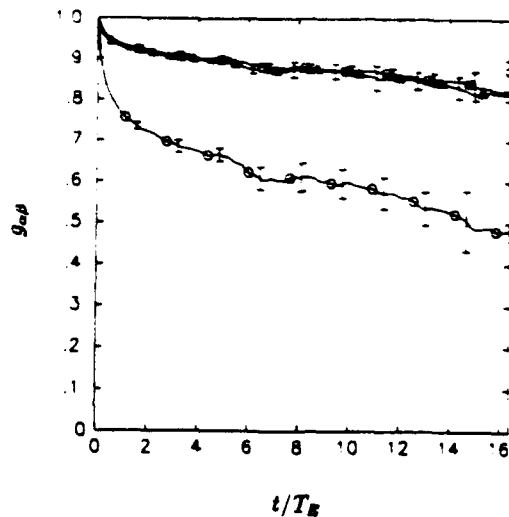


Fig. 6. Same as Fig. 5, but for correlation coefficients between the gradients of the different scalars.

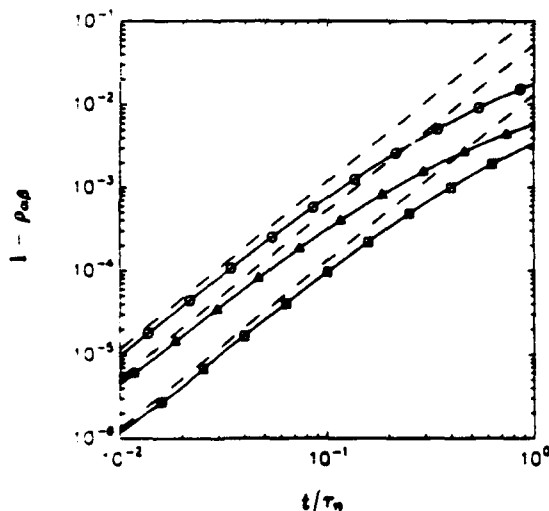


Fig. 7. Comparison of the evolution of two-scalar correlation coefficients at very small diffusion times (normalized by the Kolmogorov time scale τ_n) with prediction from analysis of the diffusion equation (Eq. 13). The scalar pairs are: $Sc = (0.25, 0.5)$ (Δ), $Sc = (0.25, 1.0)$ (\circ), and $Sc = (0.5, 1.0)$ (\square).

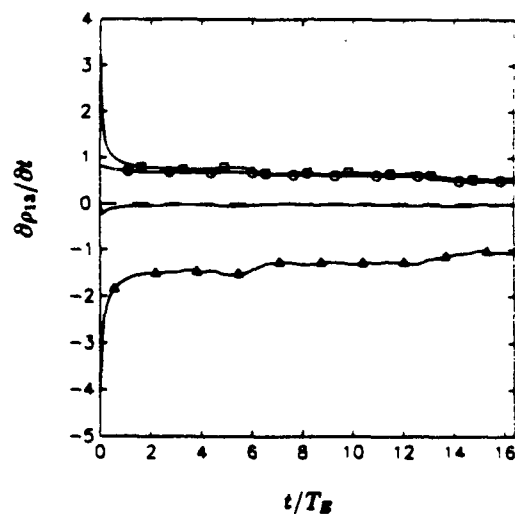


Fig. 8. Breakdown of the rate of change of the correlation coefficient (un-marked solid line) between the $Sc = 0.25$ (ϕ_1) and 1.0 (ϕ_2) scalars into three terms according to Eq. 4: $-\langle \phi_1^2 \rangle \langle \phi_2^2 \rangle \chi_{12}$ (Δ), $\frac{1}{2} \langle \phi_1 \phi_2 \rangle \langle \phi_1^2 \rangle \chi_2$ (\circ), and $\frac{1}{2} \langle \phi_1 \phi_2 \rangle \langle \phi_2^2 \rangle \chi_1$ (\square), all normalized by $[\langle \phi_1^2 \rangle \langle \phi_2^2 \rangle]^{3/2}$.

Linear Eddy Simulations of Mixing in a Homogeneous Turbulent Flow

Patrick A. McMurtry and Todd C. Gansauge

Department of Mechanical Engineering, University of Utah, Salt Lake City, UT 84112

Alan R. Kerstein

Combustion Research Facility, Sandia National Laboratories, Livermore, CA 94550

Steven K. Krueger

Department of Meteorology, University of Utah, Salt Lake City, UT 84112

ABSTRACT

The linear eddy mixing model is used to predict the evolution of a decaying scalar field in statistically steady homogeneous turbulent flow over a wide range of Reynolds and Schmidt numbers. Model results at low Reynolds number and order unity Schmidt number are shown to be in good overall agreement with direct numerical simulations. Results at higher Schmidt and Reynolds numbers reproduce conventional scaling properties of the scalar statistics. Predictions of Schmidt number and Reynolds number sensitivity of the evolution of the scalar concentration probability density function are presented and interpreted.

1. INTRODUCTION

The decay of a scalar field in a homogeneous turbulent flow has emerged as a standard test problem for models of mixing in turbulent flow fields. Two broad classes of models are commonly considered. The classical treatment of turbulent flows is based on a decomposition of the dependent variables into mean and fluctuating components (Reynolds decomposition). Solutions for the mean values are sought, with scalar transport modeled by assuming gradient diffusion. Turbulent transport is handled by introducing an *effective diffusivity* that is determined by flow field conditions. Other approaches are based on solving for the probability density function (pdf) of the scalar field. If the one-point pdf is known, moments and other one-point statistical information on the scalar field can be obtained. However, evolution equations for the single point pdf require information on the joint statistics of the scalar and its dissipation rate. Several models have been developed in an attempt to describe the mixing process.^{1,2} These models do not fully capture the underlying physical mechanisms, and none of them satisfactorily predict the scalar variance decay in a homogeneous turbulent flow field.³

The problems associated with modeling molecular mixing and chemical reaction can, in part, be traced to the difficulty of realistically describing and resolving the physical processes of turbulent convection (stirring) and molecular diffusion at the smallest scales of the flow - two distinctly different physical processes. Turbulent stirring is effective at redistributing the scalar field at all length scales above the Kolmogorov scale, while molecular diffusion acts most effectively at the smallest scalar length scales of the flow. An accurate description of mixing thus requires a realistic treatment of the flow at the smallest hydrodynamic and scalar length scales. Most mixing models involve an ad-hoc treatment of the small-scale processes that include no distinction between turbulent stirring and molecular diffusion.

Investigations of mixing in homogeneous turbulence using direct numerical simulation have provided an extensive data set on the evolution of the scalar field statistics.^{3,4} These studies have involved the use of a pseudo-spectral scheme to simulate the evolution of the scalar field on a 64^3 grid with periodic boundary conditions. Owing to the extreme range of length scales in turbulent reacting flows, resolution of all relevant length scales is computationally demanding. Complete resolution of the dynamic range of length and time scales was achieved by restricting the simulations to low-Reynolds number ($Re_\lambda \approx 50$, or $Re_\tau \approx 100$) and order unity Schmidt number, Sc . Since all relevant length scales were resolved and highly accurate numerical methods were employed, the statistics computed can be confidently treated as predictions of the scalar field behavior under the condition of low Re , homogeneous flow in a periodic domain.

Eswaran and Pope⁴ investigated the evolution of the scalar field pdf and the effects of various initial scalar length scales on the scalar field statistics. Their initial scalar field consisted of blobs of scalar concentration of -1 and +1, with some smoothing to ensure that the scalar field was resolved numerically. The computational domain was a three-dimensional box, and the velocity field was numerically "forced" to maintain a statistically steady state. The initial velocity to scalar length scale ratio was shown to have a large effect on the initial rate of scalar variance decay, but the decay rate eventually became independent of the initial scalar length scale ratio. This observation differed from the experimental results of Warhaft and Lumley,⁵ which showed a lasting dependence of the scalar variance decay on the initial scalar length scale. It was suggested by Eswaran and Pope that the difference between the experiments and simulation was a physical consequence of the adoption of a statistically steady velocity field in the simulation, in contrast to a decaying turbulence field in the experiments. This interpretation is supported by a recent DNS study of a similar configuration involving a decaying turbulence field.⁶

McMurtry and Givi³ studied a configuration similar to Eswaran and Pope using direct simulation. The velocity field was forced at the lowest wave numbers, and the initial scalar field ϕ , consisted of two slabs, one with $\phi = 1$, the other with $\phi = -1$. In addition to pure mixing, they also investigated the evolution of the statistics of a reacting scalar. The primary objective of this work was to assess a number of mixing models^{1,2,7} and study the effect of reaction on the scalar statistics. None of the models investigated predicted the correct behavior for the scalar pdf. It was shown that the reacting scalar did not tend toward a Gaussian distribution.

For a passive scalar, the question of the asymptotic form of the scalar pdf in steady, homogeneous turbulence has been addressed in a number of recent modeling studies, as well as in DNS studies. Using DNS, Eswaran and Pope found that the shape of the scalar pdf as it evolved in time was not sensitive to the initial length scale ratio, and it evolved from the initial bimodal form towards a Gaussian. Valiño and Dopazo⁶ obtained a family of pdfs in good agreement with the DNS results using a model that, by construction, yielded a Gaussian pdf in the limit of vanishing variance. Mapping closure³ generates a family of pdf's that is also in good agreement with DNS,^{10,11} yet the scalar statistics display persisting non-Gaussian behavior as the scalar variance vanishes.^{11,12} Another model indicating non-Gaussian behavior has also been developed.¹³

Interpretation of these results is hindered by the narrow range of Re and Sc accessible by DNS and by the insensitivity of predicted families of pdfs to these parameters. (In the aforementioned models, these parameters influence the rate of evolution but not the family of pdfs that is obtained.) A complete mechanistic description of turbulent mixing, with regard to pdf shape evolution or any other measurable property, should reflect the sensitivity of the mixing process to all the governing parameters. On this basis, it is evident that the analytical and computational methods employed to date have not provided a complete characterization of the mixing process.

In this paper Kersteins^{14,15} linear eddy model is used to study the evolution of a scalar field in a steady, homogeneous turbulent flow field over a wide range of Reynolds and Schmidt numbers. One of the features that distinguishes the linear eddy model from other more commonly-used mixing models (e.g., eddy diffusivity, coalescence-dispersion models, mapping closure) is that all relevant length scales, even for relatively high- Re flows, are resolved. This is achieved by reducing the description of the scalar field to one spatial dimension. By resolving all length scales, the mechanisms of turbulent convection and molecular diffusion can be treated distinctly, even at the smallest diffusion scales. Parametric sensitivities can therefore be addressed on the basis of the underlying physical mechanisms.

In previous work, the linear eddy model has been applied to mixing in spatially developing flows and to a homogeneous, statistically steady mixing configuration. These applications served both to validate aspects of the model and to provide mechanistic interpretations of measured properties in a unifying framework.

A statistically steady configuration can be obtained by imposing a uniform scalar gradient on a homogeneous turbulent flow field, resulting in relaxation of the mean scalar variance to a constant nonzero value after a transient interval. Computations for this configuration reproduced key features of the scalar power spectrum, including dependences of Reynolds and Schmidt numbers, and scaling properties of higher-order scalar statistics, thus validating the model representation of micromixing kinematics.¹⁵

The applications to spatially developing flows collectively demonstrate that the diverse phenomenology observed in such flows may be viewed as various manifestations of a simple underlying kinematic picture. In such applications, configuration-specific aspects are reflected in the initial and boundary conditions of the computations and in the model analogs of quantities such as Re , Sc ,

and Da (Damköhler number), but the underlying kinematic picture is the same in all cases. On this basis, the model reproduces the following measured properties: (1) three distinct scaling regimes governing turbulent plume growth, and spatially resolved scalar fluctuation statistics within such plumes;^{4,16} (2) the spatially resolved cross-correlation of diffusive scalars in a three-stream mixing configuration;¹⁶ (3) Da dependences of reactant concentrations in a two-stream configuration;¹⁶ (4) spatially resolved scalar fluctuation statistics in free shear flows, and the dependence of local and overall shear-flow mixing on Re and Sc ;¹⁷⁻¹⁹ and (5) scalar fluctuation statistics reflecting differential molecular diffusion effects.¹⁶ The unification of this diverse phenomenology achieved by linear eddy modeling is unprecedented.

A category of mixing configurations to which the model has not previously been applied is spatially homogeneous, transient mixing. Spatial homogeneity facilitates the interpretation of results in terms of simple scaling ideas, while transient effects introduce some of the phenomenological richness of spatially developing flows. It is largely for these reasons that the DNS study of such a configuration by Eswaran and Pope⁴ has come to be regarded as a paradigm of the turbulent mixing problem and has motivated many subsequent numerical and analytical studies.

The objectives of the present study are twofold. First, linear eddy computations, based on a formulation that incorporates high- Re inertial-range scalings, are compared to the results of Eswaran and Pope in order to demonstrate the applicability of such a picture to their moderate- Re results. Second, computations are performed beyond the limited range of Re and Sc accessible by DNS in order to extrapolate the DNS results to other regimes of physical interest. Re and Sc dependences of computed quantities are found to be consistent with simple scalings based on dimensional considerations, where such considerations are applicable. Novel qualitative features of the evolution of the concentration probability density function (pdf) for high Sc are identified. Higher moments of the concentration field are found to relax to values that exhibit Sc - and Re -dependent deviations from Gaussian values. These features, which are shown to be intuitively reasonable, constitute experimentally testable predictions.

2. LINEAR EDDY MODEL

The development of the linear eddy model has been described in detail elsewhere,^{14,15} and is only briefly outlined here. This approach has a number of unique features that distinguish it from other more commonly used mixing models (e.g., eddy diffusivity and coalescence-dispersion models). In particular, the distinction between molecular diffusion and turbulent convection is retained at all scales of the flow in a computationally affordable simulation by reducing the description of the scalar field to one spatial dimension. Diffusion and convection have very different effects on scalar field evolution; accounting for these differences is crucial to accurately describe the species field, especially when chemical reactions are involved. This distinction has not been achieved by any previously proposed mixing model.

Velocity field statistics are inputs into the model, although no explicit velocity field appears. The required model parameters that describe the flow field include the turbulent diffusivity (D_T), the integral length scale (L),

and the Reynolds number, Re (which determines the Kolmogorov scale, η). Thus, the flow field properties are inputs to the linear eddy model, not predictions of the model. The formulation of the model presented here is reparameterized in terms of L , Re , and τ_L , where τ_L is the large eddy turnover time in the model and is defined as $\tau_L \equiv L^2/D_T$.

The first mechanism acting on the scalar field, molecular diffusion, is simply implemented by the numerical solution of the diffusion equation, $\frac{\partial \phi}{\partial t} = D_M \frac{\partial^2 \phi}{\partial x^2}$, over the linear domain.

The key feature of the model is the manner in which turbulent convection is treated. This is implemented by random rearrangements of the scalar field along a line. The frequency of these rearrangements is determined by requiring that the stochastic rearrangement events result in a turbulent diffusivity consistent with accepted scalings for high- Re turbulent flows. Each rearrangement event involves spatial redistribution of the species field within a randomly selected spatial domain. The size of the selected domain, representing the eddy size, is sampled from a distribution of eddy sizes that is obtained by applying Kolmogorov scaling laws. In this model, the spatial redistribution of a segment of length l represents the action of an eddy of size l . A rearrangement event is illustrated and described in Fig. 1.

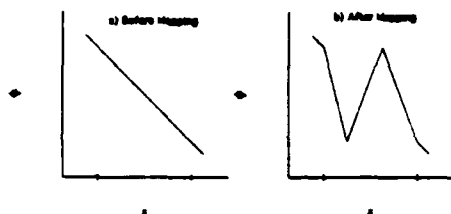


Figure 1: The scalar rearrangement (turbulent stirring) process is carried out by the use of the "triplet" map. The triplet map involves selecting a segment of the linear domain for rearrangement, making three compressed copies of the scalar field in that segment, replacing the original field by the three copies, and inverting the center copy. a) Initial scalar field, chosen in this illustration to be a linear function of spatial location. b) Scalar field after rearrangement.

The rearrangement process is governed by two parameters: λ , which is a rate parameter with dimensions $[L^{-1}t^{-1}]$, and $f(l)$, a pdf describing the segment length distribution. These parameters are determined by recognizing that the rearrangement events induce a random walk of a marker particle on the linear domain. Equating the diffusivity of the random process with scalings for the turbulent diffusivity provides the necessary relationships to determine λ and $f(l)$. For a high- Re turbulent flow described by a Kolmogorov cascade, the result of Kerstein¹⁵ can be expressed as

$$f(l) = \begin{cases} \frac{1}{3} \frac{l^{-5/3}}{\eta - l/3}, & \eta \leq l \leq L; \\ 0, & \text{otherwise} \end{cases} \quad (1)$$

$$\lambda = \frac{54}{5} \frac{1}{L\tau_L} \left(\frac{L}{\eta}\right)^{5/3} \quad (2)$$

where the model turnover time τ_L is related to a particular empirically defined turnover time τ_o by a constant factor, $\tau_L = c\tau_o$ (see §3.3). Equation (1) defines model Kolmogorov and integral scales η and L , respectively, that bound the range of segment lengths.

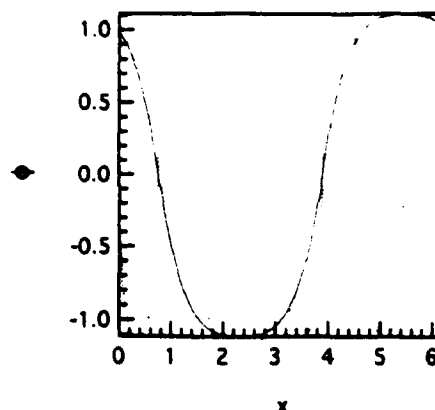


Figure 2: Typical realizations of the initial scalar field on the linear domain $[0, 2\pi]$. (— $k_s/k_0 = 1$, --- $k_s/k_0 = 4$).

Given an initial scalar distribution, the evolution of the scalar field is governed by the molecular diffusion process, punctuated by the random rearrangement events parameterized by $f(l)$ and λ . This formulation provides an approximate, yet physically sound description of turbulent mixing. Namely, molecular diffusion is accounted for explicitly by numerical solution of the diffusion equation, while turbulent stirring (convection) is modeled by the stochastic scalar rearrangement events. By limiting application to one dimension, all relevant length and time scales can be resolved.

The scalar information within the linear eddy domain provides a statistical description of the scalar field. The one-dimensional representation of the three-dimensional scalar field can be interpreted as a space curve aligned with the local scalar gradient.¹⁶ This interpretation is not unique, and it can be instructive in other cases to view the linear eddy domain as a particular spatial coordinate in the flow field.¹⁶

3. APPLICATION TO SCALAR MIXING IN A HOMOGENEOUS TURBULENT FLOW

3.1 Scalar Field Initialization

The linear eddy model is applied here to mixing of a scalar field, ϕ , in a homogeneous turbulent flow field. (The analogous physical configuration is a three dimensional flow field with periodic boundary conditions in a box of size B in each spatial dimension.) Within this domain the scalar field is initially distributed in blobs of concentration -1 and 1, with smooth transition layers at the interfaces. The transition layers are necessary to satisfy numerical resolution requirements in direct numerical simulations. The numerical specification of this scalar field for a three-dimensional DNS study is described by Eswaran and Pope.⁴ In particular, the initial length scale of the scalar field is generated in a manner such that the initial scalar-energy spectrum is equal to a specified function, $f_\phi(k)$, where $f_\phi(k)$ is a top-hat function of width k_0 , centered on a selected integer wavenumber k_s ; (k_0 is the smallest nonzero wavenumber resolved in the simulation). The ratio k_s/k_0 thus determines the integral length scale of the scalar field, ϕ . In the linear eddy model results presented here, the one-dimensional analog of this initialization is applied to a

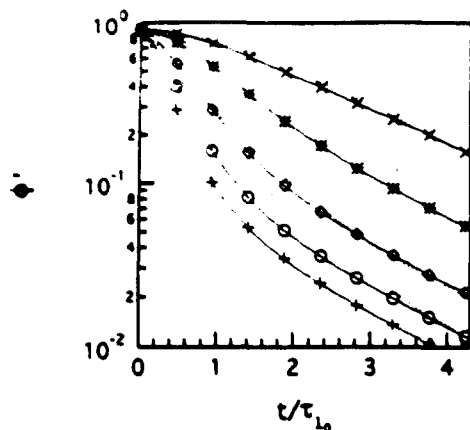


Figure 3: Time evolution of the scalar rms ϕ' for simulations at $Re_S = 90$ and $Sc_S = 0.7$, compared with DNS of Eswaran and Pope (--- Eswaran and Pope (1988), — linear eddy simulation). (\times , $k_s/k_0 = 1$), (\circ , $k_s/k_0 = 2$), (\bullet , $k_s/k_0 = 4$), (\circ , $k_s/k_0 = 6$), ($+$, $k_s/k_0 = 8$). Time is normalized by $\tau_{L_0} = l_0/u'$.

linear domain of $B = 2\pi$. For comparison with the results of Eswaran and Pope, various initial scalar fields with different scalar length scales were constructed by varying the ratio k_s/k_0 . All additional parameters of the initialization are as specified by Eswaran and Pope. The one-dimensional implementation of their initialization procedure generates non-random scalar fields, but they are soon randomized by the spatial rearrangement events (eddy action). Figure 2 illustrates two of the different initial one-dimensional scalar fields that were used in this modeling study.

3.2 Algorithm and Implementation

The total number of computational elements along the domain must be chosen to resolve the largest and smallest scales in the flow. The computational domain was selected to include one integral scale, i.e., $B = L$. From Kolmogorov scalings, the ratio of the largest to smallest length scales in the flow is approximately $L/\eta = Re^{3/4}$. For $Re = 10^4$, this ratio is 1000. By taking six computational elements to resolve the eddies at the Kolmogorov scale (i.e., $n_\eta = 6$), 6000 elements are needed to resolve the complete flow field for $Re = 10^4$. Scalar field resolution requirements can be more stringent. The Batchelor scale, l_B , which must be resolved, is smaller than the Kolmogorov scale in high- Sc flows. Scaling arguments yield $\eta/l_B \sim Sc^{1/2}$. A numerical sensitivity analysis indicated that approximately twice this number of grid points ($2Sc^{1/2} \times n_\eta$) is needed per Kolmogorov scale before multi-point statistics (e.g., scalar dissipation) become insensitive to resolution.

The molecular diffusion process is implemented by regularly advancing the one-dimensional diffusion equation using a space-centered finite difference technique. To implement each rearrangement event, a location is randomly selected within the domain. The segment size is also randomly chosen, but in such a way as to satisfy the probability distribution given by $f(l)$. One rearrangement takes place per time interval $\frac{1}{\Lambda_B}$. The process is repeated until a desired time has elapsed.

The complete model is implemented as a Monte Carlo simulation of many individual flow field realizations. The statistics are then computed by averaging the ensemble of realizations. For each of the simulations presented below,

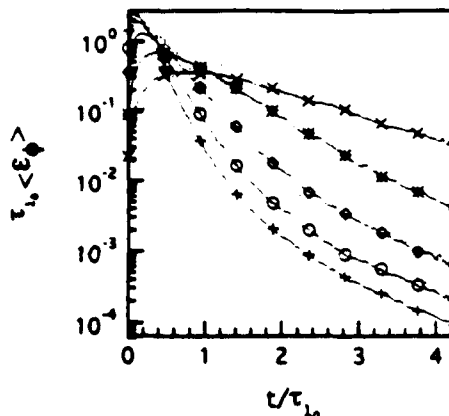


Figure 4: Evolution of mean scalar dissipation rate for same cases as Fig. 3.

the scalar field statistics were averaged over 1000 separate realizations (except the $Re_S = 10,000$ case in which 300 realizations were taken), yielding sufficient statistical precision for quantitative comparison to DNS results.

3.3 Model Parameters

The early applications of the linear eddy model involved no parameter adjustments. The model is built upon scaling laws for high Re flows, and order unity coefficients implicit in the scale relationships were set equal to one. However, some parameter adjustments must be done to achieve direct quantitative comparisons. In particular, the model analogs of Sc , Re , and L must be related to their physical (DNS) counterparts.

The large-scale Reynolds number in the DNS of Eswaran and Pope was calculated to be $Re_L \equiv u'l_0/\nu = 107$. The linear eddy analog of Re_L is $Re_S \equiv (L/\eta)^{4/3}$, where L is the integral scale of the model. Based on this definition, the model Reynolds number Re_S was selected to give approximately the same range of eddy sizes as in the DNS. This was achieved as follows: The DNS used here to compare model results contained a wave number ratio of $k_{max}/k_0 = 30$, where k_{max} and k_0 are the largest and smallest nonzero wavenumbers in the simulation. Applying an eddy size - wavenumber analogy²⁰ yields an equivalent length scale ratio, $L/\eta = \left(\frac{2\pi}{k_0}\right) / \left(\frac{2\pi}{k_{max}}\right) = k_{max}/k_0 = 30$, resulting in a model Reynolds number $Re_S \approx 90$. NOTE: The nominal Kolmogorov scale quoted by Eswaran and Pope is not necessarily the smallest resolvable eddy in their flow, but is the scale that satisfies $\eta = (\nu^3/\epsilon)^{1/4}$, which in their simulation corresponds to roughly 1/3 of the grid spacing. The Schmidt number of the model Sc_S is taken to be $Sc_S = 0.7$, equal to the physical Schmidt number.

The final consideration is the relationship between the integral scale defined in the model, L and the measured integral scale in the DNS, l_0 . The two are not equivalent since L is defined as the largest allowable eddy for a given flow, while l_0 represents a "typical" eddy size. As pointed out by Kerstein,¹⁶ the relationship between L and l_0 is not universal since the definition of l_0 for different flows is not always consistent. The value of L in the model is taken as the domain size, $L = 2\pi$. The data of Eswaran and Pope yield $l_0 = 1.01$, giving $L = 6.22l_0$. This is close to the value of $L = 5.6l_0$ found by Kerstein¹⁶ in simulating the

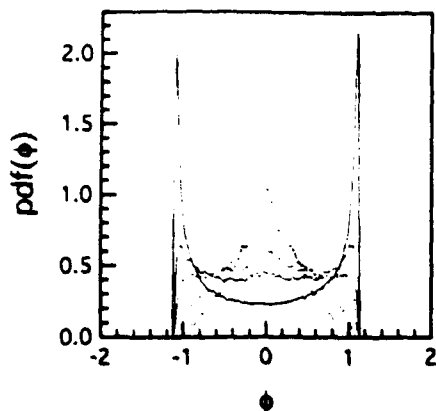


Figure 5a: Computed scalar pdf from linear eddy model for $Re_S = 90$ and $Sc_S = 0.7$, $k_s/k_0 = 1$. (solid line, $\phi'/\phi'_0 = 0.89$), (dots, $\phi'/\phi'_0 = 0.72$), (dash, $\phi'/\phi'_0 = 0.63$), (long dash, $\phi'/\phi'_0 = 0.47$), (dot-dash, $\phi'/\phi'_0 = 0.34$)

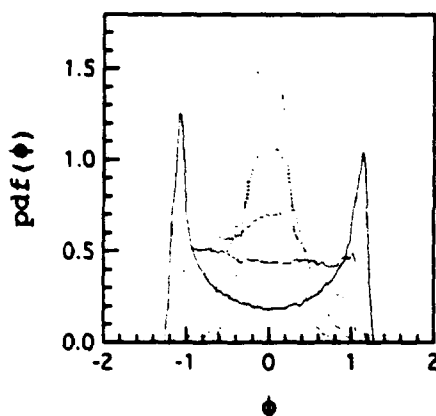


Figure 5b: Computed scalar pdf from DNS of Eswaran and Pope for $k_s/k_0 = 1$: (solid line, $\phi'/\phi'_0 = 0.99$), (dots, $\phi'/\phi'_0 = 0.73$), (short dash, $\phi'/\phi'_0 = 0.55$), (long dash, $\phi'/\phi'_0 = 0.40$), (dot-dash, $\phi'/\phi'_0 = 0.27$).

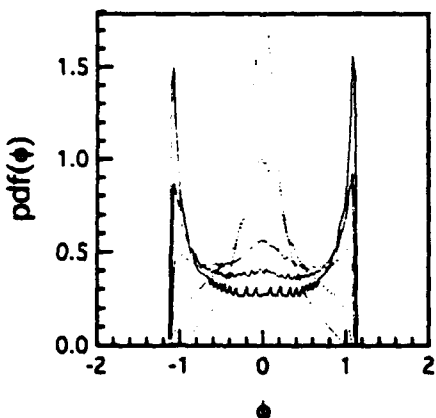


Figure 5c: Computed scalar pdf from Linear eddy model for same case as (a) except $k_s/k_0 = 4$. (solid line, $\phi'/\phi'_0 = 0.93$), (dots, $\phi'/\phi'_0 = 0.78$), (dash, $\phi'/\phi'_0 = 0.70$), (long dash, $\phi'/\phi'_0 = 0.63$), (dot-dash, $\phi'/\phi'_0 = 0.40$)

concentration field downstream of a line source in decaying homogeneous turbulence. With these model parameters determined, all computed statistical properties of the scalar field are predictions that can be compared directly with the simulation results.

To perform direct quantitative comparisons, the large eddy turnover time of the linear eddy model $\tau_L \equiv L^2/D_T$, must be related to the large eddy turnover time in the DNS, $\tau_a \equiv l_0/u'$. This was done by inferring the relationship between τ_a and D_T from the data reported in Eswaran and Pope. The chosen linear eddy model parameters imply a turbulent diffusivity based on the model definition $D_T/D_M = Re_S Sc_S = 63$. The given molecular diffusivity used in the DNS ($D_M = 0.035$) then implies a turbulent diffusivity $D_T = 2.205$. From the reported values of u' and l_0 by Eswaran and Pope, a relationship for the turbulent diffusivity of the DNS can be expressed as $D_T = 0.82u'l_0$. The time scale ratio between the linear eddy model and the DNS for the runs reported in the following is thus $\tau_L/\tau_a = L^2/(0.82l_0^2) \approx 47$. In all model/DNS comparison reported in §4.1 the time axis is scaled by τ_a . For the Schmidt and Reynolds number effects reported in §4.2, time is scaled by the linear eddy turnover time, τ_L .

In addition to the comparisons presented in §4 on the basis of the foregoing parameter assignments, additional comparisons have been performed in which different combinations of input parameters were varied by a factor of two or more. The quality of the agreement with simulation results was found to be only mildly sensitive to input parameter values, so the inferences drawn in §4 are not strongly dependent on the mechanistic basis of the parameter assignments.

With regard to direct quantitative comparisons, it is noted that the parameters defining the linear eddy model (see Eqs. 1 and 2) are developed based on Kolmogorov inertial range scalings, while the direct simulations that have been performed of scalar mixing to date display only a barely perceptible inertial range. As a result, the distribution of eddy sizes and frequencies in the linear eddy model and in the direct simulations cannot be made to match exactly. This can contribute to differences between model results and DNS data. Furthermore, it is expected that there will be some inherent limitations when describing the full three-dimensional turbulent mixing process in one dimension. However, previous results and the comparisons that follow demonstrate the ability of the linear eddy model to realistically represent the turbulent mixing process.

4. MODEL RESULTS

Validation of the linear eddy model in the configuration studied here was achieved by direct comparison to low- Re DNS. The model was then applied to study the mixing characteristics over a wide range of Reynolds and Schmidt numbers.

4.1 Comparison with Direct Numerical Simulation

The decay of the scalar rms ϕ' for various initial scalar length scales is compared to DNS results in Fig. 3. The overall agreement is good, with better agreement seen in the cases with the larger initial scalar length scale. Both linear eddy and DNS indicate that in the final state of scalar variance decay, the decay rate becomes independent of the initial scalar length scale. It was suggested by Eswaran and Pope, and shown numerically by Mell *et al.*,⁴ that this independence of the initial scalar length scale

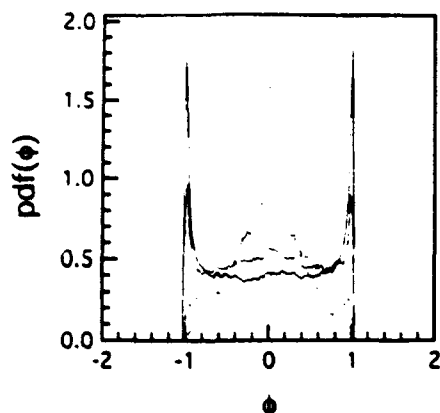


Figure 6a: Computed scalar pdf with initial scalar field given by double delta distribution (no transition region) for $Re_S = 90$ and $Sc_S = 0.7$. Linear eddy model results one period, (solid line, $\phi'/\phi_0 = 0.66$), (dots, $\phi'/\phi_0 = 0.58$), (small dash, $\phi'/\phi_0 = 0.43$), (long dash, $\phi'/\phi_0 = 0.32$)

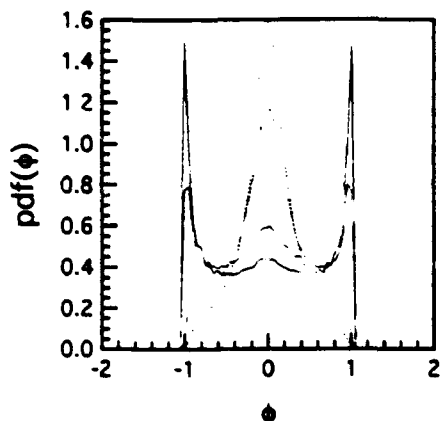


Figure 6b: Computed scalar pdf with initial scalar field given by double delta distribution (no transition region) for $Re_S = 90$ and $Sc_S = 0.7$. Linear eddy model results four periods, (solid line, $\phi'/\phi_0 = 0.68$), (dots, $\phi'/\phi_0 = 0.61$), (small dash, $\phi'/\phi_0 = 0.43$), (long dash, $\phi'/\phi_0 = 0.34$)

is a characteristic of scalar decay in a statistically steady turbulent flow. In decaying turbulence this is not observed.

Based on the interpretation of the linear eddy computational domain as a space curve aligned with the scalar gradient, the model analog of the mean scalar dissipation, defined by Eswaran and Pope as $\langle \epsilon_s \rangle \equiv D_M(\nabla \phi \cdot \nabla \phi)$, is $D_M((\partial \phi / \partial z)^2)$. This quantity is computed by first-differencing the discretized one-dimensional scalar field. The evolution of the mean scalar dissipation is shown in Fig. 4. The agreement with the DNS data is again good. The largest discrepancy is seen to occur at early times, where the dissipation computed by the linear eddy model consistently grows at a faster rate than in the DNS. At later times the dissipation decays at a rate which is approximately independent of the initial scalar length scale.

The evolution of the concentration pdf for $k_s/k_0 = 1$ is shown in Fig. 5a. At $t = 0$ the initial field is approximately represented by a double delta distribution, indicating the initially unmixed scalar field. As time proceeds, turbulent

mixing and molecular diffusion yield a mixed fluid concentration peaking at $\phi = 0$. Figure 5b shows the development of the pdf as predicted by the DNS of Eswaran and Pope for the same value of k_s/k_0 . The family of pdfs evolving from the double delta function distribution to the final peak at the mixed fluid concentration is well represented by the linear eddy model. In particular, the transition from a bimodal to unimodal form is found to involve an intermediate form (at $\phi'/\phi_0 \approx 0.6$) with a broad plateau, as in the DNS results.

The evolution of the concentration pdf for $k_s/k_0 = 4$ is shown in Fig. 5c. For this initialization the pdf displays some qualitative differences during its evolution from the case of $k_s/k_0 = 1$. Namely, there is an indication of trimodality during intermediate stages of the evolution. Some differences in the pdf evolution for different values of k_s/k_0 are also apparent in the higher order moments (Figs. 7 and 8), as will be discussed shortly. This behavior was not observed by Eswaran and Pope, who found little dependence of the pdf evolution on k_s/k_0 .

To further investigate the dependence of the pdf on the scalar field initialization, two additional simulations were run with an initial scalar field consisting of discrete regions of $+1$ and -1 , with a sharp transition between these values. (The initial scalar field pdf in this case is a pure double delta distribution.) Results of this are shown in Fig. 6 for initial scalar fields consisting of one period and four periods of the $-1, +1$ regions, respectively (corresponding to the scalar length scales of the cases $k_s/k_0 = 1$ and 4). Under this initialization the two families of pdfs that are obtained are essentially the same.

The linear-eddy results indicate the joint influence of two scalar length scales: the scalar integral scale governed by k_s , and the transition layer width governed by a cutoff wavenumber k_c in the initialization algorithm. As in the DNS study, the ratio k_c/k_s has been set equal to 2, except for the double-delta case (Fig. 6), which corresponds, in effect, to infinite k_c . The linear-eddy results indicate that the occurrence of a trimodal intermediate stage of pdf evolution exhibits a dependence on the magnitude of k_s , such that large k_s favor trimodality.

Trimodal pdf's indicate intermittency in the scalar field in the following sense. Sharp scalar interfaces are subject to rapid stirring by small eddies acting on relatively short time scales. This results in completion of local mixing near interfaces (and hence, development of the central peak of the pdf) before large-scale mixing depletes the initial unmixed peaks. It is evident that the degree of sensitivity indicated by the linear-eddy results is not supported by DNS. Nevertheless, the mechanistic plausibility of the trend suggests that a wider-ranging DNS parameter study to check the qualitative prediction would be worthwhile.

Related considerations bearing on the Sc sensitivity of pdf evolution are discussed in §4.

To analyze the structure of the pdf in more detail, it is instructive to examine some of the higher-order moments of the concentration field. In Figs. 7 and 8 the standardized fourth and sixth moments are presented. Two significant features can be pointed out. First, the asymptotic values of these moments relax to a constant value that is independent of the initial scalar length scale. However, the manner in which the curves approach the final value is seen to depend on the initial state of the scalar field. At early times, the simulations initialized with the smaller scalar length scales

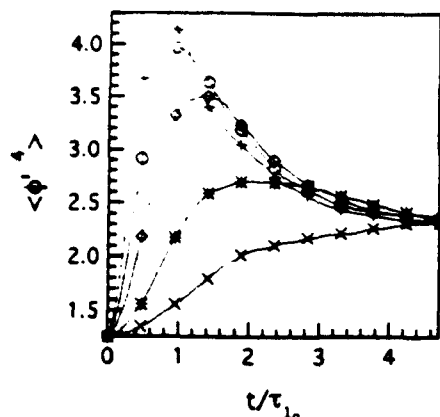


Figure 7: Evolution of kurtosis (normalized 4th moment) from linear eddy model for $Re_S = 90$, $Sc_S = 0.7$. (\times , $k_s/k_0 = 1$), (\circ , $k_s/k_0 = 2$), (\circ , $k_s/k_0 = 4$), (\circ , $k_s/k_0 = 6$), ($+$, $k_s/k_0 = 8$)

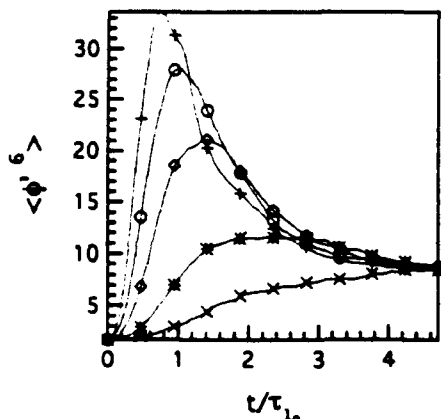


Figure 8: Evolution of superskewness (normalized 6th moment) from linear eddy model for same cases as Fig. 7.

show a rapid increase in their higher order moments before relaxing to their final state. In the case presented here, the final values of the fourth and sixth moment are somewhat less than the corresponding Gaussian values of 3 and 15. It was indicated both by Eswaran and Pope⁴ and McMurtry and Givi³ in their DNS studies that the pdf apparently tended towards Gaussian in the limit as the scalar variance became small. However, more recent analytical work¹² and simulations¹³ suggest that non-Gaussian behavior may persist throughout the mixing process. Further discussion of this matter is deferred to §4.2a.

The dependence of ϵ_ϕ on ϕ can be examined by computing the correlation function $\rho \equiv (\phi^2 \epsilon_\phi) / ((\phi^2)(\epsilon_\phi)) - 1$. Comparison of this quantity with the DNS results is shown in Fig. 9. Quantitative and qualitative differences are apparent. For the conditions considered ($Sc_S = 0.7$, $Re_S = 90$), the model predicts that ρ converges to a nonzero value, while DNS indicates eventual convergence to a different value. The linear eddy result indicates a lasting dependence of ϵ_ϕ on ϕ , consistent with the persistence of non-Gaussian behavior¹¹ evident in Figs. 7 and 8. This quantity also displays a Sc_S dependence as shown in §4.2a.

As mentioned in §3.3, the quantitative discrepancy between the linear eddy results and the DNS results shown

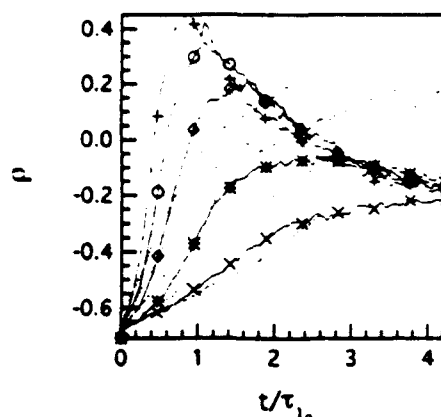


Figure 9: Evolution of the scalar variance dissipation correlation function for same cases as Fig. 7. DNS results indicated by dashed lines.

in Figs. 7-9 may reflect the use of high- Re scalings in a moderate- Re application. High- Re scaling may result in a larger contribution of the small scales to the mixing process than occurs in a low- Re DNS. This is consistent with the differences observed in the decay of the scalar rms at smaller initial scalar length scales and in the initial development of the scalar dissipation for all cases. On the other hand, the differences between the linear eddy results and the DNS may reflect a fundamental limitation of the linear eddy model with respect to its representation of mixing kinematics. This issue can be resolved on the basis of DNS and/or laboratory experiments at higher Re .

In general, the linear eddy model is found to accurately represent important features of the turbulent mixing process. The agreement is particularly remarkable considering that the scaling laws upon which the model is built are based on high- Re turbulent flows, and the DNS results have been obtained for relatively low- Re flows.

4.2 Reynolds and Schmidt Number Sensitivities

Owing to the severe computational requirements of DNS, previous DNS of turbulent mixing has necessarily been limited in the range of Re and Sc that could be treated. The effects of Re and Sc on the overall mixing process have not as yet been quantified. However, with the computationally economical one-dimensional formulation of the linear eddy model, a much wider range of length scales can be treated, allowing parametric Re and Sc studies. In the simulation results that follow, results are parameterized by Re_S and Sc_S , whose relation to the physical quantities Re and Sc is discussed in §3. The initial scalar fields for all simulations that follow were initialized with a value of $k_s/k_0 = 1$ unless otherwise noted.

4.2a Schmidt Number Dependence

The linear eddy model was used to perform simulations spanning a range of $Sc_S = 0.1 - 1000$ for $Re_S = 90$. The low- Re case was selected for Sc_S comparisons as resolution requirements become severe when resolving the Batchelor scale for high Schmidt number flows even in one spatial dimension. Sc_S sensitivities are shown in Figs. 10-13.

Figure 10 indicates that the computed early growth rate of scalar dissipation increases with increasing Sc_S . This is reasonable since the effects of molecular diffusion decrease

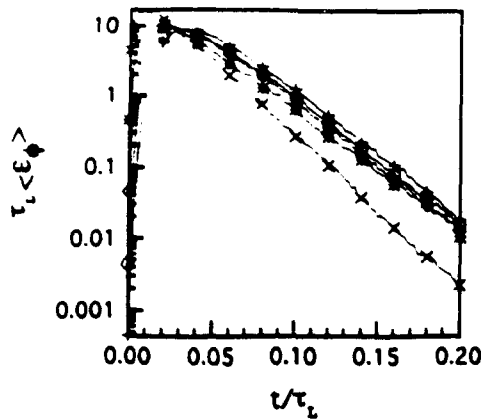


Figure 10: Evolution of the scalar dissipation for $Re_S = 90$, $k_0/k_0 = 1$ at different values of Sc_S as computed from linear eddy model. (\times , $Sc_S = 0.1$), (\circ , $Sc_S = 1.0$), (\bullet , $Sc_S = 10$), (\diamond , $Sc_S = 100$), ($+$, $Sc_S = 1000$).

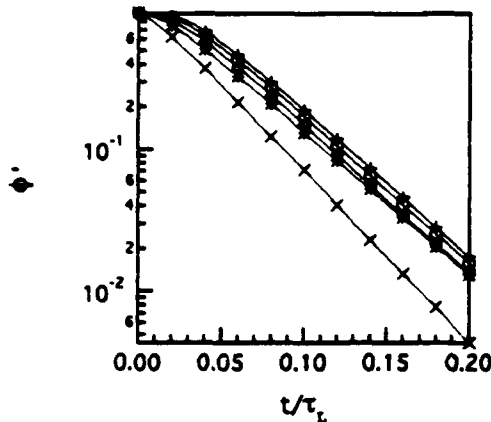


Figure 11: Evolution of the scalar field rms for same cases as Fig. 10.

as Sc_S is increased, resulting in less molecular smoothing of scalar gradients. Subsequently, the magnitude of the dissipation, when scaled by the large eddy turnover time, τ_L , is independent of Sc for $Sc_S \geq 1$. This is consistent with $\epsilon_0 \sim \phi^2/\tau_L$, where ϕ is an order unity quantity.

The time at which the scalar dissipation peaks is also consistent with conventional scaling analysis. The maximum dissipation will occur when the scalar length scale is reduced to the Batchelor scale, l_B . For $Sc > 1$, this time, \hat{t} can be estimated in two steps, $\hat{t} = t_1 + t_2$, where t_1 is the time to reach the Kolmogorov scale, and t_2 is the additional time to reach the Batchelor scale. To estimate t_1 , consider the size evolution $l(t)$ of a scalar blob initially of size $l(0) = L$. Based on dimensional considerations applicable to the inertial-range cascade, that evolution is governed by $dl/dt = -l/t_l$, where the characteristic eddy time t_l scales according to $t_l \sim (l/L)^{2/3}\tau_L$. Integrating from the integral scale L to η gives $t_1/\tau_L = [1 - (\eta/L)^{3/2}] = 1 - Re^{-1/2}$. (Numerical coefficients are suppressed here, but are restored shortly.) This demonstrates the Re sensitivity (vanishing at high Re) of the time (in units of τ_L) for a scalar blob to traverse the inertial range. Further length scale reduction to the Batchelor scale l_B occurs at an exponential rate.

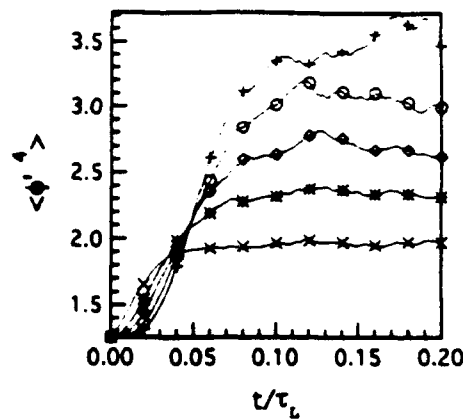


Figure 12: Evolution of kurtosis of the scalar field for same cases as Fig. 10.

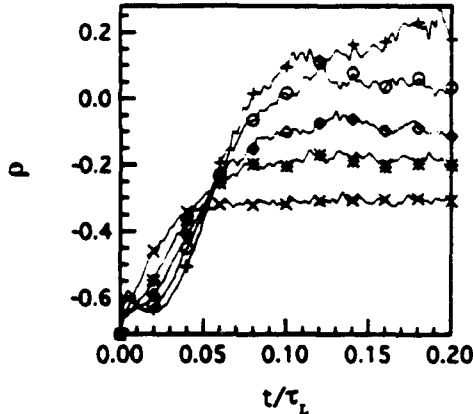


Figure 13: Evolution of the scalar variance-dissipation correlation function for same cases as Fig. 9.

For $Sc \geq 1$, $l_B = \eta \exp[-t_2/\tau_K]$, where τ_K is the Kolmogorov time and $\eta/l_B = A Sc^{1/2}$, where A is a coefficient. Since $\tau_K = B Re^{-1/2}\tau_L$, where B is another coefficient, t_2 gives $t_2/\tau_L = B[\ln A + (1/2)\ln Sc]Re^{-1/2}$. Combining t_1 and t_2 , \hat{t} can be expressed in the general form

$$\hat{t}/\tau_L = c_1 + Re^{-1/2}(c_2 + c_3 \ln Sc), \quad (3)$$

where the coefficients c_1 and c_3 are positive, but c_2 can be of either sign. This relationship can be interpreted in terms of the model quantities Re_S and Sc_S . The $\ln Sc_S$ dependence on the time of peak dissipation is borne out in Fig. 10.

The decay of the scalar rms (Fig. 11) shows little Sc_S dependence for $Sc_S > 1$. The behavior of the scalar variance is consistent with the scalings presented above and the behavior of the scalar dissipation shown in Fig. 10.

The higher-order moments display an interesting Sc_S dependence (Fig. 12) which is also reflected in the scalar variance-scalar dissipation correlation function (Fig. 13). In general, the low- Sc simulations give values of the kurtosis and superskewness well below Gaussian values. As Sc_S is increased, the values of both the kurtosis and superskewness increases. This trend is apparent over the Sc_S range studied. For Sc_S of order one, the moments are below their Gaussian values, while for high Sc_S , the final values of the higher order moments are near the Gaussian values.

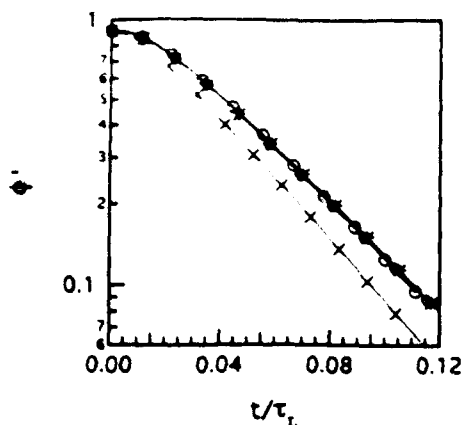


Figure 14: Evolution of the scalar rms ϕ' for $Sc_S = 0.7$ at different values of Re_S . (\times , $Re_S = 10$), (\circ , $Re_S = 100$), (\circ , $Re_S = 1000$), ($+$, $Re_S = 10000$).

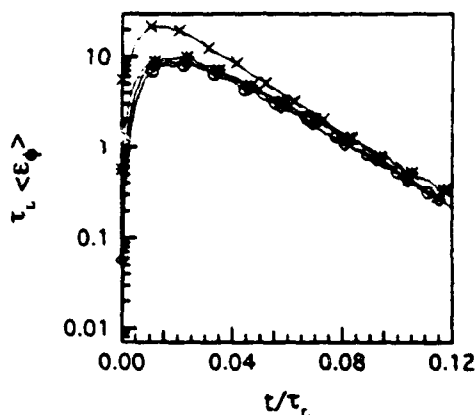


Figure 15: Evolution of the scalar dissipation for $Sc_S = 0.7$, $k_s/k_0 = 1$ for same cases as Fig. 14.

The occurrence of non-Gaussian pdf's can be understood as follows. If fine-scale mixing is fast relative to large-scale stirring, small regions will become well mixed while large-scale variations of ϕ are still present. Each small, mixed region converges to a Gaussian distribution whose mean corresponds to the local mean value of ϕ , which generally differs from the global mean value $\phi = 0$. Therefore the core of the spatially averaged pdf consists of a superposition of Gaussians with different mean values, yielding a distribution that may be longer-tailed or shorter-tailed than Gaussian. Since this mechanism is predicated on the relative efficacy of the fine-scale mixing, it implies that the linear-eddy results reflect a larger contribution of the small scales to the mixing process than occurs in the DNS. In this regard, the results for the higher moments are consistent with the results for pdf evolution, discussed in Sec. 4.1.

4.2b Reynolds Number Effects

The decay rate of the scalar variance is shown in Fig. 14 for $Re_S = 10 - 10,000$ and $Sc_S = 0.7$. With time nondimensionalized for each case by its large eddy turnover time, τ_L , all curves at or above $Re_S = 100$ collapse. This indicates that, in terms of the model parameters, high Reynolds number similarity is obtained at $Re_S = 100$. For the case of

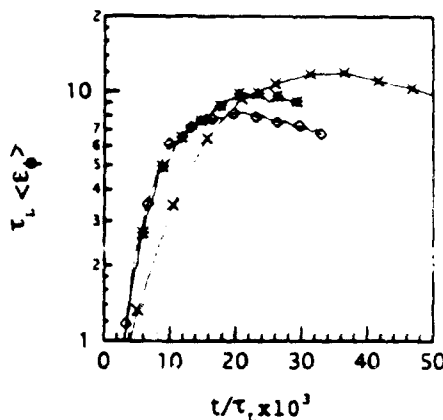


Figure 16: Initial development of the scalar dissipation for $Sc_S = 10$, $k_s/k_0 = 1$ at different values of Re_S (\times , $Re_S = 10$), (\circ , $Re_S = 100$), (\circ , $Re_S = 1000$), ($+$, $Re_S = 10000$).

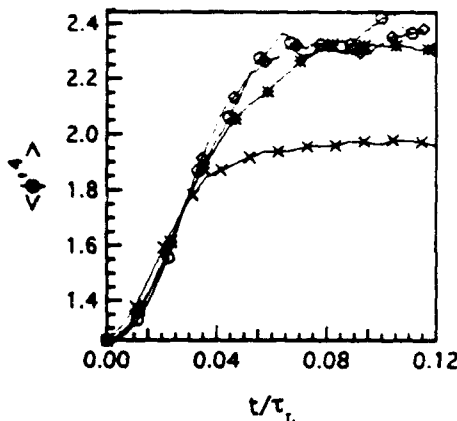


Figure 17: Evolution of kurtosis of scalar field for same cases as Fig. 14.

$Sc_S = 0.7$ considered here, the scalar dissipation decreases rapidly at the Kolmogorov scale. The time to reach this scale, as discussed in §4.2a, is $t_1 = \tau_L (1 - Re^{-1/2})$. This is consistent with the small Re_S effect, which vanishes at high Re_S , seen in the model results.

The effects of Re_S on the scalar dissipation evolution are shown in Fig. 15. The maximum value of the scalar dissipation is independent of Re_S when scaled with τ_L . This agrees with the scaling analysis outlined in §4.2a. Furthermore, the time at which the scalar dissipation peaks can also be interpreted by the scaling analysis summarized by Eq. 3. First, Eq. 3 indicates there will be a unique value of Sc_S at which the Re_S dependence will vanish. The lack of Re_S sensitivity in Fig. 15 indicates that $Sc_S = 0.7$ is near this value. Second, as Sc_S is increased above this value, the Re_S sensitivity should increase. Computed results for $Sc_S = 10$ exhibit this trend (Fig. 16).

The evolution of the scalar pdf as described by the higher-order moments does not show a strong Re dependence beyond $Re_S = 100$ (Fig. 17). This and the foregoing results indicate that Re effects may be sufficiently well characterized by studying a limited range of Re . However, a complete understanding of Sc effects may require wider-ranging study and improved analytical methods.

5. CONCLUSIONS

Various aspects of the time evolution of a passive scalar field in steady homogeneous turbulence have been addressed here using the linear-eddy modeling approach. The model formulation in one spatial dimension incorporates the mechanisms needed to represent the dependences of mixing properties on Re and Sc .

Detailed comparisons with low- Re DNS for Sc of order unity indicate that the model captures the dependence of scalar variance and scalar dissipation evolution on the initial scalar length scale. Principal features of scalar pdf evolution are reproduced. Quantitative discrepancies with respect to structural properties of the mixing field may reflect inherent limitations of the model, or may reflect the fact that low- Re DNS does not fully conform to the inertial-range scaling laws built into the model. DNS or laboratory experiments at higher Re could resolve this ambiguity.

Parametric sensitivities were investigated based on Sc and Re variations over several orders of magnitude. The parametric study demonstrates that the computed transient evolution of the scalar field obeys the appropriate high- Re scaling properties and exhibits finite- Re departures from scaling that are consistent with the classical picture of mixing kinematics in the inertial and viscous subranges. These observations complement a previous study¹⁵ which demonstrated conformance of the model to that picture in the context of steady-state homogeneous mixing. Collectively, these results highlight the common origin of the steady-state spectral scalings and the scalings governing a transient mixing field in steady homogeneous turbulence. Moreover, these results demonstrate that a comprehensive picture of turbulent mixing kinematics can be embodied in a mathematical formulation of reduced spatial dimensionality provided that the underlying physical processes and their associated length and time scales are explicitly represented.

The parametric study provided new insights into the mechanisms underlying the evolution of the scalar pdf. Qualitative as well as quantitative features of this evolution were found to be sensitive to Sc and to the initial width of the scalar interfaces, consistent with a simple mechanistic picture. This picture indicates that the shape of the pdf in the final stages of mixing depends on mechanistic details not represented in other models that have been applied to the question of pdf evolution. Improved analytical methods are needed in order to quantify the impact of these mechanisms, and to determine why models lacking the mechanisms governing Sc sensitivity agree well with DNS results for a particular value of Sc . Tests of the predicted sensitivities, by means of high- Sc laboratory experiments or DNS, would serve both to check the predictions and to stimulate further analytical study.

ACKNOWLEDGEMENTS

This work was supported in part by the Office of Naval Research under grant N0001491J1175; the Division of Engineering and Geosciences, Office of Basic Energy Sciences, U.S. Department of Energy; and the Advanced Combustion Engineering Research Center. Funds for the research center are received from the National Science Foundation, the state of Utah, 26 industrial participants, and the U.S. Department of Energy.

REFERENCES

1. R.L. Curl, "Dispersed Phase Mixing: I Theory and Effects in Simple Reactors," *AIChE J.* 9, pp. 175-181 (1963).
2. D. Dopazo and E.E. O'Brien, "Statistical Treatment of Nonisothermal Chemical Reactions in Turbulence," *Combust. Sci. Tech.* 13, pp. 99-122 (1978).
3. P.A. McMurtry and P. Givi, "Direct Numerical Simulations of Mixing and Reaction in a Nonpremixed Homogeneous Turbulent Flow," *Comb. and Flame* 77, pp. 171-185 (1989).
4. V. Eswaran and S.B. Pope, "Direct Numerical Simulations of the Turbulent Mixing of a Passive Scalar," *Phys. Fluids* 31 (3), pp. 506-520 (1988).
5. Z. Warhaft, "The Interference of Thermal Fields From Line Sources in Grid Turbulence," *J. Fluid Mech.* 144, pp. 363-387 (1984).
6. W.E. Mell, G. Kosaly, and J.J. Riley, "The Length Scale Dependence of Scalar Mixing," *Phys. Fluids A* 3 (10), pp. 2474-2476 (1991).
7. J. Janicka, W. Kolbe, and W. Kollmann, "Closure of the Transport Equation for the Probability Density Function of Turbulent Scalar Fields," *J. Non-Equilib. Thermodyn.* 4, pp. 47-66 (1979).
8. L. Valiño and C. Dopazo, "A Bimodal Langevin Model for Turbulent Mixing," *Phys. Fluids A* 3, pp. 3034-3037 (1991).
9. H. Chen, S. Chen, and R.H. Kraichnan, "Probability Distribution of a Stochastically Advected Scalar Field," *Phys. Rev. Lett.* 63, pp. 2657-2660 (1989).
10. S. B. Pope, "Mapping Closure for Turbulent Mixing and Reaction," in *Studies in Turbulence: In Recognition of Contributions by John Lumley*, edited by T. B. Gatski, S. Sarkar, and C. G. Speziale, Springer-Verlag, Berlin, pp. 255-270 (1991).
11. E. E. O'Brien and T.-L. Jiang, "The Conditional Dissipation Rate of an Initially Binary Scalar in Homogeneous Turbulence," *Phys. Fluids A* 3, pp. 3121-3123 (1991).
12. F. Gao, "Mapping Closure and Non-Gaussianity of the Scalar Probability Density Functions in Isotropic Turbulence," *Phys. Fluids A* 3 (10), pp. 2438-2444 (1991).
13. F. Gao, Y. Kimura, and R.H. Kraichnan, "Non-Gaussianity of a Scalar Probability Density Function (PDF) Induced by Random Advection," *Bull. Amer. Phys. Soc.* 36, 10, p. 2662 (1991).
14. A.R. Kerstein, "Linear Eddy Model of Turbulent Scalar Transport and Mixing," *Combust. Sci. and Tech.* 60, pp. 391-421 (1988).
15. A.R. Kerstein, "Linear Eddy Modeling of Turbulent Transport. Part 6. Microstructure of Diffusive Scalar Mixing Fields," *J. Fluid Mech.* 231, pp. 361-394 (1991).
16. A.R. Kerstein, "Linear Eddy Modeling of Turbulent Transport. Part 7. Finite-Rate Chemistry and Multi-Stream Mixing," *J. Fluid Mech.*, in press (1992).
17. A.R. Kerstein, "Linear Eddy Modeling of Turbulent Transport II: Application to Shear Layer Mixing," *Comb. and Flame* 75, pp. 397-413 (1989).
18. A.R. Kerstein, "Linear Eddy Modeling of Turbulent Transport. Part 3. Mixing and Differential Molecular Diffusion in Jets," *J. Fluid Mech.* 216, pp. 411-435 (1990).
19. J.E. Broadwell and M.G. Mungal, "Large-Scale Structure and Molecular Mixing," *Phys. Fluids A* 3, pp. 1193-1206 (1991).
20. H. Tenenbaum and J.L. Lumley, "A First Course in Turbulence," The MIT Press, Cambridge, Mass. pp. 258-259 (1974).

DIFFUSIVE MIXING IN TURBULENT JETS AS REVEALED BY A PH INDICATOR

by

A.F. Corriveau and W.D. Baines
Department of Mechanical Engineering
University of Toronto
Toronto, ON, CANADA, M5S 1A4

This paper describes an experimental study which is currently being conducted to investigate the mixing in turbulent jets and plumes. The objective is the description of the structure of turbulent flows from a coherent picture of the entrainment and mixing process. An essential component of this research is the application of pH sensitive dyes to view the three-dimensional structure of the flow by identifying all fluid exceeding a predetermined concentration of source fluid. This is best described as a threshold technique on the concentration: the specified concentration is located on the surface of the coloured fluid. The technique facilitates the examination of the interrelations of large and small turbulent structures through the observation of the instantaneous threshold contaminant distribution. Photographs have indicated that the source fluid of the jet is contained in thin sheets whose thickness is of the order of the Batchelor microscale; the distribution of which is fitted by a Gamma distribution. The spacing between the sheets are of the order of the Kolmogorov microscale. Observations of the colour distribution using a permanent inert dye in a jet showed that the Gaussian distribution cannot be a valid description of the concentration at the edges of the jet. These show that all of the contaminant is contained within an envelope of width kb , where b is the characteristic velocity radius and k has a value of 1.86. This has led to a simple equation based on the conservation of mass for predicting the time averaged mean front location within the jet. This equation compares well to the experimental results. The normalized r.m.s. values of the concentration locations are also presented.

1 Introduction

Central to many problems encountered in engineering practice is the phenomenon of turbulent mixing and this is often produced by jets and plumes. The structure of these flows determine the rate of entrainment from the surroundings and the rate of stretching and deformation of the fluid particles. Consequently this structure regulates the mechanism of mixing and thus controls the rate of chemical reactions such as flammability or instantaneous concentration of contaminants.

In turbulent flow, it is the small eddies convection which intensify the concentration gradients over short distances. The result is a mixing rate orders of magnitude larger than that in laminar flow. The concentration at a point is a function of the Reynolds and Schmidt numbers but the precise relationship cannot be ascertained by analysis. The flow is always unsteady so statistical properties must be used to describe the concentration such as the time mean concentration. This time mean is the value quoted for toxic limits and used in chemical processes. However, the fluctuation of concentration, although usually of an order smaller in magnitude, produces instantaneous large values and these should be the concentrations considered. For example, the presence of a concentrated, highly toxic pollutant can be damaging to health. The time mean value at any point would be small if these parcels were widely spaced and so passed over a measuring point rarely. In this case it is the maximum dosage, not the time averaged dosage, that is of importance.

For a complete description of the fluctuations of concentration the probability distribution must be determined. From the probability distribution the second moment gives the r.m.s. value and the third and fourth moments define the skewness and flatness factor. In most cases the measurements fit a Gaussian distribution so the mean and r.m.s. values are the only measurements of practical interest.

The next section is a description of a simple, versatile technique for investigating the diffusive mixing in turbulent flows of water. In section 3, some observations made using this technique with forced plumes are presented to illustrate the potential for identifying turbulent structures and examining the interactions of these structures. Section 4 outlines the derivation of a conservation equation for the time averaged mean front location. A comparison of this calculated mean is made with the experimental results obtained using the pH sensitive dyes. Finally an estimate for the concentration r.m.s value is made.

2 pH Sensitive Dye Technique

The introduction of a pH sensitive dye makes possible the identification of all fluid with a concentration above a preset value. The technique involves observing the progress of the acid-base titration occurring within the experimental tank. The tank fluid is made acidic with the addition of an acid, and a base is added to the source fluid. During the experiment, the entrained environment fluid mixes with the alkaline source fluid. Mixing and diffusive mixing are used interchangeably. Both refer to the diffusion of a pollutant across an intermaterial surface resulting in the fluid being molecularly mixed. If the source fluid neutralized the entrained fluid, the pH indicator in the entrained fluid becomes the base colour. When the source fluid is finally neutralized by the entrained acidic fluid, the pH indicator in the source fluid changes to the acidic colour. The specified concentration is located on the surface of the

fluid with the base colour. The dilution of the source fluid at which the colour changes, is controlled by the relative strengths of the acid and base. Hence, the photographs of the flow field show clearly all fluid for which the concentration is above the predetermined value.

The main assumption, in the conceptualization of this technique, is that the neutralization of the base (the source fluid) by the acid (the entrained fluid) will produce a distinct and abrupt change in colour at a specific concentration. This can only be achieved if (1) the neutralization curves for the acid and base have a sharp

transition through the equivalence point, (2) the reaction is diffusion limited, and (3) the indicator responds within the transition zone. The first requirement is satisfied by using a strong acid with a strong base (Laitinen 1960). Hydrochloric Acid and Sodium Hydroxide were chosen which satisfies the second criteria (Cussler 1984). Phenol-Red was chosen as the indicator because it responded within the sharp pH transition.

The dilution for an experiment was defined as the number of unit volumes of the environment, one unit from the source would neutralize. The concentration at which the colour change occurred can be calculated by,

$$c = \frac{c_0}{DIL + 1} \quad (1)$$

where c_0 is the initial concentration and DIL is the dilution set for the experiment.

3 Turbulent Structures

The two photographs of Figures 1 and 2, which are salt water plumes, are typical examples of the structures which are revealed if the dilution for colour change is 5 and 12.5 respectively. There are several points of interest in the first photograph. There appears to be very little source fluid at the core of the flow near the start: in other words it appears hollow. This was observed for all jets which emerge laminar from the orifice. Perhaps more important is



Figure 1. Apparent structures have been identified: (a) hollow core, (b) "bubble" structures, (c) shadowgraph effect, (d) spherical vortex. Scale: 3.7:1.0, $Re = 235$ and dilution = 5.

the absence of the lumps of fluid which appear as the big eddies in Figure 1. All of the source fluid has been stretched into sheets. These three-dimensional sheets, on close inspection, are interconnected and continuous as they stretch and roll up with engulfed environmental fluid. Within the flow, there are three additional features. Bubble-like structures are visible in several locations. These structures look similar to the photographs of a starting vortex (Auerback 1987). Further investigation with a high speed movie camera is planned to facilitate frame by frame measurement of individual structures for correct classification. The second structure is the shadowgraph effect which is evident throughout the upper half of the photograph. This indicates that the concentration of source fluid in these areas is below the preset value and the remaining salt is diffusing out of the sheets. The third structure visible in the photograph appears to be a spherical vortex above the mid-plane and to the right. Again further investigation capable of following an individual structure is planned to ascertain if these are truly spherical vortices or merely fluid elements in solid body rotation.

The second picture clearly shows that all the source fluid has been stretched into sheets. Bubble structures are evident here too. Note the open ended vortex midway in the photograph. One concludes that the vorticity extends into the environmental fluid or the other side of the ring is diluted. This structure is often observed in the plumes.

The detail in Figure 2 provides the opportunity to obtain characteristic length scales of the structures found in the flow. The diameter of the bubble-like structures varied between 5.6mm to 2.1mm. The interpretation of the lines in the photograph are sheets of original fluid with concentrations above the threshold value, perpendicular to the camera. Typical line spacing averaged 0.13mm. The line or sheet spacing should be related to the

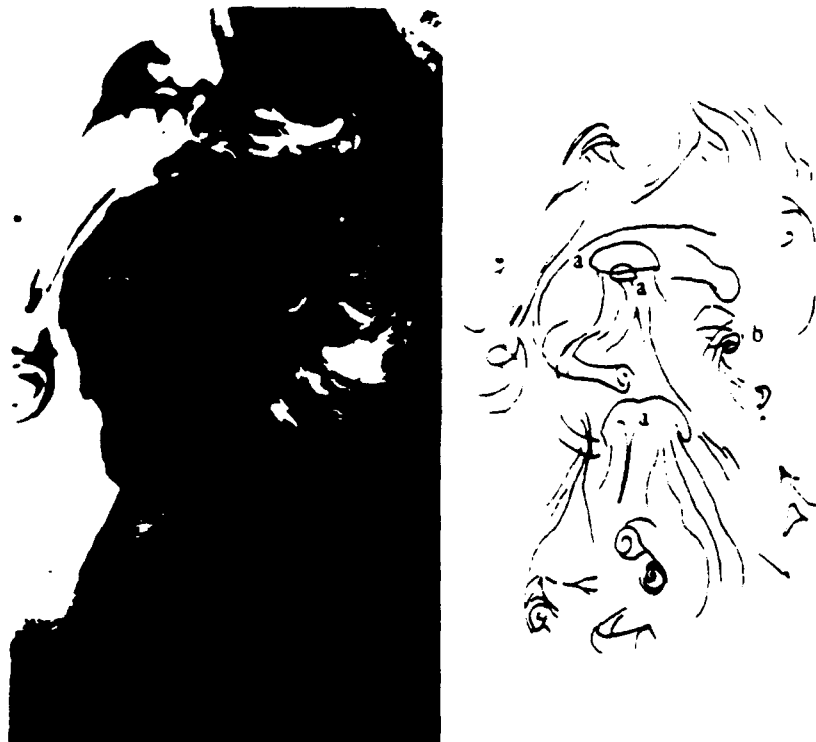


Figure 2. Close-up photograph clearly shows all the source fluid has been stretched into sheets. Identified structures: (a) "bubble" structures, (b) the end of a vortex ring. Scale: 4.8:1.0, $Re = 440$, dilution = 12.5.

smallest velocity fluctuations found in the flow. These can be estimated using Kolmogorov microscale which is defined by the dissipation rate per unit mass ϵ (m^2/sec^3) and the viscosity ν (m^2/sec) (Tennekes and Lumley 1972). For the plume it was assumed that the rate of energy dissipation was proportional to the buoyancy flux per unit area. Based on this assumption the estimated Kolmogorov's microscale for Figure 2 is 0.26mm. This is the same order of magnitude as the measurements for the sheet spacing. The width of the lines were measured in increments of 0.005mm. Line widths ranged from 0.010mm to 0.16mm. The line widths were found to have a Gamma distribution. The most frequent width was 0.020mm. The sheet thickness should be on the order of the concentration fluctuations expected in the flow. The concentration fluctuations can be estimated using the Batchelor microscale which is 0.014mm. Again the measurements are of the same order of magnitude as those predicted.

4 Measurements and Analysis

A turbulent jet is one of the simplest flows with vigorous mixing. Fluid is injected from a circular opening into an environment at rest. The intense shear on the edge of the jet generates large turbulent eddies which entrain fluid from the environment. Thus the width of the jet expands and the mean velocity decreases at sections downstream. Dimensional consistency requires that the width expand linearly with x , the coordinate along the centerline. The conservation of momentum and mass of a pollutant dictate that mean velocity and concentration on the centerline vary with $1/x$. These trends have been verified in many experimental studies and these have also described the properties of the turbulent flow. Recent publications by Papanicolaou and List(1988) and Dahm and Dimotakis(1990) present the properties obtained by the technique of laser-induced

fluorescence of a dye. The lateral profiles of both mean velocity and mean concentration follow Gaussian distributions. A characteristic width of the velocity profile is defined by the radius b at which the value is $1/e$ of the centerline value and the conservation of momentum sets $b = 2 \alpha x$. Experiments give a value of 0.057 for the entrainment coefficient α . The concentration profile is wider and the width is quoted as the ratio λ of this width to b . Experiments give λ the value 1.16. Distributions of the r.m.s. of both velocity and concentration across the jet show a drop-off from the



Figure 3. All source fluid is contained within a half angle of 12° . The experiment used Potassium Permanganate. $Re = 3,225$.

center to the edge. On the centerline the r.m.s. longitudinal velocity component is about 0.25 of the mean velocity while the r.m.s. concentration is 0.2 of the mean.

4.1 Contaminant Envelope and Flame Fronts

Observation of the colour distribution using a permanent, inert dye in a jet shows that the Gaussian distribution cannot be a valid description of the concentration at the edges of the jet. This is demonstrated by the photograph of Figure 3 which is a jet containing potassium permanganate. There is a distinct edge of the jet which is contorted and lumpy from the large eddies. All of the coloured water is contained within an envelope of width kb . This and other photographs define a half angle of 12° which corresponds to $k = 1.86$. Measurements of both the mean and r.m.s. concentration reported in recent papers give finite values beyond this edge. There must be a slow oscillation of the jet not evident in the instantaneous picture which leads to finite values when a time mean is taken.

Another view of the mixing is obtained by taking instantaneous photographs of the jet with a pH sensitive dye for comparison with the inert dye photograph of Figure 3. The coloured region has the shape of a brush or a flame front and the length increases with dilution as expected. There were two distinct zones, an inner dark region and a surrounding lighter region. These are sketched on Figures 4 and 5 for different concentrations. The lighter zone initially coincides with visible edge from Figure 3. This confirms the conjecture that the visible edge is an envelope for all of the source material. In the downstream part there are large lumps of colour visible which show the effect of turbulence. A sequence of photographs taken at 0.2 s intervals showed that these lumps changed shape but a mean position of the edge of the region could be defined. The magnitude of the excursion of the downstream end was about the total width of the jet, which mirrors the passage of one of the largest eddies. Figure 4 is a plot of several photographs which illustrate the variations in shape of the coloured region. There is only a small variation of the edge near the source.

4.2 Mean Front Location

A simple conservation equation for the time averaged mean concentration can be derived by assuming the velocity and concentration profiles are Gaussian. In the case of the concentration, the Gaussian profile is only valid from $r = 0$ to $r = kb$: all of the source material is contained within the visible edge. Thus,

$$\begin{aligned} u &= u_m \exp\left[-\frac{r^2}{b^2}\right] \\ c &= c_m \exp\left[-\frac{r^2}{\lambda^2 b^2}\right] \end{aligned} \quad (2)$$

where u is the velocity, c is the time mean concentration and the subscript m is the centerline value. Conservation of

momentum requires that the momentum at the source, which is assumed to have a top hat profile, is equal to that found at some axial distance from the source. This gives,

$$\frac{\pi}{4} U_o^2 D_o^2 = \frac{\pi}{2} u_m^2 b^2 \quad (3)$$

where U_o is the top hat velocity of the source and D_o is the diameter of the source. Similarly conservation of the scalar contaminant gives,

$$\rho \frac{\pi}{4} U_o c_o D_o^2 = \rho \int_0^{2b} u c 2\pi r dr \quad (4)$$

Substituting into the expression for u and c , using Eq.(3) and evaluating with the values for α , λ and k leads to

$$\frac{c}{c_o} = 5.415 \frac{D_o}{x} \exp \left[\frac{-57 r^2}{x^2} \right] \quad (5)$$

This is essentially the same scaling constant of 5.4 found experimentally by Dahm and Dimotakis(1990).

The edge of the deep colour zone is plotted in Figure 5. For comparison, X's indicate where Eq.(5) estimates the mean concentration to be the value set in the experiment. The deviation of the locus of points found using Eq.(5) is due to the small set of experiments from which the mean was derived. However, the agreement is quite good.

4.3 Diffusion from the Sheets

Outside this deep colour zone the time averaged mean concentration is less than the one set for the experiment. Here the colour is contained in the thin sheets described above. These are thickness λ_o , the Batchelor microscale which is, following the measurements of Dahm and Dimotakis(1990)

$$\lambda_D = 200 \alpha Re^{-\frac{3}{4}} Sc^{-\frac{1}{2}} x \quad (6)$$

Eq.(6) shows that λ_o increases linearly with x . This rate of thickening is much larger than the rate of diffusion of Na^+OH^- ions out of the sheet. Thus most of the Na^+OH^- in the sheet when it was established remains in it. The concentration decreases as the Na^+OH^- diffuses into the fluid being added onto the surface of the sheets. If the concentration profile is similar as this progresses, then the concentration in the center times λ_o is constant. Thus it would be expected that the point x_c on the centerline where colour disappears would be inversely proportional to the defined concentration. This is indeed satisfied by the mean positions of the three dilutions plotted on Figure 6. The mean concentration also decreases with $1/x$ as seen in Eq.(5), so there is a constant ratio of the lengths where the colour changes and where the concentration is the mean. The measured value of this constant from these experiments



Figure 4. Tracing of the outline for $Re=3.225$ using Phenol-Red. Everything above 6.25% original source fluid is visible.

is 1.65. The linear variation in Eq.(6) can be used to show that the maximum concentration in the thin sheets relative to the mean at the same point is equal to the length ratio. List and Papanicolaou(1988) measured the maximum concentration at the centerline using Rhodamine G dye and found that it was 1.65 times the mean. Thus, the same value was obtained for species of different diffusivity. This supports the conjecture that the rate of thickening of the sheets is larger than the rate of diffusion.

4.4 Turbulence Properties

A series of 4 experiments were performed to give a comparison to turbulent measurements found in the literature. The experiments were performed at a Reynolds Number of 3000 to match those published by Papanicolaou and List (They measured the

longitudinal and radial velocities and Rhodamine 6G dye concentrations simultaneously at the same point by a Laser-Doppler Velocimeter {LDV} combined with a Laser-Induced-Fluorescence {LIF} system). Each experiment consisted of 40 photographs which were taken at a rate of 3 per second. This time interval is large enough so that each photograph is statistically independent; meaning each photograph was of a different large scale structure. This independence was later confirmed when the correlation between sequential photographs was found to be near zero. The film and lens were selected to closely match the measurement resolution of the published data of 0.2mm. The maximum location of the contaminant was recorded for each photograph along the center line of the jet as well as for increments of three degrees off the center line from minus twelve to plus twelve degrees.

The normalized r.m.s. concentration positions for the jet are plotted in Figure 7. The measurements are flat between $|r/z| < 0.15$ and are consistent with the shape of Papanicolaou's r.m.s. measurements in a jet for this range of r/z . The measured r.m.s. value of 0.1 is less than the value of 0.2 found by Papanicolaou and List for the r.m.s. concentrations



Figure 5. Tracing for $Re = 3,225$. Everything above 4.26% is visible. The dark zone is contained within the lighter zone. X's mark the zone given by Eq.(5).

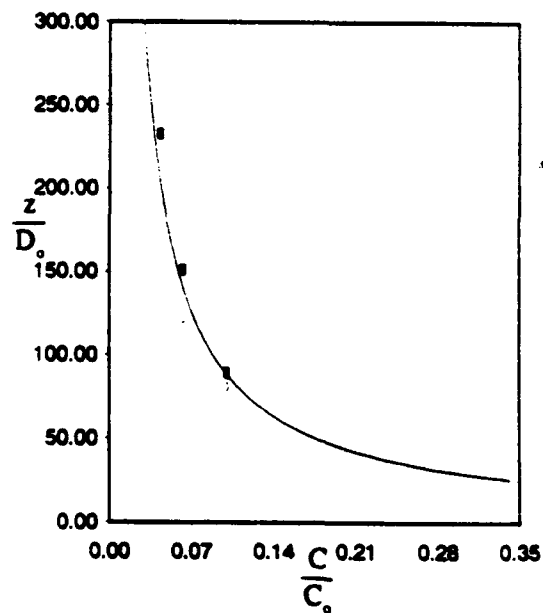


Figure 6. Plot of the maximum axial distance observed using Phenol-Red. The line corresponds to Eq.(5) with a coefficient = 1.65 and $r = 0$.

of Rhodamine 40 dye. However, these two sets of measurements may not be the same property. In Figure 7 the r.m.s. of the locations of a concentration are shown whereas, Papanicolaou and List measured the r.m.s. of the concentration at a point.

In Figure 8 the maximum recorded position normalized by the mean centerline value (given by Eq.(5)) are plotted versus r/z . The profiles have a maximum value around 1.6 and are quite self-similar. This is in excellent agreement with Papanicolaou and List who measured the maximum concentrations at a given location (normalized by their mean centerline values). Provided both experiments have the same resolution, the measurements are equivalent.

5 Summary

The picture which emerges from these photographs is a field of turbulent eddies which are diffusing the pollutant down the gradient as in a conventional diffusion. All of the pollutant is contained within an envelope of width kb . Buried in this field and widely distributed through it are thin sheets which contain high concentrations of original source fluid. The thickness and spacing of these sheets are of the order of the Batchelor and Kolmogorov microscales respectively. The concentration within these sheets is slowly decreasing as new fluid is added to the sheets and the contaminate within diffuses into the new fluid. Thus,

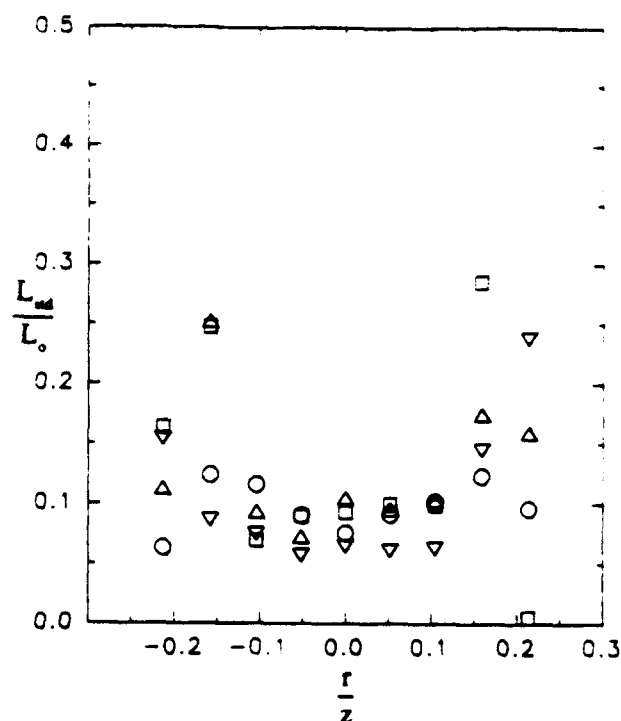


Figure 7. Normalized r.m.s. profile of maximum concentration location across a turbulent jet; $Re = 3000$.

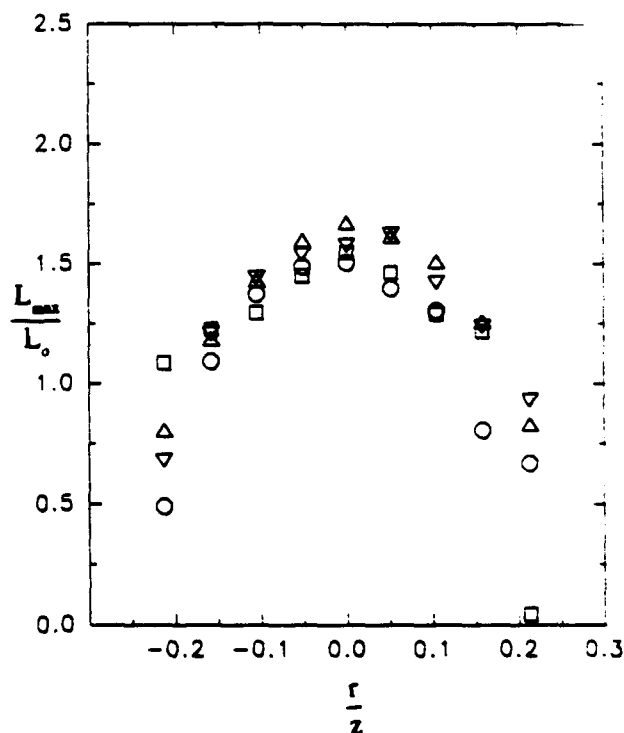


Figure 8. Maximum recorded position normalized by the mean centerline value for a turbulent jet. $Re = 3000$.

λ increases. The added fluid had previously been entrained from the environment by the biggest eddies and much of it is of very low concentration when it comes in contact with the sheets.

The pH sensitive dyes facilitate the observation of turbulent structures through the examination of the instantaneous contaminant distribution. The conservation equation presented above for the time averaged mean front agrees with the pH sensitive dye experiments as well as with other investigators. This has lead to an estimation of the r.m.s. of the concentration and provided an intuitive picture of the physical mixing process in turbulent flows.

Future work will investigate the characteristics of the lines and the identification of turbulent flow structures. The pH technique is uniquely suited for this type of investigation.

References

- Auerback, D. 1987 "Experiments on the trajectory and circulation of the starting vortex", *J. Fluid Mech.*, **183**, pp 185-198.
- Cussler, E.L. (1984), Diffusion: Mass Transfer in Fluid Systems, Cambridge University Press, [328-377].
- Dahm, W.J.A. and Dimotakis, P.E. 1990 "Mixing at large Schmidt numbers in the self-similar far field of turbulent jets", *J. Fluid Mech.*, **217**, pp 299-330.
- Laitinen, H.A. (1960), Chemical Analysis an Advanced Text and Reference, McGraw Hill Book Company, Inc. [pp 38-40].
- List, E.J. (1982), "Turbulent Jets and Plumes", *Ann. Rev. Fluid Mech.*, **14**, [pp. 189-212].
- Papanicolaou, P.N. and List, E.J. (1988), "Investigation of round vertical turbulent buoyant jets", *J. Fluid Mech.*, **195**, pp 341-391.
- Prasad, R.R. and Sreenivasan, K.R., (1990), "Quantitative Three-Dimensional Imaging and the Structure of Passive Scalar Fields in Fully Turbulent Flows", *J. Fluid Mech.*, **216**, [pp. 1-34].
- Tennekes, H. and Lumley, J.L., (1972), A First Course in Turbulence, The MIT Press, [pp 19-24].

A STUDY OF REACTING FLOWS IN
STATIONARY ISOTROPIC TURBULENCE
USING ONE-POINT PDF AND TWO-POINT
CORRELATION FUNCTIONS

Kuo-chen Tsai
Department of Mechanical Engineering
SUNY at Stony Brook, NY 11794-2300

Edward E. O'Brien
Department of Mechanical Engineering
SUNY at Stony Brook, NY 11794-2300

1 Introduction

Turbulent reacting flows have been studied for many decades and are widely recognised for the challenges they pose to both the turbulence community and those whose primary interest is in the chemistry. Neither the transport aspect nor the chemical kinetic detail necessary to predict such flows can be considered to be well understood even when the role of density fluctuations is unimportant, as may happen in aqueous solutions.

One of the problems is the necessity to describe turbulent transport in a flow consisting of enough species to represent the chemical kinetics adequately. Two elements of progress have been established in the last two decades with respect to this problem; the introduction of the joint probability density (pdf) of concentrations[7] and the exploration of Monte-Carlo techniques to minimise computational effort[18] as the number of species increases.

A pdf framework is essential for any realistic study of reactive flows, but it is especially important for flows with complicated chemistry because the reaction terms cannot be treated accurately by moment methods. The Monte-Carlo process is also important when the number of species is large; it has only been developed for the one-point pdf which has the disadvantage of not representing directly the relative motion of particle pairs. This motion is a fundamental property of turbulence and is particularly dominant when the turbulence has a high degree of symmetry as in homogeneous cases.

Recent studies have seen the development of a fully two-point pdf model of homogeneous turbulent reactive flow which successfully mimics the results of direct numerical simulation (DNS)[13]. It is, however, limited to the two species kinetic scheme $A + B \rightarrow \text{Product}$, with the conclusion that it would be uneconomical to extend the model to more reacting species.

In this paper we develop a less computationally intensive alternative to Jiang's fully two-point pdf model. This is achieved by noting that scalar correlation functions carry all the two-point information needed for the representation of the effects of advection and molecular diffusion while the one-point pdf fully represents the role of chemical kinetics. The model, as developed in the body of the paper, features a parallel evolution of the one-point pdf and the scalar correlation functions, the latter providing a time scale for the former.

As a consequence of the reduction in dimensions that follows dropping from a two-point to a one-point pdf it is possible to treat kinetic schemes with up to five reactants. This progress is obtained at the expense of a similarity assumption, which connects the moments of the one-point pdf at any instant to the correlation functions at the same instant.

The model is first evaluated for the two species reaction $A + B \rightarrow \text{Products}$ against Jiang's model and DNS data obtained for the same reaction[11]. It is then extended to a four-species consecutive reaction of the type



where A, B, C and P are four different chemical species. D is the desired product, P is the by-product and k_1 and k_2 are reaction constants. The temperature effect on reaction rates is ignored. Furthermore, we also assume the chemical reaction rates are bilinear which means the chemical reaction rate is a first order function of the reactants A and B or A and D.

The model allows prediction of the effects of Schmidt, Reynolds and Damköhler numbers on the evolution of means, variances, cross-variances and microscales. A full range of predictions can be found in the Ph.D dissertation of the first author [20]. In this manuscript we present a few samples of the results to indicate the model's performance.

2 Problem formulation

The governing equations for an isotropic scalar field $\phi(\mathbf{x}, t)$ advected and diffused by a stationary isotropic velocity field $\mathbf{u}(\mathbf{x}, t)$ can be written as:

$$\frac{\partial \mathbf{u}}{\partial t} + \mathbf{u} \cdot \nabla \mathbf{u} = -\nabla p + \nu \nabla^2 \mathbf{u} + \mathbf{f} \quad (3)$$

$$\nabla \cdot \mathbf{u} = 0 \quad (4)$$

$$\frac{\partial \phi_i}{\partial t} + \mathbf{u} \cdot \nabla \phi_i = D_\phi \nabla^2 \phi_i + \dot{\omega}_i, \quad i = A, B, D \text{ and } P \quad (5)$$

where the constant density of fluid is taken to be unity, ν is the kinematic viscosity, p is pressure, D_ϕ is the molecular diffusivity of ϕ and $\dot{\omega}$ is the chemical production term. Following Eswaran and O'Brien [10], We adopt a time-splitting scheme which separates equation (5) into three parts and each part is treated separately at each time step. With time-splitting, three equations are obtained

$$\frac{\partial \overline{\phi_{i,A}\phi_{i,B}}}{\partial t} = -2 \frac{\partial \overline{\phi_{i,A}\phi_{i,B}(u_i)_B}}{\partial \xi_j} \quad (6)$$

$$\frac{\partial \overline{\phi_{i,A}\phi_{i,B}}}{\partial t} = D_\phi \frac{\partial^2 \overline{\phi_{i,A}\phi_{i,B}}}{\partial \xi_j \partial \xi_j} + D_\phi \frac{\partial^2 \overline{\phi_{i,A}\phi_{i,B}}}{\partial \xi_j \partial \xi_j} \quad (7)$$

$$\frac{\partial \overline{\phi_{i,A}\phi_{i,B}}}{\partial t} = 2 \overline{\phi_{i,A}\dot{\omega}_{i,B}} \quad (8)$$

Of these, equations (6) and (8) are not closed; more unknowns will be generated by the averaging process than there are equations. For equation (6), many models are available. An EDQNM closure is adopted for the advection process, and this is discussed in the next section. Equation (8) is usually very troublesome. Because the non-linear chemical production term $\overline{\phi_{i,A}\dot{\omega}_{i,B}}$ varies with different chemical reaction schemes, this makes the modeling extremely difficult. In the present study, we take advantage of the one-point pdf formulation and the DNS data of Gao [11] to use a similarity assumption to close this equation. The details of this assumption are given in the next section. Because we are only interested in the bilinear reaction rate ($\dot{\omega} \sim k\phi_A\phi_B$), the second-order equations listed above for two-point correlation functions are enough to serve the purpose.

The one-point pdf evolution equation, which is to be used in conjunction with equations (6), (7) and (8), is as follow,

$$\frac{\partial P_1}{\partial t} + \frac{\partial}{\partial \phi} (P_1 v) = 0, \quad (9)$$

where

$$v(\phi, t) = D_\phi \lim_{\mathbf{x}_2 \rightarrow \mathbf{x}_1} \nabla_{\mathbf{x}_2}^2 E(\phi_2 | \phi_1) + \dot{\omega}(\phi_1). \quad (10)$$

$E(\phi_2 | \phi_1)$ is the expectation of $\phi(\mathbf{x}_2, t)$ at point \mathbf{x}_2 conditional on its value at \mathbf{x}_1 . In this formulation, the transport terms disappear because of homogeneity. Instead, this information is implicitly included in the first term on the RHS of equation (10). The steps for calculating the evolution of the one-point pdf are straightforward.

1. Calculate (6) for the advection process using a turbulent transport closure.
2. Calculate (7) for the diffusion process.

3. Use the time scale information derived from step 2 and a molecular diffusion closure to calculate the one-point pdf equation (9).
4. Calculate one-point second-order moments from the one-point pdf, then use this information and a similarity assumption to calculate two-point correlation functions after chemical reaction.
5. Repeat for the next time step.

By this method, a simulation for any chemical reaction scheme which involves only four or five reacting scalars is possible. There are two closure approximations and a similarity assumption in the model; these are outlined in the next section.

3 Modeling assumptions

Following the method of Eswaran and O'Brien[10] using time-splitting to separate advection, diffusion and reaction, we are able to treat each process separately and with more flexibility. The closures used in this study are not the most sophisticated ones, but rather they are the most suitable. The derivations shown here are based on the single-species case[20].

Modeling turbulent advection

In homogeneous turbulent advection, the one-point pdf of scalars remains unchanged. This point can be observed by looking at (9) from which the advection terms are missing because of homogeneity. However, the advection terms still exist in the equations for two-point correlation functions. By determining the micro-scale these functions affect the evolution rate of the one-point scalar pdf due to molecular diffusion. A modified EDQNM model is adopted to represent advection. It is a physical space version[10] for an isotropic which interprets the turbulent advection effect as an eddy viscosity ν , which is determined by the turbulence spectrum.

The EDQNM model is not the most advanced spectral closure. Others, such as DIA and LHDIA[12], have been proven to be more dynamically satisfactory. But the computability of the EDQNM closure makes it more accessible. Some recent research[10] has shown the ability of this model to predict the correct scalar dissipation rate when compared with experimental data. The numerical comparison with DNS data by Jiang[13], who used the EDQNM advection closure in a fully two-point pdf model, has also been found to be satisfactory.

Modeling molecular diffusion

Closure modeling of the transport of the pdf due to molecular diffusion has long been a challenging part of the pdf approach for turbulent reacting flow. Because the subsequent chemical reaction is closed in the pdf formulation, an accurate prediction of pdf evolution in molecular diffusion is the key point for the pdf to represent the chemical process correctly. There are two main difficulties in modeling the diffusion equation of the pdf. The first is the anti-diffusive behavior of a scalar pdf in this process. When a scalar is diffused in a flow field, although the mean value of scalar remains unchanged, the fluctuation is smoothed out as time goes on. This phenomenon, reflected in the phase space of the pdf, is such that the pdf will become a delta function at the mean value of the scalar in the final stage of molecular diffusion. Such a pdf equation is numerically unstable. The second difficulty comes from the same phenomenon, which is, no matter what the initial condition of the scalar pdf, it should, asymptotically, approximate a Gaussian. So far, only the mapping closure developed by Chen et. al.[4] preserves such a property. The others, such as an integral-type closure[6], assumed pdf[21] and linear mean square estimations (LMSE) do not possess such behavior.

Linear mean square estimation (LMSE) is a well established method to estimate a conditional expectation[17]. It is also the simplest way to modify the expectation term in equation (10). Which can be written as[16],

$$E(\phi_2 - \phi_1) = \phi(\underline{x}_2, t) + \rho(\underline{x}, t) \frac{\sigma_{\phi_1}(\underline{x}_1, t)}{\sigma_{\phi_1}(\underline{x}_1)} [\phi - \phi(\underline{x}_1, t)] \quad (11)$$

where $\rho = \frac{\phi(\underline{x}_2, t) - \phi(\underline{x}_1, t)}{\phi - \phi(\underline{x}_1, t)}$ and ρ , σ , and $\bar{\phi}$ are the usual correlation coefficient, variance, and mean of $\phi(\underline{x}, t)$. Although this is a Gaussian closure, a correct evolution equation for second order moments is reproduced[8]. This property is especially useful when a multi-scalar case is of interest. For a two-species bilinear reaction, if the time scale can be derived correctly, then the scalar means and second order moments should also be correct.

The pdf equation, with molecular diffusion terms only, for a two-species case in an isotropic field is

$$\begin{aligned} \frac{\partial P(\phi_a, \phi_b)}{\partial t} = & -D_{\phi_a} \frac{\partial}{\partial \phi_a} \lim_{\underline{x}' \rightarrow \underline{x}} \nabla_{\underline{x}'}^2 [E_a(\phi_a' | \phi_a, \phi_b) P(\phi_a, \phi_b)] \\ & -D_{\phi_b} \frac{\partial}{\partial \phi_b} \lim_{\underline{x}' \rightarrow \underline{x}} \nabla_{\underline{x}'}^2 [E_b(\phi_b' | \phi_a, \phi_b) P(\phi_a, \phi_b)] \end{aligned} \quad (12)$$

where the subscripts a and b denote two different chemical species, (\cdot) represents the second physical position, D_{ϕ_a} and D_{ϕ_b} are the diffusivity constant of scalar ϕ_a and ϕ_b . E_1 and E_2 have the same definitions as in (10), but this time the expectation value is conditioned on both $\phi_a(\underline{x}, t)$ and $\phi_b(\underline{x}, t)$. By LMSE closure, E_1 and E_2 can be expressed as,

$$E_a = \alpha_1(\phi_a - \bar{\phi}_a) + \beta_1(\phi_b - \bar{\phi}_b) + \bar{\phi}_a \quad (13)$$

$$E_b = \alpha_2(\phi_a - \bar{\phi}_a) + \beta_2(\phi_b - \bar{\phi}_b) + \bar{\phi}_b \quad (14)$$

where

$$\alpha_1 = \frac{\overline{\phi_a \phi_a' \phi_b^2} - \overline{\phi_b \phi_a' \phi_a \phi_b}}{\overline{\phi_a^2 \phi_b^2} - \overline{\phi_a \phi_b}^2} \quad (15)$$

$$\beta_1 = \frac{\overline{\phi_b \phi_a' \phi_a^2} - \overline{\phi_a \phi_a' \phi_b \phi_a}}{\overline{\phi_a^2 \phi_b^2} - \overline{\phi_a \phi_b}^2} \quad (16)$$

$$\alpha_2 = \frac{\overline{\phi_a \phi_b' \phi_b^2} - \overline{\phi_b \phi_b' \phi_a \phi_b}}{\overline{\phi_a^2 \phi_b^2} - \overline{\phi_a \phi_b}^2} \quad (17)$$

$$\beta_2 = \frac{\overline{\phi_b \phi_b' \phi_a^2} - \overline{\phi_a \phi_b' \phi_b \phi_a}}{\overline{\phi_a^2 \phi_b^2} - \overline{\phi_a \phi_b}^2} \quad (18)$$

With this approximation equation (9) is closed and from it the evolution equations for second-order moments due to molecular diffusion can be recovered by multiplying (12) successively by ϕ_a^2 , ϕ_b^2 and $\phi_a \phi_b$ and integrate over ϕ_a and ϕ_b .

Modeling chemical reaction

As we mentioned earlier, the chemical reaction term in equation (5) is always a challenge for a moment closure but requires no approximation in the pdf formulation. However, to match the pdf model for reaction with the two-point models for advection and molecular diffusion it is necessary, in principle, to use a two-point pdf formulation[14,13]. To avoid the computational intensity of the two-point pdf we have chosen instead to use a one-point pdf representation of reaction combined with a similarity assumption which approximates the effects of reaction on the scalar correlation functions. Gao's DNS data[11] shows an insensitivity of the dissipation rate with respect to chemical reaction in the one-species case with second order reactions and in the two-species case with a bilinear reaction. This suggests that an assumption that the shapes of two-point correlation functions are not significantly altered during chemical reaction may be reasonable. We examine this assumption as follows.

The evolution equations for the two-point second order moments are,

$$\frac{\partial \overline{AA'}}{\partial t} = -2k \overline{A^2 A'} \quad (19)$$

which corresponds to a one-species second order reaction, and

$$\frac{\partial \overline{AA'}}{\partial t} = -2k_1 \overline{A'AB} \quad (20)$$

$$\frac{\partial \overline{BB'}}{\partial t} = -2k_2 \overline{B'AB} \quad (21)$$

which correspond to a two-species bilinear reaction. A and B are two different chemical species. (') denotes the second point, and k , k_1 and k_2 are chemical reaction rate constants.

In equation (19), a similarity assumption means that $\overline{AA'}$ should have the same shape as $\overline{A^2A'}$. For the two-species bilinear reaction of equation (20) and equation (21), it assumes $\overline{AA'}$ has the same shape as $\overline{A'AB}$ and $\overline{BB'}$ has the same shape as $\overline{B'AB}$. This assumption is very likely to be true for the first case. An analytical solution for this case derived by O'Brien[15] shows a strong resemblance to this assumption. However, for the other case it is not very obvious. Another theoretical study on this topic is by Corrsin[5], who studied the effect, in spectral space, of a first-order reaction with a single scalar. Fortunately, in such a case, the evolution equation for the two-point correlation function is exact. This can be seen in the following equation.

$$\frac{\partial \overline{AA'}}{\partial t} = k \overline{AA'} \quad (22)$$

Here, we apply the similarity assumption to the two-point autocorrelation functions. By doing this, several properties can be deduced and these properties can further be used to close the evolution equation for two-point cross-correlation functions. Returning to the bilinear reaction case with (20) and (21), we separate

$$A = \overline{A} + a \quad (23)$$

and

$$B = \overline{B} + b, \quad (24)$$

where a and b are the fluctuation parts of the variables A and B . With this, the evolution equations of the two-point correlation functions follow.

$$\frac{\partial \overline{aa'}}{\partial t} = -2k(\overline{aa'} \overline{B} + \overline{a'b} \overline{A} + \overline{a'ab}) \quad (25)$$

$$\frac{\partial \overline{bb'}}{\partial t} = -2k(\overline{ab'} \overline{B} + \overline{bb'} \overline{A} + \overline{abb'}) \quad (26)$$

$$\frac{\partial \overline{ab'}}{\partial t} = -k(\overline{ab'} \overline{B} + \overline{bb'} \overline{A} + \overline{abb'}) - k(\overline{aa'} \overline{B} + \overline{a'b} \overline{A} + \overline{a'ab}) \quad (27)$$

Once the similarity relations are assumed in (25) and (26), the evolution of $\overline{ab'}$ can be found by

$$\frac{\partial \overline{ab'}}{\partial t} = \frac{1}{2} \frac{\partial \overline{aa'}}{\partial t} + \frac{1}{2} \frac{\partial \overline{bb'}}{\partial t}. \quad (28)$$

Readers should keep in mind that the assumption made here only affects the shape of two-point quantities. Because all one-point quantities can be derived exactly from the one-point pdf, all two-point quantities should be renormalised by the exact one-point quantities derived from the pdf. A similar analysis for the four-species reaction can be found in Tsai's dissertation[20].

4 Numerical method

The closed evolution equations of two-point correlation functions for turbulent advection have the following form.

$$\frac{\partial}{\partial t} \overline{\phi_i \phi_j} = \frac{1}{r^2} \frac{\partial}{\partial r} (\nu_e(r, t) r^2 \frac{\partial \overline{\phi_i \phi_j}}{\partial r}), \quad (29)$$

where ν_e is the eddy viscosity. This equation has a similar form to equation (7), and both equations are solved by the Crank-Nicolson algorithm. The exact form of ν_e is not listed here, the interested reader can find it in Eswaran and O'Brien[10]. In order to calculate ν_e , a Glenshaw-Curtis quadrature is employed to integrate the turbulent velocity spectrum[9,13]. The

chosen functional form of the spectrum has a form similar to that adopted in Jiang's study[13] which is determined by turbulence intensity, Taylor micro-scale and the integral scale. The details can be found in Tsai's dissertation[20].

Numerical integration of the pdf equation (9) is far more difficult. Following the method of Jiang, a flux-split, upwind second-order MacCormack scheme[19] is combined with the multi-dimensional FCT[1] algorithm proposed by Zalesak[22]. However, we find this hybrid scheme cannot have a satisfactory solution because of the numerical ripples that always occur in a hyperbolic system. Although Zalesak has suggested some useful tricks in his paper, monotonicity of the solution in multi-dimensions is still not guaranteed. We propose the following limiting algorithm (a two-dimensional example) which can really enforce monotonicity on the solution in all directions.

$$\begin{aligned}
 z_{max} &= \max(\rho_{i-1,j}^n, \rho_{i,j}^n, \rho_{i+1,j}^n) \\
 \rho_{i,j}^n &= \max(\rho_{i,j}^n \exp((-\nabla \cdot \mathbf{u})_{i,j} \Delta t), \rho_{i,j}^L) \\
 z_{min} &= \min(\rho_{i-1,j}^n, \rho_{i,j}^n, \rho_{i+1,j}^n) \\
 \rho_{i,j}^n &= \min(\rho_{i,j}^n \exp((-\nabla \cdot \mathbf{u})_{i,j} \Delta t), \rho_{i,j}^L) \\
 y_{max} &= \max(\rho_{i,j-1}^n, \rho_{i,j}^n, \rho_{i,j+1}^n) \\
 \rho_{i,j}^n &= \max(\rho_{i,j}^n \exp((-\nabla \cdot \mathbf{u})_{i,j} \Delta t), \rho_{i,j}^L) \\
 y_{min} &= \min(\rho_{i,j-1}^n, \rho_{i,j}^n, \rho_{i,j+1}^n) \\
 \rho_{i,j}^n &= \min(\rho_{i,j}^n \exp((-\nabla \cdot \mathbf{u})_{i,j} \Delta t), \rho_{i,j}^L).
 \end{aligned} \tag{30}$$

then

$$\begin{aligned}
 \rho_{i,j}^{max} &= \min(z_{max}, y_{max}) \\
 \rho_{i,j}^{min} &= \max(z_{min}, y_{min}).
 \end{aligned} \tag{31}$$

where ρ is the dependent variable (probability density in this case), subscript L represents the low-order solution and superscript n the solution at the previous time step. Instead of defining the bounds based on all the neighboring points of (i, j) , this procedure defines the bounds according to the largest and smallest values in each direction. Therefore, the above algorithm actually enforces monotonicity on every direction and does not keep the pdf value from becoming a delta function. In tests for two- and four-dimensional computations, this procedure is virtually free of the oscillations created by higher order algorithms.

5 Results and discussion

In order to check the validity of the proposed model, comparisons have been made with DNS data and the fully two-point pdf calculations of Jiang[13]. We compare our results with Gao's DNS data for one-scalar second-order reactions, two-scalar bilinear reactions and four-scalar consecutive reactions. The data of Jiang was also compared with our results in the case of a two-scalar bilinear reaction. A DNS calculation of the same case was performed by Chakrabarti and Hill[3] for decaying turbulence, but comparison with their data is not appropriate because of the stationary spectrum adopted in the present study. Besides the comparisons with other data, we also computed the four-scalar consecutive reaction case, for a range of Schmidt numbers and Reynolds numbers beyond those which are accessible to DNS.

There were five velocity spectra adopted in the study. Each of them refers to a different initial velocity field in the DNS data of the fully two-point pdf calculation. These parameters are listed in Tables 1 and 2. The initial parameters for the

the fields are listed in Tables 2, 3 and 5.

All the governing equations and variables in the present study are in dimensionless form. To avoid confusion, several dimensionless parameters and variables need to be defined clearly. The Damköhler numbers are defined as

$$Da = \frac{k\bar{\phi}_{a0}l}{u} \quad (32)$$

where k is the reaction constant, $\bar{\phi}_{a0}$ the initial scalar mean and l/u the eddy turnover time of the turbulence field. The dimensionless time is defined as $\tau = tu/l$. The evolution of cross-variance is studied through the variable $\gamma_{ij} = \overline{\phi_i\phi_j} / (\overline{\phi_i}^2 \overline{\phi_j}^2)^{1/2}$. Following Corrsin[5], the scalar micro-scale is defined as follow

$$\lambda_\phi = 2 / \frac{\partial^2 \rho}{\partial r^2} \quad (33)$$

where $\rho = \overline{\phi\phi'} / \overline{\phi^2}^{1/2}$. Another variable of interest is the selectivity factor in a consecutive chemical reaction, which is defined as [2]

$$X_s = \frac{2\bar{\phi}_p}{\bar{\phi}_d + 2\bar{\phi}_p} \quad (34)$$

where $\bar{\phi}_d$ is the mean concentration of the desired product D while $\bar{\phi}_p$ is that of the by-product P . X_s is zero for perfect selectivity and unity when only P is obtained.

The initial pdf in the single-scalar case is chosen to be an inverted parabola to simulate the double-spike initial condition similar to the initial condition for the DNS data. For the two-scalar cases, all the initial pdfs are chosen to be multi-variate Gaussian. In the consecutive reaction case, four scalars are involved, two pre-existing species A and B , main product D and by-product P . We choose a joint-normal distribution for A and B and a top-hat distribution in the first three grids for C and D . This is because of the difficulty in representing the delta functions of a pdf numerically.

A complete set of numerical results can be found in graphical form in the dissertation of Tsai[20]. For this paper we limit ourselves to a small sample of the results, enough to demonstrate that the model has promise and can effectively treat four species reactions.

The upper graph in Fig. 1 presents the model predictions of concentration variance evolution for a single species second order reaction in a range of Damköhler numbers from 0 to 3.0. In the lower graph we show the corresponding predictions from DNS. The agreement is excellent and is as good for the scalar mean and dissipation, which are not reproduced here.

Fig. 2 show a similar level of agreement between the model and DNS for the cross-variance in a two-species reaction for a range of Damköhler numbers from 0 to 1.0. Similar levels of agreement with DNS are also obtained (but not shown) for concentration means, variances and microscales.

We also obtained very good agreement with Jiang's model results for these same quantities both when the Schmidt numbers of A and B are equal and when they differ by a factor of 3. Figure 3 shows a comparison of the scalar dissipation for two Schmidt number ratios at a Damköhler number of 2.5.

Fig. 4 summarises the predictions of the model with respect to means, variances and cross-variances for the four-species consecutive reaction as a function of Reynolds number. Damköhler numbers and Schmidt numbers are held constant in the calculations. It is clear that Reynolds number has a profound effect on second order quantities as would be expected give the important role of turbulent advection in enhancing particle pair separation and thereby increasing the influence of molecular diffusion.

Figure 5 shows the effects of greatly increased Schmidt number on the evolution of concentration means, variances and cross-variances. The Damköhler numbers are held fixed and are the same as in Fig. 4. The Reynolds number, Re_λ , is also held constant at 21.69. An increase in Schmidt number by two orders of magnitude has the same effect as a seven-fold increase in Re_λ under the particular circumstances of this calculation. It is no surprise that an increase in molecular diffusivity, as

represented by Schmidt number, gives results qualitatively similar to an increase in Re_λ . The differences in the second order quantities which are apparent in the lower graphs of Fig. 4 and 5, indicate that the structure of the turbulent field can play a role in determining the evolution of a reaction, beyond merely enhancing diffusivities.

Figure 5 show a typical evolution of the selectivity factor (Eqn. 34) as a function of the Damköhler numbers of species A and B. Damköhler number ratio is a dominant factor as expected but the initial superiority (lower X_s) of the case ($Da_1 = 5.0$, $Da_2 = 1.0$) over ($Da_1 = 1.0$, $Da_2 = 0.1$) reveals an interesting dependence on Damköhler numbers as well as on their ratio.

The model agrees well with existing DNS data and the fully two-point pdf predictions of Jiang. It has been shown to easily handle 4 species and may be able to treat 1 or 2 more. It should be a useful predictor for other kinetic schemes with this number of species and a testing ground for simpler models of chemically-reacting, homogeneous turbulent flows.

Acknowledgment

The authors acknowledge the support from the National Science Foundation under grant CTS-8706246. Part of the computation was carried out on the Cornell National Supercomputer Facility, which is supported in part by the National Science Foundation, the State of New York and the IBM corporation.

References

- [1] Boris, J. P., Book, D. L.-J. Comp. Phys., 11, 38(1973).
- [2] Bourne, J. R., Kosicki, F., Rys, P.- Chem. Eng. Sci., 36, 1643(1981).
- [3] Chakrabarti, M., Hill, J. C.-Symp. on Turbulence, Rolla, MO(1990).
- [4] Chen, H., Chen, S. and Kraichnan, R.H.-Phys. Rev. Lett. 63, 2657(1989).
- [5] Corrsin, S.-Phys. Fluids A, 1, 421(1983).
- [6] Curl, R. L.-AICHE J., 9, 175(1963).
- [7] Dopazo, C.-Ph.D thesis, SUNY Stony Brook, NY(1973).
- [8] Dopazo, C.-Acta Astronautica, 3, 853(1976).
- [9] Engels, H.-Numerical Quadrature and Cubature.(Academic Press, New York, 1980).
- [10] Eswaran, V., O'Brien, E.E.-Phys. Fluids A, 1(3), 537(1989).
- [11] Gao, F.-Ph.D thesis, SUNY at Stony Brook, NY(1990).
- [12] Herring, J.R., Schertzer, D., Lesieur, M., Newman, G.R., Cholet, J.P., Larcheveque, M.-J. Fluid Mech. 124, 411(1982).
- [13] Jiang, T.L.-Ph.D thesis, SUNY at Stony Brook, NY(1990).
- [14] Kuo, Y.Y., O'Brien, E.E.-Phys Fluids, 24, 194(1981).
- [15] O'Brien, E.E.-Phys. Fluids, 9, 1661(1966).
- [16] O'Brien, E.E.-Turbulent Reacting Flows, Chap. 5, Springer-Verlag(1980).
- [17] Papoulis, A.-Probability, Random Variables, and Stochastic Process (2nd Ed.), McGRAW-HILL(1984).
- [18] Pope, S.B.-Prog. Energy Comb. Sci. 11, 119(1985).
- [19] Steger, J. L., Warming, R. F.-J Comp. Phys., 40, 263(1981).
- [20] Tsai, K.-Ph.D thesis, SUNY at Stony Brook(1992).
- [21] Valiño, L., Dopazo, C.-Phys. Fluids A, 2, 1204(1990).
- [22] Zalesak, S. T.-J. Comp. Phys., 31, 335(1979).

Table 1: Specifications of initial velocity fields of DNS (v1 & v3) and fully two-point pdf (SC3.4)

Vel. Field	η	l	λ	l/u	Re_λ
v1	0.0429	1.2156	0.5754	0.6012	46.54
v3	0.0874	1.3585	0.8006	2.0057	21.69
SC3.4	0.036	1.009	0.463	0.38	49.2

Table 2: Specifications of initial velocity fields of present study

Vel. Field	η	l	λ	l/u	Re_λ
v1	0.505	1.274	0.58	0.66	44.93
v3	0.0863	1.691	0.729	2.273	21.69
SC3.4	0.0425	1.056	0.4915	0.4217	49.2
v4	0.07396	3.9872	2.1584	2.302	150.0

Table 3: Specifications of initial scalar fields of DNS

PDF	Cases	l_ϕ/l	$\lambda_{\phi_{rms}}, \lambda$
v1pd	pds2	0.536	0.749
v3pb	pbs2	0.577	1.367
	pbs3	0.385	0.977
	pbc3	0.444	1.068

Table 4: Specifications of initial scalar fields for SC3 and SC4 in fully two-point pdf calculation

Cases	$\langle \phi_a \rangle_0$	$\langle \phi'^2 \rangle_0^{1/2}$	$\langle \phi'_a \phi'_b \rangle_0$	Sc_a	Sc_b
SC3	0.266	0.1382	-0.000756	0.7	0.7
SC4	0.266	0.1382	-0.000756	0.7	2.1

Table 5: Specifications of initial scalar fields in the present study

Cases \Rightarrow	v1pds2	v3pbs2s2	v3pbs2s3	v3pbs3s3	v3pbs2c3	v4pbs2c3
$\langle \phi_a \rangle$	0.5	0.5	0.5	0.5	0.5	0.5
$\langle \phi_b \rangle$	0.5	0.5	0.5	0.5	0.5	0.5
$\langle \phi_c \rangle$	*	*	*	*	0.1	0.1
$\langle \phi_d \rangle$	*	*	*	*	0.1	0.1
$\langle \phi_a'^2 \rangle^{1/2}$	0.4453	0.2381	0.2388	0.2381	0.2365	0.2365
$\langle \phi_b'^2 \rangle^{1/2}$	*	0.2381	0.2388	0.2381	0.2365	0.2365
$\langle \phi_c'^2 \rangle^{1/2}$	*	*	*	*	0.05774	0.05774
$\langle \phi_d'^2 \rangle^{1/2}$	*	*	*	*	0.05774	0.05774
$\langle \phi_a \phi_b' \rangle$	*	0.00744	0.0	0.003	0.01983	0.01983
$(\lambda_\phi/\lambda)_a$	0.741	1.352	1.352	0.966	1.352	1.4961
$(\lambda_\phi/\lambda)_b$	*	1.352	0.966	0.966	1.056	1.1477
$(\lambda_\phi/\lambda)_c$	*	*	*	*	1.352	1.4691
$(\lambda_\phi/\lambda)_d$	*	*	*	*	1.352	1.4691
$(l_\phi/l)_a$	0.5228	0.5772	0.5772	0.3852	0.5772	0.5772
$(l_\phi/l)_b$	*	0.5772	0.3852	0.3852	0.444	0.444
$(l_\phi/l)_c$	*	*	*	*	0.5772	0.5772
$(l_\phi/l)_d$	*	*	*	*	0.5772	0.5772

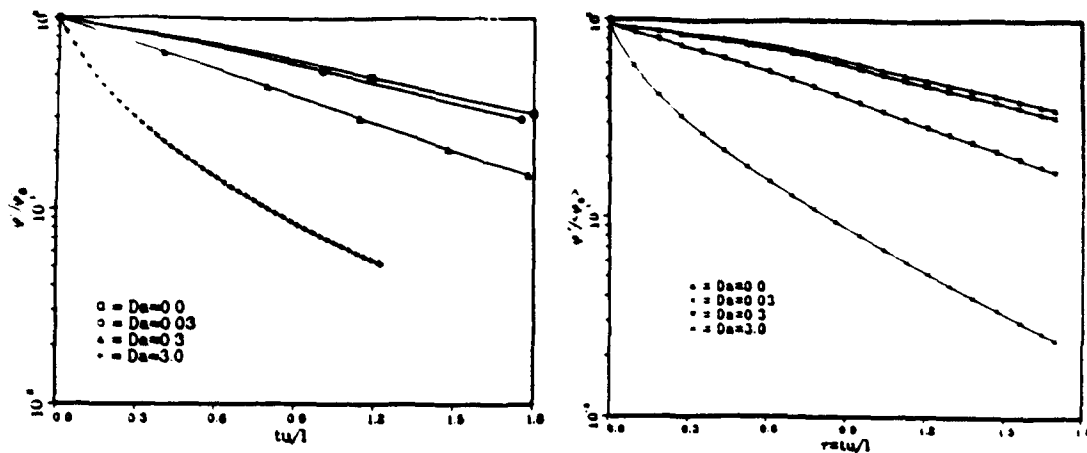


Figure 1: Evolution of variances for second order reactions under different reaction rates (v1pd-s2). Present study (left); DNS (right).

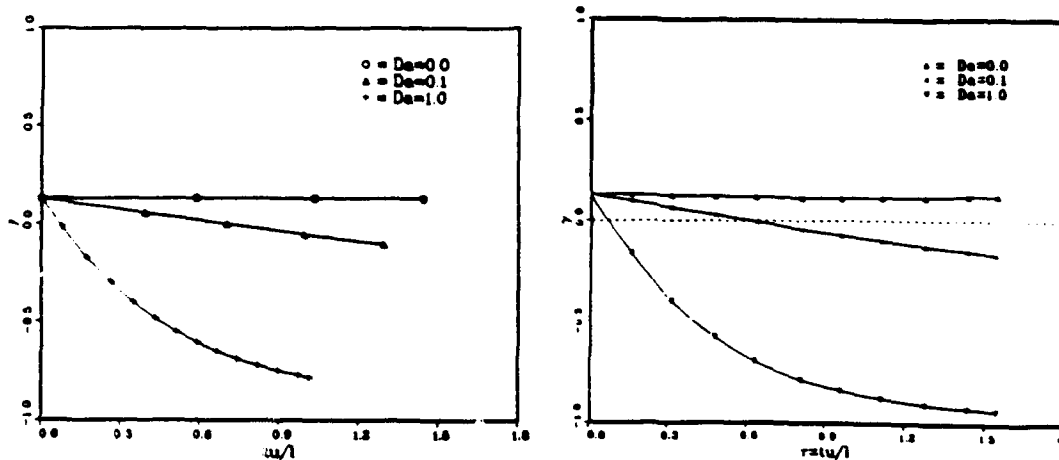


Figure 2: Evolution of γ under different reaction rates (v3pb-s2s2). Present study (left); DNS (right).

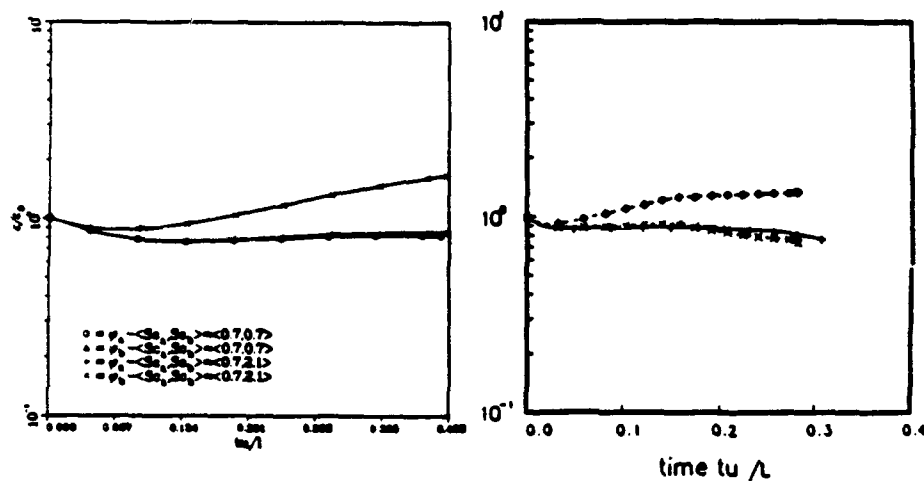


Figure 3: Evolution of scalar dissipation rates with $Da=2.5$ (SC3 and SC4). Present study (left); Jiang's data (right).

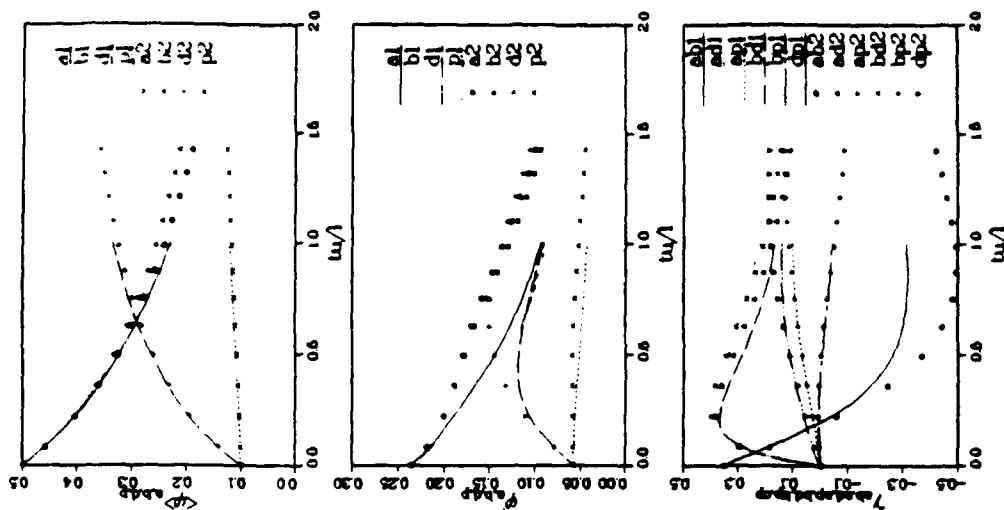


Figure 4: Evolution of scalar means, variances and $\gamma_{i,j}$ with the same reaction rates ($Da_1 = 1.0$, $Da_2 = 0.1$) but different Reynolds number $Re_\lambda = 21.69$ (v3pb-s2c3)(line) and $Re_\lambda = 150$ (v4pb-s2c3)(symbol).

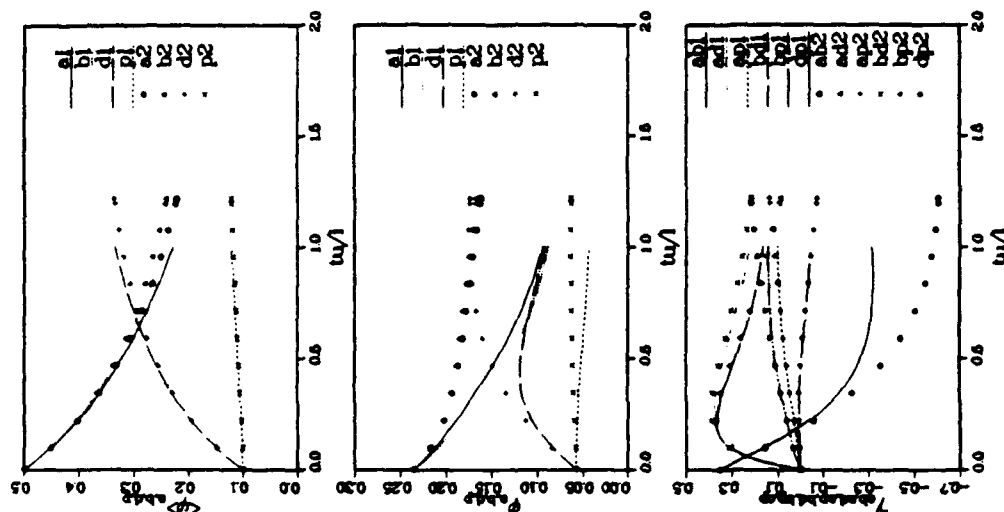


Figure 5: Evolution of scalar means, variances and $\gamma_{i,j}$ with the same reaction rates ($Da_1 = 1.0$, $Da_2 = 0.1$) but different Schmidt number $Sc, = 1.0$ (v3pb-s2c3)(line) and $Sc, = 100.0$ (v3pb-s2c3)(symbol).

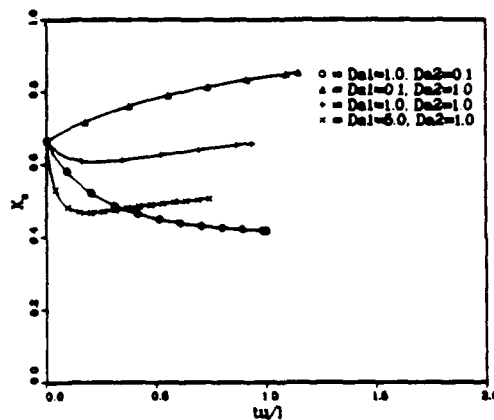


Figure 6: Evolution of X , under different Damköhler number ratios (v3pb-s2c3). Present study (upper); DNS (lower).

A LINEAR EDDY SUB-GRID MODEL FOR TURBULENT REACTING FLOWS: APPLICATION TO HYDROGEN-AIR COMBUSTION

(To Appear In *Proceedings of the 24th Symposium (International) on Combustion*, 1992)

Patrick. A. McMurtry
University of Utah
Salt Lake City, UT 84112

Suresh Menon
Quest Integrated, Inc.
Kent Washington

Alan R. Kerstein
Sandia National Laboratories
Livermore, CA 94550

ABSTRACT

A new sub-grid mixing model for use in large eddy simulations of turbulent combustion is presented and applied to a hydrogen-air diffusion flame. The sub-grid model is based on Kerstein's *Linear Eddy Model* (*Comb. Sci. Tech.*, 60, 1988). The model is first used to predict the mixing of a conserved scalar in a turbulent shear flow. The model correctly predicts the behavior of the pdf of the scalar field and displays a non-marching peak at the preferred mixture fraction as the shear layer is traversed. It is then illustrated how a reduced chemical mechanism can be implemented within the linear eddy subgrid model formulation. The model is used to predict NO formation in hydrogen-air diffusion flame using a reduced chemical mechanism involving nine reactive scalars.

1. INTRODUCTION

Conventional turbulent mixing models based on gradient diffusion assumptions are not capable of accurately predicting mixing and reaction rates in most practical combustion devices. Furthermore, at the small scales, most conventional models make no distinction between turbulent convection and molecular diffusion. This distinction is critical for the accurate description of the mixing and reaction process. In addition, it is known that turbulent mixing and entrainment processes in shear flows are dominated by unsteady large scale vortical motions. The spatial and temporal evolution of these large scale structures is difficult to model and must therefore be explicitly computed for accurate predictions.

Modeling the subgrid scalar mixing in turbulent flows provides challenges not present in subgrid models for momentum transport. Turbulent mixing, and particularly reaction, is an inherently small-scale process, and any predictive scheme must contain a description of the flow field down to the diffusion scales. This is much more stringent than the resolution requirement for modeling momentum transport, where the small scales basically provide dissipation for the large scales. As such, subgrid models for momentum transport which utilize various formulations of a subgrid eddy viscosity can be expected to give reasonable predictions of the large scale transport.

In this paper, a new subgrid modeling technique is described for use in large eddy simulations of turbulent mixing and reaction. In particular, a model for mixing and chemical reactions at the subgrid level is developed based on the Kerstein's^[1-3] *linear eddy* approach. A unique feature of this model is the separate treatment of *turbulent convection* and *molecular diffusion* at the smallest scales of the flow. This distinction is critical for predicting the small scale mixing process and capturing Schmidt number dependency and the effects of finite rate reaction. The model potentially has the capability to treat reacting and non-reacting flows at both low and high Mach numbers. Thus, it should be applicable to many reacting flow fields of interest.

The model is first applied to mixing of a conserved scalar in a turbulent shear flow. To test the subgrid mixing model, the velocity field is described by an analytical function describing vortex rollup in a shear flow. Turbulent fluctuations are added to the velocity field at each time step. Thus, the velocity field is taken as an input, and is not computed directly. This allows the testing and validation of the subgrid model without the complication of simultaneously solving for the velocity field. The subgrid model is then applied to a hydrogen-air diffusion flame. Predictions of combustion radicals as well as major species are computed.

In the following section, a basic description of the linear eddy model is given. Next, the implementation of the linear eddy model as a subgrid model for use in large eddy simulation is presented. In section 3.1, the model is applied to mixing of a conserved scalar, while the hydrogen-air combustion problem is treated in section 3.2.

2. MODEL FORMULATION

2.1 The Linear Eddy Model

Turbulent mixing can be envisioned as consisting of two distinct processes: 1) turbulent stirring, and 2) molecular diffusion. The unique aspect of the linear eddy model is that this distinction is retained at all length scales of the flow by resolving all relevant length scales. The model is formulated in one spatial dimension, allowing fully resolved computations even for relatively high Reynolds number flows - a computationally unfeasible task in two and three dimensions.

In the linear eddy model, the processes of molecular diffusion and turbulent stirring are treated as described below. Diffusion is simply implemented by the numerical solution of the diffusion equation over the linear domain for each species k ,

$$\frac{\partial \phi_k}{\partial t} = D_k \frac{\partial^2 \phi_k}{\partial x^2}. \quad (1)$$

The scalar field is regularly updated during a simulation to account for molecular diffusion.

The key feature of the model is in the manner in which turbulent convection is treated. This is implemented in a stochastic manner by random, instantaneous rearrangements of the scalar field along the line. Each event involves spatial redistribution of the species field within a specified segment of the spatial domain. The size of the selected segment represents the eddy size, and the distribution of eddy sizes is obtained by applying Kolmogorov scaling laws. In this model, rearrangement of a segment of size l represents the action of an eddy of size l . A detailed description of the rearrangement events is given in Ref. 3.

The rearrangement events are specified by two parameters; λ , which is a rate parameter with dimensions $[L^{-1}t^{-1}]$, and $f(l)$, which is a pdf describing the length scale distribution. The value of these parameters is determined by recognizing that the rearrangement events induce a random walk of a marker particle on the linear domain. Equating the diffusivity of the random process with scalings for the turbulent diffusivity provides the necessary relationships to unambiguously determine λ and $f(l)$. For a high Reynolds number turbulent flow described by a Kolmogorov cascade, the result is³

$$f(l) = \frac{5}{3} \frac{l^{-8/3}}{\eta^{-5/3} - L^{-5/3}} \quad (2)$$

$$\lambda = \frac{54}{5} \frac{\nu Re_L}{L^3} \left(\frac{L}{\eta} \right)^{5/3} \quad (3)$$

where η is the Kolmogorov scale and L is integral scale.

Given an initial scalar distribution, scalar redistributions (turbulent mixing) are carried out governed by the parameters described above, while molecular diffusion is implemented at each time step according to the discretized form of Eq. 1.

This formulation allows one to resolve *all* relevant length and time scales for flows of practical interest.

The model was originally developed to investigate the qualitative mixing properties of turbulent flows and has so far been applied as a stand-alone model in application to homogeneous turbulent flows,^{1,3} planar mixing layers,² and turbulent jets.⁴ The important qualities of this model stem from the fact that the basic physics of turbulent mixing are incorporated. Molecular diffusion is treated in a deterministic manner by numerical solution of the diffusion equation, and turbulent convection is modeled in a physically sound manner by the stochastic scalar rearrangement events. The distinction between molecular diffusion and turbulent convection, particularly at the subgrid scales, is crucial to the accurate description of the evolution of the species field, especially when chemical reactions are involved. This distinction is not made in most turbulent mixing models.

2.2 Implementation of the subgrid model in an LES code

The classical implementation of large eddy simulations involves filtering out the small scales of motion, and explicitly computing the larger scale motions which can be resolved on a numerical grid. The modeling process is then concerned with modeling only the small scale motions, and their interactions with the large scales. Subgrid models for momentum transport have primarily been based on ideas of a subgrid eddy viscosity. The eddy viscosity idea is a reasonable approach to the extent that the small scale motions primarily provide a mechanism for energy dissipation and transfer at the larger scales. For turbulent mixing and reaction processes, however, it is not possible to characterize the overall statistical state of the scalar field in such a manner. This is a result of the subtle interactions between turbulent stirring, molecular diffusion, and chemical reaction at the smallest scales of the flow. A reliable subgrid model should therefore attempt to provide a description of these different physical mechanisms, even at the subgrid level.

The linear eddy model has proven to be an effective tool for studying scalar field mixing processes by retaining this distinction at all relevant length scales. In the previous applications, the model has been implemented as a stand-alone mixing model in which the statistics of the velocity field (i.e., turbulent diffusivity, D_t , and length scale, L) have been assumed inputs. The previous applications of the linear eddy model suggest its potential as the basis for developing a subgrid model to be used in large eddy simulations.

The procedure developed here for implementing the linear eddy model as a subgrid model involves performing separate linear eddy calculations in each large eddy or computational grid cell. With the Reynolds number of the flow as an input parameter, classical scaling arguments lead to an approximation for the range of eddy sizes in the flow, and thus, the range of eddy sizes in the subgrid range. Because the small scales have much higher frequencies than the large scales, a number of scalar rearrangement events, along with the Fickian diffusion process at the subgrid level, must be performed between each time step in the LES.

Within each large eddy cell, or computational grid cell, the linear eddy simulation corresponding to that cell represents mixing and diffusion at the unresolved scales. No directional dependency is associated with the linear eddy simulation. In this situation the linear domain may be viewed as a time varying space curve aligned with the local scalar gradient. This interpretation is consistent with the action of the rearrangement events, which always result in an increase in scalar gradient.

The unresolved length scales can thus be accounted for with a one dimensional line of scalar information. Therefore, if the ratio of the smallest relevant length scale to the large eddy grid-cell spacing is N , the scalar information can be computed with an array of size N , irrespective of large eddy grid dimensionality. Full simulations in two dimensions would require array of N^2 , and in three dimensions, N^3 . The economy of this method compared to direct simulation of the multidimensional convection-diffusion-reaction equations is apparent.

Besides the rearrangement events (turbulent convection) and molecular diffusion which are treated in the linear eddy simulation associated with each grid cell, other events must be carried out to couple the subgrid mixing process to the large eddy transport and to the mixing processes occurring in neighboring grid cells. These events are associated with the convective transport across each grid cell (large scale transport) by means of the resolvable velocity field. In the present model this is carried out by *splicing* events, in which mixing processes associated with neighboring grid cells undergo a transfer of material based on the scalar flux across each grid cell interface, as computed from the resolvable grid scale velocity. This transfer is implemented by excising a portion of the linear eddy domain associated with the donor grid cell and splicing it into the linear eddy domain associated with the receiver grid cell. In Fig. 1 the processes involved in the linear eddy subgrid algorithm are illustrated.

In addition to the resolved velocity field, random turbulent fluctuations will result in additional scalar transport across grid cells. The flux across each grid cell is modified to account for this flux by adding the subgrid rms velocity vectorially to the resolvable velocity field. The direction of this perturbation is randomly chosen at each time step, so the mean flux is not affected by this fluctuating component.

In summary, the subgrid implementation consists of two processes: 1) the linear eddy calculations in each grid of the computational domain, and 2) the splicing events which account for the convective flux of the scalar field across computational grid cells. An explicit species transport equation is not solved, since the large scale convection

is accounted for by the splicing events and the small scale convection and diffusion is modeled by the linear eddy simulations.

It is noted here that the splicing events associated with the exchange of scalar material among grid cells can in principle result in an additional, unphysical contribution to the turbulent diffusivity through the generation of discontinuities in the scalar field. However, the frequency of scalar rearrangement events scales as $U Re^{5/4} / \Delta$ while the frequency of splicing events is the inverse of the large eddy time step, on the order of U / Δ , where U is the large scale convective velocity and Δ is the grid size. For high Reynolds number flows, the rearrangement events occur at a much higher rate. Therefore, the spurious scalar dissipation caused by splicing events is not statistically significant.

3. RESULTS

3.1 Scalar Mixing

The linear eddy subgrid model has been implemented using a deterministic velocity field representing vortex roll-up in a shearing flow. A deterministic, analytically explicit velocity field is used to reduce computational requirements and to isolate the characteristics of the subgrid mixing model. However, the subgrid model implementation is the same as it would be with a full Navier-Stokes solver. The assumed velocity field is

$$u(x, y, t) = \left(\frac{\Gamma}{2a} \right) \frac{\sinh \left(\frac{2\pi y}{a} \right)}{\cosh \left(\frac{2\pi y}{a} \right) - \cos \left(\frac{2\pi x}{a} \right)} - \left(\frac{\Gamma}{2\pi} \right) \frac{y}{x^2 + y^2} e^{-(x^2 + y^2)/4\nu t} \quad (4)$$

$$v(x, y, t) = \left(-\frac{\Gamma}{2a} \right) \frac{\sin \left(\frac{2\pi x}{a} \right)}{\cosh \left(\frac{2\pi y}{a} \right) - \cos \left(\frac{2\pi x}{a} \right)} - \left(\frac{\Gamma}{2\pi} \right) \frac{x}{x^2 + y^2} e^{-(x^2 + y^2)/4\nu t} \quad (5)$$

This velocity field has been used previously in studies of molecular mixing by Cetegen and Sirignano.⁵ The subgrid turbulent fluctuations were specified as 5% of the mean velocity difference across the mixing layer. In more comprehensive calculations, the subgrid turbulent kinetic energy would, in general, vary from location to location in the flow. The subgrid rms velocity would in this case be determined from the subgrid model used to determine the momentum transport in the flow.

The domain is chosen to extend from $[-\pi, \pi]$ in both the x - and y -directions, with an initial scalar field of 0 for $y \leq 0$ and 1 for $y > 0$. The velocity field is resolved on a 32×32 grid. A linear eddy simulation with a maximum array size of $N = 100$ elements is implemented for each grid cell, giving an effective Reynolds number of 5000 for the simulations. (This allows for 6 linear eddy elements to resolve the Kolmogorov scale.)

The initial scalar field consists of $\phi = 0$ for all x and $y > 0$ and $\phi = 1$ for all x and $y \leq 0$. The development of the scalar field with time is shown in Fig. 2. This figure is based on a representative scalar concentration for each grid cell obtained by averaging over the linear eddy array for that cell. The characteristic roll-up structure

is reproduced by the exchange of scalar elements across grid surfaces. These exchange (splicing) events are seen to accurately represent the large scale roll-up of the shear layer

The statistical state of the scalar microfield within each grid cell is represented by the linear eddy model. The pdf of the scalar field across the mixing layer (Fig. 3) gives some indication of the effects of the small scales. The pdf was computed at several transverse locations across the mixing layer at a time of $t = 6$. The pdf's at each transverse location were computed by sampling the data in each grid cell over all x (streamwise direction) for a constant value of y (vertical coordinate). Beside the two peaks in the pdf at 0 and 1, (corresponding to the unmixed free stream concentrations), a broad, third peak can be seen in the distribution. This corresponds to a mixed fluid concentration which is relatively independent of the transverse location. The qualitative features of this pdf compare favorable with those computed for laboratory experiments.⁶

3.2 Hydrogen-Air Flame

Chemical reactions within the linear eddy model can be accounted for in a straightforward manner by including a reaction term in the diffusion equation (Eq. 1). An additional linear eddy array must be used to account for each of the separate chemical constituents. Although this approach is fundamentally sound, practical complications arise when several chemical species must be tracked and when the reaction rates cover a wide range of time scales. In the work performed for this study some of the complications associated with treating full chemical kinetics are avoided by employing a reduced chemical mechanism for the hydrogen-air flame as used by Chen and Kollmann.^{7,8} The reduced mechanisms can be conveniently incorporated into the linear eddy subgrid model formulation. In the hydrogen-air problem treated here, ten elementary reactions are considered. The total number of scalars in the reaction mechanism is 10, of which seven are active chemical species (H_2 , O_2 , H_2O , O , H , OH , HO_2), plus temperature, density and pressure.

The advantage of the reduced mechanisms is that the number of scalars that need to be tracked during the simulation is minimized. In the simplified scheme, three scalars are tracked throughout the simulation: the mixture fraction, ϕ , a progress variable describing the extent of reaction, η , and the NO concentration. The reaction mechanisms used are solved beforehand to generate a look-up table that can be used to interpolate for the species whenever required. The mechanism used to model the formation of NO in the H_2 -air combustion process is based on thermal pathways characterized by the well-known Zeldovich mechanism. A detailed description of the reaction mechanisms and reduced mechanism formulation used in this work can be found in Ref. 9.

The simulation starts from mixture fraction values corresponding to air in the upper stream ($y > 0$), and hydrogen in the lower stream ($y < 0$). The velocity field given by equations 4 and 5 is used. Combustion is initiated by setting several elements of the linear eddies located along $y = 0$ equal to their stoichiometric values ($\phi = 0.028$) and equilibrium chemical states.

The mixture fraction evolves as shown in Fig. 2. At this stage of model development, effects of combustion heat release on the velocity field and on transport properties has not been addressed, although such effects can be accounted for within the linear eddy model.⁹ The temperature field at $t = 6$ is shown in Fig. 4, and the NO concentration at the same time is shown in Fig. 5. The stoichiometric temperature of 2500K occurs across the flame front, although the temperature is not uniform across the flame front. The flame is located at the outer regions of the vortex, extending into the air side

of the shear layer. The flame penetrates into the air side of the stream because the stoichiometric mixture fraction is less than 0.5. (The free stream reactants for this test are hydrogen and ambient air, respectively.)

The concentration of OH is shown in Fig. 6. Comparison between Figs. 4 and 6 indicate that OH production occurs where the temperature is a maximum. However, accumulation of NO over time is more widely distributed over the mixing region.

4. Discussion

The implementation of the linear eddy model as a subgrid model has been shown to realistically represent important features of the turbulent mixing process. This extension of the linear eddy model from its original formulation as a one-dimensional, stand-alone model is significant as it allows for a realistic description of the scalar field at the smallest scales of the flow for multi-dimensional flow simulations. It has also been shown that rather complex chemical mechanisms can be incorporated into the model formulation in a relatively straightforward manner.

For full three-dimensional large eddy simulations, computational requirements will become an issue, as a large one-dimensional array is needed to account for the scalar field distribution within each grid cell. Furthermore, regardless of the form of the subgrid model, numerical integration of reaction mechanisms will continue to be severe as the sophistication of the chemical models implemented in the simulations is increased. However, it should be noted that the present model formulation is ideally suited for implementation on parallel processing machines. Most of the work in the mixing subgrid model is confined to individual linear eddy arrays. If a separate processor is used for each linear eddy, communication between processors is necessary only during the large scale convection process - an infrequent event with respect to the rearrangement and diffusion processes ongoing within each cell.

Acknowledgment

This work was supported in part by NASA AMES Research Center under Contract NAS2-13354, the Division of Engineering and Geosciences, Office of Basic Energy Sciences, U.S. Department of Energy, and the Advanced Combustion Engineering Research Center.

References

1. Kerstein, A.R. (1988) "Linear Eddy Model of Turbulent Scalar Transport and Mixing," *Comb. Sci. and Tech.* Vol. 60, pp. 391-421.
2. Kerstein, A.R. (1989) "Linear Eddy Modeling of Turbulent Transport II: Application to Shear Layer Mixing," *Comb. and Flame*, Vol. 75, pp. 397-413.
3. Kerstein, A.R. (1991) "Linear Eddy Modeling of Turbulent Transport VI: Microstructure of Diffusive Scalar Fields," *J. Fluid Mech.*, Vol. 231, pp. 361-394.
4. Kerstein, A.R. (1990) "Linear Eddy Modeling of Turbulent Transport III: Mixing and Molecular Diffusion in Jets," *J. Fluid Mech.*, Vol 216, pp. 411-435.
5. Cetegen, B.M. and Sirignano, W.A. (1988) "Study of Molecular Mixing and a Finite

Rate Chemical Reaction in a Mixing Layer," *Twenty-Second Symposium (International) on Combustion*/The Combustion Institute.

6. Koochesfahani, M.M. and Dimotakis, P.E. (1986) "Mixing and Chemical Reaction in a Turbulent Liquid Mixing Layer," *J. Fluid Mech.*, Vol. 170.
7. Chen, J.-Y., and Kollmann, W. (1990) "Chemical Models for Pdf Modeling of Hydrogen-Air Nonpremixed Turbulent Flames," *Combust. Flame*, Vol. 79, pp. 75-99.
8. Chen, J.-Y., and Kollmann, W. (1991) "Pdf Modeling and Analysis of Thermal NO Formation in Turbulent Nonpremixed Hydrogen-Air Jet Flames," submitted to *Combust. Sci. Tech.*
9. Menon, S. (1991) "A New Unsteady Mixing Model to Predict NO_x Production During Rapid Mixing in a Dual-Stage Combustor," Phase I Final Report Prepared for NASA Under Contract NAS3-26242.

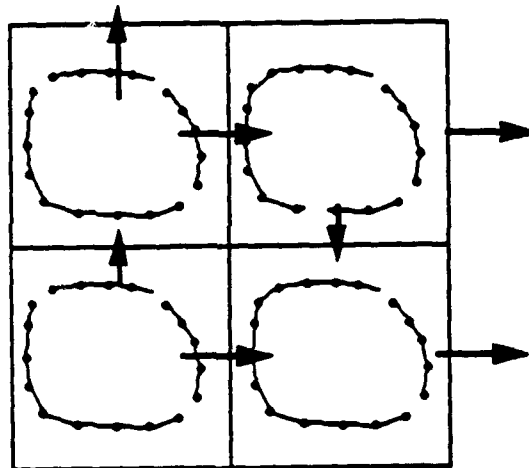


Figure 1. Schematic illustration of linear eddy subgrid model. The one-dimensional elements within each grid cell represent the on-going linear eddy calculations that are performed in each cell. At each large eddy times step, linear eddy elements are exchanged across neighboring grid cells, accounting for large-scale transport. The arrows indicate the components of convective flux across the grid cells, which determines the amount of scalar information contained in the linear eddies that is exchanged at each large eddy time step.

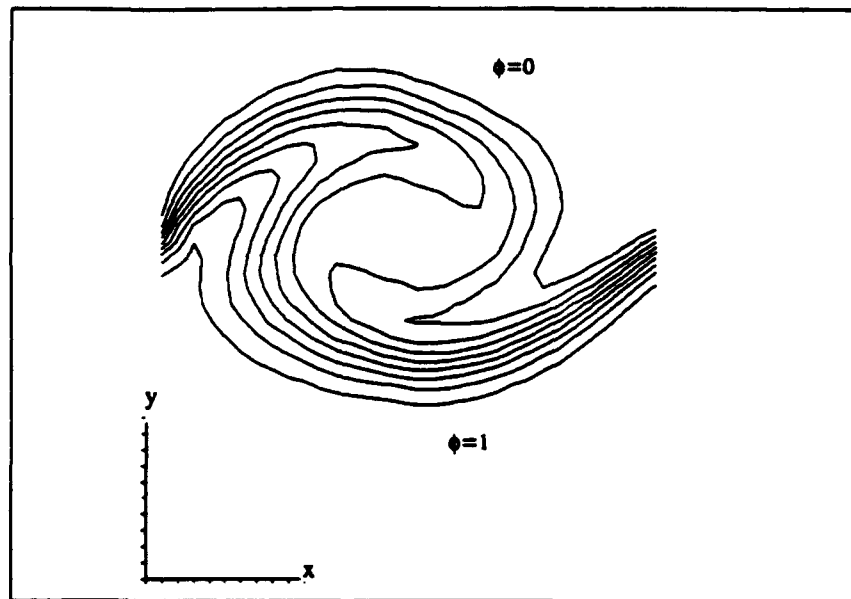
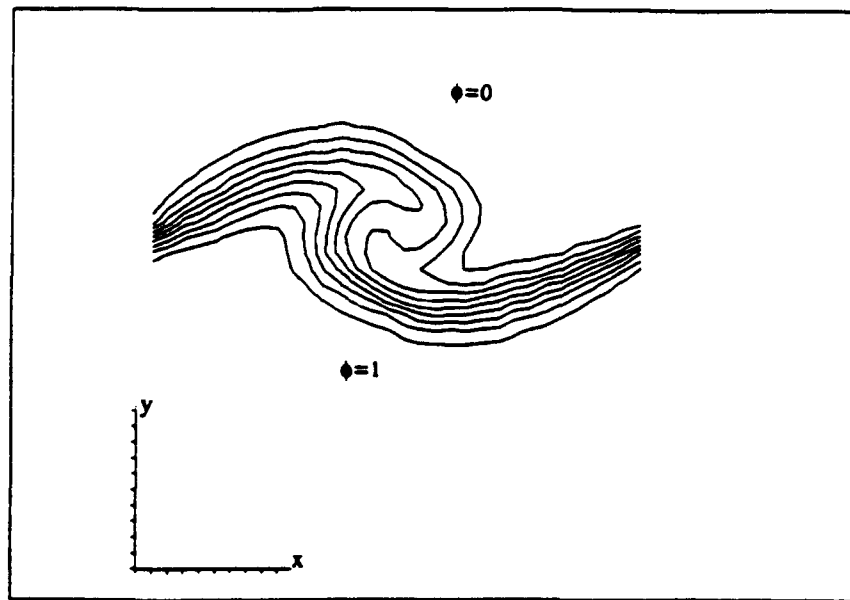


Figure 2. Contours of grid averaged mixture fraction. Within each grid cell, the linear eddy elements are averaged to give the local scalar average value for each grid cell. a) $t=2$, b) $t=6$.

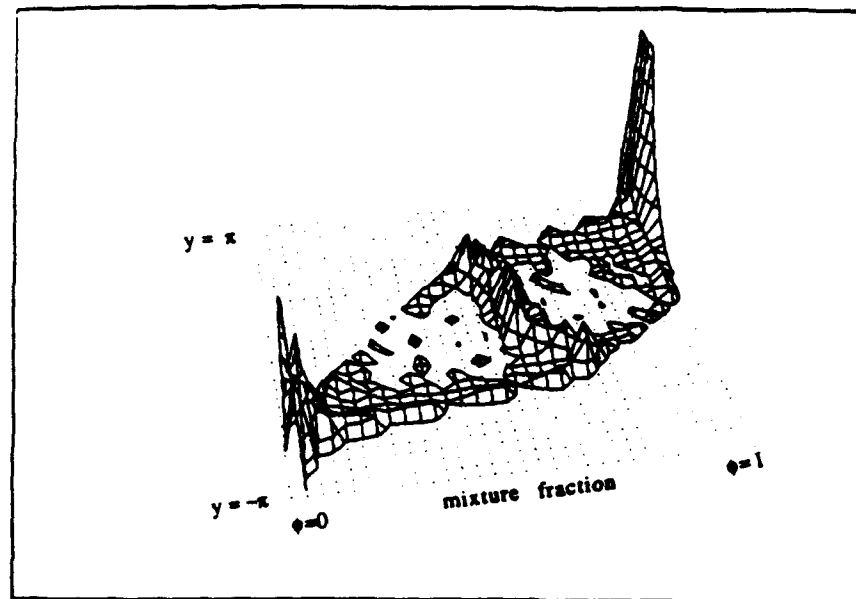


Figure 3. Pdf of scalar value at several transverse locations across the shear layer.

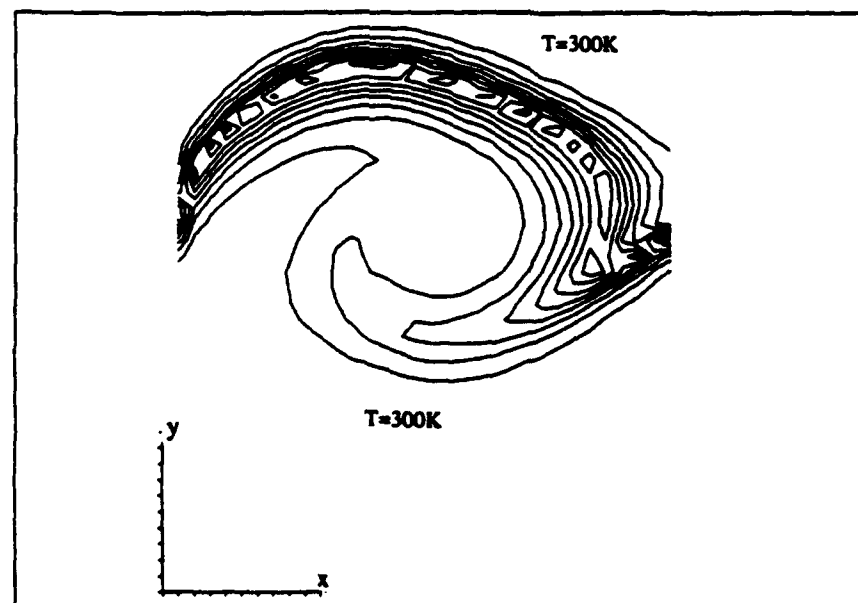


Figure 4. Temperature concentration contours for the hydrogen-air flame at time $t=6$.

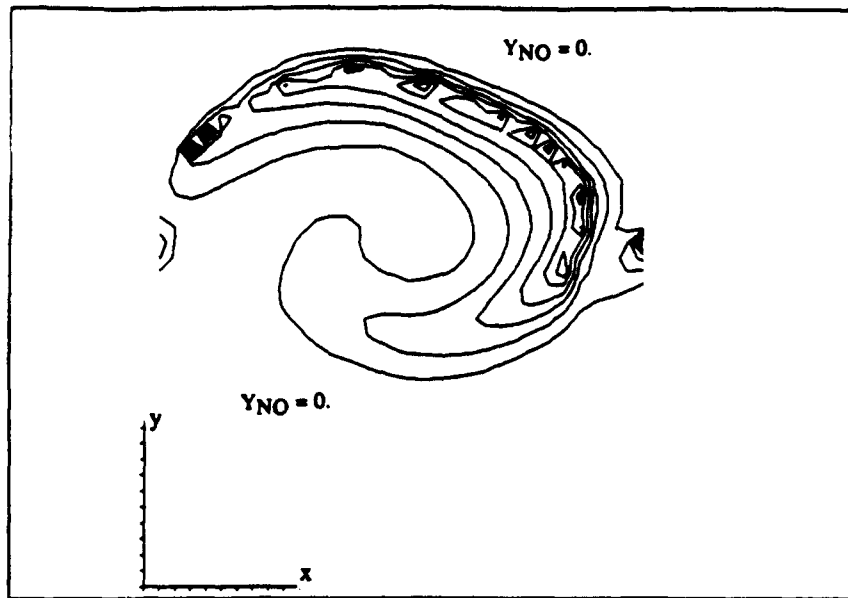


Figure 5. NO Concentration, $t=6$.

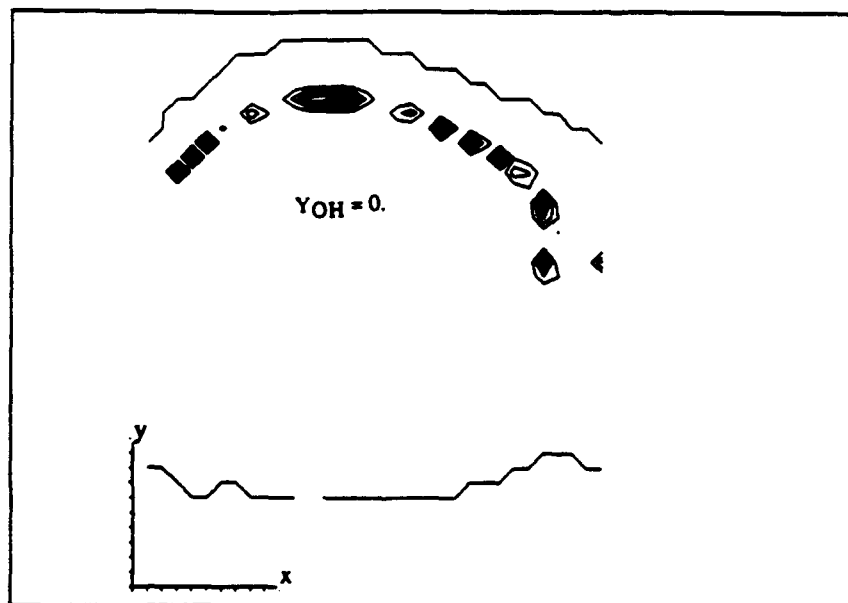


Figure 6. OH concentration, $t=6$

THE EFFECT OF CHEMICAL REACTIONS ON TURBULENT DIFFUSIVITIES

H.L. Toor

Department of Chemical Engineering
Carnegie Mellon University
Pittsburgh, PA 15213

ABSTRACT

A mixing length model is used to explain and model the recently observed (Bilger *et al.*, 1991) effect of chemical reactions on turbulent diffusivities. This coupling between microscale reactions and macroscale mixing occurs because reaction rate is a quasi-transferable property which causes more reaction in fluctuating fluid lumps leaving regions of high rate than low rate. The net effect is to either raise or lower reactant diffusivities depending upon a characteristic macromixing time and the rate at which the mean reaction rate changes with mean concentration.

$$\frac{\epsilon_A}{\epsilon} = 1 - \tau_M \frac{d\bar{r}_A}{d\bar{C}_A}$$

The model shows observed qualitative behavior and also appears to be in quantitative agreement with much of the existing data. It adds an apparent flux, $\epsilon \tau_M \nabla \bar{r}_i$, to the convective diffusion equations which can either enhance or hinder the normal turbulent fluxes.

Two kinds of closure problems arise when the convective diffusion equations for a dilute, reacting Fickian system with non-linear chemistry are averaged to give

$$\frac{\partial \bar{C}_i}{\partial t} + \bar{y} \cdot \nabla \bar{C}_i = \nabla \cdot (D_i \nabla \bar{C}_i - \bar{y} \bar{C}_i) - \bar{r}_i, i = A, B, \dots \quad (1)$$

The closure problem in the reaction term follows from non-linear chemical rate laws which lead to correlated concentration covariance terms—terms which decrease reaction rates in non-premixed systems. These *micromixing* (or more accurately, *microsegregation*) effects have been studied in one dimensional systems where they can have a very large effect on reaction rates and where models have been developed to handle them in such systems (Harada, *et al.*, 1962; Kattan and Adler, 1967; Mao and Toor, 1970; Toor, 1969; Treleaven and Tobgy, 1972; Mehta and Tarbell, 1983; Li and Toor, 1986; Baldyga and Bourne, 1989).

On the other hand the velocity-concentration covariance term, which has little effect in one dimensional systems, is more likely to dominate multidimensional systems like jets and wakes (Hanks, 1991). This term has a long history in non-reacting systems where it has been usefully modeled with a turbulent diffusivity (Taylor, 1915; Hinze, 1959; Tennekes and Lumley, 1983). Since the term is non-zero only in the presence of gradients of the time average concentration it describes *macromixing*. Because it apparently has the same significance in reacting as well as non-reacting systems it is tempting to treat it with the normal turbulent diffusivity, i.e. to assume that the reaction does not affect the turbulent diffusivity. This is almost surely true with slow enough reactions, but is less likely with faster reactions—reactions whose half lives are comparable to or less than the integral time scale (Corrsin, 1974; Klimenko, 1992). Since recent measurements of Bilger *et al.* (1991) show a significant effect of faster reactions on turbulent diffusivities, the novel effects need to be treated in order to close Eq. (1). A way around this coupling of the reaction with the turbulent diffusivity (*micro-macro coupling*) is to dispense with both terms and recognize that both effects are different manifestations of imperfect mixing, as is done in the recent conditional mean methods (Bilger, 1991; Klimenko, 1990). The alternative, adopted here, is to accept the coupling and relate turbulent diffusivities in a reacting system to both the reaction and the turbulent diffusivities in the analogous non-reacting (passive) system.

The Experiment

Bilger *et al.* (1991) studied the reaction between non-premixed dilute nitric oxide (reactant A) and dilute ozone (reactant B) behind a splitter plate with grid generated turbulence. With Damköhler Numbers of 0.3 and 1.8 they deduced turbulent diffusivities for the reactants as well as the passive non-reacting value and their non-dimensional diffusivity results for a Reynolds Number (based on grid mesh and mean velocity) of 11,700 are reproduced in Figure 1. Their non-dimensional mean concentration and reaction rate data are also reproduced in Figures 2 and 3. Both their nomenclature as well as that used here are shown. All the data are 21 grid spacings downstream. They pointed out that the turbulent diffusivities for the reactants "are substantially higher than those for the mixture fraction on the side of the layer from which the reactant comes but are much lower on the other side. In this latter region the diffusivities also show a dependence on N_D with values for high N_D being smaller than those for low N_D ." (The effects are seen more clearly in Figures 6 through 9.)

It was subsequently shown that for the particular chemistry which was used, $A+nB \rightarrow \text{products}$ (Toor, 1991), that the three turbulent diffusivities are related by

$$(\epsilon_A - \epsilon) \nabla \bar{X}_A = \beta (\epsilon_B - \epsilon) \nabla \bar{X}_B \quad (2)$$

Equation (2) is qualitatively consistent with this non-premixed experiment where the gradients are of opposite sign although, as will be seen, some of the data do not quantitatively satisfy the equation. Equation (2) *does*

suggest that the individual reactant turbulent diffusivities will depend upon the mean concentration gradients. It is explicit relationships for these individual reactant diffusivities which are needed for closure of Eq. (1) and we will use a mixing length model (Taylor, 1915; Hinze, 1959; Tennekes and Lumley, 1983) to attempt to do so.

A Qualitative Explanation

We first show that the qualitative features of Bilger *et al.*—that in their particular experiment reactant turbulent diffusivities are increased on the side from which they come and are decreased on the other side—are predicted by a mixing length model which also brings out the underlying physical cause. (The Damköhler Number effect is more easily seen in the next section.)

Figure 4 is a sketch of data of Bilger *et al.* which shows the mean concentrations and reaction rate as a function of position transverse to the main flow. The time average velocity in the transverse direction is zero so transport in this direction is caused by velocity fluctuations which exchange lumps of fluid between regions of different concentrations (large scale molecular transport is negligible). Thus in the absence of reaction this model leads to a positive turbulent diffusivity which depends upon the intensity of the velocity fluctuations and the distance (mixing length) traveled by the lumps before they mix with the surrounding fluid, i.e. before they are *micromixed*. During this motion, since the lump is not in equilibrium with its environment it can exchange a passive tracer with the surrounding fluid by molecular diffusion leading to an effect of molecular diffusivity on turbulent diffusivity. Any *micromixing* inside a non-uniform lump, since it conserves material, could only affect the macro-transport indirectly by affecting the interchange between the lump and its surroundings and even this "leak" will normally be small (Tennekes and Lumley, 1983). (It is this small interchange which leads to the idea of transferable properties and mixing length models.) However a *reaction* which takes place *inside* a lump, a microscale phenomenon, does *not* conserve material even in the absence of a leak, and, as will be seen, is the apparent cause of the observed effects.

Consider the situation in Figure 4, focus on reactant A on the right side of the centerline and consider two imaginary parallel planes perpendicular to the y direction and separated by a small distance. Lumps are interchanging between these planes, but now a reaction takes place *inside* the lumps—in this case removing reactant A. Because the integral scale lumps are much larger than the Kolmogorov scale, the microscale at which the reaction takes place, lumps will sample the mean reaction rate as well as mean concentration of their birthplace. Consequently lumps leaving from the right plane will leave on the average with the time average concentration and time average reaction rate at that plane so less A will reach the left hand plane in that lump than would occur in the absence of reaction. Similarly, lumps leaving the left plane on the average leave with the time average concentration and reaction rate in that plane and this lump will carry less A to the right than it would if there were *no* reaction. But note, however, that if the reaction rate in the left and right leaving lumps were the same during their flight the net transport and hence turbulent diffusivity would *not* be affected by the reaction.

The transport and turbulent diffusivity is affected because the reaction rates *are* different and they are different because of the small leakage from the lumps during their flight so the initially different reaction rates *persist*. (If conversion in a lump is small, rate will be essentially conserved, but even if not the two average rates will differ so long as the lumps do not immediately equilibrate with their surroundings. Reaction rate is in this sense at least a *quasi-transferable* property.)

The right leaving lumps leave with a lower reaction rate (see Figure 4) and this lower rate persists so less A is lost from these lumps than is lost from the left leaving lumps which start with and continue with a higher reaction rate as they move right. Hence as observed experimentally (Figure 1), the net transport from right to left is increased—the turbulent diffusivity of A on the right—the side from which A comes is *increased* by the reaction as observed, but it is increased because of the persistence of the reaction rate bias—it is not an eddy leak—it is a true microscale effect *within* the lumps.

On the left side of the centerline the gradient of the mean concentration of A and its rate are both in the *same* direction. Again consider two parallel planes on the left of the centerline. Now left leaving lumps are reacting more slowly than right leaving lumps so more A is lost by the right leaving lumps than the left leaving ones. Hence less A is transported down the mean gradient—the turbulent diffusivity is *decreased* by the reaction—again as observed. Reactant B merely mirrors the behavior of A—same arguments and conclusions. Although this elementary mixing length viewpoint is qualitatively in accord with experiment and affords a simple explanation for the micro-macro coupling, practice requires a quantitative result which is presented in the next section.

Quantitative Development

We will use unidirectional definitions of the turbulent fluxes

$$\bar{N} = \overline{v'C'} = -\epsilon \frac{d\bar{C}}{dy} \quad (3)$$

$$\bar{N}_A = \overline{v'C'_A} = -\epsilon_A \frac{d\bar{C}_A}{dy} \quad (4)$$

If 2λ is the mixing length, lumps cross a plane carrying their transferable properties from within distances of 2λ on either side of the plane, so the *average* distance of travel to the plane is λ if statistical properties do not change over the distance 2λ . Hence in order to relate ϵ and ϵ_A we consider the two imaginary planes discussed earlier (now drawn in Figure 5) to be the distance 2λ apart and determine the net flux from left to right crossing a parallel plane midway between the two planes. All the lumps crossing the midplane are thus taken to have traveled the average distance λ .

A lump moving with the velocity u from left to right carries $u \bar{C}_{A1}$ moles A/time area to the right and the amount carried across the midplane is given by

$$u \left(\bar{C}_{A1} - \frac{\lambda}{\bar{u}} r_{A1} \right) \quad (5)$$

It is assumed that there is no leak from the lump and that r_{A1} is the average reaction rate in these left leaving lumps based on the average flight time λ/\bar{u} .

The amount of A crossing the midplane in right leaving lumps is then

$$u \left(\bar{C}_{A2} - \frac{\lambda}{\bar{u}} r_{A2} \right)$$

so for two equal and opposite moving lumps the net flux across the midplane is

$$N_A = u \left[(\bar{C}_{A1} - \bar{C}_{A2}) - \frac{\lambda}{\bar{u}} (r_{A1} - r_{A2}) \right] \quad (6)$$

As usual, for small λ (see Tennekes and Lumley (1983) for other justifications)

$$\bar{C}_{A1} - \bar{C}_{A2} = -2\lambda \frac{d\bar{C}_A}{dy} \quad (7)$$

There are two opposing tendencies within a lump—conversion *decreases* reaction rate while micromixing *increases* rate. To avoid the difficult problem of evaluating the net effect we assume negligible rate change during the lifetime of any lump. Then for small λ

$$r_{A1} - r_{A2} = -2\lambda \frac{dr_A}{dy} \quad (8)$$

Combining (7), (8) and (9) and averaging

$$\bar{N}_A = -2u\lambda \left[\frac{d\bar{C}_A}{dy} - \frac{\lambda}{\bar{u}} \frac{dr_A}{dy} \right] \quad (9)$$

When r_A is set equal to zero, Eqs. (3) and (9) identify $2u\lambda$ as ϵ so

$$\bar{N}_A = -\epsilon \left[\frac{d\bar{C}_A}{dy} - r_M \frac{dr_A}{dy} \right] = -\epsilon_A \frac{d\bar{C}_A}{dy} \quad (10)$$

The flux is enhanced or diminished, depending upon the relative signs of the gradients of \bar{C}_A and \bar{r}_A .

Rearranging Eq. (10) gives the relationship between the two turbulent diffusivities which closes the macromixing term in Eq. (1).

$$\frac{\epsilon_A}{\epsilon} = 1 - \tau_M \frac{d\bar{r}_A}{d\bar{C}_A} \quad (11)$$

The non-dimensional form is

$$\frac{\epsilon_A}{\epsilon} = 1 - N_{DM} \frac{d\bar{R}_A}{d\bar{X}_A} \quad (12)$$

where the Damköhler Number which arises is the ratio of the flight time or characteristic *macromixing* time, $\tau_M = \frac{\lambda}{u}$, to the characteristic reaction time, τ_R .

$$N_{DM} = \frac{\tau_M}{\tau_R} \quad (13)$$

Equation (12) is presumably valid for any chemistry but if the reaction is described by the mass action law

$$r_A = k \bar{C}_A \bar{C}_B \quad (14)$$

then $\tau_R = 1/k C_{B0}$, $\bar{R}_A = \bar{X}_A \bar{X}_B$,

$$N_{DM} = \frac{\lambda}{u} k C_{B0} \quad (15)$$

and

$$\frac{\epsilon_A}{\epsilon} = 1 - N_{DM} \frac{d \bar{X}_A \bar{X}_B}{d \bar{X}_A} \quad (16)$$

The equation for B is

$$\frac{\epsilon_B}{\epsilon} = 1 - \frac{N_{DM}}{\beta} \frac{d \bar{X}_A \bar{X}_B}{d \bar{X}_A} \quad (17)$$

β appears in this equation because of the choice of N_{DM} made in Eq. (15).

This form is not particularly useful for an instantaneous reaction, but closure is not needed here since the solution to Eq. (1) at this limit is known in terms of the solution to the analogous non-reacting problem (Toor,

1962). This is known as the "Conserved Scalar" method in the combustion literature (Bilger *et al.*, 1991).

Equation (11) can also be derived by determining the effect of the reaction on the reactant concentration fluctuations. A reaction which consumes a reactant decreases positive fluctuations and enhances negative fluctuations. Equation (11) also follows from this viewpoint because of the persistence of the bias in the reaction rates.

Proceeding any further with Eq. (16) and (17) requires a micromixing model since

$$\overline{X_A X_B} = \overline{X_A} \overline{X_B} + \overline{X'_A X'_B} \quad (18)$$

However this is not needed with first order reactions which are unaffected by micromixing so Eq. (8) always overestimates the amount of reaction in the case. With

$$\bar{r}_A = k \bar{C}_A \quad (19)$$

Eq. (11) becomes

$$\frac{\epsilon_A}{\epsilon} = 1 - k \tau_M \quad (20)$$

The diffusivity is always decreased by the reaction because the reaction rate is always higher at the high reactant concentration.

This first order reaction is not very interesting in its own right, but it does allow examination of the approximation introduced by Eq. (8) since the reaction rate in a lump is now simply given by Eq. (19). The result obtained by summing the reaction effects in all lumps originating within a distance 2λ on either side of a given plane is

$$\frac{\epsilon_A}{\epsilon} = \frac{1 - (1 + 2k\tau_M) e^{-2k\tau_M}}{2(k\tau_M)^2} \quad (21)$$

so Eq. (20) is only valid for small values of the macro Damköhler Number, $k\tau_M$. Unfortunately this does not help much in determining the error in Eq. (11) for other kinds of reactions which are sensitive to micromixing.

Comparison with Experiment

Returning to Eq. (11) (or (12)) we first note that with its counterpart for reactant B it satisfies the consistency condition of Eq. (2) because $\bar{r}_B = n \bar{r}_A$ for the single step reaction. Secondly we observe that Eq. (12) has the correct overall behavior—it shows the behavior observed by Bilger *et al.* (1991)—for their experiment: (1) the reactant turbulent diffusivities are higher than the ordinary (passive) values on the side from which the reactant comes (because of the sign of $d\bar{r}_A/d\bar{X}_A$), (2) are *much* lower than the ordinary values on the other side (because the rate of change of reaction with concentration is *much* larger on that side), and (3) in this latter region

there is a Damköhler effect with diffusivity values for the high N_D smaller than for the low N_D (obvious from Eq. (12)).

Because τ_M is not precisely fixed by the model it would be reasonable to take τ_M as an adjustable parameter. However it is interesting to evaluate τ_M with measured quantities. The mixing length 2λ should be approximately the integral length scale (Tennekes and Lumley, 1984), \bar{u} the RMS velocity fluctuation, and since Bilger *et al.* (1991) has measured these values we can estimate a single value of τ_M from their measurements. Using the average measured integral scale of 0.25m and \bar{u} of 0.025 m/s (Saetran, 1989) gives an average micromixing time, τ_M , of 5.0s.

The macromixing Damköhler Number in Eq. (12) is related to that used by Bilger by

$$N_{DM} = \frac{\lambda}{M} \frac{\bar{u}}{\bar{u}} \frac{\beta}{1 + \beta} N_D$$

The mean velocity \bar{u} is 0.55 m/s and M is 0.32 m. $\beta = 0.94$ in the experiment with $N_D=1.81$ and 1.02 in the experiment with $N_D = 0.3$. Then for $N_D = 1.8$, $N_{DM} = 7.61$ and for $N_D = 0.3$, $N_{DM} = 1.30$.

We read \bar{R}_A , \bar{X}_A and \bar{X}_B off Figures 2 and 3, determined $\frac{d\bar{R}_A}{d\bar{X}_A}$ and $\frac{d\bar{R}_B}{d\bar{X}_B}$ by finite differences and then interpolated to obtain a value of $d\bar{R}_A/d\bar{X}_A$ for each reported value of $\hat{\epsilon}$. Equation (12) was then used to calculate $\hat{\epsilon}_A$ and Eq. (17) to calculate $\hat{\epsilon}_B$. Figures 6 through 9 compare these values with experiment. They all show $\hat{\epsilon}$ and both experimental and predicted values of $\hat{\epsilon}_A$ or $\hat{\epsilon}_B$ and $\hat{\epsilon}$.

Figures 6 and 7 are at the higher N_D of 1.81. In Figure 6 the experimental values of $\hat{\epsilon}_A$ left of the centerline are much lower than $\hat{\epsilon}$. We do not have an estimate of the uncertainty in these values, but the predictions of Eq. (12) captures this behavior surprisingly well, as it also does on the other side, the side from which A comes. There, Eq. (12) predicts a small increase in $\hat{\epsilon}_A$ for all points—close to experiment for most of the data (some of the reaction rate data here is questionable so we have used the rate data from the left side of Figure 4). $\hat{\epsilon}_B$, shown in Figure 7 is predicted almost as well by Eq. (17), except for the cluster of very high points, near left center. It is possible that these $\hat{\epsilon}_B$ data are incorrect since the reported $\hat{\epsilon}_A$ and $\hat{\epsilon}_B$ data do not satisfy Eq. (2).

We have recalculated $\hat{\epsilon}_B$ from Eq. (2) by assuming that the reported $\hat{\epsilon}_A$ are correct and these corrected values, shown in Figure 7, are much closer to the predictions of Eq. (17), which may lend some credence to the suggestion that the data are in error here.

Figures 8 and 9 repeat 6 and 7 at a lower N_D . The decrease in diffusivities, on the left in Figure 8 and right in Figure 9, less than at the higher Damköhler Number in Figures 6 and 7, is very nicely predicted by Eqs. (12) and (16). The small increase on the other side is also handled well, although there are more anomalous high data points in both figures. The reported values of $\hat{\epsilon}_A$ and $\hat{\epsilon}_B$ are inconsistent with Eq. (2) in such a random manner that there seems little point in recalculating $\hat{\epsilon}_B$ (or $\hat{\epsilon}_A$) as was done before.

In all the calculations we assumed τ_M to be constant, the mixing length 2λ to be the measured integral length scale, \bar{u} to be the measured average RMS velocity fluctuation and obtained reasonably satisfactory agreement with experiment—unexpectedly good in many cases, but the model cannot explain the very high values of $\hat{\epsilon}_A$ and $\hat{\epsilon}_B$ in Figures 7, 8 and 9. Is this a failure of the model or are these data erroneous? Further data are needed to answer the question.

Convective Diffusion Equation

Retaining the diffusivities as scalars while generalizing Eqs. (3), (4) and (12) to three dimensions gives the final result,

$$\frac{\partial \bar{C}_i}{\partial t} + \bar{u} \cdot \nabla \bar{C}_i = \nabla \cdot (D + \epsilon) \nabla \bar{C}_i - \nabla \cdot \epsilon \tau_M \nabla \bar{r}_i - \bar{r}_i \quad (18)$$

The new term, $\nabla \cdot \epsilon \tau_M \nabla \bar{r}_i$, contains the macro properties ϵ and τ_M and the reaction term which depends upon micromixing. This is a true macro-micro coupling which causes an apparent flux, $\epsilon \tau_M \nabla \bar{r}_i$, which can either enhance or hinder the normal turbulent flux, $-\epsilon \nabla \bar{C}_i$. How important a role it plays in the overall reactive mixing process remains to be determined.

Equation (18) still requires evaluation of the concentration covariance term or terms which appear in the mean reaction rate term. There is much less information available in multidimensional than in unidimensional systems as to how to handle these micromixing effects. Bilger *et al.* (1991) found that Toor's closure (Toor, 1969) predicted their reaction rate moderately well. This closure assumes that the concentration covariance term, $\overline{C_A C_B}$, which arises with the single step bimolecular reaction, is the value which would exist with an instantaneous reaction. Assuming perfect micromixing ($\overline{C_A C_B} = 0$) did less well, but this avoids the micromixing problem altogether and closes Eq. (18) for all chemistries. Because macrotransport tends to control in multidimensional systems (Hanks, 1991) this naive closure may well give acceptable results in practice, but this speculation requires further study.

Nomenclature

A, B	reactants A and B
C	concentration in nonreacting systems, mole/m ³
C _i	concentration of reactant i, mole/m ³
$\bar{C}_{A1}, \bar{C}_{A2}$	average concentration of A in lumps leaving positions 1 and 2, respectively, mole/m ³
D _i	molecular diffusivity of i, m ² /s
k	reaction velocity constant, m ³ /mole s for a second order reaction, s for a first order reaction
M	pitch of grid in experiment
n	stoichiometric coefficient
N	flux in absence of reaction, moles/m ² s
N _A	flux with reaction, moles/m ² s
N _D	Damköhler No., $\frac{M}{U} k (C_{A0} + C_{B0})$

N_{DM}	macro Damköhler No., $\frac{\tau_M}{\tau_R}$. For a second order bimolecular reaction = $\frac{\lambda}{u} k C_{BO}$
r_i	reaction rate mole/m ³ s
r_{A1}, r_{A2}	average reaction rate during flight in left and right leaving lumps, respectively, m ³ /mole s
R_i	non-dimensional reaction rate, $r_i \tau_R / C_{iO}$. For a second order bimolecular reaction = $r_i / k C_{AO} C_{BO}$
t	time, s
u	lump velocity, m/s
\bar{U}	mean experimental flow velocity, m/s
\bar{u}	average lump speed, m/s
v	vector fluid velocity, m/s
v'	velocity fluctuation
X_i	non-dimensional concentration of i, $\frac{C_i}{C_{iO}}$
y	distance normal to flow, m
Greek	
β	stoichiometric ratio of feed, $C_{BO}/n C_{AO}$
δ	width of mixing layer, m
ϵ	passive turbulent diffusivity—no reaction, m ² /s
ϵ_A, ϵ_B	reactant turbulent diffusivities, m ² /s
λ	half mixing length, m
τ_M	characteristic macromixing time, $\frac{\lambda}{u}$, s
τ_R	characteristic reaction time, $1/k C_{BO}$ for a bimolecular second order reaction, $1/k$ for a first order reaction, s
Subscripts	
i	reactant A or B
O	initial value
$-$	vector
Superscripts	
$-$	time mean value
\wedge	non-dimensionalized by $1/\bar{U}M$

Literature Cited

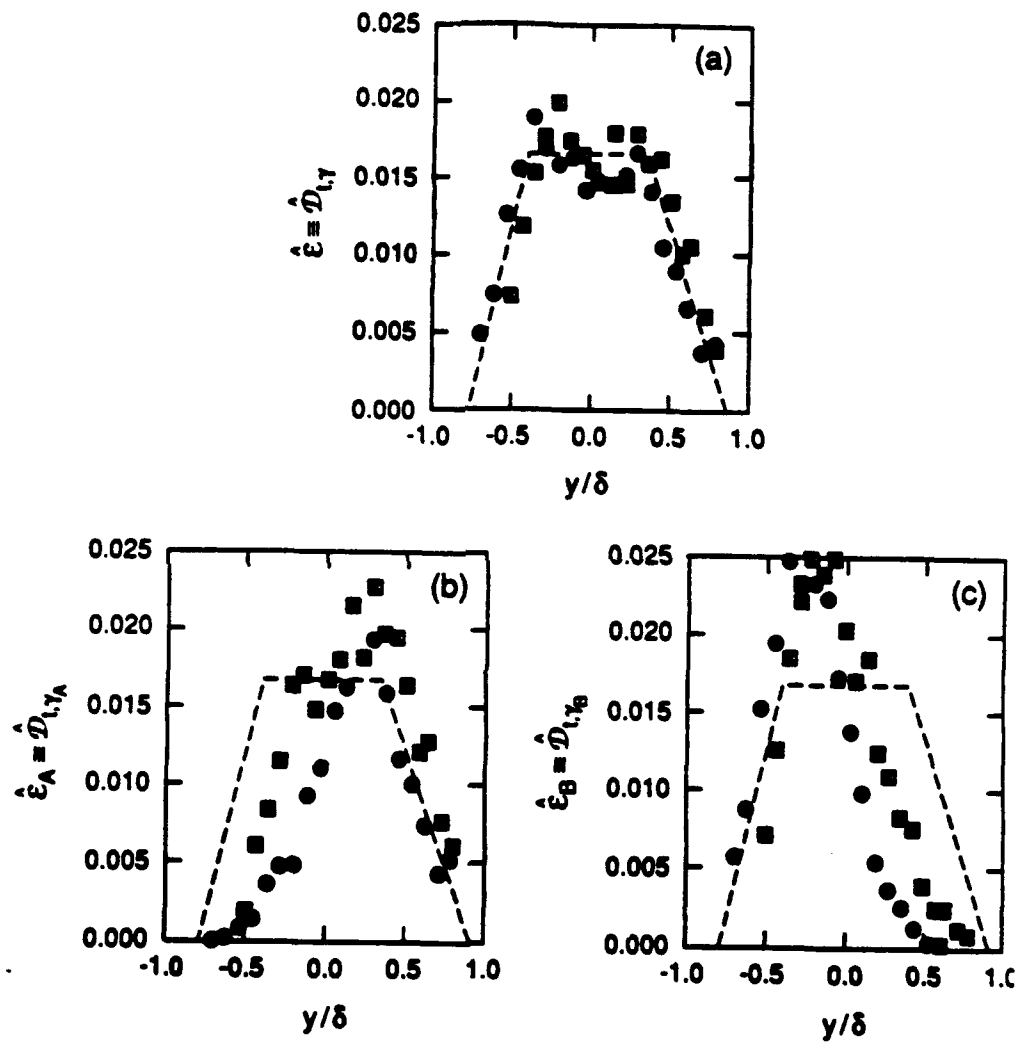
- Baldyga, J. and J.R. Bourne, "A Fluid Mechanical Approach to Turbulent Mixing and Chemical Reaction," *Chem. Eng. Commun.*, **28**, 259 (1984).
- Bilger, R.W., L.R. Saetran and L.V. Krishnamoorthy, "Reaction in a Scalar Mixing Layer," *J. Fluid Mech.*, **233**, 211 (1991).
- Bilger, R.W., "Conditional Moment Methods for Turbulent Reacting Flow using Crucco Variable Conditions." Submitted, *Physics of Fluids* (1991).
- Corrsin, S., "Limitations of Gradient Transport Models in Random Walks in Turbulence," *Advances in Geophysics*, **18A**, 25 (1974).
- Hanks, M.L., "A Study of Micromixing in Turbulent Free and Confined Cross-Flow Jets," Ph.D. Thesis, Carnegie Mellon University (1991).
- Harada, M., K. Arima, W. Eguchi and S. Nagata, "Micromixing in a Continuous Flow Reactor," *Mem. Fac. Eng. Kyoto Univ.*, **24**, 431 (1962).
- Hinze, J.O., *Turbulence*, McGraw-Hill, New York (1959).
- Kartan, H. and R.J. Adler, "A Stochastic Model for Homogeneous Turbulent, Tubular Reactors," *AIChE J.*, **13**, 580 (1967).
- Klimenko, A. Yu., "Multicomponent Diffusion of Various Scalars in Turbulent Flow," *Fluid Dynamic*, **25**, 327 (1990).
- Li, K.T. and H.L. Toor, "Turbulent Reactive Mixing with a Series-Parallel Reaction: Effect of Mixing on Yield," *AIChE J.*, **32**, 1312 (1986).
- Mao, K.W. and H.L. Toor, "A Diffusion Model for Reactions with Turbulent Mixing," *AIChE J.*, **16**, 49 (1970).
- Mehta, R.V. and J.M. Tarbell, "Four Environment Models of Mixing and Chemical Reaction," *AIChE J.*, **29**, 320 (1983).
- Taylor, G.I., "Eddy Motion in the Atmosphere," *Phil. Trans. A*, **215**, 1 (1915).
- Tennekes, H. and J.L. Lumley, *A First Course in Turbulence*, MIT Press, Cambridge (1983).
- Toor, H.L., "Mass Transfer in Dilute Turbulent and Non-turbulent Systems with Rapid Irreversible Reactions and Equal Diffusivities," *AIChE J.*, **8**, 70 (1962).

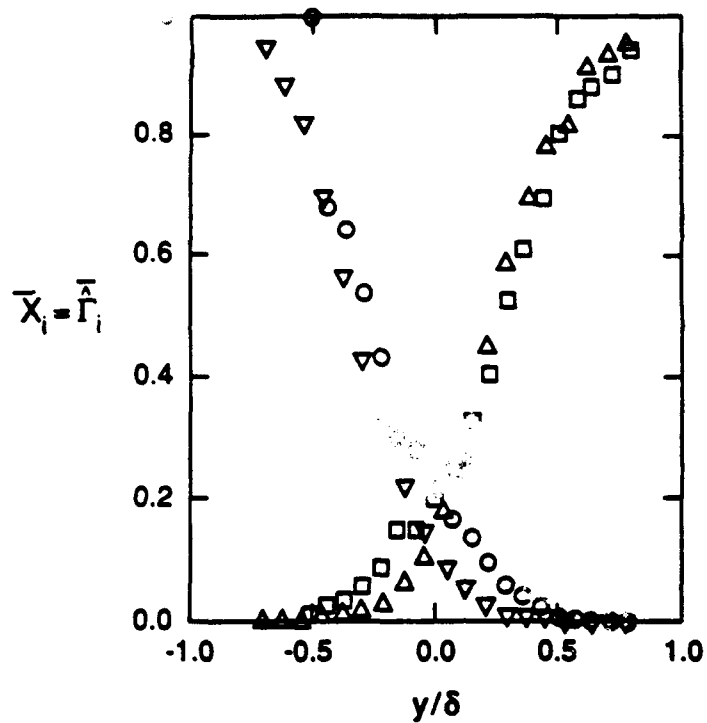
- Toor, H. L., "Turbulent Mixing of Two Species with and without Chemical Reaction," *Ind. Eng. Chem. Fund.*, 8, 655 (1969).
- Toor, H. L., "Turbulent Diffusivities in Reacting Systems," *AIChE J.*, 37, 1737 (1991).
- Saetran, L. R., D. R. Honnery, S. H. Stårner and R. W. Bilger, "Scalar Mixing Layer in Grid Turbulence with Transport of Passive and Active Species," in *Turbulent Shear Flows*, Vol. 6 (ed. J. C. Andre, J. Costeux, F. Durst, B. Launder, F. Schmidt and J. Whitelaw), p 109, Springer (1989).

List of Figures

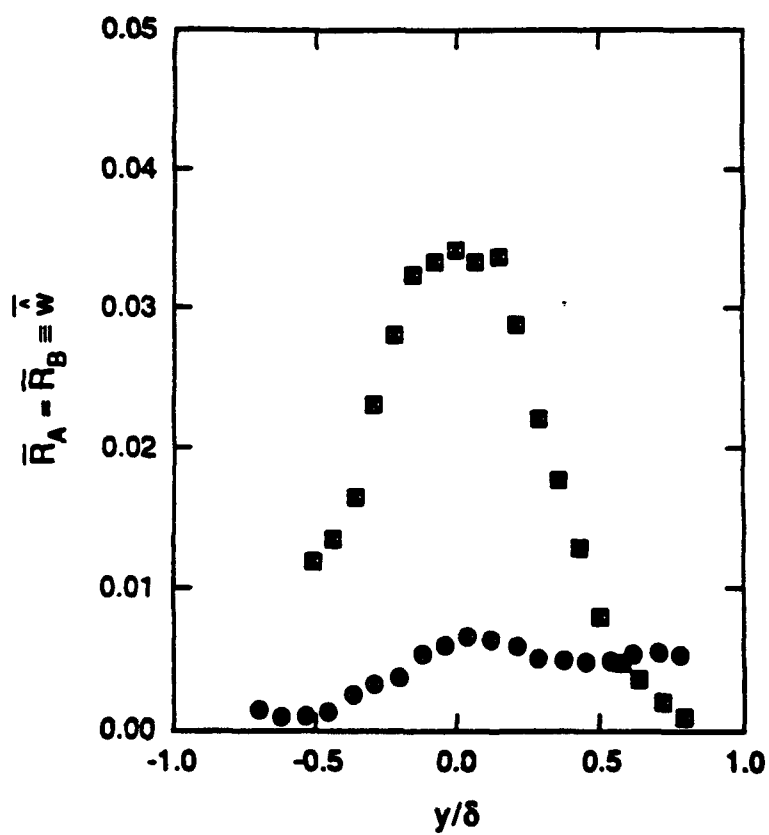
- Figure 1 Turbulent Diffusivity Data from Figure 15 of Bilger *et al.* (1991). \otimes , $N_D=1.81$; \boxtimes , $N_D = 0.3$. Same dashed line drawn on each figure for orientation. (a) Non-reacting; (b) Species A; (c) Species B.
- Figure 2 Mean Reactant Concentration Profiles from Figure 8 of Bilger *et al.* (1991). $N_D=1.81$: Δ , Species A; ∇ , Species B. $N_D = 0.3$: \square , species A; \circ , Species B.
- Figure 3 Mean Reaction Rate vs. Position from Bilger *et al.* Figure 18. \boxtimes , $N_D = 0.3$; \otimes , $N_D = 1.81$.
- Figure 4 Mean Reaction Rate and Species Concentrations vs. Position During Reactant Mixing.
- Figure 5 Mixing Length Model.
- Figure 6 Turbulent Diffusivities of Species A at $N_D = 1.81$; \otimes from Figure 1b; \circ , from Eq. (12); Δ , Non reacting Diffusivity from Figure 1a.
- Figure 7 Turbulent Diffusivities of Species B at $N_D = 1.81$; \otimes , from Figure 1c; \circ , from Eq. (17); Δ Non-reacting Diffusivity from Figure 1a. $\cup \hat{e}_B$ from Eq. (2).
- Figure 8 Turbulent Diffusivities of Species A at $N_D = 0.3$; \boxtimes from Figure 1b; \square from Eq. (12); Δ Non-Reacting Diffusivity from Figure 1a.
- Figure 9 Turbulent Diffusivities of Species B at $N_D = 0.3$; \boxtimes from Figure 1c; \square , from Eq. (17); Δ Non-Reacting Diffusivity from Figure 1a.

Toor
Figure 1

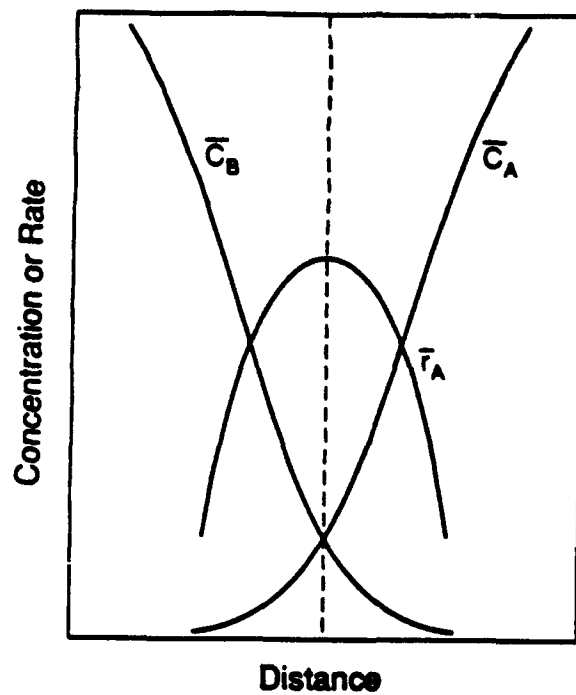




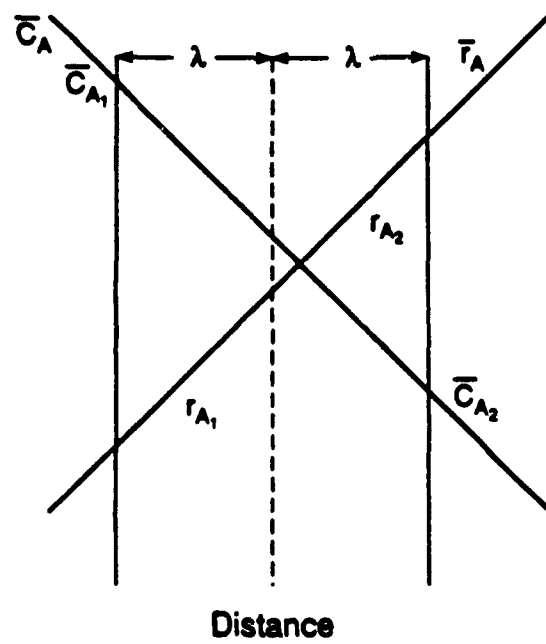
Test
Figure 2



Test
Figure 3

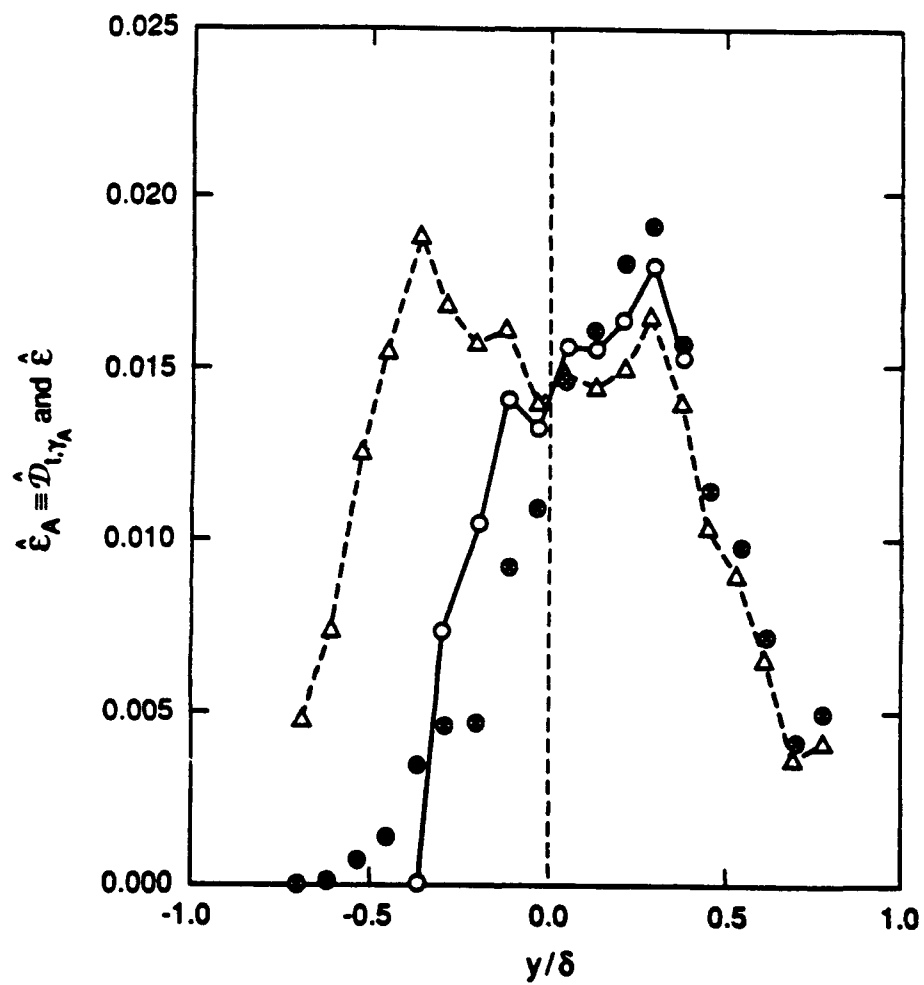


Toor
Figure 4

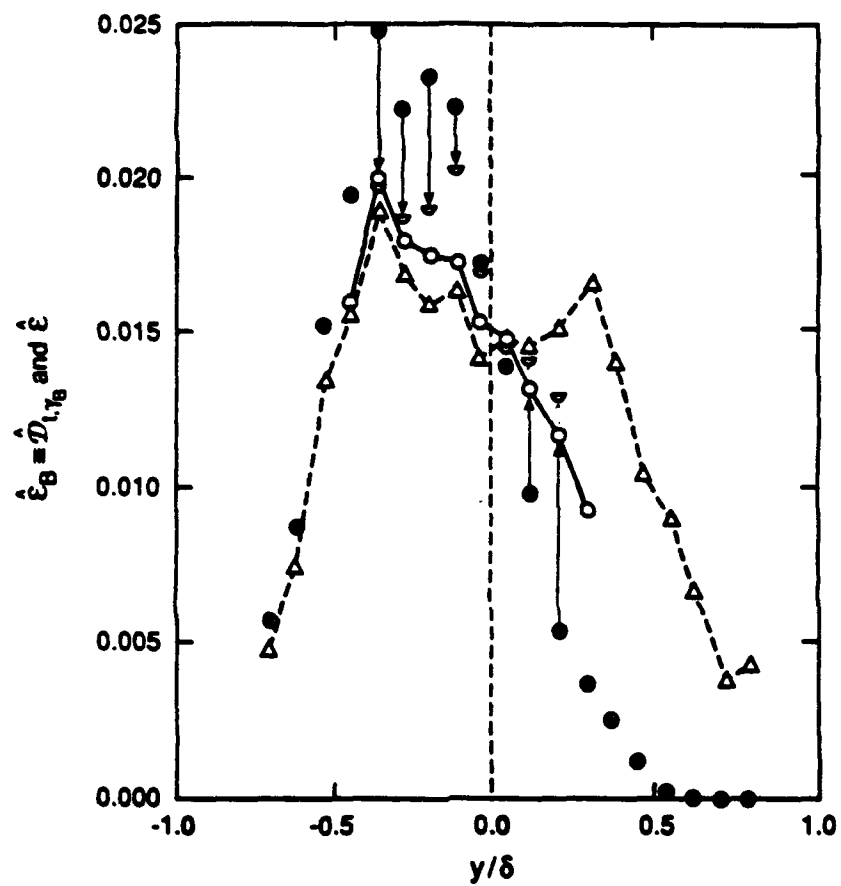


Toor
Figure 5

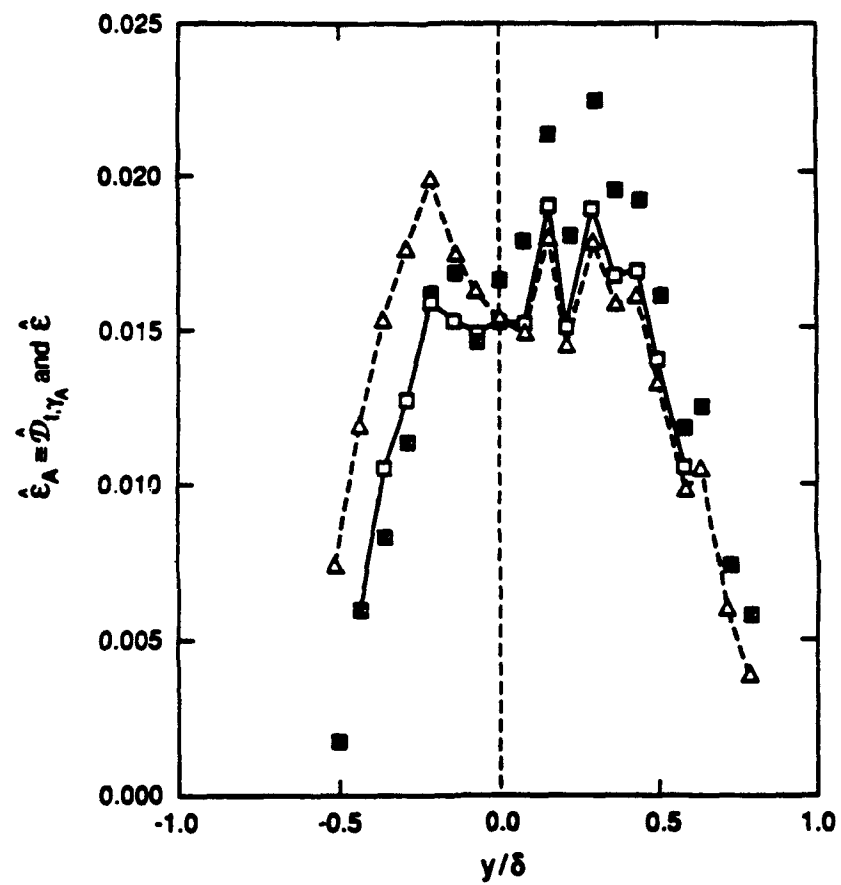
Toor
Figure 6



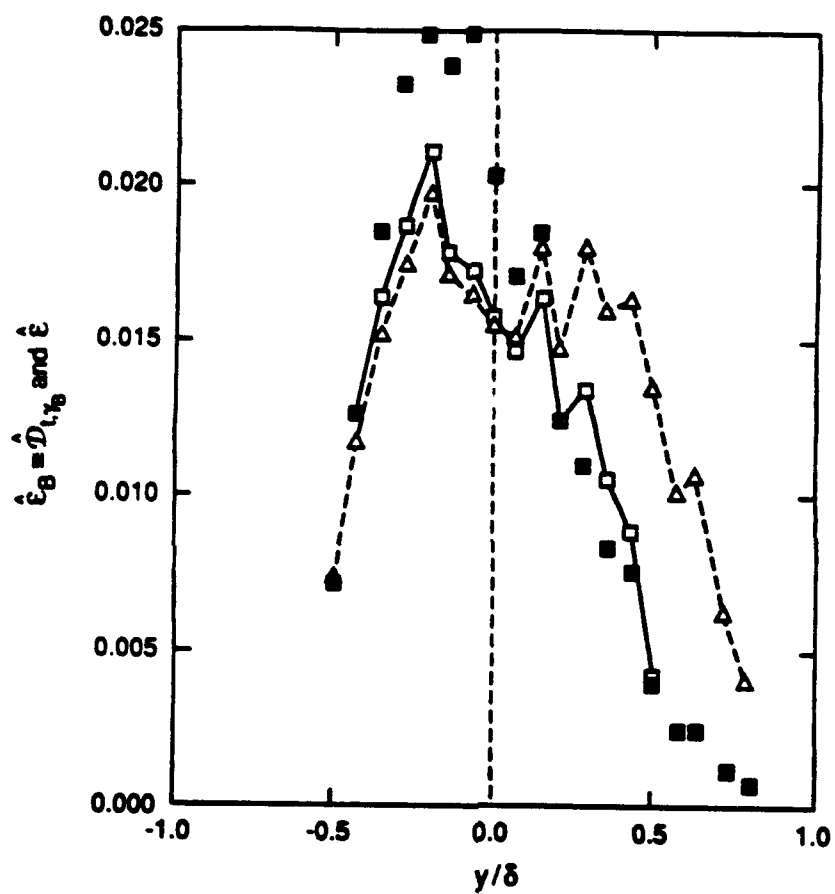
Toor
Figure 7



Toor
Figure 1



Toor
Figure 9



CHEMICALLY REACTING TURBULENT MIXING LAYERS WITHOUT HEAT RELEASE

Robert A. Gore
Francis H. Harlow
Group T-3, MS B216
Los Alamos National Laboratory
Los Alamos, NM 87545

ABSTRACT

A new model for the velocity and concentration profiles in a reacting mixing layer is proposed. The concentration model is based on a two-point turbulence model such that the small scales of turbulence which can enhance the mixing of individual species is correctly accounted for. Comparison with experiments and direct numerical simulation are made.

INTRODUCTION

We consider the far subsonic mixing of two chemically reactive species separated by a free shear layer. This classification of flow has been studied in some detail due to its generic appearance in many practical situations. These investigations have included direct numerical simulations (e.g., McMurtry *et al.*, 1986 and Riley *et al.*, 1986), experiments (e.g., Mungal and Dimotakis, 1984, and Batt, 1977) and theoretical or modeling studies (e.g., Broadwell and Breidenthal, 1982, and Borghi, 1988). The present approach applies a two-point turbulence model coupled with moment closure for the averaged species equation. The advantage of using a two-point approach is that the total energy in the turbulent fluctuations is decomposed to give the amount at each wavenumber (or heuristically, each "eddy" size). Knowledge of the turbulent energy at each scale is important to correctly quantify the mixing of reactant species occurring at the fine scale. This mixing will greatly enhance the ability of molecules to come into direct contact which is necessary for chemical reaction to occur.

At this stage of the investigation we assume a temperature-independent reaction between two species with no heat release and thus no change in overall fluid density. This decouples the equations for the turbulent velocity field and the species conservation. Also the reaction rate is assumed to be infinitely fast such that its magnitude will not have an effect on the mean velocity and concentration profiles and thus the rate at which product is formed is limited by turbulent mixing and molecular diffusion. Comparisons are made with numerical simulation and experiments in which these assumptions are valid.

For latter investigations, we will be interested in the regime where $T_a/\bar{T} \ll 1$ and $T'/\bar{T} < 1$, or flows at high temperatures and low activation energies. Staying in this regime allows us to neglect the effect of fluctuating temperature on the averaged reaction rate where typically the reaction rate is written as $\omega_f = -B \exp(-T_a/T) Y_F Y_O$ before averaging.

MODEL DEVELOPMENT

The model used in calculating the turbulent velocity field is a spectral transport model first described in Benard, Harlow, Rauenzahn, and Zemach (1990) and applied to nonreactive mixing layers in Gore, Harlow, and Zemach (1991). The latter investigation showed that the model predictions are in good agreement with experiments for that class of flows. In essence, the model describes the transport of the turbulent energy spectrum (in wavenumber space) through the physical processes of mean flow coupling, viscous and turbulent diffusion, cascade in wavenumber space, viscous dissipation, and a return to isotropy. The equation for which is:

$$\begin{aligned} \frac{\partial E_{ij}}{\partial t} = & -u_n \frac{\partial E_{ij}}{\partial x_n} - 2\nu k^2 E_{ij} + \frac{1}{2}\nu \frac{\partial^2 E_{ij}}{\partial x_n^2} - (1 - C_B)(u_{i,n} E_{j,n} + u_{j,n} E_{i,n}) \\ & - C_B \frac{2}{3} \delta_{ij} u_{k,n} E_{kn} + C_D \frac{\partial}{\partial x_n} \left\{ \nu_T \frac{\partial E_{ij}}{\partial x_n} \right\} - C_1 \frac{\partial}{\partial k} \left\{ k^2 \sqrt{kE} E_{ij} \right\} \\ & + C_2 \frac{\partial}{\partial k} \left\{ k^3 \sqrt{kE} \frac{\partial E_{ij}}{\partial k} \right\} - C_m k \sqrt{kE} \left(E_{ij} - E \frac{\delta_{ij}}{3} \right) \end{aligned} \quad (1)$$

where $E = E_{ii}$ and $\nu_T = \int_0^\infty \sqrt{kE}/k^2 dk$. The above-modeled equation was deduced from an exact derivation of $E_{ij}(\bar{x}, k)$, which followed from two steps. First the two-point velocity correlation was Fourier transformed and then integrated over shells in wavenumber space. The latter was done to reduce the modeling of interactions in wavenumber space from those between vectors to that between scalars. Mathematically these steps are represented by

$$R_{ij}(\bar{x}, \bar{k}) = \int e^{-i\bar{k} \cdot \bar{r}} R(\bar{x} + \bar{r}/2, \bar{x} - \bar{r}/2) d\bar{r}$$

and

$$E_{ij}(\bar{x}, k) = \int R_{ij}(\bar{x}, \bar{k}) \frac{k^2 d\Omega}{(2\pi)^3}$$

where it is noted that

$$R_{ij}(\bar{x} + \bar{r}/2, \bar{x} - \bar{r}/2) = \overline{u'_i(\bar{x} + \bar{r}/2) u'_j(\bar{x} - \bar{r}/2)}$$

and

$$\overline{u'_i(\bar{x}) u'_j(\bar{x})} = 2 \int E_{ij}(\bar{x}, k) dk. \quad (2)$$

Equation (1) was solved coupled with the ensembled averaged Navier-Stokes equation:

$$\frac{\partial \bar{u}_i}{\partial t} + \bar{u}_j \frac{\partial \bar{u}_i}{\partial x_j} = -\frac{1}{\rho} \frac{\partial P}{\partial x_i} + \nu \frac{\partial^2 \bar{u}_i}{\partial x_j \partial x_j} - \frac{\partial \overline{u'_i u'_j}}{\partial x_j} \quad (3)$$

to give a complete description of the turbulent flow field. The equations were coupled through the calculation of the Reynolds stress terms by (2).

The equations were simplified in the present situation by the assumption of 1-D flow, Fig. 1. In this configuration mean fluid properties vary only in the y or cross-stream direction and time. By making this assumption computational costs were greatly reduced without loss of the ability to compare to experiments (for nonreactive flows see Gore, Harlow, and Zemach, 1990).

The instantaneous form of the species transport equation with chemical reaction is:

$$\frac{\partial Y_i}{\partial t} + u_k \frac{\partial Y_i}{\partial x_k} = \frac{1}{\rho} \frac{\partial}{\partial x_k} \left\{ \rho D_i \frac{\partial Y_i}{\partial x_k} \right\} + \omega_i, \quad (4)$$

where i denotes species i . In the following, the simple reaction $A + B \rightarrow C$ is considered so that

$\omega_A = \omega_B = -A/\rho Y_A Y_B$ and $\omega_c = -2\omega_A$, where A is the reaction coefficient and Y_i is the mass fraction of species i . As mentioned, the reaction rate is considered to be so large that its value will not have an effect on the flow properties. So while the form of A may be considered to be of the Arrhenius form, it will not be modeled as such and will remain a constant albeit a very large one such that its value (which may in reality be fluctuating due to temperature fluctuation if there were any) does not result in any significant changes in the solution. The constraints on this assumption for a nonisothermal case are discussed in the introduction.

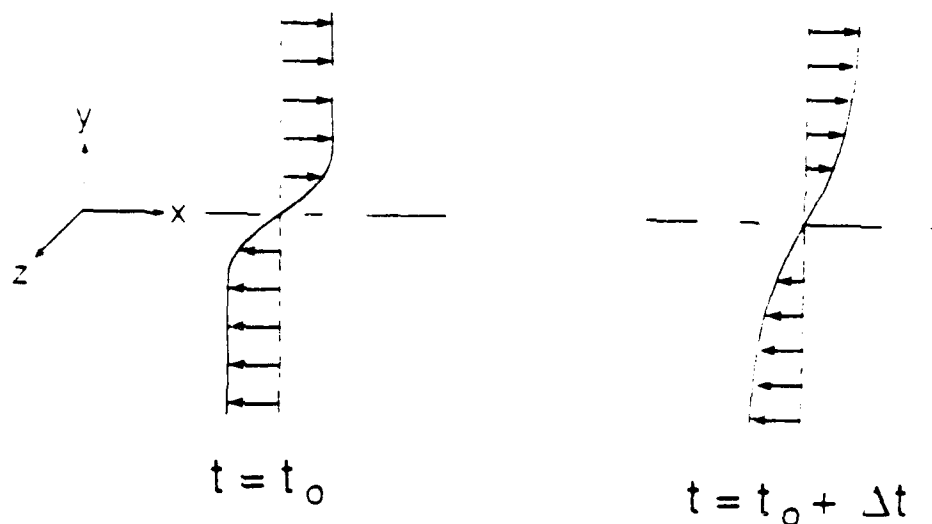


Fig. 1. Schematic of computational domain.

Ensemble averaging of Eq. (4) yields various terms that need to be modeled. First $\overline{u_k \frac{\partial Y_i}{\partial x_k}} = \overline{u_k} \frac{\partial \overline{Y_i}}{\partial x_k} - C_D \frac{\partial}{\partial x_k} \left\{ \nu_T \frac{\partial \overline{Y_i}}{\partial x_k} \right\}$, which describes the disordered (diffusional) part of the turbulent transport and neglects the ordered (or large-scale) part that can lead to a counter-gradient flux. The other term in need of modeling is $\overline{\omega_i}$. For species A , $\overline{\omega_A} = -A/\rho Y_A Y_B$ or, since A and ρ are constants, $\overline{\omega_A} = \frac{A}{\rho} \overline{Y_A Y_B}$. The first step we used in modeling $\overline{Y_A Y_B}$ is to obtain a transport equation for that quantity. This is accomplished by multiplying Y_B by the equation for Y_A (Eq. (4)) and adding to that the product of Y_A and the equation for Y_B , then averaging. This gives an equation for the transport of $\overline{Y_A Y_B}$ which can be reduced by the homogeneous-time steady assumption (i.e., $\frac{\partial(\cdot)}{\partial t} = \frac{\partial(\cdot)}{\partial z} = 0$) and the length scale assumption (i.e., $\frac{\partial(\cdot)}{\partial z} \frac{\partial(\cdot)}{\partial z} = \frac{\lambda}{s_{chem}^2} (\cdot)'(\cdot)'$). This procedure for obtaining $\overline{Y_A Y_B}$ is analogous to the procedure for "deriving" the Boussinesq assumption in single species turbulent flows; $-\overline{u_i' u_j'} = \nu_T \left(\frac{\partial \overline{u_i}}{\partial x_j} + \frac{\partial \overline{u_j}}{\partial x_i} \right) - \frac{2}{3} K \delta_{ij}$.

The resulting equation is:

$$0 = -\frac{A}{\rho} \overline{Y_A Y_B (Y_A + Y_B)} - \frac{\lambda}{s_{chem}^2} (D_A + D_B) \overline{Y_A' Y_B'} \quad (5)$$

One of the most important parameters in the present model is the definition of s_{chem} as defined in the length scale assumption described above. It is an "average" scale over which the chemical reactions will be most affected by turbulence, or conversely it is the scale at which the small scale turbulent motion enhances the molecular mixing of individual species. This scale is derivable from a spectral analysis similar to that used to derive the spectral transport model for the turbulent fluctuation, Eq. (1). This derivation follows.

First we define $W_{ij}(\bar{x}_1, \bar{x}_2) = \left(\frac{\partial}{\partial x_1} \right)_i \left(\frac{\partial}{\partial x_2} \right)_j Q(\bar{x}_1, \bar{x}_2)$ where $Q(\bar{x}_1, \bar{x}_2) = \overline{Y_A'(x_1) Y_B'(x_2)}$. By defining $\bar{x} = (\bar{x}_1 + \bar{x}_2)/2$ and $\bar{r} = (\bar{x}_1 - \bar{x}_2)$ and making this substitution in the preceding equation one obtains after performing the Fourier transform of $W_{ij}(\bar{x}, \bar{r})$

$$W_{ij}(\bar{x}, \bar{k}) = \int e^{-i\bar{k} \cdot \bar{r}} W_{ij}(\bar{x} + \bar{r}/2, \bar{x} - \bar{r}/2) d\bar{r} = \left(\frac{1}{2} \frac{\partial}{\partial x_1} + ik \right) \left(\frac{1}{2} \frac{\partial}{\partial x_2} - ik \right) Q(\bar{x}, \bar{k})$$

By neglecting the higher order derivative terms, this is simplified to

$$W_{ij}(\bar{x}, \bar{k}) \simeq k_i k_j Q(\bar{x}, \bar{k})$$

In keeping with the approximations that lead to Eq. (1), we examine only the variation of W_{ij} as a function of magnitude of wavenumber vector, thus we let

$$W(\bar{x}, k) = k^2 Q(\bar{x}, k)$$

Note that $\int Q(\bar{x}, k) dk = \overline{Y'_A Y'_B}$, where $Q(\bar{x}, k)$ is the turbulent concentration energy spectrum.

This was done to obtain the single point correlation $\overline{Y'_A Y'_B}$ which is needed to close the ensemble-average concentration equation. Thus, by definition

$$\begin{aligned} \int W(\bar{x}, k) dk &\equiv \frac{\partial Y'_A}{\partial x} \frac{\partial Y'_B}{\partial x} \\ &\simeq \int k^2 Q(\bar{x}, k) dk \end{aligned}$$

It is postulated that $Q(\bar{x}, k)$ can be modeled as a function of $E(\bar{x}, k)$ so that

$$\frac{Q(\bar{x}, k)}{\int_0^\infty Q(\bar{x}, k) dk} \propto \frac{E(\bar{x}, k)}{\int_0^\infty E(\bar{x}, k) dk}$$

This gives

$$\begin{aligned} \frac{\partial Y'_A}{\partial x} \frac{\partial Y'_B}{\partial x} &= \int W(\bar{x}, k) dk \\ &= \int k^2 Q(\bar{x}, k) dk \\ &= \int k^2 \left[\lambda \frac{\int_0^\infty Q(\bar{x}, k') dk'}{\int_0^\infty E(\bar{x}, k') dk'} \right] E(\bar{x}, k) dk \\ &= \lambda \frac{\int_0^\infty Q(\bar{x}, k') dk'}{\int_0^\infty E(\bar{x}, k') dk'} \int k^2 E(\bar{x}, k) dk \\ &= \lambda \overline{Y'_A Y'_B} \frac{\int_0^\infty k^2 E(\bar{x}, k) dk}{\int_0^\infty E(\bar{x}, k) dk} \end{aligned}$$

The limits of integration as they now stand would lead to a divergent sum for $\int_0^\infty k^2 E(\bar{x}, k) dk$ since E goes as $k^{-5/3}$ for k and Re approaching infinity. Of course finite values for molecular viscosity and diffusion would limit these integrals such that

$$\frac{\partial Y'_A}{\partial x} \frac{\partial Y'_B}{\partial x} = \lambda \overline{Y'_A Y'_B} \frac{\int_0^{k_D} k^2 E(\bar{x}, k) dk}{\int_0^{k_D} E(\bar{x}, k) dk} \quad (6)$$

where k_ν , the Kolmogorov wavenumber is equal to $(\epsilon/\nu^3)^{1/4}$ and $k_D = \sqrt{Sc} k_\nu$, where Sc is the Schmidt number. This value for k_D is obtained from the cut-off of the so-called viscous-convective range as presented in Lesieur (1987). After this cutoff the spectrum of the concentration fluctuation decreases exponentially and any values beyond this point are considered to be insignificant. For $Sc < 1$ it is postulated that the smallest scales in the concentration spectrum are those created by turbulence and as such $k_D = k_\nu$, although later we test both approximation ($k_D = k_\nu$ and $k_D = \sqrt{Sc} k_\nu$) for $Sc < 1$. This results in the postulated spectrum for

Q given in Fig. 2. The final result, Eq. (6), is the length scale assumption:

$$\frac{\partial \overline{Y_A'}}{\partial x} \frac{\partial \overline{Y_B'}}{\partial x} = \overline{Y_A' Y_B'} \left(\frac{\lambda}{s_{\text{chem}}^2} \right)$$

where

$$s_{\text{chem}}^2 = \frac{\int_0^{k_v} E(\overline{\tau}, k) dk}{\int_0^{k_D} k^2 E(\overline{\tau}, k) dk}$$

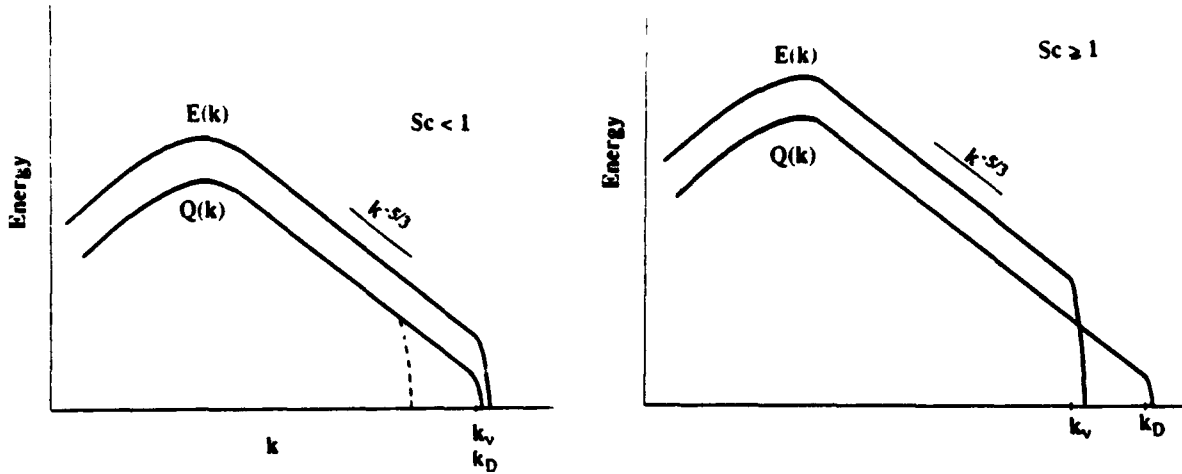


Fig. 2. Postulated spectra for E and Q .

This procedure results in a defined s_{chem} scale to be used in (5):

$$0 = -\frac{A}{\rho} \overline{Y_A Y_B (Y_A + Y_B)} - \frac{\lambda}{s_{\text{chem}}^2} (D_A + D_B) \overline{Y_A' Y_B'}$$

for which the first term on the right-hand side is still in need of modeling since, through appropriate expansion

$$\begin{aligned} \overline{Y_A Y_B (Y_A + Y_B)} &= (\overline{Y_A + Y_B}) (\overline{Y_A Y_B} + 2 \overline{Y_A' Y_B'}) \\ &\quad + \overline{Y_A Y_B' Y_B'} + \overline{Y_B Y_A' Y_A'} + \overline{Y_A' Y_B' (Y_A' + Y_B')} \\ \text{or} \quad &= \overline{Y_A Y_B} (\overline{Y_A + Y_B}) + 2 (\overline{Y_A + Y_B}) \overline{Y_A' Y_B'} + Z \end{aligned}$$

$$\text{where } Z = \overline{Y_A Y_B'^2} + \overline{Y_B Y_A'^2} + \overline{Y_A' Y_B' (Y_A' + Y_B')}.$$

It is then proposed that Z be a linear combination of the preceding terms in the above expression, that is,

$$Z = (1 + \alpha) \overline{Y_A Y_B} (\overline{Y_A + Y_B}) + \alpha (\overline{Y_A + Y_B}) \overline{Y_A' Y_B'}$$

$$\text{where } \alpha = \frac{\overline{Y_A Y_B'^2} + \overline{Y_B Y_A'^2} + \overline{Y_A' Y_B' (Y_A' + Y_B')} - \overline{Y_A Y_B} (\overline{Y_A + Y_B})}{(\overline{Y_A + Y_B}) (\overline{Y_A Y_B} + \overline{Y_A' Y_B'})}.$$

From examining the direct numerical simulation data from Riley, Metcalfe, and Orszag (1986), it was found that to a good approximation α can be considered constant.

This yields, for species A, the final modeled form for the species concentration equation:

$$\frac{\partial Y_A}{\partial t} + u_i \frac{\partial Y_A}{\partial x_i} = \frac{\partial}{\partial x_k} \left\{ (D_A + C'_D \nu_T) \frac{\partial Y_A}{\partial x_k} \right\} - \frac{A}{\rho} Y_A Y_B \left[\frac{1}{1 + \frac{A s_{chem}^2 (Y_A + Y_B)}{\rho \lambda (D_A + D_B)}} \right] \quad (7)$$

$$\text{where } \frac{1}{s_{chem}^2} = \int_0^{k_D} k^2 E(k, t) / \int_0^{k_v} E(k, t) dk$$

with λ being the only new variables to be fit by comparison to experiments. C'_D was taken as $1.5 C_D$ as the typical value used in scalar diffusion of concentration.

As A approaches infinity the ensemble average reaction term approaches a finite value of $\lambda s_{chem}^2 Y_A Y_B \frac{D_A + D_B}{(Y_A + Y_B)}$, which does not depend on A , consistent with the idea presented earlier that the reaction rate will be some large value that does not affect the final solution.

RESULTS

The results presented in this section have used the value $\lambda = .18$ to optimize the comparison with available information. This comparison is chiefly made with two sets of results. One is the direct numerical simulation of Riley *et al.* (1985) and the other is the experimental investigation of Mungal (1983). The comparison is presented in Fig. 3. As shown, the comparison is quite good but some discussion of parameters is needed. The present model has been matched to the data of Mungal using the parameters of their system, i.e., $Sc \sim 1$ and $Re \sim 30,000$, which are the values used in the present model. The simulation of Riley has a $Sc = 0.6$ and a Re of approximately 300. They found a good match between their simulation and Mungal's data despite these differences. As will be shown in the following figures our model would predict different product concentrations depending on the value of Sc . Note that for the present model the profile presented in Fig. 3 is the final self-similar form and as such does not change with time.

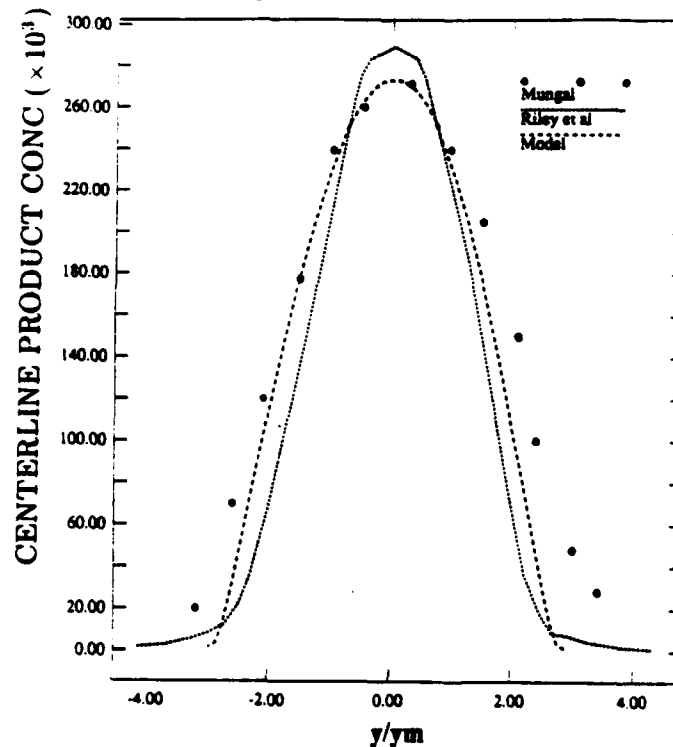


Fig. 3. Comparison of model with experiment and direct numerical simulation.

In Fig. 4 is shown the variation of the production concentration as a function of time for two Schmidt numbers. Time, though, can be linearly correlated with Re (based on width of the layer) since the width varies linearly with time. Demonstrative values of Reynolds number are also shown. As can be seen, the centerline production concentration quickly converges to its final self-similar value.

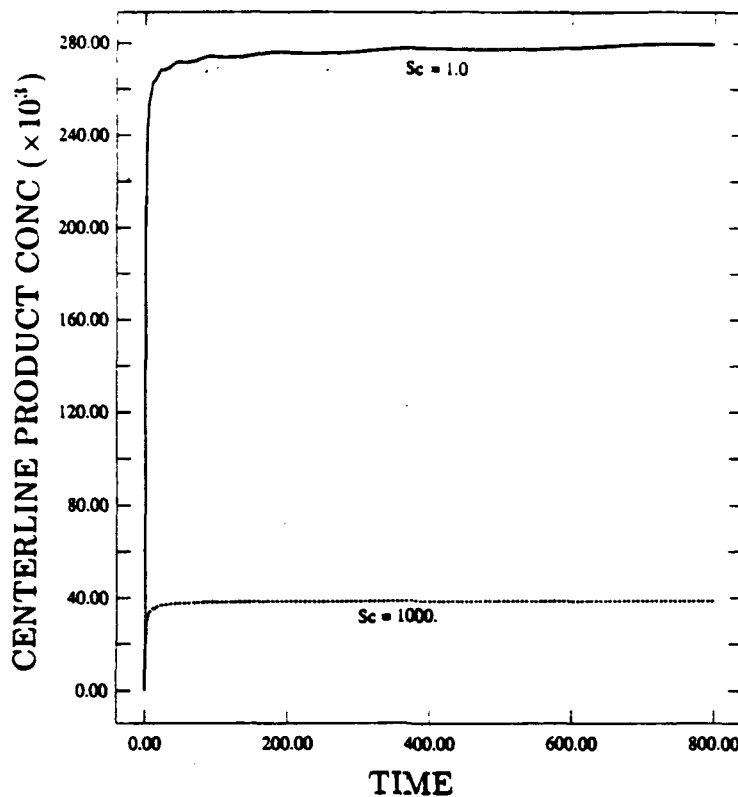


Fig. 4. Centerline product concentration as a function of time (or Reynolds number)

The variation of the centerline product concentration at a Reynolds number of 30,000 is shown in Fig. 5. The results of the two possibilities of $k_D = k$, and $k_D = \sqrt{Sc} k$, for $Sc < 1$ are presented. The theoretical foundations for the turbulent concentration spectrum for Sc less than one are much less established and in need of further experimental verification. Regardless, the general trend is consistent with other models and theories in that the centerline product concentration decreases with increasing Sc .

As can be inferred from Eq. (7), the variation of a reactant species, say A , with time, dY_A/dt , will come from two sources, reaction and diffusion. The relative magnitude of these terms is shown in Fig. 6. In this figure the cross-stream location is nondimensionalized by the momentum thickness, and each of the values for dY_A/dt , reaction and diffusion are normalized by the maximum value of the diffusion term. The values were taken after self-similarity has been reached, and therefore Fig. 6 is independent of time.

Finally, the self-similar value of the chemical reaction scale, s_{chem} , can be correlated with the various parameters of the flow, namely, θ , ν , D , and ΔU . Forming the proper nondimensional groups, one obtains

$$\frac{s_{chem}}{\theta} = f\left(\frac{\nu}{D}, \frac{\theta \Delta U}{\nu}\right).$$

Curve fitting the calculation of the present model leads to

$$\frac{s_{chem}}{\theta} = 5.125 \left(\frac{\nu}{D}\right)^{-0.332} \left(\frac{\theta \Delta U}{\nu}\right)^{-0.506} \quad (8)$$

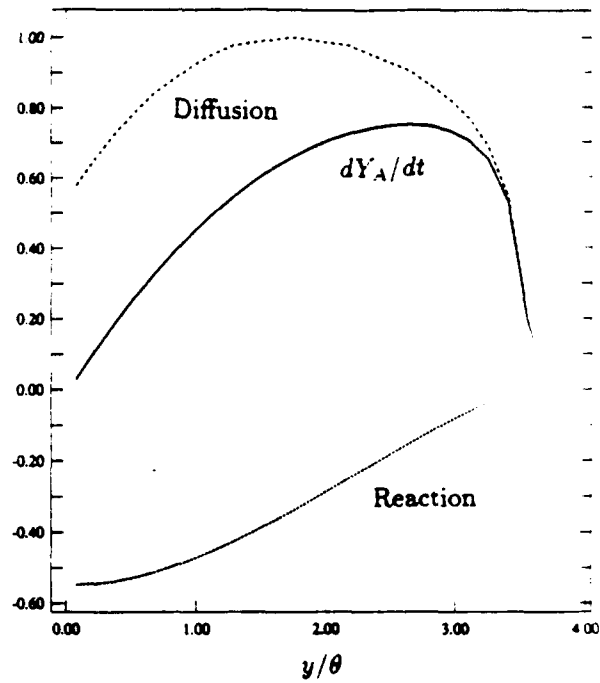
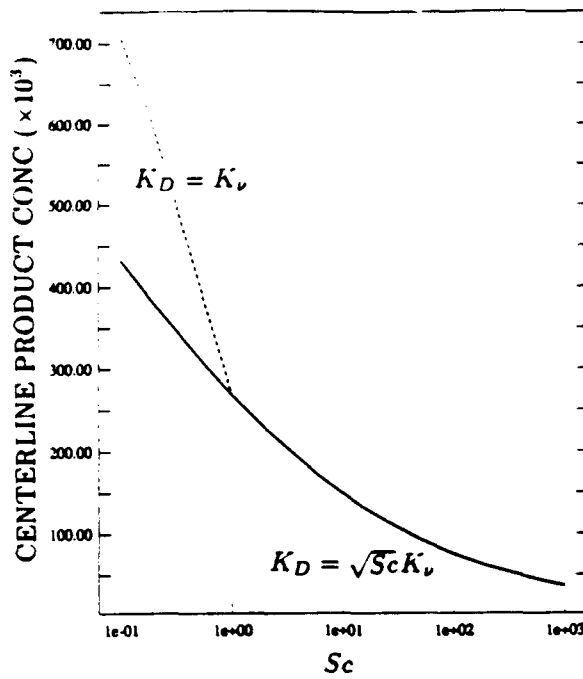


Fig. 5. Centerline product concentration as a function of Sc . Fig. 6. Contribution to the change in Y_A .

This form can be obtained approximately by making various assumptions. First, by definition

$$s_{\text{chem}}^2 = \frac{\int_0^{k_D} E(k) dk}{\int_0^{k_D} k^2 E(k) dk} = \frac{\int_0^{(\frac{1}{\nu})^{1/4}} E(k) dk}{\int_0^{(\frac{1}{\nu})^{1/4}} (\frac{1}{\nu})^{1/2} (\frac{1}{\nu})^{1/4} k^2 E(k) dk}$$

Then by making the assumption that

$$E(k) \simeq \begin{cases} E_m \left(\frac{k}{k_m} \right)^3 & k \leq k_m \\ E_m \left(\frac{k}{k_m} \right)^{-5/3} & k > k_m \end{cases}$$

where k_m is the wavenumber at which E is a maximum, E_m . This gives

$$s_{\text{chem}}^2 = \frac{\int_0^{k_m} E_m \left(\frac{k}{k_m} \right)^3 dk + \int_{k_m}^{(\frac{1}{\nu})^{1/4}} E_m \left(\frac{k}{k_m} \right)^{-5/3} dk}{\int_0^{k_m} k^2 E_m \left(\frac{k}{k_m} \right)^3 dk + \int_0^{(\frac{1}{\nu})^{1/4}} (\frac{1}{\nu})^{1/2} (\frac{1}{\nu})^{1/4} k^2 E_m \left(\frac{k}{k_m} \right)^{-5/3} dk}$$

or by performing the integration

$$s_{\text{chem}}^2 = \frac{7/4 E_m k_m - 3/2 E_m k_m^{5/3} \left(\frac{\nu^{1/2}}{\epsilon^{1/3}} \right)}{3/4 E_m k_m^{5/3} \left(\frac{\epsilon^{1/3}}{D^{2/3} \nu^{1/3}} \right) - 7/12 E_m k_m^3}$$

In the limit as $\nu \rightarrow 0$ or $Re \rightarrow \infty$ the previous equation reduces to

$$s_{\text{chem}}^2 = \frac{7/4 E_m k_m}{3/4 E_m k_m^{5/3} \left(\frac{\epsilon^{1/3}}{D^{2/3} \nu^{1/3}} \right)}$$

$$= c_1 k_m^{-2/3} \epsilon^{-1/3} D^{2/3} \nu^{1/3}$$

or with the scaling of $k_m \sim 1/\theta$ and $\epsilon \sim \Delta U^3/\theta$

$$s_{chem} \sim \theta^{1/2} \Delta U^{-1/2} D^{1/3} \nu^{1/6} \text{ or}$$

$$\frac{s_{chem}}{\theta} \sim \left(\frac{\nu}{D}\right)^{-1/3} \left(\frac{\theta \Delta U}{\nu}\right)^{1/2}$$

which is very close to the form found through curve fitting the results from the computer simulation, Eq. (8). An alternate form of Eq. (8) can be obtained by using the scaling $\theta \sim s$ (the scale of the most energetic eddy) and $\Delta U \sim \sqrt{k}$ (the square root of the turbulent kinetic energy). This results in

$$\frac{s_{chem}}{s} = 2.6 \left(\frac{\nu}{D}\right)^{-.332} \left(\frac{\sqrt{k}s}{\nu}\right)^{-.506}$$

CONCLUSIONS

The present investigation is the preliminary attempt at modeling the turbulence-chemistry interaction in a mixing layer when the reaction rate is very large. The comparison with the limited experimental evidence is encouraging and the use of a model of the turbulent concentration energy spectrum to obtain the length scale approximation leads to a good approximation of the physics. As the Reynolds number becomes large and the energy spectrum becomes self-similar, one can correlate the length scale associated with the most energetic eddy and the scale of turbulence that most affects the chemical reaction. With this scaling the ensembled averaged concentration equation can be used with a simpler one-point turbulence model such as $k - \epsilon$.

ACKNOWLEDGMENT

The first author would like to thank Chuck Zemach of Los Alamos National Laboratory for this helpful discussions on the initial derivation of the length scale assumption that leads to the expression for s_{chem} .

REFERENCES

- Benard, D. C., Harlow, F. H., Rauenzahn, R. M., and Zemach, C. 1990, "Spectral Transport Model for Turbulence." Los Alamos National Laboratory Technical Report LA-11821-MS.
- Gore, R. A., Harlow, F. H., and Zemach, C. 1991, "Computation of Mixing Layers by a Spectral Transport Model." 8th Symposium on Turbulence Shear Flows, Munich, Germany.
- Lesieur, M. 1987, *Turbulence in Fluids*, Martinus-Nijhoff Publishers.
- Mungal, M. G. 1983, Ph.D. thesis, California Institute of Technology.
- Riley, J. J., Metcalfe, R. W., and Orszag, S. A. 1985, "Direct Numerical Simulations of Chemically Reacting Turbulent Mixing Layers," *Phys. Fluids* **29** (2).

VISUAL STUDY OF THE NEAR-COMPLIANT-WALL FLOW STRUCTURE IN A TURBULENT BOUNDARY LAYER

T. Lee and W.H. Schwarz
The Johns Hopkins University
Baltimore, Maryland

The near-wall flow structure of a fully developed turbulent boundary layer with a single-layer passive viscoelastic compliant surface was studied using the hydrogen-bubble technique. Low-speed compliant-wall streaks with increased spanwise spacing and elongated spatial coherence were found and were compared to those obtained on a rigid surface. More interestingly, an intermittent laminarization-like phenomenon was observed at lower Reynolds number for the particular compliant surface investigated. Apparently, the observed changes in the near-compliant-wall flow structure are caused by the stable interaction between the compliant surface and the turbulent flow field. The visual results are then linked to the optical holographic interferometry compliant surface displacement and laser-Doppler-velocimetry mean velocity and turbulence intensity measurements so as to better understand the physics of the stable interaction between a turbulent boundary layer and a passive compliant surface.

1. INTRODUCTION

The idea of using a compliant coating to delay the laminar-to-turbulence transition and to affect the turbulent boundary layer so as to produce significant drag reduction was introduced by Kramer¹. The search for such a surface has been elusive, despite reports of substantial drag reduction by some investigators. Irreproducibility seems to be an outstanding characteristic of compliant surface experiments. The interaction between a passive compliant surface and a turbulent boundary layer is still not well understood. Recently, Hansen *et al.*², Gad-el-Hak *et al.*³, and Riley *et al.*⁴ observed hydroelastic instabilities, in the form of large-amplitude static-divergence waves, which are developed on viscoelastic compliant surfaces when the ratio of U_s (onset velocity of the static-divergence waves) to the transverse-wave speed in the solid $C_t (= (G/\rho_s)^{1/2}$, where G is the shear modulus of the compliant material, and ρ_s is the density of the solid) exceeds an asymptotic value of about 3. The presence of these unstable surface responses was always accompanied by an increase in the skin friction drag. It is, therefore, necessary that the amplitude of the surface motions must be kept low enough to avoid causing a "roughness" effect which would increase, rather than decrease, the drag.

For a zero-pressure-gradient, flat-plate turbulent boundary layer, the production and transport of the turbulence are dominated by the formation of the well-organized spatially and temporally dependent wall structures and their interaction with other portions of the flow through a process of gradual lift-up, then sudden oscillation, bursting, and ejection in the near-rigid-wall region (Kline *et al.*⁵). Blackwelder and Eckelmann⁶ suggested that the flow in the sublayer and wall adjacent regions is featured by counter-rotating pairs of streamwise vortices which dominate the bursting events or frequency (f_b) and the associated turbulence production. It seems, therefore, that a promising candidate for the compliant-surface drag reduction would somehow be able to generate a small-amplitude, stable

surface displacements (in the absence of unstable static-divergence waves) to disrupt this bursting process. Bushnell *et al.*⁷ hypothesized that a successful compliant coating would modulate the "preburst flow" in the turbulent boundary layer by providing a pressure field that would tend to inhibit or suppress the burst formation. This would result in a reduced number of bursts occurring per unit time and consequently a lower skin-friction drag. It is also hypothesized that any variation in the magnitude of dimensionless wall-streak spacing λ^* ($=\lambda u_*/v$, where λ is the wall-streak spacing, and u_* is the friction velocity) is accompanied by a change in skin-friction coefficient.

The correlations among λ^* , dimensionless streamwise wall-streak coherence κ_s^* ($=\kappa_s u_*/v$), f_b^* ($=f_b v/u_*^2$) and the skin-friction coefficient C_f have been investigated by researchers elsewhere. Grass⁸ reported that the nature of the interaction between the inner and outer regions remains quite similar whether the wall is smooth or covered with roughness elements protruding up to about 80 wall units (v/u_*), well outside the viscous region. This may be interpreted as minimizing the importance of streaks. On the other hand, smooth-wall data in drag reduction by polymer addition (e.g., Tiederman *et al.*⁹) show that there is a direct correlation among increased λ^* , decreased f_b^* and C_f reduction. However, Gad-el-Hak *et al.*³ reported that no significant differences were observed in the number or the length of recorded streaks for a PVC plastisol-gel compliant surface, and no measurable variations in the skin-friction coefficient was observed as long as the magnitude of the compliant-surface displacements are less than 30 μ m in a turbulent boundary layer.

The objective of the present study was to use the hydrogen-bubble technique to determine if the presence of a small-amplitude compliant-surface undulations would modify the spatial structure of the wall streaks and if this modification leads to any changes in the velocity and turbulence intensity and C_f measurements. In other words, it is important to examine that if any observed changes in the compliant-wall-streak spacings would lead to: (1) an alteration of the turbulent flow structure; and (2) a wall shear stress reduction or increase. Optical holographic interferometry and laser-Doppler-velocimetry techniques were also employed to obtain the corresponding basic parameters of the turbulent boundary layers examined and the whole-field flow-induced small compliant-surface displacement measurements so as to better understand the physics of the stable interaction between a turbulent boundary layer and a passive compliant surface.

2. EXPERIMENTAL APPARATUS AND METHODS

2.1. Test Facility and Compliant Material

The closed-loop, low-turbulence water tunnel at the National Institute of Standards and Technology was used in the present experiments. The test section is 0.6 m in diameter and 3.6 m in length. A stainless steel flat plate (3.6x0.6x0.048 m) with a highly polished top cover is rigidly mounted within the test section along the centerline to generate a fully developed turbulent boundary layer. A tail flap was mounted on the downstream end of the plate to control the pressure distribution along the plate, as well as the angle of attack at the leading edge. The momentum-thickness Reynolds numbers (Re_θ) investigated ranged from 900 to 8650. The single-layer isotropic passive viscoelastic compliant materials were made by mixing commercially available RTV silicone elastomer (Dow-Corning Sylgard 184) and silicone oil (Dow-Corning 200 series silicone oil). The mixture were chosen in accordance with Duncan's¹⁰ theoretical results to produce small amplitude, stable surface displacements on the compliant surface which represent the "footprints" (see figure 1 from Hess *et al.*¹¹) of the flow structure in the shear layer. The amount and viscosity of the oil in the mixture can be varied to change the viscoelastic properties of the compliant material and allows one to alter the response of the compliant surface to the flow Reynolds numbers of



Figure 1. Compliant surface response for $R_\theta = 7200$; compliant material 9/91-100 cSt oil; photographed region: 22.3x28.6 cm; spacing between hot-film prongs: 0.3 cm (photograph is reproduced from figure 5 in Hess *et al.*¹¹).

interest. The compliant surfaces were prepared in 3.8 cm deep plexiglas trays which were placed flush within the flat plate and which cover about 10 percent of the working surface. A compliant material with 91 percent by weight of 100 cSt oil and 9 percent of elastomer (9/91-100 cSt) was used in the present experiment. The shear modulus of this compliant mixture was measured with a Weissenberg rheogoniometer at the Johns Hopkins University, and found to be about 2300 dynes/cm².

2.2. Near-Wall Flow Structure Visualization

The near-wall flow structures were tagged with time lines of bubbles generated using the hydrogen-bubble technique as described by Schraub *et al.*¹². A simple and inexpensive electronic circuit which followed the design of Budwig and Peattie¹³ was built for delivering high-voltage (0 to 395 volts) pulses to the bubble wire. The pulse circuit is triggered by a TTL input signal, which allows great flexibility in its operating frequency (f_p). The anode is set at the ground potential to eliminate the electrical shock hazard. A platinum wire, of diameter 25 μ m and length 30 cm, was used as the cathode of the electronic circuit to generate small hydrogen bubbles. The hydrogen-bubble time-lines were made visible by lighting (using three 500 W incandescent bulbs) at an oblique angle of about 45° to the view direction or with the line of sight of the camera. Two specially-designed hydraulic pistons driven by two separate micrometers (each with a resolution of 2.5 μ m) were built to accurately position the bubble wire. A cathetometer with a maximum resolution of 10 μ m was used to determine the distance of the wire above the surface (based on the distance between the wire and its reflection from the surface). A 35 mm Nikon camera with a shutter speed set at 4 millisecond and with the lens aperture set at f2.8 was used to view and record the hydrogen-bubble time lines. The films used were Kodak Tmax rated at 400 ASA. The still photographs were used in negative form for projection to an enlarged scale where measurements could be easily obtained.

2.3. Turbulent Boundary Layers Characterization

The Dantec 60x Fiberflow series fiber-optic laser Doppler anemometer (LDA) was used to acquire the mean-velocity and turbulence-intensity data for the turbulent boundary layers. A 4-watt argon-ion laser (Spectra-Physics 2016) yielding 1.6 watts of power at a wavelength of 514 nm was used for the LDA. The measuring

volume is 75 μm in diameter and 0.63 mm in length which corresponded to about 4 wall units at $Re_\tau = 900$. The small measuring volume in combination with the fast signal-processing electronics permits high-bandwidth time-resolved measurements of the fluctuating velocities. The probe head was mounted on a specially-built traverse mechanism (with five degrees of freedom and a resolution of 1 μm) to measure the turbulent flow field properties over the surface.

LDA signal processing and validation are obtained using a Dantec 57N10 Burst Spectrum Analyzer (BSA) signal processor. The BSA performs an Fast Fourier Transform on the burst produced by each particle when it crosses the fringes (up to a 624 KHz maximum data rate). The fully computer-controlled BSA is capable of working in conditions of poor seeding; i.e., low signal-to-noise ratio (SNR), and in conditions of severe reflections from nearby surfaces. Compared with a conventional counter, its SNR threshold is, according to the manufacturers, about 15 dB lower. This means that bursts of small particles, which are usually buried in the signal noise, can now be "seen". The water flow is seeded with silicone carbide particles (TSI Model 10081), of a mean diameter of 1.5 μm , to obtain good signals in the present backscatter operation. The mean-velocity measurements are estimated to have about a 2 percent experimental uncertainty. This estimate is based on the maximum value of each quantity.

3. RESULTS AND DISCUSSION

3.1. Near-Wall Flow Structures

The near-wall flow structures were visualized using hydrogen-bubble time-lines at $Re_\tau = 2350, 1950, 1350$ and 900, respectively. Plan-view pictures of the spanwise low-speed wall streaks at different locations above both the rigid and compliant surfaces are presented with the flow direction from top to bottom.

3.1.1. Rigid surface case

Figure 2 summarizes the low-speed wall-streak structures observed in the present investigation at various Re_τ which are consistent with those of previous investigators using the same hydrogen-bubble technique (e.g., Kline *et al.*⁵, Lu and Smith¹⁴, and others). Figure 2a shows the low-speed wall-streak flow structure in the viscous sublayer. The collection of the hydrogen bubbles into a streaky structure is characteristic of this region. Figure 2b shows that the streaks become less noticeable in the buffer region. The streaks ejected from the near-wall region interact as they enter the outer regions of the flow. Figure 2c shows the flow structure in the log region. The streaks become less visible as compared to those shown in figures 2a and 2b. Various scales of motions are evident, also the entire flow appears to be turbulent.

Figure 3 shows the collection of all the data available^{5,15-19} on the values of the mean dimensionless spanwise spacing of the wall streaks using the hydrogen-bubble technique at different Re_τ . The present observed λ^+ values are in good agreement with the values given by Kline *et al.*⁵ and the values obtained by nearly all subsequent investigators. A mean value of λ^+ of 95 for $y^+ = 2 - 5$ was found from the present study. Figures 2 and 3 also show clearly that low-speed streaks are essentially invariant with Re_τ .

3.1.2. Compliant surface case

Visual observations with the presence of surface compliance indicated, in general, a similar low-speed wall-streak appearance compared to the rigid surface case, but with larger values of λ^+ (as indicated by the solid squares in figure 3). Also, the compliant-wall streaks appear to be more quiescent. More interestingly, an intermittent laminarization-like flow phenomenon over our particular compliant surface was observed at $Re_\tau = 1350$ and 900 with

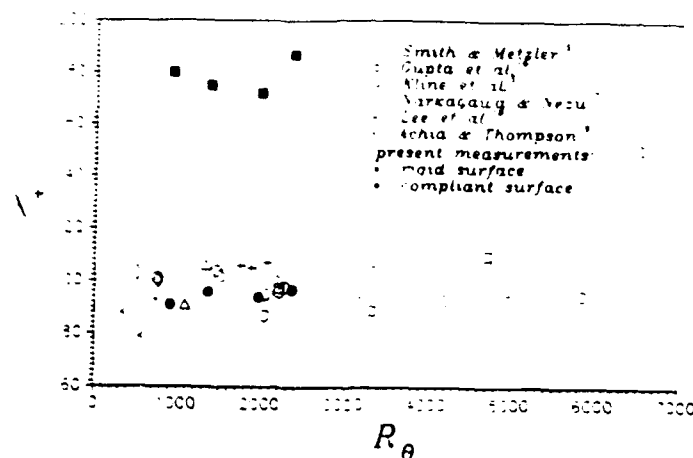


Figure 3. Variations of mean dimensionless spanwise wall-streak spacing with Reynolds number.

the bubble wire pulsed at $f_p = 20$ Hz and positioned at $y^* = 46$ for $R_\theta = 1350$ and $y^* = 17, 20$ and 26 for $R_\theta = 900$, respectively.

Figures 4a, 4b and 4c show the plan views of the near-compliant-wall flow structure at three different time sequences at $y^* = 20$ for $R_\theta = 900$. The time intervals were specified but arbitrary. Apparently, there is a stable interaction taking place between the present particular compliant surface and the turbulent flow field. Results show that at time t_1 , large scales of motions are more evident than that at the previous time t_1 and t_2 . The flow structure became more (quasi-) laminar-like or quiescent as time elapsed. The observed laminarization or the reversion of a turbulent boundary layer implies that either the turbulence production is being turned off suddenly, or dramatically reduced, or the energy dissipation is much larger than the turbulence production, which then infers that the present compliant surface may be an effective energy absorber. In other words, this particular compliant surface seems to effect a change in the balance between the turbulence production and dissipation and to exert a large net influence on the turbulence as a whole. Similar laminar-like observations were found for a y^* of 26 at two different time sequences (figures 5a and 5b). Figure 5a shows the plan views of the near-compliant-wall flow structures at time t_1 . Figure 5b shows that at time t_2 , the flow structure became quiescent or laminar from a original turbulent boundary flow condition. The corresponding instantaneous peak-to-valley amplitudes and the *rms* value of surface displacements obtained by the non-invasive optical holographic technique over a 5 cm diameter area are: 1.67 m and 0.32 m for $R_\theta = 900$, 2.93 m and 0.38 m for $R_\theta = 1350$, and 3.82 m and 0.72 m for $R_\theta = 1950$, respectively. A typical photograph and isometric phase map of the reconstructed interferometric fringes at $R_\theta = 1950$ are shown in figure 6. The details of both the optical arrangement for hologram recording and reconstruction and the determination of the compliant-surface displacement from the interferometric fringe patterns are given in Lee *et al.*²⁰.

3.2. Turbulent-Boundary-Layer Characteristics

A series of time-mean velocity and turbulence-intensity profiles were investigated for $900 < R_\theta < 8650$. The mean-velocity data were fitted to appropriate empirical correlations, and these correlations were used to establish the parameters for the visual studies.

Surface Displacement (um)

0.55 -

(b)

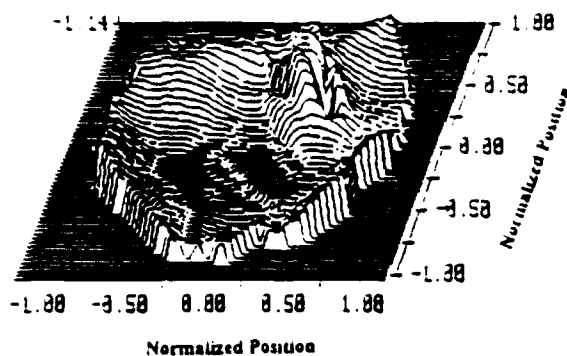


Figure 6. Photograph and the isometric phase map of the reconstructed interferometric fringes at $Re = 1950$: (a) interferogram, and (b) isometric phase map (photograph and figure are reproduced from figures 11 and 12a in Lee *et al.*²⁵).

3.2.1. Rigid surface case

Figure 7 shows the mean-velocity profiles in the wall-variable form at seven different Re . The nondimensionalized parameter u_+ was obtained using the Clauser's²¹ cross-plot method. Results show that the law-of-the-wall is independent of Reynolds number but the extent of the logarithmic region was found to decrease with decreasing Re . The existence of the fully developed turbulent boundary layer at the lowest Re ($= 900$) investigated in the present study is assured by comparing this value to the minimum Re determined by investigators elsewhere. The lower and upper bound of the minimum Re for which fully developed turbulent flow could be observed experimentally on a rigid-surface plate boundary layer are 354 and 738 as reported by Smits *et al.*²² and Granville²³, respectively. The existence of the turbulent boundary layer at $Re = 900$ can also be demonstrated from the visual observations shown in figure 2a.

Figure 8 shows the variation of the skin-friction coefficient with the Reynolds number. The present C_f measurements are a little larger than Purtell *et al.*'s²⁴ data (indicated by open circles) and Coles's²⁵ proposed values for an equilibrium turbulent boundary layer ($Re > 5000$, dashed line). Figure 9 shows the streamwise turbulence-intensity profiles for $Re < 5000$. Results show that the peak in the turbulence intensity profile increased with decreasing Re compared to the values of equilibrium conditions (dashed line) from Klebanoff²⁶. This tendency is consistent with the measurements of Purtell *et al.*¹⁹ and Erm and Joubert²⁷, except that the LDA turbulence data are slightly higher than hot-wire measurements. Figure 9 also indicates that the Reynolds number effect penetrates the boundary layer much deeper in terms of the turbulence intensity than it does for the mean velocity (see figure 7).

3.2.2. Compliant surface case

Figures 10a through 10f show the comparisons of the mean-velocity profiles of the compliant-surface case (circles) with that of rigid-surface case (squares) at six different Re . All these point-velocity measurements are made in the absence of the large-amplitude static-divergence waves. The compliant-surface mean-velocity data were nondimensionalized by u_+ which were obtained using the wall-slope method (in which the wall shear stress is obtained from the slope of the mean velocity profile near the wall). Results show that the compliant-surface $u^+ - y^+$ profiles

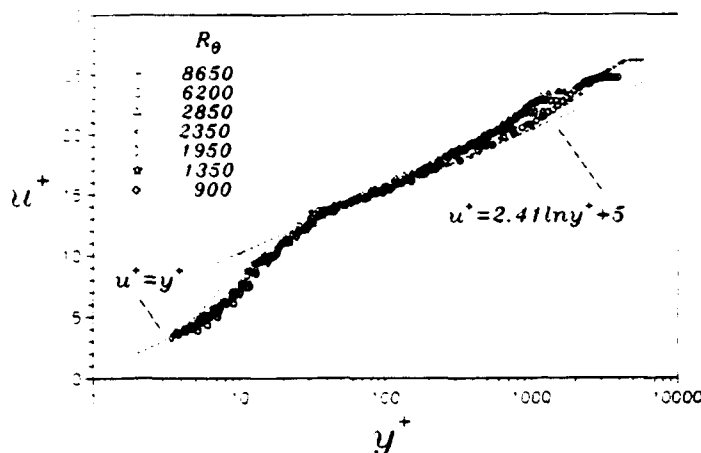


Figure 7. Mean velocity profiles at seven different Reynolds number.

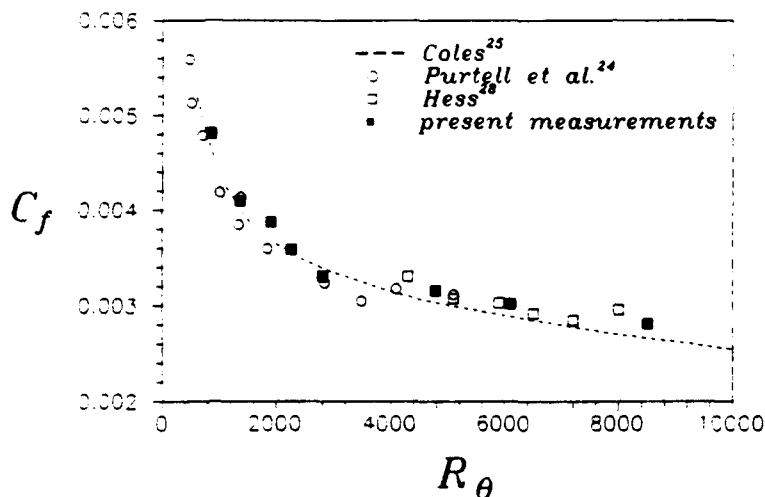


Figure 8. Variation of skin-friction coefficient with Reynolds number.

always had well-defined logarithmic and wake regions, but with a slight shift in the log-wall region at low R_θ (see figures 10c, 10d, and 10e). The magnitude of this shift increases with decreasing R_θ . The shift in the compliant-surface log-wall region at low R_θ is accompanied by: (1) a slightly broadened buffer region (see figures 10c, 10d and 10e); (2) a lower u_+ or C_f ; (3) a higher value of λ^+ (figure 3); and (4) a reduction in the streamwise velocity fluctuation (figure 9) compared to the rigid-surface data. Figures 10c through 10f in connection with the visual results (figures 2 through 5) indicate that the mean-velocity flow fields were altered by the stable interaction of this particular compliant surface with the turbulent flow field. Apparently, the formation of the low-speed wall-streaks is suppressed by the presence of the compliant-surface undulations which in turn yields a lower skin-friction coefficients and also a possible decrease in the average bursting rate. In other words, vortex stretching which responsible for the transfer of turbulent energy and vorticity is modulated by the surface compliance or the stable fluid/compliant-surface interaction. However, the physical mechanism responsible for this favorable interaction of the compliant surface with the fluid is still not understood. No significant changes in the compliant-surface u^+-y^+ profiles (see figures 10a and 10b) were found compared to the corresponding rigid-surface measurements as the Reynolds number approaches or becomes larger than the value for the equilibrium conditions. The results of the present compliant-surface u^+-y^+ measurements (in figures 10c and 10f) and the C_f thus determined, compared to the

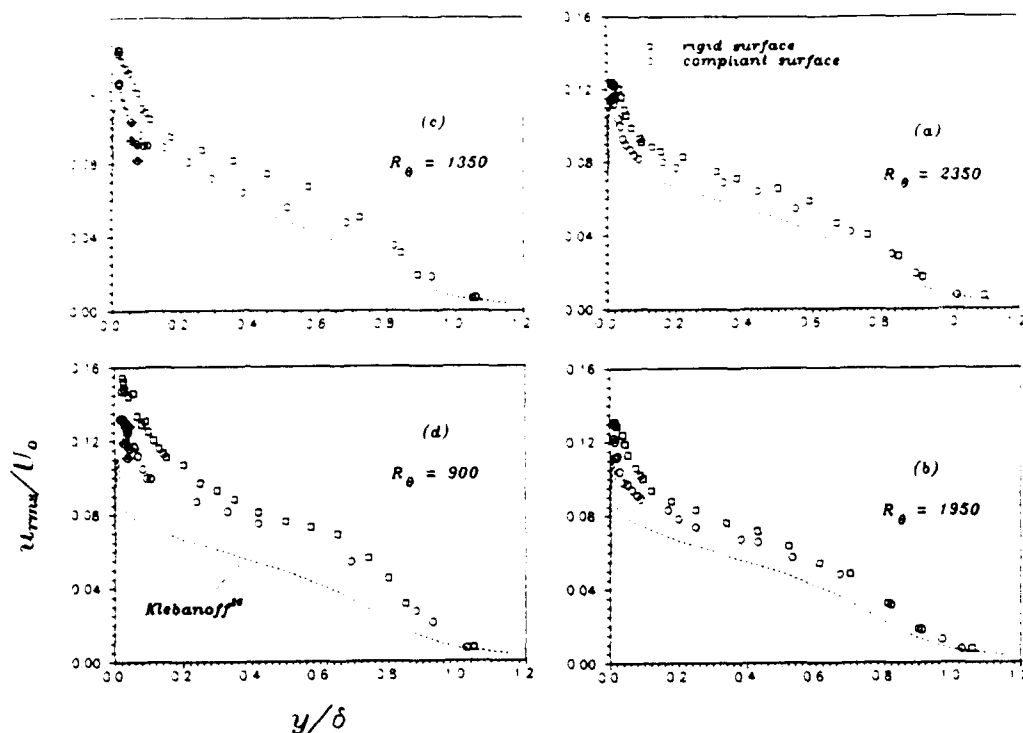


Figure 9. Comparisons of streamwise turbulence-intensity measurements between rigid- and compliant-surface cases at four different Reynolds numbers.

values of rigid surface, are not consistent with the measurements of Gad-el-Hak *et al.*³. Gad-el-Hak *et al.* concluded that the mean-velocity and the *rms* velocity-fluctuation measurements for a turbulent boundary layer over a PVC plastisol-gel compliant surface (with $G = 50$ -125000 dyne/cm² and 0.05-0.7 cm thickness) did not differ from that on a rigid surfaces as long as the static-divergence waves were absent. They also found that no significant differences were observed in the number or the length of recorded streaks for displacement-thickness Reynolds numbers ranging from 400 to 6,000.

The disappearance of the log wall region shown in figure 10f at $R_\theta = 900$ is consistent with the observed intermittent laminarization-like phenomena discussed above in Section 3.1.2. This phenomenon is accompanied by the following experimental observations: (1) an increase in the compliant-wall streak spacing (see figure 3); (2) the appearance of the intermittent laminarization-like flow structures (typical photos are shown as figures 4 and 5); (3) a decrease in the streamwise turbulence-intensity measurements (figure 9); and (+) the break-up of the log wall region (figure 10f) demonstrated that the stable interaction between the present compliant surface and the turbulence flow field at $R_\theta = 900$ does strongly modulate the near-compliant-wall flow structure. This modulation may be attributed to the relative increase in dissipation occurs when the Reynolds number goes down in a flow especially with the present compliant surface, or to the hypothesis that the compliant surface inhibits vortex stretching and leads to a quiescent state. The mechanism responsible for the appearance of the laminar-like flow phenomenon is still not clear.

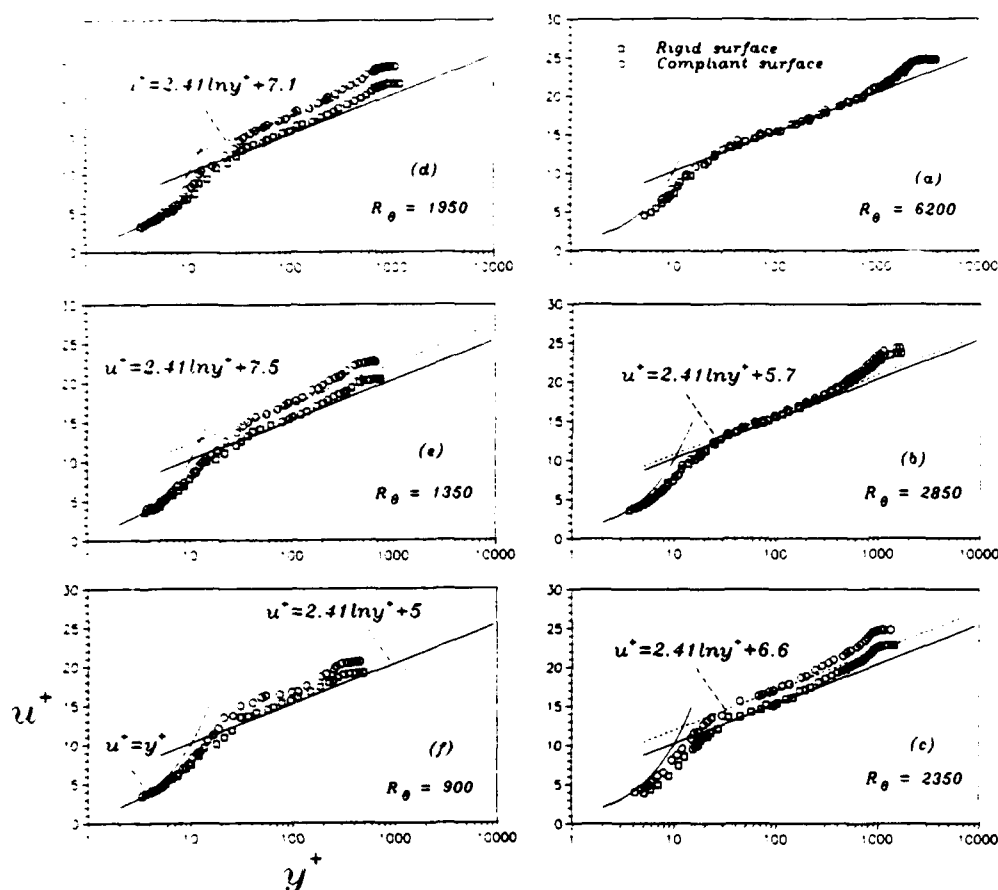


Figure 10. Comparisons of mean-velocity measurements between rigid- and compliant-surface cases at six different Reynolds numbers.

4. SUMMARY AND CONCLUSIONS

The stable interaction of the present single-layer passive viscoelastic compliant surface with a fully developed turbulent boundary layer was visualized with hydrogen-bubble time lines in connection with surface-displacement and flow field measurements. For low Reynolds number flows, a small-amplitude stable fluid/compliant-surface interaction was found from the following experimental results (compared to the values of rigid surface case): (1) an increase in λ^* and x_i^* which imply an associated decrease in the bursting rate; (2) the appearance of intermittent laminarization-like flow phenomena near the compliant wall; (3) a slight broadened buffer region; (4) a shift in the compliant law-of-the-wall; (5) a decrease in the streamwise velocity fluctuation; (6) a reduction in the skin-friction coefficient.

In summary, visual studies associated with the mean-velocity and turbulence-intensity measurements indicate that the compliant surface motion was modulating the flow field close to the wall and that the feedback loop which allows the turbulence to be self-sustaining seems to be modified at low Reynolds numbers. However, the mechanism responsible for the above observations is still not well understood. Detailed turbulent flow field measurements and the statistical measures of the real-time random topography of the compliant surface are needed in order to better understand the nature of the stable fluid/compliant-surface interaction.

ACKNOWLEDGMENTS

This work was supported by the Office of Naval Research under contract N00014-87-0126. Grateful acknowledgement is made to the staff of the Fluid Dynamics Group of the National Institute of Standards and Technology, especially David E. Hess, George E. Mattingly and Norman Meese without whose assistance this work could not have been accomplished.

REFERENCES

1. M.O. Kramer, *J. Aero. Sci.* **41**, 259 (1957).
2. R.J. Hansen, D.L. Hunston & C.C. Ni, *J. Sound & Vibration* **68**, 317 (1980).
3. M. Gad-el-Hak, R.F. Blackwelder & J.J. Riley, *J. Fluid Mech.* **140**, 257 (1984).
4. J.J. Riley, M. Gad-el-Hak & R.W. Metcalf, *Ann. Rev. Fluid Mech.* **20**, 393 (1988).
5. S.J. Kline, W.C. Reynolds, F.A. Schraub & P.W. Runstadler, *J. Fluid Mech.* **30**, 741 (1967).
6. R.F. Blackwelder & J.H. Haritonidis, *J. Fluid Mech.* **94**, 577 (1979).
7. D.M. Bushnell, J.N. Hefner & R.L. Ash, *Phys. Fluids* **20**, S31 (1977).
8. A.J. Grass, *J. Fluid Mech.* **50**, 233 (1971).
9. W.G. Tiederman, T.S. Luchik & D.G. Bogard, *J. Fluid Mech.* **156**, 419 (1985).
10. J.H. Duncan, A.M. Waxman & M.P. Tulin, *J. Fluid Mech.* **158**, 177 (1985).
11. D.E. Hess, R.A. Peattie & W.H. Schwarz, to appear in *Exp. Fluids* (1992).
12. F.A. Schraub, S.J. Kline, J. Henry, P.W. Runstadler & A. Littell, *J. Basic Engr.*, 429 (1965).
13. R. Budwig & R. Peattie, *J. Phys. E: Sci. Instru.* **22**, 250 (1989).
14. L.J. Lu & C.R. Smith, *J. Fluid Mech.* **232**, 303 (1991).
15. C. R. Smith & S. P. Metzler, *J. Fluid Mech.* **129**, 27 (1983).
16. A. K. Gupta, J. Laufer & R. E. Kaplan, *J. Fluid Mech.* **50**, 493 (1971).
17. H. Narkagawa & I. Nezzu, *J. Fluid Mech.* **104**, 1 (1981).
18. M. K. Lee, L. D. Eckelman & T. J. Hanratty, *J. Fluid Mech.* **66**, 17 (1974).
19. B. U. Achia & D. W. Thompson, *J. Fluid Mech.* **81**, 429 (1976).
20. T. Lee, M. Fisher & W.H. Schwarz, to appear in *Exp. Fluids* (1992).
21. F.H. Clauser, *Adv. Appl. Mech.*, **4**, 1 (1956).
22. A.J. Smits, N. Matheson & P.N. Joubert, *J. Ship Research* **27**, 147 (1983).
23. P.S. Granville, *J. Ship Research* **21**, 1 (1977).
24. L.P. Purtell, P.S. Klebanoff & F.T. Buckley, *Phys. Fluids* **24**, 802 (1981).
25. D. Coles, Appendix A of Rand R-304-PR (1962).
26. P.S. Klebanoff, NBS Report 2454 (1953).
27. L.P. Erm & P.N. Joubert, *J. Fluid Mech.* **230**, 1 (1991).
28. D.E. Hess, Ph.D. dissertation, Johns Hopkins Univ. (1990).

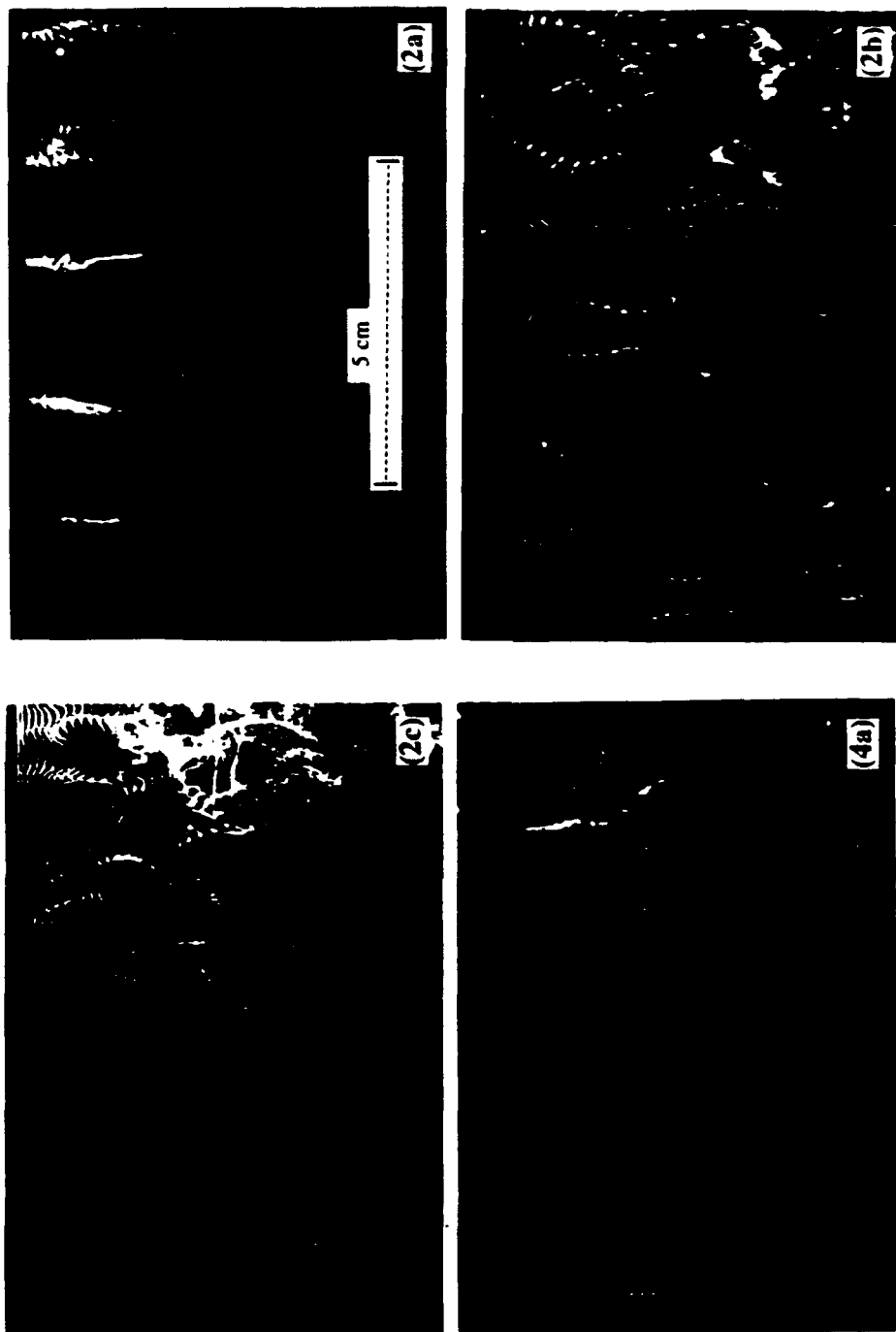


Figure 2. Plan views of low-speed streaks over a rigid-surface, flat plate turbulent boundary layer: (a) $y^* = 2$, $t_p = 40$ Hz and $R_\theta = 900$; (b) $y^* = 24$, $t_p = 20$ Hz and $R_\theta = 900$; and (c) $y^* = 64$, $t_p = 40$ Hz and $R_\theta = 900$.

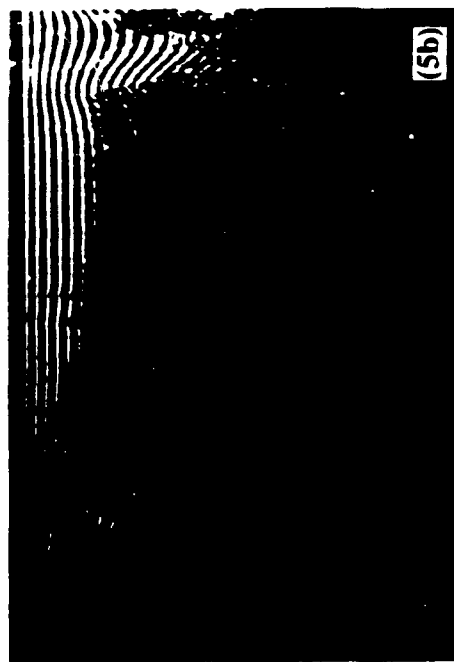
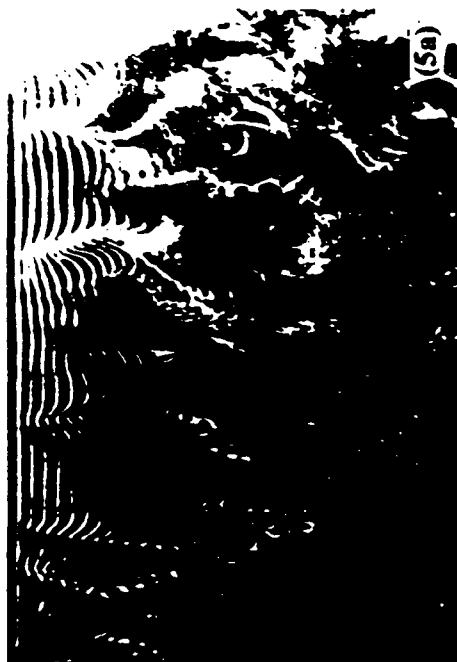


Figure 5. Plan views of intermittent laminar-like flow structures over the present compliant surface at two different time sequences for $R_0 = 900$. The bubble wire is located at $y^* = 26$ and pulsed at $f_p = 20$ Hz: (a) at time t_0 , and (b) at time t_1 .

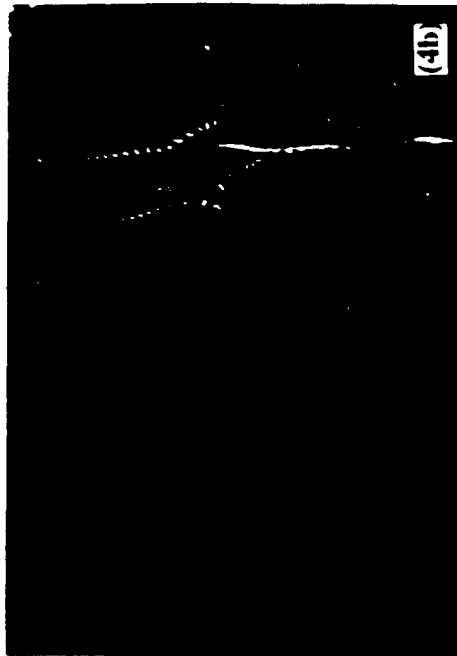


Figure 4. Plan views of intermittent laminar-like flow structure over the compliant surface at three different time sequences for $R_0 = 900$. The bubble wire is located at $y^* = 20$ and pulsed at $f_p = 20$ Hz (note the time intervals are not constant): (a) at time t_0 , (b) at time t_1 , and (c) at time t_2 .

MODELLING THE TIME DEPENDENT FLOW OVER V AND U GROOVE RIBLETS

S. Tullis and A. Pollard ¹

Department of Mechanical Engineering
Queen's University at Kingston
Canada. K7L 3N6

Abstract

The flow over V-groove and U-groove riblets is examined computationally using a time dependent model of the viscous wall region. This "2 1/2 D model", developed by Hatzivramidis and Hanratty (1979) and modified by Nikolaidis (1984) and, Chapman and Kuhn (1981,1986) assumes homogeneity in the streamwise direction so that the flow is solved only in the cross-sectional plane. The flow at the upper bound of the computational domain ($y^+ \simeq 40$) is described using a streamwise eddy model consisting of two scales, one of the streak spacing ($\lambda^+ \simeq 100$) which dominates vertical momentum transport, and a larger scale accounting for the influence of large outer flow eddies.

A control volume finite element method utilizing triangular meshes is used to exactly fit the riblet cross-sectional geometry. Results obtained using fairly large drag-neutral riblets compare well with the limited experimental data available. Observations of the transient flow conditions for both larger drag-neutral and smaller drag-reducing riblets suggest that the riblets limit the lateral spread of intrushes towards the wall and retain low momentum fluid in the riblet valleys effectively isolating much of the wall from such intrushes. The generation of intermittent secondary vortices within the riblet valleys also occurs; however, these appear to be quite weak and fairly short-lived.

1 Introduction

The ability of riblets to produce significant skin friction reductions in turbulent boundary layer flows is well established. Walsh (1990) and Savill (1989) have suggested that the viscous effect of the riblets in accumulating slow, low shear stress flow in the riblet grooves plays a major role in the skin friction reduction. The effect of riblets, however, has been observed by Benhalilou *et al.* (1991) and Choi (1989) to extend well above the viscous wall region. This has led these authors to the conclusion that at least some portion of the drag reduction is a result of the influence of riblets on near wall turbulent coherent structures.

In the very near wall region ($y^+ \leq 30-40$), the dominant turbulent structures appear to be quasi-periodic streamwise eddies (Bakewell and Lumley, 1967; Robinson *et al.*, 1990). These eddies act as a mechanism for the transport of streamwise momentum to and away from the wall which then contribute to the high Reynolds stress and turbulence production close to the wall. The near-wall low-speed streaks, which have a characteristic spanwise "streak" spacing of $\lambda^+ \simeq 100$, are generally accepted (Smith *et al.*, 1989) to be the lift up of low momentum fluid from the wall by an adjacent streamwise eddy. The

¹ to whom all correspondence should be addressed

surface drag reduction effect of riblets then seems to involve some sort of influence on these near wall eddies. An increase in the streak spacing and a decrease in their spanwise motions over riblet surfaces has been noted experimentally by many researchers, including Gallager & Thomas (1984), Bacher & Smith (1985) and Choi (1989). Both of these effects are similar to the drag reduction produced by dilute polymer solutions (Tiederman, 1989).

Until very recently, the modelling of the flow over riblets has usually been performed with simple half or single riblet geometries and with either laminar flow or mixing-length turbulence models (Djenidi *et al.*, 1990; Benhalilou *et al.*, 1991) and, more recently, $k-\epsilon$ turbulence models (Djenidi, 1991; Launder and Li, 1991). These approaches have used Reynolds-averaged and often parabolized equations to produce steady-state solutions. These methods do not consider multiple riblet interactions with any specific near wall turbulent structures, particularly streamwise vortices, and depend critically on the near wall damping assumptions made.

The approach taken here is to use a "simple eddy" or "coherent structure" model to directly model quasi-periodic streamwise eddies in the very near wall region. The model was originally developed for flat wall turbulent boundary layers by Hatziaivramidis and Hanratty (1979) and developed and refined by Chapman and Kuhn (1981, 1986) and Nikolaides (1984). The model is not intended to exactly predict the flow; it is a representation of near wall streamwise eddies and their time development — although the models do provide good agreements with experimentally measured mean velocity, Reynolds stress and turbulence intensity, skewness and flatness profiles for flat walls.

2 Turbulent Boundary Layer Modelling

2.1 Governing Equations

The model of the turbulent boundary layer is time dependent with the coordinates oriented such that the downstream direction is along the x axis, the y direction is perpendicular to the wall and the z axis is across the flow in the spanwise direction. With the streamwise eddies and low speed streaks being highly elongated (Smith and Metzler, 1983; Kasagi, 1989) a major assumption is made that the streamwise velocity derivatives can be neglected in comparison to the cross-stream velocity derivatives.

The governing equations are then:

$$\frac{\partial v^+}{\partial t^+} + \frac{\partial v^{+2}}{\partial y^+} + \frac{\partial w^+ v^+}{\partial z^+} = -\frac{\partial p^+}{\partial y^+} + \frac{\partial^2 v^+}{\partial y^{+2}} + \frac{\partial^2 v^+}{\partial z^{+2}} \quad (1)$$

$$\frac{\partial w^+}{\partial t^+} + \frac{\partial v^+ w^+}{\partial y^+} + \frac{\partial w^{+2}}{\partial z^+} = -\frac{\partial p^+}{\partial z^+} + \frac{\partial^2 w^+}{\partial y^{+2}} + \frac{\partial^2 w^+}{\partial z^{+2}} \quad (2)$$

$$\frac{\partial v^+}{\partial y^+} + \frac{\partial w^+}{\partial z^+} = 0 \quad (3)$$

and,

$$\frac{\partial U^+}{\partial t^+} + \frac{\partial v^+ U^+}{\partial y^+} + \frac{\partial w^+ U^+}{\partial z^+} = \frac{\partial^2 U^+}{\partial y^{+2}} + \frac{\partial^2 U^+}{\partial z^{+2}} \quad (4)$$

All of the quantities in equations 1-4 are normalized by the friction velocity, u_τ , with $u_\tau = \sqrt{\tau_w/\rho}$, where τ_w is the flat wall shear stress. Wall normalized units will be used for the remainder of this paper, so the superscript "+" will be dropped.

It can be noted that the cross-stream velocities v and w and the downstream velocity U are not coupled; the cross-stream velocities can be solved using equations 1-3, then U can be solved directly using equation 4. Because of this feature, this type of model is often referred to as a "2 1/2 D" model. There is also no downstream pressure gradient.

2.2 Boundary Conditions

The computational domain consists of a cross-sectional y - z plane with $0 \leq y \leq y_0$ where y_0 is typically 40. The spanwise size of the domain depends on the particular variation of the model but is usually in the range of 100–200 wall units.

The main modelling assumption of the method is in the specification of the velocities along the upper edge, $y_0 \simeq 40$, of the domain. These specifications can vary depending on the specific model; however, in all of the models, the velocity components specified at the upper boundary are periodic in time and spanwise location (z) and have overall magnitudes of the experimentally determined turbulence intensities at that distance from the wall. The downstream velocity U is specified to consist of two components: a fluctuating component u and a constant component \bar{U} which is determined, for flat walls, from experimental measurement or from the log-law relationship.

The fluctuating velocity components usually have two scales: one which dominates vertical momentum transport and roughly the size of the streak spacing and a larger scale accounting for the influence of all large "outer flow eddies". The full form as given by Nikolaides (1984) is:

$$U = \bar{U} + \hat{u}_1 \cos\left(\frac{2\pi}{T_1}t + \phi_{u1}\right) \cos\frac{2\pi}{\lambda_1}z + \hat{u}_2 \cos\left(\frac{2\pi}{T_2}t + \phi_{u2}\right) \cos\frac{2\pi}{\lambda_2}z \quad (5)$$

$$v = \hat{v}_1 \cos\left(\frac{2\pi}{T_1}t + \phi_{v1}\right) \cos\frac{2\pi}{\lambda_1}z + \hat{v}_2 \cos\left(\frac{2\pi}{T_2}t + \phi_{v2}\right) \cos\frac{2\pi}{\lambda_2}z \quad (6)$$

$$w = \hat{w}_1 \cos\left(\frac{2\pi}{T_1}t + \phi_{w1}\right) \sin\frac{2\pi}{\lambda_1}z + \hat{w}_2 \cos\left(\frac{2\pi}{T_2}t + \phi_{w2}\right) \sin\frac{2\pi}{\lambda_2}z \quad (7)$$

The periods in the spanwise direction, λ_1 and λ_2 , are typically set respectively as 100, the size of the flat wall streak spacing, and 400 or infinity as a larger period accounting for the influence of all larger scale eddies. The time periods T_1 and T_2 are usually set to roughly the same values as λ_1 and λ_2 to agree with bursting frequencies and because it is reasoned that the larger scale transient and convective terms should be of the same order (Nikolaides, 1984). The model used in this study is basically that of Chapman and Kuhn (1986). The parameters used are summarized in table 1.

λ_1	100	$\lambda_2(u, v, w)$	$\infty, -, \infty$
T_1	143	$T_2(u, v, w)$	143, -, 286
u_1	1.8	u_2	2.53
v_1	1.0	v_2	0
w_1	2.0	w_2	1.175
ϕ_{u1}	0 (reference)	ϕ_{u2}	0
ϕ_{v1}	0	ϕ_{v2}	-
ϕ_{w1}	$\pm \frac{\pi}{2}$	ϕ_{w2}	$\frac{2\pi}{3}$

Table 1: Parameters used in Chapman and Kuhn's (1986) model.

The sides of the computational domain (at $z = 0$ and $z = z_0$) are treated with cyclic boundary conditions. The wall surface has the simple no-slip condition: $U = v = w = 0$. The specification of the upper $y_0 = 40$ conditions requires a definition of the location of the $y = 0$ surface. For flat walls, this surface location is simply the wall surface. For riblets walls, the protrusion height as defined and calculated by Bechert and Bartenwerfer (1989) is used to provide a specification of the $y = 0$ location.

2.3 Numerical Scheme

The numerical solution procedure used in this study is a Control Volume Finite Element Method (CVFEM) based on the work of Saabas (1991). The approach is an equal order co-located control volume method and is a development of earlier work by Baliga and Patankar (1979,1983) and Prakash and Patankar (1985). The computational domain is divided into three-node triangular elements which are able to fit exactly such complex geometries as riblets in cross-section. Control volumes are constructed about each node with the complete discretized equations assembled for each control volume on an element-by-element basis. Interpolation functions are used within each element to evaluate the velocity components. These exponential flow oriented functions correctly simulate the nature of convection, resulting in a substantial reduction of false diffusion (Baliga, 1979; Tullis, 1992). A time-stepping procedure was incorporated into the CVFEM using an implicit scheme similar to that of Patankar (1980). A structured grid is used with the triangular elements constructed by connecting the diagonals of a rectangular grid. This allows the use of line-by-line solvers.

3 Presentation and Discussion of Results

Five different cases are considered in this study: flow over a flat wall and flow over both V-groove and U-groove riblet walls for two different sizes of riblets. The larger sized riblets ($2h^+ = s^+ = 33.3$) are in the drag-neutral size range (Walsh, 1990) with three complete riblets in the computational domain. These riblets correspond well with the experimentally investigated cases of Vukoslavčević *et al.* (1987) and Benhalilou *et al.* (1991). The grids used for these larger riblets and the flat wall case are approximately 21×43 (y and z directions) with more grids in the y direction for the riblet cases. The flat wall and V-groove cases use uniform grids while a non-uniform grid is used to produce the semi-circular U-groove riblets. Drag-reducing riblet geometries are also considered: V-groove riblets with $h^+ = s^+ = 16.7$ and U-groove riblets with $2h^+ = s^+ = 16.7$. A 32×85 (y and z directions) grid is used with extensive grid refinement about the riblet peaks. The solutions consist of approximately 500 time steps with a time step size of $\Delta t^+ = 2$. This time step size was selected from a comparison of solutions obtained using the particular spatial grid sizes and various time step sizes. The initial solution within the computational domain used at $t = 0$ is simply Bechert and Bartenwerfer's (1989) solution for the downstream velocity (U) with no cross-stream velocities ($v = w = 0$). The effects of using this simple initial solution are not significant after two of the larger scale time periods (T_2).

The results of this study are be divided into two sections: the first section presents a comparison of calculated mean velocity profiles and streamwise turbulence intensities above the larger drag-neutral V-groove riblets and the experimental measurements of Vukoslavčević *et al.* (1987) and Benhalilou *et al.* (1991) using similar riblets; the second section deals with general observations of the time-dependent interaction between the near-wall streamwise vortices and riblets of various sizes and shapes. Although the comparisons of the first section can be presented graphically, the time-dependent general observations are more difficult to present here. The thesis and accompanying video of Tullis (1992) provide better presentation of this aspect of the results.

3.1 Mean velocity profiles

The model provides good agreement with experimental measurements for the mean streamwise velocity profile over a flat wall, as observed by Chapman and Kuhn (1986). There is, however, a noticeable discrepancy near the outer edge of the domain. This effect can be also noticed in many of the other computational results, particularly the turbulent statistics. This irregularity has been observed by

Chapman and Kuhn (1986) and Nikolaides (1984) who have suggest that it is the result of too restrictive boundary conditions, probably on the smaller scale eddies. Both Chapman and Kuhn and Nikolaides consider that this effect is limited to the outer 10–20% of the domain.

The calculated mean streamwise velocity profiles over the drag-neutral V-groove riblets agree reasonably well with the experimental measurements of Vukoslavčević *et al.* (1987) as shown in figure 1. The velocity gradient distribution at the riblet surface shows the same features observed by Vukoslavčević *et al.*

As depicted in figure 2a, the wall shear stress drops nearly to zero in the angled valleys of the V-groove riblets. The wall shear stress over the riblet peaks is much larger than over the flat wall — the increase is approximately 150%. This increase is larger than that noted by both Vukoslavčević *et al.* and Benhalilou *et al.* (1991) but may be exaggerated by the relatively coarse grid used in the present calculations. A similar surface drag distribution is observed over the U-groove riblets (figure 2b). The wall shear stress in the rounded riblet valleys drops to about 25% of the flat wall case while the increase above the riblet peaks is approximately the same size as for the V-groove riblets.

3.2 Streamwise Turbulence Intensity

The calculated turbulence intensities over a flat wall show fairly good agreement with experimental data, as was demonstrated by Chapman and Kuhn (1986). Experimental measurements of turbulence intensities within and above riblets are very limited. Vukoslavčević *et al.* have measured profiles of streamwise velocity fluctuation intensity (u') while Benhalilou *et al.* were also able to obtain spanwise velocity fluctuation intensity (w') profiles with similarly large-sized V-groove riblets. Consequently, attention will be concentrated on the streamwise turbulence intensity profiles. The two sets of experimental data collapse quite well when plotted using wall coordinates (u'^+ versus y^+); however, there are significant differences. With increasing distance from the wall, Benhalilou *et al.* observed a rapid increase in the u' intensity over the riblet peaks followed by nearly as rapid decrease, as can be seen in figure 3. The intensity over the riblet valley reaches a much lower maximum value and the peak and valley intensities appear to converge to a flat wall value of approximately 1.5, significantly lower than most other flat wall experimental values such as those of Clark (1968) and Ueda and Hinze (1975), at a height of $y^+ = 35$. Vukoslavčević *et al.*, in contrast, observe very little decrease in the u' intensity profiles after they reach their maxima — with the peak and valley profiles converging at a higher than flat wall value of $u'^+ \sim 2.4$. The computationally calculated u' intensity profiles resemble those of Vukoslavčević *et al.* close to the wall, although the valley profiles appear to reach slightly larger values closer to the wall. In the upper half of the calculation domain, however, the peak and valley profiles converge while steadily decreasing to a value of approximately 1.8 at the outer edge of the domain. In this aspect, the calculated results are roughly between the two sets of experimental data.

3.3 General Observations

As the transient vortices develop close to the wall, intermittent, rapidly decaying secondary vortices can be observed within the riblet valleys for all of the riblet configurations examined. This is essentially the same phenomenon that Bacher and Smith (1985) suggested as a mechanism in the weakening of the original primary vortices. However, the computationally observed vortices are generated and driven by the periodic outer edge conditions, so the strengths of these primary vortices would not be expected to be changed by the riblets. For the smaller drag-reducing riblets, there is a definite lag-time between the start of a roughly horizontal flow over the top of a riblet and the development of a secondary vortex within the riblet valley. This lag-time is only marginally shorter than the time taken for the reversal

of the flow above any particular riblet. It is then speculated that this is the reason why the calculated secondary vortices are quite weak; the maximum transverse velocity observed in valley of a V-groove riblet is approximately one-twentieth of the maximum in the adjacent flow above the riblet. These low secondary vortex strengths may, in contrast with the ideas of Bacher and Smith, actually help reduce the overall surface drag. Strong secondary vortices would be a mechanism for the transport of high downstream momentum fluid into the riblet valleys, resulting in high shear stresses and drag in the riblet valleys. The development of only relatively weak and short duration secondary vortices does not allow this momentum transfer to occur. The stability of such low momentum fluid in the riblet valleys has been experimentally observed by many researchers including Gallagher and Thomas (1984) and Bacher and Smith (1985). For the larger drag-neutral riblets, these secondary vortices are still quite weak but are significantly stronger than those in the valleys of the smaller riblets.

The other significant effect that can be observed is the influence of riblets on inflows towards the wall that occur beside and between vortices. These inflows carry high streamwise momentum fluid towards the wall and, when reaching a flat wall, spread laterally. This creates an extended area of the surface with a high streamwise velocity gradient and, consequently, a high wall shear stress. The riblets appear to impede this lateral motion of the inrush at the wall. The size of the region with a high wall shear stress is then decreased. This is essentially the same effect noticed in the direct numerical simulation of Chu (1992) and hypothesized by Smith *et al.* (1989) and Choi (1989). The impact of an inflow is most noticeable as an increase in the pressure at the wall and, with riblets, this is often present only in the riblet immediately below the inflow. Even within riblets directly beneath such inrushes, the riblet valleys appear to retain most of their low momentum fluid. The main increase in wall shear stress appears to occur, for the most part, on the riblet peaks. So, not only is the inflow confined in the spanwise direction, it is also effectively unable to influence large areas of the surface within the riblet valleys.

4 Conclusions

A 2 1/2 D model of the viscous wall region has been used to investigate the flow over surfaces with both V-groove and U-groove riblets. Visual observations of the transient flows suggest that the riblets limit the lateral spread of inrushes towards the walls and retain low momentum fluid in the riblet valleys effectively isolating much of the wall surface from such inrushes. The riblets also appear to interact with the near wall streamwise vortices through the generation of transient secondary vortices in the riblet valleys in a manner similar to that proposed by Bacher and Smith (1985). The magnitude of these vortices, however, seems to be relatively minor which probably helps account for the experimentally observed stability of the low momentum fluid in the riblet valleys.

Further work with the results of these simulations is required; in particular, comparisons with the direct numerical simulations of Chu (1992). The mean and turbulent flow statistics for the various riblet geometries should also be examined in detail, especially for the drag reducing riblet sizes. In addition, the use of alternate riblet configurations (e.g. compound riblets) could be investigated.

Acknowledgements

The authors would like to acknowledge the financial support of the Natural Science and Engineering Research Council of Canada.

References

- Bacher, E.V., Smith, C.R.: 1985, AIAA Paper 85-0548.
- Bakewell, H.P., Lumley, J.L.: 1967, *Phys. Fluids* 10, 1880.
- Baliga, B.R.: 1978, Ph.D. Thesis, Dept. of Mech. Eng., University of Minnesota.
- Baliga, B.R., Patankar, S.V.: 1983, *Numerical Heat Transfer* 6, 245.
- Bechert, D.W., Bartenwerfer, M.: 1989, *J. Fluid Mech.* 206, 105.
- Benhalilou, M., Anselmet, F., Liandrat, J., Fulachier, L.: 1991, *Proc. of the 8th Symp. on Turb. Shear Flows, Munich*.
- Chapman, D.R., Kuhn, G.D.: 1981, AIAA Paper 81-1024.
- Chapman, D.R., Kuhn, G.D.: 1986, *J. Fluid Mech.* 170, 265.
- Choi, K.: 1989, *J. Fluid Mech.* 208 417.
- Chu, D.C.: 1992, M.Sc. Thesis, Dept. of Mech. and Aerospace Eng., Princeton University.
- Clark, J.A.: 1968, *Trans. ASME, J. Basic Engng.*, 90, 455.
- Djenidi, L., Squire, L.C., Savill, A.M.: 1990, *5th European Drag Reduction Working Meeting*, British Maritime Technology, Teddington.
- Djenidi, L.: 1991, *6th European Drag Reduction Working Meeting*, Eindhoven, (abstract).
- Gallager, J.A., Thomas, A.S.W.: 1984, AIAA paper 84-2185.
- Hatzivramidis, D.T., Hanratty, T.J.: 1979, *J. Fluid Mech.* 95, 655.
- Kasagi, N.: 1990, Near-Wall Turbulence: 1988 Zoran Zarić Memorial Conference. eds. Kline, S.L., Afgan, N.H. Hemisphere.
- Launder, B.E., Li, S-P.: 1991, *6th European Drag Reduction Working Meeting*, Eindhoven, (abstract).
- Nikolaides, C.: 1984, Ph.D. Thesis, Dept. of Chem. Eng., University of Illinois, Urbana.
- Patankar, S.V.: 1980, *Numerical Heat Transfer and Fluid Flow*. Hemisphere.
- Prakash, C., Patankar, S.V.: 1985, *Numerical Heat Transfer* 8, 259.
- Robinson, S.K., Kline, S.J., Spalart, P.R.: 1990, Near-Wall Turbulence: 1988 Zoran Zarić Memorial Conference eds Kline, S.L., Afgan, N.H. Hemisphere.
- Saabas, H.J.: 1991, Ph.D. Thesis, Dept. of Mech. Eng., McGill University.
- Savill, A.M.: 1989, *Proc. IUTAM Symp. on Structure of Turbulent and Drag Reduction*, Zurich.
- Smith, C.R., Metzler, J.: 1983, *J. Fluid Mech.* 129, 27.
- Smith, C.R., Walker, J.D.A., Haidari, A.H., Taylor, B.K.: 1989, *Proc. IUTAM Symp. on Structure of Turbulent and Drag Reduction*, Zurich.
- Tiederman, W.G.: 1989, *Proc. IUTAM Symp. on Structure of Turbulent and Drag Reduction*, Zurich.
- Tullis, S.: 1992, M.Sc. Thesis, Dept. of Mech. Eng., Queen's University, Kingston (in preparation).
- Ueda, H., Hinze, J.O.: 1975, *J. Fluid Mech.*, 67, 125.
- Vukoslavčević, P., Wallace, J.M., Balint, J.-L.: 1987, *Proc. RAeS Int. Conf. on Turbulent Drag Reduction by Passive Means*, London.
- Walsh, M.J.: 1990, *Progress in Astronautics and Aeronautics*, eds Bushnell, D.M., Hefner, J., 123.

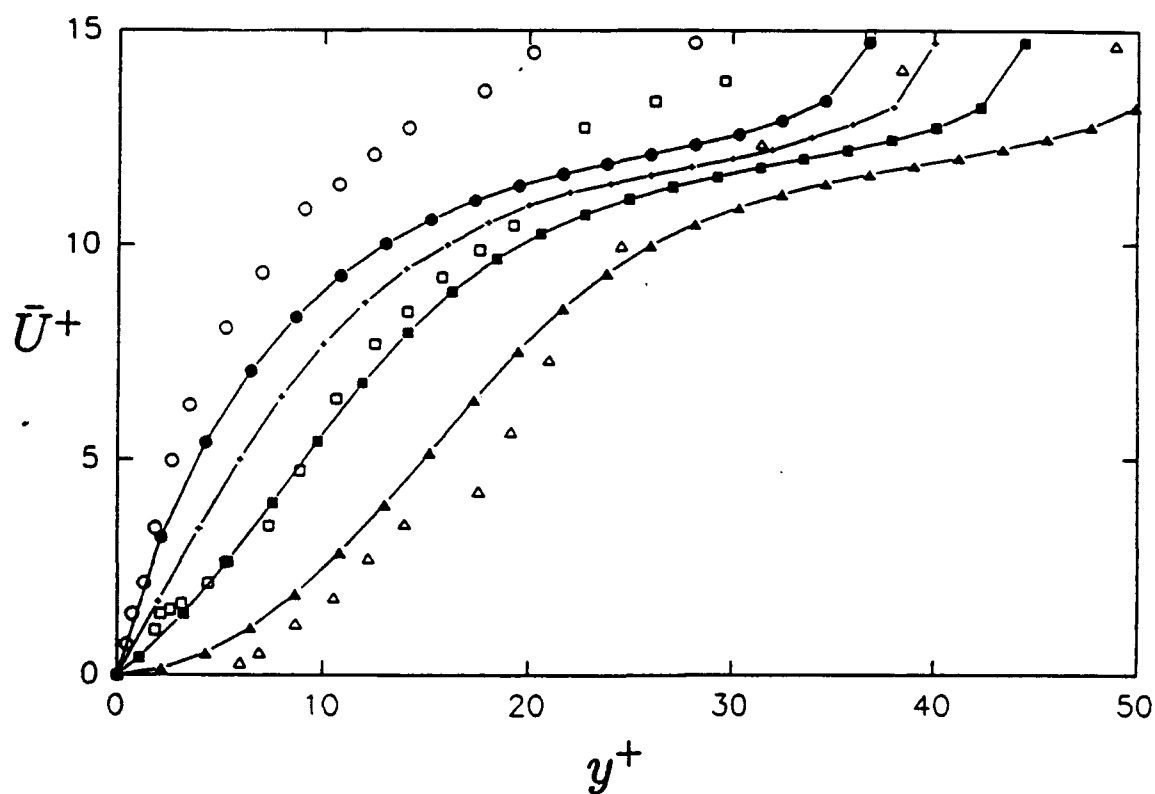


Figure 1: Mean streamwise velocity profiles over larger drag-neutral V-groove riblets ($2h^+ = s^+ = 33.3$). Comparison of the calculations ($\bullet, \square, \triangle$) and experimental results ($\circ, \square, \triangle$) from Vukoslavčević *et al.* (1987) for the riblet peaks, mid-point between peaks and valleys, and valleys. The calculated flat wall velocity profile is also shown (+).

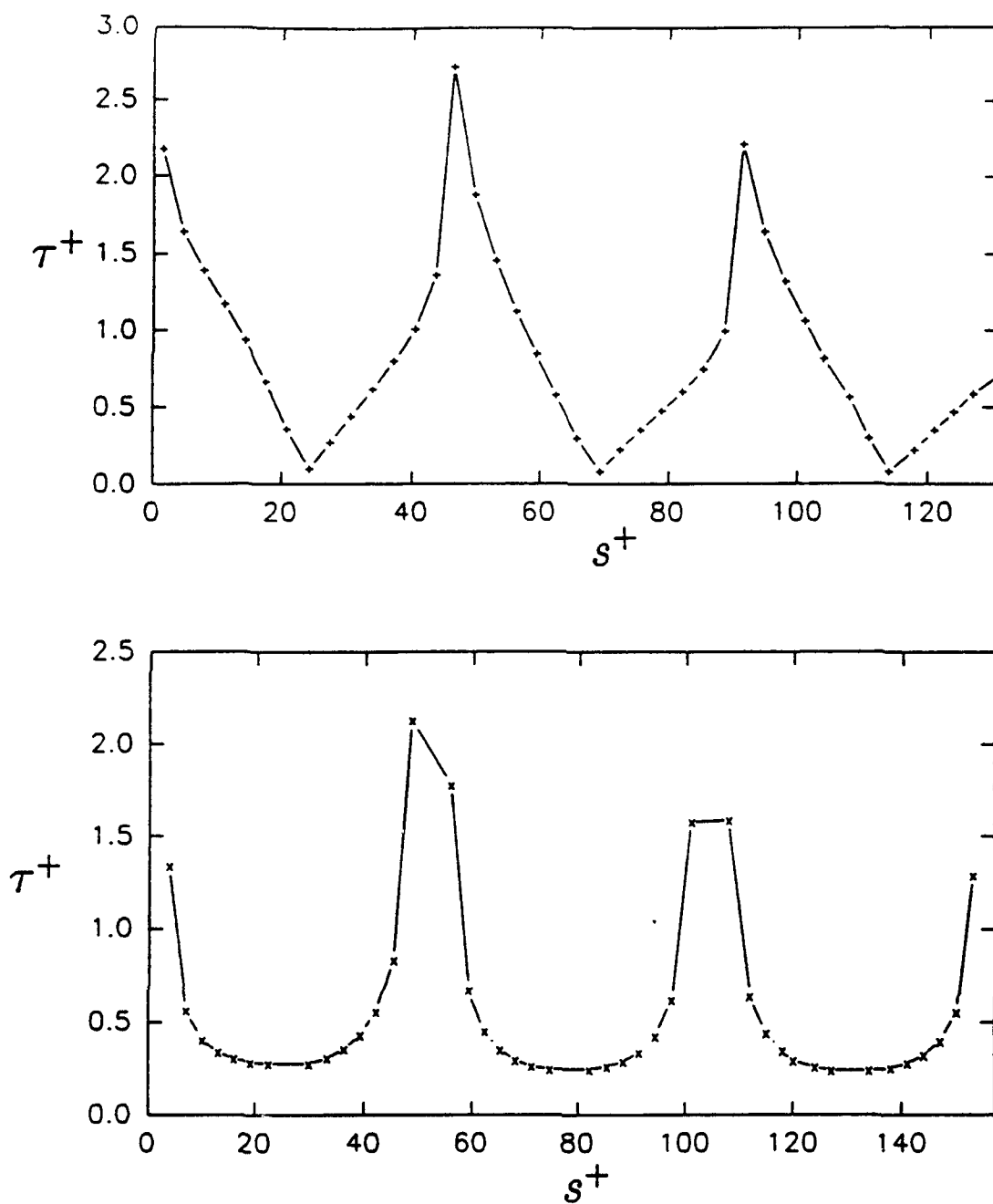


Figure 2: Calculated dimensionless wall shear stress ($\tau^+ = \tau/\tau_w$) spanwise distributions for: a) the larger V-groove riblet wall, and b) the larger U-groove riblet wall. The spanwise dimension s is measured along the wall surface.

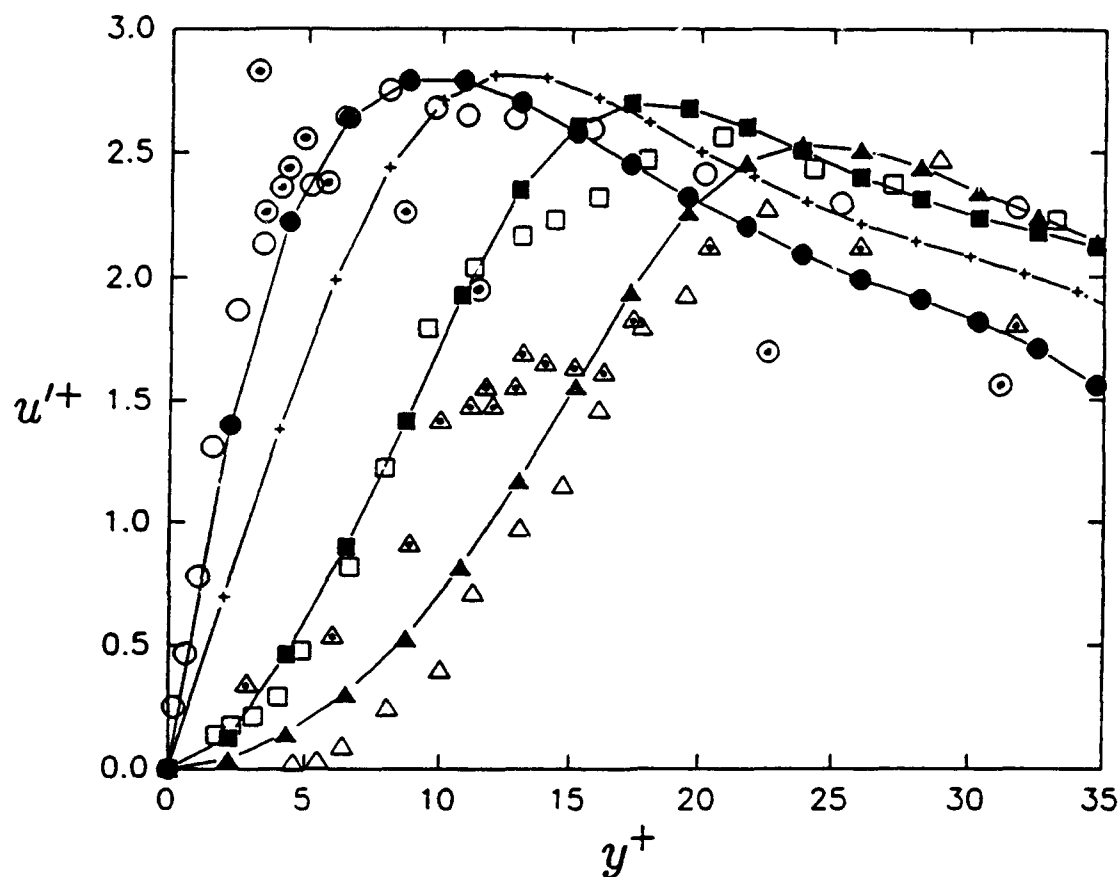


Figure 3: Streamwise turbulence intensity profiles over the larger V-groove riblets. Comparison of the calculations (\bullet , \square , \triangle) and experimental results from Vukoslavčević *et al.* (\circ , \square , \triangle) and Benhalilou *et al.* (\odot , \triangle) for the riblet peaks, mid-point between peaks and valleys, and valleys respectively. Data from Benhalilou *et al.* do not include results for the profile above the mid-point between peaks and valleys.

AN EXPERIMENTAL STUDY OF THE FLOWS ASSOCIATED WITH CIRCULAR CAVITIES

E Savory and N Toy

Fluid Mechanics Research Group
Department of Civil Engineering
University of Surrey
Guildford GU2 5XH
United Kingdom

Abstract

This paper presents some findings from a study of circular cavity flows that has been undertaken as part of a wider project to examine the flows associated with different three-dimensional cavity geometries having elliptical, rectangular or square planforms.

1. Introduction

Surface cut-outs occur in many aerodynamic applications including equipment housings, panel handles, cargo bomb bays, rivet depressions and flap recesses. They are often the cause of undesirable effects such as parasitic drag and noise generation. Our knowledge of the effects of surface cut-outs and cavities is mainly limited to the overall drag increments due to single or multiple holes, such as the early data obtained by Weighardt (1946), Tillmann (1951), Roshko (1955) and Tani et al (1961) using essentially two-dimensional rectangular slots normal to the flow direction. Weighardt and Tillmann, along with Friesing (1936), Gaudet and Johnson (1971), Gaudet and Winter (1973) and Pallister (1974), also provided data concerning the overall drag due to cavities of varying depth but with circular planform. Much of the early research was summarised by Hoerner (1965), whilst AGARDograph 264, Young and Paterson (1981), provides an excellent presentation of the best drag data in a form that may be used for design purposes. However, apart from a few surface pressure distribution measurements by a limited number of workers, such as Roshko (1955), Maull and East (1963), Rossiter (1964) and, more recently, Sinha et al (1982) and Plentovich (1990), the drag data has been derived from force balance measurements which provide very little insight into the flow regimes occurring within the cavities. Hence, the present work provides data which should be of use, not only in aerodynamic design, but also in the development

of turbulence models for cavity flow problems. The next section outlines the experimental arrangements and this is followed by a discussion of some of the results obtained.

2. Experimental details

A wind tunnel with working section dimensions of 1.37m height x 1.07m width x 9.0m length was employed for all the measurements. A 20mm high metal wall fence was placed across the tunnel near the contraction to produce a thick boundary layer with good lateral uniformity. Across the tunnel the velocity was uniform to within $\pm 2\%$, whilst the rms turbulence intensity was within 5%. These boundary layer profiles were obtained at a freestream velocity of 12m/s which was the speed used in most of the subsequent experiments. The principal boundary layer parameters were: $\delta = 320\text{mm}$, $\delta^* = 27.9\text{mm}$, $\Theta = 21.2\text{mm}$ and $c_f = 0.00265$.

The circular cavity model has a diameter of 75mm and is constructed from brass. There is a single line of thirty five 0.5mm diameter pressure tapings down the cavity wall, spaced 2.5mm apart beginning at 1mm from the rim. There are also fifteen tapings in the base of the hole at 5mm intervals centred on a line across the diameter of the base. Ten tapings are located on the rim of the hole to allow measurements on the tunnel wall close to the lip of the cavity. These begin at 1.5mm out from the rim and are spaced 2.5mm apart. A linear position transducer may be used to accurately set the depth of the cavity for each test.

A typical apparatus arrangement for the mean surface pressure measurements is illustrated in figure 1. The model was mounted flush with the tunnel interior and a pitot-static tube was positioned in the freestream, directly across the tunnel at the same downstream location, for measurement of the reference dynamic pressure. The model position was on the wall at 4.5m downstream of the tunnel contraction. The pressure tapings on the model were attached to connectors which, in turn, were inserted into Scanivalve switch mechanisms. This allowed the connection of each tapping to one side of a differential pressure transducer. The other, reference, side of the transducer was connected to the freestream static pressure, via a damper to ensure that unwanted fluctuations were removed. A series of transducers were used in the experiments, with ranges from $\pm 1\text{mm WG}$ to $\pm 10\text{mm WG}$, since the magnitudes of the pressures varied enormously from the high positive values at the reattachment point of the separated shear layer to the very small pressures deeper into the cavity. A PC was used to acquire the pressure data via an amplifier and A-D converter system and the data was used to compute the mean pressure coefficients (C_p). The computer also controlled the operation of the Scanivalve system via a relay switch arrangement. Typically, a delay time of 15 seconds was used after each switching of a Scanivalve port to allow settling of the pressure at the transducer. Similarly, the sampling times were 30 seconds at each port to permit

determination of reliable mean values. The reference dynamic pressure was monitored throughout each experiment and the accuracy of the data was estimated to be ± 0.003 in C_p . The overall drag coefficients, based on the model planform area and the freestream dynamic pressure, were obtained by integrating the wall pressures and resolving the force components in the appropriate direction. The drag increment due to the cavity, ΔC_D , was determined by subtracting the skin friction coefficient from the drag coefficient.

In order to obtain direct measurements of the drag coefficients, for comparison with the data from integrated pressure distributions, a force balance was designed and installed into the floor of the tunnel. The balance has a plan area of 0.5m length x 0.3m width into which ground boards containing models can be inserted. Essentially, the balance mechanism is a parallelogram in which rotation can occur at each corner on frictionless bearings. This mechanism is attached to a rigid frame which, in turn, is fastened to the underside of the tunnel. A load cell is incorporated into the framework and a small threaded shaft on one upstream vertical arm of the balance impinges upon the load cell sensor. On the other upstream vertical member is a cantilever upon which weights may be placed to pre-load the load cell. The gap between the balance plate and its surrounding frame at the tunnel floor is of the order of 0.05mm but the actual position of the plate within the frame is set by adjusting the cantilever loading and the threaded shaft. The frame surrounding the balance plate is pressure tapped, with six tappings on both the upstream and downstream faces and two tappings on the two side faces. This was carried out in order to assess the effect of any flow through the gaps on the loading on the sides of the balance plate. However, for these cavity models at least, there is no measureable difference between the pressures on the upstream face and those on the downstream face. The ground board is constructed from timber with a circular hole cut in the centre where the models may be inserted. The board is screwed down onto the plate with packing material underneath to ensure a flush finished surface.

The balance is located approximately 6m downstream of the tunnel contraction and, in order to generate a boundary layer similar to that used in the pressure measurements, an identical 20mm metal fence was used across the tunnel floor. The skin friction coefficient measured at the balance is approximately 0.00257 which is within 3% of that measured on the tunnel wall for the cavity pressure measurements.

The output from the load cell is taken to a unit which contains a precision high gain amplifier. This provides an accurate output with a calibration of 76.19 grammes/volt and repeated calibration tests using small weights showed that hysteresis was less than $\pm 0.0002V$ or $\pm 15mg$. Since only mean loads were of interest in the present work the amplified output was filtered at 5Hz before being sampled by a PC via an A-D converter system. Before

each set of experiments the load cell and digitisation system were calibrated in-situ to an accuracy of better than 0.001V, that is 70mg

For each model configuration the load with no airflow was measured and this was then subtracted from the load measured at the test velocity. A similar procedure was adopted for measuring the load on the plate without a cavity present. From this data the net drag coefficient due to the cavity, $\Delta C_{D,c}$, could be computed by taking the load increment and dividing by the cavity model planform area and the freestream dynamic pressure. A sampling time of 40 seconds was used for each measurement and several data sets were taken for each configuration to ensure reliability and to assess the experimental scatter. The model used in these experiments had a plunger-type base to allow variation of the cavity depth. The cavity had a diameter of 103mm, with sides constructed from uPVC pipe and the base from timber.

3. Results and discussion

Mean pressure coefficient distributions on the base, side wall and surrounding ground plane for the circular cavities with $h/D=0.1$ to 0.7 are illustrated in figures 2 to 8. The upper part of each figure shows the wall distribution "unwrapped" with the extreme upstream location (0°) at the ends and the extreme downstream location (180°) at the middle. The base distribution is given in the lower left hand plot, whilst the right hand distribution shows the pressures around the cavity on the tunnel wall.

For the shallowest cavity, with $h/D=0.1$, the flow pattern displays an essentially open regime with a symmetrical pressure distribution. The pressures on the base rise almost linearly from zero to just greater than 0.2 in the region where the separated shear layer reattaches. This value is similar to that typically found just after reattachment downstream of a 2-D backward-facing step. It would appear that shear layer reattachment occurs near the base on the downstream wall with subsequent separation at the cavity lip. This separation over the downstream half of the rim circumference gives rise to a strong pressure gradient on the tunnel wall close to the cavity with high suction values at the lip. However, the magnitudes of the pressures in this region are considerably lower than those typically occurring immediately downstream of a 2-D forward-facing step. The wall pressure distributions indicate that at this depth there is no strong vortex present within the cavity. With an increase in depth to $h/D=0.2$ a pressure distribution broadly similar to that found by Friesing (1936) is established. Here, the pressure rise on the base as reattachment is approached is more rapid. The maximum pressure on the downstream face (at about 180°) occurs near the lip where the shear layer reattaches, resulting in less strong separation at the rim in this region and reduced suction pressures on the tunnel wall downstream of the cavity. On the downstream

face there is a pressure minimum about half way up the wall, together with lower pressures over the wall at around 90° and 270° . This indicates the formation of an identifiable symmetrical vortex pattern. For the slightly deeper cavity with $h/D=0.3$ the vortex becomes more pronounced, with a pressure minimum occurring across the base from about 100° to 260° . The flow is still symmetrical and the extent of the region influenced by separation from the downstream lip remains the same.

At $h/D=0.4$ there is the onset of asymmetry as one side of the main vortex rises (almost 240°) and appears to shed some vorticity, causing a change in the pressure distribution on the tunnels wall in this region. The mean vortex line rotates slightly and no longer runs normal to the freestream flow direction. With the depth at $h/D=0.5$ the flow regime in and around the cavity becomes extremely asymmetrical with the separated flow near the upstream lip reattaching slightly to one side of the centre-line (around 80°). The greater stagnation pressure here may be due to the entrainment of higher momentum fluid from further out in the boundary layer. The main cavity vortex appears to be formed by two vortex sheets, the upper one rolling up from a spiral point on the side wall and engulfing a lower one emanating from the floor, as noted by Gaudet and Winter (1973). As a result, the mean vortex line lies across the cavity at about 45° to the freestream direction with the downstream raised arm (about 225°) shedding vorticity from the cavity. The upstream end, at about 45° , remains well within the cavity. The pressure distribution asymmetry shows the same hand as the oil film visualisation of Gaudet and Winter (1973). There is good agreement between the visualised flow and the pressure field. Within the cavity the maximum reversed flow velocity near the base, is approximately $0.25U_R$ (measured using a pulsed-wire anemometer) which is similar to that found in two-dimensional rectangular cavity flows. This velocity is slightly greater at about 90° than on the other side of the cavity at around 270° . The flow regime for a slightly deeper cavity, with $h/D=0.6$, shows a rapid return to more symmetric conditions. Here, the wall pressure distribution indicates that both ends of the main vortex are within the cavity, although the downstream arm is slightly higher than the upstream portion. The vortex line is still at about 45° to the freestream direction but shedding of vorticity from the cavity appears to have greatly reduced. For the final cavity studied, with $h/D=0.7$, the cavity flow is symmetric and dominated by a single large vortex positioned laterally across the hole. The pressure minima around the entire circumference of the wall at about half the cavity depth, together with the minima across the base, is evidence for a stable vortex regime, as shown by Roshko (1955).

The variation of the overall drag increment due to the cavity with depth is illustrated in figure 9. The graph shows both the integrated pressure values and the direct drag balance data, together with the results from previous workers. There is a peak in the drag coefficient at about $h/D=0.45$ associated with the asymmetric flow pattern

described above. The present data lies well within the large scatter of the previous results and there is reasonably good agreement between the balance and pressure data. The length of the bars for the balance data points indicates the range of the results obtained at each depth. The large scatter in the results from previous workers is principally due to the different experimental apparatus used and the differences in the approach flow boundary layer conditions. The asymptotic drag value at large depths is about 0.01 which is typical of deep 2-D rectangular cavity flows.

In an attempt to provide a rational basis for presenting circular cavity drag coefficient data Gaudet and Johnson (1971) noted that the drag depends upon the depth ratio, the roughness Reynolds number ($U_\infty D/\nu$), the skin friction coefficient and the Mach number. It was found that the data could be represented by the expression shown in figure 10 in which at each depth the normalised drag increment is related to the roughness Reynolds number by two parameters A and B. Parameter B was dependent solely on the Mach number and at low subsonic speeds took the value of 0.31. The parameter A varied with the depth ratio and is plotted in the figure. It may be seen that there is good agreement between the pressure and balance data and that the peak at about $h/D=0.5$ is again evident. The early data of Wieghardt (1946) and Tillmann (1951) appeared to show a second, much reduced, peak drag value at around $h/D=1.0$ possibly associated with the formation of deeper secondary vortices. However, Gaudet and Winter's results (unpublished, private communication) showed no evidence of this peak and their data followed the lower bound of the previous data. The present values obtained at a low subsonic Reynolds number, appear to follow an upper bound to the previous data which may be reasonable if, as stated above, Gaudet and Winters' data at very high Reynolds number represents a lower limit. Certainly, the results of Friesing (1936) and Pallister (1974) lie within this region and do not indicate the presence of a peak at $h/D=1.0$.

4. Conclusions

The pressure distributions show the development of highly asymmetric flow conditions at a depth/diameter ratio of about 0.5, associated with strong vorticity shedding and high drag. The distributions at this depth illustrate that the main vortex is aligned at approximately 45° to the freestream direction and the results also agree well with the surface oil film visualisation of Gaudet and Winter (1973). The data for overall drag coefficients obtained from the integrated pressure distributions and the force balance measurements are in reasonable agreement and also concur well with existing data. No evidence has been found to support the presence of a second peak in the drag versus depth/diameter curve at around $h/D=1.0$ which had been noted by some early workers. The pressure distributions on the ground plane near the lip of the cavities exhibit very strong gradients associated with flow

separation at the downstream rim. It is clear that further study of these distributions is necessary if the gradients are to be ameliorated by any changes in rim profile carried out to reduce cavity drag.

5. Acknowledgements

Much of this work was funded by the UK Dept of Trade and Industry under Agreement No 2064 120. The authors are indebted to Mr L Gaudet, formerly of DRA (Bedford), for his advice and encouragement.

6. Nomenclature

A_p	planform area of model
C_D	pressure drag coefficient ($F_D / (A_p \cdot q)$)
ΔC_D	drag coefficient increase due to cavity ($C_D - c_i$)
c_i	local skin friction coefficient
C_p	surface pressure coefficient ($(p - p_\infty) / q$)
D	diameter of cavity
F_D	drag force
h	depth of cavity
p	surface pressure on model
p_∞	freestream static pressure
p_t	freestream total pressure
q	freestream dynamic pressure ($p_t - p_\infty$)
Re	Reynolds number ($U_\infty \cdot D / \nu$)
U_∞	freestream reference velocity
U_s	shear velocity

7. References

- Friesing H (1936) "Measurement of the drag associated with recessed surfaces: cut-outs of rectangular and elliptical planform". Z.W.B.F.B. 628 (RAE Lib Trans 1614, 1971)
- Gaudet L & Johnson P (1971) "Measurements of the drag of excrescences immersed in turbulent boundary layers at Mach numbers between 0.2 and 2.8". RAE Tech Report 71181
- Gaudet L & Winter K G (1973) "Measurements of the drag of some characteristic aircraft excrescences immersed in turbulent boundary layers". RAE Tech Memo Aero 1538 (also AGARD CP124, 1973)
- Hoerner S F (1965) "Fluid dynamic drag". pp 5.10-5.11. published by author
- Mauld D J and East L F (1963) "Three-dimensional flow in cavities". J Fluid Mech. 16, 620-632
- Pallister K C (1974) "Wind tunnel measurements of the transonic drag of excrescences immersed in a turbulent boundary layer". ARA Report 37
- Plentovich E B (1990) "Three-dimensional cavity flows at subsonic and transonic speeds". NASA TM 4209, Sept
- Roshko A (1955) "Some measurements of flow in a rectangular cutout". NACA TN 3488, August
- Rossiter J E (1964) "Wind tunnel experiments on the flow over rectangular cavities at subsonic and transonic speeds". ARC R & M 3438, October
- Sinha S N, Gupta A K and Oberai M M (1982) "Laminar separating flow over backsteps and cavities. Part II: Cavities". AIAA J. 20, 370-375
- Tani I, Iuchi M and Komoda H (1961) "Experimental investigation of flow separation associated with a step or groove". Aero Res Inst Univ of Tokyo, Res Rep No 364, 119
- Tillmann W (1951) "Additional measurements of the drag of surface irregularities in turbulent boundary layers". NACA TM 1299 (also in "New resistance measurements with surface irregularities in the turbulent boundary layer". Forschungshefte fur Schiffstechnik. 2, 81-88, (BSRA Trans No. 322), 1953)
- Wiegardt K (1946) "Increase in turbulent frictional resistance caused by surface irregularities". Min of Air Prod R&T No 103, Trans of FB1563 (also in Forschungshefte fur Schiffstechnik. 2, 65-81, (BSRA Trans No. 322, 1953)
- Young A D & Paterson J H (1981) "Aircraft Excrescence Drag". NATO AGARD-AG-264, J L Jones, Editor

The schematic diagram illustrates the experimental setup. At the top, a horizontal line represents the 'Piezo-static tube' with an arrow labeled U_R indicating flow direction. A vertical line descends from this tube, passing through a 'Static Damper' (labeled P_3) and a 'Switch'. The tube then enters a 'Cavity model' (labeled P_1) which contains a 'Scanvalve'. The 'Scanvalve' is connected to a 'Control Unit' and a 'PC'. The 'Control Unit' is also connected to the 'PC'. The 'Switch' is connected to two '10mm WG Trans' (transducers). These transducers are connected to 'Amplifiers and A-D-Cs', which in turn are connected to the 'PC'.

Fig 4 Pressure distributions on cavity with $h/D=0.3$

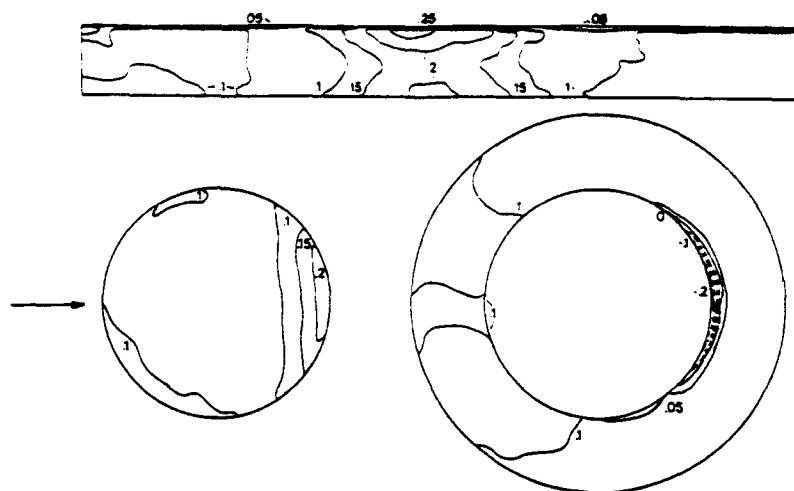


Fig 5 Pressure distributions on cavity with $h/D=0.4$

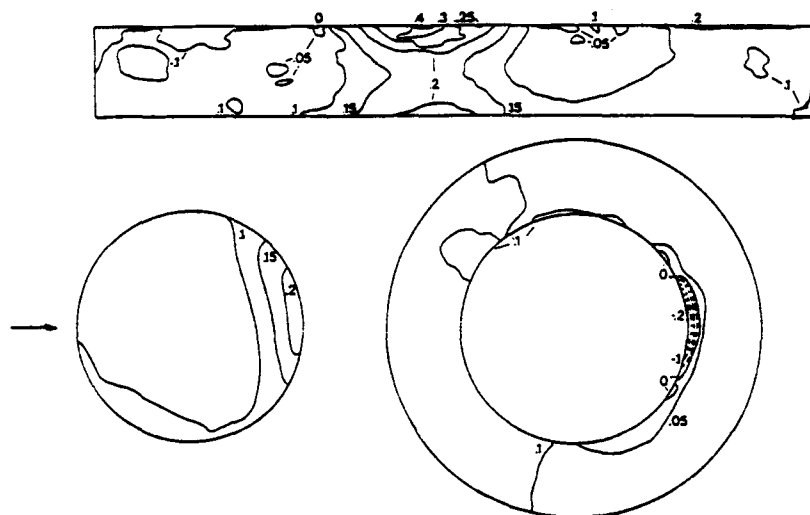
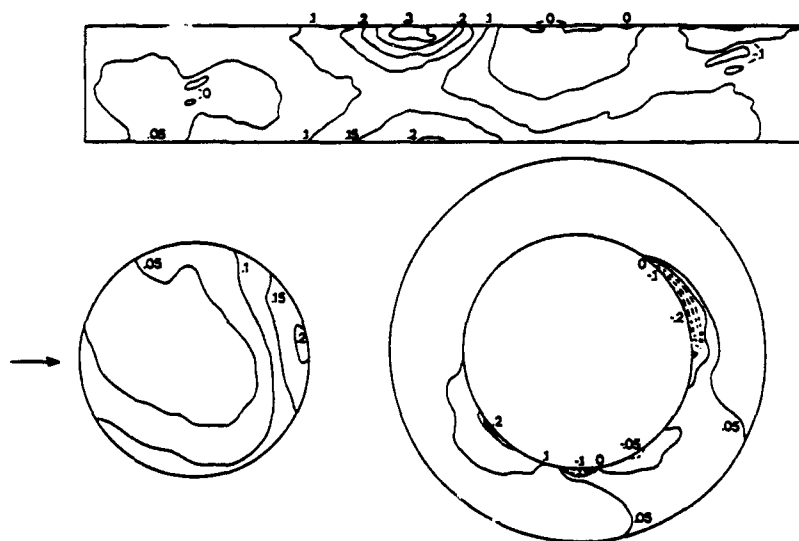


Fig 6 Pressure distributions on cavity with $h/D=0.5$



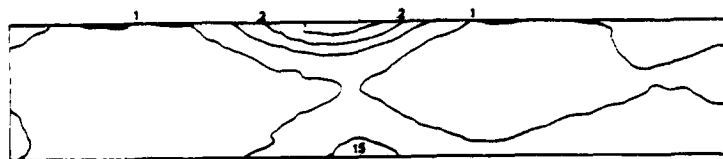


Fig 7 Pressure distributions on cavity with $h/D=0.6$

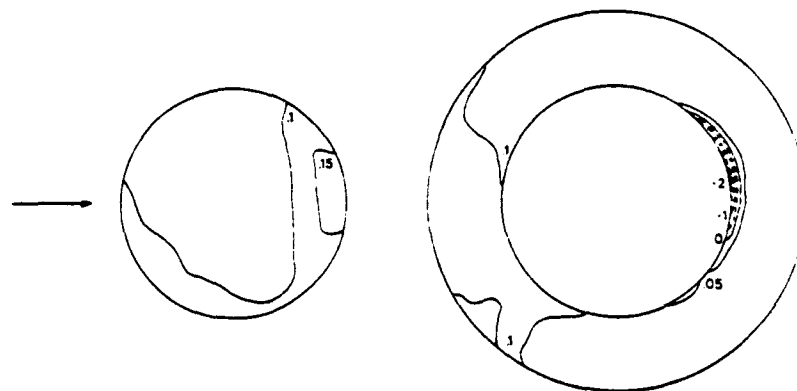


Fig 8 Pressure distributions on cavity with $h/D=0.7$

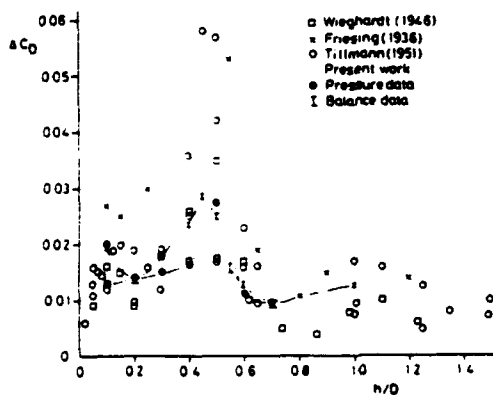


Fig 9 Variation of drag coefficient with depth/diameter ratio

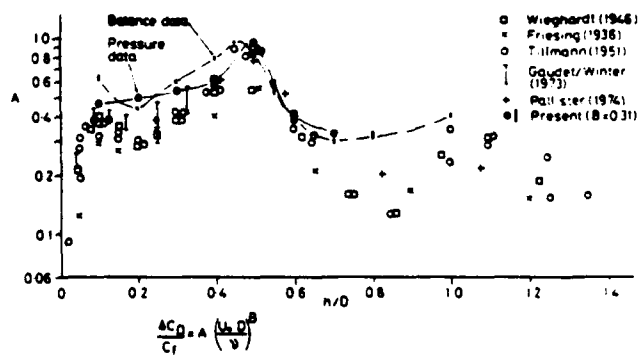


Fig 10 Variation of parameter A with depth/diameter ratio

Towards a Direct Numerical Simulation Procedure for Inhomogeneous Turbulence in High-Speed Flows

By FOLUSO LADEINDE

Department of Mechanical Engineering, SUNY Stony Brook

In this paper we sketch a procedure which, if properly implemented, could provide a means of obtaining high-order calculations of the type needed for the direct numerical simulation (DNS) of turbulence in the supersonic flow regime. We are interested in a procedure that handles more complicated geometries and boundary conditions than those currently receiving attention. The proposed procedure is based on the so-called essentially non-oscillatory schemes, which is here formulated in terms of the finite element method. Parallel implementation for arbitrary complex geometries on the Intel i860 hypercube is discussed. More work is needed for a cost-effective implementation.

1. Introduction

The present work is numerical, and has the objective of providing a sketch for a procedure which, if properly implemented, could provide a means of obtaining high-order calculations of the type needed for the direct numerical simulation (DNS) of turbulence in the supersonic flow regime. We are interested in a procedure that handles more complicated geometries and boundary conditions than those currently receiving attention, and in which inhomogeneity is more realistic than those in channels or boundary layers. However, the procedure will be limited to low R_λ 's, as is the case for all DNS calculations.

Of the three common procedures for calculating shocks the capturing approach has the best chance for complicated systems. However, and as pointed out by Hussaini and Speziale¹, the numerical viscosity, in various forms, which is required for the procedure seriously distorts small-scale features, making most capturing approaches suspect for DNS. Moreover, calculations usually degrade to first order in the vicinity of strong discontinuities, even in TVD (total-variation-diminishing) schemes that are otherwise formally high-order in the smooth part of the flow.

The basic ingredients for the formulation presented in this work are available in Harten and Osher² and Harten, Engquist, Osher, and Chakravarthy³, on essentially non-oscillatory (ENO) finite difference calculation of the Euler equations. ENO has been used in other contexts, for example, to refer to procedures where *any* unphysical oscillations in the solution are prevented, by whichever means. Moreover, in many papers distinctions are usually not made between oscillations in the smooth part of the flow and those resulting from discretization across discontinuities. Although the two are related they require different considerations with respect to the ability to obtain high-order accuracy. ENO is used in the present context in connection with oscillations associated with discontinuities which, in the ENO procedure, are inhibited, not by an artificial viscosity, but by avoiding the cause of the oscillations: discretizing across discontinuities.

The ENO procedure, again in the sense used here, has its origin from the earlier work of Godunov⁴, and the correction by van Leer⁵. The Godunov scheme is first-order accurate while van Leer's is second. Generalization of the Godunov scheme to obtain higher-order accuracy as well as the introduction of the ENO terminology came with the work of Harten and his colleagues. We think it is safe to say that most of the work on ENO originated from the group of Professor Osher in the Mathematics Department at the University of California, Los Angeles.

That the ENO procedures could be suitable for DNS came with the work of Os-

her and Shu⁶ and Shu et al.⁷. This is a welcome news at a time when interest in compressible turbulence is growing, coupled with the realization that the spectral method, which would be the choice for "simple" flows and has dominated DNS, is not directly applicable to flows with strong discontinuities. The problem with the spectral method is its sensitivity to nonlinear instability. The method also has difficulties with complicated geometries and boundary conditions. As for finite difference, highly-accurate calculations for compressible flows are possible with the fourth-order MacCormack scheme^{8,9} and the compact methods^{10,11}. However, we are not aware that these schemes do not degenerate to first-order in the vicinity of discontinuities. The spectral element method is suitable (and has been used) for low Mach number flows. However, as far as we know, we are the first to suggest the use of lower-order finite elements for DNS¹².

The ENO procedure of Shu and his colleagues is a simplified version of the original one by Harten, Osher, and others. The procedure can achieve uniformly high-order accuracy with sharp, essentially non-oscillatory shock transitions. This is accomplished by using an adaptive stencil interpolation based on difference tables, whereby the data for interpolation is selected from the smooth regions of flow. Because we try to avoid discretization across discontinuities we inhibit the Gibbs phenomenon and (hopefully) remove the need for artificial dissipation for shock capturing.

The Shu's code is a very valuable tool for DNS research, and a version we have rewritten for parallel processing on the i860 hypercube has been used for many DNS calculations. However, the implementation of the schemes in the code to handle more realistic systems is bound to be very complicated and less cost-effective than of procedures based on finite element. Further, the dimension-by-dimension fashion in which the convective terms are treated, both in the component-by-component approach and the approach based on local characteristic directions, might give a "blurred" resolution of bow-type shocks, or otherwise complex shock patterns not

aligned with the coordinate directions along which discretization is done.

A recent finite difference/volume procedure by Harten and Chakravarthy¹³ avoids the forgoing difficulties. In the present work we formulate the procedure for the finite element method (FEM), as we believe that the latter is capable of giving the flexibility needed for a cost-effective implementation for realistic systems. The price we pay for this flexibility is the requirement of a more advanced programming skill. Implementation for complicated geometries in an environment of parallel processing with the Intel i860 hypercube is given. It is hoped that other researchers of high Mach number turbulence will find sufficient interest to pursue the procedure to establish survivability in terms of computational cost.

2. A Base Scheme

The equations to be solved for DNS are those governing the conservation of mass, momentum, and energy, at high speeds. The nondimensional form in Ladeinde¹² is used. A base numerical scheme is needed for the ENO procedure discussed here. There is some flexibility in the choice of spatial interpolation for the base scheme in that one could, conceptually, use a linear element or a higher-order element. At the present we are experimenting with the 8-node linear element and a 64-node cubic element, both of the Lagrange type. With the cubic element we are pushing FEM towards its spectral limit. This element is less attractive from parallel processing standpoint, and may share some of the difficulties with the spectral method. Our interest in the element is to establish these facts, since the element has such a powerful interpolation potential compared to the linear one. In the present paper we will assume that the 8-node element is used.

We also need a time integration scheme which, from the onset, must be high-order (third, fourth, ...), explicit^{0†}, or implicit. For the explicit approach high-order Lax-

^{0†}There is no finite element scheme that is truly explicit in the sense that finite difference is, but we frequently manipulate the so-called mass matrix (for example, by lumping, or "throwing" terms to the right-hand-side), to obtain a matrix-free approach.

Wendroff applied to forward Euler formula is a possibility, as are explicit Runge-Kutta procedures. For the latter, the third-order TVD scheme of Shu⁷ could be used since it has been tested extensively. Our approach is to allow both explicit and implicit schemes in any one simulation; the one actually used in a region will depend on the (expected) local flow field (that is, implicit near solid walls, and explicit away from walls). The latter is quite straight-forward with the domain decomposition approach used for parallel processing. For an implicit procedure we have used a two-stage, third-order semi-implicit Runge-Kutta approach that is both $A-$ and algebraically stable. The first stage of this scheme is essentially backward Euler, and the second is a trapezoid rule¹².

Finally, depending on the approach used to obtain non-linear stability (SUPG, upwind elements, or other upwind approaches), we could have for the base scheme, a Galerkin system:

$$\sum_{j=1}^N B(w_h^j, w_h^i) u_h^j = (f, w_h^i), \quad 1 \leq i \leq N, \quad (1)$$

where familiar notations have been used in this equation.

3. The ENO Procedure

Whatever is used for the base scheme we can always express the problem in the form $u_j^{l+1} = u_j^l + \Delta t \operatorname{div} f$ or, for convenience, in the undiscretized form

$$u_t + \operatorname{div} f(u) = 0; \quad x \in D \subset \mathbb{R}^s, \quad u(x, 0) = u_0(x); \quad x \in D \quad (2)$$

∂D is the boundary of D . In the foregoing a vector equation is implied, and s is the dimension of the space, $= 3$. It is pointed out that D is, in the present context, a subdomain from the decomposition of the original domain, but we are giving up notational formalities, for clarity. In the same token the fact that the subdomains could be overlapped is also suppressed. We will now give the finite element formulation, using the notations in the paper by Harten and Chakravarthy,

for easy reference.

D is assumed one-piece but partitioned into finite elements (cells) C_j where,

$$D = \bigcup C_j; \quad C_j \cap C_k = \emptyset \quad (3)$$

We define

$$|C_j| = \int_{C_j} dV,$$

$$\bar{x}_j = \frac{1}{|C_j|} \int_{C_j} x dV \equiv A(C_j)x,$$

and,

$$\bar{u}_j = \frac{1}{|C_j|} \int_{C_j} u(x) dV \equiv A(C_j)u(x).$$

Given element-averages $\bar{u} = \{\bar{u}_j\}$ of $u(x)$ in D , we denote by $R(x; \bar{u})$ a reconstruction of $u(x)$ from \bar{u} , which satisfies

$$R(x; \bar{u}) = u(x) + O(h^r), \quad (4)$$

where u is smooth, and requires for consistency, that

$$A(C_j)R(x; \bar{u}) = \bar{u}_j \quad (5)$$

We denote the reconstructed polynomial in element C_i by $R_i(x; \bar{u})$. Taylor series expansion of R_i about \bar{x}_i gives

$$R_i(x; \bar{u}) = \sum_{k=0}^{r-1} \frac{1}{k!} \sum_{|l|=k} (x - \bar{x}_i)^l D_l; \quad x \in C_i \quad (6)$$

Above, we have used the multi-index notation, and

$$l = (l_1, l_2, \dots, l_s); \quad |l| = l_1 + l_2 + \dots + l_s; \quad \zeta^l = (\zeta_1)^{l_1} \cdot (\zeta_2)^{l_2} \dots (\zeta_s)^{l_s} \quad (7)$$

Also,

$$\sum_{|l|=k} = \sum_{l_1=0}^k \sum_{l_2=0}^k \dots \sum_{l_s=0}^k; \quad l_1 + l_2 + \dots + l_s = k, \quad (8)$$

$$D_l = \frac{\partial^l u}{\partial x^l} |_{(\bar{x}_i)} + O(h^{r-|l|}); \quad 0 \leq |l| \leq r-1, \quad (9)$$

so that,

$$D_0 = R_i(x_i; \bar{u}) = u(\bar{x}_i) + O(h^r); \quad \left(D_l = \frac{\partial^l u}{\partial x_1^{l_1} \partial x_2^{l_2} \dots \partial x_s^{l_s}} \right) \quad (10)$$

The following remarks on R might be useful. R is a polynomial which has the dimension of velocity, and it interpolates velocity to $O(h^r)$. Thus we must choose r so that R meets the desired order of accuracy of the scheme, and R must be differentiable upto order $r-1$. Also R must be constructed by using elements (nodes) from the smooth part of the flow, as much as possible, and in a way that retains the conservative properties of the scheme. (For example, an element must always be included in the stencil for calculating its R , even when the element harbors a discontinuity^{0†}.) R is very important: it is used to evaluate the flux term, the latter multiplying the (large) Reynolds number, and hence the source of the hyperbolicity and nonlinearity in the flow. If we can construct R in the manner outlined above we are sure that when R is differentiated to obtain the flux we will not be discretizing across discontinuities. Hence the Gibbs phenomenon will be inhibited, and no artificial viscosity will be needed for this purpose. Thus, when we look at the behavior of the inner scales, for example in the turbulence spectrum, we can be sure we are not seeing the effect of artificial viscosity, and we can confidently make statements about the physics of flow. The details of our procedure for stencil selection are available in Ladeinde¹².

^{0†}We learnt from a private discussion with Dr. Chakravarthy that this has not caused problems.

To obtain D_l needed for the reconstruction we average $R_i(x, \bar{u})$ over all elements in a stencil $J(i)$ associated with element C_i :

$$A(C_j)R_i = \bar{u}_j; \quad j \in J(i), \quad (11)$$

The matrix problem for D_l is

$$\sum_{k=0}^{r-1} \sum_{|l|=k} a_{j,l} D_l = \bar{u}_j; \quad j \in J(i) \quad (12)$$

where

$$a_{j,l} = \frac{1}{k!} A(C_j)(x - \bar{x}_i)^l = \frac{1}{k! |C_j|} \int_{C_j} (x - \bar{x}_i)^l dV \quad (13)$$

(Note that the foregoing equation has to be written for each element in $J(i)$.)

In the present work we consider $r = 4$ and $s = 3$. The equation for an element in the stencil becomes:

$$\begin{aligned} & a_{j,(0,0,0)}D_{(0,0,0)} + a_{j,(0,0,1)}D_{(0,0,1)} + a_{j,(0,1,0)}D_{(0,1,0)} + a_{j,(1,0,0)}D_{(1,0,0)} + a_{j,(0,0,2)}D_{(0,0,2)} + \\ & a_{j,(0,1,1)}D_{(0,1,1)} + a_{j,(0,2,0)}D_{(0,2,0)} + a_{j,(1,0,1)}D_{(1,0,1)} + a_{j,(1,1,0)}D_{(1,1,0)} + a_{j,(2,0,0)}D_{(2,0,0)} + \\ & a_{j,(0,0,3)}D_{(0,0,3)} + a_{j,(0,1,2)}D_{(0,1,2)} + a_{j,(0,2,1)}D_{(0,2,1)} + a_{j,(0,3,0)}D_{(0,3,0)} + a_{j,(1,0,2)}D_{(1,0,2)} + \\ & a_{j,(1,1,1)}D_{(1,1,1)} + a_{j,(1,2,0)}D_{(1,2,0)} + a_{j,(2,0,1)}D_{(2,0,1)} + a_{j,(2,1,0)}D_{(2,1,0)} + a_{j,(3,0,0)}D_{(3,0,0)} = \bar{u}_j \end{aligned} \quad (14)$$

We write this equation as $AD_l = \bar{u}$. It can be seen that twenty elements are needed in a stencil, giving a 20×20 matrix problem for D_l . (The matrix is full, unfortunately.) We assume an irregular geometry from the onset and employ the usual finite element procedure of coordinate transformation. Further, for this preliminary work, a Gauss-Legendre procedure is used for numerical integration. With this we have

$$|C_j| = \int |J| d\xi d\eta d\zeta = \sum_i \sum_j \sum_k |J|(q_i, q_j, q_k) W_i W_j W_k$$

$$|C_j| \bar{x}_i = \sum_i \sum_j \sum_k \sum_m x_m N_m(q_i, q_j, q_k) |J|(q_i, q_j, q_k) W_i W_j W_k$$

$$|C_j| \bar{u}_j = \sum_i \sum_j \sum_k \sum_m u_m N_m(q_i, q_j, q_k) |J|(q_i, q_j, q_k) W_i W_j W_k$$

$$k! |C_j| a_{j,(l_1, l_2, l_3)} = \sum_i \sum_j \sum_k (\sum_m x_m N_m(q_i, q_j, q_k) - \bar{x}_i)^{l_1} \bullet$$

$$(\sum_m y_m N_m(q_i, q_j, q_k) - \bar{y}_i)^{l_2} (\sum_m z_m N_m(q_i, q_j, q_k) - \bar{z}_i)^{l_3} |J|(q_i, q_j, q_k) W_i W_j W_k$$

Above, the physical coordinates (x, y, z) have been transformed to the computational coordinates (ξ, η, ζ) , via the the Jacobian J , with determinant $|J|$. (q_i, q_j, q_k) are quadrature points of the Gauss-Legendre procedure, with associated weights (W_i, W_j, W_k) . The N 's are the finite element basis functions. Upon solution for D_i , we obtain $R(x; \bar{u}) \equiv R(q_\alpha; \bar{u})$, $\alpha \in i \otimes j \otimes k$, (or, $q_\alpha \in q_i \otimes q_j \otimes q_k$) at the α th quadrature point of C_i using

$$R(q_\alpha; \bar{u}) = \sum_{k=0}^{r-1} \frac{1}{k!} \sum_{|l|=k} (x(q_\alpha) - \bar{x}_i)^{l_1} (y(q_\alpha) - \bar{y}_i)^{l_2} (z(q_\alpha) - \bar{z}_i)^{l_3} D_{(l_1, l_2, l_3)} \quad (15)$$

Note that l_1, l_2, l_3 will be 0, 1, 2, 3 according to equation (14).

In the present work we represent the convective terms by

$$- \sum_j \int N_{i,m} N_j R(x; \bar{u}_m) dV (\rho u_n)^j, \quad (16)$$

where $R(x; \bar{u}_m)$ is a reconstruction from the element-average values, and

$$\bar{u}_m = \frac{1}{|C_j|} \int u_m dV \quad (17)$$

Of course the actual form of the convective terms will depend on the procedure used to control non-linear instability. A non-Galerkin approach is a sure possibility.

4. Parallel Implementation

The current state of scientific computing is such that only low R_λ values can be simulated in DNS. Even then, one would need those front-end computers with parallel architecture to generate DNS data for these cases. In our work we are experimenting with the Intel iPSC/860 (hypercube) parallel supercomputer. Currently we are using

the 32-node, 16-megabytes, one processor per node Delta machine. (This will soon be replaced by the 56-node, 32-megabytes Paragon machine, with two processors per node.)

The hypercube is an MIMD machine. We use the domain decomposition procedure and pregenerate the subdomains using standard (isoparametric) polynomial mappings. The host node is used for the start-up processes - input data, further mesh generation, despatching data to other nodes, and so on. We make extensive use of disk I/O and out-of-core procedures during start-up. The latter is necessary because of the relatively small memory size of a node. In our code there is no global indexing of any array or data, and grid is structured, (i, j, k) .

Finally, our codes are written so that subdomains can be overlapped (Figure 1), the extent of overlapping varying from 0 to 3 elements, depending on user's choice. Overlapping results in a faster convergence and reduced interprocessor communication, as grid data need not be communicated. There is, of course, an overhead from overlapping: more unknowns to solve, but this becomes less critical for large subdomains. (At any rate, we do not believe that a time-accurate solution can be obtained, in a cost-effective manner, with non-overlapping subdomains.) The solution in the regions of overlap is obtained by some form of interpolation, for which the simple-minded approach in Figure 2 is currently used.

5. Conclusion

What seems to be important at this point is the design of ways to cut down on the cost of simulation. From a naive implementation of the schemes presented here we observed a two- to three-fold increase in computational cost, using 32^3 grid points, compared to a non-ENO code with first-order accuracy at discontinuities. More details on the computational cost are available in Ladeinde¹² where we also give some suggestions on possible ways to cut down on the costs. At the present time we are trying out some of the suggestions.

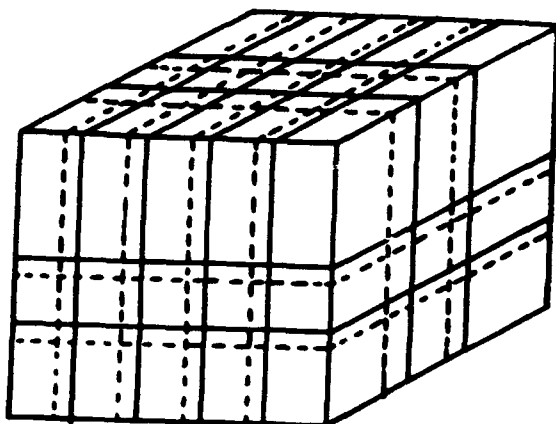


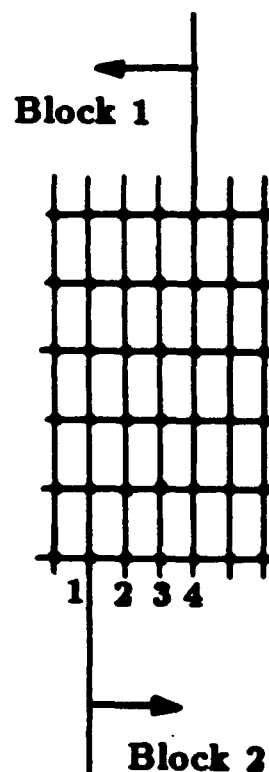
Figure 1
Overlapped Blocks

$$\begin{aligned}\phi_1 &= \phi_1^{[1]} \\ \phi_2 &= \alpha_1 \phi_2^{[1]} + (1 - \alpha_1) \phi_2^{[2]} \\ \phi_3 &= \alpha_2 \phi_3^{[1]} + (1 - \alpha_2) \phi_3^{[2]} \\ \phi_4 &= \phi_4^{[2]}\end{aligned}$$

$[1] \rightarrow \text{Block 1}$

$[2] \rightarrow \text{Block 2}$

Figure 2 Solution in region of overlap



7. References

1. Kuman, M. Y. & Spensley, C. G. 1988. *Weather Turbulence? Lecture notes in Physics* 357. Springer-Verlag.
2. Harten, A. & Osher, S. 1987. *SIAM J. Numer. Anal.* 24, pp. 279-309.
3. Harten, A., Engquist, B., Osher, S. & Chakravarthy, S. 1987. *J. Comp. Phys.* 71, pp. 231-303.
4. Godunov, S. K. 1959. *Matematicheskii Sbornik* 47, pp. 271-299.
5. van Leer, B. 1979. *J. Comp. Phys.* 33, pp. 101-130.
6. Osher, S. & Shu, C.-W. 1990. *Proc. of the Intl. workshop in compressible turbulence*, Princeton, Springer-Verlag.
7. Shu, C.-W., Eriehocher, G., Zang, T. A., Whitaker, D., & Osher, S. 1991. *ICASE Report 91-38*.
8. Tang, W., Komarath, N., & Senhar, L. 1990. *AIAA Paper 90-0376*.
9. Ragab, S. A. & Shuen, S. 1990. *AIAA Paper 90-1000*.
10. Loh, S. K. 1990. *AIAA Paper 90-0376*.
11. Sandham, N. D. & Reynolds, W. G. 1990. *Proc. 7th Symp. turbulent shear flows*.
12. Lodiada, F. 1992. *Proc. Conf. Parallel Comp. Fluid Dyn.*, Princeton, Editor: J. Hämmer. Elsevier Science Publ., The Netherlands. In Press.
13. Harten, A., & Chakravarthy, S. 1991. *ICASE Report 91-70*.

A PRELIMINARY STUDY OF TWO-DIMENSIONAL TURBULENT CHANNEL FLOW UTILIZING PARALLEL COMPUTATION

M.S.Pervaiz, P.R.Smith and G.A.Reynolds

Department of Mechanical Engineering

New Mexico State University

Las Cruces, NM 88003

Abstract

Two-dimensional turbulent channel flow was studied. Jones and Launder's $k-\epsilon$ model at low Reynolds number was applied to model the Reynolds' stresses. Patankar's algorithm SIMPLE was adapted to solve numerically on a parallel processor the decoupled partial differential equations for turbulent kinetic energy, mean velocity and rate of dissipation. The computer codes were developed in Fortran 90 and run on Connection Machine 200. The parallelly computed results for mean velocity, kinetic-energy and rate of dissipation compare well with experimental data of J. Laufer and serially computed data by S.W.Kim.

1 INTRODUCTION

The necessity for extremely small grid spacing and the iterative nature of solution algorithms for solving turbulent flow problems leads to very long run time on serial-type digital computers. Parallel processors have the potential of speeding up these calculations and offer hope of someday allowing real-time solution of at least some types of turbulent flow problems. In this paper we examine, as a preliminary step toward achieving more efficient turbulent calculations, a simple two-dimensional duct flow, as shown in Fig 1, with a known pressure gradient and requiring a relatively small number of internal nodes. This problem was chosen since very extensive experimental measurements have been made of the velocity profiles, kinetic-energy profiles and dissipation profiles. Furthermore, the problem has been solved carefully on serial machines using a two-equation model, i.e., the $k-\epsilon$ model. Hence by solving the two-equation model on a parallel machine, we can check the results against both experimental data and computational data. This will give us some insight into how well parallel algorithms work, before the technique is extended to problems with unknown pressure fields (requiring another level of iteration) and problems requiring very large numbers of internal nodes (say on the order of 10^6 or more).

Reynolds equation for a two-dimensional conduit are solved. Jones and Launder's [1] $k-\epsilon$ model at low Reynolds number is used to model the Reynolds stresses. Patankar's [2] method to solve the non-linear partial differential

equations is adapted to develop the parallel algorithm. The spacing of the grid is variable from wall surface to the centerline of the duct and grid spacing in stream wise direction is kept constant (see Fig 2). The no-slip boundary condition at the wall surface and vanishing gradient of the variables at the centerline of the duct are adapted. The computer code was developed in the parallel mode using Fortran 90 and run on the Connection Machine 200.

2 GOVERNING EQUATIONS

The main governing equation is the Reynolds' equation of motion for turbulent flow, which can be developed from the Navier-Stokes equations [5]:

$$\rho \bar{u}_i \frac{\partial \bar{u}_j}{\partial x_i} = -\frac{\partial \bar{P}}{\partial x_j} + \frac{\partial}{\partial x_i} [\mu \frac{\partial \bar{u}_j}{\partial x_i} - \rho \overline{(u'_i u'_j)}], \quad i, j = 1, 2, 3 \quad 0 \leq t \leq \Delta T. \quad (1)$$

Where the terms with the overbar are the time averaged values and the primed terms are the fluctuations about the time average. The terms $-\rho \overline{(u'_i u'_j)}$ are called Reynolds' stresses which must be modeled. Let's replace \bar{u} , and \bar{P} by u and P for simplicity. For two-dimensional steady state flow in the x_1 direction, eqn (1) can be written as:

$$\rho u_1 \frac{\partial u_1}{\partial x_1} + \rho u_2 \frac{\partial u_1}{\partial x_2} = \frac{\partial}{\partial x_1} [\mu \frac{\partial u_1}{\partial x_1} - \rho \overline{u'_1 u'_1}] + \frac{\partial}{\partial x_2} [\mu \frac{\partial u_1}{\partial x_2} - \rho \overline{u'_1 u'_2}] - \frac{\partial P}{\partial x_1} \quad (2)$$

$$\rho u_1 \frac{\partial u_2}{\partial x_1} + \rho u_2 \frac{\partial u_2}{\partial x_2} = \frac{\partial}{\partial x_1} [\mu \frac{\partial u_2}{\partial x_1} - \rho \overline{u'_1 u'_2}] + \frac{\partial}{\partial x_2} [\mu \frac{\partial u_2}{\partial x_2} - \rho \overline{u'_2 u'_2}] - \frac{\partial P}{\partial x_2} \quad (3)$$

In fully developed turbulent two-dimensional duct flow, the variation of mean values of fluctuating quantities w.r.t. x_1 should be zero [3], i.e. the flow pattern is independent of the stream wise direction, therefore pressure is independent of x_2 . Further, assuming that u_2 is zero, then eqn (3) can be dropped.

The two equation model assumes that Reynolds' stresses are equal to mean rate of strain times the turbulent viscosity [1].

$$-\rho \overline{(u'_1 u'_2)} = \mu_T \frac{\partial u_1}{\partial x_2} \quad (4)$$

where μ_T is the turbulent viscosity, ([6], [7]). The turbulent viscosity is assumed to have the form

$$\mu_T = C'_\mu \rho k^{\frac{1}{2}} l \quad (5)$$

where C'_μ is a constant, k is turbulent kinetic energy and l is the turbulent length scale. Equation (5) can be recast as ([8], [9], [10])

$$\mu_T = C_\mu \rho \frac{k^2}{\epsilon}, \quad (6)$$

where C_μ is a constant of proportionality. The variables k and ϵ (the turbulent dissipation) can be calculated for

steady, two-dimensional flow from the following two differential transport equations at low Reynolds' number ([2] and [11]):

$$\rho u_i \frac{\partial k}{\partial x_i} = \frac{\partial}{\partial x_j} \left[\left(\mu + \frac{\mu_T}{\sigma_k} \right) \frac{\partial k}{\partial x_j} \right] + \mu_T \frac{\partial u_i}{\partial x_j} \left[\frac{\partial u_i}{\partial x_j} + \frac{\partial u_j}{\partial x_i} \right] - 2\mu \left[\frac{\partial k^{\frac{1}{2}}}{\partial x_j} \right]^2 - \rho \epsilon, \quad i, j = 1, 2 \quad (7)$$

$$\rho u_i \frac{\partial \epsilon}{\partial x_i} = \frac{\partial}{\partial x_j} \left[\left(\mu + \frac{\mu_T}{\sigma_\epsilon} \right) \frac{\partial \epsilon}{\partial x_j} \right] + C_1 \mu_T \frac{\epsilon}{k} \frac{\partial u_i}{\partial x_j} \left[\frac{\partial u_i}{\partial x_j} + \frac{\partial u_j}{\partial x_i} \right] - C_2 \rho \frac{\epsilon^2}{k} + 2\mu \mu_T \left(\frac{\partial^2 u_i}{\partial x_j \partial x_i} \right)^2, \quad i, j = 1, 2 \quad (8)$$

where

$$C_\mu = 0.9 \text{Exp}(-2.5/(1.0 + R_T/50)) \quad (9)$$

$$C_2 = 2.0(1.0 - 0.3 \text{Exp}(-R_T^2)). \quad (10)$$

C_1 , σ_k and σ_ϵ are usually assumed to have the values 1.45, 1.0, and 1.3, respectively ([2], [11]).

The continuity equation for the mean flow is

$$\frac{\partial u_i}{\partial x_i} = 0. \quad (11)$$

Equations (2), (4), (7), (8) and (11) represent a complete set of equations for the steady turbulent flow through a two-dimensional duct. Equations (2), (7) and (8) can be represented in the general form as:

$$\frac{\partial}{\partial x_j} (\rho u_i \Phi) = \frac{\partial}{\partial x_j} \left(\Gamma \frac{\partial \Phi}{\partial x_j} \right) + S \quad j = 1, 2 \quad (12)$$

where Φ , Γ and S are as defined in Table 1 for the three equations.

Table 1. Variable values for eqn. (12)

Eqn.	Φ	Γ	S
2	u	$\mu + \mu_T$	$-\frac{dP}{dx_1}$
7	k	$\mu + \frac{\mu_T}{\sigma_k}$	$\mu_T \left(\frac{\partial u_i}{\partial x_j} \right)^2 - \rho \epsilon - 2\mu \left(\frac{\partial k^{\frac{1}{2}}}{\partial x_j} \right)^2$
8	ϵ	$\mu + \frac{\mu_T}{\sigma_\epsilon}$	$C_1 \mu_T \frac{\epsilon}{k} \left(\frac{\partial u_i}{\partial x_j} \right)^2 - C_2 \rho \frac{\epsilon^2}{k} + 2\mu \mu_T \left(\frac{\partial^2 u_i}{\partial x_j \partial x_i} \right)^2$

3 DESCRIPTION OF THE ALGORITHM

Equation (12) is a set of non-linear coupled partial differential equations. These equations can be decoupled and solved by different methods, (e.g. see [2], [12], and [13]), but in the current study a modified SIMPLE algorithm [2] is adapted. A staggered grid is used, as shown in Fig. 3. The pressure is assumed known at the center (main) grid point p and the velocity, turbulent kinetic energy, and dissipation are calculated at the 1/2 grid points e , w , n , s . Note that the main grid points are the intersection of the grid lines shown in Fig. 2. Now, let

$$\frac{\partial J_{x_1}}{\partial x_1} + \frac{\partial J_{x_2}}{\partial x_2} = S, \quad (13)$$

where

$$J_{x_1} = \rho u_1 \Phi - \Gamma \frac{\partial \Phi}{\partial x_1} \quad \text{and} \quad J_{x_2} = \rho u_2 \Phi - \Gamma \frac{\partial \Phi}{\partial x_2}.$$

Integrating eqn (13) over the control volume shown in Fig 2 gives

$$J_e - J_w + J_n - J_s = (S_c + S_p \Phi_p) \Delta x_1 \Delta x_2. \quad (14)$$

The quantities J_e, J_w, J_n, J_s are the total integrated fluxes over the control volume faces, e.g., J_e stands for $\int J_{x_1} dx_1$ over the interface e , etc. Integrating the continuity equation times density (eqn (11)* ρ) over the control volume gives,

$$F_e - F_w + F_n - F_s = 0, \quad (15)$$

where F_e, F_w, F_n, F_s are the mass flow rates through the faces of the control volume. If ρu_1 at e is constant,

$$F_e = (\rho u_1)_e \Delta x_2. \quad (16)$$

The other mass flow rates are found in the similar way. Multiply eqn (15) by Φ_p and subtract it from eqn (14):

$$(J_e - F_e \Phi_p) - (J_w - F_w \Phi_p) + (J_n - F_n \Phi_p) - (J_s - F_s \Phi_p) = (S_c + S_p \Phi_p) \Delta x_1 \Delta x_2 \quad (17)$$

which becomes

$$a_p \Phi_p = a_E \Phi_E + a_W \Phi_W + a_N \Phi_N + a_S \Phi_S + b, \quad (18)$$

where

$$a_p = a_E + a_W + a_N + a_S - S_p \Delta x_1 \Delta x_2$$

$$a_E = D_e A(|P_e|) + [-F_e, 0] \quad a_W = D_w A(|P_w|) + [F_w, 0]$$

$$a_N = D_n A(|P_n|) + [-F_n, 0] \quad a_S = D_s A(|P_s|) + [F_s, 0]$$

$$b = S_c \Delta x_1 \Delta x_2$$

$$D_e = \frac{\Gamma_e \Delta x_2}{(\delta x_1)_e} \quad D_w = \frac{\Gamma_w \Delta x_2}{(\delta x_1)_w} \quad D_n = \frac{\Gamma_n \Delta x_1}{(\delta x_2)_n} \quad D_s = \frac{\Gamma_s \Delta x_1}{(\delta x_2)_s}$$

and the Peclet numbers are

$$P_e = \frac{F_e}{D_e} \quad P_w = \frac{F_w}{D_w} \quad P_n = \frac{F_n}{D_n} \quad P_s = \frac{F_s}{D_s}$$

and $\Delta x_i, \delta x_i$ are defined in Figs 3 and 4, respectively. The function $A(|P|)$ was selected as [2],

$$A(|P|) = [0, (1.0 - 0.1 |P|)^4], \quad (19)$$

where [...] represents the maximum of the bracket. Equation (18) represents the equations for u_1 , k and ϵ (i.e. Φ) which must be solved at internal node p . Γ_e can be approximated by

$$\Gamma_e = \frac{2\Gamma_p\Gamma_E}{\Gamma_p + \Gamma_E} \quad (20)$$

if $(\delta x_1)_e$ is midway between p and E [2]. A similar equation results for Γ_w in terms of Γ_p and Γ_W .

If the source term is linear and depends on Φ , we can treat it as a linear function i.e.,

$$S = S_c + S_p\Phi_p \quad (21)$$

When the source term is non-linear and depends on Φ , the source term can be linearized in the following way.

$$S = S^* + \left(\frac{dS}{d\Phi}\right)^*(\Phi_p - \Phi_p^*), \quad (22)$$

where star terms are calculated on the previous iteration and Φ_p is the new value which will be calculated. The constants S_c and S_p will become

$$S_c = S^* - \left(\frac{dS}{d\Phi}\right)^*\Phi_p^* \quad \text{and} \quad S_p = \left(\frac{dS}{d\Phi}\right)^*.$$

The values of S_c and S_p are calculated on every iteration.

In order to maintain conservation of mass and to ensure the stability of the calculation, the following rules must be obeyed:

- 1) When a face is common to two adjacent control volumes, the flux across it must be represented by the same expression in the equation for the two control volumes.
- 2) All coefficients i.e. a_E, a_W, a_S, a_N, a_p must be positive at all times during the calculation.
- 3) When the source term is linearized as $S = S_c + S_p$, the coefficient S_p must be less than or equal to zero.
- 4) Sum of the neighboring coefficients should be equal to a_p .

The system of equations were solved along one horizontal grid line by substituting the estimated values of Φ in the neighboring lines. This is called the line-by-line technique. The equation for two dimensions can be written as:

$$a_p\Phi_p = a_E\Phi_E + a_W\Phi_W + a_N\Phi_N + a_S\Phi_S + b \quad (23)$$

For this study the line-by-line technique it is applied only in the x_1 -direction. The estimated values of Φ_N and Φ_S will be substituted into eqn (23). The resulting equation is:

$$a_i\Phi_i = b_i\Phi_{i+1} + c_i\Phi_{i-1} + d_i \quad i = 1, 2, 3, \dots, N_{x_1}, \quad (24)$$

in which $\Phi_i = \Phi_o$, $\Phi_{i+1} = \Phi_E$, $\Phi_{i-1} = \Phi_W$, $a_i = a_p$, $b_i = a_E$, $c_i = a_W$ and $d_i = a_N \Phi_N^* + a_S \Phi_S^* + b$, where Φ_N^* and Φ_S^* are the estimated values of the neighbouring lines. N_{x_1} is the number of central nodes in the x_1 direction. the subscript i is the grid point location in the x_1 -direction and a_i, b_i, c_i and d_i are the known coefficients in the equation. To begin the calculation the values of the velocities, turbulent kinetic energy and the dissipation at all internal nodes are set to the entrance values assumed at $x_1 = 0$. Beginning on the $m_{x_2} = 1$ line, eqn (24) yields an N_{x_1} by N_{x_1} tridiagonal matrix in the Φ_i ($i = 1, 2, 3, \dots, N_{x_1}$) which can be solved by a parallelized tridiagonal matrix solver. Solving gives new approximations to the Φ_i on the $m_{x_2} = 1$ line. These new values of Φ_i are used in calculating the Φ_i on the $m_{x_2} = 2$ line, but the entrance conditions are still used as the approximation for all the values of Φ_i on the m_{x_2} lines above the $m_{x_2} = 2$ line. This procedure is repeated for all 160 m_{x_2} lines. One completion of the calculation of the Φ_i for all 160 m_{x_2} lines represents one iteration toward the complete solution. We now have new approximations to the values of u_1 , k and ϵ at all the internal nodes. We return to the $m_{x_2} = 1$ line and begin the procedure again, using the new approximations to the Φ_i . This procedure continues until the maximum relative difference between successive iterative values of a flow parameter at all nodes is less than the specified convergence criteria for that particular parameter.

Variable grid spacing in the x_2 -direction and constant grid spacing in the x_1 -direction were used. The cross-channel half-width of 0.0635 meter was divided into one hundred and sixty grid points. The grid spacing was calculated from a second degree polynomial:

$$\Delta x_2 = 0.00003 + 0.03055x_2 - 0.24056x_2^2 \quad (25)$$

The laminar sublayer contains twenty one nodes. The near wall region contains seventy eight nodes and the turbulent core region contains sixty one nodes.

A no-slip boundary condition was used at the wall, i.e. at.

$$x_2 = 0, \quad u_1 = u_2 = u_3 = 0 \quad \text{and} \quad k = \epsilon = 0.$$

The x_1 -direction grid spacing was held constant at 0.001 meter and 110 x_1 nodes were used for all calculations.

The gradient of Φ was kept zero at the center line of the duct, i.e.

$$\left(\frac{\partial u_1}{\partial x_2}\right)_d = 0, \quad \left(\frac{\partial k}{\partial x_2}\right)_d = 0, \quad \left(\frac{\partial \epsilon}{\partial x_2}\right)_d = 0.$$

The inflow boundary condition at $x_1 = 0$ was assumed to be the entering profiles of u_1, k, ϵ . The out-flow boundary condition was determined after calculating all the unknowns at the interior nodes.

Since we are interested in the fully developed turbulent flow, the entering turbulent mean velocity profile at $x_1 = 0$ was provided by empirical relations [5] (similar methods are used by other authors ([1], [4]), who showed that the entrance profiles assumed have little influence on the final fully developed flow) and the problem treated as an entrance length problem. The flow proved to be fully developed before the $N_{x_1} = 110$ node was reached.

4 RESULTS AND DISCUSSION

The parallelly computed results for turbulent kinetic energy, rate of dissipation and mean velocity are compared with experimental results by Laufer [3] and with serially computed results by Kim [4] in Figs 5, 6, 7, 8 and 9. Turbulent kinetic energy results are shown in Fig. 5. The magnitude and location of maximum and minimum turbulent kinetic energy are in good agreement for all three methods. The results for normalized turbulent kinetic energy ($k^+ = \frac{k}{\frac{1}{2}\rho u_\tau^2}$ and $Y^+ = \frac{\nu x}{u_\tau}$) near the wall are shown in Fig. 6. The location and magnitude of the overshoot is in good agreement for all three techniques.

The results for normalized rate of dissipation ($\epsilon^+ = \frac{\epsilon}{\frac{1}{2}\rho u_\tau^3}$) near the wall are shown in Fig. 7. These results are compared with semi-empirical data [4]. The location of maximum overshoot is in good agreement with the available data. The semi-empirical data is actually the mean value of many experimental data or the turbulent quantities obtained from the analysis of various experimental data.

The results for the turbulent mean velocity are shown in Fig. 8. The parallelly computed results are in good agreement with serially computed results and within 10% of the experimental results. In this study the pressure gradient was taken from Laufer's publication [3]. The same pressure gradient was used by Kim [4]. The normalized turbulent mean velocity ($u^+ = \frac{u}{u_\tau}$) near the wall is shown in Fig. 9. The parallelly computed velocity prediction in the laminar sublayer is in excellent agreement with the available data but deviates from it somewhat in the fully developed region.

5 CONCLUSION

A numerical technique utilized on a parallel processor for determining the fully developed turbulent flow of known pressure gradient in a two-dimensional conduit has been demonstrated. The technique appears to predict the turbulent mean velocity, the turbulent kinetic energy and the turbulent dissipation as accurately as a similar numerical calculation which is completely serial in nature.

ACKNOWLEDGEMENTS

We gratefully acknowledge the support provided by the Army High Performance Computing Research Center. Special thanks are also due to Mrs. Mariagrazia Giannelli Pervaiz for her assistance in preparing the typescript.

REFERENCES

- [1] W. P. Jones and B. E. Launder, "*The Prediction of Laminarization with Two-Equation Model of Turbulence*", Int. J. Heat Mass Transfer Vol. 15(1972).
- [2] S. V. Patankar, "*Numerical Heat Transfer and Fluid Flow*", Hemisphere Pub. Corp, Washington D. C. 1980.
- [3] J. Laufer, "*Investigation of Turbulent Flow in a Two-Dimensional Channel*", NACA TN-2123, 1954.
- [4] S. W. Kim, "*Near-Wall Turbulent Flow in a Fully Developed Turbulent Channel and Pipe Flows*", Numerical Heat Transfer, Part B, Vol. 17(1990).
- [5] F. M. White, "*Viscous Fluid Flow*", McGraw-Hill, Inc. New York 1974.
- [6] H. W. Emmons, "*Shear Flow Turbulence*", Proc. 2nd U.S. National Congress App. Mech. ASME(1954).
- [7] B. E. Launder and D. B. Spalding, "*The Numerical Computation of Turbulent Flows*", Comp. Methods in App. Mech and Engg 3(1974).
- [8] K. H. Ng and D. B. Spalding, "*Some Application of a Model of Turbulence for Boundary Layers Near Walls*", Physics Fluids Vol. 15(1972).
- [9] W. Rodi and D. B. Spalding, "*A Two-Parameter Model of Turbulence and its Applications to Free Jet*", Wärme und Stoffübertragung, Vol. 3(1970).
- [10] F. H. Harlow and P. I. Nakayama, "*Transport of Turbulence Energy Decay Rate*", LA-3854, University of California Las Alamos New Mexico(1968).
- [11] W. P. Jones and B. E. Launder, "*The Calculation of Low Reynolds' Number Phenomena with a Two-Equation Model of Turbulence*", Int. J. Heat Mass Transfer Vol. 16(1973).
- [12] S. V. Patankar and D. B. Spalding, "*A Finite Difference Procedure for Solving the Equation of the Two-Dimensional Boundary Layer*", Int. J. Heat Mass Transfer Vol. 10(1967).
- [13] D. A. Anderson, "*Computational Fluid Mechanics and Heat Transfer*", Hemisphere Pub. Corp, Washington D. C. 1980.

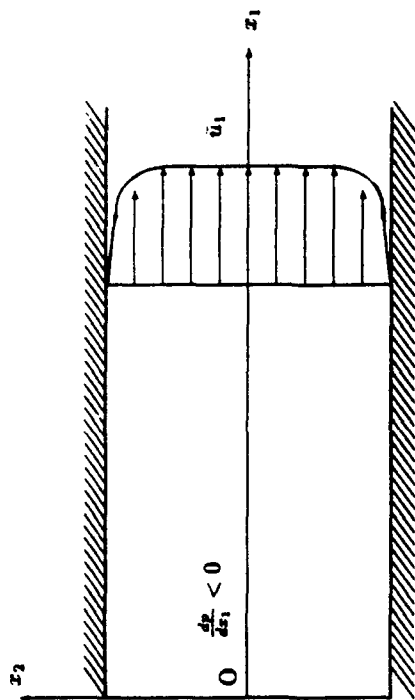


Figure 1: Two-Dimensional Duct Flow

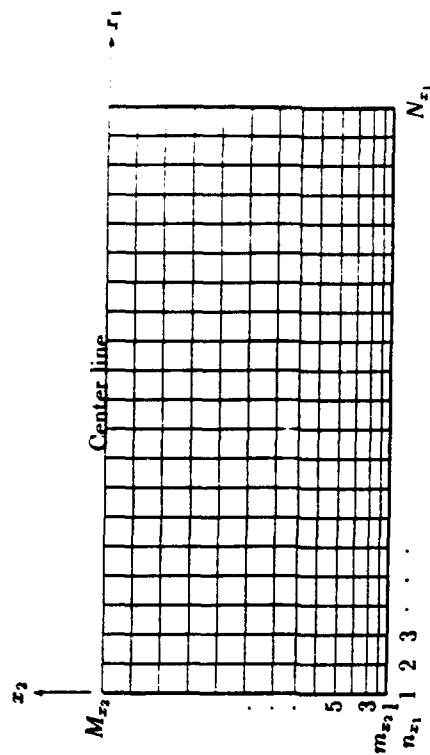


Figure 2: Two-Dimensional Computational Grid

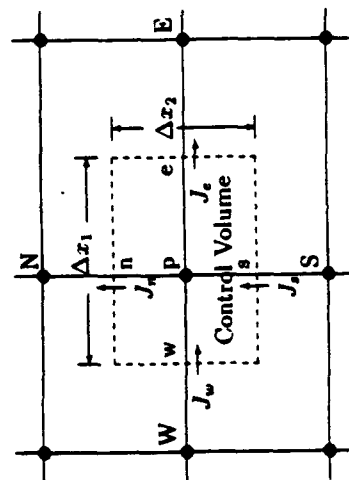


Figure 3: Two-Dimensional Control Volume

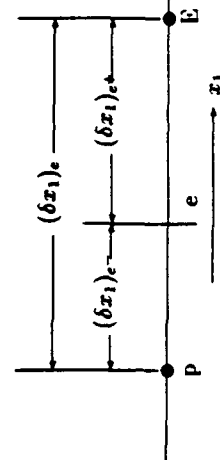


Figure 4: Distance Between Two Grid Points

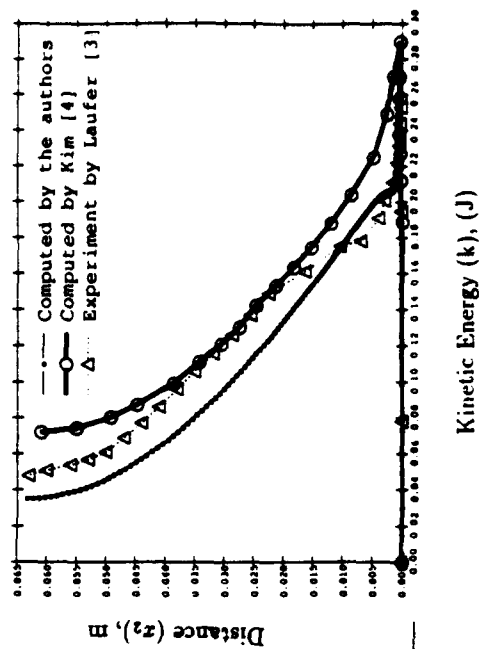


Figure 5: Kinetic Energy Distribution

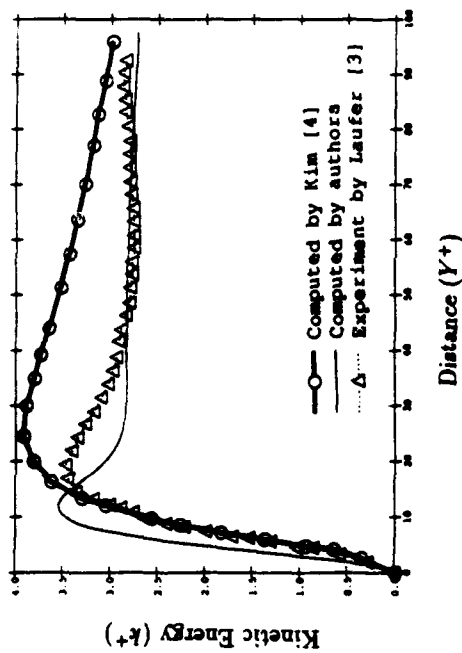


Figure 6: Normalized Kinetic Energy Distribution

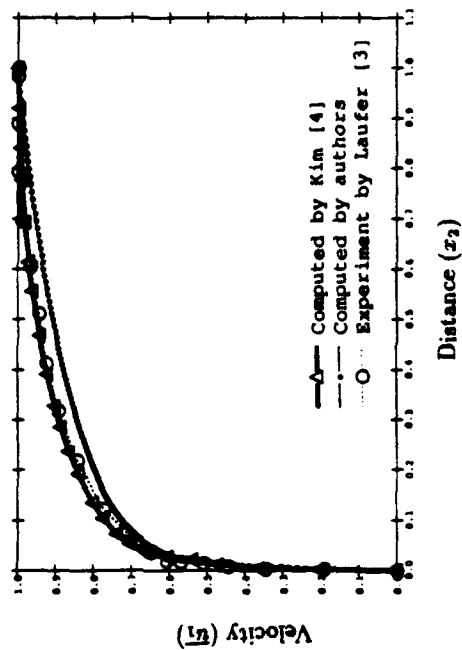


Figure 8: Mean Velocity Distribution

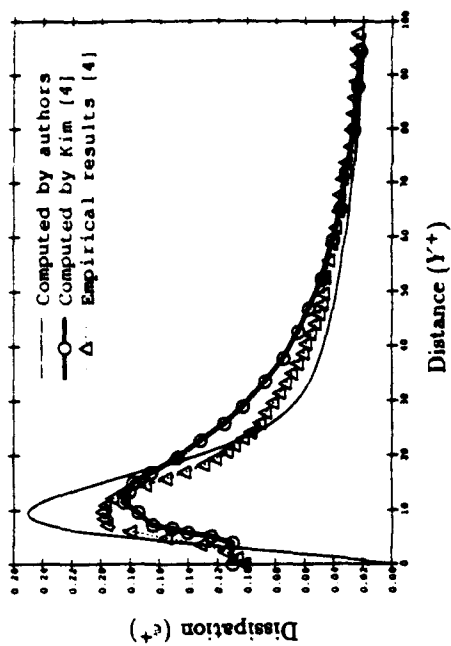


Figure 7: Normalized Rate of Dissipation

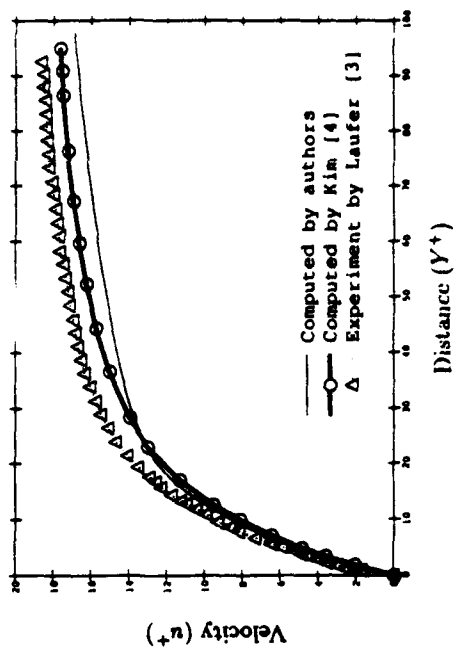


Figure 9: Normalized Velocity Distribution

AN IMPROVED $k-\epsilon$ MODEL FOR PREDICTION OF ADVERSE PRESSURE GRADIENT TURBULENT FLOWS

By G. Chukkapalli and O.F. Turan⁺

Mechanical Engineering Department
McMaster University
Hamilton, Ontario L8S 4L7
Canada

ABSTRACT

A modified $k-\epsilon$ model is proposed to predict complex, adverse pressure gradient, turbulent diffuser flows. A fuller treatment of the rate of kinetic diffusion terms is incorporated in modeling the transport equations for both k and ϵ . A third structural parameter is introduced. A three-layer representation is proposed for each structural parameter. Improved prediction is obtained with the present model.

I. INTRODUCTION

Prediction of adverse pressure gradient (APG) turbulent internal flows finds practical applications in designing turbomachinery passages, wind tunnels and diffusers in general. Such flows are complex (Bradshaw, 1976), and as a result, numerical prediction is difficult. The main reasons for this complexity are wall effects which are common to all wall bounded flows, and the effects due to adverse pressure gradients. The effect of wall on turbulence structure is two-fold. First, viscous effects surface due to reduced local turbulence Reynolds number. Secondly, wall effects preferentially suppress transverse normal Reynolds stress and distort turbulent eddies, thus making turbulence structure anisotropic. On the other hand, the effects of adverse pressure gradients on turbulence structure are many fold. First, the assumption of self preservation in the longitudinal direction becomes questionable. Additional mechanisms of production, dissipation and transport of turbulence, such as through lateral vortex stretching, appear. Most prominent physical phenomena responsible for this additional activity are irrotational strains and lateral divergence.

The present study is a step towards practical numerical prediction of turbulent diffuser flows. In the representation of Reynolds stresses, the concept of structural parameters is compared with the Boussinesq formulation. A modified $k-\epsilon$ model is proposed with structural parameters, and the triple correlation model of Hanjalić and Launder (1972, hereafter referred to as HL) is incorporated. The prediction of k , and of its rate of dissipation, ϵ , in an eight degree conical diffuser with a fully developed inlet is compared with the prediction using a conventional eddy viscosity $k-\epsilon$ model.

II. MODELING DIFFICULTIES

Turbulent diffuser flows with the complexities mentioned above are still

⁺ Address correspondence to this author.

Tel. (416) 525 9140 Ext. 7296/7321, Facs. (416) 572 5944.

out of reach for direct numerical simulation or large eddy simulation, due to their wide range of time and length scales. As a result, the prediction of these common turbulent flows have to depend on the averaged, unclosed Navier-Stokes equations and closure modeling. A popular closure approach is to solve the transport equations for turbulence kinetic energy, k , and its rate of dissipation, ϵ , along with the averaged N-S equations. By using the Boussinesq formulation, the Reynolds stresses which appear in the mean momentum equations, are linked to the mean gradients through the eddy viscosity which is derived from k and ϵ . The unmodeled transport equations for k and ϵ in tensor form are given below:

$$Dk/Dt = \underbrace{-\partial/\partial x_i \{ \overline{u_i (p/\rho + k)} \}}_{D} - \underbrace{\overline{u_i u_j} \cdot \partial U_j / \partial x_i}_{P_k} + \underbrace{\nu \cdot \partial/\partial x_i \{ \overline{u_j (\partial u_i / \partial x_j + \partial u_j / \partial x_i)} \}}_{D_\nu} - \underbrace{\nu \cdot (\partial u_i / \partial x_j + \partial u_j / \partial x_i) \partial u_j / \partial x_i}_{\epsilon} \quad (1)$$

$$D\epsilon/Dt = - \underbrace{2 \cdot \nu \cdot \partial U_i / \partial x_k (\partial u_i / \partial x_k \cdot \partial u_k / \partial x_i + \partial u_i / \partial x_i \cdot \partial u_k / \partial x_k)}_{P_\epsilon} - \underbrace{2 \cdot (\nu \cdot \partial^2 u_i / \partial x_k \partial x_i)^2}_{\epsilon_\epsilon} - \underbrace{(\nu/\rho) \cdot \partial/\partial x_i (\partial p / \partial x_i \cdot \partial u_i / \partial x_i)}_{D_p} - \underbrace{2 \cdot \nu \cdot \partial u_i / \partial x_k \cdot \partial u_i / \partial x_k \cdot \partial u_k / \partial x_i}_{P_{\epsilon T}} - \underbrace{\partial/\partial x_i (\overline{u_i \epsilon})}_{D_\epsilon} \quad (2)$$

where D , P_k , D_ν and ϵ of Equation 1 represent the rates of kinetic (turbulent) diffusion, production, viscous diffusion and anisotropic rate of dissipation, respectively, of turbulence kinetic energy, k . Similarly, P_ϵ , $P_{\epsilon T}$, ϵ_ϵ , D_ϵ and D_p of Equation 2 represent the rates of production due to mean field, production due to turbulence, destruction, turbulent diffusion and pressure diffusion, respectively, of ϵ . The kinetic diffusion and dissipation terms of the k -equation and most of the ϵ -equation terms, have to be modeled in terms of k , ϵ and mean gradients in order to obtain a closed form. The pressure diffusion is neglected here based on the available experimental data for the k -equation (Turan and Azad, 1992).

BASIC k- ϵ MODEL

Various terms of the k -equation are modeled as follows. The kinetic diffusion is given by,

$$D = \partial/\partial x_i (\nu_T \partial k / \partial x_i), \quad (3)$$

where $\nu_T = C_\mu k^2 / \epsilon$ is the turbulence eddy viscosity. Reynolds stresses are modeled by using the Boussinesq formulation as, $\overline{u_i u_j} = \nu_T \cdot (\partial U_i / \partial x_j + \partial U_j / \partial x_i) / 2 + \delta_{ij} k$. Thus, the rate of production becomes, $P_k = [\nu_T \cdot (\partial U_i / \partial x_j + \partial U_j / \partial x_i) + 2/3 \cdot \delta_{ij} k] \cdot \partial U_i / \partial x_j$. The following isotropic form is used for the rate of dissipation: $\epsilon = \nu \cdot (\partial u_i / \partial x_j)^2$. Similarly, the terms of ϵ -equation are modeled as follows: $P_\epsilon = C_{\epsilon 1} \cdot P_k \cdot \epsilon / k$; $\epsilon_\epsilon = C_{\epsilon 2} \cdot \epsilon^2 / k$; $D_\epsilon = \partial/\partial x_i (\nu_T \partial \epsilon / \partial x_i)$ where C_μ , $C_{\epsilon 1}$ etc. are the model constants.

The high Reynolds number basic k - ϵ model, fails to produce correct trends and most importantly, the correct limiting behavior, as the wall is approached; yet the wall behavior is important in engineering applications. The main reasons for this discrepancy are, the assumption of isotropy and neglecting viscous effects.

Large number of modified two-equation models have appeared in the literature to remedy the drawbacks of the basic k - ϵ model. Earlier models use

high Reynolds number forms with wall functions. In more recent models, high Reynolds number models are modified for low Reynolds number applications by using wall damping functions. A comprehensive review of near wall models is given by Patel et al. (1985), and more recently by So et al. (1991) and Speziale et al. (1992). In order to obtain the correct near wall behavior of various turbulence quantities, P_ϵ and ϵ_ϵ of the ϵ -equation and ν_t are multiplied by wall damping functions f_1 , f_2 and f_μ , respectively. These are appropriate functions of y^+ and become unity away from the wall. With these corrections to the basic k - ϵ model, most wall bounded flows, especially their mean flow fields, can be predicted with accuracy (Lai et al. 1989). Still, these modified models fall short of predicting the turbulence fields of arbitrary adverse pressure gradient flows.

The reason for this shortfall can be examined from three points of view: First, the response and recovery rates of the mean and turbulence fields to the disturbances, such as due to an APG, are quite different; whereas history effects are not taken into account when the Boussinesq approximation is used. Reynolds stresses cannot respond instantaneously to the rapid change of strain rates as modeled by an eddy viscosity model. Secondly, scalar gradient diffusion model is expected to yield poor results when turbulent transport is dominated by large eddies. Another disadvantage of this model is the assumption of isotropic diffusion such that diffusion of all normal Reynolds stresses in all three directions is taken to be similar. Thirdly, almost all k - ϵ models use the isotropic ϵ -equation, because of the shear complexity of the anisotropic one. In addition, various terms such as production, transport and destruction of the isotropic ϵ -equation are modeled on similar grounds to that of the k -equation, even though there is not experimental evidence of both scalars being governed by similar physics.

III. PRESENT MODEL

STRUCTURAL PARAMETERS

There is outstanding experimental evidence that turbulence Reynolds stresses are closely related to turbulence kinetic energy (Bradshaw, 1967, Fernholtz and Vagt, 1981, Cutler and Johnston, 1989, Saddoughi and Joubert, 1991). In the present study, the eddy viscosity concept is replaced by structural parameters to relate various Reynolds stresses to the turbulence kinetic energy as follows:

$$\overline{uv} = a_1 \cdot k; \quad (4a) \quad \overline{u^2 - v^2} = a_2 \cdot k; \quad (4b) \quad \overline{w^2 - v^2} = a_3 \cdot k, \quad (4c)$$

where structural parameters a_2 and a_3 represent the flow anisotropy in transverse and span-wise directions, respectively. From Equations 4b and 4c and $k = (\overline{u^2} + \overline{v^2} + \overline{w^2})/2$, the following relationships between normal Reynolds stress components and k can be obtained: $\overline{u^2} = b_1 \cdot k$; $\overline{v^2} = b_2 \cdot k$; $\overline{w^2} = b_3 \cdot k$; where $b_1 = (2 + 2 \cdot a_2 + a_3)/3$; $b_2 = (2 - a_3 + a_2)/3$; $b_3 = (2 - a_2 - 2 \cdot a_3)/3$.

a_1 (Bradshaw et al. 1967) and a_2 (Hanjalić and Launder, 1980) were assumed previously to be constants throughout the flow field. As it is shown in Section IV, the structural parameters a_1 , a_2 and a_3 are not constants. The parameter a_3 is proposed in the present study.

THE KINETIC DIFFUSION TERM OF THE k-EQUATION

The triple velocity correlations in term, D, of Equation 1, are modeled using HL's symmetric expansion into gradients of Reynolds stresses which was shown to yield most acceptable results (Ammano and Goel 1987).

$$\overline{u_i u_j u_k} = -C_k k / \epsilon \left(\overline{u_i u_l} \frac{\partial \overline{u_j u_k}}{\partial x_l} + \overline{u_j u_l} \frac{\partial \overline{u_i u_k}}{\partial x_l} + \overline{u_k u_l} \frac{\partial \overline{u_i u_j}}{\partial x_l} \right). \quad (5)$$

This model replaces the isotropic scalar gradient diffusion form of the k-ε models found in the literature. When expanded in the r-θ coordinates the turbulent diffusion term yields,

$$-\partial/\partial x_i (\overline{u_i k}) = \partial/\partial x \{ C_k k / \epsilon [\overline{u^2} (\partial k / \partial x + \partial \overline{u^2} / \partial x) + \overline{uv} (\partial k / \partial r + \partial \overline{u^2} / \partial r + \partial \overline{uv} / \partial x) + \overline{v^2} \partial \overline{uv} / \partial r] \} \\ + 1/r \cdot \partial/\partial r \{ r C_k k / \epsilon [\overline{u^2} \partial \overline{uv} / \partial x + \overline{uv} (\partial k / \partial x + \partial \overline{uv} / \partial r + \partial \overline{v^2} / \partial r) + \overline{v^2} (\partial k / \partial r + \partial \overline{v^2} / \partial r)] \}. \quad (6)$$

The Reynolds stresses in Equation 6 are then expressed in terms of k by using the structural parameters. Equation 3 can be obtained from Equation 6 by invoking isotropy. With the assumption of isotropy, the relationship between C_μ , σ_k and C_ϵ can be obtained as, $C_\mu / \sigma_k = (10/9) C_\epsilon$. The model constants of the present study are given in Section V.

Complete production term, P_k , is incorporated without neglecting any normal stresses as the axial mean gradients and additional strains due to conical geometry are not negligible. Thus the production of k, P_k is:

$$-\overline{u_i u_j} \cdot \partial u_j / \partial x_i = k \cdot [\underbrace{a_1 (\partial U / \partial r + \partial V / \partial x)}_{\text{I}} + \underbrace{a_2 \partial U / \partial x}_{\text{II}} + \underbrace{a_3 V / r}_{\text{III}}]. \quad (7)$$

Here, term I represents the production due to basic shear; term II represents production due to irrotational strain; term III represents production due to lateral divergence specific to conical geometry.

THE ε-EQUATION

The terms of the ε-equation, Equation 2, are modeled similar to the basic k-ε model, as in Section II, except for the rate of turbulent diffusion, D_ϵ , and the rate production, P_ϵ . The turbulent diffusion of dissipation rate was modeled according to HL's model (1972):

$$D_\epsilon = -\partial/\partial x [C_\epsilon k / \epsilon (\overline{u^2} \partial \epsilon / \partial x + \overline{uv} \partial \epsilon / \partial r)] + 1/r \cdot \partial/\partial r [r C_\epsilon k / \epsilon (\overline{uv} \partial \epsilon / \partial x + \overline{v^2} \partial \epsilon / \partial r)]. \quad (8)$$

Generation of ε is taken as similar to that of k production with the inclusion of $C_{\epsilon 3}$: $P_\epsilon = -\epsilon/k [[C_{\epsilon 1} \cdot a_1 (\partial U / \partial r + \partial V / \partial x) + C_{\epsilon 3} a_2 \partial U / \partial x + a_3 V / r]] \quad (9)$

IV. MODEL EVALUATION

STRUCTURAL PARAMETERS

Four adverse pressure gradient diffuser flows, namely, *Flow 0141*, *Flow 0142* and *Flow 0143* of the 1981 AFOSR-HTTM conference (Kline, Cantwell and Lilly 1981) and an eight degree conical diffuser (Turan 1988, referred as *Flow TU* hereafter) were selected for the evaluation of structural parameters. The APG characteristics of these flows are different enough to help assess generality of the structural parameter concept. Flow 141 is an increasingly APG planar diffuser flow; whereas the others are decreasing APG conical diffuser flows. Flow 143 has high core turbulence. Flow TU has a fully developed inlet; whereas others are boundary layer flows.

In the present study, it has been observed that the constant structural parameter assumption is not valid in these flows, especially close to the wall, consistent with the results of Gillis and Johnston (1983) and Fernholtz and Vagt (1981). The behavior of each structural parameter is similar in the decreasing APG flows examined. Detailed comparison is given by Chukkapalli and

Turan (1992). Four zones are identified in these flows in the transverse direction as shown by an example in Figures 1 to 3 for the structural parameters, a_1 , a_2 and a_3 :

1. The wall region, $y^+ < 10$. Asymptotic analysis is invoked in which channel flow simulation data of Kim et al. (1987) are used.

2. The logarithmic region, $20 < y^+ < 250$. In this region, parameters a_1 , a_2 and a_3 follow a logarithmic variation with respect to y^+ .

3. The constant region in which all the structural parameters are approximately constant, $y^+ > 250$.

4. The core region where large scatter of the structural parameters was found. This can be attributed to the low values of both the numerator, a Reynolds stress, and the denominator, the turbulence kinetic energy, in calculating the structural parameters. As a result, the uncertainty in the calculations due to experimental error is high in this region. Constant structural parameters may be assumed in the core region without causing large errors as both turbulence and mean gradients are weak in this region.

The extent of the constant region depends on core turbulence and increasing or decreasing APG. The constant region expands when the flow approaches equilibrium; whereas the logarithmic region is observed in all three decreasingly APG flows tested. In Flow 141, in increasing APG, only two of the four regions identified above in decreasing APG, are present, namely, the constant region and the core region. The reason for this observation can be due to lack of experimental data for $y^+ < 100$ in this flow, where the logarithmic region is expected.

As a result of these observations, it can be concluded that the structural parameters can be expressed as follows at any station:

$$a_1 = (\beta_1 \cdot y^+) + (a_{L1} + b_{L1} \cdot \log y^+) + (a_{c1}), \quad (10a)$$

$$a_2 = (\alpha_2 - \beta_2 \cdot y^+)^2 + (a_{L2} - b_{L2} \cdot \log y^+) + (a_{c2}), \quad (10b)$$

$$a_3 = \underbrace{(\alpha_3 - \beta_3 \cdot y^+)}_{y^+ < 10} + \underbrace{(a_{L3} - b_{L3} \cdot \log y^+)}_{20 < y^+ < 250} + \underbrace{(a_{c3})}_{y^+ > 250}. \quad (10c)$$

Using the coefficients given by Kim et al. from channel flow simulation at $Re = 6,500$, the following wall region values can be obtained: $\beta_1 = 0.0087$, $\alpha_2 = 1.56$, $\beta_2 = 0.0009$, $\alpha_3 = 0.44$. The constant region values, a_{c1} , a_{c2} and a_{c3} , respectively, are, 0.11, 0.33 and 0.15. In APG flows due to production of k by irrotational strain, lower values exist than in zero-pressure gradient flows. The modeled behavior of a_1 , a_2 and a_3 is also illustrated in Figures 1, 2 and 3, respectively.

The use of structural parameters is more advantageous than an eddy viscosity model due to two reasons. First, structural parameters are expected to be more general than eddy viscosity, since the constraint for applicability of structural parameters is similarity of averaged turbulence structure; whereas the eddy viscosity concept requires that flows have similar mean and turbulence fields. The second advantage of the structural parameter concept over the eddy viscosity model is the correct near wall behavior of the predicted Reynolds stresses; whereas the eddy viscosity model Reynolds stresses have to be corrected by an appropriate wall damping function such as f_μ . The predictions can be carried out up to the wall by using structural

parameters without using wall damping functions.

EVALUATION OF THE KINETIC DIFFUSION TERM

Flow II has been used for evaluating the modeled triple correlations and diffusion term, since triple velocity correlation measurements are not available for the other three APG flows examined here. In Figures 4a and 4b respectively, comparison is presented of experimental and modeled $\overline{u^2v}$ and $\overline{v^3}$ correlations at station $x = 66\text{cm}$. These correlations are chosen as the best and worst examples. Comparison of the total diffusion term, Equation 6 (HL model), with experimental data and the scalar gradient representation, Equation 3, is shown in Figure 5. Agreement with experimental data is observed except for the oscillations in modeled terms around the centerline and close to the wall due to differentiation of discrete experimental values. The asymptotic variation of the unmodeled diffusion term is $O(y^+)^3$; whereas the scalar gradient and HL modeled diffusion terms were found to have $O(y^+)^4$ and $O(y^+)^6$ variations, respectively. Similarly, the HL modeled triple correlations vary as $O(y^+)^3$ higher than their asymptotic equivalents as $y^+ \rightarrow 0$. Since the rate of turbulent diffusion close to the wall is negligible compared to the rate of viscous diffusion and dissipation, the incorrect near-wall behavior has been found not to affect k and ϵ predictions here.

V. COMPARISON OF PREDICTED k AND ϵ WITH EXPERIMENTAL DATA

A turbulence model which can predict turbulence quantities well is expected to predict the mean field equally well, if not better. Hence, only the k and ϵ transport equations are solved here by inputting the necessary mean data. The equations are solved radially by inputting the axial gradients. Control volume approach is used with Patankar's power law scheme (Patankar, 1980). Grid and initial guess independence has been verified.

The computations were carried out first for a fully developed pipe flow. The Reynolds number based on the centreline velocity was 139,000 (Turan, 1988). This flow at the inlet of Flow TU was chosen as a simple test case. For comparison with the present model, an eddy viscosity k - ϵ model was also used. Out of the several model constants tried, the constants derived from the re-normalization group (RNG) methods by Yakhot and Orszag (referred to as Y-0 hereafter, Speziale 1991) gave the best results. These model constants are,

$$\sigma_k = 0.7179; \sigma_\epsilon = 0.7179; C_\mu = 0.0837; C_{\epsilon 1} = 1.42; C_{\epsilon 2} = 1.7215.$$

The pipe results are presented in Figures 6a and 6b. As can be seen from these plots, both k and ϵ predictions are within experimental error.

The computations failed to converge when the eddy viscosity k - ϵ model is used with the same constants in the diffuser flow, Flow TU, along with $C_{\epsilon 3}$ in the ϵ -equation to account for the enhanced dissipation due to irrotational strains. Slight modifications to these coefficients gave good prediction of experimental results both in the pipe and diffuser flows, as can be seen in Figures 7a to 10b. In these figures, the k and ϵ predicted by the present modified k - ϵ model and by the eddy viscosity k - ϵ model with the modified Y-0 constants are compared with the experimental data. The modified Y-0 constants are as follows:

$$\sigma_k = 0.7319; \sigma_\epsilon = 0.7319; C_\mu = 0.0730; C_{\epsilon 1} = 1.42; C_{\epsilon 2} = 1.7235.$$

$C_{\epsilon 3} = 4.44$ (Rodi and Scheuerer, 1986) was used in the diffuser flow predictions. These modified constants were calculated with a minimum nodal residual criterion.

The constants of the present model are as follows:

$$C_k = 0.11; C_\epsilon = 0.15; C_{\epsilon 1} = 1.395; C_{\epsilon 2} = 1.92.$$

These coefficients are similar to Hanjalić and Launder's (1972). Here, $C_{\epsilon 1}$ is derived from $C_{\epsilon 2}$ and C_ϵ by using the following expression: $C_{\epsilon 1} = C_{\epsilon 2} - 3.5C_\epsilon$ as derived by Hanjalić and Launder (1972) for a constant shear layer. A $C_{\epsilon 3}$ of 2.5 was used by Hanjalić and Launder (1980). This value was modified to 4.44 and 5.6, respectively, by Rodi and Scheuerer (1986) and Henau et al. (1990). In the present study, the following range is calculated as the optimum values for Flow TU: $3.5 \leq C_{\epsilon 3} \leq 6.5$.

From a comparison of Figures 6a and 6b with Figures 7a and 7b, it can be seen that the eddy viscosity k - ϵ model with the unmodified Y-O constants gives better prediction of both k and ϵ in the fully developed pipe flow. This result is expected, since the eddy viscosity k - ϵ model and the Y-O constants were developed for simpler turbulent flows. In the APG diffuser flow as seen from Figures 8a to 10b, an improvement can be observed in the predicted k and ϵ when the present modified model is used, in comparison with the predictions obtained with the eddy viscosity k - ϵ model with modified Y-O constants. The improvement is in that the predicted slopes are closer to the experimental ones when the present model is used. Since the gradients of Reynolds stresses calculated by using structural parameters are needed in the averaged mean equations, the present model is expected to give better prediction of the mean flow field for engineering applications.

The improvement obtained in predicting k and ϵ with the present model is less than expected with the improved representation of Reynolds stresses and kinetic diffusion. This discrepancy can be attributed to the poor modeling of the terms of the ϵ -equation, as also indicated by the lack of generality of the model constant $C_{\epsilon 3}$. Experimental results from complex cases, or direct numerical simulation data of simple flows, are needed of the terms of the exact ϵ -equation for testing the modeled terms. Thus, measurement of these terms in an APG diffuser flow is the direction of further research in this work.

VI. CONCLUSIONS

A third structural parameter, a_3 , is introduced to account for the production of k due to lateral strain for conical cases. The development of structural parameters a_1 , a_2 and a_3 is examined in four APG plane and conical diffuser flows. It is shown that the structural parameters are not constant in these flows. A four-region three-layer description is proposed for each structural parameter, which includes the limiting behavior for $y^+ < 10$ followed by a logarithmic region and a constant region. Near wall limiting behavior of a_1 , a_2 and a_3 is derived from the asymptotic behavior of Reynolds stresses.

A modified k - ϵ model is developed which uses structural parameters instead of the Boussinesq approximation in estimating Reynolds stresses. The rate of kinetic diffusion of k is derived from the expansion of triple correlations by using the HL model which reduces to the conventional scalar gradient diffusion

form if isotropy is assumed. Similarly, the rate of kinetic diffusion of ϵ of the full Reynolds stress model of HL is introduced in conjunction with the structural parameters into the ϵ -equation. With these changes, the modified model enables better prediction of k and ϵ in an APG turbulent diffuser flow. The present results indicate the need for further improvement of the ϵ -equation modeling.

ACKNOWLEDGEMENTS

The authors greatly acknowledge the financial support provided for this work by Natural Sciences and Engineering Research Council of Canada.

REFERENCES

- Amano, R.S., and Goel, P., Investigation of third-order closure model of turbulence for the computation of incompressible flows in a channel with a backward-facing step, ASME J. Fluids Engineering, vol. 109, pp. 424-428, 1987.
- Bradshaw, P., The turbulent structure of equilibrium boundary layers, J. Fluid Mech., vol. 29, pp. 625-645, 1967.
- Bradshaw, P., Complex turbulent flows, Theoretical and Applied Mechanics, (Ed. W. T Koiler) North Holland Publishing Co., pp. 103-113, 1976.
- Bradshaw, P., Ferris, D. H., and Atwell, N. P., Calculation of boundary-layer development using the turbulent energy equation, J. Fluid Mech., vol. 28, pp. 593-616, 1967.
- Chukkapalli, G., and Turan, O. F., Structural parameters and prediction of adverse pressure gradient turbulent flows: An improved k - ϵ model, Submitted to ASME J. Fluid Engineering, 1992.
- Cutler, A. D., and Johnston, J. P., The relaxation of a turbulent boundary layer in adverse pressure gradient, J. Fluid Mech., vol. 200, pp. 367-387, 1989.
- Fernholtz, H. H., and Vagt, J. -D., Turbulence measurements in an adverse pressure gradient three-dimensional turbulent boundary layer along a circular cylinder, J. Fluid Mech., vol. 111, pp. 233-269, 1981.
- Gillis, J. C., Johnston, J. P., Turbulent boundary layer flow and structure on a convex wall and its redevelopment on a flat wall, J. Fluid Mech., vol. 135, pp. 123-153, 1983.
- Hanjalić, K., and Launder, B. E., A Reynolds stress model of turbulence and its application to thin shear flows, J. Fluid Mech. vol. 52, pp. 609-638, 1972.
- Hanjalić, K., and Launder, B. E., Sensitization the dissipation equation to irrotational strains, ASME J. Fluids Engineering, vol. 102, pp. 34-40, 1980.
- Henau, V. De., Raithby, G. D., and Thompson, B. E., Prediction of flows with strong curvature and pressure gradient using k - ϵ turbulence model, ASME J. Fluids Engineering, vol.112, pp. 40-47, 1990.
- Kim, J., Moin, P., and Moser, R. D., Turbulence statistics in fully developed channel flow at low Reynolds number, J. Fluid Mech., vol. 177, pp 133-186, 1987.
- Kline, S. J., Kantwell, B. J., and Lilly, G. M., AFOSOR-HTTM- Stanford conference on complex turbulent flows: Comparison of computation and experiment, 1980-81.
- Lai, Y. G., So, R. M. C., and Hwang, B. C., Calculation of planar and conical diffuser flows, AIAA. J., vol. 27, pp. 542-548, 1989.
- Patankar, S. V., Numerical Heat transfer and Fluid Flow, Hemisphere publications, 1980.
- Patel, V. C., Rodi, W., and Scheuerer, G., Turbulence models for near-wall and low Reynolds number flows: A review, AIAA. J. vol. 23, no. 9, pp. 1308-1319,

1985.

Rodi, W., Scheuerer, G., Scrutinizing the k- ϵ turbulence model under adverse pressure gradient conditions, ASME J. Fluids Engineering, vol. 108, pp. 174-179, 1986.

Saddoughi, S. G., and Joubert, P. N., Lateral straining of turbulent boundary layers Part I, Streamline divergence, J. Fluid Mech., vol. 229, pp. 173-204, 1991.

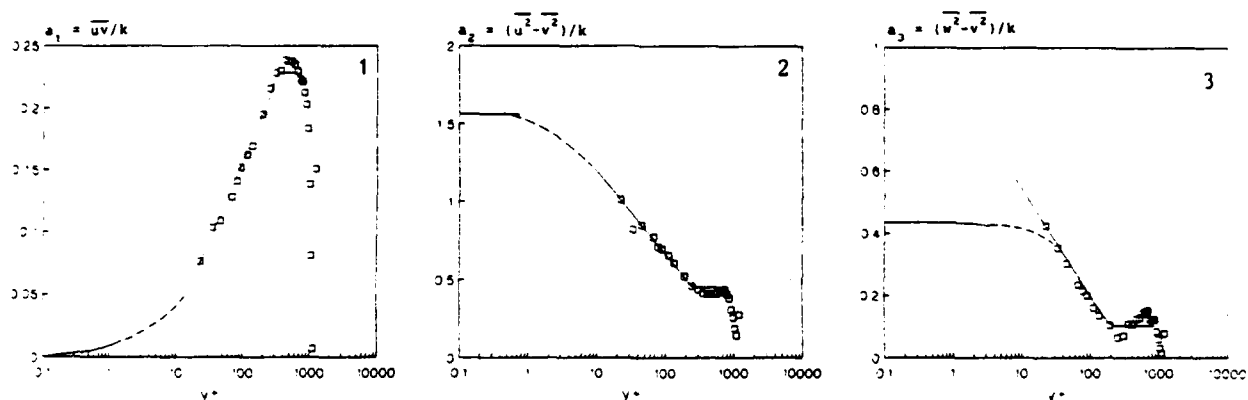
So, R. M. C., Lai, Y. G., Zhang, H. S., and Hwang, B. C., Second order near-wall closures: A review, AIAA J., vol. 29, no. 11, pp. 1819-1835, 1991.

Speziale, C. G., Analytical methods for the development of Reynolds stress closures in turbulence, Annual Review of Fluid Mechanics, vol. 23, pp. 107-157, 1991.

Speziale, S. p., Abid, R., and Anderson, E. C., Critical evaluation of two-equation models for near-wall turbulence, AIAA J., vol. 30, No. 2, pp. 324-331, 1992.

Turan, O. F., Further study of a new method of evaluating turbulence dissipation, Ph. D. Thesis, Mechanical Engineering Department, University of Manitoba, 1988.

Turan, O. F., and Azad, R. S. Comparison of the zero-wire-length dissipation technique with spectral corrections and the effect of high turbulence intensity, to appear in Exp. Thermal Fluid Sci., 1992.



Figures 1, 2 and 3. The four-region representation of the structural parameters a_1 , a_2 and a_3 , respectively, given by Equations 10a, 10b and 10c. The experimental data from the last station of Flow TU are shown as an example.

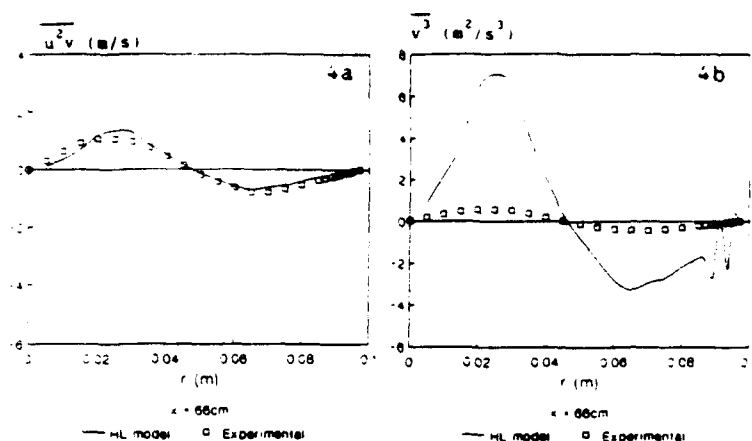


Figure 4. Comparison of the HL modeled and experimental triple velocity correlations $u_i u_j u_k$ in the last station, $x = 66\text{cm}$, of Flow TU.

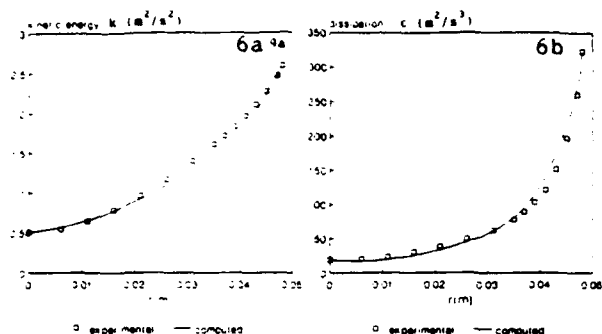


Figure 6. Comparison of the predicted k and ϵ with experimental data from a fully developed pipe flow (inlet of Flow TU, $Re = 139,000$, Turan 1988). The eddy viscosity k - ϵ model was used in the prediction with the unmodified Y-0 constants.

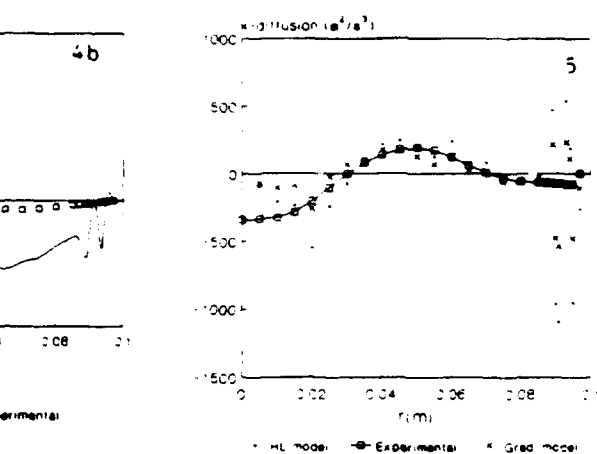
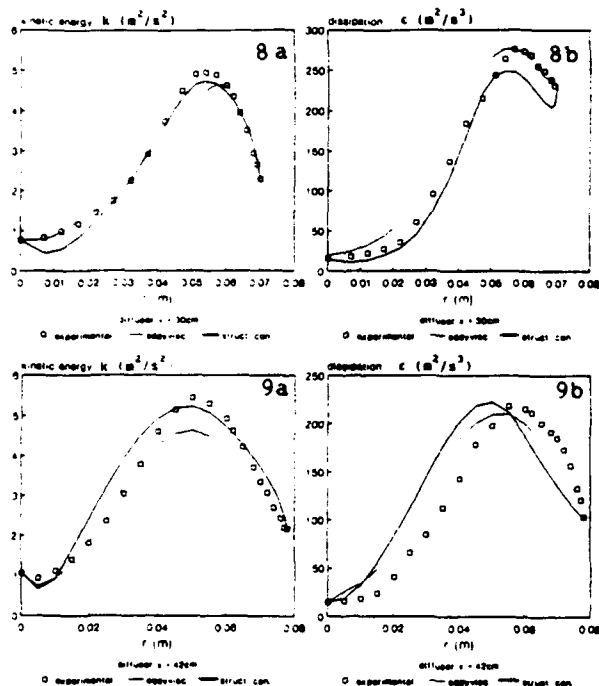


Figure 5. Comparison of the HL modeled rate of kinetic diffusion of k (Equation 6) with experimental data and with isotropic scalar gradient diffusion model (Equation 3) of the eddy viscosity k - ϵ model. The experimental data are from the last station, $x = 66\text{cm}$, of Flow TU.

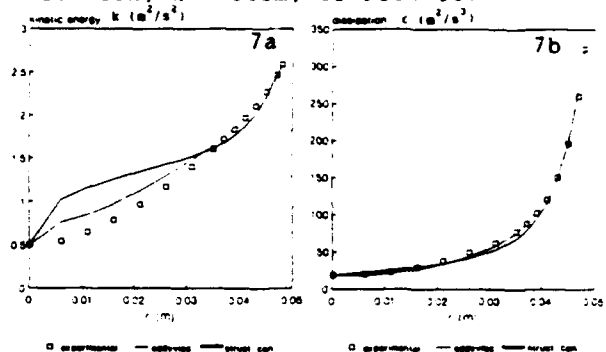
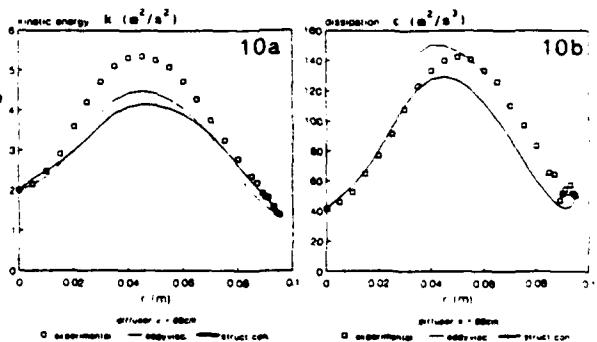


Figure 7. Comparison of the k and ϵ variations predicted with the eddy viscosity k - ϵ model using the modified Y-0 constants and the present model with experimental data from the same fully developed pipe flow as in Figure 6.



Figures 8, 9 and 10. Comparisons of the k and ϵ variations predicted with the eddy viscosity k - ϵ model using the modified Y-0 constants and the present model with experimental data from $x = 30\text{cm}$, 42cm and 66cm of Flow TU.

Two Variations of the $k - \epsilon$ model and their Application to Wall-Bounded Flows

H. Ozem^{a,1}, H. A. Becker^b, E. W. Grandmaison^b, A. Pollard^{a,2} and A. Sobesiak^a

Centre for Advanced Gas Combustion Technology

^aDepartment of Mechanical Engineering

^bDepartment of Chemical Engineering

Queen's University in Kingston, Ontario, Canada

Abstract

Two new turbulence models ($k - \epsilon - S$ and $k - k\tau - \epsilon$) based on the $k - \epsilon$ model of turbulence have been implemented and tested on simple wall bounded flows at various Reynolds numbers. Encouraging results have been obtained and preliminary plots of mean and turbulence quantities are presented. The consistency of the constants over a wide range of wall bounded flows in both models is immediately apparent, although the constants still need to be adjusted to achieve accurate predictions of the flows considered.

Introduction

The $k - \epsilon$ model was used as a basis for the development of two new turbulence models. These models are being tested to provide a novel way of calculating wall bounded turbulent flows. In particular, the $k - \epsilon - S$, Lumley [1] and the $k - k\tau - \epsilon$, Zeierman and Wolfshtein [2] and Arad and Wolfshtein [3] models are further developed. The motivation behind this work is to obtain a relatively simple yet widely applicable model for turbulent flow which could be used in an industrial setting.

Model 1: $k - \epsilon - S$, Lumley [1]

In the search for a non-local model for turbulence, Lumley [1] has scrutinized the dissipation equation in the $k - \epsilon$ model of predicting turbulent flow. Lumley has proposed an auxiliary equation and a new time scale for the modelling of the dissipation of the turbulent kinetic energy.

The new time scale, T has the following form:

$$T = c_{time} 2 \left(\frac{\ell}{u} \right) (1 - 1.29 R_\ell^{-\frac{1}{2}}) \quad (1)$$

Where C_{time} is a constant to be determined, ℓ is the turbulent length scale, u is the integral velocity scale and $R_\ell = \ell u / \nu$. The resulting dissipation equation is then:

$$U_i \frac{\partial \epsilon}{\partial x_i} + \frac{\partial \overline{u_i \epsilon}}{\partial x_i} = -C'_1 \frac{\partial U_i}{\partial x_j} \left(\frac{\overline{u_i u_j}}{T} \right) - C'_2 \frac{\epsilon}{T} \quad (2)$$

The time scale is derived only for the dissipation equation. It is intended to more accurately model the time associated with the dissipation of the turbulent kinetic energy from small wave numbers through to the high wave numbers, the latter of course being associated with the

¹Graduate student, all others appear in alphabetical order

²To whom all correspondence should be addressed

Kolmogorov scales. The time scale incorporates a time lag for the dissipative scales to receive all of their energy from higher wave numbers.

Boussinesq approximations are employed for the time-averaged fluctuating correlations ($\overline{u_i \epsilon}$ and $\overline{u_i u_j}$); of course, other practices could be employed. The resulting dissipation rate equation is of the form:

$$U_i \frac{\partial \epsilon}{\partial x_i} + \nu_T \frac{\partial^2 \epsilon}{\partial x_i^2} = \frac{C'_{lum1}}{T} \nu_T 2S_{ij} - \frac{C_{lum2} \epsilon}{T} \quad (3)$$

Where C_{lum1} and C_{lum2} are Lumley constants, the values of which need to be determined. The generation term in the dissipation rate equation ($\nu_T 2S_{ij}$) is now replaced by the auxiliary variable (S), which takes into account an averaging of the magnitude of the mean strain rates in areas from which the fluid is advected to the point in question. The rate at which energy enters the spectral pipeline should be determined by the local value of the energy and the local value of the time scale. The auxiliary equation gives a spreading Gaussian average with a fading exponential memory of scale \mathfrak{S} (again, \mathfrak{S} being the local time scale) back along the mean streamline [1].

The auxiliary (S) equation has the following form:

$$U_j \frac{\partial S}{\partial x_j} = c_S \frac{\{[S_{ij} S_{ij}]^{\frac{1}{2}} - S\}}{\mathfrak{S}} + \nu_T \frac{\partial^2 S}{\partial x_j \partial x_j} \quad (4)$$

where:

$$\nu_T = C_\mu \frac{k^2}{\epsilon}, \quad \mathfrak{S} = c_1 \frac{k}{\epsilon} \quad (5)$$

The resulting ϵ equation is:

$$U_i \frac{\partial \epsilon}{\partial x_i} + \nu_T \frac{\partial^2 \epsilon}{\partial x_i^2} = \frac{C_{lum1} \frac{kS}{\mathfrak{S}} - C_{lum2} \epsilon}{T} \quad (6)$$

The new time scale is also incorporated into the turbulent viscosity. Since the turbulent viscosity is proportional to a turbulent length scale multiplied by a turbulent velocity scale, the turbulent viscosity must also be revised to account for the new turbulent time scale. This is done as follows:

$$\nu_{T(\epsilon)} = c_2'' V_{turb} \ell_{turb} = c_2' V_{turb}^2 T \quad (7)$$

Where V_{turb} is the turbulent velocity scale. As the Boussinesq approximation is employed, the turbulent viscosity is approximated by the square root of the turbulent kinetic energy [Prandtl, 1945; Kolmogorov, 1942], resulting in:

$$\nu_{T(\epsilon)} = \frac{2}{3} C_\mu c_2 k T \quad (8)$$

final form of the dissipation equation is:

$$U_i \frac{\partial \epsilon}{\partial x_i} + \nu_{T(\epsilon)} \frac{\partial^2 \epsilon}{\partial x_i^2} = \frac{C_{lum1} \frac{kS}{\mathfrak{S}} - C_{lum2} \epsilon}{T} \quad (9)$$

Due to the multiple time scale, the new model also contains multiple viscosities. These two changes introduce many new constants to be evaluated. A summary of the constants for the three flow fields are given in Table 1.

To our knowledge, the use of $k - \epsilon - S$ has never been applied to wall bounded flows and the new time scale has not been used in conjunction with the auxiliary (S) equation. Preliminary

Table 1: Preliminary values of the constants for the $k - \epsilon - S$ model

Constant	Channel Flow - $Re=5600$	Pipe Flow - $Re=50000$	Pipe Flow - $Re=380000$
σ_k	1.2	1.2	1.2
σ_ϵ	1.2	1.2	1.2
c_{time}	1.0	1.0	1.0
c_2	0.1	0.1	2.0
C_{lum1}	0.1	0.1	0.1
C_{lum2}	1.0	1.0	1.0
c_s	0.625	0.625	0.625

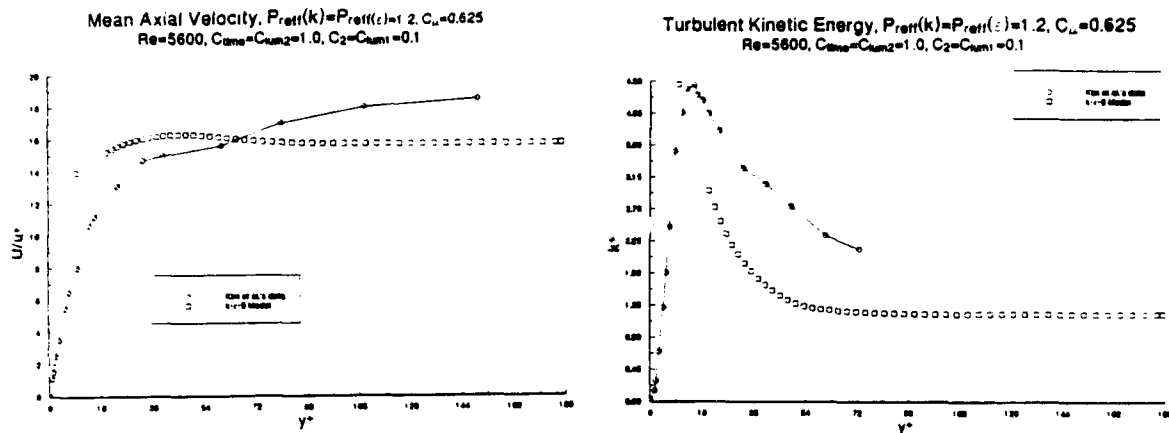


Figure 1: The $k - \epsilon - S$ model compared to channel flow simulations [7] at a Reynolds number of 5600; (a) Mean axial velocity; (b) Turbulent kinetic energy.

results for channel flow at a Reynolds number of 5600 and two pipe flows at Reynolds numbers of 50000 and 380000 are given in figures 1, 2, and 3. These results are compared against data from Laufer [4], Lawn [5], Nikuradse [6], and the direct numerical simulation data of Kim et al. [7].

The consistency of the constants for the various flow fields is very encouraging for a robust model of turbulent flow. The model, however, over-predicts the turbulent kinetic energy in the core of the flow field away from the walls and under-predicts the diffusion of the mean flow variables.

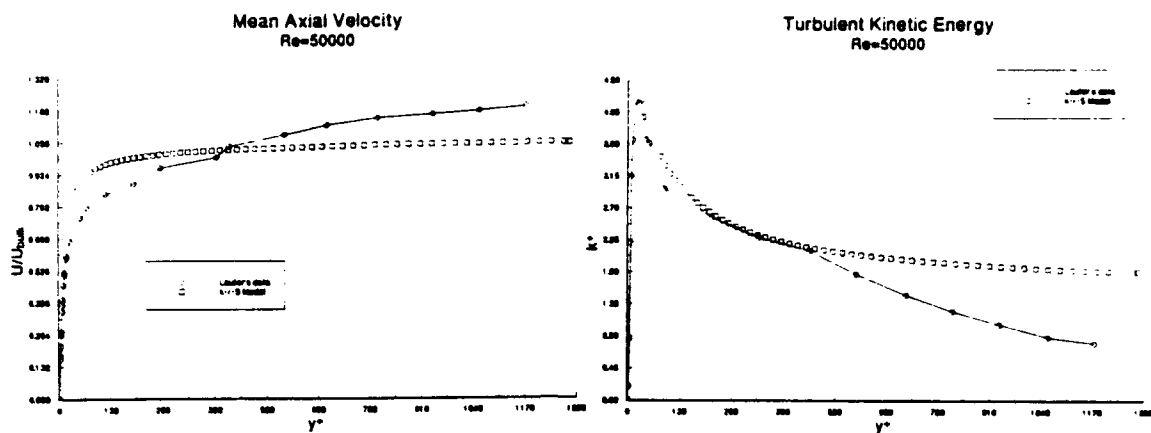


Figure 2: The $k - \epsilon - S$ model compared to pipe flow data [4] at a Reynolds number of 50000; (a) Mean axial velocity; (b) Turbulent kinetic energy.

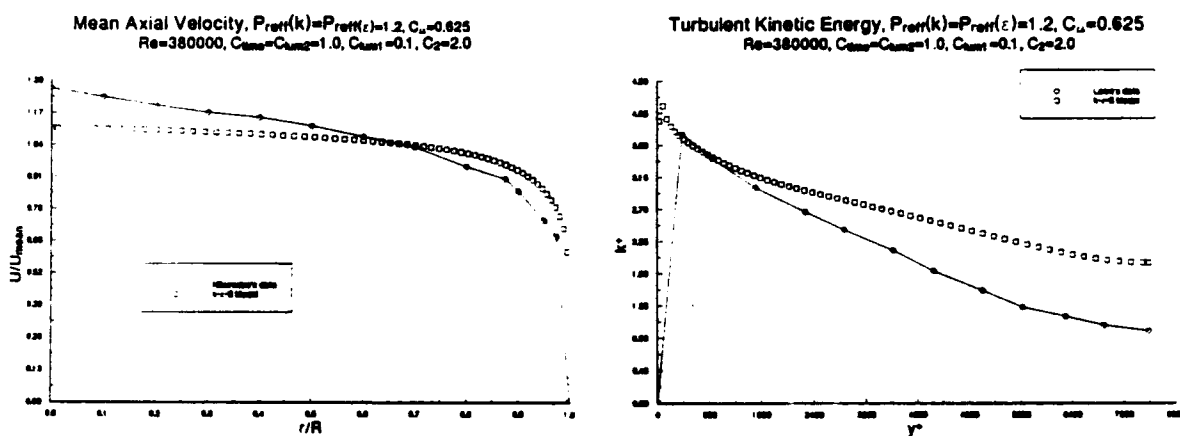


Figure 3: The $k - \epsilon - S$ model compared to pipe flow [5] at a Reynolds number of 380000; (a) Mean axial velocity; (b) Turbulent kinetic energy.

Model 2: $k - k\tau - \epsilon$, Zeierman and Wolfshtein [2] and Arad and Wolfshtein [3]

The basic $k - \epsilon$ model uses a single local turbulent time scale to model the flow field. The problem with the $k - \epsilon$ model of turbulence, recognized by Wolfshtein and Arad [3], is that the energy carrying and dissipative scales are not the same, yet the same scale is used to model both the energy production and the energy dissipation. Using two scales, one for the energy producing scale and one for the dissipative scale, ought to permit better prediction of turbulent flow fields than standard two-equation models.

The $k - k\tau - \epsilon$ model uses a turbulent time scale based upon the integral scale of turbulence to model the flow field, where the new time scale is determined explicitly in the solution algorithm from its own conservation equation. This multiple time-scale approach recognizes that dissipation occurs in the smallest scales of turbulence; thus, the dissipation is modelled based on local values for the dissipation time scale [2].

To implement this model, the energy content of the small eddies is assumed to be negligible compared to that of the larger eddies so that in the outer domain of the flow (away from walls) the integral time scale is used to model the production of energy. The new turbulent viscosity has the form:

$$\nu_t = C_\mu k\tau \quad (10)$$

where τ is the integral time scale.

The turbulent kinetic energy equation and the momentum and continuity equations have the same form as noted previously except that the turbulent viscosity has incorporated into it the new time scale. The integral time scale is solved via [2]:

$$\rho \frac{Dk\tau}{Dt} = \frac{\partial}{\partial x_j} \left[\left(\mu + \frac{\mu_t}{\sigma_\tau} \right) \frac{\partial k\tau}{\partial x_j} \right] + C_{g\tau} \tau P_k - \rho C_{d\tau} k \quad (11)$$

The dissipation rate equation then becomes:

$$\rho \frac{D\epsilon}{Dt} = \frac{\partial}{\partial x_j} \left[\left(\mu + \frac{\mu_t}{\sigma_\epsilon} \right) \frac{\partial \epsilon}{\partial x_j} \right] + \rho \frac{\epsilon_p \epsilon}{k} - \rho C_{d\epsilon} \frac{\epsilon^2}{k} \quad (12)$$

where $\epsilon_p = C_{g\epsilon} \frac{k}{\tau}$.

The dissipation rate responds slowly to the applied mean strain (this gives a better representation of a rapidly changing turbulence field [3]); however, the decay term of the dissipation rate equation depends on the high wave number turbulence scales.

Near solid walls, where the turbulence and mean flow quantities have the largest gradients, very high spatial resolution is required. Wolfshtein and Arad [3] avoid this problem by using the two layer method (see Wolfshtein [8] or Chen and Patel [9]) to bridge the core region of the flow to that in the near wall region. The turbulent kinetic energy equation is solved to the wall and the ϵ and $k\tau$ equations are only solved in the outer domain. In the inner domain (the region close to the wall) both $k\tau$ and ϵ are solved using algebraic equations. These algebraic equations are matched to the outer domain values and used as boundary conditions for the outer domain. Chen and Patel [9] recommend, and this has been confirmed in more complicated flows, Waddington [10], that the interface between the two domains be taken at a turbulent Reynolds number of 250 ($Re_\tau = \sqrt{k}y/\nu$). It has been found however, that the matching interface can not be taken at a constant turbulent Reynolds number in order for the matching interface to remain outside the viscous sublayer and yet still be inside the one dimensional zone adjacent to the wall. Using the y^+ wall coordinate or $R_T = k^2/\nu\epsilon$ to set the location of the matching interface may be a more appropriate variable. The turbulent kinetic

Table 2: Preliminary values of the constants for the $k - k\tau - \epsilon$ model

Constant	Channel Flow - $Re=5600$	Pipe Flow - $Re=50000$	Pipe Flow - $Re=380000$
σ_k	1.2	1.2	1.2
σ_ϵ	1.2	1.2	1.2
α_μ	0.000006	0.0006	0.0002
α_ϵ	0.05	0.05	0.05
Re_y	60	65.0	540.0

energy is still integrated down to the wall using the time and length scales calculated from the algebraic equations.

The algebraic equations are derived from known asymptotic behavior of the length scales near the wall. For the low wave number scales:

$$L_\mu = \frac{-\overline{uv}}{k^{\frac{1}{2}} \frac{\partial U}{\partial y}} \quad (13)$$

and for high wave number scales:

$$L_\epsilon = \frac{k^{\frac{3}{2}}}{\epsilon} \quad (14)$$

Substitution of a Taylor series expansion of the velocities into the above equations yields the following relations for the two length scales:

$$L_\mu = \left(\frac{L_\mu}{y}\right)_m y (1 - \exp(-\alpha_\mu Re_y)) \quad (15)$$

$$L_\epsilon = \left(\frac{L_\epsilon}{y}\right)_m y (1 - \exp(-\alpha_\epsilon Re_y)) \quad (16)$$

Where $\left(\frac{L_\mu}{y}\right)_m$ and $\left(\frac{L_\epsilon}{y}\right)_m$ are the values of the length scale at the matching interface between the inner and outer domains, and Re_y is the turbulent Reynolds number based on the distance from the wall.

In the inner domain the turbulent viscosity is calculated using:

$$\mu_t = \rho L_\mu k^{\frac{1}{2}} \quad (17)$$

and the dissipation is calculated using the dissipative length scale:

$$\epsilon = \frac{k^{\frac{3}{2}}}{L_\epsilon} \quad (18)$$

Some preliminary results of the $k - k\tau - \epsilon$ model for channel flow at a Reynolds number of 5600 and for two pipe flows at Reynolds numbers of 50000 and 380000 are compared to those data sets noted above and are given in Figures 4, 5, and 6. For a summary of the constants used, see Table 2.

The constants in the $k - k\tau - \epsilon$ model are consistent, implying that the model of turbulence is robust. For the simple, parabolic flows considered, the value used for normalisation of the

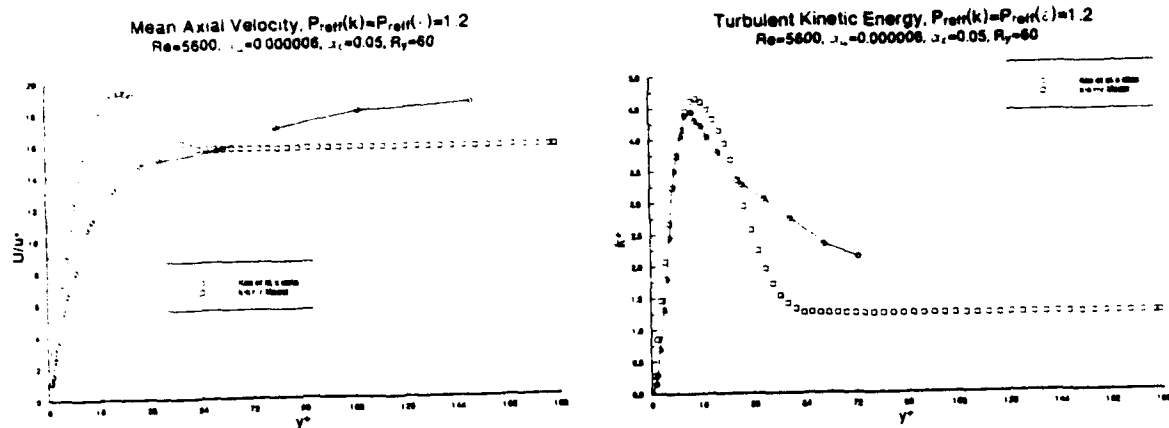


Figure 4: The $k - k\tau - \epsilon$ model compared to channel flow data [7] at a Reynolds number of 5600; (a) Mean axial velocity; (b) Turbulent kinetic energy.

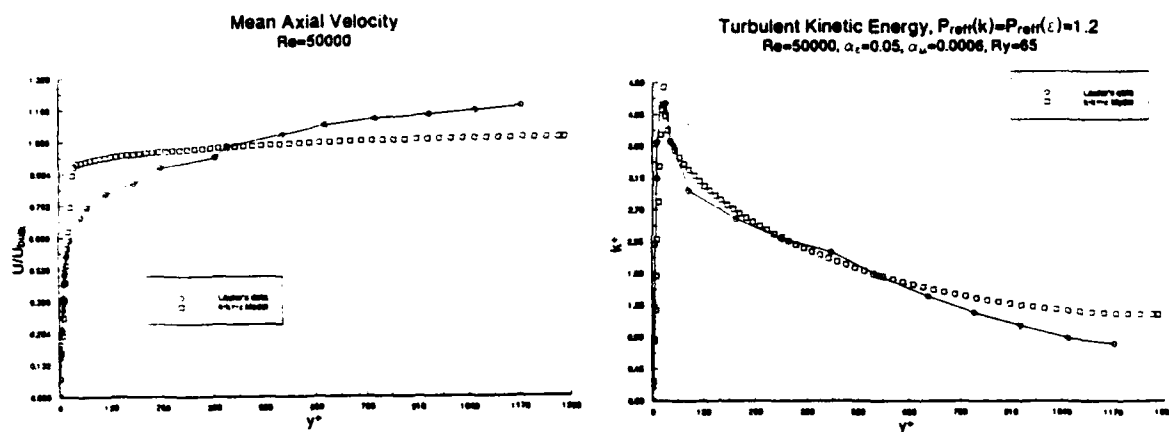


Figure 5: The $k - k\tau - \epsilon$ model compared to pipe flow data [4] at a Reynolds number of 50000; (a) Mean axial velocity; (b) Turbulent kinetic energy.

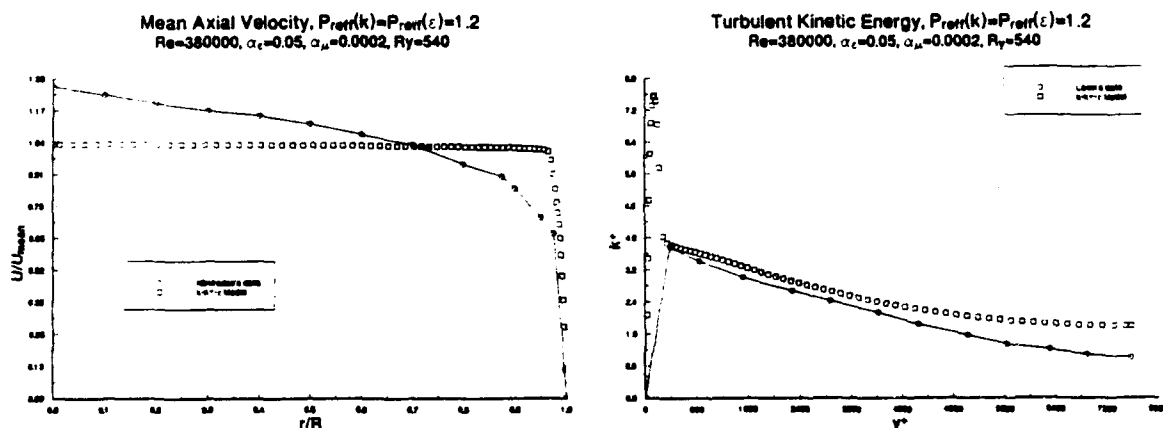


Figure 6: The $k - k\tau - \epsilon$ model compared to pipe flow data [5] at a Reynolds number of 380000; (a) Mean axial velocity; (b) Turbulent kinetic energy.

distance from the wall in the inner wall region apparently should be the turbulent Reynolds number based on the distance from the wall. It can also be seen that the various Reynolds numbers examined have different values of the turbulent Reynolds number for the matching interface indicating that the parameter that should be used for finding the matching interface should be the normalized wall coordinate, y^+ .

Summary

The $k - \epsilon - S$ and $k - k\tau - \epsilon$ models of turbulence have both been implemented and applied to simple wall bounded flows. Preliminary results have been presented and it is obvious that further work needs to be done. The $k - \epsilon - S$ model works for a variety of flow fields with no change in any of its constants; however, it is apparent that these constants still need some adjustment to account for the over prediction of the turbulence quantities in the core region of the flow field and the under prediction of the diffusion of the time-averaged flow variables.

The $k - k\tau - \epsilon$ model predicts the flow field well when the inner layer algebraic equations reflect the near-wall behavior. However, the inner layer equations do not accurately predict a variety of flow fields for a given set of constants. A more robust set of algebraic equations for the inner wall layer is required for the $k - k\tau - \epsilon$ model to perform well.

Acknowledgements

The authors wish to acknowledge the financial support of the Natural Science and Engineering Research Council of Canada, the Ontario Graduate Scholarship Society and Queen's School of Graduate Studies.

References

- [1] J. L. Lumley. Some comments on turbulence. *Phys. of Fluids A*, 4(2):203-211, February 1992.
- [2] S. Zeierman and M. Wolfshtein. Turbulent time scale for turbulent flow calculations. *AIAA Journal*, 20(10):1606-1610, 1986.
- [3] E Arad and D. G. Wolfshtein. Two-scale double-layer model in wall bounded turbulent flow. In *Eighth symposium on Turbulent Shear Flows*, Technical University of Munich, September 1991.
- [4] John Laufer. The structure of turbulence in fully developed pipe flow. Technical Report 1174, United States National Advisory Committee for Aeronautics, 1954.
- [5] C. J. Lawn. The determination of the rate of dissipation in turbulent pipe flow. *J. Fluid Mech.*, 48:477-505, 1971.
- [6] J. Nikuradse. Gesetzma β ig keit der turbulenten stromung in glatten rohren. Technical Report 356, Verein Deutscher Ingenieure-Forschungsheft, 1932.
- [7] J. Kim, P. Moin, and R. Moser. Turbulence statistics in fully developed channel flow at low reynolds number. *J. Fluid Mech.*, 177:133-166, 1987.
- [8] M. Wolfshtein. The velocity and temperature distribution in one-dimensional flow with turbulence augmentation and pressure gradient. *International Journal of Heat and Mass Transfer*, 12:301-318, March 1969.

- [9] H. C. Chen and V. C. Patel. Near-wall turbulence models for complex flows including separation. *AIAA Journal*, 26(6):641-648, June 1988.
- [10] G. Waddington. Modelling the turbulent flow inside a multi-jet, recessed burner. Master's thesis, Queen's University, Department of Mechanical Engineering, 1992.

LARGE EDDY SIMULATION OF FLOW IN A SQUARE DUCT

E. Balaras and C. Benocci
von Karman Institute for Fluid Dynamics,
Environmental and Applied Fluid Dynamics Department,
Chaussée de Waterloo 72 1640 Rhode S. Génèse, Belgium

Abstract

The dynamic subgrid model is implemented in the frame of a finite difference Large Eddy Simulation (LES) solver and used to investigate turbulent flow in a square duct at equilibrium. The results show a much improved agreement with available experimental data, in comparison with the standard Smagorinsky model.

1. INTRODUCTION

For many applications LES appears to be a most attractive compromise, which avoids both the prohibitive cost of the Direct Simulation [1] and the forever increasing complexity of the full Reynolds Stress Transport model [2]. However, the lack of suitably general boundary conditions and subgrid scale models, as well as the difficulty of developing flow solvers of sufficient accuracy and efficiency, has, up to now, restricted the applicability of LES to quite simple flow geometries at moderate Reynolds numbers.

In particular, for a long time relatively small effort has been devoted to the development of SGS models, and the Smagorinsky model [3] has remained at present the standard tool in LES. Although, modifications of this model have been successfully applied to LES of transitional and turbulent flows, it remains fundamentally handicapped by the need to use one single "universal constant" to relate resolved and modelled part of turbulence, which is unlikely to be a realistic representation of the wide variety of flow phenomenologies which can be encountered in nature. Moreover, the subgrid scale viscosity produced by this model does not vanish in laminar flows, does not have the correct limiting behavior close to solid boundaries, and cannot account for energy transfer from small to large scales (backscatter).

Different new models [4, 5] have attempted to overcome these limitations. A particularly promising new approach is the "dynamic SGS model" proposed by Germano et. al. [6] which is based upon the idea of calculating locally the model coefficient, function of the instantaneous resolved velocities. This model has already been successfully applied [6, 7] to some cases of simple turbulent flows. Here the model has been extended to the fully 3D case of equilibrium duct flow, with impressive results, as will be discussed below.

2. GOVERNING EQUATIONS

The LES approach is based on the application of a filtering process to the dependent flow variables, in order to decompose them in a large scale contribution to be resolved numerically, and a small scale contribution to be modeled.

Applying the filtering operation, signified by the overbar, to the continuity and Navier-Stokes equations, the corresponding equations for the large scales are obtained:

$$\frac{\partial \bar{u}_i}{\partial x_i} = 0 \quad (1)$$

$$\frac{\partial \bar{u}_i}{\partial t} + \frac{\partial \bar{u}_i \bar{u}_j}{\partial x_j} = -\frac{\partial P}{\partial x_i} + F_i - \frac{\partial \tau_{ij}}{\partial x_j} + \frac{1}{Re} \frac{\partial^2 \bar{u}_i}{\partial x_j \partial x_j} \quad (2)$$

where Re is the Reynolds number based on average shear velocity $\langle u_\tau \rangle$ and half height δ of the cross section and $F_i = (F_1, 0, 0)$ is a forcing term representing the average pressure drop in the longitudinal direction. The influence of the small scales upon the resolved part of turbulence appears in the SGS stress term :

$$\tau_{ij} = \bar{u}_i \bar{u}_j - \bar{u}_i \bar{u}_j \quad (3)$$

The basic assumption of the LES technique is that the subgrid part of turbulence is *isotropic* and can, therefore, be modeled in terms of a fictitious diffusivity coefficient, the *subgrid viscosity* ν_t , relating the subgrid stress tensor to the strain rate S_{ij} of the resolved scales, giving the well known Smagorinsky model [3] :

$$\tau_{ij} - \frac{1}{3} \tau_{kk} \delta_{ij} = -2c \Delta^2 |\bar{S}| \bar{S}_{ij} \quad (4)$$

where $|\bar{S}|$ is :

$$|\bar{S}| = (2\bar{S}_{ij} \bar{S}_{ij})^{\frac{1}{2}} \quad (5)$$

and Δ is the length scale associated with the filtering procedure. In a finite difference discretization the size of the filter is determined by the mesh itself. Therefore:

$$\Delta = (\Delta_1 \Delta_2 \Delta_3)^{\frac{1}{3}} \quad (6)$$

and c is the coefficient relating mesh size to filter size.

As it was mentioned in the previous paragraph, in the above model c is a constant, theoretically universal and practically a function of the discretisation, [8]. Germano [6] proposed a dynamic estimation of this coefficient obtained sampling the smallest resolved scales and using this information to model the SGS. To this end, a coarser spatial filter, denoted by a tilde over the overbar, is applied to the equations and the SGS stress is redefined as:

$$T_{ij} = \bar{\tilde{u}_i \tilde{u}_j} - \bar{\tilde{u}_i} \bar{\tilde{u}_j} \quad (7)$$

Using the same approach as in (4) T_{ij} is approximated by:

$$T_{ij} - \frac{1}{3} T_{kk} \delta_{ij} = -2c \tilde{\Delta}^2 |\tilde{S}| \tilde{S}_{ij} \quad (8)$$

Consistency between (4) and (8) depends on the proper choice of c , which can be found by subtracting the test scale average of τ_{ij} from T_{ij} :

$$L_{ij} = T_{ij} - \bar{\tau}_{ij} \quad (9)$$

where L_{ij} are the resolved turbulent stresses representing the contribution to the Reynolds stresses by the scales whose length is intermediate between the grid and the test filter. L_{ij} can be explicitly computed and compared to the rhs of (9). From equations (3), (7) and (9) it is :

$$L_{ij} = -2c M_{ij} \quad (10)$$

where

$$M_{ij} = \bar{\Delta}^2 \left| \bar{S} \right| \bar{S}_{ij} - \bar{\Delta}^2 \left| \bar{S} \right| \bar{S}_{ij} \quad (11)$$

Equation (11) represents six independent equations in one unknown, and there is no unique value of c which satisfies all six. Lilly [9] proposed to derive c minimizing the square of the error of (10), which yields:

$$c(x, y, z, t) = -\frac{1}{2} L_{ij} M_{ij} / M_{ij}^2 \quad (12)$$

3. NUMERICAL ASPECTS

3.1 Numerical scheme

The integration of the equations in time is done using an Adams-Bashfort fractional step method:

$$U_i^n = U_i^{n-1} + (1.5H_i^n - 0.5H_i^{n-1} + 0.5 \frac{\partial P^{n-1}}{\partial x_i}) \Delta t \quad (13)$$

$$1.5\Delta t \frac{\partial^2 P^n}{\partial x_i^2} = \frac{\partial U_i^n}{\partial x_i} \quad (14)$$

$$U_i^{n+1} = U_i^n - 1.5\Delta t \frac{\partial P^n}{\partial x_i} \quad (15)$$

where H includes all the right hand side terms minus the contribution of the pressure. All spatial derivatives are approximated with second-order central differences.

Equation (14) is solved using a Direct Poisson Solver based on Fast Fourier Transform. The constraints imposed by the Direct Poisson solver lead to choose a staggered discretization with uniform mesh spacing in the three coordinate directions x_i . At each time step the step size at all mesh points was chosen to respect the advective and diffusive stability limits. Following Horiuti [10], the advection term is recast in the Arakawa form which offers optimal conservation properties close to the walls.

It has been shown [8] that, when using a staggered mesh, it is important to compute the S_{ij} and ν_i in such a way as to minimize averaging between different mesh points and the consequent smoothing of the perturbations. Following this argument three different turbulent viscosities were defined: ν_i is computed at the same location as \bar{u}_i and is used in the corresponding momentum transport equation. The S_{ij} are computed at their physical locations as shown in fig. 1; in this way the absolute minimum of averaging operations is used in all three momentum equations.

The values of $c(x, y, z, t)$ were derived using equation (12). The test filter was represented by a grid with spacing twice that actually used to solve equations (13) to (15), (1 coarse cell for 8 fine cells, fig. 2). All test filter quantities in (12), assumed to be constant over one coarse cell, were obtained by averaging the corresponding resolved quantities over the 8 fine cells. A value of c was then obtained for each coarse cell and transferred to the appropriate position of the fine mesh by interpolation. Practically, it was found that, following this procedure, c can occasionally become quite large at some grid points, or a considerable number of negative values can occur, possibly leading to computational instability, (see also Germano et. al. [6] and Lilly [9], who discuss the occurrence of similar problems). The approach here taken to overcome this difficulty was to define an upper and a lower bound for $c(x, y, z, t)$ and truncate accordingly the computed values.

3.2 Initial conditions and boundary conditions

The initial solution was obtained taking the experimental mean velocity profiles from [11] and superimposing to them a divergence free perturbation.

Periodic boundary conditions are used for the streamwise direction, while a more critical problem lies with the modeling of the region close to the wall. In fact, getting closer to a wall the scales of turbulence become progressively smaller and a prohibitive number of mesh points would be needed to maintain the resolution required by the LES approach, [12].

For this reason most authors adopt *wall conditions* based upon the assumption that the first internal mesh point is located within the logarithmic layer and that local velocity and average wall shear stress τ_w are related. In a previous study [13], the present authors found that the *ejection* boundary condition [14] which takes into account the influence of the velocity normal to the boundary (turbulent filaments moving towards the wall increase the shear stress in the longitudinal direction and filaments moving away from the wall decrease it) gives the best results for the square duct problem. For $x_3 = 0$ the resulting formulation is:

$$\tau_{12}(x_1, 0, x_3) = \langle \tau_w \rangle - C u_\tau \bar{u}_2(x_1 + h_1, h_2, x_3) \quad (16)$$

$$\bar{u}_2(x_1, 0, x_3) = 0 \quad (17)$$

$$\tau_{32}(x_1, 0, x_3) = \frac{\langle \tau_w \rangle}{\langle \bar{u}_1(x_1, h_2, x_3) \rangle} \bar{u}_3(x_1, h_2, x_3) \quad (18)$$

where $h_1 = \Delta_2 \alpha g \Theta$ represents the shift in the correlation between velocity and wall stress, h_2 is the distance from the wall $x_3 = 0$ to the first internal mesh point, and C is a coefficient of order 1. Due to the lack of specific data to optimize Θ for the duct problem, in the present simulation the value 0 was taken. The average shear velocity and wall shear stress are determined for each mesh line assuming the logarithmic law to be valid :

$$\frac{\langle \bar{u}_1(x_1, 0, x_3) \rangle}{u_\tau} = 2.5 \ln \left(\frac{\Delta_2 u_\tau}{\nu} \right) + 5.5 \quad (19)$$

4. RESULTS AND DISCUSSION

4.1 Test conditions

The equations were integrated over a rectangular domain of size $4\pi \times 2\delta \times 2\delta$, in x_1, x_2, x_3 , directions respectively. The simulation was performed at Reynolds number $Re_\tau = 1125$. The adoption of approximate wall boundary conditions makes possible the use of relatively coarse meshes and a mesh of $40 \times 20 \times 20$ was used for the parametric study. Moreover, previous tests [13] had shown that a 50% refinement of the mesh in the directions normal to the walls does not affect significantly the results.

In all computations 6 non-dimensional time units ($t_{un} = u_\tau t / \delta$) were necessary for the initial perturbation to disappear. Then the mean values of the resolved quantities (U_{av}, V_{av}, W_{av}), the *rms* of the turbulent fluctuations ($\bar{u}_{rms}, \bar{v}_{rms}, \bar{w}_{rms}$) and the Reynolds stress $\bar{u}v$ were obtained averaging both in time over 10 non-dimensional time steps and in space over the homogeneous streamwise direction. In Fig. 3 contours of mean streamwise velocity and secondary velocity vectors at a cross section are shown and it is clear that the present averaging is sufficient to obtain a fair degree of symmetry over the quadrants. Further integration in time was found to have small effect on the computed averages.

For the comparisons with experimental or other LES data, all the cross sectional averaged variables were further averaged over the four quadrants. Following this procedure the sample size is effectively quadrupled. All the flow quantities shown in the following figures are normalized with respect to the centerline velocity and all distances are normalized with respect to half the duct height. Moreover, taking into account the symmetry of the flow field, all profiles are given only for one of the wall bisectors.

4.2 Comparisons with Smagorinsky model

Several tests with different values for the upper and the lower bound for $c(x, y, z, t)$ were done. In a first approach the upper bound was the computed mean value and the lower bound was set to 0.01, (bound 1). Then the range was increased and the upper bound was set to 0.05 and the lower to 0.004, (bound 2). Both combinations gave good results, without causing instabilities in the computation. Isolines of c averaged in space and in time over the different cross sections for both cases are given in fig. 4. The build in damping properties of the model are evident in the smooth decrease of c close to the walls, while in the core of the flow c is nearly a constant.

Isolines of the mean streamwise velocity and the Reynolds stress $\overline{u'v'}$, compared with the corresponding experimental data [11], are given in fig. 5 and fig. 6 respectively. The agreement is fairly good, taking in to account that the experimental data available refer to a higher Reynolds number ($Re_\tau = 1900$).

In fig. 7 profiles of turbulent intensities (\tilde{u}_{rms} , \tilde{v}_{rms} , \tilde{w}_{rms}) and Reynolds stress $\overline{u'v'}$ along the left wall bisector are shown, in comparison with the corresponding profiles obtained with the standard Smagorinsky model and experimental data [15]. The optimum value of c for the Smagorinsky model was found to be $c = 0.15$. To demonstrate the sensitivity of the model to the value of c , another computation with $c = 0.18$ is also presented. It is evident that even for this 15% change in c all turbulent quantities are affected, specially close to solid boundaries. For both turbulent intensities and the Reynolds stress, the predictions with the new dynamic SGS model are much improved compared with those obtained with the standard Smagorinsky model. Especially in the region close to the wall, in most of the cases, the data obtained with the new model are following fairly well the slope of the experimental data, due to the fact that the model can provide the correct asymptotic behavior close to solid boundaries. Moreover, the limiting bounds of c were found to have a small effect on the results. Modest improvement can be observed for some of the statistics when the larger bounds are used.

5. CONCLUSIONS

The dynamic eddy viscosity subgrid scale model has been applied to the fully 3D case of equilibrium flow in a square duct. Very good agreement was obtained between LES prediction and experimental data. However, the bounds presently applied to c in order to avoid computational instabilities also eliminate the possibility of backscatter whose importance is a quite important property of the original model. A detailed study of the best formulation for the bounding of c is progressing together with the investigations of alternative ways of extracting information from the smallest resolved scales.

References

- [1] P. Moin J. Kim. *J. Fluid Mechanics*, 177 (1987), 133-166.
- [2] B.E. Launder. *Int. J. Heat and Fluid Flow*, 10 (1989) 282-300.
- [3] J. Smagorinsky. *Mon. Weather Rev.* 91, 99 (1963).
- [4] M. Lesieur. In *Turbulence in Fluids*, Martinus Nijhoff, Dordrecht, The Netherlands, 1987.
- [5] C. Leith. *Phys. Fluids A2*, 3 (1989) 277-299.
- [6] P. Moin M. Germano, U. Piomelli and W. Cabot. *Phys. Fluids A3*, 7 (1991) 1760-1765.
- [7] P. Moin U. Piomelli, W. Cabot and S. Lee. *Phys of Fluids A3*, 7 (1991) 1766-1771.
- [8] N.S. Callen P.J. Mason. *J. Fluid Mechanics*, 162 (1986) 439-462.
- [9] D.K. Lilly. *Phys. of Fluids A4*, 3 (1992) 633-635.
- [10] K. Horiuti. *J. Comput. Phys.*, 71 (1987) 343-370.
- [11] J.H. Whitelaw A. Melling. *J. Fluid Mechanics*, 78 (1976) 289-315.
- [12] J. Kim P. Moin. *J. Comput. Phys.*, 35 (1980) 381-389.
- [13] C. Benocci E. Balaras. In *First European CFD conference*, Brussels, Sep. 1992.
- [14] P. Moin U. Piomelli, J.H. Fersinger. " Models for Large Eddy Simulation of turbulent channel flow including transpiration ". Technical report, Thermoscience Div, Dep. of Mechanical Engineering, Stanford University, 1987. Report TF-32.
- [15] W. Baines E. Brundrett. *J. Fluid Mechanics*, 18 (1964) 375-349.

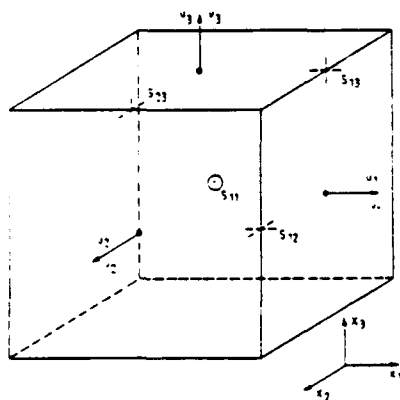


Figure 1: Positions of ν_i and U_i on staggered mesh

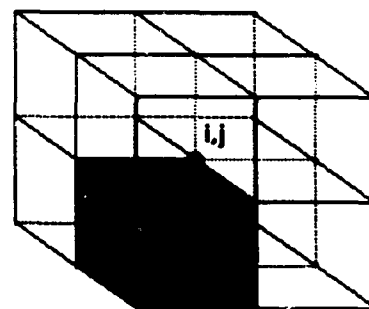


Figure 2: Relation between fine and coarse grid

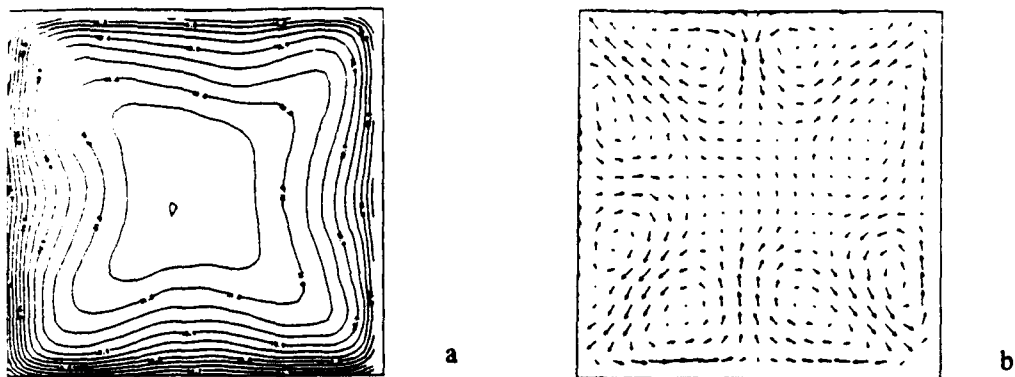


Figure 3: a)Contours of mean streamwise velocity, b)secondary velocity vectors, at a cross section

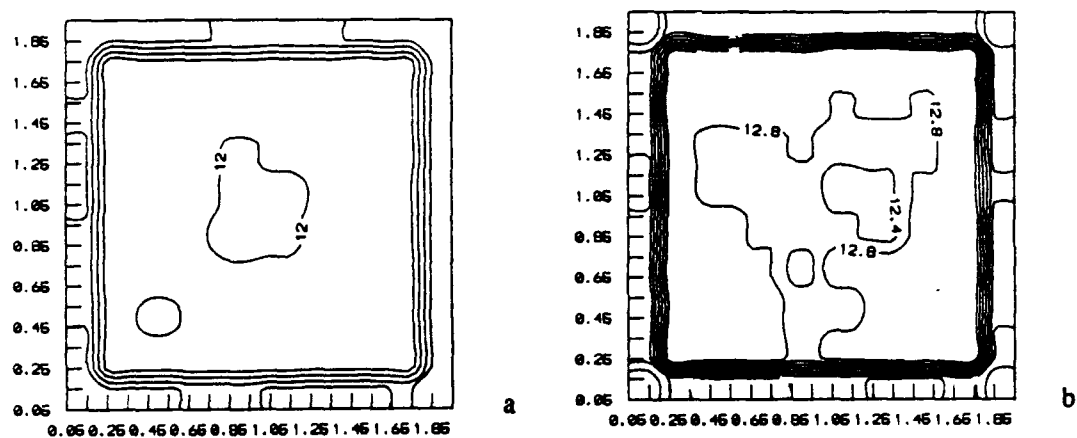


Figure 4: Isolines of the space-time averaged values of c. a)bound1 b)bound2

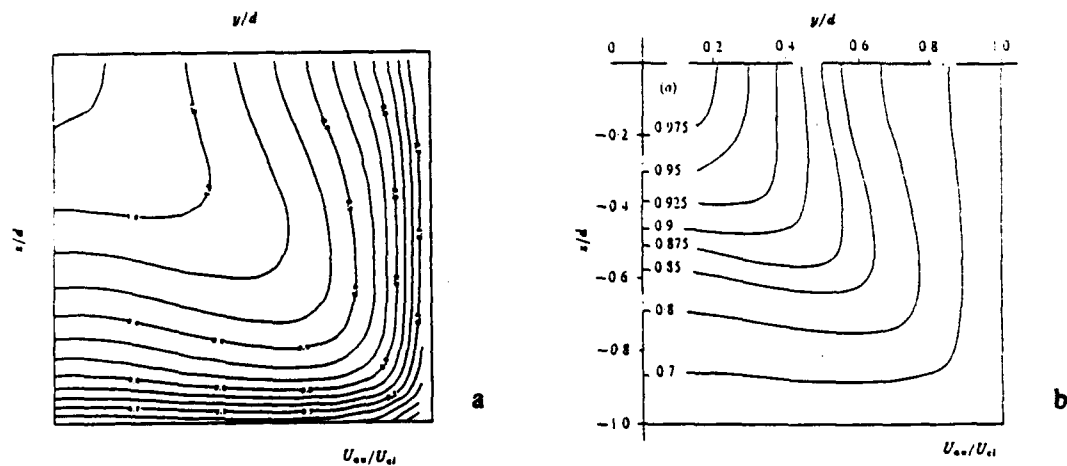


Figure 5: Mean streamwise velocity isolines in a quadrant, nondimensionalized with respect to the centerline velocity. a) Computed, $Re_\tau = 1125$, b) Experimental data (11), $Re_\tau = 1125$

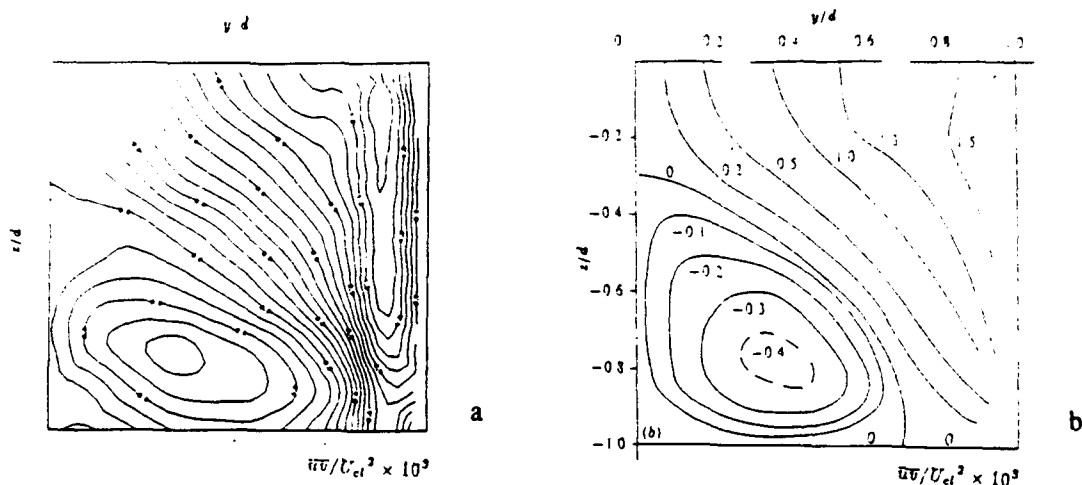


Figure 6: Reynolds stress $\overline{u'v'}$ isolines in a quadrant, nondimensionalized with respect to the centerline velocity. a) Computed, $Re_\tau = 1125$, b) Experimental data (11), $Re_\tau = 1125$

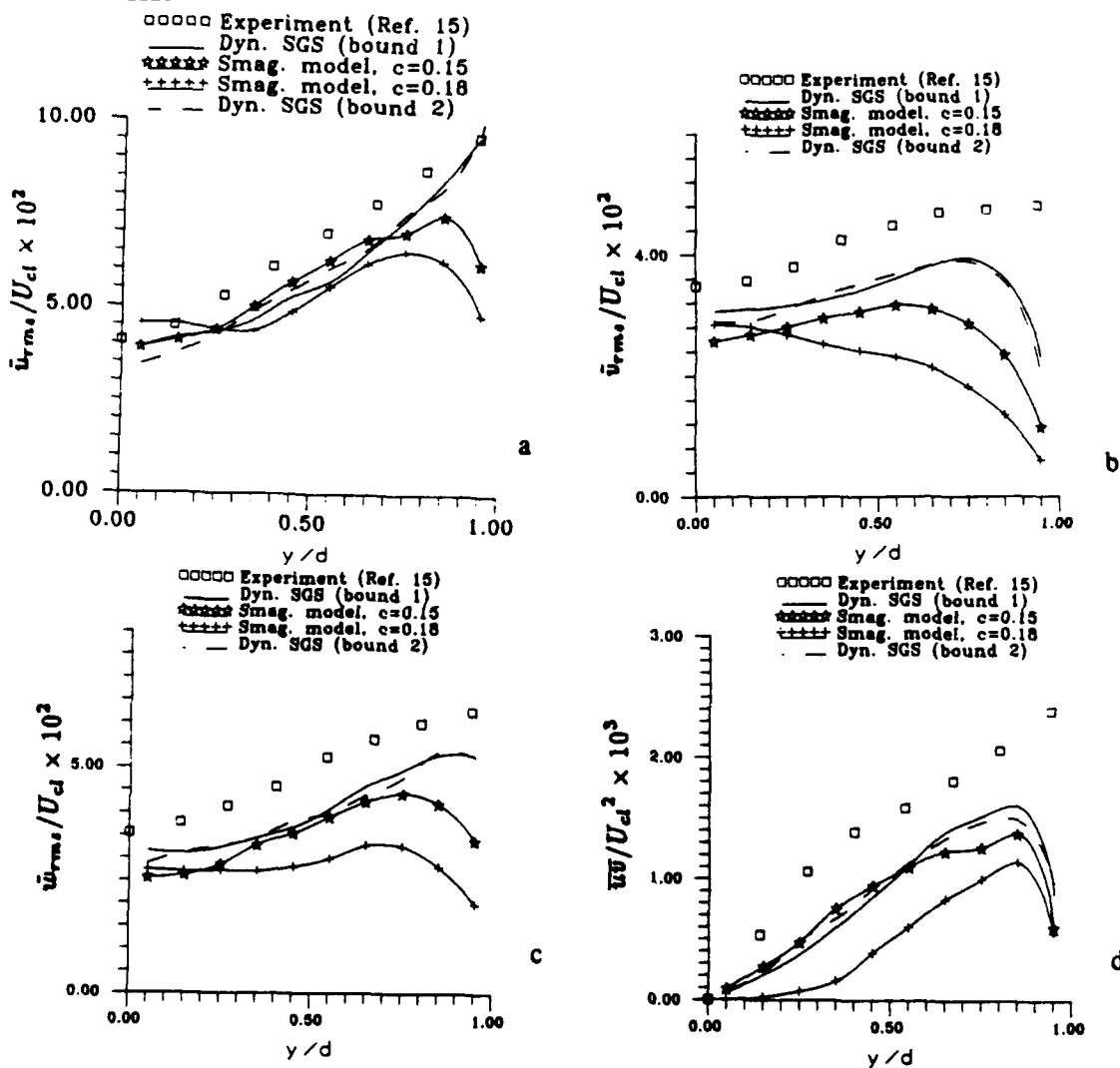


Figure 7: Profiles of a) \bar{u}'_{rms} , b) \bar{v}'_{rms} , c) \bar{w}'_{rms} , d) $\bar{u'v'}$, nondimensionalized with respect to the centerline velocity, along the right wall bisector

STOCHASTIC ESTIMATION OF WALL SHEAR STRESS FOR LARGE EDDY SIMULATION

Ted G. Bagwell, Ronald J. Adrian,
Department of Theoretical and Applied Mechanics, University of Illinois, Champaign, Illinois 61801.

Robert D. Moser and John Kim
Center for Turbulence Research, NASA Ames Research Center, Moffett Field, California 94305.

ABSTRACT

A new wall shear stress approximation has been formed using stochastic estimation for future use in large eddy simulations. The stochastic estimation method resolves the coherent structures of the wall layer using empirical correlation functions, and will be used to provide an accurate estimation of the wall shear stress in channel flow. Initial *a priori* calculations show that the method is more accurate than previous wall shear stress models. The method has also been used to approximate shear stress boundary conditions in direct numerical simulations with promising results as compared to previously published no slip results.

1. INTRODUCTION

In large eddy simulation (LES), only the large energy containing scales of motion are predicted accurately, while the energy transfer to the smaller, sub-grid scales (SGS) of motion is parameterized. For wall bounded flow, computational efficiency also dictates that the wall layer be unresolved, and thus forces the use of approximate boundary conditions and near wall SGS models that approximate the effects of the boundary layer on the large scale flow. These models must implicitly contain information on the unresolved coherent structures that are thought to be responsible for much of the momentum and energy transfer from the boundary layer. Conventionally, this has been handled through wall shear stress boundary conditions. Of course, accurate wall shear stress estimation is also important in the analysis of fluid machinery as it is the fluctuating lift and drag force on the solid body. Previous models have typically been based only on the statistically first order law of the wall, with little knowledge of the structural characteristics of the wall layer turbulence.

It would be useful to incorporate more of the recent knowledge gained in coherent structure studies to model the effect of the solid wall. The present study seeks to develop a new approximation to the wall shear stress using the coherent structure information contained in stochastic estimation. Previous results (Adrian *et al.* 1987; Adrian *et al.* 1988) confirm that the two-point spatial correlation tensor contains enough information to specify the average character of the

wall layer structures, such as hairpin vortices and near wall streaks. Thus, multi-point stochastic estimation could be used to factor coherent structure information into the near wall LES models.

Here, an approximate wall shear stress boundary condition is formulated for direct numerical simulations (DNS) of channel flow. Results of these initial calculations show that the method is more accurate than previous wall layer models in *a priori* tests and is capable of emulating the wall condition when applied as a boundary condition to the DNS. Although the method is more reliant on empirical knowledge than previous estimates, it is potentially useful if the correlation tensor can be obtained and expanded to general geometries and Reynolds numbers.

2. LARGE EDDY SIMULATION WALL SHEAR STRESS MODELING

In large eddy simulation, only the large energy containing scales of motion are computed accurately, in order to save computational time and memory. The technique relies on a spatial filtering formalism (Leonard 1974; Schumann 1975) that separates the flow, f , into a resolved scale field, \bar{f} , to be calculated on the numerical grid, and a sub-grid scale field, f' , whose effect on the resolved scales must be modeled. Current SGS models generally take the form of algebraic equations of state (Germano et al. 1991; Smagorinsky 1963), similar to the zero-equation models for the Reynolds stress found in the Reynolds averaged Navier-Stokes equations. A more comprehensive review of LES modeling may be found in Rogallo and Moin (1984).

This formalism works well for homogeneous flow, or for inhomogeneous flow far from solid boundaries, where the SGS stresses are more nearly isotropic and easier to model. However, in the vicinity of the wall, the energy containing eddies become smaller and more anisotropic. If these scales of motion are to be computed accurately, a large number of grid points must be located in the wall region. To ease this requirement, it becomes necessary to employ anisotropic, near-wall SGS models and approximate boundary conditions to model the momentum transfer to the boundary layer. Conventionally, this has been achieved mainly through the approximate boundary conditions.

The most popular approximate boundary conditions used to date have been shear stress boundary conditions in the tangential directions coupled with a zero velocity condition in the normal direction. An excellent review of current models is given in Piomelli *et al.* (1989), from which the following summary is taken. Schumann (1975) proposed the following boundary condition:

$$\overline{\tau_{w1}}(x,z) = \left. \frac{\partial \bar{u}}{\partial y} \right|_{\text{wall}} = \frac{\langle \overline{\tau_{w1}} \rangle}{\langle \bar{u}(y_e) \rangle} \bar{u}(x,y_e,z), \quad (1.a)$$

$$\overline{\tau_{w3}}(x,z) = \left. \frac{\partial \bar{w}}{\partial y} \right|_{\text{wall}} = \frac{\bar{w}(x,y_e,z)}{y_e - y_{\text{wall}}}, \quad (1.b)$$

$$\bar{v}(x,z) \Big|_{\text{wall}} = 0, \quad (1.c)$$

where y_e , the event location, is the first interior computational grid point and the $\langle \rangle$ operator represents the ensemble average. The directions x_1 , x_2 , and x_3 ; or x , y , and z ; will refer to the streamwise, wall normal, and spanwise directions respectively. The ratio of the ensemble averages in equation 1.a forms an empirical constant that may be estimated using the law of the wall. For instance, in channel flow, $\langle \tau_{w1} \rangle$ is equal to the mean pressure gradient divided by the molecular viscosity. $\langle \bar{u}(y_e) \rangle$ can be found using $\langle \tau_{w1} \rangle$ and the law of the wall.

Piomelli *et al.* (1989) extended the Schumann model by making use of inclined structure information known to exist in the wall region. Experimental evidence (Rajagopalan and Antonia 1979) indicates that the wall shear stress correlates best with the velocity condition taken downstream. From this, they formulated the shifted boundary condition by incorporating an optimal displacement, Δ_s , into the Schumann model:

$$\bar{\tau}_{w1}(x,z) = \langle \tau_{w1} \rangle \frac{\bar{u}(x+\Delta_s, y_e, z)}{\langle \bar{u}(y_e) \rangle}, \quad (2.a)$$

$$\bar{\tau}_{w3}(x,z) = \langle \tau_{w1} \rangle \frac{\bar{w}(x+\Delta_s, y_e, z)}{\langle \bar{u}(y_e) \rangle}, \quad (2.b)$$

$$\bar{v}(x,z) \Big|_{\text{wall}} = 0.0. \quad (2.c)$$

Again, the relationship between the ensemble averages may be taken empirically from the law of the wall. The optimal displacement is approximately equal to $|y_e - y_{\text{wall}}| \cot(8^\circ)$ for $30 < y_e < 50-60$.

While boundary conditions of this type are not strongly grounded, they do satisfy the law of the wall in the mean and compare well to experiments in the region away from the wall. However, the model should also contain enough information to accurately emulate the fluctuating effects of the boundary layer on the core flow. This is a region of strong anisotropy and statistical inhomogeneity in which coherent structures play a crucial role. Hence, a better model would be one that accurately predicts the wall's influence in generating coherent structures such as wall streaks and streamwise vortices.

3. LINEAR STOCHASTIC ESTIMATION

The wall shear stress models employed to date are generally based on first order statistics. One could also form the approximation by requiring that the model be the best mean square estimate given some event, E , where the event may be obtained directly from the velocities on the computational grid. This best mean square estimate is the conditional average of τ_{wi} , $\langle \tau_{wi} | E \rangle$. Further, the conditional average may be approximated by its linear stochastic estimate (LSE), defined as,

$$\langle \tau_{wi} | E \rangle = \hat{\tau}_{wi} = L_{ij} E_j \quad j=1,2,3,\dots,N, \quad (3)$$

where N is the number of events being considered, and L_{ij} is an estimation coefficient relating τ_{wi} to E_j . By forcing the coefficients to satisfy a minimum mean square error between τ_{wi} and $\hat{\tau}_{wi}$, a set of linear equations can be found for L_{ij} as,

$$\langle \tau_{wi} E_k \rangle = \langle E_k E_j \rangle L_{ij} . \quad (4)$$

These form the equations governing LSE. The main difficulties left are obtaining the correlation functions, $\langle \tau_{wi} E_k \rangle$ and $\langle E_k E_j \rangle$, (which must be known empirically) and the proper selection of the events that best characterize the structure of the random wall shear stress.

To date, stochastic estimation has been primarily a tool for investigating coherent flow structures. These coherent flow structures have been termed conditional eddies, to distinguish them from actual flow structures that may exist. Conditional eddies display features similar to actual flow structures found in experiment. Using simple one point events, linear stochastic estimation predicts a vortex ring structure in isotropic flow (Adrian 1979). In homogeneous shear flow, Adrian & Moin (1988) found that linear stochastic estimation, based on local kinematics (velocity plus deformation), predicted a hairpin-like structure in homogeneous shear flow, thought to be a dominant structure in shear flows. In channel flow for example, a single-point Q2 event specified at $y^+ = 103$, will predict a fluctuating flow field that is structurally similar to a hairpin vortex. This is shown in Figure 1. In this figure, the large vector indicates the single-point velocity event, which is located beneath the head of the vortex and between the two legs. The lines reside on a surface of constant fluctuating vorticity magnitude, which form the head and trailing legs of the hairpin-like vortex. Although it is not evident from this picture, the single point event is also capable of predicting the alternating streak structure in the viscous sublayer. Hence, stochastic estimation may be regarded ... a technique that reorganizes the structural information contained in the two point, second order correlation tensor into a realizable random vector field (Adrian 1988).

A logical extension to this research is to use averaged structure information, based on stochastic estimation, to predict the statistics of the wall layer in large eddy simulations. This may in general include estimating both the sub-grid scales stress and approximating the boundary conditions. In keeping with the current wall modeling in LSE, it would be useful to try to emulate the effect of the solid wall, through the wall shear stress boundary condition. Although this will not eliminate the artistry involved in selecting the best form of closure and the event field, it is a clear mathematical framework one may follow to minimize the error in the mean square sense.

4. RESULTS

To evaluate its ability to estimate the statistics of the wall layer, LSE has been used in a direct numerical simulation (DNS) of channel flow with stochastically estimated wall shear stress boundary conditions. Using a well resolved DNS calculation with approximate boundary conditions allows the dynamic impact of the boundary conditions to be assessed without contamination from SGS estimation error that would occur in a LES. The necessary correlations for the LSE have been taken from an existing numerical database available from NASA Ames (Moin and Moser 1989). This DNS was for

turbulent channel flow at $Re_m = 5600$ ($Re_m = 2 U_m \delta / \nu$, δ = channel half width).

The LSE of the wall shear stress has been estimated from an event field consisting of all velocities at a single horizontal plane:

$$\hat{\tau}_{wi} = \int dx' \int dz' L_{ik}(x-x', y_e, z-z') u_k(x', y_e, z'), \quad (5)$$

$$k=1,2,3 \quad i=1,3, \text{ and}$$

$$y_e = \text{event plane.}$$

The stochastic estimation coefficients, L_{ik} , satisfy a coupled set of three convolution integrals,

$$\begin{aligned} \langle \tau_{wi}(x, z) u_j(x-r_x, y_e, z-r_z) \rangle = \\ \int dr_x' \int dr_z' \langle u_j(x-r_x, y_e, z-r_z) u_k(x-r_x', y_e, z-r_z') \rangle L_{ik}(r_x', y_e, r_z'), \\ j=1,2,3. \end{aligned} \quad (6)$$

The form of equation 5 was chosen because it is simple to implement in a spectral computation and because it has a form similar to the Schumann boundary condition. Taking the Fourier transform of equation 6 results in a set of three linear equations for each wave number,

$$\begin{aligned} \langle \tau_{wi}(k_x, k_z) u_j^*(k_x, y_e, k_z) \rangle = \langle u_j^*(k_x, y_e, k_z) u_k(k_x, y_e, k_z) \rangle L_{ik}(k_x, y_e, k_z), \\ j=1,2,3, \end{aligned} \quad (7)$$

where the superscript, *, refers to the complex conjugate. This linear set of three equations may be inverted to obtain the stochastic estimation coefficients in wave space. In an integration of a DNS, estimating the wall shear stress from equation 5 is a small computational burden.

To gauge the model's validity, it is useful to perform *a priori* tests on the model. These are tests that may be constructed from previously determined statistics and hence do not require the model be used in an expensive calculation. Both *a priori* tests presented here were computed using the correlation database of Moin and Moser (1989). It should be noted, however, that these tests are not conclusive as they do not take into account dynamic feedback between the modeled wall shear stress and the event field in actual calculations (Piomelli 1987).

The relative mean square error is a suitable *a priori* reliability criterion;

$$\text{relative mse} = \frac{\langle (\tau_{wi} - \hat{\tau}_{wi})^2 \rangle}{\langle \tau_{wi}^2 \rangle}. \quad (8)$$

An exact model would have zero relative mean square error. Figure 2 compares the relative mean square error for the streamwise wall shear stress using the shifted model in equation 2 to LSE models using one and multiple planes of velocity data as events. On this graph, the abscissa refers to the y^+ location of the event. In the multiplane LSE, the event field consists of all velocity planes in a channel core extending from the indicated y_e^+ location to the opposite wall y_e^+ location, and hence is the most accurate possible LSE. The *a priori* test in Figure 2 thus confirms that the stochastic estimate is more accurate in the mean square sense.

A priori tests may also be formulated to give an indication of the turbulent structure that will emerge when the model is used in a simulation. For example, the mean streak spacing, λ^+ , in the wall layer may be estimated from the first minimum of the estimated wall shear stress correlation:

$$0 = \frac{\partial}{\partial r_z} \langle \hat{\tau}_{w1}(x, z) \hat{\tau}_{w1}(x+r_x, z+r_z) \rangle \Big|_{r_x=0} r_z=\lambda^+/2 \quad (9)$$

This estimate of the streak spacing has been plotted in Figure 3 for the actual value, the single plane LSE, and the shifted model vs. the event distance from the wall. This test indicates that the LSE will be better able to predict the mean streak spacing than the shifted model. The new length scale information is only available if the event field is multipoint.

The *a priori* tests previously mentioned are only one indication of the model's validity. A more stringent test is to use the model as a boundary condition in a dynamic simulation. To this end, a DNS calculation has been performed using the spectral code of Kim *et al.* (1987), modified for wall shear stress boundary conditions in the horizontal directions. No penetration is still enforced in the wall normal direction. No changes were made to the solution algorithm. The wall shear stress was estimated using equation 5, with the velocity events taken from the previous timestep at $y_e^+ \approx 30$. However, the wall region is still well resolved in the sense that all computational grid points were retained in the region below the event plane. The channel was discretized on a 128 X 129 X 128 grid, the same resolution as Moin and Moser (1989). Mass flux boundary conditions and 2/3 rule de-aliasing control were used in the homogeneous directions.

The calculation was carried out for 4.64 δ/u_τ time units, where the last 2.24 δ/u_τ time units were used for statistical sampling. Due to the computational expense, the statistical sampling is rather sparse, resulting in an estimated statistical error of $\pm 5\%$. Time histories (not shown) confirm that the boundary condition is capable of sustaining the turbulent kinetic energy. The various low order statistics, non-dimensionalized by the channel half width, δ , and wall shear velocity, u_τ , are plotted in Figures 4 through 7 with comparisons to results from Moin & Moser (1989), where the natural no slip boundary conditions were applied. Various global statistics are given for comparison in Table 1. Figure 4 shows the mean velocity vs. y^+ . While the mean slip velocity at the wall was 8% of the centerline velocity, the velocity does converge to the law of the wall in the log layer. The rms velocities plotted in Figure 5 show a substantial deviation from the true values for $y^+ < \sim 20$. The incurred rms slip velocity at the wall is 10% of the mean centerline velocity. Figure 6 shows the mean Reynolds stress and total shear stress profiles. Theoretically, the total shear stress in the channel should be $\sigma = -y$, which is accurately predicted here. Figures 7 a and b show the spanwise wall shear stress spectra and

correlations, clearly indicating the loss in amplitude prominent at high wave numbers that typically occurs when LSE is used to predict a field. Hence, the small scale structure will be overly damped. The net result is primarily a large rms slip velocity from the reduced gradients at the wall. This tends to drive down the turbulent kinetic energy dissipation while increasing the production in the near wall region. The effect is somewhat negated by the increased turbulent kinetic energy at the event plane, which in turn increases the wall shear stress and dissipation. Hence, the model is dynamically stable. The wall shear stress correlation fields of Figure 7.b indicate that the streak spacing in the wall layer is being accurately modeled.

5. CONCLUSIONS

Using the coherent structure information contained in linear stochastic estimation offers many possibilities for use in modeling turbulence, such as the wall shear stress model presented here. The method is a clear mathematical framework from which estimates may be constructed and is inexpensive to implement once the correlation data is known. The major expense of LSE is that the correlation tensor must be known empirically, either from experiments or from DNS simulations. This factor will be offset somewhat if the correlation tensor can be expanded to general geometries and Reynolds numbers and if a reliable estimate may be formed with fewer event points than those considered here. It would be advantageous to attempt stochastic estimates that can be obtained reasonably from experiments, thus expanding the scope of problems to be considered.

The LSE model is able to capture the salient features of the wall shear stress enough to accurately account for the wall influence in DNS. Overall, the statistics deviate from the true values only in the region of $y^+ < 20$, but agree well for the core of the channel, which is what one expects from an approximate wall boundary condition.

ACKNOWLEDGEMENTS

This work was supported by the Air Force Office of Scientific Research under contract 90-0169. Computer time was provided by the University of Illinois' National Center for Supercomputing Applications.

REFERENCES

- Adrian, R. J. 1979 Conditional eddies in isotropic turbulence. *Physics of Fluids*. 22, No. 11, 2065-2070.
- Adrian, R. J. 1988 Linking correlations and structure: stochastic estimation and conditional averaging. *Zoran P. Zaric Memorial International Seminar on Near Wall Turbulence, Dubrovnik, Yugoslavia*. May 16-20, 1988.
- Adrian, R. J., Moin, P. & Moser, R. D. 1987 Stochastic estimation of conditional eddies in turbulent channel flow. *Proceedings of the 1987 CTR Summer Program, NASA-Ames Research Center, Stanford, CA*. 1987.
- Adrian, R. J. & Moin, P., 1988 Stochastic estimation of organized turbulent structure: homogeneous shear flow. *Journal of Fluid Mechanics*. 190, 531-559.

- Germano, M., Piomelli, U., Moin, P. & Cabot, W. H. 1991 A dynamic subgrid-scale eddy viscosity model. *Physics of Fluids A*. 3, 1760-1765.
- Kim, J., Moin, P. & Moser, R. 1987 Turbulence statistics in fully developed channel flow at low Reynolds number. *Journal of Fluid Mechanics*. 177, 133-166.
- Leonard, A. 1974 Energy cascade in large-eddy simulations of turbulent fluid flows. *Advances in Geophysics*. A18, 237-248.
- Moin, P. & Moser, R. D. 1989 Characteristic-eddy decomposition of turbulence in a channel. *Journal of Fluid Mechanics*. 200, pp. 471-509.
- Piomelli, U. 1987 *Models for Large Eddy Simulations of Turbulent Channel Flows Including Transpiration*. Ph.D. Thesis, Stanford University, Stanford, California.
- Piomelli, U., Ferziger, J., Moin, P. & Kim, J. 1989 New approximate boundary conditions for large eddy simulations of wall-bounded flows. *Physics of Fluids A*. 1, No. 6, 1061-1068.
- Rajagopalan, S. & Antonia, R. A. 1979 Some properties of the large structure in a fully developed turbulent duct flow. *Physics of Fluids*. 22, 614-622.
- Rogallo, R. S. & Moin, P. 1984 Numerical simulation of turbulent flows. *Annual Review of Fluid Mechanics*. 16, 99-137.
- Schumann, U. 1975 Subgrid scale model for finite difference simulations of turbulent flows in plane channels and annuli. *Journal of Computational Physics*. 18, 376-404.
- Smagorinsky, J. 1963 General circulation experiments with the primitive equations. I. the basic theory. *Monthly Weather Review*. 91, 99.

Table 1. Comparison of DNS statistics from LSE shear stress BCs to no slip BCs.

	no slip	LSE shear stress
$Re_\tau = u_\tau \delta / \nu$	180.	178
U_m / u_τ	15.6	15.6
$C_f = 2 \nu \langle \tau_{w1} \rangle / U_m^2$	8.20×10^{-3}	8.23×10^{-3}
$\tau_{w1,rms} / (Re_\tau u_\tau^2)$	0.360	0.196
$\tau_{w3,rms} / (Re_\tau u_\tau^2)$	0.271	0.129

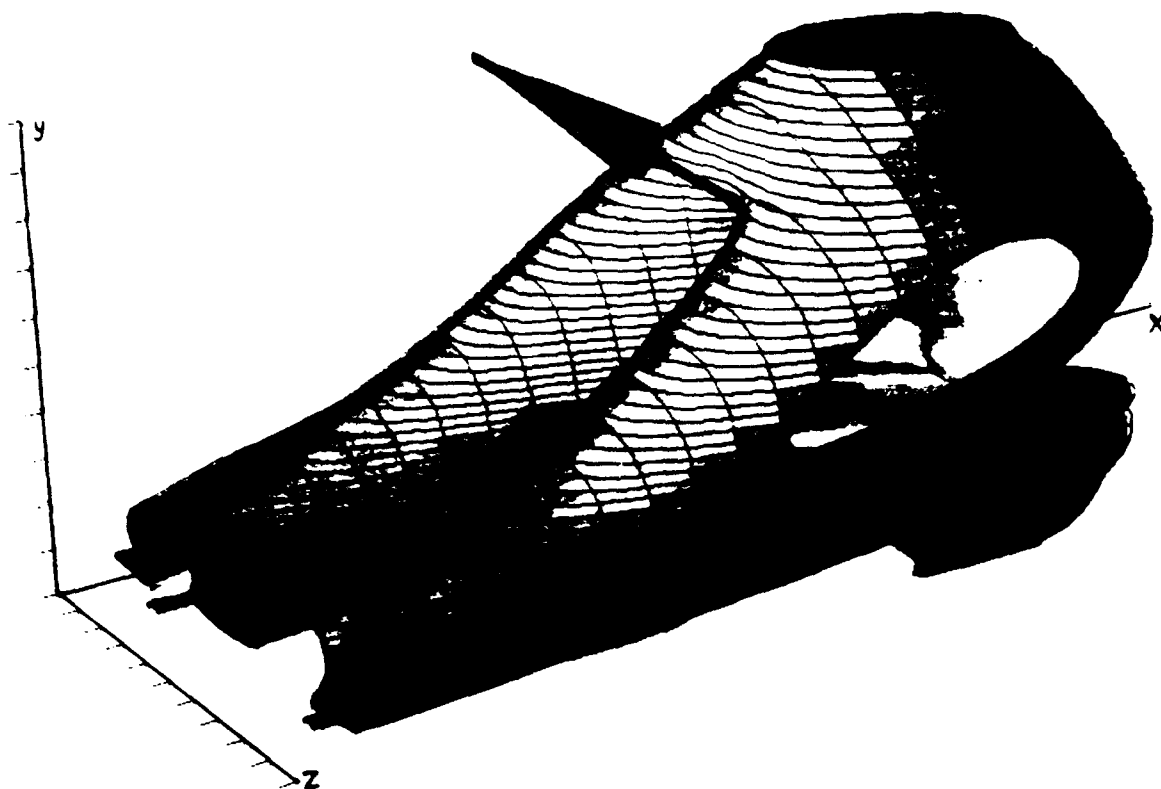


Figure 1. Hairpin-like structure resulting from the Q2 event specified at $y^*=103$.

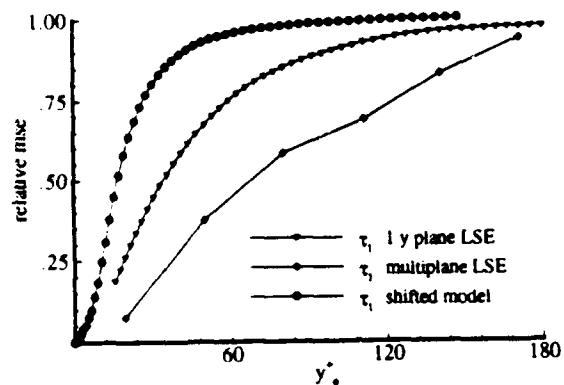


Figure 2. Relative mse for τ_{w1} estimate vs. y^* location of event.

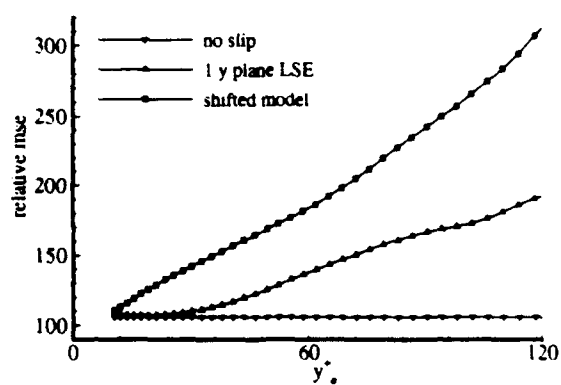


Figure 3. Mean streak spacing based on τ_{w1} estimate.

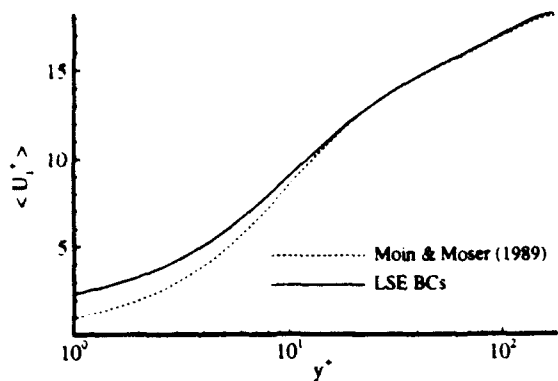


Figure 4. Mean velocity profile in wall coordinates.

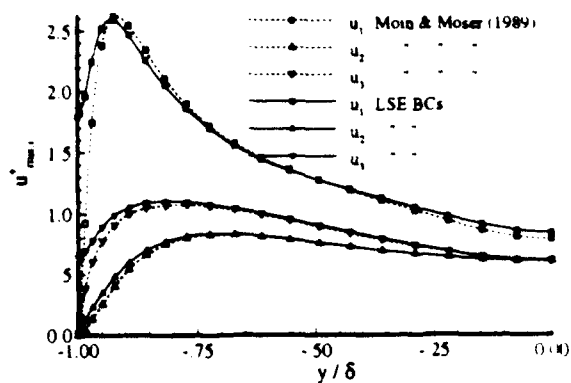


Figure 5. Rms velocities vs. y. (-1=wall ; 0=centerline)

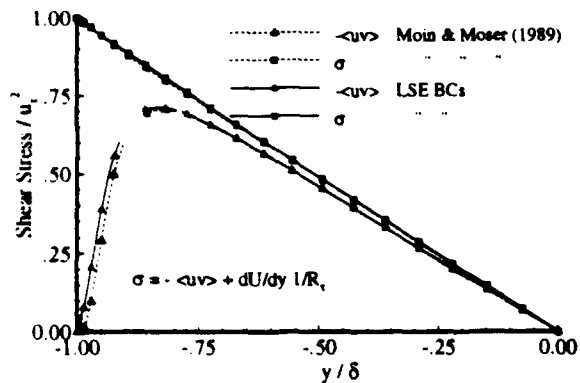


Figure 6. Mean shear stresses vs. y. (-1=wall ; 0=centerline)

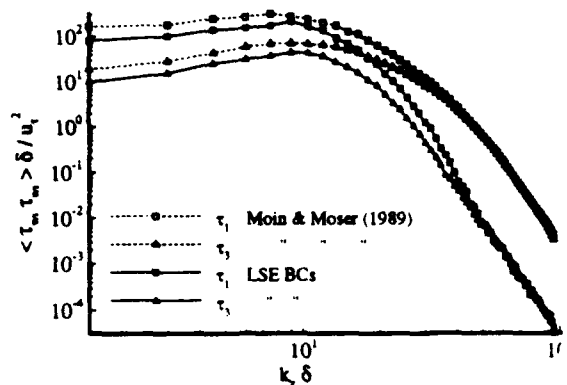


Figure 7.a. τ_{mn} spanwise spectrum vs. k_x .

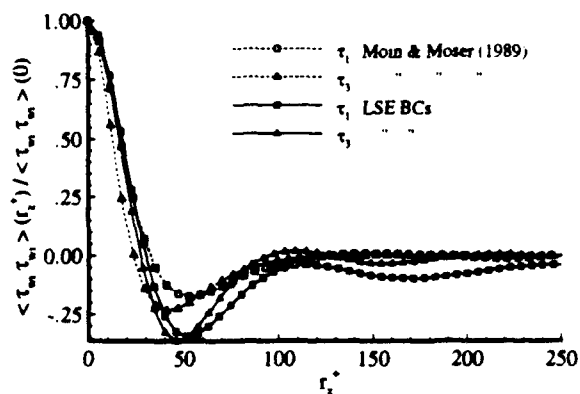


Figure 7.b. τ_{mn} spanwise correlation coefficient vs. r_x .

CORRELATION BETWEEN REATTACHMENT LENGTH DOWNSTREAM A BACKSTEP AND STRUCTURE OF THE INCIDENT FLOW

A Aroussi and A Senior
Department of Mechanical Engineering,
Nottingham University, Nottingham, NG7 2RD, UK.

Abstract

The fluid motion behind a rearward facing step is scrutinised as a function of the characteristics of the primary flow approaching the step. The flow properties measured with optical anemometers are predicted numerically with a model of turbulence. The measured velocity values are used to adjust the numerical solution until satisfactory simulation is obtained. These measured and predicted values are compared to each other and to results reported by other workers.

1. Introduction

Separated flows are of common occurrence in engineering applications and are characterised by abrupt changes in pressure which invariably lead to oscillations. These flows are encountered in numerous engineering devices such as turbomachines, heat exchangers and chemical process equipments as well as in gaps or openings in moving objects, valves, sudden expansion of pipes and flow over hills and mountains. In fluid devices, for example, flow separation produces significant losses in the performance of the machines.

Generally, the type of flow separation studied is that on a flat plate, behind a rearward facing step or within cavities. In addition to their practical applications, cavity flows and those downstream a step are usually used to test numerical techniques and mathematical models of turbulence. The presence of fixed geometry with one or two free boundaries and the certain presence of vortices makes an efficient environment for computational work and the testing of numerical techniques.

The flow pattern behind a typical rearward facing step is shown in figure 1. The important features of this flow event are the separation point, at the corner of the step, the recirculation zone behind the step, and the reattachment point. The turbulent intensities and shear stress reach maxima in the reattachment zone, and decay rapidly after the reattachment. The reattachment length is taken as the distance from the back of the step to the reattachment point. The boundary layer downstream of the reattachment point interacts with the shear layer over it and approaching from upstream. The structure of the fluid motion resulting from this complex interaction between the separated shear layer and the adjacent flow depends on the characteristics of the approach flows. consequently, comparisons of data on the reattachment length must take into account the characteristics of the incident flow. The reattachment point is an important property of any reattaching flow. Practically it may indicate deposition of

fluid particles; particularly in two phase flows. For comparison with other work, the reattachment length gives a quantitative result which is easier to correlate than a general flow pattern.

It is how this reattachment length varies with different inlet conditions which this paper investigates experimentally, using LDA and PIV, and numerically using a model of turbulence. The inlet conditions specifically examined are the velocity, and the degree of turbulence in the approaching flow.

2. Literature review

The fluid motion behind rearward facing step has been the subject of numerous studies in the past. A comprehensive review of these is given by Kim et al (1980). The present survey examines more recent and pertinent experimental and theoretical work as well as any relevant publication not included in the review by Kim et al. The present survey is split into two sections; namely experimental and theoretical.

Experimental work:

The fluid behaviour downstream a rearward facing step has been scrutinised using flow visualisation and devices such as pitot tubes, hot wire anemometers pulsed wire anemometers, laser Doppler anemometers and particle imaging velocimeters. For example, a study by Moss and Baker (1980) uses a pulsed wire anemometer and gives the reattachment length as 5.2 step heights, at $Re=50000$. This value of the reattachment length is lower than the 6.7 reported by Bandyopadhyay (1990) also using a hot wire. A similar device is used in the investigation into the effect of inlet turbulence and reported by Hanson and Al-Ohali (1988). A loudspeaker is used to induce a varying intensity of pressure perturbations. Increasing the turbulence level causes the reattachment point to move upstream, from 7.0 to 5.5 step heights.

A laser Doppler anemometer based investigation by Etheridge and Kemp (1977), gives a reattachment length of 5 step heights. However, Makiola and Buck (1990) use a similar device and report a reattachment length of 8.3 step heights at $Re=33000$. Armaly et al (1982) also using LDA report an almost linear relationship between the reattachment length and Re in the laminar flow region ($600 > Re > 70$) and higher Re values give higher reattachment lengths. For turbulent flow, the reattachment length is found to be more constant, slowly decreasing to a value of about 7 step heights.

Another laser based anemometer; namely a particle imaging velocimetry technique is used by Grant et al (1990) to study the flow event at $Re=45000$ and gives a reattachment length of 7.1. Various measuring devices are employed by Kim et al (1980) to study the flow at $Re=1300$. The authors find that although the reattachment point fluctuates with time, the mean reattachment length is 7.1.

The effect of turbulence on the reattachment length is investigated by Isomato and Honani (1989), who find the reattachment point tends to move upstream with increases in turbulence. The study concentrates on a turbulence intensity range between 10% and 12%. This is induced by a rod or a cavity at the inlet.

Theoretical work:

Theoretically, bluff body flows have been extensively investigated. However, these studies tend to differ in their purpose and in the techniques used. A vast number of these investigations choose bluff body flows purely as a medium to test their theoretical techniques. Consequently, the aim is generally to predict the overall flow pattern. Some relevant publications from this plethora of studies are reviewed next.

Analytical methods. In the past, theoretical studies of flows around bluff bodies have used conformal mapping

or the solution of the linearised equations of motion. The success of these methods has been limited, since the streamlines and pressure distributions obtained, are mostly applicable to two dimensional flows with little turbulence.

Of the analytical work of interest to this research, is that of Tani et al (1961) on the wake and re-attachment behind a backward facing step. The main feature of such a flow is the relatively steady vortex behind the rear face. Conformal mapping is used to predict the downstream re-attachment point at a distance of 1.7 times the model's height; this prediction has subsequently proved unrealistic since the range of practical values is 4 to 18.

A study by Kim and Chang (1989) uses Prandtl's turbulent flow data to investigate the region close to reattachment. The reattachment length is calculated as 6.5 step heights.

Numerical studies Back step flows are often used to test newly developed numerical techniques and mathematical models of turbulence in the handling of re-circulating flows. However, most of the investigations reported have concentrated on the generation of reverse flow rather than on the accuracy of the results or on their practical applications.

A solution of the two equation $k-\epsilon$ model by a finite element technique is reported by Sohn (1988). The reattachment length is given as 5.59 step heights for $Re=69610$. The author attributes the underprediction to the possible unsuitability of the $k-\epsilon$ model, to bluff body flows, and to numerical diffusion in the solution procedure.

A similar numerical investigation of various cases of differing Re and turbulence intensity is reported by Lovgren (1985). For turbulent flow ($Re=7000$), the reattachment point moves downstream with the increasing turbulence. This contradicts the findings of AL-Ouali (1988). For a degree of turbulence of 1% at the inlet, the reattachment length is 6.7, whilst for 2% it is 7.6 step heights.

Autret et al (1987) employ a Galerkin finite element method to solve the $k-\epsilon$ model, providing a reattachment length of 5.22 for $Re=42000$. This low value is thought to be due to the diffusive terms in the momentum equation. The authors state that improvements can be made to the conventional $k-\epsilon$ model by expressing C_μ as a function instead of a constant. This is shown by Gooray et al (1972), who find the reattachment length changes from 4.5 to 5.8 step heights by implementing the function. Other models of turbulence have also been used. For example, Spalding et al (1983), compare the KW model with the $k-\epsilon$ model. A reattachment length of 7.2 predicted by both models, indicates a good performance by both.

The Reynolds stress model when applied by Celerligil and Mellor (1985) gives a reattachment point at 7.89 step heights. Morinishi and Kobayashi (1990) use the Smagorinsky model, with various values for the Smagorinsky coefficient, to determine the reattachment length. The most accurate result, compared to experimental work, is a reattachment length of 7.1. This is for $Re=46000$.

To compute the flow, Kwon and Pletcher (1986), apply a zonal method. The flow domain is divided into 3 different flow modules, each of which is modeled by a different technique, namely, viscous or inviscid. Some turbulence modelling is still required, for which the KL model and L model are used. These give reattachment length of 7.65 and 7.2 respectively.

Karniadakis and Orszag devised a way of modelling the flow based on renormalization theory, using spectral element methodology. Two cases are performed; when $Re=4444$, the reattachment length is 9 and when doubled to $Re=8888$, the flow reattaches at 6.8 step heights.

This short review has shown the unreliability and the limited applicability of some of the experimental work and most of the analytical methods. However, three numerical studies are found to be particularly useful in respect to the present study in that they review the influence of turbulence on the reattachment length. The study by Isomato and Honami (1989) is used as a comparison with the present results. The findings of Hanson and Al-Ohali (1988) are presented in qualitative style and consequently are only used for general comparison. However, the results of Lovgren (1985) are not used since they contradict the first two studies and only cover a very narrow range of turbulence.

3. Experimental programme

The measurements are conducted in an open circuit wind tunnel and in a water channel. The wind tunnel has a maximum speed 10ms^{-1} and an adjustable flow profile in the working section. This is made of perspex to allow access to the laser beams of the LDA system. Similarly, the flume has an adjustable flow to the test section, but the maximum speed is only 2ms^{-1} . The water is driven by a submerged pump which provides a maximum flow rate of $90\text{m}^3\text{h}^{-1}$. The working section is built of 4mm glass. In both devices, the incident flow is controlled by the introduction of screens upstream of the test section. These are flow smoothing screens and slatted screens for the generation of turbulence. These are located downstream of the honeycomb straighteners. The model of the step is made of perspex and mounted on the floor of the flow channel. The optical anemometers used to acquire the flow properties are a two component Laser Doppler Anemometer (LDA) and a Particle Image Velocimeter (PIV).

PIV is used in conjunction with the water channel and involves the recording of multiple images of scattering particles on a single photographic negative. If the displacement of separate scattering particles images and the time between consecutive exposures can be measured, the velocity of the flow local to each such particle can be calculated.

The light source for the PIV system used is provided by an 18W, continuous wave, Argon Ion laser. This type of laser is employed because the light produced is in the blue-green region of the spectrum, and has the lowest absorption-attenuation characteristics in water. The arrangement used is such that the beam passes through a mechanical chopper in the form of a rotating disk with a transparent segment, which allows the generation of the required discrete images, and then a glass rod to produce a light sheet, 2mm thick, in the investigated flow area (Fig 2). The water is seeded by a commercially acquired powder of naturally buoyant particles. The analysis of the flow images recorded by the PIV is as shown in figure Fig 3.

The second anemometer in the form of a digital correlator based two component LDA system is used with the wind tunnel to obtain the longitudinal and vertical components of the mean velocity. This system uses a 15mW HeNe laser and a back-scatter arrangement mounted on a traversing mechanism. The relative position of the control volume is determined to an accuracy of $\pm 0.5\text{mm}$ and the air flow is seeded with smoke generated by the vaporisation of a light mineral oil.

These two techniques are shown to provide complementary information. LDA offers the opportunity for time series (and thus spectral) information at various measurement stations while PIV enables the spatial distribution of instantaneous fluctuating flows to be measured.

4. Computational programme

The turbulent and recirculating fluid flows generated downstream of the step by the separation of the free stream

are elliptic in nature. The primary eddy is formed when the separated shear layer reattaches downstream of the step after which the flow returns to its normal boundary layer state. Between the step and the reattachment point a large vortex is maintained by the energy in the shear layer above it. As the primary vortex sweeps backwards it is forced upwards by the vertical boundary generating a recirculation zone in the bottom corner. These flow features are mathematically approximated by most one and two equation models of turbulence (Launder and Spalding 1972).

The initial intention of this study was to examine the performance of three models of turbulence; namely the Constant Viscosity model (CV), the two equation Kε model and the Algebraic Stress model. However, the rigidity and to an extent the uniqueness of solution of the CV model has excluded it from the present paper. On the other hand the flexibility in prediction of the Kε model and the strong dependence of the solution on the inlet boundary conditions dictate a full devotion of the present numerical work to it.

The aim is to simulate the flows measured with the optical anemometer and assess the accuracy of the solution of the Kε model and evaluate the dependence of such a solution on the inlet boundary conditions. Furthermore, establish a relationship between the degree of turbulence at the inlet boundary and the reattachment length.

The Kε effective viscosity model This is the simplest mathematical model of turbulence in dealing with elliptical equations that govern the recirculating flow associated with backward facing steps and rectangular grooves. The two dependent variables solved for are the turbulence energy K and its dissipation rate ε. These two quantities are related by the equation

$$\epsilon = \frac{C_D K^{3/2}}{l}$$

where C_D is a constant usually set to unity. The Kε model expresses the Reynolds shear stresses according to the Boussinesq hypothesis, that is a product of the mean velocity gradient and the turbulent viscosity μ_t

$$(-\rho \bar{u}_i \bar{u}_j) = \mu_t \left(\frac{\partial U_i}{\partial x_j} + \frac{\partial U_j}{\partial x_i} \right)$$

The turbulent viscosity is calculated from the local values of K and ε :

$$\mu_t = \frac{C_\mu \rho K^2}{\epsilon}$$

The empirical constant $C_\mu = 0.09$. In many applications the empirical constant of the Kε model are varied "to tune" the predictions to fit the experimental results. However for bluff body flows, other workers found that predictions did not improve by changing these constants (Vasilic-Melling 1977); therefore the values of these constants have not been altered in this study and are those specified by Launder and Spalding (1972).

Treatment of wall regions The Kε turbulence model is designed to simulate flow regions of high Reynolds number. However, near solid boundaries a viscous sublayer exists because the mean velocity components and the

turbulent viscosity fall to zero, due to the no-slip condition. The $K\epsilon$ model does not lend itself to the near wall, low Reynolds number flow. The alternative approach is to use the "wall function" method which connects the sublayer with special functions which bridge the conditions at its outer edge to those at the wall, thus avoiding this low Reynolds number region (Launder and Spalding 1972).

The numerical procedure used to solve these differential equations involves an up-wind finite difference technique and the algorithm "SIMPLEST" of Spalding (1983). This technique is adopted in order to ensure stability at high Reynolds numbers. The grid used for the solution is 81×91 , rectangular and non-uniform with a fine mesh in areas of steep gradients, particularly in the shear layer and close to walls.

5. Results and discussions

This study concentrates on the effect of increasing the amount of turbulence in the flow approaching the step on the reattachment length downstream. Numerically, the turbulence is specified as a uniform profile at inlet, just above the back face of the step, and covers a range from 1% to 90%. Experimentally, the turbulence intensity range at the inlet is 5% to 40%.

The changes in flow pattern caused by increasing the inlet turbulence are such that at low turbulence intensities the vortex is long and slender giving a long reattachment length, but at high turbulence level the vortex shrinks in size, resulting in the reattachment point being closer to the step. The centre of the vortex is also nearer to the back face of the step.

This is illustrated in the comparison of the predicted vertical profiles of the U-velocity at 10% and 90% turbulence intensities at the inlet (Figs 4 and 5). Each of these profiles is taken at a different location downstream of the step. At $X/H=0$, which corresponds to the back face of the step the profiles show the uniform velocity stated at inlet. Obviously the velocity at the back face of the step is zero, since it is a solid boundary. Further downstream the vortex is shown by the fact that the profiles indicate positive longitudinal velocity at high Y/H and negative values at the lower end. The end of the vortex is indicated by a return to a positive value by the whole of the profile. This also defines the reattachment point. From Figure 4 the reattachment point is approximately 6 step heights downstream of the step. Examination of the raw data of the velocity in the flow domain gives the more accurate value of $X/H=5.8$. Similar profiles are shown in Figure 5 for 90% turbulence. These profiles straighten out more quickly than the previous 10% turbulence case. The cross-over point of the profiles occurs at $Y/H=1$ in figure 4 and at $Y/H=0.94$ in figure 5 which indicates that the flow develops more rapidly, due to the high mixing forces within the flow. This higher turbulence level of 90% results in a shorter reattachment length, of about 4 step heights.

At values of $Y=0$ on the floor of the domain, both sets of profiles, obtained numerically, indicate a negative velocity. This is impossible due to the no slip condition at walls; the velocity at these points should be zero. The reason for this error is the poor treatment of the wall region. As explained earlier, the region close to the wall is bridged by a "wall function". The distance covered by the wall function is taken as one cell height. Although the profiles are shown to $Y=0$, they do in fact stop one cell height short of this level. The error in these profiles is due to the dense grid close to $Y=0$; hence the wall function only bridges a small gap.

The variation of the turbulence kinetic energy gives an indication of the flow development (Figs 6 and 7). These profiles are taken at similar locations to the velocity profiles. At 10% turbulence it is apparent that although the

initial degree of turbulence energy is low, the energy contained within the turbulence lasts well downstream. The initial sharp peak of turbulence energy spreads out due to the mixing behind the step. The momentum of the fluid, and thus its kinetic energy is conserved until well downstream. This contrasts with the case of 90% inlet turbulence (Fig 7), where the turbulent energy spreads quickly across the height of the domain giving a flat profile. The energy also decays rapidly, shown by the low values of turbulence energy at each of the profiles, compared with the initial energy at $X/H=0$.

To validate the use of the computational results over the whole flow domain, profiles of velocity and turbulence energy are compared with present experimental results and those reported by other researchers. For example, a comparison of the present vertical profiles of the longitudinal velocity at 10% turbulence intensity are shown with those of Baker and Moss in Figure 8. The profiles at $X/H=2$ give a good correlation, but further downstream at $X/H=4$, the predictions compare favourably with the present measurements but give lower velocities than Baker's.

The profiles of turbulent energy at 10% inlet turbulence energy and at $X/H=2$ and $X/H=4$ are compared with the present LDA measurements and with the hot wire results of Baker and Moss (Fig 9). The shapes and maximum values of the profiles compare well indicating that the turbulence energy is well modelled. The KE is known to underpredict behind a step by up to 20% (Kim et al 1980). Here it also underpredicts at $X/H=2$ and 4. The maximum error in the present predictions in comparison to Baker's results at $X/H=4$ is 16%. There is a larger error between the profiles at $X/H=2$ for low values of Y (around $0.5H$). This is due to different inlet conditions. Baker's experiment naturally produces a profile velocity inlet, but a uniform velocity inlet is modelled here.

This project concentrates on determining a relationship between the reattachment length and inlet turbulence. By varying the uniform inlet turbulence profiles from 1% to 90% a relationship is obtained. Overall, the results show that at low turbulence levels the reattachment point decreases rapidly with increasing inlet turbulence. As the turbulence increases, the reattachment length decreases more slowly in an exponential form. At 60% turbulence a steady state is reached. Even with increasing turbulence the reattachment length remains at 3.5 step height downstream of the step. The present LDA results cover the inlet turbulence rate 5% to 40% only. The measurements compare extremely well to the predictions and also show an exponential decay of the reattachment length with increases in the turbulence energy. These findings are plotted against the experimental results obtained by Isomota and Honami (1989), (Fig 10). Their study examines the effect of inlet turbulence between 10% and 12% on the reattachment length. A very strong linear relationship between turbulence and the reattachment length is indicated. Increasing the turbulence by 2% moves the reattachment point upstream by two step heights. Although the present study does indicate a lower value of reattachment length at 10% turbulence, the values at 12% compare well. If the results of Isomota and Honami are interpolated to slightly high turbulence, the curves indicated by present predictions and those of Isomota would join to form a reasonably smooth curve of exponential form. This shows that the present predictions closely agree with the trend indicated by the experiments, and the exponential form of the graph is correct.

5. Conclusions

This study demonstrates that higher inlet turbulence results in great mixing in the flow. This causes the profiles of the variables to become uniform more quickly in high turbulence flows and the reattachment point can form further upstream. At very high turbulence the flow is saturated with mixing and an increase in the inlet turbulence

has no effect on the re-attachment length.

In modelling the rearward facing step some simplifications have been made. All the cases which have been considered have modelled 2-dimensional effects only. In any practical situation of flow behind a step, the step would have a finite width and it is known that cyclic three dimensional effects exist in the flow. These have been found to affect the reattachment length. A second simplification made in this study is the use of a uniform inlet velocity profile. In practical situations, the flow will have developed a boundary layer before reaching the back face of the step.

This study concentrates on the effect of varying the inlet turbulence. To fully investigate how the reattachment point changes with inlet conditions, other flow parameters need to be investigated. A more comprehensive study of the effect of inlet velocity is needed. It is shown here that the reattachment length decreases with increasing turbulence. This indicates that the rate of decay of turbulence ϵ may also affect the reattachment length.

NOMENCLATURE

U	Longitudinal velocity	ρ	Density of fluid	U_{∞}	Free stream velocity
K	Turbulence kinetic energy	V	Vertical velocity	ϵ	Kinetic energy dissipation rate
μ_t	turbulent viscosity	H	Step height	X,Y	Longitudinal & vertical directions

REFERENCES

- 1) Kim, C S and Chang, P K, "Analysis for Two Dimensional Incompressible Reattaching and Redeveloping Flow Behind a Rearward Step", *Jnl of the Franklin Inst*, 1980, pp 547-570.
- 2) Sohn, J L, "Evaluation of FIDAP on some Classical Laminar and Turbulent Benchmarks", *International Jnl for Numerical Methods in Fluids*, 1988, pp 1469-1490.
- 3) Grant et al, "Particle Image Velocimetry Measurements of the Separated Flow Behind a Rearward Facing Step", *Optics and Lasers in Engineering*, 1991.
- 4) Launder and Spalding, "Mathematical Models of Turbulence", Academic Press, 1972.
- 5) Etheridge, D W and Kemp, P H, "Measurement of Turbulent Flow Downstream of a Rearward Facing Step", *Jnl Fluid Mech*, Vol 86, pp 545-566, 1976.
- 6) Moss, W D and Baker, S, "Recirculating Flows Associated with 2-Dimensional Steps", *Aeronautical Quarterly*, 1978, pp 151-170.
- 7) Bandyopadhyay, P R, "On Instabilities and Large Structures in Reattaching Boundary Layers", 1990, pp A 4.1- A 4.9, Twelfth Turbulence Symposium.
- 8) Lovgren, "Numerical 2-D Air Flow Simulation over a Backward Facing Step and Block", *Phoenix Users Conference*, London, 1985.
- 9) Cerierlight, M C and Mellor, G L, "Numerical Solution of 2-D Turbulent Separated Flows Using a Reynolds Step Closure Model", *Jnl Fluids Engineering* 1985 vol 107, pp 467-76.
- 10) Hanson, M A and Al-Ohali, "Controlled Perturbation of Reattaching Flow", *Forum on Unsteady Flow*, 1988, pp 47-49.
- 11) Vasilic-Melling D " Three dimensional turbulent flows past rectangular bluff bodies" *Phd thesis*, Imperial College, London, 1977.
- 12) Armaly, B F et al, "Experimental and Theoretical Investigation of Backward Facing Step Flow", *Jnl Fluid Mech*, 1983, vol 127, pp 473-496.
- 13) Autret A et al, "Finite Element Computation of a Turbulent Flow over a Two Dimensional Backward Facing Step", *Int Jnl for Numerical Methods in Fluids*, vol 7, pp 89-102, 1987.
- 14) Spalding D B and Hegbusi, "Turbulent Flow Downstream of a Backward Step", pp 18.20-18.25, 1983.
- 15) Gooray et al, "Improvements to the $K\epsilon$ Model for Calculations of Turbulent Recirculating Flow", *Symposium on External Flows*, Bristol, pp 18.26-18.29, 1972.
- 16) Karmalakis, G E et al, "Large Eddy/RNG Simulation of Flow over a Backward Facing Step", *Engineering Turbulence Modelling and Experiments*, Elsevier Science Publishing Co, Inc 1990 pp 269-278.
- 17) Spalding D B " Turbulence models: a lecture course. Imperial College, London, Report CFD/82/4, 1983.
- 18) Makiola, B and Buck, "Experimental Investigation of a Single Sided Backward Facing Step Flow with Inclined Step Geometries", *Eng. Turb. Modelling & Experiments*, Elsevier Sc. Publ., 1990, pp 487-497.
- 19) Kim J, Kline, S J and Johnstone, J P, "Investigation of a Reattaching Turbulent Shear Layer: Flow Over

- a Backward Facing Step", Jnl of Fluids Engineering, vol 108, pp 64-75, 1985.
- 20) Kwon, O K and Pletcher, "A Viscous-Inviscid Interaction Procedure", pp 64-74, Jnl Fl. Eng., vol 108, 1986.
 - 21) Fletcher, C A and Barbuto, "Flow in Rearward Facing Cavities" pp 176-184, Appl Math. Mod., vol 10, 1986.
 - 22) Isomoto, K and Honami, S, "The Effect of Inlet Turbulence Intensity on the Reattachment Process over a Backward Facing Step", 1989.

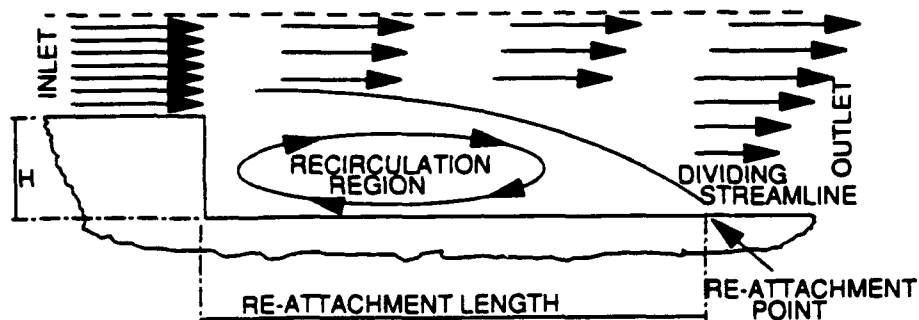


Fig 1: Flow regime behind a rearward facing step

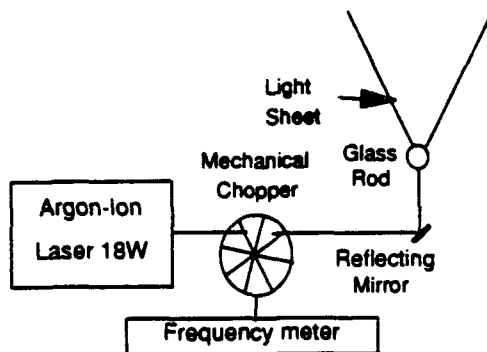


Fig 2: Transmitting optics

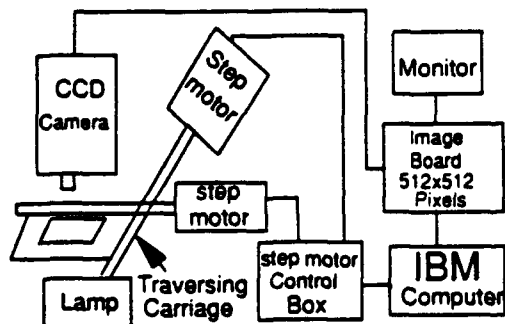


Fig 3: Image processing system

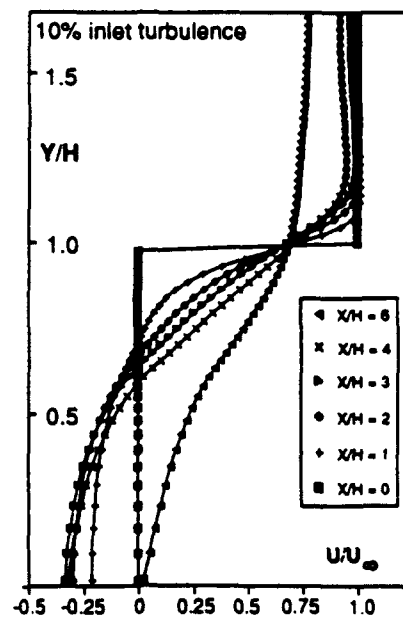
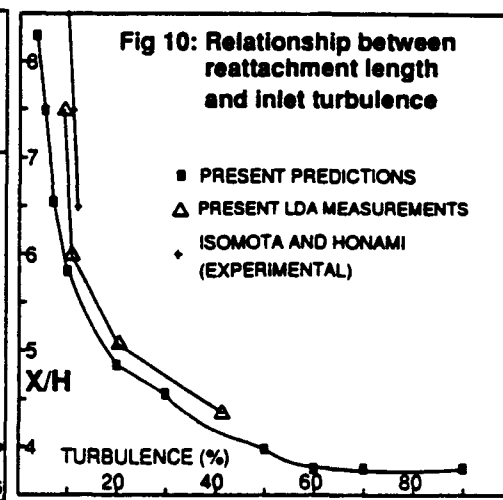
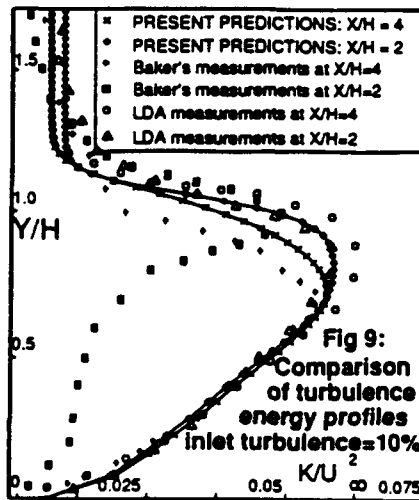
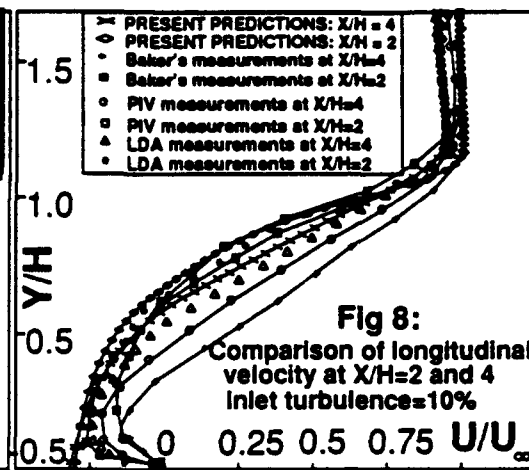
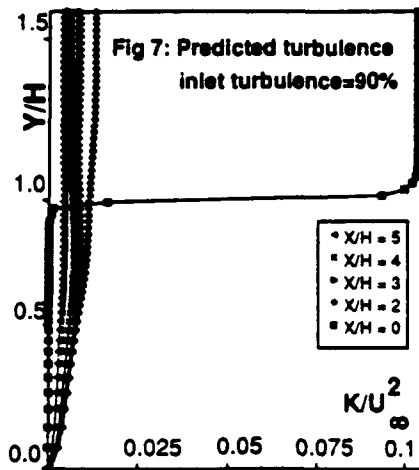
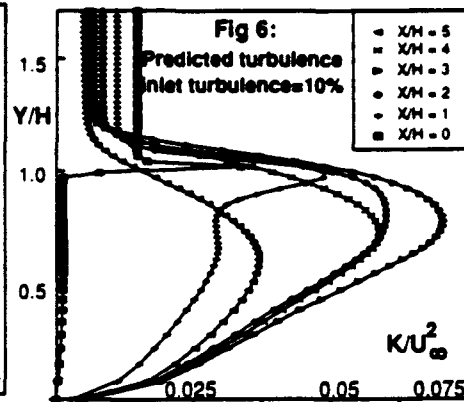
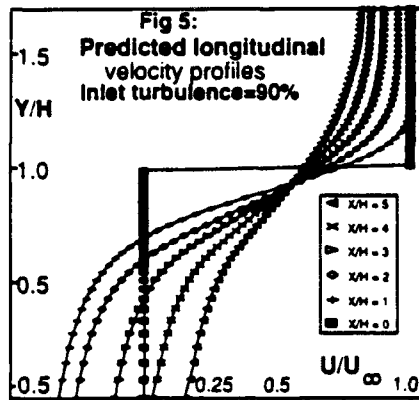


Fig 4: Longitudinal velocities



QUASI-TWO-DIMENSIONAL TURBULENCE AND STOCHASTIC TRAVELING
WAVES IN THE STRATOSPHERE AND IN THE LABORATORY

H. Branover, A. Bershadskii, A. Eidelman, and M. Nagorny

Center for MHD Studies

Ben-Gurion University of the Negev

P.O.B. 653, Beer Sheva, Israel

Abstract

On the basis of data produced by measurements conducted in the stratosphere and in laboratory models (by the authors and other researchers), it has been shown in this paper that turbulence in the stratosphere is of a quasi-two-dimensional type. Such a turbulence appears as a secondary stable regime after the loss of two-dimensional turbulence stability because of three-dimensional disturbances (helical traveling waves). The energy spectra pertaining to this type of turbulence are considerably different from energy spectra of two-dimensional turbulence. Nevertheless, inverse energy transfer actually exists, albeit it has essentially a different nature than in the case of two-dimensional turbulence (transfer from vortexes to helical waves).

1. Instability of Two-dimensional Turbulence in the Stratosphere and the Laboratory

Initial theoretical works on two-dimensional turbulence acknowledged its instability in three-dimensional space [1]. However, secondary turbulent motions ensuing as a result of two-dimensional motion-instability can be stabilized by such external stabilizing factors as stratification, rotation or strong magnetic fields if the liquid has a high conductivity. These secondary, quasi-two-dimensional motions, having become stable, are actually the ones which arise in natural surroundings. In some cases, the stabilizing factor is so strong that it overwhelms

the instability of the initial two-dimensional motion caused by three-dimensional disturbances, and then, intrinsic two-dimensional turbulence can take place.

Instability of two-dimensional turbulence in three-dimensional space will primarily display itself by exciting waves which bend the two-dimensional motion-planes. These travelling waves will bring about fluctuation of average turbulent energy dissipation rates ($\bar{\epsilon}$). As is generally known [1-3] the value $\bar{\epsilon}$ plays a major role in spectrum formation on such scales when direct viscosity influence can be ignored and where everything depends only on energy transfer between fluctuations of different scales in the so-called inertia-interval.

If the space-scale of the principle mode of these waves L is much larger than scale L^* on which energy is injected into turbulence, then in the scale-interval between L and L^* , $\bar{\epsilon}$ will not be the most important parameter any more the crucial one will be average rate of ϵ -fluctuation, i.e. a value $|\partial \bar{\epsilon} / \partial z|$ where z is the coordinate along the z perpendicular to the two-dimensional turbulence-plane. Thus, the two-dimensional plane-bending waves will propagate specifically along axis in three-dimensional space. In those cases when $\bar{\epsilon}$ was the only crucial parameter it was decided on the basis of dimensional consideration [1,3] to express the energy spectrum in the following way:

$$E \sim (\bar{\epsilon})^{2/3} k^{-5/3} \quad (1)$$

where E is the spectral density of kinetic energy and k - the wavenumber.

On a scale interval, when $L \gg r \gg L^*$, where the only crucial parameter is $|\partial \bar{\epsilon} / \partial z|$ dimensional consideration leads to:

$$E \sim \left| \frac{\partial \bar{\epsilon}}{\partial z} \right|^{2/3} k^{-7/3} \quad (2)$$

As we can see, the difference between the two spectral laws (1) and (2) is considerable. As to the direction of energy transfer on a scale-range between L and L^* , it is clear that energy exciting the three-dimensional oscillations of two-dimensional turbulence planes is supplied from the same source as the rest of the energy generating two-dimensional turbulence. Since $L > L^*$, the energy going into motion on $\sim L^*$ - scales must be transferred towards larger scales $\sim L$, i.e. from the smaller scales to the larger ones. Hence, in the scale-range which obeys the spectral law (2) inverse-energy transfer will take place. However, the nature of this inverse transfer is essentially different from that of two-dimensional turbulence proper [1-3].

Secondary motion as travelling three-dimensional waves, can be stabilized by external stabilizing factors. In this case a quasi-two-dimensional turbulence on a certain large-scale interval characterized by inverse energy transfer would be brought about.

Recent spectral data obtained in the framework of "Global Atmospheric Sampling Program" (GASP) for the stratosphere is presented in Fig. 1 [2]. Older data [4] is presented in Fig. 2. The straight lines in Figs. 1 and 2 are included so as to compare with the dependence (2). In Fig. 3 one can see the results of spectral energy transfer - function measurements corresponding to measurements shown in Fig. 2. The negative values of the spectral transfer function correspond with inverse energy transfer. Similar results (a spectrum of the type (2) and inverse-energy transfer on the same scale interval) were also obtained in the laboratory measurements of turbulent stratified liquid flow generated by a hydrodynamic grid [5].

The situation considered above pertains to the case when the initial two-dimensional turbulent spectrum was determined by spectral energy transfer (parameter $\bar{\epsilon}$). In the case of two-dimensional turbulence inertial spectra determined by enstrophy transfer are also possible [2,3]. For the case when the only crucial external parameter in the inertial interval is ϵ_ω again from dimensional considerations, the following spectral law was established [2,3]

$$E \sim (\bar{\epsilon}_\omega)^{2/3} k^{-3} \quad (3)$$

And in this case, the instability of two-dimensional turbulence in three-dimensional space leads to changes in the spectral law. Similarly to the transformation of law (1) to law (2), formula (3) is also transformed to the following:

$$E \sim \left| \frac{\partial \bar{\epsilon}_\omega}{\partial z} \right|^{2/3} k^{-11/3} \quad (4)$$

As to the inverse energy transfer, all the previous discussions remain valid. However, the structure of travelling waves bending the two-dimensional turbulence surface in this case will be different. This interesting issue will not be discussed in detail here. We will just note that problems relevant to wave structure distinction in the first and second cases depend on different types of breaking reflexion symmetry and are related to such fundamental concepts as helicity and superhelicity [6].

Spectral energy data shown in Fig. 4 was obtained in laboratory where quasi-two-dimensional turbulence was generated by a grid-bars parallel to uniform magnetic field B[7]. Straight lines are plotted in Fig. 4 so as to compare them with laws (2) and (4). The electrical conductivity of liquid mercury is high enough to allow an external magnetic field to exert a strong force influencing its motion.

In order to demonstrate in a direct manner the presence of inverse energy transfer in this type of turbulence, the wake of a separate grid-bar, parallel to the external magnetic field was investigated. The development of the wake behind the bar in the presence of magnetic field and in its absence is shown in Fig. 5. It is evident that in the absence of a magnetic field the velocity profile in the wake behind the bar becomes flatter at greater distances from the bar. This is accounted to energy transfer from fluctuations of large space-scales to

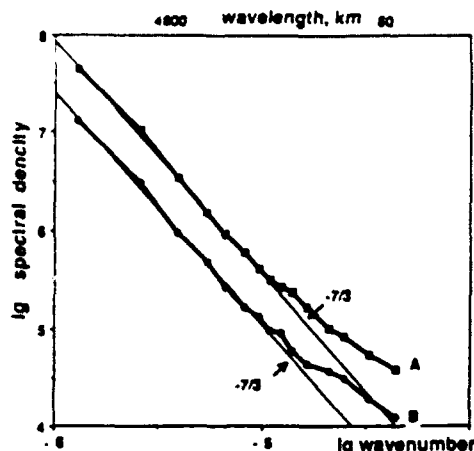


FIGURE 1. Spectra from the GASP flights in stratosphere at least 4800 km long: A-kinetic energy; B-temperature.

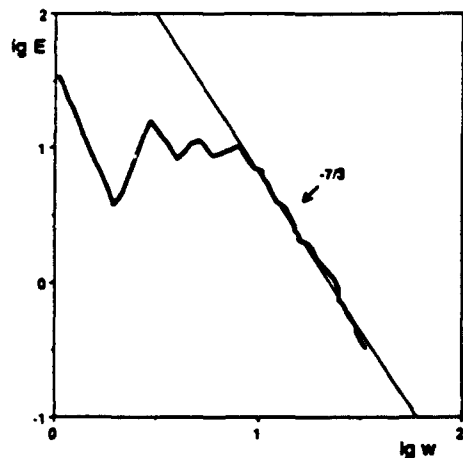


FIGURE 2. Kinetic energy spectrum, arbitrary units.

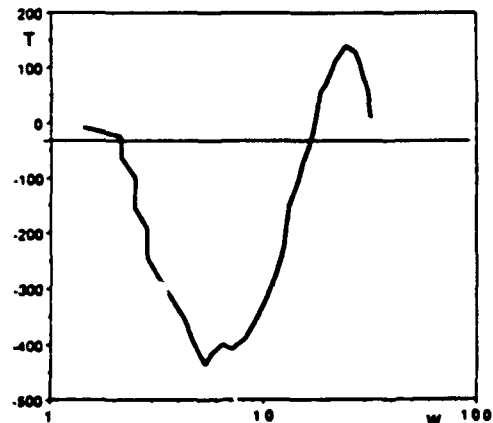


FIGURE 3. Integrated values of the resolved part of the nonlinear kinetic energy flux term. Negative values imply upscale transfer from higher to lower wave numbers.

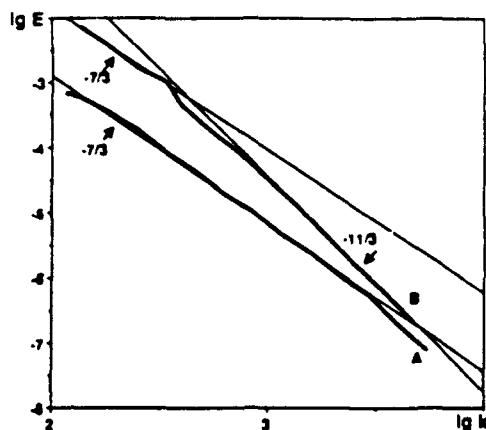


FIGURE 4. Turbulent spectra in the channel with bars parallel to the magnetic field for different values of $Ha/Re \cdot 1000$: A - 4.8; B - 10.

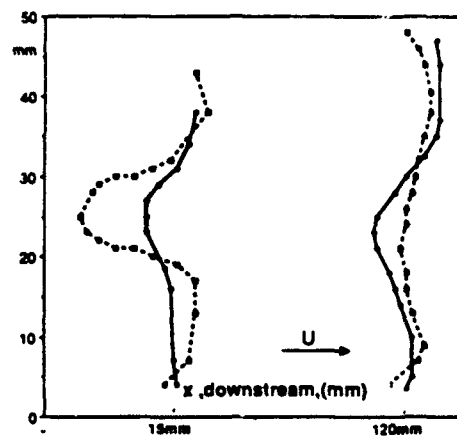


FIGURE 5. Composite normalized velocity profiles downstream of bar, solid lines-magnetic field 0.39 T, dashed lines - 0.

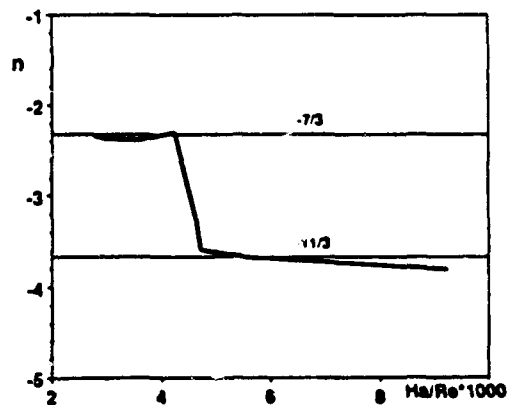


FIGURE 6. The loss of stability and violation of symmetry change the power n in the spectral law.

fluctuations of smaller space-scales, and their subsequent dissipation associated with viscosity. As to the wake behind the bar in the presence of a magnetic field it behaves in quite an unusual manner. Instead of the velocity profile getting flatter it preserves its convex form at great distances away from the bar. This is caused by the inverse-energy transfer.

Fig. 6 demonstrates that the change of motion regimes described by spectral laws (2) and (4) are associated with the loss of stability and violation of symmetry. In this figure the vertical axis is used for values of power in the spectral law for the longitudinal fluctuations component of the velocity field ($E \sim k^{-n}$) and the horizontal axis — for values of parameter Ha/Re , ($Ha \sim |B|$). From Fig. 6 it can be seen that the sharp change of the stable quasi-two-dimensional turbulence from (2) to (4) takes place when the external stabilizing parameter (in this case-magnetic field B) passes a certain critical value.

Measurements conducted in the stratosphere indicate the validity of just one formula (2). This fact shows that factors stabilizing the quasi-two-dimensional turbulence in the stratosphere usually are not strong enough to keep in force the second quasi-two-dimensional regime (4).

2. Quasi-two-dimensional Turbulence Diffusion of Passive Scalar

Dimensional considerations employed in section 1 for deriving scaling spectral laws can also be used to obtain the dependence of the effective value of diffusivity K^* on scale L . If, indeed the only dimensional parameter in the inertial interval is the value $|\overline{\partial \epsilon / \partial z}|$, then, taking into account dimensional considerations, we obtain

$$K^* \sim |\overline{\frac{\partial \epsilon}{\partial z}}|^{1/3} L^{5/3} \quad (5)$$

Another measurable quantity characterizing the diffusion of passive impurity is the mean square relative velocity of particle pairs as a functional relative separation L :

$$(\frac{\partial L}{\partial t})^2 \sim |\overline{\frac{\partial \epsilon}{\partial z}}|^{2/3} L^{4/3} \quad (6)$$

We should note that for intrinsic two-dimensional turbulence, $K^* \sim L^{4/3}$ in the energy transfer interval, and $K^* \sim L^2$ in the interval of enstrophy transfer. At the same time $|\overline{\partial L / \partial t}|^2 \sim L^{2/3}$ in the energy transfer interval and $|\overline{\partial L / \partial t}|^2 \sim L^2$ in the interval of enstrophy transfer. In both cases the laws are substantially different from those of (5) and (6).

Experimental data obtained in the lower layers of the stratosphere [8] for K^* and for $(\partial L / \partial t)^2$ are shown in Figs. 7,8. The straight lines are meant to be compared with the laws (5) and (6). Similar results have been obtained in the experiment devoted to passive impurity diffusion in a rotating liquid [9] (Fig. 9).

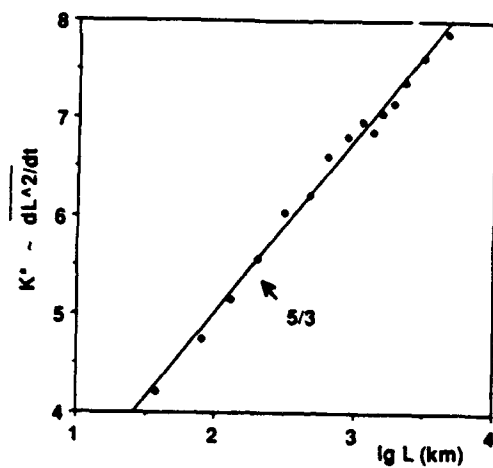


FIGURE 7. Mean diffusivity in the stratosphere

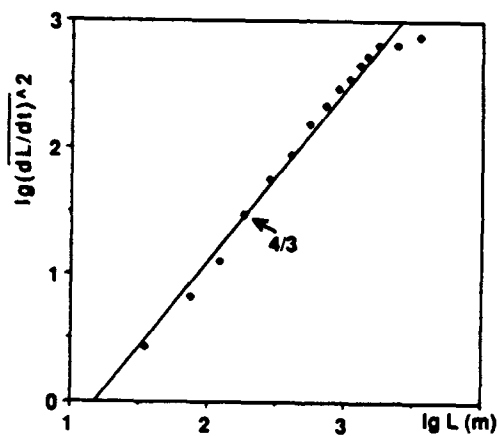


FIGURE 8. Mean square relative velocity of balloon pairs in the stratosphere.

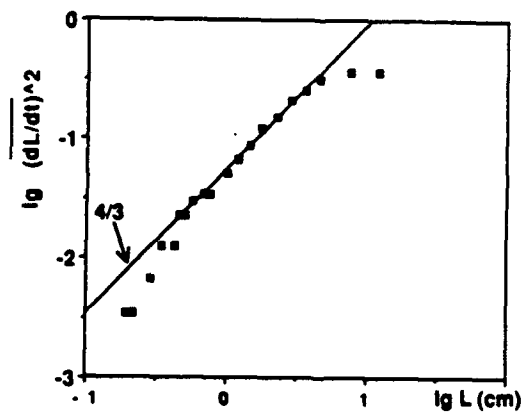


FIGURE 9. Mean square relative velocity of pair of particles in rotating fluid.

3. Fractal Dimension of Surfaces in the Quasi-two-dimensional Turbulence.

First of all a strictly two-dimensional turbulence obeying spectral law (1) will be examined. The expanding passive scalar patch of a turbulized liquid is to be monitored. Approximately the boundary of the patch formed by sections of equal length $\eta(t)$ - Kolmogorov scale. Assuming the effective radius of the patch to be $R(t)$, the number of η -sections in the broken line being approximated

$$N \equiv \left(\frac{\eta}{R}\right)^{D_p} \quad (7)$$

where D_p is the fractal dimension of the patch-boundary. Determining the effective increase of the patch-area dS during a time-period of dt , we introduce an effective instant velocity $v(\eta, t)$ of the η -section motion in a direction perpendicular to this section. Then

$$dS \equiv \eta(v \cdot dt)N \quad (8)$$

Substituting (7) into (8):

$$dS \equiv \eta(v \cdot dt) \left(\frac{\eta}{R}\right)^{D_p} \quad (9)$$

The expression (9) can be written as:

$$dS \equiv F(t)R^{D_p} dt \quad (10)$$

where

$$F(t) \equiv \eta^{1-D_p} v(\eta, t) \quad (11)$$

If scale R belongs to the inertial interval, then $F(t)$ can depend only on $\bar{\epsilon}$ for Kolmogorov's turbulence and

$$dS = c(\bar{\epsilon})^x R^{D_p} dt \quad (12)$$

where c and x are certain non-dimensional constants. D_p and x can be determined by dimension considerations:

$$dS = c_1(\bar{\epsilon})^{-1/3} R^{4/3} dt \quad (13)$$

Consequently, in the two-dimension case with Kolmogorov's turbulence, $D_p = 4/3$ in the inertial interval. This result has been known and experimentally proved, see, for instance, the review [10].

Above consideration can also be readily conducted in quasi-two-dimensional turbulence for which the crucial dimensional parameter is $|\partial \epsilon / \partial z|$. In this case, correspondingly, we obtain

$$ds = C \left| \frac{\partial \epsilon}{\partial z} \right|^{1/3} R^{5/3} dt \quad (14)$$

Hence, for turbulence of such kind

$$D_p = 5/3 \quad (15)$$

The data obtained in laboratory simulation with stratified rotating liquid [11] is shown in Fig. 10. Here, $D_p = 4/3$ at small scales, and $D_p = 5/3$ at large scales, are marked by straight lines. Atmospheric observations conducted on scales $\leq 10^3$ km showed $D_p \equiv 4/3$ [10]. One can expect a value $D_p = 5/3$ on scales $\geq 10^3$ km (Fig. 1).

4. Solitons in Quasi-two-dimensional Turbulence

Travelling waves after having lost their stability appear as a secondary stable regime, gain the capacity to engender space-localized three-dimensional (helical) formations of a soliton nature (e.g. [12-14]). The physical structure of these solitons can be easily understood, provided that the vortex perpendicular to the two-dimensional turbulence plane are represented in filament form [3,12]. The initially small disturbance of such a filament will bring about two helical local formation, propagating in both directions [12-14]. Hasimoto [15] has conducted an analytical study of these helical solitons for a laminar case. The question is: how will the show-up of these solitons in large scale turbulence influence its behavior. It is clear that these solitons are going to act as a supplementary sink of energy driven into motion on smaller scale (see section 1 about the mechanism of inverse-energy transfer into travelling waves). However, these energy sinks are space-localized, so the energy spectrum corresponding to them would not be determined by the space-density dissipation as in the case of space-distributed energy sinks), but by the total dissipation.

$$\epsilon_0 = \int_V \epsilon(\vec{r}) d\vec{r} \quad (16)$$

So, taking into account dimension considerations, a scaling dependence of large scale spectral energy density can be presented:

$$E \sim \epsilon_0^{2/3} k^{1/3} \quad (17)$$

This would essentially be a long-wave energetic spectrum of "turbulence with solitons". In the short wave range of the spectrum, structures based on discrete discontinuities described by Saffmen [16] will, most likely, dominate [17]. Accordingly, in the short wave range, the spectrum law "-11/3" will tend to transfer to law "-4".

The spectra shown in Fig. 11 we obtained in the same conditions as data presented in Fig. 6 beyond the critical point. A very broad low frequency range of the spectrum, corresponding to the soliton spectral law of "1/3" (17) can be noticed.

It is also evident that as the stabilizing factor (magnetic field) grows, so the energy of the longitudinal velocity fluctuations arise, mainly because of the "soliton" part of the spectrum. This was accompanied by a growth of the number of soliton states. A typical oscillogram segment of the longitudinal velocity fluctuations in

a magnetic field $B \cong 1T$ is shown in Fig. 12. Also, a "soliton mode" was accomplished at high angular rotation rates in a numerical turbulence experiment, described in [18], see Fig. 13 and in laboratory experiment [19]. One can suppose that such phenomena as tornado and related atmospheric cataclysms can be, to a certain extent, attributed to the "soliton mode" of a quasi-two-dimensional turbulence.

References

1. Batchelor, G.K., The theory of homogeneous turbulence, Cambridge University Press, London, 1953.
2. Gage, K.S. and Nastrom, G.D., Theoretical interpretation of atmospheric wavenumber spectra of wind and temperature observed by commercial aircraft during GASP. *J. Atmos. Sci.* 43, N7, 729-740 (1986).
3. Kraichnan, R.H. and Montgomery, D., Two-dimensional turbulence, *Repts. Prog. Phys.*, 43, 547-619 (1979).
4. Boer, G.J. and Shepherd, T.G., Large-scale two-dimensional turbulence in the atmosphere, *J. Atmos. Sci.* 40, 164-184 (1983).
5. Itsweire, E.C. and Helland, K.N., Turbulent mixing and energy transfer in stably stratified turbulence, *Seventh Symposium on Turbulence and Diffusion, Colorado*, 172-175 (1985).
6. Kida, S., Takaoka, M. and Hussain, F., Collision of two vortex rings, *J. Fluid Mech.* 230, 583-646 (1991).
7. Branover, H., Sukoriansky, S., Turbulence peculiarities caused by interference at magnetic fields with the energy transfer phenomena. *AIAA, Progress in Astronautics and Aeronautics*, 112, 87-99 (1988).
8. Morel, P. and Larcheveque, M., Relative dispersion of constant-level balloons in the 200-mb general circulation, *J. Atm. Sci.*, 31, 2189 (1974).
9. Mory, M. and Hopfinger, E.J., Structure functions in a rotationally dominated turbulent flow, *Phys. Fluids*, 29 (7), (1986).
10. Sreenivasan, K.R., Fractals and multifractals in fluid turbulence. *Annu. Rev. Fluid Mech.*, 23, 539 (1991).
11. Tseng, R.-S. and Maxworthy, M., The dynamics and geometry of two-dimensional turbulent front, *Phys. Fluids*, A(27), 1224 (1990).
12. Betchov, P., Transition in: *Handbook of turbulence*, v. 1, Plenum Press, N.Y. (1977).
13. Goldstein, R.E., Gunaratne, R.E., Gil, L. and Couillet, P., Hydrodynamic and interfacial patterns with broken space-time symmetry, *Phys. Rev. A* 43, 6700 (1991).

14. Couillet, P., Goldstein, R.E. and Cunarathne, G.H., Parity-breaking transitions of modulated pattern in hydrodynamics systems, *Phys. Rev. Lett.*, 63, 1954 (1989).
15. Hasimoto, H., A soliton on a vortex filament, *J. Fluid Mech.*, SI, 477 (1972).
16. Saffman, P.G., On the spectrum and decay of random two-dimensional vorticity distributions at large Reynolds number, *Stud. Appl. Math.*, 50, 377 (1971).
17. Pomeau, Y., Pumir, A. and Pelce, P., Intrinsic stochasticity with many degrees of freedom, *J. Stat. Phys.* 37, 39 (1984).
18. Roy, P., Numerical simulation of homogeneous turbulence submitted to two successive plane strains and to solid body rotation, *Prog. Astron. and Aeron.*, 100, 174 (1985).
19. Hopfinger, E.J., Browand, F.K. and Gagne, Y., Turbulence and waves in a rotating tank, *J. Fluid Mech.*, 125, 505 (1982).

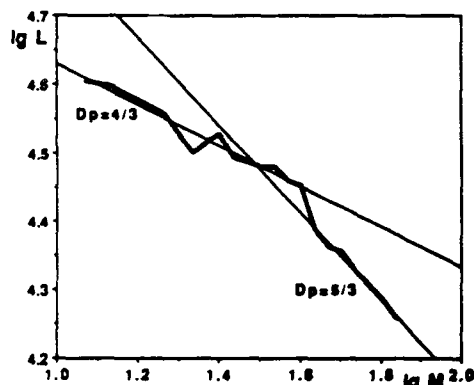


FIGURE 10. Interface length L measured with a certain gauge length M versus the value of M itself.

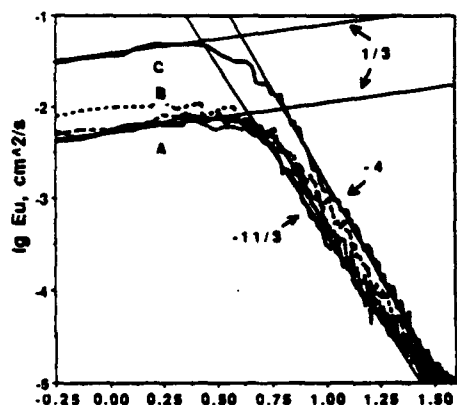


FIGURE 11. Turbulent spectra in the channel beyond the critical value Ha/Re : A - $Ha/Re \cdot 1000 = 5.5$, B - 13.2, C - 17.3.

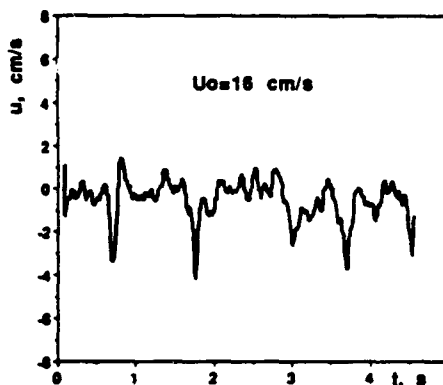


FIGURE 12. A typical oscillogram segment of the longitudinal velocity disturbances at $Ha/Re \cdot 1000 = 17.2$.

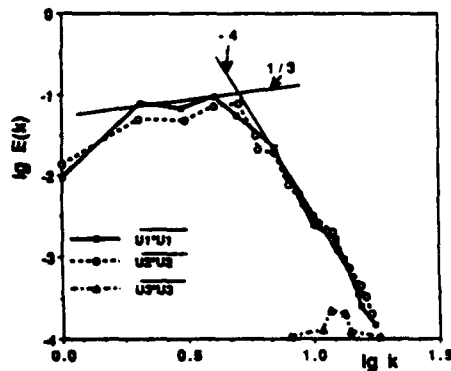


FIGURE 13. Energy spectra for numerical simulation of homogeneous turbulence in rotating fluid.

VORTICITY AND MIXING DYNAMICS IN AXIALLY
PERTURBED COFLOWING JETS

C. Cuerno and A. Viedma
E.T.S. de Ingenieros Aeronáuticos
Universidad Politécnica de Madrid
Pl. Cardenal Cisneros 3
28040 Madrid, Spain

Abstract

The development of coherent structures formed between coflowing vertical jets at moderate Reynolds numbers has been studied experimentally. By means of LDV and flow visualization it has been possible to produce data enough to describe the flow subjected to the effects of axial forcing. Flow mapping includes axial and radial phase-averaged velocity profiles, vorticity maps and streamlines. Vorticity dynamics inferred from these data shows a good agreement with numerical simulations. Mixing between the streams is also analyzed, improving with higher levels of forcing amplitude.

1 Introduction

The axisymmetric instability of a cylindrical laminar shear layer is well understood, both from a theoretical and experimental point of view (Becker and Massaro (1968), Beavers and Wilson (1970), Crow and Champagne (1971), Michalke (1984)). This instability produces the roll up of the cylindrical vorticity sheet into periodic vortex rings. The evolution has also been detected in transitional and turbulent jets (Yule (1978), Tso and Hussain (1989)).

Some authors (Yule (1978) have shown that the transition to turbulence in jets involves a relatively orderly three-dimensional deformation of the initial vortex rings. This suggests that a global comprehension of the growth and development of the initial and round vortex rings formed at the jet exit nozzle can give the key to understand some aspects of the transition to turbulence.

The actual investigations of axisymmetric coflowing jets are focused mainly on flow visualization due to its simplicity to produce results faster

than other experimental techniques (Agüi and Hesselink (1988), Chao et al (1990), Lasheras et al (1990)) although some numerical simulations are found (Acton (1980), Agüi and Hesselink (1988), Martin and Meiburg (1991)). Being these works very interesting, it is clear that detailed quantitative experimental results of velocity profiles, vorticity and mixing are needed. The experiment described in this paper is an attempt to characterize the flow topology, using LDV to obtain quantitative data of velocity and vorticity distributions and mixing evolution, in coflowing jets that are axially forced to lock to a given value the frequency and wavelength of the jet's vortex rings and to increase the periodicity which allows a phase locking of the measuring systems. The effects of more intense structures due to perturbation on vorticity and mixing are also reported.

2 Experimental Apparatus and Equipment

The experiments were conducted in a high versatile, atmospheric pressure, open return and vertical wind tunnel where either non-reacting, heat transfer or combustion experiments can be conducted. A layout of the flow facility is shown in Figure 1. The wind tunnel consists of three coflowing, low-speed axisymmetric streams independently created. The inner stream is produced through a circular nozzle with an outer diameter of 24.3 mm. This jet is surrounded by a coflowing concentric gas stream which discharges into the test section through a round nozzle, 160 mm in diameter. The tertiary coflowing jet is formed by atmospheric air drawn into the square-cross test section, through the ejection-like effect produced by these coflowing streams discharge. A detailed description of the experimental apparatus can be found elsewhere (Lasheras et al (1990)).

The periodic streamwise forcing is produced through a vibrating membrane located in the settling chamber of the inner flow. At the base of a small chamber, a loudspeaker fed with a sinusoidal wave generates pressure pulses that result in the periodic displacement of the membrane in a piston-like type fashion. The membrane fluctuation adds a streamwise velocity perturbation of a given amplitude and frequency to the inner jet.

Velocity measurements have been carried out with a two-component, Ar-Ion LDV system arranged in forward-scatter mode. A counter-type processor was used for laser signal handling. Two Bragg cells were installed to detect reverse

flow produced by the forcing external perturbations. Incense smoke and oil drops have been the kind of particles used for seeding the flow.

Flow visualization has been the first step before the LDV study and a helpful tool to understand the dynamics of the structures. Images of the forced flow have been obtained visualizing with a laser sheet TiO_2 particles at the interface of the two jets. These particles appear in the reaction between TiCl_4 , present in the dry air of the inner jet, and the atmospheric air of the surrounding jet. More detailed descriptions of the LDV and visualization systems can be found elsewhere (Lasheras et al (1990), Cuerno (1992)).

3 Results and Discussion

As a preliminary study, LDV data from the unforced flow have been processed to obtain mean axial velocity profiles and turbulence levels up to $z/D = 8$ (Cuerno (1992), Cuerno and Viedma (1992)). These profiles show that the mixing layer is not completely developed and the flow is still dominated by the nozzle wake effect showed by a loss of momentum in the mean axial velocity profiles and a peak in the turbulence levels. The turbulent fluctuations at the exit in the primary jet are about 1%, as in other experiments (Crow and Champagne (1971), Hussain and Zaman (1981)), and 2% for the secondary jet. The exit boundary layer shape factor for the primary jet is $H = \delta_1/\theta = 2.49$ close to the Blasius profile for the laminar boundary layer, and $Re_D = 1000$.

Also, the instability frequencies of this configuration have been studied. Through the estimation of autocorrelations and power spectra of axial velocity data in the primary and secondary jets have been detected two values, 10 and 16 Hz. Each value is associated to a zone of the flow. The frequency of 16 Hz appears up to $z/D = 6$ where coexists with 10 Hz. For $z/D > 6$ the spectrum is dominated by 10 Hz. So it seems that 16 Hz is associated to some initial instability and 10 Hz to other process. The Strouhal number based on the initial momentum thickness is 0.019 for 16 Hz and the Strouhal number based on the jet diameter is 0.36 for 10 Hz. These values fall in the range of St for the initial instability (which depends on the initial velocity profile and vorticity distribution) and the preferred mode (or jet column mode, which is defined as the most amplified mode at the end of the potential core and is related to some global jet instability) for axisymmetric jets (Gutmark and Ho (1983)). The first one was selected as the forcing frequency because locking

the excitation at that value the generation of structures in the flow is more repetitive, enabling the use of phase-locked analysis.

Once this value being obtained, the flow has been forced streamwise with a single sinusoidal wave at 16 Hz and two different amplitudes of forcing corresponding to 28 and 54 % in velocity (% amplitude of forcing = $(V_{zmax} - V_{zmin} / V_{zmax} + V_{zmin}) \times 100$). The lower one is the most common condition found in other works and the higher one was selected due to the apparition of small counter-rotating vortex rings. Figures 2 and 3 show phase-locked visualizations of the selected excitation conditions. Phase-locked LDV measurements of axial and radial velocity have been obtained at four downstream distances $z/D = 0.16, 1, 2$ and 3 in order to get a detailed description of the forced near field, measuring up to 59 radial positions along 29 mm at each profile.

Applying phase average processing to these measurements has been possible to map the response of the flow along the cycle of perturbation. The details about the scheme used to interpolate the axial velocity for $z/D < 3$, the estimation of the convection velocity of the structures and the estimations of the phase-averaged streamlines and vorticity can be found elsewhere (Cuerno (1992), Cuerno and Viedma (1992)). As a first qualitative result, at every downstream station where we measured and in both conditions of amplitude of forcing, velocity maps as the one showed in Figure 4 have been obtained. In this map we present simultaneously, in a reference system moving with the convection velocity, radial and axial phase-averaged velocities in terms of radius and phase. This kind of figures allow a preliminar identification of structures in the flow.

More complete information about the evolution of the structures can be found in the study of the streamlines due to its strong linking with the flow visualization. As the flow is periodic, axisymmetric and incompressible the phase-averaged stream function can be estimated in moving or fixed reference systems, which allow to obtain phase-averaged streamlines for the whole flow ($z/D \leq 3$) just interpolating the axial velocity profile using (1). Figure 5 shows the evolution of the streamlines for the higher excitation case in moving reference system for six phase positions along the cycle of perturbation (one cycle is subdivided into 30 intervals), giving a clear image of a section of the vortex rings and their downstream evolution along the cycle.

The next step is going to be the study of the phase-averaged vorticity. Figures 6 and 7 show the vorticity maps at $z/D = 0.16, 1, 2$ and 3 for the lower and higher excitations cases. At $z/D = 0.16$ for the lower case the positive vorticity is distributed along the interface between the streams in a way like the unforced flow. With increasing values of z/D the positive vorticity concentrates forming vortex rings with almost circular section. For the higher case, the effect of the increasing amplitude of excitation can be seen as a greater concentration of positive vorticity to form rings even from $z/D = 0.16$. From $z/D = 1$ there are secondary negative vorticity zones between consecutive vortex rings and seem to be associated to the counter-rotating small vortex, as the ones showed in Figure 3, that appear when the excitation levels grows (Lasheras et al (1990)).

In both cases of excitation the positive vorticity distribution in terms of radius and phase is conical, being the levels of the maximum almost double for the higher case than for the lower. The behavior of these distributions are analogous: the maximum decreases with increasing downstream distances and the vorticity concentrates to form rings although the perturbation level intensify this effect.

These results have been compared with recent works on numerical simulation of jets subjected to axisymmetric perturbations (Martin and Meiburg (1991)) showing a great agreement specially with the lower excitation case: the evolutions of vorticity distributions are analogous, the free stagnation points (in moving reference system) do not form at the center of the region between consecutive vortex but are shifted towards the jet axis (see Figure 4) and as a result the upstream neighborhood of the vortex rings becomes depleted of vorticity more rapidly than the downstream side (see Figure 6).

Finally the variation in mixing between the two streams is going to be analyzed using information from visualization together with streamlines. Comparing phase-locked photographs taken in several phase positions with the streamlines in moving reference systems is possible to measure the radial position of the interface separating mixed from unmixed primary flow for different downstream distances at several phase positions along the cycle. Taking these parameters into the streamlines maps in fixed reference system, the phase-averaged unmixed primary flow can be estimated in terms of downstream distance because there is a proportionality between the flow rate through a

section and the values of the streamfunction at the borders of that section. Figure 8 shows, for both excitation cases, the evolution of the unmixed primary flow with downstream distance. In the near region and for the higher values of z analyzed the mixing levels are analogous, but the great difference is in the intermediate zone. For $0.8 \leq z/D \leq 2.5$ mixing is much more effective with increasing levels of forcing amplitude, for instance, at $z/D = 1.6$ a 70 % of primary flow is mixed for the lower case and 92 % for the higher. Another fact is that the non-linear behavior grows with amplitude levels, as was expected. Although the quantitative data are not completely accurate, this process allow to compare the mixing efficiency with increasing levels of forcing and to show how mixing grows with structures having greater concentrations of vorticity.

4 Conclusions

Using LDV and flow visualization we have been able to produce data enough to obtain a detailed quantitative description of the vorticity and mixing dynamics in the flow formed between axially forced axisymmetric coaxial jets at moderate Reynolds numbers. This study takes flow visualization images of the flow as a first aid to generate a complete quantitative velocity and vorticity description using LDV data, that can be used to complete theoretical models for the behavior of axisymmetric jets.

First of all, the unexcited configuration has been analyzed being comparable to other works. Also, the values of the Strouhal numbers obtained for the instability frequencies are confirmed with the ones presented in other works (Gutmark and Ho (1983), Ho and Huerre (1984)).

The forced flow has been documented with phase-averaged axial and radial velocity profiles, phase-averaged streamlines and vorticity. Basically this configuration is characterized by ring shaped structures associated to positive vorticity that are formed from the exit plane and are convected while develops. An increase in the forcing amplitude means greater intensity of the structures and also the formation of small counter-rotating vortex rings with negative vorticity between consecutive mean structures. The vorticity distributions obtained for the lower excitation case show a very good agreement with numerical simulations (Martin and Meiburg (1991)) not only in the shape but in the dynamics.

Finally, the study about the effect of the amplitude of perturbation on

mixing gives the expected conclusion: mixing improves with increasing levels of forcing due to the more intense structures that produces faster and higher vorticity concentrations.

5 References

- Acton, E. 1980: A modelling of large eddies in an axisymmetric jet. J. Fluid Mech. 98, 1-31
- Agüí, J.C.; Hesselink, L. 1988: Flow visualization and numerical analysis of a coflowing jet: a three-dimensional approach. J. Fluid Mech. 191, 19-45
- Beavers, G.S. and Wilson, T.A. 1970: Vortex growth in jets. J. Fluid Mech. 44, 97-112
- Becker, H.A.; Massaro, T.A. 1968: Vortex evolution in a round jet. J. Fluid Mech. 31, 435-448
- Chao, Y.C.; Han, J.M.; Jeng, M.S. 1990: A quantitative laser sheet image processing method for the study of the coherent structure of a circular jet flow. Exp. Fluids 9, 323-332
- Crow, S.C.; Champagne, F.H. 1971: Orderly structure in jet turbulence. J. Fluid Mech. 48, 547-591
- Cuerno, C. 1992: Experimental study of the coherent structures dynamics in reacting and non-reacting axisymmetric jets (in spanish). Doctor Engineering Thesis, Universidad Politécnica de Madrid
- Cuerno, C.; Viedma, A. 1992: LDA phase mapping of velocity and vorticity in axially perturbed coflowing jets. To be presented at the Sixth Int. Symp. on Appl. Laser Tech. to Fluid Mech., Lisbon 20-23 July
- Gutmark, E.; Ho, C-M. 1983: Preferred modes and the spreading rates of jets. Phys. Fluids 26, 2932-2939
- Hussain, A.K.M.F.; Zaman, K.B.M.Q. 1981: The preferred mode of the axisymmetric jet. J. Fluid Mech. 110, 39-71
- Lasheras, J.C.; Lecuona, A.; Rodríguez, P. 1990: Three-dimensional structure of the vorticity field in the near region of laminar, co-flowing forced jets. In: The global geometry of turbulence. (ed. Jiménez Sendín, J.). Plenum Publishing Corporation
- Martin, J.E.; Meiburg, E. 1991: Numerical investigation of three-dimensionally evolving jets subject to axisymmetric and azimuthal perturbations. J. Fluid Mech. 230, 271-318

- Michalke, A. 1984: Survey on Jet instability theory. Prog. Aerospace Sci. 21, 159-199
- Iso, J.; Hussain, A.K.M.F. 1989: Organized motions in a fully developed turbulent axisymmetric jet. J. Fluid Mech. 203, 425-448
- Yule, A.J. 1978: Large-scale structure in the mixing layer of a round jet. J. Fluid Mech. 89, 413-432

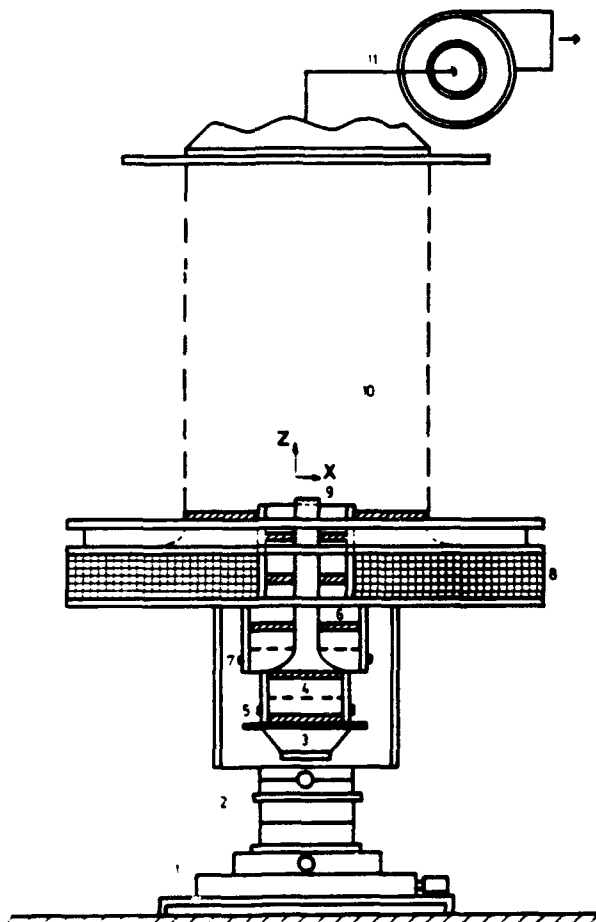


Fig. 1. Schematics of the experimental set-up.
1, 2: horizontal and vertical traversing systems; 3: loudspeaker; 4, 6: primary and secondary settling chambers; 5, 7: primary and secondary flow inlets; 8: tertiary flow inlet; 9: nozzles; 10: test section; 11: exhaust fan.

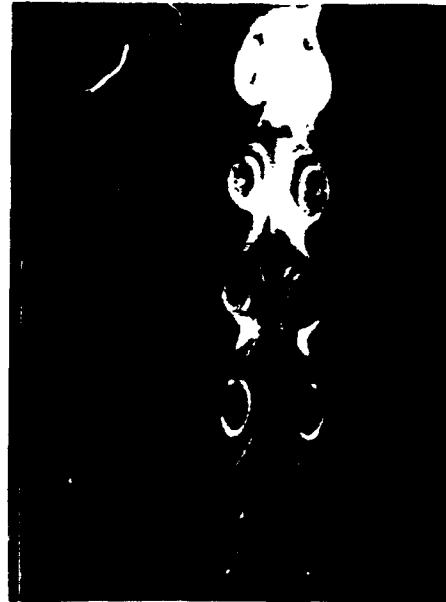


Fig. 2. Phase-locked image of the flow forced at 16 Hz and 28% of perturbation amplitude.

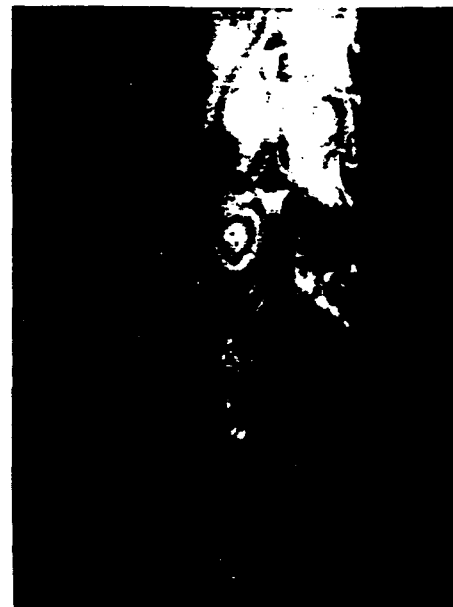


Fig. 3. Phase-locked image of the flow forced at 16 Hz and 54% of perturbation amplitude.

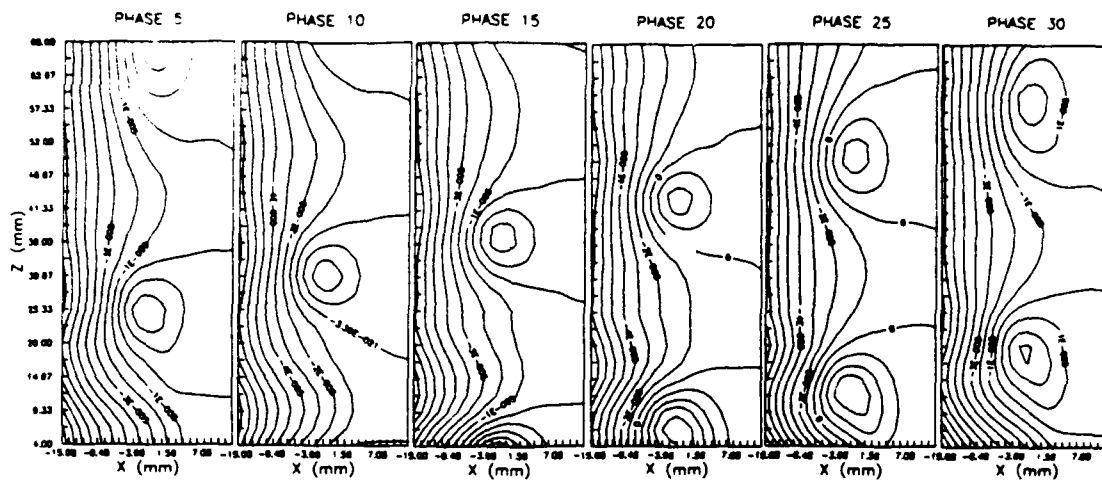


Fig. 5. Evolution of the streamlines in moving reference system for the higher excitation case along the cycle.

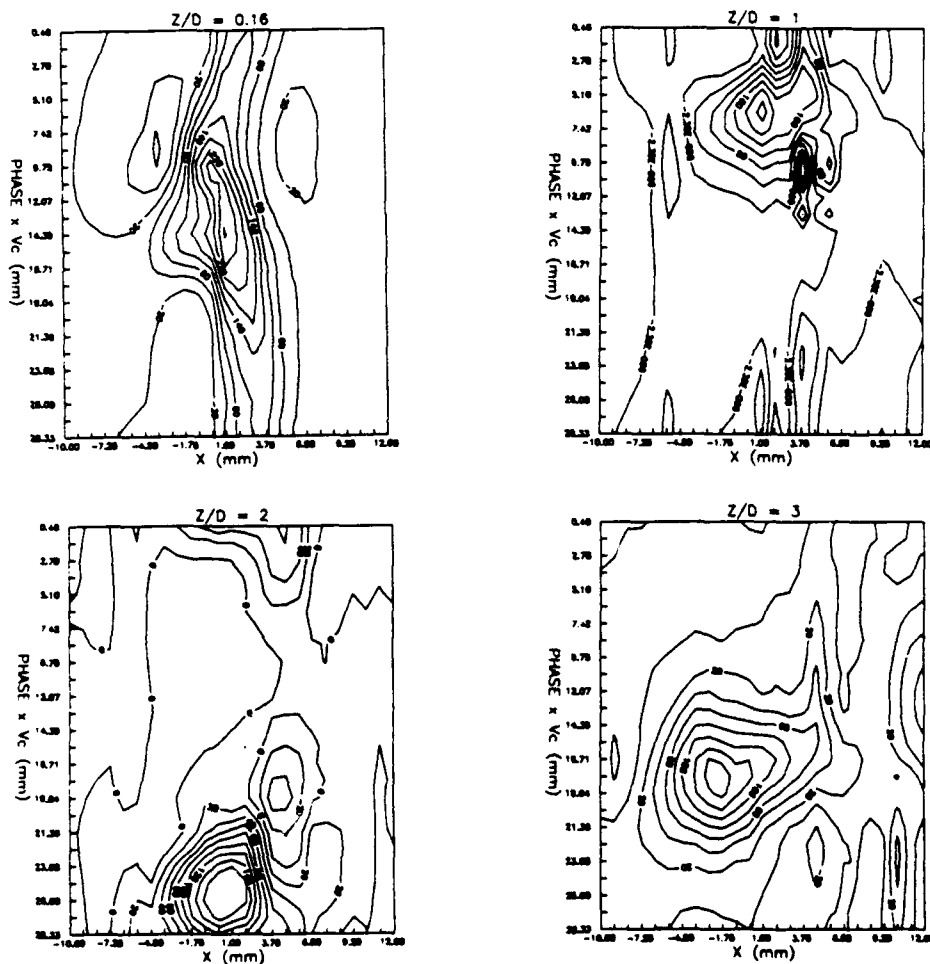


Fig. 6. Vorticity maps at $z/D = 0.16, 1, 2$ and 3 for the lower excitation case. The associated values of ω_{\max} are $300, 240, 160$ and 140 s^{-1} .

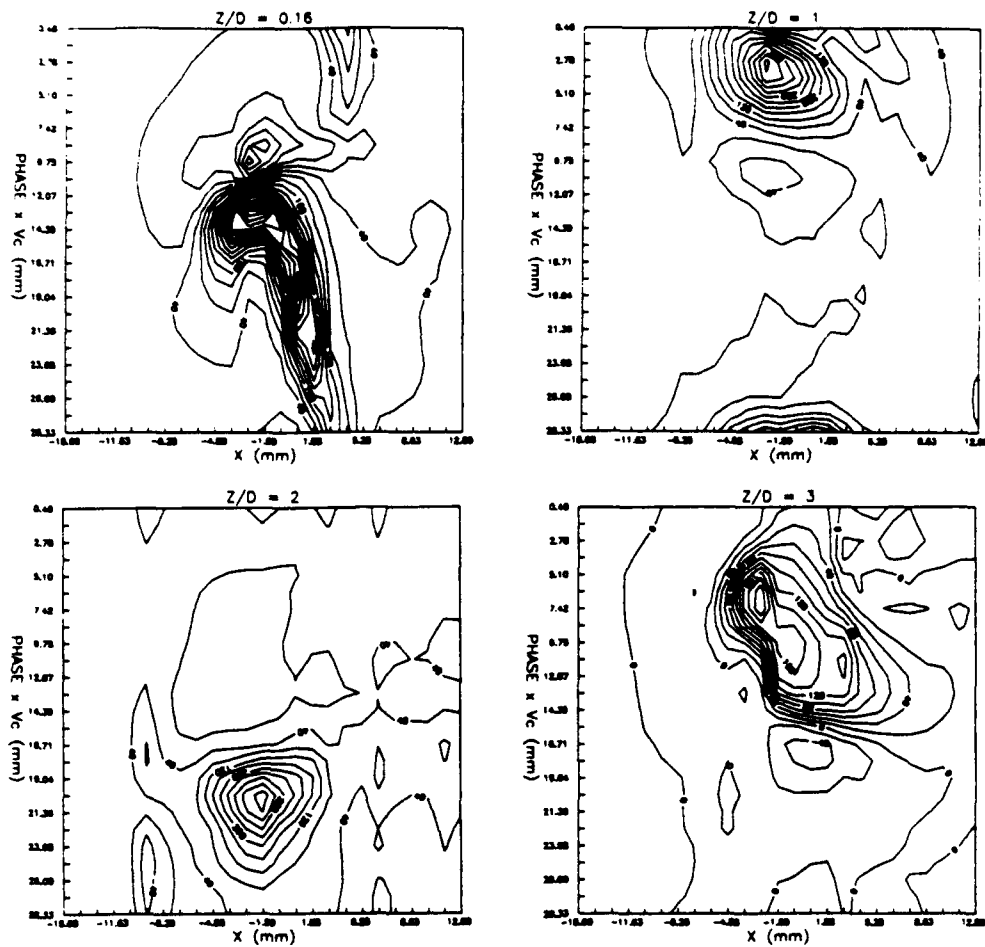


Fig. 7. Vorticity maps at $z/D = 0.16, 1, 2$ and 3 for the higher excitation case. The associated values of ω_{\max} are $560, 440, 360$ and 200 s^{-1} .

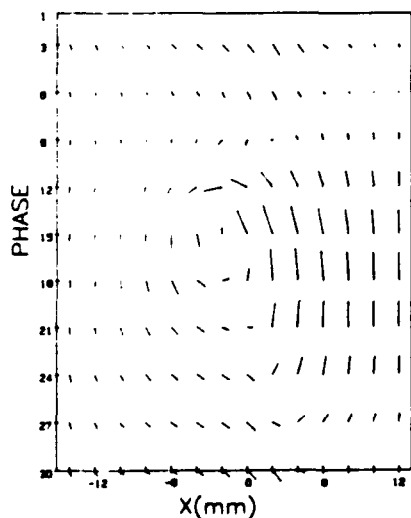


Fig. 4. Velocity map at $z/D = 0.16$ for the higher excitation.

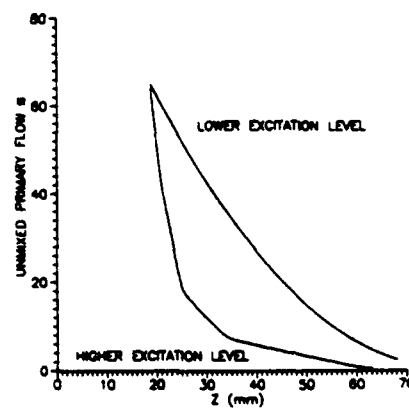


Fig. 8. Evolution of the unmixed primary flow in terms of downstream distance.

LONGITUDINAL VORTICES IMBEDDED IN THE TURBULENT CHANNEL FLOW

S. Lau, V. Schulz¹, V.I. Vasanta Ram
Institut für Thermo- und Fluiddynamik
Ruhr-Universität Bochum
Universitätsstr. 150, D 4630 Bochum, Germany

Abstract

This paper reports results of experiments at Reynolds numbers of 12000 and 36000 in the turbulent channel flow in which imbedded longitudinal vortices are generated by a circular cylinder placed with its axis perpendicular to the walls. Flow surveys were conducted in this geometry using a quadruple hot-wire probe and the wall shear stress vector was measured "directly" by a sublayer fence pair. The probe output was processed to obtain the development of all the Reynolds stress terms in this complex flow. The results show that the Reynolds stress terms containing the spanwise velocity component dominate over others in this disturbed flow. Analysis of the time dependent $u'w'$ - signals indicate the possibility of a significant clustering of events around a characteristic nondimensional time TU_c/D of 2.7.

Nomenclature

H	semi channel height
U_c	centre line velocity of fully developed undisturbed channel flow
D	cylinder diameter
(x,y,z)	streamwise, crosswise and spanwise coordinates, origin located at centre of cylinder on one of the channel walls
U,V,W	mean velocity components
u',v',w'	fluctuating velocity components
u_τ	friction velocity derived from the pressure gradient measurement of the wall shear stress in the undisturbed fully developed channel flow
$\Delta(\)$	denotes incremental stress in () normalised with u_τ^2
T	averaging time in VITA-algorithm
VITH	threshold in VITA-algorithm
$\text{var}(f(t,T))$	variance of $f(t)$ averaged over the time T
σ	ratio, $\text{var}(f(t,T))/\text{var}(f(t,\infty))$

1. Introduction

Large scale longitudinal vortices imbedded in a turbulent shear flow are a prominent feature of many flows in engineering. They are invariably present in current aeronautical applications where wing-sweepback and wing-fuselage junctions are the more immediately obvious sources of longitudinal vortices, see eg. Bradshaw and Cutler (1987). Longitudinal vortices are also purposely generated in heat-transfer augmentation devices, see eg. Eibeck and Eaton (1985), Fiebig et al. (1991), Zhu et al. (1991) and Tiggelbeck et al (1992), and as corrective measures for stabilisation and improvement of

¹) present address: Betriebsforschungsinstitut, Sohnstr.65, D 4000 Düsseldorf, Germany

diffusor performance, see eg. Senoo and Nishi (1974). Streamwise vortices are certain to have been present in the experiments of Anderson and Eaton (1989) in the boundary layer profile skewed by a wedge. Their attention is however focussed mainly on the three dimensional boundary layer outside the region of imbedded longitudinal vortices. All these studies show a strong departure of the turbulence structure of the three dimensional shear layer from that in the more conventional kinds of shear layer. Since most of the turbulence models of the present day are based on experimental data on the more conventional kinds of shear layer, the flow with imbedded longitudinal vortices presents a challenge to turbulence models. Here, the quantity of primary interest whose accurate prediction is often regarded as the test for a turbulence model, is the wall-shear stress vector. Clearly there is a need for experimental data on the evolution of Reynolds stresses, on other details of the turbulent motion and, not the least, on the wall shear stress in flows with imbedded longitudinal vortices. The motivation for the present work has been to provide these experimental data in a flow configuration that is relatively simple, yet retaining the essential features of these flows. Earlier flow investigations in the configuration of a circular cylinder with axis placed perpendicular to the walls of a large aspect ratio channel at the moderately high Reynolds number of 75000, were reported by Schulz and Vasanta Ram (1989), see also Schulz (1989). In the present study we have conducted experiments in the same geometry at Reynolds numbers of 12000 and 36000. These are lower than in the study of Schulz (1989) and are closer to the transitional flow. The wall shear stress vector has been measured directly by a sublayer fence pair. Instantaneous values of the local mean velocity vector and of all the six components of the Reynolds stresses have been obtained with a specially fabricated quadruple hot-wire probe, see Schulz (1989).

2 Experiments

A schematic diagram of the experimental facility is shown in fig. 1. The dimensions of the channel are 40mm \times 720mm \times 7550mm. The large aspect ratio of 1:18 ensured two-dimensionality of the oncoming flow. The diameter D of the cylinder spanning the channel walls with its axis perpendicular to the walls, was the same as the channel height $2H$, with $D=2H=40$ mm. The experiments were conducted at centerline velocities of the fully developed oncoming channel flow U_c of 9m/s and 27m/s, which correspond to Reynolds numbers based on the semi-channel height H , $Re=U_c H/\nu$, of 12000 and 36000 respectively.

The V-patterned sublayer fence pair for measurement of the wall shear stress vector is sketched in fig. 2a. The pressure difference across the fence was measured by a commercially available pressure transducer (Baratron of MKS Instruments Inc., Andover, Massachusetts, USA) of the range 0-1mbar or 0-1Torr as required. The fence height was 0.03mm which, in our experiments, gave rise to Reynolds numbers based on

the wall friction velocity and the fence height in the range of 1–3. The device was calibrated for both magnitude and direction of the wall shear stress vector in the undisturbed fully developed channel flow, a state that could be realised with ease in our facility by removing the cylinder. The calibration map of our sublayer fence pair is presented in fig.2c.

A dimensioned sketch of our quadruple hot-wire probe with a wire-arrangement as in Eckelmann et al. (1984) fabricated in our laboratory is shown in fig. 2b. The four wires of the probe were driven independently of each other by commercially marketed constant temperature hot-wire sets without linearizer (make of AA-Labs, Tel Aviv, Israel). Since the "cosine law" method of accounting for the angular response was found to be unsatisfactory for the individual wires in the quadruple probe arrangement, the probe was calibrated for its behaviour with respect to the velocity vector at 77 pairs of angles within the region of a cone of semi-apex angle 25° . The calibration data were arranged in a computer readable look-up table.

The four signals from the quadruple hot-wire probe were recorded for a duration of two seconds after passing them through an analog/digital-converter of 12-bit resolution (make of Keithley-Instruments, Munich, Germany) installed in a 386 MS-DOS computer. 2000 samples per channel were acquired in the sample-&-hold mode with a sampling rate of 1 kHz. Discrete time series of the three components of the instantaneous velocity vector were therefore available from which long-time averages and correlations of the fluctuating quantities could be obtained in a straightforward manner.

The profile measurements were conducted over half the channel height at 21 points in the y-direction (perpendicular to the channel walls) at 18 x-z-locations in the 'near field' which we define here to be the region $2 \leq x/D \leq 7.5$, $0 < z/D < 1.5$, see Schulz (1989). Here, x and z are streamwise and spanwise distances respectively from the center of the cylinder, see fig.3.

3. Data analysis

The disturbance generated by the cylinder to the channel flow is of a highly complex nature influencing the turbulent motion over a broad range of time and length scales. The long-time averages of the mean and fluctuating quantities as well as the spectra and other details of the fluctuating motion are all therefore affected. In order to keep the length of this communication within set limits, we restrict ourselves in this paper to reporting the results of data analysis from two points of view, one with respect to the long-time averaged stresses and the other to the search of structures, if any, in the flow. Insofar as the long-time averaged quantities are concerned we have examined the departures of these quantities from those in the undisturbed fully developed channel flow. In our search for structures the time-dependent quantities have been analysed with the VITA-algorithm.

Long-time averaged quantities

Fig. 4 shows the conventionally normalised U -component measured with our quadruple hot wire probe in the fully developed flow with the cylinder removed. The friction velocity for normalisation in this plot has been obtained from the pressure drop measurement. The measured mean velocity data are well represented by a logarithmic law, with a slope of 2.43 and 1.64 at Reynolds numbers of 36000 and 12000 respectively. This difference in slope is consistent with observations in literature, which show a departure of the Karman constant from a value of 0.41 at lower Reynolds numbers. The agreement with the log-law also provides a test of confidence for the technique of measurement by the quadruple hot-wire probe.

Fig. 5 is a plot of the "directly" measured local wall shear stress vector for $Re=36000$. From the measurement of the instantaneous velocity vector, the various long-time averaged quantities of interest that enter turbulence models, viz. the mean velocity, the Reynolds stresses and triple correlations of the fluctuating velocity components may be obtained. To preserve clarity of presentation in the midst of the voluminous data we reproduce here a selection of results which exhibit salient features of the departures from the fully developed flow*. These are in the Reynolds stresses $\overline{u'^2}$, $\overline{w'^2}$, $\overline{u'w'}$. It is also meaningful to view these quantities in terms of their differences from their profiles in the fully developed channel flow. We refer to these differences as incremental Reynolds stresses.

Figs. 6 and 7 show the streamwise evolution of the incremental Reynolds stresses at the channel centre and at $y/H=0.5$, nondimensionalised with respect to the friction velocity of the undisturbed channel flow. We draw the reader's attention to the following points in this figure.

1. The incremental Reynolds stresses that contain the spanwise component w' dominate over the others. The stress term containing the cross component (v') is generally lower than the others.
2. The location of the maximum disturbance at a certain wall distance shifts downstream as the observer moves across spanwise away from the plane of symmetry. This feature is retained at all wall distances.
3. At the location given by the normalised x - and z - coordinates (2, 0.75), which, in the two-dimensional flow past a circular cylinder of long span would lie in the region of the wake, there is hardly any departure from the fully developed undisturbed channel flow discernible. Clearly, the reason for this is the strongly confining effect of the channel walls on the wake past the cylinder. The gradual spreading of the disturbance into the adjacent fully developed region is evident on comparing the streamwise plots of the incremental Reynolds stresses at different values of z with each other.
4. The incremental Reynolds stresses at the different wall distances clearly pass through a turning point at the locations given by the normalised x -, z -

*) The complete measurement data are obtainable from the authors on request.

coordinates (3.25, 0.75) and (4.5, 1.5), downstream of which they decay. The streamwise evolution of the incremental stresses downstream of the cylinder is therefore not monotonic.

Analysis of the time series

The discrete time signals of the instantaneous Reynolds stress $u'w'$ at a few selected stations were analysed both by FFT-methods and by a VITA-algorithm. We present here the results obtained at the point $x/D=3.25$, $y/H=0.5$ and $z/D=0.75$. The significance of this location may be seen on referring to Fig. 7. It lies just within the border of the disturbed region at $x/D=3.25$ and half way between the wall and the channel center. Straightforward spectral analysis of both u'^2 and $u'w'$ by standard FFT-methods showed that the spectrum of the disturbed flow is broadbanded, but discrete frequencies with a significantly higher energy content are indeed discernible at nondimensional frequencies fD/U_c of 0.18 and 0.36, the former being more dominant for $u'w'$ and the latter for u'^2 .

Signals of both u'^2 and $u'w'$ were subjected to analysis by the VITA-algorithm for a range of averaging times and thresholds along lines laid out by Blackwelder and Kaplan (1976), Narasimha and Kailas (1987) and Morrison et al. (1989). This analysis was done for both the undisturbed fully developed channel flow and the flow disturbed by the imbedded longitudinal vortices. Fig 8a,b shows a perspective view of the count of events in the two flows as a function of the averaging time and the threshold. We have adopted the following as the criterion for detecting an event:

The quantity $\sigma = \frac{\text{var}(f(t, T))}{\text{var}(f(T=\infty))}$ should exceed the threshold VITH, (cf.

Narasimha and Kailas (1987), Morrison et al. (1989)), with the additional constraint that the duration over which σ exceeds the threshold VITH is not less than 50% of the longest duration encountered within the data set.

A comparison between the two shows that whereas in the undisturbed fully developed flow a large number of events occur around a nondimensional averaging time $U_c T/D$ of around 2 in the flow disturbed by the cylinder, not only is the count of events around this averaging time considerably larger but also they occur at several other averaging times too. Noteworthy here is that the nondimensional averaging time of 2.7, at which there is a large number of events, is consistent with the location of the peak of the spectrum with the nondimensional frequency of 0.36.

4. Concluding remarks

Measurement of the components of the Reynolds stress tensor and of the wall shear stress vector has been conducted in the turbulent channel flow with imbedded longitudinal vortices generated by a cylinder placed with axis perpendicular to the channel walls. The results shed light on some salient features of the Reynolds stress

development and structures in this flow.

Acknowledgements

The research work reported in this paper was supported financially by the Deutsche Forschungsgemeinschaft (DFG). The authors owe a special debt of thanks to S. Göllner and T. Reutter for their help at hot-wire anemometry and programming of the VITA-algorithm. The benefit of discussions with Prof. P. Bradshaw and Dr. K. Klemp is gratefully acknowledged. They also wish to thank Messers R.Königsmann and D. Schönhoff without whose assistance the laboratory work could not have been done, and Professor K. Gersten, Director of the Institute, for his encouragement and tacit support of the work.

REFERENCES

- ANDERSON, S.D. and EATON, J.K. (1989) Reynolds stress development in pressure-driven three-dimensional boundary layers. *Jour. Fluid Mechanics*, Vol. 202, 263-294.
- BLACKWELDER, R.F. and KAPLAN, R.E. (1976) On the wall structure of the turbulent boundary layer. *Jour. Fluid Mechanics*, Vol. 76, 89-112.
- BRADSHAW, P. and CUTLER, A.D. (1987): *Three-dimensional flows with imbedded longitudinal vortices. Perspectives in Turbulence Studies*, Springer, pp. 382-413.
- ECKELMANN, H., KASTRINAKIS, E.G. and NYCHAS, S.G. (1984): Vorticity and velocity measurements in a fully developed turbulent channel flow. *Turbulent and Chaotic Phenomena in Fluids* (Ed.: T. Tatsumi), Proceeding of IUTAM Symposium, Kyoto 1983, North Holland, pp. 421-426.
- EIBECK, P.A. and EATON, J.K. (1985): An experimental investigation of the heat transfer effects of a longitudinal vortex embedded in a turbulent boundary layer. Report MD-48 of the Thermosciences Division Dept. of Mech. Engg., Stanford University.
- FIEBIG, M., ZHU, J.X. and MITRA, N.K. (1991): Embedded longitudinal vortex arrays, velocity and temperature fields, loss and heat transfer augmentation. Eighth Symposium on Turbulent Shear Flows, Munich, September 9-11, 1991, 17-3.
- MORRISON, J.F., TSAI, H.M. and BRADSHAW, P. (1989): Conditional sampling schemes for turbulent flow, based on the variable-interval time averaging (VITA) algorithm. *Experiments in Fluids*, Vol. 7, pp. 173-189.
- NARASIMHA, R. and KAILAS, S.V. (1987) Energy events in the atmospheric boundary layer. In *Perspectives in Turbulence Studies*, Springer-Verlag, 188-222.
- SCHULZ, V. (1989): Der Wellencharakter der Turbulenzstruktur einer ebenen räumlich gestörten Kanalströmung. VDI-Fortschrittberichte, Reihe 7: Strömungstechnik, Nr. 153, VDI-Verlag, Düsseldorf, Germany (Dr.-Ing. Dissertation, Fak. für Maschinenbau, Ruhr-Universität Bochum, Germany).
- SCHULZ, V. and VASANTA RAM, V.I. (1989): The disturbance to the turbulent channel flow produced by a cylinder with axis perpendicular to the walls: a study with a quadruple hot-wire probe. Seventh Symposium on Turbulent Shear Flows, Stanford University, August 21-23, 1989, pp. 8.4.1-8.4.6.
- SENOO, Y. and NISHI, M. (1974): Improvement of performance of conical diffusers by vortex generators. *ASME Jour. of Fluids Engineering*, 96, no. 4, 4-10.
- TIGGELBECK, S., MITRA, N. and FIEBIG, M. (1992): Flow structure and heat transfer in a channel with multiple longitudinal vortex generators. *Experimental Thermal and Fluid Science*, Vol. 5, 425-436.
- ZHU, J.X., MITRA, N.K. and FIEBIG, M. (1991): Numerical simulation of periodically fully developed turbulent flow and heat transfer in a channel with longitudinal vortex generators. Eighth Symposium on Turbulent Shear Flows, Munich, September 9-11, 1991, 17-2.

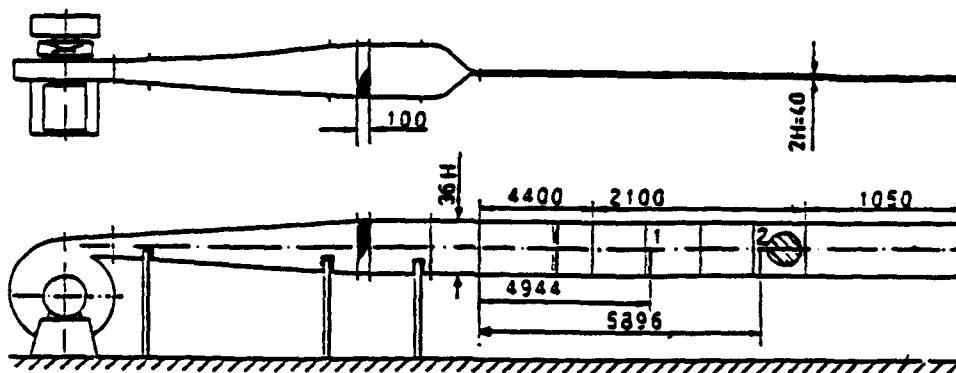


Fig.1: channel flow facility, dimensions in mm
cylinder located at pos.2 for the near field survey

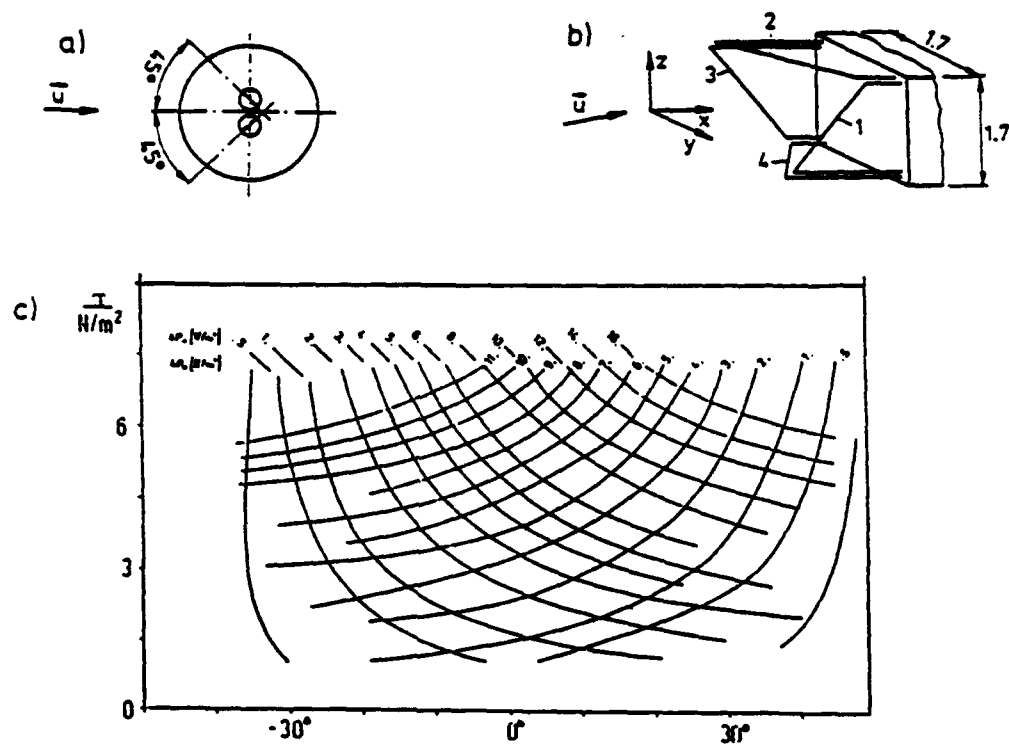


Fig.2: probes, dimensions in mm
a) V-patterned sublayer fence pair
b) quadruple hot wire probe
c) calibration map of sublayer fence pair

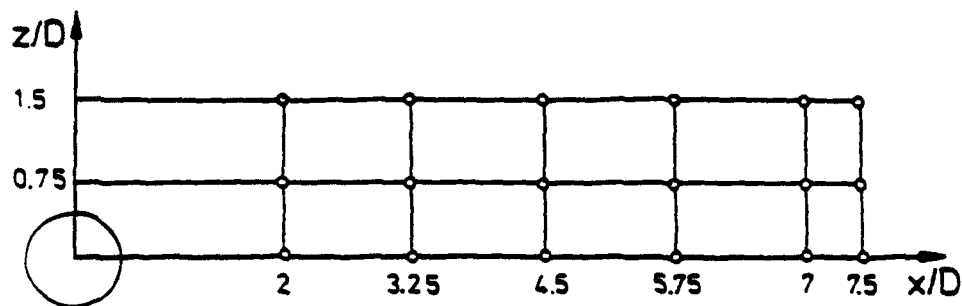


Fig.3: location of the measurement stations

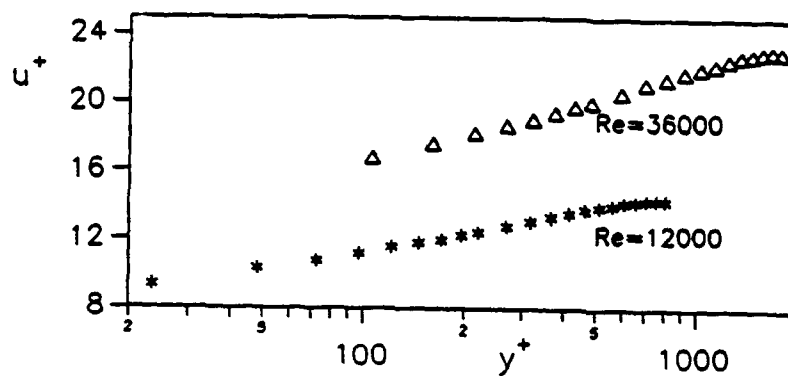


Fig.4: normalised mean velocities in the channel flow

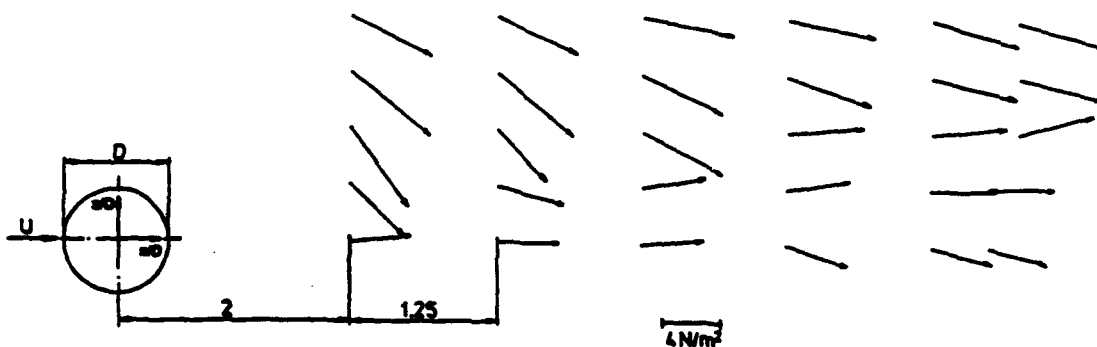


Fig.5: wall shear stress vector at $Re=36000$
angles are shown amplified by a factor 5

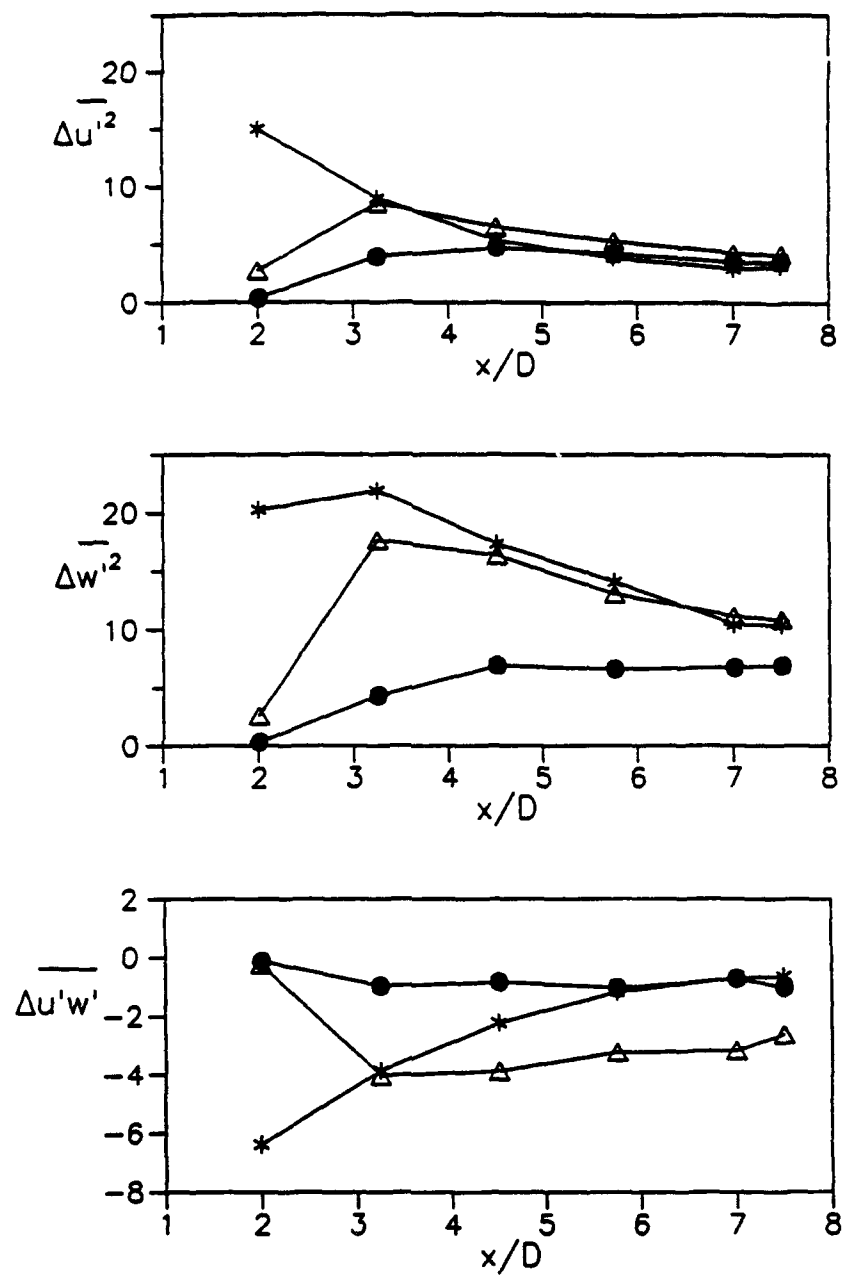


Fig.6: incremental stresses at $y/H=1$
 \bullet $z/D=0$; Δ $z/D=0.75$; $*$ $z/D=1.5$

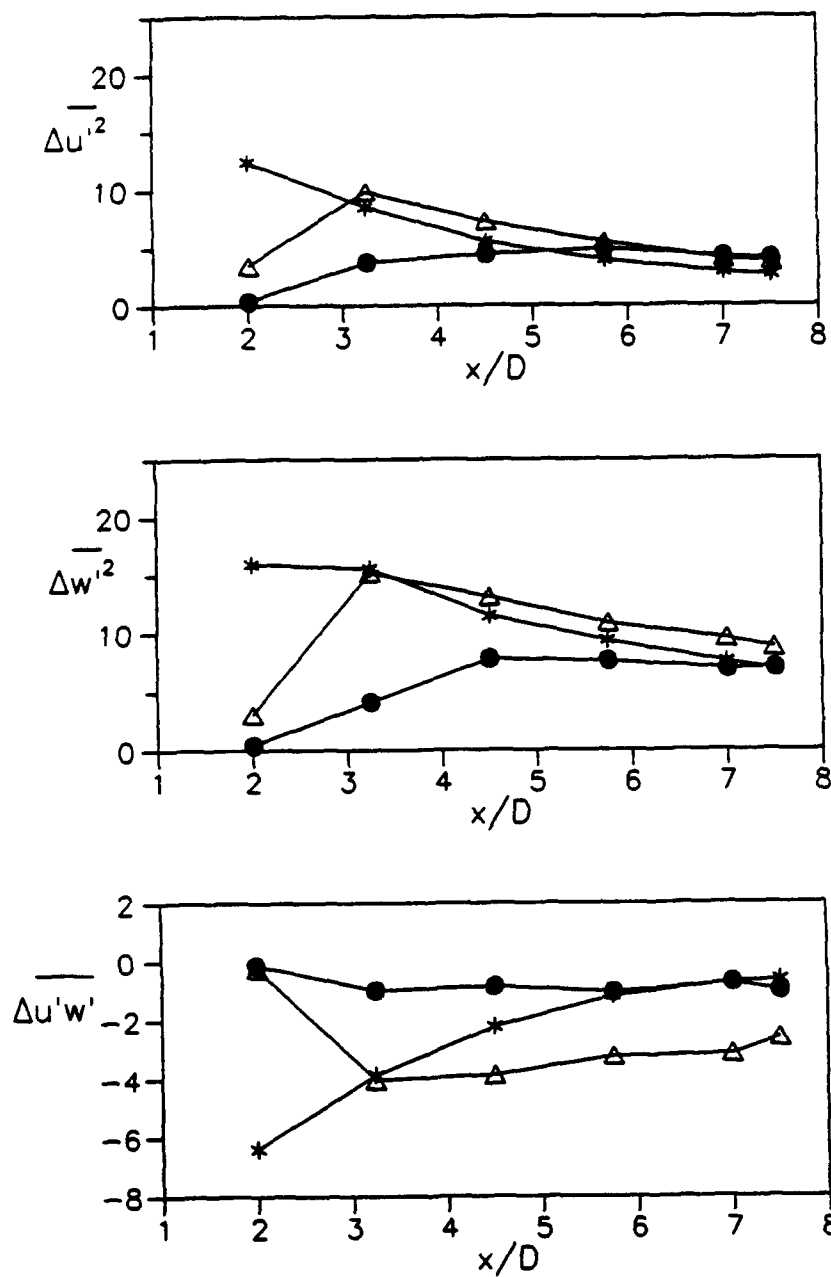


Fig.7: incremental stresses for $y/H=0.5$
 • $z/D=0$; Δ $z/D=0.75$; * $z/D=1.5$

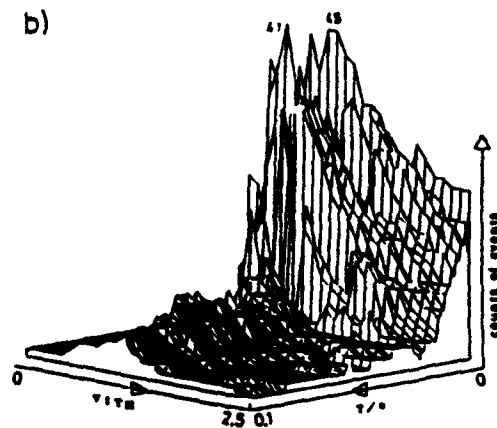
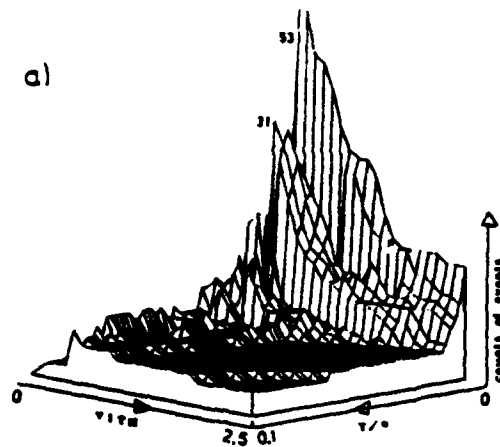


Fig.8: perspective view of event counts against averaging time T and threshold $VITH$ at $Re=12000$
 a) undisturbed turbulent channel flow
 b) channel flow disturbed by the cylinder
 at $x/D=3.25$, $y/D=0.5$, $z/D=0.75$

A COMPARISON OF SPATIAL CORRELATION AND AUTOCORRELATION MEASUREMENTS IN AN AXISYMMETRIC SUDDEN EXPANSION FLOW USING LDV

R. D. Gould and L. H. Benedict
Mechanical and Aerospace Engineering
North Carolina State University
Raleigh, NC 27695

ABSTRACT

Two-point velocity correlation measurements were made in the anisotropic flow field of an axisymmetric sudden expansion using two single component LDV systems. Both longitudinal and lateral spatial correlations were measured. The integral length scales and Taylor microscales were estimated and compared with those obtained from autocorrelation measurements in conjunction with Taylor's hypothesis. The agreement of the integral scales was within 20 % and the values obtained scale well with the flow geometry. Agreement of the microscales was within 43 %, however, the classical parabolic shape near zero separation was not found in any of the correlations. This may be due to insufficient resolution of the correlation functions near zero separation and possible spatial integration effects of the probe volume length.

1. INTRODUCTION

Few two-point velocity correlation measurements have been made using laser Doppler velocimetry(LDV) primarily due to the difficulty in obtaining suitable optical access when the laser probes are separated by large distances. In general, two independent single component LDV systems are required to make completely general two-point measurements. One LDV probe volume must be movable relative to the other in a very precise fashion. In addition, it may be difficult to collect the scattered light from each probe volume at all probe locations due to space or optical access limitations, possible signal cross-talk, and stray reflections from windows and lenses. Because of these difficulties and also because the LDV is a relatively new instrument, most spatial correlation measurements reported in the literature have been obtained using either hot wire or hot film probes. Spatial correlation measurements have been made in a variety of flows using hot wires including: free jets, grid generated turbulence flows, wake flows behind bluff bodies and boundary layer flows. Of course, hot wire correlation measurements require wake corrections(Champagne et al. (1970)) whereas LDV measurements do not. In contrast, autocorrelation measurements using LDV are numerous due to the fact that a single component LDV system with time recording capability is all that is required to make these measurements. Theoretical discussions of turbulent correlation functions(spatial and auto) and their physical interpretation can be found in the texts by Batchelor (1953), Bradshaw (1971), Tennekes and Lumley (1972), Hinze (1975), and Townsend (1976) to name a few.

Morton and Clark (1971) were among the first to make spatial correlation measurements using LDV. They used two single component reference beam LDVs to make both longitudinal and lateral correlation measurements in turbulent pipe flows using water for Reynolds numbers ranging from slightly above transition to 18,100. Their measurements agreed well with other published turbulent pipe flow measurements. Pfeifer (1986) has written a rather complete review paper on the topic of correlation measurements using LDV and thus is a good general reference. Lateral spatial correlation measurements using LDV were made by Fraser et al. (1986) on the centerline of fully developed pipe flow ($Re_D = 11,800$ based on centerline velocity). An elongated probe volume($\lambda = 514.5\mu m$) oriented such that the axial velocity component could be measured was used. Axial velocity measurements separated by as much as 9 mm in the radial direction could be made with this system. Two photo detectors oriented 90° from the forward scattering direction were used to collect the signals. The apertures of the two photo detectors were mounted on a traversing mechanism and thus determined the separation distance of the two axial velocity measurement points. Correlation measurements at separation distances closer than 1 mm were not possible with this system due to signal cross-talk problems. In another study, Absil (1988) made lateral spatial correlation measurements in the wake of a circular cylinder using a single LDV probe volume ($\lambda = 514.5\mu m$). Correlation measurements were made at three radial locations at a plane 125 diameters downstream of the circular

cylinder. The probe volume in this study was 600 μm in diameter and 31 mm in length. The two signals were detected using a setup similar to the one mentioned above. Autocorrelation measurements were also made in this study. Cenedese et al. (1991) investigated the validity of Taylor's hypothesis in a channel flow at a Reynolds number of 4,500. The turbulence intensity ranged from 20 % at the entrance of the tunnel (close to a honeycomb grid) to 7 % at the exit. The optical set up allowed spatial correlation measurements to be made both in the axial and transverse directions at a maximum separation distance of 1 cm corresponding to half the minimum channel dimension. The spatial correlations were compared to autocorrelations transformed using Taylor's hypothesis. They concluded that Taylor's hypothesis was valid even in the high turbulence regions when the separation distance was small. Agreement between the spatial correlation coefficient and the transformed autocorrelation coefficient deteriorated as separation distance increased.

2. EXPERIMENTAL APPARATUS

2.1 Flow Geometry

An axisymmetric sudden expansion flow geometry was produced by joining a 101.6 mm (4 in.) inside diameter entry pipe to a 152.4 mm (6 in.) inside diameter clear acrylic test section. The entry pipe was 3.5 m long so that a fully developed pipe flow velocity profile existed at the entrance to the sudden expansion. The step height for this geometry was 25.4 mm (1 in.). The entry pipe and sudden expansion face were mounted on a movable table and thus could be positioned at various axial locations in the rigidly fixed test section as shown in Figure 1. This arrangement allowed for measurements at various downstream positions within the sudden expansion flow field without having to move the LDV probe volume location in the axial direction. The face of the sudden expansion was moved to position the probe volume at a new x/H location; hence optical access was accomplished using a relatively small window with this apparatus. A felt gasket was used to seal the small gap between the sudden expansion face and the inside diameter of the test section.

Air was provided by well regulated shop air compressors and was monitored using a calibrated orifice plate located upstream of a large settling chamber which preceded the entrance pipe. Flat quartz windows 50 mm \times 152 mm \times 3.2 mm ($2 \times 6 \times .125$ in) were mounted in flanges on both sides of the 152.4 mm diameter test section such that the inner flat surfaces were flush with the inside diameter of the test section.

2.2 LDV System

Two TSI single component dual-beam LDV systems, both operating in backscatter mode, were used in this study. Both systems were oriented to measure the axial velocity component on the diameter of the test section as shown in Figure 2. The stationary LDV system was adjusted so that the probe volume was located on the diameter of the test section ($z = 0$) and at the required axial, x , and radial, r , measurement location. Once this "home" position was located, this LDV system was locked in place. The 514.5 μm laser line from a Model 2025 Spectra Physics argon ion laser was used in this system. A Bragg cell shifted the frequency of one beam by 40 MHz causing the fringes to move in the downstream direction. Fringe spacing and half-angle were measured and found to be $1.886 \mu\text{m} \pm .006$ and $7.838^\circ \pm .025$, respectively. A second LDV system (TSI Model 9277 190 mm fiber optic probe), mounted on a precision xyz positioning table with resolution of $\pm 2.5 \mu\text{m}$ in each axis, was located on the opposite side of the test section (see Figure 2). The 488 μm laser line from a Model 165 Spectra Physics argon ion laser was used in this system. A frequency shift of 40 MHz was used causing the fringes of this system to move in the upstream direction. Fringe spacing and half-angle were measured and found to be $1.728 \mu\text{m} \pm .006$ and $8.117^\circ \pm .025$, respectively. Both LDV systems employed $3.75\times$ beam expansion optics and gave probe volumes approximately 60 μm in diameter and 450 μm in length.

A 20 μm diameter pinhole mounted on a fixture supported on a spare test section window was used to find the position where both laser beam probe volumes overlapped. This fixture was used prior to each test sequence, thus ensuring that both probe volumes overlap at the zero separation distance point. Specially designed beam blocks were fabricated to block reflections from the LDV focusing lens (they face one another) and from test section windows. Narrow bandpass filters were placed in front of each photomultiplier tube to eliminate cross-talk between the two channels.

Two TSI Model 1990C counter processors interfaced to a custom built coincidence timing unit were used in the data collection and processing system. High and low pass filters were set to 10 MHz and 50 MHz, respectively, for the stationary LDV system, and 20 MHz and 100 MHz, respectively, for the fiber optic LDV system. Both processors were set to make a single measurement per burst, count 16 fringes and use a 1 % comparator. A hardware coincident window was set at 20 μs for all of the tests. Data (two velocities and the running time for

each realization: were transferred through two DMA ports to a MicroVax minicomputer and later uploaded to a VAX 8650 for analysis.

The flow field was seeded using titanium dioxide (TiO_2) particles generated by reacting dry titanium tetrachloride (TiCl_4) with the moist shop air. Craig et al. (1984) measured the particle sizes generated by this device and found that they were fairly uniform and in the $0.2 - 1\mu\text{m}$ diameter range. Data validation rates varied between 5000 and 500 per second on each counter processor and depended mainly on how well the chemical reaction proceeded. This seemed to be very sensitive to shop air temperature and relative humidity. Coincident data validation rates ranged from 1000 to 50 measurements per second.

3. EXPERIMENTAL PROCEDURE

All flow conditions were maintained at near constant values throughout the testing procedure. The inlet centerline velocity, U_{cl} , was maintained at $18.0 \text{ m/s} \pm 0.1 \text{ m/s}$ ($59 \text{ ft/s} \pm 0.3 \text{ ft/s}$) giving $Re_D = 114,000$ based on centerline velocity and inlet diameter. Spatial correlation statistics and histograms were formed by using 5000 individual realizations for each velocity channel at each measurement point. Autocorrelations were formed by using 50000 individual realizations from the stationary LDV system.

A two step process was used to eliminate noise from the data prior to computing statistical turbulence parameters. In the first step, a 5% threshold level was applied to the raw velocity data in an effort to estimate the standard deviation of the valid data. This estimate was made by creating a histogram of the raw velocity data with 100 equally spaced bins bounded by the actual maximum and minimum velocity. Next, the bin containing the maximum number of samples in it was found. Finally, all bins having at least 5% of the number of samples found in this "maximum" bin were located. The width of the data which met this threshold criteria was then used to estimate the standard deviation of the "good" data. Upper and lower cutoff limits were then set by adding and subtracting, respectively, 2.5 times the half-width of the data which met this 5% threshold. Applying this technique to a Gaussian distribution is equivalent to setting cutoff limits which correspond to ± 4.1 standard deviations and thus this first step is used only to remove spurious data. This method is a variation of the method suggested by Meyers (1988) and is used to eliminate spurious data which if not removed would give an abnormally large value for the standard deviation and thus wider cutoff limits. In the second step, the mean and standard deviation of the remaining data (spurious data removed) were calculated. This data was then further filtered to remove data which deviated more than 3 standard deviations from this new mean. Finally, revised statistics were calculated once these additional outliers were discarded. For a properly operating LDV system very few points are removed during the first step (typically less than 10 out of 5000) and less than 1% of the data should be discarded after both steps. It should be noted that ensemble averages were used to calculate statistical parameters in this study and that no effort was made to account for velocity bias (McLaughlin and Tiederman (1973), Edwards (1987), Gould et al. (1989)).

4. DEFINITIONS OF TURBULENCE PARAMETERS

Two-point axial velocity correlation measurements were made at three locations in the axisymmetric sudden expansion flow field as shown in Figure 3. The first two spatial correlation measurements were made at an axial location of ten step heights ($x/H = 10$) downstream of the sudden expansion plane, one on the centerline of the flow ($r/H = 0$) and the other at the same radial location as the step ($r/H = 2$). The third spatial correlation measurement was made at an axial location of six step heights and at the same radial location as the step ($x/H = 6$, $r/H = 2$). These locations are where the stationary LDV probe volume remained fixed for each set of correlation measurements. Spatial correlations were obtained by positioning the movable LDV probe volume (fiber optic system) at various separation distances from the stationary probe volume.

Longitudinal spatial correlations defined by,

$$R_{11}(\Delta x) = f(r) = \frac{\overline{u'(x)u'(x + \Delta x)}}{\sqrt{\overline{u'^2(x)}}\sqrt{\overline{u'^2(x + \Delta x)}}} = \frac{\overline{u'_1 u'_2}}{\sqrt{\overline{u_1'^2}}\sqrt{\overline{u_2'^2}}} \quad (1)$$

were made at two locations in both the plus and minus Δx directions and at one location in the plus Δx direction. In this equation the prime denotes a fluctuation about the mean (i.e. $U_1 = \overline{U_1} + u'_1$), the overbar denotes time averaging, and Δx is the separation distance in the axial direction. The notation used in the right most formula of Equation (1) shows that the spatially separated velocities are simply two independent measurements (analogous to the axial and radial velocities obtained with a standard two-component LDV system) and thus standard LDV

software and existing coincidence timing hardware were used to obtain this correlation coefficient. Lateral spatial correlations defined by,

$$R_{11}(\Delta y) = g(r) = \frac{\overline{u'(y)u'(y + \Delta y)}}{\sqrt{\overline{u'^2(y)}}\sqrt{\overline{u'^2(y + \Delta y)}}} = \frac{\overline{u'_1 u'_2}}{\sqrt{\overline{u_1'^2}}\sqrt{\overline{u_2'^2}}} \quad (2)$$

were made at two of the locations ($x/H = 6$, $r/H = 2$ and $x/H = 10$, $r/H = 2$) in both the plus and minus Δy (same as Δr) directions. Both directions (plus and minus) were considered in this study to determine the homogeneity of the flow. It should be noted that turbulent flows are three-dimensional and that these measurements give only the one-dimensional correlation coefficient. In addition to these spatial correlation measurements, autocorrelation measurements were also made at the two $x/H = 10$ locations.

Longitudinal spatial correlation measurements were made with a minimum separation distance equal to 254 μm (0.010 in) and a maximum separation distance equal to 101.6 mm (4.0 in). The same minimum separation distance was used for lateral spatial correlation measurements, but different maximum separation distances, depending upon whether the direction was toward the wall (where $\Delta y_{\text{max}} = 22.86 \text{ mm}$ (0.9 in)) or toward the centerline (where $\Delta y_{\text{max}} = 50.8 \text{ mm}$ (2.0 in)), were used. The spatial correlation data were fit to a curve having the form $R(r) = C \exp(-r/\Lambda)$, where r is the separation distance, using a weighted "least squares" error criteria. These curve fits are shown on each figure by a solid or dashed line and show that a higher weighting was given to the data with small separation distance.

The integral length scales defined as,

$$\Lambda_f = \int_0^\infty f(x) dx \quad \text{or} \quad \Lambda_g = \int_0^\infty g(y) dy \quad (3)$$

give a measure of the longest connection, or correlation distance, between velocities at two points in the flow field. This is because for a given separation distance, r , only eddies larger than r will contribute to the correlation function while eddies smaller than r will not. If the data can be fitted with the simple exponential function given above then Equation (3) gives the integral length scale as equal to the coefficient, Λ , in the exponential curve fit.

Dissipation or Taylor length scales were estimated by performing a Taylor series expansion on the correlation coefficient curve near zero separation distance (see Hinze, 1975). The dissipation length scales, λ_f and λ_g , which result from fitting a parabola to the appropriate correlation functions near x or $y = 0$ were obtained from,

$$R(x) \approx 1 - \frac{x^2}{\lambda_f^2} \quad \text{or} \quad R(y) \approx 1 - \frac{y^2}{\lambda_g^2} \quad (4)$$

These length scales give an estimate of the average dimension of the smallest eddies in the flow which are responsible for viscous dissipation. The practice of "fitting" a parabola to the discrete spatial correlation functions involves anchoring the parabola at $R_{11}(0)$ and using the next measurement (i.e. $R_{11}(x = \Delta x)$ or $R_{11}(y = \Delta y)$) to find λ_f or λ_g . An estimate of the isotropic turbulent viscous dissipation rate can be made once these microscales and the turbulence intensity are known (see Hinze, 1975) using:

$$\epsilon = 30\nu \frac{\overline{u'^2}}{\lambda_f^2} \quad \text{or} \quad \epsilon = 15\nu \frac{\overline{u'^2}}{\lambda_g^2} \quad (5)$$

Discrete autocorrelation measurements were made using the slotting technique described by Jones (1972) and Mayo, et al. (1974). The lag time axis was divided into bins of equal width and the exact lag products of all points up to the maximum lag time were accumulated in appropriate bins. The discrete autocorrelation function,

$$R_E(\tau) = \frac{\overline{u'(t)u'(t + \tau)}}{\overline{u'^2(t)}} \quad (6)$$

evaluated at the midpoint of each bin, was found by summing the autoproductions in each bin and dividing each of these values by the number of autoproductions in each corresponding bin. The data was first filtered using the previously described method to eliminate noise before the discrete autocorrelation was estimated. Slot width and segment length were then varied parametrically to study the effect of these parameters on the discrete autocorrelation function. In addition, the zero-lag autoproductions were not included in the first bin in order to minimize the ambiguity spectrum due to uncorrelated noise (Gaster and Roberts, (1975), Srikantiah and Coleman, (1985), Lau, (1988), Absil, (1988)). The Eulerian integral scale was estimated by finding the area under

the autocorrelation curve as given by,

$$\mathcal{T}_E = \int_0^{\infty} R_E(t) dt \quad (7)$$

The Eulerian dissipation(micro) time scale was estimated by applying a Taylor series expansion to the autocorrelation function near $t = 0$. The equation for an osculating parabola at the vertex of the $R_E(t)$ curve is,

$$R_E(t_1) \approx 1 - \frac{t_1^2}{\tau_E^2} \quad (8)$$

Here the Eulerian micro time scale, τ_E , is a measure of the most rapid changes that occur in the fluctuations of $U(t)$. Taylor's hypothesis, which is valid only if the flow field has uniform mean velocity, \bar{U} , and small turbulence intensity, gives a relationship between temporal and spatial quantities(i.e. $x = \bar{U}t$). If Taylor's hypothesis applies the relations, $\Lambda_f = \bar{U}\tau_E$ and $\lambda_f = \bar{U}\tau_E$, result. Note that only the longitudinal length scales can be estimated with Taylor's hypothesis. Taylor's hypothesis was applied to the autocorrelation functions at the $x/H = 10, r/H = 0$ and $x/H = 10, r/H = 2$ locations. The resulting spatial correlation functions were then compared to the measured spatial correlation functions.

5. EXPERIMENTAL RESULTS

5.1 Single-Point Turbulence Measurements

Before correlation measurements were made, axial velocity measurements at three axial planes($x/H = 1, 6, 10$) were made using the moveable fiber optic LDV system. This was done in an effort to validate that the flow was symmetric and to ensure that the flow was what was expected. Turbulence statistics were calculated using 5000 samples for each measurement point and the filtering procedure described above. The inlet mean velocity profile was found to be similar to that of a fully developed turbulent pipe profile. This data, presented in Gould et al. (1992), indicated that the spatial correlation measurements made at $r/H = 2$ were in regions of large velocity gradient and high turbulence. The turbulence intensities($TI = \sqrt{u'^2}/\bar{U}$) at this radial location and at $x/H = 10$ and $x/H = 6$ were found to be 45% and 264%, respectively. The turbulence intensity at $x/H = 10, r/H = 0$ was found to be approximately 8%. A more complete experimental mapping of this flow field is given by Gould et al. (1990).

An estimate of the turbulent kinetic energy(TKE) was made by assuming that $k \equiv \sqrt{u'^2 + v'^2 + w'^2} \approx \bar{u}'$ which was found to be a good approximation for this flow field(Gould, et al. (1990)). The Kolmogoroff length scale, $\eta = (\nu^3/\epsilon)^{1/4}$, was estimated by assuming that the turbulent viscous dissipation rate, ϵ , equaled three-fourths the production of TKE(i.e. not quite in local mechanical equilibrium). The other one-fourth of the turbulent kinetic energy produced was assumed to be either convected or diffused in the flow. Gould, et al. (1990) noted that the production of TKE in this flow field occurs primarily from the $\bar{u}'v'\partial\bar{U}/\partial r$ term. An estimate of the production of TKE in this flow was obtained by using Bradshaw et al.'s (1967) model (i.e. $\bar{u}'v' \approx 0.35k$) for the shear stress and the measured mean velocity gradient in the above equation. Single point turbulence statistics obtained from direct measurements and these estimates of k , ϵ , and η are included in Table 1 below.

Table 1. Single-Point Turbulence Statistics.

Location	$x/H=10, r/H=0$	$x/H=10, r/H=2$	$x/H=6, r/H=2$
\bar{U} (m/s)	15.69	7.54	1.35
$\sqrt{u'^2}$ (m/s)	1.35	3.36	3.93
TI	0.08	0.45	2.64
k (m ² /s ²)	1.82	11.29	12.74
ϵ (m ² /s ³)	10	740	1340
η (μ m)	200	50	40

5.2 Correlation Measurements

Figures 4 through 8 show the measured spatial correlation coefficients and autocorrelation coefficients transformed to the spatial domain by using Taylor's hypothesis as a function of separation distance at the three measurement points mentioned above. Figures 4, 5 and 7 show the longitudinal spatial correlations while Figures 6 and 8 show the lateral spatial correlations. Values for the estimated integral length scales based on the spatial

correlation measurements are summarized in Table 2. Numbers appearing in brackets in this table refer to length scales obtained with negative separation distances.

The integral length scales were found to vary between 23 and 35 mm in both separation directions for the longitudinal spatial scale and were found to vary between approximately 8 and 15 mm for the lateral spatial scale. These results indicate that the flow appears reasonably homogeneous in the axial flow direction but is non-homogeneous in the radial direction where the wall influences the flow field. Also, the lateral integral length scales, Λ_y , were found to be approximately one-half the value of the longitudinal integral length scales, Λ_x , indicating strong anisotropy of the large scales.

By definition all correlation coefficients should equal one when the separation distance is zero. However, when measuring spatial correlations, the signal to noise ratio in the two sampling volumes determines a practical maximum correlation coefficient less than unity (Morton and Clark, (1971)). So as not to affect the integral and microscales, all spatial correlation measurements presented here were normalized to unity at zero separation. The same normalizing factor was then used to correct all measured values for varying separation distance. Actual measured maximum values for $R_{11}(0)$ varied between 0.92 and 0.98. It should also be noted that low values of correlation coefficient could occur if the sample were to include measurements of velocities separated by distances greater than the actual probe volume separation distance. This could occur if seed particles passed through opposite ends of each probe volume. The effective separation distance could be as large as $\sqrt{(\Delta x)^2 + \ell^2}$, where ℓ is the probe volume length and is assumed to be the same for both probe volumes in this simple formula. Note that the effective probe volume separation approaches the actual probe volume separation as Δx or Δy become large. Placing the photo detectors 90° to the forward direction would minimize this spatial integration effect by making the effective probe volumes smaller.

Dissipation or Taylor length scales were estimated using the method discussed above and are also summarized in Table 2. The longitudinal and lateral microscale measurements were found to scale according to Equation (5) (i.e. $\lambda_g = 0.707\lambda_f$) reasonably well suggesting that the measurements are self-consistent. However, the dissipation rates obtained by using these microscales (see Table 2) in Equation (5) were found to be approximately a factor of 5 lower (for the $r/H = 2$ cases) when compared to the estimates of dissipation rate obtained by assuming they equaled three-fourths the production of TKE. The dissipation rates obtained from the turbulent kinetic energy balance are believed to be more correct as this flow field is not isotropic. The effects of the probe volume length (giving an erroneous value for $R_{11}(x)$) and the practice of fitting a parabola to discrete spatial correlation data which may not be as highly resolved near $\Delta x \rightarrow 0$ as needed add uncertainty to the estimates of the microscales. Of course, this is also true when using hot wires. Browne et al. (1991), using a single hot wire probe and recording du'/dt , showed that the correct viscous dissipation rate can be obtained only if the probe length is smaller than approximately five times the Kolmogoroff scale. For the hardware used in this study this limit requires that the Kolmogoroff scale be greater than 100 μm .

Table 2. Spatial Correlation Results.

Location	$x/H=10, r/H=0$	$x/H=10, r/H=2$	$x/H=6, r/H=2$
Λ_x (mm)	29.6(29.8)	34.4(32.1)	27.5(—)
Λ_y (mm)	—	11.3(14.8)	8.0(11.7)
λ_f (mm)	7.0	6.9	5.5
λ_g (mm)	—	4.2	3.7

Figures 4 and 5 also show the autocorrelation functions transformed to spatial correlations using Taylor's hypothesis (solid symbols). Table 3 gives a summary of the temporal and spatial scales obtained from these autocorrelation measurements. Comparisons of the integral length scales obtained from autocorrelation measurements with those obtained directly from spatial correlation measurements show that the autocorrelation method gives an integral length scale $\approx 17\%$ too large at the low turbulence location and gives an integral length scale approximately 20% too small at the location in the shear layer. Considering the limitations of Taylor's hypothesis the spatial correlation integral length scale estimates are believed to be more reliable.

The microscales obtained using the autocorrelation measurements along with Taylor's hypothesis gave a value 43% higher than the spatial correlation microscale estimate at the low turbulence location and gave a value 16% lower than the spatial correlation microscale estimate in the shear layer. Large values of microscales can result from poor resolution of transformed autocorrelation functions near zero separation. When using the slotting

technique of Jones (1972) and Mayo (1974) one is free to choose slot widths as small as needed, however, care must be used to assure that each slot contains enough lag products to accurately estimate the autocorrelation coefficient at that lag time. Thus, there is a compromise between high resolution and statistical accuracy of the autoproductions.

Table 3. Autocorrelation Results.

Location	$x/H=10, r/H=0$	$x/H=10, r/H=2$
U (m/s)	15.69	7.54
T_E (s)	.0022	.0035
r_E (s)	.00064	.00077
Λ_f (mm)	34.8	26.3
λ_f (mm)	10.0	5.8

Figures 9 and 10 illustrate one of the concerns associated with decreasing the slot width arbitrarily. Slots 40 μ s in width at the low turbulence location each contained approximately 6000 lag products and gave statistical scatter of $\pm 3\%$. In the shear layer, 40 μ s slots each contained approximately 3000 lag products giving a statistical uncertainty at each delay time of $\pm 6\%$. These values of uncertainty are consistent with the uncertainty in determining the mean of the quantity $\overline{u'u'}$ as estimated from the sample size and standard deviation of the sample in each slot (Yanta, (1973)). Evidently, an overall sample size of 50,000 at the mean data validation rate present in the data of this study is insufficient to temporally resolve this flow with an uncertainty less than 3%. Since the statistical uncertainty decreases as $1/\sqrt{N}$, it is recommended that each slot contain 20,000 or more autoproductions.

As the slotting technique is widespread, but often taken for granted, the authors would like to offer some additional commentary on the method. Often, the suggestion is made that data sets might be broken up into segments to speed implementation of the slotting algorithm. This practice can be dangerous as the block means determined from the individual segments may have large variance as was found in this study. This effect results in larger uncertainty of the slot autoproduction values. It has long been noted that inclusion of zero lag products in the first slot leads to a spiking effect in the autocorrelation at zero time. This effect has been attributed to "uncorrelated" noise in typical LDV data sets (Mayo (1974), Lau (1980)), however, a similar albeit smaller effect was noticed as the slot width approached zero although autoproductions with zero lag time were excluded (Figure 11). This may suggest a slight correlation of noise in LDV data. Researchers making multiple sample measurements per burst should be aware that this tends to amplify this effect. In general, it should be noted that the slotting technique is a statistical process with inherent subtleties that must be used with caution.

6. CONCLUSIONS

Successful two-point velocity correlation measurements were made in the anisotropic flow field of an axisymmetric sudden expansion. Both longitudinal and lateral spatial correlations were measured. The integral length scales and Taylor microscales were estimated and compared with those obtained from autocorrelation measurements in conjunction with Taylor's hypothesis. The agreement of the integral scales was within 20% and the values obtained scale well with the flow geometry. Agreement of the microscales was within 45%, however, the classical parabolic shape near zero separation was not found in any of the correlations. This may be due to insufficient resolution of the correlation functions near zero separation and possible spatial integration effects of the probe volume length.

ACKNOWLEDGMENTS

This investigation was performed at Aeropropulsion and Power Directorate, Wright Laboratory (WL/POPT) under the Summer Faculty Research Program supported by AFOSR. The author would like to thank Dr. A. S. Nejad for the use of his laboratory and equipment and for all the help he provided. Thanks are also due to Mr. C. Smith for his technical support in the laboratory.

REFERENCES

- Absil, L. H. J., (1988), "Laser Doppler Measurements of Mean Turbulence Quantities, Time and Spatial-Correlation Coefficients in the Wake of a Circular Cylinder," Proc. of the 4th Int'l Sym. on Appl. of Laser Anem. to Fluid Mech., Lisbon, Port., p. 1.1.
- Batchelor, G. K., (1953), *The Theory of Homogeneous Turbulence*, Cambridge Univ. Press, New York.

Bradshaw, P., Ferriss, D. H. and Atwell, N. P., (1967), "Calculation of Boundary Layer Development using the Turbulent Kinetic Energy Equation," *J. Fluid Mech.*, **28**, pp. 593-616.

Bradshaw, P. (1971), *An Introduction to Turbulence and its Measurement*, Pergamon Press, Oxford.

Browne, L. W. B., Zhu, Y. and Antonia, R. A., (1991), "Dissipation Estimates in Turbulent Flows using the Zero-Wire-Length Technique," *Experiments in Fluids*, **11**, pp. 197-199.

Cenedese, A., Romano, G. P. and Di Felice, F., (1991), "Experimental Testing of Taylor's Hypothesis by LDA in Highly Turbulent Flow," *Experiments in Fluids*, **11**, pp. 351-358.

Champagne, F. H., Harris, V. G. and Corrsin, S., (1970), "Experiments on Nearly Homogeneous Turbulent Shear Flow," *J. Fluid Mech.*, **41**, pp. 81-139.

Craig, R. R., Nejad, A. S., Hahn, E. Y. and Schwartzkopf, K. G., (1984) "A General Approach for Obtaining Unbiased LDV Data in Highly Turbulent Non-Reacting and Reacting Flows," AIAA Paper. No. 84-0366.

Edwards, R. V., ed., (1987), "Report of the Special Panel on Statistical Particle Bias Problems in Laser Anemometry," *J. Fluids Engineering*, **109**, pp. 89-93.

Fraser, R., Pack, C. J. and Santavicca, D. A., (1986), "An LDV System for Turbulence Length Scale Measurements," *Experiments in Fluids*, **4**, pp. 150-152.

Gaster, M. and Roberts, J. B., (1975), "Spectral analysis of Randomly Sampled Signals," *J. Inst. Math. Appl.*, **15**, pp. 195-216.

Gould, R. D., Benedict, L. H., Nejad, A. S. and Ahmed, S. A., (1992), "Two-Point Velocity Correlation Measurements in an Axisymmetric Sudden Expansion Using LDV," Proc. of the 6th Int'l Sym. on Appl. of Laser Tech. to Fluid Mech., Lisbon, Port., July 20-23.

Gould, R. D., Stevenson, W. H. and Thompson, H. D., (1989), "A Parametric Study of Statistical Velocity Bias," *AIAA Journal*, **27**, pp. 1140-1142.

Gould, R. D., Stevenson, W. H. and Thompson, H. D., (1990), "Investigation of Turbulent Transport in an Axisymmetric Sudden Expansion," *AIAA Journal*, **28**, pp. 276-283.

Hinze, J. O., (1975), *Turbulence*, McGraw-Hill.

Jones, R. H., (1972), "Aliasing with Unequally Spaced Observations," *J. Appl. Meteorology*, **11**, pp. 245-254.

Lau, J. C., (1980), "Laser Velocimeter Correlation Measurements in Subsonic and Supersonic Jets," *J. of Sound and Vibration*, **70**, pp. 85-101.

Mayo, W. T., Shay, M. T. and Ritter, S., (1974), "The Development of New Digital Data Processing Techniques for Turbulence Measurements with Laser Velocimetry," AEDC-TR-74-53.

McLaughlin, D. K. and Tiederman, W. G., (1973), "Bias Correction for Individual Realization of Laser Anemometer Measurements in Turbulent Flows," *Physics of Fluids*, **16**, pp. 2082-2088.

Meyers, J. F., (1988), "LV Data Acquisition and Real Time Processing using a Microcomputer," Proc. of the 4th Int'l Sym. on Appl. of Laser Anem. to Fluid Mech., Lisbon, Port., p. 7.20.

Morton, J. B. and Clark, W. H., (1971), "Measurements of Two Point Velocity Correlations in a Pipe Flow using Laser Anemometers," *J. Phys. E: Scient. Instrum.*, **4**, pp. 809-814.

Pfeifer, H. J., (1986), "Correlation and Spectral Density Measurements by LDA," Proc. of the 5th Int'l Congress on Appl. of Lasers and Electro-Optics, Arlington, Va., **58**, pp. 59-77.

Srikantaiah, D. V. and Coleman, H. W., (1985), "Turbulence Spectra from Individual Realization Laser Velocimetry Data," *Experiments in Fluids*, **3**, pp. 35-44.

Tennekes, H. and Lumley, J. L., (1972), *A First Course in Turbulence*, Clarendon Press, Oxford.

Townsend, A. A., (1976), *The Structure of Turbulent Shear Flow*, Cambridge Univ. Press, London.

Yanta, W. J. and Smith, R. A., (1973), "Measurements of Turbulence Transport Properties with a Laser Doppler Velocimeter." AIAA Paper 73-169.

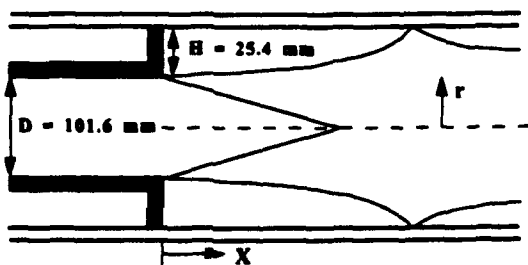


Figure 1. Axisymmetric sudden expansion geometry.

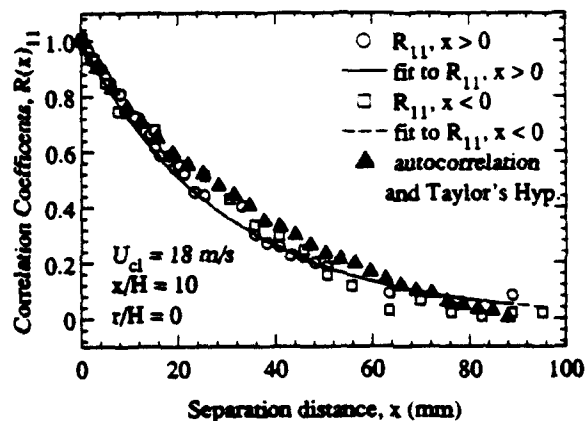


Figure 4. Longitudinal spatial correlation and transformed autocorrelation measurements ($x/H=10$, $r/H=0$).

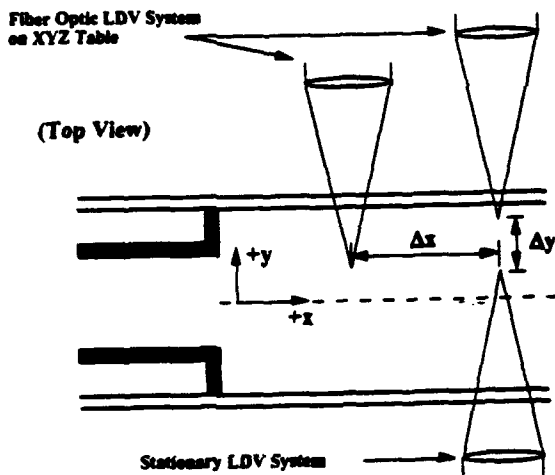


Figure 2. LDV orientation.

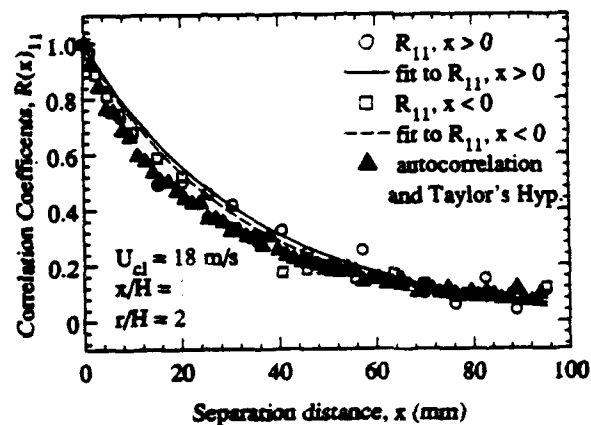


Figure 5. Longitudinal spatial correlation and transformed autocorrelation measurements ($x/H=10$, $r/H=2$).

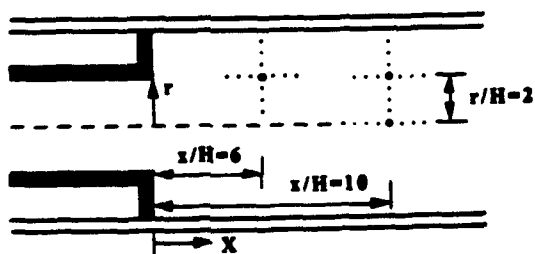


Figure 3. Measurement locations (top view).

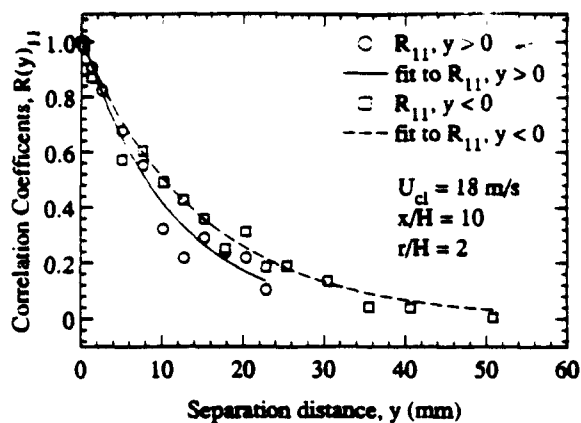


Figure 6. Lateral spatial correlation measurements ($x/H=10$, $r/H=2$).

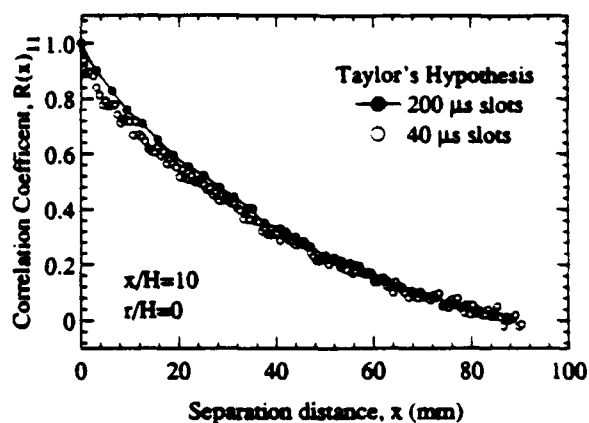


Figure 9. Autocorrelation function resolved with 40 and 200 μ s slots ($x/H=10$, $r/H=0$).

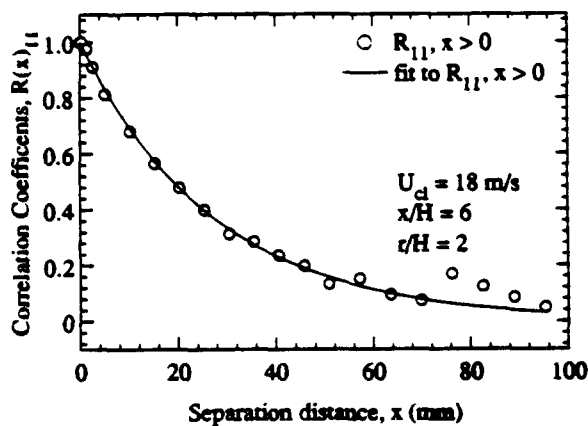


Figure 7. Longitudinal spatial correlation measurements ($x/H=6$, $r/H=2$).

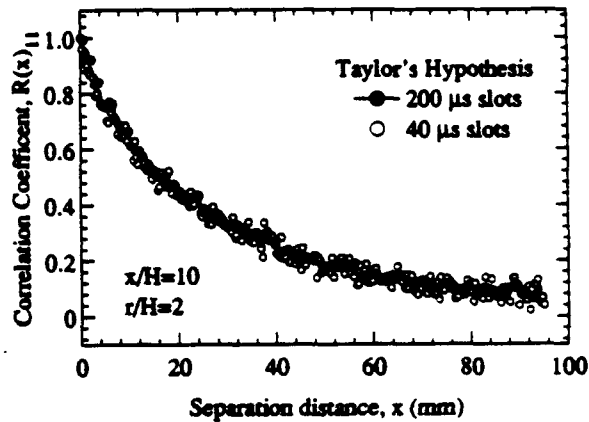


Figure 10. Autocorrelation function resolved with 40 and 200 μ s slots ($x/H=10$, $r/H=2$).

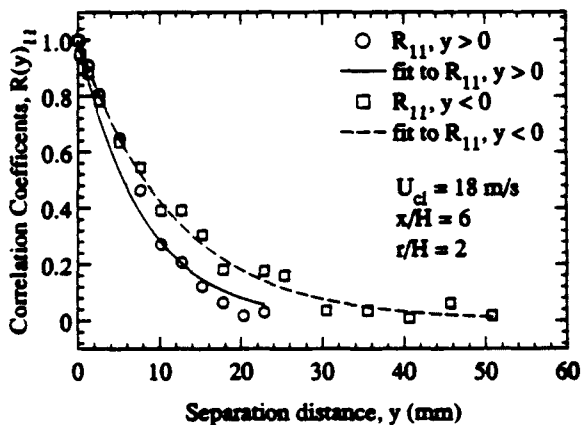


Figure 8. Lateral spatial correlation measurements ($x/H=6$, $r/H=2$).

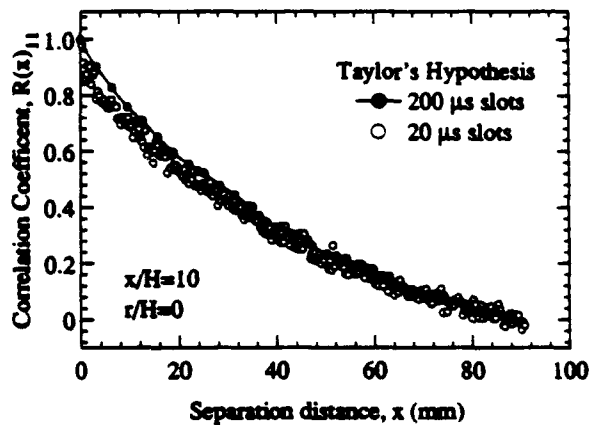


Figure 11. Autocorrelation function resolved with 20 and 200 μ s slots ($x/H=10$, $r/H=0$).

PREDICTION OF THE TURBULENT COMPRESSIBLE FLOW THROUGH
LABYRINTH SEALS FOR HIGH SPEED TURBOMACHINERY

Hassan A. El-Gamal
Dept. of Mechanical Engineering
Alexandria University
Alexandria, Egypt

Abstract

A theoretical approach is presented for predicting the compressible turbulent fluid flow through labyrinth seals of high speed turbines and rotary high performance compressors . The treatment is based on the assumption that adiabatic conditions exist and that the height of the seal to the radius of the shaft ratio is small as is always the case in turbomachines . The theoretical work is capable of handling single or multi-cavity labyrinth seals of arbitrary geometrical configurations and takes into account the shaft lateral misalignment . The analysis is restricted to subsonic flow and the proposed theoretical model has the advantage of being free from any uncertainty associated with assuming a mean kinetic energy carry-over coefficient for the seal .

Performance curves for single cavity seals are presented for different height to width ratios , eccentricity ratios and rotational inlet Mach numbers . Performance curves for multi-cavity seals are also given .

1. Introduction

Effective sealing in turbomachines is required in order to minimize the leakage of high energy working fluid, thus reducing the adverse effects of seal leakage on overall engine performance. To increase the sealing effectiveness and to reduce leakage rates it is necessary to improve and develop the labyrinth seal design both from the theoretical and experimental point of view. Advancement in labyrinth seal design will lead the turbomachine cycles to continue to advance toward higher operating temperature and pressure ratios. Some of the early design methods available in the literature are purely analytical [1-3] and others are analytical-experimental [4-7]. The large differences occurred in leakage predictions using these methods are due to the neglect of the effect of kinetic energy carry over in some cases and the inclusion of uncertain assumptions concerning its mean value in the overall seal geometry in the other cases. On the other hand Benvenuti, Ruggeri and Tomassini [8] made a comparative study of these methods and made some experiments to gain better knowledge of the flow phenomena in the labyrinth seal. However, Stoff [9] reported a theoretical and experimental study of the incompressible turbulent flow through a labyrinth seal of the straight-through grooved shaft type and was the first to reliably include the effect of shaft rotation in the analysis. It was found by Rhode et al [10] that labyrinth seal solutions using the differencing scheme of Stoff [9] may suffer from the so called false diffusion numerical error depending on the flow field conditions. They however, presented an approach to overcome the difficulties encountered when using the scheme of Stoff. They also adopted for a typical cavity configuration a simple stairstep approximation to the curved solid walls. For the purpose of predicting the stiffness and damping coefficients for labyrinth seals Wyssmann, Pham and Jenny [11] solved the time averaged Navier Stokes equations employing the $k-\epsilon$ model of turbulence. The results were used for modeling the flow field for the eccentric seal and to correlate the turbulence parameters used. An analysis for the eccentric seal was also presented by Nelson and Nguyen [12] and calculated its dynamic coefficients. They integrated the zeroth-order incompressible flow momentum equations together with Moody's friction equation in order to obtain the pressure distribution inside the seal. On the other hand Rhode and Sobolik [13] extended the method presented in [11] to include the effect of compressibility on the seal performance. They computed the pressure across a single cavity at different leakage flow Mach numbers and then used it to predict the leakage rate. The computer code used in the analysis of [11] and [13] is quite costly and cannot be applied directly to multicavity labyrinth seals as a whole. This is because of the unknown boundary conditions at the inlet of a particular cavity. This has led the

present author to treat the problem of the compressible turbulent flow through eccentric labyrinth seals of arbitrary geometry making use of the smallness of the height of the seal to shaft radius ratio as a simplifying feature to the governing equations. Adiabatic conditions for the flow are assumed and a particular toothed labyrinth seal shape is selected for the numerical computations.

2. Analysis

The geometrical configuration of the labyrinth seal selected and the coordinate system used in the analysis are shown in Fig. 1. By making an order of magnitude analysis noting that $b/R_s \ll o(1)$ the time averaged momentum and continuity equations may be expressed in the following form,

$$\begin{aligned} \frac{1}{R_s} \frac{\partial \bar{p}}{\partial \theta} &= \frac{\partial}{\partial y} \left[\bar{\mu} (1 + \epsilon_m / \nu) \frac{\partial \bar{u}}{\partial y} \right] \\ \frac{\partial \bar{p}}{\partial y} &= 0 \\ \frac{\partial \bar{p}}{\partial z} &= \frac{\partial}{\partial y} \left[\bar{\mu} (1 + \epsilon_m / \nu) \frac{\partial \bar{w}}{\partial y} \right] \\ \frac{1}{R_s} \frac{\partial (\bar{u} \bar{p})}{\partial \theta} + \frac{\partial (\bar{v} \bar{p})}{\partial y} + \frac{\partial (\bar{w} \bar{p})}{\partial z} &= 0 \end{aligned} \quad (1)$$

Where the bars denote time averaged dependent variables. Equations 1 are based on the assumption that turbulence is homogeneous and the radial pressure variation is negligible in comparison to the relatively large axial and tangential pressure gradients. The turbulence model which is found suitable for the present analysis is that described in [14]. The coefficient of eddy viscosity may be expressed as,

$$\epsilon_m / \nu = K \left[\eta h_c^* - \delta_1^* \tanh \eta h_c^* / \delta_1^* \right] \quad (2)$$

with $K = .4$ and $\delta_1^* = 10.7$
 where $h_c^* = (h/\nu) \sqrt{|\tau_c|/\bar{p}} = \sqrt{R_e} \frac{h}{\nu} \int_0^1 \frac{d\eta}{(1 + \epsilon_m / \nu)}$

Substituting from 2 into equs. 1 and integrating twice formally with respect to y we obtain in a dimensionless form the velocity distribution,

$$\begin{aligned} u^* &= \frac{h^2}{\mu^*} \frac{\partial p^*}{\partial \theta} \left[q_1(\eta) - \frac{q_1(1)}{q_2(1)} q_2(\eta) \right] R_e (b/R_s) + \frac{q_2(\eta)}{q_2(1)} \\ w^* &= (R_s/L) \frac{h^2}{\mu^*} \frac{\partial p^*}{\partial z} \left[q_1(\eta) - \frac{q_1(1)}{q_2(1)} q_2(\eta) \right] R_e (b/R_s) \end{aligned} \quad (3)$$

Satisfying the boundary conditions,

$$\begin{aligned} u^*(\theta, 0, z^*) &= 1, \quad u^*(\theta, 1, z^*) = 0 \\ w^*(\theta, 0, z^*) &= w^*(\theta, 1, z^*) = 0 \end{aligned} \quad (4)$$

$$\text{with } q_1(\eta) = \int_0^\eta \frac{\xi d\xi}{(1+\xi_m/\mu)}, \quad q_2(\eta) = \int_0^\eta \frac{d\xi}{(1+\xi_m/\mu)}$$

Substituting for u^* and w^* in equ. 1d and making a spatial average for the equation on the grounds that $\frac{\partial p^*}{\partial y} = 0$ we obtain ,

$$\frac{\partial}{\partial \theta} \left[\frac{\rho^* h^3}{\mu^* k_z} \frac{\partial p^*}{\partial \theta} \right] + (R_s/L)^2 \frac{\partial}{\partial z} \left[\frac{\rho^* h^3}{\mu^* k_z} \frac{\partial p^*}{\partial z} \right] = \frac{\partial}{\partial \theta} (\rho^* h^* F^*) \quad (5)$$

$$\text{where } 1/k_z = \int_0^1 \int_0^\eta (\frac{1}{2} - \xi) G_1(\xi) d\xi d\eta, \quad 1/k_z = \int_0^1 \int_0^\eta (\frac{1}{2} - \xi) G_2(\xi) d\xi d\eta,$$

$$F^* = [1 - q_1(1)/q_2(1)] / R_e (b/R_s)$$

$$\text{Here } G_1(\eta) = [1 - g(\eta)/(1 + \xi_m/\mu)] / \mu^* (1 + \xi_m/\mu),$$

$$G_2(\eta) = 1/\mu^* (1 + \xi_m/\mu), \quad g(\eta) = \frac{1}{2} K \eta h_c^* \tanh^2(\eta h_c^*/\delta_1^*)$$

Equation 5 is a generalization of that devised in [14] and applied to turbulent fluid flow in journal bearings [15]. The solution to equ. 5 for p^* requires the simultaneous solution of the energy equation incorporating the evaluation of the time averaged density ρ^* from the equation of state for the ideal gas and introducing the viscosity temperature power law for the gas (see [16]). Assuming adiabatic conditions to exist we may therefore write in dimensionless form ,

$$\rho^* \left[u_{av}^* \frac{\partial T^*}{\partial \theta} + (R_s/L) w_{av}^* \frac{\partial T^*}{\partial z} \right] = E \left[u_{av}^* \frac{\partial p^*}{\partial \theta} + (R_s/L) w_{av}^* \frac{\partial p^*}{\partial z} + \mu^* \Phi_{av}^* \right] + (b/R_e)(1/R_e P_r) \left[\frac{\partial^2 T^*}{\partial \theta^2} + (R_s/L)^2 \frac{\partial^2 T^*}{\partial z^2} \right] \quad (6)$$

$$p^* = [(\gamma - 1)/E\gamma] \rho^* T^* \quad (7)$$

$$\mu^* = T^{*\beta} \quad (8)$$

where Φ_{av}^* is the dimensionless time averaged dissipation function .

An expression for Φ_{av}^* is given in Appendix 2 .

Equation 6 is spatially averaged in radial direction and is to be solved for the time averaged temperature T^* together with eqs. 5 , 7 and 8 .

It is to be noted that although the order of magnitude analysis shows that the conduction terms in equ. 6 are small compared to convection , work of compression and dissipation terms they are retained here in order to keep the nature of the energy equation intact .

Equations 5 and 6 are modified using eqs. 7 and 8 in order to speed up the convergence of the numerical solution using iterative methods . They may be rewritten in the following forms ,

$$\frac{\partial^2 p^*}{\partial \theta^2} + (k_z/k_z)(R_s/L)^2 \frac{\partial^2 p^*}{\partial z^2} = Y_0(\theta, z^*) \quad (9)$$

$$\frac{\partial^2 T^*}{\partial \theta^2} + (R_s/L)^2 \frac{\partial^2 T^*}{\partial z^2} = X_0(\theta, z^*) \quad (10)$$

Expressions for $Y_0(\theta, z^*)$ and $X_0(\theta, z^*)$ are given in Appendix 2 .

Equations 9 and 10 are subject to the boundary conditions ,

$$\frac{\partial p^*}{\partial \theta}(0, z^*) = \frac{\partial p^*}{\partial \theta}(2\pi, z^*) = \frac{\partial T^*}{\partial \theta}(0, z^*) = \frac{\partial T^*}{\partial \theta}(2\pi, z^*) = 0$$

$$p^*(\theta, 0) = p_1^* \quad , \quad p^*(\theta, 1) = p_e^* \quad , \quad T^*(\theta, 0) = 1 \quad , \quad \frac{\partial T^*}{\partial z}(\theta, 1) = 0$$

It remains here to specify the geometry of the seal by providing an expression for h^* . For the eccentric toothed straight through seal selected here (see Fig. 1) we may write ,

$$h^* = 1 - \left[\left(\frac{1-c^*}{2} \right) (1 + \cos 2\pi n z^*) \right] + \epsilon c^* \cos \theta \quad (11)$$

where n and ϵ are the number of cavities and the eccentricity ratio respectively . Arbitrary geometrical configurations , however , may be used but this has to be subject to optimization techniques to search for the shape leading to minimum leakage rate . A problem worth considering in a separate publication .

The dimensionless leakage rate may be calculated from ,

$$\dot{m}^* = \dot{m} \sqrt{RT_1} / 2\pi R_s p_1 c = \left(\frac{p_0 \omega R_s^2 b \sqrt{RT_1}}{2\pi R_s c p_1} \right) \int_0^{2\pi} \int_0^1 \rho^* w^* dy^* d\theta \quad (12)$$

Solutions are obtained using mesh sizes of .05 in z^* and η and $\pi/36$ in θ . The data for the fluid and conditions of operation are given in Appendix 3.

3. Results and discussion

Figure 2 shows the results obtained for three concentric single cavity labyrinth seals having height to width ratios $b/a = .5$, 1 . and 2 . . This in fact implies that for a specific value of the height of the seal to radius of shaft ratio , taken in the present work equal to $.1$, the corresponding values of the ratio of the shaft radius to the overall length of the seal R_s/L will be equal to 5 , 10 and 20 respectively . The results clearly demonstrate that the smaller the ratio b/a the better the performance of the seal especially at lower values of the pressure ratio . Results for concentric seals having $b/a=1$. and with single , five and ten cavities are plotted in Fig.3 . The decrease in leakage rate when increasing the number of cavities is more pronounced at lower values of the pressure ratio . On the other hand for a given pressure ratio the percentage decrease in leakage rate resulting from increasing the number of cavities does not increase linearly . That is by doubling the number of cavities from 5 to 10 the percentage decrease in leakage rate will not be doubled . Figure 4 shows the effect of shaft eccentricity on the

performance of a single cavity seal having $b/a=1$. . The results show that increasing the eccentricity ratio increases the leakage rate . This increase is more pronounced at lower pressure ratios and higher values of the eccentricity ratio . The plots presented in Figs.2 , 3 and 4 here pertain to inlet Mach number $M=.5$. To examine the effect of changing M on the performance of the single cavity seal results are obtained for $b/a=1$. and for $M=.15$, $.25$, $.35$, $.40$, $.45$, $.50$ and $.75$. The decrease in M results in an increase in the leakage rate and this increase becomes very small as M approaches $.15$ irrespective of the value of the pressure ratio .

4. Conclusions

A simple approach to the turbulent compressible flow problem through labyrinth seals of arbitrary shapes has been developed . The theoretical model enabled the effect of shaft eccentricity on the performance of the seal to be included . It is found that for eccentricity ratios exceeding $.2$ the leakage rate is greatly increased . Further , the model provided a straight forward treatment of multi-cavity seals without the need to find the unknown inlet conditions for each cavity in the seal . The effect of the height to width ratio of the seal is easily demonstrated and found that the smaller the ratio the better the performance of the seal . It is also found that decreasing the value of the rotational Mach number increases the leakage rate up to $M=.15$ where the variations in it become small .

References

1. H.M.Martin, Labyrinth packings,Engineering, Jan. 10,1908,pp 35-36 .
2. M.J.Gercke, Berechnung der Ausflussmengen von labyrinthdichtungen, Die Wärme,N^o32, Aug 11,1934,pp513-517 .
3. F.Dollin and W.S.Brown, Flow of fluids through openings in series, Engineering,Aug 27,1937,pp 223-224 .
4. A.Igli, The leakage of steam through labyrinth seals,Trans. ASME, vol. 57,1935,pp 115-122 .
5. B.Rodkinson, Estimation of the leakage through a labyrinth gland, Proc. of Inst. Mech. Eng.,vol. 141,1939,pp 283-286 .
6. J.Jerie, Flow through straight-through labyrinth seals,Proc. of the 7th Int. Conf. for Appl. Mech.,vol. 2,1948,pp 70-82 .
7. G.Vermees, A fluid mechanics approach to the labyrinth seal leakage problem,Journal of Engineering for power,April 1961,pp 161-169 .
8. E.Benvenuti,G.Ruggeri and E.P.Tomassini, Analytical and experimental development of labyrinth seals for process centrifugal compressors, ASME,N.Y.,1979,PP 278-285 .

9. H.Stoff, Incompressible flow in a labyrinth seal, J.Fluid Mechanics, vol. 100, part 4, 1980, pp 817-829 .
10. D.L.Rhode, J.A.Demko, U.K.Traegner, G.L.Morison and S.R.Sobolik, Prediction of incompressible flow in labyrinth seals, J. of fluids Engineering, vol. 108, March 1986, pp 19-25 .
11. H.R.Wyssmann, T.C.Pham and R.J.Jenny, Prediction of stiffness and damping coefficients for centrifugal compressor labyrinth seals, J. of Engineering for gas turbines and power, vol. 106, Oct. 1984, pp 920-926 .
12. C.C.Nelson and D.T.Nguyen, Analysis of eccentric annular incompressible seals: Part 2 -Effects of eccentricity on rotordynamic coefficients, Journal of tribology, vol. 110, April 1988, pp 361-366 .
13. D.L.Rhode and S.R.Sobolik, Simulation of subsonic flow through a generic labyrinth seal, J. of Engineering for gas turbines and power, vol. 108, Oct. 1986, pp 674-680 .
14. C.W.Ng and C.H.T.Pan, A linearized turbulent lubrication theory, Trans. ASME, ser. D, vol. 87, 1965, pp 675-688 .
15. A.Z.Szeri, Tribology, friction, lubrication and wear, Hemisphere pub. Co., Mc Graw Hill book Co., N.Y., 1979 .
16. H.Schlichting, Boundary layer theory, 6th ed., Mc Graw Hill book Co., 1968 .

Appendix 1 : Nomenclature

a	Width of the cavity (mm)
b	Maximum height of cavity (mm)
c	Clearance (mm)
c*	Dimensionless clearance ($c^* = c/b$)
E	Eckert number ($E = \omega^2 R_s^2 / c_p T_o$)
h	Cavity local height (mm)
h*	Dimensionless local cavity height ($h^* = h/b$)
k _o	Fluid thermal conductivity ($W m^{-1} ^\circ C^{-1}$)
L	Length of seal (mm)
m	Mass flow rate ($kg s^{-1}$)
M	Inlet rotational Mach number ($M = [E/(\gamma-1)]^{1/2}$)
n	Number of cavities
\bar{p}	Fluid pressure (Pa)
p*	Dimensionless pressure ($p^* = \bar{p} / \rho_o \omega^2 R_s^2$)
P _r	Prandtl number ($P_r = \mu_o c_p / k_o$)
R _s	Shaft radius (mm)
R _e	Rotational Reynolds number ($R_e = \rho_o \omega R_s b / \mu_o$)
\bar{T}	Fluid temperature ($^\circ C$)
T*	Dimensionless temperature ($T^* = \bar{T} / T_o$)

$\bar{u}, \bar{v}, \bar{w}$	Time averaged velocity components in θ , y and z directions respectively ($m s^{-1}$)
u^*, w^*	Dimensionless time averaged velocity components in θ and z directions respectively ($u^* = \bar{u}/\omega R_s$, $w^* = \bar{w}/\omega R_s$)
y, z	Radial and axial coordinates (mm)
y^*, z^*	Dimensionless radial and axial coordinates ($y^* = y/b$, $z^* = z/L$)
β	Fluid viscosity index
γ	Ratio of specific heats ($\gamma = c_p/c_v$)
ϵ	Eccentricity ratio ($\epsilon = e/b$)
η	Dimensionless coordinate ($\eta = y/h$)
ω	Shaft angular velocity (s^{-1})
θ	Tangential coordinate (rad)
$\bar{\rho}$	Fluid density ($kg m^{-3}$)
ρ^*	Dimensionless density ($\rho^* = \bar{\rho}/\rho_0$)
$\bar{\mu}$	Fluid viscosity (mPa s)
μ^*	Dimensionless viscosity ($\mu^* = \bar{\mu}/\mu_0$)
ϵ_m	Eddy diffusivity ($m^2 s^{-1}$)
ν	Fluid kinematic viscosity ($m^2 s^{-1}$)

Appendix 2 : Expressions for ϕ_{av}^* , $Y_0(\theta, z^*)$ and $X_0(\theta, z^*)$

$$Y_0(\theta, z^*) = Y_1(\theta, z^*) + [Y_2(\theta, z^*) + Y_3(\theta, z^*)](\gamma - 1)/E\gamma, \quad X_0(\theta, z^*) = X_1(\theta, z^*) + X_2(\theta, z^*)$$

$$\phi_{av}^* = \left[\left\{ Q_3(1) - Q_1^2(1)/Q_2(1) \right\} Z_0(\theta, z^*) + \left\{ 1/Q_2(1) \right\} \right] / h^{2\beta} R_e (b/R_s)$$

$$\text{where } Y_1(\theta, z^*) = \mu^* k_\theta \left[\frac{\partial(\rho^* h^* F^*)}{\partial \theta} \right] / \rho^* h^{*3}$$

$$Y_2(\theta, z^*) = -\mu^* k_\theta \left[\frac{\partial}{\partial \theta} \left(\rho^* \mu^{*1/\beta} \right) \right] \left[\frac{\partial(\rho^* h^{*3})}{\partial \theta} / \mu^* k_\theta \right] / \rho^* h^{*3}$$

$$Y_3(\theta, z^*) = -\mu^* k_e (R_s/L)^2 \left[\frac{\partial}{\partial z} \rho^* \mu^{*1/2} \right] \left[\frac{\partial (\rho^* h^{*3} / \mu^* k_z)}{\partial z} \right] / \rho^* h^{*3}$$

$$X_1(\theta, z^*) = \left[u_{av}^* \frac{\partial \mu^*}{\partial \theta} + (R_s/L) w_{av}^* \frac{\partial \mu^*}{\partial z} \right] \rho^* \mu^{*1/2} P_r R_e R_s / \beta b$$

$$X_2(\theta, z^*) = - \left[u_{av}^* \frac{\partial p^*}{\partial \theta} + (R_s/L) w_{av}^* \frac{\partial p^*}{\partial z} + \mu^* \phi_{av}^* \right] E P_r R_e R_s / b$$

$$Z_0(\theta, z^*) = \left[\left(h^2 \frac{\partial p^*}{\partial \theta} \frac{1}{\mu^*} \right)^2 + (R_s/L)^2 \left(h^2 \frac{\partial p^*}{\partial z} \frac{1}{\mu^*} \right)^2 \right] R_e^2 (b/R_s)^2$$

$$Z_3(1) = \int_0^1 \frac{\eta^2 d\eta}{(1 + \epsilon_m/\nu)}$$

Appendix 3 : Fluid and seal data

Inlet fluid temperature

$$T_0 = 20^\circ \text{C}$$

Fluid density at 20°C

$$\rho_0 = .123 \text{ kg m}^{-3}$$

Fluid specific heat

$$c_p = 718 \text{ J kg}^{-1} \text{ } ^\circ \text{C}^{-1}$$

Fluid viscosity at 20°C

$$\mu_0 = .018 \text{ mPa s}$$

Fluid viscosity index

$$\beta = 1.$$

Fluid thermal conductivity

$$k_0 = .025 \text{ W m}^{-1} \text{ } ^\circ \text{C}^{-1}$$

Maximum height of cavity

$$b = 5 \text{ mm}$$

Shaft radius

$$R_s = 50 \text{ mm}$$

Clearance

$$c = .5 \text{ mm}$$

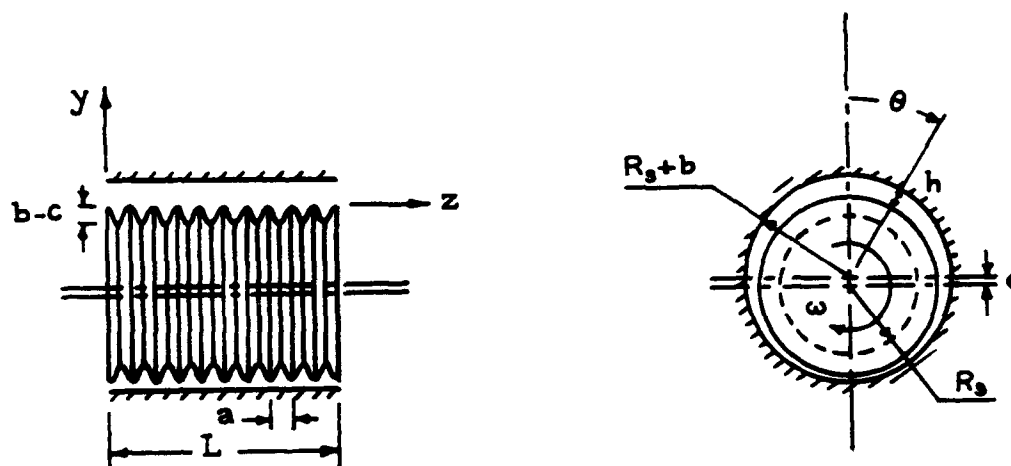


Fig.1 The geometrical configuration of the seal and the coordinate system .

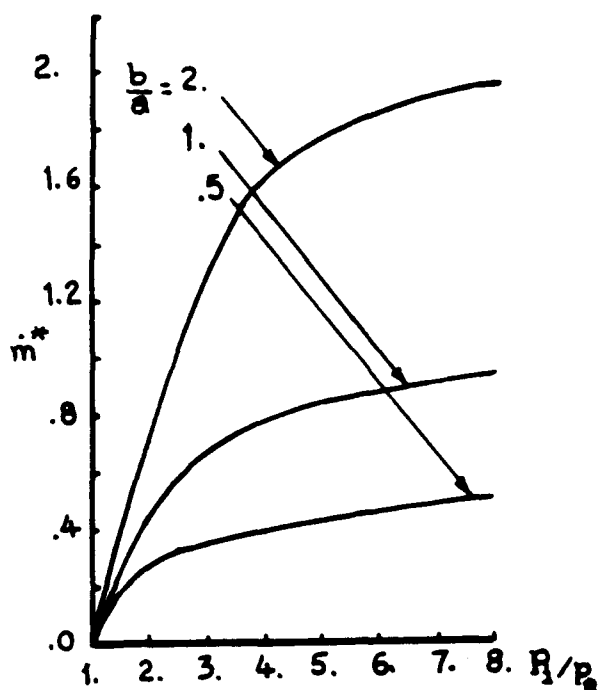


Fig. 2 Performance of single cavity seals having different b/a .
($E=0$, $M=.5$)

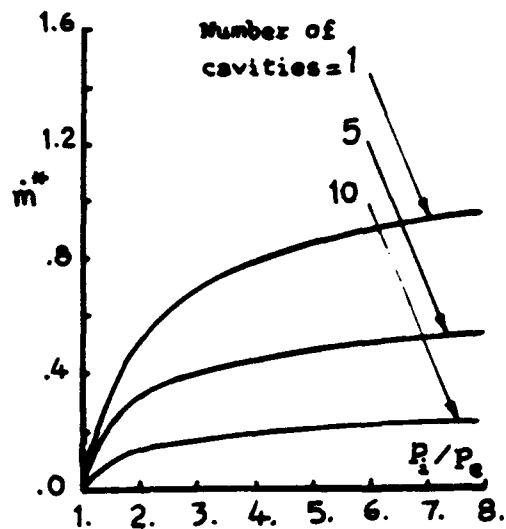


Fig. 3 Performance of seals having different number of cavities.
($E=0$, $M=.5$, $b/a=1$)

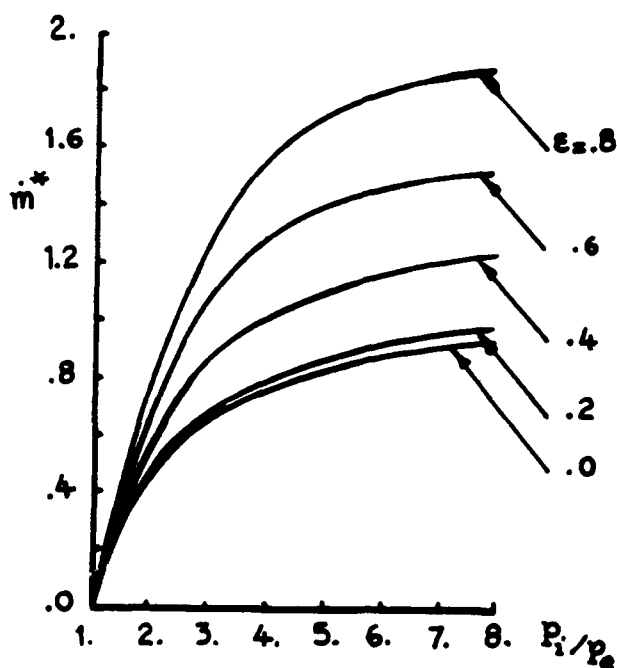


Fig. 4 Effect of eccentricity on the performance of single cavity seals.
($M=.5$, $b/a=1$)

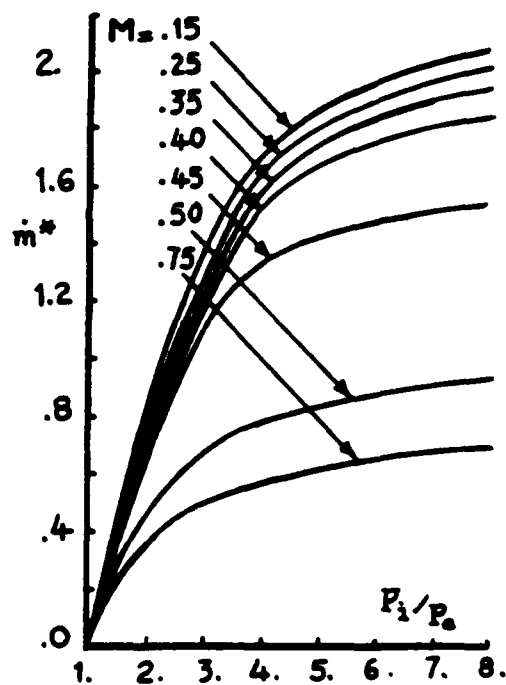


Fig. 5 Effect of inlet Mach number on the performance of a single cavity seal. ($E=0$, $b/a=1$)

The Formation of Streamwise Vortices Around the Circumference of Underexpanded Supersonic Axisymmetric Jets

Arnette, S.A., Samimy, M., and Elliott, G.S.
Department of Mechanical Engineering
The Ohio State University
Columbus, Ohio 43210

ABSTRACT

Pitot pressure measurements and flow visualizations were used to investigate streamwise vortices previously observed in underexpanded jets. A converging nozzle and a converging-diverging nozzle of design Mach number 1.5 were used to generate jet flows of equivalent Mach numbers up to 2.5. By operating the nozzles fully expanded, overexpanded, and underexpanded, insight was gained into both the occurrence and cause for formation of the vortices. Spatially-stationary streamwise vortices were found to exist in the near-field region around the circumference of underexpanded jets in the vicinity of the jet boundary. Short exposure visualizations show the vortices persist much further downstream without average organization. Visualizations suggest adjacent vortices have streamwise vorticity of opposite sign, so the action of adjacent vortices is to either pump jet fluid radially outward or entrain ambient fluid radially inward towards the jet. The downstream extent, strength, and number of vortices around the jet circumference increase with degree of underexpansion. A large number of vortices is found near the nozzle exit. Fewer vortices of larger scale are found further downstream, indicative of a merging process. The absence of the vortices in fully expanded and overexpanded jets suggests the vortices result from a Taylor-Görtler instability.

INTRODUCTION

The shock cell structure of jets operated at underexpanded conditions is well known. Adamson and Nicholls¹ found the main characteristics to be those presented in Fig. 1. Upon encountering the lower ambient pressure at the nozzle exit, the gas passes through an expansion fan. The expansion waves reflect from the jet boundary as compression waves, which coalesce to form the intercepting shock. At low pressure ratios, the intercepting shocks meet at the jet axis. For higher pressure ratios, however, these shocks are connected by a normal shock, or Mach disk, as shown in Fig. 1. In both cases, reflected shocks are formed which intersect the jet boundary and reflect as expansion waves. The cell structure repeats itself downstream until the flow becomes subsonic everywhere in the jet.

Zapryagaev and Solotchin² used Schlieren photography and pressure measurements to demonstrate the presence of stationary streamwise vortices in an underexpanded jet issuing from a conical Mach 1.5 nozzle at a pressure ratio of 10. The vortices are proposed to be of the Taylor-Görtler type with adjacent vortices having streamwise vorticity of opposite sign. A vortex merging process is suggested by Schlieren images which show the number of vortices to decrease with increasing downstream distance. Novopashin and Perepelkin³ used Rayleigh scattering to generate average cross-sectional density maps of high¹ expanded axisymmetric jets (stagnation-to-ambient pressure ratio of 100) issuing from a sonic orifice and found a periodic departure from axisymmetry. They proposed the lobed nature of the density maps was a consequence of stationary streamwise vortices. Krothapalli et al.⁴ demonstrated the

existence of stationary streamwise vortices in a moderately underexpanded axisymmetric jet issuing from a converging nozzle at a pressure ratio of 5.1. Pitot pressure measurements show sinuous type variation of the total pressure around the jet circumference, suggesting streamwise vortices exist and possess significant strength. Laser sheet lighting visualizations of jet cross-sections were obtained by collecting the scattering from condensed water particles formed when the water originally present in the ambient air as vapor was entrained and mixed with cold supersonic fluid. Indentations into the region marked by the condensed water particles support the presence of streamwise vortices.

The main objective of this study was to further investigate streamwise vortices in supersonic jets with methods similar to those employed by Krothapalli et al.⁴ Jets covering a wide range of pressure ratios were investigated, issuing from both a converging nozzle and a converging-diverging nozzle of design Mach number 1.5. Unlike the conical Mach 1.5 nozzle used by Zapryagaev and Solotchin², the Mach 1.5 nozzle in this study was designed with the method of characteristics to generate uniform flow at the nozzle exit. The cited studies indicate streamwise vortices are important in underexpanded jets. In this work, fully expanded, overexpanded, and underexpanded jets were studied to draw more general conclusions concerning the relevance of the observed streamwise vortices to supersonic jets.

EXPERIMENTAL PROCEDURE

The experiments were conducted at The Ohio State University Aeronautical and Astronautical Research Laboratory. An air storage capacity of 41 m³ at pressures up to 16.5 MPa allows the jet facility to be run continuously. The stagnation pressure of the jet was maintained to within $\pm 1\%$ of the set point. This along with the variation of the ambient pressure led to a small run-to-run variation in the equivalent Mach numbers about the reported values.

Pitot pressure measurements and flow visualizations were performed on sonic and Mach 1.5 nozzles with exit diameters of 12.7 mm and 19.05 mm, respectively. Experiments are referred to in terms of equivalent Mach number (M_e), which is the Mach number that would result in an isentropic expansion from a given stagnation pressure to ambient pressure. The cases investigated, along with the Reynolds numbers based on throat conditions, are presented in Table 1.

Pitot pressure data was acquired with a standard probe mounted on a three-axis traversing system. The system allowed positional accuracy to ± 0.013 mm along each axis. The probe sensing diameter was 0.76 mm. A Bourdon tube pressure gage capable of measurements to within ± 3.5 kPa was used. Measurements were taken through 180° of the jet circumference. The number of measurement points was determined by dividing the 180° arc length for the given measurement radius by the sensing diameter of the probe. Adjacent measurement points are separated by an arc length equal to the sensing diameter of the probe. Because of the non-parallel flow in overexpanded and underexpanded jets, the pitot pressure measurements are not of the true total pressure ahead of the probe. Only the component of the total pressure corresponding to flow velocity perpendicular to the pitot probe face, which is aligned

Table 1. Investigated flow conditions.

Nozzle	M_1	$p_{\text{stag}} / p_{\text{amb}}$	$Re_D / 10^6$
Sonic	1.0	1.89	0.375
Sonic	1.25	2.59	0.515
Sonic	1.5	3.67	0.727
Sonic	1.75	5.33	1.05
Sonic	2.0	7.82	1.55
Sonic	2.25	11.6	2.29
Sonic	2.5	17.1	4.26
Mach 1.5	1.5	3.67	1.03
Mach 1.5	2.0	7.82	2.19
Mach 1.5	2.5	17.1	4.79
Mach 1.5	1.3	2.70	0.756
Mach 1.5	1.18	2.36	0.661

parallel to the nozzle exit cross-section, is measured. However, since the interest is in azimuthal variation due to vortices, the measurements are useful.

Light scattered from condensed moisture in the jet mixing region was used to visualize the jet flow. Sheets parallel to the face of the nozzle were used to obtain jet cross-sections. Some images were recorded with the aid of a molecular iodine filter. Without the filter, the technique is the commonly employed laser sheet lighting. A Spectra Physics model 2020 continuous-wave argon-ion laser was used in conjunction with a CCD camera set to a "long" exposure time to collect average cross-sections. This technique is beset by unwanted reflections from the outer nozzle surfaces and scattering from stray particles in the ambient fluid outside the jet. For these reasons, the molecular filter was employed in a filtered Mie/Rayleigh scattering technique for the collection of all instantaneous images. Miles et al.⁵ demonstrated that a molecular filter containing iodine vapor can be used in conjunction with 532 nm Nd:YAG illumination to eliminate unshifted background light. The illuminating light was provided by a frequency-doubled Spectra Physics Nd:YAG laser at 532 nm, injection-seeded to provide a narrow linewidth and approximately 50 GHz tuning capability. The pulse duration was 9 ns, effectively freezing the flow. Images were collected with a CCD camera. A more complete description of the facility and instrumentation is provided by Arnette⁶.

Condensed water particles formed around the periphery of the jet when moist ambient air was entrained and the ambient water vapor encountered the low temperature, high speed jet fluid. The jet air is dried to low moisture levels. This method of visualizing condensed particles in the mixing region has been used in the investigation of supersonic jets by many investigators.^{6,9} Dibble et al.⁷ estimated the condensed particle size as 100 nm in similar experiments. Taking this value as a characteristic diameter (assuming spherical particles) gives an r/λ ratio of 0.094 (where r is the particle radius), which falls in the transitional region between Mie and classical Rayleigh scattering

theories. This estimate seems reasonable for the current study. A distinct polarization direction effect on the scattered intensity was present, but the scattering could not be attenuated to near extinction by varying the polarization direction. This suggests the scattering was near the transition between Rayleigh and Mie scattering, so the term filtered Mie/Rayleigh scattering is used. Fourguette et al.⁹ studied a Mach 1.5 air jet with the same method of condensed water particle formation. Using the results of Samimy and Lele¹⁰, an estimate of 350 nm is found for the maximum allowable particle size.⁹ Assuming a particle size on the order of 100 nm as suggested previously, the particles should accurately follow the flow.

RESULTS AND DISCUSSION

Figure 2 presents pitot pressure measurements taken around the circumference of an $M_j = 2.0$ jet issuing from the sonic nozzle at $X/D = 2.00$. Measurements are presented at various measurement radii, r (non-dimensionalized with the nozzle exit radius, R), non-dimensionalized by the average pitot pressure at each radius. More complete results and discussion can be found in Arnette^{6,11}.

The axial location of the measurements in Fig. 2 ($M_j = 2.0$) is 5 mm downstream of the Mach disk. Six local minima are seen in the figure, and the maximum variation level is approximately 230 kPa at $r/R = 1.20$ (61% of the average pitot pressure at $r/R = 1.20$). As proposed previously³, each of the indentations in the azimuthal pressure measurements is thought to indicate the presence of two counter-rotating, spatially-stationary, streamwise vortices. Adjacent counter-rotating vortices gives rise to a pumping action. Depending on the senses of rotation of the adjacent vortices, either jet fluid is pumped radially outward or ambient fluid is entrained radially inward.

Figures 3 and 4 present azimuthal pitot pressure profiles for the $M_j = 1.5$ and 2.5 cases issuing from the sonic nozzle at $X/D = 2.00$, respectively. Strong indentations are located in the $\theta = 90^\circ - 110^\circ$ region. As proposed previously³, this suggests the departure from axisymmetry results from the amplification of perturbations supplied by the nozzle. No noticeable imperfections were found in the nozzle. The data of Fig. 4 ($X/D = 2.00$) was collected 6.5 mm upstream of the Mach disk. The maximum variation level of approximately 360 kPa occurs at $r/R = 2.20$ (81% of the average pitot pressure at $r/R = 2.20$), and the profile exhibits approximately 11 local minima.

Azimuthal pitot profiles were collected at several downstream locations. The measurement radius displaying maximum variation was not the same for all downstream locations. Instead, it varied similarly to the radial distance between the jet boundary and the jet centerline in the underexpanded jet (see Fig. 1), suggesting the vortex tubes experience curvature like the flow in the vicinity of the jet boundary. The number of indentations encountered in the azimuthal profiles decreased with increasing distance from the nozzle exit, suggesting that vortex merging occurs.

The azimuthal pitot pressure profiles for all of the M_j cases listed in Table 1 display clear trends (data not included is presented by Arnette^{6,11}). For the jets issuing from the sonic nozzle, M_j is a convenient indicator of the degree of underexpansion (i.e. the degree of underexpansion increases with M_j). At a given downstream location, both the number and dimensional 'strength' of the indentations increase with degree of underexpansion. Each of the

indentations is believed to result from the presence of two counter-rotating vortices. The vortices persist in an average sense for a greater downstream distance with increasing equivalent Mach number. A model presented by Arnette et al.¹¹, in which the underexpanded jet is surrounded by a hypothetical "vortex sheet" shear layer (infinitesimally thin), gives the largest possible azimuthal pitot pressure variation that could be caused by the action of counter-rotating vortices. Variation magnitudes calculated with the model compare favorably to the measurements.¹¹

Pitot pressure azimuthal profiles were also generated for the Mach 1.5 nozzle at various M_j . The fully expanded and overexpanded jets displayed axisymmetry, indicating an absence of vortices. Although the azimuthal pitot profiles of the underexpanded jets issuing from the Mach 1.5 nozzle displayed variations similar to Fig's. 2-4, two trends were clear: 1) the variations were smaller than those found in jets of the same M_j issuing from the sonic nozzle and 2) the variations in the azimuthal pitot profiles existed further downstream in the jets issuing from the sonic nozzle. These comparisons indicate the vortices are stronger and persist further downstream with increasing degree of underexpansion.

Since the flow curvature and radial velocity gradient in the underexpanded jet increase with M_j for a given nozzle, the strength of the vortices would increase with M_j for a given nozzle if the vortices result from the Taylor-Görtler instability. This was seen to be the case in the azimuthal pitot profiles. Likewise, since the degree of underexpansion is much less in a Mach 1.5 nozzle than in a sonic nozzle operated at the same M_j , the strength of the streamwise vortices would be much greater in the plume of the underexpanded sonic nozzle if the vortices are the Taylor-Görtler type. Again, this was the case.

To further investigate the flow features discussed above, flow visualizations were performed. Long exposure laser sheet lighting images are presented in Fig. 5 for the $M_j = 2.0$ jet issuing from the sonic nozzle. All presented cross-sections are slightly distorted due to the off-axis position of the camera. In all cases, the presented pitot pressure measurements were taken from the top center of the jet ($\theta = 90^\circ$) to the bottom center ($\theta = 270^\circ$), traversing around the circumference in a counter-clockwise fashion referenced to the image observer. The different sizes of the condensation rings in the images is a result of camera positioning only. Indentations in the condensation ring become more noticeable with increasing equivalent Mach number, similar to the variations in the pitot pressure azimuthal profiles. Image A at $X/D = 1.00$ displays many small indentations. The left half of Image B ($X/D = 2.00$) displays six well defined indentations, which corresponds exactly to the pitot pressure azimuthal profiles of Fig. 2 for the same angular region. The center of the condensation ring in Image B is at approximately $r/R = 1.50$. The indentations in the condensation rings of Images C and D ($X/D = 3.00$ and 5.00 , respectively) become less noticeable, although indentations are clearly still present at $X/D = 3.00$.

Figure 6 presents instantaneous filtered Mie/Rayleigh scattering images of the $M_j = 2.0$ jet issuing from the sonic nozzle. Images A, B, C, and D were collected at $X/D = 1.00, 2.00, 3.00$, and 5.00 , respectively. While vortices are clearly present and stationary in an average sense from the azimuthal pitot profiles and long exposure

images, instantaneous images suggest significant deviation from the average distribution is present at any given instant. Strong counter-rotating streamwise vortices appear to be present instantaneously at $X/D = 5.00$, although they have lost their average spatial organization.

CONCLUSION

The existence and nature of streamwise vortices in high Reynolds number, axisymmetric jets operating in overexpanded, fully expanded, and underexpanded regimes have been studied. The measurement of the azimuthal variation of the pitot pressure was used as an indirect measure of the vortices' strength. Long exposure laser sheet lighting and instantaneous filtered Mie/Rayleigh scattering were used as visualization techniques. The presence of spatially-stationary, streamwise vortices has been demonstrated indirectly in underexpanded jets issuing from sonic and Mach 1.5 nozzles. The counter-rotating vortices form indentations in the region between the intercepting shock and the outer edge of the shear layer surrounding the jet. The downstream development of these vortices for equivalent Mach numbers from 1.0 to 2.5 was investigated. As reported previously by Zapryagaev and Solotchin² and Krothapalli et al.⁴, the vortices exist in the vicinity of the jet boundary and are spatially-stationary for the first few exit diameters downstream. Good agreement was found between the visualizations and pitot measurements concerning the number and angular location of the vortices circumference. Visualizations and pitot measurements indicate significant merging of adjacent vortices occurs, leading to an increase in scale of the vortices with increasing downstream location. The vortices appear to result from the Taylor-Görtler instability, as originally suggested by Zapryagaev and Solotchin². This is strongly suggested by the absence of the vortices in perfectly expanded jets issuing from both converging and converging-diverging nozzles and overexpanded jets issuing from a converging-diverging nozzle. Supporting arguments are: 1) the vortices occur in counter-rotating pairs, 2) the vortices do not exist at the same radius for all downstream locations, but instead experience curvature with the flow as is typical of Taylor-Görtler vortices, and 3) the vortices display the expected trend of increasing strength with increasing curvature and radial velocity gradient.

The effect of increasing M_j is: 1) the vortices exist in an average sense further downstream, 2) the vortices at a given downstream location are increased in strength, and 3) there is a larger number of vortices. The vortices exist instantaneously downstream of where they cease to be spatially-stationary.

ACKNOWLEDGEMENTS

The authors thank fellow graduate students V. Belovich, M. Reeder, D. Glawe, and J. Dawson for help in the experiments. Thanks also go to AARL staff and J. Dawson for the fabrication of the nozzles. The support of NASA Lewis under Cont. NAG3-764 with Dr. K.B.M.Q. Zaman is appreciated. Fellowships from NSF to Arnette and Ohio Aerospace Institute to Elliott are gratefully acknowledged.

REFERENCES

- ¹ Adamson, T.C., Jr. and Nicholls, J.A., 1959, "On the structure of jets from highly underexpanded nozzles into still air," *J. Aero. Sci.*, 26, 16-24.

- ² Zapryagaev, V.I. and Solotchin, A.V., 1988, "Spatial structure of flow in the initial section of a supersonic underexpanded jet," (in Russian) Academy of Sciences USSR, Siberian section, Institute of Theoretical and Applied Mechanics Preprint No. 23-88, UDK 533.6.011.
- ³ Novopashin, S.A. and Perepelkin, A.L., 1989, "Axial symmetry loss of a supersonic preturbulent jet," *Phys Let. A*, 135, 290-293.
- ⁴ Krothapalli, A., Buzyna, G., and Lourenco, L., 1991, "Streamwise vortices in an underexpanded axisymmetric jet," *Phys Fluids A*, 3, 1848-1851.
- ⁵ Miles, R.B., Lempert, W.R., and Forkey, J., 1991, "Instantaneous velocity fields and background suppression by filtered rayleigh scattering," AIAA-91-0357.
- ⁶ Arnette, S.A., 1992, "An experimental investigation of the structure of high reynolds number supersonic jets," MS Thesis, The Ohio State University.
- ⁷ Dibble, R.W., Barlow, R.S., Mungal, M.G., Lyons, K., Yip, B., and Long, M.B., 1989, "Use of Rayleigh scattering from condensed water vapor as a means of imaging an underexpanded supersonic jet," STAR Mtg., Nashville, TN.
- ⁸ Samimy, M., Zaman, K.B.M.Q., and Reeder, M.F., 1991, "Supersonic jet mixing enhancement by vortex generators," AIAA-91-2263.
- ⁹ Fourquette, D.C., Mungal, M.G., and Dibble, R.W., 1991, "Time evolution of the shear layer of a supersonic axisymmetric jet," *AIAA J.*, 29, 1123-1130.
- ¹⁰ Samimy, M. and Lele, S.K., 1991, "Motion of particles with inertia in a compressible free shear layer," *Phys. Fluids A*, 3, 1915-1923.
- ¹¹ Arnette, S.A., Samimy, M., and Elliott, G.S., 1992, "On streamwise vortices in high Reynolds number supersonic axisymmetric jets," submitted to *Phys Fluids A*.

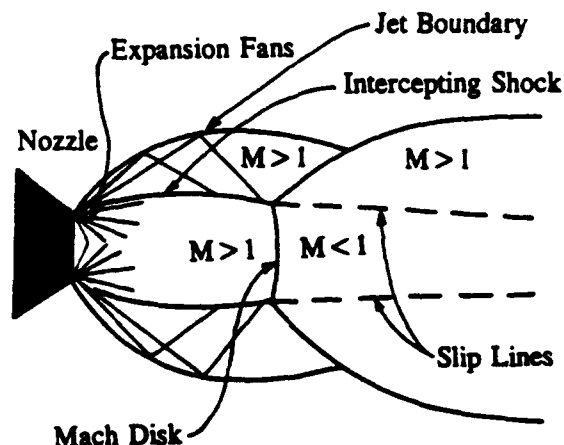


Fig. 1. Shock cell structure in the plume of an underexpanded jet.

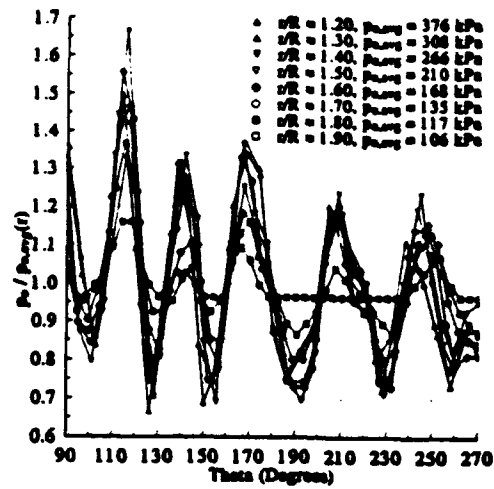


Fig. 2. Azimuthal variation of the pitot pressure for $M_j = 2.0$ issuing from sonic nozzle at $X/D = 2.00$.

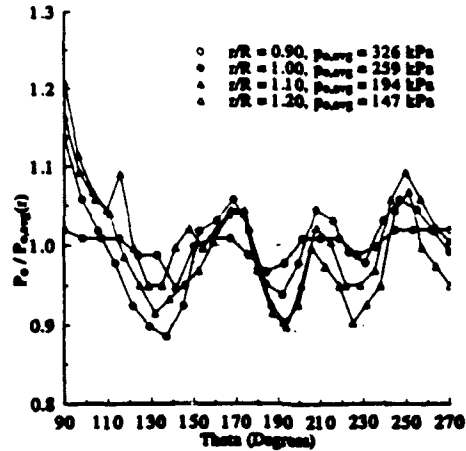


Fig. 3. Azimuthal variation of the pitot pressure for $M_j = 1.5$ issuing from sonic nozzle at $X/D = 2.00$.

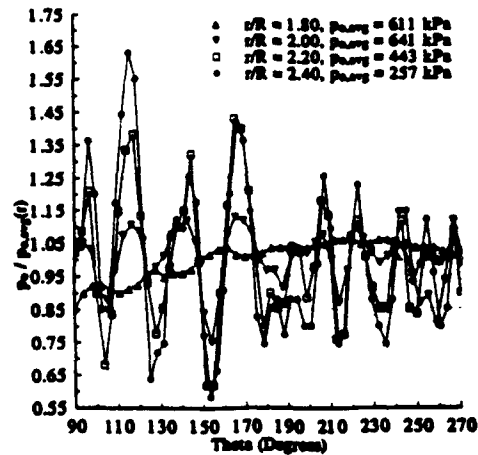


Fig. 4. Azimuthal variation of the pitot pressure for $M_j = 2.5$ issuing from sonic nozzle at $X/D = 2.00$.

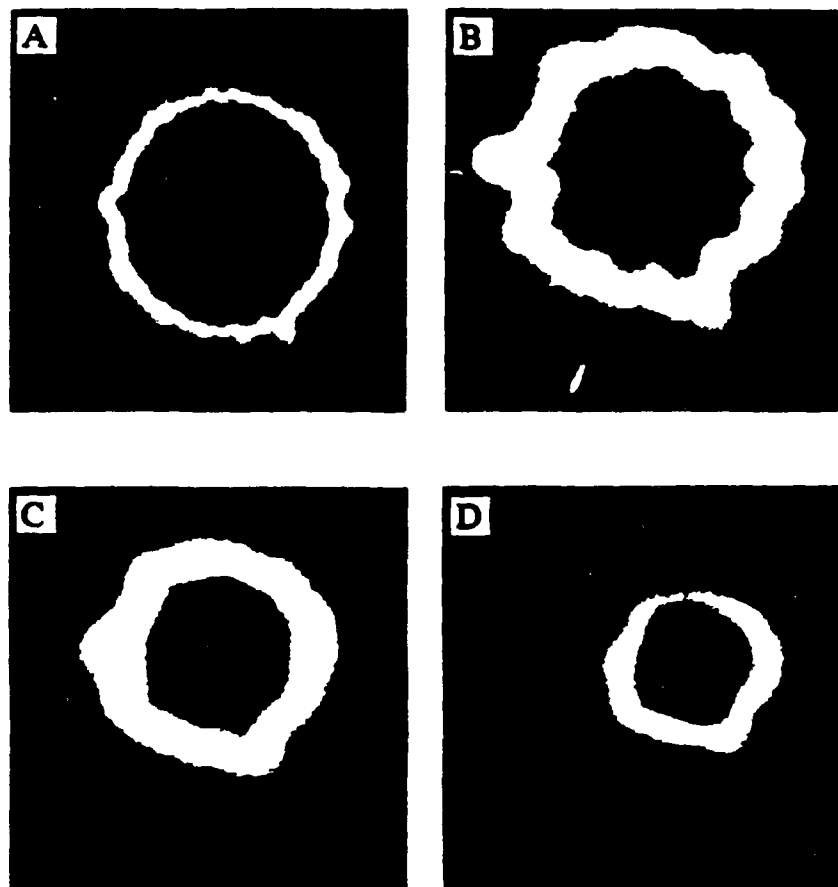


Fig. 5. Long exposure laser sheet lighting images of $M_j = 2.0$ jet issuing from sonic nozzle. Images A, B, C, and D were collected at $X/D = 1.00, 2.00, 3.00$, and 5.00 , respectively.

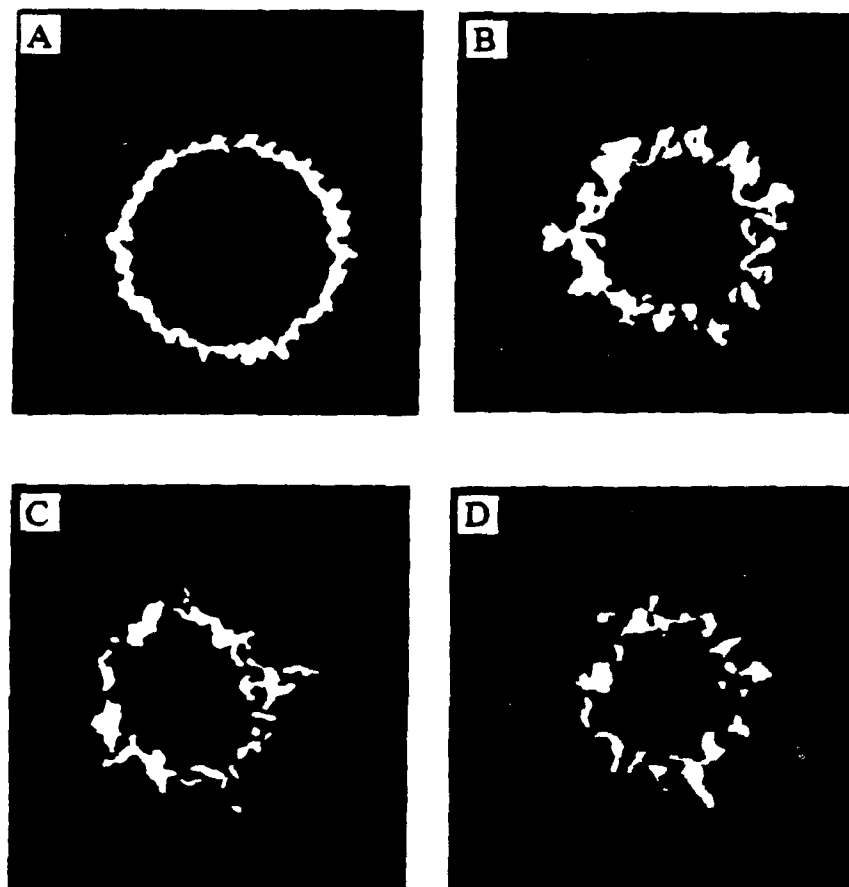


Fig. 6. Filtered Mie/Rayleigh scattering images of $M_j = 2.0$ jet issuing from sonic nozzle. Images A, B, C, and D were collected at $X/D = 1.00, 2.00, 3.00,$ and $5.00,$ respectively. No specific time relationship exists between the individual images.

TURBULENT FLOW OF AN ANNULUS WITH INNER ROTATING CYLINDER AND A DEAD END WALL

Parviz Meratiⁱ, Joseph C. Parkerⁱⁱ, and William V. Adamsⁱⁱⁱ

ⁱAssociate Professor, Department of Mechanical and Aeronautical Engineering, Western Michigan University, Kalamazoo, Michigan 49008

ⁱⁱGraduate Research Assistant, Department of Mechanical and Aeronautical Engineering, Western Michigan University

ⁱⁱⁱVice President, Research and Development, Durametallic Corporation, Kalamazoo, Michigan 49001

Abstract

Laser Doppler Velocimetry is used to measure mean flow velocity and turbulence intensity in an annulus with inner rotating cylinder and a dead end wall. In addition, root mean square values of the velocity fluctuations are measured. Snell's law is used to predict the measurement volume locations and the angles between the laser beams in the annulus.

The flow Taylor number and Reynolds number are 4.4×10^9 and 3.6×10^5 , respectively. Flow in the annulus is three dimensional and turbulent. A toroidal vortex with a centerline passing through the annulus centerline extends along its length. In this vortex, mean components of the velocity in the radial and axial directions are small compared with the mean azimuthal component. Flow particles follow helical paths in the annulus. Mean flow is toward the end wall in the region close to the outer cylinder. The flow particles occupy the region close to the inner cylinder as they travel toward the annulus throat. There is a constant flow exchange through the open annulus end.

The axial turbulence intensity is larger in the central region of the annulus flow compared with the regions close to the annulus walls. For the azimuthal turbulence intensity component, the largest magnitudes are obtained near the stationary wall where there is a sharp gradient of the mean azimuthal velocity component.

Nomenclature

b	Annulus clearance
D	Inner cylinder diameter
d	Particle mean diameter
f	Frequency
n	Refractive index
p	Pressure
Re	Reynolds number
r	Radius of the inner cylinder
Ta	Taylor number
U	Time-mean velocity component
u	Velocity component
\bar{u}	Root mean square value of the velocity component fluctuations
X,Y,Z	Laboratory coordinate system
κ	Half angle between laser beams
λ	Wave length of laser light
μ	Dynamic viscosity
ν	Kinematic viscosity
ρ	Density
τ	Period of particle fluctuation in a fluid
ϕ	Angle between the bisector of the beams and the outer cylinder tangent
ω	Inner cylinder angular speed

Subscripts

a	Average
D	Doppler
g	Glass
p	Particle
r	Radial direction
s	Surface of the inner cylinder
f	Fluid
x	X-direction
θ	Azimuthal direction

I. Introduction

Turbulent annular flow is found in various rotating machinery such as cooling systems in gas turbine rotors, flow passages of turbomachinery, heat exchangers, electric rotating machinery, journal bearings, and mechanical seals in pumps. Knowledge of the fluid stress distribution, velocity variation with passage length and radius, turbulence structure, and pressure drop characteristics in a turbulent annular flow with inner rotating cylinder are important for effective analysis and design. Fluid flow and heat transfer properties of the flow in this type of geometry are necessary for an optimum performance with regard to the maximum temperature and power rating.

Oklishi and Serovy¹ measured the mean velocity distribution in smooth annuli with radius ratios 0.344, 0.531, and 0.781 in the range of Reynolds numbers 12,000 to 100,000. Polkowski² investigated theoretically the turbulent flow between coaxial cylinders with the inner cylinder rotating. Yamada³ measured the torque between co-axial cylinders with the inner cylinder rotating by the water flow. Morrison, et al.⁴ measured the flow field inside an annulus with a 0.00127 m clearance, Reynolds number 27,000, and Taylor number 6,600.

The previous research mostly dealt with either a closed cavity or an annulus having an inlet on one end and an outlet on the other. The present experimental investigation is performed in an annulus with one dead end wall and inner cylinder rotating. The open end of the annulus is located in the wake of an impeller.

II. Experimental set-up and procedure

IIa. Operating Conditions

A Duriron Group II pump with balance holes (impeller diameter 25.4 cm), a Plexiglas casing, and an annulus with a Plexiglass wall were used for ease of access by laser beams for LDV measurements and flow visualization. Schematic of the pump with the annulus is shown in Figure 1. The inner cylinder is set-screwed to the shaft to maintain and provide face loading, axial position, and drive.

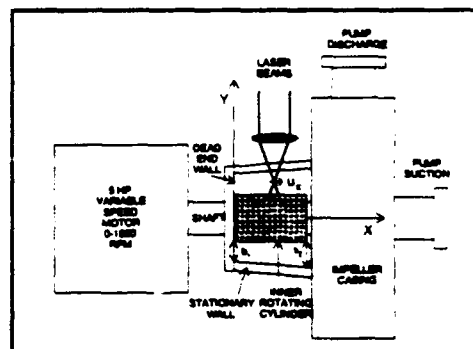


Figure 1. Schematic of the pump, the annulus, and a set-up for u_x measurements

The inner cylinder rotates at 1,750 RPM and the volumetric flow rate for the pump is 435 lit/min. Water temperature in the recirculating tank was raised 17 °C during the three initial hours of the tests. This temperature rise was mainly due to the frictional heat at the seal face located at X=0 and the turbulent viscous dissipation. A 15.24 m long, 1.27 cm copper conduit carrying cool tap water was placed inside the main water tank to remove the heat. The large flow mixing generated by the pump discharge in the tank provided adequate conditions for heat transfer. The water temperature remained constant at 20 °C during the duration of the tests.

The flow Taylor number $Ta = (\omega^2 r b_a^3)/\nu^2$ for the annulus is 4.25×10^9 . The average clearance is represented by $b_a = (b_1 + b_2)/2$. b_1 and b_2 are shown in Figure 1. The flow Reynolds number is $Re = U_s D/\nu = 3.52 \times 10^5$. Experiments were performed under the following conditions:

$$\omega = 183 \text{ rad/sec}$$

$$U_s = 5.67 \text{ m/sec}$$

$$r = 0.031 \text{ m}$$

$$b_1 = 0.015 \text{ m}$$

$$b_2 = 0.017 \text{ m}$$

$$\nu_w = 10^{-6} \text{ m}^2/\text{sec at } 20^\circ\text{C}.$$

For LDV measurements, water is seeded with silver coated particles to produce a signal with adequate signal to noise ratio. This ensures that the particles follow flow fluctuations of highest frequencies existing in this type of flow⁵. The silver coated particles have a specific gravity of 2.6 and a mean diameter $d = 9 \mu\text{m}$. Calculations based upon $f = 1/(2\pi\tau)$, where

$$\tau = \frac{\rho_p d_p^2}{18\mu_w} \quad (1)$$

show that in water, these particles follow flow fluctuations which possess frequencies up to 13,603 Hz.

11b. Mean Velocity and Turbulence Intensity Measurements

A dual beam one component LDV system was used for velocity measurements. To measure the axial component u_x , the plane of the two beams is formed in the X-Y plane as shown in Figure 1. By rotating the plane of the two beams 90 degrees around the optical axis, the azimuthal u_θ and radial u_r components

of velocity are measured as shown in Figure 2. Back scattering technique is used for mean velocity and turbulence intensity measurements.

The measurement volume location, κ , and λ change due to the beam refraction in Plexiglas and water. The half angle between the beams in water inside the chamber represented by κ , and the radial location of the measurement volume with respect to the shaft axis were measured and

predicted using Snell's law by Merati, et al.⁶ The wave length of laser light in water is $\lambda_w = \lambda/n_w$. Refractive indices of water n_w and Plexiglas n_p are measured to be equal to 1.33 and 1.49, respectively.

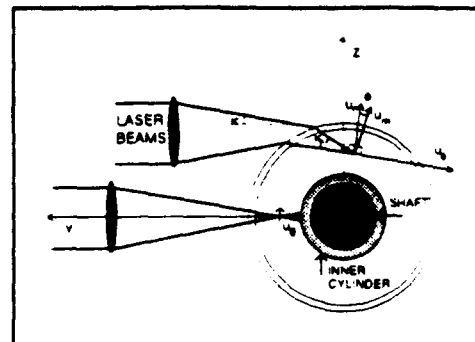


Figure 2. Experimental set-up for measurement of azimuthal and radial components

For u_r measurements, the bisector of the two beams is not tangent to the cylinder as shown in Figure 2. Thus, the measured component u_m is contaminated with the azimuthal component u_θ according to the following relationship:

$$u_m = u_r \cos \phi + u_\theta \sin \phi \quad (2)$$

By photographing the refracted beams, ϕ was found to be constant and equal to 0.79° over the annulus length. Equation (2) is used to obtain U , since $U_\theta \sin \phi$ is not negligible relative to U_m . The one component LDV system and the present experimental set-up is not capable of measuring u_r , because of the contaminating effect of the azimuthal velocity component. In addition, u_r was not measured in the region $Z \geq 39$ mm due to the severe beam refraction and reflection near the outer cylinder wall.

III. Results

IIIa. Velocity and Turbulence Intensity Field

The azimuthal, axial, and radial components of the mean velocity are shown in Figures 3, 4, and 5 respectively. The azimuthal component is dominant with a maximum value near 8 m/sec and is approximately equal to 5.67 m/sec on the surface of the inner cylinder. The linear speed of the inner cylinder's surface is 5.67 m/sec. The radial and axial components have maximum values of 0.1 m/sec and -0.7 m/sec, respectively. The azimuthal velocity component between $Y=36-40$ mm increases as X decreases, i.e., as the dead end wall approaches. Conversely, the azimuthal velocity component between $Y=40-48$ mm

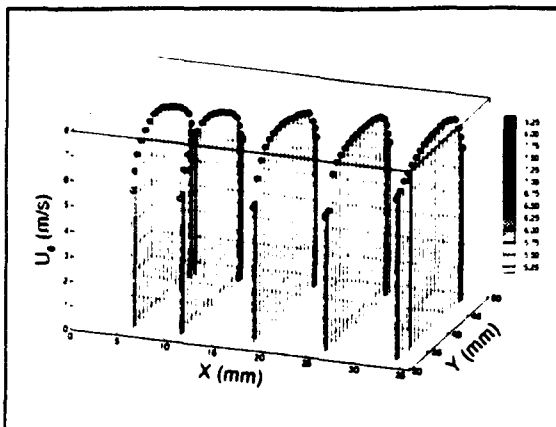


Figure 3. Azimuthal mean velocity component

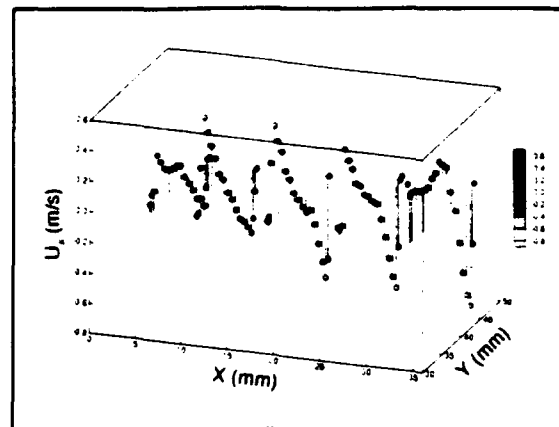


Figure 4. Axial mean velocity component

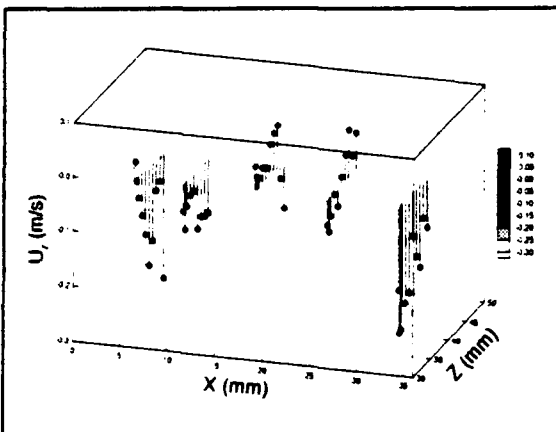


Figure 5. Radial mean velocity component

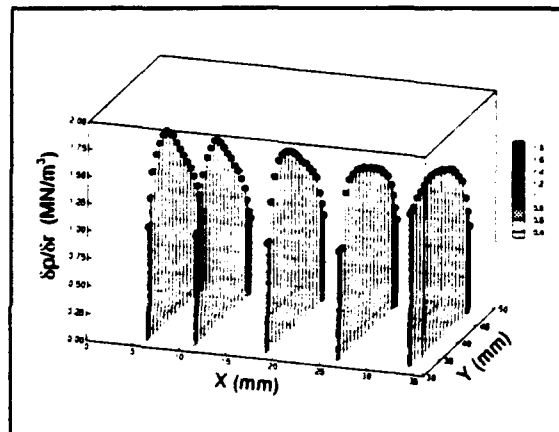


Figure 6. Radial mean pressure gradient

decreases as X decreases. The dominant terms in the momentum equation for the radial direction simplify to Equation (3).

$$U_\theta^2 = \frac{\rho}{r} \frac{\partial p}{\partial r} \quad (3)$$

Therefore, the change in U_θ along the X -axis is driven by the varying pressure gradient $\partial p / \partial r$ as shown in Figure 6.

Assuming azimuthal symmetry for the axial component of the velocity, continuity of mass is not satisfied at some of the X -constant planes. This asymmetry is possibly due to the existence of non-symmetrical inlet conditions at the open end of the annulus.

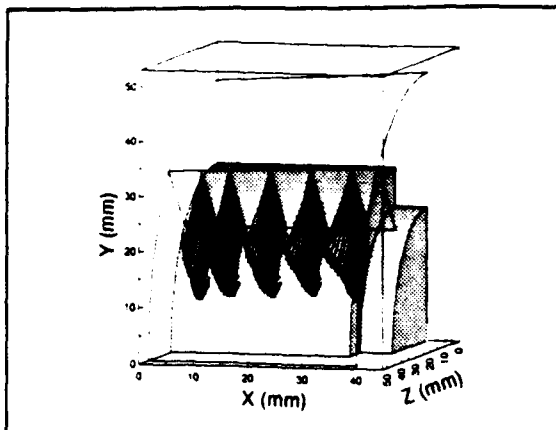


Figure 7. Total velocity vector including U_x , U_y , and U_z .

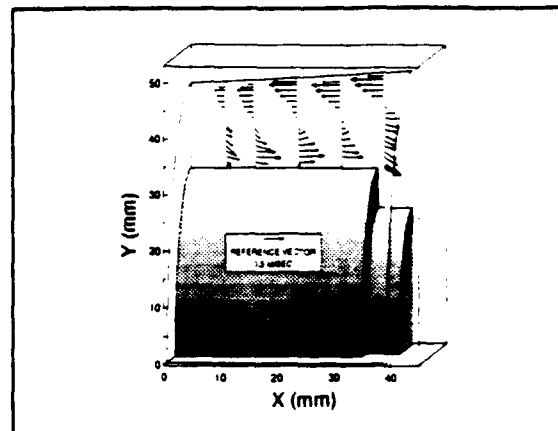


Figure 8. Cross flow velocity vectors including U_x and U_y .

The total velocity vectors of Figure 7 show that at $X=34$ mm, flow enters the annulus near the outer cylinder wall and leaves the annulus near the inner rotating cylinder. The plane of the velocity vectors becomes more parallel to the Y-Z plane as the dead end wall is approached. Thus, a fluid particle most likely enters the chamber near the outer cylindrical wall and follows a helical path until it reaches the dead end wall. Due to the large pressure field at the corner of the outer cylinder and the dead end wall, the particle is forced toward the inner rotating cylinder to follow the rest of its helical journey toward the open end of the annulus. Depending on its proximity to the annulus conical midplane, the particle either leaves or is directed back into the annulus as shown by flow vectors of Figure 8.

Assuming azimuthal symmetry, velocity vectors of Figures 7 and 8 show a toroidal vortex extending the length of the inner cylinder with its circular center line approximately passing through the annulus centerline. The radial velocity component was not measured at the same location as azimuthal and axial components. However, since the radial components are small compared with the azimuthal components, the overall flow behavior is adequately represented by the measured flow vectors.

The azimuthal and axial components of the turbulence intensity profiles are shown in Figures 9 and 10, respectively. For the azimuthal turbulence intensity component, the largest magnitudes ($\approx 20\%$) are obtained near the stationary annulus wall where there is a sharp gradient of the mean azimuthal velocity component. The axial turbulence intensity components are higher in the central region of the secondary flow

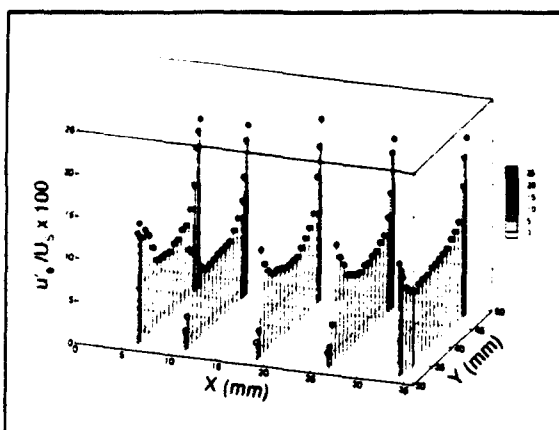


Figure 9. Azimuthal turbulence intensity

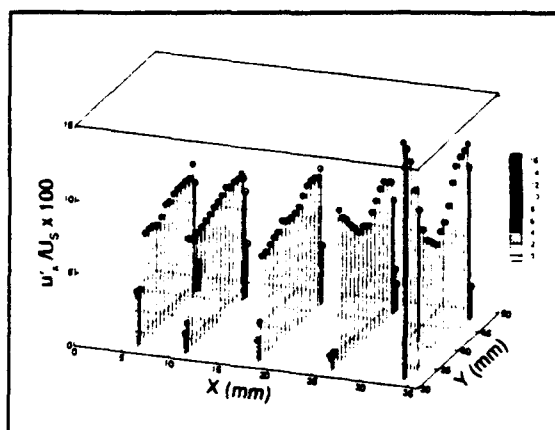


Figure 10. Axial turbulence intensity

compared with the regions near the walls. The large values of u'_θ / U_θ near the shaft at $X=34$ mm, which is slightly downstream of the inner cylinder, are due to the separated flow at the edge of the inner cylinder.

IV. Conclusions

LDV measurements showed that flow in the annulus located downstream of an impeller is three dimensional and turbulent. A toroidal vortex spans the axial length of the annulus. The cross section of this vortex on a constant θ plane has a center approximately located at the middle of this plane. In this vortex, mean components of the velocity in the radial and axial directions are small compared with the mean azimuthal component. The shape of the U_θ profile is largely determined by the pressure field of the annulus flow since U_θ is the dominant component of the mean velocity.

Flow particles follow a helical path as they move toward the dead end wall in a region close to the outer cylinder and return toward the open throat in a region close to the rotating inner cylinder. There is a constant flow exchange through the open annulus end.

For the azimuthal turbulence intensity component, the largest magnitudes were obtained near the stationary wall where there is a sharp gradient of the mean azimuthal velocity component. The axial turbulence intensity is higher in the central region of the annulus flow compared with the regions close to the walls.

V. Acknowledgement

The authors thank the National Science Foundation under grant number MSS-9114453 and Durametallic Corporation in Kalamazoo, Michigan for their financial support.

VI. References

¹Oklishi, T.H., and Serovy, G.K., 1964, "Experimental Velocity Profiles for Fully Developed Turbulent Flow in Air in Concentric Annuli," ASME Paper 64-WA/FE-32.

²Polkowski, J.W., 1984, "Turbulent Flow Between Coaxial Cylinders with the Inner Cylinder Rotating," Transactions of the ASME, Vol. 106.

³Yamada, Y., 1962, "Torque Resistance of a Flow Between Rotating Co-Axial Cylinders Having Axial Flow," Bulletin of J.S.M.E., Vol. 5, No. 20, pp. 634-642.

⁴Morrison, G.L., Johnson, M.C., and Tatterson, G.B., 1988, "3-D Laser Anemometer Measurements in an Annular Seal," ASME Gas Turbine and Aeroengine Congress, Amsterdam, the Netherlands.

⁵Technical Data on "Laser Velocimeter Techniques," 1979, Published by TSI incorporated.

⁶Merati, P., Parker, J. C., Biek, K.T., Glas, R. W., 1991, "Flow Measurements in Chambers of Mechanical Seals Using Laser Doppler Velocimetry Technique," Proceedings of the 1991 NSF Design and Manufacturing Systems Conference, pp. 275-279.

EFFECT OF BOUNDARY LAYER CONTROL ON FLOW THROUGH AN OFFSET DUCT

J.A. Mathis, Assistant Professor
Wu Tong, Graduate Research Assistant
Mechanical Engineering Department
Wichita State University
Wichita, KS 67208-1595

INTRODUCTION

The flow of air through curved ducts has been studied experimentally and numerically. This particular area of study is inspired by problems that require the delivery of a fluid from an inlet to an exit where physical constraints preclude a straight path. The particular configurations that occur in aircraft inlet ducts have been the studied in the propulsion laboratory at the National Institute for Aviation Research. Rectangular S-shaped ducts models, two-dimensional representations of inlet ducts geometries (found, for example in aircraft such as the Boeing 727 and Lockheed L-1011) have been the subject of studies investigating curvature effects, non-constant cross-sectional area and imposed inlet boundary layers. The purpose of this project was to investigate the effect of boundary layer control, in the form of wall suction, on the flow through an S-shaped duct with constant cross-sectional area. Suction was obtained by the obvious method of applying an external vacuum source, and in addition, by forming a by-pass system, wherein the naturally occurring areas of high and low pressure are used to good advantage in a self contained system. Velocity profiles and turbulent intensity levels across the duct were measured. These studies were undertaken as fundamental flow investigations and with the assumed goal that such measures as boundary layer control are intended to influence a flow for maximum mass flow rate, uniform exit velocity profiles, minimal turbulence levels and stabilization of the flow against separation at those areas deemed critical.

REVIEW

Several general features of flow through curved channels has been identified through experiment and analysis. Ramaprian and Shivaprasad(1) have demonstrated that curvature has very definite effects on the turbulent structure. At the convex wall, turbulence is inhibited; diffusion of turbulent energy from the wall is decreased, integral time scales are decreased, and the turbulent kinetic energy distribution shifts to higher wave numbers. The opposite situation occurs at the concave wall, hence, in general, the convex wall is said to "stabilize" turbulence, while the concave wall is said to "destabilize" it.

When a fluid enters an S-shaped duct (see Figure 1), a radial pressure gradient develops, forcing the pressure to increase outward from the center of curvature, while the velocity decreases. At the transition of the first bend, and the second, reversed bend, the pressure and velocity field changes are reversed. However, when entering the second bend, the boundary layer thickness has of course increased. Hence, the thickened boundary layer, when forced to proceed through the adverse pressure gradient along the concave wall becomes a critical area in the flow, and is subject to flow separation when the mass flow rate is increased or when the flow is subjected to external disturbances. If the duct were to be a diffusing duct, rather than constant cross-sectional area, this would be even more critical.

Butz(2) obtained hot wire anemometer data in rectangular (2-D) S-shaped ducts. His turbulence measurements supported the convex/concave expectations; centerline velocity measurements clearly showed the distortion of velocity profiles due to curvature effects. Profiles shown later in this paper in Figures 4-5 are similar.

Experimental work performed at the NIAR propulsion lab includes the investigations in several areas. Reyman(3) investigated changes in cross-sectional area and curvature in a 2-D rectangular duct, and developed optimization criteria to design a duct for maximum pressure recovery while avoiding flow separation. Kitchen(4) obtained 2-D laser velocimeter data in 2-D rectangular S-shaped ducts of constant cross-sectional area to verify simultaneous development of computational techniques. Said(5) studied the effect of imposed inlet boundary layer on flow through a S-shaped duct of constant cross-sectional area. He found very little apparent difference in pressure, velocity or turbulence data with inlet boundary layer thicknesses equal to 3%, 25% and 30% of the duct width. Tohmaz(6) designed and constructed a set of inlet lips. This design, based on Borda Mouthpiece streamlines, was made to be used with the 2-D duct rig in order to provide a smooth and uniform inlet flow. The lip design is shown in Figure 2. These inlet lips were used in this study.

EXPERIMENTAL SET UP AND MEASUREMENTS

The set up for testing engine inlet and nozzle structures consists of the components shown in Figure 3. Velocity measurements are obtained with a laser velocimeter, whose system components included a 2-W Argon Ion laser, Dantec 55X optics producing a three-beam system, one photo-multiplier and one Dantec counter processor. Seeding for velocity measurements was provided by spraying monodisperse polystyrene spheres mixed with ethanol near the duct inlet. A particle size of 1.2 microns was used. Pressure measurements were made with a Scanivalve system,

and all data collected on a PC in the laboratory. The duct model used in these experiments was a constant cross-sectional area duct made of two 45-degree circular arcs. The curved top and bottom sidewalls were made of fiber-composite, the straight vertical side walls were clear acrylic, for LDV measurements. Static pressure taps were located on the top and bottom walls along the duct centerline. The inlet lips shown in Figure 2 were attached to the front of the duct.

Two fan speeds were chosen for study; mean inlet velocities of 73.5 fps (speed 1), and 119 fps (speed 2) with corresponding Reynolds numbers (based on the duct height) of 1.06×10^5 and 1.73×10^5 . At each speed, velocity profiles and turbulence measurements were obtained along the traverse lines indicated in Figure 1. Velocity profile results are presented in Figures 4-5. From these figures the nature of the flow through the S-shaped duct is clearly indicated. At the inlet, the flow is immediately influenced by the radial acceleration and the uniform inlet flow is distorted with higher velocities near the top of the duct and lower velocities near the bottom. This trend continues as the flow proceeds through the curve; the velocity profiles at plane B show an increasing amount of deflection. At the inflection plane, curvature in the opposite direction begins to straighten the flow, and the distortion of the velocity profiles is reversed. At plane D the velocity profile was found to be nearly reversed from that found at plane B. At the outlet traverse, the profile appeared to be returning to an undistorted profile.

Turbulence levels were also measured, in the flow direction only. This data is presented in Figures 6-7.

There seems to be little difference in core turbulent intensities. The data does show rather clearly in a qualitative way, the diffusion of turbulent kinetic energy away from the walls. An inspection of the turbulent energy levels at the inflection traverses shows that the expected effect of concavity versus convexity on the diffusion of turbulent energy is verified--turbulence levels are higher nearer the top wall than the bottom wall. Further downstream, at the outlet traverse, the opposite situation has occurred, and here the measurements indicate that the diffusion of turbulent kinetic energy is more rapid from the bottom wall.

After obtaining these measurements, the duct was modified to allow a study of some flow control schemes. The first of these was the installation of a wall suction system. At plane D, a series of holes were drilled into the top and bottom walls, a chamber was constructed over the openings of the holes which was in turn connected to the building vacuum supply. Since the purpose of this flow control measure is intended to produce a more uniform and less turbulent outlet

velocity profile, measurements were taken at the outlet plane. Results are shown in Figure 8-9. The outlet velocity profiles, compared to those without the suction, are not markedly different. At the higher speed, the outlet turbulent intensities do show some variation, with higher turbulent intensities located in the center of the flow with the suction system operating.

Another form of flow control was investigated. Rather than using a vacuum system for suction, the chambers at the top and bottom of the duct were joined with a vent. The intent was to induce flow from the high pressure region. Again, outlet velocity profiles and turbulent intensities were obtained, and are shown in Figures 10 and 11.

CONCLUSIONS

The data presented here represents some exploratory investigations into the use of vacuum and by-pass flow control applied to the S-Shaped duct. No appreciable change in the exit velocity profiles was noted with either method. At the higher of the two speeds studied, both methods resulted in higher but more uniform turbulent intensity levels across the center of the duct. The by-pass system was especially effective in producing a fairly uniform turbulent intensity across a large extent of the duct width.

Many variables remain to be explored in the use of such method, such as the exact placement and area of the porous surfaces. In a duct with sharper turns, or a diffusing duct, where the available speeds in the test rig would be high enough to produce flow separation, removal of the high pressure fluid along the upper wall could be significant in preventing or delaying flow separation.

REFERENCES

1. Ramaprian, B.R. and Shivaprasad, B.G., "Structure of Turbulent Boundary Layers Along Mildly Curved Surfaces", Journal of Fluid Mechanics, Vol. 85, March, 1978.
2. Butz, L.A., "Turbulent Flow in S-Shaped Ducts", M.S. Thesis, Purdue University(1980).
3. Reyman, F., "Air Flow Through S-Shaped Ducts with Area Change", Ph.D. Thesis, Wichita State University(1989).
4. Kitchen, B.J., "Toward the Optimization of a Non-Diffusing, Two-Dimensional, S-Shaped Duct", Ph.D. Thesis, Wichita State University(1989).
5. Said, M.J., "Effect of Imposed Inlet Boundary Layer on Flow Through a 45°-45° S-Shaped Duct, M.S. Thesis, Wichita State University(1990).

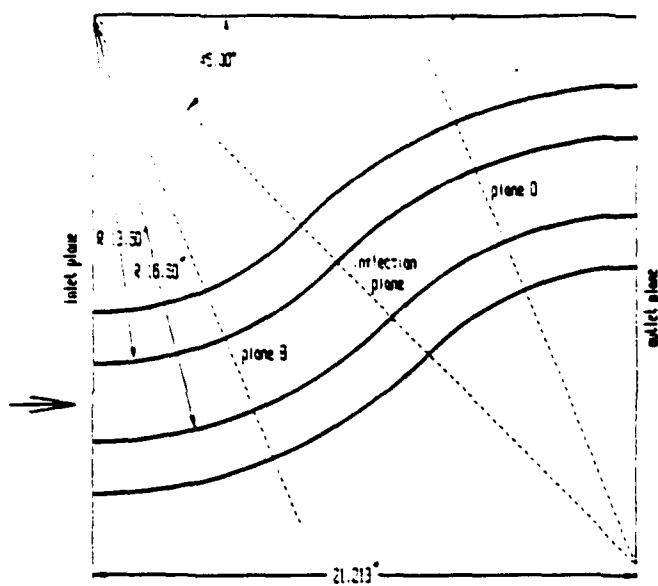


Figure 1.
S-Shaped Duct, Dimensions and
Location of Velocity Measurements

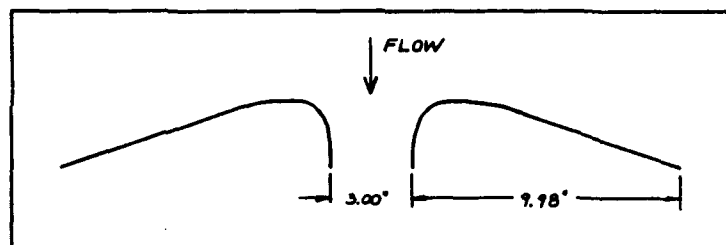


Figure 2.
Duct Inlet Lips

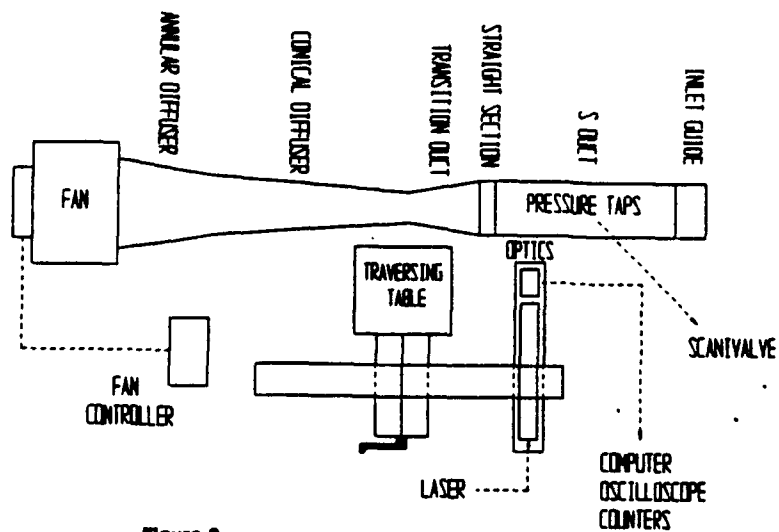


Figure 3.
Experimental Facilities

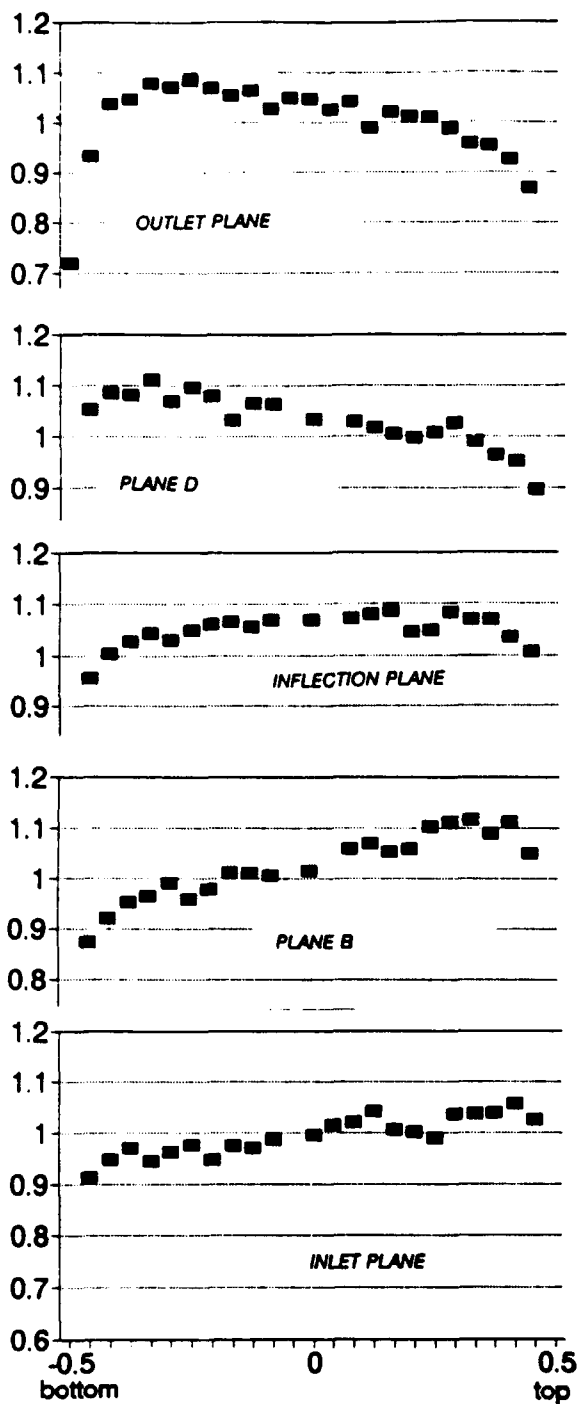


Figure 4.
Velocity Profiles at Speed 1
Velocities are Non-Dimensionalized by
Inlet Average Velocity

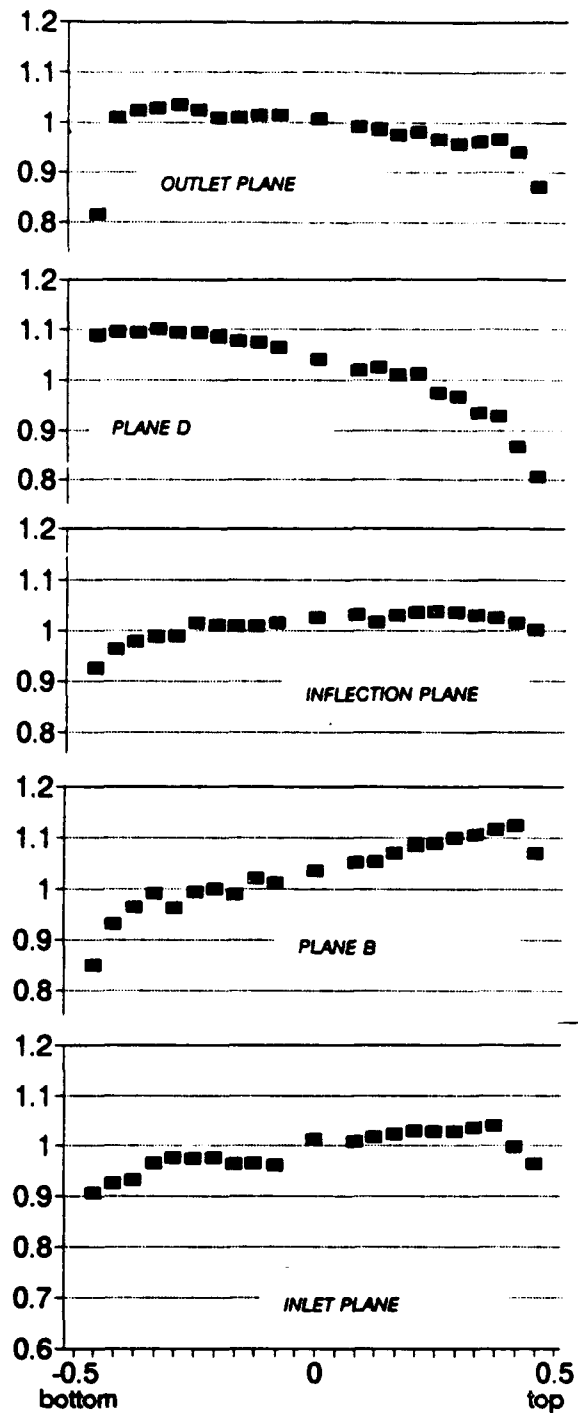


Figure 5.
Velocity Profiles at Speed 2
Velocities are Non-Dimensionalized by
Inlet Average Velocity

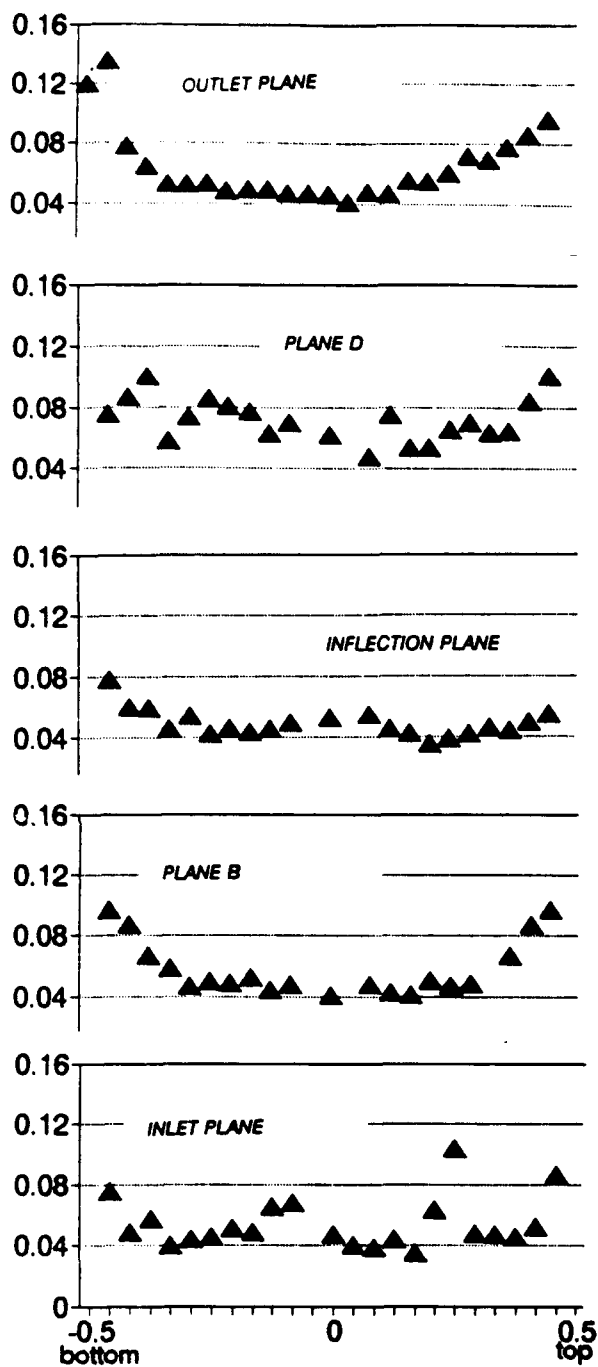


Figure 6.
Turbulent Intensities at Speed 1

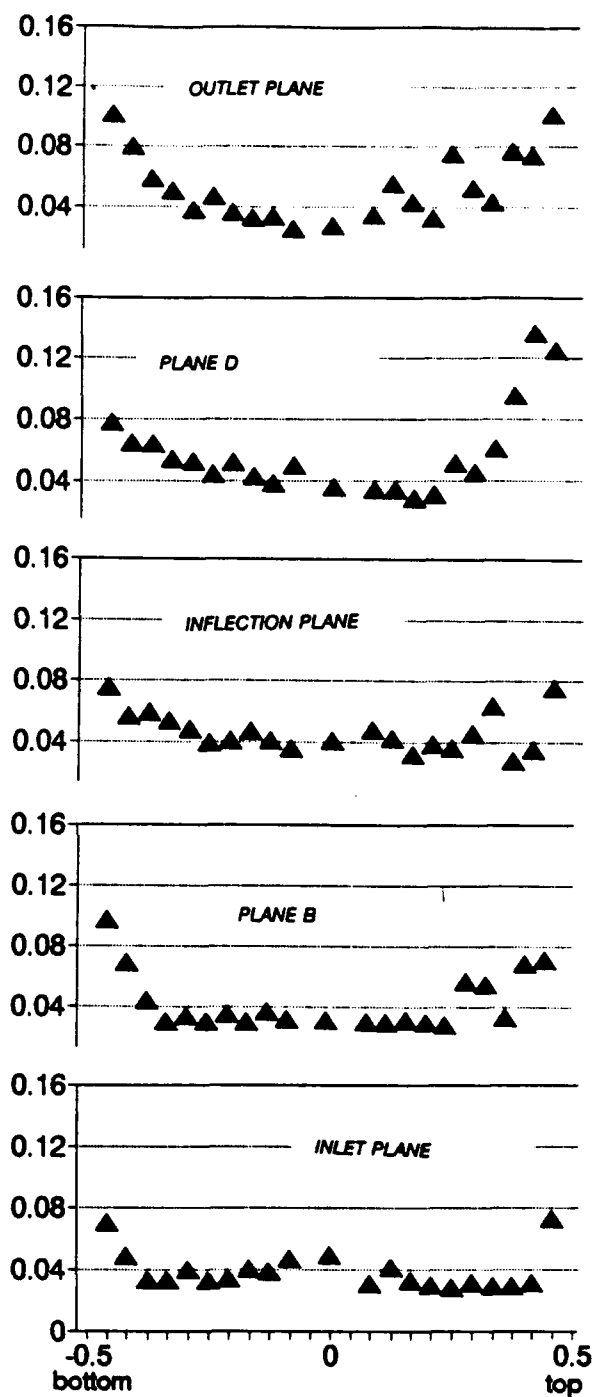


Figure 7.
Turbulent Intensities at Speed 2

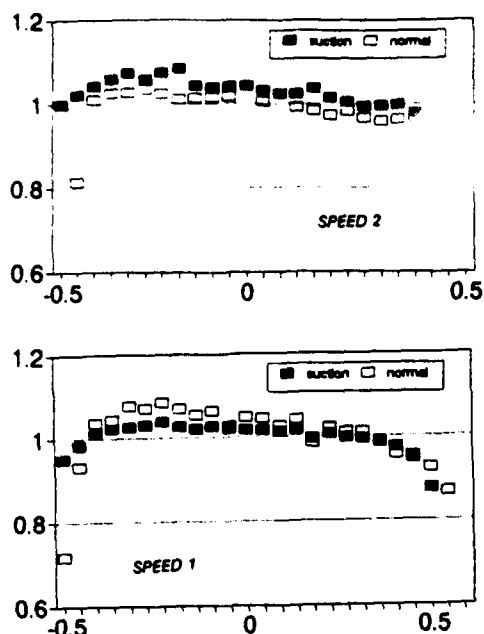


Figure 8.
Outlet Plane Velocity Profiles with Suction System
Compared with normal duct flow at same speed

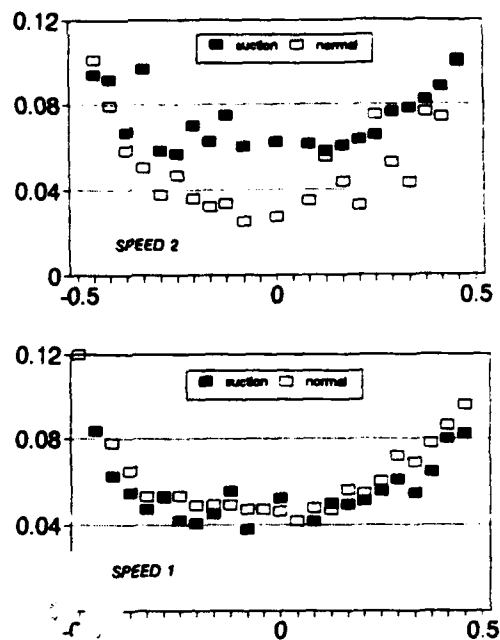


Figure 9.
Outlet Plane Turbulent Intensities with Suction System
Compared with normal duct flow at same speed

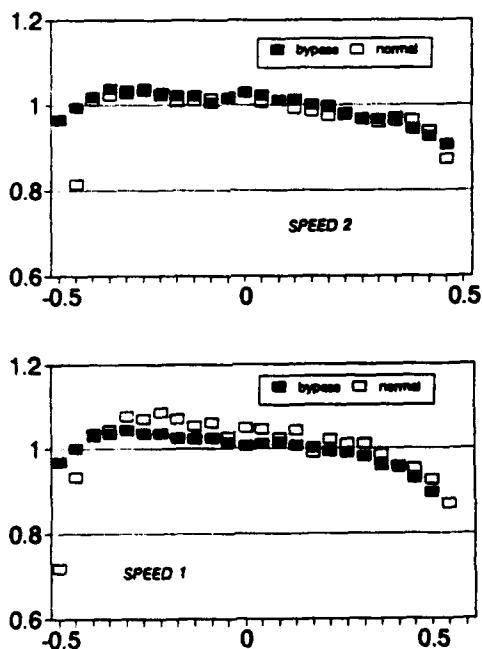


Figure 10.
Outlet Plane Velocity Profiles with By-Pass System
Compared with normal duct flow at same speed

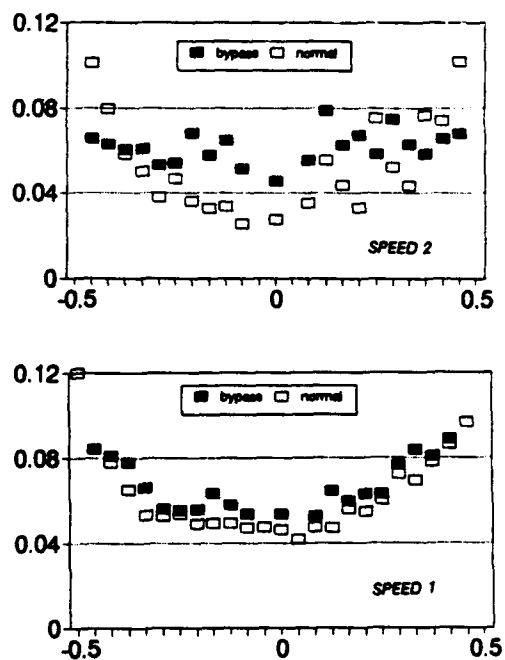


Figure 11.
Outlet Plane Turbulent Intensities with By-Pass System
Compared with normal duct flow at same speed

Turbulence in a Two-Dimensional Wall-Jet Experiments and Modelling

by

H. Abrahamsson*, H.I. Andersson, B. Johansson* and L. Löfdahl***

* Department of Thermo and Fluid Dynamics
Chalmers University of Technology
S-412 96 Göteborg, Sweden

** Division of Applied Mechanics
The Norwegian Institute of Technology
N-7034 Trondheim, Norway

ABSTRACT

An experimental and numerical investigation of the turbulence field in a two-dimensional wall-jet has been carried out in a well-defined geometry. The measurements were performed using hot-wire technique and the calculations were carried out with a standard $k-\epsilon$ model as well as an algebraic stress model (ASM), using elliptic solvers. For the mean velocity field, good agreement was found between the measurements and the calculations. The measurements of the turbulence intensities reveal two maxima in the streamwise and spanwise components, while only one maximum was found in the normal component. Also in the shear stress two maxima were found. A comparison between calculations and measurements indicates that improved turbulence models are needed.

1. INTRODUCTION

To improve turbulence models, well-defined, simple and fundamental experiments are needed. Together with direct numerical simulations of turbulence, these experiments yield a good base for the improvement on the modelling of different terms in the transport equations for the Reynolds stresses. The wall-jet is a fundamental, well-defined and simple flow case, where an interaction between a wall boundary layer and a free shear layer forms a complex flow field. A comprehensive survey of the literature on wall-jets has been carried out by Launder and Rodi (1981), who studied a large number of different, wall-jet experiments. Their main conclusion was that there is a lack of well-defined experiments in fundamental geometries. It was also pointed out that many of the studied flow cases did not fulfil the basic condition of two-dimensionality. Although more than ten years have passed since the survey by Launder and Rodi was published, very few investigations have been reported where wall-jets have been studied.

The purpose of the present work is to measure and compute the turbulence field in a two-dimensional wall jet, in a simple and also well defined geometry. The geometry of the present work differs slightly from earlier investigations in the sense that a backwall is employed above the inlet to the wall-jet chamber. However, the present choice of geometry establishes well defined boundary conditions. Furthermore, the choice of geometry also enables a future comparison with results obtained in a parallel experiment carried out in water using LDA technique, Karlsson et al. (1992).

2. EXPERIMENTAL ARRANGEMENT AND MEASURING TECHNIQUE

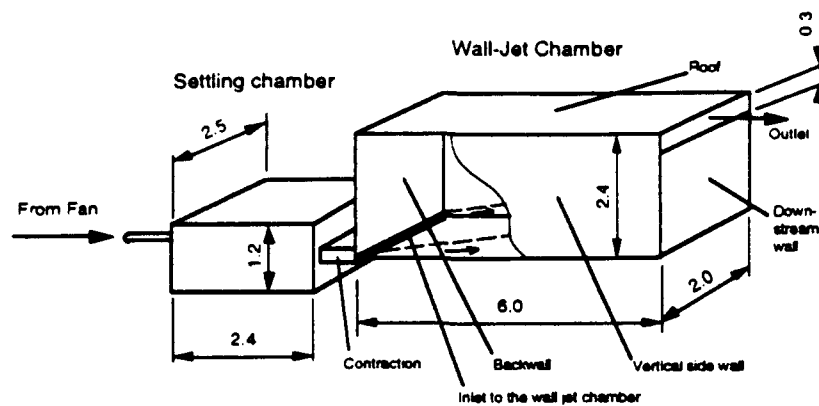


Figure 1: The wall-jet rig. (m)

The wall-jet rig consists of two parts, a settling chamber and a wall-jet chamber, see Figure 1. An ordinary fan blows air into a settling chamber, and from this chamber outlet, the wall-jet is formed over a horizontal flat plate, which is surrounded by vertical side walls. To obtain well defined boundary conditions and to be able to compare the present measurements with a parallel experiment carried out in water using LDA technique, Karlsson et al. (1992), the wall-jet rig is equipped with a roof and a downstream wall.

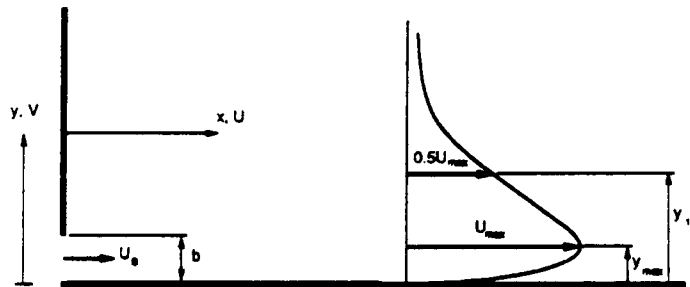


Figure 2: Configuration and nomenclature for the wall-jet. ($b=0.01$ m, $U_0=15.2$ m/s)

To obtain a uniform mean velocity profile, with low turbulence intensity, at the inlet to the wall jet chamber, the outlet of the settling chamber is equipped with a honeycomb and two screens with different mesh sizes, designed according to Groth and Johansson (1988). A large contraction with a ratio of 10:1, designed according to Morel (1975), is used between the settling chamber and the wall jet chamber, see Figure 1. Figure 3a shows the uniform mean velocity profile in the inlet to the wall jet chamber. Measurements of the turbulence level show a low value, of order 0.4%, over the central part of the profile, see Figure 3b. The slot aspect ratio is 200, which is sufficient to obtain good two-dimensionality.

The velocity measurements were performed using a constant temperature anemometer system, Dantec 5600, with standard single- and cross-wire probes, 55P01 and 55P61, respectively. The output signal of the anemometer was digitized, and a computerized evaluation procedure was employed. Siddal and Davies' (1972) calibration law was

employed for the conversion of the anemometer voltages into velocities. Conventional methods, Perry (1982), were used for the evaluation of the mean velocities, the Reynolds stress components and the triple correlations. All these acquisition methods have been tested in a two-dimensional turbulent flat plate boundary layer, see Lófdahl et al. (1992). In the measurements integration times of up to 300s have been used to achieve a good statistical accuracy and the band width was 0.1 Hz through 10 kHz in the turbulence measurements.

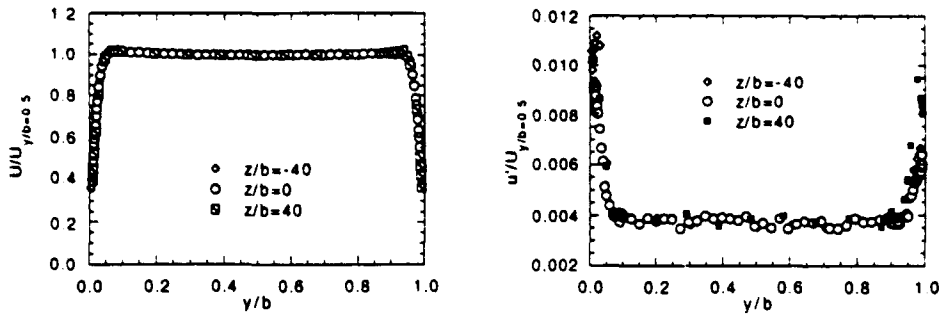


Figure 3a, b: Mean velocity and turbulence profiles in the inlet to the wall jet chamber.

3. MATHEMATICAL MODEL AND NUMERICAL METHOD

3.1 Governing mean flow equations

For a steady and incompressible flow, the conservation equations for mass and mean momentum in Cartesian tensor form are:

$$\frac{\partial U_i}{\partial x_i} = 0 \quad (1)$$

$$\frac{\partial}{\partial x_j} (U_i U_j) = -\frac{1}{\rho} \frac{\partial P}{\partial x_i} + \frac{\partial}{\partial x_j} \left(\nu \frac{\partial U_i}{\partial x_j} - \overline{u_i u_j} \right) \quad (2)$$

For a two-dimensional flow problem, the mass continuity equation (1) and the Reynolds-averaged momentum equations (2) form a set of three partial differential equations with seven unknown variables.

3.2 Turbulence models

Both a standard k- ϵ model and an algebraic stress model (ASM) was used to approximate the correlations of the fluctuating velocities, $\overline{u_i u_j}$.

3.2.1 k- ϵ model

In the standard k- ϵ model, the modelling of the Reynolds stresses is based on the eddy-viscosity concept according to Boussinesq

$$-\overline{u_i u_j} = \nu_t \left(\frac{\partial U_i}{\partial x_j} + \frac{\partial U_j}{\partial x_i} \right) - \frac{2}{3} \delta_{ij} k \quad (3)$$

where the eddy viscosity, ν_t , can be written

$$\nu_t = c_\mu \frac{k^2}{\epsilon} \quad (4)$$

The development of the turbulent kinetic, k , energy is given by a modelled transport equation and its dissipation rate, ϵ , is modelled by a similar equation

$$\frac{\partial}{\partial x_j} (U_j k) = \nu_t \left(\frac{\partial U_i}{\partial x_j} + \frac{\partial U_j}{\partial x_i} \right) \frac{\partial U_i}{\partial x_j} - \epsilon + \frac{\partial}{\partial x_j} \left(\frac{\nu_t}{\sigma_k} \frac{\partial k}{\partial x_j} \right) \quad (5)$$

$$\frac{\partial}{\partial x_j} (U_j \epsilon) = c_{\epsilon 1} \frac{\epsilon}{k} \nu_t \left(\frac{\partial U_i}{\partial x_j} + \frac{\partial U_j}{\partial x_i} \right) \frac{\partial U_i}{\partial x_j} - c_{\epsilon 2} \frac{\epsilon^2}{k} + \frac{\partial}{\partial x_j} \left(\frac{\nu_t}{\sigma_\epsilon} \frac{\partial \epsilon}{\partial x_j} \right) \quad (6)$$

Standard values ($c_\mu=0.09$, $c_{\epsilon 1}=1.44$, $c_{\epsilon 2}=1.92$, $\sigma_k=1.0$ and $\sigma_\epsilon=1.3$) of the constants have been used in the calculations.

3.3.2 Algebraic stress model (ASM) closure

To approximate the correlations of the fluctuating velocities in the algebraic stress model, the following coupled set of algebraic equations are adopted

$$\frac{\overline{u_i u_j} - \frac{2}{3} \delta_{ij} k}{k} = \frac{1}{\epsilon} \frac{(1 - c_2) (P_{ij} - \frac{2}{3} \delta_{ij} P_k) + \Phi_{ij,w}}{(\frac{P_k}{\epsilon} - 1) + c_1} \quad (7)$$

Here, P_{ij} is the production term due to mean shear

$$P_{ij} = - \left(\overline{u_i u_k} \frac{\partial U_j}{\partial x_k} + \overline{u_j u_k} \frac{\partial U_i}{\partial x_k} \right) \quad (8)$$

and $P_k = P_{ii} / 2$ denotes the production of turbulent kinetic energy. If the wall correction, $\Phi_{ij,w}$, is zero, expression (7) reduces to the ASM-model proposed by Rodi (1976). In the present application, however, pressure reflections from the walls are important and the wall correction

$$\Phi_{ij,w} = \left(c_{1w} \frac{\epsilon}{k} \left(\overline{u_i^2} \delta_{ij} - \frac{3}{2} \overline{u_i u_i} \delta_{ij} - \frac{3}{2} \overline{u_i u_j} \delta_{ii} \right) + c_{2w} \left(\phi_{n n,2} \delta_{ij} - \frac{3}{2} \phi_{n i,2} \delta_{n j} - \frac{3}{2} \phi_{n j,2} \right) \right) f \quad (9)$$

due to Gibson and Launder (1978) is employed to account for wall effects on the pressure-strain processes. While n denotes the direction normal to a wall, the wall proximity function

$$f = \frac{c_w k^{3/2}}{\epsilon r} \quad (10)$$

decreases linearly with the distance r from that wall. The function $\phi_{ij,2}$ represents the isotropization-of-production model frequently used to represent the rapid part of the pressure-strain interactions

$$\Phi_{ij,2} = -c_2 (P_{ij} - \frac{2}{3} \delta_{ij} P_k) \quad (11)$$

It is already observed that the algebraic representation of the Reynolds stresses (7) is related to k and ϵ , which are obtained from their respective modelled transport equations

$$\frac{\partial}{\partial x_j} (U_j k) = \frac{\partial}{\partial x_j} ((\nu \delta_{ij} + c_k \frac{k}{\epsilon} \overline{u_i u_j}) \frac{\partial k}{\partial x_i}) + P_k + \epsilon \quad (12)$$

$$\frac{\partial}{\partial x_j} (U_j \epsilon) = \frac{\partial}{\partial x_j} ((\nu \delta_{ij} + c_\epsilon \frac{k}{\epsilon} \overline{u_i u_j}) \frac{\partial \epsilon}{\partial x_i}) + \frac{\epsilon}{k} (c_{\epsilon 1} P_k - c_{\epsilon 2} \epsilon) \quad (13)$$

In the calculations, standard model constants ($c_1=1.80$, $c_2=0.60$, $c_{1w}=0.50$, $c_{2w}=0.30$, $c_w=0.40$, $c_k=0.22$, $c_\epsilon=0.17$, $c_{\epsilon 1}=1.44$ and $c_{\epsilon 2}=1.92$) have been used.

3.3 Numerical solution method

The numerical method, used in the present study, was an adapted version of the elliptic, finite-difference solvers TEAM-KE and TEAM-ASM, Huang and Leschziner (1983) and Huang (1986), employing primitive variables U_i , P in a staggered grid. The convective terms were approximated by the Power-Law Differencing Scheme (PLDS), while the SIMPLE-algorithm (Semi-Implicit Method for Pressure-Linked Equations) handled the velocity-pressure linkage. The resulting difference equations were solved by the TDMA-algorithm.

3.4 Computational domain

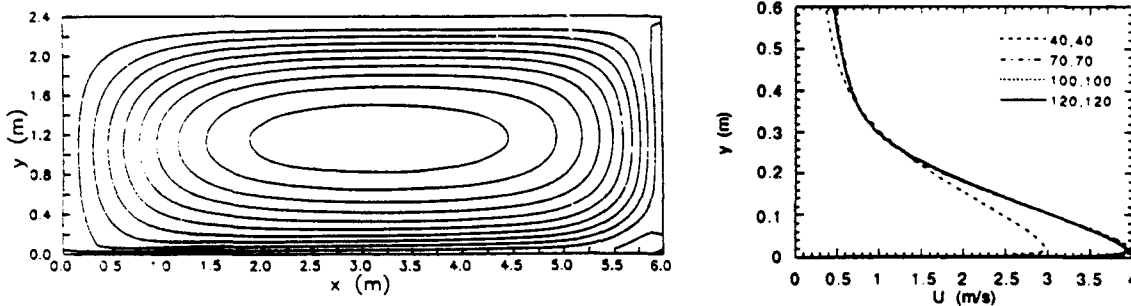


Figure 4a, b: Streamlines in the wall-jet chamber and mean velocity profiles at $x/b=200$.

Computations of the flow field in the entire wall-jet chamber have been carried out in order to get the turbulence field in the wall-jet region, see Figure 4a. To bridge the viscous sublayer along the walls, a standard wall-function approach based on the log-law has been used. Rectangular grid cells with non-uniform spacing in both directions have been used in the computations. To verify grid independence, the computations have been carried out with different grid sizes, see Figure 4b, which shows the k - ϵ computations of the mean velocity at $x/b=200$ for different grid sizes. A plausible assumption is

that the ASM-calculations achieve grid independence at approximately the same mesh size as the standard k- ϵ model. In the following figures the computations with the standard k- ϵ model has been carried out with a 100x100 mesh, and with 60x80 grid cells in the ASM-closure.

4. RESULTS AND DISCUSSION

The here presented measurements were made at an inlet Reynolds number of 10^4 . Measurements of mean velocities, Reynolds stresses and triple correlations were carried out at several downstream positions ($x/b=20, 40, 70, 100, 150, 200, 250, 300$) in the wall jet region. Spanwise measurements were made at several of the above mentioned positions in order to verify the two-dimensionality of the wall jet. The flow showed a very good two-dimensionality in the measuring position on the centre line in the wall jet chamber. In the present paper comparisons between experiments and calculations are carried out and discussed at 70 and 150 x/b , since these positions are typical for the experiment.

4.1 Mean velocities

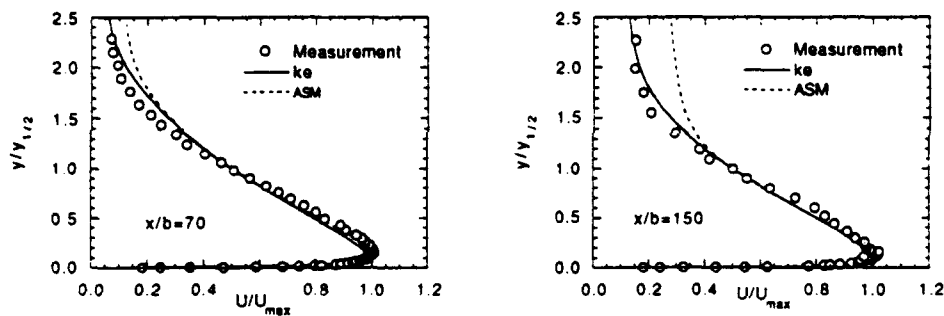


Figure 5a, b: Mean velocity profile at 70 and 150 x/b .

The mean velocity profiles at 70 and 150 x/b are shown in Figure 5a and 5b, respectively. All these measurements were performed using a single hot wire, and up to a distance of approximately $y_{1/2}$ a good agreement between measurements and calculations can be noted. This region is from an experimental point of view favourable, since the local turbulence intensities are fairly low, the mean velocities are relatively high and the influence from the outer secondary flow is negligible. Outside the half width, the uncertainty of the hot-wire measurements increases due to higher local turbulence intensities. Furthermore, in this region the mean velocity in the normal direction is comparatively high as is shown in Figure 4a. These two effects cause an overpredicted mean velocity in the streamwise direction. Looking at the computed mean velocity profiles, outside the half width a clear deviation can be noted between the measurements and the two employed turbulence models. The deviation between the measurements and the k- ϵ model is fairly low, and it seems to be independent of the position. However, the ASM obtains larger deviations, which increase in the downstream direction. The explanation of this overprediction can be found in Figure 6, which shows the mean velocity profile in the entire wall jet chamber. In this figure it is seen that the ASM yields a stronger recirculation, and a larger mean velocity gradient. In Figure

7, a traditional logarithmic plot of the mean velocity profile is shown. In the scaling of this diagram, the friction velocities was obtained using Preston tubes. It may be observed that the extension of the logarithmic region is very short, as compared to a flat plate boundary layer.

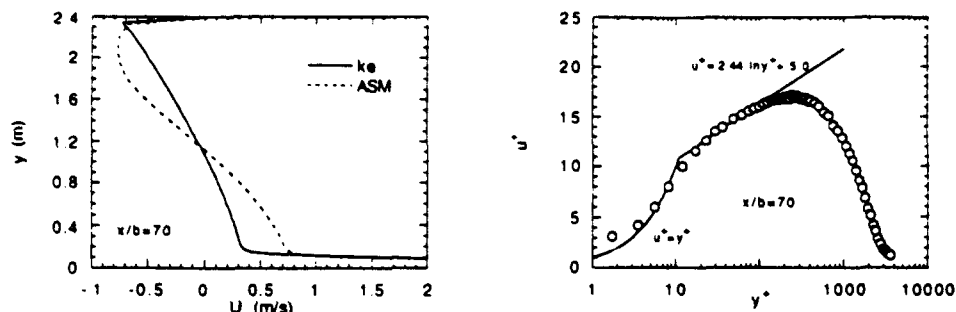


Figure 6 and 7: Mean velocity in the entire wall jet chamber, and a traditional logarithmic plot.

From the mean velocity profiles the growth of the wall-jet is estimated to 8.0 %, see Figure 8. This value is somewhat higher than the values stated by Launder and Rodi (1983). The explanation of this deviation is due to differences in the boundary conditions. In the present investigation a negative pressure gradient is prevailing in the outer portion of the wall-jet, while Launder and Rodi (1981) state a constant or positive pressure gradient in the outer portion of the wall-jet. In the present investigation a pressure difference might be created perpendicular to the wall, thus enhancing the growth of the wall-jet. Furthermore, it can also be observed that the growth of the wall-jet is not perfectly linear. This is due to the fact that the velocity profiles do not exhibit self-preservation, since no characteristic velocity and length could be found due to the prevailing secondary flow in the wall-jet chamber.

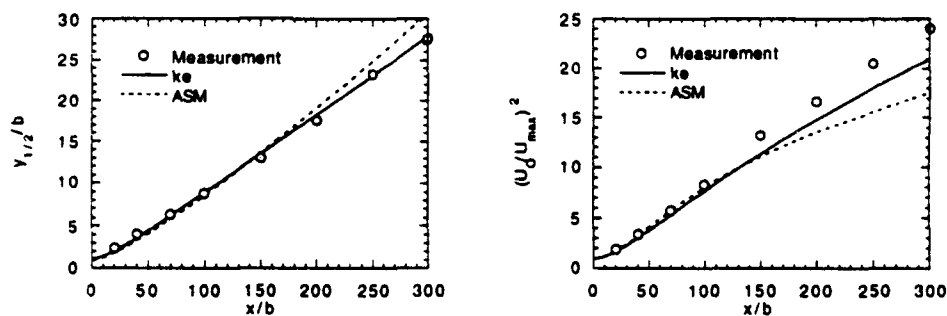


Figure 8 and 9: Growth of the wall-jet and decay of maximum velocity.

The decay of the maximum velocity is shown in Figure 9. A good agreement can be observed up to approximately $x/b=100$. Further downstream both models overpredict the maximum velocities, due to the momentum in the recirculated flow, see Figure 6. This effect is prevailing in the entire wall jet chamber, however most accentuated downstream $x/b=100$.

4.2 Reynolds stresses

Figures 10a and 10b show the normal stress in the streamwise direction. Single and cross wires have been used in the measurements and it can be noted that both probes give an acceptable repeatability. In the measurements two maxima of the normal stress can be observed and should also be expected since the wall-jet is considered to consist of a wall boundary layer and a free shear layer. The calculations fail to predict the inner maximum, however at both positions the outer maximum is captured. This maximum is overestimated for $x/b=70$, while a correct value is obtained at $x/b=150$. The high level of the calculated normal stress in the streamwise direction around $0.55 y_{1/2}$ at $x/b=70$ can be associated with the production term since the turbulent shear stress (see Fig 13a) is higher than its corresponding experimental value.

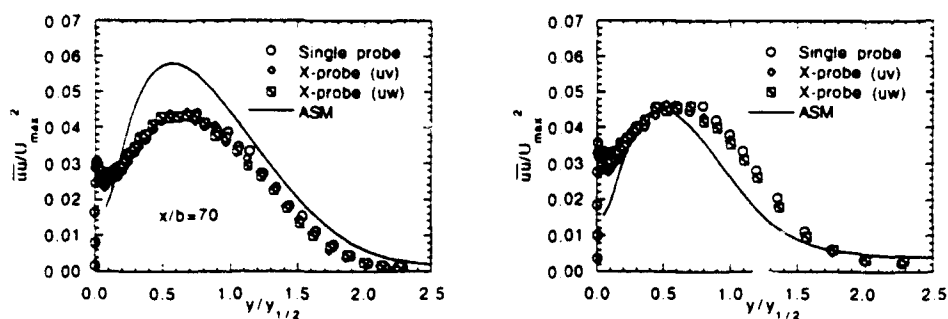


Figure 10a, b: Normal stress in the streamwise direction at 70 and 150 x/b .

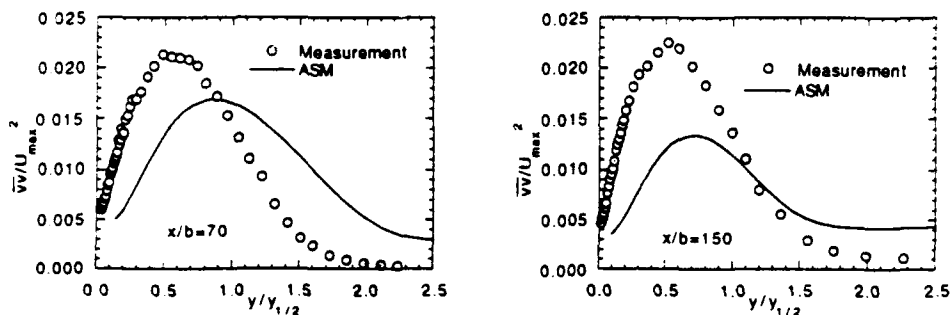


Figure 11a, b: Normal stress perpendicular to the wall at 70 and 150 x/b .

The normal stress perpendicular to the wall is shown in Figure 11a and 11b. Generally, their level is lower for this component as compared to the streamwise normal stress. The measurements do not indicate an inner maximum, which neither should be expected if the wall-jet is viewed as a wall boundary layer and an outer shear layer. The measured maximum of this component seems to coincide with the outer maxima of the streamwise normal stress and the positive maxima of the shear stress. In the calculations, it can be observed that the level of this normal stress is underpredicted while the streamwise normal stress is too high compared to the measurements in the region around $0.5 y_{1/2}$. This indicates that the wall correction has transferred a too small amount of energy from the streamwise- to the perpendicular normal stress. In the outer region, the measurements show a too low level which can be explained by the prevailing

intermittency and the high local turbulence intensity. Furthermore the ASM overpredicts the level in the outer region, due to the large gradients predicted in the secondary flow. A similar observation can be made in the spanwise normal stress as well as in the shear stress.

Figure 12a and 12b show the normal stress in the spanwise direction. The measurements of this component were carried out with the wires in a plane parallel to the wall. Although, this wire positioning may cause a lower accuracy due to mean velocity gradients, the two expected maxima were captured. The calculations are consistent with the measurements in the central region of the wall-jet.

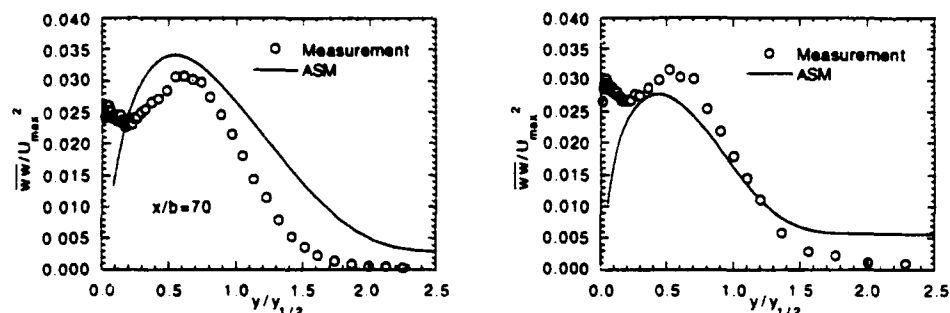


Figure 12a, b: Normal stress in the spanwise direction at 70 and 150 x/b .

The shear stress is shown in Figures 13a and 13b. The expected change of signs of the shear stress occurs at approximately $0.8 y_{max}$. Hence, the change of signs does not coincide with the position of maximum velocity where the mean velocity gradient is zero. This observation enhances that all Boussinesq approaches in the turbulence modelling will fail to predict the present flow case. Both profiles reveal that the positive stress maxima is of larger magnitude than the negative wall shear stress. Good agreement between calculations and measurements can be found in this component. The high shear stress level at approximately $y_{1/2}$ is well captured in the calculations.

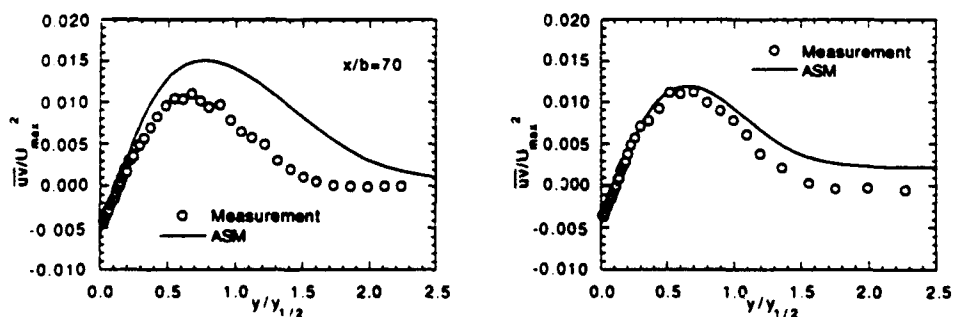


Figure 13a, b: Shear stress at 70 and 150 x/b .

5. CONCLUSIONS

Turbulence measurements and calculations of the flow field of a well-defined, fundamental and simple two-dimensional wall-jet have been carried out. From this investigation, the following main conclusions can be drawn:

- Mean velocity comparisons yield fairly good agreements between measurements and calculations. The growth of the wall-jet was determined to be 8.0%.
- Measurements of the normal stress in the streamwise and spanwise directions show two maxima, an inner associated to the wall layer and an outer in connection with the free shear layer. In the normal direction, only one maximum was found
- From the shear stress measurements, two maxima were found, a negative inner maximum and a positive outer. The change of signs does not coincide with the point of maximum velocity.
- In the comparison between measurements and calculations of the Reynolds stresses, good agreement were obtained for the normal stresses in the streamwise as well as the spanwise direction and for the shear stress. The normal stress perpendicular to the wall reveals, however, large deviations.

ACKNOWLEDGEMENTS

Support from Swedish National Board for Industrial and Technical Development is gratefully acknowledged. H. Abrahamsson acknowledges the support from NORDTEK and Bengt Ingeström Scholarship Fund.

REFERENCES

- Gibson, M.M., and Launder, B.E., 1978, "Ground effects on pressure fluctuations in the atmospheric boundary layer", J. Fluid Mech., Vol. 86, pp. 491-511.
- Groth, J., and Johansson, A., 1988, "Turbulence reduction by screens", J. Fluid Mech., Vol. 197, pp. 139-155.
- Huang, P.G., 1986, Ph.D. thesis, UMIST, Dept. Mech. Eng.
- Huang, P.G., and Leschziner, M.A., 1983, UMIST, Dept. Mech. Eng., Report TFD/83/9(R).
- Karlsson, R.I., Eriksson, J., and Persson, J., 1992, "LDV measurements in a plane wall jet in a large enclosure", The sixth international symposium on applications of laser techniques to fluid mechanics.
- Launder, B.E., and Rodi, W., 1981, "The turbulent wall-jet", Prog. Aerospace Sci., Vol. 19, pp. 81-128.
- Launder, B.E., and Rodi, W., 1983, "The turbulent wall jet", Ann. Rev. Fluid Mech., pp.429-459
- Löfdahl, L., Stemme, G., and Johansson, B., 1992, "Silicon based flow sensors used for mean velocity and turbulence measurements", Exp. Fluids, Vol. 12, pp. 270-276.
- Morel, T., 1975, "Comprehensive design of axisymmetric wind tunnel contractions", J. Fluids Eng., Vol. 97, pp. 225-233.
- Perry, A.E., 1982, "Hot-Wire Anemometry", Oxford Science Publication, Clarendon Press, Oxford.
- Rodi, W., 1976, "A new algebraic relation for calculating the Reynolds stresses", ZAMM, Vol. 56, pp. T219-T221.
- Siddal, R.G., and Davies, T.W., 1972, "An improved response equation for hot-wire anemometry", Int. J. Heat Mass Transfer, Vol. 15, pp. 367-368.

THE DEVELOPMENT OF THE INTERFACE REGION BETWEEN TWIN CIRCULAR JETS AND A NORMAL CROSSFLOW

N Toy^{*}, P. J. Disimile^{*}, F. Savory^{*}
and S. McCusker^{*}

^{*} Fluid Mechanics Research Group, Dept of
Civil Engng, Univ of Surrey, Guildford, UK

^{*} Dept of Aero Engng and Engng Mech,
Univ of Cincinnati, Ohio 45221, USA

Abstract

The present work is an experimental investigation of the interface region between a twin jet arrangement and a normal crossflow, together with the single jet case, utilising smoke flow visualisation in association with a quantitative video digital imaging technique. Measurements involving a single jet, side-by-side twin jets and in-line twin jets for a velocity ratio of 8 show that the extent of the mixing region at any downstream location (defined as the distance between the inner and outer limits of the fluctuating jet boundary) is similar in magnitude to the jet half-width (as defined by the mean interface location) at that location. The growth rates in the downstream direction of both the mixing region and the half-width are also similar. The spectra of the lateral fluctuations of the interface in each downstream plane across the jet show that, in almost all cases, energy is transferred from lower to higher frequencies with increasing distance from the wall.

1. Introduction

The case of circular jets issuing into a crossflow is of interest in many branches of engineering from V/STOL aerodynamics and jet steering systems to effluent plume dispersal and combustion chamber mixing. Whilst there has been considerable research into the classical configuration of a single jet issuing into a crossflow, the cases of twin side-by-side or in-line jets have received relatively little attention. Ziegler and Wooler (1973), Schwendemann (1973), Makihata and Miyai (1979), Isaac (1982) and Isaac and Jakubowski (1985). In a recent paper the present

authors published the findings from an investigation of twin side-by-side jets issuing into a crossflow. Savory and Tey (1991). The effects of nozzle spacing (S/D), which was varied from 1 to 5, and jet velocity/crossflow velocity ratio (α), varied from 6 to 10, were examined using a novel technique for real-time video analysis of smoke visualised jets. Tey and Wisby (1988a,b). Data were presented in the form of contour maps of intermittency in YZ planes across the jets from which the development of the jets in the downstream direction and the overall penetrations and widths were assessed. It was found that the development of the widely spaced jets (such as $S/D=5$, where the crossflow passes on both sides of each jet) is fundamentally different from that of closely spaced jets (such as $S/D=1$, where there is no crossflow penetration between the jets). In all cases the inner vortices of the two counter-rotating pairs rapidly disappeared within the first few jet diameters downstream from the nozzles, such that the two jets combined to form a large jet with single jet characteristics, as noted by Isaac (1982) and Isaac and Jakubowski (1985).

The present work is an extension of the earlier study in which one jet nozzle spacing, $S/D=5$, and one typical velocity ratio, $\alpha=8$, has been systematically investigated for three different cases, namely the single jet, twin side-by-side jets and twin in-line (or tandem) jets. The same quantitative image processing apparatus has been utilised but in the present study time-histories of the jet/crossflow interface location have been obtained at different downstream locations to permit determination of the interface statistics, notably intermittency, probability density functions and power spectra. The next section briefly outlines the experimental approach and this is followed by a discussion of some of the results obtained.

2. Experimental details

The experiments were carried out in a purpose built, open-circuit, smoke tunnel facility, shown in figure 1, which has working section dimensions of $0.75 \times 0.62\text{m}$ and a turbulence level of 0.2%. High efficiency filters are installed at the outlet to remove practically all the smoke particles. A Concept Genie generator was used to produce the smoke, via a small centrifugal fan, and the jets issued from 13.5mm diameter copper nozzles inserted into a common plenum chamber. The generator and plenums were mounted on the tunnel roof in an arrangement which allowed variation in the orientation of the jets to the crossflow direction. The experiments were conducted with a freestream velocity of 1m/s, giving a Reynolds number of 9.3×10^4 based on nozzle diameter. The approaching roof boundary layer had a thickness of 60mm, that is $4.44D$. The jet velocity was 8m/s, which gave $\alpha=8$, and measurements were undertaken in lateral YZ planes at downstream locations X/D of 5, 10, 15, 20, 25 and 30 for the single jet case and for twin jets with nozzle spacing $S/D=5$.

Details of the jet crossflow interface structure were obtained at each location by illuminating the flow at a series of heights, spaced $2.5D$ apart, using a 10mW He-Ne laser beam directed across the flow. The laser, together with a monochrome CCD camera for recording the laser-line traces, was attached to a computer-controlled two-dimensional traversing mechanism, as illustrated in figure 2. The position of the camera and laser were fixed relative to each other with each digitised pixel representing a flow area of approximately $0.58 \times 0.58\text{mm}$.

Video digitisation and analysis were undertaken by a PDP-11 73 minicomputer-based system using Imaging Technology boards for analogue processing (AP-512), arithmetic logic operations (ALU-512), histogram computations (HF-512) and frame buffer storage (FB-512). The system is shown as a block diagram in figure 3. Previous work has demonstrated that the video analysis system can be used to obtain quantitative data, including interface statistics, by utilising the smoke as a turbulent/non-turbulent discriminator. Toy and Wisby (1988a,b). In the present experiments the fully turbulent jets were seeded with smoke, whilst the crossflow, which was non-turbulent (outside the wall boundary layer) was unseeded. Hence, when the interaction region was viewed by the camera the white portions of each laser illuminated line (smoke present) represented regions of turbulent flow and the black regions (no smoke) represented non-turbulent flow regions.

Experiments were carried out at each horizontal location to determine the time history of the position of the interface between the jet and the crossflow (that is, the edge of the smoke seeded region). In each case a time series of 50000 points was obtained (requiring a sampling time of 16.7 minutes) and five 10000 point, 250 lag autocorrelations were then computed and summed. A cosine transform was then carried out to produce the power spectrum up to the Nyquist frequency of 25Hz (imposed by the image transfer rate of 50Hz) at intervals of 0.1Hz. The edge time history was also used to compute the probability density function of the interface location, together with the mean, variance, skewness and kurtosis. Although the image transfer rate in these experiments was 20msecs the camera shutter was electronically controlled to give an acquisition time of only 4msecs, thereby minimising image blur.

3. Results and discussion

Considering first the probability density functions associated with the interfaces for the different jet configurations, figure 4 shows typical profiles for the single, in-line and side-by-side jet cases, each taken in the YZ plane at $X/D=30$ along a Z/D location near the region of maximum jet width. These profiles are Gaussian in shape and illustrate that the twin jet interfaces are of similar width but about $1D$ broader than the single jet interface at the same downstream location. The mean interface location shows that the jet half-width is largest for

the side-by-side case, being about 1D wider than the in-line case and 3.5D wider than the single jet configuration. Hence, it is clear that the mixing region associated with two jets is more extensive than that for the single jet. The difference in width between the side-by-side jets and the other cases may be due, in part, to the "initial" half-width in the side-by-side case that is provided by the 5D nozzle spacing. Since the present work has only examined the lateral extents of the jets it is not possible to precisely compare overall jet penetrations between the three cases. However, from consideration of the vertical height of the maximum half-width positions in each downstream plane, it would appear that the single and side-by-side jet penetrations are broadly similar whilst the in-line combined jets penetrate further, as noted by Isaac (1982) and Isaac and Jakubowski (1985).

The plots in figures 5, 6 and 7 show the mean lateral locations (defined by the mean of the p.d.f) and extents of the mixing regions (defined by the inner and outer limits of the p.d.f) at $X/D=15$ and 30 for the single, in-line and side-by-side cases, respectively. The increases, in the downstream direction, of both the mean width and maximum extent of the interface are evident in all cases. This is further illustrated in figure 8 which shows that the width of the single jet interface is slightly greater than the mean half-width of the jet and that the former grows at a slightly greater rate than the latter. In the case of the in-line jets the interface width and mean half-width are almost identical, with similar growth rates that are close to those of the single jet. The side-by-side jets interface shows a similar growth rate to that of the in-line jets although in this case the mean half-width is slightly greater than the lateral extent of the mixing region. The three sets of results suggest that the interface width at any downstream location is considerably less sensitive to changes in nozzle geometry than the mean width of the jets. In addition, in all cases there appears to be a rapid growth in the jets within the first 2D downstream from the geometrical centre of the nozzle arrangement followed by slower growth rates that are broadly similar in all the configurations examined.

Typical examples of the energy spectra associated with the interface fluctuations are shown in figures 9, 10 and 11 for the single, in-line and side-by-side jets, respectively. In each case two spectra are shown at $X/D=30$, both just within the jets with one near the top and one near the underside. In almost all the cases considered there is a distinct transfer of energy to the higher frequencies as the point of measurement is moved from the wall side to the top of the jets. This is indicated in the figures by the extent of the flat portion of the spectra shifting from a wave number of about 6 to approximately 31, together with an increase in the slope of the profiles at the higher frequency end. These logarithmic spectra profile slopes are summarised in figure 12 which clearly shows the wide range of the measured results. The present data are not conclusive but the general trend appears to be an increase in the slope towards the top of the jets and then a smaller decrease as the outer edge of the interface is

approached. This tendency is very noticeable for the single and side by-side jet cases but less evident for the in-line configuration. A possible explanation for the changes in the energy profiles may be that the flow near the underside of the jets is dominated by the large-scale, low frequency motion associated with the contrarotating vortices whilst the interaction in the top region is largely between the two nominally co-flowing regimes of the jet and the crossflow. None of the measured spectra show any evidence of periodic "vortex shedding" associated with the jet flows which had been noted by earlier workers investigating the wakes of single jets, McMahon et al (1971), Moussa et al (1977). However, as revealed by Fric and Roshko (1989), the jet does not itself shed vortices but, rather, it sweeps up vorticity from where the wall boundary layer has separated near the nozzle due to the adverse pressure gradient in that region. This vorticity is then incorporated into the jet wake with a periodicity broadly similar to that associated with a circular cylinder in uniform flow. Since the wall boundary layer was not seeded with smoke it is clear that the present experimental technique would not directly detect any such vorticity.

4. Concluding remarks

The present work has highlighted the relationship between the overall growth of single and twin jets in a crossflow and the growth of the mixing region between the jets and the crossflow. In general, the mean half-width, as defined by the p.d.f. of the lateral interface location, and the overall lateral extent of the mixing region are very similar in magnitude. However, the intermittency data (not presented here), together with the velocity and turbulence measurements provided by Isaac and Jakubowski (1985), suggest that it is unlikely that any similarity profiles exist within the jets which could provide a single definition of the three different jet configurations. Although not a specific aim of the present work, the results confirm that twin in-line jets penetrate further than either single or side-by-side jets of the same velocity ratio. The spectra associated with the lateral fluctuations of the interfaces do not indicate any significant differences between the three jet cases. However, there is a trend for a shift of energy to higher frequencies with increasing distance outwards towards the top of the jets, which may be associated with a change from the contrarotating vortex regime on the lower side of the jet to a nominally co-flowing mixing layer on the outward side.

5. Nomenclature

- D Jet nozzle diameter
- E(F) Energy associated with interface frequency, F
- F Frequency, Hz
- k Wave number ($=2\pi F/U_R$), m^{-1}
- n Slope of logarithmic energy spectrum

P Probability density function
 S Spacing between nozzle centres
 U_g Crossflow velocity, m/s
 VAR Variance of the interface fluctuation amplitude
 W_i Lateral width of interface (distance between inner and outer limits)
 \bar{W}_j Mean half-width of the jet (defined by mean of p.d.f)
 X Cartesian coordinate in crossflow direction, with origin at geometrical centre of any given nozzle arrangement
 Y Cartesian coordinate in lateral direction
 Z Cartesian coordinate normal to ground plane
 α jet velocity / crossflow velocity ratio

6. References

- Eric T F and Roshko (1989) "Structure in the near field of the transverse jet". Proc 7th Symp on Turbulent Shear Flows, Stanford Univ. USA, pp 6.4.1-6.4.6
 Isaac K M (1982) "Experimental and analytical investigation of multiple jets in a cross-flow". PhD thesis, Virginia Polytechnic Institute and State University, Blacksburg
 Isaac K M and Jakubowski A K (1985) "Experimental study of the interaction of multiple jets with a crossflow". ALAA J, 23, 1679-1683
 Makhata T and Miyai Y (1979) "Trajectories of single and double jets injected into a crossflow of arbitrary velocity distribution". ASME J Fluids Engng, 105, 91-97
 McMahon H M, Hester D D and Palfrey J G (1971) "Vortex shedding from a turbulent jet in a crosswind". J Fluid Mech, 48, 73-80
 Moussa Z M, Trischka J W and Eskinazi S (1977) "The near field in the mixing of a round jet with a cross-stream". J Fluid Mech, 80, 49-80
 Savory E and Toy N (1991) "Real-time video analysis of twin jets in a crossflow". ASME J Fluids Engng, 113, 68-72
 Schwendemann M F (1973) "A wind tunnel investigation of stratified jets and closely spaced jets exhausting into a crossflow". Northrop Aircraft Division, Hawthorn, CA, USA. Rept NOR73-98, May
 Toy N and Wisby C (1988a) "The real time image analysis of a visualised turbulent wake" Proc 1st National Fluid Dynamics Congress, Cincinnati, USA, July, pp 695-702, ALAA Paper No 88-3552-CP
 Toy N and Wisby C (1988b) "Real-time image analysis of visualized turbulent flows". Proc 11th Biennial Symp on Turbulence, Univ of Missouri-Rolla, USA, October, pp A21.1-21.10
 Ziegler H and Wooler P T (1973) "Analysis of stratified and closely spaced jets exhausting into a crossflow". NASA CR-132297

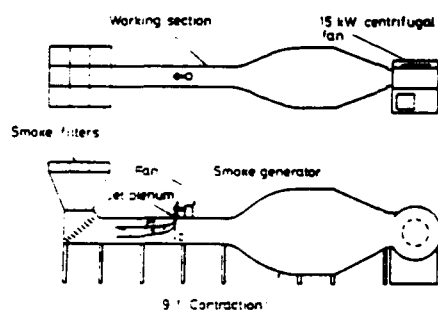


Figure 1 Smoke tunnel facility

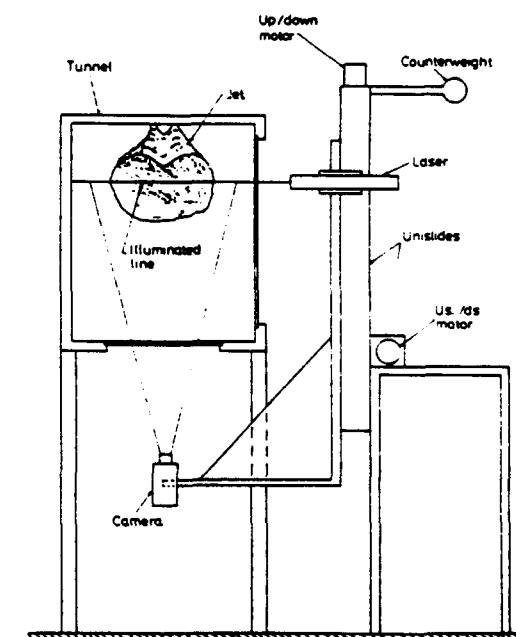


Figure 2 Laser and camera traversing system

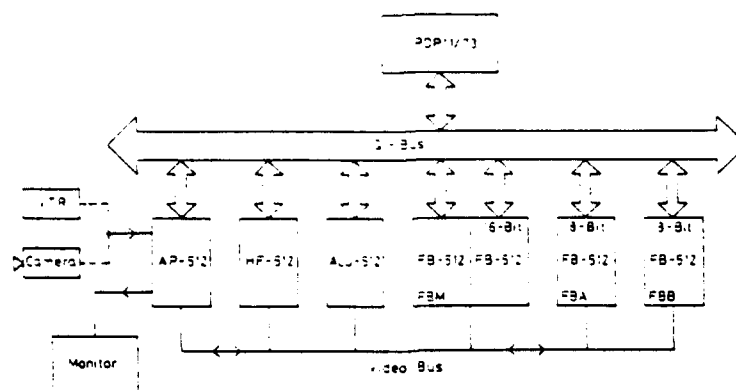
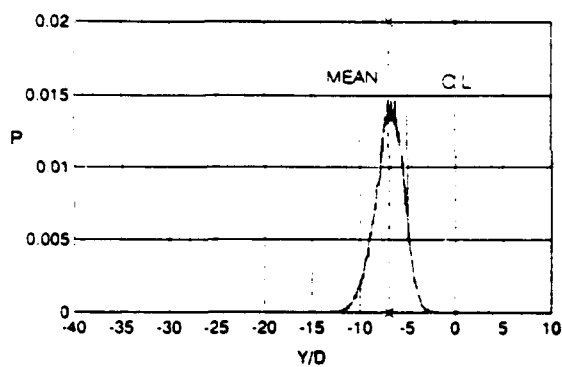
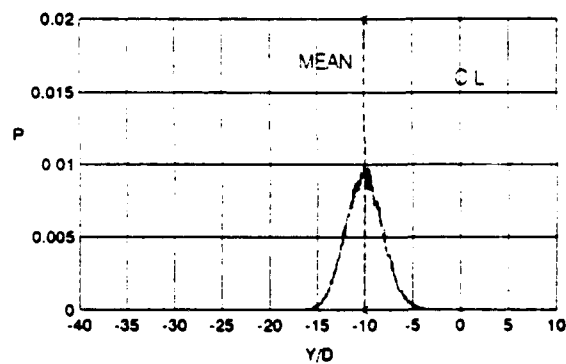


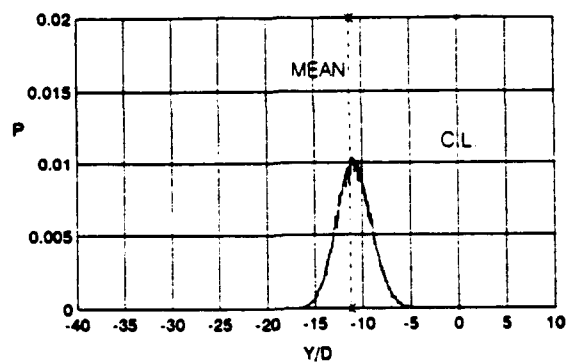
Figure 3 Block diagram of image processing system



SINGLE JET : $X/D=30$: $Z/D=12.5$

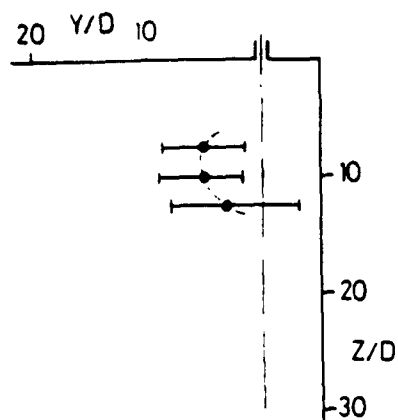


IN-LINE JETS : $X/D=30$: $Z/D=25$

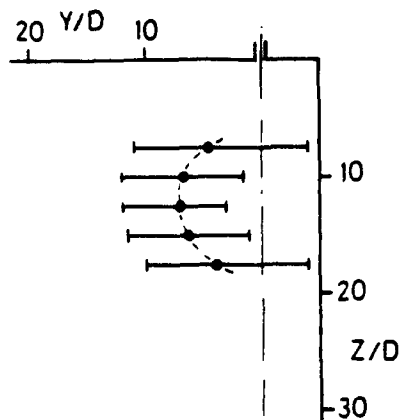


SIDE-BY-SIDE JETS : $X/D=30$: $Z/D=15$

Figure 4 Typical p.d.f distributions associated with the lateral fluctuations of the interfaces for the single, in-line and side-by-side jet configurations at $X/D=30$

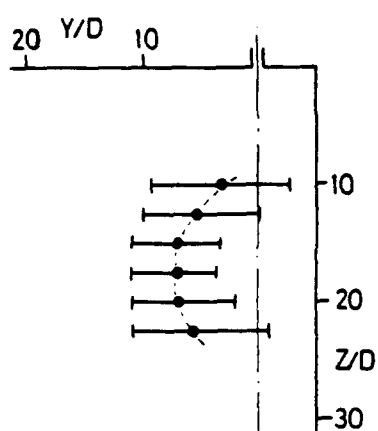


(a) $X/D=15$

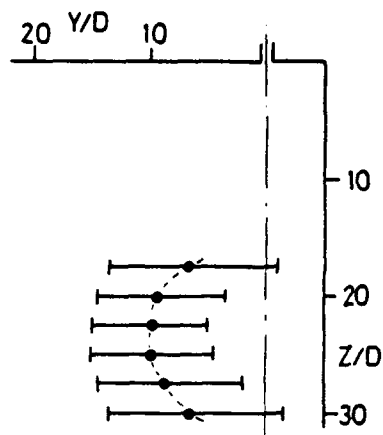


(b) $X/D=30$

Figure 5 Mean interface location (●) and extent of mixing region (—) in two YZ planes for single jet

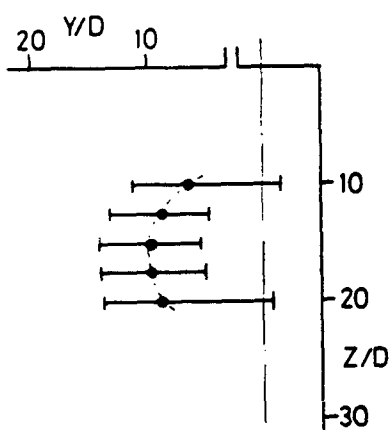


(a) $X/D=15$

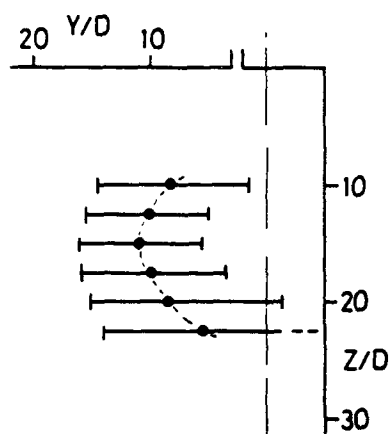


(b) $X/D=30$

Figure 6 Mean interface location (●) and extent of mixing region (—) in two YZ planes for in-line jets

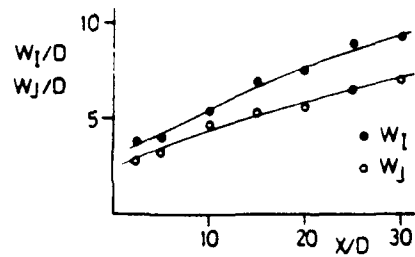


(a) $X/D=15$

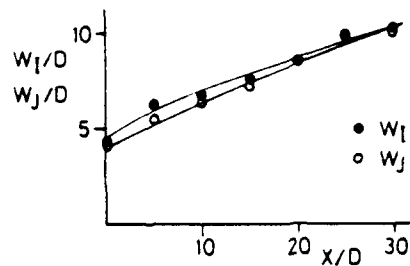


(b) $X/D=30$

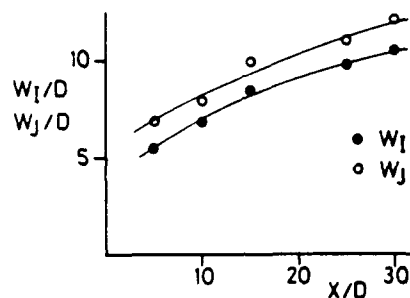
Figure 7 Mean interface location (●) and extent of mixing region (—) in two YZ planes for side-by-side jets



(a) Single jet

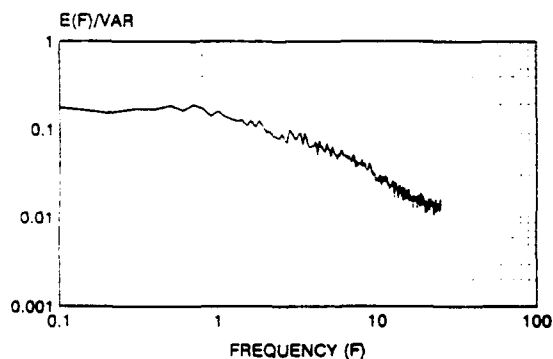


(b) In-line jets

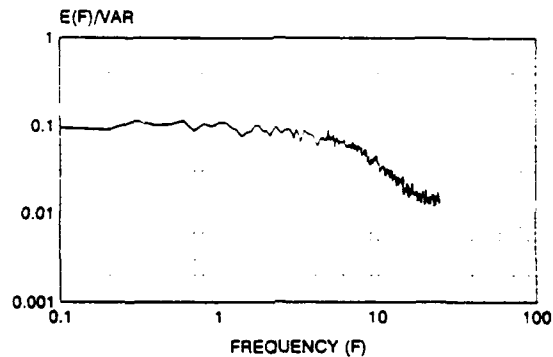


(c) Side-by-side jets

Figure 8 Variation of width of interface (W_I) and mean jet half-width (W_J) with downstream distance for the three jet configurations

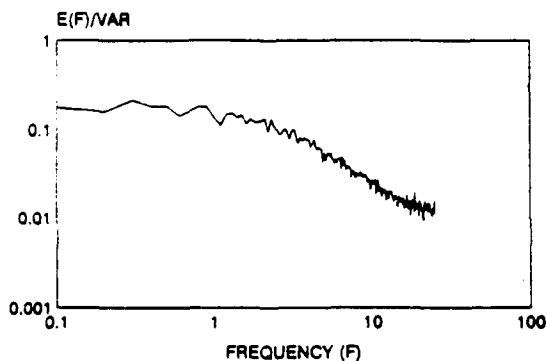


SINGLE JET : $X/D=30$: $Z/D=7.5$

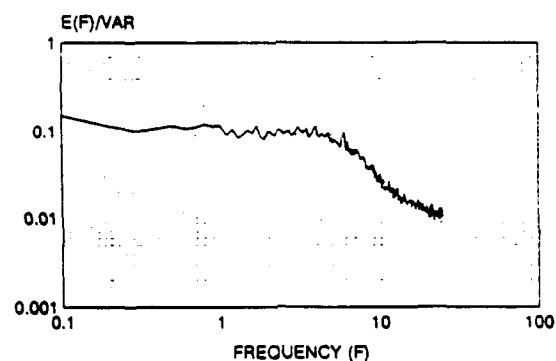


SINGLE JET : $X/D=30$: $Z/D=17.5$

Figure 9 Interface energy spectra for two heights within the single jet at $X/D=30$

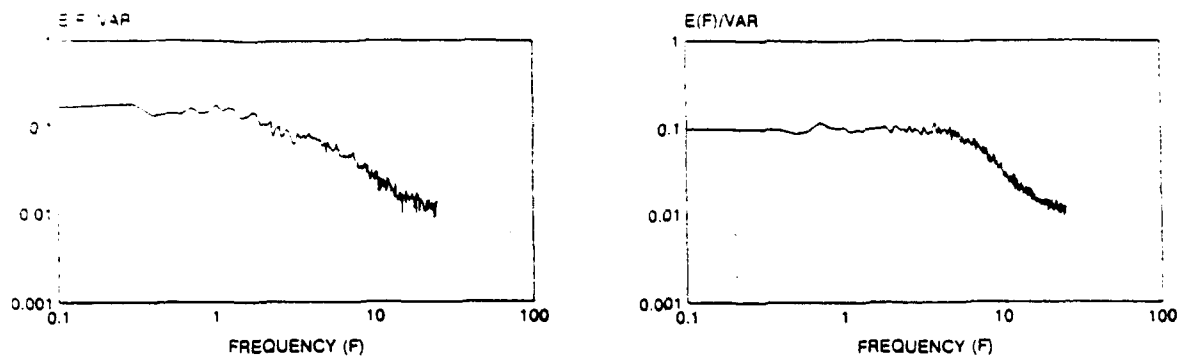


IN-LINE JETS : $X/D=30$: $Z/D=17.5$



IN-LINE JETS : $X/D=30$: $Z/D=30$

Figure 10 Interface energy spectra for two heights within the in-line jets at $X/D=30$



SIDE-BY-SIDE JETS : $X/D=30$: $Z/D=10$

SIDE-BY-SIDE JETS : $X/D=30$: $Z/D=22.5$

Figure 11 Interface energy spectra for two heights within the side-by-side jets at $X/D=30$

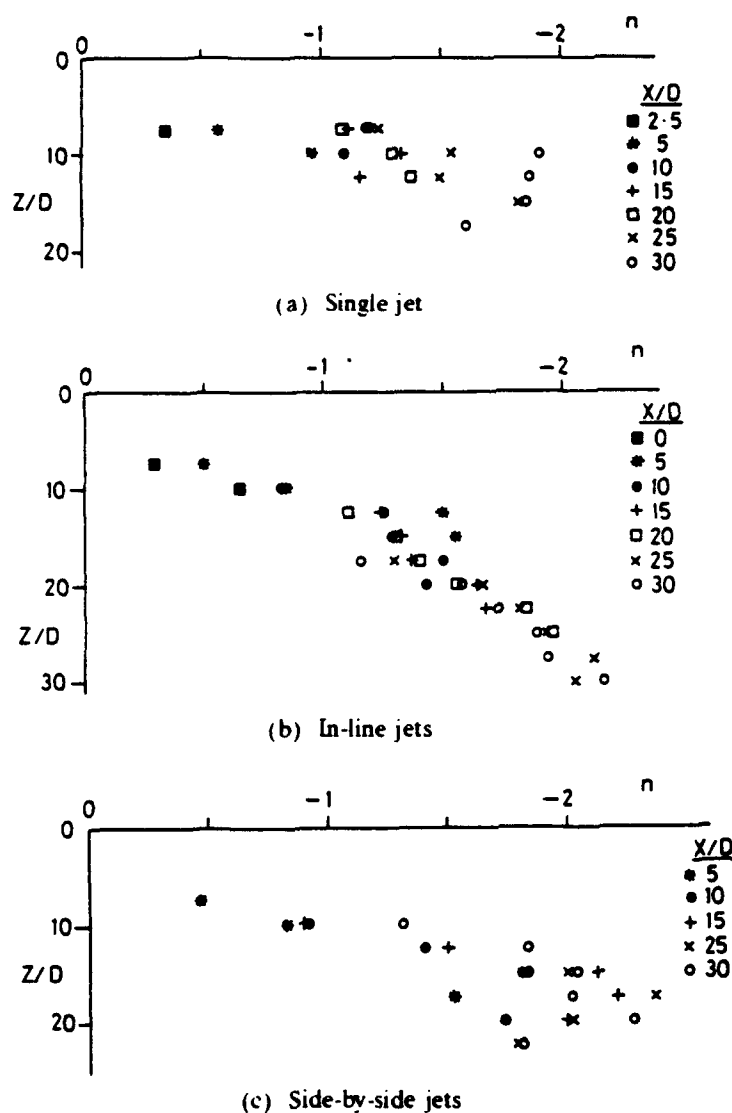


Figure 12 Variation in slope of logarithmic spectra profiles with location within jet and downstream distance

MIXING BETWEEN A SHARP-EDGED RECTANGULAR JET AND A TRANSVERSE CROSS FLOW

A.J. Humber, E.W. Grandmaison and A. Pollard*
Department of Chemical Engineering
* Department of Mechanical Engineering
Queen's University
Kingston, Ontario K7L 3N6
Canada

Abstract

The scalar mixing field of a turbulent rectangular jet issuing from a sharp-edged orifice with an aspect ratio of 10 into a cross stream flow in a square duct is investigated using marker nephelometry. Jet-to-cross stream velocity ratios of 2.0 and 3.4 are examined in this work. Results include contour plots and transverse profiles of the mean and concentration fluctuation intensity and jet trajectory paths and half concentration lengths expressed as a function of downstream position along the jet trajectory.

1. Background

The mixing field arising between a jet and a transverse cross flow has received considerable attention in the engineering literature. This research arises from a wide interest in this flow geometry for applications including turbine heat transfer, VTOL applications, pollutant dispersion and chemical mixing problems. Of particular interest in this regard is the case of a round jet with an average exit velocity U_j mixing with a cross stream of uniform velocity U_0 . The resulting flow patterns including descriptions of the jet trajectory and complex three-dimensional vortex structure have been investigated for the single jet [1 - 19] and multiple jets [20 - 27] in cross flows. The scalar mixing field arising from the round jet in a cross flow also has been examined, [3, 5, 10] and [28 - 30]. Mathematical modelling of this complex flow system has been based on integral methods [31 - 33] and numerical methods [34 - 38].

In the present work, interest was focussed on the mixing field of a rectangular jet in a transverse flow with particular attention being paid to providing data on the scalar mixing behaviour of this flow for applications in secondary and tertiary ducts in industrial boiler/furnace systems. The jet trajectory, Fig. 1, can be described in terms of cartesian coordinates (X, Y, Z) or an orthogonal system (ξ, η, ζ) with the ξ -axis located on the jet trajectory. In the industrial applications of interest air is induced into a furnace chamber under negative pressure (on the order of 0.25 KPa) resulting in velocity ratios, R, typically in the range of $2 < R < 4$. A description of the jet trajectory and cross stream profiles were of interest for comparison with the larger quantity of literature already available for the round jet case. The jet nozzle was a sharp edged rectangular orifice with an aspect ratio of 10 - this geometry was chosen for its ease of construction and for comparison with some properties already published for the free jet behaviour of this jet geometry [39 - 41].

The flow field arising from a sharp-edged rectangular jet has been extensively studied (described in references [41, 42]). The essential features of this flow include: (i) a saddle-back profile of the mean velocity and nozzle scalar fluid in the plane or major axis of the rectangular jet; (ii) transverse jet scales (as measured by the half velocity or concentration points on the major and minor axes) that are initially smaller along the minor axis but tend to a similar magnitude farther downstream; and (iii) high entrainment rates as indicated by the centreline mean concentration decay.

Weston and Thames [43] have studied some features of the flow arising from a rectangular jet with an aspect ratio of 4 injected into a cross flow. Krothapalli, Lourenco and Buchlin [44] have also examined the separated flow region upstream of rectangular jets in a cross flow. They found that the normalized separation distance reached a maximum near $U_j/U_0 \approx 5$ and subsequently decreased in a linear manner at larger velocity ratios. This phenomena was attributed to the entrainment characteristics of the jets with a lower entrainment rate likely occurring for lower velocity ratios.

The dimensionless parameters relevant for the jet in a cross flow have been discussed by Keffer and Baines [1], Pratte and Baines [2] and Rathgeber and Becker [29] - for the present system, the jet trajectory can be described by the form:

$$X/RD_j = f(Z/RD_j) \quad \dots (1)$$

$$\text{or,} \quad X/RD_j = f(\zeta/RD_j) \quad \dots (2)$$

The rectangular jet diameter can also be expressed in terms of the diameter of round jet with the same cross sectional area, D_e . ($= 3.34 D_j$ in this case) however the correlations presented in this work are not sensitive to this refinement. The majority of the results presented in this work are for the near field region where the narrow jet dimension is deemed to be the most relevant scaling parameter.

The purpose of this paper is to present results of the scalar concentration field of a sharp-edged rectangular jet injected into a cross stream flow in a square duct. The mean and concentration fluctuation field were measured by marker nephelometry [45]. The bulk of the results are presented in the form of contour maps and transverse profiles of the mean and fluctuation fields at various downstream locations as well as results of the jet spreading rate.

2. Experimental

A schematic diagram of the flow system used in this work is shown in Fig. 2. The transverse duct flow originated from a wind tunnel which had a 0.836 m^2 (square) cross-section. At the exit of the wind tunnel the cross section was reduced to a square working section, 228.6 mm, on each side with Plexiglas walls. This area reduction provided a contraction ratio of 16:1 with a turbulence intensity of less than 0.1% in the cross stream flow. The wind tunnel working section had a 1.37 m length with the rectangular jet located 203 mm from the entrance to the working section as shown in Fig. 2. The jet was aligned with the jet deflection occurring parallel to the major jet axis. An oil condensation smoke [47] was used as a tracer for the marker nephelometry technique to measure the mean and fluctuation concentration of the jet source fluid.

The jet employed in the present work was a sharp-edged orifice cut from thin aluminum plate and mounted in the wall of the plexiglas test section in such a way as to be flush with the inside wall of the wind tunnel. The cross section of the jet nozzle is shown in Fig. 3. The orifice was sharp-edged with rounded corners, its length, $L_j = 63.5 \text{ mm}$ and width, $D_j = 6.35 \text{ mm}$ (an aspect ratio of 10) with the jet mounted in the vertical position (the long dimension of the jet) relative to the jet flow. Pollard and Iwaniw [46] have shown that the rectangular jet with square and rounded corners has similar characteristics including the presence of a saddle-back behaviour as noted above. The upstream cross section of the jet nozzle was a tapered section from a 12.7 mm air supply line to a $63.5 \times 94.9 \text{ mm}$ rectangular section at the nozzle exit. Steel wool was used as an upstream flow distributor to produce a uniform exit velocity profile. A pitot probe traverse at the jet exit confirmed the presence of a saddle-back behaviour similar to that observed by Quinn, Pollard and Marsters [39 - 40] and Pollard and Iwaniw [46]. The marker nephelometry system was employed with a 5 mW He-Ne laser and Philips 150 AVP photo-multiplier tube - the laser and photo-multiplier were mounted as a solid unit which could be traversed in three dimensions with traversing distances of $1.2 \times 0.6 \times 0.25 \text{ m}$ in the longitudinal, transverse and cross stream directions, respectively. The laser beam was reflected by a mirror above the working section to provide a light source passing through the flow cross section with a control volume on the order of 1 mm^3 as observed by the photo-multiplier tube. The photo-multiplier tube voltage was processed by a Princeton Applied Research model 113 preamplifier with a gain of 100 and high frequency filter of 10 KHz. The output from the filter was fed to a DISA 55D35 rms meter and TSI model 1076 voltmeter. The data were stored in an Analogic Data Precision 6000 digital oscilloscope (14-bit resolution at 100 KHz). A 50 s sampling time was employed for both mean and fluctuation concentration measurements. The data obtained in this manner were then transferred to a microcomputer system for later processing and storage. Appropriate corrections for the marker nephelometry signals as outlined by Becker [45] were employed in the present work.

The experimental flow conditions employed in the present work were:

- (i) $R = 2.0$; $U_j = 8.4 \text{ m/s}$ and $U_o = 4.1 \text{ m/s}$
- (ii) $R = 3.4$; $U_j = 8.4 \text{ m/s}$ and $U_o = 2.5 \text{ m/s}$

The jet velocity corresponded to a Reynolds number of 34,000 based on the long dimension of the nozzle, 3,400 based on the narrow dimension and 11,400 based on the hydraulic diameter of a round jet with the same area. The Reynolds numbers for the cross stream flow based on the dimension of the duct working section were 59,700 for $R = 2.0$ and 36,400 for $R = 3.4$.

3. Results

Contour plots of the mean and fluctuation concentration field for $R = 2.0$ and 3.4 are shown in Figs. 4 - 5 respectively for three downstream locations for each velocity ratio (these plots were typically based on a grid of 200 - 300 measurement points). Humber [48] provides profiles at more intermediate locations which show the evolution of the jet concentration field in greater detail. The three contour plots in each of Fig. 4 and 5 show the concentration and fluctuation field (i) in the near field, (ii) in an intermediate region where there is deformation of the mean concentration contour field into a kidney shape and (iii) in a region farther downstream where the concentration contours have evolved to a more circular shape. After exiting the nozzle, the jet source fluid concentration field exhibits a horseshoe or kidney shape similar to, but not as extreme as, that noted by Rathgeber and Becker [29]. In particular, a distinct bifurcation of the jet flow is not indicated for the present flow system (Kamotani and Greber [5] and Rathgeber and Becker [29] have observed such a flow structure with $R > 4$ for round jets in a cross flow). It can also be noted that this kidney shape occurs at lower values of Z/D_j for the higher velocity ratio, $R = 3.4$ as shown in Fig. 5. Further downstream, near $Z/D_j \approx 20$, the contours become symmetrical in both cross stream axes. In general, the concentration fluctuation intensity in the core region of the jet was small and this is probably attributable to a lower rate of entrainment for this type of flow. It should be noted that the present work did not extend beyond $Z/D_j = 20$, corresponding to a region of 6 nozzle diameters if the nozzle dimension is based in terms of a round jet with the same area.

Estimates of the jet trajectory in the X-Z plane are shown in Fig. 6 and can be described by the power law form:

$$X/RD_j = 1.91 (Z/RD_j)^{0.342} \quad \dots (3)$$

This correlation agrees reasonably well with the correlation of Pratte and Baines [2] for a round jet in a cross flow but with less deflection near the nozzle and more deflection further downstream. These data also show less deflection than the rectangular jet with aspect ratio of 4 and $R = 4$ reported by Weston and Thames [43] (for velocity field data) - the data shown by the open squares in Fig. 6 are described by the power law form:

$$X/RD_e = 1.19 (Z/RD_e)^{0.266} \quad \dots (4)$$

The mean concentration trajectory data of Rathgeber and Becker [29] at small values of jet to pipe diameter gives

$$X/RD_j = 1.93 (Z/RD_j)^{0.20} \quad \dots (5)$$

and this relation shows close agreement with the present results near $Z/RD_j \approx 1$ but less jet penetration further downstream. Close examination of Fig. 6 reveals that the power-law fit to the data is marginal, especially for $1 < Z/RD_j < 10$. It is also apparent from the general flow structure depicted in Figs. 4 and 5 that the mean concentration contours evolve to a circular cross section sooner for the case with $R = 3.4$ - this change occurred beyond $Z/D_j \approx 12$ for $R = 2$ and $Z/D_j \approx 6$ for $R = 3.4$. This also corresponds to points in Fig. 6 where, for $1 \leq Z/RD_j \leq 20$, X/RD_j remains about constant for each velocity ratio. However, if the jet penetration is expressed in terms of the jet trajectory, ξ , as shown in Fig. 7, these two regions are more apparent. In this graph, the jet penetration initially follows a single relation for the initial region for each velocity ratio where $X/RD_j \propto \xi/RD_j$; however as each jet approaches a circular cross section the tendency at each R is to follow a power law relation, where $X/RD_j \approx \text{constant}$ as ξ/RD_j increases. These data are described by the relations:

$$\xi/RD_j \leq 3.4: \quad X/RD_j = (\xi/RD_j)^{0.815} \quad \dots (6)$$

$$R = 2, \xi/RD_j \geq 3.3: \quad X/RD_j = 2.21 (\xi/RD_j)^{0.167} \quad \dots (7)$$

$$R = 3.4, \xi/RD_j \geq 5: \quad X/RD_j = 2.90 (\xi/RD_j)^{0.169} \quad \dots (8)$$

Keffer and Baines [1] and Pratte and Baines [2] observed that $X/RD_j \approx \xi/RD_j$ for low

values of ξ over a wide range of jet penetration values, $0.1 \leq \xi/RD_j \leq 1$. Following this initial high penetration rate Pratte and Baines observed a gradual transition ($1 \leq \xi/RD_j \leq 3$) to a lower penetration rate described by a 1/3 power law for $\xi/RD_j > 3$. In the present work, accurate estimates of the jet trajectory could not be made below $\xi/RD_j \approx 1.5$, but the present results, equation (6), do not differ significantly from these observations and it is interesting to note that the power law exponents in equations (7) and (8) are nearly equal for each velocity ratio. The data of Weston and Thames [43] shown in the top graph of Fig. 7 are limited to the region $\xi/RD_j < 4$ but their results do appear to tend to be of the form of equation (6) for $\xi/RD_j < 1.0$ and a power law form similar to equations (7) and (8) farther downstream.

The jet trajectory can also be described by the relation, Fig. 7 (bottom graph),

$$\xi/RD_j = 1.32 + 1.03 Z/RD_j \quad \dots (9)$$

in close agreement with the result of Rathgeber and Becker [29], $\xi/RD_j = 1 + Z/RD_j$, for the trajectory of a round jet in a pipe flow.

The concentration half width, defined as that point in the Y or X-plane where $\bar{\Gamma}/\bar{\Gamma}_{\max} = 0.5$, provides a measure of the spreading rate of the jet flow as it proceeds downstream. The results are presented in Fig. 8 and exhibit good symmetry in the Y-plane (the plane of bilateral symmetry); however, the results for the X-plane will differ on each side of the jet trajectory and these values are denoted by $+b_x$ and $-b_x$ for the upstream and downstream sides of the jet respectively. Those data for the Y-direction are shown in the top graph of Fig. 8 and are described by linear relations,

$$R = 2: \quad b_y/RD_j = 2.28 + 0.109 \xi/RD_j \quad \dots (10)$$

$$R = 3.4: \quad b_y/RD_j = 1.34 + 0.159 \xi/RD_j \quad \dots (11)$$

The data in the X-direction are shown in the two middle graphs of Fig. 8 and are described by power law relations,

$$-b_x/RD_j = 0.871 (\xi/RD_j)^{0.572} \quad \dots (12)$$

$$+b_x/RD_j = 0.925 (\xi/RD_j)^{0.458} \quad \dots (13)$$

Rathgeber and Becker [29] also observed a power law behaviour and a similar degree of scatter for the half concentration width in the plane of bilateral symmetry for the round jet in a cross flow (they did not report measurements comparable to the b_y data noted above). The present results for $R = 2$ indicate that the half concentration width is comparable in both planes while the results for $R = 3.4$ indicate a higher spreading rate on the leading edge of the jet than on the trailing edge in the plane of bilateral symmetry. Further downstream, the half concentration widths for both flow conditions appear to tend to similar values in both planes. From the contour plots obtained in this work it is also possible to define an equivalent half concentration radius of the form,

$$b_{1/2} = (A_{1/2}/\pi)^{1/2} \quad \dots (14)$$

where $A_{1/2}$ is the area described by the contour $\bar{\Gamma}/\bar{\Gamma}_{\max} = 0.5$ (a length scale proposed by Kamotani and Greber [5]). The data for this half concentration radius are described by a linear relation, Fig. 8 (lower graph),

$$b_{1/2}/RD_j = 1.41 + 0.162 \xi/RD_j \quad \dots (15)$$

The transverse profiles of the mean concentration are shown in Fig. 9 where the transverse position is normalized with respect the appropriate half concentration width. These results exhibited good symmetry within the experimental error expected for these measurements and the data are presented with the data "folded over" along the jet trajectory.

The Gaussian type distribution observed in free jets (eg. Becker, Hottel and Williams [49]) is also shown in these graphs.

Transverse profiles of the concentration fluctuation intensity are shown in Fig. 10 for both transverse planes and velocity ratios. The data for the plane of bilateral symmetry (Y-plane) are depicted with an "open" and "closed" symbol for results on opposite sides of the jet trajectory (the fluctuation intensity is the most critical test of symmetry for the measurements in the present work). Within the experimental error expected for these measurements, the results for the Y-plane exhibit good symmetry and a steep gradient in the fluctuation intensity for $Y/b_y > 1$. The results for the X-plane are not necessarily symmetrical and these data are shown with an "open" symbol to denote the upstream side of the jet and a "closed" symbol to denote results for the leeward side of the jet. The greatest difference in these results occurred for $R = 2$ in the near field, typically $Z/RD_j = 1$ and 2, where the results for the upstream side of the jet were higher. These results in Fig. 10 generally exhibit the expected behaviour with low values of y'/Γ in the core region rising to higher values near the edge of the jet in both planes. It should be noted that fluctuation intensities on the order of $y'/\Gamma = 0.05$ are close to the noise level of the marker nephelometry technique used in this work and estimates in the core region of the jet are thus subject to larger experimental error. Generally, the fluctuation intensity rises above this low core region level near (Y/b_y or X/b_x) ≈ 1.0 and tends to values typical of those found in a free, round jet [50]. Higher fluctuation intensities were observed in the Y-plane for each flow condition and these data also exhibited a higher gradient in the cross stream values of y'/Γ than the X-plane or those of a round jet. The action of the cross stream fluid thus causes a rapid mixing towards the edge of the jet in the plane of bilateral symmetry. However in the core of the jet there is less mixing as indicated by the lower fluctuation intensities for the X-plane and for $Y/b_y < 1$ in the Y-plane.

4. Discussion of Results

The contours of the mean and fluctuation concentration fields, Figs. 4 and 5, provide a clear picture of the development of this type of flow system. At $Z/D_j = 2.0$, a kidney shaped profile is clearly evident for $R = 3.4$ and to a lesser extent for $R = 2.0$. The greater penetration of the jet for $R = 3.4$ is also evident at this downstream location. At the next downstream location shown in Figs. 4 and 5, ($Z/D_j = 12$ for $R = 2.0$ and $Z/D_j = 6.0$ for $R = 3.4$), both jets have developed into a kidney shaped contour (typically the maximum jet deformation observed for each flow condition). At this point, the mean concentration mappings are quite similar and this indicates that the jet deformation occurs faster for $R = 3.4$. These mean concentration contours are also similar to the cross sectional shape observed by Rathgeber and Becker [29] in the near field of a round jet in a cross flow. At the last downstream contour profile for each flow condition, the jet cross section approaches a circular form where the width of the jet in the Y and Z-planes are almost equal in magnitude. In this region, the rectangular cross flow jet differs from the round jet which forms and maintains a distinct bifurcated structure as noted by Rathgeber and Becker [29]. Grandmaison et al [41] also observed that the free, rectangular jet approached a circular cross section (as indicated by the half concentration widths) beyond $X/D_e \approx 30$. It is also apparent that the cross flow has a significant effect on this flow development as the jet with $R = 3.4$ (greater penetration into the cross flow) tended to a circular cross section faster than the jet with $R = 2.0$. It is also likely that the development of the jet with $R = 2$ is affected by the closer proximity of the wall boundary - Keffer and Baines [1] first noted a wall hindrance effect on jet entrainment for $R = 2$ in a round jet in a cross flow.

It should be noted that the jet trajectory data described by equation (3), Fig. 6, exhibit scatter similar to previous measurements of this parameter for round jets in a cross flow. However, there is also a trend in the residuals for each flow condition, with lower trajectory values predicted at intermediate values of Z/RD_j . It is interesting to note that this region also corresponds to the point where the maximum jet deformation takes place ($Z/D_j \approx 12$ for $R = 2$ and $Z/D_j \approx 6$ for $R = 3.4$) and this suggests that a change in trajectory path occurs as the jet changes from an initial rectangular shape to the circular cross section observed farther downstream. This effect is confirmed by the correlation shown in Fig. 7 with the jet trajectory expressed in terms of $X-\xi$ coordinates. In the initial region, $\xi/RD_j \leq 3$, both jets appear to follow a similar path - this corresponds to the zone of maximum jet

deflection noted by Keffer and Baines [1] and Pratte and Baines [2]. In these previous studies a linear relation, $X/RD_j \approx \xi/RD_j$, was observed for $\xi/RD_j \leq 1.5$ followed by a transition region to a power law region (the vortex zone noted by Pratte and Baines [2]). $X/RD_j \propto (\xi/RD_j)^{1/3}$, farther downstream, $\xi/RD_j \geq 3$. The present data for $\xi/RD_j \leq 3$ appear to follow a transition behaviour similar to that observed by Pratte and Baines [2] but more data would be required at lower values of ξ to confirm the linear form noted above. It can also be noted that the shape of the rectangular jet in the cross flow undergoes some changes in the nozzle region (the case for $R = 3.4$, Fig. 5, best demonstrates this behaviour). Farther downstream the present results also tended to power law forms where $\xi/RD_j \propto (X/RD_j)^n$ with $n \approx 0.17$ for each flow rate. The start of this region occurred at $\xi/RD_j \approx 5$ for $R = 2$ and $\xi/RD_j \approx 3$ for $R = 3.4$ and corresponds to the point where there is a large distortion in the jets, Figs. 4 and 5, leading to a more circular cross section farther downstream. The displacement of these power law regions for each jet velocity corresponds to a different effective source for the new jet shape as the flow progresses in the downstream direction. Grandmaison et al [41] observed that the free rectangular jet tended to a nearly circular cross section (as indicated by equal half concentration values in the cross stream direction) near $X/D_c \approx 30$ and this indicates that the effect of the cross flow on the jet is more pronounced than for the free jet case.

The fluctuation intensity contour plots in Figs. 4 and 5 show a region of relatively low, constant values in the central core of the jets. These contour plots do not appear to change significantly as the jet develops, nor do they vary substantially between the two flow conditions. The low fluctuation intensity values observed in the core region for the rectangular cross flow jet is significantly different from the round jet case where the bifurcated flow leads to very high fluctuation intensities, on the order of $\gamma'/\Gamma \approx 0.4$, along the jet trajectory [29]. The effect of the cross flow on the rectangular jet with an aspect ratio of 10 is clearly not sufficient to produce the enhanced mixing observed in a round jet in a cross flow for $R \leq 3.4$ [29].

The concentration half width provides a good parameter with which to measure the spreading rate of the jets. In the Y-plane, the concentration half width should be equal on both sides of the jet since this plane defines the plane of bilateral symmetry. In the X-plane, the concentration half width for a round jet in a cross flow is typically shorter during early stages of the flow development on the leading edge than on the trailing or downstream edge [29]. While this behaviour is suggested by the correlations presented in equations (12) and (13) and the results shown in Fig. 8 (two centre graphs), the effect is not large and within the scatter of the present data the half concentration width in both the Y and X-planes appears to be nearly equal farther downstream, near $Z/RD_j \approx 10$. The half concentration width expressed in terms of the effective radius of the 50% mean concentration contour, $b_{1/2}$, exhibited a good linear relation for both flow conditions over the downstream positions examined in this work. The jet spreading rate, $b_{1/2} \approx 0.162 \xi$, given by equation (15) is comparable to the spreading rate in the free rectangular jet with the same aspect ratio, where $b_z \approx 0.130 \xi$ and $b_y \approx 0.152 \xi$ [41].

The transverse profiles of the mean concentration, Fig. 9, indicate a certain amount of scatter in these data but no distinctive pattern is obvious except that the X-plane data appear to approach a Gaussian type distribution faster than the Y-plane data for both flow conditions. Kamotani and Greber [5] and Rathgeber and Becker [29] also observed a Gaussian type behaviour for the plane of bilateral symmetry for a round jet in a cross flow, particularly for $1 \leq \Gamma/\Gamma_{max} \leq 0.5$. It is also worth noting that, within the accuracy of the mean concentration measurements, there is no evidence of the saddle-back behaviour observed in the free rectangular jet emanating from a sharp edged nozzle [41]. This point is discussed in more detail later.

Transverse profiles of the concentration fluctuation intensity in the present work showed good symmetry for the Y-plane while the data for the Z-plane exhibited some asymmetry in the near field for the case of $R = 2.0$ where there appeared to be higher values on the leading edge of the jet. Rathgeber and Becker [29] also observed higher values of the fluctuation intensity on the upstream side of a round jet in a cross flow. The low values of γ'/Γ in the core region of the jet indicate a lower level of mixing than is encountered for a round jet in a cross flow. This is consistent with the general shape of the concentration contour diagrams which do not indicate a bifurcated flow pattern. There does, however, appear to be intense

mixing on the outer edge of the jet. $Y \geq b_y$ in the Y-plane. In this region, there is a sharp increase in the fluctuation intensity due to the interaction with the cross stream flow. The transverse gradient in the γ'/Γ profiles in the Y-plane for $Y/b_y > 1.0$ appear to be higher than those of a free round jet in quiescent surroundings [49]. This rapid mixing and the distortion of the jet in the Y-plane due to the cross flow stream also appears to counter the persistence of the saddle-back behaviour of the mean concentration profiles at a much earlier stage than observed in the free rectangular jet. This saddle-back phenomena has been observed in the near field region ($X/D_e \leq 10$) of jets issuing from a sharp-edged orifice near $Y/b_y \approx 0.6 - 0.8$ [39] - [41] and a wall jet flow issuing from a sharp edged rectangular orifice [42]. The near field contour plots shown in Figs. 4 and 5 do not indicate such behaviour for the rectangular jet in a cross flow near $Z/D_j \approx 2$. The transverse mean concentration data, Fig 9, exhibit a mean concentration decay, $\Gamma/\Gamma_{\max} \approx 0.8 - 0.85$, in the near field near $Y/b_y \approx 0.6 - 0.8$.

The data presented in this paper represent an intermediate range of the velocity ratio, R . Krothapalli, Lourenco and Buchlin [44] found that the normalized upstream separation distance increased in the range $R \leq 5$ and decreased for higher velocity ratios. They attributed the increase at lower R values to a weaker entrainment on the leeward side of the jet and the present results appear to confirm this hypothesis. The mean and fluctuation field contour diagrams, Figs. 4 and 5, show that the leeward side of the nozzle fluid field extends to the wall region ($X = 0$) and that there is a lower level of mixing in the core region of the jet compared to the more intense mixing observed in the round jet in a cross flow stream at larger values of R . Kamotani and Greber [5] have noted that the scalar field exhibited a peak mean value off the plane of bilateral symmetry for $R \approx 8$ but the peak value remained on the bilateral symmetry plane for $R \leq 4$ in the round jet cross flow system. This phenomena was attributed to more rapid mixing as the jet is able to entrain cross stream fluid more readily with less wall boundary interference at larger velocity ratios. It thus appears that such a phenomena may indeed occur with rectangular jets but with a slightly higher critical velocity ratio, $R \approx 5$.

5. Conclusion

The scalar concentration field of a sharp-edged rectangular jet with an aspect ratio of 10 mixing with a cross stream flow has been examined using marker nephelometry. Measurements include the fields of the mean and fluctuation concentration fields for $\xi/RD_j \leq 6$ for $R = 3.4$ and $\xi/RD_j \leq 20$ for $R = 2.0$. The principle findings of this work are:

- (1) The jet trajectory follows an initial high penetration region similar to that of a round jet followed by a power law region further downstream where the jet path is proportional to $(\xi/RD_j)^{0.17}$.
- (2) The half concentration length in the Y and X-planes follow linear and power law forms respectively as a function of the distance along the jet trajectory. The half concentration length based on the effective radius of the $\Gamma/\Gamma_{\max} = 0.5$ contour follows a linear relation with a spreading rate that is slightly larger than the free rectangular jet.
- (3) Transverse profiles of the mean concentration field in the plane of bilateral symmetry were closer to a Gaussian type behaviour than those data in the Y-plane. The fluctuation intensity data were significantly lower in the plane of bilateral symmetry than in the Y-plane.
- (4) The jets exhibited a kidney shape similar to a round jet in a cross flow but the rectangular jet did not exhibit a bifurcated structure for $R = 2.0$ and 3.4 . In the core region of the jets there was a relatively low fluctuation intensity indicating a lower mixing intensity than round jets in a cross flow at larger values of the velocity ratio.
- (5) The sharp-edged rectangular jet in a cross flow did not exhibit a saddle-back behaviour in the mean concentration field in the near field region ($Z/D \approx 2$). The action of the cross flow stream thus appears to counter the mechanism for the persistence of this phenomena more quickly than the free rectangular jet.

ACKNOWLEDGEMENT

This work was supported by grants from the Natural Sciences and Engineering Research Council of Canada.

REFERENCES

1. J.F. Keffer and W.D. Baines, *J. Fluid Mech.* **15**, 481-496 (1963).
2. B.D. Pratte and W.D. Baines, *J. Proc. Amer. Soc. Civil Eng.* **93**, HY-6 53-64 (1967).
3. M.A. Patrick, *Trans. Instn. Chem. Engrs.* **45**, T16-T31 (1967).
4. H.M. McMahon, D.D. Hester and J.G. Palfrey, *J. Fluid Mech.* **48**, 73-80 (1971).
5. Y. Kamotani and I. Greber, *AIAA J.* **10**, 1425-1429 (1972).
6. R.L. Stoy and Y. Ben-Haim, *ASME J. Fluids Eng.*, **95**, 551-556 (1973).
7. P. Chassaing, J. George, A. Claria and F. Sananes, *J. Fluid Mech.* **62**, 41-64 (1974).
8. J. Sucec and W.W. Bowley, *ASME J. Fluids Eng.*, **98**, 667-673 (1976).
9. T. Makiyama and Y. Miyai, *J. Fluids Eng.* **101**, 217-223 (1979).
10. D. Crabb, D.F.G. Durao and J.H. Whitelaw, *J. Fluids Eng.* **103**, 142-153 (1981).
11. J. Andreopoulos, *J. Fluids Eng.* **104**, 493-499 (1982).
12. J. Andreopoulos and W. Rodi, *J. Fluid Mech.*, **138**, 93-127 (1984).
13. R. Fearn and R.P. Weston, *AIAA J.* **12**, 1666-1671 (1974).
14. Z.M. Moussa, J.W. Trischka and S. Eskinazi, *J. Fluid Mech.* **80**, 49-80 (1977).
15. D. Crabb, D.F.G. Durao and J.H. Whitelaw, *ASME J. Fluids Eng.*, **103**, 142-153 (1981).
16. J. Andreopoulos, *ASME J. Fluids Eng.*, **104**, 493-499 (1982).
17. J.E. Broadwell and R.E. Breidenthal, *J. Fluid Mech.* **148**, 405-412 (1984).
18. J. Andreopoulos, *J. Fluid Mech.* **157**, 163-197 (1985).
19. R.H. Nunn, *AIAA J.* **23**, 473-475 (1985).
20. P.R. Sterland and M.A. Hollingsworth, *J. Mech. Eng. Sci.* **17**, 117-124 (1975).
21. Z.A. Khan and J.H. Whitelaw, *J. Heat Transfer* **102**, 391-392 (1980).
22. L.S. Cohen, L.J. Coulter and W.J. Egan, *AIAA J.* **9**, 718-724 (1971).
23. H. Ziegler and P.T. Wooller, *J. Aircraft*, **8**, 414-420 (1971).
24. J.D. Holdeman and R.E. Walker, *AIAA J.* **15**, 243-249 (1977).
25. K.M. Isaac and J.A. Schetz, *J. Fluids Eng.* **104**, 489-492 (1982).
26. T. Makiyama and Y. Miyai, *J. Fluids Eng.* **105**, 91-97 (1983).
27. K.M. Isaac and A.K. Jakubowski, *AIAA J.* **23**, 1679-1683 (1985).
28. J.W. Ramsey and R.J. Goldstein, *J. Heat Transfer* **94**, 365-372 (1971).
29. D.E. Rathgeber and H.A. Becker, *Can. J. Chem. Eng.* **61**, 148-157 (1983).
30. J. Andreopoulos, *Phys. Fluids* **26**, 3201-3210 (1983).
31. D. Adler and A. Baron, *AIAA J.* **17**, 168-174 (1979).
32. M.L. Bojic and S. Eskinazi, *AIAA J.* **17**, 1050-1054 (1979).
33. S.L.V. Coelho and J.C.R. Hunt, *J. Fluid Mech.* **200**, 95-120 (1989).
34. J.C. Chien and J.A. Schetz, *ASME J. Applied Mech.*, **42**, 575-579 (1975).
35. S.V. Patankar, D.K. Basu and S.A. Alpay, *ASME J. Fluids Eng.*, **99**, 758-762 (1977).
36. A.O. Demuren, *Comp. Meth. Appl. Mech. and Engng.*, **37**, 309-328 (1983).
37. Demuren, A.O. and Rodi, W., *J. Heat Transfer*, **109**, 113-119 (1987).
38. M. Fairweather, W.P. Jones and A.J. Marquis, *Comb. Sci. and Tech.* **62**, 61-76 (1988).
39. W.R. Quinn, A. Pollard and G.F. Marsters, 4th Symp. on Turbulent Shear Flows, pp. 7.1 - 7.6 (1983).
40. W.R. Quinn, A. Pollard and G.F. Marsters, *AIAA J.* **23**, 971-973 (1985).
41. E.W. Grandmaison, A. Pollard and S. Ng, *Int. J. Heat Mass Transfer* **34**, 2653-2662 (1991).
42. A. Pollard and R.R. Schwab, "The Rectangular Wall Jet", submitted to *Journal of Fluid Mechanics* (1992).
43. R.P. Weston and F.C. Thames, *J. Aircraft*, **17**, 701-707 (1979).
44. A. Krothapalli, L. Lourenco and J.M. Buchlin, *AIAA J.*, **28**, 414-420 (1990).
45. H.A. Becker, "Marker Nephelometry, Concentration Fluctuations and Turbulent Mixing", *Studies in Convection*, Vol. 2 (ed. B.E. Launder), 45-105 (1977).
46. A. Pollard and M.A. Iwaniw, *AIAA J.* **23**, 631-633 (1985).
47. E.W. Grandmaison, S. Ng and H.A. Becker, *J. Phys. Series E: Scient. Instrum.* **20**, 606-608 (1987).
48. A. Humber, M.Sc. Thesis, Dept. of Chemical Engineering, Queen's University, Kingston, Ont. Canada (1991).
49. H.A. Becker, H.C. Hottel and G.C. Williams, *J. Fluid Mech.*, **30**, 285-303 (1967).

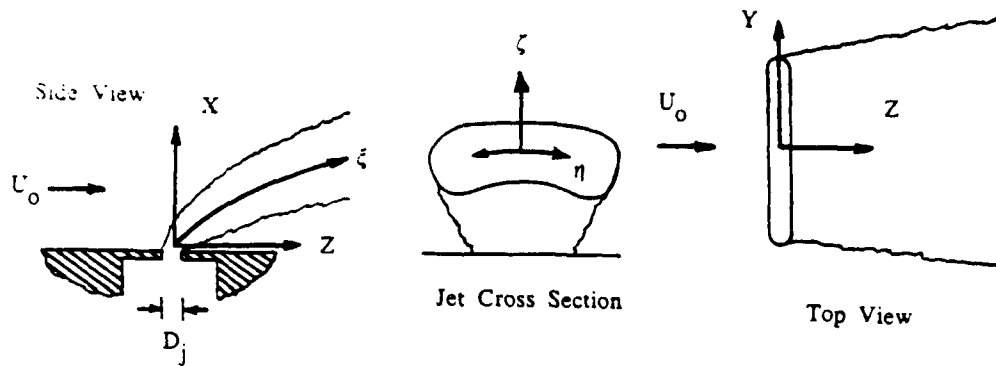


Fig. 1. Schematic diagram of the rectangular jet in a cross flow stream.

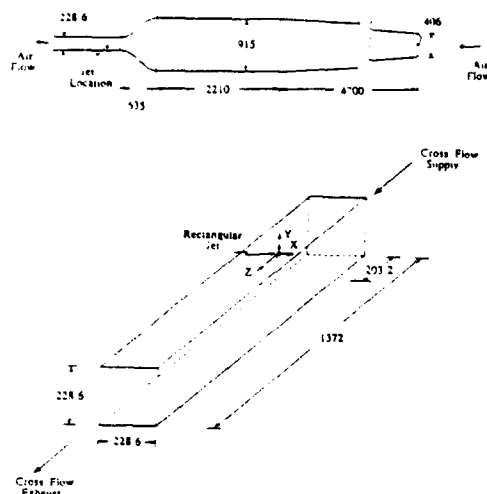


Fig. 2. Schematic diagram of wind tunnel flow system for the cross flow stream (top) and the wind tunnel working section with the cross flow jet - all dimensions in mm.

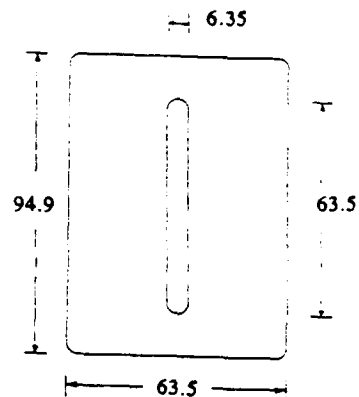


Fig. 3. The rectangular jet nozzle face - all dimension in mm.

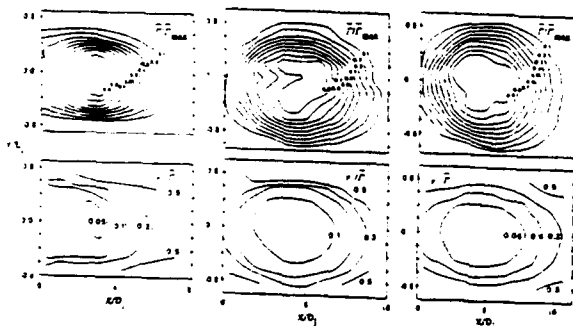


Fig. 4. Contour plots of the mean and concentration fluctuation intensity for $R = 2.0$. $Z/D_j = 2$ (left), $Z/D_j = 12$ (centre) and $Z/D_j = 20$ (right).

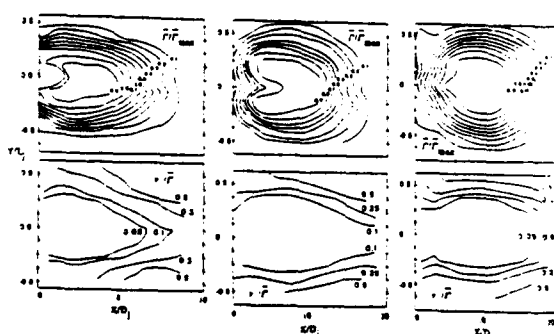


Fig. 5. Contour plots of the mean and concentration fluctuation intensity for $R = 1.4$. $Z/D_j = 2$ (left), $Z/D_j = 6$ (centre) and $Z/D_j = 12$ (right).

Fig. 6 Jet trajectory expressed in terms of cartesian coordinates.

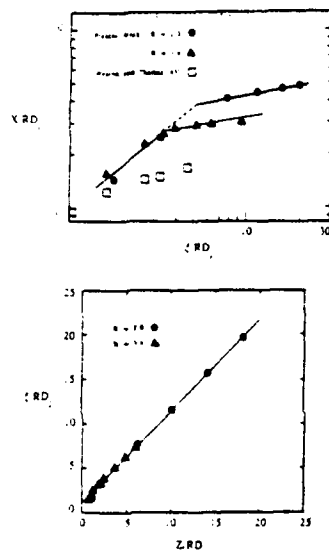
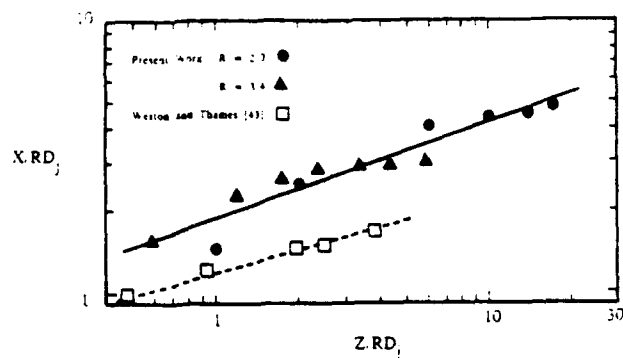


Fig. 7 Jet penetration as a function of trajectory path (top graph) and jet trajectory as a function of cartesian coordinates position in the downstream direction (bottom graph).

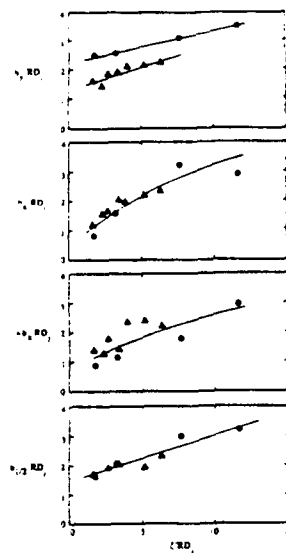


Fig. 8 Jet half concentration lengths as a function of distance along the jet trajectory; from top to bottom, graphs display $b_{1/2}$, $b_{1/2}$, $b_{1/2}$ and $b_{1/2}$. $R = 2.0$ (circles) and $R = 3.4$ (triangles).

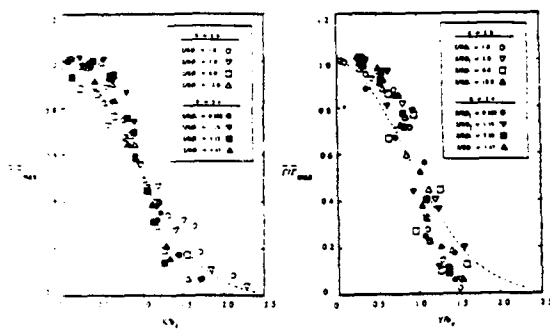


Fig. 9 Transverse profile of the mean concentration decay from the maximum value (\bar{C}_{max}) along the jet trajectory. Dashed line represents a Gaussian type distribution, $\exp(-0.693X/b_{1/2}^2)$ or $\exp(-0.693Y/b_{1/2}^2)$.

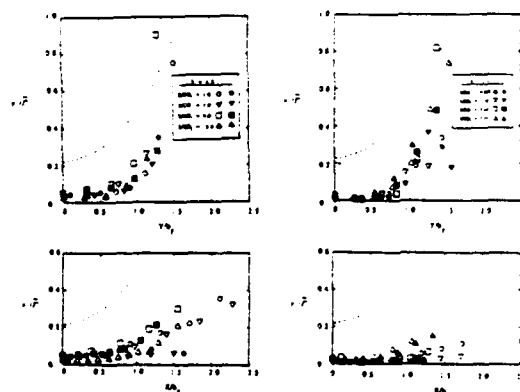


Fig. 10 Transverse profiles of the concentration fluctuation intensity. "Open" and "Closed" symbols represent data on opposite sides of the jet trajectory for the Y-plane and the upstream and downstream side of the jet for the X-plane. Dashed line represents the free turbulent jet in quiescent surroundings.

LDV MEASUREMENTS OF THE TURBULENT FLOW
IN GAS CYCLONES

T.L. Liem & H.E.A. van den Akker
Kramers Laboratorium voor Fysische Technologie
Delft University of Technology
Prins Bernhardlaan 6
2628 BW Delft, Netherlands

Abstract. Laser Doppler measurements were made of axial and tangential velocities (mean values and root mean square of the fluctuations) in a model of a reverse flow gas cyclone. The effect of geometry changes was examined. In the axis region the measured mean velocities and r.m.s.-values were significantly affected by the precession of the vortex core. A method was devised to measure the amplitude of the precession and to correct the measured velocity profiles.

1 Introduction

Gas cyclones are widely used in industry to separate particles from gas flows. A cyclone is a very simple apparatus (Fig. 1): it consists of an oblong cylindrical vessel of typically 0.3 to 1 m diameter. A strongly swirling motion is imparted to the particle laden flow by letting it enter the cyclone through a tangential inlet. The inlet velocity is typically 15 to 20 m/s. The particles are 'centrifuged' outward, and travel along the wall to the solids outlet. The gas leaves the cyclone through the central exit pipe. Depending on the side on which this gas exit pipe is located the cyclone is described as 'reverse flow' or 'through-flow'.

The separation efficiency depends on the particle diameter: small particles remain in the gas flow. The particles that have 50 % separation are said to be of 'cut size'. In principle increasing the inlet velocity lowers the cut size and increases the overall efficiency. At the same time more turbulence is created, which interferes with the separation process. There is an optimum inlet velocity (and therefore an optimum cyclone size at a given gas flow rate).

The pressure drop across an industrial cyclone is of the order of 10^3 Pa. This is seldom a limiting factor. Running costs of cyclones are low compared to other dust-separation methods; they are cheap to manufacture, reliable, and suitable for rough conditions such as high temperatures. There is still room for improvement though, especially in the class of high efficiency cyclones (cut size smaller than $10\text{ }\mu\text{m}$). Geometrical alterations can for instance significantly diminish the reentrainment of particles near the solids outlet. An improved exit pipe shape can contribute to a stronger vortex with less turbulence, thus directly influencing the separation process.

The work presented in this article is part of a project aimed at increasing the role of computational fluid dynamics (CFD) in the process of developing more efficient gas cyclones. Costly and laborious experiments could be replaced by simulation on a computer. This would make it far easier to examine the consequences of alterations in the cyclone geometry, but at the same time it places a considerable emphasis on the understanding of the physics of the flow, and the way it is modelled in the computer program. The flow in a cyclone is turbulent, but the strong swirl forces the turbulence to become non-isotropic, which makes it difficult to model (Lilley 1976).

In our group the commercial flow simulation program FLUENT is used as a tool in chemical

engineering research. To be able to judge its performance in swirling flows it is necessary to have reliable gas velocity measurements.

Laser Doppler Velocimetry (LDV) in cyclones that are actually separating dust is very difficult, because at very low dust loads the flow is already opaque. Besides this it was not possible with our LDV system to distinguish between the velocities of the various particle sizes as they are separated, and the velocity of the gas flow (measured with 'seeding' particles). For this reason only 'seeding' particles were admitted into the gas during this study.

Related studies found in literature are those of Boysan et al. (1983), Escudier et al. (1980, not a cyclone but a vortex tube with water as fluid), Reydon & Gauvin (1981, a vortex chamber), Tryman & Collin (1989, a cyclone combustor) and Hargreaves & Silvester (1990, a deoiling hydrocyclone).

Depending on the geometry and the flow rate the vortex in a cyclone can be moving around in a phenomenon called 'vortex precession'. It 'blurs' the velocity profiles and to enhance velocity fluctuations. When measuring the velocity field it is necessary to try to correct the average velocity profiles and to distinguish between the turbulent fluctuations and those of coherent movements or structures.

2 The flow in a cyclone

The flow in a cyclone can be classified as a swirling flow: an axisymmetric turbulent flow in which both tangential (rotational) and axial velocity components are important.

The tangential velocity profile of a swirling flow is characterized by an outer 'free vortex' region and an inner 'forced vortex' region. The shape of the profile suggests that in the outer region fluid going radially inward accelerates according to conservation of angular momentum ($w \cdot r = \text{constant}$). In reality the relationship is more like $w \cdot r^\alpha = \text{constant}$ with $\alpha \approx 0.7$ in a cyclone. Near the swirl centre the flow behaves as a solid body, i.e. as a region dominated by viscosity. Here $w/r = \text{constant}$.

In swirling flows two dimensionless numbers are important:

- the Reynolds number $Re = U \cdot D / \nu$ (The choice made for the velocity U and the characteristic diameter D is to be specified. ν is the kinematic viscosity of the gas.)
- the Swirl number S , a measure of the degree in which the swirl component dominates the flow

$$S = \frac{\text{axial flux of angular momentum}}{(D/2) \cdot \text{axial flux of axial momentum}} \quad (1)$$

Neglecting the turbulent and pressure contributions to the fluxes is often possible without introducing significant errors (Gupta et al. 1984). Then the swirl number can be calculated as

$$S = \frac{\int_0^R \rho u w r \, 2\pi r \, dr}{\frac{D}{2} \cdot \int_0^R \rho u^2 \, 2\pi r \, dr} \quad (2)$$

(u indicates average axial velocities, w average tangential velocities)

Because the flow pattern in a reverse flow cyclone is complicated it is difficult to define one characteristic swirl number. S varies with the height in the cyclone, because the axial flow rate is not constant. In a cyclone the simplified definition of Gupta et al. (1984) is frequently used as an overall swirl number, which does not take into account local variations:

$$S = \frac{\pi D_o D_c}{4 A_i} \quad (3)$$

A_i is the inlet surface area, D_o the exit pipe diameter, D_c the cyclone diameter. This definition can be understood as a rough estimate of the tangential velocity divided by the axial velocity.

The shape of the tangential velocity profile of a swirling flow is not very sensitive to swirl number alterations. In contrast the axial velocity profile can change dramatically. Flow reversals (gas travelling in the opposing direction to the mean flow) are known to appear around the flow axis at swirl numbers greater than 0.6 (Schetz 1980). They are caused by the tendency of high swirl fluid to avoid the central area of the flow. This sets up an adverse pressure gradient that draws back fluid with less swirl. The flow then becomes sensitive to changes in the downstream flow conditions, like bends and obstacles, even outside the cyclone. This flow condition is called 'subcritical', a term emanating from the theory of free-surface flows, where it indicates the flow regime whereby surface waves can propagate upstream (Benjamin 1962). When the swirl number is large enough the flow becomes virtually two-dimensional, with no velocity gradients at all in tangential or axial direction. The turbulent eddies in a swirling flow experience strong Coriolis forces; momentum exchange is either amplified or attenuated, depending on the local gradient of the swirl velocity (Leschziner 1990). Moreover swirl causes anisotropy in the levels of the normal stresses (Lilley 1976). When modelling swirling flows a turbulence model has to be used that calculates the turbulent stresses from transport equations (a so-called Reynolds stress turbulence model).

A phenomenon that is still poorly understood hydrodynamically is 'vortex precession'. The rotational axis of the flow moves around the geometrical axis of the cyclone, in the direction of the tangential flow, with a distinct frequency. The vortex is as it were a selective amplifier of disturbances, i.e. an oscillator. Chanaud described the phenomenon already in 1965. He found that there was a linear relationship between the frequency emitted by a so-called vortex whistle and the mean axial velocity. Two dimensionless numbers governed the precession: the Reynolds number and the Rossby number, which is closely related to the inverse of the swirl number. Below a critical Re no precession was found at all, and at any given Re above the critical there is a Rossby number above which no precession will be present. When the Rossby number is decreased (increasing swirl) the precession would eventually make way for more and more irregular oscillations.

Garg & Leibovich (1979) measured dominant frequencies of around 10 Hz in so-called 'vortex breakdown' fields. They pointed out that the oscillations can be explained using linearized inviscid stability analysis of the undisturbed axisymmetrical flow.

3 Experimental setup

3.1 The cyclone model

A gas cyclone model 29 cm in diameter and with a height of 1.5 m was used (Fig. 2). It consisted of interchangeable perspex sections. A section made of precision glass was used to measure through. The air flow rate was 44 l/s. The inlet velocity through the tangential inlet was 3.5 m/s and the Reynolds number $1.3 \cdot 10^4$, based on a superficial velocity through the cross-sectional area of the cyclone body of 0.67 m/s. As mentioned before, no particles were present in the gas except seeding droplets. There was no 'underflow' through the particle outlet; all gas left the cyclone upward through the exit pipe.

According to Van den Akker & De Kort (1988, measurements at Shell Amsterdam) fitting a conical section to the exit pipe brings about an improvement of the separation. The effect this change had on the velocity field was investigated.

Three exit pipe geometries were used:

- A. A straight exit pipe with an inside diameter of 18.8 cm and a length of 30 cm
- B. An exit pipe fitted with a conical section of 18.8 cm inside diameter at the top and 11 cm at the 'mouth' (length of cone 7.5 cm; length overall 33 cm)
- C. An exit pipe of type B fitted with an additional straight section of 16.1 cm length and inside diameter of 11 cm

A further geometry change that was studied was the insertion of a so-called stabilizer into the bottom part of the cyclone. This is simply a disk of 17 cm diameter mounted on a rod of 2.5 cm diameter. The end of the rod is meant to 'capture' the vortex and stabilize it. The disk forces the particles to travel to the solids outlet along the wall, inhibiting reentrainment.

Five geometries were studied in total. They will be referred to as A, B, BN, C and CN (N = no stabilizer).

3.2 The LDV system

The LDV measurements were carried out with a 4 W two-dimensional system (TSI fiber optics, Spectra Physics 2016 Ar-ion laser). Signal processing was achieved by two TSI IFA 550 'intelligent flow analyzers' (Jenson et al. 1988). The measurements were made in a vertical plane through the cyclone axis, in full back-scatter mode. The axial and tangential velocity components were measured. The measuring volume had a length of 3 mm and a width of 0.15 mm. The Doppler frequency was 192 kHz per m/s ($\lambda = 514.5 \text{ nm}$).

3.3 Seeding

Seeding particles were produced by atomizing a 10 % solution of glycerol (trihydroxypropane) in water with a paint spray gun. By spraying tangentially into a 'knock out vessel' (in fact a crude cyclone) larger droplets were removed (Durst & Ruck (1987) suggested this as an effective way of boosting the data rate of the LDV measurement). Stable droplets of approximately 2 μm diameter were produced in sufficient quantities. The diameter of the droplets was measured with a Malvern 2600 Particle Sizer.

The ability of the particles to follow turbulent fluctuations was checked by calculating the reaction of one particle subjected to a sinusoidal air flow (Drain 1980). At a frequency of 4 kHz the velocity amplitude of a 2 μ m particle turned out to be 95 % of the driving velocity amplitude. The droplets were considered acceptable flow followers. The centrifugal forces acting on a droplet combined with an assumed Stokes drag force (Durst et al. 1976) resulted in an estimated radial velocity of approximately 2 cm/s. Measuring the velocity of one particle takes about 10 μ s. The radial displacement of a particle during measurement is therefore negligible.

4 Data processing

4.1 Spectrum analysis

An LDV measurement consisted of 2000 to 4000 data points. The data rate varied from around 50 Hz near the axis to 300 Hz in the outer vortex. Spectrum analysis is applied to find dominant frequencies in the time-dependent velocity signals. Because the data points in a measurement are not equidistant in time direct application of Fast Fourier Transformation (FFT) is impossible. Instead a discretized auto-covariance function is calculated first, using the 'slotting method' (Mayo 1978).

4.2 Precession

To be able to correct the measured velocity profiles and to distinguish between turbulence and the fluctuations caused by vortex precession it is necessary to study the measured time-dependent velocity. In situations where the movement of a flow feature is exactly periodic it is generally possible to use 'time slotting', whereby each slot corresponds to an angular position. In this way it is for instance possible to map the detailed flow around a stirrer blade in a stirred vessel with respect to a rotating frame of reference. Vortex precession is not externally synchronized, and after each turbulent perturbation phase information is lost, so time slotting cannot be applied.

Instead an attempt was made to extract as much information as possible from the average height and fluctuation of the peaks in the graphs of measured velocity versus time, combined with knowledge of the general shape of the average velocity profiles. A simple computer program was written to seek out the peaks. They were defined as those data points that were 'higher' or 'lower' than 2n neighbours. The optimum n depends on the data rate, the frequency of the precession and the properties of the turbulence.

5 Results

5.1 Time averaged velocity profiles

The swirl number according to definition (3) is 3.4 for the geometry with exit pipe A and 2.0 for the geometries with exit pipe B or C.

In Fig. 3 the measured average tangential velocity profiles are shown for three geometries: the wide exit pipe (A) and the lengthened conical exit pipe with and without the stabilizer (C and CN). These profiles are not corrected for the effect of vortex precession (this correction

will be applied later).

The profiles show the expected shape of a combined vortex. The differences between the profiles measured on different heights in one geometry were very small, in accordance with the tendency for 'two-dimensionality' of swirling flows. There is little residual asymmetry of the single tangential inlet, except for a small shift of the vortex axis in geometry A. The angular velocity of the vortex core increases by a factor of 5 when the exit pipe is fitted with the 'long' conical section. The maximum tangential velocity only increases by a factor of about 2.2, from 3.8 m/s (A) to 8.8 m/s (CN). The core is much narrower: 45 mm instead of 90 mm. The vortex is much more 'concentrated', and all radial gradients are amplified. The acceleration experienced by particles rotating at the maximum tangential velocity increases from the order of 40 times earth gravity to 400 times. This explains the improved separation found by Van den Akker & De Kort (1988). The swirl number is lowered from 3.4 to 2.0 by narrowing the exit pipe. Intuition suggests that a higher swirl number enhances separation. The overall swirl number definition of Gupta et al. (1984) is inadequate here. Local swirl numbers have to be taken into account.

The results of the geometries B and BN are not shown in Fig. 3. The profiles are similar to those of geometries C and CN, but the shortening of the exit pipe results in a slight decrease of the maximum tangential velocity of 15 %. This is probably due to an increase of turbulence in the region of the 'mouth' of the exit pipe. The stabilizer did not influence the tangential velocities very much, which was surprising. A slight decrease of the maximum velocity (10 %) was noted when it was inserted.

In Fig. 4 the measured average axial velocity profiles are shown. As with the tangential velocity profiles no corrections have been applied here for the effect of vortex precession. The symmetry in axial and tangential directions already noted in the tangential velocity profiles is again present in the outer flow. Along the vortex axis some axial gradients are visible.

The axial velocities are downward along the cyclone wall and upward nearer the vortex centre, as was expected. As with the tangential velocities the maximum axial velocities are much larger with geometry CN (4.9 m/s) than with geometry A (1.6 m/s).

There is a distinct 'dip' or velocity minimum, broadly corresponding to the 'inner' vortex, in geometries A and CN. In C it is present only near the exit pipe. Clearly the central flow is decelerated by the already mentioned swirl induced adverse pressure gradient, but no flow reversals are visible.

The diameter of the 'dip' is approximately 85 mm for geometry A and 40 mm for geometry CN. The presence of the stabilizer inhibits the occurrence of an axial velocity minimum in the greater part of the cyclone body. This can be attributed to increased radial velocities, because the same flow has to travel inward within a reduced effective cyclone height.

The axial velocity profiles of the B and BN geometries are not shown in Fig. 4. Broadly the same conclusion can be reached here as with the tangential velocities: the lengthening of the conical exit pipe causes an additional intensification of the vortex.

5.2 Velocity fluctuations

Straightforward calculation of the root mean square (r.m.s.) of the velocity fluctuations

$(u(t) - u_{\text{average}})$ yields a profile that is similar for axial and tangential velocities: an almost constant value near the wall, a sharp peak in the centre, and a gentle slope around the peak up to a radius of about 60 mm (Fig. 5). The peak height varies from 1.5 to 4.0 m/s for geometries B, BN, C and CN and 1 m/s for geometry A. The peak width is directly related to the width of the vortex core. Near the wall an axial velocity r.m.s.-value of 0.4 m/s is found and a tangential velocity r.m.s.-value of 0.3 m/s.

Leschziner (1990) deduced from turbulence theory that turbulence is attenuated by solid-body rotation and amplified by free-vortex rotation. When the measured r.m.s.-velocities are considered as turbulence intensities there is an apparent contradiction. Either the turbulence theory is incorrect, or there is a fluctuating velocity component that is not turbulent. The solution lies in the analysis of the time-dependent velocity signal that will be presented in the next section.

5.3 Corrections for vortex precession

Analysis of the power spectrum revealed a distinct precession frequency of 7 Hz in the time-dependent velocity signals of geometries B, BN, C and CN (all with a conical exit pipe). It was present in both velocity components, in a region of 60 mm radius around the centre of the flow.

The amplitude of the precession in the centre of the measured vortex was calculated by averaging the peak heights in the graph of the tangential velocity versus time (Fig. 6), and dividing this average peak velocity by the slope of the measured tangential velocity profile. It is assumed that:

- the precession amplitude is smaller than the radius of the vortex core without precession (assuring a linear relationship between radial displacement and velocity shift),
- the vortex precession does not alter the slope at the centre of the measured tangential velocity profile.

The calculated precession amplitude was 5 mm.

The presence of a stabilizer did not influence either the frequency or the amplitude of the precession. The same could be said of the lengthening of the conical exit pipe.

The precession component in the velocity signals of geometry A (wide exit pipe) was too indistinct to be measured correctly. A comparison with the precession in the other geometries was therefore not possible. This problem will probably be solved when more data points per measurement are used.

Corrections were attempted of the measured average velocity profiles and of the measured profiles of the turbulence intensity (the r.m.s. of the velocity fluctuations).

It is assumed that precession consists of a circular movement of the whole vortex core and a region around it. The average velocity profiles are distorted in two ways:

- Maxima and minima are blunted.
- The positions of maxima and minima are shifted in the radial direction away from their steepest slope.

Maxima in the profiles occur on the rim of the vortex core, and at the centre of the axial velocity profiles. In geometry CN, when traversing the measuring point radially at an axial position of 65 cm, a frequency component of 14 Hz was noticeable in both velocity components,

at radial positions 15 and 20 mm from the symmetry axis of the measured flow. The corresponding time-dependent velocity signals appeared strongly non-sinusoidal. Clearly in these cases the measuring volume straddled the maximum position (two peaks in the velocity signal per precession period), or was so close to it that the non-linearity generated harmonics of the precession frequency.

At a radius of 20 mm the peak height was averaged (bearing in mind the right sign), resulting in a corrected value for the maximum axial or tangential velocity. For both components the corrected value was 0.8 m/s higher than the measured value. The corrected maximum axial velocity in geometry CN was 5.7 m/s, the corrected maximum tangential velocity 9.6 m/s.

The corrected radius of maximum velocity could not be determined accurately; $15 \text{ mm} < r_{\text{max}} < 20 \text{ mm}$ remains the best estimate.

The measured minimum at the centre of the axial velocity profiles will be too high due to vortex precession. Here the negative peak values of the time-dependent velocity signal do not provide an estimate of the 'true' minimum axial velocity at the vortex axis, because most of the time the precessing minimum will 'miss' the measuring volume. The 'true' minimum will always be lower than the average of the negative peaks in the velocity signal.

In geometry C the uncorrected central minimum in the axial velocity profile was 5.0 m/s (measured at the 65 cm axial position). 'Peak analysis' revealed that the true minimum was at least 3.4 m/s lower. The corresponding values for geometry CN were 1.7 m/s and 1.8 m/s respectively. This means that there is a central flow reversal of at least 0.1 m/s.

Estimates of the corrected r.m.s.-velocities were obtained by calculating the r.m.s.-value of the deviations from the average peak height. In the outer vortex ($r < 60 \text{ mm}$) the outcome was in fact no different from the r.m.s.-values near the wall. More surprisingly, the same result was obtained when correcting the r.m.s.-values measured at a radius of 20 mm, on the rim of the vortex core. For geometry CN the corrected r.m.s.-values at the centre of the vortex were calculated. The axial r.m.s.-value was 1.0 m/s, the tangential r.m.s.-value 1.3 m/s. Both are well above the corrected outer vortex values. The apparent contradiction with turbulence theory mentioned before is still not resolved. It has to be borne in mind that the number of data points is greatly reduced by only using the peaks; typically there are 300 peaks in one measurement.

6 Conclusions

Velocity measurements in a gas cyclone reveal aspects of swirling flows that have to be considered if a validation of computational fluid flow programs is to be possible: flow reversals, sharp gradients near the centre and precession of the vortex core.

An overall swirl number is inadequate. The level and the variation of the local swirl number have to be taken into account to characterize the velocity field.

Modifications in cyclone geometry induce changes in the velocity field. How these changes influence the separation efficiency is still to be assessed.

The presence of a stabilizer does not influence either the frequency or the amplitude of the vortex precession. It does inhibit the occurrence of axial flow reversal.

It is possible to correct the measured velocity profiles for the effect of vortex precession if there is a clear precession frequency in the velocity signal. The corrections apply to

the value and radial position of the maxima and minima in the profiles of average axial and tangential velocities. To correct the measured r.m.s.-velocities more data points per measurement are needed.

Acknowledgement

The cooperation of Mr. A.K. Lahr is gratefully acknowledged. He carried out the experiments in the framework of his graduate project.

References

- Akker, H.E.A. van den; Kort, C.J.M. de 1988: Improved swirl tube separator. Patent application (UK) No. 8822348
- Benjamin, T.B. 1962: Theory of the vortex breakdown phenomenon. *J. Fluid Mech.* 14, 593-629
- Boysan, F.; Ewan, B.C.R.; Swithenbank, J.; Ayers, W.H. 1983: Experimental and theoretical studies of cyclone separator aerodynamics. I. Chem. E. Symposium series No. 69 (POWTECH Conference)
- Chanaud, R.C. 1965: Observations of oscillatory motion in certain swirling flows. *J. Fluid Mech.* 21, 111-127
- Drain, L.E. 1980: The laser doppler technique. *J. Wiley & Sons*
- Durst, F.; Melling, A.; Whitelaw, J.H. 1976: Principles and practice of laser-doppler anemometry. Academic Press
- Durst, F.; Ruck, B. 1987: Effective particle size range in laser-doppler anemometry. *Exp. Fluids* 5, 305-314
- Escudier, M.P.; Bornstein, J.; Zehnder, J. 1980: Observations and LDA measurements of confined turbulent vortex flow. *J. Fluid Mech.* 98, 49-63
- Garg, A.K.; Leibovich, S. 1979: Spectral characteristics of vortex breakdown flowfields. *Phys. Fluids* 22, 2053-2064
- Gupta, A.K.; Lilley, D.G.; Syred, N. 1984: Swirl Flows. Abacus Press
- Hargreaves, J.H.; Silvester, R.S. 1990: Computational fluid dynamics applied to the analysis of deoiling hydrocyclone performance. *Trans. I. Chem. E.* 68, 365-383
- Jenson, L.; Menon, R.K.; Fingerson, L.M. 1988: An automatic signal processor for LDV systems. Proc. 4th Symp. Applications of Laser Anemometry, Lisbon
- Leschziner, M.A. 1990: Modelling Engineering flows with reynolds stress turbulence closure. *J. Wind Eng. Ind. Aerodyn.* 35, 21-47
- Lilley, D.G. 1976: Nonisotropic turbulence in swirling flows. *Acta Astro.* 3, 919-933
- Mayo, W.T. 1978: Spectrum measurements with laser velocimeters. Proc. Dynamic Flow Conference, Marseille & Baltimore
- Reydon, R.F.; Gauvin, W.H. 1981: Theoretical and experimental studies of confined vortex flow. *Can. J. Chem. Eng.* 59, 14-23
- Schetz, J.A. 1980: Injection and mixing in turbulent flow. Martin Summerfield
- Tryman, R.; Collin, R. 1989: The gas flow field in a cyclone combustor: measurement and prediction by mathematical model. Proc. 9th IFRF-members Conf. Noordwijkerhout

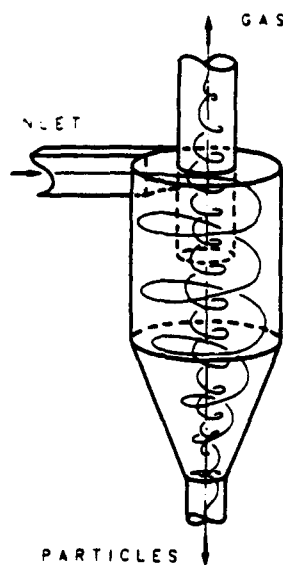


Fig. 1. A reverse flow gas cyclone

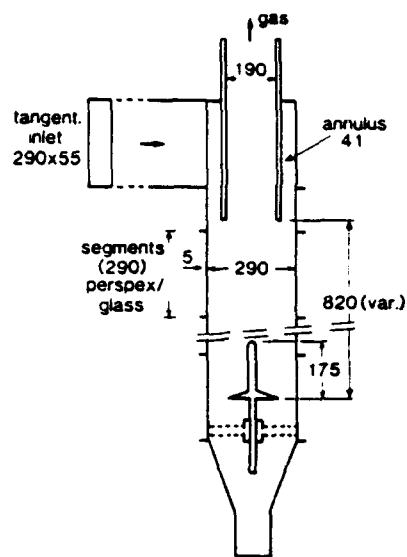


Fig. 2. The model cyclone

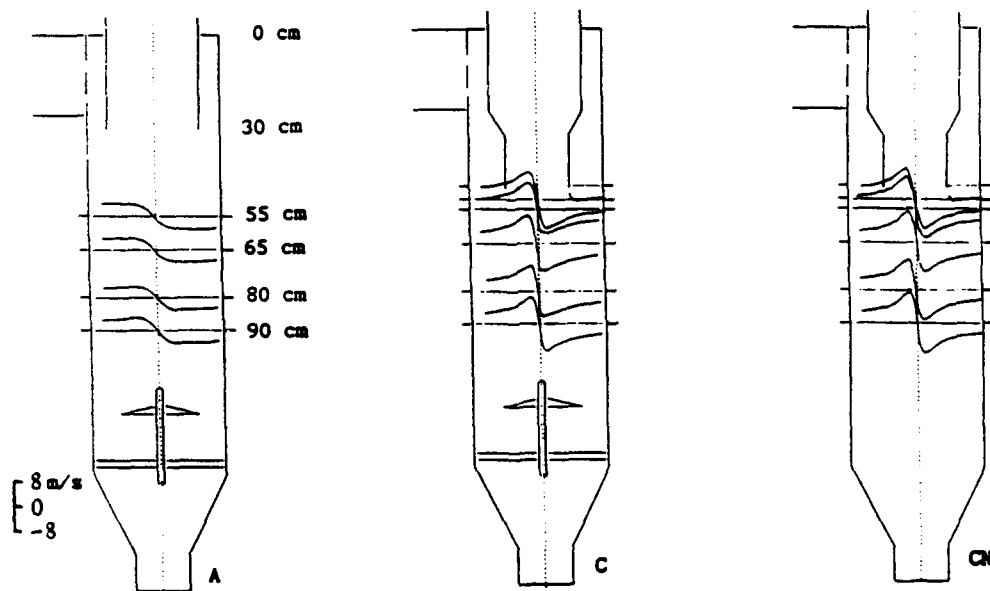


Fig. 3. Measured average tangential velocities

- A. Wide exit pipe, stabilizer
- C. Lengthened conical exit pipe, stabilizer
- CN. Lengthened conical exit pipe, no stabilizer

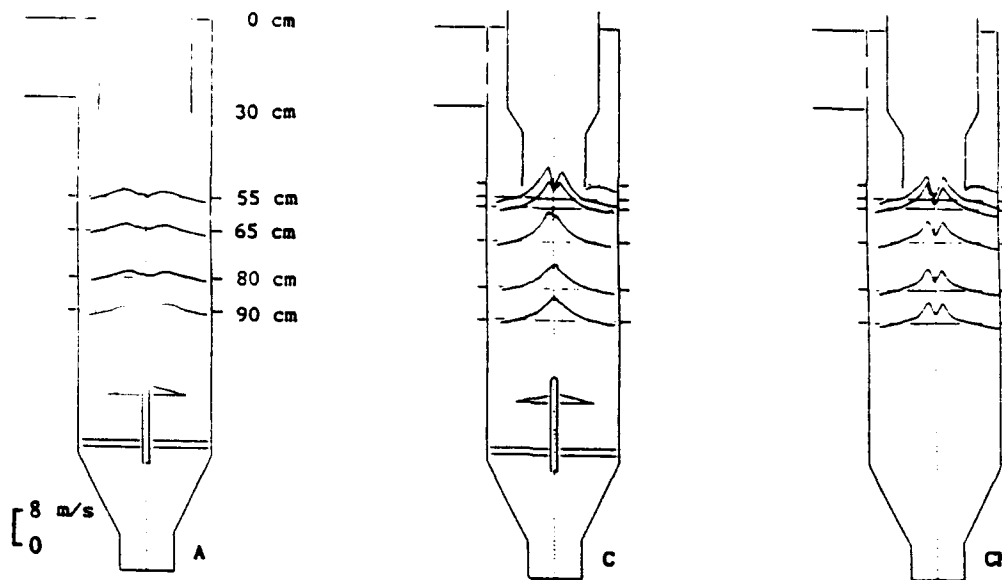


Fig. 4. Measured average axial velocities

- A. Wide exit pipe, stabilizer
- C. Lengthened conical exit pipe, stabilizer
- CN. Lengthened conical exit pipe, no stabilizer

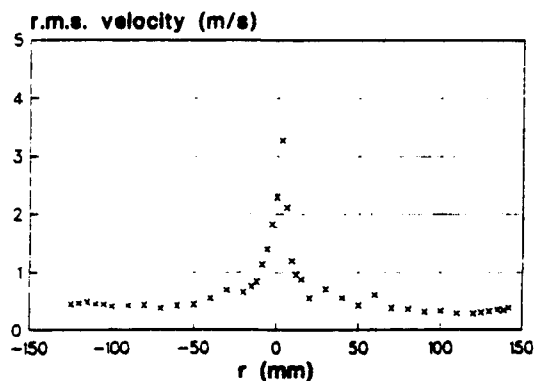


Fig. 5. Example of measured profile of r.m.s. velocity fluctuations. Tangential velocity, geometry CN, height 65 cm

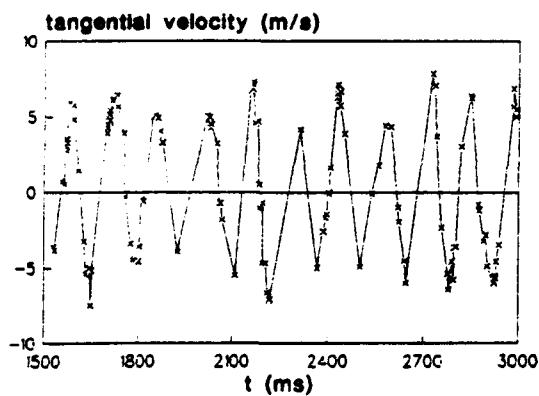


Fig. 6. Example of measured time-dependent tangential velocity at the cyclone axis. Geometry CN, height 65 cm

TWO-COMPONENT VELOCITY MEASUREMENTS IN TOP SUBMERGED GAS INJECTION SYSTEMS

D.D. Atapattu^{*}, Y.S. Morsi[#] and N.B. Gray^{*}

^{*} G.K. Williams Cooperative Research Centre for Extractive Metallurgy, Department of Chemical Engineering, The University of Melbourne, Parkville, Victoria 3052, Australia.

[#] Flowfield Modelling and Diagnostics Group, Energy Systems Engineering Centre, Swinburne University of Technology, Hawthorn, Victoria 3122, Australia.

Abstract

Top submerged gas injection through a lance is being increasingly used in the metallurgical industry for smelting operations. Bath mixing in these processes is mainly controlled by the injection technique. Swirled gas flow injection through the annular region of the lance is preferred to unswirled flow through a plain lance as this increases the lance cooling and promotes bath mixing.

The present work deals with the flow distribution within the bath of a laboratory (air-water) top submerged gas injection system. A Particle Dynamics Analyser (PDA), which utilises the phase-Doppler technique, is used for the measurement of velocity components in a vertical plane within the bath. Experimental measurements of the effect of swirl intensity and Reynolds number on the bath flow field, bubble size distribution and turbulent intensity are presented and discussed.

List of symbols

D_i	inner diameter of the annulus (mm)	w	tangential fluctuating component (m/s)
D_o	outer diameter of the annulus (mm)	Z	distance in the axial direction (mm)
D_h	hydraulic diameter of the annulus ($= D_o - D_i$) (mm)	μ	dynamic viscosity of air (kg/m s)
R	distance in the radial direction (mm)	ρ	density of air (kg/m ³)
Re	Reynolds number ($= \rho U D_h / \mu$)	ψ	swirl angle (deg.)
U	axial component of mean velocity (m/s)		
u	axial fluctuating component (m/s)		
W	tangential component of mean velocity (m/s)		

1 Introduction

Lances are used in submerged-combustion smelting processes to inject air and fuel into metal baths. Fuel is passed through the inner pipe of the lance which is made up of two concentric pipes. Air or oxygen enriched air is passed down the annular gap. The mixing process, which is a function of the dispersion of air is normally controlled by the rate of injection and the shape of the velocity profile at the exit of the lance.

The Sirosmelt submerged lancing system, developed at CSIRO in the early 1970's, utilises the characteristics of swirling flow by introducing a swirler in the annular gap. This system, where air is driven through the annular gap, has been applied to a wide range of metallurgical operations such as slag treatment, oxide smelting and sulphide smelting (Floyd and Conochie, 1984). Although gas injection is widely applied in the smelting and refining of metals, and a number of researchers have investigated the flow within the bath, little quantitative information is available.

For bottom injection and for top submerged systems without swirl, a number of workers have investigated the bubble formation within the bath (e.g. Castillejos and Brimacombe, 1987 a,b and Nilmani and Robertson, 1979). The regimes of gas discharge (e.g. Hoefele and Brimacombe, 1979) and liquid phase velocity fields (e.g. Grevet et al. 1982) have also been investigated. The two-phase region, however, is less well understood due to the analytical and experimental difficulties encountered in the determination of the flow behaviour of two-phase systems. Only a limited amount of work has been reported on flow measurements in top submerged gas injection systems.

Mazumdar and Guthrie (1985) carried out an investigation of the flow in a water model using plain lances with top submerged injection. Flow visualisation work was carried out using a suspended grid of silken threads. The results showed the nature of the flow within the bath. Experimental data on velocity fields were obtained on the basis of video recordings of the motion of small rectangular cards. They also looked at the plume geometry at different injection levels. The governing equations of motion were solved using the finite difference code TEACH-T (Patankar and Spalding, 1972), after neglecting the tangential component of the velocity.

In validating numerical predictions from the package PHOENICS, Rankin et al. (1989) compared their numerical results with flow visualisation work carried out in a 500 mm cylindrical water tank. Again only a plain lance of outer diameter 37 mm was used in their experiments and velocities were determined using streak photography. Furthermore, the package was used to validate the data of Mazumdar and Guthrie (1985) and a reasonably good agreement was found for both cases.

Schwarz and Koh (1986) used PHOENICS to predict the velocity profiles for a top injection lancing system. No measurements were taken for liquid phase velocity distributions. They compared the results of the numerical work with void fractions reported by Conchie et al. (1984) and a qualitative agreement with the predictions was reported. The authors pointed out the necessity for further work on two phase flow modelling in order to predict void fraction accurately, and concluded that, as expected, the swirled jet penetrates less deeply and creates quite a different flow to that obtained from a plain lance.

Nilmani and Conchie (1986) used a laboratory scale gas injection system (tank dimensions: 200 x 200 mm and liquid depth of 300 mm) with a lance of diameter 6.2 mm, and used an electroresistivity probe to find the bubble frequency profiles. They found that, in a water model, the swirler improves the radial dispersion of gases, minimises bath slopping and splashing and helps to create finer bubbles.

Schwarz (1989) used PHOENICS to simulate an experiment carried out by Kawakami et al. (1985) on a bottom-injected bath. Kawakami et al. (1985) used electroresistivity probes to obtain bubble rise velocity and bubble frequency.

Electroresistivity probes have been used by several researchers to measure the liquid and gas distribution in bottom injection systems (e.g. Sheng and Irons, 1991; Castillejos and Brimacombe 1987 a,b and Kawakami et al. 1985). This method of bubble distribution measurement can be used when the bubble velocities are predominantly in one direction. Measurements near the lance exit in a top submerged gas injection system requires more sophisticated techniques because the gas will have significant components of velocity in all directions. Other widely used methods used to measure the dispersion of gas, as characterised by the local time averaged gas fraction and bubble frequency, include hot-film anemometers (e.g. Jones and Zuber, 1978).

Sheng and Irons (1991) summarised techniques employed by various workers to distinguish signals obtained from each phase in order to obtain particle/bubble velocity, size and void fraction. The signal discrimination, in these techniques, is based on the signal wave form, signal analysis and light blocking or the velocity distribution.

All the above LDA methods may be used in gas-liquid flows if the flow consists of a low void fraction chain of small bubbles. Sheng and Irons (1991) proposed a new technique, the combined LDA-electroresistivity probe technique, which may overcome some of the limitations in other LDA techniques described above. The main disadvantage of their proposed method is that it is intrusive.

The above literature review clearly indicates that experimental work related to top submerged swirled gas injection is lacking.

The objective of our ongoing research program is to develop design criteria for top submerged gas injection systems. Initially, a detailed understanding of the turbulent swirling flow in an annulus has been gained through comprehensive numerical and experimental investigations of the effect of swirl intensity and Reynolds number in heated and non-heated flows (e.g. Morsi, 1983, Dave and Gray, 1991, Morsi et al., 1992). Currently we are dealing with the experimental aspect of the gas-liquid interaction taking place in the bath. Emphasis is given to obtaining detailed velocity component measurements in the liquid phase. A Particle Dynamics Analyser system from Dantec has been used to determine liquid phase point velocities and bubble size distribution for a given plane within the bath. The performance of various swirlers, including a plain lance, is evaluated together with the effect of gas flow Reynolds number.

2 Experimental setup

2.1 The water model

A schematic diagram of the experimental apparatus is shown in Figure 1. The model consists of a 230 mm internal diameter cylindrical perspex vessel, placed inside a square glass tank. The inner cylindrical tank and the outer square tank were filled with water to minimise distortion of the laser beam due to the curvature of the inner cylinder. Injection of compressed air was through the annulus of a lance which was fitted to the vessel lid and positioned at the centre of the vessel.

The air flow rate was metered using a standard rotameter. The present results are reported for one level of submergence and a liquid depth in the vessel of 230 mm. The inside and outside diameters of the lance annulus are 12.7 and 17.2 mm, respectively. Table 1 summarises the experimental conditions. The Reynolds number range (6720 - 8040) used in these experiments was limited by the injection system used and the difficulties encountered in obtaining sufficient data in high gas fraction flows.

Run No.	Type of Lance	Level of Submergence	Reynolds Number	Swirl Angle (Deg.)
1	Plain	2/3	6720	0
2	Swirl (No. of starts = 2)	2/3	6720	57.5
3	Swirl (No. of starts = 2)	2/3	8040	57.5

Table 1 Experimental conditions of the study

2.2 LDA/PDA equipment

Figure 1b shows a schematic representation of the measuring system. A 4W Argon Ion laser was used to obtain a green beam (wave length of 514.5 nm). The transmitting optics consist of a collimator, polarisation rotator, a dispersion prism, a beam splitter, a Bragg cell, a beam spacer and a fibre optic module with a 100 mm focal length lens. In setting up the transmitting optics, attention was paid to such factors as mode structure, polarisation, optical path length balancing and correct beam waist positioning in the measurement volume. A frequency shift of 40 MHz was introduced in one of the crossing laser beams to overcome the sign ambiguity of the velocity measurements.

The standard Dantec Particle Dynamics Analyser (PDA) system was used in the reflection mode as receiving optics. The PDA simultaneously measures the size and velocity of spherical particles (or bubbles) which allow correlation of these two quantities. The velocity is calculated from the frequency of

the Doppler burst and the size measurement is based on the phase difference of signals from two detectors located at different scattering angles. A scattering angle of 128° was used in the present investigation.

In determining the measuring point, the refractive index of both the walls and the water was taken into account. Particular attention was given to the choice of the seeding particles. After a number of experimentations using different type of particles, $9\text{ }\mu\text{m}$ metallic coated powder which have small terminal velocities, were found to give sufficient validated signal. The velocity-diameter correlation for scattering particles present in the flow was obtained and a typical plot is shown in Figure 2. It can be seen from the figure that the mean particle velocity remains constant for the size range studied. Measurements were taken not only from the seeding particles but also from the small bubbles present in the bath. Data was acquired for particles in the size range of $0 - 980\text{ }\mu\text{m}$. However, only data corresponding to particle sizes below $200\text{ }\mu\text{m}$ were processed to ensure that the particles for which the results are reported follow the flow exactly.

3 Results and discussion

The results presented here are for different swirl angles and Reynolds numbers as summarised in Table 1. The measurements were taken on the plane X-X shown in Figure 1a. Instantaneous velocity components were measured at grid points on a rectangular mesh (spacing 10 mm). Data could not be obtained at some points either due to the presence of large bubbles or due to a high void fraction.

The axial velocity contours for different swirl intensities ($\psi = 0^\circ$ and $\psi = 57.5^\circ$) are shown in Figure 3a and b, respectively. A higher velocity zone is present in the vicinity of the lance at the top part of the bath. A similar finding was reported by Schwarz and Koh (1986). These figures also show a high velocity zone at the exit of the lance, and the velocity vectors tend to increase in magnitude toward the top of the bath. The effect of the swirl intensity is shown by comparison of Figures 3a and 3b. As expected, the swirl introduces a large recirculation zone at the top of the bath. The effect of Reynolds number on the distribution of the flow around the lance appears to be small for the range of Reynolds numbers investigated.

Figures 4 and 5 show the axial velocity distribution at different bath depths. It is evident that bath mixing is mainly taking place in the top part of the bath, i.e., the region above the lance exit. These figures also show that vertical mixing in the region below the lance is minimal in all cases, irrespective of the swirl angle and the Reynolds number under the conditions employed in this investigation. The tangential velocity component for a swirled lance is higher than that for plain lance in the region below the lance exit (see Figure 6).

Furthermore, the measured data indicate a higher axial velocity for a plain lance than a swirled lance. This finding implies that swirlers help to reduce splashing above the bath. Such reductions in splashing were clearly observed during the course of experiments. It was also observed that there was a larger number of fine bubbles in the bath with swirled lances.

3.1 The distribution of turbulence intensity

There are several definitions of turbulence intensity relating to the fluctuating velocity components, including root mean square (RMS) values and the ratio of the root mean square value to the characteristic velocity or its square. For the sake of convenience, here we shall define the turbulence intensity as the RMS value, i.e., $\overline{u^2}$, where the overbar denotes a time average. Figures 4 and 5 show the effect of swirl and Reynolds number on the distribution of turbulence within the bath. The turbulence intensity is higher in the vicinity of the lance and increases in magnitude vertically upward. The effect of Reynolds number on the RMS values appears to be small in the range studied.

4 Conclusions

This work has demonstrated that the phase-Doppler technique can be used to gather useful information in the bath for a top submerged injection air/water system. The model study shows that the momentum associated with the injected air in the case of a plain lance is mainly transferred to high axial velocities which could cause high splashing. In the case of swirled lances, the axial velocities in the bath are significantly less for a given Reynolds number. Swirled gas flow creates more fine bubbles and the high

liquid-gas contact area associated with the fine bubbles can lead to high reaction rates in bath smelting systems. The turbulent intensity is found to be higher in the vicinity of the lance and the effect of Reynolds number on the turbulent intensity is small in the range studied.

It can be concluded that the performance of swirled lances is better than that of plain lances with regard to gas dispersion and splashing. The work is being extended to higher Reynolds numbers to more closely simulate a real top submerged injection system.

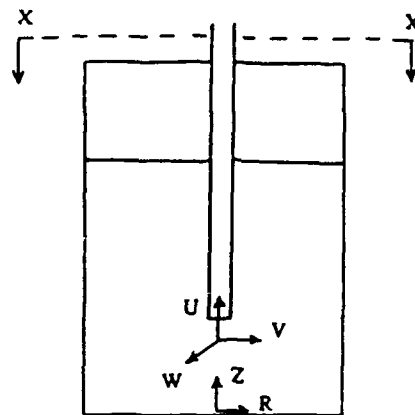
Acknowledgments

The authors acknowledge the financial support provided for this work by the Australian Research Council. The co-operation of G.K. Williams Cooperative Research Centre of the University of Melbourne and the Flow Field Modelling and Diagnostic Group of Swinburne University of Technology in using their facilities is gratefully acknowledged. The authors are also thankful to Mr. G.D. Laird and Mr. F. Othman for their support in the experimental work.

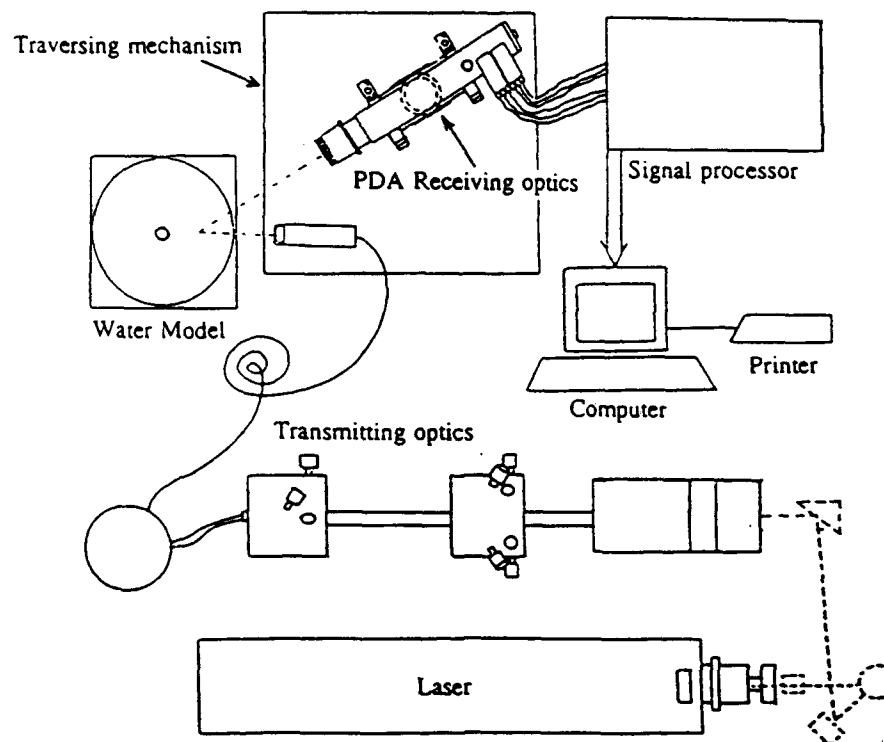
References

- Castillejos, A.H.; Brimacombe, J.K. 1987 a: Measurement of physical characteristics of bubbles in gas-liquid plumes: Part I. An improved electroresistivity probe technique. *Met. Trans. B*, 18B, 649-658
- Castillejos, A.H.; Brimacombe, J.K. 1987 b: Measurement of physical characteristics of bubbles in gas-Liquid plumes: Part II. Local properties of turbulent air-water plumes in vertically injected jets. *Met. Trans. B*, 18B, 649-658
- Conochie D.S.; Orton T.H.; Floyd J.M. 1984: Model studies of the SIROSMELT gas injection lance. Paper presented at 113th AIME Ann. Meet., Los Angeles
- Dave, N.; Gray, N.B. 1991: Fluid flow through lances with constant and variable pitch swirled inserts. *Met. Trans. B*, 22B, 13-20
- Floyd, J.M.; Conochie, D.S. 1984: Sirosmelt - the first ten years. *Extractive Met. Symp. AusIMM*, Melbourne, 1-8
- Grevet, J.H.; Szekely, J.; El-Kaddah, N. 1982: An experimental and theoretical study of gas bubble driven circulation systems, *Int. J. of Heat Mass Transfer*, 25, 487-497

- Hoefele, E.O.; Brimacombe, J.K. 1979: Flow regimes in submerged gas injection, *Met. Trans. B*, 10B, 631-648
- Jones, O.C.; Zuber, N. 1978: A.I.Ch.E. Symposium Series, 74, 191-204
- Kawakami, M.; Kitazawa, Y.; Nakamura, T.; Miyake, T.; Ito, K. 1985: Dispersion of bubbles in molten iron and nitrogen transfer in the bubble dispersion zone at 1250°C, *Trans I.S.I.J.*, 25, 394-402
- Mazumdar D.; Guthrie R.I.L. 1985: Hydrodynamic modelling of some gas injection procedures in ladle metallurgy operations. *Met. Trans. B*, 16B, 83-90
- Morsi, Y.S.M. 1983: Analysis of turbulent swirling flows in axisymmetric annuli, PhD Thesis, University of London
- Morsi, Y.S.; Solnordal, C.B.; Atapattu, D.D.; Gray, N.B. 1992: Numerical validation of measurements of isothermal and non-isothermal swirling flows in annuli, to be presented at Australasian Fluid Mechanics Conf., Hobart
- Nilmani M.; Conochie D.S. 1986: Gas Dispersion with swirled lances. SCANINJECT IV: Proc. 4th Int. Conf. on Injection Metallurgy, *MEFOS*, 7:1-7:19.2
- Nilmani, M.; Robertson, D.G.C. 1979: Symposium on gas injection into liquid metals, Newcastle-upon-tyne, B1-B35
- Patankar, S.V.; Spalding, D.B. 1972: A calculation procedure for heat, mass and momentum transfer in three-dimensional parabolic flows, *Int. J. of Heat and Mass Transfer*, 15, 1787-1805
- Rankin, W.J.; Jorgenson, F.R.A.; Nguyen, T.V.; Koh, P.T.L.; Taylor, R.N. 1989: Process engineering of SIROSMELT reactors: lance and bath-mixing characteristics, *Extraction Metallurgy '89, IMM*, 577-600
- Schwarz, M.P. 1989: Two and three dimensional models of a gas-stirred bath of molten pig iron, *PHOENICS J.*, 1, 3, 282-310
- Schwarz, M.P.; Koh, P.T.L. 1986: Numerical modelling of bath mixing by swirled gas injection. SCANINJECT IV: Proc. 4th Int. Conf. on Injection Metallurgy, *MEFOS*, 6:1-6:17
- Sheng, Y.Y.; Irons, G.A. 1991: A combined laser Doppler anemometry and electrical probe diagnostic for bubbly two-phase flow, *Int. J. Multiphase Flow*, 17, 5, 585



(a) Geometry and nomenclature



(b) LDA/PDA setup

Fig. 1 Schematic diagram of the experimental facility.

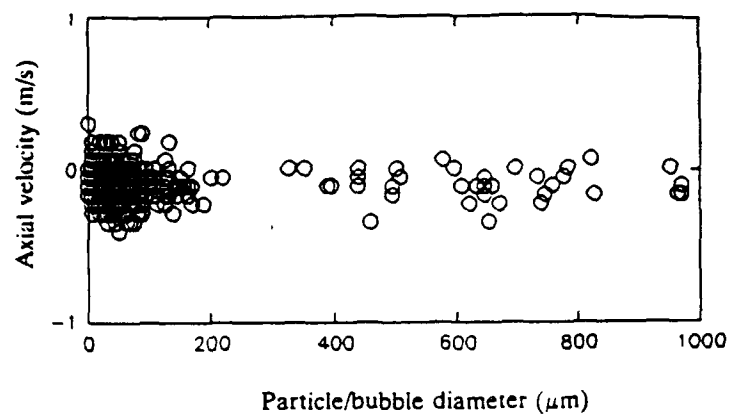


Fig. 2 A typical plot of the velocity-diameter correlation

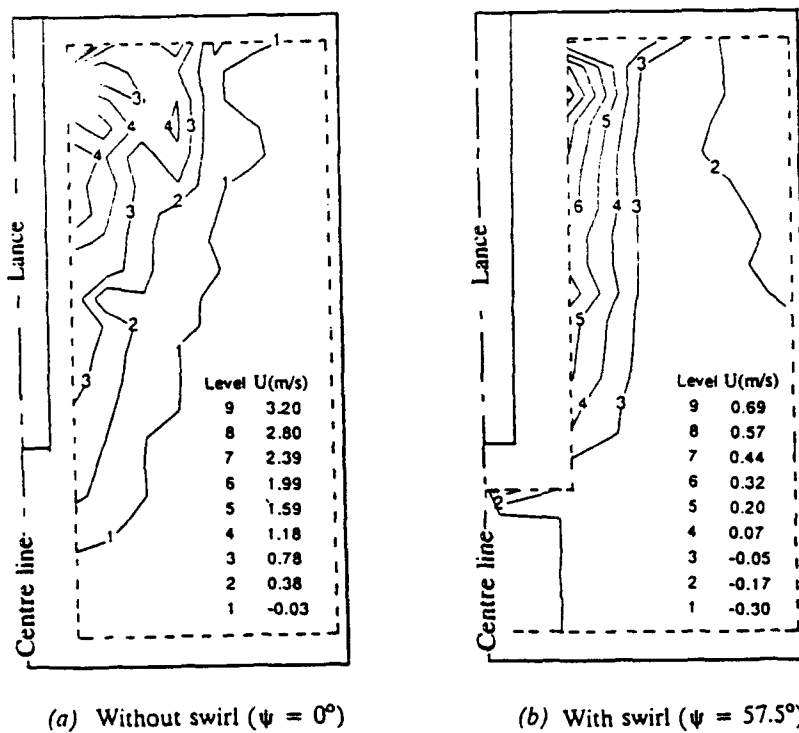


Fig. 3 Axial velocity contours for $Re = 6720$

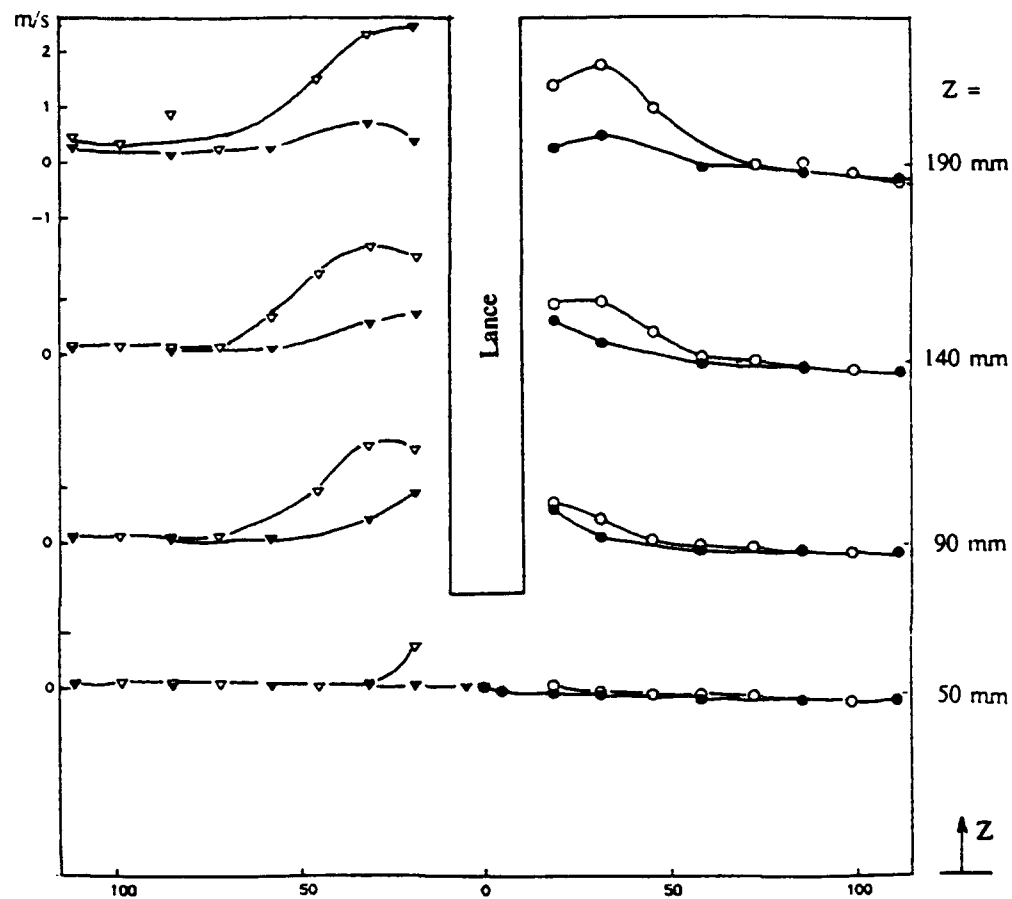


Fig. 4 Axial velocity distribution (mean and RMS values) at various depths for different swirl angles ($Re = 6720$): \circ U ($\psi = 0^\circ$); \bullet U ($\psi = 57.5^\circ$); ∇ $\sqrt{u^2}$ ($\psi = 0^\circ$); \blacktriangledown $\sqrt{u^2}$ ($\psi = 57.5^\circ$).

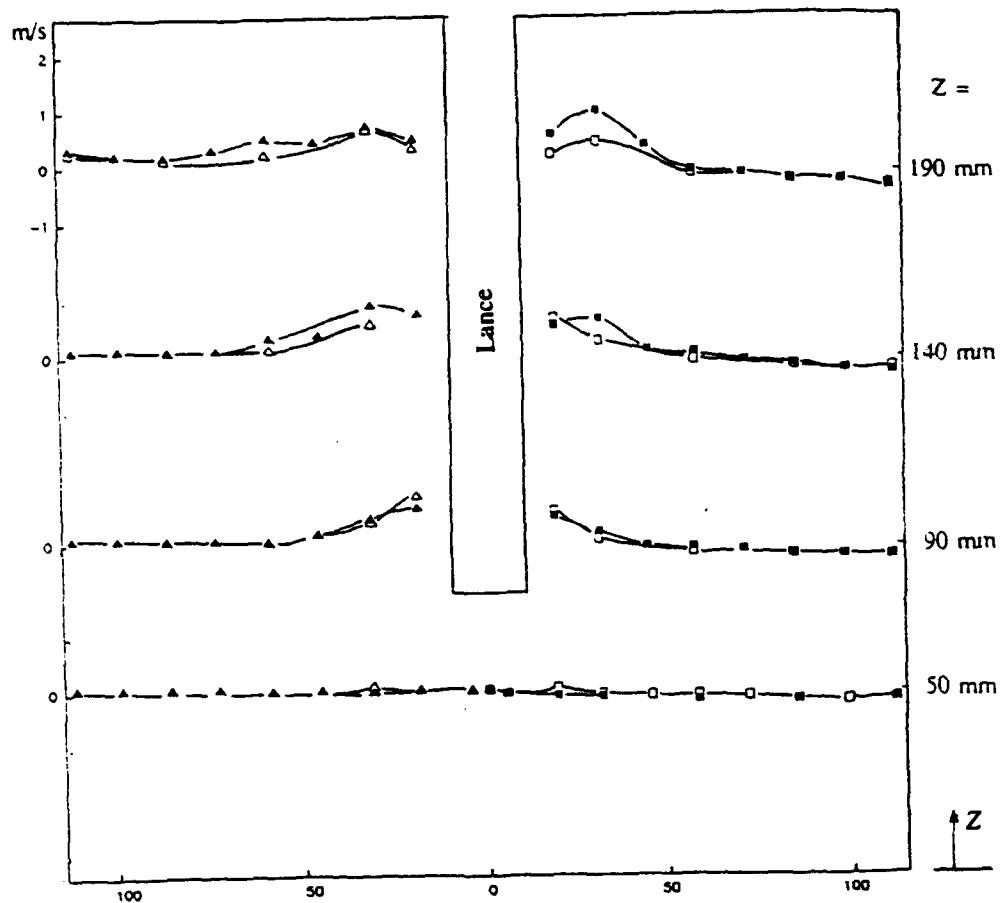


Fig. 5 Axial velocity distribution (mean and RMS values) at various depths for different Reynolds numbers ($\psi = 57.5^\circ$): \square U ($Re = 6720$); \blacksquare U ($Re = 8040$); \triangle $\sqrt{u^2}$ ($Re = 6720$); \blacktriangle $\sqrt{u^2}$ ($Re = 8040$).

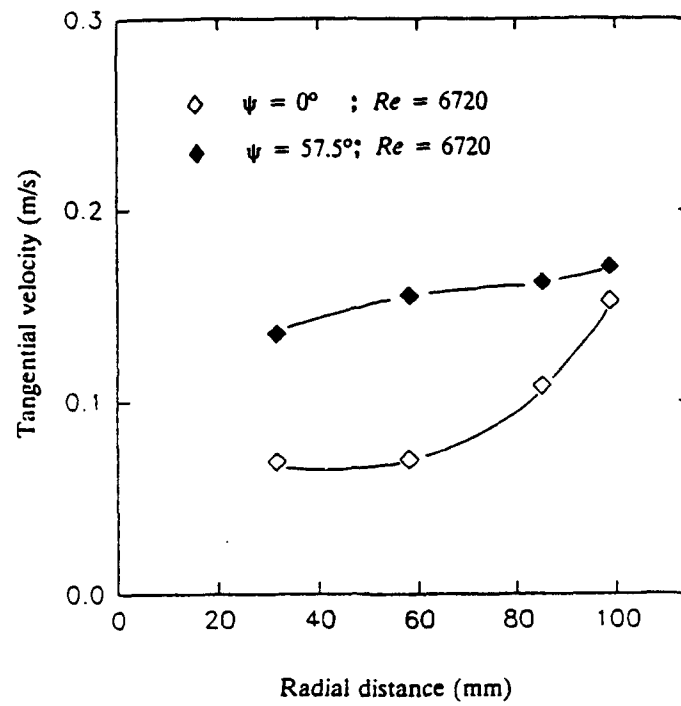


Fig. 6 Tangential velocity profiles for $Z = 50$ mm

TURBULENCE ENERGY DISSIPATION
IN
FLOW THROUGH POROUS MEDIA

By
Charles D. Morris, Ph.D., P.E.
Associate Professor
Civil Engineering
University of Missouri-Rolla

Acknowledgments

The Associated Electric Cooperative, Inc. funded this study, providing support to faculty, graduate, and undergraduate students at the University of Missouri-Rolla. Graduate students at the University of Missouri-Rolla assisted with physical and mathematical modeling, and collected data on experimental measurements of head loss and turbulence. The author would also like to acknowledge Messrs. Gerry Diddle and Jim McNabb of Associated Electric Cooperative, Inc. for their support of this research.

Abstract

Darcy's Law fails to hold for higher flow velocities. Many situations have arisen where a different relation between head loss and velocity is needed for higher flow velocities. Such a situation is flow around large diameter rock forming a dike or dam. If pipe and porous media flow are analogous, the head loss should be proportional to the velocity head. As the velocity of flow through the porous media increases the inertial effect gradually increases and at some higher velocity the onset of turbulence occurs. At the onset of turbulence, the mixing length scale may become the predominant factor in describing energy dissipation, with the mixing length scale being a function of the size and gradation of the media. Experimental evidence based on turbulence measurements and evolved turbulent theory seems to support this view. Turbulence flow was measured directly via a fast-response, constant temperature, hot-film, anemometer. A two-dimensional finite element code was modified during this investigation to solve the turbulent flow case. The flow can be two dimensional planar or axially symmetric, laminar (Darcy's Law) or turbulent flow.

Introduction

Most of the literature on flow through porous media involves "creeping flows." However, since the last century it has been realized that Darcy's Law fails to hold for higher flow velocities. Thus, while many practical problems of flow through porous materials can be correctly solved using the assumption of Darcy's Law, many situations have arisen where a different relation between head loss and velocity is needed for higher flow velocities. Such a situation is flow around large diameter rock forming a dike or dam.

A finite element, mathematical model (SEEP-2DFE-T) was developed for finding flow through porous media for turbulent flow. Neither the turbulent mathematical (computer) model nor the physical evaluation of the energy loss coefficient for turbulent flow for this type of media exists in the literature. The basic contributions of this research include development of energy dissipation theory for turbulent flow through porous media, experimental results used to evaluate the energy loss coefficient and a mathematical model for turbulent flow through porous media.

Literature

There are two approaches to mathematically predicting the turbulent (nonlinear) flow through porous media. One approach, Forchheimer (1901) suggested replacing Darcy's Law with a nonlinear, empirical equation in which the negative total head gradient is equal to a constant times the velocity plus another constant times the velocity head squared. He later added a third order term of a constant times the velocity cubed. The third order term was added to the original expression based on experimental evidence.

Many authors have supported the Forchheimer's relationship based on experimental evidence [Lindquist (1933), Morcom (1946), and Ward (1964)]. The Forchheimer relationship has also been derived theoretically for certain flow conditions [Kristianovich (1940), Irmay (1958)]. Stark and Volker (1967) carried out experimental and analytical investigations of flow through idealized media. Missbach (1937) postulated an equation of the general form where the negative total head gradient is a function of a constant times the velocity raised to a variable power. This relationship is called the empirical-velocity approach. This approach recognized that the head loss gradient through porous media is proportional to the velocity. Also, the term, empirical-head-loss equations or empirical-exponential relation may be applied to this approach.

Although the head loss relationships for porous media have been derived on an empirical basis by Ahmed (1969), Cedergren (1977), Soni (1978), and Volker (1969), most of the resulting equations is dimensional and have limited applicability. Most workers [Dudgeon (1966), Johnson (1971), Leps (1973), Parkins (1966), and Wilkins (1956)] prefer a relationship of the form of the empirical-velocity approach. The velocity is equal to a variable "a" times the negative total head raised to a variable "b" power in the empirical-velocity approach. The applicability of this type of equation is dependent on the units used and the characteristics of the medium.

A non empirical and pipe flow analogous approach has the advantage of not being limited by units used or the characteristics of the medium. In addition, it seems logical that the value of (b) in the above empirical-velocity approach should converge toward two for fully developed turbulent pipe flow where the head loss should be proportional to the velocity head, if the pipe flow and porous media are analogous. Attempts to correlate head loss with velocity squared have met with limited success [Ahmed (1969), Dudgeon (1966)]. However, these studies attempted to correlate the head loss with the real velocity, v/n where n is the porosity of the aquifer (volume of voids per unit volume of aquifer). By analogy with the flow in conduits, the head loss should be proportional to real velocity squared divided by the quantity of the gravitational constant times the hydraulic mean radius. The proportionality constant "c", friction factor, depends on the Reynolds number. For a large Reynolds number, (C) may be a function of the media size, shape and roughness.

If pipe and porous media flow are analogous, the head loss should be proportional to the velocity head. Attempts to correlate head loss with velocity squared have met with limited success [Ahmed (1969), Dudgeon (1966)]. However, these studies attempted to correlate the head loss with the real velocity, v/n where n is the porosity of the aquifer (volume of voids per unit volume of aquifer). By analogy with the flow in conduits, the head loss should be proportional to real velocity squared divided by the quantity of the gravitational constant times the hydraulic mean radius. The proportionality constant (C-friction factor) is a function of the Reynolds number. For large Reynolds Numbers, (C) may be a function of the media size, shape and roughness.

Before modern digital computing systems, analysis of practical problems involving nonlinear flow equations has been largely neglected probably because the complex differential equations involved have been too difficult to handle by analytical mathematics. Another difficulty is that most research of flow through porous media has been conducted at lower Reynolds Numbers (R). Stephenson, (1979) using the hypothesis that (C) is constant for large (R-greater than ten thousand), conducted tests at these higher (R).

These tests indicated that these values of (C) become approximately independent of (R) at the higher values of (R). These tests also suggest that the relationship between (C) and (R) is not fully understood. It appears that (C) is not just a function of (R) but, may also be a function of the porosity, aggregate shape, roughness, size and gradation (Dudgenon, 1966). This is due both to the inertia effect and the onset of turbulence. As the velocity of flow through the porous media increases the inertial effect gradually increase and at some higher velocity the onset of turbulence occurs. A predominate factor that affects dissipation of energy, at the onset of turbulence, is the mixing length scale. The mixing length scale is most likely found by the size and gradation of the aggregate. Experimental evidence on the dispersion of dye streams seems to support this view.

Experimental Model

A six-inch PVC pipeline was installed in the hydraulic laboratory with a removable, two foot long test section located near the end of the pipeline. The flow through the pipeline was measured with a 60 degree v-notch weir at the end of a large tank. The rock was placed and retained in the test section by a wire mesh (one quarter inch hardware cloth). Manometers were used to measure the upstream and downstream differential head on the test section. This pipe data is a one-dimensional measure of the energy loss through the media used to attain the energy loss coefficient.

Porosities of different media size and gradation were found by measuring the volume of the media, filling the voids between the media with water; removing the media, then measuring the volume of the remaining water. The volume of the water divided by the volume of the media was used to find the porosity of the media. The measurements were repeated three times with the average reading being recorded.

Turbulent Energy Dissipation Model

Turbulence is a hierarchy of scales, loosely termed eddies, with transfer of kinetic energy down the scales from the larger to the smaller. The energy is dissipated, or transferred into heat via the action of viscosity at the smallest scales, i.e. by the smallest eddies. Small scale components lose energy via the action of viscosity much faster than the large ones. The action of the non linear inertia terms in the equations of motion is responsible for the transfer of energy from the large scale motions, which is extracted from the mean flow, to the small scale motions where it is dissipated. The energy is extracted from the mean flow by the larger scales or eddies to maintain an overall constant turbulent structure.

Turbulence may be measured directly via a fast-response, hot-film, velocity anemometer. Because the root-mean-square value of the turbulence velocity fluctuation (u') is a definite quantity in a given turbulent motion and represents a suitable statistical measure of the magnitude of the fluctuations, it is termed the level of the turbulence. A ratio of this value to the mean flow velocity is termed the intensity. The rate of turbulent energy dissipation is simply related to quantities already defined. In isotropic (independent of location and direction) turbulence, the energy of the turbulence is

$$e' = \frac{3}{2} \rho u'^2$$

where: ρ is the mass density of fluid, and rate of dissipation per unit volume (Robertson, 1965) is found to be

$$\phi = 15\nu \left[\frac{u'}{\lambda} \right]^2$$

λ is the scale of the dissipating eddies, ν kinematic viscosity of fluid, and u' is the turbulent level.

Many researchers have searched for a relationship between the characteristics of porous media and the flow versus energy loss relationship for different media. The selected approach for analysis of this relationship is analogous to the flow through narrow tubes. The real fluid velocity through the tubes is the velocity through the media, i.e., the discharge divided by the cross-sectional area, divided by the porosity where porosity is the volume of voids per unit volume of the media. In fact, the real velocity will also depend on the pore size and shape, and the wetted surface area of the media per unit volume. Note that Bakhmetoff (1937) expressed real velocity in the voids as velocity divided by the porosity raised to the two thirds power which is justified with a cubic model. The real velocity in the voids is therefore, somewhere between the velocity divided by porosity and the porosity raised to the two thirds power. The flow path is tortuous and consequently it is probably closer to velocity divided by porosity than to the cubic model of porosity raised to the two thirds power.

If the rate of dissipation is proportional to the cube of the velocity, as it is where the Reynolds's stresses are proportional to the squares of the turbulent components of velocity, λ "the average size of the smallest eddies," which are responsible for the dissipation of energy by viscosity, is proportional to the square root of (Lv/u') (Taylor, 1958) where L is some dimension defining the scale of the system. If the L scale is defined as the mean diameter of the media, then the variation in turbulent energy dissipation over a flow field is roughly proportional to the cube of the turbulent intensity divided by the mean diameter of the media. Thus, the rate of energy dissipation per unit volume is:

$$\phi = Cu^3/L$$

This relationship provides a means of examining the physical effects of different size and gradation of the media on the head loss and facilitates a more complete understanding of the energy dissipation process. The ultimate goal is to be able to predict the effect of media size and gradation on the head loss coefficient so that the head loss through any porous media can be found.

Energy Loss Model

The energy loss coefficient for laminar flow ($R \leq 0.001$) is

$$K_1 = 800 / R$$

where

$$R = (n v) / (v d)$$

and

n = porosity of the media
 v = kinematic viscosity of fluid
 v = apparent velocity or Q/A
 d = media diameter.

The turbulent head loss coefficient [K ($R > 100,000$)] is independent of (R) is

$$K_1 = 2.$$

Both energy loss coefficients (turbulent and laminar) were found empirically. Therefore, in the transition region the energy loss coefficient " K " is

$$K = K_1 + K_2.$$

Because, the hydraulic gradient is

$$i = V / k = (V^3 K) / g d n^3.$$

Thus, the gradient is related to rate of energy dissipation as follows:

$$i = \phi = u'^3 / L = K_t V^3 / g d n^3 .$$

Therefore, the energy loss coefficient is related to rate of energy dissipation as follows:

$$K_t = (u'/U)^3 u'.$$

Turbulence measurements were made using a constant temperature anemometer system (hot-wire or hot-film anemometer). The hot-film probe is less fragile than its hot-wire counterpart but is not as sensitive due to a larger surface area. The model anemometer used is the DISA Type 55D01 and the model hot-film probe is the TSI 1219-W.

Correlation Coefficient Squared (R^2) for Energy Loss versus Turbulent Energy Dissipation, ϕ

GRAVEL:	R^2
Size[range]:(inches)	H_f vs. ϕ
0.50[0.25-0.75]	0.962
0.75[0.5-1.0]	0.938
1.25[50%0.75-50%1.0]	0.980
1.75[1.5-2.0]	0.986
SPHERES:	R^2
Size[range]:(inches)	H_f vs. ϕ
0.750	0.975
0.750	0.968
1.000	0.966
1.000	0.988
1.125[50%1.5-50%0.75]	0.978
1.125[50%1.5-50%0.75]	0.984
1.500[50%1.0-50%2.0]	0.991
1.500	0.977
1.500	0.969
1.750[50%1.5-50%2.0]	0.990
1.750[50%1.5-50%2.0]	0.979
1.750[50%1.5-50%2.0]	0.979
2.000	0.973
2.000	0.997
2.000	0.978
2.000	0.984

This shows a high correlation of measured energy loss with measured turbulent energy dissipation. This result suggests that the primary mode of energy dissipation may be through the generation of turbulence from the mean flow. The result also suggests that a relationship may be developed that will predict the K value from measurements of the turbulence.

Mathematical Model

(SEEP-2DFE-T) a mathematical model uses a two-dimensional finite element method of solution. This approach is used because of the complex geometry, material anisotropy, spatial and temporal variations of the parameters such as the applied heads and fluxes. In the past more general and simplified approaches were used for solving problems of fluid-flow through porous media. Analytical closed form solutions, such as the electrical analogy method, Hele-Shaw viscous flow model and graphical sketching are some commonly used classical procedures. Most of these procedures can be applied to simplified geometry and linear behavior, which is not the situation for turbulent flow through porous media.

The program code (SEEP-2DFE-T) is based on the finite element method and is intended for the

solution of general seepage including such categories as steady confined and unsteady (transient) unconfined flow. The flow can be two dimensional plane or axially symmetric, laminar (Darcy's Law) or turbulent flow. Finite element equations can be obtained by using a number of different formulation procedures. The reader should consult Desai, (1972, 1975, 1977, and 1978) for further details of the procedures used in this program code. The original code (SEEP-2DFE) was obtained from Drs. T. Kuppusamy and C. S. Desai, (Department of Civil Engineering, Virginia Polytechnic Institute and State University, Blacksburg, Virginia, July 1978). This code was developed to solve only laminar or Darcy's Law type flow problems. The original code was modified during this investigation to solve the turbulent flow case.

A flow domain is divided into several discrete finite elements with the code based on an isoparametric quadrilateral element using a 4-node element and simple Euler type integration. The procedure used to decide the initial free surface, equal potential, and flow lines are the electrical analogy method, solution of the Laplace equations, or assumed flow net. The initial free surface, equal potential, and flow lines are input to the program by giving the x-y coordinates of the nodal intersection of equal potential lines and flow lines. These initial positions of the free surface and flow lines are subsequently corrected by iterations until they approximately satisfy the boundary conditions.

The procedure for solving the steady unconfined flow is based on the inputted free surface location. This free surface is considered impervious or a "no" flow, boundary condition. Thus, for the first iteration, values of nodal heads are computed at all nodes including those on the assumed free surface. If the assumed free surface is indeed the actual free surface, then the boundary condition, should be identically satisfied. If not, the difference between the computed head and the free surface or phreatic surface elevation is found. Now the free surface nodes are shifted by a weighted amount of the differences. This procedure is repeated until an acceptably small change occurs.

The material parameters required for input to this code are the energy loss coefficient as a function of Reynolds Number (Reynolds Number is only a function of velocity for a given media) and porosity. The values of nodal heads and velocities are computed at all nodes. If the assumed Reynolds number (velocity) and corresponding energy loss coefficient is correct, i.e., the change in velocity is small then the solution is complete. If not, the new Reynolds Number is used to find the corresponding energy loss coefficient (K). With this new (K), values of nodal heads and velocities are computed at all nodes. This procedure is repeated until an acceptably small change in velocity occurs.

This code can handle most, if not all, of the nonhomogeneous and anisotropic media, and various categories of seepage. In the case of the phreatic surface, the inclination of the interfaces in layered media should be vertical or near vertical. If they are horizontal and the phreatic surface crossed them, the code may involve computational difficulties. The output quantities printed include the potentials at the nodes, the quantity of flow across a given section and the velocity through each element. Graphical plotting of the results can be obtained by specifying that option. The program code was verified using measured data published by Volker, 1975. His experimental results allowed verification of the computed flow net, discharge, velocity distribution for unconfined non-Darcy turbulent flow.

Results

This mathematical model and these physical modeling results were verified using data measured during this study and other authors' experimental data. Verification and examination of the modeling results are congruous.

Volker, (1975) performed two-dimensional flow experiments in an open flume 2 feet wide and 2 feet deep. The gravel used in the flow experiments was 3/16 inch effective size and no difficulty was

encountered with surface tension effects. Flow net positions were recorded on the clear side of the flume and measurements of piezometric surface were obtained from tapping points on the other side of the flume. The gravel was retained between two vertical sheets of gauze placed perpendicular to the direction of flow. The discharge measured experimentally by Volker was 0.052 cfs while the discharge predicted by (SEEP-2DPE-T) using a K_f value of 2.0 and inputting his measured flow net and porosity was 0.0501 cfs.

Results of the physical modeling (one-dimensional pipe flow model) provided a prediction of the energy loss coefficient (K) as a function of the nominal media size and gradation. The pipe flow modeling results were also used to evaluate the ability of the mathematical model to predict two-dimensional flow through a rock dike in a flume.

Different nominal media sizes and gradations were selected for the rock dike to give a range of different materials so the data collected could be used to predict the behavior of K , i.e., find a relationship between the material and the energy loss coefficient. The largest media used was the nominal six-inch size. This nominal six-inch size was retained on a five-inch mesh and passed through a seven-inch mesh. The nominal four-inch size was retained on three inch mesh screen and passed through a five-inch screen. The nominal two inch media was retained on one inch and passed through a three-inch screen. The nominal one inch size was retained on a one-half inch screen and passed through a one and one-half inch screen, etc.

An extensive investigation was performed to learn the relationship that would best fit the energy loss coefficient K versus Reynolds Number data. For each size of gravel or sphere a relationship for laminar energy loss coefficient K_f was calculated by dividing the Reynolds number into eight hundred and then using least squared difference to find the K_f value. After analysis was completed, it was decided that the relationship presented in Figure 1 best represents the data. Both the gravel and sphere data suggest that as the Reynold's Number is increased the K_f value tends to approach two. These results indicate that the shape, gradation, and roughness have little or no effect on the energy loss coefficient K . These results are shown in Figure 1. However, this figure shows some scatter in the relationship with nominal size and aggregate gradation, but no trend is observed. It is hypothesized that the scatter is due mainly to the measured data being in the transition zone between laminar and turbulent flow. The transition zone is where values are uncertain because the flow may be either laminar or turbulent. Secondly, placement and shape or packing (arrangement) of the aggregate in the test facility may also cause some scatter in the data.

The total longitudinal force exerted by a moving fluid upon immersed media necessarily consists of the summation of the longitudinal components of all normal and tangential stresses upon the media surface. Here the reduction of pressure intensity in the region of discontinuity will so outweigh the boundary shear so that the drag is almost entirely due to the unbalanced normal forces on the front and rear of the media. These forces can only be evaluated by measurement and integration of the pressure distribution. Within the region of discontinuity downstream from the point of boundary-layer separation, the mean intensity of pressure is essentially the same as that of the surrounding flow; because the separation generally occurs at a point of increased velocity - and hence of decreased pressure - a low pressure will prevail throughout the region of reverse flow. Separation is a source of instability, conversion of mean flow energy to turbulent energy. This leads too fully developed turbulence in the wake of the media. This leads to the occurrence of energy dissipation through turbulence. In an attempt to separate the effects of boundary shear or the effects of surface roughness, if any, an analysis similar to that performed on the gravel was performed on spheres. The results are similar to that for the gravel. Therefore, the predominate mode of energy dissipation is through the conversion of mean flow energy to turbulent flow energy. The result for the spheres is shown in Figure 2.

Verification of the relationship presented in Figure 1 and the mathematical computer model was accomplished by comparing the computer model's predicted flow rate with the measured flow through

porous media dikes built in the hydraulic flume. Because the computer model is very sensitive to the assumed free surface and flownet for the dike, it was very time consuming to determine the flownet accurately by an electrical analog model. Initially it is decided to only develop an average flownet for each head range. Evidently to get better predictions of the measured values require an electrical analog model to be input to the mathematical model. All prototype predictions should be based on an electrical analog model being input to the mathematical model before a solution is obtained. The following solutions were obtained by inputting an approximate flownet and the fitted relationship for K. Some of these results are presented in Table 1.

Table 1 - Some Comparisons of (SEEP-2DFE-T) Results and Measured Flows

Nominal 6 inch size media: Q(cfs)			
RUN	Q(measured)	Q(predicted)	ERROR
6	1.140	1.294	+14%
4	0.801	0.755	-6%
Nominal 4 inch size media: Q(cfs)			
RUN	Q(measured)	Q(predicted)	ERROR
5	0.703	0.602	-14%
6	0.522	0.538	+3%
Nominal 2 inch size media: Q(cfs)			
RUN	Q(measured)	Q(predicted)	ERROR
1	1.019	1.034	+1%
4	0.801	0.882	+10%
Nominal 1 inch size media: Q(cfs)			
RUN	Q(measured)	Q(predicted)	ERROR
1	0.348	0.358	+3%
2	0.347	0.345	-1%

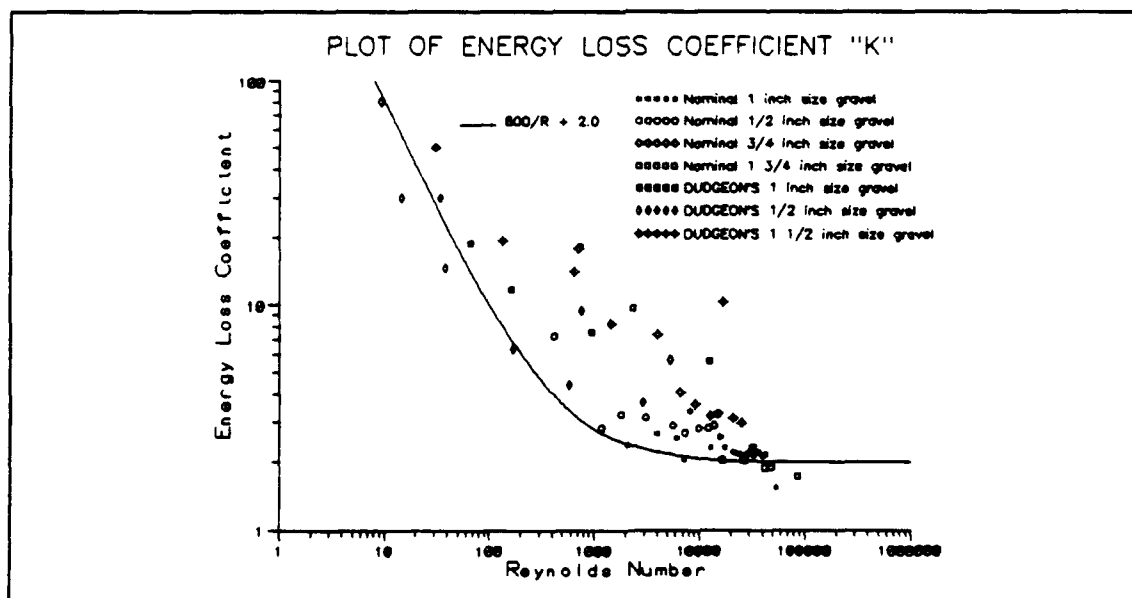


Figure 1

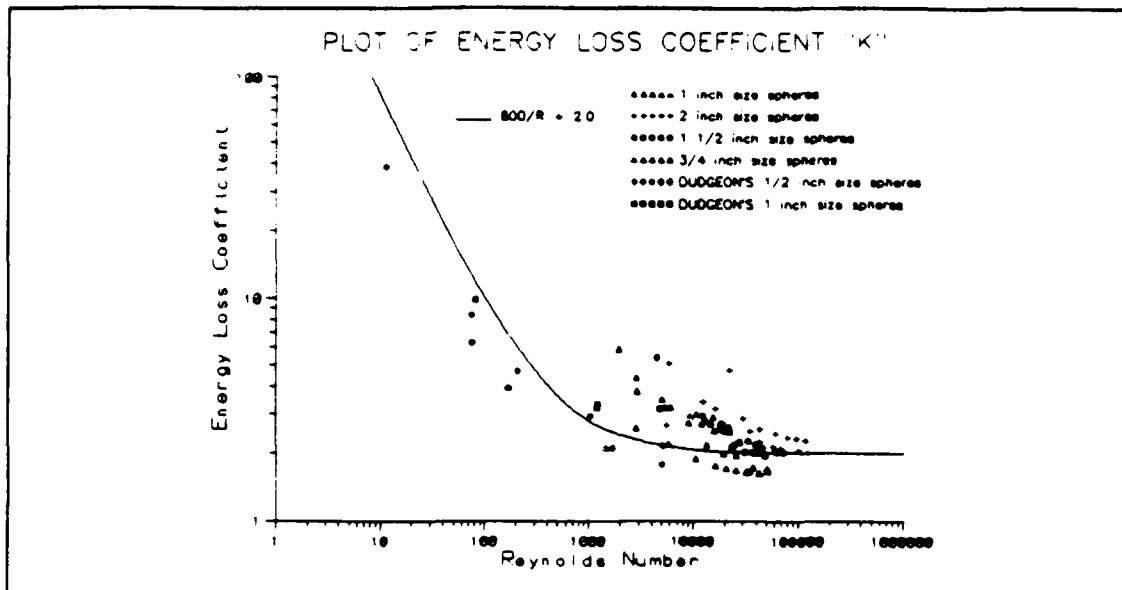


Figure 2

The energy loss coefficient relationship found from the one-dimension physical model is input to the mathematical computer model varying the porosity and aggregate diameter. The porosity for various size of aggregate approaches 52% for the nominal six inch media.

References

- Ahmed, N. and Sunada, D.K., 1969, "Nonlinear Flow in Porous Media", Proc. ASCE, Journal Hyd. Div. HY6, 6883, Nov.; 1847-1857.
- Cedergren, H.R., 1977, "Seepage, Drainage and Flow Nets", J. Wiley and Sons, New York, 534 pp.
- Desai, C. S.: Seepage Analysis of Earth Banks Under Drawdown, J. of S. M.F.E., ASCE, Vol.98, No. SM1, November, 1972.
- Desai, C. S. and Able, J. F., Introduction to the Finite Element Method: A Numerical Method for Engineering Analysis, Von Nostrand Reinhold Co., New York, 1972.
- Desai, C. S.: Finite Element Methods for Flow in Porous Media, Chapter 8 in Gallaghern R. H. et. al. (Eds.), "Finite Elements in Fluids," John Wiley & Sons Limited, London, 1975.
- Desai, C. S.: Flow Through Porous Media, Chapter 14, Desai C. S. and Christian, J. T. (Eds.), "Numerical Methods in Geotechnical Engineering," McGraw-Hill Book Company, New York, 1977.
- Desai, C. S. and Kuppusamy T., User's Manual and Background for A Computer Code For General Seepage Analysis (SEEP-2DFE), Department of Civil Engineering, Virginia Polytechnic Institute and State University, Blacksburg, Virginia, 1978.
- Dudgeon, C.R., 1966. "An Experimental Study of the Flow of Water Through Coarse Grained Media", Houille Blanche, 7; 785-801.
- Fenton, J.D., "Hydraulic and Stability Analysis of Rockfill Dams," Department Report, DR 15, Department of Civil Engineering, University of Melbourne, Parkville, Victoria, Australia, July 1968.
- Forchheimer, P.H., "Wasserbewegung durch Boden", 2. Ver. dt. Ing., 1901, p. 1782.
- Friedlander, S. K. and Topper, Leonard, (edited by), "Turbulence - Classic Papers on Statistical Theory," Interscience Publishers, Inc., New York, 1961, pp.34-40.
- Hedar, A., "Design of Rockfill Backwaters," Proceedings, Minnesota International Hydraulic Convention, September 1953.
- Irmy, S., "On the Theoretical Derivation of Darcy and Forchheimer Formulae", Transactions, American Geophysical Union, Vol. 39, 1958 pp. 702-707.

- Johnson, H.A., "Flow Through Rockfill Dams," Journal of Soil Mechanics and Foundation Engineering Division, ASCE, Vol. 97, No. SM2, February 1971, pp. 329-340.
- Kristianovich, S.A., "Movement of Groundwaters Violating Darcy's Law", Journal of Applied Math and Mech., Vol. 4, 1940, pp. 33-52.
- Lawson, J.D. and Curtis, R.P., "Flow Over and Through Rockfill Banks," Journal of Hydraulic Division, ASCE, Hyd 5, 1967, pp. 1-22.
- Laps, T.M., 1973, "Flow Through Rockfill", In: Hirschfeld, R.C. & Poulos, S. J. (Editors), Embankment Dam Engineering, J. Wiley & Sons, New York pp. 87-105.
- Lindquist, E., "On the Flow of Water Through Porous Soil", Report to the First Congress on Large Dams, Vol. 5, Stockholm, 1933, pp. 81-101.
- Morcom, A.R., "Fluid Flow Through Granular Materials", Transactions, Instit. of Chem. Engrs., Vol. 24, 1946, pp. 30-43.
- Morris, C.D. 1987. "Feasibility study on the use of a porous rock dike as a fish screen at the Harry S. Truman Dam and Reservoir". Report submitted to Associated Electric Cooperative, Inc., pp. 1-27.
- Oliver, H., "Through and Overflow Rockfill Dams - New Design Techniques," Proceedings, Institution of Civil Engineers, Vol. 36, March 1967, pp. 433-471.
- Parkin, A.K., Trollope, D.H. and Lawson, J.P., "Rockfill Structures Subjected to Waterflow," Journal of Soil Mechanics and Foundation Engineering Division, ASCE, SM 6, November, 1966, pp. 135-151.
- Parkin, A.K., "Field Solutions for Turbulent Seepage Flow," Journal of Soil Mechanics and Foundation Engineering Division, ASCE, January 1971, pp. 209-218.
- Robertson, James M., "A Turbulence Primer," University of Illinois Engineering Experiment Station Circular No. 79, Volume 62, Number 71; March 1965, pp. 14-15.
- Soni, J.P., Islam, N. and Basak, P., 1978, "An Experimental Evaluation of Non-Darcial Flow in Porous Media", J. Hydro., 38, 3/4, Aug., pp. 231-241.
- Volker, R.E., 1969, "Non-linear Flow in Porous Media by Finite Elements", Proc. ASCE., Journal Hydraulics. Div., (HY6), Vol. 95; pp. 2093-2114.
- Volker, R.E., 1975, "Solution for Unconfined Non-Darcy Seepage", Proc. ASCE., Journal of the Irrigation and Drainage Division., (IR1), Vol. 101; 11203, pp 53-65.
- Ward, J.C., "Turbulent Flow in Porous Media", Journal of the Hydraulics Division, ASCE, Vol. 90, No. (HY5), Proc. Paper 4019, Sept. 1964, pp. 1-13.
- Wilkins, J.K., 1956, "Flow of Water Through Rockfill and Its Application to the Design of Dams", Proc. 2nd Australia, NZ, Soils Conference.
- Wilkins, J.K., "The Stability of Overtopped Rockfill Dams," Proceedings, 4th Australian - New Zealand Conference on Soil Mechanics and Foundation Engineering, 1963.

FLOW REGIMES IN ALUMINIUM REDUCTION CELLS

E.E. Khalil and M.F. El-Demerdash
Cairo University, Faculty of Engineering,
Cairo, Egypt

ABSTRACT

Aluminium reduction technology is a very intensive energy process that requires consumptions of energy (electric) in the order of 14000 Kw hr/ton. Such energy is used ultimately for the decomposition of the ore and to its reduction to aluminium. Aluminium Reduction Cells (ARC) normally operate at small DC volt and high current (may exceed 200 K amp.). Cells of the Hall Herrolt type are widely used to reduce aluminium through a series of magneto-hydrodynamic and thermal interacting processes. Flow and heat transfer in the cell cavity that contains the heavier molten metal and the electrolytic bath, are important indicators of cell performance, productivity and cost.

Attempts are made to thoroughly understand the electromagnetic, flow regimes and turbulence, mixing and interdiffusion as well as thermal balance of the cell. However earlier attempts made use of simplified modelling assumptions both for electromagnetics representation of busbar system and cell steel structure as well as using low order modelling of flow and turbulence.

The present work made use of a full elliptic representation of flow and turbulence characteristics and took account of ledge formation mechanism and development of metal topology.

The cell considered in the present work is that of Egyptalum, Egypt designed as Soderberg with prospects to raise current to 200 K amp., using same cell cavity, and operating as prebaked cell.

The results presented and discussed in this paper were obtained with the

aid of a two-dimensional turbulent flow solver, marching in the third direction. A two equation turbulence model was incorporated with appropriate modified wall functions.

The present predictions demonstrate the characteristics of the cell in terms of melt velocities, turbulence, isopressure and interface contours.

The predicted results show, once more the ability of the present modelling technique to adequately represent cell characteristics in an actual full scale production cell.

I. Introduction to Prebaked Cell

I.1. General

Aluminium industry is one of the largest energy consuming sectors, and with souring energy and raw materials prices, modernization of plants becomes inevitable. Most of Soderberg Aluminium Reduction Cells "SARC" are intensive energy consumers with energy consumption of the order of 15500 Kwhr/ton with current efficiencies of the order of 88% and current densities about 0.7 A/cm². The corresponding cell voltage drop is 4.46 V and anode paste consumption is about 490 kg/tons of produced aluminium. New trends suggest the use of the more efficient multianode prebaked cells to reduce energy consumption and to raise productivity and production economy.

At Nage Hammady, Egyptalum smelter comprises 460 cells each producing about 1 ton/day at current of 155 KA, thus producing 175,000 metric tons/year. Through a series of energy auditing and management [1], the cell energy consumption was reduced to about 15,100 Kwhr/ton. It was found inevitable to change over to prebaked cell technology with optimum utilization of existing end-to-end facilities.

I.2. Criteria for Proposed Prebaked Aluminium Reduction Cells "PARC"

The proposed PARC were based on the following criteria :

Current efficiency not less than	93%
Aluminium production per cell	1.479 t/day
Energy consumption	135,000 Kwh/ton
Carbon consumption for anodes	440 kg/ton

The new designs were obtained with the aid of computer program "PACEM2" designed to mathematically represent prebaked aluminium cells in end-to-end and side-by-side arrangements under various operating conditions. This is carried out under the formulation of the governing conservation equations in finite elements and finite difference techniques and solving these equations in an iterative manner at a grid mesh superimposed on the cell plane in question.

A multi anode design is proposed with 24 similar anodes with side and longwise clearances, central channels and overall cavity dimensions of 10 x 4 m. and depth of 0.30 m between cathode and anode bottom. Figure 1 shows the general cell configuration.

In the second section, description of the computational procedure, equations, model assumption and wall conditions is given. The third section presents results of computations and discussion is devoted to show merits of present procedure and its limitations. The paper ends with a brief summary of conclusions.

II. Computation of Flow Field and Melt Velocities

II.1. General

The current distribution within the aluminium reduction cell was obtained from the Ohm's law and applying the current conservation equation at all grid nodes in the cell. The value of the electric conductivity was taken to vary from one location to other as previously described by El-Maghraby et al. [2] and Aly [3]. The current density distribution was determined within the cell and consequently the magnetic field strength and direction at any location in the cell were determined. This was achieved by the application of the Biot-Savart law in the integral form. The current densities and magnetic fields being calculated within the cell, the electromagnetic stirring forces can be readily obtained from the Lorentz law [2].

Such forces are three dimensional in nature and were calculated at all preset grid nodes.

II.2. Melt and Electrolyte Velocities

In aluminium reduction cells, the electrolyte and molten metal move under the influence of the prevailing forces. Namely the electromagnetic steering

force components, inertia forces, bouyancy forces and turbulent interactions. In the present work, these forces are considered; it is worthnoting that the first type of forces is generally dominant. The general governing equations of mass and momentum are incorporated in the present analysis. The general form of these equations are show as;

$$\frac{\partial}{\partial x_j} (\bar{\rho} U_j \phi + \bar{\rho} \overline{u_j \phi}) = \frac{\partial}{\partial x_j} \Gamma_\phi \frac{\partial \bar{\phi}}{\partial x_j} + S_\phi \quad (1)$$

The above equation is general with ϕ representing any conserved dependent variable; ϕ can represent U, V or W velocity components. This yields the three momentum equations. For ϕ equals unity, equation (1) is then reduced to the continuity equation. The second term on the left hand side of equation (1) represents the turbulent flux of the entity ϕ in question due to fluctuations of velocity component U_j and fluctuations of ϕ .

In turbulent flow analysis, a commonly adopted technique, is to use the eddy viscosity concept of Launder and Spalding [4], hence the correlation $\overline{u_j \phi}$ can be represented as;

$$\bar{\rho} \overline{u_j \phi} = - \Gamma_\phi \frac{\partial \bar{\phi}}{\partial x_j} \quad (2)$$

where ϕ represents velocity components, then Γ_ϕ is the effective viscosity defined as;

$$\Gamma_\phi = \mu_e = \mu_t + \mu \quad (3)$$

and using the two equation k- ϵ model of Launder et al. [4],

$$\mu_t = 0.09 \rho \frac{k^2}{\epsilon} \quad (4)$$

where μ is Laminar viscosity

k kinetic energy of turbulence

ϵ dissipation rate of kinetic energy of turbulence

ρ is local average density

The values of k and ϵ at every grid node can be readily obtained from their respective transport equations expressed in the form (1) with ϕ equals to k or ϵ respectively [5].

The term S_ϕ denotes the source/sink of the entity ϕ . In momentum equations, S_u , S_v and S_w contains the electromagnetic force components F_x , F_y and F_z , respectively. Details of this model and its applications and validation can

be found in reference 5, 6, 7 and 8. In the present work, the values of F_x , F_y and F_z were obtained from reference (8) and incorporated in the flow prediction code.

III. Numerical Computations of Flow Characteristics :

Results and Discussions

III.1. Predicted Parameters

In numerical procedure outlined in the previous section was applied to the prebaked cell configuration shown earlier in Figure 1 for side-by-side cell arrangements. The present demonstrations were carried out for the situation of 24 anode blocks. The numerical procedure utilizes a 24 x 24 grid arrangement superimposed on the cell horizontal plane at various distances z from bottom of cathode, for a 200 Ka cell.

Predictions of current density J_{xy} , magnetic flux density B_{xy} , B_x , B_y and B_z were obtained with the aid of the electromagnetic model of El-Maghraby et al. [8] and are shown here in Figures 2a, b, c, d and e for completeness, as the present contribution is devoted to flow regimes and interface characteristics.

The results of Figure 2 are obtained for $z = 0.275$ m from cathode bottom. The corresponding flow field vectors are shown in Figure 3 which shows two large eddies to the upstream end and smaller eddies near the downstream side. The flow is not symmetrical along the longitudinal axis of the cell due to effect of the two neighbouring cell fields upstream and downstream of this cell. The order of magnitude of the velocities is 4.0 cm/s.

The corresponding pressure distribution in the same horizontal x - y plane is shown in Figure 4. The pressure distribution is non-symmetrical along the longitudinal cell axis and larger pressure drop are observed near the upstream side. The maximum pressure drop is of the order of 40 N/m².

The corresponding cell characteristics at $z = 0.2$ were obtained under the same operating conditions and are shown in Figures 5, 6 and 7. Figures 5A, B, C, D and E shows the current density J_{xy} , B_{xy} , B_x , B_y and B_z . The values of B_{xy} , B_x , B_y , and B_z are near those shown in Figure 2A while the current density changes due to field changes from electrolyte to molten metal.

Figure 6 shows the velocity vectors in xy plane at $z = 0.2$, the velocities are higher than those at $z = 0.275$ m and is attributed to the strong forces at this plane.

The predicted pressure distribution is shown in Fig. 7 and it shows better symmetry than that observed in Fig. 4. The maximum pressure drop is 42 N/mm^2 .

Figure 8 shows the obtained interface contours and Fig. 9 presents a three dimensional display of the interface that shows two large troughs in the middle of cell and larger peaks at the vicinity of the four corners of the cell.

Table 1 shows the maximum values of cell properties at three different locations of $z = 0.125$ (mid aluminium), $z = 0.2$ m and $z = 0.275$ mid electrolyte.

Table 1

Property			$z=0.125^*$	$z = 0.2$	$z=0.275$
J_{xy} , A/m^2	Max.		1644	2364	444
J_x			1589	2195	444
J_y			1133	-1485	130
J_z			-5161	-5738	-5622
B_{xy}	Gaus		114.3	113.34	118.29
B_x			51.5	54.01	58.3
B_y			107.8	105.6	110.17
B_z			40.82	40.81	41.65
U_{xy}			11.9	13.74	3.916
U_x	Abs		11.9 -ve	13.7 -ve	3.89 -ve
U_y	Abs		9.11	10.5	2.92 -ve
P			4	+29	44

*See reference [8].

From Table 1, it can be seen that current density increases in the core of the flow and decreased towards the electrolyte zone. The corresponding current density in the z-direction J_z does not change drastically as the other two components which are affected by the existance of ledge, walls, ... etc. The magnetic flux density vector B_{xy} shows minimal changes within 3%, same remark applies for B_x , B_y and B_z . The magnetic force density F_{xy} is obtained from current density vector J_{xy} and magnetic flux density B_{xy} by equation of Lorentz, $F = J \times B$. The magnetic forces change in magnitude and direction due to the

changes of flux and current densities and hence affects the momentum balance. As expected, this would change velocities and pressures, demonstrated in Table 1.

III.2. Discussion

From results described above, one can conclude that the magnetic flux distribution is almost the same at different z sections. This approximation is reasonable since the depth of liquid is small compared to cell and busbar dimensions. On the other hand, flow results show remarkable changes along the cell depth. In mid electrolyte, the fluid is relatively calm, while in the metal velocities can reach more than four times those in electrolyte. It seems that the zone just below the interface suffers the most violent flow.

These results stress the role of current distribution on flow characteristics along cell depth. When the magnetic flux is considered constant along the depth, then, current distribution is the only factor that affects force distribution; the basic input of flow equations. This is true as shown in Table (1) where a good correlation can be held between horizontal currents and flow values. Flow velocities clearly increases as horizontal currents increase. These horizontal currents cause the development of forces that disturb the relatively stable force field caused by vertical current.

Horizontal currents developed in the cell depend upon the geometry of cell cathode in relation to anode blocks. Also, the thickness of ledge and bottom ridge affect the geometry of cell where current is forced to fill. In the electrolyte, the central channel between anodes affects current distribution as shown in Fig. 2A. The current in the electrolyte does not suffer large divergence towards cell walls. In the metal, the effect of central channel is screened out and the current flows towards the walls to fill cell cavity and then converges back to escape from the cell hearth.

One can stress the geometry effect on flow characteristics of the prebaked cells.

IV. Summary of Conclusions

The present work addressed the mathematical modelling of flow field, turbulence and interface topography in Prebaked Aluminium Reduction Cells "PARC"

under normal operating condition. The following are the more important conclusions of this work :

1. A numerical finite difference procedure was developed and utilized to predict local flow characteristics in "PARC". The procedure solved fully the time averaged conservation equations of mass, three momentum and energy in the cell at discretized grid nodes mapping the horizontal and vertical planes.
2. Twenty four prebaked anodes of dimensions 1.65 x 0.72 x 0.6 m were used.
3. The model ability to adequately predict cell properties was demonstrated by parametric investigations. Model calculations can be readily used to yield the effect of end and quarter risers and busbar arrangements. The model is a usefull tool for engineering design.

Acknowledgement

This work was carried out under contract between Egyptalum and Cairo University, financial support from Egyptalum is kindly acknowledged. Thanks and gratitude are due to Prof. M.G. El-Maghraby and S.M. El-Raghy for technical support.

References

1. El-Maghraby M.G., et al., Energetics in Metal Industries, Cairo Univ./MIT project report 2, 1984.
2. El-Maghraby, M.G. et al., Analysis and Modelling of Aluminium Reduction Cells, FRCU project 842014, 1988.
3. Ali, K.F., Private Communication, 1992.
4. Launder, B.E. and Spalding P.B., Mathematical Models of Turbulence, Academic Press, 1972.
5. Khalil, E.E., Modelling of Furnaces and Combustors, 1983, Abacus Press.
6. Khalil, E.E., Numerical Computations of Flow Pattern in Aluminium Reduction Cells, Proc. 10th Symposium on Turbulence, 1986.
7. Khalil, E.E., Mathematical Modelling of Aluminium Cells, ECI, Chapter 52, Proc. ICES88, U.S.A.
8. El-Maghraby, M.G. et al., Modelling and Analysis of Aluminium Reduction Cells, Interium Report, Jan. 1992, Egyptalum, Egypt.

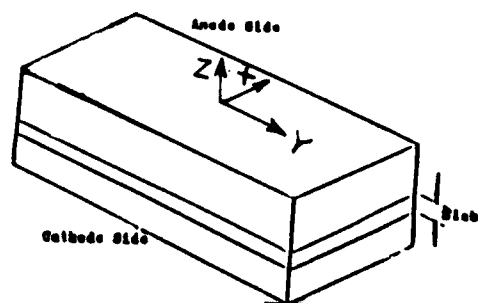


Fig. (1) : General cell configuration.

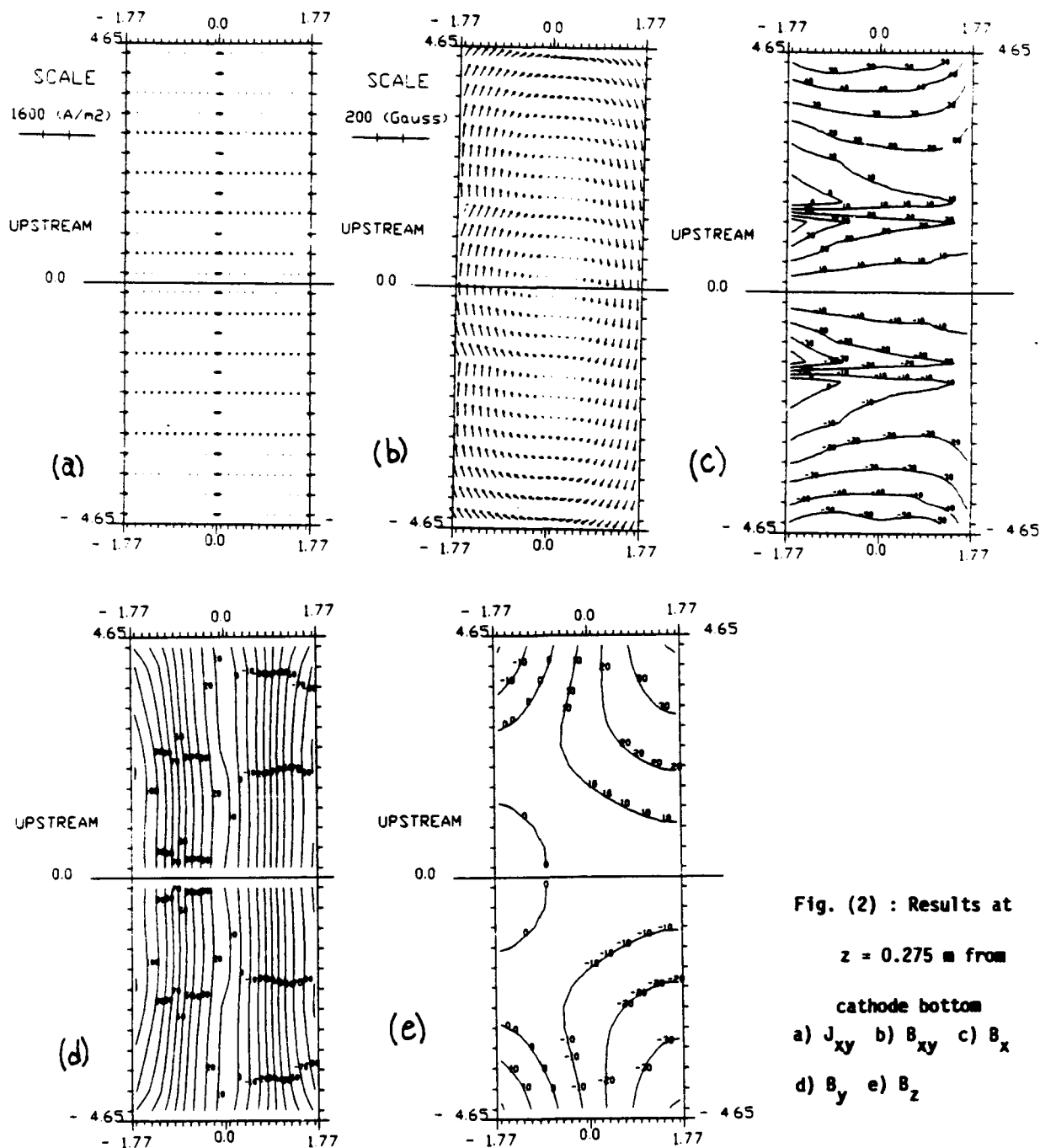


Fig. (2) : Results at

$z = 0.275$ m from

cathode bottom

a) J_{xy} b) B_{xy} c) B_x

d) B_y e) B_z

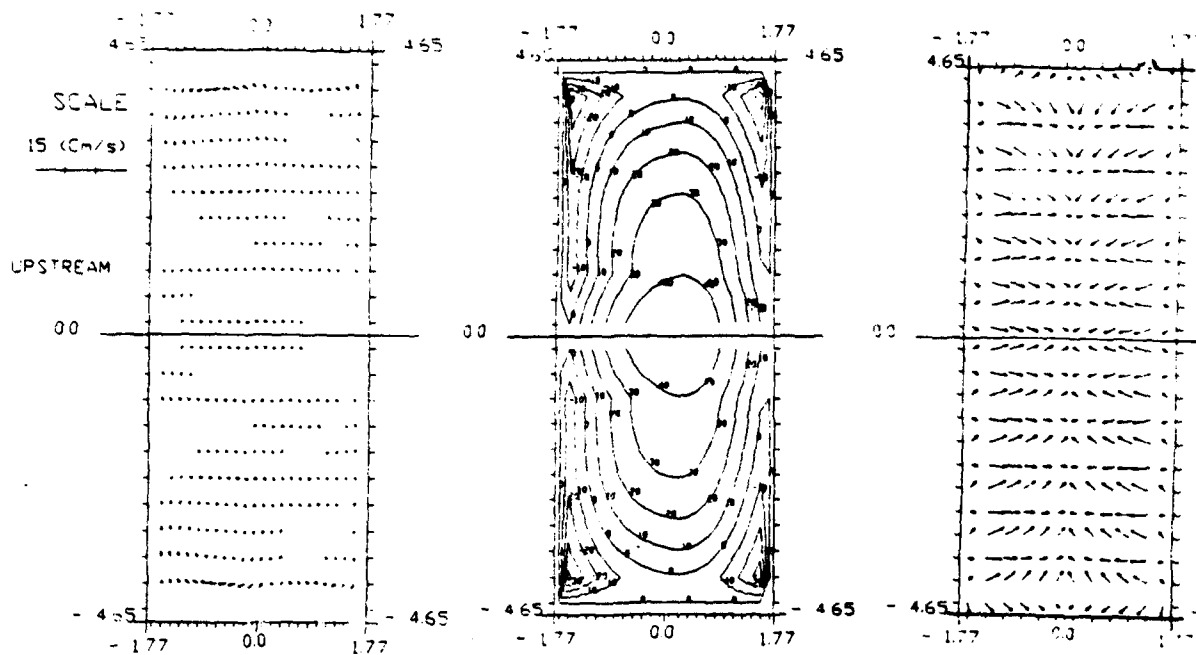


Fig. (3) : Flow field vectors at $z = 0.275$ from cathode bottom.

Fig. (4) : Pressure distribution at $z = 0.275$ from cathode bottom.

(A)

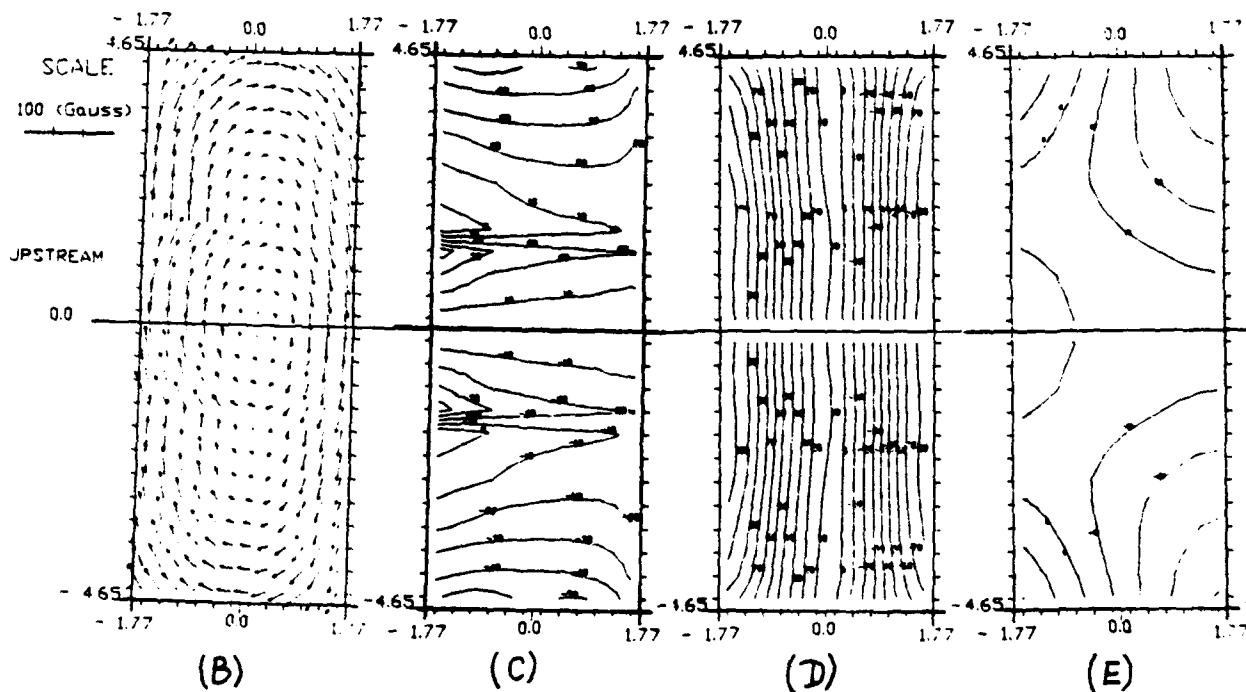


Fig. (5) : Results at $z = 0.2$ m from cell cathode
A) J_{xy} B) B_{xy} C) B_x D) B_y E) B_z

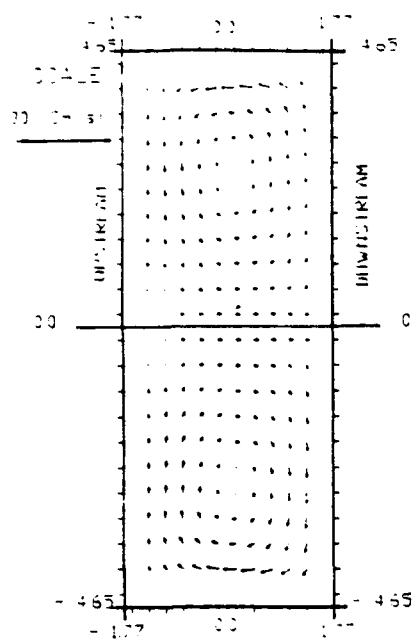


Fig. (6) : Flow field vectors at $z = 0.2$ m.

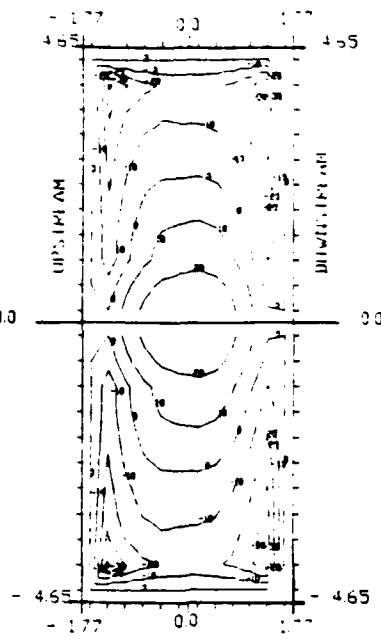


Fig. (7) : Pressure distribution at $z = 0.2$ m

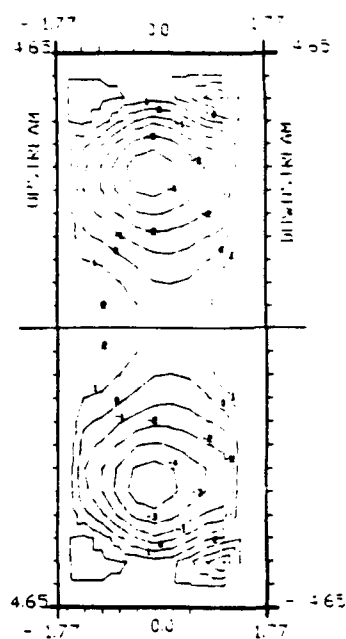


Fig. (8) : Contours of interface.

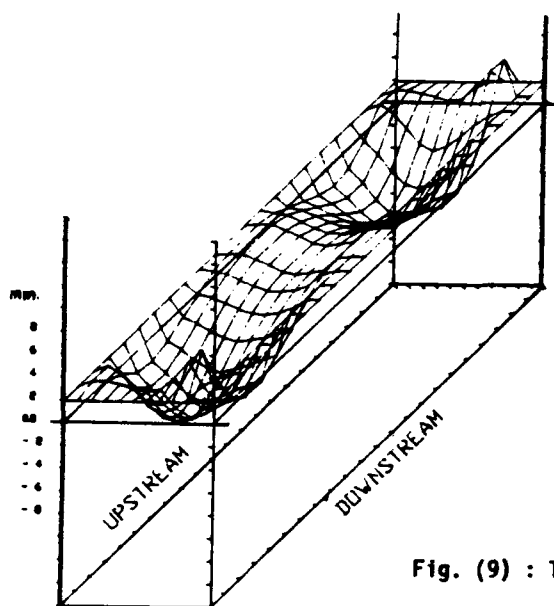


Fig. (9) : Three-dimensional interface.

AN ANALYSIS OF LIFT FORCES ON
AEROSOLS IN A WALL BOUNDED
TURBULENT SHEAR FLOW

P. Cherukat and J. B. McLaughlin

Department of Chemical Engineering
Clarkson University, Potsdam, N.Y 13699-5705

Abstract

This paper describes work that will lead to a better understanding of the role of lift forces in the deposition of aerosols on the walls bounding a turbulent shear flow. After providing some background information about aerosol trajectories that has been obtained from computer simulations, new results for the lift force in the relevant parameter ranges are presented.

I. Introduction

Aerosols follow the streamlines of a turbulent shear flow fairly well except in the viscous wall region. Although the inertia of the aerosols is small, the extremely rapid spatial variations of the fluid velocity in the viscous wall region can cause aerosols that are bigger than about a micron to depart from the streamlines and travel toward the wall. Computer simulations by Kallio and Reeks¹ and McLaughlin² indicate that as they pass through the viscous wall sublayer, aerosols that deposit on the wall develop Reynolds numbers of order unity. The cause of the large Reynolds numbers is the large streamwise slip velocity that develops as the aerosols pass through the viscous sublayer. Thus, in spite of their small size, it is possible that inertial effects could play a significant effect in the deposition of aerosols. It has been pointed out^{1,2} that the Saffman lift formula³ would suggest a significant lift force on the aerosols as they pass through the viscous sublayer. Although the force predicted by the Saffman formula is small compared to the maximum normal component of the Stokes drag force, it acts on the aerosol in a region of nearly stagnant fluid. As a consequence, it can increase the predicted rate of deposition by an order of magnitude. However, McLaughlin¹ pointed out that Saffman's assumptions are not satisfied by the aerosols that deposit as they move through the viscous sublayer.

Saffman pointed out that there are two Reynolds numbers that characterize a small, freely-rotating sphere that translates through an unbounded

linear shear flow. One Reynolds number, Re_s , is based on the sphere diameter and the velocity of the sphere relative to the surrounding fluid. The other Reynolds number, Re_G , is based on the sphere diameter and fluid shear rate. He assumed that Re_s and Re_G were small compared to unity and that $Re_s \ll Re_G^{1/2}$, where $Re_s = v_s d / \nu$ and $Re_G = G d^2 / \nu$; the symbol d denotes the particle diameter, G denotes the velocity gradient, and v_s denotes the magnitude of the particle's slip velocity. However, McLaughlin's² computer simulations indicate that Re_G is of order 10^{-2} and Re_s is of order unity. Thus, two of Saffman's assumptions are not satisfied for most of the aerosols that deposit as they pass through the viscous sublayer. In addition, Saffman's analysis ignores wall effects.

The goal of the work to be discussed has been to obtain a better understanding of the lift force for the Reynolds number ranges of interest for aerosol deposition and to include wall effects. In Section II, asymptotic results that give the dependence of the lift force on the ratio $Re_G^{1/2} / Re_s$ and the distance of the aerosol from the wall will be presented. These results assume that Re_G and Re_s are small compared to unity and that the distance of the aerosol from the closest wall is large compared to the aerosol radius. Since numerical simulations indicate that Re_s is order unity for most of the aerosols that deposit as they pass through the viscous sublayer, it is necessary to have results for finite Reynolds numbers. In Section III, the results of direct numerical simulations of the three-dimensional flow field around a sphere in an unbounded linear shear flow will be discussed. The results help to assess the usefulness of the asymptotic results at finite Reynolds numbers. At the present time, no numerical results are available that include both finite Reynolds number effects and wall effects. In Section IV, some experimental measurements will be presented and compared with the asymptotic and numerical results. Finally, the new results are summarized in Section V.

II. Asymptotic Results

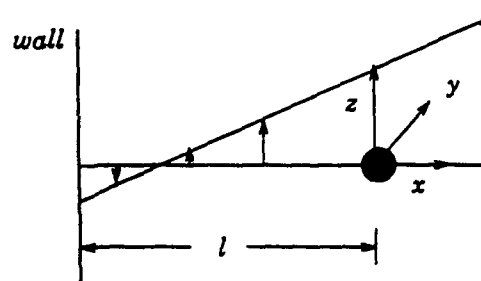


Figure 1. Sphere translating in a wall bounded shear flow.
(Reference frame translates with the sphere)

In this section, results for the lift force on a small sphere in a wall-bounded linear shear flow will be discussed. The derivations have been given elsewhere^{4,5}. The geometry of interest is shown in Fig. 1. The center of the sphere is located at a distance l from the wall. The problem is formulated in a frame of reference where the sphere is at rest. The origin of the coordinate system is at the center of the sphere. The wall is located at $x = -l$. The undisturbed fluid velocity is

$$v = (Gx + v_s)e_3, \quad (1)$$

where e_3 is a unit vector in the z -direction. Such a situation could arise, for example, by the sedimentation of a negatively buoyant sphere in a vertical channel flow provided that the sphere is close enough to one of the channel walls that the curvature of the undisturbed fluid velocity may be neglected. Unless an external force constrains the sphere, it will migrate laterally. It may be verified after the fact that the migration velocity is a small fraction of v_s . Thus, the situation in Fig. 1 may be viewed as quasi-steady. An alternative is to assume that an external force prevents the sphere from moving in the x -direction. In either case, it is assumed that the velocity of the sphere relative to the surrounding fluid is $-v_s e_3$. In the laboratory frame of reference, the wall is at rest. In this frame, positive values of G and v_s correspond to a negatively buoyant sphere in an upward flow. If $v_s < Gl$, the sphere moves upward, but it lags the surrounding fluid. As pointed out in the Section I, in the motion of aerosols, the slip velocity arises because of the aerosols' inertia and the rapid variations in the fluid velocity in the viscous wall region. However, in discussing the results for the lift force, it will be convenient to picture the slip velocity as being caused by the sedimentation of the sphere in a vertical shear flow. The sphere lags the fluid if $v_s > 0, G > 0$ or $v_s < 0, G < 0$. The sphere leads the fluid if $v_s > 0, G < 0$ or $v_s < 0, G > 0$. Considerations of symmetry indicate that the lift force (or migration velocity) depends only on whether the sphere leads or lags the fluid. Thus, one may assume that $G > 0$ and consider the cases $v_s > 0$ or $v_s < 0$.

The results to be discussed are based on the following assumptions:

$$a \ll l \quad (2)$$

$$Re_G \ll 1 \quad (3)$$

$$Re_s \ll 1. \quad (4)$$

No assumption is made about the ratio $\epsilon = Re_G^{1/2}/Re_s$. The assumptions about Re_G and Re_s imply that, near the sphere, the convective term in the Navier-Stokes equation is small compared to the viscous term. However, this assumption is not necessarily valid at large distances from the sphere. In an unbounded fluid, inertial effects are comparable with viscous effects when the distance from the sphere, r , satisfies $r \sim \min(L_G, L_s)$, where

$$L_G = \left(\frac{\nu}{G}\right)^{1/2} \quad (5)$$

$$L_s = \frac{\nu}{v_s} \quad (6)$$

It may be seen that L_G and L_s are both large compared to a when Re_G and Re_s are small compared to unity. Thus, as pointed out by Saffman³, inertial effects must be treated with singular perturbation methods. Saffman considered the case $\epsilon = \infty$ and showed that the lift force, F_L , was

$$F_L = 6.46a^2v_s\left(\frac{G}{\nu}\right)^{1/2}, \quad (7)$$

where it is assumed that $G > 0$. To leading order, one may obtain an expression for the inertial migration velocity by assuming a Stokes drag coefficient:

$$v_m = \frac{F_L}{6\pi\mu a}, \quad (8)$$

where μ denotes the dynamic viscosity of the fluid.

McLaughlin⁴ showed that the singular perturbation methods used by Saffman may be generalized to obtain a result for the lift force in an unbounded linear shear flow ($l = \infty$) that is valid for arbitrary values of ϵ :

$$F_L = \frac{9}{\pi}\mu a^2v_s\left(\frac{G}{\nu}\right)^{1/2}J. \quad (9)$$

In Eq.(9), J denotes a dimensionless three-dimensional integral that depends only on ϵ . As ϵ goes to infinity, J approaches 2.255 and Eq.(9) reduces to Saffman's formula in Eq.(7). For large but finite values of ϵ , J is given by the asymptotic form:

$$J = 2.255 - \frac{0.6463}{\epsilon^2}, \quad (10)$$

while, for small ϵ ,

$$J = -32\pi^2\epsilon^5\ln(1/\epsilon^2). \quad (11)$$

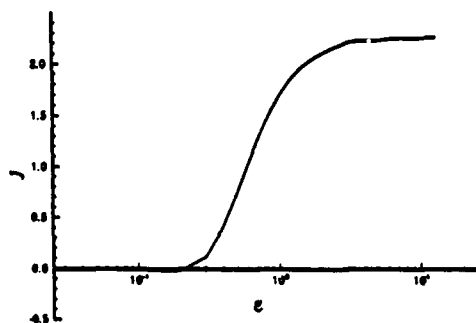


Figure 2. J as a function of ϵ .

In Fig. 2, J is plotted as a function of ϵ . When ϵ is smaller than unity, the Saffman formula significantly overpredicts the magnitude of the lift force. This raises doubts about the validity of aerosol trajectories computed with the Saffman expression for the lift force.

The above asymptotic theory ignores wall effects. However, wall effects may have a significant effect on the lift force experienced by aerosols in the viscous sublayer. This may be seen by considering the relative sizes of a^+ and L_G^+ , where the plus sign denotes a value in "wall units" based on the friction velocity and the kinematic viscosity. Since the friction velocity is based on the average wall shear rate, one may take $L_G^+ = 1$. Since the lift force is caused by inertial effects at distances of order L_G from the sphere, it is likely that the presence of a wall will modify the lift force at most points within the viscous sublayer. Wall effects will also change the drag coefficient⁶, but only when the sphere is within a few radii from the wall and a^+ is typically on the order of 0.1 for aerosols in the range where lift forces may be important.

Cox and Brenner⁷ developed a theory for the lift force on a sphere that is close enough to the nearest wall that $l \ll \min(L_G, L_s)$. Under these conditions, the leading order approximation to the lift force may be calculated by regular perturbation methods. They also assumed that $a \ll l$ so that a non-neutrally buoyant sphere may be treated as a point force to leading order. Cox and Hsu⁸ used the theory to compute the lift force on a sphere in a vertical parabolic flow bounded by a planar wall. Close to wall, the parabolic flow may be linearized. The Cox-Hsu result for a linear flow is

$$F_L = 6\pi\mu a \left(\frac{3}{32} \frac{av_z^2}{\nu} + \frac{11}{64} \frac{Gav_z l}{\nu} \right). \quad (12)$$

For future reference, it is convenient to express the lift force in Eq.(12) in terms of the dimensionless "outer" coordinate $l_* = l/L_G$:

$$F_L = \frac{9\pi}{16} \mu a^2 \left(\frac{1}{\epsilon} + \frac{11}{6} l_* \right). \quad (13)$$

Using the dimensionless parameter J defined by Eq. (9), the Cox-Hsu result is

$$J = \frac{\pi^2}{16} \left(\frac{1}{\epsilon} + \frac{11}{6} l_* \right). \quad (14)$$

The Cox-Hsu theory is valid when $l \ll \min(L_G, L_s)$, while the Saffman and McLaughlin theories are valid for $l \gg \max(L_G, L_s)$. Recently, McLaughlin⁵ has shown that it is possible to establish a general result for the lift force that reduces to the above results in the appropriate limits and is also valid at intermediate values of l . The general result is

$$F_L = F_L^u + F_L^w, \quad (15)$$

where F_L^u is the lift force on the sphere in an unbounded, linear shear flow and F_L^w is the correction due to the wall. Both F_L^u and F_L^w are obtained by Fourier transforming an Oseen-like (linear) approximation to the Navier-Stokes equation and solving an ordinary differential equation for the Fourier transform of the disturbance flow. The result for F_L^u is given by Eq.(9) and Fig. 2. McLaughlin⁵ shows that F_L^w may be expressed in terms of integrals of the Airy function, Ai .

In the limit $l_* \ll 1$, the result for F_L reduces to the Cox-Hsu result as may be seen in Fig. 3 which shows the dimensionless lift force, J , as a

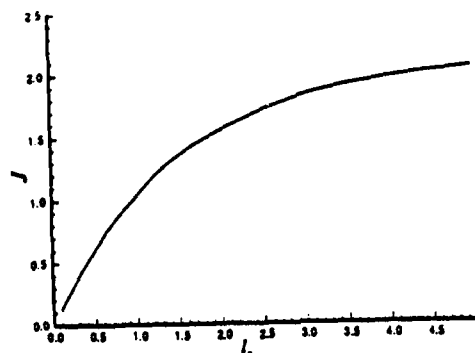


Figure 3. J as a function of l_0 for $\epsilon = \infty$.

function of l_0 for $\epsilon = \infty$. It may be seen that J approaches the Saffman value (2.255) as l_0 goes to infinity. For $\epsilon = \infty$, the lift force points away from the wall for all values of l_0 . For $\epsilon = -\infty$, the lift force points toward the wall at all distances satisfying $l >> a$. For positive values of ϵ larger than about 0.22, the lift force points away from the wall at all distances. An example of the dependence on l_0 is shown in Fig. 4 which shows the dimensionless lift force for $\epsilon = 1$. However, for $\epsilon = -1$, the lift force points toward the wall for large values of l_0 and away from the wall for small values of l_0 as may be seen in Fig. 5. For values of ϵ , that are small in magnitude, the lift force points away from the wall at all values of l_0 satisfying $l_0 << 1/\epsilon$. The lift force in this case may be approximated by the Vasseur-Cox⁹ expression for the lift on a sphere sedimenting next to a vertical, planar wall in a stagnant fluid. This may be seen in Fig. 6 which shows results for $\epsilon = 0.2$.

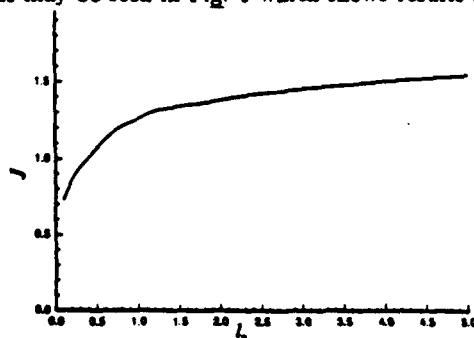


Figure 4. J as a function of l_0 for $\epsilon = 1$.

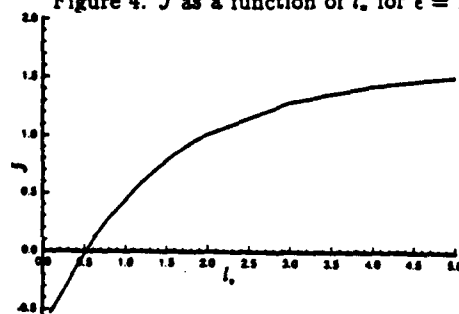


Figure 5. J as a function of l_0 for $\epsilon = -1$.

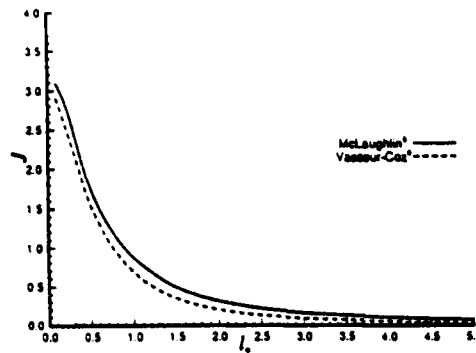


Figure 6. Comparison of J according to McLaughlin's⁵ expression with Vasseur-Cox⁹ expression for $\epsilon = 0.2$.

The asymptotic theory described in this section provides detailed information about the dependence of the lift force on aerosol Reynolds numbers and the distance from the wall. However, before applying the theory to trajectory calculations, it is important to determine whether the theory makes accurate predictions at finite Reynolds numbers. This issue will be addressed in Sections III and IV.

III. Numerical Simulations

To calculate the lift on a sphere at finite Reynolds numbers, it is necessary to solve the three-dimensional Navier-Stokes equation for the flow around the sphere. The governing equations are

$$\mathbf{v} \cdot \nabla \mathbf{v} = -\nabla p / \rho + \nu \nabla^2 \mathbf{v} \quad (16)$$

$$\nabla \cdot \mathbf{v} = 0 \quad (17)$$

$$\mathbf{v} = \boldsymbol{\Omega} \times \mathbf{r}, |\mathbf{r}| = a \quad (18)$$

$$\mathbf{v} = (G\mathbf{x} + v_s)\mathbf{e}_3, |\mathbf{r}| = R. \quad (19)$$

In Eqs.(16-19), \mathbf{v} denotes the velocity of the fluid, p is the pressure, and ρ is the fluid density. In Eq. (18), $\boldsymbol{\Omega}$ is the angular velocity of the sphere. In Eq. (19), R is the radius of an imaginary outer boundary. On this artificial surface, the disturbance created by the sphere is assumed to vanish. Ideally, R would be infinity. In the work to date, $R = 50a$. In the limit of vanishing Reynolds numbers, there is an exact solution for a freely rotating sphere that translates relative to a linear shear flow¹⁰. According to the Stokes flow solution, the disturbance flow is on the order of two percent at $r = 50a$. Furthermore, the effect of inertia is to cause the disturbance flow to decay more rapidly at large distances^{10,11}.

A hybrid finite volume-spectral method is used to solve Eqs. (16-19). The equations for the Cartesian components of the fluid velocity are written in a spherical coordinate system. Spectral methods are applied in the azimuthal coordinate. The region between $r = a$ and $r = R$ is divided into control volumes with surfaces that are defined by constant values of the spherical coordinates. The momentum and continuity equations are integrated over

and control volume and are expressed in terms of surface integrals¹². The convective term is expressed in a semi-implicit form. The velocity and pressure at each time step are obtained by solving the discretized momentum and continuity equations simultaneously. This large system of linear algebraic equations (typically about 50,000) is solved by the GMRES¹³ method.

The results obtained to date appear to show the same trend with ϵ as the asymptotic results in Eq.(9) and Fig. 2. In Fig. 7, the dimensionless lift force, J , is plotted versus ϵ . Also plotted in Fig. 7 is the asymptotic result for J . The numerical results were obtained for values of Re_G ranging from 0.10 to 3.0. To date, wall effects have been ignored in the numerical simulations.

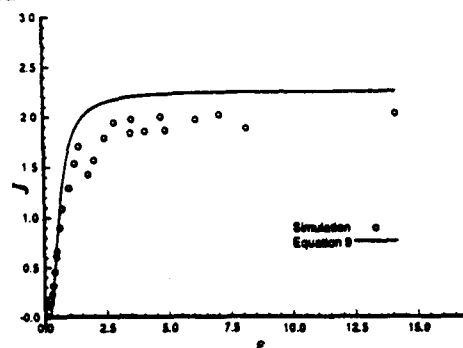


Figure 7. J computed by flow simulation as a function of ϵ .

IV. Experiments

To test the asymptotic and numerical results, it is necessary to perform experimental measurements. Ideally, one would measure the lift force. However, it is much easier to measure the lateral migration velocity. When the sphere Reynolds numbers are small compared to unity, one may use the Stokes drag coefficient to relate the lift force to the migration velocity. At finite Reynolds numbers, one should use a drag coefficient that is appropriate to the flow around the sphere. However, at small ϵ (weak shear), it seems reasonable to use the drag coefficient for axisymmetric flow around a sphere to approximate the drag coefficient.

The strategy of the experiments is to measure the lateral migration velocity of a sphere sedimenting through a vertical linear shear flow. A homogeneous flow apparatus (HFA) (fig. 8) similar to the one used by Graham and Bird¹⁴ is used to produce a linear shear field. The HFA consists of two timing belts rotating in the same sense in a liquid. the liquid is contained in the space between two Plexiglas walls in the front and rear and aluminum blocks at the top, bottom and sides. It has been verified by experiments and simulation using the CFD software NEKTON[†] that the flow profile is linear in the middle 60 percent of the region between the Plexiglas walls.

The migration velocities have been measured for polymethylmethacrylate (pmma) balls (2mm dia.) and polyacetate balls (2mm and 1.5mm dia) in aqueous solutions of polyalkylene glycol (viscosities between 20cp and 60cp and specific gravities in the range 1.03 - 1.05).

[†] NEKTON is a registered trademark of Nektonics Inc. and M.I.T.

In Fig. 9, the dimensionless lift force obtained from the experiments is plotted versus ϵ for values of Re_s between 0.1 and 1.0 and ϵ between 0.3 and 1.0. Also shown in Fig. 9 is the asymptotic result in Eq.(9) and Fig. 2.

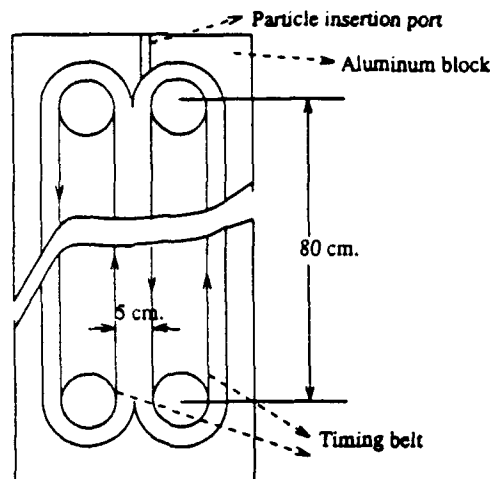


Figure 8. Homogeneous Flow Apparatus (HFA).

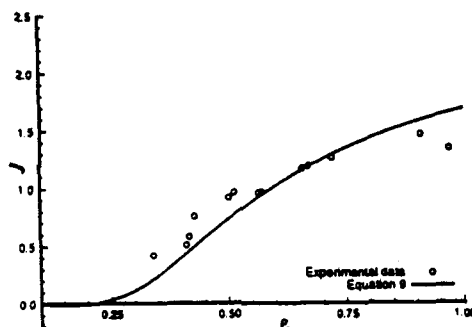


Figure 9. Experimentally measured values of J as a function of ϵ .

V. Conclusion

The numerical and experimental results are for situations in which wall effects may be neglected. They show that the asymptotic predictions are robust in the sense that they make reasonably accurate predictions even when the slip Reynolds number is of order unity. No numerical results are available for comparison with the asymptotic results for wall-bounded flows. However, Cherukat and McLaughlin¹⁵ reported measurements of the inertial migration velocity of a sphere sedimenting next to a vertical planar wall in a stagnant liquid. Their results agree well with the small ϵ limit of the asymptotic theory even though the slip Reynolds numbers were as large as 3.

At the present time, it is not clear what role the lift force plays in inertial aerosol deposition. For small values of l_s or small values of ϵ , the lift force points away from the wall. The Saffman formula would indicate that the lift force points toward the wall. Thus, the actual lift force may introduce

greater variation for a given value of the dimensionless particle relaxation time τ^* than one might expect on the basis of the Saffman formula.

Acknowledgement

The HFA used in this work was based on a prototype developed by Mr. James Abbott and Dr. Alan Graham. The authors also gratefully acknowledge the assistance of Dr. David Dandy with the numerical work. The computations were performed on the IBM RISC 6000 workstation in Clarkson's AVS laboratory.

This work was supported by the United States Department of Energy under contract DE-FG02-88ER13919.

References

1. G.A. Kallio and M.W. Reeks. 1989 *Int. J. Multiphase Flow* 15 433.
2. J.B. McLaughlin. 1989 *Phys. Fluids A* 1, 1211.
3. P.G. Saffman 1965 shear 1965 *J. Fluid Mech.* 22, 385.
4. J.B. McLaughlin. 1991 *J. Fluid Mech.* 224, 261.
5. J.B. McLaughlin, "The lift on a small sphere in wall-bounded linear shear flows," *J. Fluid Mech.* (accepted for publication, 1992).
6. R.G. Cox and H. Brenner. 1967 *Chem. Eng. Sci.* 22, 1753.
7. R.G. Cox and H. Brenner. 1977 *Chem. Eng. Sci.* 23, 147 (1977).
8. R.G. Cox and S.K. Hsu. 1977 *Int. J. Multiphase Flow* 3, 201.
9. P. Vasseur and R.G. Cox. (1977) *J. Fluid Mech.* 80, 561.
10. G.K. Batchelor, "An introduction to fluid dynamics," *Cambridge University Press* London (1970).
11. C.W. Oseen. 1910 *Ark. Mat. Astr. Fys.* 6, No. 29.
12. D.S. Dandy and H.A. Dwyer. 1990 *J. Fluid Mech.* 216, 381.
13. Y. Saad and M.H. Schultz. 1986 *SIAM J. Sci. Stat. Comput.* 7, 856
14. A.L. Graham and R.B. Bird. 1984, *Ind. Eng. Chem. Fundam.* 23 406
15. P. Cherukat and McLaughlin J.B. 1990, *Int. J. Multiphase Flow* 16 899

EVALUATION OF EJECTION DETECTION SCHEMES IN TURBULENT WALL FLOWS

Renard G. Tubergen and William G. Tiederman
School of Mechanical Engineering
Purdue University
West Lafayette, IN 47907-1288

Velocity techniques for detecting ejections have been systematically examined by separating the detection schemes into trigger and delimiter algorithms. A new technique for grouping ejections based on a period of quiescence between bursts was also developed. The combination of improved ejection detection and the new grouping technique have reduced the error in the time between bursts from 25% to 10%. There is a similar improvement in the uncertainty.

1. Introduction

Coherent structures within the turbulent boundary layer have been identified using many different techniques. Each uses one particular aspect of the structure for detection. This approach often provides knowledge about the detected feature without providing a complete picture of the structure.

The most complete view of the turbulent boundary layer structure was generated using Spalart's (1988) full numerical solutions of the boundary layer equations. Robinson et al. (1990), using the $Re_\delta = 680$ boundary layer from this data base, identified a Reynold Stress Producing Vortical Structure (RSPVS) containing all previous observations attributed to the wall-layer structure.

The most straightforward method to answer questions about how the RSPVSs are conceived, mature and die would be to observe a large number of samples from real flows. However, the insitu identification of RSPVSs is a problem that precludes a straightforward approach. Investigators have often tried to identify the wall-layer structure by the ejection of low-speed fluid away from the wall. Ejections are the outward excursions of fluid from a low-speed region near the wall (Kline et al., 1967). Since multiple ejections may occur within a single event named a burst (Offen & Kline, 1975, Bogard & Tiederman, 1981), ejections were subsequently grouped into bursts, which were considered to be the event of interest. These ejection/burst events were identified along the inboard side of the leg and below the neck of the RSPVS.

Techniques that have been used to identify parts of what was believed to be the dominant structure are summarized in Table 1. U is the instantaneous streamwise velocity and u is the fluctuation about the mean.

Table 1 Comparison of ejection detection techniques

Mathematical Description of Ejection Detection Techniques				
Technique	Defining Variable	Threshold Equation	Ejection Criteria	References
VITA	$\hat{v}\bar{a}r(x_i, t, T) = \hat{u}^2(x_i, t, T) - (\hat{u}(x_i, t, T))^2$ where: $\hat{u}(x_i, t, T) = \frac{1}{T} \int_{t-\frac{1}{2}T}^{t+\frac{1}{2}T} u(x_i, s) ds$	$\hat{v}\bar{a}r > k\hat{u}^2$	$\frac{du}{dt} \Big _{\text{begin}} < 0$ $\frac{du}{dt} \Big _{\text{center}} < 0$ $u < 0$	Blackwelder & Kaplan (1976) Chen & Blackwelder (1978) Bogard & Tiederman (1986) Tuberger (1991)
Zaric	$Z_1 = u \left(\frac{du}{dt} \right)$ $Z_2 = \left(\frac{du}{dt} \right)$ $Z_3 = u$	$ Z_1 > k_1(u) \left[\frac{du}{dt} \right]$	$Z_3 < 0$	Zaric (1975) Zaric (1982)
uv-Level		$uv(t) < -hu'v'$	$u(t) < 0$ and $v(t) > 0$	Lu & Willmarth (1973) Wallace et al. (1972)
u-Level		$u(t) < -Lu'$		Lu & Willmarth (1973)

An overbar denotes the mean value while a prime identifies the root mean square of the fluctuation. Blackwelder & Kaplan (1976) identified sharp shear layers that occur at the interface of burst events (Bogard & Tiederman, 1987). These sharp shear layers were located at the interface of the streamwise vortex, or "leg", and also the transverse vortex, or "head" of the RSPVS. Wallace et al. (1977) used a characteristic velocity pattern that was postulated to result from the Reynolds stress producing structure. Willmarth & Lu (1973) and Wallace et al. (1972) used a second quadrant (in u-v coordinates) technique to identify regions of the flow having low streamwise velocity and a large velocity, v, away from the wall. Zaric (1975) attempted to identify the RSPVS by searching out the regions in the flow where the streamwise momentum was changing rapidly. In addition to these techniques, a handful of new schemes created by using the older techniques as building blocks have also been tested (Aouad & Brodkey, 1990, Mao-Zhang & Bradshaw, 1988, Falco & Gendrich, 1988, Luchik & Tiederman, 1987).

With each technique identifying a part of the RSPVS, there is a need to determine which technique can identify the RSPVS most effectively. The question of single point technique performance has been considered by Bogard & Tiederman (1986), and Luchik & Tiederman (1987). However, new techniques have been published since the last critical review. One purpose of this study is to develop a systematic approach to determine which Eulerian, single point technique or combination of techniques performs the best.

A data set containing simultaneous flow visualization and two-component velocity records from the two-

dimensional channel flow of Bogard & Tiederman (1986) was used to test the techniques. The flow visualization technique based on florescent dye seeping through a wall slot was calibrated using a hydrogen bubble wire. Velocity was measured with a miniature x-wire hot film probe located at y^+ of 15.

2. Evaluation Procedure

In order to evaluate and to understand newer, compound techniques that use multiple algorithms and multiple thresholds, it was necessary to separate the components of each compound techniques for analysis. All the new compound techniques use one characteristic to turn on the detector and a separate characteristic to turn off the detector. Therefore it was natural to separate the components into a trigger or "on" function and the delimiter or "off" function. The trigger is the algorithm used to find an extreme value having a very high likelihood of being part of a detected ejection. The delimiting function, searching forward and backward from the trigger detection, determines the beginning and end of an event. Thus, the delimiter yields the amount of time that the event is taking place.

The trigger functions were evaluated using two variables, $P(A_T)$ and $P(V_T)$, defined by

$$P(A_T) = N_{AV}/N_A \quad \text{and} \quad P(V_T) = N_{VA}/N_V \quad (1)$$

N_A corresponds to the number of events detected with the algorithm, N_V corresponds to the number of events detected visually, N_{AV} is the number of algorithm detected events corresponding to some portion of a visually detected events, and N_{VA} is the number of visually detected events corresponding to some part of an event detected with the algorithm. Figure 1 contains plots which demonstrate typical records used to evaluate the terms in Equation 1. The second line represents the events detected with the VITA algorithm applied to the uv signal with threshold $k = 0.4$. For this example N_{VA} is 4, N_V is 6 and $P(V_T)$ is 0.67. In a similar fashion, $N_{AV}=7$, and $N_A=8$ so that $P(A_T)=0.875$.

Figure 2 shows that both $P(A_T)$ and $P(V_T)$ are functions of the threshold level which is used. An increasing threshold results in more accurate detections. An increasing threshold also results in fewer detections which decreases the number of visual events that correspond to the detections. Therefore the increasing threshold decreases the value of $P(V_T)$ which is the probability of a visual event being detected. When $P(A_T)$ is plotted as a function of $P(V_T)$ the accuracy of the detector is seen as a function of the probability of a visually identified ejection being detected by the trigger. This allows direct comparison of different triggers.

The trigger function is required to have a total "on" time that is less than the "on" time of the visual detection file. This limit allows the trigger to be used with a separate delimiter. Since the TPAV algorithm did not satisfy this condition, it was considered to be a complete detection algorithm by itself. Thus TPAV algorithms are considered when the trigger and delimiter are evaluated as a total scheme.

The delimiter functions were evaluated using two variables similar to those given by Equations 1. These new variables reflect the amount of time that the functions are correct. The second two variables are:

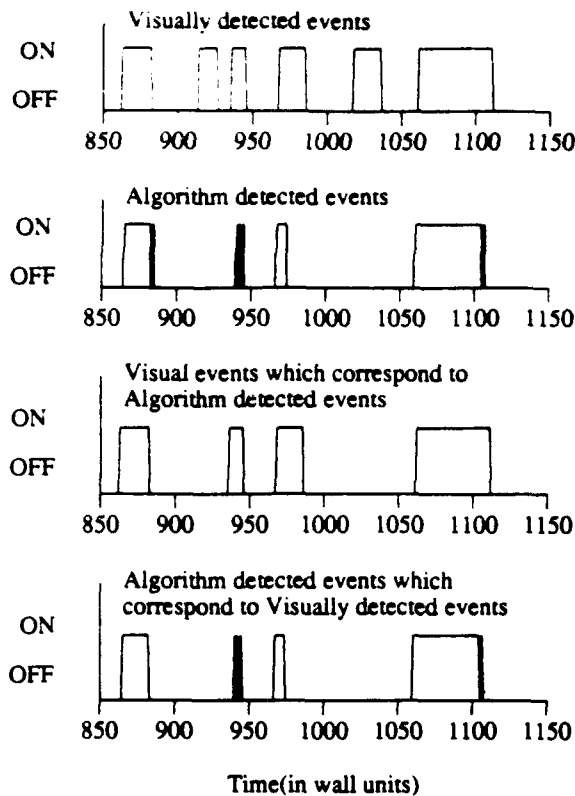


Figure 1 Example of temporal records of visual and trigger detections

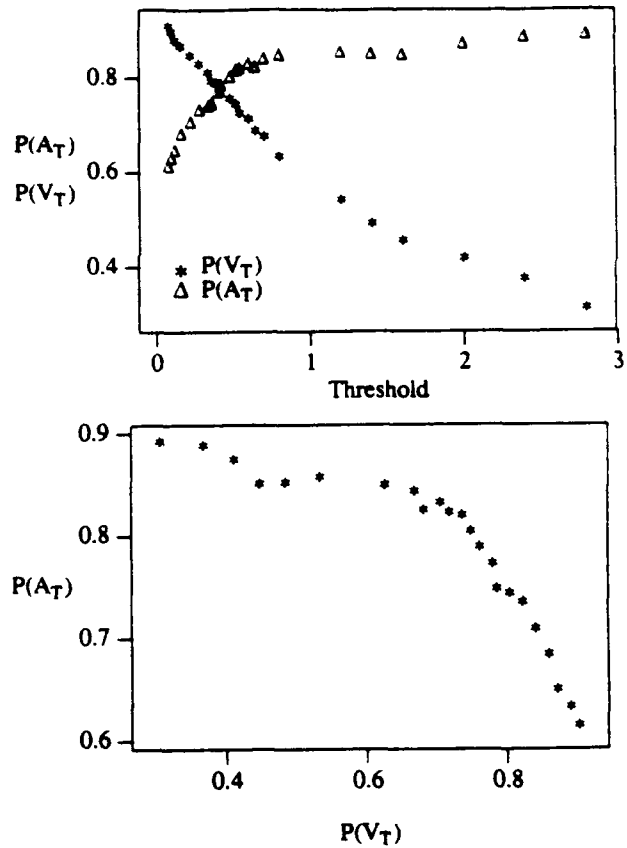


Figure 2 Cross-plot evaluation of VITA(uv)

$$P(A_D) = T_{AV}/T_A \quad \text{and} \quad P(V_D) = T_{AV}/T_V \quad (2)$$

T_A corresponds to the on time of the algorithm detected events, T_V corresponds to the on time of the visually detected events, and T_{AV} corresponds to those points in time where both detectors are "on".

Examples of the signals used to determine the quantities used in Equations 2 are demonstrated in Figure 3. The second line is from a file where VITA applied to uv is the trigger and u-level is the delimiter (VITA(uv)+u-Level) with $k=0.4$ and $h=0.15$, respectively. For the example, the visual detector identifies 124 units of time as active. The detection algorithm yielded 78 units as active, of which 70 units were also detected by the visual detector. $P(A_D)$ for this example is $70/78 = 0.92$, and $P(V_D)$ is $70/124 = 0.56$. These two variables are also functions of the threshold. As the delimiter threshold increases, the detector becomes more selective which results in less but more accurate detection of the event. $P(A_D)$ is the conditional probability of the detector being "on" and correct. $P(V_D)$ is the conditional probability that the point within a visually detected ejection was identified by the detector as an ejection. These are cross plotted so that different delimiters can be compared on the same graph.

By optimizing these four variables, a combination of trigger and delimiter can be found that has not only the highest percent of accurate detections, but also correctly represents the beginning and end of the event in time. With this division, the effectiveness of the total algorithm is more dependent upon the trigger function

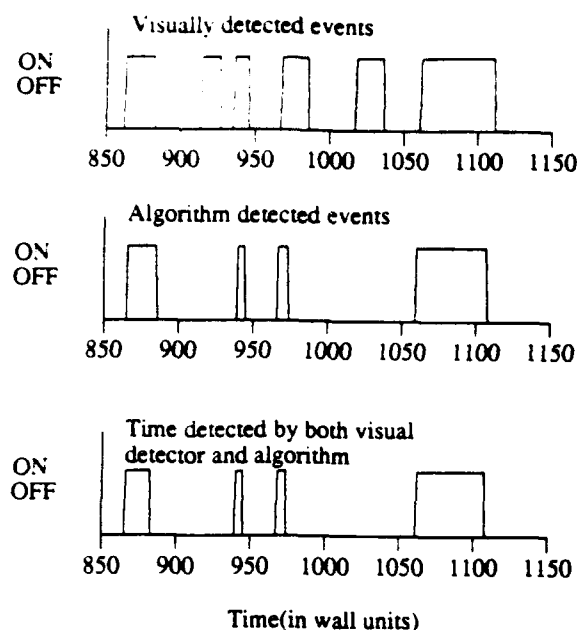


Figure 3 Example of temporal records of visual and trigger and delimiter algorithm detections

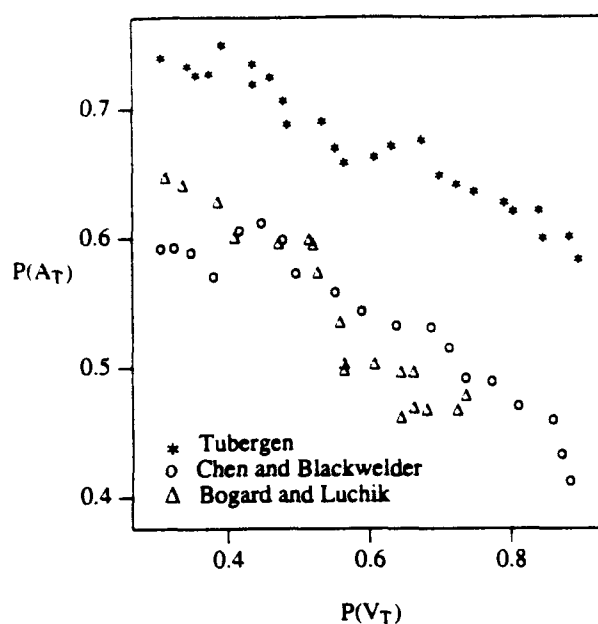


Figure 4 Signal Trigger Techniques Comparison of Slope Techniques and Sign as Second Condition with VITA

because the delimiter can not detect ejections missed by the trigger, nor can it reject false trigger detections.

The number of velocity components in the algorithm has obvious consequences. More than one velocity component increases the experimental difficulty; but, the additional data should yield a better detector. Therefore it is useful to determine both the best one-component technique, and the best overall technique.

3. Results

A random number generator was used as an ejection detector to provide a basis for comparison. The effectiveness of any technique had to surpass that of the random number generator in order to be considered. The random number generator yielded a value of 31% for $P(A_T)$ for all values of $P(V_T)$. That is, it was 31% percent accurate regardless of how many of the ejections it had detected.

The VITA technique applied to the u signal has 3 different conditions used to determine whether the detected event was an ejection or a sweep as shown in Table 1. Figure 4 shows that the Tubergen(1991) technique performs best so this is the technique used in this paper. An averaging time of 15 wall units was chosen for the VITA technique to correspond to Alfredsson & Johansson (1984) and Johansson & Alfredsson (1982). This was within a range in which the detector showed minimal change about some optimum point.

3.1. Trigger and Delimiter Analysis

The VITA and the Level techniques operate on either the u or uv product signal, while Zaric's technique functions only on the u signal. Figure 5 shows the accuracy of these techniques used as a trigger. The VITA detector operating on the uv product is slightly more accurate than the uv -Level and Zaric detectors.

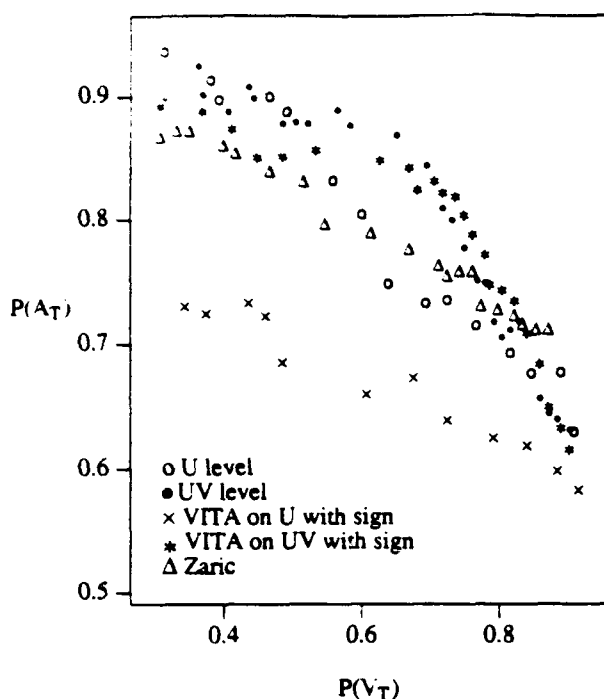


Figure 5 Comparison among trigger techniques

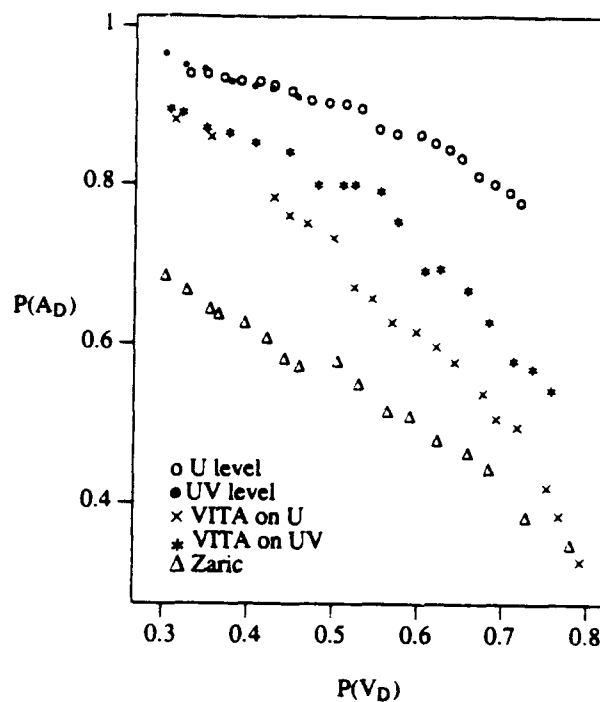


Figure 6 Comparison among delimiting techniques

Figure 6 shows the performance of the techniques used as delimiters. The Level detector schemes are the most accurate with the only distinction between them being the limited interval over which the uv-Level works. This limitation is due to the highly intermittent fluctuations in v causing the uv event to shift into quadrant III which terminates the detection. It is also interesting to note that the Zaric technique, which does well as a trigger, is the poorest performer as a delimiter.

3.2. Analysis of Compound Techniques

Luchik & Tiederman (1977) compared schemes at thresholds where the schemes were detecting the same number of ejections as detected visually. For a more rigorous comparison, the intent of this study was to match as closely as possible both the number of detections (164) and the percentage (approximately 31%) of active time between the detection scheme and the visual detections.

It is not clear whether a comparison based on the number of detections or time of detections is more appropriate. A perfect detector would match both the number and time. Of the existing techniques, only the modified u-Level (Luchik & Tiederman, 1987) could match both the time and number of detections. The remaining techniques were evaluated at two separate sets of thresholds which both appear in Table 2. One set was used to match the number of detections, while the second was used to match the active time of the flow. Additional information about the detector is gained by examining both sets of thresholds.

The most recent (Mao-Zhang & Bradshaw, 1988) improvement to detection schemes is an application of the VITA technique to the uv signal with an additional requirement on the uv level. In this study, these

Table 2 Evaluation of ejection detection schemes

Evaluation of Ejection Detection Schemes								
Technique	Threshold	Detections	P(A _T)	P(V _T)	Time	P(A _D)	P(V _D)	
	Trigger	Delimiter						
Schemes Tested by Luchik & Tiederman (1987)								
uv ₁₂	1.21	1.21	163	0.646	0.859			
VITA with Slope	0.40	0.40	166	0.579	0.613			
u-Level	1.28	1.28	163	0.634	0.773			
mu-Level	1.00	0.25	166	0.756	0.747			
Schemes Recently Proposed								
TPAV+u-Level								
Brodkey thresholds	1.500	0.400	111	0.390	0.658	11.8	0.249	0.662
Most Detections	1.500	0.100	126	0.433	0.611	14.8	0.285	0.605
VITA(uv)+uv-Level								
Match Detections	1.900	0.000	166	0.362	0.869	12.0	0.263	0.696
Match Active Time	0.400	0.000	581	0.773	0.723	31.5	0.545	0.547
TERA								
Match Detections	0.625	0.625	161	0.963	0.665	72.7	0.853	0.372
Match Detections	1.650	1.650	165	0.540	0.776	7.4	0.177	0.760
Match Active Time	0.900	0.900	298	0.847	0.667	30.4	0.534	0.557
mu-Level								
Both Matched	1.000	0.200	165	0.779	0.645	31.2	0.644	0.654
New Schemes Developed as a Result of This Study, Both Detections and Time Matched								
VITA(uv)+u-Level	0.400	0.150	167	0.773	0.755	29.3	0.626	0.678
Modified Zaric	1.050	0.150	165	0.791	0.739	30.8	0.642	0.660

concepts were used in a VITA(uv)+uv-Level method where the trigger was based on the uv product. The sign of the u-signal, as suggested by Figure 4 was used to separate ejections from sweeps and the delimiter was based on uv-Level. These changes add up to significant increases in the effectiveness of the scheme as shown in Table 2. The technique cannot simultaneously match the number of bursts and the active time so two different sets of thresholds were used. The first set matched the number of ejections, and the second matched the active time of the flow. The scheme cannot match both criteria because the rapid fluctuation in the v signal turns off the detector. The scheme detects the ejections at their beginning and end, but is dropping out somewhere in the middle, possibly multiple times. This is because the uv-level is not the best delimiter. When detecting the correct number of ejections, the system is very accurate but it detects portions of only 36% of the ejections. When the time is matched, however, approximately 600 detections are made, giving an indication of the extent of dropout.

The TERA technique of Falco & Gendrich (1988) was examined as a function of its one threshold. Thresholds in the range suggested ($k_1 < 0.4$) by Falco & Gendrich (1988) were found to be too low. At $k_1 = 0.625$, the number of detections was matched. This threshold had smoothed together much of the flow identifying 70% of it as active. To get a reasonable active time, the threshold was increased which caused dropout to appear. The system identified 300 ejections when matching the correct active time. Approximately 100 of these were the second detection of an event. At even higher thresholds the system again match the correct number of detections by eliminating some of the second detections and incorrect detections. This reduced the "on time" to 7.4%. This is less than the "on time" for the VITA(uv)+uv-Level technique showing an even greater problem with dropout. This performance is consistent with the techniques poor

performance as a delimiter.

The modified u-level thresholds used by Luchik & Tiederman (1987) were very close to the optimum found by this study when the active time was also considered. Using the time constraint, the delimiter threshold was lowered to 20%. This yielded a closer match to the active visual time. Note that in this study, the delimiter is applied both forward and backward in time. With this new delimiter, more detected events were grouped increasing $P(V_T)$, and lowering $P(A_T)$. The trigger threshold was not changed.

The mu-level technique has remained the most accurate single component technique of those that had been tested before. This is due in part to the excellent performance of the delimiter. Based on matching the number and active time of the visual detector, the mu-level outperformed all other, 1- or 2-component, techniques which existed prior to this study.

3.3. New Schemes

A new technique which combines the best trigger and delimiter should perform better than previous techniques. VITA on uv should be the trigger and u-Level the delimiter. This combination yields a slight (3%) improvement in the accuracy of the detector, $P(A_T)$, but a 15% improvement in $P(V_D)$ and a 25% increase in $P(A_D)$ compared to Mao-Zhang & Bradshaw (1988). As expected the majority of the gains are made in the detection of active time due to the change in delimiter.

As suggested by the figures the best single component ejection detector is a combination of the trigger of Zaric with a u-level delimiter. This simple modification of the Zaric technique was termed the Modified-Zaric technique. This technique performs approximately as well as the VITA(uv)+u-Level, while not having the experimental complexity of using two-component velocity data.

4. Bursts

Grouping ejections into bursts yielded a region of thresholds where the average time between burst is independent of the threshold. As the optimum thresholds for each detector has been set using only one flow, it is important that this region of threshold independence exist so that the techniques may be applied successfully to other flows. This region of threshold independence may imply that the grouped events correspond to the RSPVS.

The grouping of ejections has been done by using a grouping time (τ_g) which assumes all ejections separated by less than τ_g are from the same burst and those with greater spacing are from different bursts. Ideally, a histogram of the time between ejections would have two separate distributions; one for ejections from the same burst and one for ejections from different bursts. In reality, the two distributions have some overlap. Even though the concept of a single grouping time has some inherent error, a single grouping time can be used to determine a region of threshold independence for the detection techniques. For overlapping distributions, a grouping time is determined using the histogram of the time between ejections plotted on a semi-log scale. The distribution of times between ejections within the same burst and the time between

ejections in different bursts should both decrease exponentially, yielding two linear sections with a region in between where the distributions overlap. A grouping time is then chosen between τ_1 and τ_2 which indicate the extent of the overlap region. White (1989) used an average of τ_1 and τ_2 . The uncertainty in τ_g was half of the width between τ_1 to τ_2 . The propagation of this uncertainty was the major contributor to the uncertainty in the normalized time between burst events $\overline{T_B}$.

This technique of grouping shows the VITA(uv)+u-Level (Figure 7) technique has a region independent of both the trigger and the delimiter threshold ($0.4 < k < 0.8$, $0.1 < h_D < 0.2$). The Zaric+u-Level technique does not exhibit a threshold independent region.

In an attempt to reduce the uncertainty and to improve the estimate of $\overline{T_B}$, velocity signals were investigated to see if they could be used to determine the division between ejections in the same and different bursts. It was hypothesized that between ejections from different bursts, there should exist some time in which the flow is in an quiescent phase. This would not be true of the period of time between ejections from the same bursts. An additional detector is needed that would detect quiet time instead of active time.

The VITA detector was chosen to detect quiet time because minima in the VITA signal correspond to quiet time. This appears to be the only detector which would detect quiet time effectively. The other techniques detect extrema associated with ejections, while the opposite extrema is associated with sweeps. Some average level occurs during quiet times.

Using the VITA signal to determine quiescent period of flow requires an additional threshold which was set by using the same probability graph used for the τ_g technique. Since τ_1 corresponds to the smallest separation time between two ejections from different bursts, the VITA(uv) threshold was set so that all ejections with spacings below τ_1 were grouped. This threshold level varied but was typically in the range of $0.01 < k < 0.10$.

Since only approximately 75 bursts exist in Bogard's data file, the semi-log plots of τ_g are not as smooth as those from larger data sets. This leads to uncertainty in the value for τ_1 . This was overcome by choosing two points which were the upper and lower limits for τ_1 . The lower bound was chosen by being hyper-sensitive in determining the first deviation from the first linear portion of the graph. The upper bound was established by requiring an obvious deviation. These values were also used to determine the uncertainty in $\overline{T_B}$.

In evaluating the data and the technique, both values were to determine the threshold for the VITA(uv) grouping. The lower value of τ_1 yielded a lower threshold and grouped fewer events causing a value for $\overline{T_B}$ which was too low compared to the visual result. The second value of τ_1 had the opposite effect causing $\overline{T_B}$ to be too high. Both choices had a threshold independent region for $\overline{T_B}$ as shown in Figure 8.

To determine the value of the bursting period for a set of thresholds, the average of the upper and lower bound of τ_1 was used to yield $\overline{T_B} \approx 186$. This value is within 5% of the value obtained by Bogard using

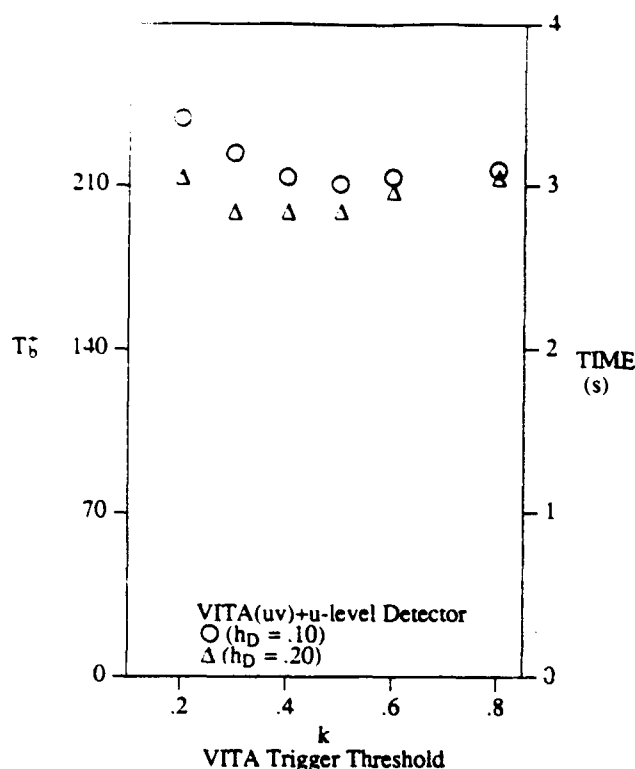


Figure 7 Dependence of bursting period for the VITA(uv)+u-Level scheme on both thresholds

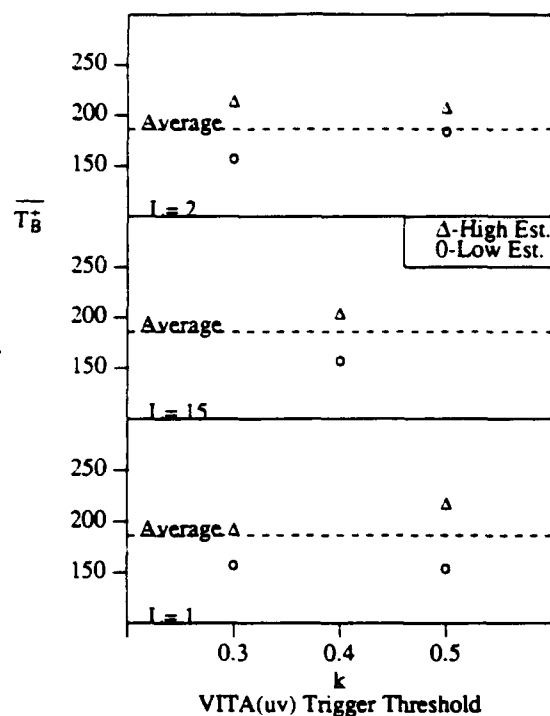


Figure 8 Dependence of bursting period for the VITA(uv)+u-Level scheme on both thresholds grouped with the VITA(uv) grouping technique.

hydrogen bubble flow visualization. The uncertainty in $\overline{T_B}$ was reduced. The previous τ_g technique had an uncertainty of about 25%. The VITA(uv) grouping technique has about 15% uncertainty. Table 3 indicates the improvements which have been made.

Table 3 Comparison of burst detection techniques

Comparison of Eulerian Techniques to Lagrangian Techniques		
Technique	Time, $\overline{T_B}$	Uncertainty
Lagrangian Techniques		
Hydrogen Bubbles	168	
Dye-Plane Lighting	172	
Dye-Full Lighting	168	
Eulerian Techniques		
uv/2 with τ_{group} grouping	212	25
mu-Level with τ_{group} grouping	225	25
VITA(uv)+u-Level with VITA(uv) grouping	186	15

VITA(u) was investigated to see if it would perform better as a grouping function on the single component techniques; however, VITA(u) yielded the wrong answer for $\overline{T_B}$ for both mu-Level and Zaric+u-Level techniques. Once it was determined that it could not produce the correct answer the investigation was discontinued. Since the other velocity characteristics identify ejections as one extrema and sweeps as the other extrema, no other systems were investigated for use as a grouping parameter.

5. Conclusions And Recommendations

The study suggests the use of either a new single-component technique or a new two-component technique. Using a single component of velocity, the Modified Zanic technique demonstrated better ejection detection but did not exhibit a region of threshold independence for ejections grouped into bursts. The best single-component ejection detector with threshold independence for bursts is the modified u-Level technique. The new two-component system, VITA(uv)+u-Level, was the best overall ejection detector and also had a region of threshold independence for the bursting period.

A new technique requiring a period of quiescent flow between two ejections from different bursts was used to group ejections into bursts. VITA(uv) was used to determine that the flow was quiescent. The VITA(uv)+u-Level technique with the VITA(uv) grouping yielded a more accurate time for the bursting period. The uncertainty in the value of $\overline{T_B}$ was reduced to 15%.

With a single probe, there is no information about which part of the event is being detected. Therefore, the most logical next step is to use multiple probe techniques. Since each ejection detector looks for a different characteristic and therefore a different part of the vortical structure, the use of multiple probes would lead to the ability to determine phase relationship between the different parts of the RSPVS. This type of phase relation would make it possible to more accurately detect turbulent structures in the flow.

REFERENCES

- ALFREDSSON, P.H. & JOHANSSON, A.V., 1984 On the detection of turbulence-generating events. *J. Fluid Mech.*, 50, 325-345.
- AOUAD, Y.G. & BRODKEY, R.S., 1990 Pattern Recognition, VITA, U-signal slope and Quadrant Splitting: A comparison for channel flow. Preprints of Symposium on Turbulence 1990, University of Missouri-Rolla.
- BLACKWELDER, R.F. & KAPLAN, R.E., 1976 On the wall structure of the turbulent boundary layer. *J. Fluid Mech.*, 76, 89-112.
- BOGARD, D.G. & TIEDERMAN, W.G., 1986 Burst detection with single-point velocity measurements. *J. Fluid Mech.*, 162, 389-414.
- CHEN, C.H. & BLACKWELDER, R.F., 1978, Large scale motion in a turbulent boundary layer using temperature contamination. *J. Fluid Mech.*, 89, 1-31.
- FALCO, R.E. & GENDRICH, C.P., 1988, The turbulence detection algorithm of Z. Zanic'. in Near-Wall Turbulence, ed. Kline, S.J. & Afgan, N.H., 911-931.
- JOHANSSON, A.V. & ALFREDSSON, P.H. 1982 On the structure of turbulent channel flow. *J. Fluid Mech.*, 122, 295-314.
- KLINE, S.J., REYNOLDS, W.C., SCHRAUB, F.A., & RUNSTADLER, P.W., 1967, The structure of turbulent boundary layers. *J. Fluid Mech.*, 30, 741-773.
- LU, S.S. & WILLMARTH, W.W., 1973 Measurements of the structure of the Reynolds Stress in a turbulent boundary layer. *J. Fluid Mech.*, 60, 481-511.
- LUCHIK, T.S. & TIEDERMAN, W.G., 1987 Timescale and structure of ejections and bursts in turbulent channel flows. *J. Fluid Mech.*, 174, 529-552.
- MAO-ZHANG, C., & BRADSHAW, P., 1988, Studies of burst-detection schemes by use of direct simulation data for fully-turbulent channel flow. Preprints of Symposium on Turbulence 1988, University of Missouri-Rolla.
- OFFEN, G.R. & KLINE, S.J., 1975, A comparison and analysis of detection methods for the measurements of production in a boundary layer. Symposium of Turbulence in Liquids, University of Missouri-Rolla. 289-320.

ROBINSON, S.K., KLINE, S.J., & SPALART, P.R., 1990, Quasi-Coherent structures in the turbulent boundary layer: Part II. Verification and new information from a numerically simulated flat-plate layer. Near-Wall Turbulence, ed. Kline, S.J. & Afgan, N.H., 218-247.

SPALART, P., 1988, Direct simulation of a turbulent boundary layer up to $Re = 1410$. *J. Fluid Mech.*, 187, 61-98.

TUBERGEN, R.G., 1991, Evaluation of ejection detection schemes in turbulent flow. MSE thesis, Purdue University.

WALLACE, J.M., BRODKEY, R.S. & ECKELMANN, H., 1977, Pattern-recognized structures in bounded turbulent shear flows. *J. Fluid Mech.*, 83, 673-693.

WALLACE, J.M., ECKELMANN, H., & BRODKEY, R.S., 1972, The wall region in turbulent shear flow. *J. Fluid Mech.* 54, 34-48.

WHITE, J.B., 1989, The effect of adverse pressure gradient on the turbulent burst structure in low-Reynolds number equilibrium boundary layers. MSE thesis, Purdue University.

ZARIC, Z.P., 1975, Wall Turbulence Structure and Convection Heat Transfer, *Int. J. Heat Mass Transfer.*, 18, 831-842.

ZARIC, Z.P., 1982, Conditionally Averaged Patterns of Coherent Events in a Wall-bounded Turbulent Flow. In Structure of Turbulence in Heat and Mass Transfer, ed. Zaric, Z. 7-28.

SPATIAL RESOLUTION OF WALL-TRANSFER PROBES

B. Py

Institut universitaire de technologie
29287 Brest Cedex, France

Abstract

The behaviour of both hot-film and electrochemical sensor is similarly described by the thermal or mass balance and the transfer equation at the wall. In a homogeneous field or for point transducers, the wall shear can be consistently deduced from the transfer since the number of signals and unknowns coincide. Unfortunately, owing to the finite size of the sensor, if one can no longer consider the wall shear as independent of space, new unknowns appear and the measurement method becomes inconsistent.

The influence of four parameters which characterize the non-uniformity of the velocity field is studied for low and high values of these variables. The results indicate that the evolution of the wall-shear field over the transducer introduces an uncertainty on the measurement position which is smaller than half the sensor length. For highly inhomogeneous fields, such as the vicinity of a stagnation or a separation line, some transducers also give reliable values up to distances of half an electrode length.

List of symbols

A	total area of the transducer
A_j	area of the part j of the transducer
C	concentration (or temperature)
C_∞	bulk concentration
D	diffusion coefficient
K	transfer coefficient of the electrode
K_j	transfer coefficient of the part j of the electrode
S_x, S_z	components of the wall shear
S_{x0}, S_{z0}	components of the wall shear at the center of the electrode
S_r	relative velocity gradient (S_x/S_{x0})
V	velocity
V_x, V_y, V_z	components of the velocity
L	electrode length
t	time
w	width of the electrode

x	direction of the flow
y	direction normal to the wall
z	spanwise direction
ΔK	difference between the transfer coefficients
η	similarity variable
ψ	similarity function

1. Introduction

The behaviour of both the hot-film and the electrochemical sensor is similarly described by the mass or thermal balance and the transfer equation at the wall:

$$\frac{\partial C}{\partial t} + \vec{V} \cdot \vec{\text{grad}} C = D \frac{\partial^2 C}{\partial y^2} \quad (1)$$

$$K_j = \frac{D}{C_\infty} \frac{1}{A} \iint_{A_j} \left(-\frac{\partial C}{\partial y} \right)_{y=0} dA \quad (2)$$

C is the concentration or the temperature. C is zero on the electrode and C_∞ in the bulk of the solution. V is the velocity, D the diffusion coefficient, t the time, A_j the area of the part j of the transducer and A its total area. The transfer coefficient K_j is the signal delivered on the part j of the transducer and y the distance perpendicular to the wall.

In the inverse transfer problem, the velocity field is a priori dependent on a lot of parameters. One way of making them appear consists in developing it in a Taylor series. The origin of the development is taken at the center of the transducer (index o). One takes into account the continuity equation and the no-slip condition at the wall. The first order development expresses the field versus the components of the wall velocity gradients S_{x0} and S_{z0} :

$$\begin{aligned} V_x(x,y,z,t) &= y S_{x0}(t) \\ V_y(x,y,z,t) &= 0 \\ V_z(x,y,z,t) &= y S_{z0}(t) \end{aligned} \quad \text{with} \quad \begin{aligned} S_{x0}(t) &= \left(\frac{\partial V_x}{\partial y} \right)_{\substack{x=0 \\ z=0}} \\ S_{z0}(t) &= \left(\frac{\partial V_z}{\partial y} \right)_{\substack{x=0 \\ z=0}} \end{aligned} \quad (3)$$

Then, the velocity field is characterized by two time-dependent parameters (only one in two-dimensional flow). The number of signals $K_j(t)$ received on a double electrode (simple in two-dimensional flow) very exactly corresponds to the number of flow parameters. As far as the transducer is point or the first order development sufficient, no hypothesis about the characteristics of the flow is necessary and the measurement method is consistent.

Unfortunately, owing to the finite size of the transducer, if one can no longer consider $S(t)$ as independent of space, the method becomes inconsistent. For example, if we develop the wall shear field at the second order:

$$\begin{aligned} V_x(x,y,z,t) &= y S_{x0} + xy \frac{\partial S_{x0}}{\partial x} + yz \frac{\partial S_{x0}}{\partial z} \\ V_y(x,y,z,t) &= -\frac{y^2}{2} \left(\frac{\partial S_{x0}}{\partial x} + \frac{\partial S_{z0}}{\partial z} \right) \\ V_z(x,y,z,t) &= y S_{z0} + xy \frac{\partial S_{z0}}{\partial x} + yz \frac{\partial S_{z0}}{\partial z} \end{aligned} \quad (4)$$

we make appear four extra unknowns. Two of them induce, by continuity equation, a significant velocity normal to the wall (eqs. 4). The only interest of these new parameters in the measurement technique, will be an estimation of its limits. For this purpose, we shall successively examine the influence of every new unknown parameter.

2. Streamwise evolution of the streamwise wall shear field.

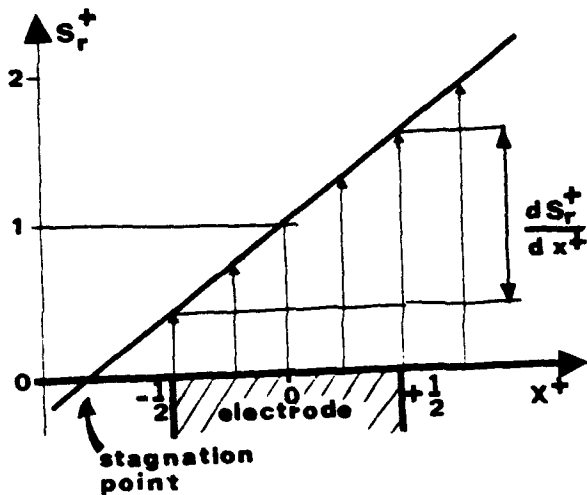


Fig. 1 Streamwise evolution of the streamwise wall shear component.

The x axis is chosen in the flow direction. The evolution of the wall shear S over each point of the transducer expresses by:

$$S = S_0 + x \frac{\partial S_0}{\partial x} \quad (5)$$

S_0 is the wall shear value at the center of the electrode and $\partial S_0 / \partial x$ is a constant. In the quasi-steady state the mass balance (1) is then described by:

$$S y \frac{\partial C}{\partial x} - \frac{\partial S}{\partial x} \frac{y^2}{2} \frac{\partial C}{\partial y} = D \frac{\partial^2 C}{\partial y^2} \quad (6)$$

The following transformation (Py 1973) in which ℓ is the total transducer length:

$$\begin{aligned} C^+ &= \frac{C}{C_\infty} & x^+ &= \frac{x}{\ell} & z^+ &= \frac{z}{\ell} \\ S^+ &= \frac{S \ell^2}{D} & K^+ &= \frac{K \ell}{D} & y^+ &= \frac{y}{\ell} S_0^{+1/3} \end{aligned} \quad (7)$$

renders dimensionless the mass balance and the transfer equation

$$\frac{S^+}{S_0^+} y^+ \frac{\partial C^+}{\partial x^+} - \frac{\partial S^+ / \partial x^+}{S_0^+} \frac{y^{+2}}{2} \frac{\partial C^+}{\partial y^+} = \frac{\partial^2 C^+}{\partial y^{+2}} \quad (8)$$

$$K^+ = S_{x0}^{+1/3} \int_{-1/2}^{+1/2} \left(\frac{\partial C^+}{\partial y^+} \right)_{y^+=0} dx^+ \quad (9)$$

By introducing the relative gradient $S_r^+ = S^+/S_0^+$ such as $S_r^+ = 1$ at the center of the transducer and $\partial S_r^+ / \partial x^+$ represents the variation of the relative wall shear over the electrode (fig. 1), the mass balance (8) becomes :

$$S_r^+ y^+ \frac{\partial C^+}{\partial x^+} - \frac{\partial S_r^+}{\partial x^+} \frac{y^{+2}}{2} \frac{\partial C^+}{\partial y^+} = \frac{\partial^2 C^+}{\partial y^{+2}} \quad (10)$$

Equations (9) and (10) can be solved by introducing the similarity variable η (Lévéque 1928) :

$$\eta = \frac{y^+}{\psi(x^+)} \quad (11)$$

It results that :

$$\frac{\partial C^+}{\partial x^+} = \frac{dC^+}{d\eta} y^+ \left(-\frac{1}{\psi^2}\right) \psi'$$

$$\frac{\partial C^+}{\partial y^+} = \frac{dC^+}{d\eta} \frac{1}{\psi}$$

$$\frac{\partial^2 C^+}{\partial y^{+2}} = \frac{d^2 C^+}{d\eta^2} \frac{1}{\psi^2}$$

When replacing these values in the mass balance equation (10), one gets :

$$- (S_r^+ \psi^2 \psi' + \frac{\partial S_r^+}{\partial x^+} \frac{\psi^3}{2}) \eta^2 \frac{dC^+}{d\eta} = \frac{d^2 C^+}{d\eta^2} \quad (12)$$

If the similarity variable is chosen such as :

$$S_r^+ \psi^2 \psi' + \frac{\partial S_r^+}{\partial x^+} \frac{\psi^3}{2} = 3 \quad (13)$$

the solution of the mass balance (12) is :

$$C^+ = \frac{\int_0^\eta e^{-\eta^3} d\eta}{0.8930} \quad (14)$$

Supposing that S_r^+ does not annulate on the electrode (no stagnation point on the electrode), the variables ψ and x can be separated in eq. (13) :

$$\frac{\psi^2 d\psi}{3 - \frac{\partial S_r^+}{\partial x^+} \frac{\psi^3}{2}} = \frac{dx^+}{1 + x^+ \frac{\partial S_r^+}{\partial x^+}}$$

The integration of this equation, taking into account the condition $x^+ = -1/2 \Rightarrow \psi(x^+) = 0$ on the leading edge of the transducer, allows the determination of the ψ function :

$$\psi^3(x^+) = \frac{6}{\frac{\partial S_r^+}{\partial x^+}} \left[1 - \left(\frac{1 + x^+ \frac{\partial S_r^+}{\partial x^+}}{1 - \frac{1}{2} \frac{\partial S_r^+}{\partial x^+}} \right)^{-3/2} \right]$$

It results that the space average which appears in the transfer equation (9), is only a function of $\partial S_r^+ / \partial x^+$:

$$\left(\frac{\partial C^+}{\partial y^+}\right)_{y^+=0} = \left(\frac{dC^+}{dn} \frac{\partial n}{\partial y^+}\right)_{y^+=0} = \frac{1}{0.8930} \frac{1}{\psi(x^+)}$$

$$\int_{-1/2}^{+1/2} \left(\frac{\partial C^+}{\partial y^+}\right)_{y^+=0} dx^+ = \int_{-1/2}^{+1/2} \frac{1}{0.8930} \frac{dx^+}{\psi(x^+)}$$

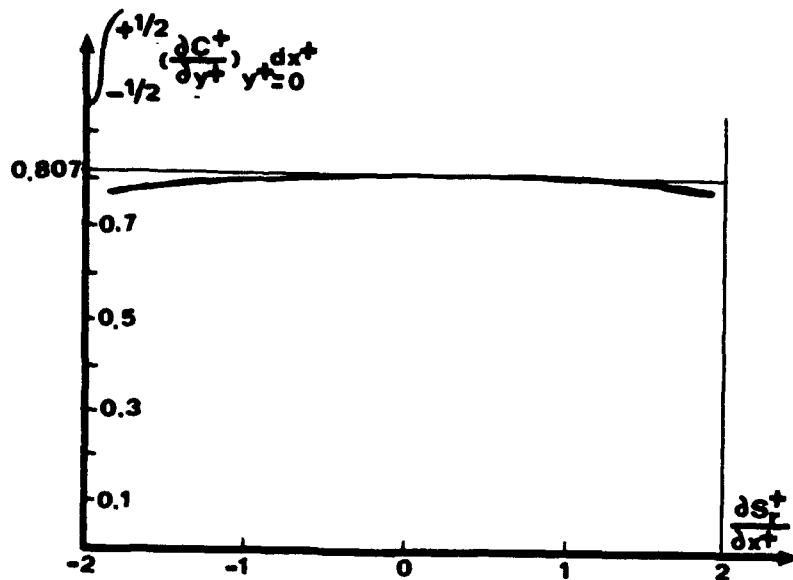


Fig. 2 Space-averaged concentration gradient versus $\partial S_r^+ / \partial x^+$.

This space average was tabulated and related on fig. 2 for the values of $\partial S_r^+ / \partial x^+$ to which it applies ($-2 < \partial S_r^+ / \partial x^+ < +2$). The result is remarkable. The space-averaged concentration gradient is nearly independent of $\partial S_r^+ / \partial x^+$ and close to the value 0.807 (Dimopoulos and Hanratty 1968) for uniform flow. The variation is only 4.5% when $\partial S_r^+ / \partial x^+ = \pm 2$, that is to say when a stagnation or a separation line is located on the leading or trailing edge of the transducer. Even in these border-line cases the sensor indicates the value of the wall shear which prevails at the center of the transducer.

differential electrodes.

As the single electrode is insensitive to the evolution of the wall shear (eq. 5), the velocity gradient at the center of the electrode is such as (eq. 9) :

$$\frac{K_1 \ell}{\varnothing} = 0.807 \left(\frac{S_0 \ell^2}{\varnothing} \right)^{1/3} \quad (16)$$

The upstream electrode constitutes an independent electrode so that we also have from eqs. (5) and (16) :

$$\frac{2K_1 \ell/2}{\varnothing} = 0.807 \left[\frac{(S_0 - \frac{\ell}{4} \frac{\partial S_0}{\partial x}) (\frac{\ell}{2})^2}{\varnothing} \right]^{1/3} \quad (17)$$

From the difference between (16) and (17), one calculates the transfer coefficient K_2 on the downstream part of the electrode :

$$\frac{K_2 \ell}{\rho} = 0.807 \left(\frac{S_0 \ell^2}{\rho} \right)^{1/3} \left[1 - \left(\frac{1}{2} \right)^{2/3} \left(1 - \frac{\ell}{4} \frac{\partial S_0}{\partial x} \frac{1}{S_0} \right)^{1/3} \right] \quad (18)$$

From (17) and (18) we deduce :

$$\frac{(K_1 - K_2) \ell}{\rho} = 0.807 \left(\frac{S_0 \ell^2}{\rho} \right)^{1/3} \left[1.260 \left(1 - \frac{\ell}{4} \frac{\partial S_0}{\partial x} \frac{1}{S_0} \right)^{1/3} - 1 \right] \quad (19)$$

Then the differential electrode is sensitive to the streamwise evolution of the wall shear. Numerical study of eq. (19) shows that the transducer indicates the value of the wall shear which prevails on its leading edge for large values of $\partial S_r^+ / \partial x^+ = (\partial S_0 / \partial x)(\ell / S_0)$. For smaller values, the first order development of (19) leads to :

$$\Delta K^+ = 0.807 \cdot 0.260 \left(1 - 0.4038 \frac{\partial S_0}{\partial x} \frac{\ell}{S_0} \right) S_0^{+1/3} \quad (20)$$

such as the measured wall shear is the wall shear which prevails on a point located on the upstream part of the electrode. Although the relative error can be important for large values of $\partial S_r^+ / \partial x^+$, the spatial resolution is always equal or better than half the electrode length for both the simple and differential sensors.

3. Spanwise evolution of the streamwise wall shear component.

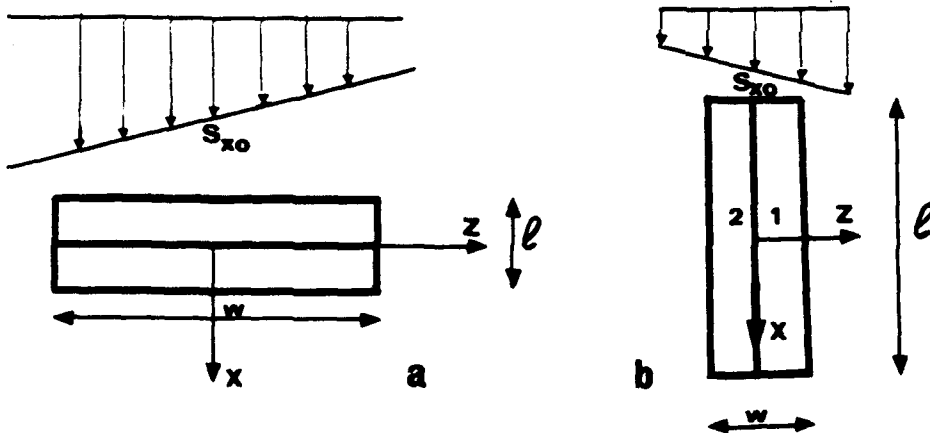


Fig. 3 a and b, Spanwise evolution of the streamwise wall shear component.

The wall shear field expresses by :

$$S_x = S_{x0} + z \frac{\partial S_{x0}}{\partial z} \quad (21)$$

and is related on fig. 3 a and b. For a given value of z , the transfer coefficient is (eq. 16) :

$$\frac{K(z) \ell}{\rho} = 0.807 \frac{(S_{x0} + z \frac{\partial S_{x0}}{\partial z}) \ell^2}{\rho}^{1/3}$$

The first order development leads to :

$$\frac{K(z) \ell}{D} = 0.807 \left(\frac{S_{x0} \ell^2}{D} \right)^{1/3} \left(1 + \frac{z}{3} \frac{\partial S_{x0}}{\partial z} \frac{1}{S_{x0}} \right)$$

If w is the width of the transducer, the space-averaged coefficient expresses by :

$$\frac{K \ell}{D} = 0.807 \left(\frac{S_{x0} \ell^2}{D} \right)^{1/3} \frac{1}{w} \int_{-w/2}^{+w/2} \left(1 + \frac{z}{3} \frac{\partial S_{x0}}{\partial z} \frac{1}{S_{x0}} \right) dz$$

which reduces to :

$$K^+ = 0.807 S_{x0}^{+1/3} \quad (22)$$

In the configuration described on fig. 3 a, the sensor is insensitive to a spanwise evolution of the wall shear. This result also applies to the differential electrodes except in the configuration of fig. 3 b. Then the response of the element 1 is :

$$\begin{aligned} \frac{2K_1 \ell}{D} &= 0.807 \left(S_{x0}^+ + \frac{w}{4} \frac{\partial S_{x0}^+}{\partial z} \right)^{1/3} \\ &= 0.807 S_{x0}^{+1/3} \left(1 + \frac{w}{12} \frac{\partial S_{x0}^+}{\partial z} \frac{1}{S_{x0}^+} \right) \end{aligned}$$

The response of element 2 is :

$$\frac{2K_2 \ell}{D} = 0.807 S_{x0}^{+1/3} \left(1 - \frac{w}{12} \frac{\partial S_{x0}^+}{\partial z} \frac{1}{S_{x0}^+} \right)$$

The difference expresses then as :

$$\begin{aligned} \frac{(K_1 - K_2) \ell}{D} &= \Delta K^+ = 0.807 S_{x0}^{+1/3} \frac{1}{12} \frac{w}{\ell} \frac{\partial S_{x0}^+}{\partial z} \frac{1}{S_{x0}^+} \\ \Delta K^+ &= K^+ \frac{1}{12} \frac{w}{\ell} \frac{\partial S_{x0}^+}{\partial z} \frac{1}{S_{x0}^+} \end{aligned} \quad (23)$$

Then an interference is introduced in the response of the split electrodes. Their advantage is the possession, in the configuration on fig. 3 b, of a very low aspect ratio w/ℓ which minimizes the influence of this signal.

4. Streamwise evolution of the spanwise wall shear component.

The evolution of the spanwise wall shear related on fig. 4, is expressed by :

$$S_z = S_{z0} + x \frac{\partial S_{z0}}{\partial x}$$

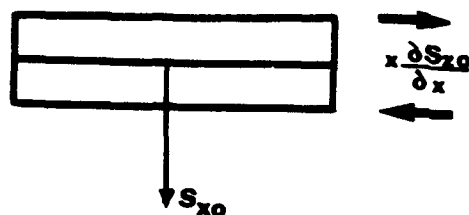


Fig. 4 Streamwise evolution of the spanwise wall shear component.

In the quasi-steady state hypothesis, the mass balance (1) expresses by :

$$y S_{x0} \frac{\partial C}{\partial x} + y S_{z0} \frac{\partial C}{\partial z} + y x \frac{\partial S_{z0}}{\partial x} \frac{\partial C}{\partial z} = \rho \frac{\partial^2 C}{\partial y^2}$$

or, introducing the transformation (7) and choosing the mean flow in the x direction :

$$y^+ \frac{\partial C^+}{\partial x^+} + y^+ x^+ \frac{\partial S_{z0}^+}{\partial x^+} \frac{1}{S_{x0}^+} \frac{\partial C^+}{\partial z^+} = \frac{\partial^2 C^+}{\partial y^{+2}} \quad (24)$$

For orientated electrodes in the flow direction or normal to the flow (fig. 4), $\partial C^+ / \partial z^+ = 0$ except at their extremities. On the other hand $(\partial S_{z0}^+ / \partial x^+) (1/S_{x0}^+)$ is a small term of the first order. It results that the product of these terms is negligible. $\partial S_{z0} / \partial x$ does not intervene in the signal.

5. Spanwise evolution of the spanwise wall shear component.

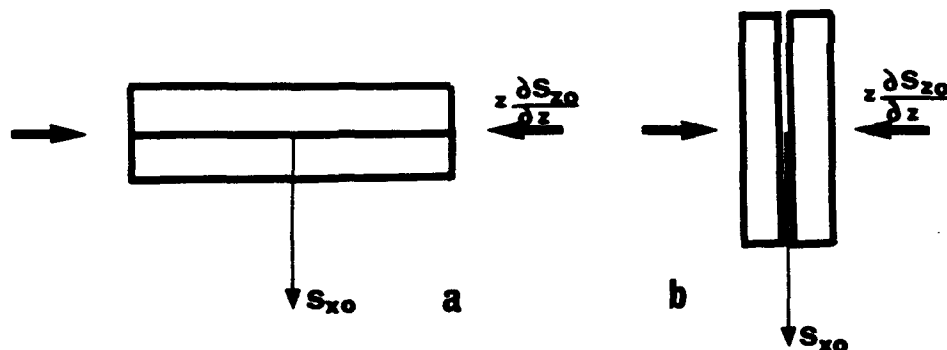


Fig. 5 a and b, Spanwise evolution of the spanwise wall shear component.

For a flow in the x direction, the wall shear field related on fig. 5 is described by :

$$S_z = z \frac{\partial S_{z0}}{\partial z}$$

For the same reasons as in the above paragraph, the effect of this term would be negligible if the continuity equation did not impose a velocity component normal to the wall whose value is (eq. 4) :

$$v_y = \gamma y^2 \quad \text{with} \quad \gamma = -\frac{1}{2} \frac{\partial S_{z0}}{\partial z}$$

In the quasi-steady state hypothesis, the mass balance (1) expresses as :

$$S_{x0} y \frac{\partial C}{\partial x} + \gamma y^2 \frac{\partial C}{\partial y} = \rho \frac{\partial^2 C}{\partial y^2} \quad (25)$$

and can be written in a dimensionless form by eqs. (7) and (26) :

$$\gamma^+ = \frac{\gamma \ell^3}{\theta} = -\frac{1}{2} \frac{\partial S_{zo}^+}{\partial z^+} \quad (26)$$

$$y^+ \frac{\partial C^+}{\partial x^+} + \frac{\gamma^+}{S_{xo}^+} y^{+2} \frac{\partial C^+}{\partial y^+} = \frac{\partial^2 C^+}{\partial y^{+2}} \quad (27)$$

Introducing as in paragraph 2, the similarity variable $\eta = y^+/\psi(x^+)$, the mass balance (27) reduces to :

$$-\eta^2 \frac{dC^+}{d\eta} (\psi^2 \psi' - \frac{\gamma^+}{S_{xo}^+} \psi^3) = \frac{d^2 C^+}{d\eta^2} \quad (28)$$

By putting :

$$\psi^2 \psi' - \frac{\gamma^+}{S_{xo}^+} \psi^3 = 3 \quad (29)$$

one finds again eq. (14) as the solution of the mass balance (28). However, the similarity function ψ is no longer the same. It is now defined by (29) and, with the initial condition $x^+ = 0 \Rightarrow \psi(0) = 0$, integrates on the form :

$$\psi = \left[\frac{3(e^{3\frac{\gamma^+}{S_{xo}^+} x^+} - 1)}{\gamma^+/S_{xo}^+} \right]^{1/3} \quad (30)$$

As previously, the concentration gradient at the wall expresses by :

$$\left(\frac{\partial C^+}{\partial y^+} \right)_{y^+=0} = \left(\frac{dC^+}{d\eta} \right)_{\eta=0} \left(\frac{\partial \eta}{\partial y^+} \right)_{y^+=0} = \frac{1}{0.8930} \frac{1}{\psi(x^+)} \quad (31)$$

Expanding the exponential, in (30) to the second order allows to calculate the first order development of the space-averaged concentration gradient :

$$\int_0^1 \left(\frac{\partial C^+}{\partial y^+} \right)_{y^+=0} dx^+ = 0.807 \left(1 - \frac{2}{5} \frac{\gamma^+}{S_{xo}^+} \right) \quad (32)$$

and then the transfer coefficient (9) :

$$K^+ = 0.807 \left(1 + \frac{1}{5} \frac{\partial S_{zo}^+}{\partial z^+} \frac{1}{S_{xo}^+} \right) S_{xo}^{+1/3} \quad (33)$$

The sensor is sensitive to that non-uniformity of the wall shear field.
Differential electrodes.

As in paragraph 2, the upstream part of the electrode (fig. 5 a) behaves as a single electrode with a $\ell/2$ length. Then :

$$\frac{2K_1}{\theta} \frac{\ell}{2} = 0.807 \left(1 - \frac{2}{5} \frac{\gamma}{S_{xo}} \frac{\ell}{2} \right) \left(\frac{S_{xo} (\frac{\ell}{2})^2}{\theta} \right)^{1/3} \quad (34)$$

$K_2 = K - K_1$ is calculated by the difference between (33) and (34). A first order expansion of

$\pm K^+ = (K_1 - K_2) \ell / D$ leads to :

$$\Delta K^+ = 0.807 S_{x0}^{+1/3} 0.260 \left(1 - 0.284 \frac{\partial S_{z0}^+}{\partial z^+} \frac{\ell}{S_{x0}^+} \right) \quad (35)$$

The signals sum (K^+) and difference (ΔK^+) do not possess the same sensitivity to $(\partial S_{z0} / \partial z)(\ell / S_{x0})$. A linear combination of the two signals can be performed which is insensitive to this term. This is particularly important in turbulence measurements at the wall because the spanwise length scales are very small.

The case of the electrode oriented as in fig. 5 b is important. Generally it occurs in turbulence or when the electrode is over a three-dimensional separation line where the wall shear does not annulate. The enlargement or the reduction of the transfer which results from the velocity component perpendicular to the wall and induced by $\partial S_{z0} / \partial z$, is the same over the two parts of the electrode. By difference, the errors annulate and ΔK is independant of $\partial S_{z0} / \partial z$. A more detailed demonstration was published (Tournier and Py 1973).

6. Conclusion.

Elementary non-uniformity	Electrode array			
	K	Measured ΔK	Greatness K	ΔK
$\frac{\partial S_{x0}}{\partial x}$	1	$1 - 0.4038 \frac{\partial S_{x0}}{\partial x} \frac{\ell}{S_{x0}}$	1	1
$\frac{\partial S_{x0}}{\partial z}$	1	1	1	$1 + K \frac{1}{12} \frac{\ell}{z} \frac{\partial S_{x0}}{\partial z} \frac{\ell}{S_{x0}}$
$\frac{\partial S_{z0}}{\partial x}$	1	1	1	1
$\frac{\partial S_{z0}}{\partial z}$	$1 + 0.2 \frac{\partial S_{z0}}{\partial z} \frac{\ell}{S_{x0}}$	$1 - 0.284 \frac{\partial S_{z0}}{\partial z} \frac{\ell}{S_{x0}}$	$1 + 0.2 \frac{\partial S_{z0}}{\partial z} \frac{\ell}{S_{x0}}$	1

Fig. 6 Influence of the elementary non-uniformity on the transfer coefficient.

Fig. 6 summarizes the influence, on the transfer coefficients, of the non-uniformity of the wall shear field. Sixteen cases were studied following the arrangement of the transducer with respect to the streamlines and the measured greatness K or ΔK . Except in the case n° 14, where a signal independent of the measured greatness appears, the other coefficients characterize the relative error on K or ΔK .

It must not be forgotten that the introduction of these coefficients in transfer formulae does not allow an improvement of the resolution. For the fluid mechanicist these equations possess then two unknown variables. The introduction of an hypothesis (never invalidated) for solving the system deprives of value any experimental study. At the best, one can estimate the errors, speak

of uncertainty on the experimental results, and, especially, put oneself in the case where they are low, even if this can seem constraining.

Acknowledgements

Mrs A.M. Bryckaert corrected the manuscript.

References.

- Dimopoulos, H.G. Hanratty, T.J. 1968, Velocitygradient at the wall for flow around a cylinder for Reynolds numbers between 60 and 360. J. Fluid Mech., 33, 303-319.
- Lévéque, M.A. 1928, Les lois de la transmission de chaleur par convection. Annales des Mines 13, 201-415.
- Py, B. 1973, Etude tridimensionnelle de la sous couche visqueuse dans une géométrie rectangulaire par des mesures de transfert de matière en paroi. Int. J. Heat Mass Transfer, 15, 129-144.
- Tournier C. Py B. 1973, Sur la mesure du gradient pariétal de vitesse dans les zones de séparation en général. C.R. Acad. Sc. Paris, 277A, 1187-1190.

HOW TO ESTIMATE LOW WAVENUMBER TURBULENCE ENERGY

R.E. Kronauer*, P.G. Hollis*, K.J. Bullock* and J.C.S. Lai†

* Division of Applied Sciences, Harvard University, Massachusetts, 02138, USA.

† Department of Mechanical Engineering, University of Queensland, 4072, Australia

‡ Department of Mechanical Engineering, Australian Defence Force Academy, Canberra, 2600, Australia

ABSTRACT

An estimate of the low wavenumber component of surface turbulence shear stress has been obtained through measurements of the correlations of the longitudinal component of turbulent velocity made close to the surface at $y^+=7$. The data were acquired in a fully-developed turbulent pipe flow at a Reynolds number (based on centreline velocity and pipe diameter) of 268000, using two single hot-wire anemometer probes. A novel data analysis procedure has been introduced to establish the accuracy limits of the low wavenumber turbulent energy estimate for frequencies in the similarity regime of wall turbulence and the results will be compared with other measurement techniques.

NOMENCLATURE

A	area	η	normalized transverse coordinate
f	frequency	λ	wavelength
I	progressive double integral of the correlation function as defined in Equation (11)	ν	viscosity
k	wavenumber	ξ	normalized longitudinal coordinate
N	number of data points	ρ	density
Re	Reynolds number	σ	standard deviation
R	Normalized correlation function	τ	shear stress
u	fluctuating velocity	Φ, ϕ	one sided spectral density functions
U_τ	friction velocity	ω	circular frequency (rad/sec)
x	longitudinal coordinate	Superscripts	
y	distance from wall	+	quantity nondimensionalized using U_τ and ν .
z	transverse coordinate	*	near zero value
ϵ	noise	overbar	time average

1. INTRODUCTION

In engineering applications, turbulent shear stress can excite structural resonances, and although as the wavenumber, k , approaches 0, the power spectral density for these stresses vanish, the low wavenumber shear stress is still a significant component of the vibrational drive mechanism, Chase (1991). Longitudinal acceleration measurements in special towed array modules behind submarines have been used to infer the strength of turbulent shear fluctuations; however these data may be significantly influenced by surface roughness, Kronauer (1991). Morrison and Kronauer (1969) used longitudinal and transverse correlations of longitudinal velocity fluctuations (u) to generate u spectra as functions of ω and k_x or ω and k_z , where x and z are the longitudinal and transverse directions, respectively. Although Lai, Bullock and Kronauer (1989) reported full 3-dimensional spectra (function of ω , k_x and k_z), only the data of Morrison and Kronauer included locations sufficiently close to the surface such that u could be directly related to the fluctuating shear stress, τ . By assuming that the 3-dimensional spectrum could be represented as the product of the two 2-dimensional spectra which Morrison and Kronauer reported, and by extrapolating these two functions to very low k , an estimate of τ at near zero k could be formed. These estimates have proven to be typically about 3 to 5 db lower than similar low k spectra deduced from at-sea array acceleration data.

The objective of this study was to provide an estimate of the very low wavenumber turbulent shear stress for various frequencies from measured two-dimensional correlation functions of the longitudinal turbulent velocity in fully-developed pipe flow.

2. THEORY

The fluctuating shear stress, τ at the surface can be modelled by the gradient of the longitudinal turbulent velocity, u , and non-dimensionalized by the average shear stress, ρU_τ^2 , to give

$$\tau^+ = \tau / (\rho U_\tau^2) = (\rho v u / y) / (\rho U_\tau^2) = u^+ / y^+ \quad (1)$$

From Figure 4 of Morrison and Kronauer (1969), for $y^+ \leq 7$, the turbulence intensity of u fluctuations can be approximated by:

$$\overline{u^{+2}} = (y^+)^2 / 6 \quad (2)$$

If $\Phi(k_x^+, k_z^+, \omega^+)$ is the one-sided shear stress power spectral density function, then from equations (1) and (2),

$$\int_0^\infty \int_0^\infty \Phi(k_x^+, k_z^+, \omega^+) dk_x^+ dk_z^+ d\omega^+ = \int_0^\infty \Phi_\tau(\omega^+) d\omega^+ / 12 \quad (3)$$

where

$$\int_0^\infty \Phi_\tau(\omega^+) d\omega^+ = 1 \quad (4)$$

From equation (1), the shear stress spectral density, $\Phi_\tau(\omega^+)$ must be identical to the longitudinal velocity spectral density $\Phi_{uu}(\omega^+)$. Also, the normalized correlation function for u , $R_{uu}(x^+, z^+ | \omega^+)$ is identical with the

normalized correlation function for τ . Using the conventional transform relationship between the correlation function and the power spectral density,

$$\int_0^\infty R_{uu}(x^*, z^*) \omega^* e^{-i k_x^* x^* - i k_z^* z^*} dx^* dz^* = C(\omega^*) \Phi_r(k_x^*, k_z^*) \omega^* \quad (5)$$

where C is a function to be evaluated. Here, x^* and z^* represent the incremental longitudinal and transverse spacing (respectively) of the two measuring stations. The inverse of this transform is given by:

$$C \int_0^\infty \Phi_r(k_x^*, k_z^*) \omega^* e^{i k_x^* x^* + i k_z^* z^*} dk_x^* dk_z^* = (2\pi)^2 R_{uu}(x^*, z^*) \omega^* \quad (6)$$

C can be evaluated from equation (6) by setting $x^*=0=z^*$ where R_{uu} is defined to be 1.

$$C = 12(2\pi)^2 / \Phi_r(\omega^*) \quad (7)$$

From equation (5), the zero wavenumber spectrum can therefore be estimated from the integral of the two-dimensional correlation function as given by:

$$\Phi_r(0,0) \omega^* = \frac{1}{C(\omega^*)} \int_0^\infty \int_0^\infty R_{uu}(x^*, z^*) \omega^* dx^* dz^* \quad (8)$$

For $k_x^*=0=k_z^*$, this function must equal zero. However, for engineering applications, such as underwater acoustics, the low wavenumber component is of interest and can be estimated from equation (8) by terminating the integration process at finite values of x^* and z^* . If a and b are the limits of the integration process in the x and z directions respectively, then the average spectral energy over the range of wavenumbers $k_x=\pi/2a$, $k_z=\pi/2b$, can be estimated.

3. APPARATUS AND EXPERIMENTAL CONDITIONS

Experiments at $y^*=7$ were conducted in a smooth steel pipe of internal diameter 254 mm and length 14.675m. The pipe has a surface roughness of 63CLA and is circular within 0.1 mm and straight within 1 mm/m of axial length. The testing section was located downstream at stations between 53.3 and 58.3 pipe diameters. Air, supplied by a centrifugal fan powered by a shunt wound DC motor, was first passed through a heat exchanger to keep its temperature constant. Swirl and large scale turbulence generated by the fan and associated diffuser were eliminated by a settling chamber. A wire gauze was placed at the entrance of the pipe to promote flow development.

The data acquisition system consists of an AT personal computer which scheduled the operations of the various components, checked the experimental conditions by monitoring the fan speed, the fluid temperature, longitudinal and transverse separations of the two hot-wire probes which consisted of 5 μ m silver plated tungsten wires with a working length of 0.7 to 0.8 mm and operated at a constant overheat ratio of 1.3. The signals from the two hot-wire probes were first linearized on an EAI680 analogue computer, then high pass filtered to yield the fluctuating components and processed by a Bruel and Kjaer (B&K) 2034 dual channel FFT analyzer to generate cross-power frequency spectra of the longitudinal components of turbulence, u . A Hanning window with zero overlap and record length of at least 180 seconds were used. The maximum

longitudinal separation Δx^* was 18850, while the maximum transverse separation, Δz^* , was 2000 and a total of 2705 experimental grid points (arranged in an approximately triangular array) were used. The narrow band cross-power frequency spectra data were transferred from the B&K2034 analyzer to the AT computer for synthesis into narrow band filters with 7.5% bandwidth centred at selected frequencies between $\omega^* = 0.005$ to 0.35, corresponding to 20 and 1340 Hz respectively. The friction velocity used was $U_\tau = 0.61$ m/s which corresponded to a Reynolds number (based on diameter and centreline velocity) of 268000. There were two experimental runs utilizing two different frequency ranges for the spectral analysis. In the first experiment, the frequency range was 1600 Hz giving spectral lines spaced at 2 Hz while in the second, the frequency range was 400 Hz giving a line spacing of 0.5 Hz. With the 1600 Hz range, 360 spectra were averaged, requiring 3 minutes of data at each grid point for a total of 136 hours for the entire grid array. With the 400 Hz range, 120 spectra were averaged requiring 4 minutes at each point for a total of 180 hours. Data from the two experiments were averaged to improve noise suppression.

4. DATA ANALYSIS AND RESULTS

4.1 Error Analysis

In estimating the errors associated with representing the double integral by an appropriate sum of the experimental correlation values, two different sources of error must be distinguished. The first kind of error is 'deterministic'. Such errors can arise from the spatial sampling process (i.e. the discrete and finite nature of the Δx^* , Δz^* grid used). If the grid points are not sufficiently dense, they may not accurately represent the underlying continuous function while if they do not extend far enough, they may fail to measure the 'tails' of the decreasing correlation. Although the spatial sampling frequency used is adequate, the finite experimental grid was found to truncate some of the correlation data at the lower frequencies studied.

Another deterministic error occurs when the two hot-wire probes are physically close (small Δx^* and Δz^*). For these small separations, no measurement is possible hence the data must be interpolated between the $R_{uu}=1$ value at zero separation to the value at the point of closest Δx^* , Δz^* . For low frequencies, this interpolation will make a negligible contribution to the error of the double integral of the correlation because of the large spatial extent over which the integral must be taken. However, for higher frequencies, interpolation is not possible because the characteristic wavelength of the correlation function is of the same order of magnitude as the minimum separation distance. Data outside this region is still useful in estimating the contribution to the double integral from the 'tails' of the correlation function.

The second kind of error is random. The turbulence field can be considered as a succession of independent events (a Poisson process) and the variance in any estimate of the field properties is reduced by increasing the number of events to be averaged. Consider a correlation taken at a reference frequency, f_0 (Hz). Since a bandwidth of 7.5% was adopted in these experiments, the relevant frequency for the averaging process is $0.075f_0$. Suppose an independent event comprises m radians of this frequency measure, then an independent

data sample is obtained every $m/2\pi(0.075f_0)$ seconds and for 240 seconds averaging time (for the 400 Hz range experiment) there are $240.2\pi(0.075f_0)/m$ independent samples. The normalized variance of the u measured at a single point is the reciprocal of this number. Since a two point correlation involves the product of the two filtered velocity signals, the variance of the correlation is double the reciprocal. Finally, the standard deviation of each normalized correlation value is:

$$\sigma_0 = [m/2\pi(0.075f_0)]^{1/2} \quad (9)$$

A comparison with experimental correlation data (as in Figure 1a for example) leads to an estimate for m of 1.6. For most frequencies of interest, this means that the standard deviation of the normalized correlation value lies in the range 0.01 to 0.03. These seemingly modest noise levels have a serious impact on the assessment of the low wavenumber spectral density and will be discussed below.

4.2 Similarity

For any ω^* , the full data set is the two-dimensional array of u - u correlations, $R_{uu}(x^*, z^*|\omega^*)$. However, to appraise the geometric similarity, it is easier to consider the one-dimensional cuts through this spatial array, namely $R_{uu}(x^*, z^*=0|\omega^*)$ and $R_{uu}(x^*=0, z^*|\omega^*)$ which will be denoted as R_x and R_z respectively. The dominant spatial scales of these correlations represent the properties of the 'convective ridge' of the wall shear stress. If the turbulence structures are self-similar, it should be possible to find a spatial scaling parameter at any ω^* which will cause R_x and R_z to be identical for all these ω^* . Figure 1 shows the raw data for R_x and R_z over a wide range of ω^* . It is clear that R_x has the stronger characteristic shape, which includes a well-defined, early zero crossing and a strong negative extremum. Consequently, it is the shape of R_x which is used for the similarity criterion. By restricting the negative minimum to lie in the range -0.21 0.06, the similarity regime is given by $0.005 < \omega^* < 0.050$. The x^* value of the first zero crossing (which is denoted as x_0^*) is used to estimate the relative spatial scaling of the ω^* in this range.

With the introduction of the scaled coordinates (where $\lambda_x^* = 4x_0^*$),

$$\xi = x^*/\lambda_x^*, \quad \eta = z^*/\lambda_z^* \quad (10)$$

the correlation functions $R_x(\xi)$, $R_z(\eta)$, as shown in Figure 2, are almost independent of ω^* , thus supporting that the similarity regime lies in the range $0.005 < \omega^* < 0.050$.

4.3 Correlation Field

The data sets for $\omega^* = 0.02$ (400 and 1600 Hz ranges) and $\omega^* = 0.031$ (400 Hz range only) are within the similarity regime and, by being at the high end of this regime, the scale of the turbulence structures are sufficiently small so that the overall size of the sampling grid is large by comparison resulting in no truncation errors.

Using the normalized correlation function $R(\xi, \eta)$, these three data sets have been averaged and the results for the one-dimensional cuts in the data field, $R_x(\xi)$ and $R_z(\eta)$, are shown in Figure 3. They have also been

smoothed by a raised cosine (Hanning) function with bandwidths in the longitudinal and transverse directions equal to 40 percent of the x^* and z^* values of the centre of the cosine function. It is clear that the correlations decay to an insignificant level well within the range of the sampling grid.

The smoothing of the correlations reduces the variance, σ_0 , of the correlation data points. The number of data points used in the smoothing process varied from 12 to 64 depending on the x^* , z^* location of the particular point being smoothed. Using the raised cosine smoothing function, the reduction in σ_0 varies between 0.33 and 0.14 for the various number of data points used.

By fitting R_x and R_z with conventional exponential/cosine functions and by assuming product separability, the corresponding two-dimensional correlation field is shown in Figure 4a. The actual averaged and smoothed two-dimensional correlation field is shown for the combined data sets in Figure 4b which is different from Figure 4a in that Run drops off much less rapidly in the transverse direction (η direction) for $\xi > 0.25$ than it does for $\xi < 0.25$. Thus, the one-dimensional cut at $x^* = 0$ (which has been referred to as R_z) greatly underestimates the extent of the large negative band of R_{xz} lying approximately between $\xi = 0.25$ and 1.

4.4 Integration Limits

Regardless of any method of smoothing or interpolation which may be used, the double integral of the correlation function consists basically of summing weighted values at individual grid points. In order to display the effect of the change in the value of the double integral with the number of grid points, the integration has been performed outward from $\xi = 0$, $\eta = 0$ with a fixed ratio of ξ to η . The result was found to be independent of the ratio of ξ to η and a value of 10 was used. Figure 5 shows the change in the value of the progressive integral versus the limiting value of ξ used in the integration for the average of the three data sets chosen above ($\omega^* = 0.02$ (400 & 1600 Hz experiments) and 0.31). It can be seen that the progressive integral has a significant negative region. The progressive integral of the twodimensional correlation modelled by a product-separable function is also shown in Figure 5. Since the actual integral does not return to positive values until ξ exceeds 1.1, its asymptotic value depends heavily on the contributions from larger ξ (and larger η). Thus, whereas the integral for the analytic product-separable function approaches its asymptotic value at $\xi = 1$, it is necessary to extend the integral beyond $\xi = 2$ (or more than 4 times the integration area) for the experimental correlation data. The variance of the estimate of the double integral with increase in grid points included in the summation is examined as follows.

The progressive integral has been evaluated as a simple weighted sum, $I(n)$, of the individual data points, the weighting factor being the element of area associated with each point. Since the experimental data, R_n , consists of the 'true' signal (which we denote by $R_{n,s}$) and the 'noise' (ϵ_n), the progressive sum $I(n)$ of the correlation data can be expressed as:

$$I(N) = \sum_{n=1}^N R_{1,n} \Delta A_n + \sum_{n=1}^N \epsilon_n \Delta A_n \quad (11)$$

Since the noise contributions at the individual data points are uncorrelated and have uniform variance (which depends on the frequency and integration time but is independent of the signal),

$$\text{Var}[I(N)] = \left(\sum_{n=1}^N \epsilon_n \Delta A_n \right)^2 = \sigma_0^2 \sum_{n=1}^N (\Delta A_n)^2 \quad (12)$$

where σ_0 is the standard deviation of the noise at each point.

This summation of incremental areas can be calculated directly from the experimental grid and can then be combined with the standard deviations of the smoothed correlations to provide an estimate of the standard deviation of the summation. The standard deviation of the smoothed correlations is calculated by multiplying σ_0 , obtained in e 9, by the reduction caused by the smoothing process. For 30 data points in the smoothing process, which is a typical value for much of the experimental grid, the smoothed standard deviation is $0.21\sigma_0$. Hence the error estimate, σ , can be calculated for the five relevant data sets (in the similarity regime), as shown in Figure 6. Although we expect the standard deviation of the sum relative to the signal to decrease as the number (N) of grid points used in the sum increases, Figure 6 clearly shows that the inclusion of grid points at large values of ξ and η , where the signal is very small may increase the standard deviation by more (percentage-wise) than it increases the signal (percentage-wise). Thus, if we know a priori how large the signal is at any grid point and have an estimate of the point variance, we can decide how far in ξ and η the integral is to be extended. However, since the aim of the experiment is to reveal the signal, the data have to be used to decide where to terminate the integration process. Generally, as seen from Figure 6, the higher frequencies have less error at large ξ . The greatly reduced variability afforded by averaging the five data sets shows the importance of including these higher frequencies of the similarity regime.

Since the similarity regime extends down to $\omega^*=0.005$, we can consider incorporating data sets taken at $\omega^*=0.005$ and 0.01 . To do so makes no useful contribution to the accuracy of the asymptotic value of the double integral because the range of ξ and η for which the correlations at $\omega^*=0.005$ and 0.01 were taken limit the double integral to $\xi=0.77$ and 1.7 respectively and the estimated error corresponding to the average of the five sets shown in Figure 6 is satisfactory up to these values of ξ .

The progressive integral of the correlation function for the five data sets that are averaged is shown on Figure 5 and it is seen that the integral does not 'settle' to a single asymptotic value and is tending to 0 as predicted by Chase (1991) however the integral will not reach zero until much larger values of ξ . From the data in Figures 5 and 6, we can estimate the double integral of the normalized correlation function from the smoothed, averaged data sets as 0.00023 ± 0.00007 at $\xi=2.5$.

4.5 Quantifying the Low Wavenumber Spectral Density

Using this estimate of the double integral of the correlation function, the low wavenumber spectral energy can now be calculated. The integral estimate has been evaluated in terms of similarity scaled arguments, ξ and η . Equation (8) then becomes:

$$\phi_{\tau}^*(0^*, 0^*, \omega^*) = \frac{4\lambda_z^2}{C} \int_0^{\infty} \int_0^{\infty} R_{\tau}(\xi, \eta | \omega^*) d\xi d\eta \quad (13)$$

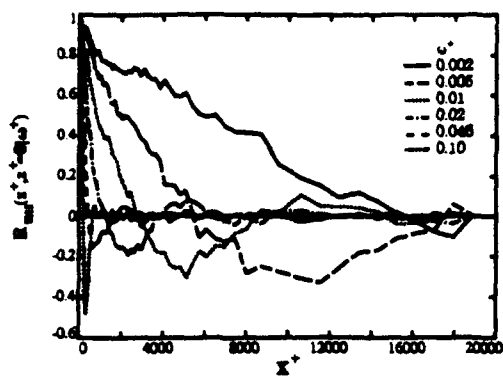
Here, 0^* is a small, non-zero value of k_1^* or k_2^* . Using values of C calculated from the data from Morrison and Kronauer (1969), the low wavenumber shear stress can now be calculated in the similarity regime. These data are shown in Figure 7 and are seen to agree well with the data obtained from Morrison and Kronauer (1969) calculated using the assumption of product separability. Agreement between the two sets of data is because the correlations in Morrison and Kronauer (1969) had larger negative values in the transverse direction than the data obtained here which consequently reduced the final value of the product-separable integral in equation (13) to agree with the value obtained from the current experiment. The data from the present experiments represent an estimate of the average spectral energy over a wave size range $k_1^* = 0.000026$ to 0.00038 and $k_2^* = 0.00026$ to 0.0038 .

5. CONCLUSIONS

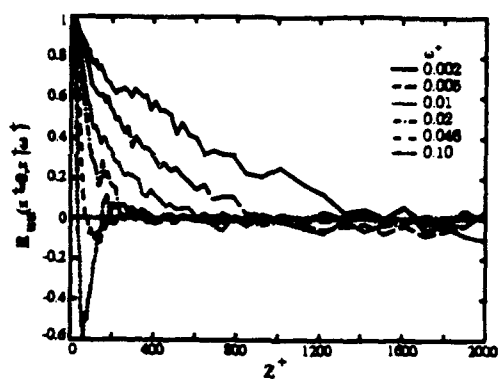
Low wavenumber turbulent energy has been estimated for non-dimensional frequencies $\omega^* = 0.005$ to 0.05 , corresponding to a wavenumber range of 0.00026 to 0.0039 , in the similarity regime of wall turbulence from measurements of two-dimensional correlations of longitudinal turbulent velocity in fully-developed turbulent pipe flow at $Re = 268000$. The results fall within the accuracy limits of towed array acceleration data and agree well with those estimated from longitudinal and transverse correlation data of Morrison and Kronauer (1969). A novel data analysis procedure has been introduced to establish the confidence limits of this estimate. It has also been shown that the lowest value of the wavenumber for which the power spectral density can be estimated cannot be reduced by expanding the experimental grid due to the random noise embedded in the correlations data. This latter error can only be reduced by a significant increase in the experimental time.

REFERENCES

- Chase, D.M. (1991) Fluctuations in wall-shear stress and pressure at low streamwise wavenumbers in turbulent boundary-layer flow, *J. Fluid Mech.*, Vol. 225, pp. 545-555.
- Kronauer, R.E. (1991) *private communication*.
- Lai, J.C.S., Bullock, K.J., and Kronauer, R.E. (1989) Structural similarity of turbulence in fully developed smooth pipe flow, *AIAA Journal*, 27, pp. 283-292.
- Morrison, W.R.B. and Kronauer, R.E. (1969) Structural similarity for fully developed turbulence in smooth tubes, *J. Fluid Mech.*, Vol. 39, Part 1, pp. 117-141.

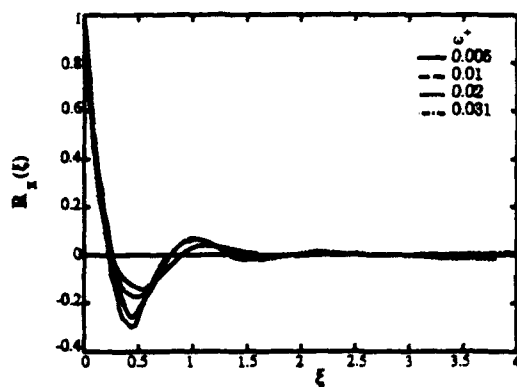


(a)

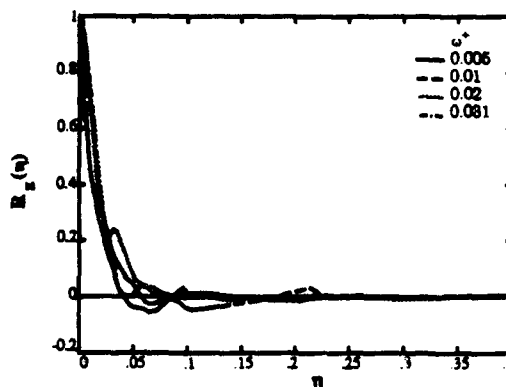


(b)

Figure 1 Experimental correlation function (a) Longitudinal direction (b) Transverse direction

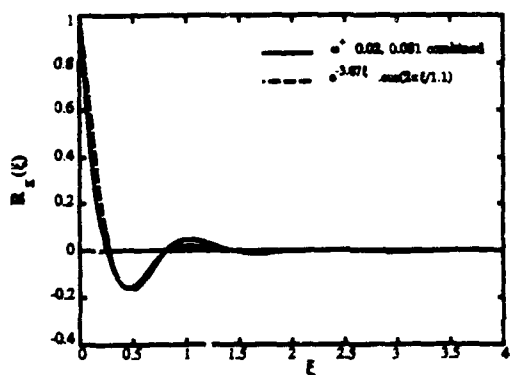


(a)

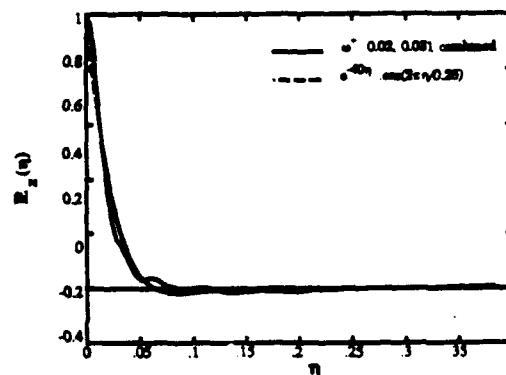


(b)

Figure 2 Variation of correlation functions with normalized coordinates (a) Longitudinal direction (b) Transverse direction



(a)



(b)

Figure 3 Averaged and analytic correlation functions (a) Longitudinal direction (b) Transverse direction

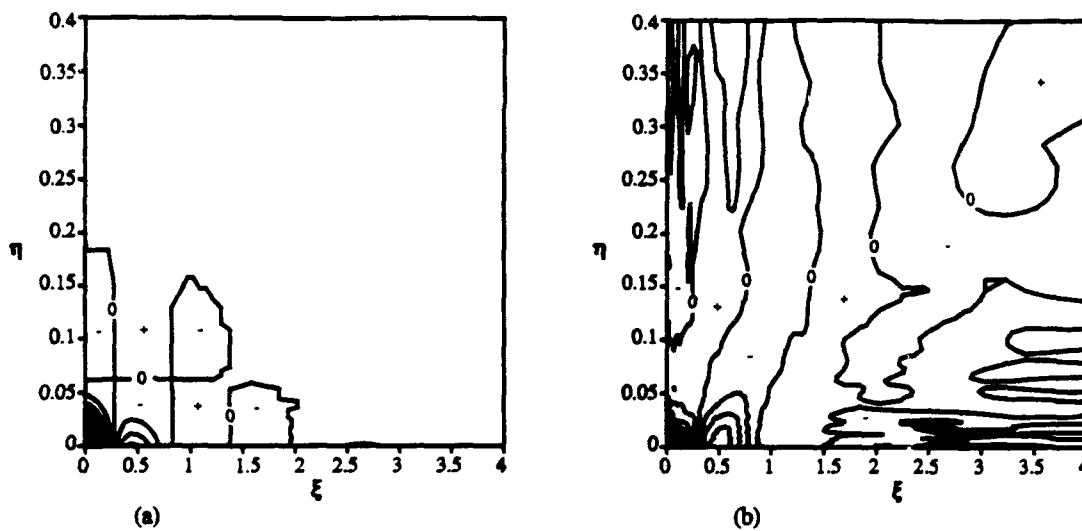


Figure 4 Two dimensional correlation field - contour spacing 0.05.
(a) Analytic function (b) Combined experimental data

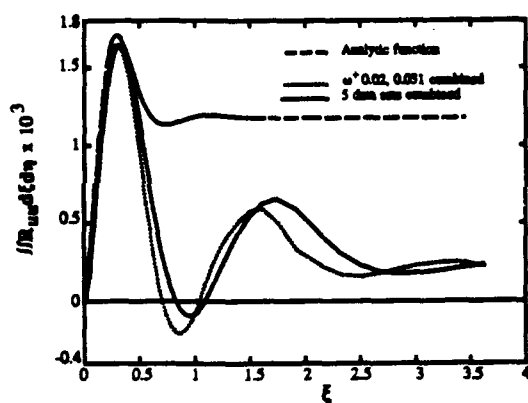


Figure 5 Progressive double integral

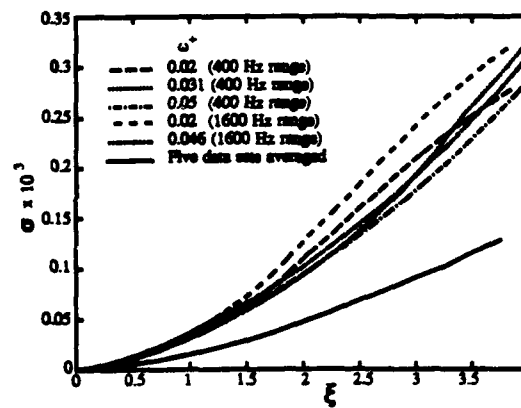


Figure 6 Standard deviation of progressive double integral

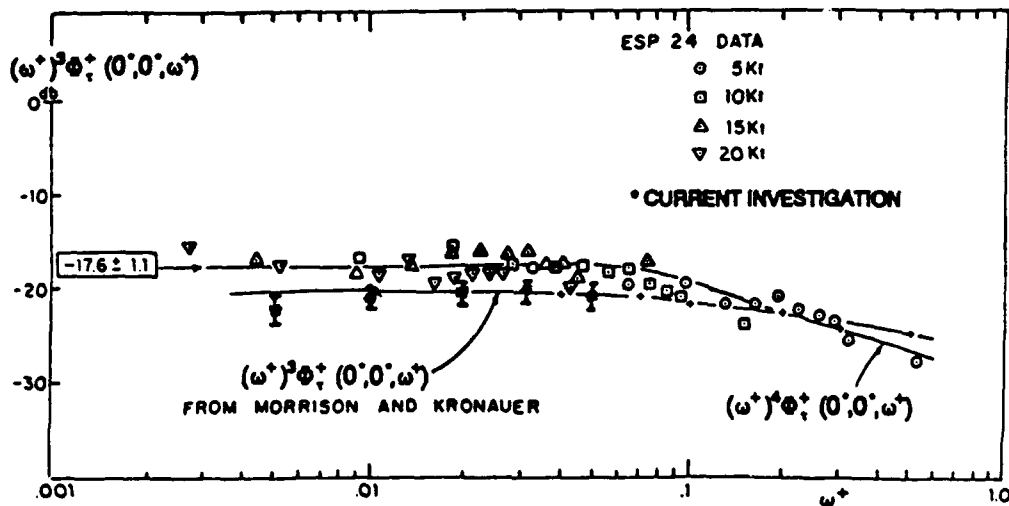


Figure 7 Low-wavenumber shear stress spectrum

RELATION BETWEEN SPECTRA OF HOT WIRE ANEMOMETER SIGNALS AND VELOCITY COMPONENTS IN HIGHLY TURBULENT FLOWS

S. Ramamoorthy*
P. K. Rajan**
S. Munukutla†

Tennessee Technological University
Cookeville, TN 38505, U.S.A.

Abstract

The relationship between the spectrum of fluctuating voltages from a hot wire anemometer signal and the spectrum of the corresponding fluctuating velocity field is studied in the case of a jet flow with high turbulence intensity. It is found that the linear analysis commonly used when converting hot wire signals into turbulence quantities gives erroneous results when determining the spectrum in high turbulence intensity flows. Excellent agreement between the spectrum of hot wire fluctuating voltages and that of the corresponding velocity field has been achieved by considering higher-order terms.

1. Introduction

Spectral analysis of turbulence quantities is performed almost routinely at the present time as part of experimental turbulence research. With the advent of modern high speed digital data acquisition systems and techniques, determination of spectra does not involve extra effort or time. Before the time data acquisition systems were used widely, analog instrumentation was used for the analysis of turbulence signals. Spectral estimation using analog instrumentation is very time consuming and, therefore, spectra were taken only when required. There are several advantages of using digital data acquisition systems. The most important advantage being that the turbulence signals can be digitally sampled and stored initially and then analyzed later using the spectral analysis technique that is most suited for the particular flow situation. Rajan and Munukutla [1, 2] have recently compared three different

*Research Assistant, Mechanical Engineering

**Professor and Chairman, Electrical Engineering

†Professor, Mechanical Engineering

techniques for estimation of turbulence energy spectrum.

There are two techniques that are currently available for measuring turbulence quantities. Hot wire anemometry is the earliest and most commonly used technique for turbulence measurements. One of the features of hot wire anemometry is that the output of the instrument which is in the form of electrical voltage fluctuations is related to the velocity fluctuations that are being sensed, via a nonlinear relationship. Care must, therefore, be exercised in deducing turbulence quantities from the instrument output.

A given turbulent flow can be thought of as being comprised of a steady mean and a fluctuating component. Thus, the instantaneous velocity in the x-direction U_i can be split into a steady mean component \bar{U} and a fluctuating component u_i . With a hot wire anemometer, an electrical voltage output E_i is generated which would comprise of a steady mean component \bar{E} and a fluctuating component e_i . The instantaneous velocity U_i and the instantaneous voltage E_i are related by the equation:

$$E_i^2 = A + B\sqrt{U_i} \quad (1)$$

where A and B are two calibration constants for the instrument. The electrical signal E_i is the one that is measured in any turbulence experiment employing hot wire anemometry. The DC component \bar{E} can be filtered and measurements can be performed on the AC component e_i . Before the advent of digital data acquisition systems, the AC component e_i was used with analog instrumentation to obtain RMS values, correlations and spectrums. The experimental quantities thus measured were converted to turbulence quantities using appropriate scale factors. All these scale factors were based on a linearized version of the voltage/velocity relation given in Equation 1.

With digital data acquisition systems, the fluctuating voltage e_i would be sampled at a prescribed sampling rate and stored. Computation of RMS values, correlations and spectrum would then be performed on the stored e_i data. Scale factors identical to those used with analog instrumentation would then be used to obtain turbulence quantities. One of the advantages of obtaining the turbulence data this way is that the noise ordinarily introduced by analog instruments is avoided. Another advantage is that once the data are stored, the processing can be done after completing the experiment, thereby reducing the experimental time. This is always advantageous with hot wire anemometry because it reduces the drift in calibration. Overall, this method of obtaining turbulence quantities is not superior to that of using analog instruments since the linearized version of the voltage/velocity relation is still being used.

There is another way of obtaining the turbulence quantities from the voltage signals by reconstructing the

instantaneous velocity field. To each e_i , the \bar{E} can be added to obtain E_i and each E_i can then be converted to U_i using Equation (1). Thus, the instantaneous velocity field is obtained. The average \bar{U} of all the U_i can be subtracted from each U_i to obtain u_i , thus giving the fluctuating velocity field. RMS values, correlations and spectra can then be obtained by analyzing the u_i data. The biggest advantage of this method is that the non-linearity of the E_i vs. U_i relationship is preserved and the results would be more accurate than those obtained by using the linearized analysis. However, it should be noted that there is an increase in computational time.

The scale factors relating the results for the fluctuating voltages to those of the turbulence quantities are well known for RMS values and correlations. These are described in standard textbooks [3]. However, the scale factors relating the spectra are not found in the literature. Ramamoorthy, Rajan and Munukutla have recently presented the results for a low turbulence intensity flow [4]. The results showed that the scale factors are different for a single wire and a two wire probe. In the case of the two wire probe, the spectrum of the cross correlation $e_1 e_2$ assumes a very important role, particularly in regions of high shear stress. In flows with high turbulent intensities, the nonlinearity plays an important role in determining the scale factors. A complete analysis of the scale factors in highly turbulent flows is presented in this paper. The results are also examined in the light of experimental data.

2. Analysis for Single Wire Probe

Substituting $U_i = \bar{U} + u_i$ and $E_i = \bar{E} + e_i$ in Equation (1), we obtain the following

$$(\bar{E} + e_i)^2 = A + B \sqrt{\bar{U} + u_i} \quad (2)$$

Rearranging Equation (2), we obtain the following relation for u_i ,

$$u_i = a_1 + a_2 e_i + a_3 e_i^2 + a_4 e_i^3 + a_5 e_i^4 \quad (3)$$

$$\begin{aligned} \text{where} \quad a_1 &= \frac{(\bar{E}^2 - A)^2 - B^2 \bar{U}}{B^2} & a_2 &= \frac{4(\bar{E}^2 - A)\bar{E}}{B^2} \\ a_3 &= 2 \frac{(3\bar{E}^2 - A)}{B^2} & a_4 &= \frac{4\bar{E}}{B^2} \end{aligned}$$

and

$$a_5 = \frac{1}{B^2}$$

Retaining terms up to the order of e_i^2 only in Equation (3) and taking the Fourier transform of the autocorrelation, the spectrum of e , is computed as

$$S u_i(f) = a_2^2 S e_i(f) + a_3^2 S e_i^2(f) + a_2 a_3 [S e_i e_i^2(f) + S e_i^2 e_i(f)] + K \delta(f) \quad (4)$$

where $K = 2a_1 a_3 \bar{e}_i^2 + a_1^2$

In Equation (4), for example, $S e_i^2(f)$ stands for the spectrum of e_i^2 and similarly the other terms. $\delta(f)$ is the Dirac delta function. It is to be noted that by retaining only the linear terms in e_i in Equation (3) the spectrum of u_i will be given by

$$S u_i(f) = a_2^2 S e_i(f) \quad (4a)$$

A comparison of the results obtained by using Equations (4) and (4a) will be presented in the Results section.

3. Analysis for Two Wire Probe

In the case of the two wire x-probe, the relationships between the instantaneous voltage and the instantaneous velocity for the two wires are

$$(\bar{E}_1 + e_{1i})^2 = A_1 + B_1 \sqrt{U + u_i + v_i} \quad (5)$$

$$(\bar{E}_2 + e_{2i})^2 = A_2 + B_2 \sqrt{U + u_i + v_i} \quad (6)$$

In the above equations A_1 , B_1 and A_2 , B_2 are the calibration constants for wires 1 and 2, respectively. u_i and v_i are the fluctuating components in the x and y direction, respectively. Rearranging Equations (5) and (6) and retaining terms up to the order of e_{1i}^2 and e_{2i}^2 , we obtain

$$u_i + v_i = b_1 + 2b_2 e_{1i} + 2b_3 e_{1i}^2 + 0(e_{1i}^3) \quad (7)$$

$$u_i - v_i = c_1 + 2c_2 e_{2i} + 2c_3 e_{2i}^2 + 0(e_{2i}^3) \quad (8)$$

where

$$b_1 = \frac{(\bar{E}_1^2 - A_1)^2 - B_1^2 \bar{U}}{B_1^2} \quad c_1 = \frac{(\bar{E}_2^2 - A_2)^2 - B_2^2 \bar{U}}{B_2^2}$$

$$b_2 = \frac{2(\bar{E}_1^2 - A_1)\bar{E}_1}{B_1^2} \quad c_2 = \frac{2(\bar{E}_2^2 - A_2)\bar{E}_2}{B_2^2}$$

$$b_3 = \frac{(3\bar{E}_1^2 - A_1)}{B_1^2} \quad \text{and} \quad c_3 = \frac{(3\bar{E}_2^2 - A_2)}{B_2^2}$$

From Equations (7) and (8), we obtain

$$u_i = L_1 + (b_2 e_{1i} + c_2 e_{2i}) + (b_3 e_{1i}^2 + c_3 e_{2i}^2) \quad (9)$$

$$v_i = L_2 + (b_2 e_{1i} - c_2 e_{2i}) + (b_3 e_{1i}^2 - c_3 e_{2i}^2) \quad (10)$$

where

$$L_1 = \frac{b_1 + c_1}{2} \quad \text{and} \quad L_2 = \frac{b_1 - c_1}{2}$$

The spectra of u_i and v_i are obtained by taking the Fourier transforms of the autocorrelations of Equations (9) and (10) and are given by

$$\begin{aligned} \begin{matrix} Su_i(f) \\ (v_i(f)) \end{matrix} &= b_2^2 Se_{1i}(f) + c_2^2 Se_{2i}(f) \pm b_2 c_2 [Se_{1i} e_{2i}(f) + Se_{2i} e_{1i}(f)] \\ &+ b_3^2 Se_{1i}^2(f) + c_3^2 Se_{2i}^2(f) + b_2 b_3 [Se_{1i} e_{1i}^2(f) + Se_{1i}^2 e_{1i}(f)] \\ &\pm b_2 c_3 [Se_{1i} e_{2i}^2(f) + Se_{2i}^2 e_{1i}(f)] \pm b_3 c_2 [Se_{2i} e_{1i}^2(f) + Se_{1i}^2 e_{2i}(f)] \\ &+ c_2 c_3 [Se_{2i} e_{2i}^2(f) + Se_{2i}^2 e_{2i}(f)] \pm b_3 c_3 [Se_{1i} e_{2i}^2(f) + Se_{2i}^2 e_{1i}(f)] + \frac{K_i}{(K_2)} \delta(f) \end{aligned} \quad (11)$$

Note that Equation (11) is a concise form for representing the spectra of u_i and v_i by one single equation. The - sign and K_2 correspond to the spectrum of v_i . In Equation (11)

$$K_1 = L_1(L_1 + 2b_3 \bar{e}_{1i}^2 + 2c_3 \bar{e}_{2i}^2) \quad (12)$$

$$K_2 = L_2(L_2 + 2b_3 \bar{e}_{1i}^2 - 2c_3 \bar{e}_{2i}^2) \quad (13)$$

and $\delta(f)$ is the Dirac delta function.

By retaining only the linear terms in e_{1i} and e_{2i} in Equations (9) and (10), the spectra of u_i and v_i will be given by

$$Su_i(f) = b_2^2 Se_{1i}(f) + c_2^2 Se_{2i}(f) + b_2 c_2 [Se_{1i} e_{2i}(f) + Se_{2i} e_{1i}(f)] \quad (14)$$

$$Sv_i(f) = b_2^2 Se_{1i}(f) + c_2^2 Se_{2i}(f) - b_2 c_2 [Se_{1i} e_{2i}(f) + Se_{2i} e_{1i}(f)] \quad (15)$$

A comparison of the results obtained by using the linear analysis (Equations (14) and (15)) with those obtained by using the nonlinear analysis (Equation (11)) is given in the results section.

4. Results

Spectra are presented for turbulence data obtained by hot wire anemometer using both single wire and cross wire probes. Measurements were made in a circular free-air jet, 7/8" diameter at jet exit. The probes were located 8" downstream of the jet exit and 1/2" off the jet axis. The turbulence level at this location was estimated to be about 44% of the mean velocity. The mean velocity in the core of the jet was nominally 100 ft./sec.

The hot wire anemometer output signals were sampled at 20 kHz for 2 seconds and stored. The data were subsequently processed in a Sun sparc workstation. In the case of single wire data and cross wire data, spectra were estimated by three different ways. First, the velocity field was constructed as explained in the Introduction and the spectrum was evaluated directly. Next, the spectrum was estimated using the linear version (Equation (4a) for single wire and Equations (14) and (15) for cross wire). Finally, the spectrum was estimated using the full non-linear version, as given by Equations (4) and (11).

The results for the single wire case are shown in Figure 1. It can be seen that the spectra obtained directly from u and that obtained by non-linear analysis agree well with each other over the entire frequency range. The linear approximation gives an error which progressively increases with the frequency. The results for the cross wire probe are shown in Figures 2 and 3. Figure 2 shows the comparison of the spectra of u and Figure 3 that of v . It can be noted that the spectra obtained directly from u and v agree very well with the corresponding spectra using non-linear analysis. However, the linear analysis is in error over the entire frequency range.

5. Conclusions

It can be concluded that the spectra of the velocity fluctuations evaluated directly from the velocity field and the spectra evaluated by using a non-linear analysis of the voltage signals agree very well with each other. This is true for single wire, as well as two wire probes. It should, however, be noted that the computations needed for converting the spectra of the fluctuating voltages to those of the velocity fluctuation are very involved. It would, therefore, be much easier to convert the voltage fluctuations to velocity fluctuations and then perform spectral analysis in highly turbulent flows.

6. References

1. "A Comparative Study of Three Techniques for Estimation of Turbulence Energy Spectrum," (P. K. Rajan and S. Munukutla) presented at Twelfth Symposium on Turbulence, September 24-26, 1990, University of Missouri, Rolla.
2. "A Comparative Study of Three Techniques for Estimation of Turbulence Energy Spectrum," (P. K. Rajan and S. Munukutla) Experiments in Fluids, 12 (1992).
3. Turbulence, Hinze, J. P., 2nd Edition, McGraw-Hill, Inc., 1975.
4. "Relation Between Spectra of Hot Wire Anemometer Fluctuating Voltages and Those of Turbulence Quantities," (S. Ramamoorthy, S. Munukutla and P. K. Rajan) Paper #AIAA 92-3958 presented at the 17th Aerospace Ground Testing Conference, July 6-8, 1992, Nashville, Tennessee.

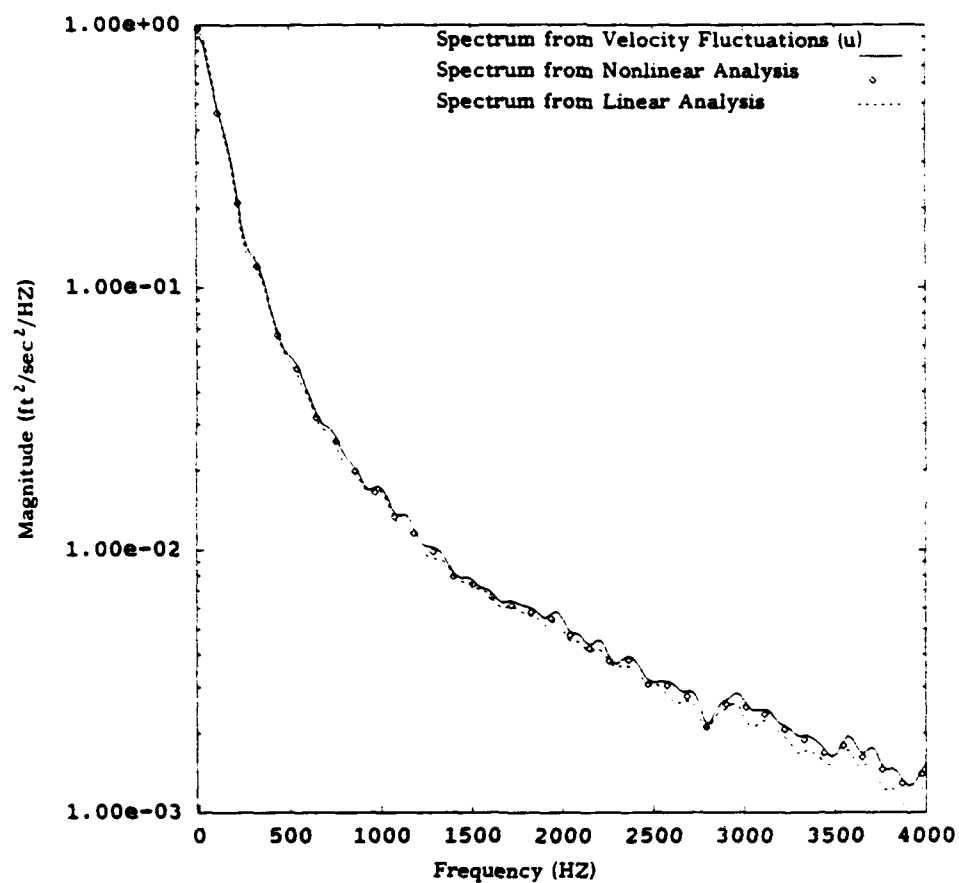


Figure 1. Comparison of u Spectra Estimated by Different Methods for a Single Wire Probe

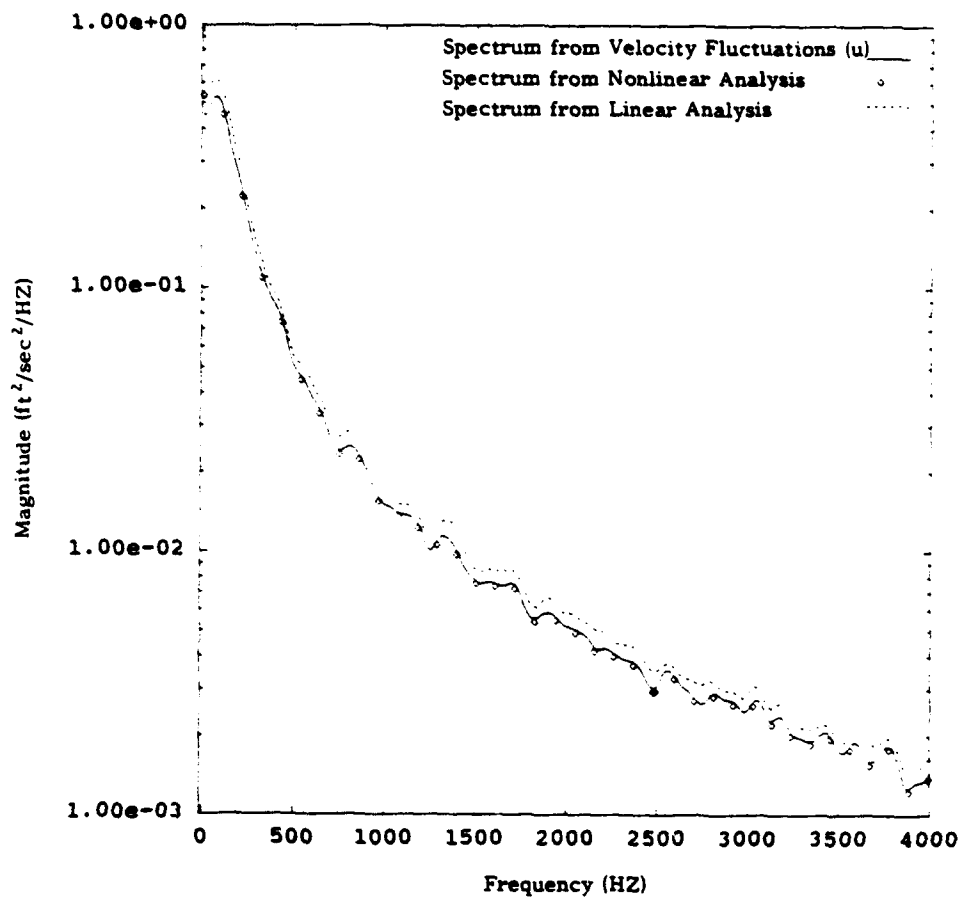


Figure 2. Comparison of u Spectra Estimated by Different Methods for Two Wire Probe

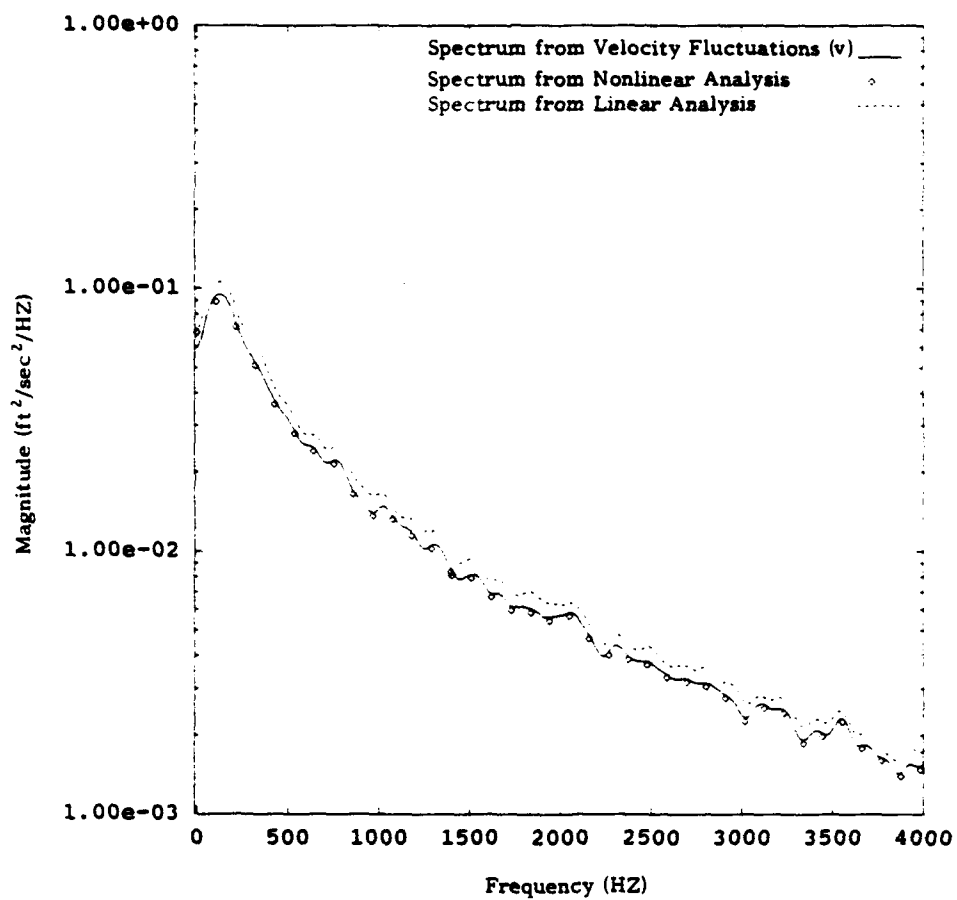


Figure 3. Comparison of v Spectra Estimated by Different Methods for a Two Wire Probe

AN ACOUSTIC DOPPLER VELOCITY PROFILER FOR TURBULENT FLOW

U. Lemmin, T. Rolland, R. Lhermitte

Laboratoire Recherches Hydrauliques
Ecole Polytechnique Fédérale
CH-1015 Lausanne
Switzerland

Abstract. This paper presents an acoustic Doppler velocity profiler (ADVP) for hydrodynamic research in channels, rivers and lakes. It is non-intrusive and, different from other existing velocity measuring instruments, it allows to take an instantaneous velocity profile across the water column in turbulent flow. Extensive tests of the ADVP system in laboratory open channel flow with optically clean water have been carried out. Spectral and autocorrelation signal processing algorithms were evaluated with respect to the extraction of the velocity information. Using a 1 MHz acoustic frequency and a pencil beam (2 degree), complete instantaneous velocity profiles of up to 128 points are obtained in a continuous mode with a resolution of 6 mm in the vertical and at a rate of 15 Hz. Profiles of mean velocity, variance and turbulence scales in uniform flow are presented showing that the instrument is well-suited for measurements in turbulent flow.

1. Introduction

Velocity and turbulence are important hydrodynamic parameters. Many instruments, working on a variety of principles, have been developed for their measurement. These instruments have two major drawbacks: they provide single point measurements and, except for the Laser Doppler Anemometer (LDA), they are intrusive, perturbing the flow. Furthermore, to establish a velocity profile either the instrument has to be displaced or several instruments have to be employed at the same time. Measurements in non-stationary or non-uniform flow become tedious and difficult. Thus, an instrument which can take instantaneous velocity profiles with a resolution in the range of turbulence scales and which at the same time is non-intrusive will be of advantage in hydrodynamic research.

We are developing such an instrument on the basis of a Doppler sonar. The potential of ultrasonic waves for the determination of flow speeds was recognized long ago in medical research. Since blood flow is typically turbulent, much of the experience gained there can be directly applied to hydraulic research. Different concepts of an acoustic velocity measuring instrument have been realized. The most versatile for hydraulic research is the so-called pulse-to-pulse coherent Doppler system developed for medical research by Baker and Watkins (1967). Its application in oceanic research was first described by Lhermitte (1983) and the feasibility for hydraulic research was tested by Lhermitte and Lemmin (1990). In this paper we

present an acoustic Doppler velocity profiler (ADVP). Based on results from measurements in an open laboratory channel we discuss the possibilities and the limitations of this instrument.

2. Principle of operation

The principle of operation of the instrument is based on the Doppler effect. The frequency at the source is $f_s = C/\lambda$, where C is the speed of sound and λ is the wavelength. A listener moving with the speed v_l will experience additional $v_l T/\lambda$ waves during a time T resulting in the frequency $f_o = (C+v_l)/\lambda$. The difference between the two is the Doppler shift frequency

$$f_d = f_o - f_s = v_l f_s / C. \quad (1)$$

A Doppler frequency for the case in which the source moves at speed v_s can be derived in a similar way. The general Doppler shift frequency becomes

$$f_d = f_s (v_l + v_s) / (C - v_s). \quad (2)$$

Assuming that v_s is small compared to C one can write

$$f_d = f_s (v_l + v_s) / C. \quad (2a)$$

Sonic waves are typically reflected at density interfaces. If the echo is returned from a moving interface, the returning signal receives a Doppler shift. In this case the interface causing the echo is acting first as a listener and then as a source, thus $v_l = v_s = v$. The Doppler shift frequency then becomes

$$f_d = f_s 2v / C. \quad (3)$$

In practical applications of this principle, the omnidirectional spherical sound source is often replaced by a narrowly focused cylindrical transducer which for technical reasons typically has a conical shaped narrow sound beam. Since only the component of the velocity directed towards or away from the transducer, called radial velocity, contributes to the Doppler shift frequency, it must now be scaled by the cosine of the angle between the velocity vector of a sound scatterer and the line connecting the axis of the transducer and the scatterer. The Doppler shift frequency can then be expressed as:

$$f_d = (2 f_s v / C) \cos \theta. \quad (4)$$

This equation can be inverted to yield the velocity of interest

$$v = C f_d / (2 f_s \cos \theta). \quad (4a)$$

The angle between the velocity direction and the sound beam becomes an important parameter in the application of the ADVP instrument. The smaller this angle, the less resolution and accuracy in the determination of the velocity can be expected. In

hydrodynamic research a profile of the horizontal velocity component u along a vertical axis is frequently sought. However from eq (4a) it is obvious that this orientation of the transducer cannot provide any information on the horizontal velocity component. ADVP-profiles will therefore always be taken along a line inclined to the vertical.

2.1 A pulse-to-pulse coherent ADVP-system

Different system concepts can be applied to provide a Doppler shift frequency. In the pulse-to-pulse coherent system of the present ADVP a single sonar transducer is used. The 'pulse' - a short train of several sinusoidal waves with frequency f_s - is emitted from the transducer into the water (Fig. 1a) at regular intervals, the 'pulse repetition frequency' (PRF). Between two emissions the transducer serves as a receiver. A wave of frequency f_0 is reflected back to the transducer. An electronic system detects the difference between the two frequencies which is the Doppler frequency and provides a signal which corresponds to the instant water velocity.

By gating the received signals to correspond to the pulse's time of flight to the point of interest, a small sampling volume (the 'gate') can be interrogated (Fig. 1b) instead of the entire length of the beam. As the depth to which one wishes to interrogate the fluid flow increases, the time interval between the emitted pulse and the sample gate increases. Each echo must be allowed enough time to return from the maximum depth of interest before the next pulse is emitted to prevent ambiguous range information. The pulse repetition frequency PRF in turn determines the maximum Doppler shift frequency that can be detected without aliasing. Since the pulsed Doppler instrument requires sampling the returning echoes at fixed times after the pulse emission, it is possible for the higher-frequency Doppler shift to alias to lower frequencies. As a result a tradeoff between the maximum sampling depth D_{\max} and the the maximum unaliased flow velocity v_{\max} exists, called the 'range-gate ambiguity' (Lhermitte, 1983):

$$v_{\max} D_{\max} = C^2 / (8 f_s \cos \theta.) \quad (5)$$

Within these limits any depth can be chosen. The method of interrogation can be extended if more than one gate is dealt with after each emitted pulse. By sampling at a certain number of gates in sequence a quasi-simultaneous profile of the velocity distribution between the transducer and D_{\max} can be obtained (Fig. 1c). At the same time the water depth can be determined if D_{\max} is chosen larger than the anticipated depth.

2.2 Determination of the velocity

The Doppler shift frequency is typically extracted by mixing the received signal with the emitted signal. If the received signal is processed in quadrature, the sign of the Doppler frequency shifts can be distinguished, indicating the direction of the flow. From the Doppler shift frequency the flow velocity is determined by eq 4a. For this purpose different methods of signal processing exist; best known are the spectral analysis and the 'pulse pair' method, an auto-covariance algorithm. Since the echoes come from turbulent flow, the time series of Doppler shift frequencies at each gate have a spectrum of finite width. These methods and their errors have

been discussed by Lhermitte and his co-workers (1983, 1984, 1990, 1991). For routine data treatment we have found the auto-covariance algorithm (Lhermitte and Serafin, 1984) to be the most efficient due to its computational simplicity and the elimination of subjective spectrum's interpretation. For each velocity estimate, an average over several consecutive measurements is taken in order to augment the statistical stability of the results.

3 Experimental apparatus and set-up

A pulse-to-pulse coherent ADVP unit operating at 1 MHz was assembled. The design allows software selection of number of gates, pulse widths and pulse repetition frequencies but most of the experiments were conducted with a 8 microsecond pulse width and a 800 - 1200 Hz PRF. The scattering volume of each of the equally spaced gates consisted of a cylinder of 20 mm diameter and 6 mm height. The above conditions are well-adjusted for measurements in the laboratory channel, providing about 0.75 m unambiguous range, 0.9 ms^{-1} unambiguous velocity (eq. 5; $\theta = 15^\circ$) and 6 mm vertical resolution. The effects of spurious signals resulting from reflections on channel walls, bottom, etc., were virtually removed in the system, by pseudo-random coding of the transmitted signal phase.

The experiments were conducted under uniform flow conditions in an open channel of 16 m total length. The measurements were made at about 12 m from the channel entrance, so that the flow profile was well-established at the measuring point. The channel width is 60 cm between glass walls which is acceptable for the 20 cm water depth set in most of the experiments. The channel bed is covered with 4 mm mean diameter gravel glued to the bottom plate.

For the experiments the sonar transducers were first mounted from the top with the face of the transducer submerged in the flow. Better results were obtained when the transducers are mounted below the channel bed looking up into the flow through a small window in the floor which was covered by Mylar film to minimize flow disturbance. Three transducers pointing in different directions as shown in Fig. 2 were installed. In this configuration the measuring installation produced no perturbation of the flow. For stationary flow the two velocity vectors u in the direction of the mean flow and w in the vertical direction can be determined by trigonometric manipulation (Lhermitte and Lemmin, 1991) from three consecutive measurements with transducers at different orientation. For this operation the ADVP system was connected to the transducers following a 1 through 3 sequence. Each time, the instrument acquired data for up to 1 min at up to 128 gates.

Experiments conducted with the ADVP system were concerned with clear water (better than 98 percent transmissivity). The water used in the channel and in the holding tank was continuously filtered to remove any particulates. There was no seeding by physically defined targets to provide tracers for the water motion. Very small size particulates (less than 50 micrometer size) could still be seen in the water. However, calculating the sonar reflectivity expected from these targets as a function of their estimated size and concentration showed that the reflectivity expected from their presence was well below (three orders of magnitude) the water reflectivity actually measured. The experiments conducted have shown that in

normal distribution. It is systematically negative indicating the probability of slightly overestimating the true velocities. Similar results with respect to sample size were obtained for the kurtosis.

4.2 Turbulence parameters

The data obtained with the ADVP were subsequently analyzed for turbulent flow characteristics. Particular attention was given to the effect of the limited transversal resolution of the acoustic beam size in the present prototype system. The profile of the standard deviation (Fig. 7) shows an increase towards the channel bed in the way reported in the literature. In this case we have investigated the effect of sample size on the resultant standard deviation. Each individual sample is calculated from a number data points by a double pulse-pair algorithm. It can be seen that for a small sample size (16 data points) the slope of the curve is correctly represented but the actual value is too high and (not shown here) has itself an important standard deviation. When the sample size is increased to 512, the curve approaches the theoretical prediction by Nezu and Rodi (1986) and the deviation is greatly reduced. This sample size represents a measuring period of about 30 seconds at about 1000 data points per second. Further increase of the sample size does not change the variance.

Turbulent energy spectra from data taken at different gates show a well-developed inertial subrange over more than one decade and self-similarity for different layers in the flow. Spectra calculated from samples which were produced by a running mean pulse-pair over 82 data points advanced by 6 data points show the $-5/3$ inertial subrange and also a -3 to -4 diffusive subrange at higher frequencies (Fig. 8). For open-channel flow a diffusive subrange with a comparable slope in the same frequency range was already reported by McQuivey and Richardson (1969) and is close to the $-13/3$ slope measured by Komatsu et al. (1989).

The spatial autocorrelation function along the profile was calculated. This function provides an estimate of the eddy size as associated with the turbulent flow. The area under the curve gives an indication of the mean eddy size in the flow direction, called macro scale L . We find a distribution of L (Fig. 8) which corresponds to profiles reported in the literature (McQuivey and Richardson, 1969; Nalluri and Novak, 1977). However, due to rough bottom and higher Reynolds number ($Re \approx 1.5 \times 10^5$), the largest scales are limited to about 30% of the water depth. This limit corresponds to Kironoto and Graf (1991) who measured in the same flow conditions in the same channel using hot film instrumentation. The micro scale was also calculated and is shown in Fig. 9. Again, we find close resemblance with the literature and results by Kironoto and Graf (1991). Thus, even though the sound beam diameter of the present instrument is rather large (about 20 mm), turbulence scales can be well-resolved with this instrumentation, because sonar echoes come from interfaces which are much smaller than the beam dimensions.

5. Conclusion

The data acquired have been analyzed to evaluate their use for the probing of boundary layer flow conditions in open channel flow. From the analysis it is apparent that the ADVP hardware and the software algorithms applied to the

turbulent flow a well-defined spectrum with a nearly Gaussian shape is always observed from clear water backscattering (Lhermitte and Lemmin, 1990).

4. Results and discussion

4.1 Mean velocity profiles

For verification of the measurements the ADVP is compared with standard instrumentation: Pitot tube and hot film. While the Doppler measurement of the ADVP is an absolute measurement and does not require calibration, certain aspects of the installation of the instrument can influence the result. One of these parameters is the inclination of the transducer. Tests have shown that the resultant velocity (eq. 4a) is strongly dependent on this angle. When comparing the ADVP mean velocity profile with one obtained by a Pitot tube (Fig. 3), it is seen that a deviation of the transducer angle of less than 2° changes the estimated speed by up to 10%. In a similar way an observed systematic deviation in the profile of the vertical mean velocity could be attributed to an angle deviation of 0.1° . Thus a carefully controlled installation of the transducers is an important prerequisite for good measurements with the ADVP. The shape of the measured mean profile corresponds to a logarithmic velocity profile, well-established for uniform open-channel flow.

Since the ADVP measures the radial velocity in the axis of the acoustic beam, measurements by a single inclined transducer cannot distinguish between contributions from the horizontal (u) and the vertical (w) components of the velocity vector. Under stationary flow conditions the two components can be obtained from measurements with a single transducer at a time if measurements are repeated at different transducer angles θ . Using the two inclined transducers 2 and 3 (Fig. 2) two profiles of the mean velocity were obtained (Fig. 4) which due to the transducer orientation are slightly different. From the two profiles the profile of the 'true' horizontal velocity vector was calculated (Lhermitte and Lemmin, 1991) and falls in between the two measured profiles (Fig. 4). The difference between the measured and the calculated velocities never exceeds 5% and can be attributed to the vertical velocity w . The w profile is shown in Fig. 5 together with the vertical velocity measured directly with transducer 1. High measured velocities near the bed are due to the change in bottom roughness caused by the smooth Mylar window of transducers 2 and 3 which is upstream from the window for transducer 1. One can see that the general trend of the two w profiles is identical but the actual values of the rather small velocity may differ. The general trend of w can be explained by a secondary circulation as suggested by Nezu and Rodi (1985) for channel flows with small width to depth ratios. Thus profiles of horizontal velocity can be measured by a single observation if not too high an accuracy is required. The results could be further improved if the angle (θ ; Fig. 2) of inclination of the transducer would be increased.

The effect of the number of data points used to calculate the velocity has been investigated by calculating higher statistical moments of the time series. The skewness, shown in Fig. 6, does not change much once the number of data points exceeds 64. For lower sample lengths a large scatter was observed. For 64 points and above, the skewness is relatively small implying a small deviation from a

extraction of the velocity vector are well suited for the analysis of turbulent flow characteristics. Without the need for a calibration procedure, mean vertical and horizontal water velocity is effectively measured by the ADVP, turbulence scales are well resolved. Measurements can be made to a degree of accuracy better than most conventional in situ sensors which can also modify the local flow conditions significantly by intruding into the flow. The ADVP is easier to operate than laser velocimeters and essentially provides instantaneous velocity profiles instead of point measurements. Up to 128 points in each ADVP-profile can be resolved. Thus a higher spatial resolution is achieved. Compared to existing instrumentation, the ADVP profile measurements take only a small fraction of the time for the same resolution. Furthermore, since ADVP profile measurements are taken simultaneously under the same flow conditions, the resultant profiles are found to be smoother than those taken in sequence by existing instruments.

Our conclusion at this point is that the high frequency ADVP is a valuable tool for hydraulic research. Turbulent clear water constitutes an appropriate backscattering medium. The relevance of more sophisticated techniques for beam focalization, data acquisition and signal processing of the Doppler information may need to be investigated before the configuration and domain of application of a high frequency ADVP designed for hydraulic research can be finalized.

References

- Baker D.W.; Watkins D.W. 1967: A phase coherent pulsed Doppler system cardiovascular measurement. Proc. 20 ACEMB. 27, 2-12.
- Kironoto, B.; Graf, W.H. 1990: Non-uniform turbulent flow in rough beds flume. Annual report of the Laboratoire de recherches hydrauliques, EPFL, Lausanne, Switzerland.
- Komatsu, T.; Shibata, T.; Matsumoto, Y. 1989: Spectra of turbulence in a viscous subrange. Proceedings 23 IAHR Congress; Ottawa, Canada. A39-A46.
- Lhermitte, R. 1983: Doppler sonar observations of tidal flow. J. Geophys. Res. 88, 725-742
- Lhermitte, R.; Serafin, R. 1984: Pulse-to-pulse coherent Doppler sonar signal processing techniques. J. Atmospheric and oceanic technology. 1, 293-308
- Lhermitte, R.; Lemmin, U. 1990: Probing water turbulence by high frequency Doppler sonar. Geophys. Res. Lett. 17, 1549-1552
- Lhermitte, R.; Lemmin, U. 1990: Open-channel flow and turbulence measurements by high resolution Doppler sonar. Annual report of the Laboratoire de recherches hydrauliques, EPFL, Lausanne, Switzerland
- McQuivey, R.S.; Richardson, E.V. 1969: Some turbulence measurements in open-channel flow. J. Hydr. Div. Proc. ASCE. 95, 209-223
- Narulli, C.; Novak, P. 1977: Turbulence characteristics in smooth open channel flow. Proc. 5th biannual symposium on turbulence, Rolla, USA, 191-204
- Nezu, I.; Rodi, W. 1986: Open-channel flow measurements with a laser Doppler anemometer. J. Hyd. Eng., Proc. ASCE. 112, 335-355
- Nezu, I.; Rodi, W. 1985: Experimental study on secondary currents in open channel flow. Proc. 21 IAHR Congress; Melbourne, Australia. 2, 115-119

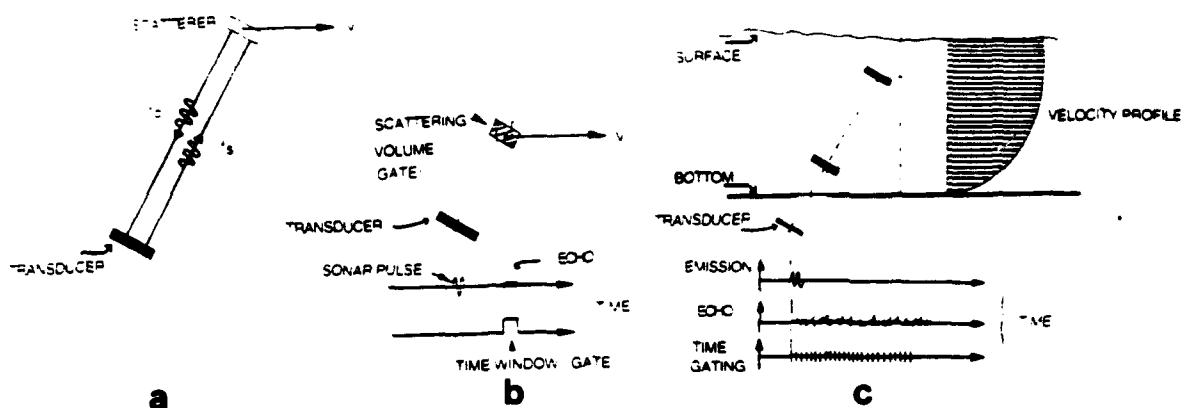


Fig. 1. Principle of operation of an ADVP. a: The change in frequency ($f_0 - f_s$) is the Doppler shift frequency which is proportional to the velocity v in the water. b: Single gate pulse-to-pulse coherent instrument. c: Multi-gate pulse-to-pulse coherent instrument.

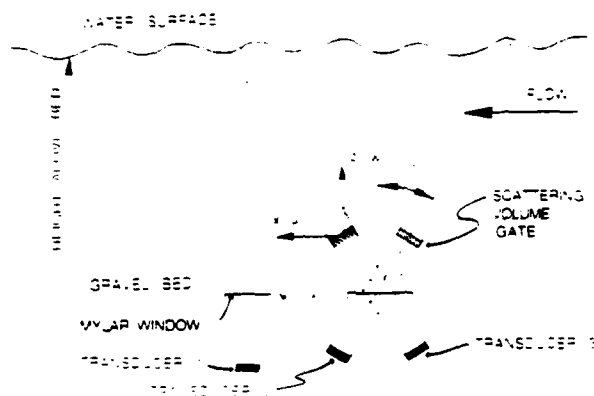


Fig. 2: Installation of acoustic transducers in the bottom of the laboratory channel.

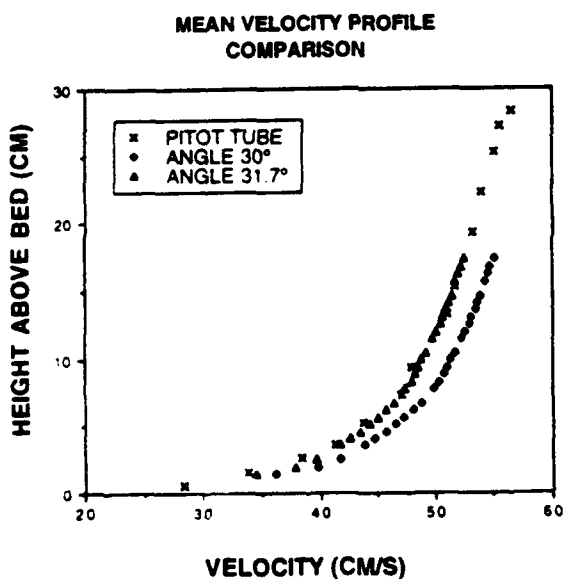


Fig. 3: Horizontal mean velocity profiles taken with an ADVP and with a Pitot tube. The angle of inclination of the acoustic transducer was changed between the two ADVP profiles.

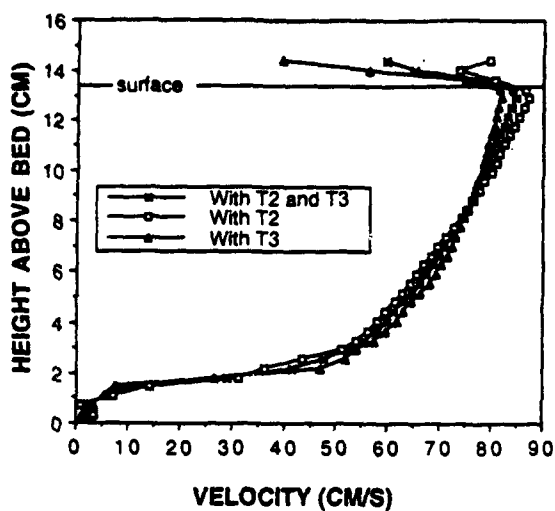


Fig. 4: Horizontal mean velocity profiles taken with the two transducers T2 and T3 (see Fig. 2) and the profile calculated from the two measurements.

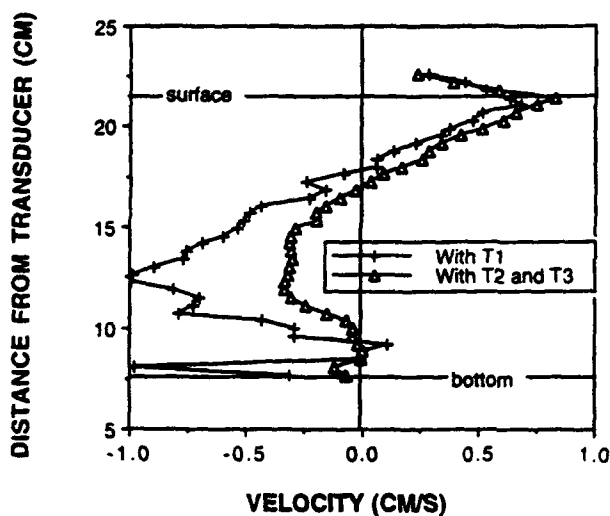


Fig. 5: Vertical mean velocity profiles a: calculated for the profiles taken by transducers T2 and T3 and b: measured by transducer T1. A positive velocity is oriented downwards.

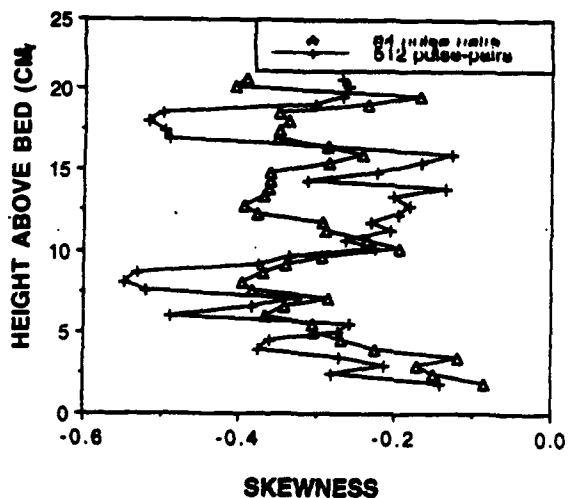


Fig. 6: Skewness profiles as function of data points used to calculate the velocity estimates.

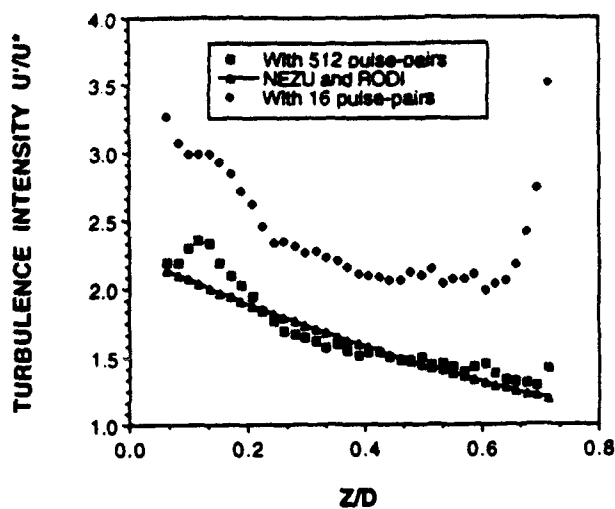


Fig. 7: Horizontal velocity variance ADVP profiles compared with the profile predicted by Nezu and Rodi (1986). The two ADVP profiles differ in the number of data points over which the variance was estimated.

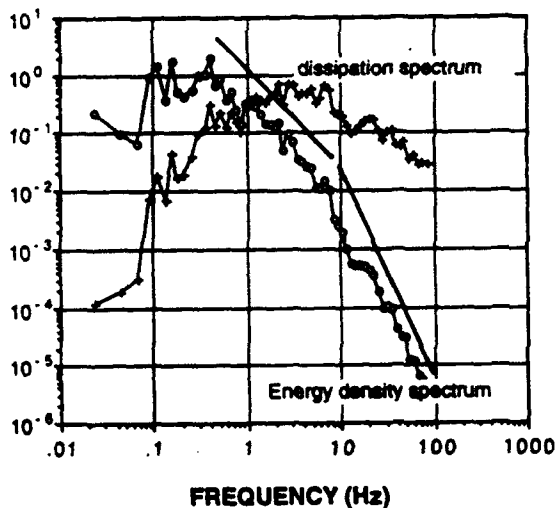


Fig. 8: Energy density and energy dissipation spectrum for a gate in the central part of the velocity profile. The $-5/3$ slope of the inertial subrange and the -4 slope in the diffusive subrange of the energy density spectrum are indicated.

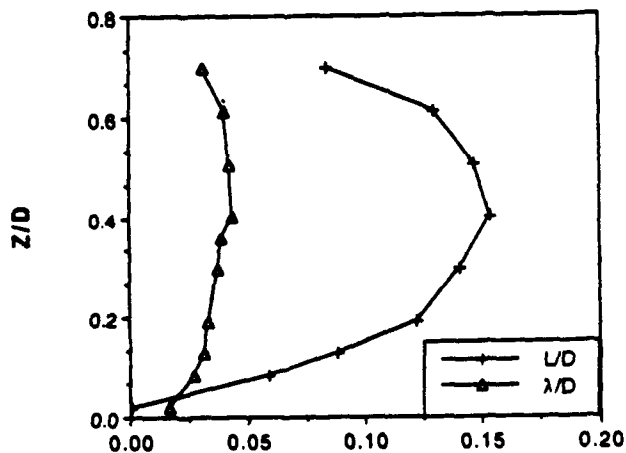


Fig. 9: Profiles of the dimensionless micro-scale λ and macro-scale L . D is the water depth, z is the vertical axis.

INCOMPRESSIBLE TURBULENT FLOW IN THE ENTRY REGION OF A TWO-DIMENSIONAL CHANNEL

Jack W. Backus and Merle C. Potter
Department of Mechanical Engineering
Michigan State University
E. Lansing, MI 48824-1226

Bashar S. AbdulNour
Department of Mechanical Engineering
University of Wyoming
Laramie, WY 82071-3295

ABSTRACT

The turbulent entry flow in a two-dimensional channel is characterized by an initial inviscid-core region followed by a profile-development region which leads to fully-developed turbulent flow. The length at which turbulent bursts initiate the transition process is very dependent on the Reynolds number. Previous studies have been carried out for high Reynolds numbers ($Re > 10^5$) only so that the transition has been assumed to start from the inlet section. For flows at low Reynolds numbers ($2,000 < Re < 12,000$), transition is observed to occur significantly downstream of the inviscid-core region; for such flows the flow resembles the laminar flow entry region up to the point of transition so that the pressure gradient prior to transition is less than that of the fully-developed turbulent flow. For intermediate Reynolds numbers ($12,000 < Re < 20,000$), transition occurs downstream of the inlet section but before the disappearance of the inviscid core. For such flows, the pressure gradient is near its fully-developed value throughout the entire entry region.

1. INTRODUCTION

The study of turbulent entry flows is important in many engineering applications, including the designs of wind and water tunnels, as well as piping and duct systems. Turbulent entry flow is characterized by an initial inviscid-core region that changes to a profile-development region. This is followed by fully-developed flow downstream. The location of a transition region in which turbulence initiates is dependent on the Reynolds number. Although researchers have developed relations for laminar entry flows that satisfactorily predict experimental findings, similar success has not been achieved for turbulent flow at all Reynolds number ranges.

Many researchers have studied turbulent entry flows in smooth pipes; these include Ross and Whippary (1956), Barbin and Jones (1963), Bowlus and Brighton (1968), Klein (1981), and Salami (1986). Wang and Tullis (1974) provided an analysis for flow in a rough pipe. In all of these studies, the analyses were carried out for higher-Reynolds-number ($Re > 10^5$) flows than studied here. One common conclusion was that the pressure gradient at the entrance to the pipe was significantly higher than the value for fully-developed flow. Moreover, it was determined that the pressure gradient reduces to its fully-developed value in less than fifteen (15) pipe diameters. Barbin and Jones (1963) estimated the entrance length (distance to achieve fully-developed flow) to be forty-four (44) pipe diameters at $Re = 388,000$. Wang and Tullis (1974) estimated the entrance length to be forty-nine (49) pipe diameters for $10^6 < Re < 3.7 \times 10^6$. In sharp contrast, Klein (1981) predicted that the entrance length may exceed one hundred forty (140) pipe diameters. Even though the entrance length was not measured, the distance at which the boundary layer filled the pipe and the inviscid core disappeared was determined. Barbin and Jones (1963) measured the inviscid-core length to be twenty-eight (28) diameters, while Wang and Tullis (1974) achieved this at thirty (30) diameters. Bowlus and Brighton (1968) developed the following equation for the inviscid-core length, L_i :

$$\frac{L_i}{D} = 6.19 \ln Re - 46$$

where D is the pipe diameter and Re is the Reynolds number based on D and the uniform velocity at the inlet section. This equation agrees with experimental data collected by Barbin and Jones (1963) within 10%. The results of past investigations of turbulent entry flows in pipes indicate a need for further research for flows at lower Reynolds numbers.

In addition to the studies in pipes, investigations have been conducted for flows in channels and ducts. Two studies of interest were conducted by Cebeci and Keller (1974) and Shcherbinin and Shklyar (1980). In these analyses, excellent agreement between predicted and experimental velocity profiles was obtained. Both studies employed the equations of motion (momentum and continuity) and an eddy-viscosity model for the turbulent structure to predict velocity profiles. These equations were solved numerically. As with studies in pipes, values for Reynolds numbers (based on average velocity and channel height) in these studies exceeded 10^5 .

Even though a great deal of research has been conducted, there appears to be little data at low to intermediate Reynolds numbers ($4,000 \leq Re \leq 18,000$) for entry flows. Additionally, data over the entire entry region to determine the entrance length for fully-developed turbulent flow is lacking. Therefore, the purpose of this study is to investigate turbulent entry flows for low to intermediate Reynolds numbers in a smooth, two-dimensional channel, with attention given to the entire entry region.

2. FLOW CHARACTERISTICS

Simplified models of turbulent entry flows depict the flow as a growing turbulent boundary layer that eventually fills the entire channel. Often, the entrance length is defined as the distance for the inviscid core to disappear and the flow is considered fully developed beyond that point. However, the flow changes considerably beyond the disappearance of the inviscid core before reaching its fully-developed velocity profile. Moreover, this simplified model does not accommodate turbulent entry flows in which turbulent bursting does not initiate at the channel inlet section. Therefore, to accurately describe flow in the entire region, a more complex model is required.

To provide a more comprehensive description of developing flow, several lengths have been defined and are shown in Figure 1. The distance from the channel inlet section to the location where turbulent bursting initiates is called the turbulence-initiation length, L_t . The turbulence-initiation length is dependent on the Reynolds number and occurs near the channel inlet section for high Reynolds numbers ($Re > 10^5$). As noted earlier, the inviscid-core length, L_i , is the distance from the inlet section to the location where inviscid core disappears as the viscous wall layer fills the channel. The distance at which the entire flow is turbulent is the established-turbulence length, L_s . The distance at which the pressure gradient achieves its fully-developed value is denoted L_p . Finally, the distance from the channel inlet section to the location where the velocity profile attains its fully-developed shape is the entrance length, L_e . It may be possible that the turbulent structure has not been completely established at L_e , as has been suggested. This study did not address that point.

The choice of a velocity profile to represent fully-developed turbulent flow varies between researchers. For this study, the one-seventh power-law velocity profile

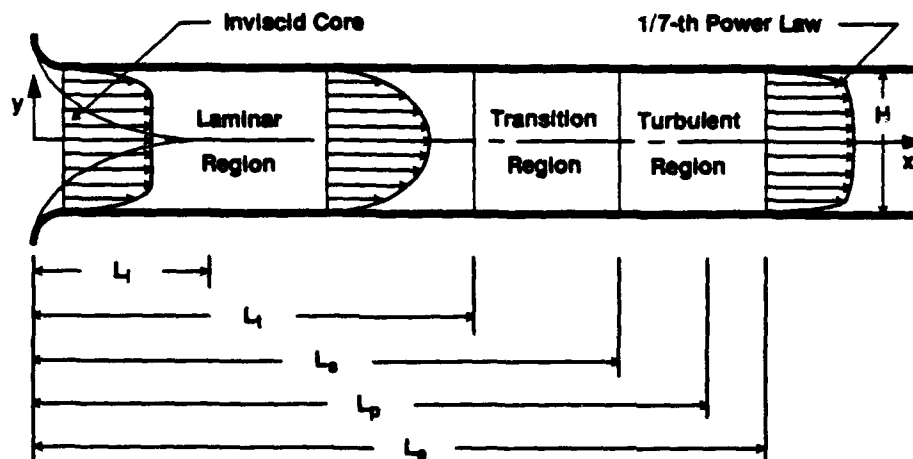


Figure 1. Definition of turbulent entrance lengths.

$$\frac{\bar{u}}{U_0} = \left(\frac{y}{H}\right)^{1/7}$$

has been selected. Here \bar{u} is the mean velocity component in the streamwise direction, U_0 is the average velocity, y is the transverse coordinate, and H is the channel height.

In addition to studying the development of the velocity profile, the development of the pressure gradient is also of interest. In earlier studies at higher Reynolds numbers, where turbulent bursts initiate near the inlet section of the channel, the pressure decreased from a relatively large value near the inlet section to its fully-developed distribution downstream. However, at lower Reynolds number flows the pressure distribution should behave quite differently. For steady developed flow, the pressure gradient is directly related to the wall shear stress, τ_w . Furthermore, wall shear stress relates to the velocity profile near the wall by

$$\tau_w = \mu \left| \frac{\partial \bar{u}}{\partial y} \right|_w$$

where μ is the dynamic viscosity.

The wall velocity gradient for laminar flow is substantially less than that of turbulent flow. For low Reynolds numbers, the flow is initially laminar and turbulent bursts initiate downstream of the channel inlet section in the profile-development region. Consequently, the pressure near the inlet section is substantially less than the pressure associated with the high-Reynolds-number flow, as shown in Figure 2. For the high-Reynolds-number flow, the pressure approaches its fully-developed value earlier in the flow, as shown. For intermediate-Reynolds-number flow, the pressure gradient distribution approximates its fully-developed value throughout the entire entry flow, a rather interesting observation.

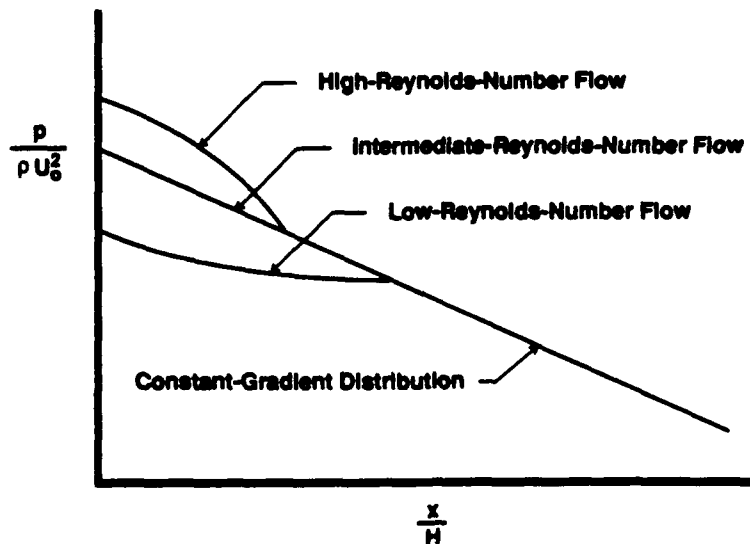


Figure 2. Proposed pressure distributions for different ranges of Reynolds number.

3. EXPERIMENTAL FACILITY

The experiments for this study were conducted in a rectangular, parallel-sided, straight channel. The channel assembly, shown in Figure 3, consisted of an entrance, a settling chamber, a plenum, a contraction, and a horizontal parallel-plate test section. A fan was located downstream of the test section to reduce flow disturbances associated with an otherwise upstream fan location. The channel occupied two rooms so that the entrance could be in a separate room sealed from the test section. This allowed for a pressurized test section which prevents highly undesirable leakage into the test section as is found for a single room arrangement with a downstream fan location.

The entrance and settling chamber consisted of a smooth inlet; a one-inch hog-hair filter; a honeycomb section filled with 7.5 inch long, 0.25 inch diameter plastic straws; and four stainless steel screens, 8 inches apart, with screen meshes of 59.5%, 57.8%, 57.4%, and 49.6%, respectively. The plenum was 48 inches long and made of plywood. The two-dimensional contraction was formed from a styrofoam block and covered with linoleum. The experimental test section was 16 feet long by 4 feet wide, with a 0.75 ± 0.005 inch wide gap. The top of the test section was constructed of acrylic sheets. The bottom surface consisted of aluminum plates covered with a sheet of linoleum, spray painted black and wet sanded smooth. The data was collected with commercially available instruments.

4. RESULTS

To provide a comprehensive description of turbulent flow development, experiments were conducted to determine the turbulence-initiation length, the inviscid-core length, the established-turbulence length, the length at which the pressure gradient achieves its fully-developed distribution, and the entrance length. These experiments were conducted for Reynolds numbers ranging from 4,000 to 18,000 and are plotted in Figure 4.

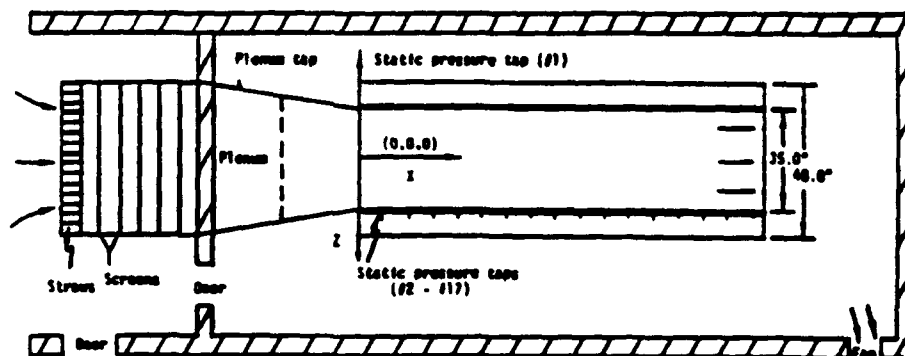


Figure 3. Experimental facility; top view.

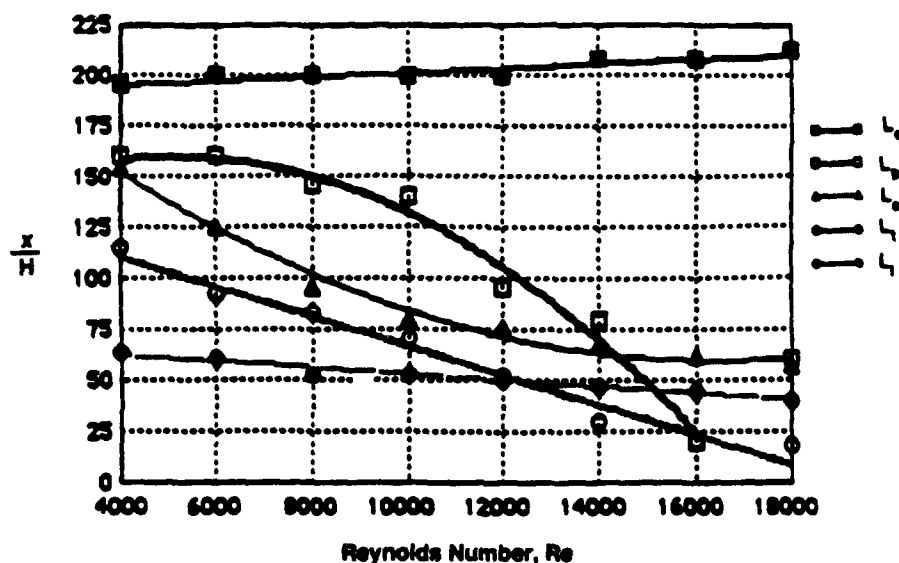


Figure 4. Various turbulent entrance Lengths as functions of the Reynolds number.

The measurements to determine the turbulence-initiation length, L_i , were taken along the channel centerline. As shown in Figure 4, L_i decreases as the Reynolds number increases. Eventually, turbulence will initiate at the channel inlet section at high Reynolds numbers. The plot of the inviscid-core length shows that L_i gradually decreases as the Reynolds number increases. This indicates that a relation of the form derived by Bowlus and Brighton (1968) for pipe flow is not applicable for the conditions in this channel flow study at the Reynolds numbers considered because the equation they proposed would lead to an increasing L_i with increasing Reynolds number. For $Re < 12,000$, the initiation of turbulent bursts occurs downstream of the inviscid-core region. Therefore, the velocity profiles and static pressure distributions for $Re < 12,000$ should resemble laminar flow conditions until turbulence initiates downstream.

Measurement of the established-turbulence length indicates that L_e decreases with increasing Reynolds number. The distance L_p at which the pressure gradient attains its fully-developed value also decreases with increasing Reynolds number for $Re < 16,000$. For $Re > 16,000$, L_p increases with Reynolds number. This change is related to the pressure gradient development and will be discussed later. The entrance length was established by curve fitting the velocity profile to a one-seventh power-law distribution. From the plot of entrance length it can be seen that unlike the other distances measured, L_e gradually increases with Reynolds number. Moreover, changes in the Reynolds number do not affect values for L_e as significantly as the other lengths measured. Because L_e is in the range of 190 to 215 channel heights, the conclusions of Klein (1981), that entrance lengths could exceed 140 pipe diameters, would tend to be supported over those of Barbin and

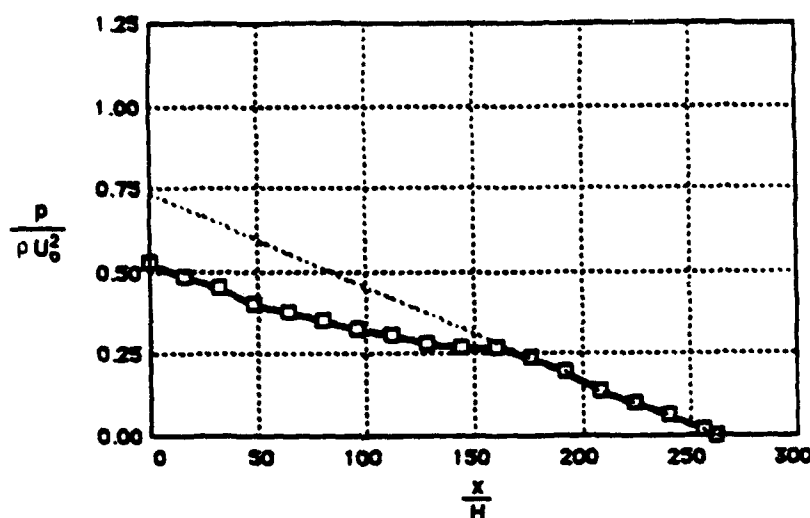


Figure 5. Low-Reynolds-number static pressure distribution; $Re = 4,000$.

Jones (1963) or Wang and Tullis (1974). This would further indicate that some past experiments for fully-developed turbulent flow were actually conducted on flows that were not yet fully developed.

Experimental streamwise static pressure distributions were measured using taps in the channel side wall. The results of ten trials at each Reynolds number were averaged. The measured distributions can be divided into three categories. The first category of static pressure distributions are designated as low-Reynolds-number distributions. These flows are represented by the curve of Figure 5 and are characterized by the disappearance of the inviscid core before the first turbulent bursts are detected (i.e., $L_i < L_t$). For this category, the pressure gradient initially follows a gradient characteristic of laminar flow. After turbulent bursts initiate, the pressure gradient deviates from the laminar gradient and approaches the fully-developed turbulent profile.

The second category of static pressure distributions are represented by the curves of Figures 6, 7, and 8, and are designated as intermediate-Reynolds-number distributions. For this case, the turbulent bursts initiate prior to but near the disappearance of the inviscid core (i.e., $L_i \leq L_t$). The pressure gradient is near its fully-developed value throughout the entry region. There is a value for which the pressure distribution remains at its fully-developed value throughout the entire flow; the available data indicates that it is approximately around $Re = 16,000$, as demonstrated in Figure 7.

The final category of pressure distributions is the high-Reynolds-number distributions. For this case, the pressure at the entrance to the channel is significantly greater than its fully-developed value. This category is not represented by data collected in this study. However, Figure 8 for flow at $Re = 18,000$ is a clear indicative of this trend.

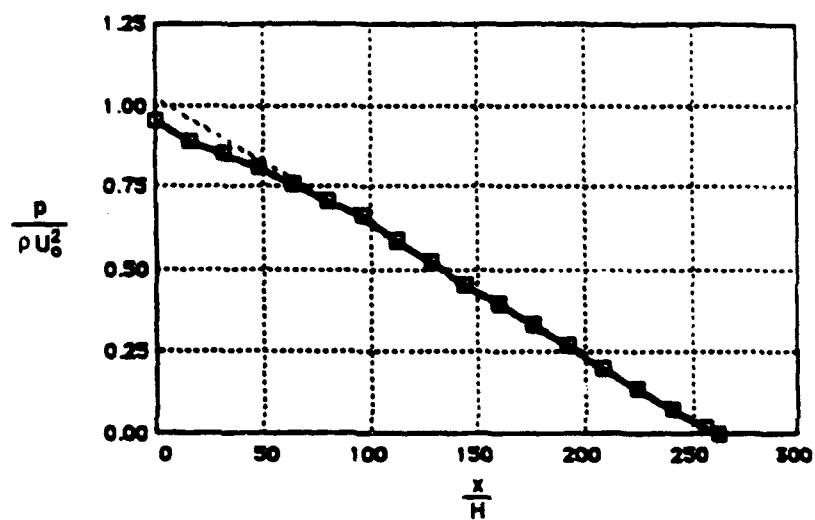


Figure 6. Intermediate-Reynolds-number static pressure distribution; $Re = 12,000$.

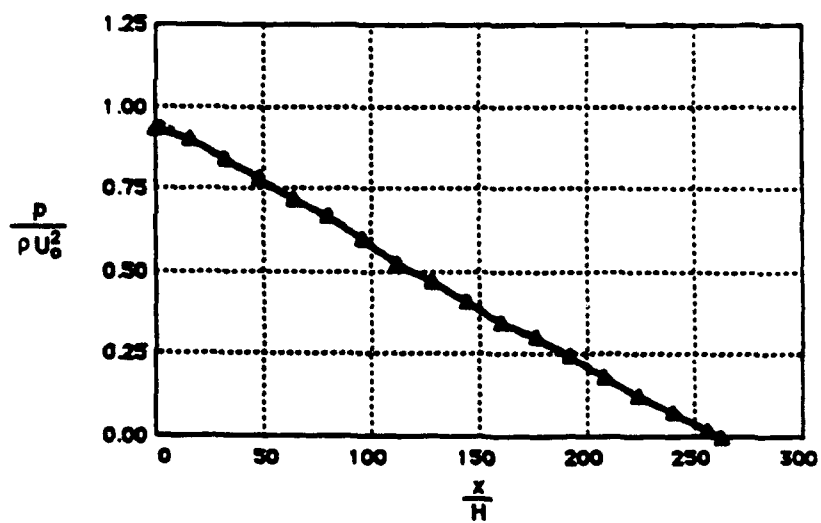


Figure 7. Intermediate-Reynolds-number static pressure distribution; $Re = 16,000$.

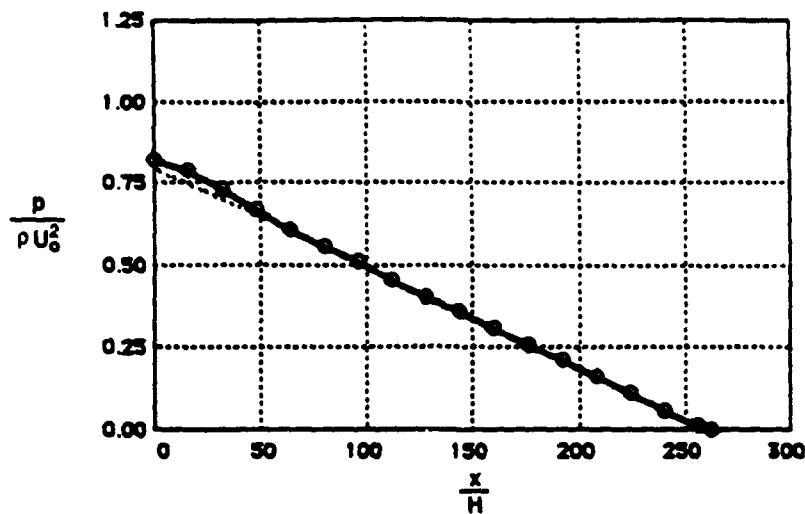


Figure 8. Intermediate-Reynolds-number static pressure distribution; $Re = 18,000$.

5. CONCLUSIONS

Based on the results of this investigation, the following conclusions can be made for flow in the entry region of a smooth channel.

1. The inviscid-core length, L_i , decreases with increasing Reynolds number. It can be approximated by the relationship

$$\frac{L_i}{H} = -0.00156 Re + 69 \quad Re < 18,000.$$

The Reynolds number is $Re = U_0 H / \nu$, where ν is the kinematic viscosity.

2. The turbulence-initiation length, L_t , decreases with increasing Reynolds number. It can be approximated by the relationship

$$\frac{L_t}{H} = -0.0072 Re + 140 \quad Re < 18,000.$$

3. The established-turbulence length, L_s , decreases with increasing Reynolds number. It can be approximated by the relationship

$$\frac{L_s}{H} = 6.8 \times 10^{-8} Re^2 - 0.008 Re + 168 \quad Re < 18,000.$$

4. The distance from the channel inlet section to the location where the pressure gradient attains its fully-developed value, L_p , decreases with Reynolds number for $Re < 16,000$. It can be approximated by the relationship

$$\frac{L_p}{H} = -6.9 \times 10^{-8} Re^2 - 0.01 Re + 220 \quad Re < 16,000.$$

For $Re > 16,000$ the value for L_p increases with increasing Reynolds number.

5. The entrance length, L_p , for the velocity profile to attain its fully-developed form, increases with Reynolds number and exceeds 190 channel heights. It can be approximated by the relationship

$$\frac{L_p}{H} = 0.00104 Re + 190 \quad Re < 18,000.$$

6. There are three categories of turbulent flows that are designated as follows:
 - a. Low-Reynolds-number turbulent flow for which $L_i < L_f$. In this category, $Re < 10,000$ and the pressure in the entry region is less than the pressure associated with the fully-developed flow distribution.
 - b. Intermediate-Reynolds-number turbulent flow for which $L_i \leq L_f$. In this category, $10,000 < Re < 20,000$ and the pressure gradient is approximated by its fully-developed turbulent values. This category includes a flow, at $Re = 16,000$, for which the pressure gradient retains its fully-developed value throughout the entire entry region.
 - c. High-Reynolds-number flows for which $L_i = 0$. In this category, $Re > 10^5$ and the pressure is above the pressure value associated with the fully-developed flow distribution and reduces monotonically to its fully-developed distribution downstream.

REFERENCES

- Ross, D., and Whippary, N. J., 1956, "Turbulent Flow in the Entrance Region of a Pipe", *Transactions of the ASME, Series D*, Vol. 78, pp. 915-923.
- Barbin, A. R., and Jones, J. B., 1963, "Turbulent Flow in the Inlet Region of a Smooth Pipe", *ASME Journal of Basic Engineering*, Vol. 85, pp. 29-34.
- Bowlus, D. A., and Brighton, J. A., 1968, "Incompressible Turbulent Flow in the Inlet Region of a Pipe", *ASME Journal of Basic Engineering*, Vol. 90, pp. 431-433.
- Klein, A., 1981, "Review: Turbulent Developing Pipe Flow", *ASME Journal of Fluids Engineering*, Vol. 103, pp. 243-249.
- Salami, L. A., 1986, "An Investigation of Turbulent Developing Flow at the Entrance to a Smooth Pipe", *International Journal of Heat and Fluid Flow*, Vol. 7, pp. 247-257.
- Wang, J.-S., and Tullis, J. P., 1974, "Turbulent Flow in the Entry Region of a Rough Pipe", *ASME Journal of Fluids Engineering*, Vol. 96, pp. 62-68.
- Cebeci, T., and Keller, H. B., 1974, "Flow in Ducts by Boundary-Layer Theory", *Proceedings of the Fifth Australian Conference on Hydraulics and Fluid Mechanics*, pp. 538-545.
- Shcherbinin, V. I., and Shklyar, F. R., 1980, "Analysis of the Hydrodynamic Entrance Region of a Plane Channel with the Application of Various Turbulence Models", *High Temperature*, Vol. 18, pp. 781-785.

EXAMINATION OF THE TWO HALF-POWER REGIONS IN TURBULENT DECREASING ADVERSE PRESSURE GRADIENT FLOWS

By G.A. Kopp and O.F. Turan⁺

Mechanical Engineering Department
McMaster University
Hamilton, Ontario L8S 4L7
Canada

ABSTRACT

From the longitudinal mean velocity profiles in eight decreasing adverse pressure gradient turbulent diffuser flows, and in similar regions of an initially increasing adverse pressure gradient diffuser flow, it can be shown that there are two half-power regions, starting outside of the viscous sublayer. In these flows, the longitudinal development of the two half-power regions indicates an entry region and a universal region. The ranges of applicability of different semi-empirical velocity profiles are also described in terms of the two half-power coefficients.

I. INTRODUCTION

Mean velocity profiles in wall-bounded turbulent flows with adverse pressure gradients is a topic which has generated much research due to the common occurrence of such flows in engineering applications. Although there is a large volume of literature on the topic, no one theory is wholly satisfactory, the reason being the high degree of complexity in these types of flows. Developing a better understanding of the mean velocity behavior in this class of flows will allow engineers to more effectively design plane or conical diffusers. In addition, such an understanding of flow development will also help in practical prediction without having to resort to expensive experimentation or direct numerical simulation.

In the present work, with the ultimate objective of more accurate semi-empirical prediction of the mean velocity field in decreasing adverse pressure gradient turbulent flows, the experimental data from the nine turbulent diffuser flows listed in Table 1 are examined. Although this is certainly not all of the experimental data available in the literature for this class of flows, it is a representative sample. Only unseparated, incompressible flows which have no swirling are considered. It has been observed that there are two half-power regions in all the flows examined. In fact, the longitudinal development of the mean flow can be described in terms of the half-power characteristics.

The nine flows listed in Table 1 include four plane diffuser flows, namely, Flows 1100, 1200, 2900 of the 1968 Stanford Conference (Coles and Hirst 1968) and Flow 0141 of the 1980-81 Stanford Conference (Kline et al. 1981). In addition, the experimental data from five conical diffuser flows of

⁺ Address correspondence to this author. Tel. (416) 525 9140 Ext. 7296 or 7321. Facs. (416) 572 5944.

ten, six and eight-degree conical angles, have been examined. The ten and six-degree conical diffuser flows are, Flows 5000 and 5100 (Coles and Hirst), and Flows 0142 and 0143 (Kline et al.), respectively. The eight-degree conical diffuser data are from Turan (1988), Kassab (1986) and Ozimek (1985). One of the plane diffusers, Flow 0141, has an increasing adverse pressure gradient over much of the length of the flow. The other eight flows have decreasing adverse pressure gradients, except for a short region at their entrances. All of the diffusers have either a developing channel (or boundary layer) or pipe flow at their inlet except for the eight-degree conical diffuser which has a fully-developed pipe flow at its inlet. The inlet Reynolds numbers of these flows are also listed in Table 1.

Based on local flow variables, three different distinct length scales can be developed in a wall-bounded adverse pressure gradient flow (Kader and Yaglom), such that $\delta_v \ll \delta_p \ll \delta$, where δ_v is the viscous length scale, $\delta_v = \nu/u_*$; δ_p is the pressure length scale, $\delta_p = u_*^2/\alpha$ ($u_* = (\tau_w/\rho)^{1/2}$ is the friction velocity and τ_w is the wall shear stress). The values of these three length scales in the eight decreasing adverse pressure gradient flows examined have been found to differ by at least an order of magnitude at a given measuring location (Kopp 1991). Therefore, these three length scales can be distinctly identified. As a result, there should be at least three different functional forms of the mean velocity at each particular measuring station.

In the following, first, the two half-power regions are discussed in detail. Subsequently, applicability of the profiles of Coles (1956), Kader and Yaglom (1978), Perry (1966), Townsend (1961), McDonald (1969), Mellor (1966), and Nakayama and Koyama (1984) are examined with respect to the development of the two half-power regions.

II. PREDICTION OF THE MEAN VELOCITY FIELD IN DECREASING ADVERSE PRESSURE GRADIENT FLOWS

A. THE TWO HALF-POWER REGIONS

It is observed that in turbulent adverse pressure gradient internal flows, there are two regions at each measuring station where the mean velocity varies with the square root of the distance from the wall. All of the flows examined here exhibit a similar development of two half-power regions. Examples of this progression is shown in Figure 1, for the plane diffuser flows, Flows 2900, 1200 and 0141. Figure 2 shows the same development in the conical diffuser flows, Flows 5100, 0142 and the eight degree conical diffuser are given as examples. Here, the inner half-power region is where the mean velocity profile can be described by,

$$U/U_\infty = C_i/U_\infty(y/\delta)^{1/2} + D_i/U_\infty, \quad (1)$$

while in the outer half-power region, the mean velocity is given as follows:

$$U/U_\infty = C_o/U_\infty(y/\delta)^{1/2} + D_o/U_\infty. \quad (2)$$

In addition to experimental evidence, the presence of the inner half-power region can be shown from a dimensional analysis, as done by Kader and Yaglom (1978) and Perry et al. (1966); or it can be analytically linked to the presence of an approximately linear turbulent shear stress distribution, as done by Townsend (1962), Mellor (1966), McDonald (1969) and Nakayama and Koyama (1984). It has been observed here for the three flows with turbulence

measurements (Flows 0142, 0143, and the eight-degree conical diffuser) that outer half-power region occurs after the peak of the Reynolds shear stress \overline{uv} , as \overline{uv} decreases in an approximately linear manner. The outer half-power region can hence be related to this linear stress layer, just as the inner half-power region is.

B. THE $C_0 < C_i$ REGION

Figures 1 and 2 show that early in the development of these flows, the outer half-power slope, C_0 is less than the inner half-power slope, C_i . As the flows develop, the inner slope decreases while the outer slope increases until they become approximately the same. The region where $C_i = C_0$ is the half-power region discussed by Perry (1966), Samuel and Joubert (1974), and Kader and Yaglom. As the flows develop, the inner half-power slope becomes smaller than the outer slope.

When $C_i > C_0$ in all of the diffusers, the blending region between inner and outer half power regions is small, indeed almost non-existent on half-power coordinates. At this point there are no substantial linear regions present in any of the flows examined, as seen in Figures 1 and 2.

C. THE $C_0 > C_i$ REGION

Once C_0 exceeds C_i , the two half-power regions begin to separate and the blending region becomes linear. Specifically, the linear blending region begins for approximately $2 < C_0/C_i < 3$ in all of the flows examined here. Further downstream, the blending region becomes longer and has a 3/2-power velocity distribution. This occurs when $4 < C_0/C_i < 5$. Examples of this development can be seen in Figures 3 and 4. Figure 3 shows the linear blending region at Station 5 ($x = 0.382$ m) in Flow 0142 on linear coordinates while Figure 4 shows the 3/2-power blending region at Station 11 of the same flow ($x = 5.92$ m) on 3/2-power coordinates. It is observed that the region of overlap can be quite long.

Trupp et al. (1986) reported the presence of two half-power regions in the eight-degree conical diffuser examined here. The experimental data examined in that paper, however, were only for the near wall region, so that towards the exit, there were no data for the outer half-power regions. Upon further examination of the experimental data of Turan, Kassab, and Ozimek from the same diffuser, it has been observed that there are two half-power regions present throughout the flow, as mentioned above.

The only exception to the above discussion is Flow 0143. This flow has a very long entry length caused by the "backward facing step" arrangement just upstream of the diffuser entrance, which was used to generate high core turbulence. The development is much slower, and C_0 becomes greater than C_i only at the last measuring station (the entry length concept is discussed further in Section E).

Flows 1100 and 1200 developed in much less extreme adverse pressure gradients. Hence, flow 1100 never develops a 3/2-power region and flow 1200 only barely develops a 3/2-power region. All of the other flows have larger adverse pressure gradients and the 3/2-power region develops more readily.

The development of the linear regions of this class of flows is related to the decreasing adverse pressure gradient. Upon examining Samuel and Joubert's increasing adverse pressure gradient flow, Flow 0141, it can be seen that the

linear blending regions between the inner and outer half-power regions are delayed until the adverse pressure gradient starts to decrease. In the other flows examined, the pressure gradient increases for a short distance from the inlet. At this point, the ratio of the outer half-power slope to the inner slope starts to increase rapidly and finally the long linear blending region between the two 1/2-power regions occurs.

As the 3/2-power blending region begins, the flow has developed sufficiently so that the pressure gradient, freestream velocity, and the friction velocity do not decrease as rapidly as upstream. The logarithmic region begins to return, or becomes longer. As a result, the mean flow field can be said to be in a moving equilibrium at this stage.

Figure 5 shows how the ratio of C_o/C_i changes with u_\star/U_x . The flows develop as u_\star/U_x decreases (right to left on this plot), with C_o/C_i increasing in this direction. Figure 6 shows that the ratio of the intercepts, D_o/D_i , also correlates well with the ratio of u_\star/U_x . The ratio of the two half-power slopes seems to be quite important, as discussed in more detail below.

D. ENTRY LENGTH AND COLES' LAW OF THE WAKE IN THE UNIVERSAL REGION

Coles (1956) showed that the mean velocity profile in the outer region is similar to that for a wake flow. He obtained a velocity profile of the form

$$U^+ = f(y^+) + g(\Pi, y/\delta), \quad (3)$$

where $f(y^+)$ is the Log Law and $g(\Pi, y/\delta)$ is the departure from the Log Law in the outer region. Coles determined that $g(\Pi, y/\delta) = \Pi(x)w(y/\delta)/x$ where $w(y/\delta)$ is called the Law of the Wake, which was determined empirically. $\Pi(x)$ is determined from

$$\frac{U_x}{u_\star} = \frac{1}{x} \ln\left(\frac{u_\star \delta}{\nu}\right) + b + \frac{\Pi}{x} w(1), \quad (4)$$

where $w(1)=2$. Hinze (1975) approximated $w(y/\delta)$ as follows:

$$w(\zeta) = 1 + \sin[(2\zeta - 1)\pi/2], \quad (5)$$

where $\zeta = y/\delta$. There is a small error in this approximation at $\zeta \approx 0.1$ and $\zeta \approx 0.8$ to 0.9 . In the outer region of the boundary layer, Coles' Law of the Wake should be valid if a logarithmic velocity profile exists and the adverse pressure gradient is not severe.

Coles' Law of the Wake fits the experimental data at every station of the plane diffuser flows examined, as shown in Figure 7a for selective stations in Flow 1100, Flow 1200 and Flow 2900, although there are a few exceptions where the agreement is not as good. These minor inaccuracies seem to be due to inaccuracies in determining the boundary layer thickness, such as in the case of Flow 2900 in Figure 7a. Sample profiles are presented in Figure 7b from the six and ten-degree conical diffusers, and in Figure 7c, from the eight-degree conical diffuser. In Figure 7b, the Log Law intercept is unmodified. In addition, u_\star was calculated from the Preston tube measurements, as opposed to Clauser's method. This figure shows that Coles' formulation predicts the data reasonably in the outer layer, although the fit is much better when the Log Law intercept is modified or the Clauser friction velocity is used.

In the entry region of these flows, Coles' Law of the Wake does not fit the experimental data, as shown in Figure 7c for the eight-degree conical diffuser Station 2 ($x = 0.18$ m). However, because Coles' Law of the Wake

reasonably fits all of the data sets after an "entry length", it is considered here to be a universal mean velocity profile. This universal mean velocity profile depends on two parameters (u_* and $\Pi(x)$), and hence, it does not collapse onto one line for all flows. This can be seen in Figure 8 which shows the data for the eight-degree and two six-degree conical diffuser flows on the usual U^+ versus $\log y^+$ coordinates. For these three flows, the outer layer occurs at varying distances from the wall.

The entry length is hence defined as the distance to the point where Coles' Law of the Wake starts to accurately predict the data. After the entry length, the universal region starts. In the universal region, the local flow parameters such as the friction velocity, freestream velocity and kinematic pressure gradient do not change very rapidly in comparison with the entry region where the gradients are large. There are not enough experimental data to examine whether the entry length is Reynolds number dependent.

E. ENTRY LENGTH IN TERMS OF THE TWO HALF-POWER REGIONS: $C_0/C_i < 3$

Since the ratio of the inner to outer half-power slopes is also related to the entry length, the mean velocity becomes universal for the flows examined here specifically in the range $1.1 < C_0/C_i < 1.4$ for the plane diffusers and $1.2 < C_0/C_i < 3.5$ for the conical geometries. This criterion is dependent on initial conditions as can be shown with the data from the six-degree conical diffuser. Flows 0142 and 0143. Flow 0142 develops a universal profile at $C_0/C_i = 3.2$; while in Flow 0143, the mean velocity profile attains the universal form at $C_0/C_i = 1.2$. Generally, the Law of the Wake predicts the experimental profile well when $C_0/C_i > 3$. A summary is given in Table 2.

Attempts were made to relate the slope and intercept for the inner half-power region to the local flow parameters so that Figures 5 and 6 can be used to evaluate C_0 and D_0 . It is observed from examining the experimental data that the inner half-power region overlaps with the Log Law, especially when the Log Law is long. Therefore, it seems reasonable to expect C_i to be a function of the friction velocity just as the Log Law is. The best non-dimensional correlation of the inner half-power slope is as shown in Figure 8 in terms of $[C_i/(U_\infty \delta^{1/2})]$ versus $[x/\delta_{inlet} * \alpha \delta/u_*^2]$. This plot is most useful in the entry length region where Coles' profile does not apply and the Log Law region is small. The Law of the Wake occurs at different distances from the wall for different flows. This causes difficulty in correlating the intercepts (or slip velocities) of the two half-power regions. The best correlation for D_i has been found to be D_i/U_∞ versus $\Delta = \alpha \nu/u_*^3$, as shown in Figure 9.

F. TOWNSEND'S AND McDONALD'S PROFILES

In the region where $C_0/C_i < 1$, the only mean velocity formulations that predict the data are those of Townsend and McDonald. Mellor's and Nakayama and Koyama's models yield profiles similar to Townsend's, as shown by Nakayama and Koyama. With the stress distribution approximated as, $\frac{\tau}{\rho} = \frac{\tau_w}{\rho} + \alpha y = u_*^2 + \alpha y$, and the same mixing length as used by van Driest (1956), $\ell = \alpha y$, Townsend's mean velocity profile is,

$$U = \frac{u_*}{x} \left(\ln \frac{(a + \alpha y)^{1/2} - a^{1/2}}{(a + \alpha y)^{1/2} + a^{1/2}} \right) + \frac{2(1 - B \operatorname{sgn}(\alpha))}{x} (a + \alpha y)^{1/2} + U_s, \quad (6)$$

where $a = u_*^2$ and x is the universal mixing constant. Using the Log Law, the

half-power law, but do not adequately predict the half-power region, except for McDonald's profile at a few stations in the entrance regions. McDonald's model can be used in the entry region of these flows with the shear stress gradient approximately 0.6 times the pressure gradient. As summarized in Table 2, McDonald's formulation works reasonably well for $C_0/C_1 < 3$ while Townsend's model works when $C_0/C_1 < 1.2$.

For plane diffuser flows there is no entry region data available, where $C_1 > C_0$; whereas in the conical diffuser flows, the inner half-power law is easily observed in the entry region since there is a multitude of entry region data for these flows, and hence, there is less uncertainty.

G. THE PROFILES OF PERRY AND KADER AND YAGLOM

As stated above, when C_0/C_1 becomes equal to approximately unity, the half-power region described by Perry, Samuel and Joubert and Kader and Yaglom begins. Perry stated that in the half-power layer, the flow is dependent primarily on the kinematic pressure gradient and the distance from the wall. Since there should be a half-power layer in adverse pressure gradient flows, and if the velocity gradient, obtained from dimensional analysis, is of the following form, $\frac{\partial \bar{u}}{\partial y} = \frac{1}{2} K_1 \frac{\alpha^{1/2}}{y}$, upon integration the half-power velocity profile is obtained. Perry also pointed out that the universal constant, K_1 , shows reasonable agreement with experimental results when the major portion of the velocity profile at a particular station varies with the square-root of y . Perry's half-power equation is as follows:

slip velocity or additive constant, U_s can be obtained, and is given by,

$$U_s = \frac{U_*}{x} \left[\ln\left(\frac{4}{\Delta}\right) - 2[1 - B \operatorname{sgn}(\alpha)] \right] + A, \quad (7)$$

where A is the intercept of the Log Law, $B \approx 0.2$ is a constant representative of the rate of turbulent kinetic energy diffusion, and $\Delta = \alpha\nu/u_*^3$.

With the stress distribution modified as, $\tau/\rho = a + \gamma\alpha y$, where a can be either positive or negative, and $\gamma < 1$ is empirically determined, McDonald's profile is given as, follows, for a positive a ,

$$U = \frac{2}{x} [(a^2 + \gamma\alpha y)^{1/2} - a^{1/2}] + \frac{a^{1/2}}{x} \ln \left(\frac{4}{\Delta} \frac{(a^2 + \gamma\alpha y)^{1/2} - a^{1/2}}{(a^2 + \gamma\alpha y)^{1/2} + a^{1/2}} \right) + U_s. \quad (8)$$

with the slip velocity matched to the velocity at the end of the buffer region. The resulting expression is similar to Equation 6 with $B = 0$, and the linear shear stress gradient is empirically or experimentally determined.

Townsend's model, in general, agrees with the measured profiles at only the first few axial stations in all of the flows if the slip velocity is modified. In these locations Townsend's model provides a moderately better approximation to the data than the Log Law. Further downstream, however, his model does not predict the mean profiles as significant amounts of advection of turbulence kinetic energy become apparent. In addition, the predicted slip velocity also becomes too large for these stations.

At all the axial stations in the entry region, McDonald's formulation is in good agreement with the six and eight-degree conical diffuser data sets over a longer region than the Log Law. This is also a substantially longer range of measuring stations than Townsend's model worked in. Far from the wall, the models of McDonald and Townsend, mathematically asymptote to the

$$v = K_1 \left(\frac{\alpha y}{u_*^2} \right)^{1/2} + \frac{K_2}{u_*} \quad (9)$$

where K_1 is a universal constant and K_2 is a function of Δ . The slip velocity is given as, $\frac{K_2}{u_*} = \frac{1}{\kappa} \ln(C/\Delta) + A$, where κ and A are the Log Law constants. $K_1 = 4.16$, and $C = 0.19$ is a universal constant. Because of Perry's definition of the slip velocity, the half-power region is to follow immediately after the logarithmic region. Perry, thus, assumed the presence of a logarithmic region in all unseparated adverse pressure gradient flows. As indicated before, it has been observed in the present study that this assumption is correct only after the 3/2-power blending region appears, for $4 < C_0/C_i < 5$.

Kader and Yaglom's half-power law, after performing a similarity analysis and obtaining the constants empirically, is as follows:

$$U^+ = K \frac{(\alpha \delta)^{1/2}}{u_*} \left(\frac{y}{\delta} \right)^{1/2} + \frac{K_2}{u_*} \quad (10)$$

where $K = (200u_*^2/\alpha\delta + 20)^{1/2}$, $\frac{K_2}{u_*} = 2.44 \ln(\Gamma) - \frac{15}{\Gamma^{1/2}} - \frac{6}{\Gamma}$, and $\Gamma = \frac{6u_*^3/\alpha\nu}{5 + 50u_*^2/\alpha\delta}$.

Kader and Yaglom's half-power slope is, thus, seen to be a function of $\alpha\delta/u_*^2$, while the intercept is a function of $\alpha\delta/u_*^2$ and Δ .

Following the half-power region (and possibly a small blending region) is the velocity defect region. Kader and Yaglom use dimensional analysis and empirical results from a wide range of experiments to obtain their defect law

$$U^+ = \frac{U_x}{u_*} - C \left(1 + \frac{\alpha\delta}{u_*^2} \right)^{1/2} \left(1 - \frac{y}{\delta} \right)^2 \quad (11)$$

where $C = 9.6$ is an empirical constant. A wide degree of scatter in the experimental data around $C = 9.6$ is indicated by Kader and Yaglom.

It is observed that Perry's and Kader and Yaglom's half-power laws have approximately the correct slope where $C_i \approx C_0$ in these flows. Kader and Yaglom's half-power law gives prediction over a wider range of axial stations in most of the flows than Perry's half-power law. It should be noted, however, that Perry's half-power law is designed to predict the half-power region only when it is the dominant region of the flow. On the other hand, Kader and Yaglom's defect profile gives better prediction in the plane diffusers than in the conical ones. These results are summarized in Table 2 (where Equations 9, 10 and 11 are referred to as Perry-1/2, KY-1/2 and KY-defect, respectively). From the presented results, it can be seen that these half-power laws work in the region $1 < C_0/C_i < 2.5$ (approximately) and the Kader and Yaglom defect law in the range around $C_0/C_i = 1.5$.

III. CONCLUSIONS

It was observed that there are two half-power regions present in the eight adverse pressure gradient flows examined. The ratios of the inner and outer half-power slopes and intercepts correlate well with the ratio of the friction velocity and the freestream velocity. The blending region between the two 1/2-power regions is small when the inner half-power slope is larger than the outer half-power slope. As the flows develop, the outer half-power slope grows larger than the inner half-power slope and the blending region becomes longer and is linear. Further into the flows, the blending region varies with the 3/2-power of the distance from the wall.

It is apparent from the experimental data that there is a universal mean velocity profile in wall-bounded adverse pressure gradient flows. This universal profile, the Log Law with Coles' Law of the Wake, occurs after the entry length, $C_0/C_1 > 3$, and before separation occurs, as the mean field comes to a moving equilibrium.

ACKNOWLEDGEMENTS

Financial support for this work has been provided by Natural Sciences and Engineering Research Council of Canada.

REFERENCES

- Coles, D.E., The law of the Wake in the turbulent boundary layer, *J. Fluid Mech.* vol. 1, pp. 191-226, 1956.
- Coles, D.E. and Hirst, E.A., *Computation of Turbulent Boundary Layers - 1968 AFOSR - IFP - Stanford Conference*, 1968.
- van Driest, E.R., On turbulent flow near a wall, *J. Aeronaut. Sci.* vol. 23, pp. 1007-1011, 1036, 1956.
- Hinze, J.O., *Turbulence*, McGraw Hill Book Co. New York, 1975, Chapter 7.
- Kader, B.A. and Yaglom, A.M., Similarity treatment of moving-equilibrium turbulent boundary layers in adverse pressure gradients, *J. Fluid Mech.* vol. 89, pp. 305-342, 1978.
- Kassab, S.Z., *Turbulence Structure in Axisymmetric Wall-Bounded Shear Flow*, Ph.D. Thesis, University of Manitoba, 1986.
- Kline, S.J., Cantwell, B.J., and Lilley, G.M., *1980-81 AFOSR - HTIM - Stanford Conference on Complex Turbulent Flows*, 1981.
- Kopp, G.A., *Mean Velocity Prediction and Evaluation of $k-\epsilon$ Models in Turbulent Diffuser Flows*, M.Eng. Thesis, McMaster University, 1991.
- McDonald, H., The effect of pressure gradient on the Law of the Wall in turbulent flow, *J. Fluid Mech.* vol. 35, pp. 311-336, 1969.
- Mellor, G.L., The effects of pressure gradients on turbulent flow near a smooth wall, *J. Fluid Mech.* vol. 24, pp. 255-274, 1966.
- Nakayama, A. and Koyama, H., A wall law for turbulent boundary layers in adverse pressure gradients, *AIAA J.* vol. 22, pp. 1386-1389, 1984.
- Ozimek, L.G., *A Comparison of Analog and Digital Data for Measurements of Turbulence Parameters*, M.Sc. Thesis, University of Manitoba, 1985.
- Perry, A.E., Turbulent boundary layers in decreasing adverse pressure gradients, *J. Fluid Mech.* vol. 26, pp. 481-506, 1966.
- Perry, A.E., Bell, J.B., and Joubert, P.N., Velocity and temperature profiles in adverse pressure gradient turbulent boundary layers, *J. Fluid Mech.* vol. 25, pp. 299-320, 1966.
- Samuel, A.E. and Joubert, P.N., A boundary layer developing in an increasingly adverse pressure gradient, *J. Fluid Mech.* vol. 66(3), pp. 481-505, 1974.
- Townsend, A.A., Equilibrium layers and wall turbulence, *J. Fluid Mech.* vol. 11, pp. 97-120, 1961.
- Townsend, A.A., The behaviour of a turbulent boundary layer near separation, *J. Fluid Mech.* vol. 12, pp. 536-554, 1962.
- Trupp, A.C., Azad, R.S., and Kassab, S.Z., Near-wall velocity distributions within a straight conical diffuser, *Experiments in Fluids*, vol. 4, pp. 319-331, 1986.
- Turan, O.F., *Further Study of a New Method of Evaluating Turbulence Dissipation*, Ph.D. Thesis, University of Manitoba, 1988.

Table 1 List of Adverse Pressure Gradient Flows Examined

experimenters	flow	classification	Re, U/ν [1/m]
Ludwig & Tillmann	1100 ^a	plane, developing	2.2 E+08
	1200 ^a	plane, developing	2.2 E+08
Perry	2900 ^a	plane, developing	2.5 E+08
Samuel & Joubert	0141 ^a	plane, developing, increasing dP/dx	1.7 E+08
Freese	3000 ^a	10 deg. conical, dev.	3.3 E+08
	5100 ^a	10 deg. conical, dev.	3.6 E+08
Pozzorini	0142 ^a	8 deg. conical, dev.	2.7 E+08
	0143 ^a	8 deg. conical, dev.	1.2 E+08
Turan, Ozimek, & Kasab	-	8 degree conical, fully developed inlet	1.4 E+08

^a 1988 Stanford Conference, + 1980-81 Stanford Conference
^b see also Trupp et al (1988)

Table 2 Range of C_0/C_1 where mean velocity models predict the data

Flow	Townsend ^a	KV-1/2	Perry-1/2	KV-defect	Coles
1100	$r < 1.0$	$1 < r < 2$	$1.5 < r < 2$	$1 < r < 2$	$r > 1.0$
1200	$r < 1.2$	$1.4 < r < 2.5$	$1.6 < r < 2.5$	$1.4 < r < 6$	$r > 1.0$
2900	$r < 1.4$	$1.4 < r < 2$	$1.4 < r < 2$	$1.6 < r < 3$	$r > 1.4$
5000	Marginally better than Log Law at all of the stations.	not at any	not at any	$0.6 < r < 1.5$	$r > 3.5$
5100	not at any	not at any	not at any	$0.6 < r < 1.6$	$r > 3.5$
0142	$r < 1.9$ ($r < 3.2$)	$1.5 < r < 2.6$	$1.2 < r < 1.5$	$1.1 < r < 4.1$	$r > 3.2$
0143	$r < 0.6$ ($r < 1.2$)	$r = 0.6$	not at any	not at any	$r > 1.2$
8 deg. conical	$r < 1.5$ ($r < 2.5$)	$2.3 < r < 2.6$	$0.7 < r < 2.3$	$2.5 < r < 6$	$r > 4$

^a The valid range for McDonald is shown in brackets [].
 In this table, $r = C_0/C_1$ and all ranges are approximate.

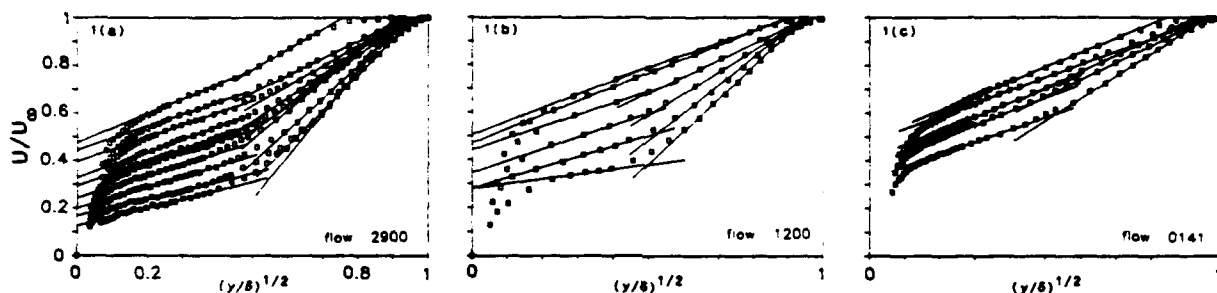


Figure 1. Half power development in plane diffuser flows. Three examples are given, namely, Flows 2900, 1200 and 0141, respectively, in Figures 1a, 1b and 1c.

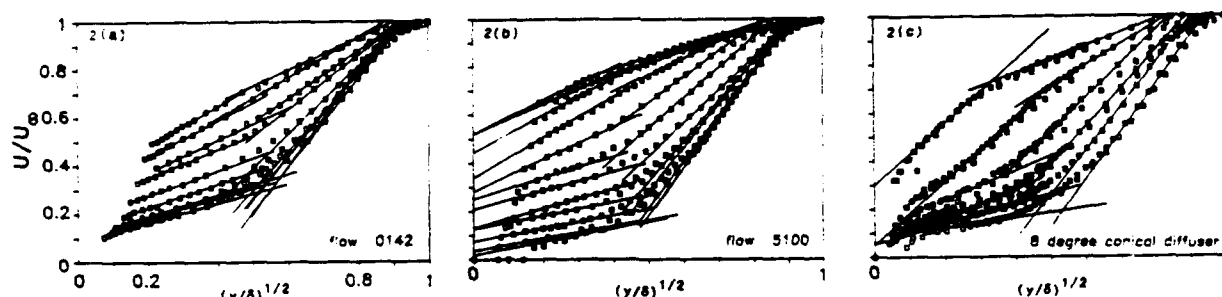
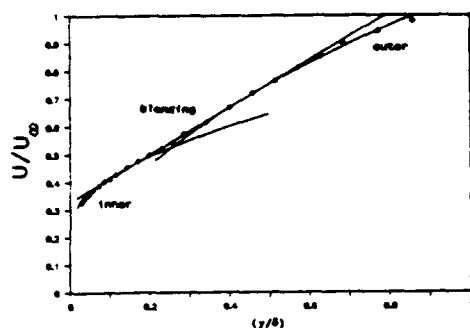
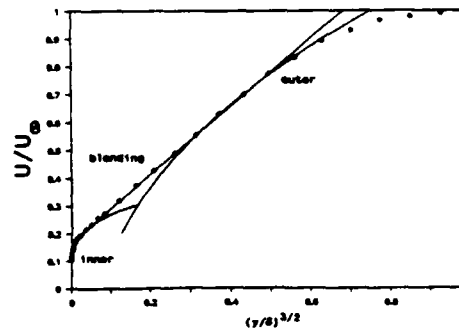


Figure 2. Half power development in conical diffuser flows. Three examples are given, namely, Flows 5100, 0142 and the eight-degree diffuser, respectively.

Figure 3. An example of the linear blending region between the inner and outer half-power regions in Flow 0142 at $x = 0.382$ m.Figure 4. An example of the $3/2$ -power blending region between the inner and outer half-power regions in Flow 0142 at $x = 1.813$ m.

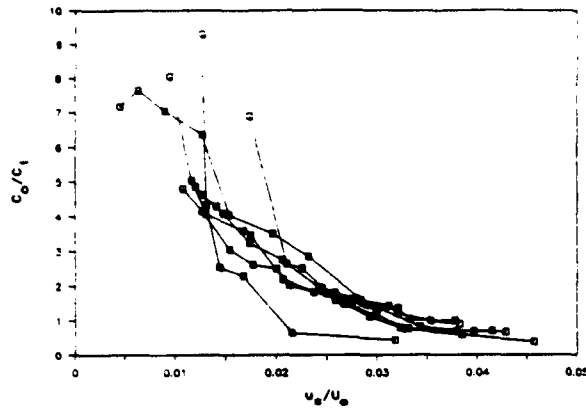


Figure 5. Variation of the outer to inner half-power slope ratio in the eight decreasing adverse pressure gradient flows examined.

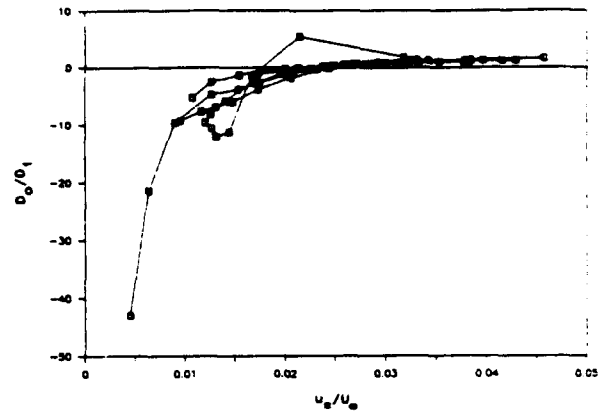


Figure 6. Variation of the outer to inner half-power intercept ratio in the eight decreasing adverse pressure gradient flows examined.

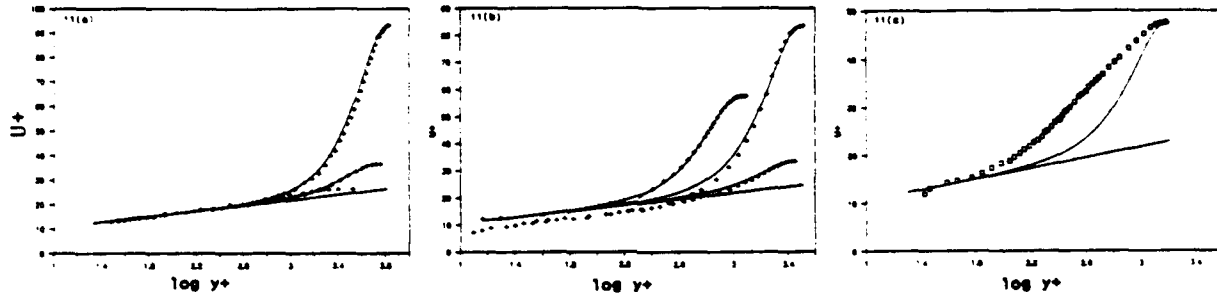


Figure 7. Coles' Law of the Wake compared with experimental data. From top to bottom in each frame, the following stations are shown: 7a, Flow 2900 ($x = 4.572\text{m}$), Flow 1100 ($x = 3.532\text{m}$), Flow 1200 ($x = 0.782\text{m}$); 7b, Flow 5000 ($x = 0.443\text{m}$), Flow 0142 ($x = 0.572\text{m}$), Flow 0143 ($x = 1.813\text{m}$); 7c, the eight-degree diffuser ($x = 0.18\text{m}$).

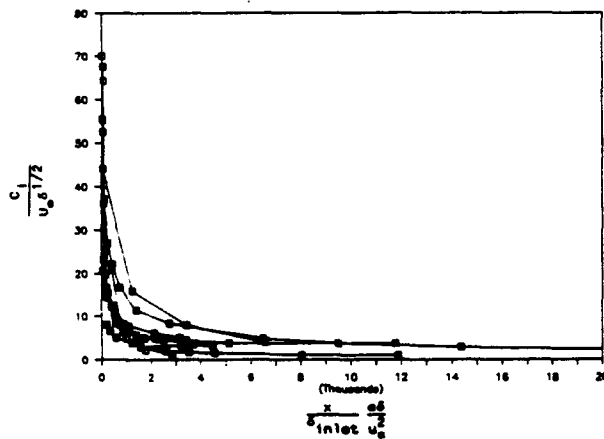


Figure 8. Variation of the non-dimensional inner half-power slope in the flows examined.

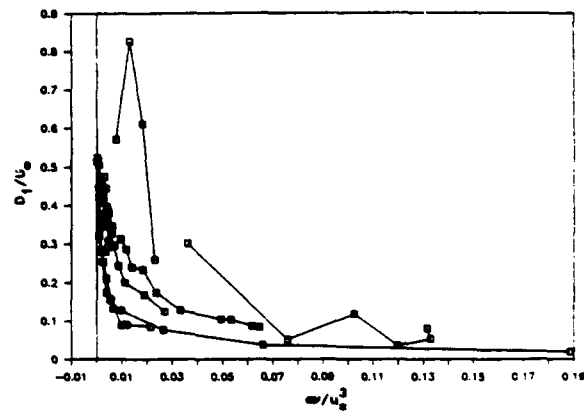


Figure 9. Variation of the non-dimensional inner half-power intercept in the flows examined.

VORTICAL MOTION CONTRIBUTIONS TO STRESS TRANSPORT IN TURBULENT BOUNDARY LAYERS

J. C. Klewicki and J. A. Murray
Physical Fluid Dynamics Laboratory
Department of Mechanical Engineering
University of Utah
Salt Lake City, UT 84112

R. E. Falco
Turbulence Structure Laboratory
Department of Mechanical Engineering
Michigan State University
East Lansing, MI 48824

ABSTRACT

Four-wire hot-wire probe measurements are used to examine the relationships between the motions bearing span-wise vorticity, ω_z , and the mechanisms responsible for turbulent stress transport. The measurements were carried out in thick zero pressure gradient turbulent boundary layers over the Reynolds number range, $1010 < Re_\delta < 4850$. Because of the scale of the flow, the spatial resolution of the probe was, in general, very good. The capabilities of the probe allowed all of the terms in the balance equation for $\langle u^2 \rangle$, except the pressure strain correlation, to be directly measured. Regarding wall region vorticity dynamics, relations between velocity-vorticity correlations and gradients of the turbulent stresses are established. In particular, ω_z statistics are examined relative to issues concerning the wall-normal transport of sublayer fluid. Relationships between the motions bearing ω_z and the sweep and ejection bursting events are examined, and the results are discussed in connection with the turbulent diffusion term in the budget for $\langle u^2 \rangle$. The overall results are discussed relative to coherent motion interactions and the known properties of the inner region vorticity field.

1. Introduction

Numerous results (see, for example, Kline et al.¹, Robinson²) indicate that the essential flow field interactions associated with the generation and maintenance of turbulent stresses in boundary layers involve motions covering a range of scales, which interact over extended space/time domains. Qualitative flow visualization as well as quantitative measurements indicate that specific phase relationships between the different scales of motion are of particular importance regarding the initiation and evolution of the stress producing events. Furthermore, there is an ever expanding body of evidence (see, for example, Wallace³, Kline et al.¹, Robinson², Smith et al.⁴, Falco⁵) indicating that the predominant motions participating in the stress production and transport have well defined vortical signatures. In general, these findings support the assertion that an increased understanding of the relationships between the vorticity field and turbulent stresses will lead to new insights pertaining to the underlying physics of boundary layer turbulence and its effective control. In this study, experimental measurements in zero pressure gradient turbulent boundary layers are examined with the intent of clarifying the roles of velocity-vorticity field interactions regarding turbulent stress production and transport.

1.1 Convecting Eddy Induced Sublayer Vorticity Redistribution

Contained within many physical models describing the turbulence production process are the dynamics associated with convecting vortical motions. Willmarth⁶ presents numerous results which lend support to the notion that convecting vortices are responsible for the instantaneous character of the viscous sublayer. Consistent with this, the studies of Falco⁵ (also see, Falco⁷, Falco et al.⁸) indicate that vortex ring-like motions convecting above and toward the sublayer are capable of causing sublayer passive contaminant rearrangements in the form of streaks and pockets, as well as initiating both upstream oriented pocket vortices, and downstream oriented hairpin vortices.

The generation, evolution, and interaction of hairpin vortices (either symmetric or asymmetric) in the wall region finds both experimental and computational support (e.g. Smith et al.⁴, Robinson et al.²) as being an integral com-

ponent of the processes responsible for sustaining boundary layer turbulence. Particularly detailed results regarding hairpin vortex dynamics have emerged from the on-going studies at Lehigh University, and are reported in the comprehensive paper by Smith et al.⁴ In their studies, connections are drawn between the flow fields associated with hairpin-like vortices convecting within the near-wall region (above the sublayer), and unsteady separation phenomena leading to rapid eruptions of sublayer fluid away from the surface. This eruptive behavior is generally preceded by a strong viscous/inviscid interaction between the sublayer fluid and the convecting hairpin vortex. The interaction then rapidly evolves to a condition of unsteady separation, which, in accord with the Moore-Rott-Sears criterion, occurs along a surface of zero vorticity. The culminating eruptive behavior is viewed as both a mechanism for $\langle uv \rangle$ production and a source of coherent vorticity in the outer layer.

While the studies by Smith et al.⁴ focus primarily on hairpin vortex induced phenomena, there is also good reason to expect that the vortex ring-like motion/sublayer interactions revealed by Fflicke⁵ lead to variations of generically the same type of phenomena. In particular, under the most commonly observed of these interactions, the topology of vorticity field is characterized by the wallward portion of the ring-like motion having spanwise vorticity, ω_x , opposite that of the mean, Ω_x ($\Omega_x = \Omega_x + \omega_x$). Given that for y^+ less than about 12 the instantaneous spanwise vorticity has the same sign (negative) as the mean vorticity over 99% of the time (Klewicky et al.⁹) the presence of positive spanwise vorticity in the buffer region necessarily indicates that a condition of zero ω_x occurs between the sublayer and the wallward lobe of the ring-like eddy. Consistent with this, the two point ω_x correlations of Klewicki¹⁰ indicate that in the region $10 < y^+ < 25$ ω_x regularly undergoes an instantaneous change in sign. Thus, the supply of positive ω_x in the buffer region provided by the ring-like eddies promotes a flow field condition essential for the onset of unsteady separation of the surface layer, as described by Smith et al.

1.2 Vortical Motions and Stress Transport

Overall, the results reviewed above support the assertion that rapid wall-normal transport from the sublayer is generically initiated by organized vortical motions convecting above the sublayer. Regarding these motions, the analysis below gives reason to expect that there exists well defined connections between their velocity and vorticity signatures and stress transport.

It can be shown (see, for example, Hinze¹¹) that the gradients of the turbulent stresses in an incompressible turbulent flow are related to velocity-vorticity correlations through the following tensor identity:

$$\frac{\partial \langle u_j u_i \rangle}{\partial x_j} = -\epsilon_{ijk} \langle u_j \omega_k \rangle + \frac{\partial \langle u_i u_j \rangle}{\partial x_i}, \quad (1)$$

where ϵ_{ijk} is the alternating tensor, and the brackets denote the long time average. For turbulent wall flows, Klewicki¹² demonstrates that the three component equations ($i = 1, 2, 3$) represented in Eq. 1 may also be derived directly from the momentum equations describing the mean flow. In the context of convecting vortical motions, Eq. 1 describes, in an average sense, how the interaction of these motions and the velocity field results in turbulent stress gradients. Furthermore, the velocity-vorticity correlations appearing in Eq. 1 may be interpreted physically in terms of body forces per unit mass associated with vortical motions (see, for example, Tennekes and Lumley.¹³)

Very few studies have presented data pertinent to the analysis of Eq. 1. Hinze¹¹ does, however, utilize the $i = 1$ form,

$$\frac{\partial}{\partial y} \langle -uv \rangle = \langle v''^2 \rangle - \langle w \omega_y \rangle - \frac{1}{2} \frac{\partial}{\partial x} (\langle v^2 \rangle - \langle u^2 \rangle - \langle w^2 \rangle), \quad (2)$$

as a means of more precisely defining the "active/inactive" motion decomposition proposed by Townsend.¹⁴ (In this decomposition, the bulk of stress production and transport is attributed to the active motions.) Under Hinze's interpretation of Eq. 2, the active motion contributions to $\partial \langle -uv \rangle / \partial y$ come from the velocity-vorticity correlation terms, while the streamwise gradient terms represent the inactive component contributions. For the present flow, Klewicki¹⁰ shows that the $\partial \langle u^2 \rangle / \partial x$ and $\partial \langle v^2 \rangle / \partial x$ terms are approximately two orders of magnitude less than the $\langle v \omega_x \rangle$ term. Conversely, however, it is also demonstrated that the variances of the streamwise gradient terms are at least as large as the variance of $v \omega_x$. The negligible magnitudes of the $\partial \langle u^2 \rangle / \partial x$ and $\partial \langle v^2 \rangle / \partial x$ terms are consistent with Townsend's original notion that most of the stress transport is attributable to the active vortical motions. The large variances of the fluctuating streamwise gradient signals indicate, however, that the active/inactive motions

decomposition is only relevant to time averaged structure -- as first suggested by Bradshaw.¹⁵

The $\partial/\partial x$ terms being very small, is good reason to believe that those motions which persistently produce single-signed contributions to the Reynolds stress gradient should be identifiable as a subset of velocity-vorticity field interactions. This point is significant since, while existing evidence indicates that the dynamics associated with coherent vorticity give rise to stress producing events, not all organized vortical motions are important in this regard. To illustrate this point, Smith et al.⁴ give non-trivial examples of locally organized vortical motions which, on average, provide very little contribution to $\langle uv \rangle$. They then use these examples to motivate the assertion that the most relevant flow field interactions are those which have on average asymmetries associated with their spatial and temporal evolution. This inherent asymmetry property results in persistent and single-signed $\langle uv \rangle$ production from these motions. Smith et al. include within this subset of motions the mechanisms for the generation of hairpin-like vortices which subsequently move outward from the surface, and the wallward sweep-type motions which follow the ejection of low momentum sublayer fluid. The results of Falco^{7,16} also reveal specific flow fields associated with the convection of coherent vortical motions (hairpin-like and ring-like) which result in persistent single-signed contributions to $\langle uv \rangle$. An underlying motivation for the present study is based on the belief that flow field interactions which produce indelible contributions to stress transport are statistically represented in the velocity-vorticity correlations contained in Eq. 2.

A logical point of departure for the study of turbulent stress transport is an analysis of the associated budget equations,

$$\begin{aligned} \frac{\partial \langle u_i u_j \rangle}{\partial t} + U_i \frac{\partial \langle u_i u_j \rangle}{\partial x_i} = & - \left[\langle u_i u_j \rangle \frac{\partial U_j}{\partial x_i} + \langle u_j u_i \rangle \frac{\partial U_i}{\partial x_j} \right] + \left\langle \frac{p}{\rho} \left[\frac{\partial u_i}{\partial x_j} + \frac{\partial u_j}{\partial x_i} \right] \right\rangle \\ & - \frac{\partial \langle u_i u_j u_i \rangle}{\partial x_i} - \frac{1}{\rho} \left[\frac{\partial \langle p u_j \rangle}{\partial x_i} + \frac{\partial \langle p u_i \rangle}{\partial x_j} \right] + \nu \frac{\partial^2 \langle u_i u_j \rangle}{\partial x_i \partial x_i} - 2\nu \left\langle \frac{\partial u_i}{\partial x_i} \frac{\partial u_j}{\partial x_i} \right\rangle. \end{aligned} \quad (3)$$

With regard to the mechanisms involved in the wall-normal transport of low momentum sublayer fluid, of particular relevance is the budget equation for $\langle u^2 \rangle$. Given that to a very good approximation the present flow exhibits streamwise homogeneity (see discussion above), this equation becomes,

$$0 = -2\langle uv \rangle \frac{\partial U}{\partial y} + 2 \left\langle \frac{p}{\rho} \frac{\partial u}{\partial x} \right\rangle - \frac{\partial \langle u^2 v \rangle}{\partial y} + \nu \frac{\partial^2 \langle u^2 \rangle}{\partial y^2} - 2\nu \left\langle \left(\frac{\partial u}{\partial x_i} \right)^2 \right\rangle. \quad (4)$$

The first term on the right of Eq. 4 is the familiar production term. The second term is the pressure-strain redistribution term, while the last two terms are the viscous diffusion and dissipation terms respectively. The third term on the right is a turbulent diffusion term which accounts for the transport of $\langle u^2 \rangle$ by v component velocity fluctuations. This term has particular relevance to the present study since its near-wall characteristics should reflect wall-normal transport of sublayer fluid.

The $\partial \langle u^2 v \rangle / \partial y$ term also has a well defined connection with the near-wall motions bearing spanwise vorticity. To show this connection, it is important to recognize that in the near-wall region the motions bearing ω_z are much more apt to be like a shear-layer than having solid body rotation. In an average sense, this fact has been verified by examining the ratio of the rms gradients $(\partial u / \partial y)'$ to $(\partial v / \partial x)'$ (not shown), which exceeds a value of 10 for y^+ less than about 12. Furthermore, the conditional averaging results of Eckelmann et al.¹⁷ indicate this property also holds during the bursting phenomena. Expansion of the turbulent diffusion term yields,

$$-\frac{\partial \langle u^2 v \rangle}{\partial y} = -2\langle uv \rangle \frac{\partial u}{\partial y} - \langle u^2 \frac{\partial v}{\partial y} \rangle. \quad (5)$$

Or, in light of the near-wall character of ω_z , one may also write,

$$-\frac{\partial \langle u^2 v \rangle}{\partial y} = 2\langle uv \omega_z \rangle - \langle u^2 \frac{\partial v}{\partial y} \rangle. \quad (6)$$

Thus, near the wall, the turbulent transport and production terms from Eq. 4 combine to represent a correlation between the uv shear product and the total spanwise vorticity, ω_z . Regarding the mean vorticity ($\Omega_z = -\partial U/\partial y$), the combination with $\langle uv \rangle$ always represents a positive contribution to the time rate of change to $\langle u^2 \rangle$. In the case of the $\langle uv\omega_z \rangle$ correlation, however, both positive and negative values may occur.

In the present study, four element hot-wire probe measurements in flat plate turbulent boundary layers are used to examine relationships between the motions bearing ω_z , and the mechanisms responsible for turbulent stress transport as described in Eqs. 2 and 4. In the next section a brief description of the experiments is given, as well as results pertaining to the spatial resolution of the measurements. In the section following, results are presented relative to the issues raised above. These results are then discussed in connection with known coherent motion characteristics and the known structure of the wall region vorticity field.

2. Experimental Procedures and Conditions

The data herein are derived from the measurements of Klewicki.¹⁰ Data were taken at the three Reynolds numbers, $R_\theta = 1010, 2870$, and 4850 . Because of the low flow speeds and the long flow development length, the boundary layers at the measurement site were about $0.2m$ thick. The measurements were obtained using a four-wire spanwise vorticity probe similar to that developed by Foss et al.¹⁹ The probe is comprised of a parallel-array and an x-array, which is positioned at the same axial and wall-normal position as the parallel-array, but offset in the spanwise, z , direction. The individual wires in the probe are 3 mm in length with a center unplated active length of 1 mm . The Δy spacing between the parallel-array wires is nominally 1 mm , as is the spacing between the wires contained in the x-array. The Δz spacing between the centers of the parallel and x-arrays is nominally 3.4 mm . For reference 1 mm is equal to about $1.85, 4.75$ and 7.75 viscous units at $R_\theta = 1010, 2870$ and 4850 respectively. For further details concerning the experiments and the accuracy of the measurements see Klewicki and Falco.¹⁸

When discussing vorticity and/or near-wall flow field behavior, issues regarding the spatial resolution of the measurement probe are of particular importance. Fig. 1 presents results concerning the resolution of the probe in the spanwise direction relevant to the measurement of the $\langle v\omega_z \rangle$ and $\langle uv\omega_z \rangle$ correlations. The results in this figure are derived from the two point ω_z probe experiments of Klewicki.¹⁰ In these experiments, correlations with spanwise probe separation were performed in the $R_\theta = 1010$ boundary layer. By correlating the v and uv fluctuations with the ω_z fluctuations for different spanwise separations, the effect of the spanwise scale of the probe on the measured value of $\langle v\omega_z \rangle$ and $\langle uv\omega_z \rangle$ can be estimated. The correlation between v and ω_z is derived from measurements at $y^+ = 6.7$, while the correlation between uv and ω_z are derived from measurements at $y^+ = 15.3$. These positions were chosen since they are near the peaks in the $\langle v\omega_z \rangle$ and $\langle uv\omega_z \rangle$ distributions shown in Figs. 3 and 8 respectively, and they are in a region where small scale motions are expected to be significant. In each of the curves of Fig. 1 the point of closest spanwise separation is derived from a single ω_z probe. Therefore, a linear extrapolation to $\Delta z = 0$ (using the two points of smallest separation) gives an indication of the spatial resolution of the probe itself -- relevant, of course, to the particular measured quantity. For the $\langle v\omega_z \rangle$ results, this procedure indicates an attenuation of about 7% . For $\langle uv\omega_z \rangle$ an attenuation of about 12% is deduced. The spanwise scale of the four-wire probe is 6.4 viscous units at $R_\theta = 1010$. The single probe results from the correlation experiments of Fig. 1 are also plotted in Figs. 3 and 8. As can be seen, the results in Fig. 1 indicate that both $\langle v\omega_z \rangle$, and especially $\langle uv\omega_z \rangle$, are quite sensitive to probe scale effects.

3. Results and Discussion

A detailed presentation of the present flow field characteristics is given in Klewicki¹⁰ and Klewicki and Falco.¹⁸ Logarithmic mean velocity profiles have been previously shown to follow the law-of-the-wall using Coles²⁰ parameters, as well as Van Driest's²¹ formula. Many of the other flow field statistics derived from the ω_z probe have been previously examined (see above references), and in general show very good agreement with other studies of comparable spatial resolution. In particular, the inner normalized Reynolds stress profiles of Fig. 2 show the expected sharp rise through the buffer region and approximate constancy in the log-law region. Furthermore, the data of Fig. 2 also exhibit the recently identified Reynolds number dependencies in both the magnitude and peak position (Sreenivasan,²² Klewicki¹⁰, Falco⁵). With regard to the present study, much of the attention will focus on velocity-vorticity interactions which contribute to the large stress gradient starting near the edge of the sublayer.

3.1 Wall-Normal Transport of Spanwise Vorticity

As indicated in Eq. 2, the correlation between v and ω_z is associated with the gradient of $\langle uv \rangle$. According to this equation, positive values of $\langle v\omega_z \rangle$ result in positive contributions to $\partial\langle uv \rangle/\partial y$. Inner normalized profiles of the

present $\langle v\omega_z \rangle$ are given in Fig. 3 for Reynolds numbers $R_\theta = 1010, 2870$ and 4850 . In the region $4 < y^+ < 20$, the $R_\theta = 1010$ and 2870 results suggest an approximate Reynolds number independence — although it is clearly recognized that the $R_\theta = 2870$ data are incomplete. Across the log-law region, however, an apparent Reynolds number dependence is observed. Of course, in assessing the validity of this observation the effects of finite probe scale must be considered. Based upon the results of Fig. 1, one would expect the $R_\theta = 4850$ data ($\Delta z^+ = 26.4$) to be attenuated to a magnitude of about 50% of the $R_\theta = 1010$ data ($\Delta z^+ = 6.4$). Near $y^+ = 100$, however, the $R_\theta = 4850$ value is less than 15% of the $R_\theta = 1010$ value. (Note also, that since the results of Fig. 1 are derived from measurements near the edge of the sublayer, the application of these results at positions farther from the wall is likely to result in an overestimation of the attenuation.) Thus, it is concluded that between $R_\theta = 1010$ and 4850 the $\langle v\omega_z \rangle$ contribution to $\partial(-uv)/\partial y$ is Reynolds number dependent across the log-law region. It is less certain, however, whether the observed differences between the $R_\theta = 2870$ and 4850 profiles are predominantly a consequence of spatial averaging effects.

In the log-law region, the Reynolds stress is nearly constant. By virtue of Eq. 2, this indicates that the contributions to the stress gradient from $\langle v\omega_z \rangle$ and $\langle w\omega_y \rangle$ are approximately equal and opposite. The deduced Reynolds number dependence indicates that at lower R_θ the individual contributions from both of these velocity-vorticity correlations are more significant. Furthermore, given that $\langle -uv \rangle / u_\tau^2$ itself has a smaller peak value with decreasing R_θ , negative contributions from $\langle v\omega_z \rangle$ in the buffer region must increasingly outweigh the positive $\langle w\omega_y \rangle$ contributions as the Reynolds number is decreased. These observations may be taken to indicate a Reynolds number dependence in the vortical motion contributions to stress transport near the surface. In connection with the mixing length based analysis of Tennekes and Lumley,¹³ one concludes that at lower R_θ the gradient transport of vorticity becomes increasingly significant in comparison with change-of-scale effects.

The positive values of $\langle v\omega_z \rangle$ in the region $4 < y^+ < 15$ indicate that this correlation has significant contributions to the rapid increase in $\langle -uv \rangle$ shown in Fig. 2. (Over this y^+ range, $\langle -uv \rangle$ begins near zero and increases to reach about 60% of its maximum value.) Positive values of $v\omega_z$ arise, of course, when v and ω_z are instantaneously of the same sign. As a result of the no-slip condition, it is expected that u and ω_z should be strongly negatively correlated in and near the sublayer. The direct measurements of $\langle u\omega_z \rangle$ by Klewicki¹² clearly indicate this to be the case. Because of this, in the sublayer one may associate positive ω_z fluctuations with low momentum fluid. Thus, it is seen that $[+], [+]$ combinations of v and ω_z are consistent with the outward motion of sublayer streaks. According to Eq. 2, this process alone (i.e. without other associated dynamics) results in a positive gradient of $\langle -uv \rangle$. Contributions to the positive correlation from simultaneously negative v, ω_z pairs results from vorticity of the same sign of the mean, and of greater magnitude than mean, being transported toward the surface. This type of process may occur when near-wall hairpin and/or shear layer-like motions are convected toward the surface, as a result of, for example, outer layer influences. This type of process is also more specifically described in the self-induced motion of pocket vortices toward the surface (see, Falco et al.⁸).

Contributions to the $\langle v\omega_z \rangle$ correlation may be revealed via two dimensional probability density functions (pdf's). The v, ω_z pdf's from the $R_\theta = 1010$ boundary layer at $y^+ = 5.3, 14.2$ and 26.3 are shown in Figs. 4, 5, and 6 respectively. Fig. 4 indicates that the contributions to the positive correlation at $y^+ = 5.2$ are approximately shared between $[+], [+]$ and $[-], [-]$ combinations — although examination of a quadrant contribution plot (not shown) indicates that the $[+], [+]$ combinations have a slightly greater contribution. Near $y^+ = 15$ the $\langle v\omega_z \rangle$ correlation exhibits a zero crossing. Given the prevalence of lifting hairpin vortices and shear layer-like motions in this region, one might expect this zero crossing to result from a shift to the fourth quadrant in the v, ω_z plane (i.e. negative ω_z , positive v combinations). Examination of Fig. 5, however, indicates that this is not the case. This figure shows that second quadrant events (i.e. positive ω_z , negative v) are predominantly responsible for the reduction in the positive correlation. Examination of the quadrant contribution plot (not shown) confirms this assertion. Farther from the wall, the $\langle v\omega_z \rangle$ correlation becomes strongly negative, and the pdf at $y^+ = 26.3$ in Fig. 6a indicates that this occurs through significant quadrant 4 and especially quadrant 2 contributions. The quadrant breakdown (derived by multiplying the probability and magnitude of $v\omega_z$) in Fig. 6b shows that at this location the greatest contribution comes from positive ω_z , negative v contributions. Furthermore, the absolute spanwise vorticity line indicates that the largest fraction of the second quadrant events arise from positive total vorticity, ω_z . Regarding the interpretation of quadrant 4 events in the context of hairpin vortices and/or lifting shear layers, it is also interesting to note that the movement of negative vorticity outward from the surface actually serves to reduce the gradient of $\langle -uv \rangle$.

The fact that $\langle v\omega_z \rangle$ makes positive contributions to $\partial(-uv)/\partial y$ in the region $5 < y^+ < 15$ and negative contributions farther from the wall suggests that motions lifting from the sublayer may generate positive and negative contributions to the stress gradient during the earlier and later phases of their evolution respectively. The likelihood of this phenomena is made more apparent when it is recognized that the mean vorticity drops to about 30% of its

maximum value by $y^+ = 15$. Thus, if one considers a motion lifting from the sublayer with an initial momentum deficit of 50%, and assumes that the vorticity of this motion remains approximately constant during this process (i.e. an initially positive ω_z fluctuation such that $\omega_z = -0.5 u_z^2/\nu$), then in the region $y^+ < 10$ this motion will make positive contributions to $\partial(-uv)/\partial y$ as it moves outward. However, near $y^+ = 10$ the ω_z associated this motion will exceed the mean, and its further outward motion from the surface will produce negative contributions to the stress gradient. Given that $\langle -uv \rangle$ reaches about 60% of its maximum value by $y^+ = 15$, the formation processes by which sublayer vorticity becomes redistributed into more locally organized motions is seen to be of greatest importance with regard to buffer region stress transport.

3.2 Vortical Contributions to $\langle u^2 \rangle$ Budget

Wall-normal transport of sublayer fluid should also leave statistical signatures in the balance for $\langle u^2 \rangle$. The $\langle u^2 \rangle$ budget (Eq. 4) from the $R_\theta = 1010$ boundary layer is shown in Figs 7a and 7b. In these figures the results of the computation of Spalart²³ ($R_\theta = 1410$) are also shown. For the turbulent transport and viscous diffusion terms, the gradients were computed by the differentiation of a moving five-point curve fit of the $\langle u^2 v \rangle$ and $\langle u^2 \rangle$ profiles respectively. These curve fits were differentiated at the center point, and thus the first two points in each of the profiles are omitted in Fig. 7. The dissipation terms were computed directly from the fluctuating gradient time records, and for convenience, the computation of the production term utilized the formula of Van Driest.²¹ The pressure strain term was the only unmeasured term, and was obtained by difference.

Comparison with Spalart's results indicates that the dissipation shows best agreement, while the experimental production profile is consistently lower. Both the present turbulent transport and viscous diffusion terms peak closer to the wall than the computational profiles. The deduced pressure-strain profile shows very good agreement until $y^+ = 10$, but then shows a strong positive excursion. This large difference is probably a consequence of the sensitivity of this deduced profile on the cumulative difference of all of the other terms -- which show large variations in this region. Overall, however, given the multiple differencing required to obtain the budget, the agreement between the experiment and computation is felt to be quite good.

Examination of Fig. 7a indicates that the turbulent transport term is positive in the sublayer, and exhibits a negative excursion in the region $5 < y^+ < 20$. Thus, in and near the sublayer, this term contributes to a gain of $\langle u^2 \rangle$, and in the buffer layer it contributes to a loss of $\langle u^2 \rangle$. The negative values of the turbulent transport term indicate that the spanwise vorticity term in Eq. 6 is also likely to be negative. Verification of this is provided in Fig. 8, which shows that the $\langle uv\omega_z \rangle$ correlation is negative in the buffer layer, and that it reaches a peak magnitude of approximately the same value and at nearly the same location as the turbulent transport term in Fig. 7a. Fig. 8 also includes the correlation of $\langle -uv\partial u/\partial y \rangle$ at $R_\theta = 1010$. This profile is nearly identical to the $\langle uv\omega_z \rangle$ profile, and thus the approximation of Eq. 6 is shown to hold. Based upon the results of Fig. 1, the lower magnitudes of the $\langle uv\omega_z \rangle$ correlation at $R_\theta = 2870$ and 4850 probably result largely from probe resolution effects. Given the results of Figs 7a and 8, one may conclude that across the buffer layer the $\langle uv\omega_z \rangle$ correlation is nearly equal to the $\langle u^2 \partial v/\partial y \rangle$ correlation in Eq. 6. (Note that the $\langle uv\omega_z \rangle$ correlation is multiplied by 2 in this equation.) In the sublayer, however, because of the lack of correlation between u and v (see Fig. 2), the magnitude of $\langle uv\omega_z \rangle$ is expected to remain small. Thus, positive turbulent transport predominantly arises from a negative value of $\langle u^2 \partial v/\partial y \rangle$. Given that u^2 is always a non-negative quantity, a negative $\langle u^2 \partial v/\partial y \rangle$ must result from negative $\partial v/\partial y$ fluctuations. As a result of the impermeability of the wall, wallward flows will, as a result of continuity, give rise to fluctuations of the in-plane velocity components, Lighthill.²⁴ The present results indicate that with regard to the transport of $\langle u^2 \rangle$ these "continuity" generated motions are predominant only in the sublayer.

In the Introduction it was shown that in the near-wall region the turbulent transport term in Eq. 2 has a vortical component. Furthermore, by expanding this term it was shown that this vortical contribution could be combined with the production term to form a total spanwise vorticity Reynolds stress correlation, $\langle uv\omega_z \rangle$ (under the condition of approximate streamwise homogeneity). The production term from Fig. 7a indicates that the mean vorticity part of this total correlation is always positive and peaks near $y^+ = 12$. The results from Fig. 8, however, indicate that the contribution from the fluctuating part is negative in the buffer layer. Based upon the $v\omega_z$ results above, it is likely that this extraction of $\langle u^2 \rangle$ in the buffer layer is associated with the formation of organized vortical motions. As discussed by Offen and Kline²⁵ and illustrated in detail in the studies of Falco et al.⁸ and Smith et al.⁴, vortical motions formed at an upstream location in the near-wall region are likely to reinitiate stress producing events at locations farther downstream.

3.3 Spanwise Vorticity and the Bursting Events

Because of their distinct contributions to $\langle uv \rangle$, the sweep (+u, -v) and ejection (-u, +v) bursting events represent a useful decomposition of the flow conditions associated with the production of new turbulence. With regard to understanding the significance of organized vortical motions and stress generation, it is therefore useful to explore the vorticity characteristics associated with the bursting events.

The data of Figs 3 and 4 give clear indications that in the region $y^+ < 12$, positive ω_z fluctuations are correlated with positive v fluctuations. By virtue of the negative correlation between u and ω_z in the sublayer, this process was associated with the lifting of low momentum fluid, and thus is descriptive of ejections. The statistical significance of this process is reinforced by the increasingly negative value of $\langle uv\omega_z \rangle$ in this region.

Near the position where $v\omega_z$ crosses zero and becomes negative ($y^+ \approx 15$), $\langle uv\omega_z \rangle$ reaches its maximum value (see Figs 3 and 8). Thus, for $y^+ > 15$, it is expected that the nature of correlation between u and ω_z changes. In particular, it is expected that u will be, on average, positive during those times in which $v\omega_z$ is negative. Furthermore, based upon the predominance of [-] v, [+] ω_z contributions in Fig. 6b, it is expected that [+] u, [+] ω_z combinations are significant. The quadrant contribution plot of u vs ω_z at $y^+ = 26.3$ in Fig. 9 clearly shows this to be the case. Furthermore, the zero vorticity line in this figure indicates that the majority of these contributions not only involve positive ω_z but positive ω_x .

Combining the above results, it is concluded that for $y^+ < 15$ the negative $\langle uv\omega_z \rangle$ correlation arises primarily from [-] u, [+] v and [+] ω_z combinations, which, by definition are associated with the ejection of low momentum sublayer fluid, and by virtue of Eq. 6 are associated with a gain in $\langle u^2 \rangle$. Conversely, for $y^+ > 15$ the negative $\langle uv\omega_z \rangle$ correlation results primarily from [+] u, [-] v, and [+] ω_z combinations, which, by definition are associated with the wallward sweep of high momentum fluid, and are associated with an extraction of $\langle u^2 \rangle$.

4. Concluding Remarks

In this study the relationships between spanwise vorticity and near-wall stress transport were examined via experimental measurements in low Reynolds number turbulent boundary layers. Overall, the results point to the importance of positive vorticity fluctuations. In the region $y^+ < 15$, these fluctuations predominantly have magnitude less than the mean, and thus represent weak but negative ω_z . For $y^+ > 15$, however, many of these positive fluctuations exceed the mean, and thus represent positive ω_z . These motions, which were shown to, on average, reduce the Reynolds stress gradient (see Eq. 2), are believed to have importance regarding the regenerative mechanism of wall turbulence. In support of this assertion, the motion of positive ω_z toward the surface is explicitly contained in the physical model of Falco et al.⁸ as an initiating mechanism for the generation of new turbulence. Furthermore, recent results regarding unsteady separation of the surface layer (described in Smith et al.⁴) indicate the importance of those motions capable of generating a zero vorticity surface above the sublayer. Positive ω_z in the buffer layer ensures this condition for the z-component by virtue of the single-signed nature of the sublayer vorticity field.⁹

5. Acknowledgement

This work was partially supported by the Air Force Office of Scientific Research, contract number 87-0047. Dr. J. McMichael was the contract monitor.

6. References

- ¹S. J. Kline and S. K. Robinson, *Quasi-Coherent Structures in the Turbulent Boundary Layer: Part I. Status Report on a Community-Wide Summary of the Data*, in *Near-Wall Turbulence* (ed. by S. J. Kline and N. H. Afgan) Hemisphere Press, 200 (1990).
- ²S. K. Robinson, *Coherent Motions in the Turbulent Boundary Layer*, *Ann. Rev. Fluid Mech.* 23, 601 (1991).
- ³J. M. Wallace, *On the Structure of Bounded Turbulent Shear Flow. A Personal View*, in *Developments in Theoretical and Applied Mechanics XI*, (ed. by T. J. Chung and G. R. Karr) Dept. Mech. Eng., University of Huntsville, 509 (1982).
- ⁴C. R. Smith, J. D. A. Walker, A. H. Haidari and U. Sobrun, *On the Dynamics of Near-Wall Turbulence*, *Phil. Trans. Proc. Roy. Soc. A* 336, 131 (1991).
- ⁵R. E. Falco, *A Coherent Structure Model of the Turbulent Boundary Layer and its Ability to Predict Reynolds Number Dependence*, *Phil. Trans. Proc. Roy. Soc. A* 336, 103 (1991).
- ⁶W. W. Willmarth, *Structure of Turbulence in Boundary Layers*, *Adv. Appl. Mech.* 15, 159 (1975).

- ⁷R. E. Falco, *New Results, A Review and Synthesis of the Mechanism of Turbulence Production in Boundary Layers and its Modification*, AIAA Paper 83-0377 (1983).
- ⁸R. E. Falco, J. C. Klewicki, K. Pan, *Production of Turbulence in Boundary Layers and Potential for Modification of the Near-Wall Region*, in *Structure of Turbulence and Drag Reduction* (ed. by A. Gyr) Springer-Verlag, 59 (1990).
- ⁹J. C. Klewicki, C. P. Gendrich, J. F. Foss and R. E. Falco, *On the Sign of the Instantaneous Spanwise Vorticity Component in the Near-Wall Region of Turbulent Boundary Layers*, *Phys. Fluids A* 2, 1497, (1990).
- ¹⁰J. C. Klewicki, *On the Interactions Between the Inner and Outer Region Motions in Turbulent Boundary Layers*, Ph.D. Dissertation, Michigan State University, East Lansing, MI (1989).
- ¹¹J. O. Hinze, *Turbulence*, McGraw-Hill, (1975).
- ¹²J. C. Klewicki, *Velocity-Vorticity Correlations Related to the Gradients of the Reynolds Stresses in Parallel Turbulent Wall Flows*, *Phys. Fluids A* 1, 1285, (1989).
- ¹³H. Tennekes and J. L. Lumley, *A First Course in Turbulence*, MIT Press, (1972).
- ¹⁴A. A. Townsend, *Equilibrium Layers and Wall Turbulence*, *J. Fluid Mech.* 11, 97, (1961).
- ¹⁵P. Bradshaw, *'Inactive' Motion and Pressure Fluctuations in Turbulent Boundary Layers*, *J. Fluid Mech.* 30, 241, (1967).
- ¹⁶R. E. Falco, *Coherent Motions in the Outer Region of Turbulent Boundary Layers*, *Phys. Fluids Suppl.* 20, S124, (1977).
- ¹⁷H. Eckelmann, S. G. Nychas, R. S. Brodkey and J. M. Wallace, *Vorticity and Turbulence Production in Pattern Recognized Turbulent Flow Structures*, *Phys. Fluids Suppl.* 20, S225, (1977).
- ¹⁸J. C. Klewicki and R. E. Falco, *On Accurately Measuring Statistics Associated with Small Scale Structure in Turbulent Boundary Layers Using Hot-Wire Probes*, *J. Fluid Mech.* 219, 119, (1990).
- ¹⁹J. F. Foss, C. L. Klewicki and P. J. Disimile, *Transverse Vorticity Measurements Using an Array of Four Hot-Wire Probes*, NASA CR 178098, (1986).
- ²⁰D. E. Coles and E. A. Hirst, *Proc. 1968 AFOSR-IFP-Stanford Conference on Computation of Turbulent Boundary Layers*, Thermosciences Division, Stanford University, (1969).
- ²¹E. R. Van Driest, *On Turbulent Flow Near a Wall*, *J. Aeronaut. Sci.*, 23, 1007, (1956).
- ²²K. R. Sreenivasan, *A Unified View of the Origin and Morphology of the Turbulent Boundary Layer Structure*, in *Turbulence Management and Relaminarization* (ed. by H. Liepmann and R. Narasimha), Springer-Verlag, 37, (1988).
- ²³P. Spalart, *Direct Simulation of a Turbulent Boundary Layer up to $Re_\theta = 1410$* , *J. Fluid Mech.* 187, 61, (1988).
- ²⁴M. J. Lighthill, *Introduction to Boundary Layer Theory*, in *Laminar Boundary Layers* (ed. L. Rosenhead), Oxford University Press, 46, (1963).
- ²⁵G. R. Offen and S. J. Kline, *A Proposed Model of the Bursting Process in Turbulent Boundary Layers*, *J. Fluid Mech.* 70, 209 (1975).

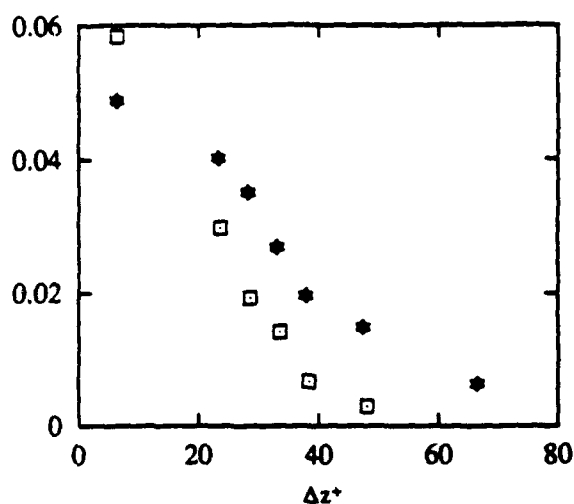


Figure 1. Inner normalized correlations of $\langle \omega_z(0)v(\Delta z) \rangle$ at $y^+=6.7$ * and $-\langle \omega_z(0)uv(\Delta z) \rangle$ at $y^+=15.3$ □, both at $R_\theta=1010$.

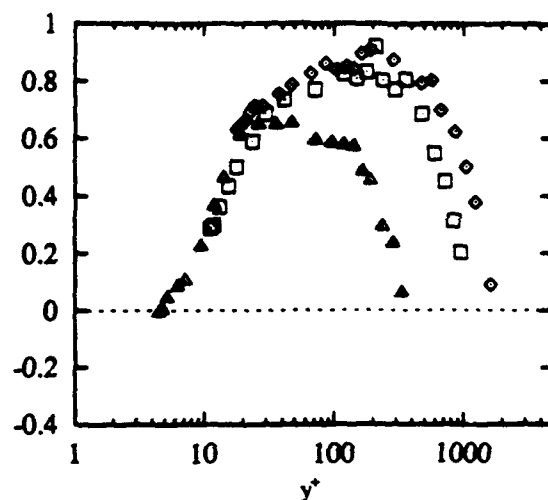


Figure 2. Inner normalized Reynolds stress profile at $R_\theta=1010$ △, $R_\theta=2870$ □, $R_\theta=4850$ ◇.

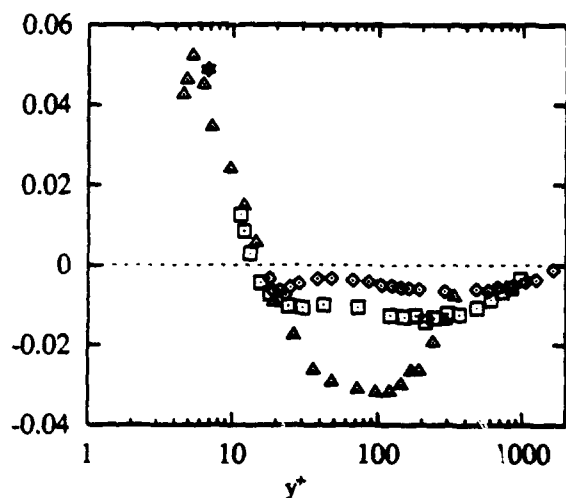


Figure 3. Inner normalized $\langle v\omega_z \rangle$ correlation (symbols same as Figure 2). Correlation point * from Figure 1, $\Delta z^+=6.4$.

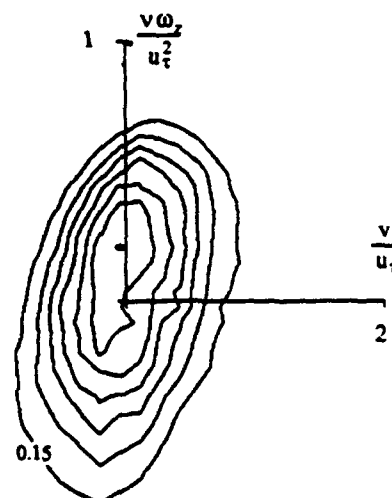


Figure 4. $\frac{v}{u_\tau}$ vs. $\frac{v\omega_z}{u_\tau^2}$ PDF at $y^+=5.3$.

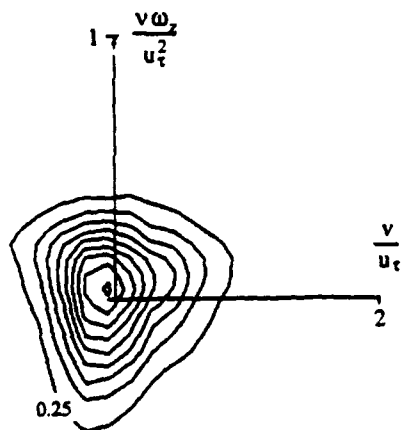


Figure 5. $\frac{v}{u_\tau}$ vs. $\frac{v\omega_z}{u_\tau^2}$ PDF at $y^+=14.3$.

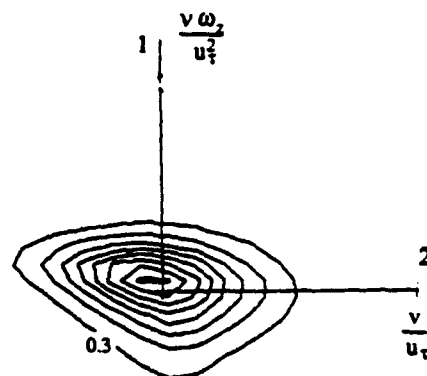


Figure 6a. $\frac{v}{u_\tau}$ vs. $\frac{v\omega_z}{u_\tau^2}$ PDF at $y^+=26.3$.

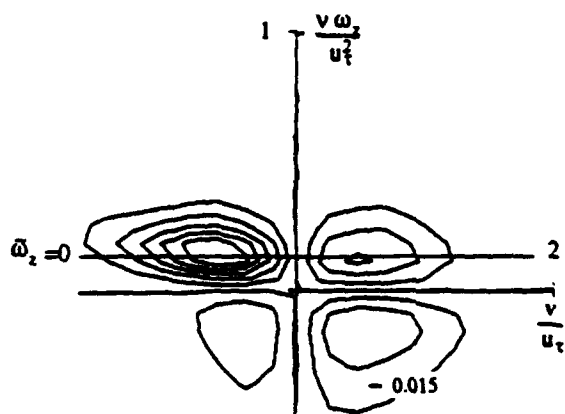


Figure 6b. Quadrant contribution of figure 6a. PDF.

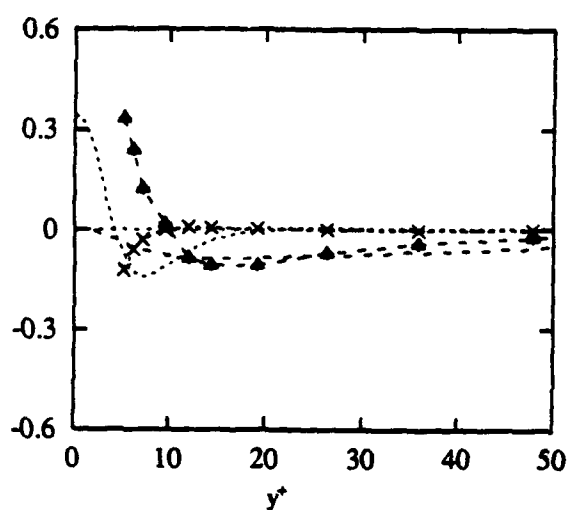


Figure 7b. $\langle u^2 \rangle$ budget at $R_\theta = 1010$.
Pressure \blacktriangle Spalart $---$
Viscous Diffusion \times Spalart \cdots

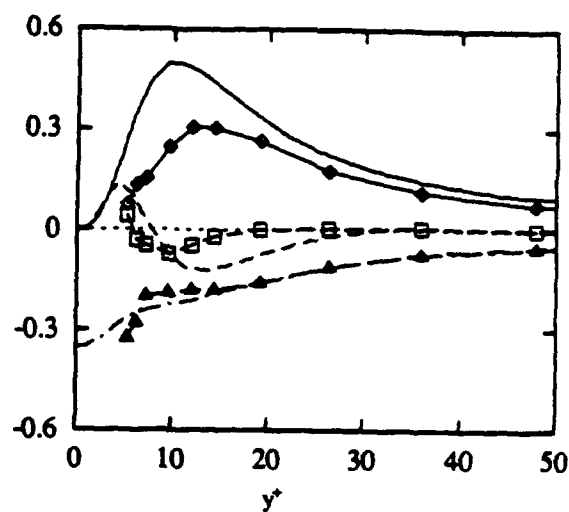


Figure 7a. $\langle u^2 \rangle$ budget at $R_\theta = 1010$.
Production \blacklozenge Spalart $---$
Turbulent Diffusion \square Spalart $---$
Dissipation \blacktriangle Spalart $---$

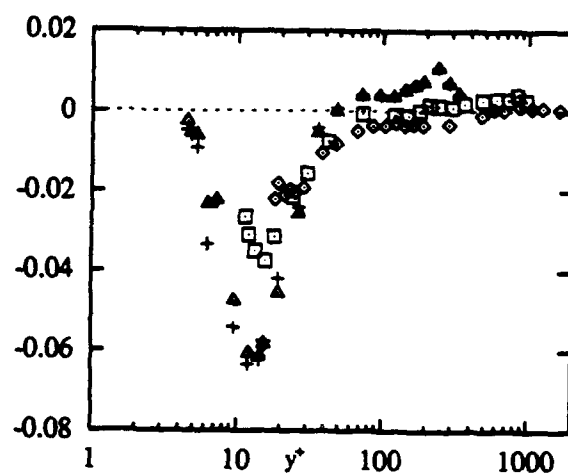


Figure 8. Inner normalized $\langle uv\omega_z \rangle$ correlation (symbols same as Figure 2.), $\langle uv \frac{\partial u}{\partial y} \rangle$ at $R_\theta = 1010$.
Correlation point from Figure 1, $\Delta z^+ = 6.4$ \star

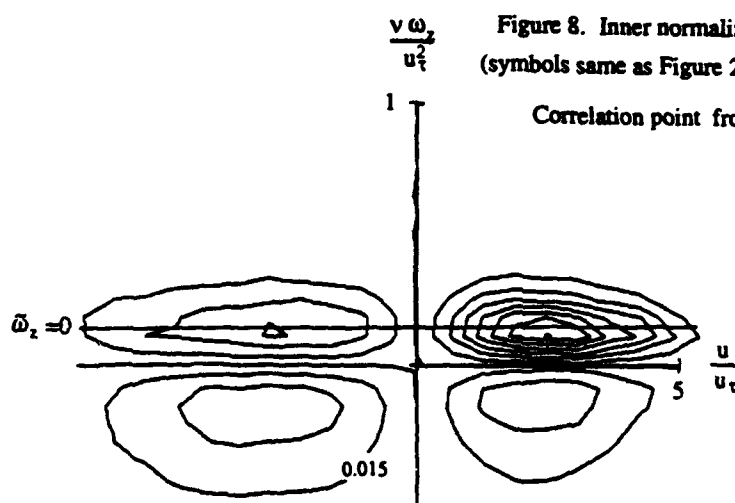


Figure 9. $\frac{u}{u_\tau}$ vs. $\frac{v\omega_z}{u_\tau^2}$ PDF at $y^+ = 26.3$.

Coherent Structures in Smooth and Rough Wall Turbulent Boundary Layer Flows

by

Atul Kohli and David G. Bogard
Department of Mechanical Engineering
The University of Texas at Austin

Abstract

Characteristics of coherent structures in boundary layer flows over smooth and rough walls have been studied using a scanning LDV capable of measuring essentially instantaneous velocity profiles. A unique spatial detection technique allowed classification of events in terms of size and maximum/minimum height from the wall, giving a more resolved description of the structures. Differences in characteristics of low speed events (bursts) for flow over smooth and rough walls indicate differences in burst dynamics. Over rough walls low speed events were larger and independent of high speed events. Burst and ejection frequencies for smooth and rough walls were found to scale with outer variables and a combination of a convection velocity and inner variables.

1. Introduction

The presence of coherent structures in turbulent boundary layers has been well established. Although there is general agreement in turbulence literature about several of the kinematic issues of coherent structures, the dynamics remain largely unsettled. The extent to which the outer region of the boundary layer interacts with the wall region is also a subject of controversy in the turbulence community. In the present study boundary layer flows over smooth and rough walls were studied to determine changes in near wall coherent structures which might give insight to the dynamics of turbulence. For experiments conducted with smooth and rough walls with nominally the same outer scaling, the inner scaling will be significantly different because of the much larger wall shear for the rough wall. Therefore finding the appropriate scaling for the spatial structure and for burst and/or ejection frequencies for the two different wall conditions would be very informative.

There are relatively few studies of boundary layer turbulence structure over rough surfaces. Grass (1971) used the hydrogen bubble technique to visualize open-channel turbulent flow over smooth and transitionally and fully rough surfaces. He found that fluid ejections and sweeps both make strong, intermittent contributions to the Reynolds stress, irrespective of the change in surface roughness. Sabot, Saleh and Comte-Bellot (1977) studied the effects of roughness on intermittent maintenance of shear stress in pipe flow. They indicate that the mean shear stress is maintained primarily by ejection events. They found that compared with smooth wall flows, ejections in rough wall pipe flows at the same Reynolds number had larger mean periods of occurrence, larger mean time duration and length scale, and larger negative instantaneous shear stress peaks.

The few studies of the effects of rough wall on ejections have obtained conflicting results on the appropriate scaling for ejection frequency. Raupach (1981), using quadrant analysis found that using δ and u_τ as scaling parameters collapsed ejection frequencies from a smooth wall and rough surfaces of different concentration. Sabot, Saleh and Comte-Bellot (1977) using quadrant analysis in smooth and rough pipe flow, found that above a certain threshold, ejections are the sole contributors to Reynolds stress. They found that the frequency of these 'violent' ejections did not scale with the generally accepted outer variables (pipe radius and centerline velocity), but did scale with a convective velocity and length scale derived from space-time correlations. Osaka and Mochizuki (1988) using VITA detection found that ejection frequencies at $y^+ = 15$ varied slightly over a range of Reynolds numbers for a rough wall when scaled with inner variables. In a definitive study of ejection frequency for smooth walls over a large range of Reynolds numbers, Blackwelder and Haritonidis (1983) found that ejection frequencies scale with inner variables.

In this study we use a unique spatial detection technique to study coherent structures using a scanning LDV. The spatial detection technique, developed by Bolton and Bogard (1992), identifies coherent regions of low or high velocity in

the flow. Unlike single point detections, the spatial detection was found to be relatively independent of threshold. Using the spatial detection technique to study flow over a smooth wall, Bolton and Bogard (1992) found that the movement of low speed structures away from the wall corresponded with the movement of a high speed structures towards the wall. In this paper we describe differences in characteristics in turbulence structure, deduced from spatial detections and single point detection, for flow over smooth and rough walls.

2. Water channel facility, scanning LDV and analysis procedures

Measurements of boundary layer flows for smooth and rough walls were conducted along the bottom wall a low speed open water channel facility with a 5 m long and 50 cm wide test section. A schematic of this facility is shown in Figure 1. Continuous time histories of essentially instantaneous streamwise velocity measurements were made using a rapid scanning LDV. A brief description of the flow facility and scanning LDV system is given in this section. Further details about the channel facility are presented by Bogard and Coughran (1987), details about the scanning LDV are given by Bolton and Bogard (1992), and details about improvements to the scanning LDV and the rough wall boundary layer are given by Kohli (1992).

Flow conditions for the smooth wall and rough wall experiments are given in Table 1. For the smooth wall flow the boundary layer was tripped 0.5 m downstream of the channel inlet with a 3 mm diameter rod. Scanning measurements were made at essentially the same $Re_\theta = 14,600$ for the smooth and rough wall flows ($Re_\theta = 1700$ for the smooth wall and $Re_\theta = 2200$ for the rough wall). As shown in Figure 1, for the rough wall studies a rough wall section was installed in the channel 1.7 m downstream of the trip. The rough wall consisted of small vertical cylinders (of height $k = 4.5$ mm, and diameter $d = 9$ mm separated by a distance $D = 16$ mm) in a square array. Measurements were made 33 boundary layer thicknesses downstream from the start of the rough wall at which the boundary layer was proven to be self-preserving by a series of velocity profiles measured from the leading edge to the measurement location. With a spanwise aspect ratio $d/k = 2$ for the roughness elements and a normalized roughness height of $k^+ = 65$, the rough wall boundary layer was well within the fully rough regime.

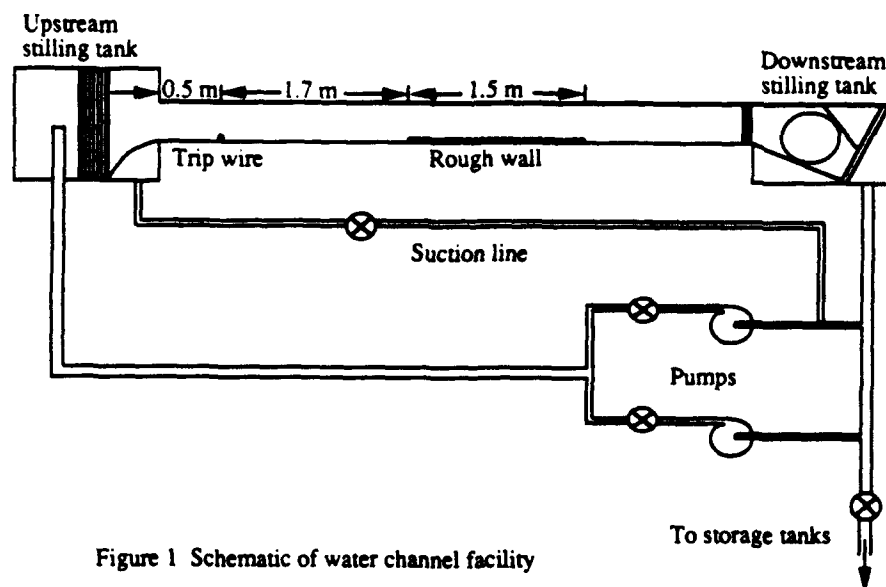


Figure 1 Schematic of water channel facility

The skin friction coefficient, C_f , for the smooth wall was obtained using a Clauser fit to the log-region of the mean velocity profiles. For the rough wall, C_f was obtained using the profile matching technique described by Bandyopadhyay (1987). The accuracy of the profile matching technique was verified by making uv Reynolds stress measurements in the constant stress region near the wall. C_f for the rough wall obtained from the Reynolds stress measurements was approximately 10% lower than that obtained with the profile matching technique. The rough wall flow had a C_f value twice that of flow over the smooth wall.

The scan rate of the scanning LDV system was rapid enough to give a continuous time history of velocity profiles. Parameters for the scanning LDV are given in Table 2. The single velocity component scanning LDV system was constructed by adding a stepper motor controlled mirror system to a TSI model 9100-10 backscatter LDV. Signals were processed using a TSI model 1998 counter, and data were acquired and processed using a Macintosh II computer. Probe volume position was determined to an accuracy of ± 0.2 mm ($\pm y^+ = 2$) using a Schaevitz model 500HR LVDT to monitor the scanning mirror position.

With 40 to 50 measurements per scan the randomly distributed measurements had an average spacing of $\Delta y^+ = 6$ to 7. To obtain profiles with uniform spacing of velocity data, the randomly placed velocity measurements were arranged in bins with an interval of $\Delta y^+ = 10$. When multiple measurements were made within a bin, the measurements were averaged. When no measurements were made within a bin, the velocity for that bin position was obtained by linear interpolation with adjacent bins. If no adjacent data were available, the velocity for the bin was left undetermined. A representative time series of velocity scans obtained following the processing described above is shown in Figure 2. As is evident from the representative sample shown in Figure 2, the scanning LDV measured essentially complete velocity profiles from $y^+ = 25$ to $y^+ = 235$; the only gaps in the velocity record occurred intermittently at the nearest wall position of $y^+ = 25$. These scanning measurements were considerably closer to the wall and had a greater range than our previously published study, Bolton and Bogard (1992).

Table 1 Flow conditions

Parameter	Smooth wall	Rough wall
U_∞	0.192 m/s	0.196 m/s
x	3.0 m	3.0 m
Re_θ	1700 ($U_\infty \theta / \nu$)	2200 ($U_\infty \theta / \nu$)
Re_δ	14600 ($U_\infty \delta / \nu$)	14700 ($U_\infty \delta / \nu$)
δ	63 mm	65 mm
ν	$0.825 \times 10^{-6} \text{ m}^2/\text{s}$	$0.864 \times 10^{-6} \text{ m}^2/\text{s}$
θ	0.74 cm	0.98 cm
u_τ	0.84 cm/s	1.24 cm/s
C_f	0.00385	0.00796

Table 2 Scanning parameters

Parameter	Smooth wall	Rough wall
Scan velocity	1.5 m/s ($7.8 U_\infty$)	1.5 m/s
Scan frequency	28 scans/s	28 scans/s
Scan distance	2.3 cm ($230 y^+$)	2.7 cm ($370 y^+$)
Scan range	$15 \leq y^+ \leq 235$	$15 \leq y^+ \leq 385$
Time for one scan	17 ms ($1.3 T^+$)	20 ms ($3.6 T^+$)
Time between scans	37 ms ($2.9 T^+$)	37 ms ($6.5 T^+$)
Average data rate	40 points/scan	50 points/scan
Velocity uncertainty	$\pm 3\%$	$\pm 3\%$
Total data acquired	26,500 scans	25,000 scans
Total time	950 s	915 s

Note: Measurements on the rough wall were made at the center of the square area defined by four adjacent roughness elements.

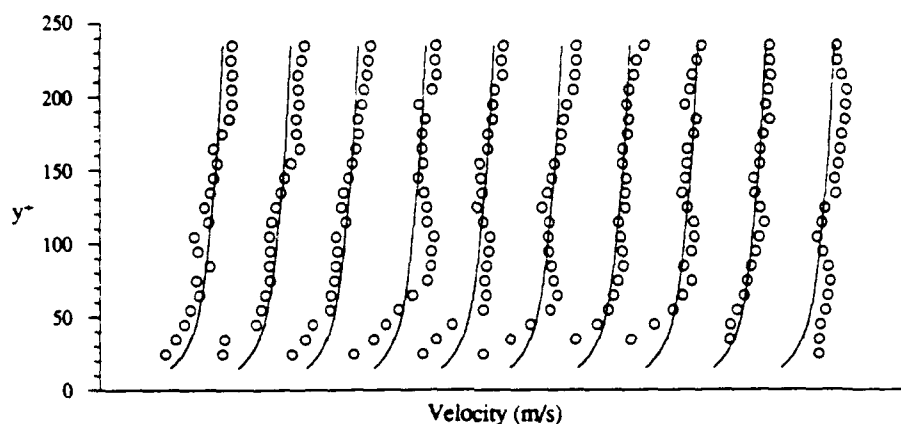


Figure 2 Typical velocity scans over the smooth wall; time between scans is $T^+ = 2.9$. Solid lines represent mean profile from 26,500 scans.

Precision error for the scanning measurements, determined as described by Ciancarelli et al. (1988) and by Bolton and Bogard (1992), was $\pm 3\%$ for each instantaneous velocity measurement. Accuracy of the scanning measurements was verified by evaluating the mean velocity profile, Figure 3(a), and the rms velocity profile, Figure 3(b). Essentially no bias error was evident from the mean velocity profile. The rms velocity profile also showed very good agreement with stationary measurements and previous data in the literature. The good agreement for the rms velocity profile indicates that precision error was negligible.

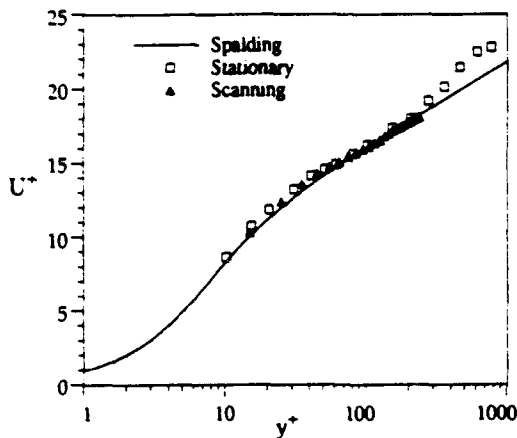


Figure 3(a) Scanning mean velocity profile compared with profile from stationary measurements and Spalding's law.

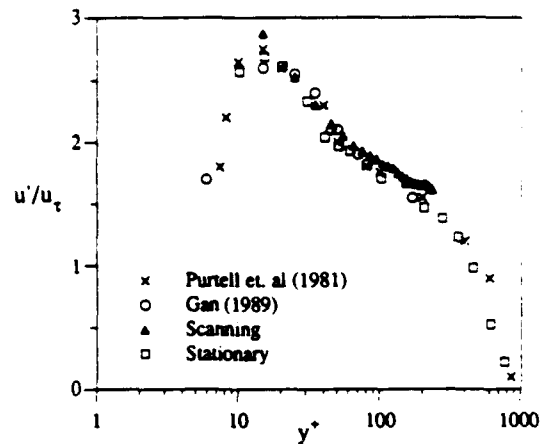


Figure 3(b) Scanning rms profile compared with rms profiles from stationary measurements, Gan (1989) and Purtell et. al (1981).

Since the time between scans was very short, essentially continuous time records of the velocity profiles were obtained. The resulting velocity field in the t - y plane was analyzed using conditional sampling based on the U-level point detection technique described by Bogard and Tiederman (1986) and the spatial detection technique described by Bolton and Bogard (1992). The U-level technique was verified by Bogard and Tiederman (1986) to be a relatively accurate burst detection technique in the near wall region. This technique detects ejections (identified by low velocities), and combines them into bursts based on the probability density distribution of the time between ejections. The spatial detection technique identifies spatially coherent regions of low or high velocity. A region of low velocity is a characteristic associated with bursts, and a region of high velocity with sweeps. Events identified by spatial detection can be classified in terms of size and position. Consequently, conditional sampling using spatial detection is more finely resolved by using only events of a particular size classification and/or at a particular height from the wall.

3. Spatial structure results

The relative effects of smooth and rough walls on spatial structure was determined using U-level detection of bursts, and using spatial detection of low speed events (associated with bursts) and high speed events (associated with sweeps). Conditional sampling using the point detection U-level technique was done for comparison with previous studies which were limited to point detection, and for comparison with the structure obtained with spatial detection. The following results show that use of the spatial detection is crucial for determining detailed characteristics of the turbulence structure.

Figures 4(a) and (b) show the smooth wall ensemble averaged burst structures detected using U-level at detection heights of $y^+ = 35$ and $y^+ = 65$, respectively. The velocity field measured in the t - y plane was transformed to the x - y plane using the average convection velocity of bursts and sweeps ($U_c^+ = 15$) over smooth walls determined by Gan and Bogard (1991). This convection velocity corresponds to the local mean velocity at $y^+ = 60$. For the rough wall, a convection velocity equal to the local mean at $y^+ = 60$ was used. As expected, the contour levels in Figure 4 show that at each height the maximum velocity deviation occurs at the point of detection. However, the general shape and scale of the structure are similar for both detection heights. The general shape and scale of the structure is also similar to that deduced by Gan (1989) using the single point quadrant detection technique. Note in particular that for both heights the ensemble averaged burst event is not associated with any significant high speed fluid.

The rough wall ensemble averaged burst structure detected at $y^+ = 35$ is shown in Figure 5. This structure, and the structure detected at $y^+ = 65$ (not shown), were very similar in scale to the burst structure detected over the smooth wall. The burst structure over the rough wall is slightly larger the structure over the smooth and does not have the distinct slope along the upstream edge.

Spatial detections of low speed structures were based on identifying coherent regions in the velocity field where negative velocity deviations were greater than $0.7u_{rms}$. High speed structures were identified as coherent regions in the velocity field where the positive velocity deviations were greater than $0.8u_{rms}$. The detection thresholds were selected to be in the center of a range of thresholds in which the number of detected events was essentially constant. Conditional sampling was based on the size of the event and the maximum height of a low speed event or the minimum height of a high speed event. The size of an event was defined as the number of discrete points grouped in a coherent region of high or low velocity. Events of different sizes were analyzed in terms of size categories as shown in Table 3. As Table 3 shows, the number of events decreases rapidly as the size of the event increases. Average streamwise and wall normal lengths for each size category are shown in Table 3 for low speed events over smooth and rough walls. In each case the detected structure is elongated in the streamwise direction, but the structure over the smooth wall tends to be more elongated than the structure over the rough wall. Of particular interest, although small in number there some very large events which extend across the full scan range. Although the smooth and rough wall had practically the same number of events in most of the size categories, the rough wall had over twice as many events in the largest size category. Characteristics for high speed events were the same as the characteristics for low speed events described above.

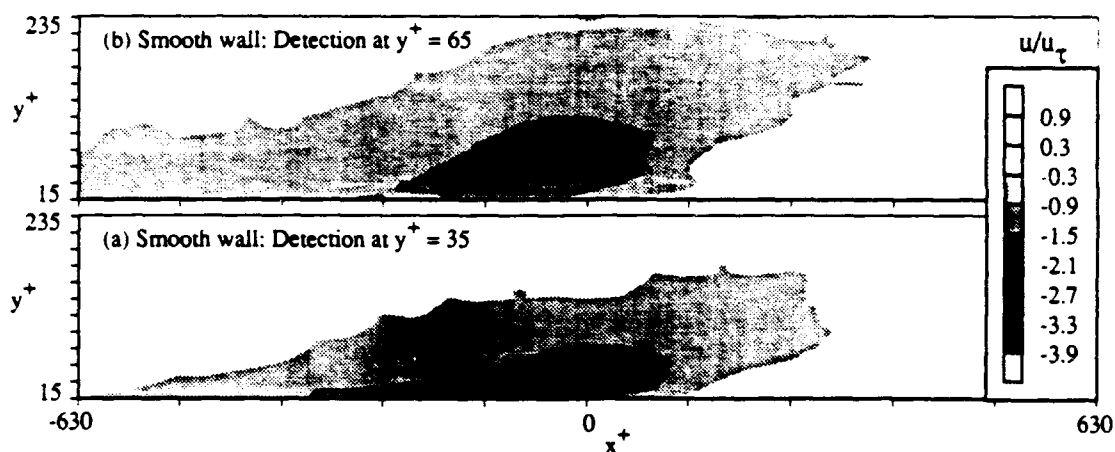


Figure 4 Ensemble averaged condition samples using single point U-level detection for the smooth wall at (a) $y^+ = 35$ (536 events) and (b) $y^+ = 65$ (552 events).

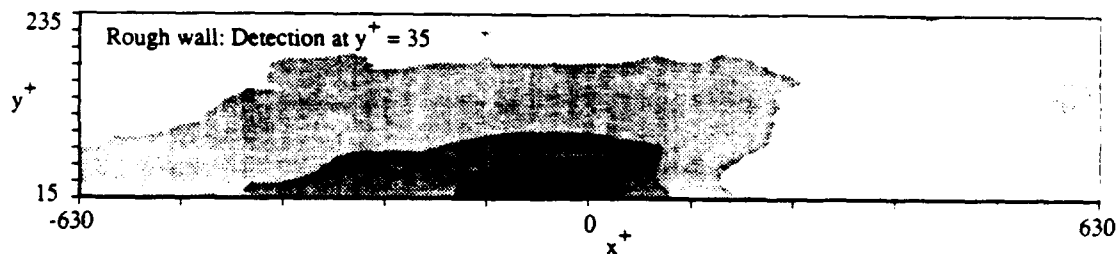


Figure 5 Ensemble averaged condition sample using single point U-level detection for the rough wall at $y^+ = 35$ (459 events). Contour levels are the same as in Figure 4.

Table 3 Characteristics of smooth and rough wall low speed events at different size categories

Size Category (no. of points)	Smooth Wall			Rough wall		
	N/Nt (%)	Avg. L_y (y^+)	Avg. L_x (x^+)	N/Nt (%)	Avg. L_y (y^+)	Avg. L_x (x^+)
1<size≤2	22.1	10	10	23.7	10	10
2<size≤4	20.7	20	30	20.4	20	30
4<size≤8	16.9	30	70	16.2	40	60
8<size≤16	13.1	50	120	12.2	60	100
16<size≤32	10.5	80	200	8.8	90	170
32<size≤64	7.1	130	300	6.8	140	270
64<size≤128	5.1	170	500	5.0	200	420
128<size≤256	3.0	210	830	3.2	280	650
size>256	1.5	-	-	3.7	-	-

where: N/N_t = Number of events in category/Total number of events
 Avg. L_y = Average wall normal extent of event
 Avg. L_x = Average streamwise extent of event

The following conditional sampling analyses of spatial structures are based on events with size ≤ 32 points, which constitute more than 80% of the total number of events. Low speed events, which are associated with bursts, were further classified in terms of the maximum height of the event. This allowed conditional sampling based on the height of the low speed event. Since bursts move away from the wall, conditional samples at increasing heights can be interpreted as following the development of the burst. High speed events, which may be associated with sweeps, were classified in terms of the minimum height of the event. All the conditional sampling analyses were phase aligned on the leading edge of the event.

Figures 6 (a) through (d) show ensemble averages of the low speed spatial event at different heights. Results at higher heights are not shown for sake of brevity. At a height $y^+ \leq 45$ the low speed spatial event is very intense, becoming less intense and larger at increasing heights. At height $85 \leq y^+ \leq 105$ the low speed structure is completely detached from the wall. Figure 6 also shows movement of a high speed structure associated with the low speed event. At the lowest height, $y^+ \leq 45$, the high speed structure appears over the low speed event. When the low speed structure is in the range $45 \leq y^+ \leq 65$ the high speed structure moves over and downstream of the low speed event. At the highest height shown in Figure 6, $85 \leq y^+ \leq 105$, high speed flow occurs above the low speed event and downstream and below the low speed event. The high speed fluid has also increased in size and extends across the full scan range. These characteristics of the low speed burst at different heights from the wall are very similar to the results obtained by Bolton and Bogard (1992).

The ensemble averaged burst structures from single point detection, shown in Figures 4(a) and (b) are bigger than the low speed spatial events described above. The single point burst detection was done at a higher threshold ($1.3u_{rms}$) compared to the spatial detection ($0.7u_{rms}$). To eliminate the effect of the higher threshold, single point burst detection was done at the threshold used for spatial detection. Even at the same threshold, the structure obtained from single point detection was larger than the spatial event, and had no high speed fluid associated with it. Thus, the spatial detection brings out details of the turbulence structure which are not resolved by the single point detection scheme.

Spatial characteristics of low speed events over the rough wall at different heights are shown in Figure 7. The low speed event is clearly larger and has larger negative velocity deviations over the rough wall. The velocity levels of the rough wall low speed events do not change rapidly with increasing height; on the other hand, the smooth wall events become very weak by height $85 \leq y^+ \leq 105$. Another distinct difference between the rough wall and smooth wall low speed events is the lack of significant high speed flow surrounding the low speed event with a rough wall.

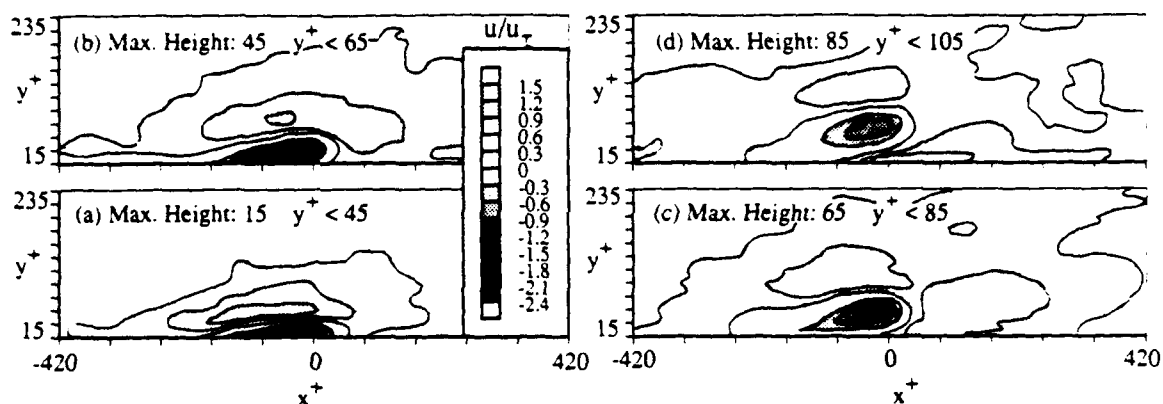


Figure 6 Low speed events over smooth wall. Conditional samples based on spatial detection. Indicated heights are a classification of events in terms of the maximum height of the event.

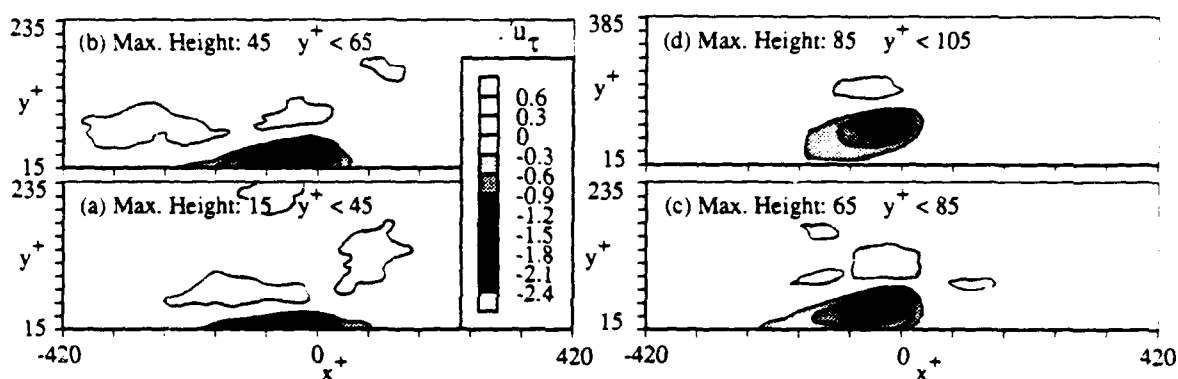


Figure 7 Low speed events over a rough wall. Conditional samples based on spatial detection. Indicated heights are a classification of events in terms of the maximum height of the event.

Results for high speed spatial events over the smooth wall are shown in Figure 8. The high speed spatial event becomes large and intense when near the wall. The low speed structure associated with the high speed spatial event is not spread out like the high speed structure associated with the low speed spatial events, but is present in small concentrated areas. The high speed events for the rough wall is shown in Figure 9. The rough wall high speed event has velocity levels and size similar to those over the smooth wall. The presence of the associated low speed fluid in small concentrated areas and its relative position with respect to the high speed event is similar to that over the smooth wall.

4. Burst and ejection frequencies

Burst and ejection frequencies were determined from single point U-level detection, to compare with previous studies, and the burst frequency was also determined from spatial detections. Figure 10 compares the single point measured burst and ejection frequencies for smooth and rough wall using three different scalings: (a) inner scaling, (b) outer scaling, and (c) scaling based on a convected velocity. Figures 10(a) shows that inner scaling cannot collapse burst or ejection frequency data from rough and smooth walls. Figure 10(b) shows that outer scaling yields good agreement for ejection and burst frequencies for rough and smooth walls. However, in the near wall region ($y^+ < 100$) there the ejection frequency is slightly greater for the smooth wall indicating that bursts over smooth wall tend to have slightly greater number of ejections.

The frequency of spatially detected low and high speed events for smooth and rough walls are shown in Table 4. The nondimensional frequencies for spatial detected events shows the same trends as the nondimensional burst and ejection frequencies from single point detection. Inner scaling fails to collapse the data for the rough and smooth walls, but outer scaling and convected scaling are reasonable.

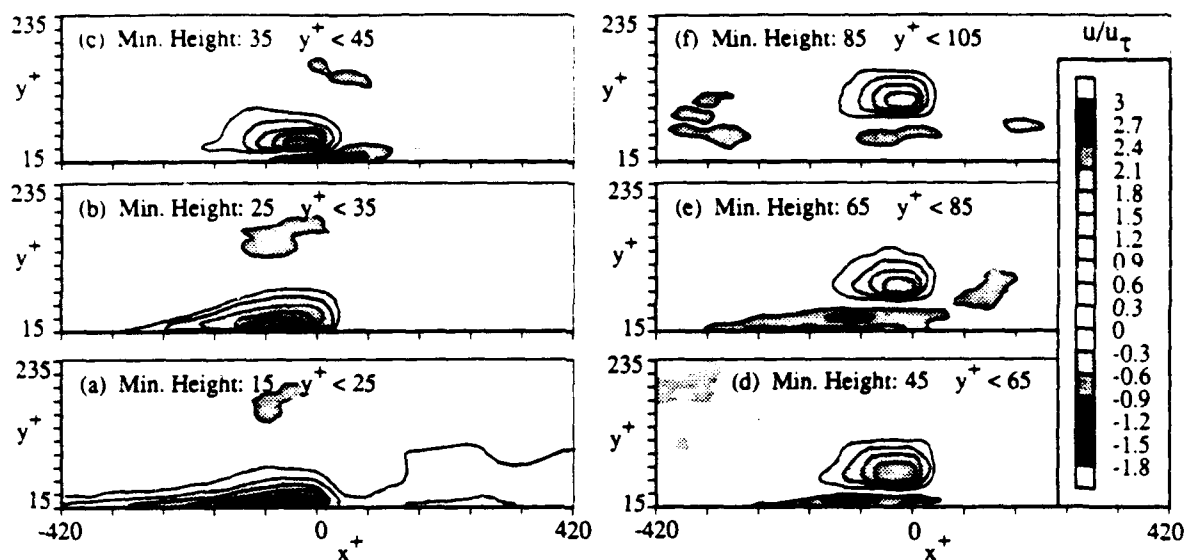


Figure 8 High speed events over a smooth wall. Conditional samples based on spatial detection. Indicated heights are a classification of events in terms of the minimum height of the event.

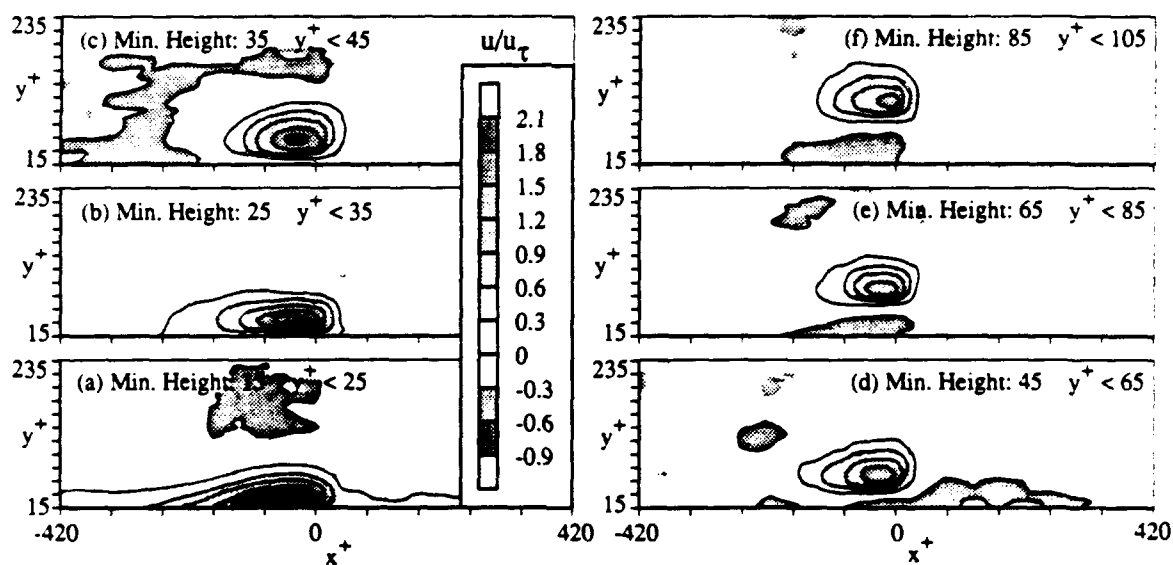


Figure 9 High speed events over a rough wall. Conditional samples based on spatial detection. Indicated heights are a classification of events in terms of the minimum height of the event.

Table 4 Frequency of spatial events

Type of event	f (s ⁻¹)	$f^+ = f\nu/u_\tau^2$	$f^0 = f\delta/U_\infty$	$f^c = f\nu/U_c u_\tau$
Low speed (smooth)	4.4	0.051	1.44	.0034
High speed (smooth)	4.3	0.050	1.41	.0033
Low speed (rough)	4.3	0.024	1.43	.0037
High speed (rough)	4.2	0.024	1.39	.0037

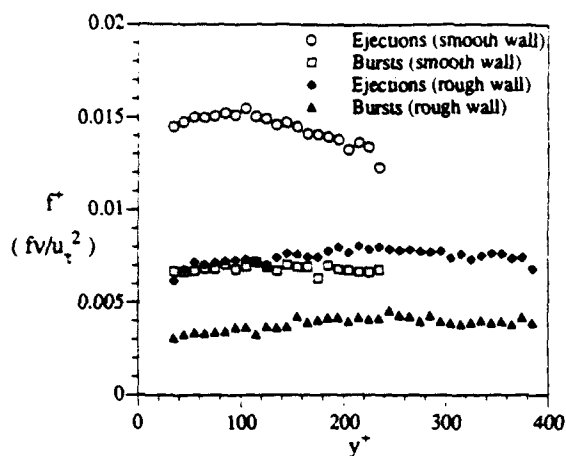


Figure 10(a) Burst and ejection frequencies scaled with inner variables.

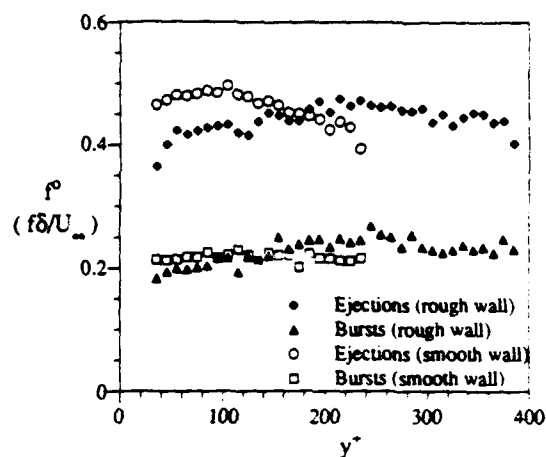


Figure 10(b) Burst and ejection frequencies scaled with outer variables.

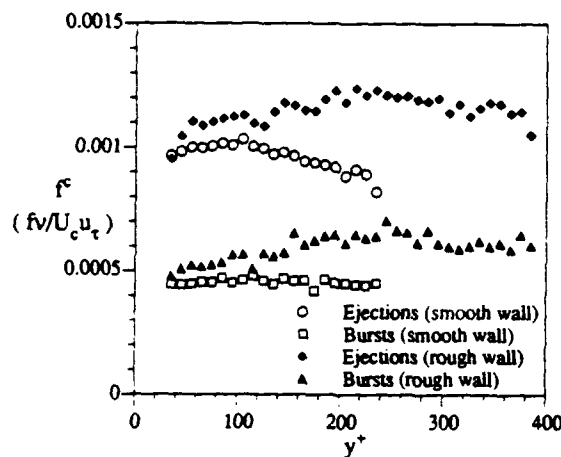


Figure 10(c) Burst and ejection frequencies scaled with convection velocity, U_c and v .

5. Conclusions

The presence of a high speed structure associated with the conditionally sampled low speed spatial event is a characteristic of near wall turbulence structure that is revealed by the spatial detection technique. Single point detection performed on the same data does not show any high speed structure associated with the burst because it groups events of all sizes and at different heights together. The spatial detection scheme allows classification of events based on their size and the height at which they occur. This gives a more realistic description of the flow field and can give more insight into the interaction of coherent structures.

Compared to the smooth wall, the low speed spatial event was bigger and had lower velocity levels over the rough wall, especially away from the wall. The high speed spatial structure on the other hand, did not undergo any significant change over the rough surface. The presence of high speed fluid above and in front of the low speed spatial event for the smooth wall and not for the rough wall indicates a significant difference in the burst dynamics for the two cases. Since the high speed fluid originates in the outer part of the boundary layer, this suggests that interaction between the inner and outer structures of the boundary layer is more significant for the smooth wall. Bursting over a rough surface may be stimulated by the wall roughness.

At the same Reynolds number, burst and ejection frequencies for the smooth and rough walls scaled with outer variables and not inner variables, which is contrary to smooth wall results of Blackwelder and Haritonidis (1983). However, reasonable scaling was also found using a combination of a convection velocity and inner variables. The frequency of spatial events also collapsed when scaled with outer or convected-inner variables. The convected-inner scaling is equivalent to conventional inner scaling for flows on smooth walls only, and hence would be consistent with the results of Blackwelder and Haritonidis (1983).

7. Acknowledgements

We gratefully acknowledge the sponsorship of the Office of Naval Research for this project. We would also like to acknowledge the contributions of Mr. Choon Gan who developed the data acquisition program used in this study.

6. References

- Bandyopadhyay, P.R. 1987: Rough-wall turbulent boundary layers in the transition regime. *J. Fluid Mech.* 180, pp. 231-266.
- Blackwelder, R.F. and Haritonidis, J.H. 1983: Scaling of the bursting frequency in turbulent boundary layers. *J. Fluid Mech.* 132, pp. 87-103.
- Bolton, B.L. and Bogard, D.G. 1992: Detection of coherent structures in a turbulent boundary layer using a scanning LDV system. *Exp. Thermal and Fluid Science* 5, pp. 274-280.
- Bogard, D.G. and Coughran, M.T. 1987: Bursts and ejections in a δ -EBU-modified boundary layer. Sixth Symposium on Turbulent Shear Flows, Toulouse, France.
- Bogard, D.G. and Tiederman, W.G. 1986: Burst detection with single-point velocity measurements. *J. Fluid Mech.* 162, pp. 389-413.
- Gan, C.L. 1989: The burst structure and its associated flow field in a turbulent boundary layer. M.S. Thesis, The University of Texas at Austin.
- Gan, C.L. and Bogard, D.G. 1991: Study of the convection velocities of the burst and sweep structures in a turbulent boundary layer. Eighth Symposium on Turbulent Shear Flows, Munich, Germany.
- Grass, A.J. 1971: Structural features of turbulent flow over smooth and rough boundaries. *J. Fluid Mech.* 50, pp. 233-255.
- Kohli, A. 1992: Detection of coherent structures in smooth and rough wall boundary turbulent boundary layer flows using a scanning LDV. M.S. Thesis, The University of Texas at Austin.
- Osaka, O. and Mochizuki, S. 1988: Coherent structure of a D-type rough wall boundary layer. In: *Transport Phenomena in Turbulent Flows*. (ed. Hirata, M. and Kasagi N.). pp. 199. New York: Hemisphere.
- Purtell, L.P., Klebanoff, P.S. and Buckley, F.T. 1981: Turbulent boundary layer at low Reynolds number. *Phys. Fluids* 24, pp. 802.
- Raupach, M.R. 1981: Conditional statistics of Reynolds stress in rough-wall and smooth-wall turbulent boundary layers. *J. Fluid Mech.* 108, pp. 363-382.
- Sabot, J., Saleh, I. and Comte-Bellot, G. 1977: Effects of roughness on the intermittent maintenance of Reynolds shear stress in pipe flow. *Phys. Fluids* 20, pp. 150.

TURBULENCE-DRIVEN SECONDARY FLOW IN A DUCT OF SQUARE CROSS SECTION.

McGrath, G., Petty, D.G. and Cheesewright, R.*
School of Engineering, Queen Mary and Westfield College
University of London, London E1 4NS.

* Department of Manufacturing and Engineering Systems
Brunel University, Uxbridge UB8 3PH, England

Abstract.

Details of an experimental study of the turbulent flow of air in a duct of square cross section are presented for a Reynolds number of 4900. The objectives of the work were to obtain data suitable for the validation of numerical predictions of turbulent flow in a duct and to demonstrate the application of a fibre-optic laser Doppler anemometer for this purpose. Detailed measurements of the first through fourth order moments of secondary (cross-stream) velocity components are presented and compared to measurements at substantially higher Reynolds number. A limited survey of primary (streamwise) velocity component is also presented.

Nomenclature.

D_H	Hydraulic diameter.
H	Duct height width.
K	Flatness factor (kurtosis).
S	Skewness factor.
u', v'	RMS fluctuating primary and secondary velocity component respectively.
U, V	Time-mean primary and secondary velocity component respectively.
x	Coordinate in streamwise direction (origin at entrance to duct).

Subscripts.

b	Bulk value.
0	Centre-line value.
v	Secondary velocity component.

Introduction.

The turbulent flow of an incompressible fluid in a duct of non-circular cross section is characterised phenomenologically by a bulging of primary- (streamwise) velocity contours towards the duct corners. This is caused by turbulence-driven secondary flow in the plane of the duct cross-section. These secondary velocities are typically of the order of less than one percent of the characteristic primary flow velocity and yet they significantly affect the overall pressure drop and heat transfer.

The accurate prediction of these secondary velocities represents an exacting test for turbulence models which attempt to model the Reynolds-stress tensor. The models are required to either adopt an anisotropic form of eddy viscosity (Speziale (1987)) or else model the transport of individual Reynolds-stress components using a model of the form proposed by Launder et al (1975). In order to conclusively differentiate between the physical

accuracy of the numerous turbulence models, an experimental data set of quantifiable accuracy is required against which comparison may be made. However, it is noticeable that in the review of numerical predictions for flow in a duct of non-circular cross section by Demuren and Rodi (1984), the conclusions drawn regarding the physical accuracy of predictions were limited because the discrepancies between the results of experimental investigations were so large and were not fully accounted for.

An important additional source of validation data is direct numerical simulation where all of the turbulence length scales are resolved and, therefore, no turbulence model is required. The results of the experimental study presented here complement those of a direct numerical simulation of turbulence-driven secondary flow in a duct of square cross-section (Gavrilakis (1989)) and were intended to provide validation for these predictions. The simulation was restricted to flows of low Reynolds number in order to enable all the turbulence length scales to be resolved and was performed for a Reynolds number of 4900 (based on duct hydraulic diameter and centre-line velocity). This Reynolds number is significant in that it is much lower than that for which turbulent flow in a duct is believed to have previously been investigated (Table.1). In order to validate this prediction a separate experiment at an identical Reynolds number was considered necessary as the characteristics of the flow were believed to be significantly different at low Reynolds numbers to those of previous experimental investigations reported in the open literature, for reasons outlined below.

A survey by Demuren and Rodi (1984) reported that for *fully developed* flows at a Reynolds number, based on bulk velocity, greater than 1.2×10^5 the ratio of centre-line velocity to bulk velocity was practically uniform at 1.2. However for Reynolds numbers below this value the ratio of centre-line velocity to bulk velocity increased, which suggests that the strength of the secondary flow is attenuated for $Re_b < 1.2 \times 10^5$. Thus in order to validate the simulation results of Gavrilakis (1989) a separate experimental study was required. Taken together, the results of these two studies were intended to provide a 'benchmark' data set which could be used to verify predictions where the Reynolds-stress tensor was modelled.

Background.

Having identified the need for a separate experimental study at low Reynolds number, it remains to account for the discrepancies in the data from previous experiments in order to understand how these error sources were avoided in the present study. In particular, two considerations which significantly influence the usefulness of the data reported by most of the previous investigations are incomplete flow development and probe interference. These are discussed in turn below as a justification of the choice of experimental method and test facility for the present study.

Inspection of the development lengths $(x/DH)_{max}$ of previous experimental investigations in Table.1 suggests that the flow was only approximately fully developed in all cases except for the results reported by Brundrett and Baines (1964). This conclusion is based on the findings of Klein (1981) who reported that, for turbulent pipe flow, the length required for fully developed flow may exceed 140 diameters. However for inlet conditions where turbulence was promoted it was found to be as low as 70 diameters. Since the secondary motion in a non-circular duct is driven by the turbulence, the development length would be expected to be at least of the same order of magnitude as for the turbulent flow in a pipe. For this reason the present study was carried out in a duct which allowed for a development length of approximately 100 hydraulic diameters.

Since the results of this study were required for validation purposes, the data had to be of quantifiable accuracy. The error due to probe interference is difficult to quantify which made laser-Doppler anemometry (LDA) the first choice of technique since it is non-intrusive. By contrast, in all previous hot-wire studies probe interference resulted in a serious mass discontinuity in the plane perpendicular to the main flow: ie the mass flow towards a wall was not equal to that away from the wall (It is difficult to comment on whether the continuity requirement was satisfied for the published results of Brundrett and Baines (1964)).

Table 1. Details of previous experimental investigations of flow in a duct of square cross-section.

Investigator	Instrument	Re_b	$(x/D_H)_{max}$	U_0/U_b
Brundrett & Baines (1964)	Single hot wire	8.4×10^4	260	1.2
Gessner (1964)	X-array hot wire	2.5×10^5	40	1.2
Gessner & Jones (1965)	X-array hot wire	7.5×10^4 to 3×10^5	84	1.2
Lauder & Ying (1972)	Single hot wire	2.2×10^4 & 6.9×10^4	69	1.2
Melling (1975)	LDA with tracker	4.2×10^4	36.8	1.2
Present study	LDA with counter	3.8×10^3 (estimate)	100	1.3 (estimate)

Where LDA has previously been used, Melling (1975) and Melling and Whitelaw (1976), the unquantifiable error due to probe interference was eliminated and the most significant source of error was quantified and attributed to misalignment of the measuring volume. In fact the accuracy of measured components of secondary mean velocity was critically dependent on the precision of optical alignment such that a fringe orientation error of as little as 0.3 degrees relative to the duct axis resulted in errors of up to 50%. As a consequence of this, the reported measurements of secondary velocity did not satisfy continuity and were no better than those obtained by hot-wire anemometry in the previous studies.

The benefits of non-intrusiveness and of quantifiable error motivated the authors to employ LDA in the present study and the measurements reported here are believed to be both the first to be made at low Reynolds number and to closely satisfy continuity.

Test facility and experimental technique.

The test facility consisted of a duct of 76.2 mm square cross-section. The duct was just over 100 hydraulic diameters, D_H , long and air was blown down the duct by a centrifugal fan. Measurements of static pressure from a series of pressure tapings in the duct revealed that the pressure gradient tended to a constant upstream of and at the station where secondary flow measurements were taken. This was taken to indicate that the flow was approximately fully developed.

Velocity measurements were made with a Dantec fibre-optic laser-Doppler anemometer (LDA), operating in back-scatter mode, fitted with a 35 mW HeNe laser. A frequency shift unit (Dantec 55N10) was used to avoid directional ambiguity and to enhance the data rate for the measurement of secondary velocities. The Doppler signals were processed by a counter processor (Dantec 55L90a). Joss-stick smoke was used as seeding and was introduced at the fan inlet to ensure adequate mixing.

For secondary flow measurements (ie flow in the cross-stream plane) the LDA probe head was aligned as shown in Fig.1. In order to assess the effect of probe interference, measurements were repeated with a side-looking probe, representing a significantly greater blockage. These measurements showed negligible difference to those made with the forward-looking probe (as shown in Fig.1) so that probe interference was estimated to be negligible in either case.

Secondary flow velocities were typically less than 1% of the primary (streamwise) velocity, therefore alignment of the fringes parallel to the streamwise axis was critical. The uncertainty in this alignment was

estimated to be less than ± 0.2 degrees which would represent a systematic error of 35% for $V=0.01$ m/s. An absolute error of such a magnitude would be apparent if the continuity requirement was grossly in error for a secondary flow profile and would be manifested as a shift in the origin of the order of 0.0035 m/s.

Measurements of streamwise (primary) velocity component had to be taken with the probe volume located 6 mm downstream of the duct exit plane because time did not permit the construction of a special working section which allowed for optical access from the side. This arrangement was felt to yield results closely representative of the enclosed flow except in the vicinity of the wall. At positions corresponding to the wall region, the decrease in width of the potential core and the entrainment of the stagnant ambient air into the flow would be expected to produce lower mean velocities and an attenuation of the velocity gradient. However, within the unmixed flow in the potential core, where most of the measurements were taken, the distribution of mean velocity would be expected to be almost identical to that just upstream of the exit (ie in the enclosed flow region).

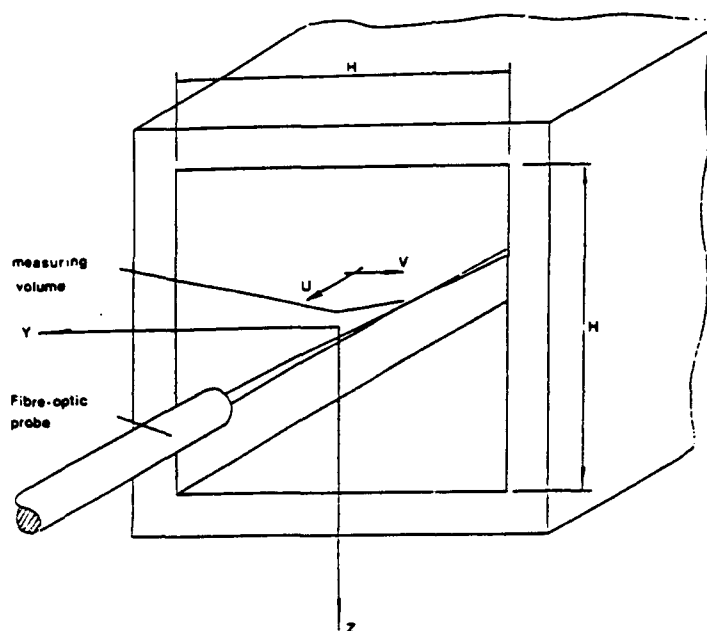


Fig.1 Orientation of fibre-optic probe for secondary flow measurements and definition diagram.

First through fourth order moments of velocity were determined from velocity estimates of 10 000 particles and the error due to this sample size was estimated to be less than 1.5% and 7% for primary and secondary velocity moments respectively.

Residence-time weighting was applied to the raw velocity data to eliminate velocity bias. However this is only believed to be equivalent to a time-averaging of the individual particle sample data if the flow is uniformly seeded (Hoesel and Rodi (1977)). There was no reason to believe that seeding density gradients existed for the flow in this configuration and the conditions for the residence-time weighting were taken to have been satisfied.

The scale of this correction was significant for the secondary flow measurements and negligible for the primary flow measurements. This result is to be expected because the velocity bias becomes increasingly significant as the particle arrival rate decreases with respect to the turbulence time scale. The data rates for the primary and secondary flow measurements were typically 50 Hz and 15 Hz respectively and a turbulence time scale of 13 Hz was calculated (as the ratio of a typical length scale, H , to a typical velocity scale, U_0 , for both the primary and secondary flow). The velocity bias might, therefore, be expected to be more significant for

secondary flow velocity measurements.

Residence time weighting was believed to be an appropriate correction for velocity bias for this flow and was applied to all velocity data which are presented in this paper.

Results and Discussion.

All measurements were taken at a Reynolds number of 4900, based on the axial centre-line velocity, U_0 , and the duct width, H unless otherwise stated. A representative sample of velocity measurements are presented here, for full details of results the reader is referred to McGrath (1991).

The secondary flow measurements, presented in Fig.2, are consistent with the expected flow pattern, where the secondary flow is dominated by large-scale counter-rotating vortices, each bounded by a duct wall and by the normal and diagonal bisectors. The velocity component along a normal bisector is directed away from the wall associated with it while the opposite is true along a corner (diagonal) bisector in accord with observations by Brundrett and Baines (1964).

Mass continuity requires that the flow of mass directed towards a wall is equal to that away from it. For the present study this was satisfied, for all secondary flow profiles, to within an average of 13% net mass flow (mass discontinuity equals net flow normalised by the mass flow in one direction). There was no directional trend for a net flow, which indicates that errors were due to misalignment of the probe and not probe interference. In view of the critical nature of the optical alignment (with a maximum systematic error estimated to be 35% for a secondary velocity of 0.01 m/s) the accuracy of the secondary velocity measurements was encouraging.

It should be noted that before each measurement run, a check was made to ensure that measurements of the secondary velocity component perpendicular to a normal bisector approximated to zero which was a requirement of flow symmetry and an indication that the probe head was aligned properly. The measured distribution along the vertical bisector was seen to be less than 0.01% of the axial centre-line velocity increasing to a maximum of 0.12% near the wall which was a satisfactory result.

The effect of the secondary velocities is manifested in the bulging of the axial velocity (ie primary velocity) contours towards the duct corner as shown in Fig.3, where comparison is made with the results of Brundrett and Baines (1964). It is noticeable that the contours for the present work do not exhibit the same

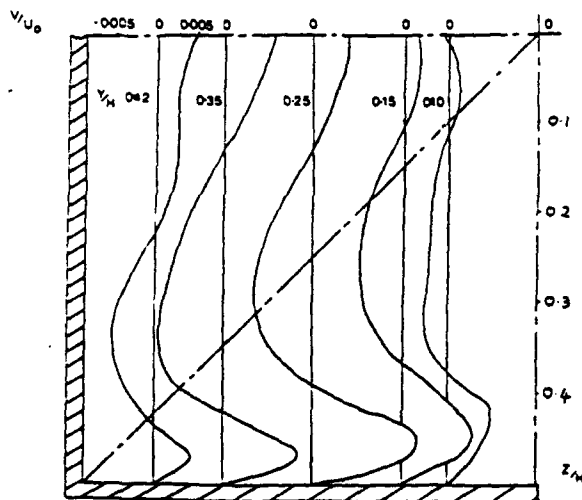


Fig.2 Profiles of secondary mean velocity in a corner of the duct (smooth lines drawn through raw data). $Re=4900$.

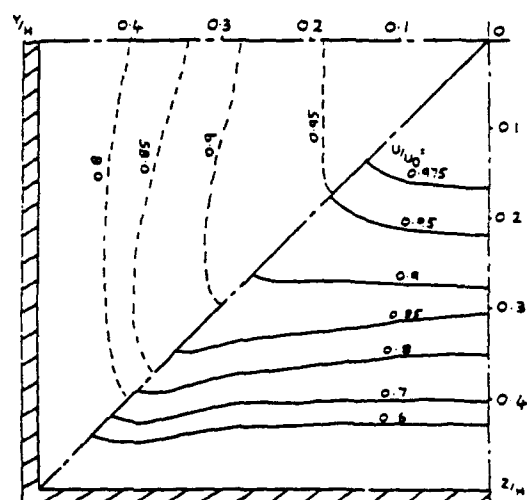


Fig.3 Contours of U/U_0 . $Re=4900$.

— Present study
 - - - - - Brundrett and Baines (1964)

degree of penetration into the duct corner and similarly the maximum magnitude of secondary velocity is approximately 7% smaller than that reported by Brundrett and Baines, at a Reynolds number of 8.3×10^4 . The difference in the two sets of results could be explained by either incomplete flow development or a low Reynolds number effect. If the flow was not fully developed the ratio of the axial centre-line velocity to bulk velocity U_0/U_b would exceed the asymptotic high-Reynolds number value for fully developed flow of 1.2 (due to incomplete momentum distribution across the duct flow area). However, the static pressure measurements taken upstream of the measurement station, indicated that the flow was approximately fully developed. Thus the attenuated secondary flow, compared to the results of Brundrett and Baines, is attributed to a low-Reynolds number effect. Indeed the ratio U_0/U_b is estimated to equal 1.3 in the present study (extrapolated from numerical predictions of Demuren and Rodi (1984)) compared to a value of 1.2 for the flow investigated by Brundrett and Baines. Attenuated secondary flow is, therefore, expected to occur in the present study. This is substantiated by the agreement between the predicted and measured values of secondary velocity shown in Fig.4.

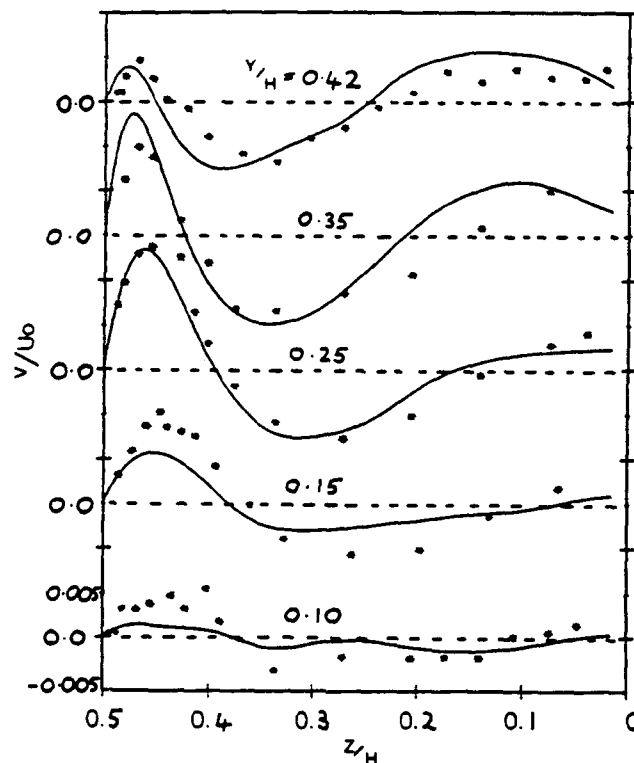


Fig.4 Comparison of secondary velocity measurements with simulation results (Gavrilakis (1989)).

* experiment — simulation

Turbulence intensity (defined, for convenience, as the RMS fluctuating component of velocity normalised by the axial centre-line velocity) is also affected by the low Reynolds number flow. The profiles of the primary component of turbulence intensity, shown in Fig.5 (where data are compared with the simulation results), have significantly higher maximum values than those previously reported for high Reynolds numbers. Values in the core flow region are over 50% greater than values reported by Brundrett and Baines in this region. This is consistent with the trend reported by Gessner (1964), whereby a 50% decrease in Reynolds number effected a 20% increase in primary Reynolds-normal-stress component. However the same does not appear to be true for the measurements of secondary Reynolds-normal stress (Fig.6) which appear practically equal for the present study and that of Brundrett and Baines.

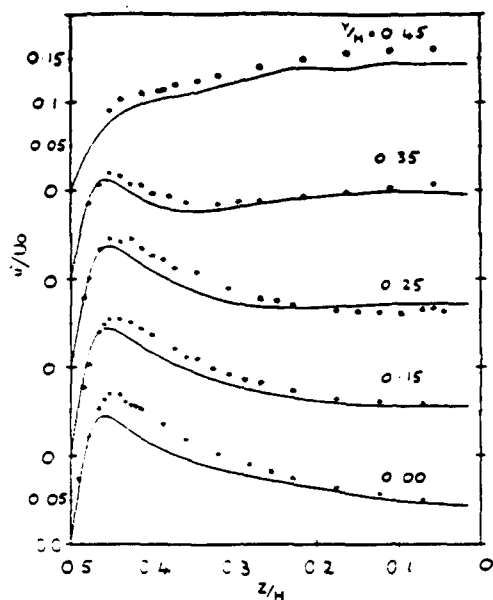


Fig.5 Profiles of primary RMS fluctuating velocity component.
* experiment — simulation

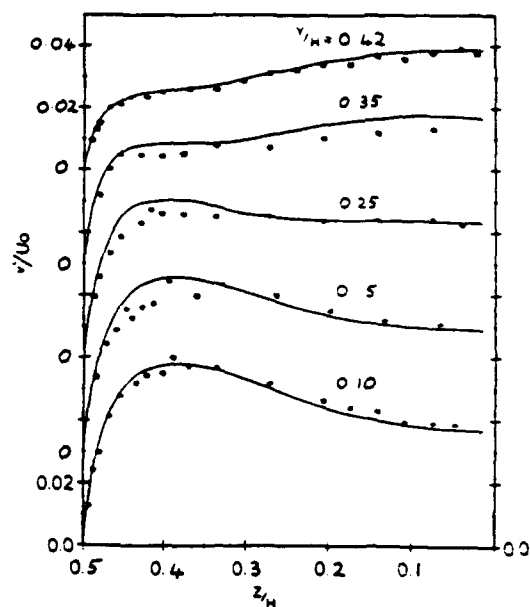


Fig.6 Profiles of secondary RMS fluctuating velocity component.
* experiment — simulation

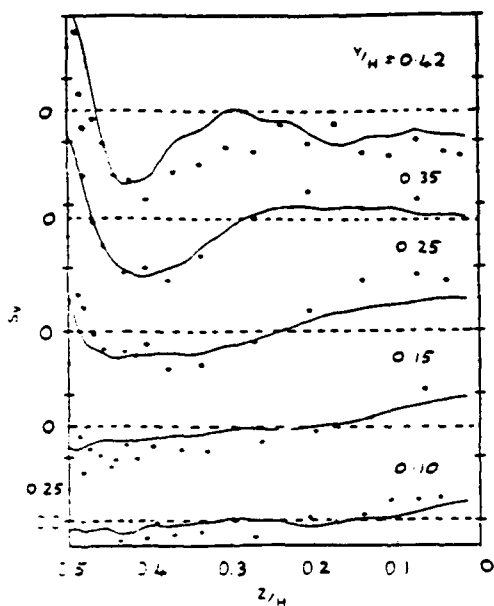


Fig.7 Profiles of secondary component of skewness.
* experiment — simulation

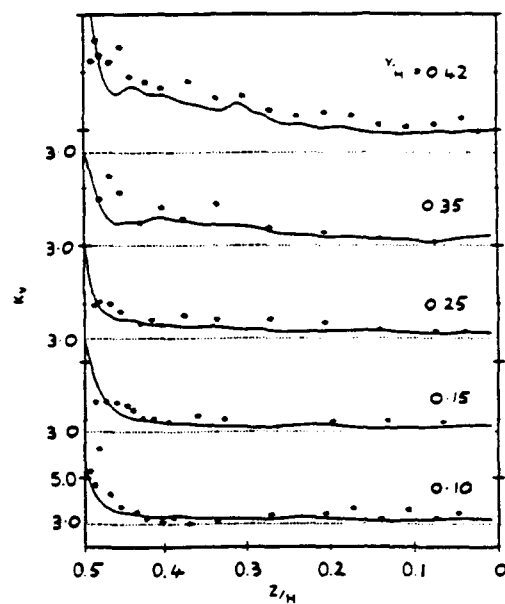


Fig.8 Profiles of secondary component of flatness (kurtosis). Note that origins are drawn through the value for a Gaussian distribution.
* experiment — simulation

Measurements of the secondary component of turbulence intensity indicate that at low Reynolds number contours of peak values of Reynolds stress would not extend as far into the corner as reported in all previous studies and is consistent with the relatively attenuated secondary flow in the present study.

The measurements of skewness and flatness factor presented here are believed to be the first for a flow in a non-circular duct. Profiles of skewness factor for the secondary flow are presented in Fig.7. Inspection of the profiles of mean velocity suggest that for the secondary flow, the relatively high velocity region occurs closest to a solid boundary such that as one approaches a wall the low speed fluid leaving the core-flow region produces the large amplitude velocity fluctuations which result in a negative skewness there.

The distributions of flatness factor in Fig.8 are seen to be largely invariant about a mean value of 3.5 in the core-flow region for the secondary component. The profiles all tend to a maximum in the wall region where the high values are normally taken to indicate that the flow is highly intermittent (Moin and Kim (1982)).

Comparison of the experimental results with the full simulation (Gavrilakis (1989)), for identical flow conditions show reasonable agreement overall. However, differences between the data sets exceed the errors estimated due to random error sources and do not exhibit any systematic discrepancy (which might be expected if probe misalignment was the principal cause of the error). The results do, however, substantiate the observation that the flow at low Reynolds number was significantly different to that for which all experiments (and predictions using turbulence models) have previously been conducted.

Conclusion.

Detailed measurements of the turbulence-driven secondary velocity have been made in a duct of square cross-section. These data are the most accurate to date with the mass continuity requirement being satisfied to within 13 % over all profiles. Measurements of third- and fourth-order moments of velocity have been reported for the first time.

The measurements were taken at a Reynolds number of 4900 which is substantially less than that for which measurements or predictions have previously been made. The magnitude of the secondary motion was seen to be significantly less than for fully developed flow at high Reynolds numbers. Consequently, contours of axial mean velocity and contours of primary and secondary flow components of Reynolds-normal stress would exhibit decreased penetration of the duct corners at this low Reynolds number.

References.

- Brundrett, E. and Baines, W.D. 1964 The production and diffusion of vorticity in duct flow. *J. Fluid Mech.* v19, p375.
- Demuren, A.O. and Rodi, W. 1984 Calculation of turbulence-driven secondary motion in non-circular ducts. *J. Fluid Mech.* v140, p189.
- Gavrilakis, S. 1989. Private communication.
- Gessner, F.B. 1964 Turbulence and mean-flow characteristics of fully-developed flow in rectangular channels. Ph.D. thesis, Purdue University.
- Hoesel, W. and Rodi, W. 1977. New biasing elimination method for laser-Doppler velocimeter counter processing. *Rev. Sci. Instrum.* v48, No7, p910.
- Launder, B.E., Reece, G.J. and Rodi, W. 1975. Progress in the development of a Reynolds stress turbulence closure. *J. Fluid Mech.* v68, p537.
- Launder, B.E. and Ying, W.M. 1972 Secondary flows in ducts of square cross-section. *J. Fluid Mech.* v54, p289.
- McGrath, G. 1991. The application of laser-Doppler anemometry to the measurement of turbulent flow in tube banks and ducts. PhD thesis. Queen Mary and Westfield College, University of London.
- Melling, A. 1975 Investigation of flow in non-circular ducts and other configurations by laser Doppler

anemometry. Ph.D. thesis, University of London.

Melling, A. and Whitelaw, J.H. 1976. Turbulent flow in a rectangular duct. *J. Fluid. Mech.* v78, p289.

Moin, P. and Kim, J. 1982 Numerical investigation of turbulent channel flow. *J. Fluid Mech.* v118, p341.

Speziale, C.G. 1987. On non-linear $k-l$ and $k-\epsilon$ models of turbulence. *J. Fluid Mech.* v178, p459.